WMHE 2026

Advancing Water Science, Engineering and Sustainability



19TH INTERNATIONAL SYMPOSIUM
Water Management & Hydraulic Engineering

OPATIJA, CROATIA

HOTEL ADMIRAL

16-19-SEPTEMBER 2026

Proceedings



PROCEEDINGS

19th International Symposium

WATER MANAGEMENT & HYDRAULIC ENGINEERING

16 – 19 September 2026

OPATIJA Croatia

Editors
Gordon Gilja
Domagoj Nakić
Hana Posavčić
Kristina Potočki

Zagreb, 2026

Published by:
University of Zagreb Faculty of Civil Engineering
Zagreb, Fra Andrije Kačića-Miošića 26, Croatia

Editors:
Assoc. Prof. Gordon Gilja, PhD
Assist. Prof. Domagoj Nakić, PhD
Hana Posavčić, PhD
Assoc. Prof. Kristina Potočki, PhD

ISSN 3027-5032

Authors are fully responsible for the content and form of manuscripts. The publisher and the Editors of the Proceedings and the organizers of the Symposium take no responsibility for the views expressed in this Proceedings.

Symposium Chairpersons

Eva Ocvirk – University of Zagreb Faculty of Civil Engineering, Croatia

Andrej Šoltész – Slovak University of Technology in Bratislava Faculty of Civil Engineering, Slovakia

Michał Szydłowski – Gdansk University of Technology Faculty of Civil and Environmental Engineering, Poland

Jaromír Říha – Brno University of Technology, Czechia

Goce Taseski – Ss. Cyril and Methodius University Faculty of Civil Engineering, North Macedonia

Helmut Habersack – BOKU University, Institute of Hydraulic Engineering and River Research, Austria

Organizing Committee

Gordon Gilja, Domagoj Nakić, Kristina Potočki, Damjan Bujak, Antonija Harasti, Hana Posavčić – University of Zagreb Faculty of Civil Engineering, Croatia

Michaela Červeňanská, Lea Čubanová – Slovak University of Technology in Bratislava Faculty of Civil Engineering, Slovakia

Piotr Zima, Tomasz Kolerski – Gdansk University of Technology Faculty of Civil and Environmental Engineering, Poland

Tomáš Julínek, Jiří Skokan, Veronika Chrástová – Brno University of Technology, Czechia

Nikola Krstovski, and Bojan Ilioski – Ss. Cyril and Methodius University Faculty of Civil Engineering, North Macedonia

Philipp Gmeiner, Marlene Haimann – BOKU University, Institute of Hydraulic Engineering and River Research, Austria

Scientific Advisory Committee

Damir Bekić, Dalibor Carević, Dražen Vouk, Meho Saša Kovačević – University of Zagreb Faculty of Civil Engineering, Croatia

Andrej Šoltész, Lea Čubanová, Michaela Červeňanská, Peter Šulek – Slovak University of Technology in Bratislava Faculty of Civil Engineering, Slovakia

Michał Szydłowski, Piotr Zima, Tomasz Kolerski – Gdansk University of Technology Faculty of Civil and Environmental Engineering, Poland

Jaromír Říha, Tomáš Julínek – Brno University of Technology, Czechia

Violeta Gjeshovska – Ss. Cyril and Methodius University Faculty of Civil Engineering

Philipp Gmeiner, Marlene Haimann – BOKU University, Institute of Hydraulic Engineering and River Research

Danko Holjević – Croatian Waters, Croatia

Scientific Committee

Mario Bačić - Faculty of Civil Engineering, University of Zagreb, Croatia

Jelena Batica - Institut za vodoprivredu "Jaroslav Černi", Serbia

Damir Bekić - Faculty of Civil Engineering, University of Zagreb, Croatia

Tamara Brleković - Faculty of Civil Engineering and Architecture, Osijek Josip Juraj Strossmayer University, Croatia

Damjan Bujak - Faculty of Civil Engineering, University of Zagreb, Croatia

Dalibor Carević - Faculty of Civil Engineering, University of Zagreb, Croatia

Michaela Červeňanská - Slovak University of Technology in Bratislava, Slovakia

Ivan Červeňanský - Faculty of Chemical and Food Technology, Slovak University of Technology in Bratislava, Slovakia

Lea Čubanová - Slovak University of Technology in Bratislava, Slovakia

Gorana Ćosić-Flajsig - Zagreb University of Applied Science, Croatia

Bojan Đurin - University North, Department of Civil Engineering, Croatia

Morena Galešić Divić - University of Split, Faculty of Civil Engineering, Architecture and Geodesy, Croatia

Gordon Gilja - Faculty of Civil Engineering, University of Zagreb, Croatia

Ivan Halkijević - Faculty of Civil Engineering, University of Zagreb, Croatia

Antonija Harasti - Faculty of Civil Engineering, University of Zagreb, Croatia

Tomáš Julínek - Brno University of Technology, Faculty of Civil Engineering, Czechia

Danijela Jurić-Kaćunić - Faculty of Civil Engineering, University of Zagreb, Croatia

Tomasz Kolerski - Gdansk University of Technology, Poland

Meho Saša Kovačević - Faculty of Civil Engineering, University of Zagreb, Croatia

Nerma Lazović - Faculty of Civil Engineering, University of Sarajevo, Bosnia and Herzegovina

Lovorka Librić - Faculty of Civil Engineering, University of Zagreb, Croatia

Ana Margarida Lopes Saraiva Alves Bento - Interdisciplinary Centre for Marine and Environmental Research (CIIMAR), Portugal

Robert Ljubičić - Faculty of Civil Engineering, University of Belgrade, Serbia

Domagoj Nakić - Faculty of Civil Engineering, University of Zagreb, Croatia

Eva Ocvirk - Faculty of Civil Engineering, University of Zagreb, Croatia

Hana Posavčić - Faculty of Civil Engineering, University of Zagreb, Croatia

Kristina Potočki - Faculty of Civil Engineering, University of Zagreb, Croatia

Jaromír Říha - Brno University of Technology, Faculty of Civil Engineering, Chechia

Adis Skejić - Faculty of Civil Engineering, University of Sarajevo, Bosnia and Herzegovina

Ivana Sušanj Čule - University of Rijeka Faculty of Civil Engineering, Croatia

Michał Szydłowski - Gdansk University of Technology, Poland

Andrej Šoltész - Slovak University of Technology in Bratislava, Slovakia

Marko Šrajbek - University North, Croatia

Željko Šreng - Faculty of Civil Engineering and Architecture, Osijek Josip Juraj Strossmayer University, Croatia

Salah Eddine Tachi - Badji Mokhtar-Annaba University, Algeria

Dražen Vouk - Faculty of Civil Engineering, University of Zagreb, Croatia

Hasnaoui Yacine - Department of Hydraulics, Laboratoire de Recherche des Sciences de L'eau, National Polytechnic School, Algeria

Piotr Zima - Gdansk University of Technology, Poland

Budo Zindović - Faculty of Civil Engineering, University of Belgrade, Serbia

Organized by

University of Zagreb
Faculty of Civil Engineering

Co-organized by

GDAŃSK UNIVERSITY OF TECHNOLOGY

STU SvF
SLOVAK UNIVERSITY OF TECHNOLOGY IN BRATISLAVA
FACULTY OF CIVIL ENGINEERING

BRNO UNIVERSITY OF TECHNOLOGY
FACULTY OF CIVIL ENGINEERING

BOKU UNIVERSITY

FACULTY OF CIVIL ENGINEERING
"Ss. Cyril and Methodius University"

Supporting Institutions

University of Rijeka
Faculty of Civil Engineering

GRAĐEVINSKI I ARHITEKTONSKI FAKULTET OSIJEK
Faculty of Civil Engineering and Architecture Osijek

SVEUČILIŠTE SJEVER

Water Institute
Josip Juraj Strossmayer

Hrvatsko društvo za zaštitu voda
Croatian Water Pollution Control Society

HHD

Croatian Hydrological Society

DHMZ

Croatian Meteorological and Hydrological Service

HDN

Croatian Society for Drainage and Irrigation

VODOVOD PULA-LABIN
d.o.o. za vodne usluge

Water Supplier Pula-Labin d.o.o.

ISTARSKI VODOVOD d.o.o
ZA PROIZVODNJU I DISTRIBUCIJU VODE, Buzet, Sv. Ivan 8

Water Supplier Istria d.o.o.

PREFACE

The responsibilities of water-oriented researchers are becoming increasingly demanding: climate change is altering hydrological regimes and intensifying water-related risks; urbanization and ageing infrastructure are placing additional pressure on water supply, sewerage and drainage systems; concerns over water quality and environmental degradation are becoming more complex; and engineering solutions are increasingly expected to combine technical efficiency with ecological sustainability and resilience. WMHE2026 takes place within this evolving scientific and professional landscape while continuing a tradition that extends over more than four decades. The Symposium series began in 1984 as a bilateral activity between the faculties of Gdańsk University of Technology and the University of Zagreb. Since the 1998 Symposium in Dubrovnik, the Slovak University of Technology, Ss. Cyril and Methodius University in Skopje and BOKU University in Vienna have participated in the series, while Brno University of Technology joined the steering group in 2013. Through this cooperation, WMHE has developed into a durable international forum for scientists, engineers and professionals working across the broad fields of water management and hydraulic engineering. The fundamental aim of the Symposium has remained unchanged: to encourage communication, exchange recent research results and professional experience, and strengthen cooperation among researchers and practitioners. Over successive editions, however, the programme has naturally evolved in response to changing scientific questions and engineering priorities.

Contributions to WMHE2026 reflect current trends in research: digitalization has moved from being an enabling tool to becoming an explicit area of research, with hydroinformatics, remote sensing and advanced monitoring receiving dedicated attention across disciplines. Contributions addressing green technologies, nature-based solutions, river and floodplain restoration, sustainable drainage, water retention and ecological considerations indicate an important transition to strengthening relationship between engineering and environmental objectives. Similarly, water supply, sewerage and treatment are increasingly approached as interconnected systems, while research into water and wastewater treatment is expanding toward questions of resource efficiency, reuse, recovery and circularity. Despite these advances, the Symposium also reminds us of the lasting importance of sound engineering fundamentals. More detailed data, more powerful computational tools and more sophisticated models are valuable only when supported by a rigorous understanding of physical processes, careful observation and engineering judgement. WMHE continues to provide a setting in which established knowledge and emerging approaches can meet, be critically examined and mutually strengthened.

We therefore hope that WMHE2026 will serve not only as a forum for presenting research results, but also that the discussions initiated here will continue well beyond the Symposium and contribute to future research, improved engineering practice and stronger professional cooperation. Above all, we hope that every participant leaves WMHE2026 with new knowledge, new professional connections and renewed motivation to advance water engineering in the service of safer, more resilient and more sustainable societies.

Organizing Committee

TABLE OF CONTENTS

PROCEEDINGS 1

ANALYSIS OF TEMPERATURE AND PRECIPITATION PARAMETERS AND THEIR INFLUENCE ON DROUGHT OCCURRANCE IN OSIJEK 2

COMPARATIVE ANALYSIS OF STATION-BASED AND CLIMATE MODEL DATA FOR FLOW MODELLING 12

EARLY WARNING SYSTEM BASED ON PRE-SIMULATED SCENARIOS FOR COMPOUND FLOODING: APPLICATION TO THE RJEČINA RIVER, RIJEKA 24

EVALUATING THE SCS-CN METHOD IN THE PAZINČICA RIVER CATCHMENT (CROATIA): MEASURED EXTREMES VS. EVENT-BASED HYDROLOGICAL SIMULATIONS 36

BIOTECHNOLOGICAL POTENTIAL OF ALGAE FOR WASTEWATER TREATMENT 51

ADVANCED WASTEWATER TREATMENT USING SEWAGE SLUDGE–DERIVED BIOCHAR AS A CIRCULAR ADSORBENT MATERIAL 64

APPLICATION OF BIOCHAR FOR THE REMOVAL OF THE PHARMACEUTICAL ZIDOVUDINE FROM WASTEWATER 77

THE USE OF ULTRAFILTRATION IN WATER TREATMENT 88

WASTEWATER TREATMENT IN SMALL SETTLEMENTS USING THE TEHNIX BIOROTOR SYSTEM 100

HYBRID ELECTROCOAGULATION–ADSORPTION TREATMENT OF AMMUNITION MANUFACTURING WASTEWATER: INFLUENCE OF PROCESS PARAMETERS ON COD, HEAVY METALS AND SULFATE REMOVAL 108

COMPARISON OF UNIVARIATE AND BIVARIATE APPROACHES TO DESIGN HYDROGRAPH DERIVATION IN CROATIAN AND SLOVENIAN CATCHMENTS 121

OPTIONS FOR FLOOD PROTECTION OF THE ZÁHORSKÁ BYSTRICA URBAN AREA 133

THE ROLE OF RETENTION RESERVOIRS IN URBAN FLOOD PROTECTION IN THE KACZA RIVER BASIN IN GDYNIA, POLAND 142

INFLUENCE OF DESIGN HYETOGRAPH CONSTRUCTION METHODS ON URBAN RUNOFF SIMULATION 152

CORRECT ADOPTION OF THE TWO-DIMENSIONAL DISPERSION TENSOR FOR POLLUTANT PROPAGATION IN WIDE RIVERS 164

URBAN AREAS AND GROUNDWATER FLOW ISSUESt 177

APPLICATION OF THE ENTROPY THEORY IN A CASE OF THE MEANDER IN A COMPLEX MORPHODYNAMICS MEDIA 189

INNOVATIVE TREND ANALYSIS (ITA) OF GROUNDWATER QUALITY PARAMETERS AT THE BARTOLOVEC WELLFIELD (CROATIA) 201

TRANSBOUNDARY WATER COOPERATION BETWEEN EU MEMBER STATES AND THE THIRD COUNTRIES 214

STRATEGIC RECONNECTION OF FLOODPLAINS FOR IMPLEMENTING THE EU 2030 BIODIVERSITY STRATEGY IN LEVEE MANAGEMENT 225

CARTOGRAPHIC MICROZONATION OF NITRATE VULNERABILITY IN THE VARAŽDIN AQUIFER THROUGH INTEGRATION OF FIELD MEASUREMENTS, HISTORICAL TIME SERIES AND LAND COVER DATA 234

A FRAMEWORK FOR URBAN CLIMATE RESILIENCE: REGULATION ELEMENTS FOR GROUNDWATER PROTECTION IN THE VARAŽDIN AQUIFER 243

PROPOSAL OF FISHPASSES BASED ON MONITORING 252

OPTIMIZATION OF THE MANNING´S ROUGHNESS COEFFICIENT VALUE FOR 1-D FISH PASS NUMERICAL MODELLING 263

SOFTWARE TOOL FOR OPERATIONAL CONTROL OF THE GABČÍKOVO HYDROPOWER PLANT ON THE DANUBE: LINKING WATER FLOW SIMULATIONS AND ENERGY MANAGEMENT 276

SAFETY ASSESSMENT OF HYDRAULIC STRUCTURES USING RISK ANALYSIS 287

ADAPTIVE DISCRETIZATION FOR 3D BRIDGE FLOW WITH SCALE-RESOLVING AIR-WATER MULTIPHASE SIMULATION 297

UNCERTAINTY QUANTIFICATION OF WAVE TRANSMISSION OF PI-TYPE FLOATING BREAKWATERS 306

HIGH-RESOLUTION UAV LASER SCANNING OF THE CHANNEL MORPHOLOGY – COMPARISON WITH TRADITIONAL SURVEYING TECHNIQUES 317

ADVANCING THE TEMPORAL DYNAMICS ANALYSIS OF THE BULAŽ SPRING CATCHMENT WATER BALANCE WITH GLOBAL MODERATE RESOLUTION SOIL MOISTURE DATASETS 329

FLOOD RISK ASSESSMENT AND HYDRAULIC CAPACITY ANALYSIS OF THE UNGAUGED ROKALOVO KARST CATCHMENT 341

EVALUATION OF REANALYSIS AND CLIMATE PRODUCTS FOR WIND FORCING OF A MID-ADRIATIC NUMERICAL WAVE MODEL 349

WATER RETENTION MEASURES IN THE CENTER OF TURANY NAD ONDAVOU VILLAGE 360

REVITALIZATION OF A DRAVA RIVER SIDE BRANCH USING 2D NUMERICAL MODELLING 367

INTEGRATING HYDRODYNAMIC HABITAT MODELLING AND NATURE-BASED SOLUTIONS FOR THE RESTORATION OF THE NOSKOVAČKA BARA SIDE-ARM 377

NATURE-BASED SOLUTIONS IN THE WATER SECTOR IN SERBIA AND THE EU: FROM REGULATORY ALIGNMENT TO IMPLEMENTATION CHALLENGES 389

COMPARATIVE HYDRAULIC ANALYSIS AND OPTIMISATION OF THE WATER SUPPLY SYSTEM IN A RESIDENTIAL AND TOURIST AREA 401

HYDRAULIC ANALYSIS AND OPTIMISATION OF AN ANNULAR WATER SUPPLY SYSTEM IN AN URBAN AREA 416

HYDROLOGICAL MODEL CALIBRATION USING SWAT-CUP 429

NUMERICAL ASSESSMENT OF AN IMPROVED HYDRODYNAMIC VORTEX SEPARATOR FOR STORMWATER TREATMENT 441

MODELLING OF SNOWMELT USING SWAT IN THE CASE OF THE UPPER DRAVA CATCHMENTS 452

DISCREPANCIES BETWEEN AN UPDATED 1000-YEAR DESIGN HYDROGRAPH AND RECONSTRUCTED HISTORICAL FLOOD EVENTS 465

IMPACT OF PRIMARY PRECIPITATION DATA PROCESSING ON DIMENSIONLESS HYETOGRAPHS 477

POSSIBILITIES OF WATER RESOURCES USE FROM DRAINAGE CANALS ALONG RESERVOIRS ON THE DRAVA RIVER, CROATIA 489

SONO-ELECTROCOAGULATION FOR SIMULTANEOUS SELENIUM AND STRONTIUM REMOVAL IN A MULTI-STAGE REACTOR 501

COMPARATIVE EVALUATION OF ELECTROOXIDATION, ULTRASOUND, AND

OZONATION FOR THE INACTIVATION OF *ESCHERICHIA COLI* AND TOTAL COLIFORMS 514

WATER QUALITY ANALYSIS IN THE ORLJAVA RIVER BASIN AREA 526

METHODOLOGY FOR WHOLESALE WATER PRICING BETWEEN PUBLIC WATER UTILITIES IN CROATIA: LEGAL FRAMEWORK AND COST ALLOCATION..... 540

CALIBRATION OF ANALYTICAL MODELS FOR WAVE PREDICTION 552

CROSS-SCALE ANALYSIS OF PRECIPITATION DATA FROM HIGH AND LOW TEMPORAL RESOLUTION DATASETS 565

QUANTIFYING WIND CONTRIBUTION TO WATER EXCHANGE IN MARINAS USING AN IMPROVED ANALYTICAL FORMULATION 576

PROCEEDINGS

ANALYSIS OF TEMPERATURE AND PRECIPITATION PARAMETERS AND THEIR INFLUENCE ON DROUGHT OCCURRANCE IN OSIJEK

Tamara BRLEKOVIĆ [1*], Lidija TADIĆ [1], Josip JANJIĆ [1], Tatjana MIJUŠKOVIĆ-SVETINOVIĆ [1]

[1] *Faculty of Civil Engineering and Architecture Osijek, Croatia*

E-mail: tamaradadic@gfos.hr

E-mail: ltadic@gfos.hr

E-mail: jjanjic@gfos.hr

E-mail: tatjanam@gfos.hr

[*] *Corresponding author*

Abstract

This study investigates the long-term climatic indicators most closely associated with drought conditions represented by New Drought Index (NDI) in the Osijek region (eastern Croatia) during the 1900–2025 period. Annual climatic series were derived from meteorological observations, including temperature and precipitation-related variables such as annual and seasonal temperatures, precipitation totals, precipitation frequency, and extreme temperature indicators. The association of climatic variables with drought variability was analyzed using Pearson's correlation, Partial Least Squares (PLS) regression, and Stepwise multiple regression. Pearson correlation analysis indicated that besides annual precipitation (0.791) and average annual temperature (-0.791) which exhibited the strongest correlations with NDI, also average annual minimum and maximum temperatures as well as annual number of days with precipitation above 1 and 10 mm showed strong relationship suggesting that drought conditions in Osijek are jointly controlled by precipitation deficit and increasing temperatures. The PLS regression model demonstrated very high explanatory and predictive performance (R^2Y cum=0.940; Q^2 cum= 0.937), while the stepwise regression model served as a consistency check of the NDI formulation. The findings indicate that increasing temperatures may play an equally important role as precipitation deficits in future drought development in eastern Croatia under ongoing climate change.

Key words

New Drought Index (NDI), Osijek, Pearson's correlation, Partial Least Squares (PLS) regression, Stepwise multiple regression.

1 Introduction

Drought represents one of the most complex and damaging natural hazards affecting environmental systems, agriculture, water resources, and socio-economic activities worldwide (Wilhite, 2000; Orimoloye et al., 2022). Unlike most natural hazards, drought develops slowly and is characterized by prolonged periods of below-normal water availability resulting from complex interactions among precipitation deficits, atmospheric conditions, evapotranspiration, soil moisture dynamics, and hydrological processes (Wilhite, 2000).

In recent decades, rising global temperatures and changing precipitation patterns have heightened concerns about the frequency, duration, and severity of drought events under ongoing climate change (Tsegai et al., 2022; Lloyd-Hughes et al., 2012). According to IPCC reports, a +2°C of global warming could raise drought risk by 50%.

Traditionally, drought has been primarily associated with precipitation deficits. However, numerous studies have demonstrated that rising temperatures can substantially amplify drought conditions by increasing evapotranspiration and accelerating soil moisture depletion. Dai (2011) emphasized that global warming contributes to increasing aridity and drought severity even in regions where long-term precipitation trends remain relatively unchanged. Similarly, Trenberth et al. (2014) noted that elevated temperatures intensify drought by increasing atmospheric moisture demand, accelerating drought onset and increasing its severity.

Given the complexity and frequency of drought worldwide, several methods, known as indices, have been developed to calculate drought. They are primarily based on meteorological (precipitation and temperature) and hydrological parameters (discharges and water levels), but can also be based on soil moisture content, groundwater levels, and remote sensing data (Svoboda and Fuchs, 2016). The most commonly used are those based on meteorological data, such as the Standardized Precipitation Index (SPI), Rainfall Anomaly Index (RAI), Standardized Precipitation Evapotranspiration Index (SPEI), and Palmer Z Index. In recent years, due to climate change and rising air temperatures, new indices have been developed, such as the New Drought Index (NDI) (Bonacci et al., 2023).

The Pannonian Plain and southeastern Europe are considered particularly vulnerable to future drought intensification due to projected increases in air temperature, more frequent heat waves, and changes in precipitation variability (Crocetti et al., 2020; Trnka et al., 2016). Eastern Croatia, including the Osijek region, has already experienced increasing thermal stress and more frequent extreme climatic events during recent decades (Santos et al., 2023; Tadić et al., 2015). Since this region strongly depends on agriculture and water availability, understanding the dominant climatic controls of drought development is of considerable importance for future water management and climate adaptation strategies.

Previous drought studies have commonly focused on precipitation deficits or trend analyses of drought indices. However, fewer studies have investigated the relative importance of different climatic variables and their influence on drought occurrence. Furthermore, the relationships between seasonal temperatures, precipitation frequency, and drought development remain insufficiently explored for the Osijek region and the wider Pannonian area.

Therefore, the main objective of this study was to investigate the relationships between the New Drought Index (NDI) and broad range of annual and seasonal temperature and precipitation indicators in Osijek during the period 1900–2025. To achieve this objective, Pearson correlation analysis, Partial Least Squares (PLS) regression, and Stepwise Multiple Regression analysis were applied to evaluate the associations between the NDI and a set of climatic indicators. The combined application of these methods enabled the identification of climatic variables most strongly associated with interannual NDI variability and the assessment of the relative importance of different precipitation- and temperature-related indicators in explaining drought conditions.

2 Methods

The analysis was conducted for the Osijek region, located in eastern Croatia within the Pannonian Plain based on observations from the Osijek main meteorological station (45.53°N, 18.73°E; 89 m a.s.l.) covering the period 1900–2025. The observational record is continuous except for a short interruption caused by the war in Croatia, when measurements were unavailable from 17 October to 31 December 1991 and from 1 January to 15 February 1992. Missing values were subsequently completed using data from the meteorological E-OBS gridded dataset (ensemble mean, spatial resolution 0.25°). EOBS data showed a high correlation with measured data in Croatia in previous analyses (Santos et al., 2023), which is why this particular dataset was also used in this analysis.

Long-term meteorological records for the period 1900–2025 were used to examine the relationships between the New Drought Index (NDI) and a broad range of temperature and precipitation indicators. Annual time series were constructed from the original meteorological observations in order to obtain

homogeneous climatic indicators suitable for statistical analysis.

The analyzed temperature and precipitation-related variables are listed in Table 1. All variables were calculated on an annual scale to enable comparison with the drought index, which was also calculated on an annual scale.

Table 1. List of temperature and precipitation parameters (after Burić and Doderović, 2021)

No.	Parameter	Definition	Unit
		Temperature	
1	TY	Average annual temperature	°C
2	TW	Average winter temperature	°C
3	TSp	Average spring temperature	°C
4	TSu	Average summer temperature	°C
5	TA	Average autumn temperature	°C
6	Tyx	Average annual maximum temperature	°C
7	Tyn	Average annual minimum temperature	°C
8	FD	Total annual number of frost days Tn<0°C	Number of days
9	ID	Total number of ice days Tx<0°C	Number of days
10	SU	Total number of summer days Tx≥25°C	Number of days
11	TD	Total number of tropical days Tx≥30°C	Number of days
12	TR	Total number of tropical nights Tn>20°C	Number of days
13	T35+	Total number of days with Tx≥35°C	Number of days
14	T40+	Total number of days with Tx≥40°C	Number of days
		Precipitation	
1	PY	Annual precipitation	mm
2	PW	Winter precipitation	mm
3	PSp	Spring precipitation	mm
4	PSu	Summer precipitation	mm
5	PA	Autumn precipitation	mm
6	P1	Annual number of days with precipitation ≥1.0 mm	Number of days
7	P10	Annual number of days with precipitation ≥10 mm	Number of days
8	P20	Annual number of days with precipitation ≥20 mm	Number of days
9	P30	Annual number of days with precipitation ≥30 mm	Number of days
10	P40	Annual number of days with precipitation ≥40 mm	Number of days

Abbreviation: Tx-maximum temperature; Tn-minimum temperature

To ensure that changes in air temperatures were captured by the drought index, the recently developed NDI was used in this study. NDI presumes that drought severity is driven by precipitation deficits (below average at a given area) and by rising air temperatures (above average at a given area). So, the expression for NDI calculation is (Tadić et al., 2025; Bonacci et al., 2023):

$$NDIi = [(Pi - Pav)/\sigma_P] - [(Ti - Tav)/\sigma_{PT}] \quad (1)$$

where:
Pi- precipitation in the year or month i;
P_{av} -the average value of the analyzed series of precipitation in the obtained period;
σ_P- the standard deviation of the analyzed series of precipitation in the analysis period;
T_i -is the mean temperature in the year or month i;
T_{av}-the average value of the analyzed series of air temperature data in the analysis period;
σ_T -is the standard deviation of the series of air temperature in the analysis period.

The proposed classification of NDI values is shown in Table 2. The classification is the same as for several other drought indices, such as the Standardized Precipitation Index (SPI) and the Standardized Precipitation Evapotranspiration Index (SPEI) as used by the original author of the NDI (Bonacci et al., 2026). Although the NDI is derived using a different formulation, it is based on standardized precipitation and temperature anomalies, resulting in a dimensionless index.

Table 2. Classification thresholds applied to NDI, adopted from Li et al. (2015)

Category	NDI
Extremely wet	≥2.00
Severely wet	from 1.50 to 1.99
Moderately wet	from 1.00 to 1.49
Normal	from 0.99 to -0.99
Moderate drought	from -1.00 to -1.49
Severe drought	from -1.50 to -1.99
Extreme drought	≤-2.00

Temporal trends in selected climatic variables and the NDI drought index were evaluated using the non-parametric Mann–Kendall trend test (Mann, 1945; Kendall, 1975) and Sen's slope estimator (Sen, 1968), which are among the most widely used methods for trend detection in hydroclimatological time series. The Mann–Kendall test was applied to assess the statistical significance of monotonic trends, whereas Sen's slope estimator was used to quantify the rate and direction of change over time.

Pearson correlation analysis (Montgomery et al., 2021) was performed to examine the linear relationships between climatic variables and drought characteristics. Correlation coefficients were calculated between all temperature and precipitation indicators and the calculated drought index. The statistical significance of the correlations was evaluated at α=0.05. Correlation matrices and correlation maps were used to identify the dominant climatic controls on drought development and to assess the strength and direction of the relationships between variables.

Partial Least Squares (PLS) regression was applied to determine the relative importance of climatic variables, selected based on Pearson correlation results. PLS regression was selected due to strong multicollinearity among climatic predictors, particularly among temperature-related variables and precipitation indicators. NDI values were used as dependent variables and climatic variables were used as explanatory variables. The importance of individual climatic variables was evaluated using Variable Importance in Projection (VIP) scores. Variables with VIP values greater than 1 were considered highly influential, while variables with VIP values between 0.8 and 1 were considered moderately important (Wold et al., 2001).

Stepwise multiple regression analysis was subsequently applied as a complementary method to verify the results obtained from the PLS regression models and to identify the optimal subset of climatic predictors for each drought characteristic. Only the most relevant climatic variables identified by the correlation and PLS analyses were included in the regression procedure. The stepwise selection method iteratively added or removed variables based on their statistical significance and their contribution to model performance (Montgomery et al., 2021).

All statistical analyses were performed using XLSTAT software.

3 Results and Discussion

Mann–Kendall trend was calculated for all parameters from Table 1. The results shown in Table 3 revealed statistically significant increasing trends in all major temperature variables during the 1900–

2025 period. Mean annual temperature increased by approximately 0.011 °C/ year, while spring and summer temperatures increased by 0.010 and 0.013 °C/year, respectively. This increase in temperature over the last several decades was confirmed by several other publications (EEA, 2024; Spinoni et al., 2015; Bonacci, 2010). In contrast, annual precipitation did not exhibit a statistically significant trend ($p = 0.247$). However, the annual number of days with precipitation exceeding 1.0 showed a significant negative trend, indicating a decrease in the number of wet days over time.

Table 3. Mann–Kendall trend test and Sen's slope estimates for selected climatic variables in Osijek during 1900–2025

Parameter	Minimum	Maximum	Mean	Std. deviation	Kendall's tau	Sen's slope	P-value*
TY	8.857	14.311	11.230	0.909	0.295	0.011	**<0.0001**
TW	-4.738	6.065	1.574	2.100	0.196	0.016	**0.001**
TSp	12.114	17.628	14.643	1.059	0.239	0.010	**<0.0001**
TSu	17.939	24.417	20.440	1.171	0.270	0.013	**<0.0001**
TA	4.40	10.640	7.730	1.241	0.007	0.007	**0.045**
Tyx	15.750	20.517	17.582	0.920	0.312	0.012	**<0.0001**
Tyn	1.433	7.975	4.513	1.220	0.213	0.011	**0.000**
FD	31	119	80.040	18.275	-0.104	-0.083	0.086
ID	0	62	18.206	11.311	-0.125	-0.05	**0.040**
SU	44	134	94.032	17.207	0.182	0.130	**0.030**
TD	2	73	32.087	14.176	0.094	0.061	0.123
TR	0	24	1.714	2.953	0.260	0	**<0.0001**
T35+	0	26	3.738	4.807	0	0	0.997
PY	317	1117.8	689.027	137.024	-0.070	-0.373	0.247
PW	32.1	277.8	132.303	50.597	-0.018	-0.036	0.766
PSp	39.8	471.6	203.194	68.807	-0.082	-0.233	0.172
PSu	61.9	481	186.388	70.165	0.032	0.059	0.597
PA	21.7	372.9	168.975	67.080	-0.053	-0.131	0.383
P1	54	124	91.937	13.682	-0.176	-0.094	**0.004**
P10	6	37	20.651	5.874	-0.020	0	0.753
P20	1	14	5.841	2.855	0.012	0	0.848
P30	0	7	2.040	1.567	-0.026	0	0.687
P40	0	5	0.770	0.989	0.060	0	0.385

*Bold values are the ones that are statistically significant

Annual NDI values are calculated according to (1), and results are shown in Figure 1. Negative values, especially those below -1, indicate drought conditions according to Table 2. It can be seen that the wettest years were 1906 and 1940, and the driest were 1928, 2000, and 2024. Also, the concentration of dry years from 2000 is visible. Other researchers also confirmed that in Croatia, the driest year was 2000 (Santos et al., 2023) and that an extreme drought occurred in Croatia during 2011 and 2012 (Cindrić et al., 2016), which is also visible in Figure 1. According to the European State of the Climate 2024 report and Copernicus analyses, southeastern Europe experienced exceptionally high temperatures and severe drought conditions during 2024 (Toreti et al., 2024; Copernicus Climate Change Service, 2025). This confirmed that the chosen drought index (NDI) represents drought conditions well and can be used in further analysis.

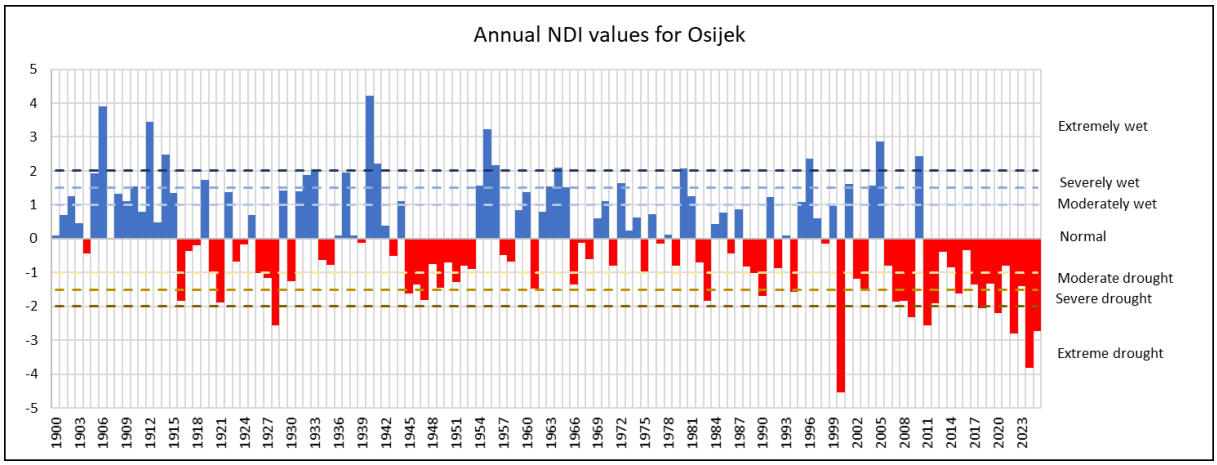


Figure 1. Annual NDI values for Osijek for the period 1900–2025 with classification from Table 2

Pearson correlation analysis revealed exceptionally strong relationships between the analyzed variables and the NDI drought index (Figure 2). Warm colors (yellow, orange, and red) indicate positive correlations, whereas cool colors (light blue, blue, and dark blue) indicate negative correlations, with darker colors indicating higher correlation. It is important to note that negative values of the drought index indicate drought conditions; thus, in this case, the negative correlations between NDI and all temperature parameters are actually positive for drought (i.e., higher temperatures are more likely to lead to drought). Table 4 shows 10 parameters with the highest correlation with NDI index. Annual temperature (TY) and annual precipitation (PY) showed the strongest correlations with NDI ($r = -0.791$ and $r = 0.791$, respectively), indicating that drought conditions in Osijek are controlled by both increasing temperatures and precipitation deficit. Strong correlations were also obtained for average annual maximum temperature (Tyx), annual number of days with precipitation (P1 and P10), and spring temperature (TSp), suggesting an important role of warming trends and precipitation continuity in drought variability.

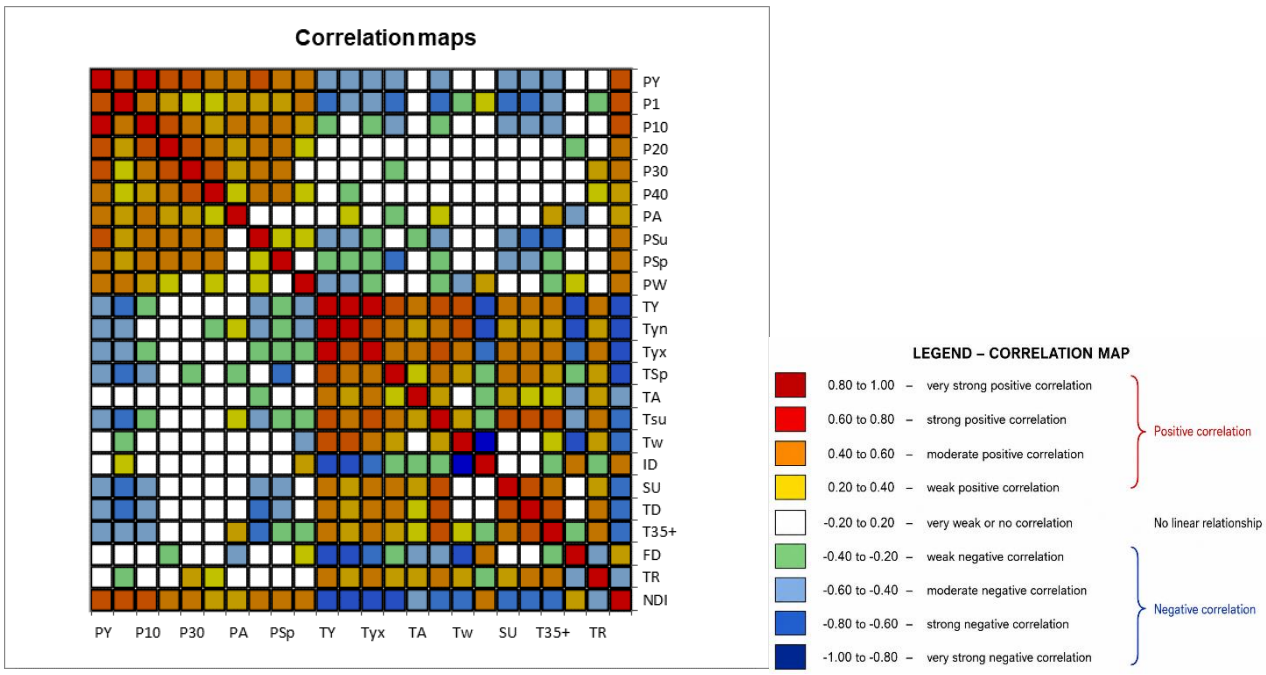


Figure 2. Correlation maps with NDI for all parameters

Table 4. Strongest Pearson correlations between climatic variables and the NDI drought index in Osijek during the 1900–2025 period

Parameter	Correlation coefficient (r)	p-values	Coefficients of determination (R^2)
TY	-0.791	<0.0001	0.626
PY	0.791	<0.0001	0.626
Tyx	-0.706	<0.0001	0.498
P1	0.694	<0.0001	0.482
Tyn	-0.668	<0.0001	0.446
P10	0.626	<0.0001	0.392
TSp	-0.613	<0.0001	0.376
Tsu	-0.599	<0.0001	0.354
PSu	0.511	<0.0001	0.261
PSp	0.487	<0.0001	0.237

Based on the Pearson correlation analysis results, 10 parameters with the highest correlations with NDI values (Table 4) are selected for further analysis. This approach was used to eliminate redundant variables for Partial Least Squares (PLS) regression and to interpret VIP scores more accurately. The PLS regression model demonstrated exceptionally high explanatory and predictive performance (R^2Y cum=0.940; Q^2 cum= 0.937). The model performance results indicate that climate variables explain about 94% of the variability in the NDI index. Variable Importance in Projection (VIP) is the most valuable result of the PLS regression model. All variables with a VIP score ≥ 1 are dominant variables. In this case, annual temperature (TY) and annual precipitation (PY) are the dominant variables of the NDI drought index, exhibiting identical VIP values 1.206. This was expected given their role in calculating NDI. Average annual maximum temperature (Tyx), the annual number of days with precipitation ≥1.0 mm (P1) and average annual minimum temperature (Tyn) also showed high importance. Regarding seasonal parameters, only spring and summer parameters were significant in this analysis according to Pearson's correlation, and the temperature VIP values are higher than those of precipitation. They contributed moderately (Figure 3).

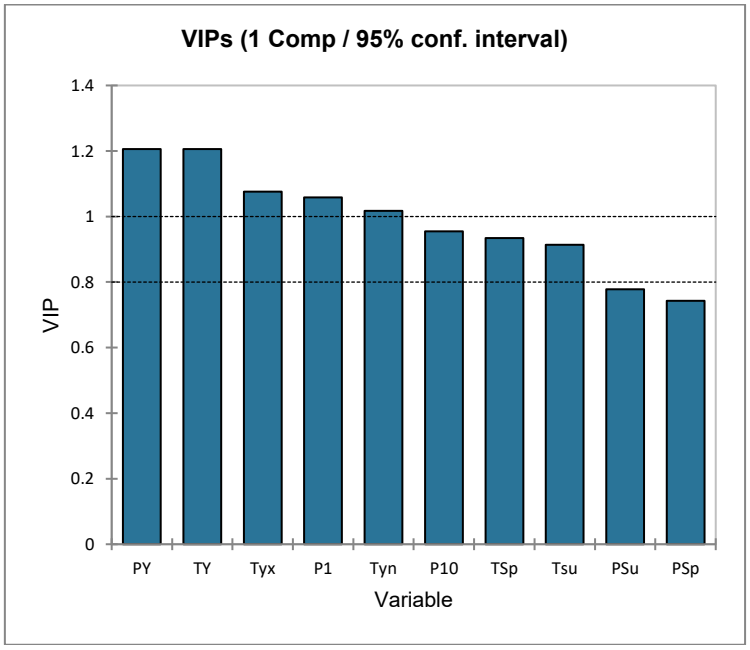


Figure 3. VIP scores obtained from the PLS regression model for the NDI drought index.

The final part of the drought analysis was the Stepwise multiple regression. In this analysis, the same 10 parameters were also included. The results (Table 5 and Figure 4) identified annual precipitation (PY) and annual temperature (TY) as the dominant climatic controls of the NDI drought index in Osijek.

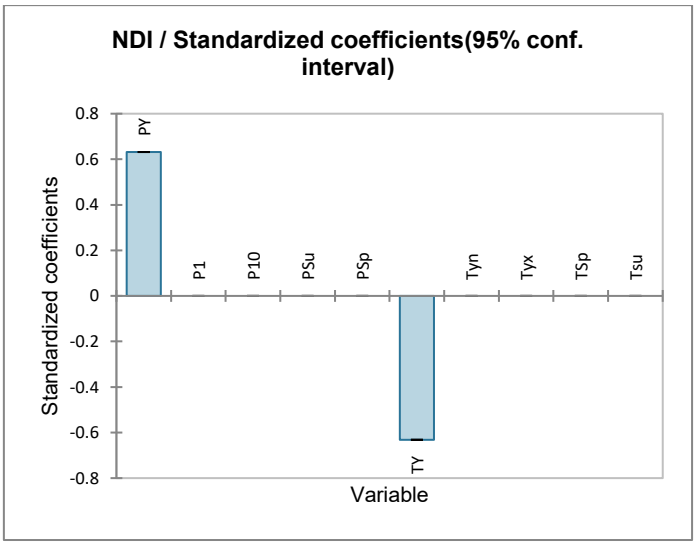


Figure 4. Results of the Stepwise multiple regression

Table 5. Final stepwise multiple regression model for the NDI drought index in Osijek (1900–2025)

Variable	Standardized coefficient (β)	p-value
PY	0.632	<0.0001
TY	-0.632	<0.0001

The stepwise regression retained only annual precipitation and annual temperature, reproducing the NDI exactly ($R^2 = 1.00$). This result confirms the mathematical consistency of the NDI formulation rather than identifying independent climatic drivers of drought.

The stepwise regression analysis confirmed that annual precipitation and annual temperature, which mathematically define the NDI, completely explained its variability ($R^2 = 1.00$). Therefore, the regression served as a consistency check of the NDI formulation rather than as an independent identification of drought predictors.

The obtained results are consistent with previous studies that identified precipitation and temperature as the dominant climatic controls of drought variability. Using PLS regression, Wu et al. (2021) reported that precipitation and evaporation were the most influential drivers of drought development in Southwest China. Similarly, Zheng et al. (2022) demonstrated that drought characteristics are controlled by the combined effects of precipitation deficits and increasing evaporative demand. The significant warming trends observed in Osijek and the strong influence of temperature on the NDI index are therefore consistent with recent findings indicating an increasing role of temperatures in drought development under changing climatic conditions.

4 Conclusion

This study investigates the long-term climatic indicators most closely associated with drought conditions represented by New Drought Index (NDI) in the Osijek (eastern Croatia) during the 1900–2025 period. The combined application of Mann–Kendall trend analysis, Pearson correlation analysis, Partial Least Squares (PLS) regression, and Stepwise Multiple Regression enabled a comprehensive assessment of the relationships between the New Drought Index (NDI) and a broad range of climatic indicators.

The Mann–Kendall analysis revealed statistically significant increasing trends in all major temperature variables, including annual, seasonal, minimum, and maximum temperatures, indicating a pronounced warming trend throughout the study period. In contrast, annual precipitation did not exhibit a statistically significant trend, whereas the frequency of precipitation days decreased significantly. These findings suggest that climatic changes in the study area are characterized primarily by increasing temperatures

and fewer precipitation events, rather than changes in annual precipitation.

Pearson correlation analysis demonstrated exceptionally strong relationships between NDI and both annual temperature (r = -0.791) and annual precipitation (r = 0.791), indicating that drought conditions are jointly controlled by precipitation deficit and increasing temperatures. High influence of those two parameters was expected due to a mathematical expression for the NDI, but this analysis quantified that influence. The PLS regression model further confirmed the dominant role of annual temperature and annual precipitation, which exhibited the highest VIP scores of 1.206, while average annual maximum temperature (Tyx), the annual number of days with precipitation ≥1.0 mm (P1) and average annual minimum temperature (Tyn) also contributed significantly to drought variability. The model showed excellent explanatory and predictive performance.

The final stepwise regression analysis served as a consistency check of the NDI formulation rather than as an independent identification of drought predictors.

Overall, the obtained findings highlight the growing importance of increased temperatures in drought development under contemporary climate conditions. Although no significant long-term decrease in annual precipitation was detected, precipitation also remains one of the most important controls of drought variability, whereas temperature shows a strong and significant increase.

Future research should focus on analysing regional and global climate model projections to assess potential changes in temperature, precipitation, and drought conditions throughout the 21st century. Such analyses would provide valuable information for evaluating future drought risk and supporting climate adaptation and water resource management strategies in eastern Croatia and the wider Pannonian region.

Acknowledgements

Funded by the European Union – Next Generation EU. However, the views and opinions expressed are solely those of the author(s) and do not necessarily reflect those of the European Union or the European Commission. Neither the European Union nor the European Commission can be held responsible for them.

References

Bonacci, O., Žaknić-Ćatović, A., Brleković, T., Roje-Bonacci, T., Filipčić, A. 2026 Assessing Drought Intensification with SPEI and NDI in Pazin, Istria (Northern Adriatic, Croatia). *Meteorology*, *5*(1), 4.
Bonacci, O., Bonacci, D., Roje-Bonacci, T., Vrsalović, A. 2023 Proposal of a new method for drought analysis. *Journal of Hydrology and Hydromechanics.* 71*,* 1–11.
Bonacci, O. 2010 Analysis of mean annual air temperature series in Croatia. *Građevinar,* 62. (9/12), 781–791.
Burić, D., Doderović, M. 2021 Changes in temperature and precipitation in the instrumental period (1951 – 2018) and projections up to 2100 in Podgorica (Montenegro). *International Journal of Climatology.* 41, 133–149.
Cindrić, K., Telišman Pretnjak, M., Herceg-Bulić, I., Mihajlović, D., Pasarić, Z. 2016 Analysis of the Extraordinary 2011/2012 Drought in Croatia. *Theoretical and Applied Climatology.* 123*,* 503–522.
Copernicus Climate Change Service. 2025 Heat and drought in southeastern Europe during summer 2025. European State of the Climate 2024. https://climate.copernicus.eu/esotc/2024 (accessed 11 June 2026).
Crocetti, L., Forkel, M., Fischer, M., Jurečka, F., Grlj, A., Salentinig, A., Trnka, M., Anderson M., Ng, W.-T., Kokalj, Ž., Bucur, A., Dorigo, W. 2020 Earth Observation for agricultural drought monitoring in the Pannonian Basin (southeastern Europe): current state and future directions. *Regional Environmental Change*. 20, 123.

Dai, A 2011 Drought under global warming: a review. WIREs Clim Change, 2:45–65. doi: 10.1002/wcc.81
European Environment Agency. 2024 European Climate Risk Assessment. EEA Report No. 01/2024. https://www.eea.europe.eu/publications/european-climate-risk-assessment (accessed 11 June 2026).
IPCC. 2021 Summary for Policymakers. In: Climate Change 2021: The Physical Science Basis. Contribution of Working Group I to the Sixth Assessment Report of the IPCC. https://www.ipcc.ch/report/ar6/wg1 (accessed 11 June 2026).
Kendall, M.G. 1975 *Rank Correlation Methods*. 4th edition, Charles Griffin, London.
Li, B., Zhou, W., Zhao, Y., Ju, Q., Yu, Z., Acharya, K. 2015 Using the SPEI to Assess Recent Climate Change in the Yarlung Zangbo River Basin, South Tibet. *Water*. 7*,* 5474–5486.
Lloyd-Hughes, B., Shaffrey, L.C., Vidale, P.L., Arnell, N.W. 2012 An evaluation of the spatiotemporal structure of large-scale European drought within the HiGEM climate model. *International Journal of Climatology*. 33/8*,* 2024–2035.
Mann, H.B. 1945. Nonparametric Tests against Trend. *Econometrica*. 13 (3), 245–259
Montgomery, D.C., Peck, E.A., Vining, G.G. 2021 *Introduction to Linear Regression Analysis.* 6th edition, John Wiley & Sons, Hoboken, NJ.
Orimoloye, I.R., Belle, J.A., Orimoloye, Y.M., Olusola, A.O., Ololade, O.O. 2022 Drought: A Common Environmental Disaster. *Atmosphere*. 13(1), 111.
Santos, F.J., Tadić, L., Portela, M.M., Espinosa, L.A., Bleković, T. 2023 Drought Characterization in Croatia Using E-OBS Gridded Data. *Water.* 15(21)*,* 3806.
Sen, P.K. 1968 Estimates of the Regression Coefficient Based on Kendall's Tau. *Journal of the American Statistical Association*. 63*,* 1379–1389.
Spinoni, J., Naumann, G., Vogt, J., Barbosa, P. 2015 European Drought Climatologies and Trends Based on a Multi-Indicator Approach. *Global and Planetary Change.* 127, 50–57.
Svoboda, M., Fuchs, B.A. 2016 *Handbook of Drought Indicators and Indices*. World Meteorological Organization (WMO) and Global Water Partnership (GWP), Geneva, 45 pp.
Tadić, L., Brleković, T., Antolović, M. 2025 Comparison of the New Drought Index with various well-known drought indices. *Advances in Civil and Architecture Engineering*. 13(31)*,* 31–43.
Tadić, L., Dadić, T., Bosak, M. 2015 Comparison of different drought assessment methods in continental Croatia. *Građevinar,* 67. (1/12), 11–22.
Toreti, A., Bavera, D., Acosta Navarro, J., Acquafresca, L., Azas, K., Barbosa, P., De Jager, A., Ficchi, A., Fioravanti, G., Grimaldi, S., Hrast Essenfelder, A., Magni, D., Mazzeschi, M., McCormick, N., Salamon, P., Santos Nunes, S., Volpi, D. 2024 *Global Drought Overview September 2024.* JRC139423, Publications Office of the European Union, Luxembourg.
Trenberth, K.E., Dai, A., van der Schrier, G., Jones, P.D., Barichivich, J., Briffa, K.R., Sheffield, J. 2014 Global warming and changes in drought. *Nature Climate Change.* 4, 17–22.
Trnka, M., Balek, J., Štěpánek, P., Zahradníček, P., Možný, M., Eitzinger, J., Žalud, Z., Formayer, H., Turňa, M., Nejedlík, P., Semerádová, D., Hlavinka, P. and Brázdil, R. 2016 Drought trends over part of Central Europe between 1961 and 2014. *Climate Research.* 70, 143–160.
Tsegai, D., Medel, M., Augenstein, P. and Huang, Z. 2022 *Drought in Numbers 2022: Restoration for Readiness and Resilience*. United Nations Convention to Combat Desertification (UNCCD), Bonn, Germany.
Wilhite, D.A. 2000 Drought as a natural hazard: Concepts and definitions. In: *Drought: A Global Assessment*, D.A. Wilhite (ed.), Vol. I, Routledge, London, pp. 3–18.
Wold, S., Sjöström, M. and Eriksson, L. 2001 PLS-regression: a basic tool of chemometrics. *Chemometrics and Intelligent Laboratory Systems.* 58 (2), 109–130.
Wu, T., Zheng, W., Yin, W. and Zhang, H. 2021 Spatiotemporal Characteristics of Drought and Driving Factors Based on the GRACE-Derived Total Storage Deficit Index: A Case Study in Southwest China. *Remote Sensing.* 13, 79.
Zheng, Y., Zhang, X., Yu, J., Xu, Y., Wang, Q., Li, C. and Yao, X. 2022 Assessing the Joint Impact of Climatic Variables on Meteorological Drought Using Machine Learning. *Frontiers in Earth Science.* 10, 835142.

COMPARATIVE ANALYSIS OF STATION-BASED AND CLIMATE MODEL DATA FOR FLOW MODELLING

Jadran BERBIĆ [1*], Eva OCVIRK [1]

[1] *Faculty of Civil Engineering, University of Zagreb*

E-mail: jadran.berbic@grad.unizg.hr

E-mail: eva.ocvirk@grad.unizg.hr

[*] *Corresponding author*

Abstract

Water resources systems, such as reservoirs, are highly dependent on future water availability, making reliable long-term flow forecasting an essential component of water resources planning and management. Since river discharge is strongly influenced by climatic variables, particularly precipitation and air temperature, the application of climate model outputs within hydrological forecasting frameworks therefore requires an assessment of their consistency with local observations. This study investigates the relationship between station-based meteorological observations and climate-model-derived data for the Cetina River basin in Croatia. Daily precipitation and temperature records from meteorological stations are compared with corresponding spatial datasets obtained from climate model simulations over the common period 2015-2022. Particular attention is given to the identification of spatial grid cells that best represent local station conditions. The analysis included comparisons of monthly climatological characteristics, correlation-based evaluation of spatial cells, and temporal lag assessment. The results provide guidance for selecting representative climate model inputs for future monthly flow modelling and represent a preliminary step towards climate-informed assessment of future water availability in the Cetina River basin.

Key words

long term planning, mean monthly flow, precipitation, air temperature, climate scenarios

1 Introduction

Reservoir operation and water resources management depend on reliable estimates of future water availability. In river basins characterized by pronounced seasonal variability, long-term water resources planning commonly relies on analyses and forecasts of mean monthly discharge, which provides the basis for decisions related to water supply, hydropower production, environmental flow maintenance, and drought management (Wurbs and James, 2002, Loucks and van Beek, 2005). Catchment response is governed by the interaction between basin characteristics and meteorological forcing. While physiographic factors (topography, geology, land cover, soil properties) determine the general hydrological response of the basin, precipitation and air temperature are the principal climatic variables controlling long term variability in runoff and streamflow (Brutsaert, 2005, Lemann et al., 2017). Furthermore, precipitation and temperature are among the most consistently available variables in both historical observations and climate projections, allowing direct comparison between station-based measurements and climate-model-derived datasets. Their widespread availability and clear physical interpretation make them suitable predictors for climate-informed flow forecasting.

Consequently, projected changes of climate are expected to alter runoff generation processes and river flow regimes (Mahmood et al., 2024, Gudmundsson et al., 2025). To assess future hydrological conditions, climate model simulations are increasingly used as inputs to hydrological forecasting models

(Mahmood et al., 2024). However, climate model outputs are typically provided as spatially distributed grid-based datasets, while most hydrological models have historically been developed using observations from point-based meteorological stations. This difference introduces an important challenge: determining how representative climate model grid cells are for local station conditions and identifying appropriate strategies for transferring station-based hydrological models to climate-model-derived inputs.

A monthly flow forecasting model has previously been developed for the hydrological station Vinalić in the Cetina River basin using precipitation and temperature observations from nearby meteorological stations (Berbić et al., 2026). To enable future applications of this modelling framework under climate change conditions, it is necessary to establish a relationship between locally observed meteorological variables and their climate-model-derived counterparts. The available observational datasets include records from the hydrological station Vinalić, meteorological station Knin, the climatological station Sinj, and the precipitation gauge Vinalić. These records are compared with daily climate model outputs available for the period 2015-2100 under several climate scenarios. Since only the period 2015-2022 is common to both observations and climate simulations, the present study focuses on this interval.

The primary objective of this study is to evaluate the correspondence between station-based and climate-model-derived precipitation and temperature data within the Cetina River basin. Specific objectives include:

- Comparison of observed and model-derived climatological characteristics;
- Identification of climate model grid cells most representative of station locations;
- Assessment of correlation strength and temporal lag relationships between station and spatial datasets;
- Investigation of alternative aggregation and modelling strategies for deriving representative climate model inputs.

The ultimate goal is to provide recommendations for selecting suitable climate-model-based predictors for future flow forecasting and to establish a methodological framework for transferring existing station-based hydrological models to climate projection datasets.

2 Methods

2.1 Available Data

A common period of daily observations (2015–2022) was extracted from the hydrological station Vinalić, the main meteorological station Knin, the climatological station Knin, and the precipitation gauge Vinalić. These datasets were compared with daily climate projections from three CMIP6 scenarios (SSP126, SSP245, and SSP585) and three global climate models (HadGEM3, IPSL, and MPI), available for the period 2015–2100 (DHMZ, 2025; C3S, 2025). All data processing, analyses, and visualizations were performed in Python using the Anaconda distribution and the pandas library (Van Rossum and Drake, 2009; Anaconda Inc., 2020; McKinney, 2010). Spatial visualizations were generated using the Cartopy and Matplotlib libraries (Met Office, 2010; Hunter, 2007). The existing ensemble supervised-learning monthly flow forecasting model for the Cetina River (Berbić et al., 2026) was developed using station-based precipitation and temperature observations together with discharge records from the Vinalić hydrological station. The model uses monthly mean, minimum and maximum temperature and monthly mean, accumulated and maximum precipitation as input variables together with 6 flow periodicity variables derived from mean monthly flow. Model development, calibration, and verification were performed using the common observation period 1951–2014 (with gap 1991-1997), while the period 2015–2022 was reserved for independent forecasting validation and for evaluating the relationship between station-based observations and climate-model-derived datasets. The present study focuses on establishing a methodological basis for augmenting these station-derived predictors with climate-model-derived datasets in future flow forecasting applications. Since precipitation and

temperature constitute the primary predictors of the existing flow forecasting model, the present study focuses on the corresponding climate-model-derived variables as a prerequisite for transferring the station-based forecasting framework to future climate projections (Table 1.).

Table 1. Available data and convention used for labeling variables

Data source	Variable	Daily variable (original temporal resolution)	Grid structure / cell size	Monthly aggregation variables	Unit	Period
HS Vinalić	Discharge	Q_d^V	/	$Q_{m,mean}^V, \hat{Q}_{m,mean}^V$	m³/s	1946–2022
MMS Knin	Temperature	T_d^K	/	$T_{m,mean}^K, T_{m,min}^K, T_{m,max}^K$	°C	1949–2022
	Precipitation	P_d^K		$P_{m,mean}^K, P_{m,acc}^K, P_{m,max}^K$	mm	
CS Sinj	Temperature	T_d^S	/	$T_{m,mean}^S, T_{m,min}^S, T_{m,max}^S$	°C	1949-2022
PS Vinalić	Precipitation	P_d^V	/	$P_{m,mean}^V, P_{m,acc}^V, P_{m,max}^V$	mm	1951–2022
HadGEM3 (SSP126, SSP245, SSP585)	Temperature	$T_d^{sc,HadGEM3,cell}$	5 x 7 1.875 x 1.25°	$T_{m,mean}^{sc,HadGEM3}, T_{m,min}^{Ksc,HadGEM3}, T_{m,max}^{Ksc,HadGEM3}$	°C	2015–2100
	Precipitation	$P_d^{sc,HadGEM3,cell}$	~150 x 140 km	$P_{m,mean}^{sc,HadGEM3}, P_{m,min}^{sc,HadGEM3}, P_{m,max}^{sc,HadGEM3}$	mm	2015–2100
IPSL (SSP126, SSP245, SSP585)	Temperature	$T_d^{sc,IPSL,cell}$	4 x 7 2.5 x 1.27°,	$T_{m,mean}^{sc,IPSL}, T_{m,min}^{sc,IPSL}, T_{m,max}^{Ksc,IPSL}$	°C	2015–2100
	Precipitation	$P_d^{sc,IPSC,cell}$	~200 x 140 km	$P_{m,mean}^{sc,IPSL}, P_{m,min}^{sc,IPSL}, P_{m,max}^{sc,IPSL}$	mm	2015–2100
MPI (SSP126, SSP245, SSP585)	Temperature	$T_d^{sc,MPI,cell}$	6 x 5 1.87 x 1.865°	$T_{m,mean}^{sc,MPI}, T_{m,min}^{sc,MPI}, T_{m,max}^{sc,MPI}$	°C	2015–2100
	Precipitation	$P_d^{sc,MPI,cell}$	~150 x 210 km	$P_{m,mean}^{sc,MPI}, P_{m,min}^{sc,MPI}, P_{m,max}^{sc,MPI}$	mm	2015–2100

Notes: sc – scenario

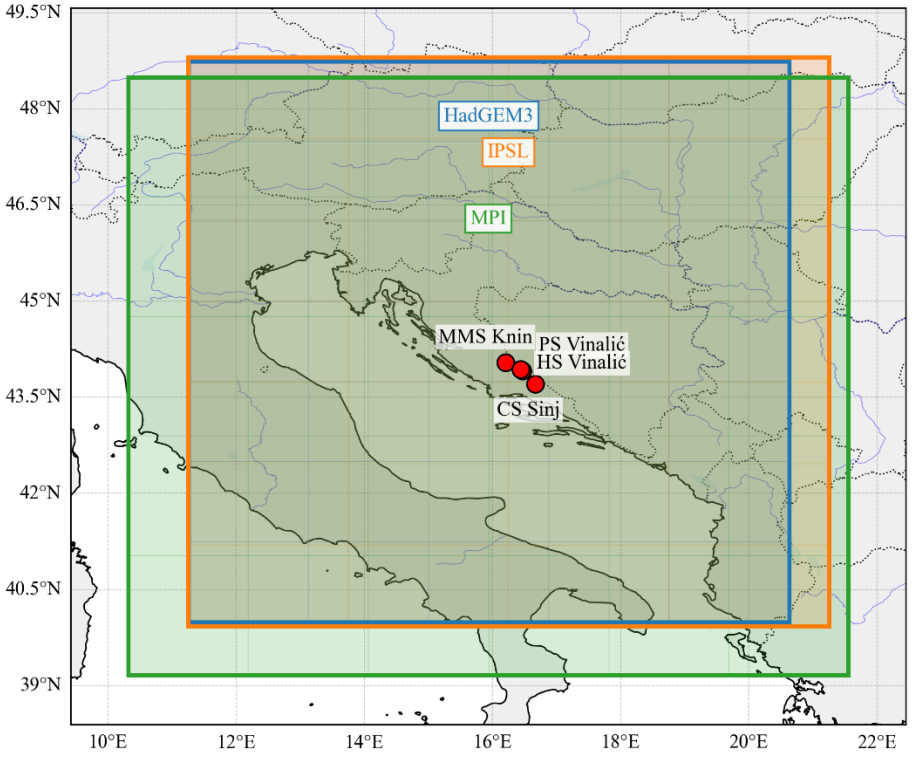


Figure 1. Stations and climate models coverage

2.2 Methodology

All analyses were provided for chronologically first 60 % of data (2015-09/2019), in order to preserve the rest of the data for subsequent calibration and verification of models. The methodology consisted of four main steps:

1. Comparison of observed station data and climate-model-derived data using monthly precipitation and temperature statistics.
2. Evaluation of climate model outputs regarding observed data based on correlation coefficients (R), bias, root mean square error (RMSE), annual means, and cumulative precipitation characteristics. One scenario (SSP245) and one climate model (HadGEM3) were selected for further analyses.
3. Lagged-correlation analysis between station observations and climate-model grid cells. Daily correlations were evaluated for temporal lags from -60 to +60 days, while monthly correlations were evaluated for lags from -12 to +12 months. For each grid cell, the temporal lag of the most significant matching with observations was identified based on the highest absolute correlation coefficient ($|r|$), while the original sign of the correlation coefficient was retained and reported.
4. Identification of the climate-model grid cells exhibiting the strongest relationships with precipitation from station observations. Monthly climatological characteristics of the selected cells were compared with station observations and analysed as potential predictors for future flow forecasting applications. The most representative cells are selected based on the highest composite matching score defined as:

$$score = r - |bias - 1| - \frac{RMSE}{\bar{P}_{obs} + 10^{-9}} \quad (1)$$

where r is the correlation coefficient, bias is the ratio between modelled and observed values, $RMSE$ is the root mean square error of grid cell values, $\bar{P}_{obs}$ is the mean observed value, while 10^{-9} is a small constant preventing division by zero. Higher score values indicate better overall agreement, while a value equal to 1 represents the ideal matching between grid-cell values and observations.

3 Results and Discussion

3.1 Overall long term aggregated statistics

A comparison between station observations and CMIP6 precipitation data (Fig. 2, Table 2) over the common period 2015-2019 indicated that the IPSL model provided the best overall agreement with observed precipitation dynamics. For cumulative monthly precipitation, IPSL achieved the highest correlation coefficients at both PS Vinalić (R = 0.84) and MMS Knin (R = 0.93), while also yielding the lowest monthly RMSE values (48.1 mm and 58.7 mm, respectively). Furthermore, the annual mean precipitation simulated by IPSL (843 mm) was within the range of station observations (731 mm at PS Vinalić and 996 mm at MMS Knin).

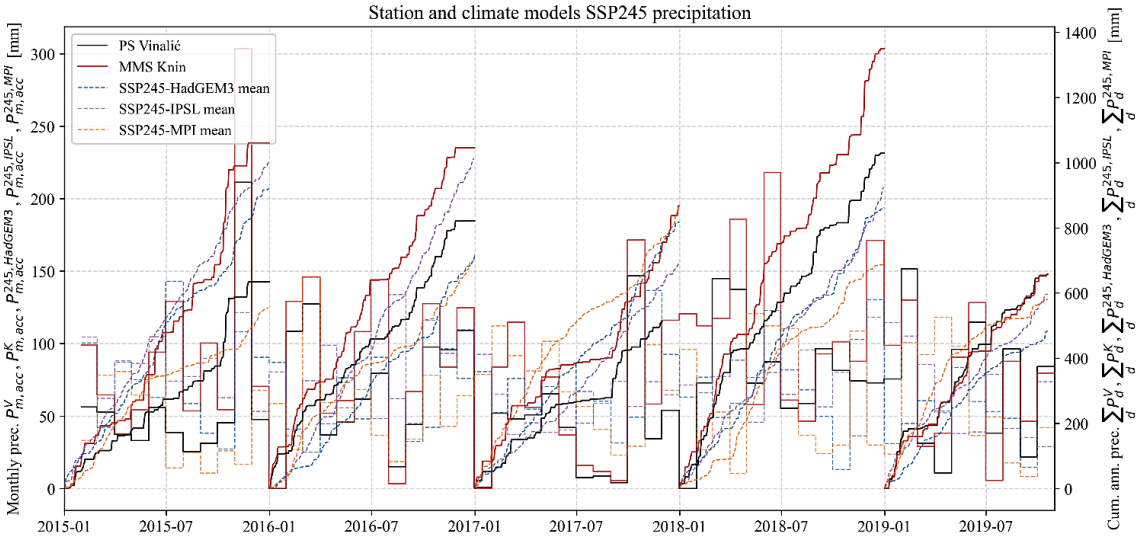


Figure 2. Accumulated monthly precipitation and cumulative annual precipitation – SSP245

Table 2. Comparison of precipitation between station observations and climate-model values

		Statistics			n	R	bias	RMSE	Obs. Mean	Mod. Mean	Obs. Ann. Mean	Mod. Ann. Mean
Station	Dataset	Spat.	Temp.	Type	[/]	[/]	[mm]	[mm]	[mm]	[mm]	[mm]	[mm]
PS Vinalić	HadGEM 3		acc	mon	58	0.02	2.5	51.7	63.0	65.6	731.1	760.6
			acc	cum	58	0.79	-10.9	153.7	419.9	409.0		
			mean	mon	57	0	0.1	1.7	2.1	2.2		
			max	mon	57	0.14	-3.3	14.5	21.9	18.6		
	IPSL		acc	mon	58	0.14	9.7	48.1	63.0	72.7		843.3
			acc	cum	58	0.84	30.6	147.9	419.9	450.6		
			mean	mon	57	0.13	0.3	1.6	2.1	2.5		
			max	mon	57	0.29	-3.5	13.4	21.9	18.4		
	MPI		acc	mon	58	-0.05	-4.3	56.8	63.0	58.7		680.9
			acc	cum	58	0.75	-16.4	159.6	419.9	403.5		
			mean	mon	57	-0.02	-0.2	1.9	2.1	2.0		
			max	mon	57	0.07	-8.8	16.6	21.9	13.1		
MMS Knin	HadGEM 3	Cells	acc	mon	58	0.26	-20.3	59.9	85.9	65.6	996.3	760.6
		mean	acc	cum	58	0.9	-146.3	206.0	555.2	409.0		
			mean	mon	58	0.24	-0.6	2.0	2.8	2.2		
			max	mon	58	0.26	-10.0	20.0	28.6	18.5		
	IPSL		acc	mon	58	0.2	-13.2	58.7	85.9	72.7		843.3
			acc	cum	58	0.93	-104.7	163.1	555.2	450.6		
			mean	mon	58	0.18	-0.4	1.9	2.8	2.5		
			max	mon	58	0.33	-10.2	19.6	28.6	18.4		
	MPI		acc	mon	58	-0.07	-27.2	73.1	85.9	58.7		680.9
			acc	cum	58	0.76	-151.8	260.0	555.2	403.5		
			mean	mon	58	-0.06	-0.9	2.4	2.8	2.0		
			max	mon	58	-0.03	-15.3	24.2	28.6	13.3		

Notes: spat – spatial, temp – temporal, perc. – percentage, obs. – observed, mod. – climate model output, ann. – annual, acc – accumulated, max – maximum, mon – monthly, cum – cumulative

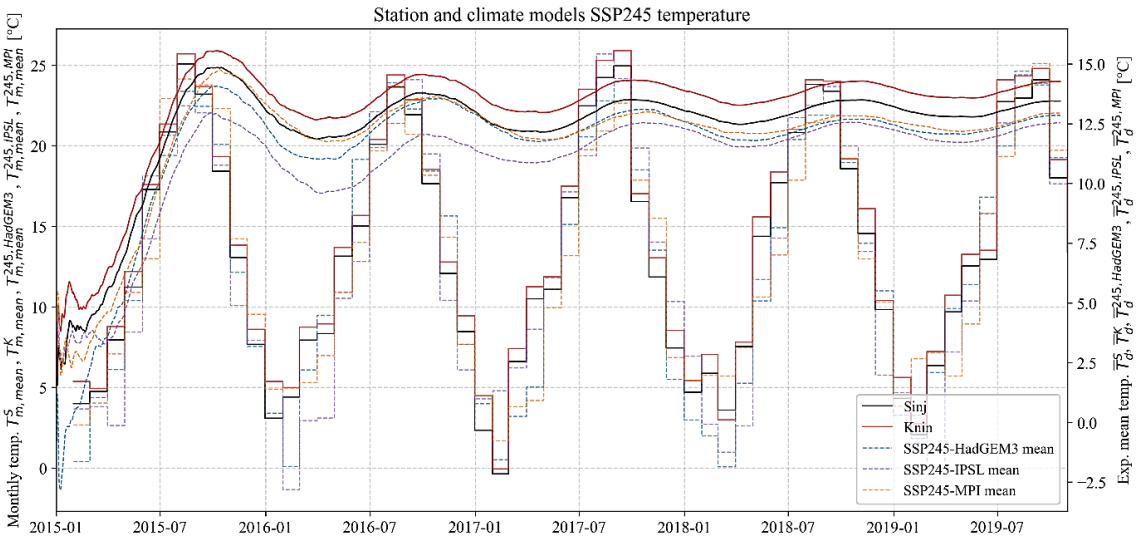


Figure 3. Mean monthly and expanding mean temperature – SSP245

For temperature (Fig. 3, Table 3), all evaluated CMIP6 models reproduced the observed seasonal cycle well, with correlation coefficients generally exceeding 0.90. HadGEM3 and MPI showed the best overall agreement with observations, exhibiting lower bias and RMSE values than IPSL. Both HadGEM3 and MPI reproduced the observed seasonal cycle very well, while IPSL showed systematically larger biases and errors. MPI exhibited slightly lower biases for several temperature statistics, while HadGEM3 generally achieved the highest correlation coefficients and comparable RMSE values.

Table 3. Comparison of temperature between station observations and climate-model values

			Statistics		n	R	bias	RMSE	Obs. Mean	Mod. Mean
Station	Dataset	Spat.	Temp.	Type	[/]	[/]	[°C]	[°C]	[°C]	[°C]
CS Sinj	HadGEM 3		mean	mon	57	0.97	-0.61	2.09	13.41	12.80
			min	mon	57	0.91	-0.76	3.63	7.99	7.23
			max	mon	57	0.92	-1.16	3.19	18.74	17.57
	IPSL		mean	mon	57	0.95	-0.95	2.69	13.41	12.45
			min	mon	57	0.93	-1.39	3.50	7.99	6.60
			max	mon	57	0.90	-1.41	3.46	18.74	17.33
	MPI		mean	mon	57	0.95	-0.51	2.36	13.41	12.89
			min	mon	57	0.92	-1.03	3.46	7.99	6.96
			max	mon	57	0.90	-0.74	3.15	18.74	18.00
MMS Knin	HadGEM 3	Cells	mean	mon	57	0.97	-1.42	2.48	14.21	12.80
		mean	min	mon	57	0.90	-1.22	3.94	8.44	7.23
			max	mon	57	0.93	-2.18	3.54	19.75	17.57
	IPSL		mean	mon	57	0.95	-1.76	3.03	14.21	12.45
			min	mon	57	0.92	-1.84	3.86	8.44	6.60
			max	mon	57	0.91	-2.42	3.90	19.75	17.33
	MPI		mean	mon	57	0.95	-1.32	2.69	14.21	12.89
			min	mon	57	0.91	-1.48	3.68	8.44	6.96
			max	mon	57	0.90	-1.75	3.39	19.75	18.00

Notes: spat – spatial, temp – temporal, perc. – percentage, obs. – observed, mod. – climate model output, ann. – annual, min - minimum, max – maximum, mon – monthly

Although IPSL showed slightly better agreement with observations for precipitation, HadGEM3 demonstrated consistently good performance across both precipitation and temperature variables. For temperature, HadGEM3 achieved the highest correlation coefficients, RMSE values comparable to those of MPI, and lower biases than IPSL. Considering the objective of selecting a single climate model for the subsequent analyses, HadGEM3 was chosen as the most balanced overall performer across the evaluated hydroclimatic variables. A more comprehensive intercomparison of climate models is beyond

the scope of the present study.

3.2 Lagged correlation analysis

3.2.1 Precipitation

Daily precipitation correlations between SSP245-HadGEM3 grid cells and station observations were consistently weak across the entire domain, with all positive correlation coefficients rarely exceeding 0.10 (Fig. 4). Even with consideration of time lags, no grid cell exhibited a strong relationship with the observed station precipitation. This result reflects the highly localized and stochastic nature of precipitation processes, which are not adequately represented at the spatial scale of individual climate-model cells.

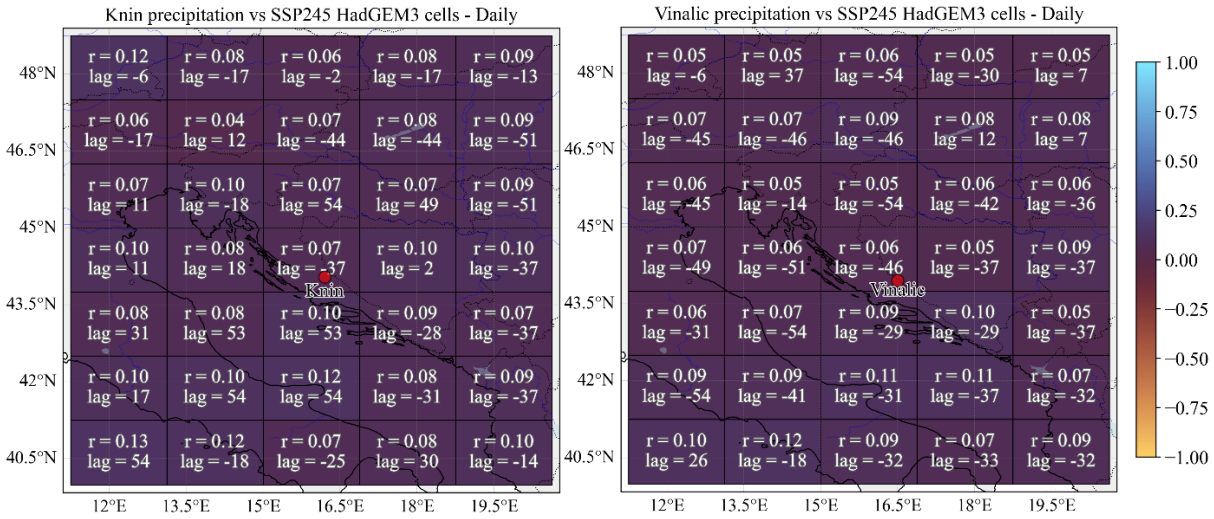


Figure 4. Lagged correlations of total daily precipitation – SSP245, HadGEM3 – MMS Knin and PS Vinalić

In contrast to the daily analysis, monthly precipitation exhibited a recognizable spatial structure, with the strongest correlations consistently occurring in grid cells located close to and south-west of the corresponding stations (Fig. 5). Furthermore, the optimal temporal lag varied considerably across the grid cells for both stations, ranging from -11 to 12 months. Smaller lag values (-1) were generally observed in the southern cells, while larger positive or negative lags (-8 and 4) occurred in the northern cells.

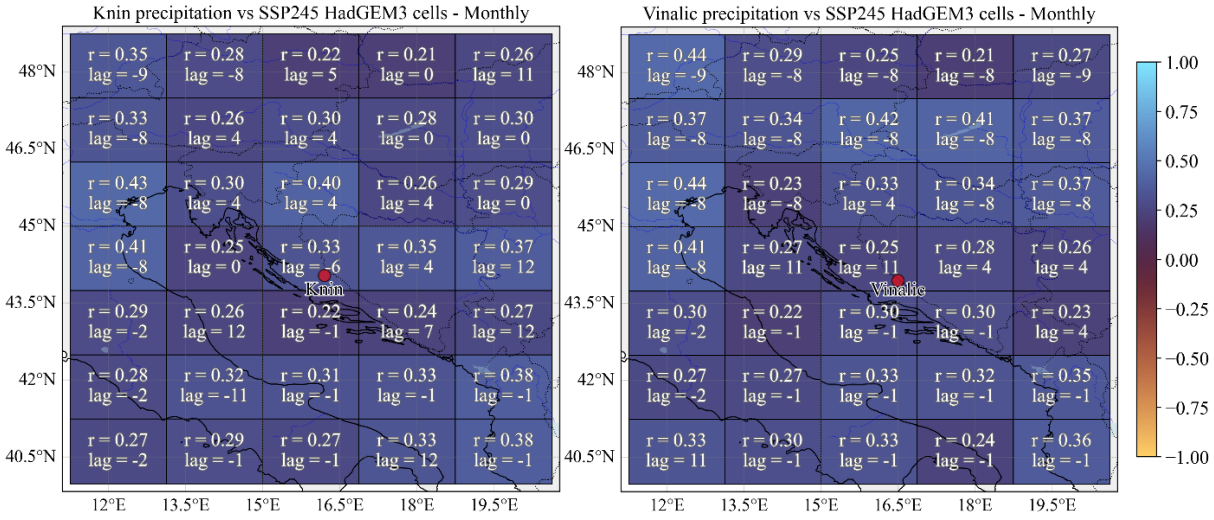


Figure 5. Lagged correlations of total monthly precipitation – SSP245, HadGEM3 – MMS Knin and PS Vinalić

This spatial pattern suggests a certain degree of consistency in the lag structure. Aggregation to the monthly scale did not fully resolve the temporal mismatch in precipitation occurrence, but it improved statistical consistency between station observations and climate-model outputs.

3.2.2 Temperature

Temperature exhibited substantially stronger relationships with climate model outputs than precipitation. Daily temperature correlations (Fig. 6) exceeded 0.80 across the entire domain, with lags mostly equal to zero or several days preceding the station data. Unlike precipitation, the spatial variability of correlations was limited, indicating a coherent regional temperature signal well represented by the climate model.

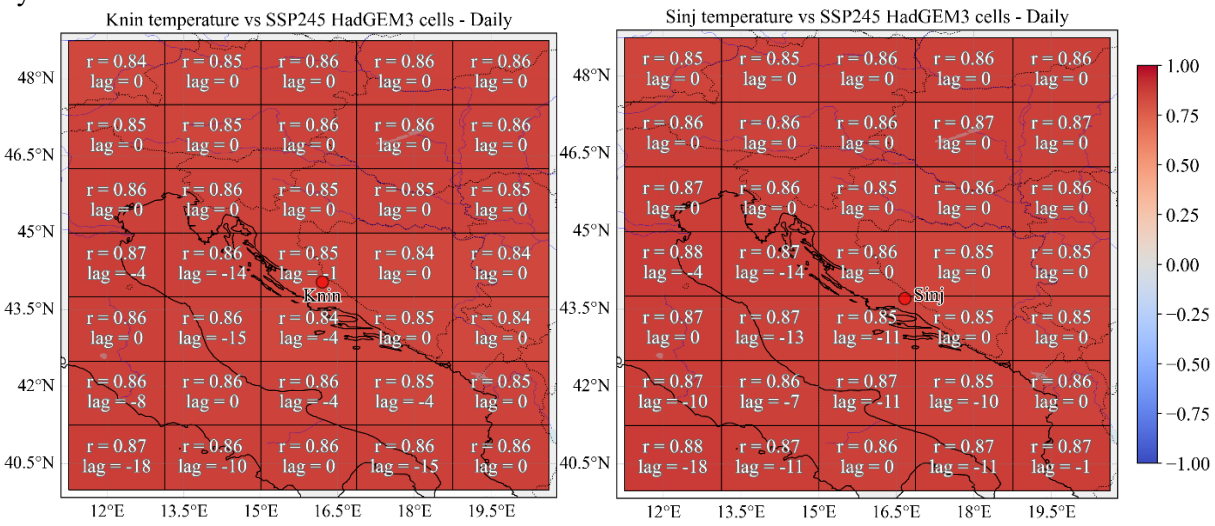


Figure 6. Lagged correlations of mean daily temperature – SSP245, HadGEM3 – MMS Knin and CS Sinj

At the monthly scale (Fig. 7), correlation exceeded 0.95 for all grid cells and both stations, with optimal lags mostly equal to 0 and, in some cases +12 months, demonstrating that climate-model temperature fields successfully reproduce the observed seasonal cycle, while the dominance of zero-lag relationships suggests good agreement in the temporal evolution of station and model temperatures.

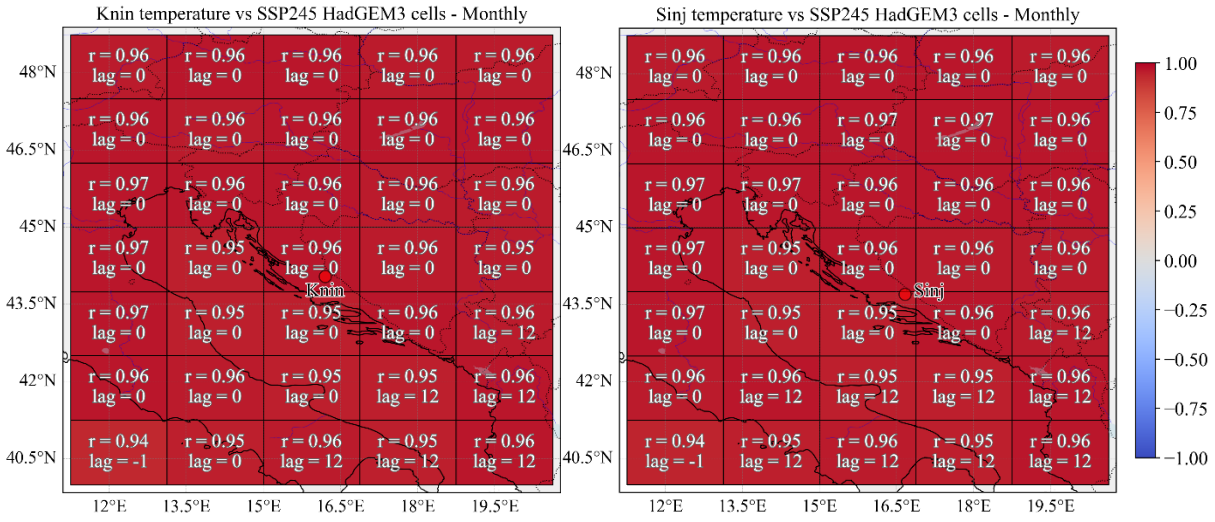


Figure 7. Lagged correlations of mean monthly temperature – SSP245, HadGEM3 – MMS Knin and CS Sinj

3.3 Monthly precipitation statistics for selected cells

The five selected cells for each station, identified according to the highest scores (equation 1) between monthly station observations and corresponding climate-model precipitation, reproduced the overall precipitation regime reasonably well (Fig. 8, Table 4). For MMS Knin, the mean annual precipitation of the five selected cells was 892.5 mm compared to 996.3 mm observed at the station, while for PS Vinalić the corresponding values were 687.5 mm and 731.1 mm, respectively. Although differences remained in individual monthly values and annual extremes, the selected-cell averages preserved the general seasonal behavior and long-term precipitation magnitude. The selected cells also reproduced the annual variability reasonably well, with annual standard deviations of 251.0 mm and 166.4 mm compared to 256.0 mm and 199.8 mm observed at MMS Knin and PS Vinalić, respectively. This indicates that the selected cells capture not only the mean precipitation regime but also a substantial part of the interannual variability. The average of the five selected cells provides a robust representation of the regional precipitation regime; however, for MMS Knin, cell K2 individually exhibits precipitation statistics closer to the observed station values.

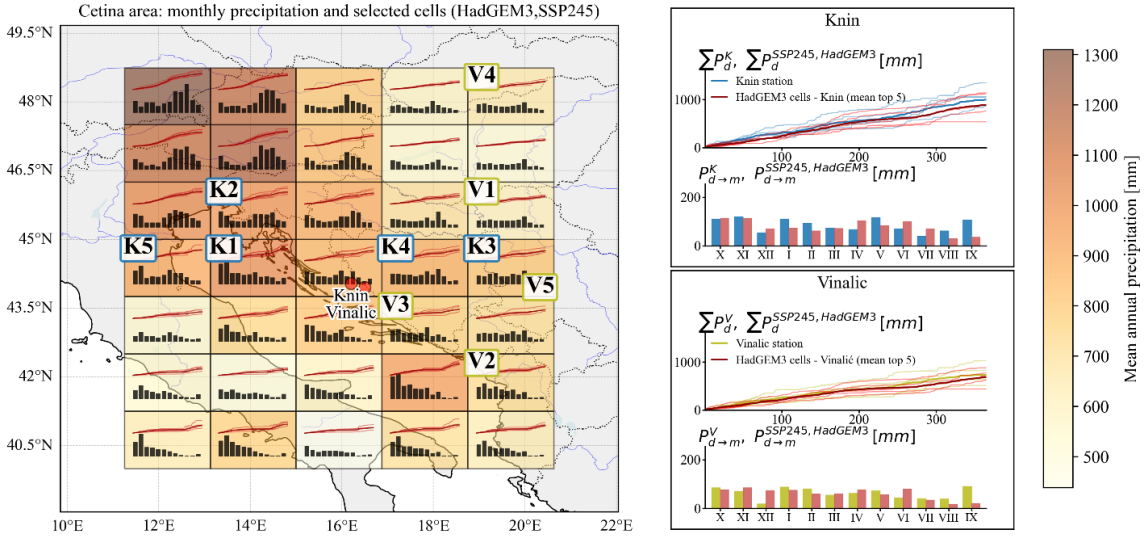


Figure 8. Precipitation characteristics of 5 selected top cells – SSP245, HadGEM3 – MMS Knin and PS Vinalić

Table 4. Comparison of precipitation between station observations and climate-model values

Dataset	n cells	Monthly mean [mm]	Monthly min [mm]	Monthly max [mm]	Annual mean [mm]	Annual min [mm]	Annual max [mm]	Annual standard deviation [mm]
Knin	/	85.9	40.5	120.5	996.3	658.6	1349.7	256.0
5 cells	5	77.5	30.4	114.4	892.5	535.1	1140.2	251.0
K1	1	86.5	21.7	180.6	983.5	513.7	1293.6	313.0
K2	1	82.3	44.9	132.6	958.9	558.6	1357.1	326.9
K3	1	67.9	22.4	110.0	785.5	545.6	1042.8	186.5
K4	1	74.0	20.1	126.0	856.0	578.3	1172.1	227.9
K5	1	76.6	25.9	153.2	878.7	479.4	1272.7	280.7
Vinalić	/	62.4	19.1	91.0	731.1	512.9	1029.6	199.8
5 cells	5	59.9	17.5	85.3	687.5	438.6	882.0	166.4
V1	1	51.4	18.3	91.9	593.6	429.0	715.6	115.1
V2	1	61.0	5.1	128.0	690.0	409.9	832.5	164.8
V3	1	64.1	8.9	118.5	733.7	449.7	1007.2	241.2
V4	1	55.3	25.4	85.8	634.8	358.6	812.2	167.9
V5	1	67.9	22.4	110.0	785.5	545.6	1042.8	186.5

3.4 Lagged correlations of precipitation and flow

Correlations between climate-model variables and discharge were generally stronger at the monthly than at the daily scale, particularly for precipitation (Fig. 9 and 10). As the analysis considered

the absolute magnitude of correlation, the reported results correspond to lags associated with the maximum absolute correlation coefficient ($|r|$). Daily precipitation exhibited a weak relationship with discharge (r = -0.15 to 0.17) and a wide range of optimal lags. At the monthly scale, correlations were substantially stronger, predominantly positive but with several negative values, while optimal lags ranged from -8 to +11 months.

Daily temperature showed consistently negative correlations with discharge (approximately r = -0.5), with relatively consistent optimal lags, mostly between 24 and 34 days. In accordance with the daily scale, at the monthly scale strong negative correlations ($|r| > 0.66$) occurred across the entire domain, all with a lag of +1, except one with +12. The relationship between station discharge and model temperature is consistently inverse across the grid cells, indicating pronounced seasonal behavior of both variables. These findings suggest that monthly climate-model variables may serve as suitable predictors for future discharge forecasting and climate-change impact assessments.

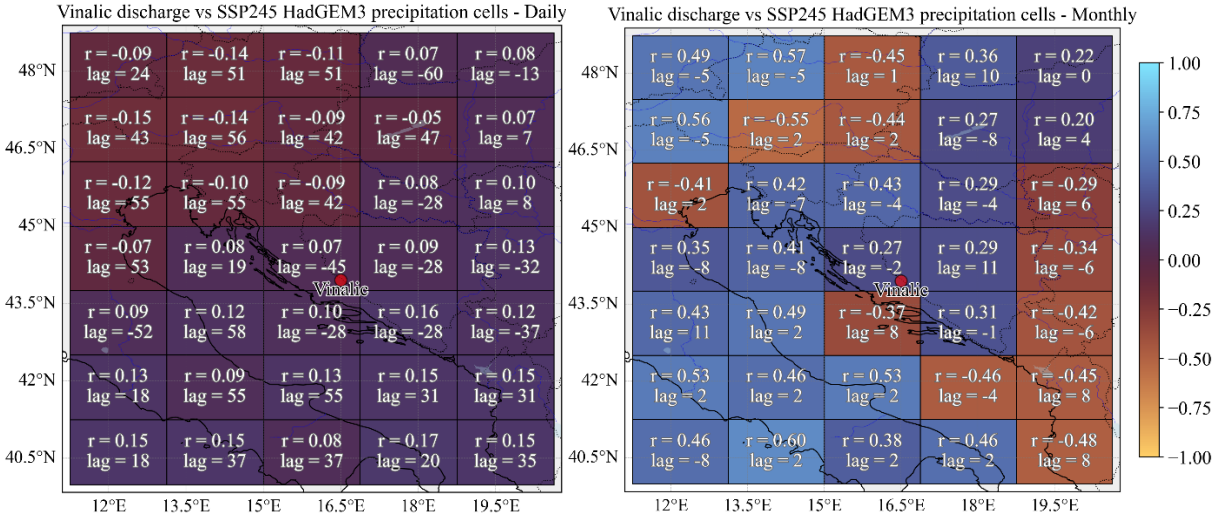


Figure 9. Lagged correlations of total precipitation (SSP245, HadGEM3) and mean flow (HS Vinalić) – daily (left), monthly (right)

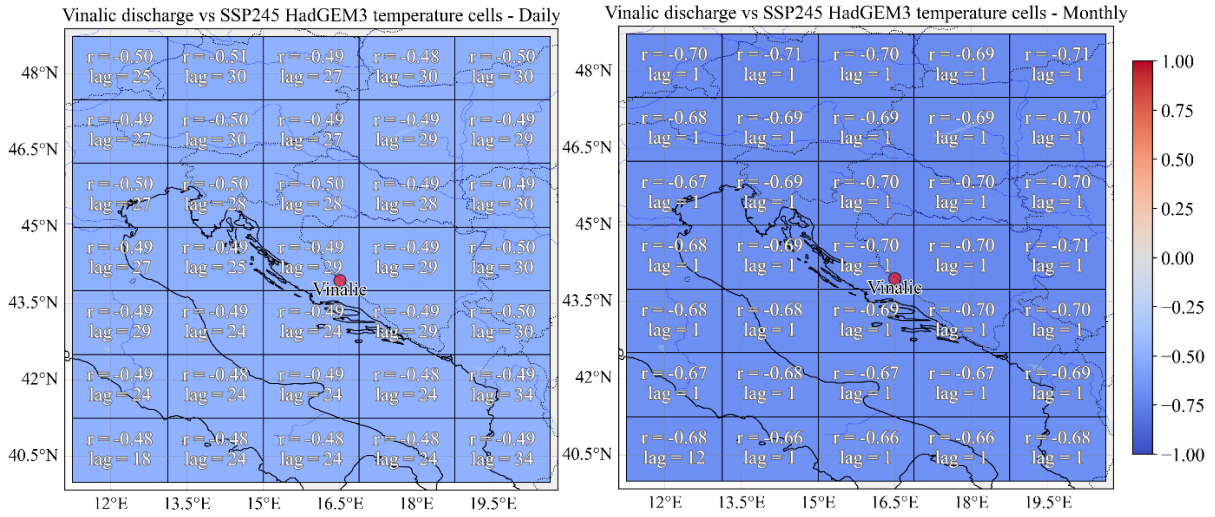


Figure 10. Lagged correlations of mean temperature (SSP245, HadGEM3) and mean flow (HS Vinalić) – daily (left), monthly (right)

It should be noted that the common observation-climate model period available for this study is relatively short, and only part of this period (2015-2019) was used in the present analyses. The remaining data were intentionally reserved for the future calibration and verification.

4 Conclusion

The results indicate that future work should primarily focus on identifying climate-model grid cells that best represent local station conditions, potentially supplemented by additional statistical techniques for establishing relationships between station observations and climate-model-derived precipitation and temperature data. Daily-scale analyses revealed relatively weak correlations, particularly for precipitation, suggesting that direct transfer of daily climate-model outputs to station conditions may be challenging. Several alternative approaches for integrating climate-model data into the existing flow forecasting framework can be considered:

1. Daily station-variable reconstruction approach - Daily station precipitation and temperature could be reconstructed from daily climate-model outputs and subsequently aggregated to monthly values. These reconstructed station series would then be used as inputs for flow forecasting. The main advantage of this approach is the large amount of available daily data. However, monthly predictor variables are not modelled directly.
2. Monthly station-variable reconstruction approach - Monthly station precipitation and temperature could be estimated directly from monthly (or aggregated daily) climate-model data and then used for flow forecasting. This approach benefits from the strong relationship between flow and station observations, as well as the generally satisfactory correspondence between station and climate-model data. Furthermore, the existing flow forecasting model has been calibrated and validated over a much longer historical period. The main limitation is the relatively short common period available for developing station–climate transfer relationships.
3. Representative grid-cell substitution approach - Selected climate-model grid cells could be used directly as substitutes for station observations. This approach is simple and operationally attractive. However, the physical and statistical justification for replacing station measurements with grid-cell values requires further investigation. In addition, the available common period remains relatively short.
4. Direct climate-to-flow modelling approach - Flow could be modelled directly from climate-model precipitation and temperature outputs without intermediate reconstruction of station variables. Preliminary results suggest that monthly climate-model variables exhibit meaningful relationships with observed flow. Nevertheless, the limited overlap period between climate-model outputs and observed discharge data would result in a relatively short calibration and validation dataset.

Based on the present results, the monthly station-variable reconstruction approach appears to be the most suitable for monthly flow forecasting, as it provides satisfactory agreement between climate-model and station data. The representative grid-cell substitution approach may also provide a practical alternative, particularly where station observations are unavailable. Overall, all four approaches appear scientifically relevant and potentially useful. A systematic comparison of their predictive performance and practical applicability represents an important direction for future research.

References

Anaconda Inc. 2020 Anaconda Distribution Documentation. Anaconda Inc., Austin, TX, USA.
Berbić, J., Ocvirk, E. and Gilja, G. 2026 Long-term supervised ensemble forecasting of monthly flows of Cetina river, Croatia, *Water* 18(13), 1641.
Brutsaert W. 2005 Hydrology: An Introduction. Cambridge University Press, Cambridge, UK.
Copernicus Climate Change Service (C3S) 2025 Climate Data Store (CDS). CMIP6 Climate Projections. European Centre for Medium-Range Weather Forecasts (ECMWF), Reading, UK.
Croatian Hydrological and Meteorological Service (DHMZ) 2025 Hydrological Database HIS 2000. DHMZ, Zagreb, Croatia.
Croatian Hydrological and Meteorological Service (DHMZ) 2025 Relational Meteorological Database. DHMZ, Zagreb, Croatia.
Gudmundsson, L., Brunner, M.I., Döll, P., Fluet-Chouinard, E., Frolova, N., Gosling, S.N., Hirabayashi, Y., Kireeva, M.B., Liu, X., Müller Schmied, H., Magritskiy, D., Slater, L.J., Stein, L., Tramblay, Y.,

Wang, K., Wasko, C., Yamazaki, D. and Zhou, X. 2025 Past and future change in global river flows. *Nature Reviews Earth & Environment* 7(1), 7–23. https://doi.org/10.1038/s43017-025-00745-z
Hunter J.D. 2007 Matplotlib: A 2D graphics environment. *Computing in Science & Engineering* 9(3), 90–95.
Lemann T., Roth V., Zeleke G., Subhatu A. T., Kassawmar T. and Hurni H. 2017 Impact of precipitation and temperature changes on hydrological processes in a tropical catchment in the Lake Tana Basin, Ethiopia. *Hydrological Sciences Journal* 62(13), 2130–2147.
Loucks D.P. and van Beek E. 2017 Water Resource Systems Planning and Management: An Introduction to Methods, Models and Applications. Springer, Cham, Switzerland.
Mahmood, S., Khan, A.U., Babur, M., Ghanim, A.A.J., Al-Areeq, A. M., Khan, D., Najeh, T., Gamil, Y. 2024 Isolating land use and climate change impact on river runoff. *Frontiers in Environmental Science* 12, 1338512.
McKinney W. 2010 Data structures for statistical computing in Python. In *Proceedings of the 9th Python in Science Conference*, Pasadena, CA, USA, 28 June–3 July, pp. 51–56.
Met Office 2010 Cartopy: a cartographic python library with a Matplotlib interface. UK Met Office, Exeter, Devon. Available at: https://scitools.org.uk/cartopy
Van Rossum G. and Drake F.L. 2009 Python 3 Reference Manual. CreateSpace, Scotts Valley, CA, USA.
Wurbs, R.A. and James, W.P. 2002 Water Resources Engineering. Prentice Hall, Upper Saddle River, New Jersey, USA.

EARLY WARNING SYSTEM BASED ON PRE-SIMULATED SCENARIOS FOR COMPOUND FLOODING: APPLICATION TO THE RJEČINA RIVER, RIJEKA

Marta Marija GRŽIĆ [1*], Nevenka OŽANIĆ [1], Nino KRVAVICA [1]

[1] *University of Rijeka, Faculty of Civil Engineering, Croatia*

E-mail: mmgrzic@gradri.uniri.hr

E-mail: nozanic@uniri.hr

E-mail: nino.krvavica@uniri.hr

[*] *Corresponding author*

Abstract

Compound flooding in coastal rivers can be a result of the interaction between river discharge and sea level, leading to greater impacts than those associated with either driver acting independently. In such environments, early warning systems should account for the main flood drivers and their interaction. This study presents an impact-based early warning system for compound flooding in the lower reach of the Rječina River, Croatia. A bivariate statistical analysis of extreme river discharge and storm surge events was performed to derive representative compound flood scenarios, which were subsequently simulated using the HEC-RAS numerical model. Based on the simulated flood characteristics, a two-level warning system was developed to represent impacts on hydraulic structures and the onset of flooding. The results show that elevated sea levels considerably reduce the river discharge required to trigger hazardous conditions, demonstrating the importance of considering the interaction between the two flood drivers. In addition to defining warning thresholds, the proposed methodology enables rapid estimation of flood extent and inundation volume through interpolation of pre-simulated scenarios. The presented framework provides a practical tool for impact-based flood risk management and can be transferred to other small coastal rivers exposed to compound flooding.

Key words

Rječina River, Compound Flooding, Numerical Modeling, Early Warning System

1 Introduction

Coastal low-lying areas are among the most valuable and densely populated regions worldwide. Approximately 15% of the global population lives within 5 km of the shoreline, occupying only 4% of the Earth's land surface (Cosby et al., 2024). These areas are particularly vulnerable to flooding due to their high population density and exposure to multiple flood drivers, including high river discharges, elevated sea levels, intense precipitation, and extreme waves (Green et al., 2025). In coastal regions, a single meteorological event, such as an atmospheric low-pressure system, can simultaneously or sequentially intensify several of these drivers, potentially resulting in an event known as compound flooding. When multiple flood drivers are generated by the same atmospheric forcing, neglecting their interactions and dependence structure may lead to an underestimation of flood hazard and risk (Ward et al., 2018).

Climate change is expected to increase the frequency and intensity of extreme events, while interactions among multiple climatic and non-climatic risk drivers will result in more frequent compound and cascading events. This will amplify overall risks to human and natural systems, making them more complex and difficult to manage (Calvin et al., 2023). Mean sea level rise (MSLR) is one of the most widely used indicators of climate change impacts in coastal compound flood studies because of its direct

influence on coastal water levels and flood extents (Corvaro et al., 2026; Ghanbari et al., 2021; Liu et al., 2025; Moftakhari et al., 2017; Wang et al., 2025).

In recent years, extensive research has substantially advanced the understanding of compound flooding processes, drivers, and impacts (Green et al., 2025). However, further efforts are needed to translate these scientific advances into practical risk management strategies, including forecasting, early warning, and adaptation measures that enhance the resilience of coastal communities to compound flood events and climate change (Gomez Rave et al., 2025).

Although flood risk cannot be completely eliminated, it can be effectively managed and mitigated through appropriate structural and non-structural measures (United Nations Office for Disaster Risk Reduction (UNDRR), 2015). To enhance preparedness and support timely response during flood events, early warning systems (EWS) have an important role in modern flood risk management (Gomez Rave et al., 2025). Traditionally, EWSs have relied on rainfall forecasting or monitoring of water levels and river discharges at hydrological stations. However, such information often provides limited insight into the potential extent of flooding and its impacts, making it difficult for decision-makers to take appropriate actions (Najafi et al., 2024). To address this limitation, modern EWSs usually rely on hydrodynamic models to predict flood inundation extent, identify areas at risk, and provide information for emergency response and flood risk management (Metallinos et al., 2026; Papadimitriou et al., 2024; Pumo et al., 2024).

The aim of this study is to develop a simple, yet effective, impact-based early warning system to support emergency response and flood risk management in the lower reach of the Rječina River in Croatia. A bivariate statistical analysis of extreme storm surge and river discharge was performed to derive representative compound flooding scenarios, which were subsequently simulated using the HEC-RAS numerical model (Brunner, 2024). Based on the simulated flood extent and water depth, a two-level warning system was proposed to represent impacts on hydraulic structures and the flood occurrence. In addition, the simulation results were used to develop interpolation-based relationships between river discharge, sea level, and flood impacts, enabling rapid estimation of flood extent and flood volume for a wide range of compound flood conditions.

This study presents an impact-based early warning system specifically developed for compound flooding in the lower Rječina River. By explicitly accounting for the interaction between river discharge and sea level, the proposed methodology enables the identification of hazardous conditions that may not be adequately represented by single-driver approaches and provides rapid estimates of inundation characteristics for a broad range of compound flood scenarios.

2 Study area

The focus of this study is the lower reach of the Rječina River. Rječina is a small coastal river located in the northern Adriatic coast of Croatia (Figure 1). The 18 km long river flows through a narrow flysch valley in its upper and middle reaches before entering an alluvial plain within the City of Rijeka (Jagodnik and Bernat Gazibara, 2025). The river ultimately discharges into the Adriatic Sea, a semi-enclosed basin connected to the Mediterranean Sea through the Strait of Otranto.

The lower Rječina River reach area is vulnerable to compound flooding resulting from the joint occurrence of high river discharges and elevated sea levels. Extreme discharges in the Rječina River are typically associated with intense precipitation events within the catchment, often driven by low-pressure systems. The same meteorological conditions can simultaneously generate storm surges, the non-tidal residual between the total sea water level and predicted tides. As these flood drivers may be influenced by the same atmospheric processes, their possible interaction and dependence structure needs to be assessed to determine the possible compound flooding hazard and associated risks.

In addition to extreme storm surges and river discharges, climate change is expected to further increase

flood hazard in the lower Rječina River area through mean sea level rise. According to the Climate Change Adaptation Strategy in the Republic of Croatia for the Period to 2040 with a View to 2070, the mean sea level along the Croatian coast is projected to rise by 32-65 cm by 2100 (Ministarstvo zaštite okoliša i energetike, 2020).



Figure 1. Study area of the lower reach of the Rječina River in Rijeka, Croatia, showing the numerical model domain, the Rječina River course, and the locations of the hydrological stations used in this study.

3 Methods

3.1 Data Preprocessing

The developed EWS is based on measured river discharges and sea levels. Observed hourly river discharge data for the period 2001-2021 were obtained from the Tvornica Papira hydrological station, located upstream of the tidal influence zone (Figure 1). Observed sea-level data were acquired from the Bakar tide gauge station, the nearest station with a sufficiently long and publicly available record (1950–2020) (Međugorac et al., 2022, 2025). The total sea level time series was decomposed into tidal components and non-tidal residual using UTide (Codiga, 2011). The non-tidal residual was calculated as a difference between the observed sea level and the predicted tidal signal and is hereafter referred to as storm surge. Additionally, hourly water level observations from the Titov Trg station (Figure 1) recorded during the high-discharge event of November 2016 were used for numerical model calibration and validation.

To characterize the dependence structure and joint occurrence probability of high river discharges and extreme storm surges, a bivariate probability analysis was conducted using the copula method and the MultiHazard approach (Jane et al., 2026). The resulting 5-, 10-, 20-, 50-, 100-, 200-, and 500-year joint return period isolines served as the basis for selecting the representative pairs of river discharge and storm surge used for the boundary conditions in the numerical model.

According to the Croatian Climate Change Adaptation Strategy, the mean sea level along the Croatian coast is projected to rise by 32–65 cm by 2100. Based on this range, a deterministic mean sea level rise scenario of +0.60 m was adopted for the study area. This scenario was implemented as a uniform vertical shift of the sea-level boundary condition while preserving the present-day dependence structure between

storm surge and river discharge. Although this simplified approach does not account for uncertainties associated with future climate projections or potential changes in storm surge characteristics, it provides a practical framework for assessing the influence of mean sea level rise on compound flooding.

To incorporate this scenario into the joint probability analysis, the joint return period isolines were shifted upward by 0.60 m along the sea level axis, while the river discharge component remained unchanged. The original and sea level rise-adjusted isolines were subsequently discretized using a regular grid with intervals of 20 m³/s for river discharge and 0.2 m for sea level (Figure 2), resulting in a total of 146 representative river discharge–sea level pairs used as boundary conditions for the numerical simulations.

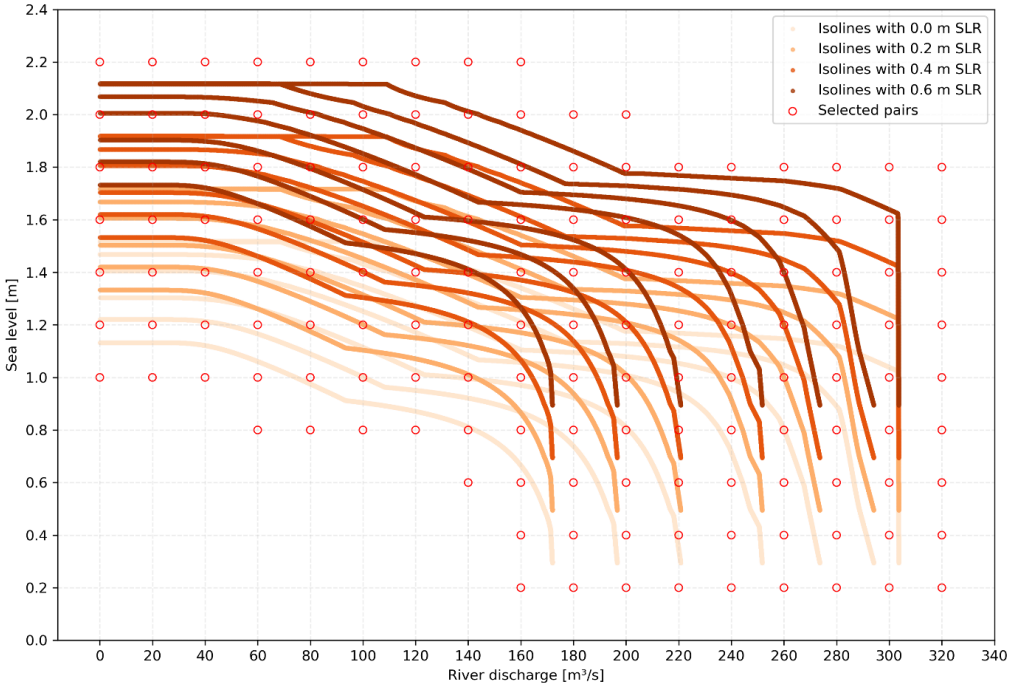


Figure 2. The selected river discharge-sea level pairs for numerical simulations based on the joint return period isolines under present and future sea level conditions.

Besides hydrological and sea level data, spatial datasets were used to define the model topography, land cover, and land use. The digital terrain model (DTM) was generated from publicly available LiDAR data provided by the Croatian State Geodetic Administration (DGU) with a spatial resolution of 1 m. Since the LiDAR dataset did not include bathymetric information, surveyed cross-sections of the Rječina River obtained within the VEPAR scientific project ("VEPAR," 2014) were integrated into the terrain model to ensure an accurate representation of the river channel geometry. The integrated terrain model was subsequently inspected and corrected where necessary using the original LiDAR point cloud. Land cover and land use information were derived from the Urban Atlas dataset povided by the Copernicus Land Monitoring Service ("Urban Atlas Land Cover/Land Use 2018 (vector), Europe, 6-yearly, Jul. 2021," n.d.), which includes 27 land cover classes and enables a detailed representation of urban surface characteristics in the hydraulic model.

3.2 Numerical Modelling

Numerical simulations of surface water flows are the basis for compound flood hazard assessment. The Engineering Center's River Analysis System (HEC-RAS 7.0) (Brunner, 2024) numerical model was used to simulate 146 river discharge-storm surge scenarios as a 2D unsteady flow simulation based on the shallow water equations (SWE) and a variable time step. This approach enables an accurate representation of flow dynamics and inundation processes within the coastal area.

The model domain covers most of the city center of Rijeka, including the lower reach of the Rječina

River and the adjacent Adriatic coastal zone (Figure 3). The computational mesh consisted of an unstructured triangular grid with cell sizes ranging from 2 to 10 m. To accurately capture the flow within the river channel, a refinement region with a structured rectangular grid with cell dimensions of 2 × 1 m was implemented and aligned with the dominant flow direction. Also, mesh refinement was concentrated around bridges, flood protection walls, and other hydraulic controls where accurate representation of flow patterns was essential. Larger cells were adopted elsewhere to reduce computational cost while maintaining sufficient accuracy in less hydraulically complex areas.

The upstream boundary condition was defined as a Rječina River synthetic hydrograph, with peak discharges corresponding to the river discharge values obtained from the bivariate probability analysis (Figure 3). The downstream boundary condition was set as a uniform stage hydrograph representing Adriatic Sea water levels corresponding to the sum of associated storm surge values and average high tides. To characterize surface roughness, Manning's roughness coefficient was used (Chow et al., 1988). Each land cover and land use class from Urban Atlas land use/land cover was assigned a different coefficient following the Natural Resources Conservation Service (2004) to allow a realistic simulation of overland flow and flood wave attenuation across different surface types.

A total of seven bridges located along the lower reach of the Rječina River were represented in the numerical model using the HEC-RAS bridge modelling approach (Figure 3). The bridge decks and piers were incorporated to accurately reproduce their influence on flow conditions and water levels. Since bridges act as hydraulic constrictions, they can induce backwater effects and locally modify flow velocities and flood propagation. Their inclusion in the model was therefore essential for reliable simulation of compound flood processes and for identifying the discharge thresholds associated with impacts on hydraulic structures.

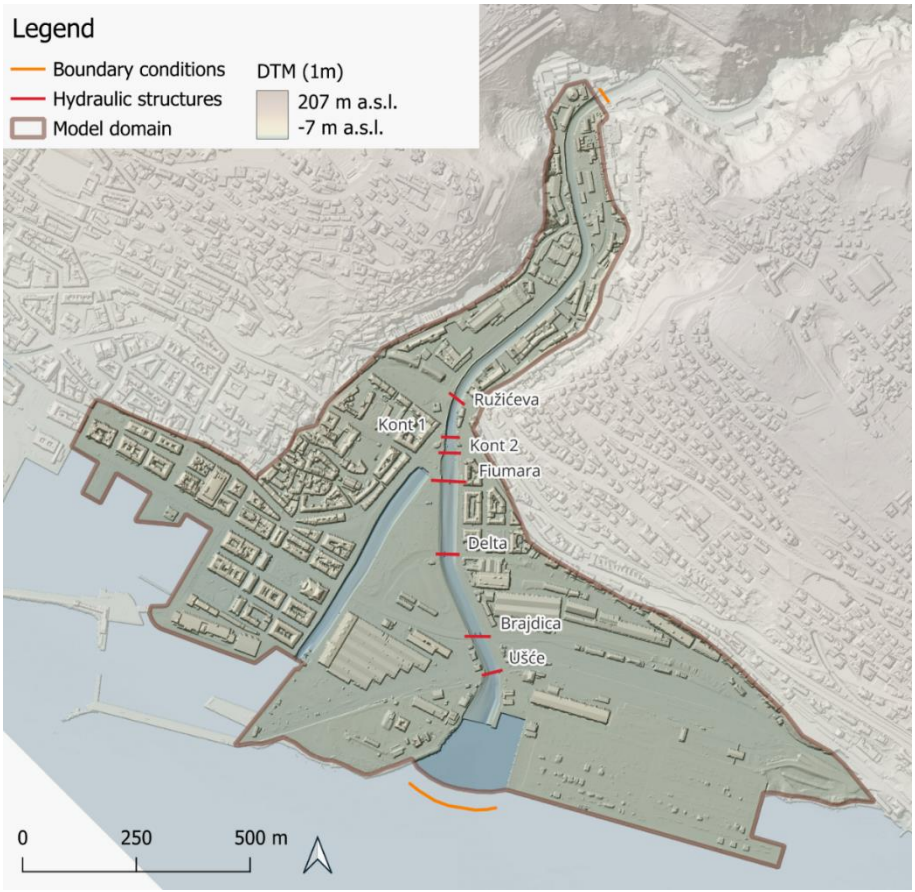


Figure 3. Numerical model setup for the lower Rječina River, including the model domain, upstream and downstream boundary conditions, and the locations of the seven bridges overlaid on the digital terrain model.

For each scenario, the maximum flood extent and water depth were extracted and analysed in QGIS to

derive flood characteristics (water levels at bridges and flood extent). The set of 146 simulations was subsequently used to establish warning thresholds and to develop the proposed early warning system. Furthermore, the simulation results database enabled the construction of bilinear interpolation surfaces connecting river discharge and sea level to flood extent and flood volume, allowing rapid estimation of flood impacts for any measured or forecasted combination of the two flood drivers within the analysed range.

3.3 Early Warning System

The proposed early warning system (EWS) for the study area consists of two warning levels: a Flood Preparedness Level and a Flood Emergency Level. The Flood Preparedness Level corresponds to conditions without inundation but with the potential for significant impacts on hydraulic structures, whereas the Flood Emergency Level represents conditions under which flooding occurs.

The two-level EWS is based on three characteristic sea-level scenarios combined with extreme Rječina River discharges. The proposed sea levels are: (1) mean sea level with tides, (2) 1-year return period storm surge with tides, and (3) 100-year return period storm surge with tides. The sea levels correspond to (1) no-compound conditions (only discharge), (2) frequent sea conditions that can cause compound effects, and (3) very rare and extreme sea conditions.

For each sea-level scenario, the corresponding discharge thresholds for the Flood Preparedness Level were derived from the results of numerical simulations defined as the minimum river discharges that can potentially cause damage to hydraulic structures. In this study, the impact was defined as the water level reaching the underside of the bridge decks along at least one of the seven bridges along the lower Rječina River reach. All seven bridges were treated equally, meaning that the Flood Preparedness Level should be triggered when the water level reached the underside of the deck at any bridge within the model domain.

The discharge thresholds corresponding to the Flood Emergency Level were defined as the minimum Rječina River discharges that, in combination with the selected sea levels, result in compound flooding within the model domain. For this warning level, any occurrence of inundation within the model domain was considered an impact because even small flood extents may already affect traffic, infrastructure, or emergency response within the densely urbanized study area.

4 Results and Discussion

4.1 Simulation results

The model was calibrated and validated using the high-flow event of November 2016. Calibration was performed by adjusting Manning's roughness coefficient (n) of the river channel to reproduce the observed water levels at the Titov Trg hydrological station. Eight Manning's coefficients ranging from 0.016 to 0.030 were tested with an increment of 0.002, and the resulting simulated water level time series were compared with the observations. Among the tested values, n=0.022 provided the best overall agreement with the observations, yielding an RMSE of 0.039 m, an NSE of 0.951, and a KGE of 0.973. Although the model slightly overestimates the peak water level, it satisfactorily reproduces the timing and overall hydrograph shape. The results of the numerical simulations presented in Figure 4 illustrate the spatial variability of flood extents associated with different combinations of river discharge and sea level. Elevated sea levels induce flooding in low-lying coastal areas even under relatively low river discharges (Figure 4, top row), whereas increasing discharge results in a progressive upstream expansion of inundation along the Rječina River corridor (Figure 4, bottom row). Similar flood extents may arise from different combinations of the two boundary conditions, demonstrating that both river discharge and sea level contribute to the overall flood response.

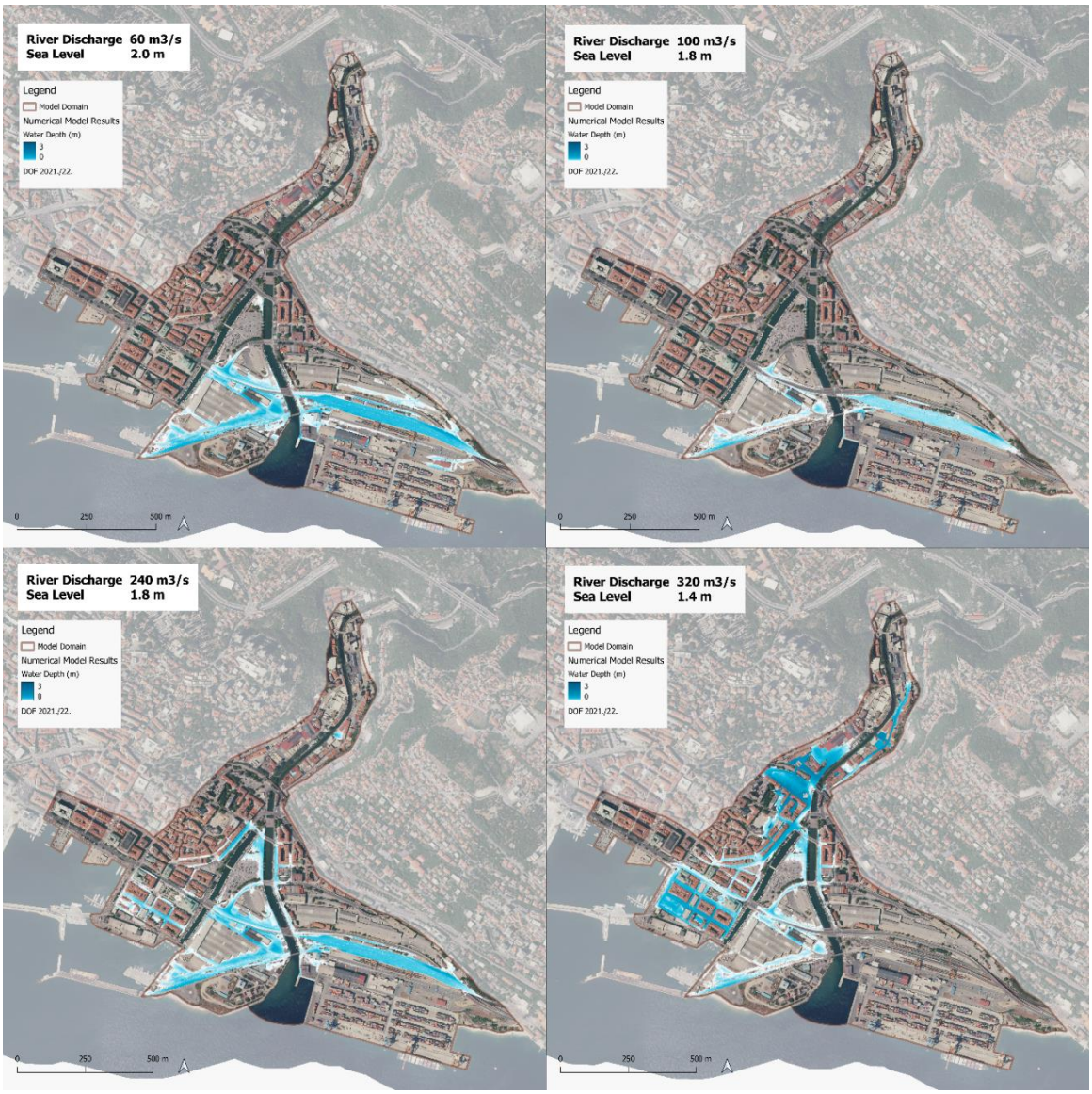


Figure 4. Spatial distribution of flood extents and water depths for selected combinations of river discharge and sea level.

4.2 Early warning system

The main outcome of the proposed two-level EWS is a set of discharge thresholds defined for different sea level conditions. These thresholds represent the minimum lower Rječina River discharges that either affect hydraulic structures or initiate flooding within the model domain. The corresponding thresholds for the Flood Preparedness Level and the Flood Emergency Level are summarized in Table 1.

The current flood warning system implemented by Croatian Waters defines three warning stages: Normal Flood Defence, Emergency Flood Defence, and a State of Emergency. The activation of these stages is based on observed or forecasted water levels at hydrological stations, with threshold values defined in the National Flood Defence Implementation Plan (Hrvatske Vode, 2022). For the lower reach of the Rječina River, the corresponding water level thresholds are +3.50, +4.00, and +4.50 m, which approximately correspond to discharges of 215, 280, and 350 m³/s, respectively.

Table 1. The Flood Preparedness and the Flood Emergency Level water levels and associated river discharge thresholds for the three sea level conditions.

Sea Level Conditions		Flood Preparedness Level	Flood Emergency Level
Scenarios	SL [m]	H_{min} [m] / Q_{min} [m^3/s]	H_{min} [m] / Q_{min} [m^3/s]
MSL + tides	+0.2	+4.00 / 280	+4.30 / 320
1-yr RP SS + tides	+0.9	+3.85 / 260	+4.15 / 300
100-yr RP SS + tides	+1.4	+2.65 / 120	+3.55 / 220

Notes: H = Water Level, Q = River Discharge, MSL = Mean Sea Level, SS = Storm Surge, RP = Return Period.

The proposed early warning system differs from the existing approach in two aspects. First, it defines two warning levels based on expected impacts: (1) the Flood Preparedness Level, associated with water levels reaching the underside of bridge decks, and (2) the Flood Emergency Level, associated with the occurrence of flooding within the study area. These levels are comparable to the Emergency Flood Defence and State of Emergency warning stages used by Croatian Waters. Second, the proposed system explicitly accounts for both river discharge and sea level, thereby considering the compound nature of flooding in the lower Rječina River.

Figure 5 compares the river discharge-sea level combinations associated with the proposed warning levels and the thresholds currently used by Croatian Waters. Under mean sea level conditions, both EWS approaches provide similar discharge thresholds, although the proposed system yields slightly lower values due to the updated extreme value analysis and the use of a higher-resolution hydraulic model. However, as sea levels increase, lower river discharges are sufficient to trigger the Flood Preparedness Level. Consequently, the existing system increasingly underestimates the potential impacts of compound flooding because it does not account for elevated sea levels. This effect becomes particularly pronounced during extreme sea level conditions, such as the 100-year return period storm surge scenario. These results demonstrate that the interaction between elevated sea levels and river discharge can substantially increase flood hazard, even when river discharges alone would not be considered critical.

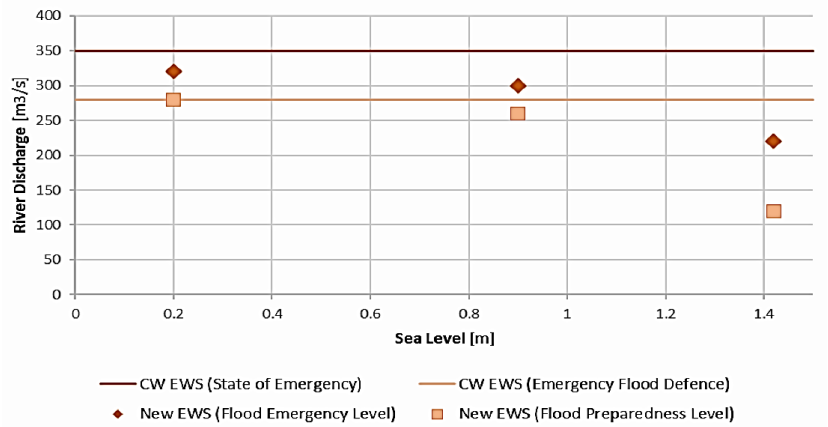


Figure 5. River discharge-sea level combinations associated with the newly proposed compound flood EWS compared with the current Croatian Waters (CW) warning thresholds for the lower Rječina River.

These results highlight the importance of compound flooding in the lower Rječina River. Elevated sea levels amplify the effects of river discharge through backwater interactions, causing critical conditions to occur at considerably lower discharges than would be expected under normal sea level conditions. Consequently, events that would not pose a threat during average sea levels may result in infrastructure impacts or flooding when combined with storm surges. This demonstrates that flood hazard in coastal rivers cannot be adequately assessed by considering river discharge or sea level independently, but rather requires accounting for their joint occurrence and interaction.

In addition to defining warning thresholds, the proposed approach provides estimates of flood extent

and flood volume for a given combination of river discharge and sea level. The results obtained from the 146 simulated scenarios were used to construct bilinear interpolation surfaces, enabling the estimation of flood characteristics for any river discharge-sea level combination within the analysed range. This allows rapid assessment of inundation extent and flood volume under a wide range of flood-driver conditions, providing an additional impact-based component to the proposed EWS.

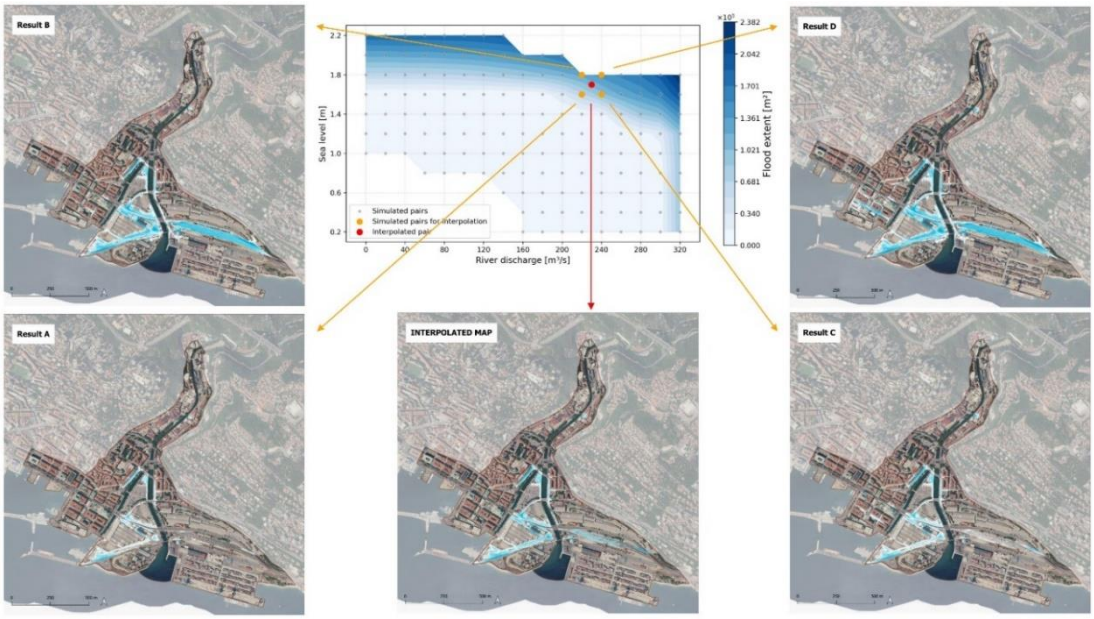


Figure 6. Conceptual framework for generating an interpolated flood extent map from neighbouring river discharge–sea level scenarios.

To enable the generation of flood maps for any combination of river discharge and sea level within the range of pre-simulated scenarios, without performing additional numerical simulations, a raster-based bilinear interpolation approach was implemented. For a target river discharge–sea level pair, the four neighbouring simulated scenarios surrounding the selected point on the response surface are identified. The corresponding maximum water depth rasters are then combined using bilinear interpolation weights derived from the relative position of the target pair within the surrounding grid cell. In this way, a new flood depth raster can be generated for any intermediate combination of boundary conditions while preserving the spatial characteristics of the inundation patterns obtained from the numerical model. Flood extent and flood volume can subsequently be derived from the interpolated raster using the same post-processing procedure applied to the original simulations. Figure 6 illustrates the interpolation procedure and provides an example of an interpolated flood map obtained from four adjacent river discharge–sea level scenarios. This approach enables rapid generation of flood maps for forecasted boundary conditions and provides the basis for the implementation of an impact-based early warning system for compound flooding.

4.3 Limitations

The proposed methodology is subject to several sources of uncertainty. The copula-based joint probability analysis depends on the selected marginal distributions, copula family, and the assumption that the present-day dependence structure between river discharge and sea level remains stationary. Similarly, the adopted +0.60 m mean sea level rise scenario represents a deterministic projection based on the Croatian Climate Change Adaptation Strategy and does not account for uncertainties associated with different climate scenarios, regional sea-level variability, or possible future changes in storm surge characteristics. Consequently, the future warning thresholds should be interpreted within the context of these assumptions.

The numerical simulations are influenced by uncertainties associated with model parameterization and bathymetry representation. River channel roughness was calibrated against observed water levels by

testing Manning's coefficients ranging from 0.016 to 0.030, together with additional combinations of roughness values for the channel bed and banks. Among the tested configurations, a uniform Manning's coefficient of n = 0.022 for the river channel resulted in the lowest RMSE (0.039 m) and the highest NSE (0.951), and was therefore adopted in the model. Nevertheless, the selected Manning's coefficient directly influences simulated water levels and, consequently, the discharge thresholds associated with the proposed warning levels. Additional uncertainty arises from the representation of the river bathymetry. The channel geometry was reconstructed from 17 surveyed cross-sections distributed along approximately 1450 m of the river reach, requiring interpolation between neighbouring cross-sections. As a result, local hydraulic conditions may not be fully captured, particularly in sections where the channel geometry changes rapidly. Similarly, bridge geometry was reconstructed from available engineering documentation, and any simplifications in the representation of bridge structures may influence local backwater effects and water levels.

The interpolation-based flood mapping substantially reduces computational time by avoiding additional hydraulic simulations. However, the adopted bilinear interpolation assumes gradual transitions between neighbouring scenarios. In locations where inundation patterns change non-linearly, for example due to bridge overtopping or activation of new flow pathways, interpolation errors may increase. Therefore, interpolated flood maps should be interpreted with appropriate caution and are intended primarily for rapid operational guidance.

Quantitative validation of the interpolation procedure was not possible because no detailed observations of recent fluvial flood extents are available for the lower Rječina River. Future validation should compare interpolated flood maps against either additional hydraulic simulations or observed inundation data if they become available. Furthermore, the accuracy of the interpolation is expected to depend on the density of the pre-simulated scenario library, with a finer scenario resolution likely reducing interpolation errors between neighbouring simulations.

One advantage of the proposed framework is that all computationally intensive simulations are performed offline, allowing rapid estimation of flood extent during operation through interpolation of pre-simulated scenarios. From an operational perspective, the proposed methodology could complement the existing Croatian Waters warning system rather than replace it. While the current Croatian Waters system relies primarily on river water levels, the proposed framework incorporates both river discharge and sea level together with impact-based warning thresholds. In its current form, the system is observation-driven rather than forecast-driven, relying on real-time measurements of river discharge and sea level. Consequently, warning lead times are limited to the natural hydrological response of the catchment. Integrating operational river discharge and sea-level forecasting systems would provide earlier identification of hazardous conditions and represents the next logical step towards a fully operational compound flood early warning system.

5 Conclusion

This study presents an impact-based early warning system for compound flooding in the lower reach of the Rječina River. The proposed two-level warning system distinguishes between impacts on hydraulic structures, represented by the Flood Preparedness Level, and the occurrence of flooding, represented by the Flood Emergency Level. In this way, the proposed approach explicitly accounts for the interaction between river discharge and sea level, providing a more comprehensive assessment of flood hazard in this coastal area.

By moving from static water-level thresholds to discharge thresholds associated with different sea-level conditions and defined by the occurrence of impacts on hydraulic structures or flooding, the interaction between river discharge and sea level is explicitly incorporated into the warning system. The results demonstrate that elevated sea levels considerably reduce the river discharge required to trigger hazardous conditions, highlighting the importance of considering both flood drivers simultaneously. The findings confirm that a single-driver approach based solely on river discharge may underestimate flood

hazard in coastal river systems affected by compound flooding. Therefore, both sea level and river discharge should be considered as key flood drivers in the lower Rječina River.

In addition to defining warning thresholds, the proposed methodology enables rapid estimation of flood extent and inundation volume through interpolation of pre-simulated flood scenarios. This provides a practical and computationally efficient tool for decision support and flood risk management.

Although developed for the lower Rječina River, the proposed framework is transferable to other small coastal rivers exposed to compound flooding, provided that site-specific hydrological, hydraulic, and impact analyses are performed. Future work should focus on integrating operational river discharge and sea-level forecasts into the framework, enabling earlier warnings and supporting the transition towards a fully operational compound flood early warning system.

Acknowledgements

This work was supported by the Croatian Science Foundation under the project number 4SeaFlood (IP-2022-10-7598). This work was also funded by the European Union - NextGenerationEU projects CroCo-Flood - uniri-iz-25-86 and HIDKLP - uniri-iz-25-34, and the URBANFLOODS Interreg IPA ADRION project.

References

Brunner, G.W., 2024 HEC-RAS River Analysis System: User's Manual.

Calvin, K., Dasgupta, D., Krinner, G., Mukherji, A., Thorne, P.W., Trisos, C., Romero, J., Aldunce, P., Barrett, K., Blanco, G., Cheung, W.W.L., Connors, S., Denton, F., Diongue-Niang, A., Dodman, D., Garschagen, M., Geden, O., Hayward, B., Jones, C., Jotzo, F., Krug, T., Lasco, R., Lee, Y.-Y., Masson-Delmotte, V., Meinshausen, M., Mintenbeck, K., Mokssit, A., Otto, F.E.L., Pathak, M., Pirani, A., Poloczanska, E., Pörtner, H.-O., Revi, A., Roberts, D.C., Roy, J., Ruane, A.C., Skea, J., Shukla, P.R., Slade, R., Slangen, A., Sokona, Y., Sörensson, A.A., Tignor, M., Van Vuuren, D., Wei, Y.-M., Winkler, H., Zhai, P., Zommers, Z., Hourcade, J.-C., Johnson, F.X., Pachauri, S., Simpson, N.P., Singh, C., Thomas, A., Totin, E., Alegría, A., Armour, K., Bednar-Friedl, B., Blok, K., Cissé, G., Dentener, F., Eriksen, S., Fischer, E., Garner, G., Guivarch, C., Haasnoot, M., Hansen, G., Hauser, M., Hawkins, E., Hermans, T., Kopp, R., Leprince-Ringuet, N., Lewis, J., Ley, D., Ludden, C., Niamir, L., Nicholls, Z., Some, S., Szopa, S., Trewin, B., Van Der Wijst, K.-I., Winter, G., Witting, M., Birt, A., Ha, M., 2023 IPCC, 2023: Climate Change 2023: Synthesis Report. Contribution of Working Groups I, II and III to the Sixth Assessment Report of the Intergovernmental Panel on Climate Change. Intergovernmental Panel on Climate Change (IPCC), Geneva, Switzerland. https://doi.org/10.59327/IPCC/AR6-9789291691647

Chow, V.T., Maidment, D.R., Mays, L.W., 1988 *Applied hydrology*, McGraw-Hill series in water resources and environmental engineering. McGraw-Hill, New York.

Codiga, D.L., 2011 Unified Tidal Analysis and Prediction Using the UTide Matlab Functions. Technical Report 2011-01. Graduate School of Oceanography, University of Rhode Island, Narragansett, RI 59.

Corvaro, S., Marini, F., Rocchi, S., Lorenzoni, C., 2026 Bivariate extreme analysis for coastal flooding in the Adriatic Sea. *Estuarine, Coastal and Shelf Science* 329, 109668. https://doi.org/10.1016/j.ecss.2025.109668

Cosby, A.G., Lebakula, V., Smith, C.N., Wanik, D.W., Bergene, K., Rose, A.N., Swanson, D., Bloom, D.E., 2024 Accelerating growth of human coastal populations at the global and continent levels: 2000–2018. *Sci Rep* 14, 22489. https://doi.org/10.1038/s41598-024-73287-x

Ghanbari, M., Arabi, M., Kao, S.-C., Obeysekera, J., Sweet, W., 2021 Climate Change and Changes in Compound Coastal-Riverine Flooding Hazard Along the U.S. Coasts. *Earth's Future* 9, e2021EF002055. https://doi.org/10.1029/2021EF002055

Gomez Rave, D.V., Scolobig, A., del Jesus, M., 2025 Review article: Rethinking preparedness for coastal compound flooding: insights from a systematic review. *Natural Hazards and Earth System*

Sciences 25, 3977–4002. https://doi.org/10.5194/nhess-25-3977-2025
Green, J., Haigh, I.D., Quinn, N., Neal, J., Wahl, T., Wood, M., Eilander, D., de Ruiter, M., Ward, P., Camus, P., 2025 Review article: A comprehensive review of compound flooding literature with a focus on coastal and estuarine regions. *Natural Hazards and Earth System Sciences* 25, 747–816. https://doi.org/10.5194/nhess-25-747-2025
Hrvatske Vode, 2022 Glavni provedbeni plan obrane od poplava.
Jagodnik, P., Bernat Gazibara, S., 2025 Engineering geological settings of the Rječina River Valley (Croatia): a LiDAR-based approach. *Journal of Maps* 21, 2539921. https://doi.org/10.1080/17445647.2025.2539921
Jane, R., Wahl, T., Pena, F., Obeysekera, J., Murphy-Barltrop, C., Ali, J., Maduwantha, P., Li, H., Santos, V.M., 2026 MultiHazard: Copula-based Joint Probability Analysis in R. *Journal of Open Source Software* 11, 8350. https://doi.org/10.21105/joss.08350
Liu, Q., Xu, H., Wu, G., Lu, C., Wei, X., Wang, J., 2025 Integrating relative sea level rise into compound flooding hazard assessment for coastal cities. *J. Hydrol.-Reg. Stud.* 58, 102276. https://doi.org/10.1016/j.ejrh.2025.102276
Međugorac, I., Pasarić, M., Orlić, M., 2022 Long-term measurements at Bakar tide-gauge station (east Adriatic). *G e o f i z i k a* 39, 149–162. https://doi.org/10.15233/gfz.2022.39.8
Međugorac, I., Pasarić, M., Orlić, M., 2025 Historical sea-level measurements at Bakar (east Adriatic). https://doi.org/10.17882/85171
Metallinos, A.S., Chondros, M.K., Papadimitriou, A.G., Tsoukala, V.K., 2026 Development of an Early Warning System for Compound Coastal and Fluvial Flooding: Implementation at the Alfeios River Mouth, Greece. *Journal of Marine Science and Engineering* 14, 110. https://doi.org/10.3390/jmse14020110
Ministarstvo zaštite okoliša i energetike, 2020 Strategija prilagodbe klimatskim promjenama u Republici Hrvatskoj za razdoblje do 2040. godine s pogledom na 2070. godinu [WWW Document]. URL https://narodne-novine.nn.hr/clanci/sluzbeni/2020_04_46_921.html (accessed 1.30.26).
Moftakhari, H.R., Salvadori, G., AghaKouchak, A., Sanders, B.F., Matthew, R.A., 2017 Compounding effects of sea level rise and fluvial flooding. Proceedings of the National Academy of Sciences 114, 9785–9790. https://doi.org/10.1073/pnas.1620325114
Najafi, H., Shrestha, P.K., Rakovec, O., Apel, H., Vorogushyn, S., Kumar, R., Thober, S., Merz, B., Samaniego, L., 2024 High-resolution impact-based early warning system for riverine flooding. *Nat Commun* 15, 3726. https://doi.org/10.1038/s41467-024-48065-y
Natural Resources Conservation Service, 2004 Hydrology National Engineering Handbook, Chapter 9: Hydrologic Soil-Cover Complexes. Part 630. [WWW Document]. URL https://www.hydrocad.net/neh.htm (accessed 3.3.25).
Papadimitriou, A.G., Metallinos, A.S., Chondros, M.K., Tsoukala, V.K., 2024 A Novel Input Schematization Method for Coastal Flooding Early Warning Systems Incorporating Climate Change Impacts. *Climate* 12, 178. https://doi.org/10.3390/cli12110178
Pumo, D., Avanti, M., Francipane, A., Noto, L.V., 2024 An Early Warning System for Urban Fluvial Floods Based on Rainfall Depth–Duration Thresholds and a Predefined Library of Flood Event Scenarios: A Case Study of Palermo (Italy). *Water* 16. https://doi.org/10.3390/w16182599
United Nations Office for Disaster Risk Reduction (UNDRR), 2015 Sendai Framework for Disaster Risk Reduction 2015 - 2030.
Urban Atlas Land Cover/Land Use 2018 (vector), Europe, 6-yearly, Jul. 2021 [WWW Document], n.d. . EEA geospatial data catalogue. URL https://sdi.eea.europa.eu/catalogue/copernicus/api/records/fb4dffa1-6ceb-4cc0-8372-1ed354c285e6 (accessed 1.30.26).
VEPAR [WWW Document], 2014 URL https://vepar.voda.hr/ (accessed 6.15.26).
Wang, Z., Leung, M., Mukhopadhyay, S., Sunkara, S.V., Steinschneider, S., Herman, J., Abellera, M., Kucharski, J., Ruggiero, P., 2025 Compound coastal flooding in San Francisco Bay under climate change. npj *Nat. Hazards* 2, 3. https://doi.org/10.1038/s44304-024-00057-0
Ward, P.J., Couasnon, A., Eilander, D., Haigh, I.D., Hendry, A., Muis, S., Veldkamp, T.I.E., Winsemius, H.C., Wahl, T., 2018 Dependence between high sea-level and high river discharge increases flood hazard in global deltas and estuaries. *Environ. Res. Lett*. 13, 084012. https://doi.org/10.1088/1748-9326/aad400

EVALUATING THE SCS-CN METHOD IN THE PAZINČICA RIVER CATCHMENT (CROATIA): MEASURED EXTREMES VS. EVENT-BASED HYDROLOGICAL SIMULATIONS

Ivona PETKOVIĆ[1*], Nevenka OŽANIĆ[1], Petra JAGODNIK[1], Nino KRVAVICA[1]

[1] *University of Rijeka, Faculty of Civil Engineering, Croatia*

E-mail: ipetkovic@gradri.uniri.hr

E-mail: nozanic@gradri.uniri.hr

E-mail: petra.jagodnik@gradri.uniri.hr

E-mail: nino.krvavica@gradri.uniri.hr

[*] *Corresponding author*

Abstract

Design peak discharge is commonly derived from event-based rainfall–runoff simulations using the SCS Curve Number (CN) method under discrete Antecedent Moisture Condition (AMC I–III) scenarios, yet the validity of this framework is rarely tested against independent, long-term discharge observations. This study evaluates the SCS-CN/AMC framework in the Pazinčica River catchment, a small flysch catchment in Central Istria, Croatia, with a torrential flow regime, through a two-part diagnostic based on a sample of peaks-over-threshold (POT) discharge extremes at the Dubravica station (1972–2024). First, design peak discharges were simulated by a semi-distributed HEC-HMS model under AMC I, II and III design storms, with calibrated runoff-transformation parameters (CN, lag time, peak rate factor) and validated against the observed hydrographs of the most extreme events. Next, design peak discharges were compared against peak discharges estimated from measured flow at the Dubravica station using POT/GPD approach. The results show that POT/GPD discharge-frequency curve falls just bellow the HEC-HMS simulations under AMC II and above AMC I, which indicates that no single AMC-based CN reproduces the observed frequency distribution reliebly. Second, effective CN values calculated by direct inversion of the SCS-CN equation for all POT events showed that CN decreases systematically with increasing rainfall depth and maximum rainfall intensity, while showing no significant relationship with antecedent precipitation computed for cumulative observed rainfall across multiple aggregation windows. These results indicate that effective CN in this catchment is governed primarily by rainfall intensity rather than by antecedent moisture state, explaining why a discrete AMC I–III classification cannot simultaneously reproduce the flow behaviour captured by the analysis of measured discharges.

Key words

SCS Curve Number (CN), Antecedent Moisture Conditions (AMC I–III), HEC-HMS rainfall-runoff modelling, Extreme value analysis, Mediterranean small catchment

1 Introduction

Design peak discharge estimation is a central task in hydrological engineering because it provides the quantitative basis for hydraulic design, flood risk mapping, infrastructure safety assessment and spatial planning. In gauged catchments, peak discharges are commonly estimated through frequency analysis of observed discharge extremes, whereas in ungauged catchments they are frequently derived from rainfall–runoff simulations using design storms. Flood-frequency analysis reflects the integrated historical response of the catchment at the gauging station, while rainfall–runoff modelling translates a

selected rainfall depth, duration and temporal pattern into discharge through assumptions about rainfall losses, initial storage, routing and hydrograph transformation. Differences between the two estimates should therefore be interpreted not only as statistical or numerical discrepancies, but also as evidence of the assumptions embedded in the modelling chain (Davison and Smith, 1990; Coles, 2001; Merz and Blöschl, 2008).

Recent European-scale studies have shown that changes in flood processes and antecedent catchment state can be as important as changes in rainfall extremes for explaining flood behaviour and flood anomalies (Tarasova et al., 2023). In Mediterranean basins, flood seasonality, rainfall intensity and antecedent wetness may interact in a non-linear manner, so the same rainfall return period does not necessarily produce the same flood return period under dry, average and wet initial conditions (Tramblay et al., 2023; Massari et al., 2023). Consequently, evaluating the validity of the SCS-CN/AMC framework in such catchments requires explicit assessment of the consistency between observed discharge extremes, design rainfall assumptions and event-scale runoff-generation parameters.

The Soil Conservation Service Curve Number (SCS-CN) method is one of the most widely used event-based loss methods in hydrological engineering because it is simple, transparent and relatively easy to set up from land cover, soil and imperviousness density (Ponce and Hawkins, 1996; Hawkins et al., 2009). However, the apparent simplicity of the SCS-CN method should not be interpreted as physical uniqueness. The Curve Number (CN) is an effective parameter that lumps together the influence of soil hydrologic properties, land cover and land use, surface condition, and antecedent moisture condition on the rainfall–runoff response, from which the potential maximum retention (S) and initial abstraction (I_a) are derived. Therefore, tabulated CN values and conventional antecedent moisture classes (AMC) can introduce substantial uncertainty if they are transferred to local design studies without calibration against observed hydrographs. Recent studies further emphasise that both CN and the initial abstraction coefficient should be treated as event-scale uncertain parameters, rather than fixed lookup values, especially where flood peaks are sensitive to pre-event conditions and runoff connectivity (Walega et al., 2020; Afrasiabikia et al., 2025).

At the same time, antecedent wetness should not be assumed to be a universal control on runoff response. In dry, high-intensity, infiltration-excess environments, measured runoff coefficients may show weak dependence on antecedent soil moisture, indicating that rainfall intensity and surface hydraulic conditions can dominate over antecedent storage (Zhang et al., 2011). In contrast, soil-tank and hillslope-scale experiments have demonstrated threshold-like responses in runoff coefficient, subsurface-flow activation, response time and hysteresis when antecedent soil moisture approaches field capacity (Zhao et al., 2015; Song and Wang, 2019). The activation soil moisture accounting concept provides a useful interpretation of this behaviour by treating antecedent state as a storage deficit or activation threshold that must be exceeded before effective runoff begins (Verma et al., 2020).

The Pazinčica River catchment in Central Istria, Croatia, provides a suitable case study for examining these issues. This is a small Mediterranean catchment on an impermeable flysch basin composed of clastic rocks with a thin weathered cover, which promotes a flow regime dominated by surface runoff with rapid flow concentration following intense rainfall, characteristic of a typical torrential regime. At the same time, the availability of long-term observed discharge data from the Dubravica hydrological station, rainfall data from two rain gauges, and a high-resolution digital elevation model provides a basis for a comparative statistical and hydrological assessment.

The objectives of this study are twofold: (i) to evaluate whether HEC-HMS design-storm simulations under AMC I, II and III, with runoff-transformation parameters calibrated and validated against the observed hydrographs of the most extreme flood events at the Dubravica station, reproduce the discharge-frequency curve independently estimated from 53 years of observed extremes (1972–2024) via a peaks-over-threshold (POT) Generalized Pareto Distribution (GPD) analysis; and (ii) to identify the source of any discrepancy by calculating effective CN values, through direct inversion of the SCS-CN equation, for the full sample of POT-exceeding historical events, and testing their relationship with storm depth, storm intensity and antecedent precipitation. The comparative analysis is not intended to

force equality between rainfall and peak discharge return periods, but to identify which antecedent-condition assumptions produce simulated peak discharges that are consistent with the discharge-frequency estimates inferred from the observed record. The novelty of the work lies in combining these two independent lines of evidence, namely, long-term discharge-frequency statistics and event-based simulation with independently validated response-timing parameters, into a diagnostic test of whether the conventional AMC I–III classification captures the dominant source of effective CN variability in a small Mediterranean flysch catchment.

2 Methods

2.1 Study area and input data

The Pazinčica River is a small torrential watercourse in Central Istria, Croatia. The catchment is developed within the central part of the Istrian flysch basin, composed almost entirely of impermeable clastic rocks overlain by a thin cover of weathered material. This geological setting results in very limited infiltration and a flow regime dominated by rapid surface runoff. Downstream of the flysch basin, the Pazinčica River sinks into the karst underground at the Pazinski ponor, where its waters become part of the regional groundwater system. During dry periods, inflow to the sink decreases markedly, and in some years the watercourse temporarily dries out. The Dubravica gauging station, used as the reference outlet for this study, is located upstream of the sink zone and is not affected by sink backwater under the observed event range. This station is located at coordinates 45°14′48.8″ N and 13°58′0.4″ E, with a gauge zero elevation of 249.59 m a.s.l.

The methodology compares two approaches for assessing design peak discharge: statistical frequency analysis of observed discharge extremes and rainfall-runoff modelling based on individual events. The statistical approach provides a reference for discharge frequency at the outlet, based on observations, while the hydrological approach isolates the effects of rainfall duration, losses, transformation, routing and the antecedent state of the catchment. Hydrological data include monthly maximum discharge observations at Dubravica for 1972-2024 and hourly discharge observations for 2001-2024. Meteorological data include 5-min precipitation records from two meteorological stations operated by the Croatian Hydrometeorological Service (DHMZ), located inside the catchment; Pazin (45°14′27.0″ N, 13°56′43.0″ E; 291 m a.s.l.) and Grdinići (45°19′11.6″ N, 14°02′25.7″ E; 425 m a.s.l.). Spatial data comprise a high-resolution digital elevation model (DEM) at 1 m resolution, vector watercourse layers, Copernicus CLCplus land-cover data and Copernicus imperviousness-density data. Specifically, land-cover information was derived from the CLCplus Backbone 2021 raster product at 10 m resolution, while impervious surfaces were represented using the 2018 Imperviousness Density (IMD) layer at 10 m resolution (Copernicus Land Monitoring Service, 2020, 2024).

2.2 Extreme value analysis of observed discharges

Design peak discharges at Dubravica (1972-2024) were estimated using a peaks-over-threshold (POT) framework with the Generalized Pareto Distribution (GPD; Coles, 2001). The POT approach was selected because it uses all observations exceeding a sufficiently high threshold and is therefore suitable for upper-tail inference when rare flood quantiles are required (Davison and Smith, 1990; Coles, 2001). The POT sample was based on monthly maximum discharges, where each value represents the highest observed discharge within a given month. The extraction interval was therefore one month, and no additional declustering was applied prior to threshold exceedance modelling. For each observation x exceeding a threshold u, the excess was defined as $y = x - u$ and its cumulative distribution function was modelled using the GPD, as given in Eq. (1).

$$H(y) = 1 - \left(1 + \frac{\xi y}{\sigma}\right)^{-\frac{1}{\xi}}, \quad y > 0, \tag{1}$$

where σ is the scale parameter and ξ is the shape parameter. The annual exceedance rate λ_u, was computed as the number of threshold exceedances divided by the record length in years. Return levels

for a return period T were estimated using Eq. (2).

$$z_T = u + \frac{\sigma}{\xi}\left[(\lambda_u T)^{\xi} - 1\right], \tag{2}$$

where z_T is the discharge return level associated with return period T. When ξ approaches zero, the logarithmic form obtained as the limiting case of Eq. (1) was applied instead, to avoid numerical instability in the general expression.

Threshold selection was performed using the empirical cumulative distribution of the monthly maximum discharge series. Candidate thresholds were defined as empirical quantiles, $u_p = F_n^{-1}(p)$, where $p = P(X \leq u)$. The tested cumulative probability levels p ranged from 0.5 to 0.99 with an increment of $\Delta p = 0.01$, and a candidate threshold was retained for evaluation only if at least 10 exceedances remained above it. The final threshold was selected using the TAILS approach (Collings et al., 2025), which compares candidate thresholds on a common scale within the upper tail of the data. For a candidate threshold u with empirical cumulative probability $\pi_u = F_n(u)$, each upper-tail probability P is converted to the conditional exceedance scale as given in Eq. (3).

$$q_{\text{cond}} = 1 - \frac{1 - P}{1 - \pi_u} \tag{3}$$

This cumulative-to-conditional transformation allows quantiles corresponding to the same upper-tail region to be compared across thresholds. For each candidate, a GPD was fitted by maximum likelihood to the excesses $Y = X - u$. The distance between empirical and theoretical upper-tail quantiles was calculated using 1000 bootstrap resamples and 500 quantile levels. The threshold that minimized the TAILS distance was selected for the final POT-GPD model.

2.3 Extreme value analysis of observed rainfall

Extreme value analysis of observed rainfall was conducted using 5-min precipitation records from the rain gauges Pazin and Grdinići. The available record covered the period 1963-2024 for Pazin and 1968-2024 for Grdinići. The analysis was carried out separately for each station in order to obtain localised estimates of design rainfall depths. For each station, continuous 5-min rainfall observations were aggregated into rainfall depths corresponding to durations of 1, 2, 3, 6, 12 and 24 h. For each duration, a separate time series of maximum rainfall depths was derived and used as input for the extreme-value analysis. The procedure was therefore repeated independently for every combination of station and rainfall duration. The statistical analysis followed the same POT-GPD framework as described in Section 2.2 for observed discharges.

2.4 Design storms

The design storm hyetographs were constructed using the Average Variability Method (AVM), originally proposed for deriving representative rainfall temporal patterns for design peak discharge estimation (Pilgrim and Cordery, 1975; Cordery et al., 1984). This approach derives a representative rainfall temporal pattern from observed storm events for a selected storm duration. After scaling by the corresponding design rainfall depth, the pattern defines the distribution of rainfall depths over the design storm duration. The use of the AVM design storm was supported by Krvavica and Rubinić (2020), who compared several design storm types for flood prediction in a partially urbanized catchment in Istria and showed that the AVM produced runoff results in the closest agreement with historical storm events.

2.5 Hydrological analysis of the catchment

Catchment geometry was prepared in QGIS (QGIS Development Team, 2024), while WhiteboxTools was used for hydrological terrain processing. The original 1 m DEM was resampled to 5 m resolution to reduce computational cost while retaining sufficient topographic detail. Roads, embankments and culverts can introduce artificial depressions or barriers in raster drainage models; therefore, the terrain model and extracted stream network were visually checked against available watercourse and

orthophoto information before final delineation. Hydrological conditioning was performed using depression breaching, followed by D8 flow-direction and flow-accumulation calculations. Depression breaching was preferred to simple filling because it removes artificial barriers while better preserving plausible drainage pathways in raster terrain analysis (Lindsay, 2016). The stream network was extracted from the flow accumulation raster. The final semi-distributed model geometry, including delineated subcatchments, stream network and monitoring stations, is shown in Fig. 1. Subcatchment land-cover and imperviousness attributes were calculated using zonal statistics. CLCplus land-cover data were used to support initial CN assignment, while the Copernicus imperviousness-density raster was used to estimate sealed-surface fractions. The resulting subcatchment layer provided the inputs required for hydrological simulations in HEC-HMS.

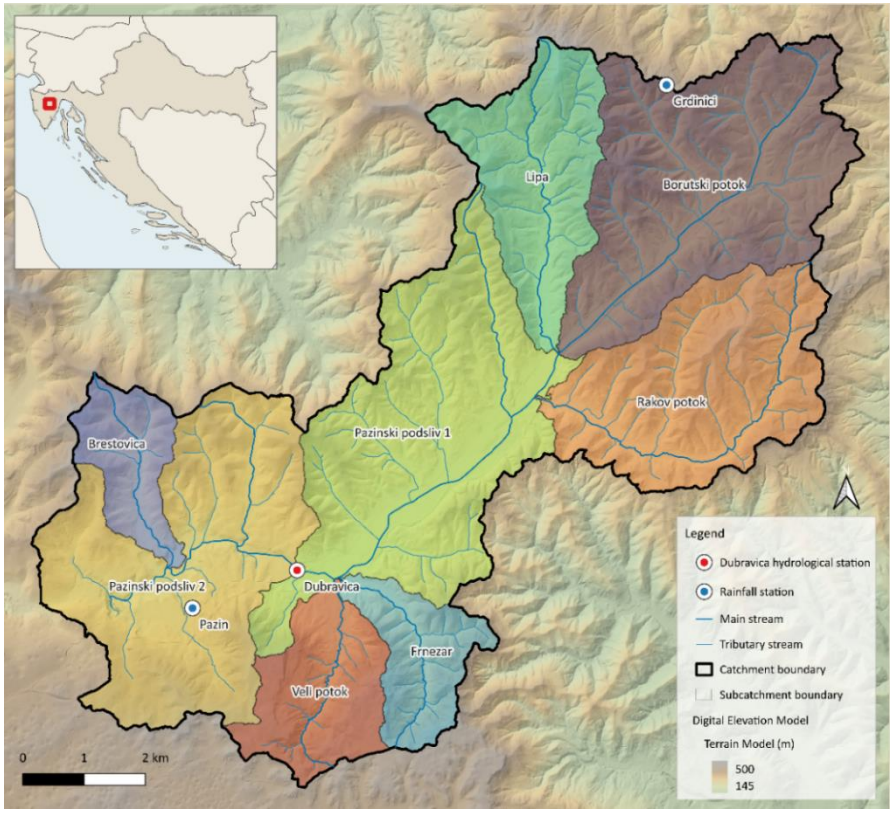


Figure 1. Semi-distributed model geometry of the Pazinčica River catchment, including subcatchments, stream network and hydrometeorological monitoring stations.

Table 1. Subcatchment characteristics, SCS-CN values and imperviousness parameters used for HEC-HMS model parameterisation (subcatchments in *italic* do not contribute to the discharges at Dubravica station).

Subcatchment	Area (km^2)	Length (m)	Slope (m/m)	CN (AMC I)	CN (AMC II)	CN (AMC III)	IMD (%)
Borutski potok	15.64	7303	0.264	51.1	71.3	85.1	0.82
Brestovica	*3.30*	*3910*	*0.281*	*50.0*	*70.4*	*84.5*	*0.31*
Frnežar	3.73	3960	0.353	50.2	70.6	84.7	0.46
Lipa	7.44	6010	0.292	50.3	70.7	84.7	0.27
Pazinčica –	17.18	9145	0.238	50.9	71.2	85.0	1.20
Pazinčica –	*15.12*	*6371*	*0.236*	*49.5*	*70.0*	*84.3*	*5.62*
Rakov potok	11.35	7690	0.313	50.5	70.8	84.8	0.25
Veli potok	5.19	4092	0.227	51.1	71.3	85.1	1.28

The GIS parameterisation produced eight hydrological subcatchments of the Pazinčica River, of which six subcatchments are draining to the Dubravica outlet. The main topographic, CN and imperviousness parameters are reported in Table 1. Subcatchment areas range from 3.30 km² to 17.18 km². The total

Pazinčica River catchment area is 78.95 km², of which 60.5 km² (six subcatchments) drains to the Dubravica gauging station; the remaining two subcatchments (Brestovica and Pazinčica – subcatchment II) do not contribute to discharges at Dubravica and are included in Table 1 for completeness of the catchment delineation. The catchment is predominantly rural and karst-influenced. Mean imperviousness is low at the catchment scale (area-weighted mean 1.68%), although Pazinčica II reaches 5.62% because it includes the strongest urban and transport-infrastructure influence around Pazin. The range of CN values derived from land cover and imperviousness is narrow, varying only from 70.0 to 71.3 under AMC II, with an area-weighted mean of 70.8.

2.6 Hydrological model

A semi-distributed, event-based HEC-HMS model (Hydrologic Engineering Center, 2026) was developed for the Pazinčica catchment to simulate hydrographs at the Dubravica outlet. The catchment was represented by a network of subcatchments, junctions and routing reaches, allowing runoff generation to be calculated at the subcatchment scale and subsequently transferred through the channel system towards the outlet. An event-based setup was selected because the objective was to reproduce selected hydrographs and to evaluate catchment response to design storms under controlled antecedent conditions, rather than to reproduce continuous water-balance processes.

Rainfall losses were represented using the SCS-CN method. This method was selected because it is widely used in engineering hydrology, requires a limited number of parameters and can be linked to land cover, soil information and imperviousness (Ponce and Hawkins, 1996; Hawkins et al., 2009).

Following the formulation given in the USDA-NRCS (2004), direct runoff depth was computed from storm precipitation depth, initial abstraction and potential maximum retention as shown in Eq. (4).

$$P_e = \frac{(P - I_a)^2}{P - I_a + S} \tag{4}$$

where P is the total storm precipitation depth, I_a is the initial abstraction and S is the potential maximum retention. The potential maximum retention is related to the Curve Number using Eq. (5).

$$S = \frac{25400}{CN} - 254 \tag{5}$$

where S is expressed in millimetres and CN is dimensionless. The initial abstraction I_a was represented as a fraction of the potential maximum retention according to Eq. (6).

$$I_a = \lambda S \tag{6}$$

where λ is the initial abstraction coefficient. Although the conventional SCS-CN formulation assumes $\lambda = 0.2$ (Hawkins et al., 2009; Afrasiabikia et al., 2025), several studies have shown that this value is often too high for event-based runoff modelling. The strongest support for using a lower value is provided by Woodward et al. (2003), who re-examined the initial abstraction ratio using a large rainfall–runoff event database and found that $\lambda = 0.05$ provided a better fit to observed runoff data than the conventional value of 0.20. Sensitivity of the calibration to the initial abstraction coefficient was also tested for the seven extreme events, for which λ values ranged from 0.01 to 0.2. A single value of $\lambda = 0.05$ was adopted for all subsequent simulations, being both the most commonly reported value in the literature (Woodward et al., 2003) and the closest to the median calibrated value.

Initial CN values were derived from land-cover and pedological maps, and they were subsequently evaluated through event calibration. Impervious areas were included in the subcatchment parameterization to account for surfaces contributing more directly to runoff. In addition to the reference CN values, the antecedent catchment state was represented using three SCS-CN scenarios: AMC I, AMC II and AMC III, corresponding to dry, average and wet conditions, respectively. AMC II was used as the reference condition. The dry-condition CN values for AMC I were derived from AMC II using the standard conversion relationship given in Eq. (7) (Texas Department of Transportation, 2019):

$$CN(I) = \frac{4.2CN(II)}{10 - 0.058CN(II)} \quad (7)$$

The corresponding wet-condition CN values for AMC III were derived using Eq. (8).

$$CN(III) = \frac{23CN(II)}{10 + 0.13\,CN(II)} \quad (8)$$

These categories were not interpreted as direct soil-moisture measurements, but as design states representing different storage deficits and degrees of hydrological connectivity. This interpretation is supported by experimental and modelling studies showing that antecedent moisture can influence runoff coefficient, subsurface-flow activation, response lag and hysteresis, while also recognising that antecedent wetness may be a weak predictor in high-intensity infiltration-excess events (Zhang et al., 2011; Zhao et al., 2015; Song and Wang, 2019; Verma et al., 2020).

Rainfall excess generated by the loss model was then transformed into discharge using the SCS Unit Hydrograph method (USDA-NRCS, 2004). The lag time parameter was used to describe the delay between rainfall excess and the resulting runoff response. The time of concentration and lag time were estimated using the SCS/NRCS lag-time relationship. The SCS lag equation was then used to estimate the lag time L, as given in Eq. (9).

$$L = \frac{\ell^{0.8}(S+1)^{0.7}}{1900Y^{0.5}} \quad (9)$$

where ℓ is the hydraulic flow length, Y is the average watershed land slope expressed as a percentage, and S is the potential maximum retention. In the original formulation, ℓ is expressed in feet and S in inches; therefore, input variables were converted to SI units before applying Eq. (9). The corresponding time of concentration T_c was obtained using Eq. (10).

$$T_c = \frac{L}{0.6} \quad (10)$$

The computed lag time was used as the subcatchment response parameter in the SCS Unit Hydrograph transform method, while subsequent adjustment during calibration was performed only within a hydrologically plausible range. Channel routing was simulated using the Muskingum-Cunge method. This method routes flow through river reaches by accounting for flood-wave translation and attenuation using reach length, channel slope, roughness and cross-sectional geometry. Length and channel slope were determined from DEM, roughness was estimated from the literature, and cross-sections were represented using simplified channel geometry, while the computational space and temporal intervals were determined automatically within HEC-HMS. No additional channel loss or gain was applied.

The HEC-HMS model was calibrated against seven of the most extreme observed flood events at the Dubravica station, using a sequential parameter-estimation strategy designed to isolate the loss, transformation-timing and transformation-shape components of the model. In the first step, the curve number (CN) for each subcatchment was adjusted so that the simulated direct runoff volume matched the observed runoff volume for each event, computed via Eq. (4)–(6) with $\lambda = 0.05$. Because CN governs only the rainfall–runoff volume relationship and does not affect the timing or shape of the resulting hydrograph, this step was performed independently of the subsequent transformation parameters, avoiding compensation between loss and transform model components. The same direct-inversion procedure (Eq. 4–6, $\lambda = 0.05$) was subsequently applied to the full sample of 25 discharge events exceeding the POT threshold used for the GPD analysis (Section 2.2), providing the basis for the CN-variability analysis presented in Section 3.4. The seven selected extreme events were retained for the subsequent lag-time and peak-rate-factor calibration steps described below, required to simulate the design-storm hydrographs in Section 3.3.

In the second step, with CN fixed from the volume calibration, several lag-time formulations

(SCS/NRCS, Kirpich, Snyder, Passini) were evaluated against the observed peak timing for each of the seven calibration events. The SCS/NRCS lag equation (Eq. 9), computed using the event-specific potential maximum retention S obtained in Step 1 together with hydraulic length and slope, provided the closest agreement with observed peak timing among the tested formulations and was retained for all subsequent simulations, including the design-storm scenarios. This preserves a consistent lag-time formulation between the historical-event calibration and the AMC design-storm runs, differing only in the AMC-specific value of S.

In the third step, with both CN and lag time fixed, the peak rate factor (PRF) was calibrated to reproduce the observed peak discharge for each of the seven calibration events. The resulting PRF values ranged from 100 to 450; a median value of 100 was adopted as a single fixed basin-scale parameter for the simulations across all AMC scenarios and return periods, consistent with the limited theoretical basis for relating unit-hydrograph shape to antecedent moisture state.

For the design-storm simulations under AMC I, II and III, lag time was recalculated for each subcatchment and scenario from Eq. (9) using the AMC-specific potential maximum retention (S_I, S_{II}, S_{III}), while the PRF was held at its calibrated median value. Consequently, AMC-driven differences in simulated peak discharge reflect two compounding effects of CN: a direct effect on runoff volume via Eq. (4)–(6), and an indirect effect on hydrograph timing via the CN-dependent lag time in Eq. (9).

We note that PRF was derived from the most extreme observed events and applied uniformly across all AMC scenarios and return periods; this is consistent with calibrating unit-hydrograph shape on the flood regime relevant to design, but implicitly assumes that peakedness is invariant with rainfall intensity. This assumption was not independently tested here.

The calibrated model was then used to simulate design flood hydrographs under different antecedent catchment conditions using design storms. Simulated peak discharges were compared with POT/GPD-based design discharges for the same return periods. The comparison was interpreted carefully, as rainfall return period and peak discharge return period are not physically equivalent: a flood peak also depends on hyetograph structure, rainfall duration, initial abstraction, available storage, catchment wetness, time lag, runoff transformation and channel routing.

The spread among AMC I, AMC II and AMC III simulations was interpreted as a measure of the simulated peak discharge's sensitivity to the assumed effective CN, representing the plausible range of catchment response under the conventional AMC framework. In this way, the resulting comparison is expressed not as a single deterministic value, but as a range bounded by observed discharge extremes, rainfall-frequency forcing and event-scale runoff-generation assumptions. The comparison itself serves as a diagnostic test of whether AMC-based scenario selection is consistent with the empirical controls on catchment response identified from the observed event record.

3 Results

3.1 Historical discharge extremes and POT/GPD discharge-frequency estimate values

The monthly maximum discharge series at Dubravica (1972–2024) confirms a strongly asymmetric flood regime, characterised by frequent moderate high-flow events and a small number of dominant extremes. The selected threshold and corresponding exceedances used for the POT/GPD analysis are illustrated in Fig. 2. Most values above the selected threshold are located close to the threshold, whereas the upper tail is controlled by a limited number of exceptional floods. During the monitoring period, the maximum discharge derived from limnigraphic data was 72.2 $m^3 s^{-1}$ in August 2002. The catastrophic October 1993 flood was considerably larger; because it was not fully represented by the available limnigraphic record, its peak discharge was reconstructed through hydraulic-hydrological modelling combined with field observations of water levels and estimated at 176 $m^3 s^{-1}$ (Rubinić et al., 2020). Including this reconstructed peak reduces the risk of underrepresenting the most extreme part of the

flood regime. The selected threshold for the POT/GPD analysis was u = 26.1 m³ s⁻¹, yielding a sample of n = 25 threshold-exceeding events. The resulting discharge estimates derived from the observed record increase from 26.8 m³ s⁻¹ for T = 1 year to 192.8 m³ s⁻¹ for T = 200 years (Fig. 5b). These values define the POT/GPD discharge-frequency reference against which HEC-HMS design-storm simulations were evaluated (hereafter the POT/GPD reference value).

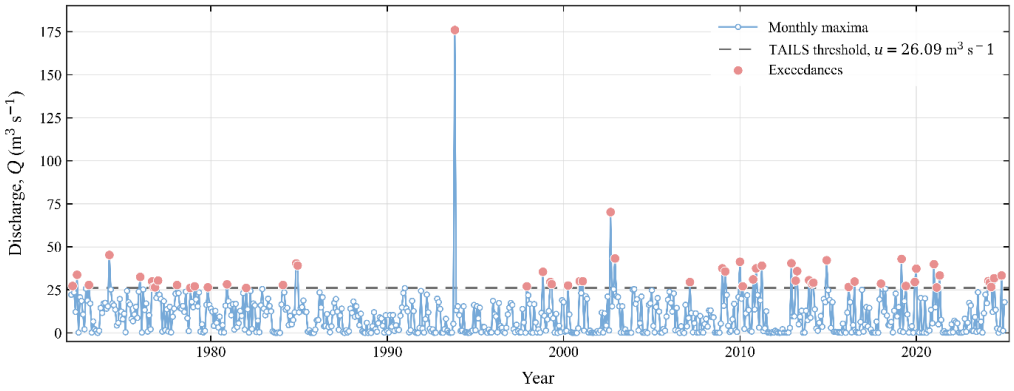


Figure 2. Monthly maximum discharge series at Dubravica with the selected POT threshold and exceedances used for GPD-based flood-frequency analysis.

The T = 200-year POT/GPD estimate (192.8 m³ s⁻¹; q ≈ 3.2 m³ s⁻¹ km⁻², based on the 60.5 km² catchment area) is not an isolated statistical artifact: it lies close to, and only slightly above, the specific discharge of the documented October 1993 flood (176 m³ s⁻¹; q ≈ 2.9 m³ s⁻¹ km⁻²), which was independently reconstructed through hydraulic-hydrological modelling combined with field water-level observations (Rubinić et al., 2020), not derived from the POT/GPD analysis itself. The consistency between an independently reconstructed historical extreme and the statistical T = 200-year estimate supports the physical plausibility of peak discharges of this order for the Pazinčica catchment at Dubravica, which is characterised by an impermeable flysch geology and a torrential flow regime favouring rapid, high-intensity runoff response.

3.2 DDF curves and design storms

Design rainfall depths were obtained from the DDF curves shown in Fig. 3. The DDF curves for Pazin were derived using rainfall data from the period 1963–2024, whereas those for Grdinići were derived using data from the period 1968–2024. The temporal distribution of the design rainfall was represented by the hyetographs shown in Fig. 4, which were derived for the Pazin station using the AVM method. This hyetograph shape was applied to both rainfall stations, while the rainfall depths for the selected durations and return periods differ between Pazin and Grdinići according to the corresponding DDF values and were used to scale the design hyetographs.

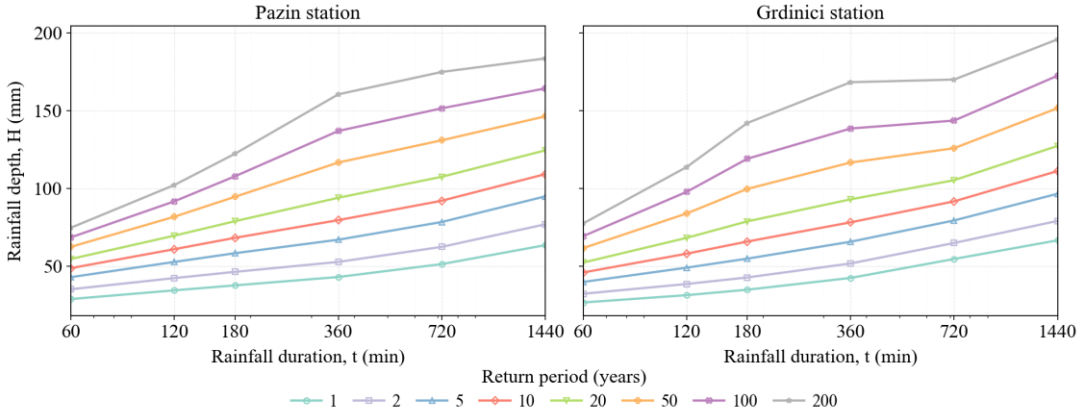


Figure 3. DDF curves for the Pazin and Grdinići stations used for design-storm scaling.

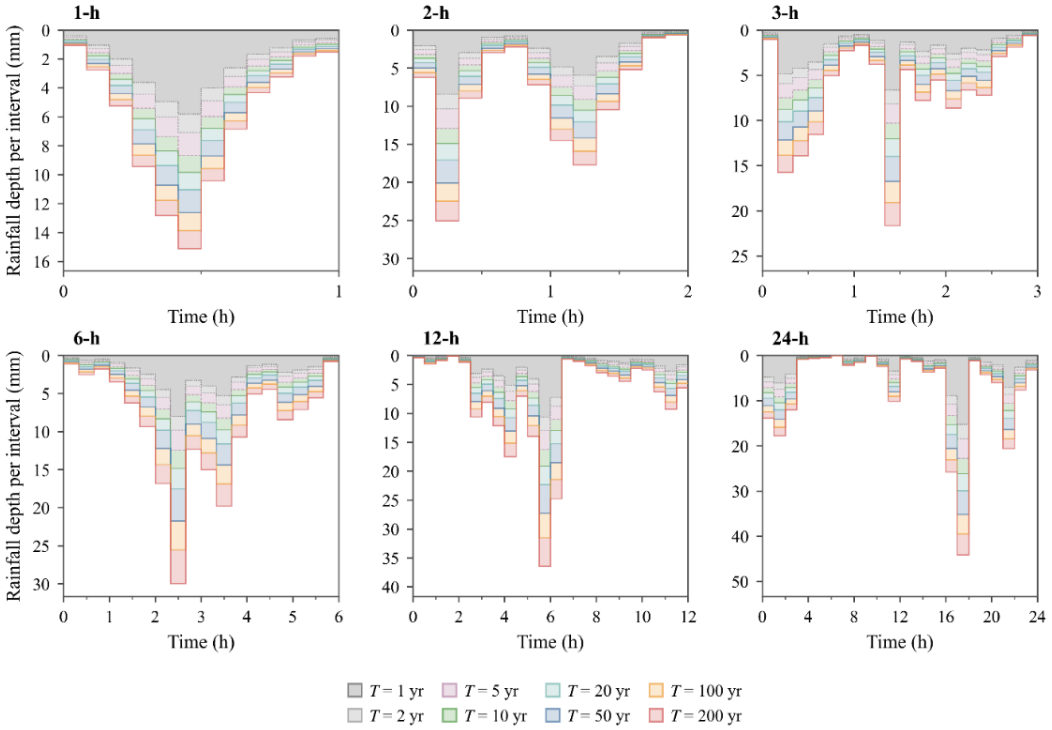


Figure 4. Design hyetographs for Pazin station scaled to selected return periods and storm durations for HEC-HMS design-storm simulations.

3.3 Design-storm response under AMC scenarios

Fig. 5a shows the simulated runoff coefficient (P_e/P) for AMC I, II and III computed for critical rainfall duration, isolating the direct effect of CN on runoff generation through the loss model (Eq. 4–6), independent of lag-time and routing effects. Across all return periods, AMC I produces the lowest runoff coefficients, AMC II intermediate values, and AMC III the highest, consistent with the higher CN values assigned under wetter antecedent conditions. For all three scenarios, the ratio increases with return period, reflecting the saturating form of Eq. (4): as rainfall depth increases, a progressively larger share of rainfall is converted to direct runoff regardless of AMC scenario. The difference between AMC III and AMC I narrows with increasing return period, from a ratio of approximately 5.3 at T = 1 year to approximately 2.0 at T = 200 years. This confirms that CN affects the volume of simulated runoff already at the loss-model stage, independent of the subsequent hydrograph transformation shown in panel (b). The POT/GPD discharge-frequency estimates and the simulated HEC-HMS peak discharges for each AMC scenario are illustrated in Fig. 5b. The simulations show that AMC scenario selection produces a pronounced, systematic difference in simulated design peak discharge, arising from the compounded effect of CN on both runoff volume (Eq. 4–6) and lag time (Eq. 9). Across all return periods, AMC I produces the lowest design peaks, AMC II intermediate values, and AMC III a substantially higher wet-catchment envelope. The relative sensitivity of simulated peak discharge to AMC scenario is strongest for frequent and intermediate return periods. For T = 1 year, the AMC III peak is approximately 5.2 times the AMC I peak, whereas for T = 200 years this ratio decreases to about 3.6, indicating that the largest design rainfall depths partly saturate the loss and timing differences between scenarios. Nevertheless, the absolute difference remains substantial even for rare events, with approximately 310 $m^3 s^{-1}$ separating AMC I and III at T = 200 years. The POT/GPD reference values are bracketed by the AMC I and AMC II envelopes across the entire range of return periods. The AMC II simulation, used as the reference condition, closely matches the POT/GPD reference value at T = 1 year, but overestimates the POT/GPD reference values at return periods beyond approximately two years, with the differences increasing progressively to a maximum of approximately 65 $m^3 s^{-1}$ around T = 200 years.

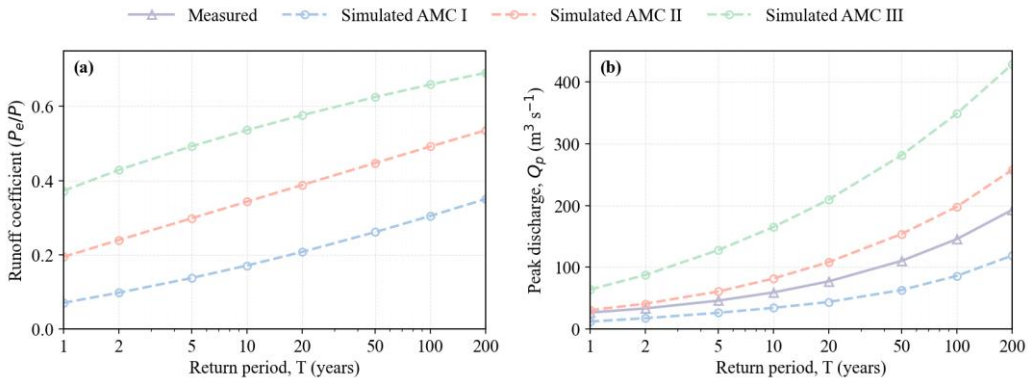


Figure 5. Simulated (a) runoff coefficient and (b) peak discharge under AMC I, II and III design-storm scenarios, compared with POT/GPD discharge-frequency estimates (panel b).

Note that the runoff coefficient in panel (a) is not a pure measure of the CN effect in isolation: because Eq. (4) is nonlinear in P, P_e/P also varies with the return-period-dependent design rainfall depth. Panel (a) should therefore be read as showing the combined effect of rainfall intensity and AMC scenario on runoff generation, rather than an isolation of CN alone.

3.4 CN variability across historical extreme events

Fig. 6 presents the relationships between calibrated CN ($\lambda = 0.05$) and four parameters: 15-day antecedent rainfall, peak discharge, total rainfall depth, and maximum 1-hour intensity for the n = 25 extreme events at Dubravica exceeding the POT threshold. The three horizontal reference lines mark the catchment-averaged AMC I (CN = 50.5), AMC II (CN = 70.8) and AMC III (CN = 84.8) values used in the HEC-HMS simulations. Three events fall below the AMC I line; five events exceed the AMC II line. Fig. 6a shows no significant correlation between CN and 15-day antecedent rainfall ($\tau = 0.12$, $p = 0.4$), with similar results for 5- and 30-day windows. CN values span the full range from 30.8 to over 90 for P <30 mm; however, the CN does stay at and above 70 for P > 30 mm. Fig. 6b shows a weak, non-significant correlation between CN and peak discharge Q_p ($\tau = -0.17$, $p = 0.22$); colour-coding by P shows that the highest-flow events are also the highest-rainfall events, again spanning the full CN range from 30.8 to over 90. Fig. 6c shows the strongest correlation in the dataset ($\tau = -0.638$, $p < 0.001$): CN declines from up to 93.4 for P < 50 mm to below 50 for the three events with P > 100 mm, with the August 2002 event (P = 181.5 mm) reaching CN = 30.8. Fig. 6d shows a negative correlation between CN and 1-hour rainfall intensity ($\tau = -0.446$, $p < 0.01$), with similar results for 3-hour and 6-hour rainfall intensities.

4 Discussion

The systematic AMC II overestimation and AMC I underestimation identified in Section 3.3 motivate the question of whether the conventional three-class AMC framework adequately represents the effective CN behaviour of the catchment's historical flood record. Section 3.4 examines this directly.

The three events falling below the AMC I reference line in Fig. 6 directly explain the AMC I underestimation in Fig. 5b: the model's lower CN bound is set too high relative to the regime governing the catchment's largest observed floods. Conversely, the AMC II line lies below the CN of most small-to-moderate events, consistent with the AMC II overestimation observed across most return periods.

The absence of a significant correlation between CN and antecedent rainfall (Fig. 6a) indicates that antecedent moisture, as represented by cumulative rainfall preceding the event, exerts no detectable independent influence on effective CN once the rainfall intensity is accounted for. This is the empirical basis for this study's central argument that the AMC I–III framework does not capture the dominant source of CN variability in this catchment.

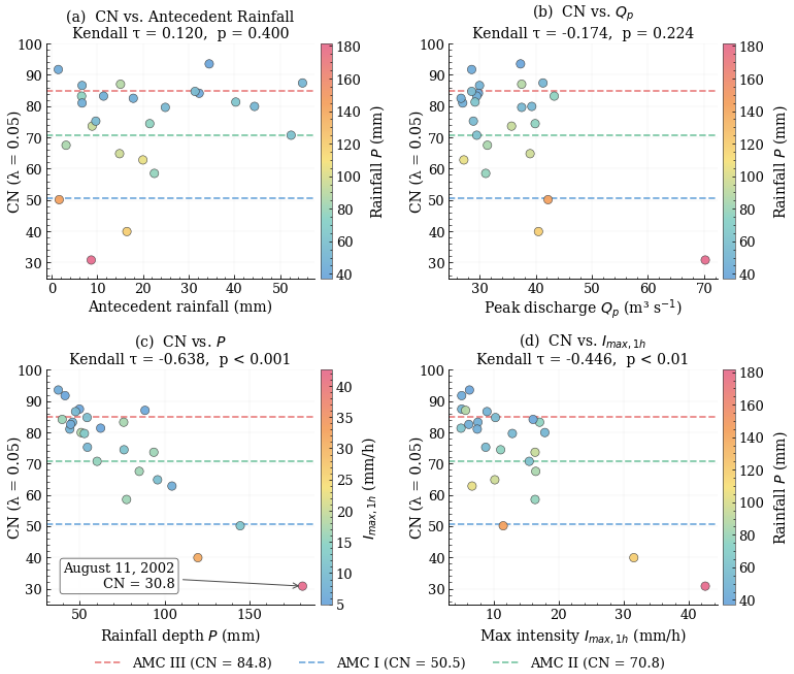


Figure 6. CN relationships with 15-day antecedent rainfall, peak discharge, total rainfall and 1-hour rainfall intensity for the n = 25 POT-exceeding events at the Dubravica station.

The weak CN–Q_p correlation (Fig. 6b) does not indicate CN stability with respect to flood magnitude; rather, since Q_p is jointly determined by P and CN, it reflects compensation between these two variables. The strong CN–rainfall-depth correlation (Fig. 6c) reproduces the Hawkins (1993) CN scale-dependency effect. The CN–intensity correlation (Fig. 6d) is consistent with an infiltration-capacity-exceedance mechanism: high-intensity rainfall exceeds the infiltration capacity of the thin flysch cover more rapidly than low-intensity rainfall of equal depth, producing a runoff response that a formulation based only on rainfall depth interprets as a lower CN.

Together, the presented results indicate that CN variability for the peak discharges relevant to this catchment is governed primarily by the depth of rainfall and, to a lesser extent, by its intensity. These two factors act independently but in the same direction, while antecedent moisture shows no detectable correlation. Consequently, no single CN value, AMC I, II, or III, can simultaneously represent the small-to-moderate events dominating low-return-period statistics and the large, high-intensity events dominating high return-period events. The AMC framework's assumption that catchment response is governed by a discrete, storm-independent antecedent-wetness state is not supported by the observed record; instead, effective CN appears to be a function of the storm itself.

5 Conclusion

The study demonstrates that combining POT/GPD discharge-frequency analysis with HEC-HMS design-storm simulation, using a common sample of historical POT extremes, provides a useful diagnostic framework for evaluating the validity of the SCS-CN/AMC framework in the Pazinčica River catchment. The POT/GPD analysis provides this reference at Dubravica, while the hydrological model shows how simulated peak discharges depend on rainfall duration, the loss assumptions and the antecedent state of the catchment. The comparison is therefore most useful as a diagnostic procedure, rather than as a direct match between the return periods of rainfall and of floods.

The results show that catchment characteristics derived from spatial data alone cannot explain the observed variability in flood response. Although the catchment has low overall imperviousness and a narrow range of CN values derived from land cover, calibrated event CN values across the n = 25 POT-

exceeding events ranged from 30.8 to 93.4. Statistical analysis of this variability shows that effective CN decreases systematically as rainfall depth increases and as maximum rainfall intensity increases, while antecedent precipitation, tested over windows of 5, 15 and 30 days, shows no significant correlation with CN. This indicates that, for this catchment, effective CN is governed primarily by the characteristics of the storm that drives the river discharge, rather than by the soil moisture state before the event that the standard AMC framework assumes.

AMC scenario selection, through its combined effect on runoff-generation volume and lag time, produces a wide envelope of simulated design peak discharge: AMC I defines a lower bound, AMC III an upper bound, and AMC II an intermediate reference. Comparison with the POT/GPD reference values shows that AMC II systematically exceeds these values at return periods beyond approximately two years, while AMC I falls below them at all return periods. This bracketing is consistent with, though not a direct mechanistic consequence of, the finding that effective CN values calibrated against historical events fall below the AMC I reference for the catchment's largest floods (Section 3.4). Both results point to the inadequacy of a single catchment-wide CN across the full range of storms, even though the CN–timing linkage differs between the historical-event calibration and the design-storm scenarios.

These results suggest that the discrepancies between simulated design discharges and the POT/GPD reference values arise less from selecting the wrong AMC class among I, II or III. Instead, they point to a structural limitation of the SCS-CN framework itself. A single catchment-wide CN, however it is chosen, cannot represent both the moderate, frequent events and the large, intense events that together define the discharge-frequency curve. This is because these two populations of events occupy distinct and only partially overlapping ranges of effective CN. For practical application at Dubravica, the results suggest that adjusting CN according to storm depth or intensity, rather than selecting an AMC class based on antecedent moisture, may offer a more robust basis for estimating flood events.

Acknowledgements

This work was supported by the Croatian Science Foundation under the project number IP-2022-10-7598 (4SeaFlood) and DOK-NPOO-2023-10-4458. This work was also funded by the European Union - NextGenerationEU projects CroCo-Flood (uniri-iz-25-86) and HIDKLP (uniri-iz-25-34), as well as project PRIMIS (PK.3.4.17.0018).

References

Afrasiabikia, P., Parvaresh Rizi, A. and Brocca, L. 2025 Improving the SCS-CN method based on adjusting the main parameters using rainfall-runoff data. *Journal of Hydrology: Regional Studies* 62, 102899. https://doi.org/10.1016/j.ejrh.2025.102899.

Coles, S. 2001 *An Introduction to Statistical Modeling of Extreme Values*. Springer, London, UK.

Collings, T.P., Murphy-Barltrop, C.J.R., Murphy, C., Haigh, I.D., Bates, P.D. and Quinn, N.D. 2025 Automated tail-informed threshold selection for extreme coastal sea levels. *Natural Hazards and Earth System Sciences* 25, 4545–4562. https://doi.org/10.5194/nhess-25-4545-2025.

Copernicus Land Monitoring Service 2020 Imperviousness Density 2018 (raster 10 m), Europe, 3-yearly. European Environment Agency, Copenhagen, Denmark. https://doi.org/10.2909/3bf542bd-eebd-4d73-b53c-a0243f2ed862.

Copernicus Land Monitoring Service 2024 CLCplus Backbone 2021 (raster 10 m), Europe, 3-yearly. European Environment Agency, Copenhagen, Denmark. https://doi.org/10.2909/71fc9d1b-479f-4da1-aa66-662a2fff2cf7.

Cordery, I., Pilgrim, D.H. and Rowbottom, I.A. 1984 Time patterns of rainfall for estimating design floods on a frequency basis. *Water Science and Technology* 16(8–9), 155–165. https://doi.org/10.2166/wst.1984.0187.

Davison, A.C. and Smith, R.L. 1990 Models for exceedances over high thresholds. *Journal of the Royal Statistical Society: Series B (Methodological)* 52(3), 393–442. https://doi.org/10.1111/j.2517-

6161.1990.tb01796.x.
Hawkins, R.H. 1993 Asymptotic determination of runoff curve numbers from data. *Journal of Irrigation and Drainage Engineering* 119(2), 334–345. https://doi.org/10.1061/(ASCE)0733-9437(1993)119:2(334).
Hawkins, R.H., Ward, T.J., Woodward, D.E. and Van Mullem, J.A. *2009 Curve Number Hydrology: State of the Practice*. American Society of Civil Engineers, Reston, VA, USA.
Hydrologic Engineering Center 2026 *HEC-HMS User's Manual*, Version 4.14. U.S. Army Corps of Engineers, Davis, CA, USA. https://www.hec.usace.army.mil/software/hec-hms/documentation.aspx (accessed 13 June 2026).
Krvavica, N. and Rubinić, J. 2020 Evaluation of design storms and critical rainfall durations for flood prediction in partially urbanized catchments. *Water* 12 (7), 2044. https://doi.org/10.3390/w12072044.
Lindsay, J.B. 2016 Efficient hybrid breaching-filling sink removal methods for flow path enforcement in digital elevation models. Hydrological Processes 30(6), 846–857. https://doi.org/10.1002/hyp.10648.
Massari, C., Pellet, V., Tramblay, Y., Crow, W.T., Gründemann, G.J., Hascoetf, T., Penna, D., Modanesi, S., Brocca, L., Camici, S. and Marra, F. 2023 On the relation between antecedent basin conditions and runoff coefficient for European floods. *Journal of Hydrology* 625, 130012. https://doi.org/10.1016/j.jhydrol.2023.130012.
Merz, R. and Blöschl, G. 2008 Flood frequency hydrology: 1. Temporal, spatial, and causal expansion of information. *Water Resources Research* 44, W08432. https://doi.org/10.1029/2007WR006744.
Pilgrim, D.H. and Cordery, I. 1975 Rainfall temporal patterns for design floods. *Journal of the Hydraulics Division* 101(1), 81–95. https://doi.org/10.1061/JYCEAJ.0004197.
Ponce, V.M. and Hawkins, R.H. 1996 Runoff curve number: Has it reached maturity? *Journal of Hydrologic Engineering* 1(1), 11–19. https://doi.org/10.1061/(ASCE)1084-0699(1996)1:1(11).
QGIS Development Team 2024 QGIS Geographic Information System. QGIS Association. https://www.qgis.org (accessed 13 June 2026).
Rubinić, J., Krvavica, N., Radišić, M., Horvat, B., Ružić, I., Kalajžić, D., Güttler, I., Gašparac, G., Biondić, R., Biondić, B., Meaški, H., Kovač Konrad, P., Jirkal, D., Jalžić, B. and Jekić, M. 2020 Istraživanje dinamike protjecanja voda u slivu Pazinčice i s njime povezanim vodnim resursima krškog vodonosnika središnje Istre te mogućih promjena, utjecaja i rješenja opskrbe vodom, zaštite od poplava i zaštite akvatičkih ekosustava [in Croatian]. Study report, *Hrvatske vode*, Rijeka, Croatia.
Song, S. and Wang, W. 2019 Impacts of antecedent soil moisture on the rainfall-runoff transformation process based on high-resolution observations in soil tank experiments. *Water* 11(2), 296. https://doi.org/10.3390/w11020296.
Tarasova, L., Lun, D., Merz, R., Blöschl, G., Basso, S., Bertola, M., Miniussi, A., Rakovec, O., Samaniego, L., Thober, S. and Kumar, R. 2023 Shifts in flood generation processes exacerbate regional flood anomalies in Europe. *Communications Earth & Environment* 4, 49. https://doi.org/10.1038/s43247-023-00714-8.
Texas Department of Transportation 2019 *Hydraulic Design Manual*. Revised September 2019. Texas Department of Transportation, Austin, TX, USA. https://www.txdot.gov/manuals/des/hyd/index.html (accessed 13 June 2026).
Tramblay, Y., Arnaud, P., Artigue, G., Lang, M., Paquet, E., Neppel, L. and Sauquet, E. 2023 Changes in Mediterranean flood processes and seasonality. *Hydrology and Earth System Sciences* 27, 2973–2987. https://doi.org/10.5194/hess-27-2973-2023.
USDA-NRCS 2004 *National Engineering Handbook, Part 630: Hydrology, Chapter 10: Estimation of Direct Runoff from Storm Rainfall*. United States Department of Agriculture, Natural Resources Conservation Service, Washington, DC, USA.
Verma, S., Singh, P.K., Mishra, S.K., Singh, V.P., Singh, V. and Singh, A. 2020 Activation soil moisture accounting (ASMA) for runoff estimation using Soil Conservation Service Curve Number (SCS-CN) method. *Journal of Hydrology* 589, 125114. https://doi.org/10.1016/j.jhydrol.2020.125114.
Walega, A., Amatya, D.M., Caldwell, P., Marion, D. and Panda, S. 2020 Assessment of storm direct runoff and peak flow rates using improved SCS-CN models for selected forested watersheds in the Southeastern United States. *Journal of Hydrology: Regional Studies* 27, 100645. https://doi.org/10.1016/j.ejrh.2019.100645.
Woodward, D.E., Hawkins, R.H., Jiang, R., Hjelmfelt, A.T., Van Mullem, J.A. and Quan, Q.D. 2003 *Runoff curve number method: Examination of the initial abstraction ratio*. In Proceedings of the World

Water & Environmental Resources Congress 2003, Philadelphia, PA, USA, 23–26 June, pp. 691–700. https://doi.org/10.1061/40685(2003)308.
Zhang, Y., Wei, H. and Nearing, M.A. 2011 Effects of antecedent soil moisture on runoff modeling in small semiarid watersheds of southeastern Arizona. *Hydrology and Earth System Sciences* 15, 3171–3179. https://doi.org/10.5194/hess-15-3171-2011.
Zhao, N., Yu, F., Li, C., Zhang, L., Liu, J., Mu, W. and Wang, H. 2015 Soil moisture dynamics and effects on runoff generation at small hillslope scale. *Journal of Hydrologic Engineering* 20(7), 05014024. https://doi.org/10.1061/(ASCE)HE.1943-5584.0001062.

BIOTECHNOLOGICAL POTENTIAL OF ALGAE FOR WASTEWATER TREATMENT

Ivan HALKIJEVIC [1*], Antonija CRNOJA [1], Katarina LICHT [1], Hana POSAVCIC [1]

[1] *University of Zagreb Faculty of Civil Engineering, Croatia*

E-mail: ivan.halkijevic@grad.unizg.hr

E-mail: antonija.crnoja@student.grad.hr

E-mail: katarina.licht@grad.unizg.hr

E-mail: hana.posavcic@grad.unizg.hr

[*] *Corresponding author*

Abstract

The paper reviews the use of algae in wastewater treatment, with emphasis on the removal of nutrients, specifically nitrogen and phosphorus. The basic properties of algae and the mechanisms by which they participate in treatment are explained, and the systems most commonly used today, open ponds and closed photobioreactors, are compared in terms of their advantages, disadvantages and practicality for industrial application. The potential use of the biomass generated during treatment is also considered, since it can serve for biofuel production, as an animal feed supplement, as fertiliser, or in the pharmaceutical and cosmetics industries. Case studies of specific wastewaters are presented with an overview of efficiency and costs. This paper is a literature-based review rather than a report of original experimental work; on the basis of the synthesised evidence, the discussion sets out implications for water utilities, the pharmaceutical and cosmetics sectors, public health and regulators, and identifies priorities for future experimental research.

Key words

algae, wastewater, wastewater treatment, photobioreactors, open ponds

1 Introduction

Freshwater is among the most heavily stressed natural resources, and its availability and quality are increasingly threatened by population growth, industrialisation and rapid economic development (Abdel-Raouf et al., 2012). Ever larger volumes of domestic, agricultural and industrial wastewater must therefore be treated before they can safely be returned to the environment, since inadequately treated effluents degrade aquatic ecosystems and limit the reuse potential of an already scarce resource (Gupta & Bux, 2019). Conventional treatment removes settleable solids and oxidises dissolved organic matter, but it is energy-intensive, depends on chemical inputs and frequently leaves the secondary effluent enriched in dissolved inorganic nitrogen and phosphorus, which promotes eutrophication in receiving waters (Jayaraman et al., 2024). Removing this residual load requires a tertiary step that is costly and chemically intensive when carried out by purely physico-chemical means.

Cultivation of algae offers an attractive biological alternative for this stage, because algae assimilate inorganic nitrogen and phosphorus for their own growth and thus polish secondary effluent while capturing carbon dioxide and oxygenating the water (Abdel-Raouf et al., 2012). Removal efficiencies of approximately 86 % for inorganic nitrogen and 70–78 % for inorganic phosphorus are documented for *Chlorella vulgaris*, and algal–bacterial systems achieve 81–96 % overall (Jayaraman et al., 2024). Algal cultures also remove heavy metals and refractory organic compounds, and the same metabolic activity generates biomass that can be valorised as biofuel, feed or high-value compounds (Kumar et al.,

2019). Costs are not negligible, since in raceway ponds the carbon-dioxide supply alone accounts for 40–60 % of operating costs at roughly 60–88 € per tonne of CO_2 (Skifa et al., 2025), but open-pond biomass has a modelled minimum selling price of about 525 € per tonne of ash-free dry weight (Klein & Davis, 2023), and in industrial practice algal treatment has eliminated up to 100 % of certain chemical-dosing costs while generating saleable biomass (Oilgae, n.d.).

In practice, algae are cultivated either in open configurations, such as waste stabilisation ponds and high-rate algal ponds, or in closed photobioreactors (Posten, 2009; Skifa et al., 2025). This paper is a literature-based review rather than a report of original experimental work; it synthesises peer-reviewed articles, book chapters, design guidelines and techno-economic assessments published mainly between 2007 and 2025 and identified in Scopus, Web of Science and Google Scholar, preference being given to studies reporting outdoor, pilot- or full-scale operation because laboratory results overstate performance at scale (Velásquez-Orta et al., 2024). The review outlines the properties of algae and the mechanisms by which they treat wastewater, compares the two families of cultivation system, considers valorisation routes for the biomass, presents selected case studies, and discusses the implications for water utilities, industry, public health and regulators.

2 Methods

2.1 Basic Properties of Algae

Algae are photosynthetic organisms that convert light, carbon dioxide and dissolved nutrients into biomass while releasing oxygen, and are among the simplest photosynthetic life-forms able to grow under harsh conditions (Shah, 2019). Microalgae, which combine microscopic size with a high surface-to-volume ratio and rapid growth, are the group most relevant to wastewater treatment (Gupta & Bux, 2019); the term as used here covers both eukaryotic microalgae, principally green algae and diatoms, and the prokaryotic cyanobacteria (Mehar et al., 2019; Pandey et al., 2019). Diatoms account for roughly 20 % of global photosynthetic carbon-dioxide fixation, and their sensitivity to physico-chemical conditions makes them useful bio-indicators (Ansari et al., 2019); cyanobacteria fix atmospheric nitrogen and grow faster than higher plants (Abdel-Raouf et al., 2012); and green algae such as *Chlorella* and *Scenedesmus* are most commonly applied because they tolerate variable effluent conditions and assimilate nutrients efficiently (Skifa et al., 2025).

Algae are also metabolically flexible: most species grow photoautotrophically, but many grow heterotrophically or mixotrophically, and cultivation of *Chlamydomonas reinhardtii* on wastewater has increased biomass and lipid yields by 144 % and 271 % respectively (Gupta & Bux, 2019; Eladel et al., 2019). Four characteristics make them well suited to treatment: they assimilate inorganic nitrogen and phosphorus directly into biomass; the oxygen released during photosynthesis supports the aerobic bacteria that oxidise organic matter, creating an algal–bacterial symbiosis within a single system (Mitra & Mishra, 2019); their cell walls sequester heavy metals; and the biomass accumulates lipids, proteins, pigments and enzymes useful for biofuel, food, pharmaceutical and cosmeceutical applications (Markou et al., 2019).

Realising these benefits depends on maintaining suitable cultivation conditions, and the reported operating, design and performance ranges are summarised in Table 1: mesophilic temperatures, near-neutral to mildly alkaline pH, and light and carbon-dioxide supply sufficient to avoid limiting photosynthesis (Jayaraman et al., 2024). Under such conditions areal productivities of roughly 10 g m^{-2} day^{-1} are typical in raceway ponds, with values as high as 17 g m^{-2} day^{-1} reported (Skifa et al., 2025).

Table 1. Typical operating, design and performance ranges for algal bioremediation of wastewater; laboratory ranges are complemented by mean values from a meta-analysis of 69 outdoor pilot-scale high-rate algal pond datasets.

Parameter	Typical range	Source
Temperature	15–30 °C (optimum 20–25 °C); pilot-scale mean 18 °C	Skifa et al. (2025); Velásquez-Orta et al. (2024)
Light intensity (PAR)	55–145 µmol m^{-2} s^{-1} (laboratory); pilot-scale mean ≈960 µmol m^{-2} s^{-1}	Jayaraman et al. (2024); Velásquez-Orta et al. (2024)
pH	7.8–8.4 (pilot-scale mean 8.2); >9 during intense photosynthesis	Jayaraman et al. (2024); Velásquez-Orta et al. (2024)
Carbon-dioxide supply	1–6 % v/v; 1.65–2.2 kg CO_2 per kg biomass produced	Jayaraman et al. (2024); Skifa et al. (2025)
Hydraulic retention time	4–10 d (pilot-scale mean 7.7 d); 3–4 d in summer, 7–9 d in winter	LGA of South Australia (2020); Park et al. (2011)
Water depth (open systems)	0.1–0.3 m (raceway ponds); 0.3–0.5 m (high-rate algal ponds)	Skifa et al. (2025); LGA of South Australia (2020)
Mixing	0.15–0.30 m s^{-1} forward velocity; turbulent, paddlewheel-driven	Skifa et al. (2025)
Influent N:P ratio (mass)	8–10 for simultaneous N and P removal; ≈30 for *Scenedesmus* sp.	Cai et al. (2013); Jose & Archanaa (2019)
Specific growth rate	≈0.54 d^{-1} (outdoor pilot scale) vs ≈1 d^{-1} (laboratory)	Velásquez-Orta et al. (2024)
Areal biomass productivity	≈10 g m^{-2} d^{-1} typical; 5.7–40 g m^{-2} d^{-1} reported	Skifa et al. (2025); Velásquez-Orta et al. (2024)
Nutrient-removal efficiency	81–96 % overall; HRAP means ≈90 % NH_4^+, 70 % COD, 50 % PO_4^{3-}	Jayaraman et al. (2024); Velásquez-Orta et al. (2024)

2.2 Quantification of Treatment and Growth Performance

Although this review is qualitative, the processes described above are conventionally quantified by a few simple expressions, given here so that the values in Tables 1 and 3 can be interpreted consistently. The removal efficiency η (%) is the fractional decrease in the concentration of a pollutant between influent and effluent, C_0 and C_t (mg L^{-1}) being the concentrations at the inlet and at time t:

$$\eta = (C_0 - C_t) / C_0 \times 100 \quad (1)$$

Because η is referenced to the influent concentration, the same efficiency corresponds to very different mass loadings in dilute and in concentrated effluents; the volumetric removal rate r (mg L^{-1} d^{-1}), where HRT (d) is the hydraulic retention time, is a useful complement:

$$r = (C_0 - C_t) / HRT \quad (2)$$

Biomass production is expressed per unit illuminated surface or volume, as the areal productivity P_A (g m^{-2} d^{-1}) and the volumetric productivity P_V (g m^{-3} d^{-1}), where V_R (m^3) is the working volume, A (m^2) the illuminated surface area and C_t and C_0 the biomass concentrations in the reactor and in the influent (Velásquez-Orta et al., 2024):

$$P_A = (C_t - C_0) \cdot V_R / (HRT \cdot A) \quad (3)$$

$$P_V = P_A \cdot (A / V_R) \quad (4)$$

Because open ponds are shallow, A/V_R is large and areal productivity is the more demanding figure of merit where land is constrained. For batch or start-up conditions the specific growth rate µ (d^{-1}) follows from the exponential growth model:

$$\mu = (\ln C_t - \ln C_0) / (t - t_0) \quad (5)$$

Reported values illustrate the scale-up penalty: µ averages about 0.54 d^{-1} in outdoor pilot-scale high-rate algal ponds against approximately 1 d^{-1} in the laboratory, so design should not be extrapolated from bench-scale data (Velásquez-Orta et al., 2024). Production of 1 g of dry biomass requires approximately 1.83 g CO_2, 0.07 g N and 0.008 g P, so a wastewater must supply at least about 70 mg L^{-1} N and 8 mg

L^{-1} P to sustain 1 g L^{-1} of biomass. The corresponding mass ratio, N:P ≈ 8.8, agrees with the practical optimum of 8–10 for *Chlorella vulgaris*, although optima are species-specific and a ratio near 30 has been reported for *Scenedesmus* sp. (Cai et al., 2013; Jose & Archanaa, 2019); where the influent ratio departs from the optimum, one nutrient remains in excess in the effluent. The same relationships underpin dynamic models of pond productivity (Lösing, 2011).

2.3 Mechanisms of Pollutant Removal by Algae

Algae contribute to treatment through several complementary mechanisms that usually act simultaneously within a single system: assimilation of nitrogen and phosphorus, oxygenation of the water, elevation of pH, binding of metals and degradation of organic micropollutants.

2.3.1 Photosynthetic oxygenation and the algal–bacterial symbiosis

The foundation of algal treatment is a mutualistic relationship between algae and bacteria: photoautotrophic microalgae assimilate dissolved nitrogen, phosphorus and carbon dioxide and release oxygen as a by-product of photosynthesis (Jayaraman et al., 2024).

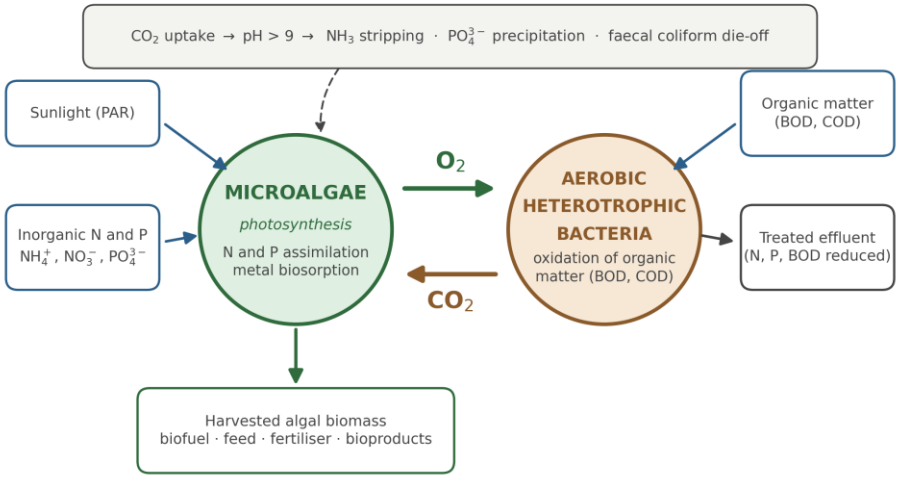


Figure 1. Schematic representation of the algal–bacterial symbiosis that underpins algal wastewater treatment, showing the oxygen and carbon-dioxide loop, the principal inputs and outputs, and the pH-mediated removal pathways (compiled from Abdel-Raouf et al., 2012; Jayaraman et al., 2024; Mohsenpour et al., 2021).

This oxygen serves as the electron acceptor for the aerobic heterotrophic bacteria that oxidise the organic load, while the carbon dioxide released by bacterial respiration is taken back up by the algae, closing the loop (Abdel-Raouf et al., 2012). In waste stabilisation ponds the oxygen required for BOD removal is supplied primarily by photosynthesis, which is why facultative ponds are loaded at only about 100–400 kg BOD ha^{-1} day^{-1}. The exchange of oxygen and carbon dioxide between the two partners, with the associated pH-mediated pathways, is summarised in Figure 1.

2.3.2 Assimilation of nutrients and pH-driven removal

The central mechanism of nutrient removal is uptake of inorganic nitrogen and phosphorus into algal biomass. Nitrate uptake and reduction are photosynthetically driven, assimilation is modulated by light, temperature, pH and carbon availability, and phosphate uptake depends approximately hyperbolically on the external concentration, so removal efficiency declines as the residual concentration falls (Abdel-Raouf et al., 2012). Because algae incorporate nutrients into harvestable cells rather than converting nitrogen to gas as in nitrification–denitrification, the nutrients are recovered rather than lost, a key advantage when the biomass is valorised. Intense photosynthesis simultaneously depletes dissolved carbon dioxide; carbonate and bicarbonate then dissociate to supply more, leaving an excess of hydroxyl

ions and driving the pH above 9. The elevated pH promotes ammonia volatilisation, favours phosphate precipitation and is lethal to faecal coliforms, and these effects can account for a substantial share of nutrient and pathogen removal in open systems (Abdel-Raouf et al., 2012).

2.3.3 Removal of metals and organic micropollutants

Heavy metals are removed by two routes: passive biosorption, in which metal ions bind to functional groups on the cell wall by adsorption and ion exchange and which proceeds even with non-living cells, and active bioaccumulation, in which living cells transport trace metals such as Co, Cu, Zn, Cr, Pb and Se intracellularly (Abdel-Raouf et al., 2012; Gupta & Bux, 2019). Which route dominates depends on the alga, the metal, the solution conditions and whether the cells are living; field systems using cyanobacteria have removed up to 99 % of dissolved and particulate metals. Organic micropollutants, including pharmaceuticals and personal-care products, are eliminated by adsorption, bioaccumulation and enzymatic degradation at rates that vary with the compound and the species, the large specific surface area of algal cells further promoting adsorption and subsequent biodegradation (Jayaraman et al., 2024). A single culture can thus address nutrients, organic load, metals and trace organics at once.

2.4 Cultivation Systems and Technologies

Algae are grown either in open systems, exposed to the atmosphere, or in closed photobioreactors (PBRs). The two represent a fundamental trade-off: open systems are cheap and simple but offer little control, whereas closed systems deliver high productivity and control at substantially higher cost. Most algal biomass worldwide is produced in open ponds, with only a few hundred tonnes per year grown in photobioreactors (Posten, 2009).

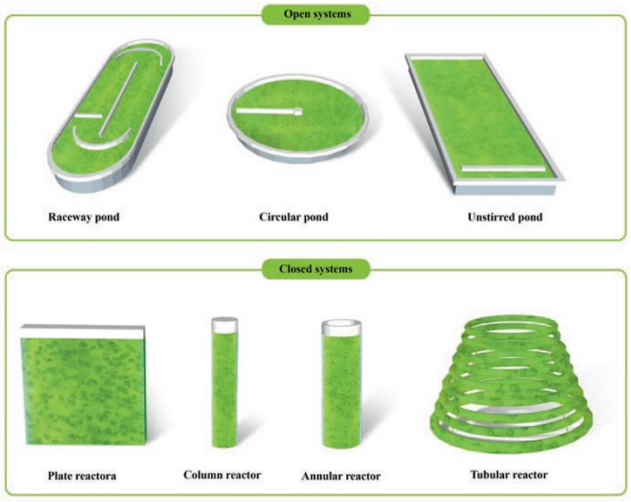


Figure 2. Examples of different types of pond systems for outdoor microalgae cultivation (Zerrouki & Henni, 2019)

2.4.1 Open systems

Open cultivation takes several forms, including raceway, circular, unstirred and thin-layer cascade ponds, simple mixed ponds and high-rate algal ponds (Skifa et al., 2025), Figure 2. Raceway ponds are the most widely used and are also employed commercially for *Spirulina*, *Haematococcus* and *Dunaliella*; a typical raceway is a closed-loop channel 0.1–0.3 m deep, mixed by a paddlewheel, with reported sizes of 100–5000 m², shallow operation improving light penetration and culture stability. Productivities range from less than 1 g m^{-2} day^{-1} in unstirred ponds to 31 g m^{-2} day^{-1} in thin-layer cascades (Skifa et al., 2025).

Waste stabilisation ponds (WSPs) are large, shallow basins in which raw sewage is treated entirely by natural processes involving algae and bacteria, and they are among the most cost-effective and easily operated methods for domestic and industrial wastewater: sunlight is the only energy input, supervision

is minimal and faecal coliform removal is particularly effective (Abdel-Raouf et al., 2012). A WSP system comprises anaerobic, facultative and maturation ponds in series, the first two removing BOD and settling solids and the last dedicated to pathogen removal (Water Corporation, 2022); the drawbacks are a large footprint and long retention times, with significant evaporative loss.

High-rate algal ponds (HRAPs) are shallow, paddlewheel-mixed raceways designed specifically to combine treatment with biomass production. Compared with a traditional facultative lagoon an HRAP offers up to a 50 % smaller footprint owing to its shorter retention time, which also lowers construction costs and evaporative losses; it provides superior ammonia removal, reported at 59–74 %, and requires less power than activated sludge or membrane bioreactors, the only significant demand being the paddlewheel, which can be solar-driven (LGA of South Australia, 2020). Independent evidence confirms substantially higher areal productivity than conventional oxidation ponds at low energy demand, although larger units perform less well than small experimental ponds (Park et al., 2011; Sutherland et al., 2020). Open systems are therefore inexpensive, energy-efficient and robust, but land-hungry, exposed to weather and contamination, subject to evaporation and of limited controllability.

2.4.2 Closed photobioreactors

Closed photobioreactors enclose the culture within transparent vessels. The main configurations are tubular reactors as horizontal arrays or helical coils, flat-plate reactors, and bubble-column and airlift reactors (Posten, 2009), Figure 2. Tubular reactors are built from glass, Perspex or PVC with tube diameters from roughly 24 mm to 24 cm, narrower tubes being favoured for their better hydrodynamics, and they offer near-linear scale-up, in contrast to paddlewheel ponds (Abdel-Raouf et al., 2012).

Effective design rests on managing three coupled phenomena: distribution of light to avoid saturation, mixing along the light gradient to exploit light/dark cycles, and aeration and mass transfer to supply carbon dioxide and strip photosynthetic oxygen (Posten, 2009). Managed well, closed systems achieve higher productivities than open ponds, reach high biomass concentrations, prevent contamination and largely eliminate evaporation.

The decisive disadvantage is cost: for low-value applications such as biofuels, photobioreactor costs would need to fall below roughly € 40 per m² and biomass concentrations to exceed about 20 g L^{-1}, yet available reactors cost several times this figure (Posten, 2009). Practical problems also persist, including overheating, accumulation of inhibitory oxygen, biofouling of the inner walls and damage to fragile cells from circulation (Abdel-Raouf et al., 2012).

2.4.3 Comparison and practicality for industrial application

Table 2 summarises the contrasting characteristics of the two approaches. For wastewater treatment, where large volumes must be processed at minimum cost and the product is of low value, open systems and HRAPs in particular are the more practical choice; closed photobioreactors are justifiable mainly where cultivation targets high-value biomass or a contamination-free monoculture.

Table 2. Comparison of open systems and closed photobioreactors for algal wastewater treatment (Abdel-Raouf et al., 2012; LGA of South Australia, 2020; Posten, 2009; Skifa et al., 2025).

Attribute	Open systems (ponds/HRAP)	Closed photobioreactors
Capital and operating cost	Low	High
Productivity	Lower (≈10 g m^{-2} day^{-1} typical)	Higher
Biomass concentration	Low	High (target >20 g L^{-1})
Land area required	Large	Smaller
Process control	Limited	High
Contamination risk	High	Low
Water loss by evaporation	Significant	Minimal
Scale-up	Difficult (ponds)	Near-linear (tubular)
Energy demand	Low	High
Best suited to	Wastewater treatment, low-value biomass	High-value biomass, monocultures

2.5 Valorisation of Algal Biomass

A major advantage of algal treatment is that the biomass generated during purification need not be a waste but can become a valuable product. Because most wastewaters are rich in nitrogen and phosphorus they serve as a cheap nutrient source, and the harvested algae can be directed to methane production, composting, liquid biofuels, animal feed, fertiliser use or fine chemicals (Abdel-Raouf et al., 2012).

Conversion to energy is the most widely studied route, either by extracting lipids for biodiesel and renewable diesel or by anaerobic digestion of the whole biomass to biogas. Because lipid-extraction technologies for waste-grown algae remain under development and lipid contents are variable, anaerobic digestion is the more appropriate near-term option at treatment plants (Abdel-Raouf et al., 2012). Algae yield somewhat less methane than sewage sludge, roughly 0.3 against 0.4 L CH_4 per gram of volatile solids, but co-digestion with carbon-rich wastes to adjust the C:N ratio to about 20–25:1 doubles the methane production rate. The attraction lies in productivity: microalgae in high-rate ponds can produce some 70 tonnes of ash-free dry weight per hectare per year, far exceeding soybeans (≈3), corn (≈9) and switchgrass or hybrid poplar (≈10–13 t ha^{-1} $year^{-1}$), without competing for arable land.

The biomass is also rich in protein and can supplement animal feed or serve as aquaculture feed (Skifa et al., 2025), and because it concentrates the nitrogen and phosphorus assimilated from the wastewater it makes an effective fertiliser and can be composted: in the alginate sector, algal treatment produced a commercially valuable fertiliser in strong market demand and eliminated residual sludge disposal entirely (Oilgae, n.d.), while nitrogen-fixing cyanobacteria further reduce the need for synthetic fertiliser when biomass is returned to land (Pancha et al., 2019).

The highest-value applications draw on the diverse biochemistry of algae, which synthesise polymers, fatty acids, enzymes, vitamins, pigments and secondary metabolites for pharmaceutical, nutraceutical and cosmeceutical products (Gupta & Bux, 2019); these command prices that justify the higher cost of closed photobioreactor cultivation. The end use must nevertheless be matched to biomass quality, since the properties that allow algae to remove metals and micropollutants mean that biomass grown on contaminated wastewater may accumulate them; such material is best directed to energy recovery or, after assessment, fertiliser use rather than food or feed.

3 Results and Discussion

Case studies of algal treatment applied to specific wastewaters confirm the performance suggested by the mechanisms described above. Selected examples are summarised in Table 3 and shown graphically in Figure 3, grouped by pollutant class: metals and phosphate are removed almost completely, nutrients and organic load consistently at 60–90 %, and micropollutants over the widest range, down to some 40–60 % for diclofenac.

3.1 Case studies by wastewater type

Municipal wastewater is the most common target, the objective being removal of residual nutrients and, increasingly, of pharmaceutical micropollutants. In two pilot high-rate algal ponds treating urban wastewater at hydraulic retention times of 4 and 8 days over a full annual cycle, more than 90 % of ibuprofen, caffeine and acetaminophen was removed, with 60–90 % of ketoprofen and naproxen and 40–60 % of the more recalcitrant diclofenac, biodegradation, photolysis and adsorption being the main pathways and removal consistently higher in the warm season (Matamoros et al., 2015). Some 99 % of micropollutants were removed within ten days in laboratory cultures of *Chlorella* sp. and *Scenedesmus* sp. (Mateescu & Zaharescu, 2019), while for nutrients *Chlorella vulgaris* has achieved about 86 % removal of inorganic nitrogen and up to 97.8 % of phosphorus (Abdel-Raouf et al., 2012).

Industrial effluents are more variable and often more concentrated, but several have been treated successfully. *Chlorella vulgaris* reduced total nitrogen by around 80 % and COD by around 90 % in

rubber-latex wastewater, while in industrial wastewater generally nitrogen removal of about 50 % and phosphorus removal of about 86 % have been reported (Abdel-Raouf et al., 2012; Jayaraman et al., 2024). A consortium of *Desmodesmus* sp., *Oscillatoria* and *Arthrospira* removed 83 % of nitrogen and 60 % of phosphorus from lagoon-plant effluent, and *Spirulina* sp. grown on aquaculture effluent removed essentially all phosphate outdoors (Jayaraman et al., 2024). Screening strains directly from the target effluent is a practical first step, as six species suitable for pulp and paper mill effluent were isolated from the mill wastewater itself (Zule et al., 2013); the constraints on operating such systems as full biorefineries have been reviewed by Letry et al. (2019).

Algal systems have also been used to target pharmaceuticals and metals. *Chlorella sorokiniana* removed 60–100 % of spiked diclofenac, ibuprofen, paracetamol and metoprolol in laboratory cultures fed with source-separated urine and anaerobically treated black water, biodegradation and photolysis dominating, whereas carbamazepine and trimethoprim were removed by no more than 30 % and 60 % respectively (de Wilt et al., 2016). Cyanobacteria in artificial pools and meanders removed up to 99 % of metals from mine wastewater (Abdel-Raouf et al., 2012), and full-scale HRAPs in South Australia have demonstrated ammonia removal of 59–74 % (LGA of South Australia, 2020).

Table 3. Selected case studies of algal wastewater treatment, showing study scale and duration and the reported removal efficiencies. n.r. – not reported in the cited source.

Wastewater	Algae	Scale and duration	Reported efficiency	Source
Urban (micropollutants)	*Chlorella*, *Stigeoclonium*, *Monoraphidium*	Two pilot HRAPs, 1.5 m² and 0.5 m³; HRT 4 and 8 d, one annual cycle	>90 % ibuprofen, caffeine, paracetamol; 60–90 % ketoprofen, naproxen; 40–60 % diclofenac	Matamoros et al. (2015)
Urban / synthetic (micropollutants)	*Chlorella* sp., *Scenedesmus* sp.	Laboratory batch, 10 d	≈99 % of micropollutants	Mateescu & Zaharescu (2019)
Domestic (nutrients)	*Chlorella vulgaris*	Laboratory and pilot values compiled in a review	86 % inorganic N; up to 97.8 % P	Abdel-Raouf et al. (2012)
Rubber-latex industry	*Chlorella vulgaris*	Laboratory, n.r.	≈80 % total N; ≈90 % COD	Jayaraman et al. (2024)
Lagoon-plant effluent	*Desmodesmus* sp., *Oscillatoria*, *Arthrospira*	Outdoor open pond, 19 d	83 % N; 60 % P	Jayaraman et al. (2024)
Aquaculture effluent	*Spirulina* sp.	Outdoor trial scale, n.r.	≈100 % phosphate	Jayaraman et al. (2024)
Source-separated urine and black water, spiked pharmaceuticals	*Chlorella sorokiniana*	Laboratory batch, n.r.	60–100 % diclofenac, ibuprofen, paracetamol, metoprolol; ≤30 % carbamazepine; ≤60 % trimethoprim	de Wilt et al. (2016)
Mine wastewater (metals)	Cyanobacteria	Full scale, artificial pools and meanders, n.r.	up to 99 % dissolved and particulate metals	Abdel-Raouf et al. (2012)
Municipal (HRAP)	Mixed culture	Full-scale field installations, South Australia; HRT 4–10 d	59–74 % ammonia	LGA of South Australia (2020)

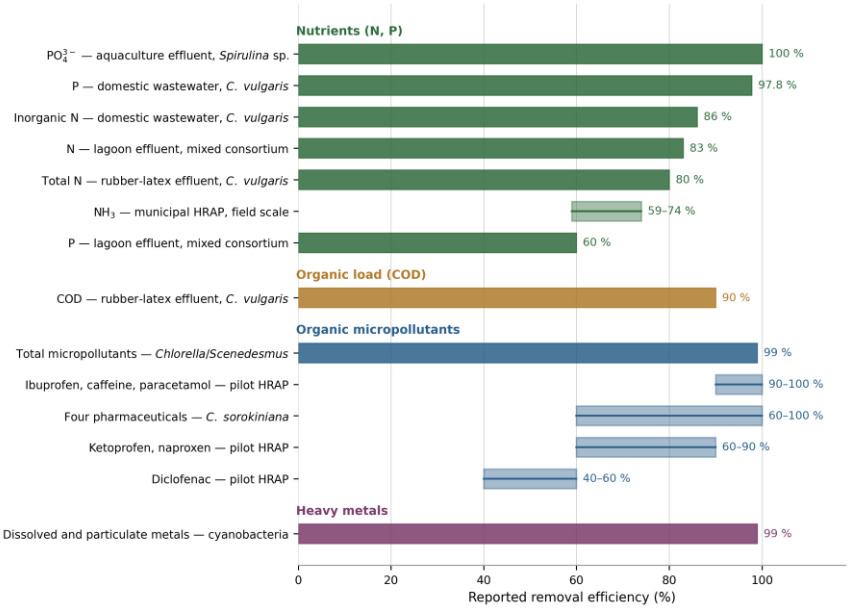


Figure 3. Reported removal efficiencies from the case studies of Table 3, grouped by pollutant class. Solid bars denote single reported values; open bars denote reported ranges. Values reported as ">90 %" are plotted as 90–100 %.

3.2 Economic perspective: an industrial cost–benefit example

A documented application in the alginate industry illustrates the economics most clearly. Replacing conventional effluent treatment with phycoremediation eliminated the annual expenditure on caustic soda used for neutralisation, a saving of around 46,000 € per year, while labour and electricity costs remained almost unchanged; the process produced no residual sludge, removing an estimated 2,750 € in annual disposal costs and instead yielding a saleable fertiliser, and it released about 75 % of the treatment-facility footprint (Oilgae, n.d.). Pollutant removal coupled with biomass valorisation can thus transform the economics of effluent treatment, although outcomes are site- and effluent-specific.

3.3 Implications for Water Utilities and Wastewater Managers

For utilities the evidence supports a differentiated rather than a universal recommendation. High-rate algal ponds are best positioned as an upgrade to existing pond-based works serving small and medium agglomerations, where land is available and the realistic alternative is a mechanical process with a considerably higher energy demand; relative to a facultative lagoon an HRAP offers up to a 50 % smaller footprint and its only significant power requirement can be driven by photovoltaics (LGA of South Australia, 2020; Park et al., 2011). Three operational conclusions follow: performance is governed primarily by solar irradiance and influent ammonium concentration, so site selection and the seasonal adjustment of depth and retention time matter most; laboratory growth rates are roughly twice those achieved outdoors, so design should rest on pilot- or full-scale data (Velásquez-Orta et al., 2024); and harvesting and dewatering rather than cultivation dominate cost, so valorisation should be appraised case by case (Acién et al., 2012).

3.4 Implications for the Pharmaceutical and Cosmetics Industries and for Public Health

For producers of pharmaceuticals and cosmetics the relevance of algal treatment is now as much regulatory as technical. Directive (EU) 2024/3019 requires producers of human medicinal and cosmetic products to finance at least 80 % of the cost of the quaternary treatment introduced to remove micropollutants from urban wastewater, an obligation that Member States must implement by 31 December 2028 (European Union, 2024); industry associations challenged these provisions, but the action was dismissed by the General Court of the European Union in February 2026, so the financial exposure may now be treated as settled (Water Europe, 2026). Algal systems are a partial rather than a

complete answer: readily biodegradable and photolabile compounds are removed efficiently, exceeding 90 % for ibuprofen, caffeine and paracetamol, whereas diclofenac is typically removed by only 40–60 % and carbamazepine by no more than 30 % (de Wilt et al., 2016; Matamoros et al., 2015). Their realistic role is a low-energy polishing stage that reduces the load reaching ozonation or activated-carbon adsorption, so co-funding demonstration-scale algal polishing may be a cheaper route to compliance than financing conventional quaternary treatment alone.

For public-health authorities, the elevated pH generated by intense photosynthesis, combined with sunlight exposure in shallow, well-mixed ponds, inactivates faecal coliforms without chemical disinfectants and hence without chlorination by-products (Abdel-Raouf et al., 2012; LGA of South Australia, 2020), which makes maturation ponds and HRAPs attractive wherever treated effluent is destined for agricultural reuse under Regulation (EU) 2020/741 (European Union, 2020). Two caveats apply: partial removal of antibiotics leaves sub-inhibitory concentrations whose implications for antimicrobial resistance warrant monitoring, and contaminants accumulate in the harvested cells, so the safety of the biomass must be demonstrated before any food or feed use (Letry et al., 2019; Markou et al., 2019).

3.5 Regulatory and Policy Implications

The recast Urban Wastewater Treatment Directive sets the frame within which algal technologies will be assessed in Europe over the next two decades. It extends secondary treatment to smaller agglomerations, makes tertiary nitrogen and phosphorus removal mandatory for plants above 150,000 population equivalents by 2039, phases in quaternary treatment between 2033 and 2045, introduces the extended producer responsibility scheme described above, sets a national energy-neutrality target by 2045 and requires Member States to promote water reuse (European Union, 2024). Nutrient removal is the core competence of algal systems, micropollutant attenuation a partial co-benefit, their low energy demand supports the neutrality target and the disinfected effluent supports reuse.

Five recommendations follow. First, compliance pathways should remain performance-based and technology-neutral, so that combined algal-plus-polishing trains can be demonstrated against the same benchmark as ozonation or activated carbon. Second, because the energy-neutrality target is set nationally rather than per plant, low-energy extensive systems at small works can offset the demand of quaternary treatment at large ones. Third, the legal status of wastewater-grown biomass under the fertilising-products and feed frameworks is the principal non-technical barrier to valorisation. Fourth, reporting should be standardised, since the evidence base is constrained less by the number of studies than by inconsistent reporting of retention time, productivity and removal efficiency (Velásquez-Orta et al., 2024). Fifth, because performance is climate-dependent and published outdoor datasets originate predominantly from Spain, New Zealand and the United States, Member States in continental and sub-Mediterranean climates, Croatia among them, need their own demonstration data.

3.6 Priorities for Future Experimental Work

The gaps identified translate into a specific experimental agenda. Year-round outdoor campaigns in continental and sub-Mediterranean climates, quantifying winter performance, culture collapse and recovery, are the single most valuable missing item of evidence (Velásquez-Orta et al., 2024). Because harvesting and dewatering dominate cost, comparative pilot trials of bioflocculation, ozone flotation, membrane filtration and gravity settling are required, with consistent energy and cost accounting (Acién et al., 2012). Closed mass balances separating biodegradation, photolysis and sorption are needed for micropollutants, together with monitoring of antibiotic resistance genes (de Wilt et al., 2016; Matamoros et al., 2015), while hybrid configurations such as photobioreactor-produced inoculum feeding open ponds, algal–bacterial membrane bioreactors and the coupling of ponds with anaerobic digestion merit pilot evaluation (Jayaraman et al., 2024). Finally, characterisation of contaminants in the biomass, life-cycle assessment under European conditions and the screening of native strains from the target effluent (Zule et al., 2013) should be combined with dynamic models calibrated on local data (Lösing, 2011).

4 Conclusion

Algae offer a versatile biotechnological route for wastewater treatment, particularly for removing the residual nitrogen and phosphorus that conventional secondary treatment leaves behind. Their value rests on rapid, metabolically flexible growth, the assimilation of nutrients into harvestable biomass, the photosynthetic oxygenation that sustains a mutualistic algal–bacterial community, pH-driven ammonia stripping, phosphate precipitation and disinfection, and the capacity to bind heavy metals and degrade organic micropollutants within a single system, with reported nutrient-removal efficiencies frequently in the 80–96 % range.

Open systems, comprising waste stabilisation ponds and, increasingly, high-rate algal ponds, are inexpensive, energy-efficient and simple to operate and presently dominate large-scale application, their limitations being a large land footprint, evaporative loss, weather dependence and limited process control; closed photobioreactors deliver higher productivity and contamination-free monocultures at a cost that remains too high for low-value applications. A defining advantage is that the biomass is a resource rather than a waste: depending on quality it can be converted to biogas or liquid biofuels, used as feed, applied as fertiliser or processed into high-value compounds, which aligns algal systems with circular-economy principles.

The findings carry different messages for different stakeholders. For water utilities, high-rate algal ponds are a credible low-energy upgrade to pond-based works serving small and medium agglomerations, provided that design rests on outdoor rather than laboratory data. For the pharmaceutical and cosmetics industries, which must finance at least 80 % of the cost of quaternary treatment, algal systems are a low-cost partial polishing step rather than a substitute for ozonation or activated carbon, since the compounds they remove least effectively are precisely the recalcitrant ones the Directive targets. For public-health authorities, pathogen inactivation without chemical disinfectants is a clear benefit, offset by the need to demonstrate biomass safety before any food or feed use. For policymakers, the priorities are technology-neutral compliance pathways, exploitation of the national energy-neutrality target, clarification of the legal status of wastewater-grown biomass, and standardised reporting. Harvesting and dewatering remain cost-intensive, open systems are climate-sensitive and closed reactors expensive; addressing these will determine how fully the potential of algae can be realised.

Acknowledgements

This research was supported by the European Regional Development Fund under the PKK 2021–2027 programme, project “Upravljanje rizicima od pluvijalnih poplava kroz mjere prilagodbe klimatskim promjenama na urbanim područjima (HORUS)” grant number PK.3.4.17.0009. The views and opinions expressed are however those of the author only and do not necessarily reflect those of the European Union or the granting authority. Neither the European Union nor the granting authority can be held responsible for them.

References

Abdelfattah, A., Ali, S.S., Ramadan, H., El-Aswar, E.I., Eltawab, R., Ho, S.-H., Elsamahy, T., Li, S., El-Sheekh, M.M., Schagerl, M., Kornaros, M. & Sun, J. 2023 Microalgae-based wastewater treatment: Mechanisms, challenges, recent advances, and future prospects. *Environmental Science and Ecotechnology, 13*, 100205.

Abdel-Raouf, N., Al-Homaidan, A.A. & Ibraheem, I.B.M. 2012. Microalgae and wastewater treatment. *Saudi Journal of Biological Sciences, 19*(3), 257–275.

Acién, F.G., Fernández, J.M., Magán, J.J. & Molina, E. 2012 Production cost of a real microalgae production plant and strategies to reduce it. *Biotechnology Advances, 30*(6), 1344–1353.

Ansari, F.A., Gupta, S.K. & Bux, F. 2019 Microalgae: A biorefinery approach to the treatment of aquaculture wastewater. In S. K. Gupta & F. Bux (Eds.), *Application of microalgae in wastewater treatment: Volume 2: Biorefinery approaches of wastewater treatment* (pp. 69–84). Springer.
Cai, T., Park, S.Y. & Li, Y. 2013 Nutrient recovery from wastewater streams by microalgae: Status and prospects. *Renewable and Sustainable Energy Reviews, 19*, 360–369.
Chisti, Y. 2007 Biodiesel from microalgae. *Biotechnology Advances, 25*(3), 294–306.
de Wilt, A., Butkovskyi, A., Tuantet, K., Hernandez Leal, L., Fernandes, T.V., Langenhoff, A. & Zeeman, G. 2016. Micropollutant removal in an algal treatment system fed with source separated wastewater streams. *Journal of Hazardous Materials, 304*, 84–92.
Eladel, H., Esakkimuthu, S. & Abomohra, A.E.-F. 2019 Dual role of microalgae in wastewater treatment and biodiesel production. In S. K. Gupta & F. Bux (Eds.), *Application of microalgae in wastewater treatment: Volume 2: Biorefinery approaches of wastewater treatment* (pp. 85–122). Springer.
European Union 2020. Regulation (EU) 2020/741 of the European Parliament and of the Council of 25 May 2020 on minimum requirements for water reuse. *Official Journal of the European Union, L 177*, 32–55.
European Union. 2024 Directive (EU) 2024/3019 of the European Parliament and of the Council of 27 November 2024 concerning urban wastewater treatment (recast). *Official Journal of the European Union, L, 2024/3019*, 12 December 2024.
Gupta, S.K. & Bux, F. (Eds.) 2019. *Application of microalgae in wastewater treatment, Volume 1: Domestic and industrial wastewater treatment*. Springer.
Jayaraman, J., Kumaraswamy, J., Rao, Y.K.S.S., Karthick, M., Baskar, S., Anish, M., Sharma, A., Yadav, A.S., Alam, T. & Ammarullah, M.I. 2024 Wastewater treatment by algae-based membrane bioreactors: A review of the arrangement of a membrane reactor, physico-chemical properties, advantages and challenges. *RSC Advances, 14*, 34769–34790.
Jose, S. & Archanaa, S. 2019. Phycoremediation of textile wastewater: Possibilities and constraints. In S. K. Gupta & F. Bux (Eds.), *Application of microalgae in wastewater treatment: Volume 1: Domestic and industrial wastewater treatment* (Chapter 14). Springer.
Klein, B., & Davis, R. 2023 *Algal biomass production via open pond algae farm cultivation: 2022 state of technology and future research* (Technical Report No. NREL/TP-5100-85661). National Renewable Energy Laboratory.
Kumar, D., Singh, B. & Ankit. 2019 Phycoremediation of nutrients and valorisation of microalgal biomass: An economic perspective. In S.K. Gupta & F. Bux (Eds.), *Application of microalgae in wastewater treatment: Volume 2: Biorefinery approaches of wastewater treatment* (pp. 1–16). Springer.
Letry, K.A., Castro, E.D., Gupta, S.K. & Kumar, M. 2019 Industrial wastewater-based algal biorefineries: Application constraints and future prospects. In S. K. Gupta & F. Bux (Eds.), *Application of microalgae in wastewater treatment: Volume 2: Biorefinery approaches of wastewater treatment* (pp. 371–392). Springer.
Local Government Association of South Australia. (2020). *High rate algal pond (HRAP) design guideline: An element in CWMS wastewater treatment trains*. Local Government Association of South Australia.
Lösing, M.B. 2011 *Modelling & simulating microalgae production in an open pond reactor* [Master's thesis, Wageningen University].
Markou, G., Wang, L., Ye, J. & Unc, A. 2019 Cultivation of microalgae on anaerobically digested agro-industrial wastes and by-products. In S. K. Gupta & F. Bux (Eds.), *Application of microalgae in wastewater treatment: Volume 2: Biorefinery approaches of wastewater treatment* (pp. 147–172). Springer.
Matamoros, V., Gutiérrez, R., Ferrer, I., García, J. & Bayona, J.M. 2015 Capability of microalgae-based wastewater treatment systems to remove emerging organic contaminants: A pilot-scale study. *Journal of Hazardous Materials, 288*, 34–42.
Mateescu, C. & Zaharescu, T. 2019 Comprehensive overview of biomethane production potential of algal biomass cultivated in wastewater. In S. K. Gupta & F. Bux (Eds.), *Application of microalgae in wastewater treatment: Volume 2: Biorefinery approaches of wastewater treatment* (pp. 427–444). Springer.
Mehar, J., Shekh, A., Malchira, N.U. & Mudliar, S. 2019 Potential of microalgae for integrated biomass production utilizing CO_2 and food industry wastewater. In S. K. Gupta & F. Bux (Eds.), *Application of*

microalgae in wastewater treatment: Volume 2: Biorefinery approaches of wastewater treatment (pp. 41–68). Springer.
Mitra, M. & Mishra, S. 2019 A biorefinery from *Nannochloropsis* spp. utilizing wastewater resources. In S.K. Gupta & F. Bux (Eds.), *Application of microalgae in wastewater treatment: Volume 2: Biorefinery approaches of wastewater treatment* (pp. 123–146). Springer.
Mohsenpour, S.F., Hennige, S., Willoughby, N., Adeloye, A. & Gutierrez, T. 2021 Integrating micro-algae into wastewater treatment: A review. *Science of the Total Environment, 752*, 142168.
Oilgae. (n.d.). *Oilgae guide to algae-based wastewater treatment* (Sample report). Oilgae (Clixoo).
Pancha, I., Chokshi, K. & Mishra, S. 2019 Industrial wastewater-based microalgal biorefinery: A dual strategy to remediate waste and produce microalgal bioproducts. In S.K. Gupta & F. Bux (Eds.), *Application of microalgae in wastewater treatment: Volume 2: Biorefinery approaches of wastewater treatment*, pp. 173–194. Springer.
Pandey, A., Srivastava, S. & Kumar, S. 2019 Phyco-remediation of dairy effluents and biomass valorization: A sustainable approach. In S.K. Gupta & F. Bux (Eds.), *Application of microalgae in wastewater treatment: Volume 2: Biorefinery approaches of wastewater treatment* (pp. 195–214). Springer.
Park, J.B.K., Craggs, R.J. & Shilton, A.N. 2011 Wastewater treatment high rate algal ponds for biofuel production. *Bioresource Technology, 102*(1), 35–42.
Posten, C. 2009 Design principles of photo-bioreactors for cultivation of microalgae. *Engineering in Life Sciences, 9*(3), 165–177.
Shah, M.M.R. 2019 Astaxanthin production by microalgae *Haematococcus pluvialis* through wastewater treatment: Waste to resource. In S.K. Gupta & F. Bux (Eds.), *Application of microalgae in wastewater treatment: Volume 2: Biorefinery approaches of wastewater treatment* (pp. 17–40). Springer.
Skifa, I., Chauchat, N., Cocquet, P.-H., & Le Guer, Y. 2025 Microalgae cultivation in raceway ponds: Advances, challenges, and hydrodynamic considerations. *EFB Bioeconomy Journal, 5*, 100073.
Sutherland, D.L., Park, J., Heubeck, S., Ralph, P.J. & Craggs, R.J. 2020 Size matters – Microalgae production and nutrient removal in wastewater treatment high rate algal ponds of three different sizes. *Algal Research, 45*, 101734.
Velásquez-Orta, S.B., Yáñez-Noguez, I., Monje Ramírez, I. & Orta Ledesma, M.T. 2024 Pilot-scale microalgae cultivation and wastewater treatment using high-rate ponds: A meta-analysis. *Environmental Science and Pollution Research, 31*(34), 46994–47021.
Water Corporation. 2022 *DS 230 design guideline: Waste stabilisation ponds* (Version 2, Revision 0). Water Corporation.
Water Europe. 2026 *CJEU confirms the application of UWWTD extended producer responsibility scheme to the pharmaceutical and cosmetic sectors*. https://watereurope.eu/cjeu-confirms-the-application-of-uwwtd-extended-producer-responsibility-scheme-to-the-pharmaceutical-and-cosmetic-sectors/
Zerrouki, D. & Henni, A. 2019 Outdoor microalgae cultivation for wastewater treatment. In S.K. Gupta & F. Bux (Eds.), *Application of microalgae in wastewater treatment: Volume 1: Domestic and industrial wastewater treatment* (pp. 81–100). Springer.
Zule, J., Weinberger, G., Ergünsel, A., & Thiebaut, Q. (2013, June 19). *Algae for wastewater treatment* [Conference presentation]. GZS, Ljubljana, Slovenia.

ADVANCED WASTEWATER TREATMENT USING SEWAGE SLUDGE–DERIVED BIOCHAR AS A CIRCULAR ADSORBENT MATERIAL

Domagoj NAKIĆ [1*], Katarina LICHT [1], Hana POSAVČIĆ [1], Danica MALJKOVIĆ [2], Anita LEOVAC MAĆERAK [3], Marko ŠRAJBEK[4]

[1] *University of Zagreb, Faculty of Civil Engineering, Croatia*

E-mail: domagoj.nakic@grad.unizg.hr

E-mail: katarina.licht@grad.unizg.hr

E-mail: hana.posavcic@grad.unizg.hr

[2] *INDELOOP d.o.o., Croatia*

E-mail: danica.maljkovic@dok-ing.hr

[3] *University of Novi Sad, Faculty of Sciences, Serbia*

E-mail: anita.leovac@dh.uns.ac.rs

[4] *University North, Department of Civil Engineering, Croatia*

E-mail: msrajbek@unin.hr

[*] *Corresponding author*

Abstract

This paper presents the initial phase of experimental investigations conducted within a newly established research project focused on advanced wastewater treatment using sewage sludge–derived biochar. The study explores the feasibility of using pristine biochar obtained through experimental semi-industrial sewage sludge gasification as a low-cost adsorbent for the removal of micropollutants, such as pharmaceuticals, heavy metals and pesticides, as well as nutrients, which represent a growing concern in conventional wastewater treatment systems. The research includes physicochemical characterization of the biochar and preliminary adsorption experiments performed under controlled laboratory conditions. The biochar is carbon-based (approximately 50%), which supports its potential suitability as an adsorbent. Removal efficiencies were evaluated through batch experiments to assess adsorption capacity and process behavior, employing single-component synthetic solutions under varying operational parameters, including pH, adsorbent dosage, initial pollutant concentration, and reaction time. Overall, high removal efficiencies were achieved (above 50%), with several target compounds exceeding 90%, highlighting the strong adsorption potential of the produced biochar even without further modification. The results indicate that sewage sludge–derived biochar may serve as an effective material in adsorption-based tertiary and quaternary wastewater treatment technologies, while simultaneously contributing to sustainable sewage sludge management and promoting the circular economy on multiple levels. These findings provide a foundation for further optimization and scale-up within the ongoing project.

Key words

sewage sludge, gasification, biochar, adsorption, micropollutants

1 Introduction

Wastewater treatment and the disposal of treatment byproducts have become major global challenges over the last few decades. The expansion of wastewater treatment plants (WWTPs) has significantly increased sewage sludge (SS) production, which is generated during all treatment stages, mainly through

separation processes in primary and secondary settling tanks. Both primary and biological sludge must be properly treated and disposed of in compliance with environmental regulations. Existing WWTPs typically produce 45-65 g of dry sludge matter per population equivalent per day (gDM/PE·d) (Vouk et al., 2022). Across the 27 EU Member States, annual SS production reaches approximately 10 million tons of dry mass and is expected to continue increasing (EUROSTAT, 2026). Figure 1 illustrates the distribution of SS disposal routes in the EU-27, Norway, and Switzerland based on EUROSTAT data for 2023 where available, while for countries lacking 2023 data, the most recent year published by EUROSTAT is indicated in parentheses; the data for Italy (*) are based on the Special Waste Report - 2023 Edition published by ISPRA for 2022. Considerable differences in SS management practices can be observed among European countries. Agricultural use and composting clearly dominate in countries such as Estonia, Ireland, Spain, Hungary, and the Scandinavian countries, whereas incineration represents the primary disposal route in Germany, the Netherlands, Austria, and Switzerland. In contrast, countries such as Croatia, Latvia, Portugal, and Slovenia rely heavily on "other" management routes, while landfill disposal remains particularly significant in Malta and Romania, reflecting the absence of a unified approach to SS management across Europe. According to the ISPRA (2024) report, Italy generated approximately 3.2 million tons of municipal SS in 2022, of which around 40% was applied to agricultural land, approximately 30% was incinerated, about 20% was landfilled, and the remaining 10% was exported, further illustrating the substantial differences in sludge management strategies observed across European countries.

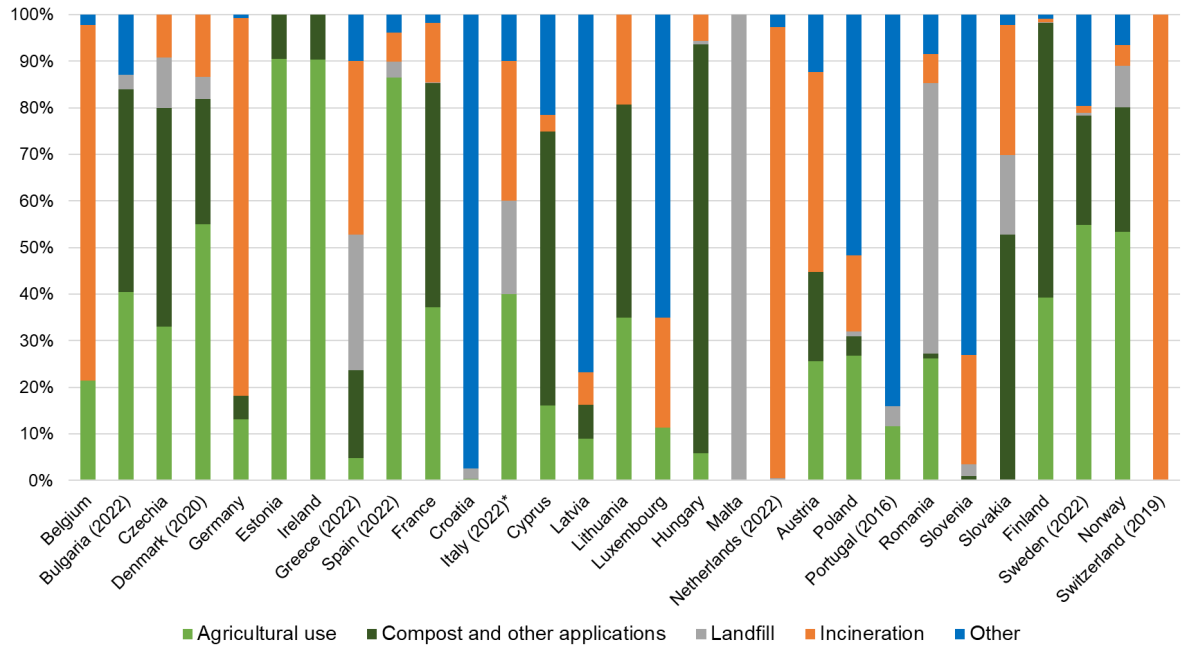


Figure 1. SS disposal routes in the EU-27 + Norway and Switzerland (EUROSTAT, 2026; ISPRA, 2024)

The most sustainable approach is to reintegrate wastewater treatment byproducts into material and energy cycles, following natural or other environmentally sustainable processes. Council Directive 91/271/EEC states that "*sludge arising from wastewater treatment shall be reused whenever appropriate*" (Article 14), promoting sludge reuse in accordance with circular economy principles. The revised Urban Wastewater Treatment Directive (EU) 2024/3019 further strengthens the principles of resource recovery, circular economy, and sustainable sludge management. At the same time, SS is commonly regarded as a problematic waste stream due to its complex physicochemical composition, high moisture content, and the presence of inorganic and potentially hazardous constituents. However, SS also represents a potentially valuable precursor for the production of carbonaceous materials because of its significant organic fraction, which can be transformed during thermochemical processing into solid carbon-rich products with potentially useful adsorption properties (Agrafioti et al., 2013; Hu et al., 2022; Ihsanullah et al., 2022; Jellali et al., 2021; Nakić et al., 2025a,b; Patro et al., 2024; Portillo et al., 2025; Rangabhashiyam et al., 2022). Consequently, SS should not be viewed exclusively as waste

requiring disposal, but also as a secondary raw material suitable for material valorization. Although SS derived adsorbents cannot be considered fully equivalent to conventional carbon adsorbents, the similarity of their general concept and functional properties confirms that the transformation of SS into adsorptive materials is scientifically and technologically justified rather than conceptually arbitrary.

The suitability of SS as a precursor for adsorbent production is nevertheless associated with several important limitations. One of the most significant drawbacks is its high mineral and ash content (Xu et al., 2015). Elevated ash levels hinder the development of the pore structure characteristic of conventional carbon adsorbents, influence surface chemistry, and may reduce the practical usefulness of the final material (Halbus et al., 2021; Mu'azu et al., 2017; Nicholas et al., 2022). Earlier studies demonstrated that chars obtained through simple pyrolysis of SS may exhibit relatively low specific surface areas of approximately 50 m^2/g, whereas chemically activated SS derived adsorbents can exceed 1000 m^2/g (Mu'azu et al., 2017). Such differences clearly illustrate the strong influence of activation procedures on structural development and adsorption performance.

Another important issue is the substantial variability in SS composition (Jellali et al., 2021). The physicochemical properties of SS may differ considerably depending on its origin, stabilization process, dewatering method, and the relative proportions of organic and inorganic fractions. In addition, SS may contain varying amounts of metals and other potentially undesirable substances, which may influence not only thermochemical conversion processes but also the environmental safety and end-of-life management of the produced adsorbents (Kominko et al., 2024; Ghacha et al., 2020). As a consequence, the evaluation of SS as a precursor material cannot be generalized easily and should always be related to the characteristics of the specific SS under investigation. At the same time, this variability does not undermine the concept of SS valorization itself. Rather, it suggests that the most practically relevant approaches are those capable of tolerating raw material variability without requiring highly sophisticated and expensive modification procedures. Such an approach is consistent with the concept of low-cost adsorbents adopted within AdSorB project ("*Advanced Wastewater Treatment by Repurposing Sewage Sludge Derived Biochar*") and this research.

The preparation of sludge-derived adsorbents often involves activation processes intended to increase specific surface area, develop pore structure, and improve the accessibility of active adsorption sites. From a laboratory perspective, activation may substantially enhance sorption performance. However, it simultaneously transforms a relatively simple waste conversion process into a more complex technology involving additional processing stages, increased energy consumption, and in some cases the use of chemical reagents associated with further economic and environmental burdens. Therefore, the practical value of SS-derived adsorbents should not be assessed solely on the basis of maximum sorption capacity or exceptionally high surface area values. Instead, evaluation should include the relationship between adsorption performance, preparation complexity, production cost, and the management of the material after its use (Ghacha et al., 2020; Ighalo et al., 2022; Xu et al., 2015). The adsorption performance of carbonaceous materials is determined not only by structural parameters such as specific surface area, pore volume, and pore size distribution, but also by surface chemistry, including the presence of functional groups, polarity, acid-base properties, and the ability to form specific interactions with adsorbates. In aqueous systems, adsorption effectiveness additionally depends on pore accessibility for larger molecules, the ionization state of contaminants, and the influence of mineral constituents on adsorption mechanisms. Consequently, materials with relatively modest surface areas may still exhibit satisfactory adsorption performance if their surface and pore properties are well matched to the target pollutants. Conversely, highly porous materials do not necessarily guarantee superior performance when pore accessibility or surface chemistry is unfavorable for the adsorption of specific compounds (Foujdar et al., 2025; Halbus et al., 2021).

An additional challenge is associated with the difference between model laboratory systems and real wastewater conditions. Real wastewater streams contain numerous dissolved and colloidal substances that may influence adsorption kinetics, compete for active sites, and reduce overall treatment efficiency. As a result, adsorbents exhibiting excellent performance toward individual model compounds may perform substantially worse under realistic conditions. Nevertheless, SS-derived adsorbents have

demonstrated promising potential in wastewater polishing processes and in the removal of selected organic contaminants from aqueous solutions (Hamda et al., 2024; Zhou et al., 2024).

From a practical perspective, the key issue is therefore not the achievement of maximum sorption capacity at any cost, but rather the balance between treatment efficiency, simplicity of material preparation, and economic feasibility. The most promising approaches appear to be those based on relatively simple preparation routes capable of producing materials suitable for specific and less demanding applications, particularly wastewater polishing after primary, secondary and/or tertiary treatment stages or the removal of selected groups of contaminants. In such applications, moderate adsorption performance may be entirely sufficient provided that the overall process remains technically simple, economically reasonable, and environmentally justified. The AdSorB project is founded on these principles and aims to investigate the efficiency and key process parameters governing the removal of various contaminants, particularly micropollutants, using pristine (unmodified) biochar produced through a specialized SS gasification process. Gasification is a high-temperature sludge treatment method that offers significantly lower emissions of harmful gases compared to other thermal processes, making it a promising focus for further research (Nakić et al., 2025c).This paper reports the initial findings regarding the removal efficiency and adsorption capacity of the biochar. The focus is placed on evaluating the overall performance of the treatment approach rather than on elucidating the underlying removal mechanisms. The results will serve as a basis for selecting specific contaminant groups for more detailed investigation and process optimization in the subsequent phases of the AdSorB project.

2 Materials and methods

Stabilized and dehydrated SS was collected from the Karlovac WWTP (Croatia), which employs tertiary treatment including nutrient removal. Samples were collected on three separate occasions over a one-month period to account for potential variations in influent composition and operational conditions. After drying at 105°C to a dry matter content exceeding 90%, the sludge was homogenized and subjected to gasification in a pilot-scale Looper reactor developed by Indeloop Ltd (Figure 2). The gasification process, designed primarily for syngas production, generates biochar as a solid by-product. This biochar was used as an adsorbent for the removal of selected contaminants from synthetic wastewater. The process was operated at temperature of ≈ 800°C, resulting in a hydrogen-rich syngas and the production of biochar for further valorization (Bubalo et al., 2022; Nakić et al., 2025b).

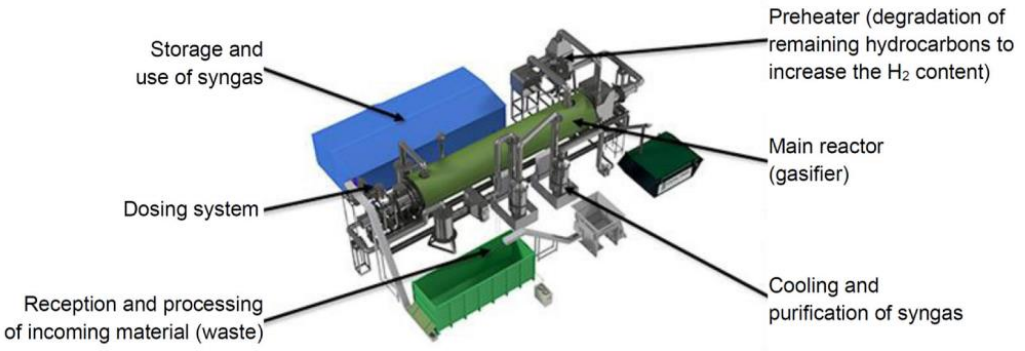


Figure 2. Process schematic of the pilot-scale gasification plant from which the studied biochar was obtained (Bubalo et al., 2022; Nakić et al., 2025b)

To evaluate the adsorption potential and environmental suitability of the produced biochar, its chemical composition, mineral content, and leaching behavior were characterized. Major elements were determined by atomic absorption spectroscopy (AAS) and expressed as their corresponding metal oxides, while trace elements were quantified using energy-dispersive X-ray fluorescence (EDXRF). In addition, leaching tests were performed in accordance with the EN 12457-2 standard to assess the potential release of metals and associated environmental risks (Bubalo et al., 2025; Nakić et al., 2017).

2.1 Adsorption experiments

Batch adsorption experiments were conducted to evaluate the removal of various pollutants, including ammonium, phosphates, selected heavy metals, the pesticide acetamiprid, and selected pharmaceuticals. The experiments were performed under different initial conditions according to a predefined experimental matrix. The parameters investigated included the initial pollutant concentration, biochar dosage, solution pH, and contact time. Experiments were carried out in 250 mL bottles containing 200 mL of solution and varying amounts of biochar. The suspensions were agitated on a rotary shaker (Reax 2, Heidolph, Germany) at 45 rpm for contact times of up to 24 h (Figure 3).

The adsorption capacity was determined according to Eq. (1).

$$q_t = V \frac{C_0 - C_t}{m} \tag{1}$$

where q_t (mg/g) is the amount of adsorbate adsorbed per gram of biochar; C_0 and C_t (mg/L) represent the initial and final concentrations of the adsorbate in the solution, respectively; V (L) is the solution volume; and m (g) represents the weight of the adsorbent (biochar).



Figure 3. Experimental setup used in the adsorption experiments

Following adsorption, the samples were filtered through 0.45 µm polyethersulfone (PES) membrane filters to remove suspended biochar particles. Residual concentrations of phosphate and ammonium were determined using a Nanocolor 500 D photometer (Macherey-Nagel, Germany) and the corresponding cuvette tests. Residual concentrations of selected heavy metals in the filtrates were measured using an inductively coupled plasma optical emission spectrometer (ICP-OES) (Agilent 5900, Agilent Technologies, USA). Initial and residual concentrations of acetamiprid and selected pharmaceuticals were determined using a UV–Vis spectrophotometer (Cary 60, Agilent Technologies, USA). Quantification was performed based on absorbance measurements at selected wavelengths and corresponding calibration curves.

3 Results and Discussion

3.1 Biochar Characterization

The produced biochar is a predominantly crystalline material composed of high-temperature aluminosilicates, mainly quartz and cristobalite (SiO_2), with smaller amounts of illite, calcite, and calcium-aluminum phosphate. Chemical characterization showed that the dominant inorganic constituents were Al_2O_3 (~16%), CaO (~15%), and Fe_2O_3 (~11%), while approximately 50% of the sample mass consisted of carbon.
The concentrations of potentially hazardous elements and heavy metals were generally low.

Furthermore, leaching tests demonstrated very limited release of most metals, indicating their stable incorporation within the biochar matrix and a low risk of environmental contamination. These findings support the potential safe application of the material as an adsorbent in water and wastewater treatment processes.

Scanning Electron Microscopy (SEM) analysis revealed irregular, agglomerated particles with a rough and highly porous surface morphology. The presence of numerous cavities, channels, and voids of different sizes contributes to a large specific surface area and a high density of active adsorption sites, which are considered key factors governing the adsorption performance of the biochar.

3.2 Results of Batch Adsorption Experiments

3.2.1 Adsorption of Pharmaceutical Micropollutants

Wastewater containing pharmaceutically active compounds represents a growing environmental concern because, despite the low concentrations of these residues, their persistent presence can disrupt microbial communities, promote antimicrobial resistance, and adversely affect biodiversity and ecosystem health (Zango et al., 2024). Due to the limited effectiveness of conventional wastewater treatment methods and the complex interactions of pharmaceuticals in the environment, there is a need to develop sustainable and cost-effective technologies for their removal from wastewater (Langbehn et al., 2021).

Among the analyzed pharmaceutical micropollutants, all four compounds (ibuprofen, zidovudine, amlodipine, and indomethacin) exhibited moderate removal efficiencies when treated with biochar produced from SS through an experimental gasification process. Under the experimental conditions, using an adsorbent dosage of 1.50 g/L (0.3 g in 200 mL solution), an initial pollutant concentration of 20 mg/L, neutral pH (7), and 5 h of agitation, removal efficiencies ranged from 37.25% for zidovudine to 58.50% for indomethacin. Similarly, the adsorption capacities of the biochar varied from 4.97 mg/g for zidovudine to 7.80 mg/g for indomethacin (Figure 4).

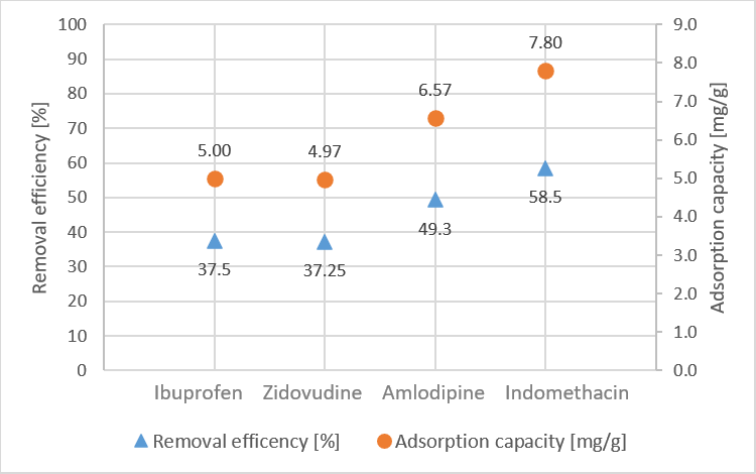


Figure 4. Removal efficiency (%) and adsorption capacity (mg/g) of the analyzed pharmaceutical micropollutants at an initial pollutant concentration of 20 mg/L, adsorbent dosage of 1.50 g/L, pH 7, and agitation time of 5 h

These results indicate a moderate adsorption potential of the investigated biochar toward pharmaceutical contaminants. The observed differences in removal efficiencies among the compounds are likely associated with variations in their physicochemical properties, such as molecular structure, hydrophobicity, and affinity toward the biochar surface. Overall, the findings demonstrate that gasification-derived SS biochar can contribute to the removal of pharmaceutical micropollutants from aqueous media, although further optimization of operational conditions may be required to achieve higher removal efficiencies. Future research will focus on a more detailed investigation of the key

parameters influencing the adsorption process, including adsorbent dosage, contact time, pH, and pollutant concentration. The preliminary results obtained for pharmaceutical pollutants provide a sound basis for further investigation and highlight the potential of this material for the removal of this specific group of micropollutants from aqueous media.

Although adsorption capacities of up to 309 mg/g have been reported for ibuprofen, such values were predominantly achieved using modified biochars. In contrast, unmodified biochars generally exhibited substantially lower adsorption capacities, with values as low as 9.69 mg g^{-1} reported for pine wood-derived biochar (Zhan et al., 2023). Using a tea-waste biochar modified with reduced graphene oxide and a glycerol-based deep eutectic solvent, Mashoene et al. (2023) achieved a maximum zidovudine adsorption capacity of 61.65 mg g^{-1} and a removal efficiency of approximately 49%. For amlodipine, Fakhrian and Baseri (2020) reported a maximum adsorption capacity of 229 mg/g and a removal efficiency of approximately 65% using a magnetic rice straw-based biosorbent. Similarly, Momčilović et al. (2025) achieved adsorption capacities of up to 320.4 mg/g using activated carbon derived from dwarf elder biomass, while increasing the adsorbent dosage from 0.125 to 1.25 g/L resulted in a decrease in adsorption capacity from 320.4 to 77.4 mg/g but an increase in removal efficiency from 40.1% to 96.8%. Unlike ibuprofen, amlodipine, and zidovudine, studies investigating the adsorption of indomethacin using biochar-based adsorbents are scarce. Most available studies have focused on activated carbon and composite adsorbents limiting direct comparison with the results of the present study. Therefore, although the adsorption performance of the pristine biochar used in this study was lower than that reported for many modified biochars and activated carbon-based adsorbents, its simpler production process, lower cost, and reduced environmental footprint make it a promising and sustainable alternative for potential wastewater treatment applications.

3.2.2 Adsorption of Nutrients (PO_4^{3-} and NH_4^+)

Nutrient pollution of water resources, particularly by nitrogen and phosphorus compounds, is a major environmental concern due to its contribution to eutrophication, water quality deterioration, and ecosystem degradation. These nutrients commonly enter aquatic environments through inadequately treated municipal, agricultural, and industrial wastewater. Consequently, efficient nutrient removal from wastewater is essential for both environmental protection and resource recovery. Conventional treatment methods include chemical precipitation, biological processes, and adsorption. However, chemical and biological approaches are often associated with operational complexity, high costs, and excessive sludge production (Kari-Ferro et al., 2024). In contrast, adsorption has emerged as a promising alternative due to its cost-effectiveness, operational simplicity, high selectivity, and particularly good performance at low nutrient concentrations. Biochar has shown considerable potential for nutrient (N/P) removal from water, although its adsorption performance largely depends on feedstock characteristics, thermal treatment conditions, and activation or modification processes (Leng et al., 2015; Singh et al., 2020).

The results presented in this study (Figure 5) reveal a marked difference in the adsorption behavior of the two nutrients. Although the experimental conditions were not identical, several observed differences are sufficiently pronounced to allow meaningful comparison. NH_4^+ adsorption was evaluated at an initial concentration of 100 mg/L, an adsorbent dosage of 1.25 g/L (0.25 g biochar in 200 mL of solution), unadjusted pH (~4.0), and an agitation time of 8 h. PO_4^{3-} adsorption was evaluated at an initial concentration of 90 mg/L, an adsorbent dosage of 5.0 g/L (0.5 g biochar in 100 mL of solution), unadjusted pH (~3.5), and an agitation time of 24 h.

Phosphate (PO_4^{3-}) exhibited a very high removal efficiency of 97.78%, indicating a strong affinity of the biochar for phosphate ions; however, the corresponding adsorption capacity was 17.60 mg/g (a direct consequence of the experimental setup). In contrast, ammonium (NH_4^+) showed a considerably lower removal efficiency of 26.47%, despite achieving a slightly higher adsorption capacity of 21.18 mg/g. These findings suggest that the pristine biochar was substantially more effective in removing phosphate than ammonium from aqueous solutions. This behavior is likely attributable to differences in adsorption mechanisms and the interactions of phosphate and ammonium species with the biochar surface. However, the differing experimental conditions, particularly the contact time, solution volume, and

biochar mass, may have influenced the adsorption performance and should therefore be considered when interpreting the results. The optimization of these parameters will be addressed in future studies.

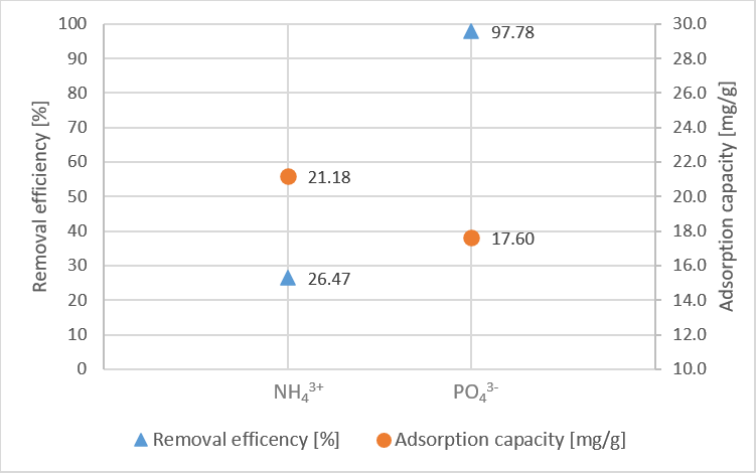


Figure 5. Removal efficiency (%) and adsorption capacity (mg/g) for NH_4^+ and PO_4^{3-}. NH_4^+ adsorption was evaluated at an initial concentration of 100 mg/L, adsorbent dosage of 1.25 g/L, unadjusted pH (~4.0), and agitation time of 8 h. PO_4^{3-} adsorption was evaluated at an initial concentration of 90 mg/L, adsorbent dosage of 5.0 g/L, unadjusted pH (~3.5), and agitation time of 24 h.

Previous studies have consistently shown that modified biochars exhibit substantially higher nutrient adsorption capacities than pristine biochars due to their larger surface area, greater abundance of functional groups, and enhanced reactivity (Xiang et al., 2020). Reported adsorption capacities for modified biochars were up to 47.5 mg/g for NH_4^+ and up to 2000 mg/g for PO_4^{3-}, with particularly high phosphate adsorption achieved by Mg, Ca, and Fe modified biochars (Saadat et al., 2018; Xiang et al., 2020; Yang et al., 2018; Yin et al., 2019). Although these values exceed those obtained in the present study, it should be noted that the biochar used here was pristine (unmodified). This is a particularly important consideration, as the absence of chemical or physical modification reduces both processing costs and environmental impacts. Therefore, despite the lower adsorption performance, the results highlight the potential of pristine biochar as a more economically and environmentally sustainable alternative to modified biochars reported in the literature, especially for phosphate removal (Nakić et al., 2024).

3.2.3 Adsorption of Heavy Metals

Heavy metal contamination of aquatic environments represents a major environmental challenge due to the persistence, non-biodegradability, and toxicity of these pollutants. Among the concerning heavy metals are lead (Pb), chromium (Cr), copper (Cu), and cadmium (Cd), which are frequently detected in wastewater and pose significant risks to ecosystems and human health. Cadmium is of particular concern because of its high toxicity and widespread occurrence in drinking water and wastewater (Shah et al., 2024). Consequently, the development of effective wastewater treatment strategies for heavy metal removal is of great importance. Among the available treatment methods, adsorption has emerged as one of the most efficient and economically feasible approaches. Previous studies have demonstrated that the adsorption performance of sewage sludge-based biochar is strongly influenced by the activation and modification process, with the type of chemical activator playing a key role in enhancing the physicochemical properties and adsorption capacity of the resulting material (Cao et al., 2024).

Among the tested combinations of biochar dosage, initial pollutant concentration, pH, and agitation time, the conditions resulting in the highest removal efficiencies for all investigated heavy metals were selected and are presented as a representative case and shown in Figure 6. The results from this study demonstrate a very high removal efficiency for all investigated metals, with values exceeding 99% for Cd, Cr, and Cu, while a slightly lower efficiency was observed for Pb (95.19%). Similarly, the adsorption capacities were comparable for Cd, Cr, and Cu (around 22.00 mg/g), whereas Pb exhibited

somewhat lower adsorption capacity (20.94 mg/g). Nevertheless, the overall results confirm the excellent performance of the biochar as an adsorbent for the removal of heavy metals from aqueous solutions, which is consistent with previous findings reported in Nakić et al. (2025b). While Cao et al. (2024) emphasized the importance of biochar modification through pre- and post-treatment processes to improve adsorption performance, the present results demonstrate that pristine biochar produced via a specialized gasification process also has potential as an effective adsorbent for the removal of heavy metals from aqueous solutions.

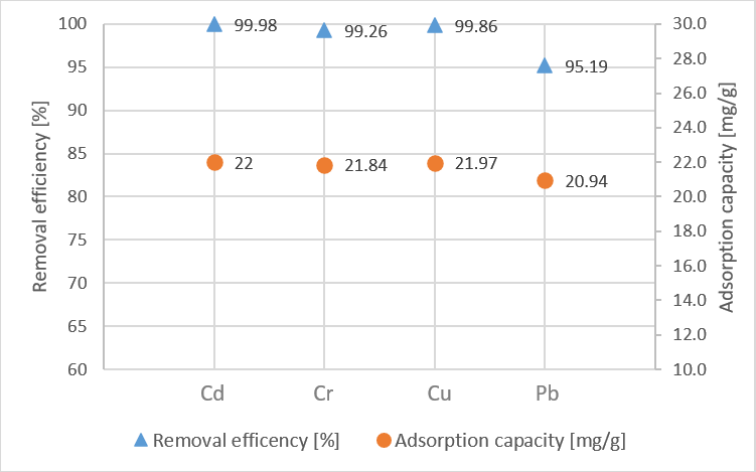


Figure 6. Removal efficiency (%) and adsorption capacity (mg/g) of the analyzed heavy metals at an initial pollutant concentration of 110 mg/L, adsorbent dosage of 5.0 g/L, pH 7, and agitation time of 24 h

3.2.4 Adsorption of Acetamiprid

The presence of pesticides in aquatic environments has become a significant environmental concern, as these contaminants can enter water bodies through both point and diffuse pollution sources (Grimene et al., 2022). Acetamiprid, a neonicotinoid insecticide extensively used in agricultural production, is frequently detected in surface and wastewater systems and may pose risks to aquatic organisms due to its persistence and biological activity. Moreover, conventional wastewater treatment processes are often unable to completely remove acetamiprid, highlighting the need for the development of efficient, sustainable, and cost-effective treatment technologies for its removal from contaminated waters.

In this study, the average adsorption capacity of biochar for acetamiprid removal was 21.15 mg/g, ranging from 0.46 to 187 mg/g. The maximum adsorption capacity (187 mg/g) was achieved at pH 9 using 0.1 g of biochar per 200 mL (0.50 g/L) of solution and an initial acetamiprid concentration of 200 mg/L, whereas the minimum value (0.46 mg/g) was recorded at same biochar dosage (0.50 g/L), pH 3 and an initial concentration of 10 mg/L. Lower biochar dosage increased adsorption capacity; however, removal efficiency decreased under these conditions. Increasing the initial acetamiprid concentration significantly enhanced both adsorption capacity and removal efficiency. The most favorable results in terms of both adsorption capacity and removal efficiency were obtained under alkaline conditions (pH 9), while the poorest performance was observed under acidic conditions (pH 3). Across all experimental conditions, the mean acetamiprid removal efficiency was 22.96%. The highest removal efficiency (54.2%) was achieved after only 1 h of contact time at an initial acetamiprid concentration of 200 mg/L, pH 9, and a biochar dosage of 1 g per 200 mL of solution. These findings indicate that alkaline conditions promote stronger interactions between acetamiprid molecules and biochar surface functional groups, resulting in enhanced adsorption performance. Furthermore, the positive effect of higher initial acetamiprid concentrations suggests that a greater concentration gradient provides a stronger driving force for mass transfer and adsorption onto the biochar surface. This is in contrast with previous studies that identified neutral to acidic pH values as the most favorable conditions for acetamiprid removal (Cao et al., 2023; Somaia et al., 2019). For comparison, Somaia et al. (2019) achieved acetamiprid removal efficiencies exceeding 99% and maximum adsorption capacities of 151.52-370.37 mg/g using

chemically activated carbons derived from orange peels and almond shells. Although these values are considerably higher than those obtained in the present study with non-modified biochar, such differences are expected due to the activation process, while non-modified biochar remains attractive because of its lower cost, simpler production, and reduced environmental footprint. On the other hand, Srikhaow et al. (2022) reported a maximum adsorption capacity of 4.87 mg/g for acetamiprid using eucalyptus woodchip-derived biochar, which is far more comparable to the results obtained in the present study.

An interesting finding of the present study is that prolonged agitation time did not necessarily lead to improved adsorption performance. Some of the highest adsorption capacities and removal efficiencies were achieved after only 1 h of contact time, whereas under identical experimental conditions, extending the contact time up to 24 h occasionally resulted in lower adsorption and removal values. This observation suggests that adsorption equilibrium may have been reached rapidly, with longer contact times providing no additional benefit. Also, the decline in performance observed in certain experiments may indicate the occurrence of partial desorption processes or the redistribution of previously adsorbed acetamiprid molecules from weaker adsorption sites, although additional kinetic and desorption studies would be required to confirm these mechanisms.

4 Conclusion

This study presented the initial results of the AdSorB project, investigating the feasibility of using pristine SS derived biochar produced through a pilot-scale gasification process as a low-cost adsorbent for advanced wastewater treatment. The results demonstrated that the produced biochar possesses favorable physicochemical properties, including significant carbon content, porous surface morphology, and low leaching potential, supporting its safe application in water and wastewater treatment processes. The adsorption experiments confirmed that the biochar can remove a wide range of contaminants, including pharmaceutical micropollutants, nutrients, heavy metals, and pesticides. Particularly high removal efficiencies were achieved for phosphate and heavy metals, with phosphate removal reaching 97.78% and heavy metal removal exceeding 95% for all investigated metals. Moderate but promising results were also obtained for pharmaceutical compounds and pesticide acetamiprid, indicating that the material has potential for the treatment of emerging contaminants despite the absence of any chemical or physical modification. Although the adsorption capacities reported in this study are generally lower than those achieved with activated or chemically modified biochars described in the literature, the investigated material offers important advantages in terms of production simplicity, lower cost, reduced environmental footprint, and compatibility with circular economy principles. The valorization of SS through gasification not only contributes to sustainable sludge management but also generates a value-added product that can be utilized in wastewater polishing and advanced treatment applications.

Overall, the findings confirm the potential of SS derived biochar as a sustainable adsorbent for wastewater treatment and provide a solid foundation for further research. Future work within the AdSorB project will focus on process optimization, adsorption kinetics and equilibrium studies, investigation of removal mechanisms, and validation under real wastewater conditions to support the future scale-up and practical implementation of this circular treatment approach. Particular emphasis will be placed on transitioning from batch adsorption experiments to continuous flow through column systems for those pollutants that demonstrate the highest removal potential under laboratory conditions, thereby enabling a more realistic assessment of process performance and operational feasibility. In the final phase of the project, the potential for the safe and permanent immobilization of spent biochar containing adsorbed pollutants will also be investigated through its incorporation into cement-based composites as a partial replacement for conventional raw materials, such as aggregates and/or cement. This approach aims to further extend the circular economy concept by providing an environmentally sound end-of-life management strategy for exhausted adsorbents while potentially delivering additional environmental and economic benefits through resource conservation and waste valorization.

Acknowledgements

This work was supported by the Croatian Science Foundation under the project number [HRZZ-UIP-2025-02-9907]: AdSorB – "*Advanced Wastewater Treatment by Repurposing Sewage Sludge Derived Biochar*"
The authors gratefully acknowledge INDELOOP d.o.o. for providing the biochar derived from sewage sludge gasification used in this research.

References

Agrafioti, E., Bouras, G., Kalderis, D., Diamadopoulos, E. 2013 Biochar production by sewage sludge pyrolysis. *J. Anal. Appl. Pyrolysis*. 101, 72-78 https://doi.org/10.1016/j.jaap.2013.02.010
Bubalo, A., Vouk, D., Maljković, D., Bolanča, T. 2022 Gasification of Sewage Sludge in a Rotary Kiln Reactor—A Case Study with Incorporation of Sewage Sludge Ash in Brick Production. *Chem. Biochem. Eng. Q*. 36, 77–87. https://doi.org./10.15255/CABEQ.2021.2030
Bubalo, A., Vouk, D., Rogošić, M., Nakić, D., Kučić Grgić, D., Ćurković, L. 2025 Microwave drying of sewage sludge: A sustainable additive for improved clay brick manufacturing. *J. Environ. Manag.* 385, 125557 https://doi.org/10.1016/j.jenvman.2025.125557
Cao, N., Ji, J., Li, C., Yuan, M., Guo, X., Zong, X., Li, L., Ma, Y., Wang, C., Pang, S. 2023 Rapid and efficient removal of multiple aqueous pesticides by one-step construction boric acid modified biochar. *RSC Advances* 13, 8765–8778 https://doi.org/10.1039/D2RA07684E
Cao, J., Jiang, Y., Tan, X., Li, L., Cao, S., Dou, J., Chen, R., Hu, X., Qiu, Z., Li, M., Chen, Z., Zhu, H. 2024 Sludge-based biochar preparation: Pyrolysis and co-pyrolysis methods, improvements, and environmental applications. *Fuel* 373, 132265 https://doi.org/10.1016/j.fuel.2024.132265
EUROSTAT 2026 Sewage sludge production and disposal from urban wastewater (in dry substance). https://ec.europa.eu/eurostat/databrowser/view/ten00030/default/table?lang=en (accessed 20 May 2026)
Fakhrian, S., Baseri, H. 2020 Production of a magnetic biosorbent for removing pharmaceutical impurities. *Korean J. Chem. Eng*. 37, 1541–1551 https://doi.org/10.1007/s11814-020-0523-4
Foujdar, A., Shersiya, M., Khandelwal, N., Agrawal, H. K., Sharma, O. P. 2025 Sewage Sludge-Derived Hydrochar for the Removal of Color Cocktails and Pharmaceutical Compounds from Complex Water Matrices. *J. Hazard. Mater.: Organics* 1 (1), 100003 https://doi.org/10.1016/j.hazmo.2025.100003
Ghacha, A., Ammari, M., Ben Allal, L. 2020 Sustainable sewage sludge management in Morocco: Constraints and solutions. *J. Water Land Dev*. 46, 71–83. https://doi.org/10.24425/jwld.2020.134199
Grimene, C., Mghirbi, O., Louvet, S., Bord, J.-P., Le Grusse, P. 2022 Spatial characterization of surface water vulnerability to diffuse pollution related to pesticide contamination: case of the Gimone watershed in France. *Environ. Sci. Pollut. Res.* 29, 17–39 https://doi.org/10.1007/s11356-021-14253-2
Halbus, A., Athab, Z., Hussein, F. H. 2021 Review on preparation and characterization of activated carbon from low cost waste materials. *Egypt. J. Chem*. 64 (12), 7255-7268 https://doi.org/10.21608/ejchem.2021.79055.3870
Hamda, A. S., Jayakumar, M., Periyasamy, S., Manivannan, S., Bacha, W. 2024 Production strategies and potential repercussion of sewage sludge biochar as a futuristic paradigm toward environmental beneficiation: A comprehensive review. *Environ. Qual. Manage*. 33 (3), 1–19 https://doi.org/10.1002/tqem.22007
Hu, M., Hu, H., Ye, Z., Tan, S., Yin, K., Chen, Z. Guo, D., Rong, H., Wang, J., Pan, Z., Hu, Z.-T. 2022 A review on turning sewage sludge to value-added energy and materials via thermochemical conversion towards carbon neutrality. *J. Clean. Prod.* 379, 134657 https://doi.org/10.1016/j.jclepro.2022.134657
Ighalo, J., Omoarukhe, F., Ojukwu, V., Iwuozor, K., Igwegbe, C. 2022 Cost of adsorbent preparation and usage in wastewater treatment: A review. *Cleaner Chem. Eng*. 3, 100042 https://doi.org/10.1016/j.clce.2022.100042
Ihsanullah, I., Khan, M. T., Zubair, M., Bilal, M., Sajid, M. 2022 Removal of pharmaceuticals from water using sewage sludge-derived biochar: A review. *Chemosphere*. 289, 133196 https://doi.org/10.1016/j.chemosphere.2021.133196

ISPRA 2024 Special Waste Report-2024 Edition (Rapporto Rifiuti Speciali - Edizione 2024). https://www.isprambiente.gov.it/it/pubblicazioni/rapporti/rapporto-rifiuti-speciali-edizione-2024 (accessed 20 May 2026)
Jellali, S., Khiari, B., Usman, M., Hamdi, H., Charabi, Y., Jeguirim, M. 2021 Sludge derived biochars: a review on the influence of synthesis conditions on pollutants removal efficiency from wastewaters. *Renew. Sustain. Energy Rev*. 144, 111068 https://doi.org/10.1016/j.rser.2021.111068
Kari-Ferro, A., Solano-Reynoso, A.M., Alvarez-Arias, C., Echegaray-Peña, N.G., Choque-Quispe, D. 2024. Activated polymeric materials for phosphorus removal in aqueous medium: study of kinetics and adsorption isotherm. *Results Eng.*, 24, 103201 https://doi.org/10.1016/j.rineng.2024.103201
Kominko, H., Gorazda, K., Wzorek, Z. 2024 Sewage sludge: A review of its risks and circular raw material potential. *J. Water Process Eng*. 63, 105522 https://doi.org/10.1016/j.jwpe.2024.105522
Langbehn, R. K., Michels, C., Soares, H. M. 2021 Antibiotics in wastewater: From its occurrence to the biological removal by environmentally conscious technologies. *Environmental Pollution* 275, 116603 https://doi.org/10.1016/j.envpol.2021.116603
Leng, L., Yuan, X., Huang, H., Shao, J., Wang, H., Chen, X., Zeng, G. 2015 Bio-char derived from sewage sludge by liquefaction: Characterization and application for dye adsorption. *Applied Surface Science* 346, 223-231 https://doi.org/10.1016/j.apsusc.2015.04.014
Mashoene, T.N., Leudjo Taka, A., Akpotu, S.O., Lawal, I.A., Klink, M.J. 2023 Surface Modification of Tea-Waste-Based Biochar Adsorbent: Synthesis, Characterization, and Batch Adsorption for the Removal of Zidovudine ARV Drug and Phenol. *Appl. Sci.* 3, 7493 https://doi.org/10.3390/app13137493
Momčilović, M.Z., Dodevski, V., Krstić, S., Petrović, M., Suručić, L., Nešić, A., Bojić, A.L. 2025 Aqueous-Phase Uptake of Amlodipine Besylate by Activated Carbon Derived from Dwarf Elder. *Processes* 13, 1483 https://doi.org/10.3390/pr13051483
Mu'azu, N. D., Jarrah, N., Zubair, M., Alagha, O. 2017 Removal of phenolic compounds from water using sewage sludge-based activated carbon adsorption: A review. *Int. J. Environ. Res. Public Health.* 14 (10), 1094 https://doi.org/10.3390/ijerph14101094
Nakić, D., Vouk, D., Donatello, S., Anić Vučinić, A. 2017 Environmental impact of sewage sludge ash assessed through leaching. *Eng. Rev*. 37, 222–234 https://hrcak.srce.hr/file/267543
Nakić, D. Vouk, D., Licht, K., Posavčić, H. 2024 Sewage Sludge Biochar as Adsorbent Used in Wastewater Treatment. *In Proc. of the* WSPA 2024 International Conference Water in Sensitive and Protected Areas, Pula 10-13 April, pp. 159-174
Nakić, D., Licht, K., Posavčić, H., Halkijević, I. 2025a Biochar from experimental sewage sludge gasification as an adsorbent for phosphate removal. *Results in Engineering*. 27, 106077 https://doi.org/10.1016/j.rineng.2025.106077
Nakić, D., Posavčić, H., Licht, K., Vouk, D. 2025b Application of Novel Biochar Derived from Experimental Sewage Sludge Gasification as an Adsorbent for Heavy Metals Removal. *Sustainability* 17, 997. https://doi.org/10.3390/su17030997
Nakić, D., Posavčić, H., Matošević, D., Tomaš, I. 2025c Perspectives on the Application of Biochar Produced From Sewage Sludge Gasification in Wastewater Treatment for Heavy Metals Removal. *Environmental Engineering - Inženjerstvo okoliša* 12 (1-2), 26-34. https://doi.org/10.37023/ee.12.1-2.3
Nicholas, H. L., Mabbett, I., Apsey, H., Robertson, I. 2022 Physico-chemical properties of waste derived biochar from community scale faecal sludge treatment plants. *Gates Open Res*. 6, 96. https://doi.org/10.12688/gatesopenres.13727.2
Patro, A., Dwivedi, S., Thakur, A., Sahoo, P. K., Biswas, J. K. 2024 Recent approaches and advancement in biochar-based environmental sustainability: Is biochar fulfilling the sustainable development goals? *iScience*. 27 (9), 110812 https://doi.org/10.1016/j.isci.2024.110812
Portillo, E., Flores, S., Carrizosa, R., Álvarez-Torrellas, S., Carbajo, J., Águeda, V. I., García, J. 2025 Sustainable adsorbents from sewage sludge: Efficient removal of cytostatic compounds in single and complex aqueous matrices. *J. Environ. Chem. Eng*. 13 (3), 116927. https://doi.org/10.1016/j.jece.2025.116927
Rangabhashiyam, S., dos Santos Lins, P.V. de Magalhães Oliveira, L.M.T., Sepulveda, P., Ighalo, J.O., Rajapaksha, A.U., Meili, L. 2022 Sewage sludge-derived biochar for the adsorptive removal of wastewater pollutants: A critical review. *Environ. Pollut*. 293, 118581 https://doi.org/10.1016/j.envpol.2021.118581

Saadat, S., Raei, E., Talebbeydokhti, N. 2018 Enhanced removal of phosphate from aqueous solutions using a modified sludge derived biochar: comparative study of various modifying cations and RSM based optimization of pyrolysis parameters. *J. Environ. Manag*. 225, 75–83 https://doi.org/10.1016/j.jenvman.2018.07.037

Shah, A., Zakharova, J., Batool, M., Coley, M.P., Arjunan, A., Hawkins, A.J., Bolarinwa, T., Devi, S., Thumma, A., Williams, C. 2024 Removal of cadmium and zinc from water using sewage sludge-derived biochar. *Sustain. Chem. Environ.* 6, 100118 https://doi.org/10.1016/j.scenv.2024.100118

Singh, S., Kumar, V., Singh Dhanjal, D., Datta, S., Bhatia, D., Dhiman, J., Samuel, J., Prasad, R., Singh, J. 2020 A sustainable paradigm of sewage sludge biochar: Valorization, opportunities, challenges and future prospects. *Journal of Cleaner Production* 269, 1-16 https://doi.org/10.1016/j.jclepro.2020.122259

Somaia G. M., Sahar M. A. 2019 Adsorptive removal of acetamiprid pesticide from aqueous solution using environmentally friendly natural and agricultural wastes. *Desalination and Water Treatment* 145, 280-290 https://doi.org/10.5004/dwt.2019.23644

Srikhaow, A., Chaengsawang, W., Kiatsiriroat, T., Kajitvichyanukul, P., Smith, S.M. 2022 Adsorption Kinetics of Imidacloprid, Acetamiprid and Methomyl Pesticides in Aqueous Solution onto Eucalyptus Woodchip Derived Biochar. Minerals 12, 528. https://doi.org/10.3390/min12050528

Vouk, D., Nakić, D., Bubalo, A., Bolanča, T. 2022 Environmental Aspects in Selecting Optimum Variant of Sewage Sludge Management. *Environmental Engineering and Management Journal.* 21 (3), 443-456

Xiang, W., Zhang, X., Chen, J., Zou, W., He, F., Hu, X., Tsang, D.C.W., Ok, Y.S., Gao, B. 2020 Biochar technology in wastewater treatment: A critical review. *Chemosphere* 252, 126539 https://doi.org/10.1016/j.chemosphere.2020.126539

Xu, G., Yang, X., Spinosa, L. 2015 Development of sludge-based adsorbents: Preparation, characterization, utilization and its feasibility assessment. *J. Environ. Manage*. 151, 221–232. https://doi.org/10.1016/j.jenvman.2014.08.001

Yang, Q., Wang, X., Luo, W., Sun, J., Xu, Q., Chen, F., Zhao, J., Wang, S., Yao, F., Wang, D., Li, X., Zeng, G. 2018 Effectiveness and Mechanisms of Phosphate Adsorption on Iron-Modified Biochars Derived from Waste Activated Sludge. *Bioresource Technology* 247, 537-544 https://doi.org/10.1016/j.biortech.2017.09.136

Yin, Q., Liu, M., Ren, H. 2019 Biochar produced from the co-pyrolysis of sewage sludge and walnut shell for ammonium and phosphate adsorption from water. *Journal of Environmental Management* 249, 109410 https://doi.org/10.1016/j.jenvman.2019.109410

Zango, Z. U., Khoo, K. S., Garba, A., Lawal, M. A., Abidin, A. Z., Wadi, I. A., Eisa, M. H., Aldaghri, O., Ibnaouf, K. H., Lim, J. W., Da, W. 2024 A review on carbon-based biowaste and organic polymer materials for sustainable treatment of sulfonamides from pharmaceutical wastewater. *Environmental Geochemistry and Health* 46, 1–51 https://doi.org/10.1007/s10653-024-01936-1

Zhan, Y., Deng, M., Wang, M., Li, H., Zhang, Y., Yang, L., Chen, H., Wang, Y., Li, Y., Wang, X. 2023 Research progress on biochar-based material adsorption and removal of ibuprofen. *Frontiers in Environmental Science* 11, 1327000 https://doi.org/10.3389/fenvs.2023.1327000

Zhou, Y., Gao, J., Yang, X., Ni, H., Qi, J., Zhu, Z., Yang, Y., Fang, D., Zhou, L., Li, J. 2024 Recent progress in sludge-derived biochar and its role in wastewater purification. *Sustainability* 16 (12), 5012. https://doi.org/10.3390/su16125012

APPLICATION OF BIOCHAR FOR THE REMOVAL OF THE PHARMACEUTICAL ZIDOVUDINE FROM WASTEWATER

Hana POSAVČIĆ [1*], Domagoj NAKIĆ [1], Katarina LICHT [1], Anđela PRKAČIN [1]

[1] *Faculty of Civil Engineering University of Zagreb, Croatia*

E-mail: hana.posavcic@grad.unizg.hr

E-mail: domagoj.nakic@grad.unizg.hr

E-mail: katarina.licht@grad.unizg.hr

E-mail: andela.prkacin@student.grad.unizg.hr

[*] *Corresponding author*

Abstract

In this study, dried sewage sludge was converted into biochar through pilot gasification process, and batch adsorption experiments were conducted to evaluate zidovudine removal. Optimal Design was used to study the effects of pH, initial concentration, biochar mass and contact time. Laboratory results showed a maximum removal efficiency of 65% and an adsorption capacity of 2.94 mg/g. Optimal performance was achieved at low pH (3–4), higher biochar dosage (5 g/L), and longer contact time (24h), underscoring the key role of acidity in the adsorption process. Results demonstrate that biochar derived from sewage sludge gasification can serve as an effective and environmentally sustainable adsorbent, and contribute to sustainable waste management.

Key words

adsorption, biochar, gasification, Response Surface Methodology, sewage sludge, zidovudine

1 Introduction

A class of micro-pollutants that has gained an increasing attention in recent years as emerging water and environmental pollutants are pharmaceutical compounds. Pharmaceuticals are biologically active substances encompassing a wide range of commonly used medical products, including antibiotics, antipyretics, anti-inflammatory drugs, analgesics, and many others, which are extensively applied in both human and veterinary medicine worldwide (Jatmiko et al., 2020; Rozaini et al., 2023). Among these compounds, analgesics and antibiotics are the most frequently detected in wastewater treatment plant (WWTP) influents. Notably, ciprofloxacin and sulfamethoxazole have been reported at particularly high concentrations, reaching approximately 16532–21635 µg/L and 734–1178 µg/L, respectively (Phoon et al., 2020).

Pharmaceuticals as ubiquitous environmental pollutants pose significant risks to both human health and ecosystems. Although they are highly beneficial due to their ability to inhibit microbial growth and eliminate pathogenic microorganisms, their large-scale production and extensive use have resulted in their widespread presence in the environment (Zhuang and Wang, 2023). A substantial proportion of administered pharmaceuticals is only partially metabolized and subsequently excreted, allowing these compounds to enter wastewater systems (Gehring et al., 2023). Numerous studies have reported the presence of pharmaceutical residues in surface water, groundwater, treated and untreated wastewater, and other environmental matrices, often at trace concentrations. Despite their low levels, exposure to these substances has been shown to induce mutagenic and genotoxic effects in both humans and aquatic organisms (Phoon et al., 2020). Owing to the global and continuous use of pharmaceuticals in human

and animal healthcare, their environmental occurrence has become a critical research focus across multiple fields, including public health, medicine, and environmental protection (Maleki and Masoumi, 2024).

Pharmaceutical compounds enter aquatic environments primarily through effluents from pharmaceutical manufacturing facilities, hospitals, and domestic sources (Zango et al., 2020). The occurrence and concentration of pharmaceuticals in wastewater are influenced by several factors, such as geographical location, seasonal variations, demographic characteristics, and economic conditions (Dinh et al., 2017). Furthermore, the structural complexity and diverse physicochemical properties of pharmaceuticals present additional challenges for their effective removal and management in wastewater treatment processes (Langbehn et al., 2021).

Despite the typically low concentrations of these chemical compounds in aquatic environments, their continuous input and persistence over time pose significant risks to both aquatic and terrestrial organisms. Consequently, these substances have been increasingly recognized as emerging environmental pollutants in recent years (Ashfaq et al., 2016). Nevertheless, conventional wastewater treatment processes are often unable to completely remove pharmaceutical residues, resulting in their discharge into natural water bodies. The presence of pharmaceutical compounds, such as antibiotics, in the environment can disrupt native microbial communities and contribute to the development and proliferation of antibiotic-resistant bacteria (Daniel et al., 2023; Zango et al., 2021). The spread of such resistant bacteria represents a serious public health concern, as it can compromise the effectiveness of existing antibiotic therapies. In addition, chronic exposure to low concentrations of antibiotics may exert sublethal effects on organisms, ultimately impairing ecosystem functioning and biodiversity (Zango et al., 2024; Imama et al., 2018).

Addressing this escalating challenge necessitates the development of efficient and sustainable strategies for the removal of various compounds from pharmaceutical wastewater. Conventional treatment methods, including membrane filtration and ozonation, are often associated with high operational costs and significant energy demands (Oguz and Mihciokur, 2014). Therefore, there is a pressing need to explore alternative approaches that are not only effective but also economically viable and environmentally sustainable.

Biochar is a porous, carbon-rich material produced through the thermochemical conversion of organic biomass under limited or oxygen-free conditions (Xiang et al., 2020). The feedstocks used for biochar production are predominantly organic waste materials, such as agricultural residues, forestry by-products, wood chips, algae, sewage sludge, paper and pulp mill sludge, and municipal solid waste (Souza et al., 2024; Xiang et al., 2020). Feedstock selection is influenced by factors including availability, cost, energy content, and the desired physicochemical properties of the resulting biochar. Variations in feedstock type can significantly affect biochar composition, porosity, surface functionality, and reactivity, thereby influencing its suitability for specific environmental applications (Wan Mahari et al., 2022).

Biochar can be produced through a variety of thermochemical conversion processes, including pyrolysis, microwave-assisted pyrolysis, hydrothermal carbonization, and gasification, whereas torrefaction and rapid carbonization are less frequently applied processes (Murtaza et al., 2022; Xiang et al., 2020).

In this study, stabilized and dehydrated sludge was used as feedstock. The dried sludge was converted into biochar, which was subsequently applied for the removal of the pharmaceutical compound zidovudine. Zidovudine is recognized as the first antiretroviral drug developed for the prevention and treatment of HIV/AIDS, and its presence can contribute to pharmaceutical pollution and may pose potential risks to ecosystems and human health (Volberding et al., 1990).

2 Materials and methods

2.1 Biochar properties

For this study, stabilized and dehydrated sludge obtained from the Karlovac (Croatia) WWTP was used as feedstock. The facility operates with a tertiary treatment stage that, in addition to the removal of suspended solids and organic matter, includes nutrient removal processes targeting nitrogen and phosphorus. Sludge samples (approximately 15 kg wet weight per sample) were collected in sealed containers and stored at room temperature prior to drying. Before drying, each sample was thoroughly homogenized to ensure uniformity. Drying was carried out in a laboratory oven at 105 °C until a dry matter content exceeding 90% was achieved. The dried sludge was subsequently converted into biochar through a gasification process conducted in a pilot-scale (experimental) Looper plant developed by Indeloop d.o.o. (Fig. 1).

Chemical composition analysis performed using atomic absorption spectroscopy (AAS) revealed that the predominant inorganic constituents of the biochar were Al_2O_3 (15.6%), CaO (14.7%), and Fe_2O_3 (10.5%). Approximately 49% of the sample mass remained undissolved, which was attributed to the carbonaceous fraction, corresponding to the organic phase of the biochar. The calculated elemental composition indicated contents of approximately 8.3% Al, 10.5% Ca, and 7.3% Fe, while potassium, magnesium, sodium, silicon, and titanium were present at concentrations below 2%.

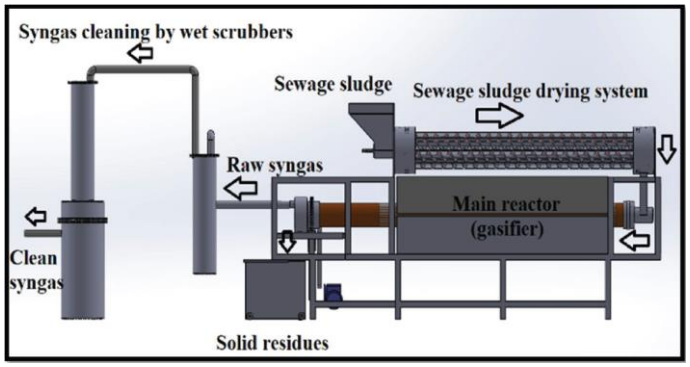


Figure 1. The Gasification pilot plant (Looper) (Bubalo et al., 2022; Nakić et al., 2024)

2.2 Zidovudine properties and preparation

Zidovudine (Fig. 2) was used as the model pharmaceutical compound, and all experiments were conducted using its aqueous solutions. A 100 mg/L stock solution was prepared by dissolving 0.1 g of pure zidovudine in a small volume of distilled water, followed by quantitative transfer into a 1000 mL volumetric flask and dilution to the mark with distilled water. Working solutions with concentrations of 1, 10, and 20 mg/L were prepared by dilution of the stock solution with deionized water.

Relatively low concentrations were selected, as pharmaceuticals are typically present in municipal wastewater at trace or sub-trace levels; therefore, even the concentrations investigated in this study may be considered extreme under realistic environmental conditions. The initial pH of the solutions was measured using a multiparameter probe (HI9829, Hanna Instruments, Italy) and adjusted to pH values of 3, 7, and 9 using 0,1 M HNO_3 or 0,1 M NaOH, as required.

Biochar dosages of 0.1, 0.5, and 1.0 g per 200 mL of solution were applied in the adsorption experiments (Table 1).

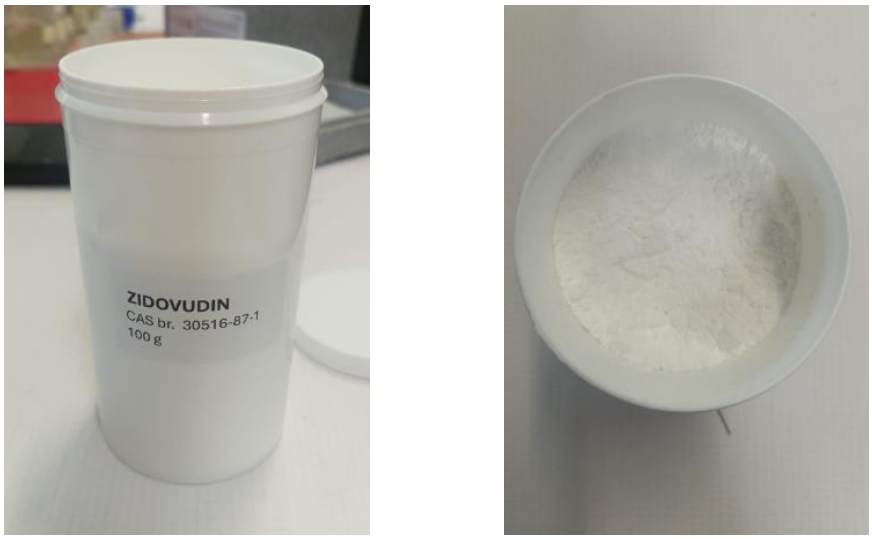


Figure 2. The pharmaceutical zidovudine – pure active substance

2.3 Adsorption experiments

The experiments were carried out in 250 mL closed bottles containing 200 mL of solution and 0.1, 0.5 or 1 g of biochar. The bottles were placed on a rotary mixer (Reax 2, Heidolph, Germany) set at 45 rpm, for contact times of 1, 6 and 24 h (Figure 3).



Figure 3. Rotary mixer

Ranges of parameters used in experimental research are shown in Table 1.

After adsorption was complete, the samples were filtered using a syringe with a 0.45 μm pore size polyether sulfone (PES) membrane filter to remove biochar. The initial and residual concentrations were determined spectrophotometrically using an Agilent Cary 60 UV-Vis spectrophotometer (Agilent Technologies, USA).

Table 1. Ranges of parameters

Parameter	Range		
A) Initial zidovudine concentration [mg/L]	1	10	20
(B) pH	3	7	9
(C) Biochar mass [g/200 mL]	0.1	0.5	1
(D) Time [h]	1	6	24

3 Results and Discussion

The experimental matrix (Table 2) was generated using the Design-Expert software package based on the Optimal (Custom) Design approach within Response Surface Methodology (RSM). This design was selected because it allows manual specification of the mean values of numerical factors, enabling the adjustment of experimental levels according to research objectives rather than being limited to purely statistical considerations. For instance, the contact time was centred at 6 h to evaluate whether most of the pollutant removal occurs during the early stages of adsorption, whereas the statistical midpoint of the investigated interval, assuming symmetrical spacing, would have been 12.5 h.

Removal efficiency represents the percentage of the initial concentration of the pollutant (zidovudine) removed from the solution after the adsorption process. It quantifies the fraction of the initially present compound that is eliminated and serves as a fundamental indicator of adsorption performance. The removal efficiency was calculated using Eq. (1):

$$RE\ [\%] = \frac{C_{in} - C_e}{C_{in}} \times 100 \tag{1}$$

where RE [%] represents removal efficiency of zidovudine, C_{in} [mg/L] initial zidovudine concentration, and C_e [mg/L] final zidovudine concentration.

No zidovudine removal was observed in experimental runs 3 and 6 (RE = 0%). Both experiments were conducted at an initial concentration of 1 mg/L, pH 9, and a contact time of 1 h, differing only in the biochar dosage (0.1 and 1.0 g/200 mL). Since increasing the adsorbent dosage by a factor of ten did not improve the removal efficiency, the amount of biochar was likely not the limiting factor. Instead, the absence of adsorption can be attributed to the unfavorable effect of alkaline pH on zidovudine adsorption, combined with the insufficient contact time to reach adsorption equilibrium. Furthermore, due to the low initial concentration of zidovudine (1 mg/L), any decrease in concentration may have been within the analytical uncertainty of the measurement method, resulting in a calculated removal efficiency of 0%.

Based on the experimental matrix (Table 2), the Design-Expert software was also used to perform regression analysis and develop polynomial models. Among the tested models, the reduced quadratic model exhibited the highest coefficient of determination (R^2 = 0.9895), indicating an excellent fit between the experimental and predicted values.

An analysis of variance (ANOVA) was conducted for the reduced quadratic model to evaluate the significance of the process variables listed in Table 1 on zidovudine removal efficiency. The results showed that the linear terms A (initial concentration), B (pH), C (biochar mass), and D (time), as well as the interaction terms AB, BC, and BD, and the quadratic terms C^2 and D^2, were statistically significant ($p < 0.05$).

Table 2. Experimental matrix

Run	(A) C_{in} [mg/L]	(B) pH	(C) m [g/200 mL]	(D) t [h]	RE [%]	q_e [mg/g]
1	1	7	0.5	6	16	0.06
2	20	7	1	24	21.5	0.86
3	1	9	0.1	1	0	0
4	1	3	1	1	47	0.09
5	10	3	1	6	48.3	0.97
6	1	9	1	1	0	0
7	10	9	0.5	24	9	0.36
8	20	3	0.5	1	14	1.12
9	20	7	0.1	24	4.05	1.62
10	1	3	0.5	6	40	0.16
11	20	7	1	1	17.7	0.71
12	1	7	0.5	6	19	0.08
13	10	7	0.5	1	9	0.36
14	10	3	0.1	24	14.7	2.94
15	1	3	1	24	65	0.13
16	20	3	0.5	24	29	2.32
17	20	7	0.1	6	3	1.2
18	10	3	0.1	6	9.5	1.9
19	1	7	0.1	24	4	0.08
20	20	9	0.5	6	17	1.36
21	1	7	0.5	6	13	0.05
22	10	7	0.5	1	13	1.72
23	10	3	1	6	43	2

The interactions between the influencing parameters are illustrated through contour plots and three-dimensional response surface diagrams (Fig. 4). The highest removal efficiencies were observed at lower pH values and lower initial concentrations of zidovudine. An increase in either parameter led to a pronounced decrease in removal efficiency. Specifically, optimal performance was achieved under acidic conditions, with pH values in the range of 3 – 4, but only at relatively low zidovudine concentrations.

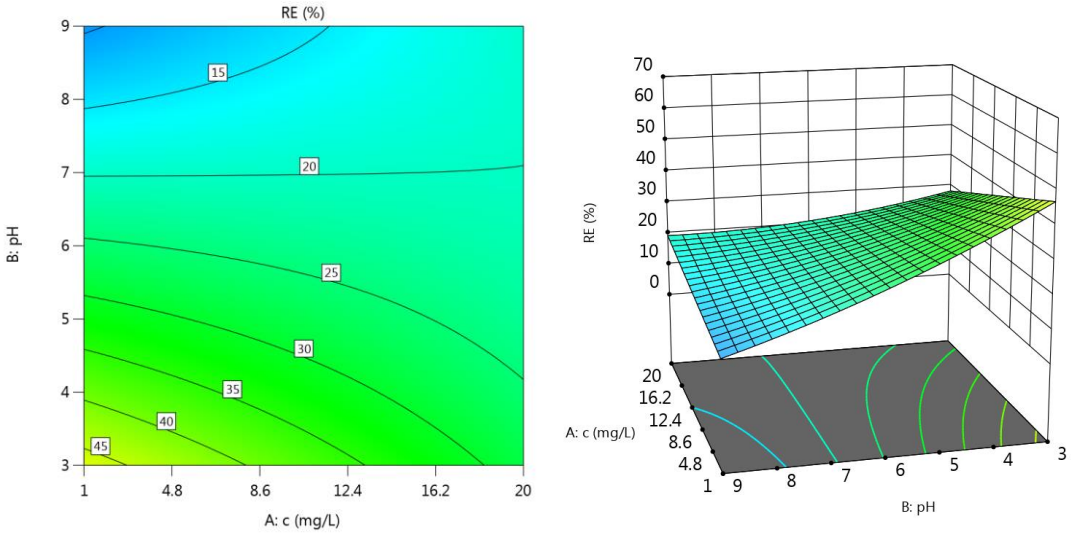


Figure 4. Contour plot (left) and 3D response surface (right) for combined effect of initial concentration and pH on zidovudine removal

Another significant interaction was observed between pH and contact time, indicating that an increase in contact time enhances removal efficiency primarily at lower pH values (Fig. 5). Under acidic conditions, extended contact time leads to a noticeable improvement in zidovudine removal efficiency. In contrast, at higher pH levels, prolonging the contact time does not result in a significant increase in removal efficiency. The most favorable operational conditions therefore involve a combination of longer contact time and low pH, highlighting the critical role of acidity in the adsorption and removal of zidovudine.

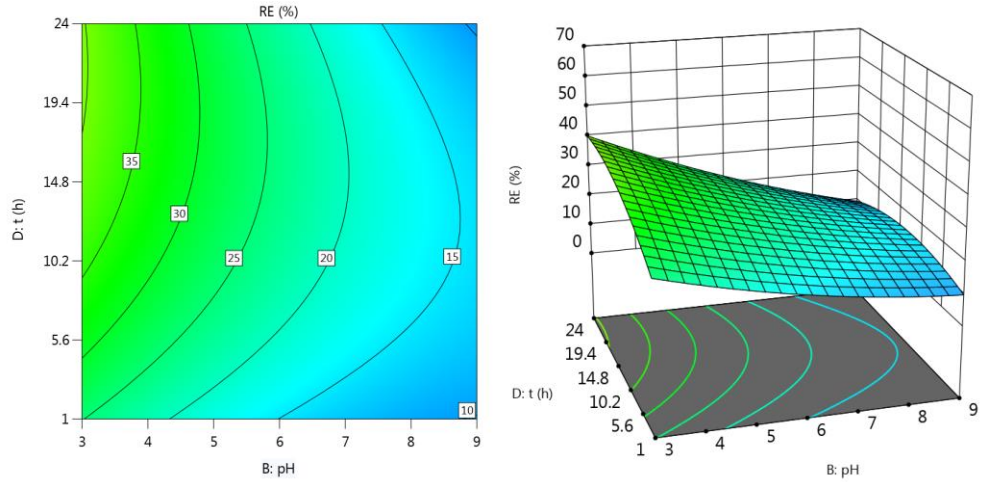


Figure 5. Contour plot (left) and 3D response surface (right) for combined effect of time and pH on zidovudine removal

The final significant interaction was observed between pH and biochar dosage (Fig. 6). At lower pH values, increasing the biochar mass resulted in a substantial improvement in removal efficiency. In contrast, under alkaline conditions, increasing the biochar dosage had a much weaker effect, and the removal efficiency remained relatively low. Overall, the highest removal efficiencies were achieved through a combination of higher biochar dosages and acidic conditions, further emphasizing the critical influence of pH on the adsorption process.

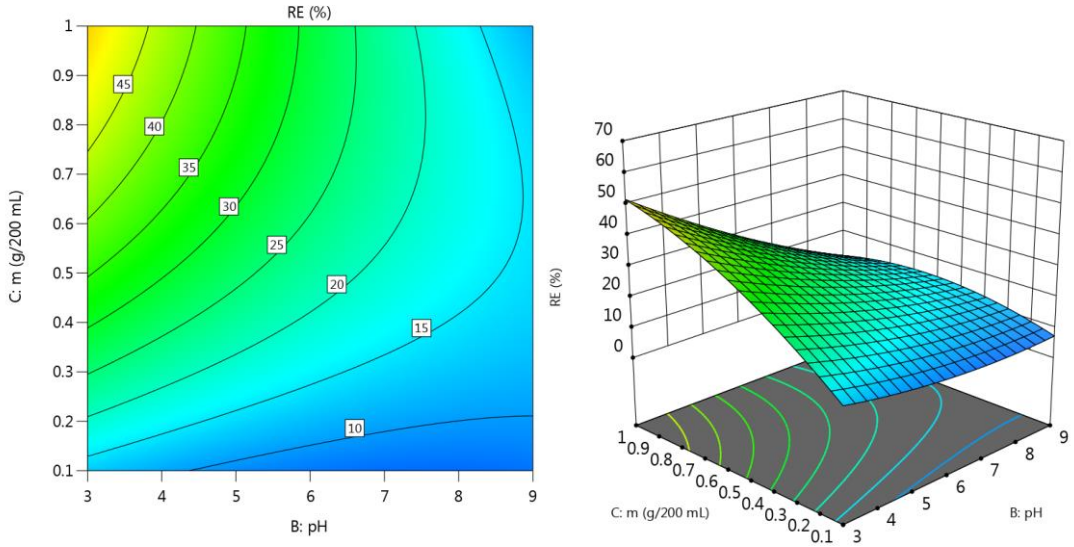


Figure 6. Contour plot (left) and 3D response surface (right) for combined effect of biochar mass and pH on zidovudine removal

Unlike removal efficiency, which does not take into account the mass of the adsorbent, adsorption capacity (q_e [mg/g]) refers to the amount of adsorbed pollutant per unit mass of biochar and is calculated by Eq (2):

$$q_e = \frac{(C_{in} - C_e) \times V}{m} \tag{2}$$

where V [L] represents volume of the solution and m [g] biochar mass.

The overall average adsorption capacity of the biochar for zidovudine removal was 0.77 mg/g, with individual values ranging from 0.05 to 2.94 mg/g (Table 2). In two experiments, an adsorption capacity of 0 mg/g was recorded, indicating no measurable pollutant removal, highlighting the need for further investigation to verify these results. Excluding these cases, the lowest adsorption capacity (0.05 mg/g) occurred at pH 7, with 2.5 g/L of biochar and an initial zidovudine concentration of 1 mg/L. The highest value (2.94 mg/g) was achieved at pH 3, with 0.5 g/L of biochar and 10 mg/L of zidovudine.

Overall, the results indicate that zidovudine removal efficiency increases with decreasing pH, reaching its maximum in the acidic range. The highest observed removal efficiency was 65%, recorded at pH 3, with 5 g/L biochar, an initial concentration of 1 mg/L, and a contact time of 24 h. As the pH increased, adsorption efficiency gradually decreased, reaching from 0% to 9% at pH 9, independent of other parameters. These findings are largely consistent with the literature (Czech et al., 2020; Jellali et al., 2023; Mashoene et al., 2023). However, while numerous studies have investigated biochar for the removal of pharmaceutical contaminants, limited attention has been given to biochar derived from sewage sludge gasification and its application for zidovudine removal.

For instance, Mashoene et al. (2023) investigated the removal of zidovudine and Phenol using biochar and reported that maximum adsorption occurred under acidic conditions (pH 2), with efficiency decreasing at higher pH. Their experiments, conducted with initial concentrations of 10 mg/L and 50 mg/L and a constant dose of modified biochar (biochar/rGO/DES-glycerol, 0.1 g/40 mL), achieved a maximum zidovudine removal efficiency of 49% and adsorption capacity of 20.2 mg/g. Compared to these results, the present study achieved a slightly higher maximum removal efficiency (65%), but a lower maximum adsorption capacity (2.94 mg/g). This difference can be attributed to variations in biochar surface properties. Mashoene et al. (2023) employed a multi-modified biochar with enhanced porosity and a higher density of active sites, whereas the current study used unmodified (pristine) biochar. Importantly, Mashoene et al. (2023) also tested unmodified biochar, which showed no

zidovudine removal (0%). The authors explained that modification produced a composite material with open cavities, unevenly distributed pores, and increased active sites, resulting in significantly improved adsorption performance.

4 Conclusion

This study investigated the potential of using biochar produced from the gasification of sewage sludge from the Karlovac WWTP for the removal of the pharmaceutical compound zidovudine from wastewater. Laboratory experiments were conducted to evaluate the adsorption capacity of the biochar and to identify the most favourable conditions for zidovudine adsorption.

The highest removal efficiency achieved was 65%, with a maximum adsorption capacity of 2.94 mg/g. Optimal removal occurred at low pH values (3 – 4), higher biochar dosages, and longer contact times, highlighting the critical role of acidity in the adsorption process. These results demonstrate that biochar derived from sewage sludge gasification can serve as an effective and environmentally sustainable adsorbent for zidovudine, while simultaneously contributing to sustainable waste management in line with circular economy principles.

Nevertheless, several limitations and uncertainties should be acknowledged. The experiments were conducted under controlled laboratory conditions using synthetic solutions, which may not fully represent the complexity of real wastewater containing dissolved organic matter and competing contaminants. In addition, adsorption mechanisms were not investigated through kinetic or isotherm modelling, limiting the understanding of the dominant interactions responsible for zidovudine uptake. The regeneration potential, long-term stability, and performance of the biochar under continuous operating conditions were also beyond the scope of this study.

To achieve a more comprehensive understanding of the adsorption process, future studies should focus on elucidating adsorption mechanisms through isotherm and kinetic analyses. Such approaches would help determine whether zidovudine removal is primarily governed by electrostatic interactions, physical adsorption and pore filling, or π–π interactions. Furthermore, exploring chemical or physical modifications of biochar to enhance surface activity and increase the abundance of functional groups could provide valuable insights into strategies for improving pharmaceutical removal efficiency compared with unmodified biochar.

The findings may benefit several stakeholder groups. For the pharmaceutical industry, the study highlights the importance of developing strategies to reduce the environmental release of pharmaceutical residues. For public health authorities, the results contribute to efforts aimed at protecting water resources from emerging contaminants. For wastewater treatment operators and water managers, the study presents sewage sludge gasification biochar as a promising supplementary treatment material that may improve the removal of pharmaceutical compounds while simultaneously promoting sustainable sludge management.

Detailed studies of this nature would also allow for the full optimization of the adsorption process, including the determination of optimal biochar dosages and contact times, with the goal of maximizing removal efficiency while minimizing resource consumption.

Acknowledgements

This work was supported by the Croatian Science Foundation under the project number [HRZZ-UIP-2025-02-9907]: AdSorB – “Advanced Wastewater Treatment by Repurposing Sewage Sludge Derived Biochar”.

References

Ashfaq, M., Khan, K.N., Rasool, S., Mustafa, G., Saif-Ur-Rehman, M., Nazar, M.F., Sun, Q., Yu, C.-P. 2016 Occurrence and ecological risk assessment of fluoroquinolone antibiotics in hospital waste of Lahore, Pakistan, *Environ. Toxicol. Pharmacol*. 42, 16–22

Bubalo, A., Vouk, D., Maljković, D., Bolanča, T. 2022 Gasification of Sewage Sludge in a Rotary Kiln Reactor – A Case Study with Incorporation of Sewage Sludge Ash in Brick Production. *Chem. Biochem. Eng. Q.* 36(1), 77–87. doi: https://doi.org/10.15255/cabeq.2021.2030

Czech, B., Konczak, M., Rakowska, M., Oleszczuk, P. 2020. Engineered biochars from organic wastes for the adsorption of diclofenac, naproxen and triclosan from water systems. *J. Clean. Prod*., 288, 125686

Daniel, M., Szymanik-Grzelak, H., Sierdzinski, J., Podsiadły, E., Kowalewska-Młot, M., Panczyk-Tomaszewska, M. 2023 Epidemiology and risk factors of UTIs in children—a single-center observation, *J. Pers. Med*. 13, 138

Dinh, Q.T., Moreau-Guigon, E., Labadie, P., Alliot, F., Teil, M.J., Blanchard, M., Chevreuil, M. 2017 Occurrence of antibiotics in rural catchments. *Chemosphere* 168, 483–490.

Gehring R., Mochel J.P., Schmerold I. 2023 Understanding the background and clinical significance of the WHO, WOAH, and EMA classifications of antimicrobials to mitigate antimicrobial resistance, *Front. Vet. Sci. 10*, 1153048

Imama, S.S., Zango, Z.U., Abdullahi, H. 2018 Room temperature synthesis of bismuth Oxyiodide with different morphologies for the photocatalytic degradation of Norfloxacin, Am. Sci. Res. J. Eng. Technol. Sci. 41, 26–39

Jatmiko, T.H., Penelitian, B., Bahan, T., Ilmu, L. 2020 Optimization of production activated carbon for removal of pharmaceuticals wastewater using Taguchi method and Grey relational Analysis*, J. Ris. Teknol. Pencegah. Pencemaran Ind.* 11, 11–18

Jellali, S., Khiari, B., Al-Harrasi, M., Charabi, Y., Al-Sabahi, J., Al-Abri, M., Usman, M., Al-Raeesi, A., Jeguirim, M. 2023. Industrial sludge conversion into biochar and reuse in the context of circular economy: Impact of pre-modification processes on pharmaceuticals removal from aqueous solutions, *Sustainable Chemistry and Pharmacy* 33, 101114, doi: https://doi.org/10.1016/j.scp.2023.101114.

Langbehn, R.K., Michels, C., Soares, H.M. 2021 Antibiotics in wastewater: from its occurrence to the biological removal by environmentally conscious technologies. *Environ. Pollut*. 275, 116603

Maleki, F., Masoumi, H. 2024 Adsorption of antibiotics, *J. Water Process. Eng*. 106186

Mashoene, T.N., Leudjo Taka, A., Akpotu, S.O., Lawal, I.A., Klink, M.J. 2023. Surface Modification of Tea-Waste-Based Biochar Adsorbent: Synthesis, Characterization, and Batch Adsorption for the Removal of Zidovudine ARV Drug and Phenol, *Applied Sciences* 13, 13: 7493. doi: https://doi.org/10.3390/app13137493

Murtaza, G., Ahmed, Z., Dai, D.-Q., Iqbal, R., Bawazeer, S., Usman, M., Rizwan, M., Iqbal, J., Akram, M.I., Althubiani, A.S., Tariq, A., Ali, I. 2022 A review of mechanism and adsorption capacities of biochar based engineered composites for removing aquatic pollutants from contaminated water. *Front. Environ. Sci.,* 10:1035865

Nakić, D., Licht, K., Vouk, D., Posavčić, H. 2024 Sewage sludge biochar as adsorbent used in wastewater treatment, *In Proceedings book of the 4th International Conference Waters in sensitive & protected areas*, 10 -13 April 2024, Pula, Croatia. 159-174.

Oguz, M. 2014 Mihciokur, H. Environmental risk assessment of selected pharmaceuticals in Turkey, *Environ. Toxicol. Pharmacol*., 38 (1), 79-83

Phoon BL, Ong CC, Mohamed Saheed MS, Show PL, Chang JS, Ling TC, Lam SS, Juan JC. 2020 Conventional and emerging technologies for removal of antibiotics from wastewater. *J Hazard Mater.* 5 (400), 122961. doi: 10.1016/j.jhazmat.2020.122961

Rozaini M.N.H., Semail N.-F., Zango Z.U., Lim J.W., Yahaya N., Setiabudi H.D., Tong W.-Y., Shamsuddin R., Chan Y.J., Khoo K.S., Sulimanm M., Kiatkittipong W. 2023 Advanced adsorptions of non-steroidal anti-inflammatory drugs from environmental waters in improving offline and online

preconcentration techniques: an analytical review, *J. Taiwan Inst. Chem. Eng*. 105020
Souza, T.F., Ferreira, G.M.D. 2024 Biochars as adsorbents of pesticides: laboratory-scale performances and real-world contexts, challenges, and prospects, *ACS EST Water*, 4 (10), 4264−4282
Volberding P.A, Lagakos S.W, Koch M.A, Pettinelli C., Myers M.W., Booth D.K., Balfour H.H. Jr, Reichman R.C., Bartlett J.A., Hirsch M.S., et al. 1990. Zidovudine in Asymptomatic Human Immunodeficiency Virus Infection: A Controlled Trial in Persons with Fewer Than 500 CD4-Positive Cells per Cubic Millimeter. *New England Journal of Medicine,* 322 (14), 941–949. doi:10.1056/NEJM199004053221401.
Wan Mahari, W.A., Waiho, K., Azwar, E., Fazhan, H., Peng, W., Ishak, S.D., Tabatabaei, M., Yek, P.N.Y., Almomani, F., Aghbashlo, M., Lam, S.S. 2022 A state-of-the-art review on producing engineered biochar from shellfish waste and its application in aquaculture wastewater treatment. *Chemosphere,* 288, 132559
Xiang, W., Zhang, X., Chen, J., Zou, W., He, F., Hu, X., Tsang, D.C.W., Ok, Y.S., Gao, B. 2020 Biochar technology in wastewater treatment: A critical review. *Chemosphere*, 252, 126539
Zango, Z.U., Sambudi, N.S., Jumbri, K., Ramli, A., Hana, N., Abu, H., Saad, B., Nur, H., Muhammad Rozaini, H.A., Isiyaka, A.M., Sulieman Osman, A. 2020 An overview and evaluation of highly porous adsorbent materials for polycyclic aromatic hydrocarbons and phenols removal from wastewater, *Water*, 12, 2921
Zango, Z.U., Jumbri, K., Soraya, N., Hanif, H., Bakar, A., Nasiru, Z., Ahmad, H., Saad, B. 2021 Selective adsorption of dyes and pharmaceuticals from water by UiO metal–organic frameworks: a comprehensive review, *Polyhedron* 210, 115515.
Zango, Z.U., Khoo, K.S., Garba, A., Lawal, M.A., Abidin, A.Z., Wadi, I.A., Eisa, M.H., Aldaghri, O., Ibnaouf, K.H., Lim, J.W., Da, W. 2024 A review on carbon-based biowaste and organic polymer materials for sustainable treatment of sulfonamides from pharmaceutical wastewater, *Env. Geochem Heal.* 46, 1–51
Zhuang, S., Wang, J. 2023 Interaction between antibiotics and microplastics: recent advances and perspective, *Sci. Total Environ.* 897, 165414

THE USE OF ULTRAFILTRATION IN WATER TREATMENT

Danka BARLOKOVÁ [1*], Ján ILAVSKÝ [1], Michal PROSŇANSKÝ [2], Mikuláš KRESCANKO [3]

[1] *Department of Sanitary and Environmental Engineering, Faculty of Civil Engineering, Slovak University of Technology, Radlinského 11, 810 05 Bratislava, Slovakia*

E-mail: danka.barlokova@stuba.sk

E-mail: jan.ilavsky@stuba.sk

[2] *PRAKTIKPUMP, Ltd., Priemyselná 444, 965 01 Ladomerská Vieska, Slovakia*

E-mail: upravavod@praktikpump.sk

[3] *ProMinent Slovensko, Ltd., Roľnícka 9239/21, 831 07 Bratislava, Slovakia*

E-mail: krescanko.mikulas@prominent.com

[*] *Corresponding author*

Abstract

The article deals with the removal of antimony from water using coagulation and ultrafiltration. The aim of the experiments is to compare the efficiency of removing antimony from water for iron coagulants (ferric sulphate, ferric chloride), to monitor the agent doses, contact time with water, filtration rate and antimony concentration in raw water, and before and after ultrafiltration. The experiments used an ultrafiltration device, with the material of membrane from polyacrylonitrile (PAN), diameter of pores 0.025 μm and membrane surface 16 m^2. To achieve the necessary contact time of water with the coagulant, a tubular reactor with a static stirrer (length > 6.0 m, volume 30 litres) will be used. The concentration of antimony in the monitored spring Brdáre ranges in the interval 80.3-97 μg/L. The results of the experiments showed that in the case of ferric sulphate, at a flow rate of 700 L/h, a dose of 320 mL/h $Fe_2(SO4)_3$ (41% solution of PIX-113) and a retention time of 2.5 min, the concentration of Sb in the treated water was less than 1 μg/L Sb, while in the case of $FeCl_3$, at a flow rate of 800 L/h, a dose of 184 mL/h $FeCl_3$ (38% solution of PIX-111) and a retention time of 2.25 min, the concentration of Sb in the treated water was 1.73 μg/L Sb. The results confirmed that the technological process used is effective in removing antimony from water.

Key words

drinking water, removal of antimony, ultrafiltration, tubular reactor, coagulation agents, iron sulphate, iron chloride, retention time.

1 Introduction

Antimony (Sb), atomic number 51, molecular weight 121.75 is a brittle silver-white metal that occurs in the Earth's crust in chemically bound forms, including minerals. Antimony is released into the environment from natural sources and from industry, while the anthropogenic emission into the atmosphere exceeds the natural resources emission. Antimony is a standard component of coal and oil. Industrial plants, emissions from car exhausts and the burning of fossil fuels are the main sources of antimony in the air. The emissions are getting into the atmosphere also from factories by melting the ore and by incineration of the municipal waste. Then they are transported from the air into the soil, lakes, rivers and bottom sediments.

Major part of antimony ends up in the soil where the antimony is strongly bound to particles containing iron, manganese or aluminium. From the soil it is released into the food chain. At lower concentration,

antimony could be found in some lakes and rivers, and even in drinking water. At the present time, it is very difficult to distinguish the anthropogenic pollution of the waters from the natural background.

Antimony is a toxic heavy metal with effects similar to arsenic and lead. The intoxication by antimony is not as much severe as it is in the case of arsenic because the compounds of antimony are absorbed slowly. Antimony is an inhibitor for some enzymes, influences the metabolism of proteins and carbohydrates, and causes a failure of glycogen production in kidneys. Its ability of accumulation in the bodies of organisms is low. Findings on health aspects related to the occurrence of some heavy metals in drinking water are summarized in publication (AWWA 1990, USEPA 1984).

Till now, the World Health Organization (WHO 2011) and institutes dealing with the monitoring of carcinogenic effects have not classified antimony as a carcinogen. The limit concentration of antimony in drinking water in Slovakia is 10 μg/L (The Decree of the Ministry of Health of the Slovak Republic No. 91/2023 Coll.). This limit value is in accordance with the WHO Recommendations (WHO 2011), EU Directive (Directive (EU) 2020/2184) and USEPA 2013.

Antimony is presented in water as Sb^{3-}, Sb^{0}, Sb^{3+} and Sb^{5+} (Sb^{3+} is ten times more toxic than Sb^{5+}), depending on the pH of the water, the oxidation-reduction potential and the oxygen content.

The most common form is antimonate – oxyanion $(H_2SbO_4)^-$ and $(HSbO_4)^{2-}$ or it can be present as antimonite ($H3SbO_3$). The organic form of antimony is very rare, especially in drinking water (Pitter 2009, WHO 2003).

Concentrations in natural waters not polluted by anthropogenic activity are in a range from tens of ng/L up to 1 μg/L. The threshold limit value (Sb = 10 μg/L) has been exceeded in Slovakia (Figure 1), for instance, in the locality of Košice and its surroundings (Zlatá Idka, the Bukovec water reservoir), the Low Tatras in the locality of Dúbrava (Liptovský Mikuláš), Spišsko-Gemerské rudohorie (Čučma, Poproč) and in the Little Carpathians (Pernek). Today, it is very difficult to distinguish between anthropogenic and natural pollution caused by antimony.

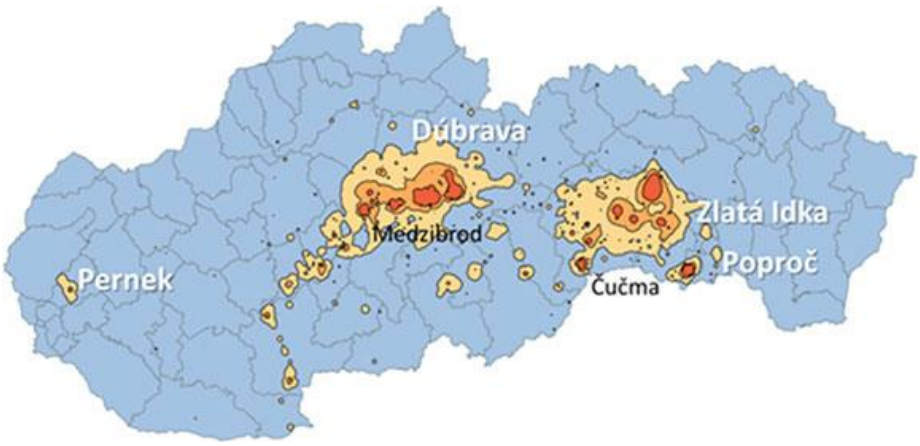


Figure 1. Areas of antimony in Slovakia

There are several technological methods of heavy metals removal, which are used in water treatment: precipitation (clarification), ion exchange, membrane technologies, adsorption, electrochemical processes and recently also biological methods (Bratby, 2006; Driehaus et al., 1998; Gannon and Wilson, 1986; Guo et al., 2009; Inam et al., 2019; Kang et al., 2000; Kang et al., 2003; MacPhee et al., 2001; Mohan et al., 2007; Nguyen et al., 2011; Zeng et al., 2008).

The most common method for the removal of heavy metals is water clarification – the **precipitation** of metal hydroxides and carbonates. This process is based on the dosing of appropriate agents (iron and aluminium salt, lime, sodium carbonate, sodium hydroxide and sulphates) to obtain the optimum pH

value of the solution in which an insoluble solid phase of precipitated heavy metal hydroxides or carbonates is formed. The effectiveness of the precipitation depends on the type of contaminant, its concentration, water composition and the type of agent.

Precipitation seems to be an ideal solution for the treatment of water containing heavy metals, provided that the process is not limited by certain effects that are reducing the effectiveness of coagulation. For example, the efficiency of precipitation is lower at a higher concentration of metals in water. If the solution is too diluted, the precipitation will be too slow. The precipitation is mainly influenced by the pH value (an acidic conditions is best for removing Sb, an alkaline environment is unsuitable) and also depending on the oxidation form (speciation) of antimony in the water. If no oxidizing agent is added, antimony remains in its original form.

In groundwater and surface waters, it occurs either as trivalent antimony Sb(III) (in a reduced environment, e.g. deep groundwater), or as pentavalent antimony Sb(V) (in an oxygenated environment, surface waters). The addition of an iron-based coagulant decreases the pH of the water. For this reason, it is necessary to determine the coagulant dosage using a coagulation test.

An overview of the efficiency in individual environments is as follows (Guo et al., 2009; Inam et al., 2021; Klimko et al., 2014; Munka et al., 2008):

1. Acidic environment (pH 4.0 – 5.5)
Acidic environment is the most efficient for this process, especially when Sb(V) is removed. Efficiency for Sb(V) removal is very high (85% – 95%). At low pH, the surface of the resulting iron hydroxide flakes $Fe(OH)_3$ has a positive charge. Pentavalent antimony occurs in solution as a negatively charged anion $[Sb(OH)_6]^-$. Due to strong electrostatic forces, excellent adsorption and binding to iron flakes occurs.

Efficiency for Sb(III) removal is high (approx. 80% – 90%). Trivalent antimony occurs in this region as the neutral molecule $Sb(OH)_3$. Although electrostatic attraction is absent, the precipitation and surface complexation mechanism works very well in the acidic region as well.

2. Neutral environment (pH 6.5 – 7.5)
In a neutral environment, which is typical for most raw waters entering treatment plants, the efficiency selectively decreases. Efficiency for Sb(V) removal is medium to low (approx. 40% – 60%). With increasing pH, the positive charge on the surface of the iron flakes decreases (the isoelectric point is reached), which weakens the bond with the negative anion $[Sb(OH)6]^-$. To achieve good efficiency in a neutral environment, it is necessary to significantly overdose $FeCl_3$.

Efficiency for Sb(III) removal is still high (80% – 90%). The removal of trivalent antimony remains stable even at neutral pH, because its sorption to ferric hydroxide is not so strictly dependent on the surface charge of the coagulant.

3. Alkaline environment (pH > 8.0)
In the alkaline range, the clarification efficiency drops dramatically and for practical use in drinking water treatment, the process is ineffective in this condition. Efficiency for Sb(V) removal is quiet low (less than 20% – 30%). The surface of the ferric hydroxide acquires a negative charge. Since Sb(V) is also a negative anion, there is a mutual electrostatic repulsion. The antimony remains dissolved in the water and passes through the filters.

The removal efficiency for Sb(III) decreases slightly (approx. 60% - 70%). At pH above 10.0, Sb(III) starts to change to the negative ion $[Sb(OH)_4]^-$, which also leads to repulsion and a decrease in efficiency, although the decrease is not as drastic as for Sb(V).

In addition, the presence of other salts (ions) in water has an adverse effect on the precipitation process. The disadvantages of precipitation are the addition of other chemicals to the treatment process and the

high production of sludge that should be processed and stored under specific conditions. After coagulation, flocculation and filtration (capturing flocs with bound antimony), it is necessary for hygienic and corrosive reasons to re-alkalize the water (e.g. with sodium hydroxide or milk of lime) back to neutral pH before distributing it into the network.

In comparison with the other metal removal methods the advantage of precipitation is its relatively low cost. The coagulants used in this process are easily available. Precipitation can be used for a wide range of metals, and an acceptable level of effectiveness is achieved through its proper operation.

Ion exchange is based on the mutual exchange of ions with the same charge between an ion exchanger (an exchangeable ion) and the treated water (captured ion). The ion exchanger is a material capable of the reverse stoichiometric exchange of cations or anions in a condition of electroneutrality.

The advantage of the ion exchange process is the relatively low cost compared to the other methods. The method is tried and tested, and all the components required for its operation are commercially available. It is possible to remove undesirable metals from water using the cation exchanger in a wide range up to the µg/L level.

The disadvantage of ion exchangers is that they disrupt the ion exchange due to the high competitiveness of some ions (selenium, fluorine, nitrates and sulphates) to finding a place in the ion exchanger. In addition, these ions reduce the efficiency due to suspended and organic substances, which may cause fouling of the ion exchanger filter. It is not possible to use the ion exchange method in the treatment of water with a high concentration of metals. Moreover, this method is sensitive to the pH value of the treated water and water quality (alkalinity, concentration of competing ions). The need to dispose of the regenerative agent used and the ion exchanger are also among the disadvantages of this material.

Adsorption processes are based on the adsorption of contaminants on the surface of an adsorption material. The molecules of the contaminant pass from the water environment to the solid adsorbent. It is possible to use activated alumina, activated carbon or new adsorption materials such as granular hydroxide or ferric hydroxide (GEH, CFH12, CFH18, Bayoxide E33) etc., for removing heavy metals. Both filtration sand and zeolite modified by higher manganese oxides (MnO_2), whether in a reactor with a fluidized bed or filter, have significant adsorption properties for the removal of antimony and arsenic. Efficiency of heavy metal removal by adsorption material depends on the pH of the water, oxidation-reduction potential of a given metal in the water, concentration of substances in the water that have a potential to affect (interfere with) adsorption or modify adsorbent surface loading, concentration of substances and colloid particles that can physically block the entry into the particle and the access to grains of adsorption media, respectively, specific surface area and distribution of pores of adsorption material, hydraulic properties of filtration media in treatment (filtration rate, the Empty Bed Contact Time - EBCT, the filter medium height).

Membrane methods belong to a group of diffuse processes in which the selective properties of membranes are used (thin semipermeable films, the thickness of whose walls range from 0.05 to 2.0 mm) to eliminate contaminants from water. Depending on the type of membrane (structure and driving force), it is possible to divide these processes into micro-, ultra-, nano-filtration and reverse osmosis.

Today, **electrochemical methods** are not commonly used in the treatment of water and wastewater. These methods are still in the process of development, but it is important to note that they may become very useful for the removal of metals from water in the future.

Biological methods are based on the production of a special microbial culture capable of using heavy metals dissolved in water as a substratum for further microbial growth.

The literature relating to water treatment deals more often with the arsenic removal, whose occurrence is more frequent in the water. Most water treatment processes proposed for antimony removal are still at the experimental stage, and the effectiveness of some of these technologies has not yet been

sufficiently demonstrated.

The aim of this work was to investigate the effectiveness of coagulation and ultrafiltration of antimony removal from groundwater source from Dúbrava, determine the optimum dose of coagulant and optimize all ultrafiltration process. As coagulation reagent was used ferric sulphate or ferric chloride.

1.1 Dúbrava water resource

The Dúbrava group water supply system in Slovakia was built in connection with the construction of the Liptovská Mara Water Reservoir. The group water supply system was supplied with water from the Dúbrava water resource (capacity of about 40 L/s). The water resource included three springs (Brdáre, Močidlo and Škripeň). Škripeň is currently the only spring used for a drinking water supply, since it contains no antimony. Two other springs are contaminated with antimony.

A deposit of antimony ore (a quartz vein containing Sb in ore from 1.5 to 5.0%) is considered to be the main cause of the increased antimony concentrations in the springs of Močidlo and Brdáre. Furthermore, a high concentration of antimony in water from mining activities as well as rain falling on antimony-rich waste rock piles and a sludge settling pond has led to higher concentrations of antimony in the relevant water resources.

The Dúbrava water source supplied the villages of the Lipt. Mikuláš and Ružomberok districts: Dúbrava, Vlachy, Ľubeľa, Liptovské Kľačany, Gôtovany, Bobrovník, Bešeňová, Ivachnová, Liptovský Michal and Potok. The Partizánska Ľupča water supply supplied the village of Partizánska Ľupča.

With the amendment of STN 75 7111 Drinking Water in 1998 and the introduction of the NMH for antimony (0.005 mg/L), antimony values exceeding the limit value specified for this element were found in the appliances of the Dúbrava water supply system. Therefore, the district hygienist in Liptovský Mikuláš issued a ban on the use of water from the Dúbrava water supply system and the Partizánska Ľupča water supply system for drinking purposes on 28 January 2000.

The pilot-plant tests for removing antimony were carried out at the Dúbrava chlorination plant (Figure 2). At present, only water from the Škripeň well is conveyed into the storage tank of the chlorination plant. After its disinfection, the water is gravitationally distributed to the point of consumption. For the experiments, there was a need to convey the water from the Brdáre spring to the chlorination plant through a separate pipe in order to avoid mixing it with the water from the Škripeň spring.



Figure 2. Dúbrava chlorination plant and a place for pilot experiments

According to the water quality monitoring data provided by the Water Company of the Region of Liptov, the selected water quality parameters for the Brdáre spring (average values) are shown in Table 1.

Table 1. Water quality of the springs of Brdáre according to selected parameters for the period 2000-2025

Parameter	Unit	Brdáre spring	Parameter	Unit	Brdáre spring
pH		7.8	water temperature	° C	6.2
conductivity	mS/m	22.3	NH_4^+	mg/L	0.015
colour	mg/L Pt	2	Fe total	mg/L	0.013
turbidity	FTU	0.40	Mn	mg/L	0.004
Absorbance at 254 nm		0.012	Na^+	mg/L	< 2.0
Alkalinity (ANC)	mmol/L	1.901	Ca^{2+}	mg/L	32.0
Acidity (BNC)	mmol/L	0.060	Mg^{2+}	mg/L	14.17
COD-Mn	mg/L	0.63	Ca + Mg	mmol/L	1.294
TDS	mg/L	145.5	Cl^-	mg/L	2.37
Sb	µg/L	80.2	NO_3^-	mg/L	2.72
As	µg/L	1.93	SO_4^{2-}	mg/L	30.25

Figure 3. shows the antimony concentrations from 2000 to 2025. Since these sources are not used, there is not much data.

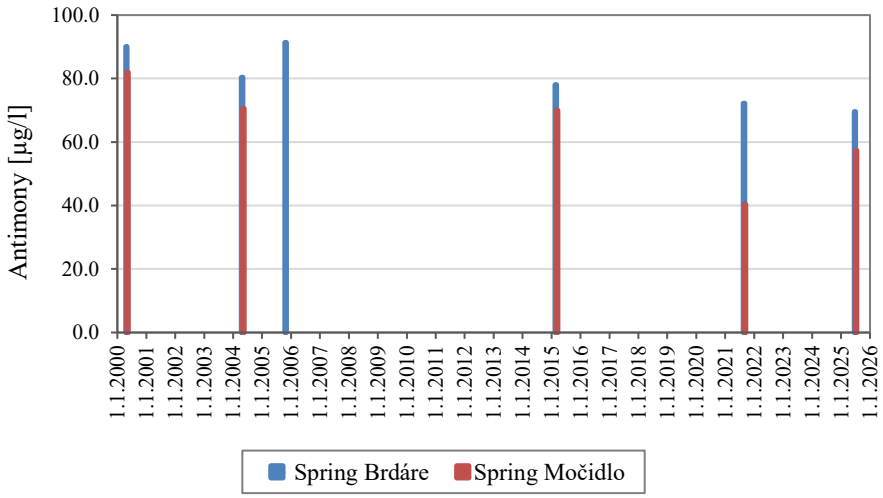


Figure 3. Concentration of antimony in springs Brdáre and Močidlo

2 Methods

The equipment used for the pilot plant experiment (Figure 4) consisted of the following devices: (1) a dosing pump to dose the coagulation agent, which was injected into the pipeline at the entry point to (2) a static mixer to homogenize the coagulant with raw water. The next step represented the (3) tubular reactor engaged to reach the retention time sufficient for antimony precipitation. (4) Before the water entered ultrafiltration, a small 50 µm mechanical filter was used to protect the UF from clogging the membrane module with small sand particles. The last water treatment step represented (5) ultrafiltration as the separation step to remove the precipitation particles with antimony. Water after treatment accumulated in the (6) tank with a pump unit for backwashing the membrane module. Backwashing was carried out using the previously mentioned pump unit. (7) Wastewater from the backwashing of the membrane accumulated in the second tank and could be treated further or discharged to the sewer.

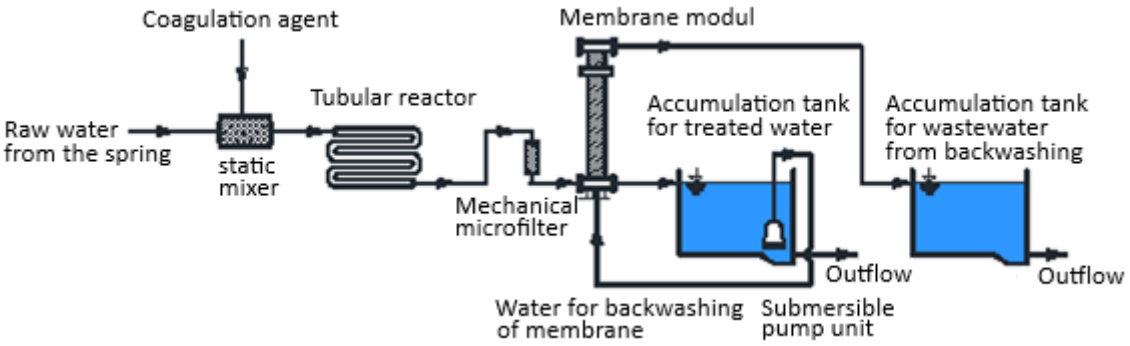


Figure 4. Technological scheme of the pilot plant experiment

Fully automated ultrafiltration equipment was applied to remove antimony from water source in Dúbrava. The equipment consisted of membrane module UA-640 (Microdyn-Nadir) with regulation system, measurement of trans-membrane pressure and backwash of the membrane by water and air with the chemical regeneration. The automat switches between filtration and backwash at regular intervals. Basic data on membrane module are listed in the Table 2.

Table 2. Basic parameters of membrane module

Membrane type	Hollow fibers module	Max flow	Up to 1.3 m^3/h
Fiber diameter	OD/ID: 2.1 mm/1.1 mm	Max trans-Membrane pressure	1 bar
Membrane material	PAN - polyakrylnitril		
Diameter of pores	0.025 µm	Max. press. of the module	2 bar
Membrane surface	16 m^2	Module diameter	168 mm
Filtration type	Direct filtration	Module length	1210 mm
Regeneration	Water and air	Max turbidity	300 NTU

Within the removal of antimony from water, it is necessary to precipitate antimony to microparticulate form. We used solution of iron sulphate and iron chloride for coagulation. To increase the removal of antimony we used the tubular reactor.

The tubular reactor was equipped with static mixer to inject the chemicals. Static mixer is designed to allow intense mixing of water with chemicals and diameter of reactor is DN25. The PVC tubes are getting wider up to DN70 and are longer more than 6.0 m. By this way the volume of tubular reactor of 30 L is reached. At the flow rate of 1.3 m^3/h the detention time above 1 minute is ensured, and slightly turbulent conditions have an impact on colloidal particles that agglomerate to adequate flocs. Tubular reactor is fixed to stainless steel construction.

A Hach DR 3900 spectrophotometer with reagents from Hach was used to analyse the monitored parameters (iron, chloride, sulphate, colour), turbidity was determined with the Hach 2100Q Portable Turbidimeter. At the same time pH and conductivity were monitored. The chemicals used were of analytical grade.

Antimony samples were collected into plastic bottles and immediately acidified with highly pure nitric acid (Merck). All bottles were submerged in 10% nitric acid solution over 3 days and triple rinsed with deionized water. Agilent 7500CE ICP-MS (ORS technology) was used to determine antimony concentration in solution. The detection limit for Sb by ICP-MS was 1 µg/L.

3 Results and Discussion

3.1 Coagulation test

Tables 3 and 4 show the results of coagulation tests with 1% solution of ferric chloride (PIX-111) or ferric sulphate (PIX-113). One litre of natural water was added into 5 beakers. After the addition of coagulation agent (1% solution of coagulant) followed 3 minutes of fast mixing (180 rpm) and 15 minutes of slow stirring (40 rpm). After sedimentation (1 hour) and filtration using filter paper, the sample was analysed. pH, conductivity, turbidity, colour, acid neutralization capacity ($ANC_{4.5}$) and the concentrations of iron, antimony, sulphate and chloride were determined.

Table 3. Result of coagulation test with ferric chloride

Dose of coagulant parameter	Unit	RW 0.00	10 ml/L 17.7 mg Fe/L	15 ml/L 26.55 mg Fe/L	20 ml/L 35.4 mg Fe/L	25 ml/L 44.25 mg Fe/L	30 ml/L 53.1 mg Fe/L
pH		7.68	6.91	6.56	6.31	5.49	4.88
conductivity	mS/m	22.9	26.1	27.0	28.1	29.5	30.5
turbidity	FNU	0.36	0.37	0.41	0.43	0.48	0.52
colour	mg/L	3	3	2	2	2	6
iron	mg/L	0.03	0.05	0.09	0.15	0.29	0.45
antimony	µg/L	87.5	45.9	30.3	15.9	2.92	1.4
$ANC_{4.5}$	mmol/L	2.814	1.843	1.206	0.737	0.201	0.067
chloride	mg/l	0.6	23.2	39.2	53.1	75.5	86.6

Table 4. Result of coagulation test with ferric sulphate

Dose of coagulant parameter	Unit	RW 0.00	10 ml/L 17.3 mg Fe/L	20 ml/L 34.6 mg Fe/L	30 ml/L 51.9 mg Fe/L	35 ml/L 60.55 mg Fe/L	40 ml/L 69.2 mg Fe/L
pH		7.68	7.21	6.84	6.40	5.93	5.15
conductivity	mS/m	22.9	24.2	25.6	27.3	27.6	28.1
turbidity	FNU	0.31	0.41	0.43	0.42	0.41	0.48
colour	mg/L	3	3	3	3	3	4
iron	mg/l	0.03	0.18	0.22	0.34	0.55	0.76
antimony	µg/L	87.5	53.8	26.1	9.87	4.98	2.61
$ANC_{4.5}$	mmol/L	2.814	1.943	1.139	0.737	0.368	0.112
sulphate	mg/l	32.0	51.2	72.8	84.8	89.2	92.1

According to the results mentioned in Table 3 it is obvious that by this coagulation test was achieved reduction of antimony to the desired value of 5 µg/L as much as about 25 ml/L of 1% $FeCl_3$, which is the equivalent around 44.25 mg/L of Fe^{3+}. Table 4 shows the results of coagulation tests with 1% solution of ferric sulphate. Antimony removal below 5 µg/l was achieved at coagulant dose 35 ml/L of 1% $Fe_2(SO_4)_3$, which is the equivalent of 60.55 mg/L of Fe^{3+}. The disadvantage of this process is the increased Fe content in the treated water and low pH, which requires additional water treatment.

The results of the coagulation test are shown in Figures 5 – 7; there is demonstrated antimony removal depending on coagulant dose, concentration of iron and pH value of water after coagulation tests.

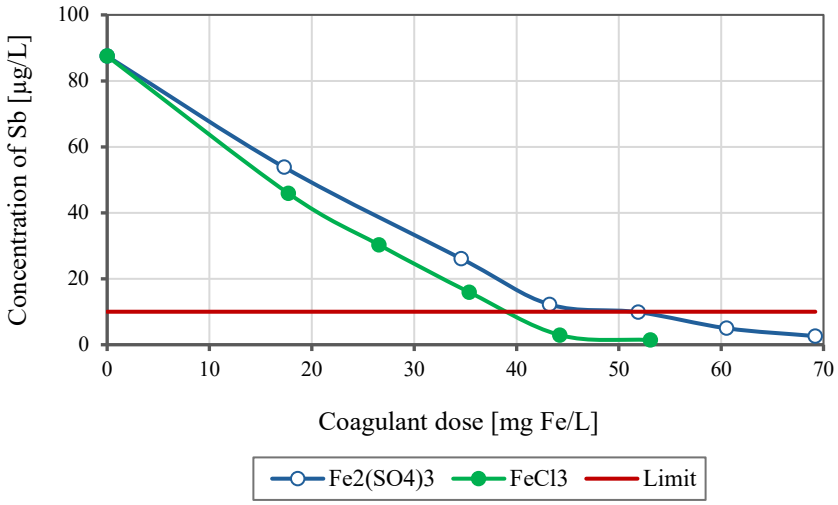


Figure 5. Comparison of the efficiency of Sb removal from water depending on the coagulant dose

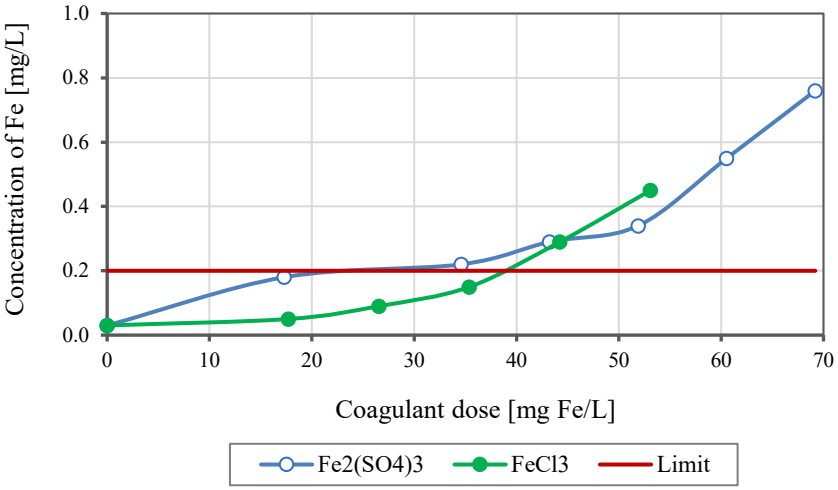


Figure 6. Iron concentration depending on coagulant dose

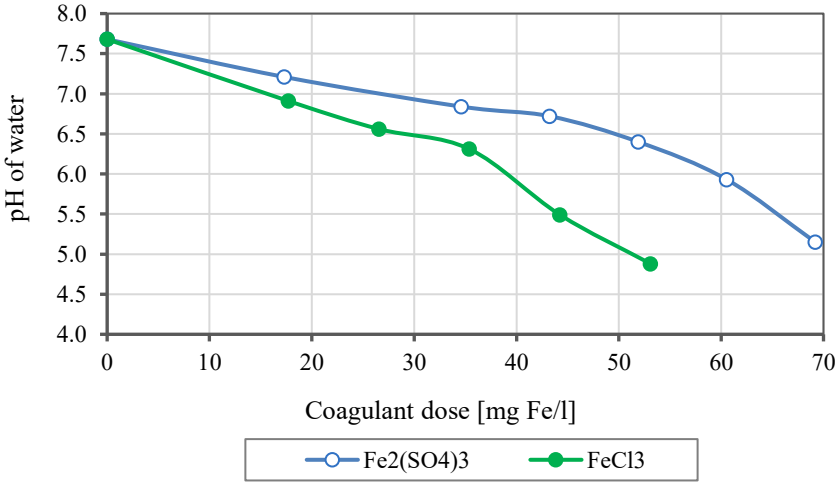


Figure 7. Effect of coagulant dosage on water pH value

3.2 Pilot plant experiment on Dúbrava water resources

Experiments were carried out directly at the Dúbrava site using coagulation with two ferric coagulants, which were dosed via a static mixer into a tubular reactor and then the water was ultrafiltered. The water retention time in the tubular reactor was 2.25 to 4.5 minutes. Water quality of raw water (RW), before (in UF) and after ultrafiltration (out UF) was monitored. The efficiency of antimony removal depends on the flow rate through UF and the coagulant dose in mg Fe per hour. Table 5 illustrates the results of experiments with the dosing of the coagulation agent $Fe_2(SO_4)_3$ and $FeCl_3$ (undiluted solution) into raw water (RW) and filtration of formed microparticles using ultrafiltration.

Table 5. Results of experiments using coagulation and ultrafiltration

Coagulant			$FeCl_3$				$Fe_2(SO_4)_3$			
Flow through UF (L/h)			400		800		400		700	
Coagulant dose (mL/h)			120		184		160		320	
parameter	unit	RW	in UF	out UF	in UF	out UF	in UF	out UF	in UF	out UF
pH		7.73	3.28	5.65	6.28	6.33	2.89	5.37	3.15	3.71
Conductivity	mS/m	17.4	36.8	31.4	33.1	33.4	65.7	44.5	42.2	29.4
$ANC_{4.5}$	mmol/L	2.68	–	0.34	–	1.58	–	0.53	–	–
Turbidity	FNU	0.36	–	0.36	–	0.38	–	1.37	8.76	1.32
Colour	mg/L Pt	0	498	0	506	1	647	107	241	64
Iron total	mg/l	0.03	10.82	0.04	6.18	0.05	9.16	4.31	6.28	1.08
Antimony	µg/l	95.3	–	4.76	–	1.73	–	< 1.0	–	< 1.0
Chlorides	mg/l	0.6	91.5	64.8	51.2	50.8	–	–	–	–
Sulphates	mg/l	19.2	–	–	–	–	5.2	24.4	101.8	94.1

The filtration cycle consisted of filtration of raw water for 1 hour and 3 minutes, followed by washing the membrane with treated water. At this mode and a flow rate of 800 L/h, the pressure conditions were stabilized. After the experiments, a 5% citric acid solution was used for CIP washing. The solution was left to act for 1 hour and was followed by another 30-minute rinsing with the solution and clean water. The efficiency of the CIP washing was also confirmed by the reduced pressure loss through the UF membrane. Before CIP washing it was transmembrane pressure (TMP) 0.72 bar and after it only 0.54 bar at a nominal flow rate of 800 L/h or a specific flow rate through the membrane of 0.05 $m^3/m^2/h$. Table 6 summarised results removal of antimony from water using coagulation and ultrafiltration, with condition of experiments.

Table 6. Removal of antimony using coagulation and ultrafiltration

Flow	Filtration Surface	Specific Flow	Retention Time	Sb Input	Sb Output	Efficiency
L/h	m^2	$L/m^2/h$	min	µg/L	µg/L	%
			Ferric chloride $FeCl_3$			
400	16	25	4.5	95.3	4.76	95.0
800	16	50	2.25	95.3	1.73	98.2
			Ferric sulphate $Fe_2(SO_4)_3$			
400	16	25	4.5	95.3	< 1.0	100
700	16	43.75	2.5	95.3	< 1.0	100

Scaling up this pilot-scale process to a full-scale drinking water treatment plant will require optimization of coagulant dosing and pH control under variable raw-water conditions, together with management of membrane fouling, backwash water and antimony-bearing sludge.

4 Conclusion

Coagulation followed by ultrafiltration for the removal of antimony from water at the Dúbrava water

source was verified. The results confirmed that the technological process used is effective in removing antimony from water. Of the coagulants used, iron sulphate was more effective, the antimony concentration at the outlet of the ultrafiltration was below the detection limit.

The results of the experiments showed that, in the case of ferric sulphate, at a flow rate of 700 L/h, a dose of 320 mL/h $Fe_2(SO_4)_3$ (41% solution of PIX-113) and a retention time of 2.5 min, the concentration of Sb in the treated water was below the detection limit (<1.0 µg/L), while in the case of $FeCl_3$, at a flow rate of 800 L/h, a dose of 184 mL/h $FeCl_3$ (38% solution of PIX-111) and a retention time of 2.25 min, the concentration was 1.73 µg/L.

Experiments will continue, their goal is to optimize the entire filtration process (filtration rate, filtration and water washing time and chemical cleaning of the membrane) and the coagulant dose (pH of water, iron content, etc.). Additionally, it will be necessary to monitor the transmembrane pressure during long-term membrane loading.

Acknowledgements

The article was prepared with the financial support of the projects VEGA 1/0666/23, VEGA 1/0615/26 and APVV-22-0610. We would also like to thank the Liptov Water Company and its employees for the opportunity to carry out these experiments at the Dubrava waterworks.

References

AWWA 1990. Water Quality and Treatment. A handbook of Community Water Suppliers.

Bratby, J. 2006. Coagulation and flocculation in water and wastewater Treatment. IWA Publishing, London, p. 407.

Driehaus, W., Jekel, M., Hildebrandt, U. 1998. Granular Ferric Hydroxide – A New Adsorbent for the Removal of Arsenic from Natural Water. *J. Water Supply: Research and Technology-Aqua* 47, 30-35.

Gannon, K., Wilson, D.J. 1986. Removal of antimony from aqueous system. Sep. Sci. Technol. 21, 475-493.

Guo, X., Wu, Z., He, M. 2009. Removal of antimony (V) and antimony (III) from drinking water by coagulation–flocculation–sedimentation (CFS). *Water Res.* 43 (17), 4327-4335. https://doi.org/10.1016/j.watres.2009.06.033.

Inam, M.A, Khan, R., Akram, M., Khan, S., Yeom, I.T. 2019. Effect of Water Chemistry on Antimony Removal by Chemical Coagulation: Implications of ζ-Potential and Size of Precipitates. *Int J Mol Sci.* Jun 17;20(12):2945. doi: 10.3390/ijms20122945.

Inam, M.A., Khan, R., Yeom, I.T., Buller, A.S., Akram, M., Inam, M.W. 2021. Optimization of Antimony Removal by Coagulation-Flocculation-Sedimentation Process Using Response Surface Methodology. *Processes* 2021, 9, 117. https://doi.org/10.3390/pr9010117

Kang, M., Kawasaki, M., Tamada, S., Kamei, T., Magara, Y. 2000. Effect of pH on the removal of arsenic and antimony using reverse osmosis membranes. *Desalination* 131 (1-3), 293-298.

Kang, M., Kamei, T., Magara, Y. 2003. Comparing polyaluminum chloride and ferric chloride for antimony removal. *Water Res*. 37, 4171-4179.

Klimko, T., Heviánková, S., Šottník, P., Jurkovič, Ľ., Lacková, E., Vozár, J. 2014. Experimentálne odstraňovanie antimónu z banských vôd (Experimental removal of antimony from mining waters.) *Acta Geologica Slovaca,* 6(2), 203–213.

MacPhee, M.J., Charles, G.E., Cornwell, D.A. 2001. *Treatment of Arsenic Residuals from Drinking Water Removal Processes*. (EPA/600/R-01/033).

Mohan, D., Pittman, Ch. U. Jr. 2007. Arsenic removal from water-wastewater using adsorbents - A critical review. *J. of Hazard. Mater*. 142 (1-2), 1-53.

Munka, K., Gajdoš, L., Karácsonyová, M. 2008. *Odstraňovanie antimónu v procese čírenia pri úprave vody (Antimony removal in the clarification process in water treatment).* In: Proceeding of conference Pitná voda 2008, s. 201-206. W&ET Team, Č. Budějovice, ISBN 978-80-254-2034-8 In Slovak).

Nguyen, V.L., Chen, W.H., Young, T., Darby J. 2011. Effect of interferences on the breakthrough of arsenic: Rapid small scale column tests. *Water Res.* 45 (14), 4069-4080.
Pitter, P. 2009. *Hydrochemie*, fourth ed., Institute of Chemical Technology Press, Praha. (in Czech).
The Decree of the Ministry of Health of the Slovak Republic No. 91/2023 Coll., which establishes indicators and limit values for drinking water quality and hot water quality, the procedure for monitoring drinking water, risk management of the drinking water supply system and risk management of house distribution systems.
Directive (EU) 2020/2184. *Quality of water intended for human consumption*.
USEPA, 2013. United States Environmental Protection Agency. *Secondary Drinking Water Regulations: Guidance for Nuisance Chemicals*; Washington, DC, USA.
USEPA 1984. *Antimony: an environmental and health effects assessment*. Washington, DC, US Environmental Protection Agency, Drinking Water Office, 1984.
WHO 2003. *Antimony in drinking-water. Background document for preparation of WHO Guidelines for drinking-water quality*.
WHO 2011. *Guidelines for Drinking-Water Quality*. 4th edition. WHO, Geneva.
Zeng, H., Arashiro, M., Giammar, D. 2008. Effects of water chemistry and flow rate on arsenate removal by adsorption to an iron oxide-based sorbent. *Water Res.* 42 (18), 4629-4636.

WASTEWATER TREATMENT IN SMALL SETTLEMENTS USING THE TEHNIX BIOROTOR SYSTEM

Mura HORVAT[1]*, Nikola GOLUB[1], Željko HORVAT[1], Dubravko HORVAT[1], Bruno ZELIĆ[2]

[1] *TEHNIX ECO INDUSTRY, Croatia*

E-mail: mura.horvat@tehnix.com

E-mail: nikola.golub@tehnix.com

E-mail: zeljko.horvat@tehnix.com

E-mail: dubravko.horvat@tehnix.com

[5] *University of Zagreb, Faculty of Chemical Engineering and TechnologyCroatia*

E-mail: bzelic@fkit.unizg.hr

[*] *Corresponding author*

Abstract

Conventional centralized wastewater treatment systems are often economically and technically unsuitable for small and sparsely populated settlements, highlighting the need for decentralized solutions. This paper presents the (TEHNIX Biorotor) as an efficient on-site wastewater treatment technology designed for small communities. The system operates on the principle of a rotating biological contactor (RBC), where a partially submerged rotating drum provides a large surface area for biofilm growth. Microorganisms attached to the rotor surface degrade organic pollutants through aerobic biological processes. The methodology includes analysis of long-term operational experience, performance data from installed systems, and evaluation of treatment efficiency based on key output parameters such as biochemical oxygen demand (BOD_5), chemical oxygen demand (COD), and suspended solids. The system demonstrates stable performance under varying hydraulic and biological loads, with removal efficiencies up to 90% for BOD_5 and COD. Results show that the TEHNIX Biorotor achieves high efficiency in secondary wastewater treatment, consistently meeting regulatory discharge standards. Additionally, the system offers potential for upgrading to tertiary treatment. Key advantages include low investment and operational costs, low energy consumption, minimal maintenance requirements, and no need for continuous supervision.

Key words

wastewater treatment, rotating biological contactor, decentralized purification systems, small settlements, biorotor.

1 Introduction

Municipal wastewater treatment is essential to prevent water pollution, eutrophication, habitat degradation, toxicity, and health risks. Untreated or inadequately treated wastewater can harm aquatic life, reduce biodiversity, and introduce toxic chemicals and heavy metals into the environment. Excess nutrients such as nitrogen and phosphorus can cause algal blooms and oxygen depletion, which damage aquatic ecosystems and disrupt food chains. Effective wastewater treatment removes or reduces pollutants before wastewater is discharged, helping protect public health and support sustainable water management. Treatment systems may be centralized, typically used in large urban areas, or decentralized, such as biorotors used in smaller communities (Nazaroff and Alvarez-Cohen, 2001; Valsaraj, 2000; Tomašić and Zelić, 2018).

A biorotor is commonly used in municipal wastewater treatment as part of a rotating biological contactor system. It consists of a large rotating drum or disc, partially submerged in wastewater and coated with microorganisms forming a biological layer. As it rotates, microorganisms contact the wastewater and decompose organic pollutants. This method efficiently removes organic matter, suspended solids, and nutrients from the water. Rotating biological contactor systems are considered economical and reliable solutions for small and medium-sized wastewater treatment plants, while reducing environmental impact (Ning et al., 2019; Suzuki and Yamaya, 2005).

The wastewater treatment process consists of three main phases: mechanical-physical treatment, biological treatment, and sludge treatment. In the first phase, wastewater passes through coarse and fine sieves with mesh sizes of 10–25 mm, where large suspended particles are removed. An automatic screw conveyor may be used for solid waste removal, while a bypass system allows wastewater to skip treatment stages during heavy rainfall or maintenance. The wastewater then enters a sedimentation chamber, where pumps break down organic matter and the inflow is equalized. At the same time, grease and sand are separated and removed by sludge pumps for temporary storage. Before biological treatment, the wastewater may also be aerated to improve treatment efficiency for heavily polluted inflows (Meena et al., 2022).

Biological treatment is carried out in a biorotor system, which uses ribbed polypropylene surfaces to support the growth of microorganisms that decompose organic pollutants (Meena et al., 2022). The slowly rotating biorotor improves aeration, mixing, and aerobic microbial activity, enabling efficient treatment under a wide range of environmental conditions. After passing through the biorotor and an aeration chamber for nitrification and denitrification, the wastewater enters a secondary clarifier. There, purified water is separated from activated sludge and discharged into the receiving environment. Part of the settled sludge is recirculated to the biological treatment stage to maintain stable treatment conditions, while excess sludge is stored and can later be used in the production of class III compost, supporting sustainable waste management and circular resource use.

2 Methods

The technological process of the Tehnix Biorotor includes the following sections: 1. collecting chamber for solid materials, rags, wood, oil and other large materials; 2. sand pit - chambers for receiving sand, gravel, ash and other fine-grained material; 3. aeration chamber; 4. pre-pumping station with built-in double sludge pumps; 5. primary sedimentation basin – biomass dispenser of the rotating polypropylene rotor; 6. rotor filled with polypropylene honeycomb blocks to maintain the biomass; 7. secondary sedimentation basin for aerobically-biologically purified water; 8. channel for removing the accumulated sludge in the secondary clarifier; 9. pre-pump system for the periodic recovery of activated sludge; 10. recirculation of activated sludge; 11. separate grid in front of the water outlet from the biorotor and a sampling point; and 12. connection for the removal of accumulated sludge from the primary basin and the secondary sedimentation basin. The process can be simplified and represented schematically as shown in Figure 1.

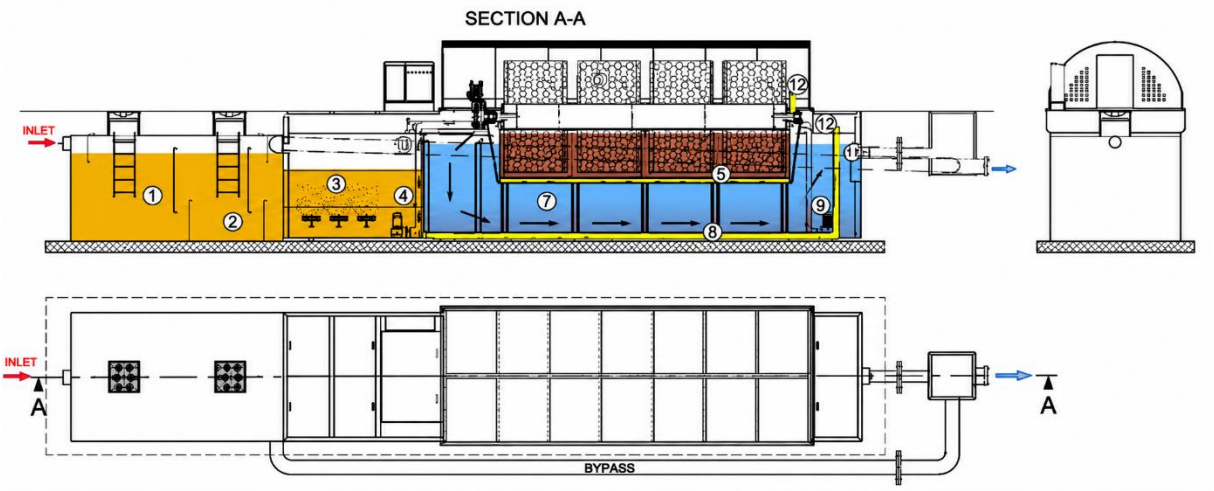


Figure 1. Scheme of the Tehnix Biorotor

3 Results and Discussion

3.1 Main characteristics of Tehnix Biorotor

Tehnix develops and manufactures biorotor- and bioreactor-based systems for the biological treatment of municipal wastewater, optimized for high-efficiency secondary treatment in compliance with applicable environmental and regulatory standards. The systems are designed with modular flexibility, enabling integration of tertiary treatment processes and adaptation through various configurable treatment solutions according to specific operational and treatment requirements (Figure 2).

Accordingly, the secondary treatment stage complies with the regulatory requirements prescribed by the Regulation on Limit Values for Wastewater Emissions (Official Gazette of the Republic of Croatia 26/20), particularly regarding key indicators such as total suspended solids, biochemical oxygen demand (BOD_5), and chemical oxygen demand (COD). The Tehnix Biorotor is designed to achieve effluent concentrations below the prescribed threshold values, namely total suspended solids < 35 mg/L, BOD_5 (20 °C) < 25 mg O_2/L, and COD < 125 mg O_2/L, in accordance with the Decision on the Determination of Sensitive Areas (Official Gazette of the Republic of Croatia 81/10, 141/15).

Compared with other decentralized municipal wastewater treatment technologies, particularly conventional activated sludge (CAS) systems and rotating biological contactors (RBCs), the Tehnix Biorotor offers several advantages for small settlements. Unlike conventional activated sludge systems, it provides effective biological treatment with lower energy consumption, simpler operation, reduced maintenance requirements, and a more compact footprint. Compared with conventional RBCs, the system incorporates an optimized process design, modern construction materials, and advanced monitoring, resulting in improved operational reliability and treatment stability while complying with European design and performance standards (EN 12255, EN 12255-1, EN 12255-7, EN 12255-10, and EN 12255-11).

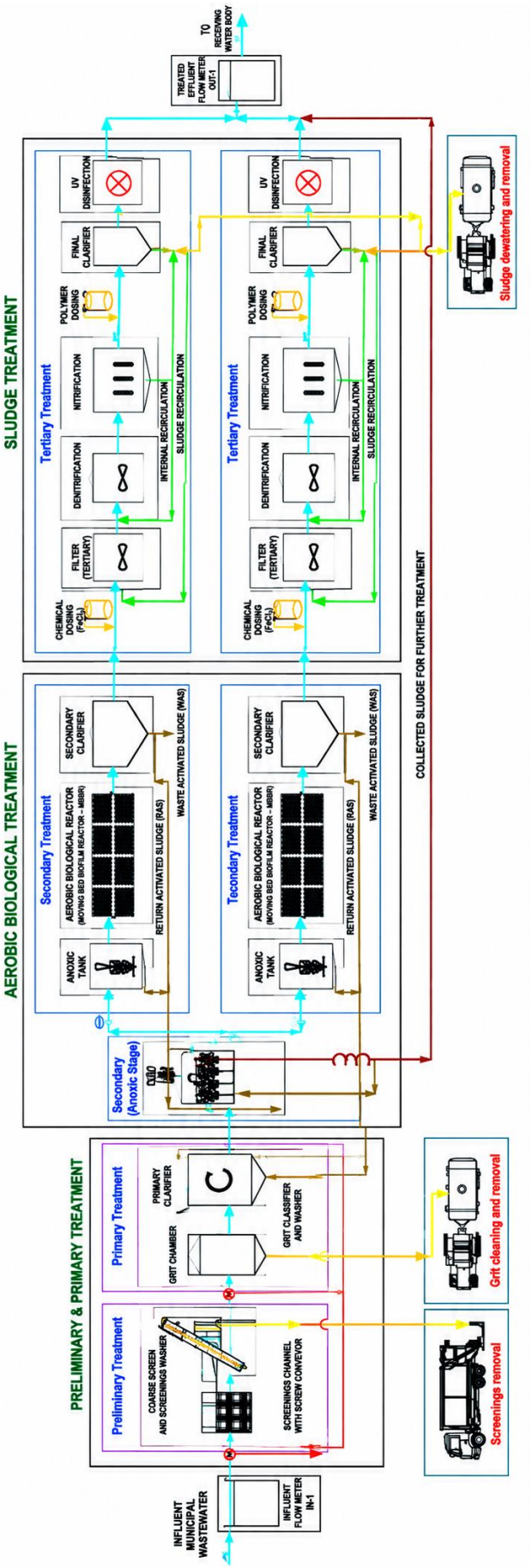


Figure 2. Scheme of the Tehnix Biorotor for the biological treatment of municipal wastewaters

The principal design and operational parameters facilitate comparison with other RBC systems. The reactor has a working volume of 12.8 m^3, is designed for a hydraulic loading of approximately 150 L PE^{-1} day^{-1}, and provides a hydraulic retention time (HRT) of 114 min (1.90 h). The rotor operates at 1 rpm, while the specific biofilm surface area of 165 m^2 m^{-3} ensures efficient microbial attachment and degradation of organic matter.

The principal advantages of the Tehnix Biorotor include:

- Designed and constructed in accordance with standardized European norms EN 12255, EN 12255-1, EN 12255-7, EN 12255-10, and EN 12255-11,
- Sustainable and integrated wastewater treatment solution based on the biological degradation of organic matter by microorganisms,
- Engineered to ensure high operational reliability, functionality, and flexibility under variable hydraulic and biological loading conditions,
- Achieves treatment efficiency in compliance with applicable legal requirements for secondary wastewater treatment, including prescribed maximum allowable concentrations (MAC) at the discharge outlet,
- Optimized technological design utilizing modern materials and equipment, enabling simple operation, process control, and maintenance without the need for continuous monitoring,
- Advanced management and monitoring systems ensure low specific energy consumption per population equivalent (PE), contributing to high economic and operational efficiency,
- Characterized by low investment, operational, and maintenance costs, combined with minimal spatial requirements due to the compact system configuration,
- Modular and adaptable design enables efficient installation and operation in decentralized systems, including inaccessible and hilly terrain,
- Supports sustainable sludge management through sludge stabilization and valorization processes, including the potential application of bioreactor composting technologies.

As with other biofilm-based technologies, the system may be affected by extreme hydraulic shock loads, prolonged low-temperature conditions, or atypical wastewater characteristics. In addition, applications requiring advanced nutrient removal or water reuse may require tertiary treatment. Nevertheless, its low energy demand, compact and modular design, operational simplicity, and reliable performance make the Tehnix Biorotor a suitable solution for decentralized municipal wastewater treatment, particularly in small communities where centralized treatment systems are economically or technically impractical.

3.2 Efficiency of Tehnix Biorotor

The efficiency of the Tehnix Biorotor is best demonstrated by the results of monitoring total suspended solids, BOD_5 and COD in a real municipal wastewater treatment plant (Table 1).

The results presented are based on monitoring conducted at the Sveti Križ Začretje and Hotiza wastewater treatment facilities, which use TEHNIX Biorotor system. The study included the evaluation of two biorotors with different treatment capacities: a BRT-400 unit designed for 400 population equivalents (PE) and a BRT-950 unit designed for 950 PE. These units were selected because they represent the lower and upper capacity limits of the medium-capacity TEHNIX Biorotor product range, allowing the assessment of treatment performance across a representative range of typical municipal applications. Monitoring was performed during both winter and summer periods to assess the influence of varying environmental conditions, particularly ambient air temperature, on TEHNIX Biorotor performance and process stability. Each seasonal monitoring campaign covered a three-month period, with treated wastewater sampled once, during the middle of the monitoring period.

Physicochemical analysis of treated wastewater was carried out by EC Inspekt, Zagreb and Bioinstitut, Čakovec using standardized analytical methods. Total suspended solids (TSS) were determined

according to HRN EN 872:2008, chemical oxygen demand (COD) according to HRN ISO 15705:2003, and biochemical oxygen demand over five days (BOD_5) according to HRN EN 1899-2:2004.

Table 1. Treatment efficiency of the Tehnix Eco Industry Biorotor expressed through removal of suspended solids, BOD_5 and COD in winter and summer seasons

Parameter	Wastewater inlet	Treated wastewater	MAC	Efficiency, %
Winter season				
		BRT-400		
Total suspended solids, mg/L	84.2	14.9	35	82.3
BOD_5, mg O_2/L	77	16	25	79.2
COD, mg O_2/L	191	51	125	73.3
		BRT-950		
Total suspended solids, mg/L	36.6	10.2	35	72.1
BOD_5, mg O_2/L	91	18	25	80.2
COD, mg O_2/L	223.7	73.4	125	67.2
Summer season				
		BRT-400		
Total suspended solids, mg/L	54.6	18.8	35	65.6
BOD_5, mg O_2/L	119	18	25	84.9
COD, mg O_2/L	296	62	125	79.1
		BRT-950		
Total suspended solids, mg/L	252.8	23.8	35	90.59
BOD_5, mg O_2/L	236	28	25	88.14
COD, mg O_2/L	593.6	105.4	125	82.24

**Applicable discharge limits differ between the Croatian and Slovenian facilities; see discussion in Section 3.2.*

The analytical results of treated wastewater indicate that the monitored effluent parameters were generally below the prescribed maximum allowable concentrations (MAC values) during both winter and summer operating conditions. Comparative evaluation of the two investigated biorotor systems demonstrated no significant variation in treatment efficiency with respect to plant capacity, expressed in PE. A slightly higher removal efficiency of TSS was observed during the winter period, whereas improved BOD_5 and COD removal efficiencies were recorded during the summer months. This trend is consistent with the enhanced metabolic and microbiological activity of aerobic microorganisms at elevated ambient temperatures.

The results presented in Table 1 are based on two representative measurements for each device (one winter and one summer samples) obtained during routine operational monitoring. Owing to the limited number of observations, statistical evaluation of the measured parameters was not performed. Therefore, the observed seasonal differences should be interpreted as indicative operational trends rather than statistically significant differences.

The results presented were obtained from two wastewater treatment facilities located at separate sites in Croatia and Slovenia, respectively, and should therefore be interpreted within the context of the applicable national regulatory frameworks. The Croatian facility was evaluated according to Croatian wastewater discharge regulations, while the Slovenian facility operates under different legal requirements, under which a BOD_5 concentration of 28 mg O_2/L is considered compliant and acceptable. In addition to the key monitored parameters, all other operational and discharge indicators remained within the limits prescribed by the respective water permits for the investigated plants.

3.3 Modularity

The modular concept of the TEHNIX Biorotor system is one of its key developmental features, enabling the system to adapt to changing user requirements and environmental protection standards. The modularity of the system is primarily demonstrated by the following possibilities:

1. Capacity expansion through standardized technological modules, allowing an increase in the hydraulic and biological treatment capacity of the plant without replacing the existing core system. This approach enables the gradual expansion of treatment capacity in line with population growth, seasonal load variations, or changes in wastewater generation patterns. Capacity enhancement is achieved by increasing the volume of technological chambers, expanding aeration tank capacities, and enlarging the biologically active rotor surface area, thereby maintaining a high level of treatment efficiency.

2. Qualitative upgrading of the treatment process. The basic TEHNIX Biorotor configuration is designed for efficient secondary treatment of municipal wastewater, while its structural and technological design allows straightforward integration of additional processes required to achieve tertiary treatment standards. Depending on site-specific requirements and receiving water body conditions, the system can be upgraded with nitrification, denitrification, and phosphorus removal processes, as well as UV disinfection units for treated effluent. This approach enables compliance with more stringent discharge limits for nitrogen, phosphorus, and microbiological parameters without significant modifications to the existing plant infrastructure.

3. Digitalization and automation of plant operation. The system allows the gradual integration of analytical sensors for continuous monitoring of key process parameters, including dissolved oxygen concentration, flow rate, nitrates, nitrites, ammonium nitrogen, phosphates, and indicators of organic loading. The collected data are used for automatic control of blowers, sludge recirculation pumps, and dosing systems, resulting in more stable operation and reduced risk of human error. Furthermore, the implementation of a SCADA system enables centralized monitoring, remote control, and real-time analysis of plant performance.

This approach increases energy efficiency, reduces operation and maintenance costs, and ensures greater reliability in decentralized wastewater treatment applications. The integration of capacity, quality, and digital modularity makes the TEHNIX Biorotor a flexible platform capable of adapting to future regulatory requirements and user needs with minimal investment.

4 Conclusion

The TEHNIX Biorotor provides a reliable, cost-effective, and environmentally sustainable solution for wastewater treatment in small settlements. Its adaptability, simplicity, and proven performance make it particularly suitable for decentralized applications where conventional systems are not viable.

References

Decision on the determination of sensitive areas, Republic of Croatia Official Gazette 81/10, 141/15
Meena, M., Yadav, G., Sonigra, P. and Shah, M.P. 2022. A comprehensive review on application of bioreactor for industrial wastewater treatment. *Letters in Applied Microbiology*, 74, pp. 131-158.
Nazaroff, W. W. and Alvarez-Cohen, L. 2001. *Environmental Engineering Science*, J. Wiley, New York
Ning, L.,Wei, Z., Yanan, Y., Baogui, W., Zaixing, L. and Yongzhen, P. 2019. Oxygen mass transfer and post-denitrification in a modified rotating drum biological contactor. *Biochemical Engineering Journal*, 144, pp. 48-56.
Regulation on Limit Values for Wastewater Emissions, Republic of Croatia Official Gazette 26/20
Tehnix: Technical solutions for biological water protection / Wastewater treatment and purification plants / Bioreactor plants. https://tehnix.hr/en/product/bioreaktorska-postrojenja/ (accessed October 23,

2023)
Tomašić, V and B. Zelić, 2018. *Environmental Engineering, Basic Principles*, De Gruyter, Berlin
Suzuki, T. and Yamaya, S. 2005. Removal of hydrocarbons in a rotating biological contactor with biodrum. *Process Biochemistry*, 40, pp. 3429-3433.
Valsaraj, K. T. 2000. *Elements of Environmental Engineering*, CRC Press LLC, Boca Raton

HYBRID ELECTROCOAGULATION–ADSORPTION TREATMENT OF AMMUNITION MANUFACTURING WASTEWATER: INFLUENCE OF PROCESS PARAMETERS ON COD, HEAVY METALS AND SULFATE REMOVAL

Dražen VOUK[1*], Katarina FANJEK[1], Katarina LICHT[1], Domagoj NAKIĆ[1]

[1] *University of Zagreb, Faculty of Civil Engineering, Fra Andrije Kačića-Miošića 26, 10 000 Zagreb, Croatia*

E-mail: drazen.vouk@grad.unizg.hr

E-mail: katarina.fanjek@student.grad.hr

E-mail: katarina.licht@grad.unizg.hr

E-mail: domagoj.nakic@grad.unizg.hr

** Corresponding author*

Abstract

Wastewater generated during ammunition manufacturing has a complex pollutant composition, making its treatment a significant technological challenge. This study investigates a hybrid process combining electrocoagulation and adsorption, with emphasis on the removal of sulfates, heavy metals, and organic load expressed as chemical oxygen demand (COD). The experimental investigation included adsorbent selection, selection of electrode configuration, and evaluation of current intensity and process sequence. Adsorption experiments were conducted using granular activated carbon and two biochar materials, while different combinations of iron and aluminum electrodes were tested during electrocoagulation. Process performance was assessed through physicochemical parameters, heavy metal concentrations, COD, and sulfate concentrations. The combined electrocoagulation–adsorption process achieved heavy metal removal efficiencies exceeding 90%. The highest COD reduction, 42.86%, was obtained in the simultaneous process using granular activated carbon and aluminum–graphite electrodes. The highest sulfate removal, 46.31%, was achieved when electrocoagulation was applied before adsorption. An additional sequential experiment using a lead electrode further improved treatment performance, achieving approximately 60% reduction of both sulfate concentration and COD value. Overall, the results confirm that the hybrid electrocoagulation–adsorption process is a promising approach for treating ammunition manufacturing wastewater and provides a basis for further selection of integrated treatment systems.

Key words

wastewater, treatment, ammunition manufacturing, electrocoagulation, adsorption

1 Introduction

Industrial activities associated with ammunition manufacturing generate complex wastewaters containing a broad spectrum of inorganic and organic contaminants, including dissolved heavy metals, sulfates, suspended solids, lubricants, oils and various organic compounds originating from machining, surface treatment and cleaning operations. Owing to their highly variable composition and elevated pollutant concentrations, these wastewaters represent a considerable environmental challenge and generally require advanced treatment technologies capable of simultaneously removing multiple contaminant groups. Conventional physicochemical treatment processes frequently exhibit limited efficiency when several pollutant classes must be removed within a single treatment train (Chen, 2004; Holt et al., 2005).

Among the contaminants commonly detected in ammunition manufacturing wastewater, dissolved heavy metals represent one of the greatest environmental concerns because of their toxicity, persistence and tendency to bioaccumulate. Metals such as lead, copper, zinc, iron and manganese may adversely affect aquatic ecosystems even at relatively low concentrations, while increasingly stringent discharge regulations require their efficient removal before wastewater discharge or reuse. In parallel, elevated sulfate concentrations may contribute to increased salinity and, under anaerobic conditions, stimulate sulfate-reducing bacteria, resulting in hydrogen sulfide formation, odour generation and accelerated corrosion of sewer infrastructure. Organic contaminants, commonly expressed as chemical oxygen demand (COD), originate primarily from lubricants, degreasing agents and production additives, and therefore constitute another important treatment objective (Chen, 2004).

Electrocoagulation (EC) has attracted considerable scientific and engineering interest over the past two decades as an effective alternative to conventional chemical coagulation. During the process, sacrificial metal electrodes generate coagulant species directly within the wastewater, promoting destabilization of colloidal particles, adsorption of dissolved contaminants, coprecipitation of heavy metals and partial oxidation or removal of organic compounds. Compared with conventional coagulation, electrocoagulation generally requires lower chemical consumption, produces less sludge and enables simultaneous removal of several pollutant groups, making it particularly attractive for complex industrial wastewaters (Mollah et al., 2001; Mollah et al., 2004; Holt et al., 2005).

Adsorption is widely recognised as one of the most effective polishing technologies for removing dissolved contaminants that remain after primary physicochemical treatment. Granular activated carbon (GAC) is considered the benchmark adsorbent owing to its exceptionally high specific surface area and adsorption capacity, while biochar has recently attracted increasing attention as a sustainable and economically attractive alternative because of its favourable surface chemistry, porous structure and low production costs. Consequently, combining electrocoagulation with adsorption offers the possibility of integrating complementary removal mechanisms, thereby improving the simultaneous removal of heavy metals, sulfate and dissolved organic matter while potentially reducing overall treatment costs (Vepsäläinen, 2012; Inyang and Dickenson, 2015).

Although electrocoagulation has been extensively investigated for the treatment of numerous industrial wastewaters, most published studies have focused primarily on evaluating the influence of electrode materials, current intensity and operating conditions on the removal of individual contaminant groups. Considerably less attention has been devoted to integrated treatment systems in which electrocoagulation is combined with adsorption as a subsequent polishing step, particularly for complex industrial wastewaters containing simultaneously elevated concentrations of heavy metals, sulfate and organic matter. Furthermore, most published investigations have evaluated only a single adsorbent material, most commonly granular activated carbon, whereas comparative assessments involving different biochar materials under identical experimental conditions remain limited.

Ammunition manufacturing wastewater represents a particularly demanding wastewater matrix because its composition varies considerably depending on production processes and typically contains a combination of dissolved heavy metals, sulfate and refractory organic compounds. Consequently, optimization of individual treatment processes alone may not provide the treatment efficiency required for increasingly stringent environmental requirements. Instead, greater attention should be directed towards integrated treatment concepts capable of exploiting complementary removal mechanisms. Despite the recognised advantages of electrocoagulation and adsorption as individual treatment technologies, only a limited number of studies have reported integrated comparisons of different adsorbent materials combined with electrocoagulation for the treatment of ammunition manufacturing wastewater under identical experimental conditions.

Building upon our previous investigation, which demonstrated the technical feasibility of electrocoagulation for the treatment of ammunition manufacturing wastewater and confirmed the significant influence of electrode materials on pollutant removal efficiency (Drušković et al., 2022), the present study extends that research by introducing adsorption as an additional treatment stage. Unlike

previous investigations (Drušković et al., 2021; Licht et al., 2024) that primarily focused on electrocoagulation alone, this work systematically compares conventional granular activated carbon with two different biochar materials under identical operating conditions while simultaneously evaluating the influence of electrode configuration and process sequence on the removal of heavy metals, sulfate and chemical oxygen demand (COD). This integrated experimental approach provides additional knowledge regarding the interaction between electrocoagulation and adsorption processes and contributes to the development of efficient and sustainable treatment strategies for complex industrial wastewaters. Therefore, the objective of the present study was to evaluate the performance of a hybrid electrocoagulation–adsorption process for the treatment of ammunition manufacturing wastewater. Particular emphasis was placed on identifying the most effective combination of electrode material and adsorbent with respect to the simultaneous removal of heavy metals, sulfate and chemical oxygen demand (COD). The findings contribute to a better understanding of hybrid electrochemical treatment systems and provide a scientific basis for further optimisation and future scale-up of integrated treatment technologies.

2 Materials and Methods

2.1 Wastewater characteristics

The experimental investigation was conducted using industrial wastewater collected from an ammunition manufacturing facility. The wastewater originated from several production processes involving metal processing, surface treatment and cleaning operations, resulting in a complex wastewater matrix containing dissolved heavy metals, sulfate ions and organic contaminants expressed as chemical oxygen demand (COD). Prior to each experimental series, the wastewater was thoroughly homogenized to ensure representative sampling and identical initial conditions for all laboratory experiments. Initial physicochemical characterization included determination of pH, electrical conductivity, total dissolved solids (TDS), temperature, turbidity, COD, sulfate concentration and dissolved heavy metals. These parameters were measured before treatment and after each experimental phase to evaluate treatment efficiency.

2.2 Experimental setup

The laboratory-scale hybrid treatment system consisted of an electrocoagulation reactor combined with an adsorption unit. Electrocoagulation experiments were performed in a transparent acrylic reactor placed on a magnetic stirrer providing continuous mixing throughout the treatment process. The electrocoagulation cell accommodated interchangeable plate electrodes positioned vertically and connected to the external DC power supply that enabled precise adjustment of the applied voltage and current during electrocoagulation. A schematic diagram of the experimental setup is presented in Fig. 1, including a cooling element immersed in the reactor, which consisted of an insulated heat-pipe, aluminium heat sink and a fan and was used to minimize water heating during electrocoagulation.

Different electrode configurations were investigated, including iron–iron (Fe/Fe), iron–graphite (Fe/C), aluminium–aluminium (Al/Al) and aluminium–graphite (Al/C), while an additional verification experiment was performed using a lead–graphite (Pb/C) electrode combination. The distance between adjacent electrodes was maintained at 1 cm throughout all electrocoagulation experiments to ensure comparable hydrodynamic and electrochemical conditions.

The adsorption stage was investigated both as an independent treatment process and as an integrated component of the hybrid electrocoagulation–adsorption system. Adsorption experiments were performed using three adsorbent materials: granular activated carbon (GAC), Biochar 1 (BC1) and Biochar 2 (BC2). Both biochars were produced by gasification of sewage sludge obtained from different municipal wastewater treatment plants and therefore differed in their composition.

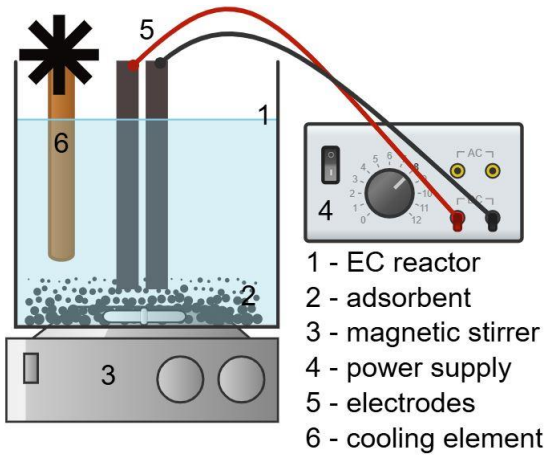


Figure 1. Experimental set-up

2.3 Experimental procedure

The experimental investigation was organised into five consecutive phases to enable systematic selection of suitable operating conditions for the hybrid treatment process.

2.3.1 Adsorbent screening

The first phase evaluated the adsorption performance of GAC, Biochar 1 and Biochar 2 using identical operating conditions. Adsorption experiments were performed using 200 mL of wastewater with an adsorbent dose of 10 g/L (2 g per experiment), a contact time of 120 min, continuous mixing at 200 rpm, and the natural pH of the wastewater. Samples were collected every 30 min to evaluate pollutant removal during adsorption.

2.3.2 Electrode configuration selection

Following selection of the most suitable adsorbent, electrocoagulation experiments were carried out to determine the most efficient electrode configuration. The efficiency of four anode/cathode combinations (Fe/Fe, Fe/C, Al/Al and Al/C) was investigated using 2.5 L of wastewater, a treatment time of 30 min, continuous mixing at 200 rpm, natural pH and a fixed electrode spacing of 1 cm, as shown in Table 1. After electrocoagulation, treated wastewater was allowed to settle for 15 min, after which the supernatant was analysed. Samples were collected at 10 min intervals during treatment.

Table 1. Electrode configurations investigated during electrocoagulation configuration set

Configuration	Anode	Cathode	Experimental purpose
Fe/Fe	Fe	Fe	Conventional iron-based electrocoagulation using iron electrodes as both the sacrificial anode and cathode
Fe/C	Fe	C	Electrocoagulation with an iron sacrificial anode and an inert carbon cathode
Al/Al	Al	Al	Conventional aluminium-based electrocoagulation using aluminium electrodes as both the sacrificial anode and cathode
Al/C	Al	C	Electrocoagulation with an aluminium sacrificial anode and an inert carbon cathode

2.3.3 Effect of current intensity

After identifying the most suitable electrode configuration, the effect of current intensity was evaluated using three applied current levels: 3, 6, and 9 A, corresponding to the minimum, medium, and maximum

operating conditions, respectively. Besides pollutant removal efficiency, the optimisation considered energy consumption, sludge production, pH variation, and electrode dissolution to identify the most appropriate operating conditions for subsequent hybrid experiments.

2.3.4 Hybrid process configuration

The fourth phase investigated three different configurations of the hybrid treatment process:

1. Electrocoagulation followed by adsorption (EC → ADS),
2. Adsorption followed by electrocoagulation (ADS → EC),
3. Simultaneous electrocoagulation and adsorption (EC + ADS).

The sequential configurations enabled evaluation of the influence of treatment order, whereas the simultaneous configuration investigated possible synergistic interactions between electrocoagulation and adsorption occurring within the same reactor.

2.3.5 Verification experiment

An additional verification experiment was performed using a Pb/C electrode configuration under the selection of most efficient hybrid operating conditions established during the previous experimental phases. This experiment was designed to further evaluate the influence of lead electrodes on sulfate removal and overall treatment efficiency.

2.4 Analytical methods

Physicochemical parameters, including pH, electrical conductivity, TDS, turbidity and temperature, were determined using a HI 9829 multimeter (Hanna Instruments) equipped with integrated sensors. COD was determined photometrically using a NANOCOLOR 500D photometer (Macherey-Nagel) in combination with NANOCOLOR CSB 60 test kits following thermal digestion in a NANOCOLOR VARIO compact thermoreactor. Heavy metal concentrations were determined by Inductively Coupled Plasma – Optical Emission Spectrometry (ICP-OES) using an Agilent 5900 SVDV ICP-OES instrument equipped with a SeaSpray concentric glass nebulizer and a double-pass glass spray chamber. Measurements were performed in triplicate using simultaneous axial and radial plasma observation, while quantification was based on weighted linear regression of calibration curves using ICP Expert software. Sulfate concentrations were determined using a Cary 60 UV–Vis spectrophotometer by the barium chloride turbidimetric method employing commercially prepared reagent packets.

3 Results and Discussion

3.1 Initial wastewater characterization

The investigation of ammunition manufacturing wastewater exhibited a complex composition, containing organic matter, sulfate ions and dissolved heavy metals. These characteristics justified the application of a hybrid electrocoagulation–adsorption process capable of simultaneously removing different pollutant groups. The initial physicochemical characteristics of the wastewater are presented in Table 2.

The relatively high electrical conductivity favoured electrocoagulation by reducing electrical resistance, while the simultaneous presence of heavy metals, sulfates and organic matter confirmed that no single treatment mechanism would be sufficient for efficient treatment. Consequently, selection of the hybrid process focused on the selection of the adsorbent, electrode configuration, current intensity and process arrangement. These initial characteristics served as the reference for evaluating the treatment efficiency presented in the following sections.

Table 2. Initial physicochemical characteristics of the investigated ammunition manufacturing wastewater

Parameter	Measurement unit	Value
pH	–	7.03
Electrical conductivity	μS/cm	1478
TDS	ppm	795
Turbidity	FNU	46
COD	mg O_2/L	38
Sulfates	mg/L	575
Al	mg/L	0.38
Cu	mg/L	0.16
Fe	mg/L	0.01
Mg	mg/L	22.75
Mn	mg/L	0.11
Pb	mg/L	0.97
Si	mg/L	6.82
Zn	mg/L	0.67

3.2 Selection of the adsorbent

Adsorption experiments were performed to identify the most suitable adsorbent for the subsequent hybrid electrocoagulation–adsorption process. In this screening phase, adsorbent selection was based exclusively on pollutant removal efficiency under identical experimental conditions; economic criteria and adsorbent capacity were outside the scope of the present study. GAC and two biochar materials designated BC1 and BC2, were evaluated under identical experimental conditions. The selection was based on the simultaneous removal of COD, sulfates and dissolved heavy metals.

Fig. 2, Fig. 3 and Table 3 summarize the treatment performance obtained after 120 min of adsorption. GAC achieved the highest COD removal of 58% (Fig. 2), while also providing the greatest sulfate removal (8,2 %) among the investigated adsorbents (Fig. 3). Both biochar materials exhibited lower overall treatment efficiencies, particularly regarding heavy metal removal.

The results demonstrated clear differences between the adsorbents investigated. GAC consistently exhibited the highest overall treatment efficiency, particularly regarding COD removal, while maintaining satisfactory removal of dissolved heavy metals. Under the investigated batch conditions and fixed contact time, GAC exhibited higher pollutant removal than both biochars. Since equilibrium adsorption capacity and adsorbent surface characteristics were not determined in the present study, the observed differences should be interpreted as comparative treatment performance under the applied experimental conditions rather than differences in maximum adsorption capacity. The superior performance of GAC can be attributed to its well-developed porous structure, high specific surface area and abundance of active adsorption sites, enabling efficient adsorption of dissolved organic compounds. Similar observations have been reported in previous studies investigating hybrid adsorption processes for industrial wastewater treatment, where activated carbon generally outperformed biochar materials for the removal of dissolved organic contaminants. Based on the obtained results, GAC was selected as the adsorbent for all subsequent hybrid electrocoagulation–adsorption experiments.

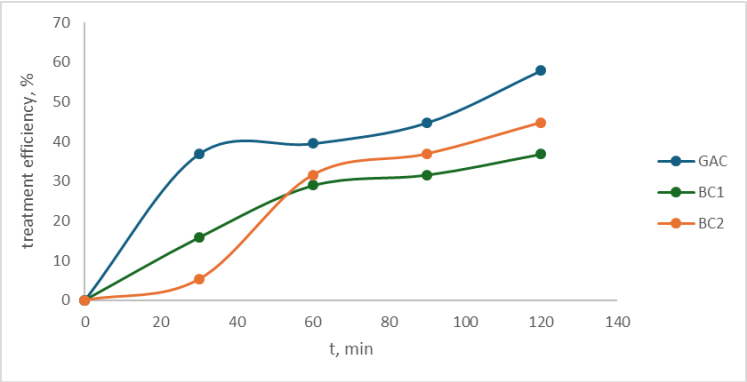


Figure 2. Efficiency of COD removal by adsorption with different adsorbents

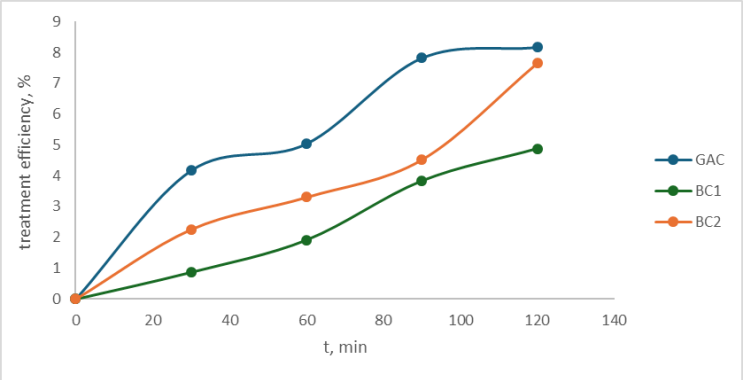


Figure 3. Efficiency of sulfates removal by adsorption with different adsorbents

Table 3. Comparison of heavy metals removal efficiencies achieved with different adsorbents

Electrode configuration	Reaction time	Treatment efficiency							
	t	Al	Cu	Fe	Mn	Pb	Zn	Si	Mg
	(min)	(%)	(%)	(%)	(%)	(%)	(%)	(%)	(%)
GAC	30	42	75	100	18	49	94	7	51
	60	63	88	100	27	63	97	12	52
	90	82	94	100	36	72	97	16	52
	120	89	100	100	45	76	99	17	53
BC1	30	5	69	0	27	37	99	12	14
	60	24	81	100	64	57	99	27	21
	90	50	88	100	82	62	99	33	27
	120	66	94	100	91	70	99	39	37
BC2	30	3	88	100	9	7	81	5	21
	60	32	88	100	18	36	94	8	45
	90	47	88	100	36	51	97	9	46
	120	61	88	100	45	70	99	12	48

3.3 Selection of the electrocoagulation configuration

Following the selection of GAC as the most suitable adsorbent, electrocoagulation experiments were performed to determine the most efficient operating conditions for the hybrid treatment process. Four electrode configurations (Fe/Fe, Fe/C, Al/Al and Al/C) were investigated under identical experimental conditions. In addition, the influence of reaction time and current intensity was evaluated to identify the operating conditions providing the highest overall removal efficiency while maintaining stable process performance. The comparison of COD removal efficiencies obtained with different electrode configurations is presented in Fig. 4, while the corresponding sulfate removal efficiencies are shown in

Fig. 5. Both parameters exhibited a gradual improvement with increasing reaction time; however, the treatment efficiency depended on the electrode material.

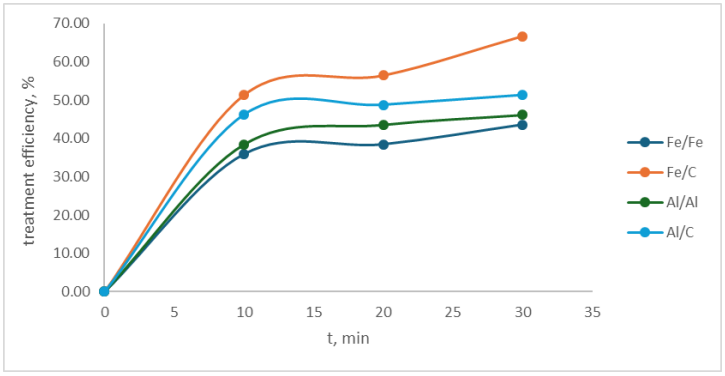


Figure 4. COD removal efficiency using different electrode configurations, with current intensity of 3A

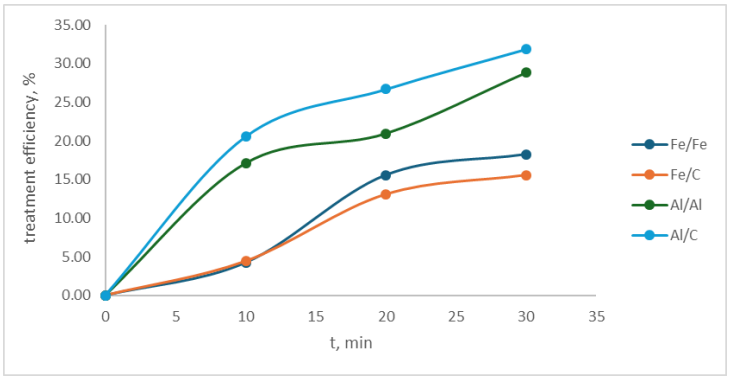


Figure 5. Sulfate removal efficiency using different electrode configurations, with current intensity of 3A

The experimental results demonstrated that the Al/C electrode configuration consistently achieved the highest overall treatment performance. After 30 min of electrocoagulation, COD removal reached approximately 51%, while sulfate removal exceeded 30%, outperforming the remaining electrode combinations. The aluminium sacrificial anode generated a high quantity of amorphous aluminium hydroxide flocs, promoting efficient sweep coagulation and adsorption of dissolved contaminants, whereas the graphite cathode ensured stable electrochemical conditions without additional metal dissolution.

The removal efficiencies achieved for the investigated heavy metals after electrocoagulation are summarised in Table 4. The obtained results confirmed that electrocoagulation was highly effective for the removal of dissolved heavy metals, with removal efficiencies exceeding 90% for most investigated elements. These findings agree well with previous studies reporting the high affinity of freshly generated aluminium hydroxide flocs towards dissolved metal ions and further support the suitability of aluminium-based electrodes for the treatment of complex industrial wastewaters. The negative removal efficiencies observed for aluminium and iron should not be interpreted as a deterioration of the treatment performance. Instead, they reflect the electrochemical dissolution of the sacrificial electrodes, which is the fundamental mechanism of the electrocoagulation process. When aluminium electrodes were used as sacrificial anodes (Al/Al and Al/C), the concentration of dissolved aluminium temporarily increased because anodic oxidation released Al^{3+} ions into the wastewater. Similarly, the Fe/Fe and Fe/C configurations produced elevated dissolved iron concentrations owing to the oxidation of the iron anode and the subsequent release of Fe^{2+}/Fe^{3+} species. These dissolved metal ions subsequently undergo hydrolysis, forming amorphous aluminium and iron hydroxides that act as highly efficient coagulants. The freshly generated hydroxide flocs destabilise suspended and colloidal particles, adsorb dissolved organic matter and heavy metals, and promote their removal by sweep coagulation and sedimentation. Consequently, the negative removal efficiencies reported for aluminium and iron represent an expected intermediate stage of the electrocoagulation mechanism rather than a reduction in treatment efficiency.

Because aluminium and iron are intentionally introduced into the wastewater during electrocoagulation, their concentrations should therefore not be interpreted in the same manner as those of the remaining heavy metals. For evaluating the effectiveness of the electrocoagulation process, considerably greater importance should be attributed to the removal of target pollutants such as lead, copper, zinc, manganese, COD and sulfates, together with the overall treatment performance.

Table 4. Comparison of heavy metals removal efficiencies achieved with different EC configuration with current intensity of 3A

Electrode configuration	Reaction time	Treatment efficiency							
	t (min)	Al (%)	Cu (%)	Fe (%)	Mn (%)	Pb (%)	Zn (%)	Si (%)	Mg (%)
Fe/Fe	10	100	78	n/a *	8	28	94	60	49
	20	100	100	n/a *	75	52	98	86	61
	30	100	100	n/a *	92	65	100	89	83
Fe/C	10	100	100	n/a *	17	25	52	33	51
	20	100	100	n/a *	75	63	98	71	55
	30	100	100	n/a *	92	71	100	91	82
Al/Al	10	64	100	50	100	13	96	89	23
	20	n/a *	100	50	100	35	96	96	62
	30	n/a *	100	100	100	45	98	99	88
Al/C	10	n/a *	100	50	100	21	83	98	65
	20	n/a *	100	100	100	48	85	99	82
	30	n/a *	100	100	100	63	88	99	86

* ..... Removal efficiency was not calculated because its very low initial concentration results in physically misleading percentage values following Fe and Al release from the sacrificial electrode.

The influence of current intensity was evaluated at three operating levels: 3, 6, and 9 A. As shown in Fig. 6, the highest COD removal efficiency was achieved at 3 A, whereas the highest sulfate removal efficiency was obtained at 9 A (Fig. 7). The better COD removal observed at the lower current intensity may be associated with the formation of larger and more stable flocs, together with lower gas evolution and reduced hydrodynamic disturbance. At higher current intensities, intensive hydrogen generation and rapid coagulant production may promote floc fragmentation or flotation, thereby reducing the effective contact between organic matter and the generated aluminum hydroxide flocs. In contrast, sulfate removal benefited from the higher current intensity because increased electrode dissolution generated a greater quantity of aluminum-based coagulant species and hydroxide precipitates. These species provide additional active sites for sulfate adsorption, incorporation into precipitates, and co-precipitation. Since sulfates were considerably more difficult to remove than the organic load, the improvement in sulfate removal at 9 A was considered more important than the higher COD removal achieved at 3 A. Accordingly, 9 A was selected for the subsequent experiments because sulfate removal was considered the primary selection criterion, while acknowledging the higher COD removal obtained at 3 A. Therefore, based on the overall treatment objectives, the Al/C electrode configuration, a current intensity of 9 A, and a reaction time of 30 min were selected as the most efficient electrocoagulation conditions and subsequently applied in the hybrid electrocoagulation–adsorption experiments described in the following sections.

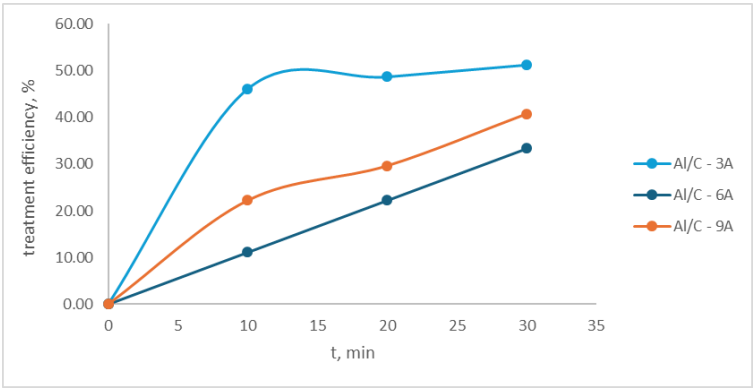


Figure 6. COD removal efficiency using Al/C electrode configurations, with different current intensities

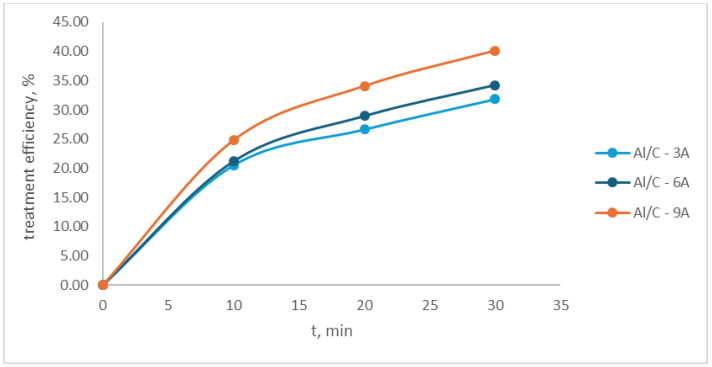


Figure 7. Sulfates removal efficiency using Al/C electrode configurations, with different current intensities

3.4 Performance of the hybrid electrocoagulation–adsorption process

Following the selection of both the adsorption and electrocoagulation stages, the hybrid treatment process was evaluated using the selected operating conditions, namely GAC as the adsorbent with 120 min of reaction time, the Al/C electrode configuration, a current of 9 A and an electrocoagulation reaction time of 30 min. Three different process arrangements were investigated: electrocoagulation followed by adsorption (EC → ADS), adsorption followed by electrocoagulation (ADS → EC) and simultaneous electrocoagulation and adsorption (EC + ADS). The comparison focused on the removal of COD and sulfates, since the previous experimental phases had already demonstrated excellent heavy metal removal efficiencies for both individual treatment processes. The COD removal efficiencies obtained for the investigated hybrid process configurations are presented in Fig. 8, while the corresponding sulfate removal efficiencies are shown in Fig. 9.

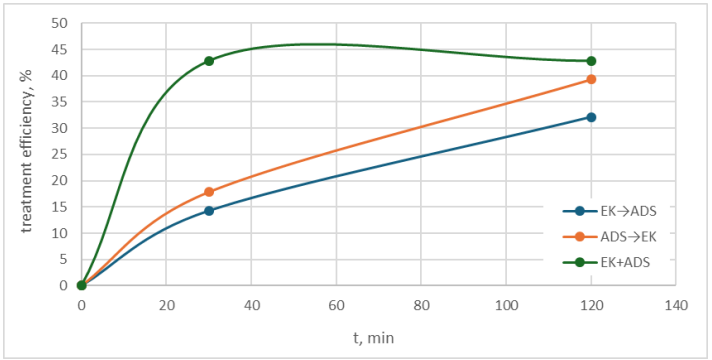


Figure 8. COD removal efficiency using different hybrid electrocoagulation–adsorption process configurations.

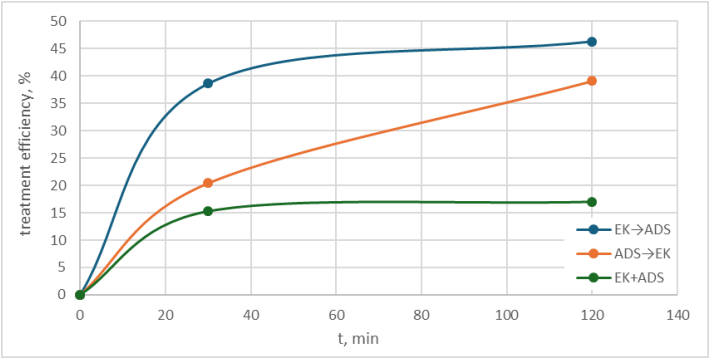


Figure 9. Sulfate removal efficiency using different hybrid electrocoagulation–adsorption process configurations.

The results demonstrate that the performance of the hybrid process depended strongly on the target pollutant and process sequence. The hybrid configurations improved sulfate removal compared with the individual processes, whereas for COD the highest removal achieved by the hybrid process remained lower than that obtained by GAC adsorption alone. However, the treatment efficiency depended strongly on the sequence in which the two processes were applied. The simultaneous electrocoagulation–adsorption configuration (EC + ADS) achieved the highest COD removal efficiency among the investigated hybrid configurations. The concurrent occurrence of electrocoagulation and adsorption enabled freshly formed aluminium hydroxide flocs and the highly porous activated carbon to act simultaneously, promoting the removal of dissolved organic compounds through complementary mechanisms of coagulation, adsorption and coprecipitation. The intimate interaction between both processes most likely reduced mass transfer limitations and enhanced the overall removal of organic matter. In contrast, the EC → ADS configuration provided the highest sulfate removal efficiency. During electrocoagulation, sulfate ions were partially removed through adsorption onto freshly precipitated aluminium hydroxides and by coprecipitation within the generated flocs. The subsequent adsorption stage further polished the treated wastewater, resulting in the highest overall sulfate removal among the investigated hybrid configurations. The ADS → EC configuration also improved wastewater quality compared with the individual treatment processes but generally exhibited lower removal efficiencies than the other two hybrid arrangements. Adsorption removed part of the dissolved organic matter before electrocoagulation; however, this sequence appeared to reduce the beneficial interaction between adsorption and the continuously generated coagulant species during electrocoagulation.

These findings indicate that the sequence of individual treatment processes plays an important role in determining the overall treatment efficiency. While simultaneous electrocoagulation and adsorption are particularly advantageous for the removal of organic contaminants, the sequential application of electrocoagulation followed by adsorption is more effective for sulfate removal. Consequently, the hybrid configuration should be selected according to the primary treatment objective.

A verification experiment was conducted using a lead anode and a graphite cathode at an applied current of 9 A for 30 min, followed by 120 min of adsorption with GAC. This treatment achieved approximately 60% removal of both sulfates and COD, together with complete or nearly complete removal of all investigated metals except Pb. Owing to the use of a Pb anode, the Pb concentration remaining in the solution after the electrocoagulation step was 348 mg/L. The subsequent adsorption stage reduced this concentration to 139 mg/L, although this value remained unacceptably high. The relatively high sulfate removal can be attributed to the precipitation of sulfate ions as poorly soluble and chemically stable $PbSO_4$, while the observed COD reduction may have resulted from a combination of electrocoagulation, precipitation, flotation, and subsequent adsorption onto GAC. Despite the favourable removal of sulfates and COD, the release of Pb from the sacrificial anode represents a major limitation because residual dissolved Pb poses a significant environmental and toxicological risk. Therefore, this electrode configuration could only be considered after further process optimisation. Possible improvements include extending the adsorption time, increasing the adsorbent dosage, introducing an additional polishing step, or applying a lower current intensity to reduce excessive Pb dissolution while maintaining sufficient sulfate removal. Further optimisation would be necessary to ensure complete

removal of residual Pb before any practical application of this treatment option.

Overall, the results confirm that integrating electrocoagulation with adsorption provides a clear performance advantage over the individual treatment processes and represents a promising treatment strategy for complex ammunition manufacturing wastewater. Considering that both adsorption and electrocoagulation individually achieved very high heavy metal removal efficiencies, while the hybrid process substantially improved COD and sulfate removal, the proposed integrated treatment system can be regarded as an efficient multi-barrier treatment approach for complex industrial wastewater.

4 Conclusion

This study demonstrated that the hybrid electrocoagulation–adsorption process represents an effective treatment approach for complex wastewater generated during ammunition manufacturing. A systematic selection of the most effective set was carried out, including the selection of the most suitable adsorbent, electrode configuration and electrocoagulation operating conditions, followed by the evaluation of different hybrid process arrangements. Among the investigated adsorbents, GAC exhibited the highest overall treatment performance and was therefore selected for subsequent experiments. The selection of the most efficient electrocoagulation set showed that the Al/C electrode configuration operated at a current intensity of 9 A and a reaction time of 30 min provided the most favourable balance between pollutant removal and process stability. Both adsorption and electrocoagulation individually achieved very high removal efficiencies for dissolved heavy metals, confirming their suitability for the treatment of industrial wastewater containing metallic contaminants. The hybrid process further enhanced the treatment performance, particularly regarding the removal of COD and sulfates. The simultaneous electrocoagulation–adsorption configuration proved to be the most effective for COD removal, whereas the sequential application of electrocoagulation followed by adsorption achieved the highest sulfate removal efficiency. These results demonstrate that the treatment sequence significantly influences process performance and should be selected according to the target pollutants. Overall, the proposed hybrid treatment system successfully combines the advantages of electrocoagulation and adsorption, providing an efficient multi-barrier approach for the simultaneous removal of organic matter, sulfates and heavy metals from ammunition manufacturing wastewater. The findings provide a basis for further laboratory-scale optimisation of the integrated treatment process. Future studies should address adsorbent capacity and breakthrough under continuous-flow conditions, as well as energy and electrode consumption, before considering pilot-scale application.

Acknowledgements

This study was conducted within the framework of the institutional project of the University of Zagreb Faculty of Civil Engineering – [ARMOR – Advanced Treatment of Ammunition Production Wastewater Using Integrated Electrochemical and Adsorptive Technologies], under the programme line for enhancing scientific excellence, financed through the National Recovery and Resilience Plan 2021–2026. The project is funded by the European Union – NextGenerationEU.
The views and opinions expressed are solely those of the author(s) and do not necessarily reflect those of the European Union or the European Commission. Neither the European Union nor the European Commission can be held responsible for them.

References

Chen, G. 2004 Electrochemical technologies in wastewater treatment. *Separation and Purification Technology*, 38(1), 11–41. DOI: 10.1016/j.seppur.2003.10.006.
Drušković, M., Vouk, D., Šiljeg, M. and Maldini, K. 2021 Treatment of Wastewater from Separators for Rainfall Runoff Using Electrochemical Oxidation Processes. *Environmental Engineering*, 8(1–2). DOI: 10.37023/ee.8.1-2.5

Druškovic, M., Vouk, D., Bolanča, T. and Posavčić, H. 2022 The Influence of Pretreatment on the Efficiency of Electrochemical Processes in Oily Wastewater Treatment. *Water*, 14(19), 2976. DOI: 10.3390/w14192976

Holt, P.K., Barton, G.W. and Mitchell, C.A. 2005 The future for electrocoagulation as a localised water treatment technology. *Chemosphere*, 59(3), 355–367. DOI: 10.1016/j.chemosphere.2004.10.023.

Inyang, M. and Dickenson, E. 2015 The potential role of biochar in the removal of organic and microbial contaminants from potable and reuse water: A review. *Chemosphere*, 134, 232–240.

Licht, K., Glavaš, M., Halkijević, I., Vouk, D., Bolanča, T. and Crnogaj, A. 2024 *Ammunition factory wastewater treatment by electrocoagulation*. In: Proc. 18th International Symposium on Water Management and Hydraulic Engineering (WMHE 2024), Štrbské Pleso, Slovakia, M. Červeňanská, A. Šoltész, D. Baroková and L. Čubanová (eds), Spektrum STU, Bratislava, Slovakia, pp. 335–342.

Mollah, M.Y.A., Schennach, R., Parga, J.R. and Cocke, D.L. 2001 Electrocoagulation (EC)-Science and applications. *Journal of Hazardous Materials*, 84(1), 29–41. DOI: 10.1016/S0304-3894(01)00176.

Mollah, M.Y.A., Morkovsky, P., Gomes, J.A.G., Kesmez, M., Parga, J.R. and Cocke, D.L. 2004 Fundamentals, present and future perspectives of electrocoagulation. *Journal of Hazardous Materials*, 114(1–3), 199–210. DOI: 10.1016/j.jhazmat.2004.08.009.

Vepsäläinen, M. 2012 *Electrocoagulation in the Treatment of Industrial Waters and Wastewaters*. VTT Science 19.

COMPARISON OF UNIVARIATE AND BIVARIATE APPROACHES TO DESIGN HYDROGRAPH DERIVATION IN CROATIAN AND SLOVENIAN CATCHMENTS

Fran VUIĆ [1*], Damir BEKIĆ [1], Nejc BEZAK [2], Kristina POTOČKI [1]

[1] *University of Zagreb Faculty of Civil Engineering, Croatia*

E-mail: fran.vuic@grad.unizg.hr,

E-mail: damir.bekic@grad.unizg.hr,

E-mail: kristina.potocki@grad.unizg.hr

[2]*University of Ljubljana, Faculty of Civil and Geodetic Engineering*

E-mail: nejc.bezak@fgg.uni-lj.si

[*] *Corresponding author*

Abstract

The design hydrograph is a key input for designing water management and hydraulic structures, defining the design peak discharge, flood volume and flood wave duration. This study compares two approaches for defining design hydrographs in gauged catchments: a simpler univariate approach based on the Typical Flood Hydrograph (TFH) method, and a more complex bivariate approach based on joint analysis of peak discharge and volume. In the TFH approach, flood frequency analysis is performed on Annual Maximum (AM) series, with distribution parameters estimated by L-Moments and goodness of fit evaluated against empirical frequencies. A representative observed hydrograph is then scaled to the design peak discharge and volume using an amplification factor. In the bivariate approach, the dependence between peak discharge and volume is modeled using copulas, and the derived bivariate return periods and design discharge–volume combinations are used to construct a synthetic design hydrograph (SDH). The analysis covers gauging stations Kupljenovo (Krapina), Farkašić (Kupa) and Zagreb (Sava) in Croatia, and Litija (Sava) and Dravograd (Drava) in Slovenia. The results highlight the advantages and limitations of both approaches, contribute to a methodological framework for design hydrograph determination and provide a basis for future classification and machine learning–based categorization of hydrograph shapes.

Key words

design hydrograph; Typical Flood Hydrograph (TFH); bivariate analysis; copulas; flood frequency analysis

1 Introduction

Floods are among the most damaging natural hazards, causing loss of life, damage to infrastructure and long-term economic costs. According to the Organisation for Economic Co-operation and Development (OECD, 2016), floods cause more than 40 billion dollars in damage each year worldwide, while the number of people living in flood-prone areas increased by 24% from 2000 to 2015 (Jongman 2021). Their impact is expected to further increase under the effects of climate change, as changes in extreme precipitation and hydrological regimes alters flood frequency and intensity.

In Europe, climate-related extremes have already caused substantial damage. At the local scale, extreme rainfall events have also been recorded in Croatia, such as the July 2020 event in Zagreb, which exceeded the 100-year return period and caused significant urban flooding (Nimac et al. 2022). At the regional

scale, for example, the August 2023 floods in Slovenia resulted in three fatalities and several billion in damages (Bezak et al. 2023). In order to mitigate these damages, more accurate flood derivations are needed when designing hydraulic structures.

The design hydrograph is one of the fundamental inputs in the design of water management and hydraulic structures. It is used to define peak discharge, flood volume, and duration of the flood wave. Traditionally the construction of the design hydrograph has been done using the univariate approach, which takes one variable, either peak flow or flood volume and uses either one of them to scale a chosen flood event to the dimension of a flood event of a desired return period. In such approaches flood frequency analysis (FFA) is done using the annual maximum method (one maximum discharge/volume per year) or the peaks over threshold method (all discharges/volumes above a chosen threshold). The return period is then obtained by choosing a best fitting probability distribution (e.g. Generalized Extreme Value (GEV), Gumbel, Pearson Type III (PE3), Log-Pearson Type III (LP3)) and using it to calculate the return period for any given discharge or flood volume (Yue et. al 2002).

-While such methods are widely applied, they do not explicitly account for the dependence between different flood characteristics, as the design flood hydrograph for the peak discharge may not provide the hydrograph for the largest volume. Several studies (Brunner et al. 2019, Rahimi et al., 2021) indicated that flood characteristics such as peak discharge (Q) and flood volume (V) are interconnected to each other. To address this dependency, multivariate approaches to design flood hydrograph construction have been developed. Multivariate approaches are based on joint modelling of key flood characteristics (Q-V). Firstly, suitable marginal distributions are fitted to each variable. Then a copula function is used to describe their dependence structure, allowing the construction of a joint distribution. This defines joint return periods for the selected design conditions (AND/OR probabilities). The corresponding values Q-V are then combined to construct a consistent design hydrograph ensuring compatibility between peak discharge and volume. Such methods provide a more realistic flood hydrographs compared to traditional univariate methods (Šraj et al., 2014; Brunner et al., 2017; Lacko et al., 2022).

Regional flood frequency studies have also been conducted for the broader Pannonian Basin, which encompasses the Sava and Drava river systems analyzed in this study, demonstrating the applicability of L-moments and Annual maximum series (AMS) methods (Leščešen and Dolinaj 2019). Also in Slovenia, there has been development of proposed methodologies for gauged basins: the univariate approach is recommended for less important applications such as roads and river cross sections, while the multivariate approach is proposed for the design of hydro power plants and larger flood protection structures (Bezak et. al. 2022). Earlier work by Šraj et al. (2014) compared classical univariate frequency analysis with bivariate copula-based methods on the Litija station in Slovenia, showing that the univariate return periods always fall between the bivariate AND OR return periods. In Croatia, Lacko et al (2022) constructed a multivariate analysis of flood hydrograph characteristics for selected stations on Sava and Drava rivers with a particular focus on selection of baseflow separation methods.

This study aims to compare the univariate TFH and bivariate copula-based approaches for design hydrograph derivation at five gauging stations in the Sava and Drava River basins in Croatia and Slovenia. The specific contributions of this paper are: (1) comparative application and methodological evaluation of TFH and copula-based SDH across selected Croatian and Slovenian gauged catchments; (2) evaluation of differences in design Q–V combinations obtained from univariate and bivariate approaches across a range of return periods; and (3) contribution to the definition of design hydrographs as input data for bridge scour assessment, which has recently been emphasized as an important application of synthetic design hydrographs under current and future climate conditions (Potočki et al., 2025). The objective is to evaluate the differences between the two approaches and to assess how the explicit consideration of dependence between flood peak and volume influences the resulting design hydrograph.

2 Data and Methods

2.1 Data

This analysis is conducted at five gauging stations: Kupljenovo (Krapina River), Farkašić (Kupa River), and Zagreb (Sava River) in Croatia, along with Litija (Sava River) and Dravograd (Drava River) in Slovenia. Figure 1 shows the locations of studied gauging stations and their corresponding basin areas, as can be seen from the pictures the basin areas of Litija and Kupljenovo are contained within the Zagreb station basin area.



Figure 1. Locations of the analysed catchments and corresponding gauging stations in Croatia and Slovenia.

Daily discharge data was obtained from the national hydrological services of Croatia and Slovenia (DHMZ - Croatian Meteorological and Hydrological Service, ARSO - National Meteorological Service of Slovenia). For each station, time series of mean daily discharge were used as the primary input dataset. Additionally, available yearly extreme data provided by DHMZ and ARSO was used to refine the annual maximum series. Yearly extreme values typically represent the actual recorded peak discharge for a given flood event, which can exceed the corresponding mean daily discharge computed by 24-hour averaging, particularly for short-duration, fast-rising flood waves. To correct for this potential underestimation, the date of each yearly extreme value was matched to the corresponding date in the daily discharge series, and the daily value was substituted with the yearly extreme value at that date.

Table 1. Characteristics of the study catchments and extracted flood event datasets

Station	Country	River	Basin area (km^2)	Period	Gap	Q_{max} (m^3/s)	Q_{mean} (m^3/s)	V_{max} ($\times 10^6$ m^3)	V_{mean} ($\times 10^6$ m^3)
Dravograd	Slovenia	Drava	12060	1965–2024	N/A	2570	311	983	42
Kupljenovo	Croatia	Krapina	1150	1964–2024	N/A	268	24	112	7
Farkašić	Croatia	Kupa	8902	2000-2024	N/A	1339	649	1598	283
Litija	Slovenia	Sava	4281	1953–2024	N/A	2580	234	1196	56
Zagreb	Croatia	Sava	12450	1951–2024	N/A	3126	548	1859.6	154.5

2.2 Methodology

Prior to the analysis, for each daily discharge value a corresponding baseflow was calculated using the base flow index (BFI) method through the R package lfstat (Koffler and Laaha, 2012), applying the package's default smoothed-minima settings. Flood volume (V) in this study is defined as the direct-

runoff volume, i.e. the volume of discharge above the estimated baseflow, integrated over the duration of the flood event. After the preprocessing we took our data and use it to construct an AM series for each station, the annual maximum method was chosen because this method ensures the chosen events are independent of each other (Leščešen and Dolinaj 2019). In accordance with Hrelja (2007) the homogeneity tests and trend analyses are done on the AM time series. Homogeneity and trend analyses tests were performed using the Mann-Kendall test for monotonic trends and the Pettitt test for change point detection. These steps ensure that the input data are suitable for frequency analysis and that any potential non-homogeneities are identified.

Flood event extraction is done in accordance with Lacko et. al. (2022) where flood events are extracted from the daily discharge time series using an event-based approach. Flood events were extracted around selected peaks using an automated event extraction procedure. Starting from the identified flood peak, the algorithm searches backwards and forwards through the daily discharge series until the total discharge equals the calculated baseflow, which are then identified as beginning and ending of the flood event. Each flood event is characterized by its peak discharge (Q), flood volume (V), and duration (D) (Lacko et. al. 2022).

To ensure that the selected peak discharge values are independent events, an independence criterion was introduced. For the purposes of this analysis, the criterion recommended by the United States Water Resources Council (USWRC 1982) and used in other studies was adopted (Bezak et al. 2014, Lacko et al. 2022). The criterion defines the minimum number of days between two peak exceedances to ensure they do not belong to the same flood event:

$$\theta < 5 + log(A) \quad (1)$$

Where **θ** is the maximum separation of days between two local peaks in a flood wave and **A** is the catchment area in square miles.

Flood frequency analysis was formed using the method of L-moments. L-moments were selected for parameter estimation because they provide robust and nearly unbiased estimators for skewed and heavy-tailed hydrological datasets, while being less sensitive to outliers than conventional moments (Mahbod et al., 2024). Several theoretical probability distributions were tested, including the Generalized Extreme Value (GEV), Gumbel, Pearson Type III (PE3) and Log-Pearson Type III (LP3) distributions. The best-fitting distribution was subsequently chosen separately for peak discharge and flood volume at each gauging station. Based on the fitted distribution, design discharges and flood volumes are chosen corresponding to selected return periods (5, 10, 100 and 500 years).

Univariate analysis

Two TFH hydrographs were derived following the scaling approach of Yue et al. (2002). This method first scales the typical flood hydrograph to match the design peak discharge (Q-based scaling), while the second scales it used to match the design flood volume (V-based scaling). The final design hydrographs (Q and V based) are obtained by scaling the typical hydrograph using the design peak discharge and design flood volume. While this approach is widely used in practice, it relies on a single design variable and does not explicitly account for dependencies between flood characteristics.

Bivariate analysis

In the bivariate approach, the annual maximum flood events were extracted from the discharge time series. Each AM peak discharge was matched with a corresponding flood volume of that event. This creates a dataset of annual maximum flood events containing both peak discharge and the appropriate flood volume.

The dependence between peak discharge and flood volume was quantified using Kendall correlation coefficients. Peak discharge was transformed and modelled using the same types of distributions as in the univariate method for both Q and V. The fitted marginal cumulative distribution functions were used

to transform both variables to uniform scale for further copula modelling.
Three bivariate copula families from the Archimedian family of copulas were tested: Gumbel-Hougaard, Clayton and Frank., and the best-fitting copula was selected based on the log-likehood and Akaike information criteria (AIC). These copulas were also tested by Šraj (2014) on the Litija gauging station and Rizwan (2019) on Pakistan's 2 major rivers Indus and Jhelum. The selected copula is then used to calculate joint probabilities and bivariate return periods for peak discharge and flood volumes.

Both OR and AND cases of bivariate return periods were considered. The OR return period represents the probability that at least one of the two variables exceeds its selected value, while the AND return period represents the probability that both variables exceed the selected values. The fitted copula and marginal distributions were then used to calculate return period curves in discharge and flood volume, allowing the joint behaviour of peak discharge to be visualised in the Q-V graph.

Following the selection of the best-fitting copula, return-period contours were derived for the selected return periods. The Equal Frequency Combination (EFC) (Rizwan et al. 2019) method was then applied to identify representative design combinations of peak discharge and flood volume. For each return period, the design point was defined as the location on the return-period contour where the marginal non-exceedance probabilities of peak discharge and flood volume were equal (u=v). The corresponding design values of peak discharge and flood volume were obtained from the fitted distributions and subsequently used for the construction of the synthetic design hydrograph. Both OR and AND return period definitions were considered when deriving the design Q–V pairs.

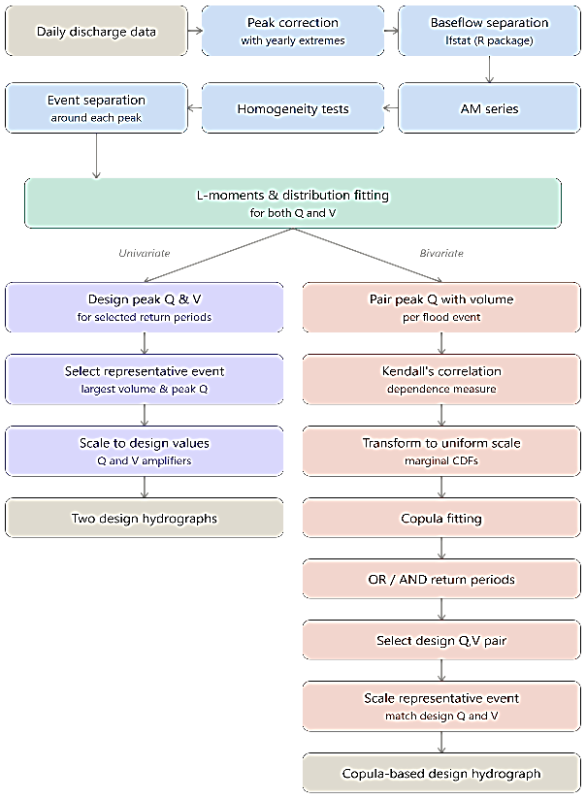


Figure 2. Methodological framework for univariate and bivariate flood frequency analysis and synthetic design hydrograph construction

The obtained design peak discharge–volume pairs were subsequently used for the construction of synthetic design hydrographs. Following the methodology based on Rizwan et al. (2019), The observed event with the closest V/Q ratio to the design pair was used as the representative hydrograph, scaled by $\alpha = Q_T/Q_{peak,obs}$ to exactly match Q_T (V verified post hoc against V_T). This single-parameter

scaling was chosen for simplicity; EFC was preferred over MLC for the same reason and because it yields more conservative design values (Rizwan et al. 2019). Given the short Farkašić record (25 years), its 100- and 500-year estimates carry larger uncertainty and should be interpreted with caution.

3 Results and discussion

3.1 Results

The- extracted annual maximum flood events were first analyzed to evaluate the suitability of the input data for both univariate and bivariate flood frequency analysis. Table 2 summarizes the results of the homogeneity and dependence analyses together with the selected marginal probability distributions and copula models for each gauging station. The Mann-Kendall (MK) and Pettitt tests were applied to assess the presence of monotonic trends and potential change points within the annual maximum series, while the dependence between peak discharge and flood volume was quantified using Kendall's correlation coefficient. Based on the goodness of fit analyses the most appropriate marginal distributions and copula families were selected for further modelling. Selected marginal distributions are then checked for goodness of fit using the Anderson Darling (AD) test.

Table 2. Summary of statistical analyses and selected probabilistic models for the analysed gauging stations

Gauging station	MK p	Pettitt p	Kendall τ	Best fit distribution (Q)	Best fit distribution (V)	Best copula
Dravograd	0.270	0.437	0.504	GEV	LP3	Frank
Kupljenovo	0.950	0.575	0.472	Gumbel	GEV	Clayton
Farkašić	0.907	0.885	0.448	Gumbel	GEV	Gumbel-Hougaard
Litija	0.579	0.909	0.351	LP3	PE3	Frank
Zagreb	0.075	0.07	0.319	LP3	PE3	Clayton

The analysed stations generally exhibited homogeneous behaviour without statistically significant trends or abrupt change points in the annual maximum series. Statistical significance of the Mann–Kendall and Pettitt tests was evaluated at the 5% significance level, meaning that p-values greater than 0.05 indicate that no statistically significant trend or change point was detected. Therefore, the obtained MK and Pettitt p-values suggest that there is no evidence of statistically significant monotonic trends or abrupt change points in the analysed annual maximum series. Positive dependence between peak discharge and flood volume was observed at all analysed stations, as indicated by positive Kendall's τ values. Kendall's τ ranges from −1 to 1, where values close to 0 indicate weak dependence, while higher positive values indicate stronger positive association. In this study, the obtained τ values, ranging approximately from 0.32 to 0.50, indicate moderate positive dependence between peak discharge and flood volume, supporting the application of bivariate copula models. Depending on the station characteristics and flood regime, different marginal distributions and copula families provided the best fit to the observed data. For peak discharge, the selected marginal distributions varied between GEV, Gumbel and LP3, while for flood volume they varied between LP3, GEV and PE3. Different copula families were selected depending on the station characteristics, with Frank, Clayton and Gumbel–Hougaard copulas identified as the best-fitting models across the analysed stations. Overall, both the best-fitting marginal distributions and copula functions were relatively non-homogeneous across the selected gauging stations in Croatia and Slovenia. The results indicate that no single marginal distribution or copula family consistently provided the best fit across all analysed gauging stations, highlighting the site-specific nature of flood peak–volume relationships. It is worth noting that for the Zagreb station the Mann-Kendall and Pettitt p-values (0.075 and 0.07, respectively) are close to the 0.05 significance threshold; while formally non-significant, this borderline result introduces some additional

uncertainty into the homogeneity assessment for Zagreb.

Based on the selected marginal distributions, design peak discharges and flood volumes corresponding to selected return periods were calculated using both univariate and bivariate approaches. Table 3 presents the comparison between univariate design values and the corresponding OR and AND bivariate design combinations derived using the fitted copula models. The comparison between univariate and bivariate (OR/AND) design values shows systematic differences depending on the variable (Q or V) and the station.For discharge (Q), the AND scenario almost always yields lower values than the univariate ones, with differences ranging from about -4% to -36%, while the OR scenario remains close to the univariate values (deviations generally within ±15%).

For volume (V), the OR scenario typically gives considerably higher values than the univariate ones (up to +80% at some stations), except at Farkašić where the opposite occurs (V_OR lower by ~20-38%). The AND scenario for V is the most variable - at Kupljenovo and Farkašić it gives lower values (up to -50%), while at Dravograd, Litija and Zagreb it is close to or slightly above the univariate values.

Table 3. Comparison of univariate and bivariate design peak discharges and flood volumes for selected return periods

Gauging station	T	Q_uni (m^3/s)	V_uni (m^3*10^6)	Q_OR (m^3/s)	V_OR (m^3*10^6)	Q_AND (m^3/s)	V_AND (m^3*10^6)
Dravograd	5	1596	615	1547	1114	1279	768
	10	1926	1127	1726	1424	1418	933
	100	2044	1401	2150	2626	1743	1458
	500	2278	2189	2366	3748	1911	1844
Kupljenovo	5	205	77	200	75	159	56
	10	260	98	227	86	176	64
	100	283	106	306	113	221	84
	500	337	121	361	144	249	95
Farkašić	5	1267	1114	1232	860	1146	664
	10	1428	1636	1304	1022	1213	819
	100	1495	1868	1532	1504	1436	1304
	500	1652	2429	1690	1814	1591	1622
Litija	5	1795	631	1738	896	1331	660
	10	2347	896	2006	1051	1508	763
	100	2584	1183	2820	1514	1983	1038
	500	3146	1652	3404	1837	2274	1205
Zagreb	5	2431	1097	2381	1620	1949	1233
	10	2929	1528	2631	1843	2143	1398
	100	3127	1705	3317	2443	2592	1808
	500	3567	2106	3757	2816	2852	2038

The differences between the univariate and bivariate approaches grow with return period, particularly when the joint behaviour of peak discharge and flood volume is considered: because the copula-based framework explicitly models their dependence, multiple Q–V combinations can correspond to the same bivariate return period.

Figure 3. illustrates this in Q–V space for the Kupljenovo station, showing observed flood event pairs together with the OR and AND bivariate return period contours. The OR contours span a wider region, while the AND contours concentrate in the upper-right, reflecting the simultaneous occurrence of large peaks and volumes. The red-yellow background represents the fitted copula function C(u,v), with lighter shades indicating higher joint non-exceedance probabilities.

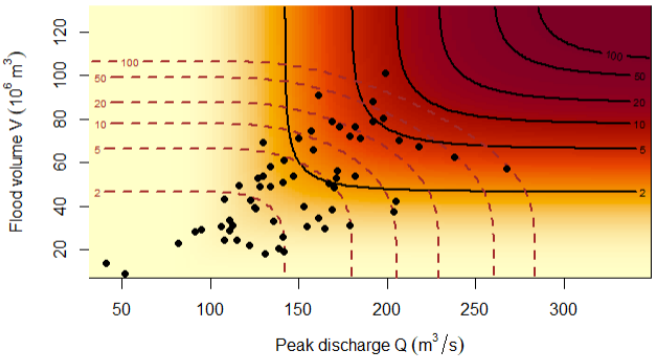


Figure 3. Observed flood events and bivariate OR (solid black lines) and AND (dashed brown lines) return period contours in the Q–V space for the Kupljenovo gauging station.

Figure 4. compares the resulting OR-based copula hydrograph with the univariate Q-based and V-based hydrographs. The V-based hydrograph has a notably lower peak, while the Q-based one has shorter duration and therefore smaller volume. The copula-based hydrograph balances both, yielding a more hydrologically consistent design event.

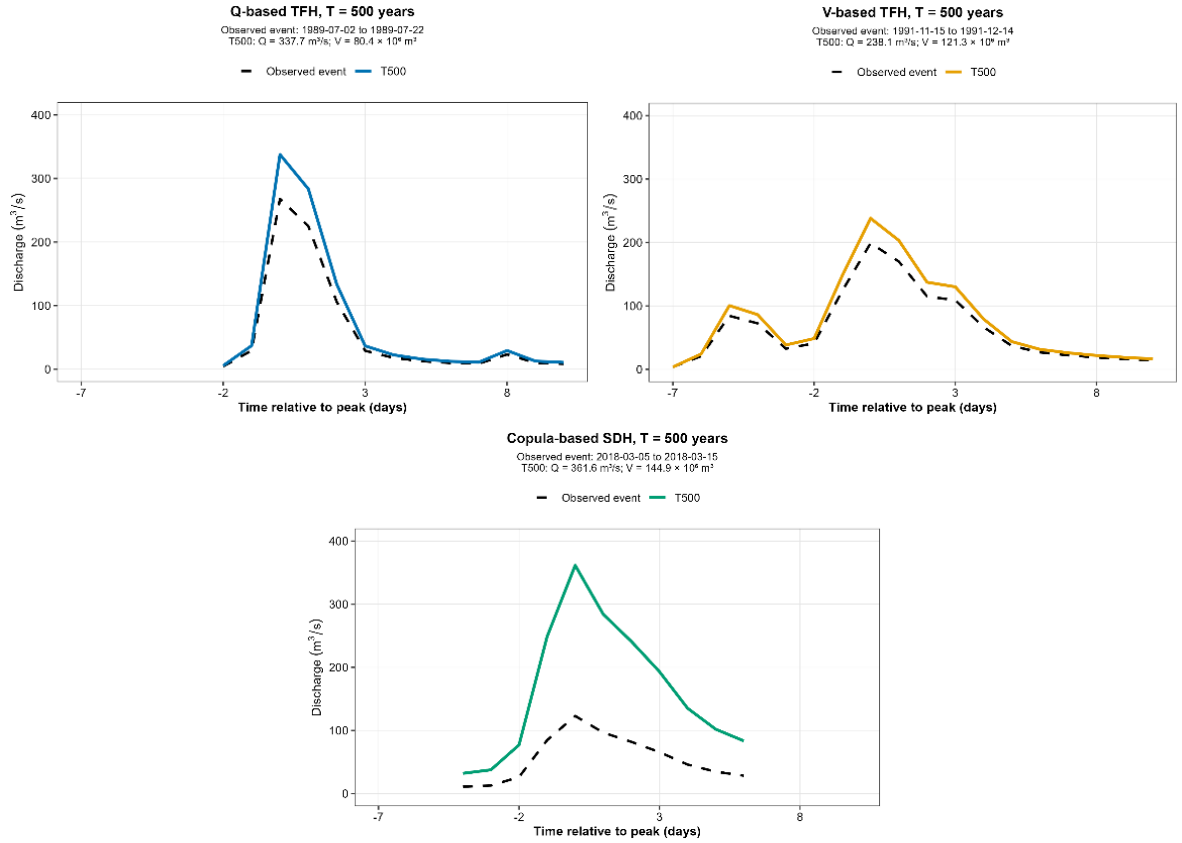


Figure 4. Comparison of Q-based, V-based and copula-based OR design hydrographs for the 500-year return period with their respective observed events used for scaling for the Kupljenovo gauging station

3.2 Discussion

Kendall's correlation coefficients ranging from 0.351 (Litija) to 0.504 (Dravograd) confirm a positive dependence between peak discharge and flood volume across all five analysed stations. This dependence has a direct and quantifiable consequence on the resulting design values: the univariate approach, by treating Q and V independently, systematically misrepresents at least one flood characteristic, and the magnitude of this misrepresentation grows substantially with return period.

The univariate flood frequency analysis results for the Litija gauging station show generally good agreement with the reference values reported by Šraj (2014). The calculated design peak discharges and flood volumes obtained in the present study were generally higher than the reference values reported by Šraj et al. (2014) across all analysed return periods. These differences are likely attributable to several factors, most importantly the different observational record length and analysed time period. Šraj et al. used data for the period 1953–2010, whereas the present study used an extended record covering 1954–2024. This extended period includes the largest recorded flood wave, with a peak discharge of 2580 m³/s observed in 2023, which can substantially influence the resulting design values. Additional differences may arise from the baseflow separation method applied prior to event extraction and from the flood wave delineation procedure. Given these methodological differences, the level of agreement between the two sets of results is considered satisfactory. The univariate flood frequency analysis for peak discharge for the Zagreb gauging station was also done by Lešćešen et al. (2022), where they got a different best fitting distribution (GEV) which can be likely attributed to different goodness-of-fit tests being used which resulted in the best fitting in this study being LP3.

The most consistent finding across all stations is that the univariate approach markedly underestimates flood volume relative to the OR bivariate definition. At Dravograd, the OR design volume for T = 100

years exceeds the univariate value by 87% ($V_{OR} = 2626 \times 10^6$ m³ vs. $V_{uni} = 1401 \times 10^6$ m³), and by 71% at T = 500 years. At Zagreb, the corresponding excess reaches 43% at T = 100 years and 34% at T = 500 years (Table 3). The practical implication is that a Q-based univariate design hydrograph, which remains standard in Croatian engineering practice, produces the target peak discharge but may provide flood volumes substantially lower than those associated with the same nominal return period under the OR exceedance concept. For applications where inundation duration and total water volume are critical, such as reservoir routing, levee breach assessment or bridge scour, this underestimation is relevant.

The choice between OR and AND return period definitions introduce divergence that grows with return period. The AND definition, requiring simultaneous exceedance of both Q and V thresholds, yields systematically lower design values than the univariate approach. At Dravograd for T = 500 years, the AND peak discharge is 16% lower than the univariate value ($Q_{AND} = 1911$ m³/s vs. $Q_{uni} = 2278$ m³/s). The spread between OR and AND peak discharges at T = 500 years ranges from approximately 35% of the univariate value at Dravograd ($Q_{OR} = 2366$ m³/s vs. $Q_{AND} = 1911$ m³/s) to less than 3% at Farkašić, reflecting how strongly station-specific dependence structure mediates this effect. This confirms the ordering $T_{OR} < T_{UNI} < T_{AND}$ reported by several studies such as Šraj et al. (2014) and Salvadori and De Michele (2007) and demonstrates that the choice of exceedance concept produces design differences of practical engineering significance.

4 Conclusion

This study compared univariate and bivariate approaches for the derivation of synthetic design hydrographs at five gauging stations in Croatia and Slovenia. The analysis was conducted using several copula functions, while the most suitable marginal distributions and copulas were selected based on statistical tests and graphical evaluation. Design hydrograph pairs were derived for both OR and AND joint return period definitions and compared against conventional univariate approaches.

The results confirmed positive dependence between peak discharge and flood volume at all analysed stations, demonstrating that these two characteristics cannot be treated independently without quantifiable consequence for the resulting design values. The univariate approach was shown to systematically misrepresent at least one flood characteristic, with discrepancies that grow with return period and vary between stations depending on the strength of dependence and the tail behaviour of the fitted copula. The choice of joint return period definition was further shown to significantly influence the resulting Q–V design pairs, with the ordering $T_{OR} < T_{UNI} < T_{AND}$ confirmed across all stations.

These findings are directly relevant to current Croatian and Slovenian hydraulic engineering practice (FGG Ljubljana (2023), Faculty of Civil Engineering, University of Zagreb, VEPAR). FGG Ljubljana (2023) explicitly identifies a critical gap in regional practice: design flood analyses predominantly yield only peak discharge, while flood volume and duration, equally important for hydraulic design, are routinely neglected. The same study further highlights a pronounced disproportion between the complexity of hydrological and hydraulic calculations, which reduces the practical value of flood studies, and recommends that design calculations incorporate multiple combinations of flood hydrograph characteristics. The results presented here respond directly to this identified need: the bivariate framework enables consistent specification of Q–V design pairs for a given return period and exceedance concept, quantifiably reducing the underestimation of design flood volumes that univariate approaches produce. Within the scope of the SERIOUS project, where design hydrographs serve as inputs to bridge scour assessment under present and future climate conditions, this more complete characterisation of the design flood event is of direct practical relevance.

Acknowledgements

This work has been supported in part by the Croatian Science Foundation under the project SERIOUS (IP-2024-05-1497) and the "Young Researchers' Career Development Project – Training New Doctoral Students" (DOK-2025-02-4645).

References

Bezak, N., Panagos, P., Liakos, L. and Mikoš, M. 2023 Brief communication: A first hydrological investigation of extreme August 2023 floods in Slovenia, Europe. *Natural Hazards and Earth System Sciences* 23, 3885–3892. https://doi.org/10.5194/nhess-23-3885-2023

Bezak, N., Mikoš, M., Lebar, K. and Šraj, M. 2022 Development of the methodology for the design hydrograph estimation in Slovenia, Europe. In *Proceedings of IAHR*, 2022.

Bezak N, Brilly M, Šraj M. 2014 Comparison between the peaks-over-threshold method and the annual maximum method for flood frequency analysis. *Hydrol Sci J.* 2014;59(5):959-77. doi: 10.1080/02626667.2013.831174.

Brunner, M.I., Sikorska, A.E., Viviroli, D. and Favre, A.-C. 2017 Flood type specific construction of synthetic design hydrographs. *Water Resources Research* 53 (2), 1390–1406.

Brunner, M.I., et al. 2019 Future trends in the interdependence between flood peaks and volumes: Hydro-climatological drivers and uncertainty. *Water Resources Research* 55 (9). https://doi.org/10.1029/2019WR024701

Faculty of Civil Engineering, University of Zagreb, 2023 n.d. *Projekt unaprjeđenja negrađevinskih mjera upravljanja rizicima od poplava u Republici Hrvatskoj (VEPAR), Unaprjeđenje hidroloških podloga, Metodologija*. https://vepar.voda.hr/ (accessed 8 June 2026)

FGG Ljubljana 2023 Razvoj metodologije za izračun visokovodnih valov na podlagi ekstremnih padavinskih dogodkov V2-2137. Univerza v Ljubljani, Fakulteta za gradbeništvo in geodezijo, Ljubljana.

Hrelja, H. 2007 *Inženjerska Hidrologija*. Građevinski fakultet, Sarajevo.

Jongman, B. 2021 The fraction of the global population at risk of floods is growing. *Nature* 596, 37–38. https://doi.org/10.1038/d41586-021-01974-0

Koffler, D. and Laaha, G. 2012 *LFSTAT - an R-package for low-flow analysis*. In EGU General Assembly Conference Abstracts, Vienna, April 2012.

Lacko, M., Potočki, K., Škreb, K.A. and Bezak, N. 2022 Joint modelling of flood hydrograph peak, volume and duration using copulas - case study of Sava and Drava River in Croatia, Europe. *Water* 14, 2481. https://doi.org/10.3390/w14162481

Leščešen, I. and Dolinaj, D. 2019 Regional flood frequency analysis of the Pannonian Basin. *Water* 11 (2), 193. https://doi.org/10.3390/w11020193

Leščešen, I., Šraj, M., Basarin, B., Pavić, D., Mesaroš, M., & Mudelsee, M. 2022. Regional flood frequency analysis of the Sava River in South-Eastern Europe. *Sustainability, 14*(15), 9282. https://doi.org/10.3390/su14159282

Mahbod, M., et al. 2024 An innovative regional frequency analysis approach for robust extreme precipitation assessment in data-rich and climatically diverse regions. *Water Resour Manage,* 39, 5079–5102 https://doi.org/10.21203/rs.3.rs-4356974/v1

Nimac, I., Cindrić Kalin, K., Renko, T. et al. 2022 The analysis of summer 2020 urban flood in Zagreb (Croatia) from hydro-meteorological point of view. *Natural Hazards* 112, 873–897. https://doi.org/10.1007/s11069-022-05210-4

OECD 2016 *Financial Management of Flood Risk*. OECD Publishing, Paris. https://doi.org/10.1787/9789264257689-en

Potočki, K., Bekić, D., Bezak, N., Conradt, T., Pintar, D., Šrajbek, M. and Lacko, M. 2025. *Synthetic design hydrographs under current and future climate for local bridge scour assessment*. EGU General Assembly 2025, Vienna, Austria, 27 April–2 May 2025, EGU25-16468. https://doi.org/10.5194/egusphere-egu25-16468

Rahimi, M., et al. 2021 Origin and variability of statistical dependencies between peak, volume, and

duration of rainfall-driven flood events. *Scientific Reports* 11. https://doi.org/10.1038/s41598-021-84664-1
Rizwan, M., Guo, S., Yin, J. and Xiong, F. 2019 Deriving design flood hydrographs based on copula function: a case study in Pakistan. *Water* 11 (8), 1531. https://doi.org/10.3390/w11081531
Salvadori, G. and De Michele, C. 2007 On the use of copulas in hydrology: theory and practice. *Journal of Hydrologic Engineering* 12, 369–380.
USWRC 1982 *Guidelines for Determining Flood Flow Frequency*. US Water Resources Council, Washington DC, USA.
Yue, S., Ouarda, T.B.M.J., Bobée, B., Legendre, P. and Bruneau, P. 2002 Approach for describing statistical properties of flood hydrograph. *Journal of Hydrologic Engineering* 7 (2), 147–155. https://doi.org/10.1061/(ASCE)1084-0699(2002)7:2(147)
Šraj, M., Bezak, N. and Brilly, M. 2014 Primerjava med klasičnimi univariatnimi verjetnostnimi analizami in bivariatnimi z uporabo funkcije kopula / Comparison between classical univariate frequency analysis and bivariate analysis with copula. *Acta Hydrotechnica* 26, 37–48.

OPTIONS FOR FLOOD PROTECTION OF THE ZÁHORSKÁ BYSTRICA URBAN AREA

Martin ORFÁNUS [1*], Andrej ŠOLTÉSZ [1], Peter ŠULEK [1], Natália BILČÍKOVÁ [1]

[1] *Department of Hydraulic Engineering, Faculty of Civil Engineering, STU in Bratislava, Slovakia*

E-mail: martin.orfánus@stuba.sk

E-mail: andrej.soltesz@stuba.sk

E-mail: peter.sulek@stuba.sk

E-mail: natalia.bilcikova@stuba.sk

[*] *Corresponding author*

Abstract

This study focuses on assessing the current state of flood protection in the Bratislava – Záhorská Bystrica district and its adjacent areas during 100-year flood events (Q100). The primary objective was to identify critical locations within the urban area and propose effective technical and nature-based measures to eliminate flood risks. The HEC-RAS 2D mathematical model (v6.3.1), utilizing the shallow water approximation of Saint-Venant equations, was employed for water level analysis and flow simulation. The model was parameterized using a high-resolution digital elevation model (1x1 m) and hydrological data provided by the SHMU. Flood scenarios were simulated for the catchments of the Bystrický Brook and Salabov Stream, including their mutual confluence. Simulation results revealed insufficient capacity of key culverts, particularly on Vrbánska Street, where overtopping into residential zones occurs. To mitigate these risks, a system of four polders (retention basins) is proposed: three within the Salabov Stream catchment and an upgrade of the existing sedimentation basin in the Bystrický Brook catchment. Additional measures include consolidation and retention check dams in the upper reaches to capture debris and sediment, as well as the installation of trash racks at culvert inlets. The study confirms the necessity of implementing integrated flood risk management that combines technical structures with landscape elements designed for debris and sediment retention.

Key words

Flood protection, HEC-RAS 2D, Záhorská Bystrica, Polder, Q_{100}

1 Introduction

The assessment of localized flood risks within the Bratislava - Záhorská Bystrica district has become a critical priority for municipal safety and civil infrastructure planning. This urgency is driven primarily by continuous urban development and the rapid expansion of residential zones directly into peripheral areas that are naturally vulnerable to torrential discharges (Bugár, 2023).

To address these vulnerabilities, this technical study was formally commissioned in February 2026. The primary focus of the research centers on modeling a 100-year flood event (Q_{100} flood wave) to evaluate current risks and design highly effective, resilient countermeasures (HYDROCOOP, 2023).

The overarching research objectives were systematically divided into five primary tasks:

- Hydrological Data Analysis,
  - Evaluating foundational input data provided by the Slovak Hydrometeorological Institute (SHMU)

- 2D Model Development,
  - Building a high-resolution, two-dimensional mathematical model tailored to the local topography
- Scenario Simulation.
  - Executing three distinct computational scenarios, including independent flood waves in both catchments as well as a simultaneous, combined confluence event
- Landscape Intervention Design
  - Proposing macro-level engineering solutions, specifically focusing on a system of retention polders.
- Urban Technical Adjustments
  - Developing micro-level localized infrastructure modifications, such as inlet protection systems.

1.1 Study Area Description

The geographic area of interest encompasses the catchments of the Salabov stream and the Bystrický stream, both of which represent integral components of the broader hydrography of the Morava River basin (Table 1).

Table 1. Main characteristics of the analyzed streams

Stream	Total length	Classification
Salabov Stream	1.90 km	Drains the southeastern slopes of the Little Carpathians and portions of the Borská nížina. It functions as a smaller, locally significant watercourse that retains the natural, unregulated character of Bratislava's outskirts.
Bystrický Stream	11.0 km	Acts as a significant right-bank tributary of the Morava River. It originates near Malý Slavín as a high-velocity mountain torrent before transitioning into a partially regulated lowland stream as it traverses the Záhorská Bystrica urban zone.

The entire municipal cadaster of the district spans an area of 32 km². For the purpose of flood risk management, this territory can be categorized into three functional zones:

- The Urbanized Core,
  - Encompassing historical village centers alongside rapid new residential developments, most notably the Strmé vŕšky and Pod vŕškami neighborhoods
- Agricultural Lands,
  - Located predominantly in the western part of the district
- Protected Forest Fund.
  - Comprising parts of the Little Carpathians mountain range, which are heavily utilized for public forestry and recreation (Slovenský vodohospodársky podnik, 2023)

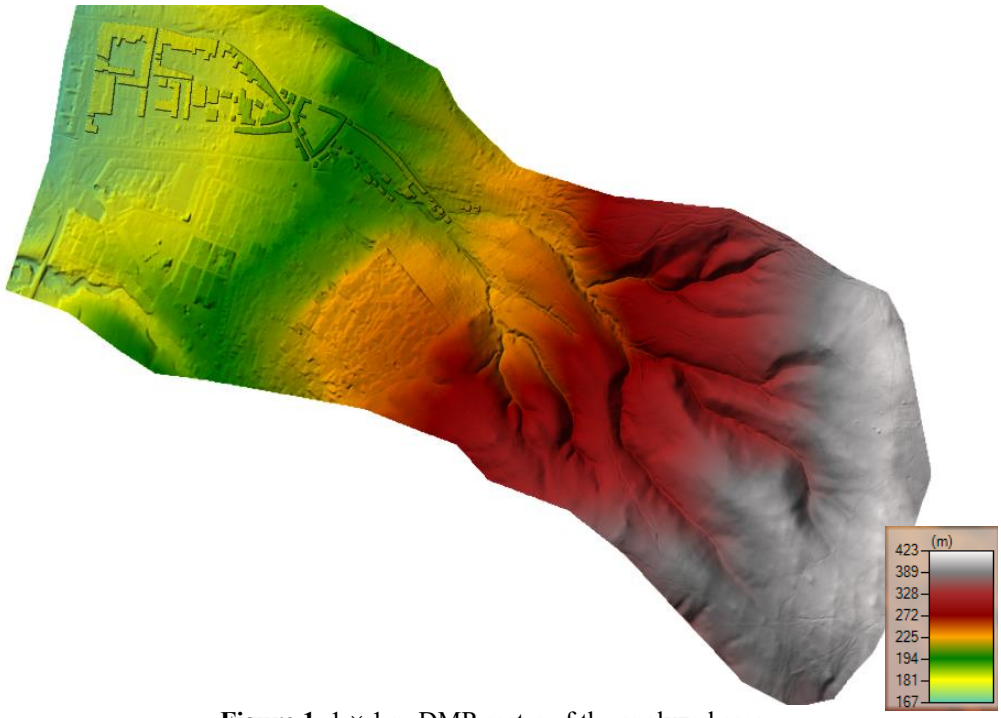


Figure 1. 1 × 1 m DMR raster of the analyzed area

Topographical Baseline: The spatial modeling relies on a high-precision Digital Relief Model (DMR) raster with a detailed 1x1 m resolution to map elevations ranging from 167 meters up to 423 meters above sea level (Fig. 1).

2 Methods

To accurately determine the water level regime and simulate complex flow dynamics across the study area, an advanced two-dimensional mathematical modeling approach was established. The framework utilizes the industry-standard HEC-RAS 2D (version 6.3.1) software package, developed by the U.S. Army Corps of Engineers. This software platform applies robust numerical finite difference methods to execute flood risk planning, mapping, and predictive analysis (HEC-RAS Documentation, 2023).

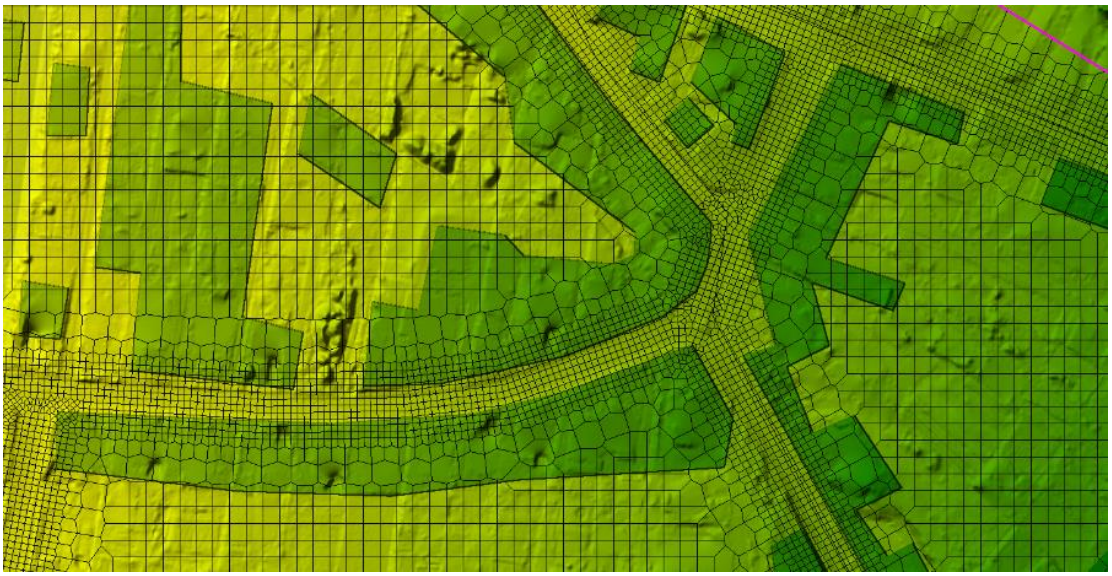


Figure 2. Computational mesh of the analyzed area – detail at the street crossing

2.1 Hydrodynamic Governing Equations

The mathematical core of the model relies on a dynamic wave scheme. Specifically, it solves the Saint-Venant equations simplified into the standard approximation of the Shallow Water Equations (SWE). This hydraulic framework operates under two core physical assumptions:

- The fluid is completely incompressible.
- Vertical velocity components are negligible compared to horizontal flow vectors.

The mathematical continuity equation utilized by the software to solve non-stationary, two-dimensional overland flow is defined as follows

$$\partial h/\partial t + \partial(hu)/dx + \partial(hv)/dy = q \quad (1)$$

where t is time, u and v are velocity components, and q is the source/inflow term.

2.2 Model Parameterization and Mesh Design

The reliability of the 2D flow simulation is heavily dependent on its structural parameterization. The model's terrain geometry was built using a high-resolution Digital Relief Model (DMR) featuring a 1x1 m cell resolution, directly extracted from the official geographic data of the ZBGIS portal. To reflect realistic hydraulic conditions, critical hydrotechnical objects (such as bridges, culverts, and retaining walls) identified during exhaustive field surveys were manually integrated into the geometric layer.

- Computational Mesh Configuration
  - As shown in Figure 2, a flexible computational mesh was generated across the terrain.
- Spatial Resolution
  - To guarantee extreme detail and capture localized flow transitions near critical infrastructure bottlenecks, the element size of the mesh scales down to approximately 0.8 m in high-risk urban zones.

2.3 Methodological Limitations & Uncertainty

Critical Note on Model Calibration: Due to a severe historical deficit in localized gauging infrastructure, no real-world water level or discharge data was available for extreme meteorological events. Consequently, the HEC-RAS 2D model could not undergo standard calibration or validation protocols. This lack of empirical calibration introduces an inherent degree of scientific uncertainty regarding the absolute interpretation of the resulting flood depths and velocities, which must be accounted for in subsequent engineering designs.

3 Results and Discussion

The analysis is centered on three computational scenarios:

Bystrický stream Scenario (Figure 3): The Q_{100} flood wave here is characterized by a sharp peak but relatively lower total volume. While the channel capacity on Vrbánska Street is sufficient, flow velocities exceed 2.0 $m \cdot s^{-1}$ necessitating channel reinforcement. The culvert at Vrbánska Street acts as a bottleneck with a capacity of only ~0.7 $m^3.s^{-1}$, causing water to overtop and flow through Kollarova, Hargašova, and Bratislavská streets with depths of ~0.15 m.

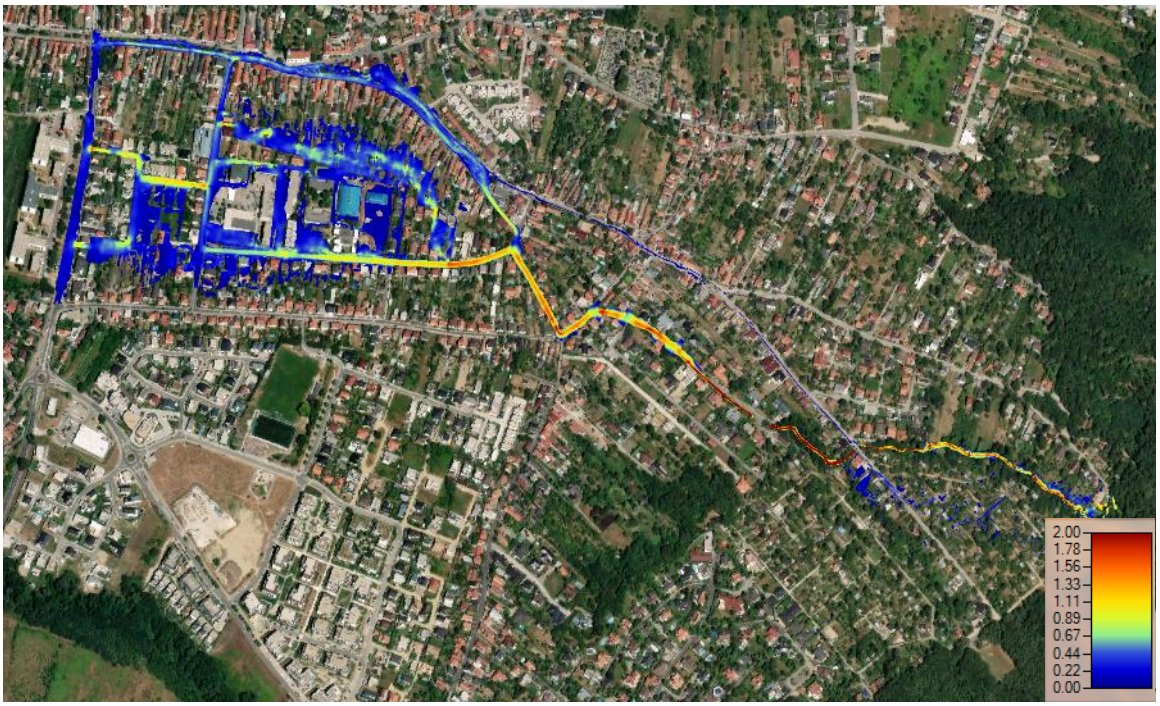


Figure 3. Bystrický stream. Q_{100} map of velocities

Salabov stream Scenario: This catchment produces a flood wave with higher volume and culmination. The Vrbánska Street culvert is significantly undersized for this load, leading to street flooding with velocities up to 2.0 $m \cdot s^{-1}$ and depths reaching ~0.5 m as shown in Figure 4. Residential properties on Hargašova Street and the intersection with Rošického Street are severely impacted.



Figure 4. Salabov stream. Q_{100} map of velocities.

Confluence Scenario: A simultaneous culmination of both streams was simulated for illustrative purposes. This combined event increases depth and velocity parameters by approximately 10% compared to the Salabov stream scenario, as shown in Figure 5.

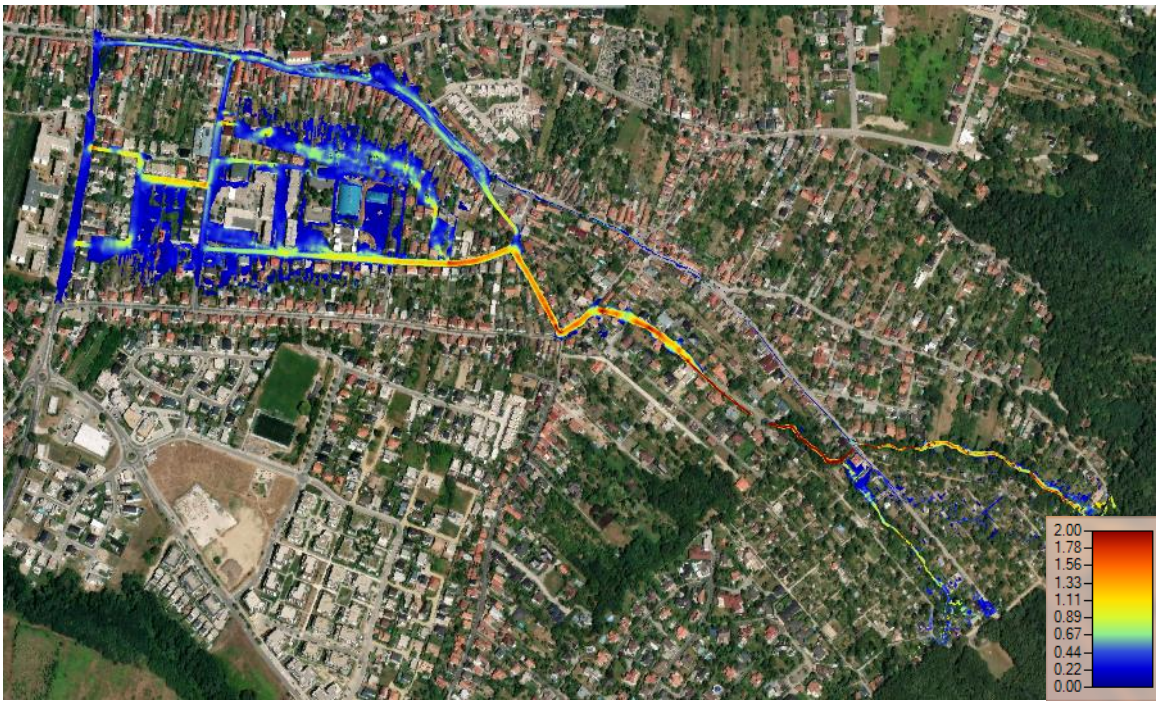


Figure 5. Confluence. Q_{100} map of velocities.

3.1 Proposed Measures

Effective protection requires a combination of landscape and urban technical measures.

- Landscape Measures (Polders): A system of polders is proposed to transform the flood discharge (Raplík, 1989)

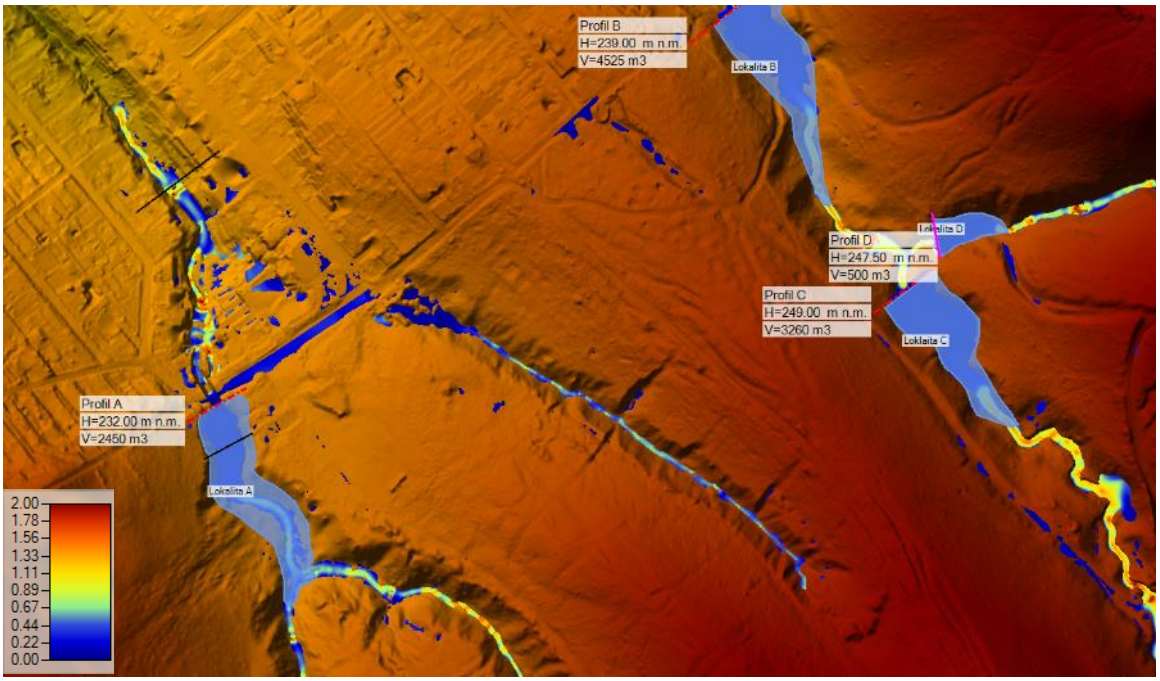


Figure 6. Situation of proposed polders

- Locations B, C, D (Salabov stream): Three new polders with dam heights up to 7 m as shown in Figure 6.
- Location A (Bystrický stream): Upgrade of the existing "Poľovník" sedimentation basin. Proposed enhancements include deepening the basin by 1.0 m, reconstructing the embankment

to an elevation of ~232.50 m a.s.l., and reducing the inlet culvert diameter to force retention.

- Debris Management: Consolidation and retention check dams are proposed in the upper reaches to prevent sediment and woody debris from clogging the polders and urban culverts (Říha et al., 2014).

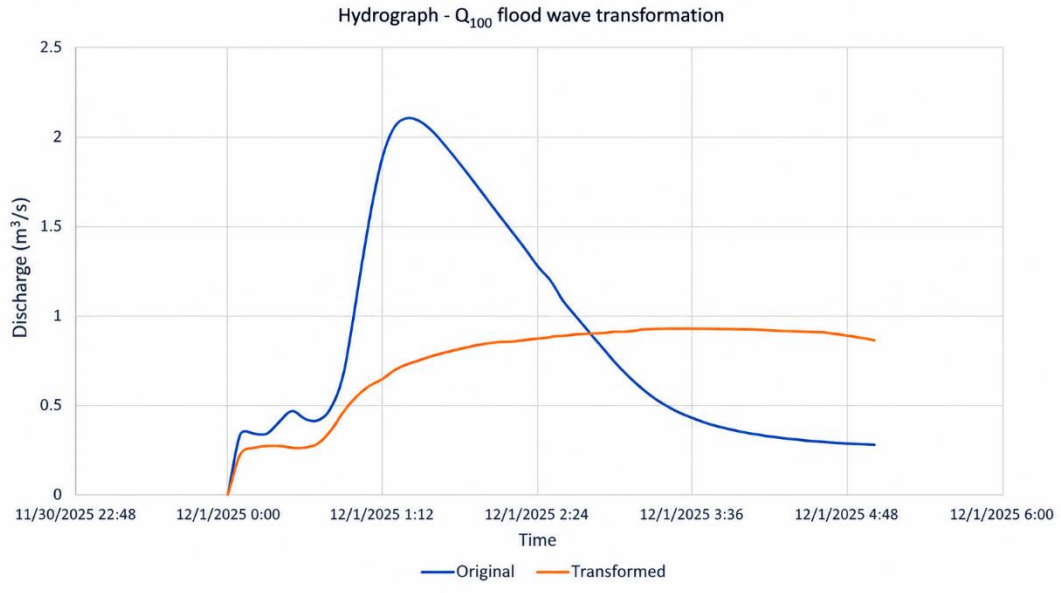


Figure 7. Flood wave transformation on Salabov stream

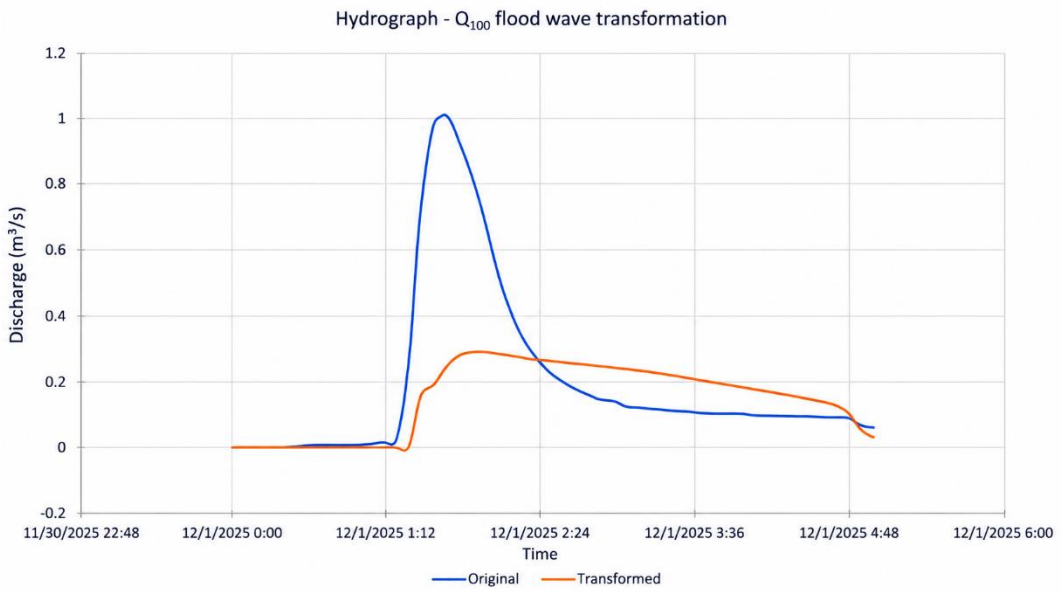


Figure 8. Flood wave transformation on Bystrický stream

3.2 Urban Technical Measures

For culverts within the village, the installation of trash racks is recommended.

- Fine Racks: 100 mm spacing, installed in a basket configuration at a 45° angle (Visser, 2020).
- Coarse Racks: 300 mm spacing, placed 10 m upstream to capture large debris (Vokurka et al., 2020) as shown in Figure 9,
- Maintenance: Expanding and reinforcing the channel bed at inlets is recommended to allow for mechanized cleaning (Rumann et al., 2025).



Figure 9. Proposed trash racks

4 Conclusion

The comprehensive hydraulic analysis of the Záhorská Bystrica urban area has provided critical insights into the flood dynamics of the Bystrický Brook and Salabov Stream catchments under Q_{100} conditions. The study confirms that the area is highly vulnerable to torrential flood waves characterized by rapid onset and significant peak amplitudes. While the primary channel capacities on streets like Vrbánska and Tešedíkova are generally sufficient to contain the flow, the existing culvert infrastructure acts as a primary bottleneck, leading to widespread urban flooding. Specifically, the simulations revealed that the culvert on Vrbánska Street has a maximum capacity of approximately 0.7 $m^3.s^{-1}$, which is insufficient for a 100-year event. For the Bystrický Brook, this results in overtopping that impacts streets such as Kollarova and Hargašova with water depths of ~0.15 m and flow velocities of 0.6 $m.s^{-1}$. The risk is significantly higher for the Salabov Stream catchment, where larger flood volumes cause street-level inundation depths of 0.5 m and dangerous flow velocities reaching 2.0 $m.s^{-1}$. These conditions pose a direct threat to residential properties on Hargašova and Rošického streets. To address these risks, an integrated flood risk management strategy is proposed, combining technical landscape interventions with urban maintenance protocols:

- Landscape Transformation: A system of three polders with dam heights up to 7 meters is recommended for the Salabov Stream catchment to achieve significant flood wave transformation as shown in Figures 7 and 8. For the Bystrický Brook, the existing sedimentation basin at the "Poľovník" cottage should be upgraded by deepening the reservoir by 1.0 m, raising the embankment to 232.50 m a.s.l., and reducing the outlet culvert diameter to force retention,
- Debris and Sediment Control: To ensure polder and culvert efficiency, consolidation and retention check dams must be implemented in the upper reaches to capture wood debris and sediment before they reach urban infrastructure,
- Urban Technical Measures: Within the village, the installation of dual-stage trash racks is critical. Fine racks (100 mm spacing) are recommended directly at inlets and coarse racks (300 mm spacing) placed 10 meters upstream at a 45-degree angle. Furthermore, the removal or redesign of speed bumps on Hargašova Street is advised, as they may unintentionally divert floodwaters toward residential parcels.

While the HEC-RAS 2D model provides a robust conceptual framework for flood behavior, the lack of historical gauging data for calibration remains a source of uncertainty. Consequently, the next phase of development must include high-precision geodetic surveys, a detailed hydrological census of all existing watercourse objects, and the integration of these findings into the municipal territorial plan. Only through this multi-layered technical approach can Záhorská Bystrica achieve a resilient level of protection against extreme flood events.

Acknowledgements

This work was supported by the Science Grant Agency - project VEGA 1/0161/24.

References

Bugár, J. 2023. *General principles of functional organization of the territory - part "A" - surveys and analyzes of the territory (VZFU part "A" - Surveys, analyzes and analysis of the current state - documentation of the Project of simple land adjustments in the section of the Lamač, Štamperky location)*. Bratislava. https://docplayer.net/43422528-Vseobecne-zasady-funkcneho-usporiadania-uzemia-cast-a-prieskumy-a-rozbory-uzemia.html (accessed 20 June 2023)

HEC-RAS Documentation, 2023. *HEC-RAS Hydraulic Reference Manual*. https://www.hec.usace.army.mil/confluence/rasdocs/ras1dtechref/latest/theoretical-basis-for-one-dimensional-and-two-dimensional-hydrodynamic-calculations/2d-unsteady-flow-hydrodynamics/hydraulic-equations (accessed 20 June 2023)

HYDROCOOP, spol. s.r.o. 2023. *Update of the territorial general of water courses and flood protection of the city of Bratislava*. Bratislava. https://cdn-api.bratislava.sk/strapi-homepage/upload/textova_cast_a73c1b7990.pdf (accessed 20 June 2023)

Raplík, M., Výbora, P., Mareš, K. 1989. *Uprava tokov*. Alfa, Bratislava. ISBN 80-08- 00128-2.

Říha, J., Sedláček, M., Smrž, P., Veselý, R., Žatecký, S. 2014. *Design and Realization of Dry Reservoirs from a Technical-Safety Supervision Perspective*. MŽP ČR, Academic Publishing CERM, Brno, 126 p.

Rumann, J. et al. 2025. Research of Hydraulic Parameters Influencing the Design of Flood Protection Measures in the Vývrat Catchment. STU in Bratislava, Bratislava.

Slovenský vodohospodársky podnik, š. p. 2023. *Flood hazard maps and flood risk maps of Slovak waterways* (according to Directive 2007/60/EC of the European Parliament and Council of October 23, 2007 on flood risk assessment and management). Selection of the class - Bratislava IV district (2). https://mpompr.svp.sk/okres.php?id=4 (accessed 20 June 2023)

Visser, R., Harvey, C. 2020. *Design of Debris Slash Traps: Considerations for NZ Plantation Forestry Operating*. School of Forestry, University of Canterbury, Christchurch.

Vokurka, A., Zlatuška, K., Barták, J., Brouček, M., Jelínek, B., Lakomá, H., Straková, M., Úradníček, L., Vaníček, M. 2020. *Technical Recommendations for Torrent and Ravine Control*. Ministry of Agriculture & Czech Society of Landscape Engineers, Prague. 94 p. ISBN 978-80-7434-557-9.

THE ROLE OF RETENTION RESERVOIRS IN URBAN FLOOD PROTECTION IN THE KACZA RIVER BASIN IN GDYNIA, POLAND

Abdata Wakjira GALATA [1*], Kamil RATKA[2], Michał SZYDŁOWSKI[2]

[1] *Doctoral School, Gdańsk University of Technology, 80-233 Gdańsk, Poland*

E-mail: abdata.galata@pg.edu.pl

[2] *Faculty of Civil and Environmental Engineering, Gdańsk University of Technology, 80-233 Gdańsk, Poland*

E-mail: kamil.ratka@pg.edu.pl

E-mail: mszyd@pg.edu.pl

[*] *Corresponding author*

Abstract

This study investigates the role of retention reservoirs in reducing outflow in the Kacza River basin. The analysis is based on the extreme rainfall event of 14-15 July 2016, which resulted in significant urban flooding. Four scenarios were proposed: (1) the basin with two reservoirs operating in 2016; (2) without reservoirs; (3) all currently existing reservoirs; and (4) the existing and planned reservoirs. Simulation results show that in the absence of reservoirs, the peak discharge at the basin outlet would have reached 52.7 m^3/s. In contrast, the presence of the two operated reservoirs in 2016 reduced the peak flow to 40 m^3/s. The inclusion of all currently existing reservoirs further decreased peak discharge to 25 m^3/s, while the future configuration with planned reservoirs would have reduced peak flow to approximately 17.3 m^3/s. In addition to peak attenuation, a noticeable delay in peak timing is revealed. Similarly, the flood-inundation area decreased from 0.30 km^2 in the scenario without reservoirs to 0.18 km^2 when all reservoirs were included. The findings demonstrate the hydrological effectiveness of retention reservoirs for urban catchment management. Future research will incorporate nature-based solutions to enhance the catchment buffering system under land use/land cover and climate change driven extreme events.

Key words

Flood mitigation, Gdynia, Kacza River, Retention reservoirs, Urban catchment.

1 Introduction

Urban flooding is an increasingly common problem in the world. It is driven by rapid urbanization and climate change. Urban expansion alters the natural hydrological cycle by increasing impervious surfaces, reducing infiltration capacity, increasing surface runoff, and runoff coefficient within urban catchments (Gao et al., 2023; Li et al., 2024). Additionally, climate variability aggravates urban flooding by increasing the frequency and intensity of extreme rainfall events (Blenkinsop et al., 2021). Consequently, urban basins tend to respond rapidly to rainfall inputs, exhibiting short lag times, sharp hydrograph peaks, and elevated peak discharges, which collectively increase the likelihood of urban flooding (Rosa et al., 2023; Song et al., 2020). Structural flood mitigation measures such as dry and wet retention reservoirs can effectively reduce peak discharge, provided that suitable locations are available for their implementation (Bezak et al., 2021). The upstream reservoirs temporarily store stormwater runoff during intense rainfall events and release it gradually, thereby reducing downstream peak discharge and flood inundation (Birkinshaw and Krivtsov, 2022a). It is important to evaluate the performance of constructed reservoirs to determine whether they are functioning as intended.

The city of Gdynia, located on the Baltic Sea coast in northern Poland, is particularly susceptible to

urban flooding due to its unique geomorphological setting. The Kacza River basin is characterized by steep moraine hills in the upstream region and densely urbanized areas in the downstream coastal zone. This topographic gradient accelerates runoff generation during intense rainfall events. In July 2016, an extreme rainfall event caused severe flooding in Gdynia, downstream of the Kacza River basin (Szydłowski et al., 2017). Following this event, additional retention reservoirs were constructed and planned to improve flood protection. The objective of this study is to evaluate the effectiveness of existing and planned retention reservoirs in mitigating urban flood in the Kacza River basin using hydrological and hydraulic modeling.

2 Methods

2.1 Study area

The Kacza River basin is located in the city of Gdynia in northern Poland (Fig.1). The basin covers an urbanized catchment characterized by strong elevation gradients between the upstream moraine plateau and the downstream coastal zone. Extending over 14.8 km, the river drains from a total area of 54.8 km², which constitutes the primary hydrological focus of this study. It is characterized by relatively steep slopes in range from 2.5‰ to 22‰. Construction is increasingly expanding into the upstream part of the basin, while the downstream section is already urbanized, with residential areas, transportation infrastructure, and commercial developments (Fig. 2). The growing impervious surfaces on steep slopes, together with established urban surfaces downstream leads to rapid runoff generation during intense rainfall events. The 2016 rainfall event analyzed in this study resulted in severe urban flooding. Retention reservoirs have been constructed in the catchment as part of Gdynia's flood mitigation strategy. During the occurrence of the flood phenomena, two reservoirs existed – Krykulec and Karwiny (Fig. 1). After the 2016 flood event, three additional reservoirs were constructed, and three more have been planned (Fig. 1).

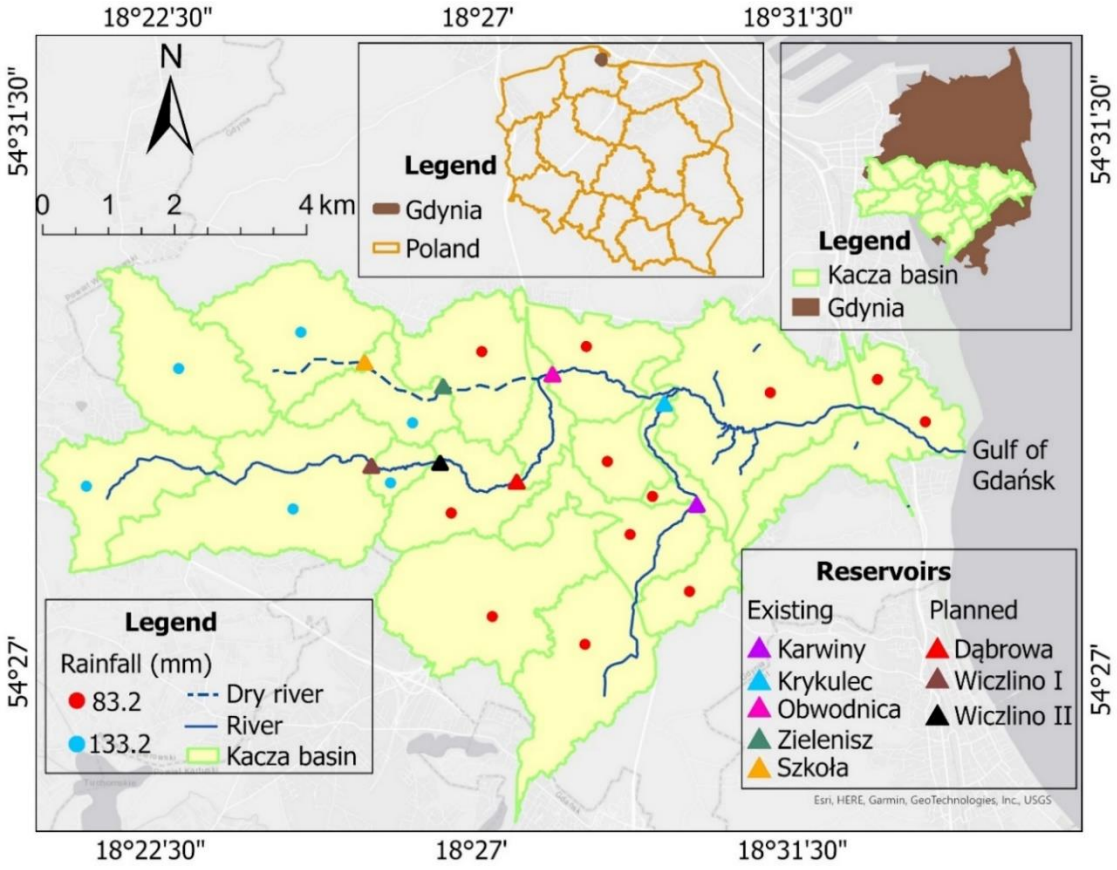


Figure 1. Geographical location of the study area: location of Poland (top left), Gdynia (top right), and the Kacza basin (bottom).

2.2 Spatial data

The study uses the 2016 land use land cover (LULC) map. Sentinel-2 Multispectral Instrument (MSI) imagery with a spatial resolution of 10 m by 10 m was processed using the Google Earth Engine platform and classified using a machine learning algorithm. The classified LULC map represents a spatial distribution of surface water, forest, green area, agricultural land, bare, and built-up area across the case study during the 2016 flood event (Fig. 2). This data was used to define hydrological parameters such as infiltration and runoff characteristics within the model. A digital elevation model (DEM) of 1m by 1 m spatial resolution is sourced from the Scalgo Live (scalgo.com) platform (Fig. 2). It was used to represent the catchment topography and support the setup of the HEC-HMS model.

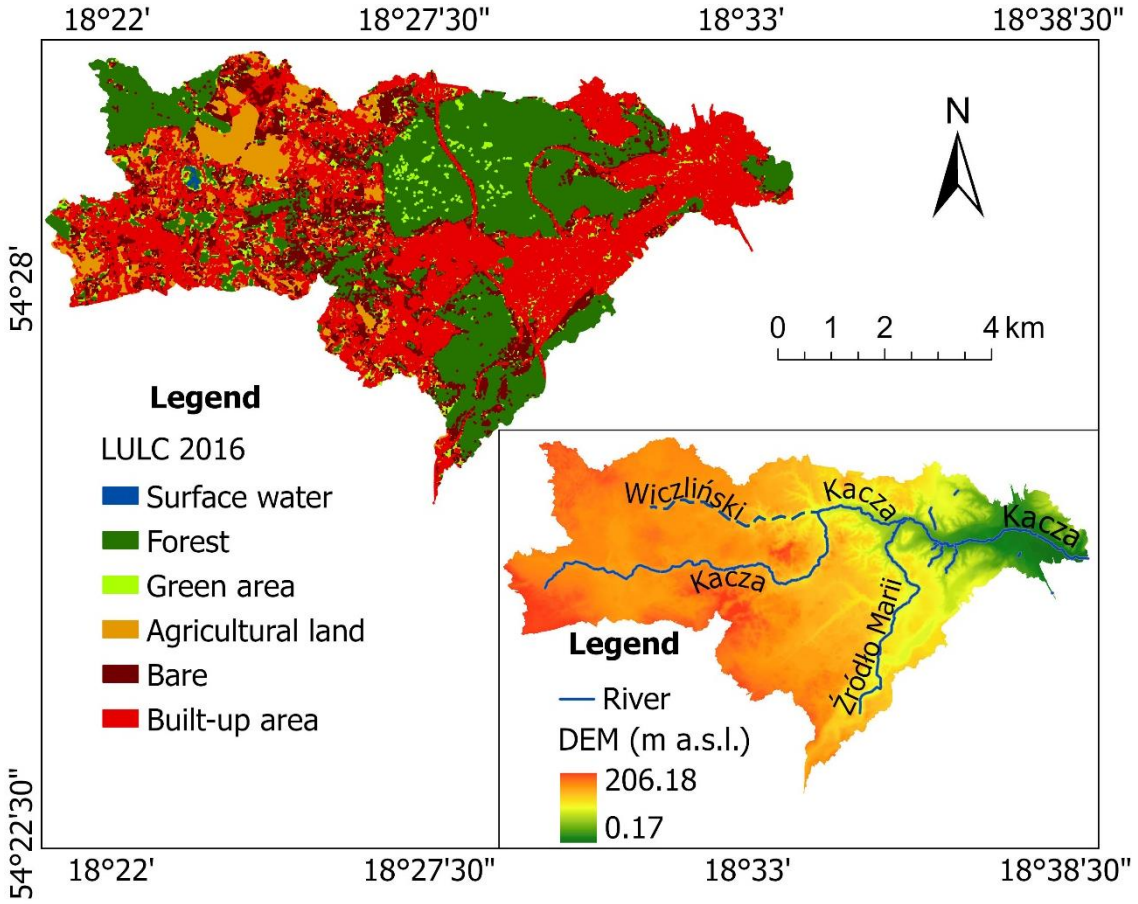


Figure 2. The 2016 land use land cover and digital elevation model of the study area.

The spatial extents of the HEC-HMS and HEC-RAS models are presented in Fig. 3. The HEC-HMS model covers the entire basin of the Kacza River, and the HEC-RAS model is limited to the downstream floodplain. The discharge hydrograph obtained from the hydrological model was used as the upstream boundary condition of the hydraulic model, which defines the temporal variation of inflow driving the hydraulic simulations. The downstream boundary is the basin outlet.

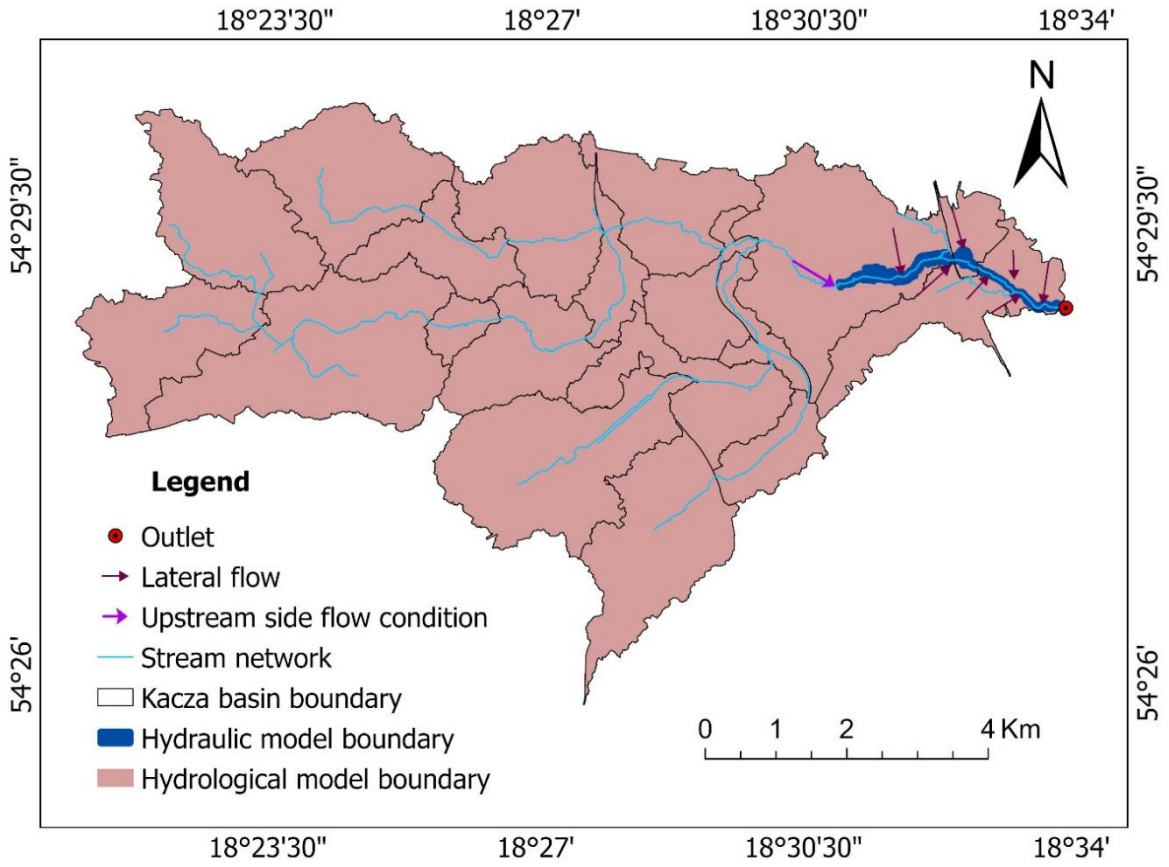


Figure 3. Spatial extent of the hydrological and hydraulic models in the Kacza River basin.

2.3 The 2016 rainfall event and urban flooding

From the afternoon of July 14 to the early hours of July 15, 2016, the Tri-City experienced heavy rainfall, accompanied at times by very strong and violent winds that resulted in the urban flooding (Szydłowski et al., 2017). Because of the catchment's varied topography, rainfall over the Kacza River basin in Gdynia was unevenly distributed that influence its intensity and distribution across the basin. It can be noted that Gdynia has only one official meteorological station, located on the coastline. During the event, a total rainfall of 83.2 mm was recorded at this station. At the same time, significant spatial variation in rainfall was observed across the Tri-City region, with respect to the lower (coastal) and upper (moraine) terraces (Szydłowski et al., 2017). To maintain similarity to the observed rainfall, spatial variation was proposed. For the lower terrace and edge zone, the rainfall amount measured at the Gdynia weather station was used, while for the upper terrace (where there is no measuring station in Gdynia), the rainfall amount measured at the Gdańsk Rębiechowo weather station was used. A higher total rainfall of 133.2 mm was used for this location, making it appropriate to represent the upper terrace due to similar terrain and regional rainfall characteristics within the Tri-City area. The temporal distributions of the rainfall were performed according to German Standardisation and Derivation of Dimensioning Values for Wastewater Facilities (German DVWK) for both magnitudes (Zima, 2018) (Fig. 4).

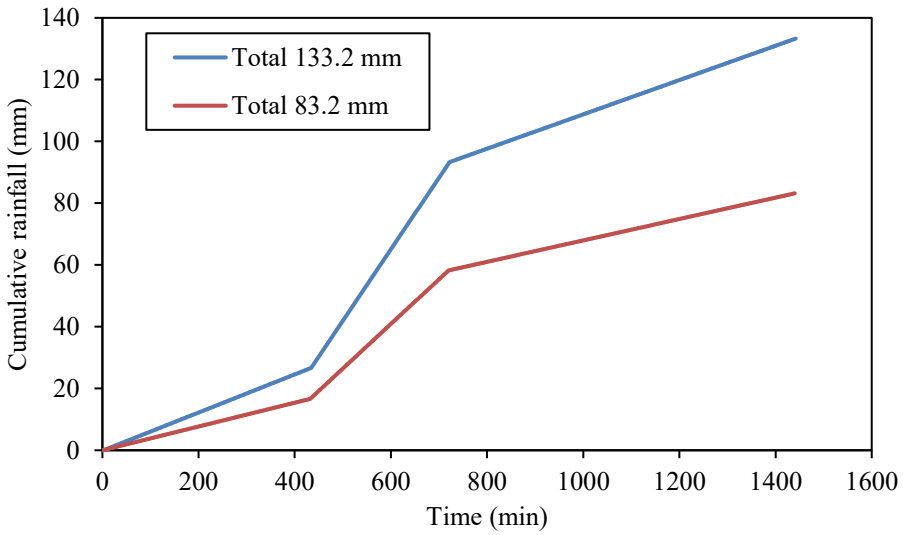


Figure 4. Cumulative rainfall curves for the July 2016 event representing DVWK rainfall distribution of 83.2 mm (coastal conditions) and 133.2 mm (upper terrace conditions).

2.4 Hydrological Modeling

The rainfall-runoff process in the Kacza River basin was simulated using the Hydrologic Engineering Center-Hydrologic Modeling System (HEC-HMS) (USACE, 2023). The model calculates surface runoff generated by rainfall and routes the flow through the river network and retention reservoirs. The hydrological model includes rainfall input from the 2016 extreme event (Fig. 4), basin characteristics derived from LULC data, reservoir storage data (Table 1), and flow routing through the river network. The main output of the hydrological model is outflow hydrograph with the peak discharge (Qmax) at the Kacza River outlet to the Gulf of Gdańsk.

2.5 Reservoir Scenarios

The study considers four reservoir configuration scenarios to evaluate their hydrological impact within the basin. Scenario 1 represents the baseline condition corresponding to the situation during the 2016 flood event, when only the two existing retention reservoirs Krykulec and Karwiny (Fig. 1) were in operation. In contrast, scenario 2 assumes the absence of any reservoirs, allowing assessment of the catchment response and providing insight into how the basin would behave without retention infrastructure. Scenario 3 builds upon the baseline by adding three additional reservoirs Obwodnica, Zielenisz, and Szkoła thereby reflecting an expanded retention strategy. Finally, scenario 4 extends this configuration further by incorporating three planned reservoirs, namely Dąbrowa, Wiczlino I, and Wiczlino II, representing a future scenario with maximum retention capacity. The main parameters of reservoirs are presented in Table 1.

Table 1. Retention reservoir's parameters.

Stream	Reservoir name	Construction year	Surface area (10^3m^2)	Storage (10^3m^3)	WSE max (m a.s.l)	Pipe number	Pipe diameter (m)	Spillway elevation (m a.s.l)
Źródło Marii	Krykulec	2002	34.48	66.65	69.0	1+1	0.8	68.5
Źródło Marii	Karwiny	2011	5.55	6.0	95.2	2+1	1.2	94.5
Kacza	Obwodnica	2017	19.32	40.64	99.7	2+1	1.0	98.7
Wiczliński	Zielenisz	2017	27.6	60.3	131.0	1+1	0.8	130.0
Wiczliński	Szkoła	2018	5.97	8.9	149.1	1+1	1.1	148.7
Kacza	Dąbrowa	planned	21.5	50.0	125.1	1+1	0.8	124.6
Kacza	Wiczlino I	planned	16.5	27.0	147.7	1+1	0.8	147.0
Kacza	Wiczlino II	planned	9.5	14.25	138.5	1+1	0.8	138.0

2.6 Hydraulic Modeling

The peak discharges calculated using HEC-HMS were used as boundary conditions for hydraulic simulations performed in Hydrologic Engineering Center-River Analysis System (HEC-RAS) (USACE, 2023). The hydraulic model calculates water levels and floodplain inundation in the downstream section of the Kacza River basin 3.7 km long from outlet (Fig. 7). Flood extent was determined for each scenario to evaluate the impact of reservoirs on downstream flooding inundation.

3 Results and Discussion

3.1 Peak Flow Reduction

As it can be seen from Table 2 and Fig. 5, increasing the number of reservoirs noticeably regulates the hydrological responses of the catchment under similar total rainfall volume of 5469.8 x 10^3 m^3. The absence of reservoirs significantly increases peak discharge, with the maximum value reaching 52.7 m^3/s. The total outflow volume calculated at this scenario is 2678.8 x $10^3 m^3$, while the outflow coefficient is 0.49. When the two existing reservoirs during the 2016 event are considered, the peak discharge decreased to 40.0 m^3/s and occurred after 60 minutes in reference to no-reservoir scenario. This result is consistent with previous calculations, which validated by geodetic measurements taken after the flood (Szydłowski et al., 2017). Consideration of the three reservoirs built after 2016 reduced the peak discharge to 25.0 m^3/s and increased peak time to 90 minutes. When all planned reservoirs are included, peak discharge decreased to 17.3 m^3/s, with the highest delay of peak discharge time (180 minutes) and the highest retention capacity (273.74 x $10^3 m^3$).

Table 2. Hydrological response parameters under different reservoir development scenarios.

Scenario	Reservoir configuration	Peak discharge (m^3/s)	Delay of peak discharge timing (min)	Total retention volume ($10^3 m^3$)
1	Two reservoirs	40.0	60	72.65
2	No reservoir	52.7	-	0.0
3	Five reservoirs	25.0	90	182.49
4	Eight reservoirs	17.3	180	273.74

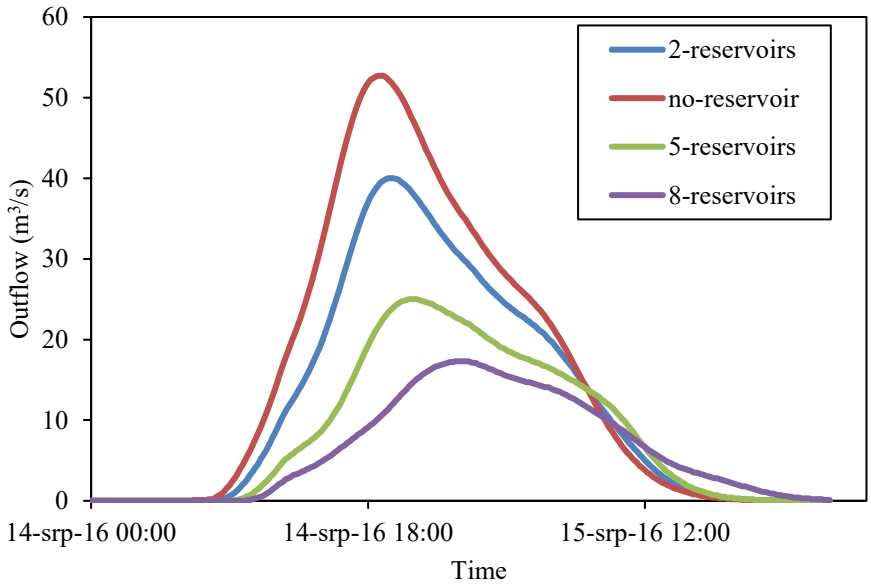


Figure 5. Simulated outflow hydrographs for various reservoir scenarios.

3.2 Flood inundation area

The hydraulic simulations show that retention reservoirs also significantly reduce the downstream flood extent (Fig. 6). The largest flood area (0.30 km²) occurs when no reservoirs are present. The existed configuration of two reservoirs reduced inundation area to 0.27 km². With five reservoirs, the flood area decreased to 0.21 km², while the inclusion of all planned reservoirs further reduced the area to 0.18 km².

Fig. 7 presents the simulated longitudinal water surface profiles for the no reservoir, two-reservoir, five-reservoir and eight-reservoir scenarios, and compares them with the observed water levels in the downstream reach of the Kacza River. The simulated profiles agree generally well with the water levels observed. The two-reservoir scenario is the best representation of the observations with the lowest RMSE of 0.31 m, followed by the five-reservoir (0.45 m) and the eight-reservoir (0.66 m) scenarios. The largest discrepancy appears in the no-reservoir scenario with an RMSE of 0.78 m. Simulations with retention reservoirs show lower downstream floodplain water levels in general. The two-reservoir case provides the best fit to the observed longitudinal water surface profile as the observed water levels were measured during a flood when the two existing retention reservoirs were already in operation. Therefore, this situation is the most representative for the real hydraulic conditions during the observation period. The five- and eight-reservoir scenarios represent hypothetical flood mitigation configurations and therefore result in lower water surface elevations compared to the existing reservoir system.

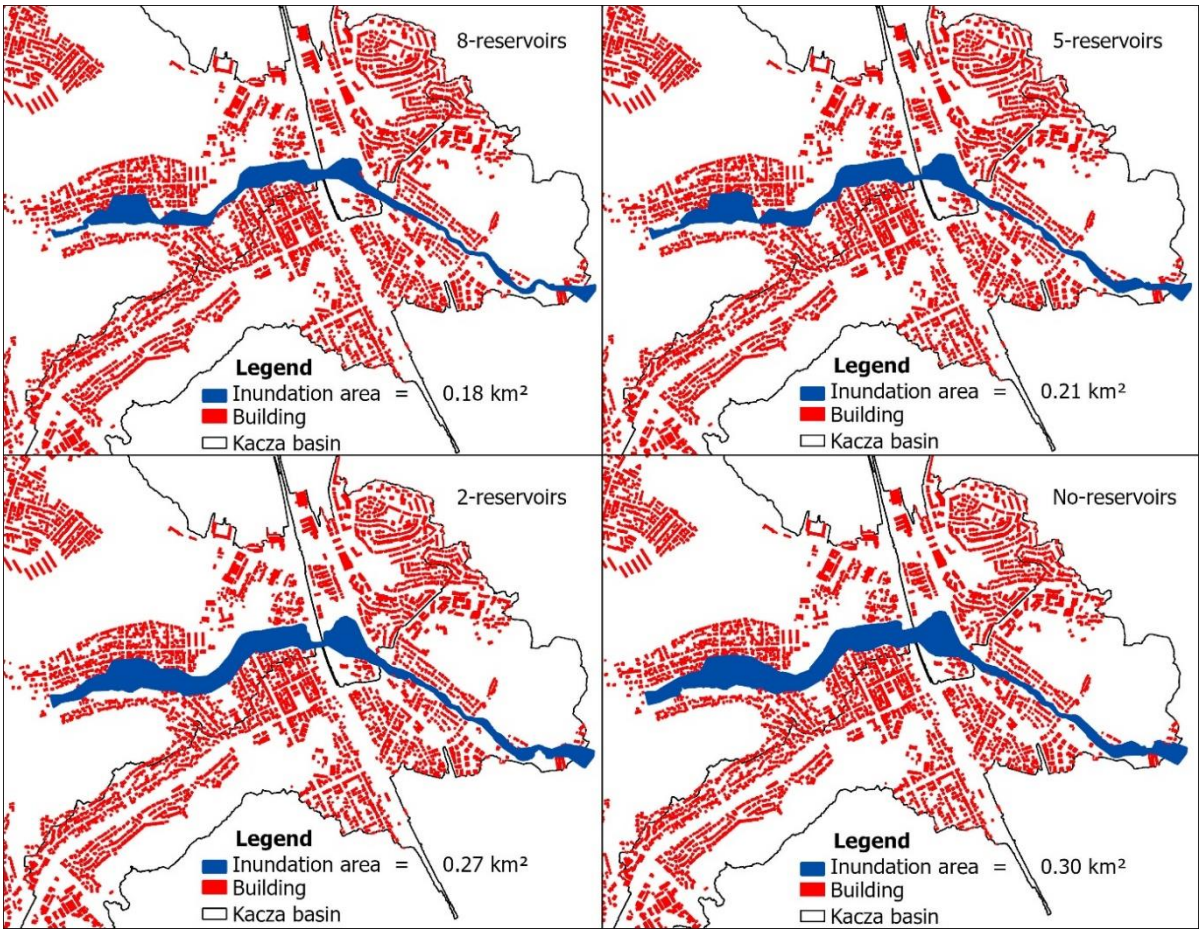


Figure 6. Flood inundation area under different scenarios.

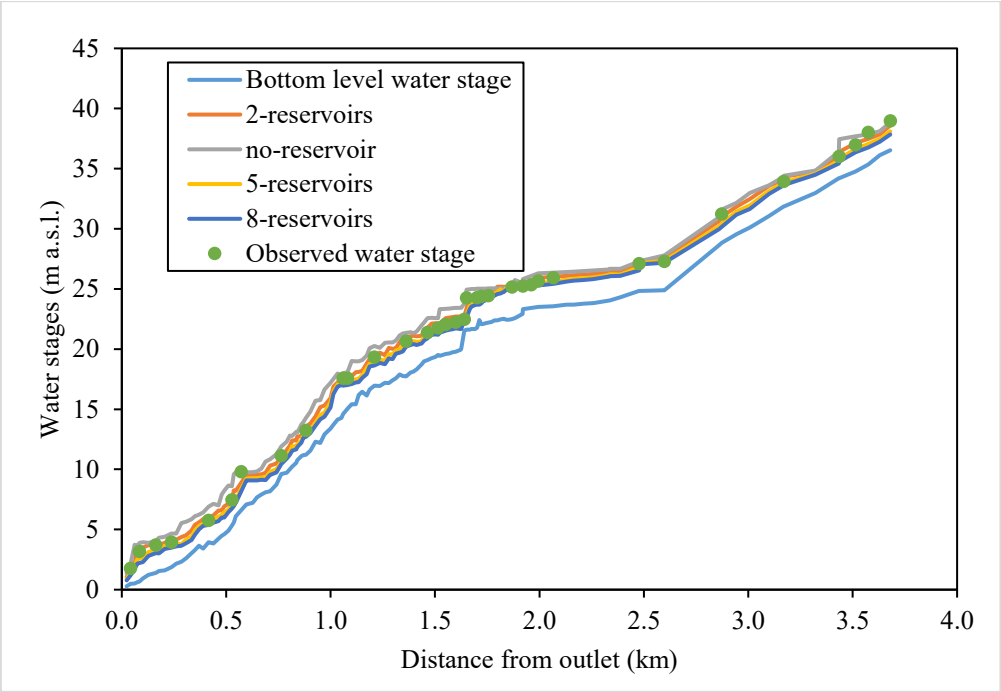


Figure 7. Comparison of simulated water surface profiles under different reservoir scenarios and observed water levels along the downstream reach of the Kacza River.

3.3 Discussion

Modeling results indicate the need for dry retention reservoirs in order to reduce the severity of urban flooding. The benefits of flood control are significant with the addition of reservoirs built after 2016, and could be further reduced with the planned reservoirs. As the comparison of the scenarios indicates, increasing the storage capacity decreases the peak flow and delays the propagation of the flood wave towards downstream metropolitan centers. This highlights the fundamental purpose of retention reservoirs, to attenuate the flood peaks by temporarily storing the excess runoff and releasing it gradually (Guarda et al., 2026; Pirone et al., 2024). Similar results have been found in urban flood management studies where storage-based approaches increase catchment resilience and minimize runoff volume (Jemberie and Melesse, 2021). These results not only help in evaluating the efficacy of retention reservoirs for flood mitigation, but also show that the reduction in peak discharge depends not only on the available retention volume but also on the spatial distribution and its hydraulic location. Reservoirs of similar storage capacity located in areas of less influence may not provide the same level of flood attenuation as those located in strategically important areas where tributaries or rapid generation of runoff play an important role in contributing to downstream flood peaks (Birkinshaw and Krivtsov, 2022b). Further work involving sensitivity analysis, optimization strategies, and geographic exploration of alternative reservoir locations would provide a more detailed understanding of the impact of reservoir placement on flood mitigation performance. Still attention is needed for peak discharge capacity in the Kacza River catchment. However, as retention reservoirs have been already constructed and planned at almost all major tributaries, the potential for major additional flood reduction by enlarging large-scale storage facilities only might become limited. Future adaptation strategies therefore focus not only on increasing retention reservoirs, but on reducing runoff generation at the source and improving distributed retention within the urban landscape. Their effectiveness can be improved by combining them with complementary strategies that increase the retention capacity of the whole catchment. Recent assessments have shown that nature-based solutions (NBS) can significantly reduce the risk of urban pluvial flood, especially when combined with traditional drainage and storage infrastructure (Huang et al., 2020). NBS can also bring other ecological and social benefits in addition to improving infiltration and reducing runoff generation (Zhou et al., 2024).

4 Conclusion

The role of retention reservoirs in reducing urban flooding in the Kacza River catchment in Gdynia was assessed by means of integrated hydrological and hydraulic modelling. The results show that increasing reservoir storage reduced peak discharge, increased the delay time of peak discharge and decreased flood inundation area. These findings indicate that a retention reservoir is a significant component of flood management strategies in Gdynia. However, limitations should be considered despite the demonstrated benefits. The analysis is limited to one urban catchment and selected hydrological scenarios, and therefore the magnitude of flood reduction cannot be directly generalized to all urban environments. Climate, topography, land use and drainage characteristics may vary and affect the effectiveness of retention measures elsewhere. Future work will explore combined structural and nature-based interventions for a broader set of rainfall scenarios, including projected climate conditions, and will integrate economic assessments more comprehensively to evaluate the cost-effectiveness of alternative adaptation pathways.

References

Bezak, N., Kovačević, M., Johnen, G., Lebar, K., Zupanc, V., Vidmar, A., Rusjan, S., 2021 Exploring Options for Flood Risk Management with Special Focus on Retention Reservoirs. *Sustainability* 13, 10099. https://doi.org/10.3390/su131810099

Birkinshaw, S.J., Krivtsov, V., 2022a Evaluating the Effect of the Location and Design of Retention Ponds on Flooding in a Peri-Urban River Catchment. *Land* 11, 1368. https://doi.org/10.3390/land11081368

Birkinshaw, S.J., Krivtsov, V., 2022b Evaluating the Effect of the Location and Design of Retention Ponds on Flooding in a Peri-Urban River Catchment. *Land* 11, 1368. https://doi.org/10.3390/land11081368

Blenkinsop, S., Alves, L.M., Smith, A.J.P., 2021 Climate change increases extreme rainfall and the chance of floods. Zenodo. https://doi.org/10.5281/ZENODO.4779119

Gao, B., Xu, Y., Sun, Y., Wang, Q., Wang, Y., Li, Z., 2023 The impacts of impervious surface expansion and the operation of polders on flooding under rapid urbanization processes. *Theor. Appl. Climatol.* 151, 1215–1225. https://doi.org/10.1007/s00704-022-04318-8

Guarda, T., Sotomayor-Cuadrado, A.J., Coronado-Hernández, O.E., Arrieta-Pastrana, A., Coronado-Hernández, J.R., 2026 An Integrated Explicit Hydrological Routing and Machine Learning Framework for Urban Detention System Design. *Water* 18, 483. https://doi.org/10.3390/w18040483

Huang, Y., Tian, Z., Ke, Q., Liu, J., Irannezhad, M., Fan, D., Hou, M., Sun, L., 2020 Nature-based solutions for urban pluvial flood risk management. WIREs *Water* 7, e1421. https://doi.org/10.1002/wat2.1421

Jemberie, M.A., Melesse, A.M., 2021 Urban Flood Management through Urban Land Use Optimization Using LID Techniques, City of Addis Ababa, Ethiopia. *Water* 13, 1721. https://doi.org/10.3390/w13131721

Li, J., Zhou, W., Tao, C., 2024. The Impact of Urbanization on Surface Runoff and Flood Prevention Strategies: A Case Study of a Traditional Village. Land 13, 1528. https://doi.org/10.3390/land13091528

Pirone, D., Cimorelli, L., Pianese, D., 2024 The effect of flood-mitigation reservoir configuration on peak-discharge reduction during preliminary design. *J. Hydrol. Reg. Stud.* 52, 101676. https://doi.org/10.1016/j.ejrh.2024.101676

Rosa, D.W.B., Das Graças Silva, T.F., De Araújo, R.P.Z., De Oliveira Nascimento, N., 2023 Hydrological impacts of urban expansion in a Brazilian metropolis – Case study of the Vargem das Flores reservoir catchment. *Urban Water J.* 20, 1618–1626. https://doi.org/10.1080/1573062X.2022.2075769

Song, M., Zhang, J., Bian, G., Wang, J., Wang, G., 2020 Quantifying effects of urban land-use patterns on flood regimes for a typical urbanized basin in eastern China. *Hydrol. Res.* 51, 1521–1536. https://doi.org/10.2166/nh.2020.110

Szydłowski, M., 2019 Hydraulic Analysis of Causes of Washout of Gdynia-Orłowo Sea-Shore During the Flood in the Kacza River Estuary. *Pol. Marit. Res.* 26, 174–182. https://doi.org/10.2478/pomr-2019-

0019
Szydłowski M., Szpakowski W., Widerski T. 2017 *Analysis of Kacza River surge in Gdynia after precipitation* of 14 July 2016, Gospodarka Wodna, No. 6/2017, 161–167.
USACE (U.S. Army Corps of Engineers) 2023 *HEC-HMS Hydrologic Modeling System User's Manual (Version 4.13)*. Hydrologic Engineering Center, Davis, CA.
U.S. Army Corps of Engineers (USACE) 2023 *HEC-RAS River Analysis System User's Manual (Version 6.4.1)*. Hydrologic Engineering Center, Davis, CA.
Zhou, K., Kong, F., Yin, H., Destouni, G., Meadows, M.E., Andersson, E., Chen, L., Chen, B., Li, Z., Su, J., 2024 Urban flood risk management needs nature-based solutions: a coupled social-ecological system perspective. *Npj Urban Sustain.* 4, 25. https://doi.org/10.1038/s42949-024-00162-z
Zima, P., 2018 *Impact of Climate Change on a Runoff Formation in Seaside Catchment Area on the Example of the Babica River Catchment,* in: 2018 Baltic Geodetic Congress (BGC Geomatics). Presented at the 2018 Baltic Geodetic Congress (BGC Geomatics), IEEE, Olsztyn, Poland, pp. 236–240. https://doi.org/10.1109/BGC-Geomatics.2018.00051

INFLUENCE OF DESIGN HYETOGRAPH CONSTRUCTION METHODS ON URBAN RUNOFF SIMULATION

Željko ŠRENG [1*], Marija ŠPERAC [1], Filip LAUŠ [1], Siniša MARIČIĆ [1], Dražen VOUK [2]

[1] *Josip Juraj Strossmayer University of Osijek, Faculty of Civil Engineering and Architecture Osijek, Vladimira Preloga 3, 31000 Osijek, Croatia*

E-mail: zsreng@gfos.hr

E-mail: msperac@gfos.hr

E-mail: filip.laus@gmail.com

E-mail: smaricic@gfos.hr

[2] *University of Zagreb, Faculty of Civil Engineering, Fra Andrije Kačića-Miošića 26, 10000 Zagreb, Croatia*

E-mail: drazen.vouk@grad.unizg.hr

[*] *Corresponding author*

Abstract

The temporal distribution of precipitation within a design storm significantly influences simulated runoff and hydraulic loading in urban drainage systems. Although intensity–duration–frequency (IDF) relationships define precipitation magnitude, the selection of the design hyetograph determines the temporal concentration of precipitation and thus the peak discharge response. This study investigates the sensitivity of an urban sewer system to different methods of constructing dimensionless design hyetographs. Design storms were derived from local high-resolution precipitation records using two approaches: the Huff curves and the Alternating Block Method. For each method, representative dimensionless hyetographs were constructed and combined with design precipitation height corresponding to selected return periods. The resulting synthetic storms were applied as input to a numerical hydraulic model developed in the SWMM (Storm Water Management Model) software for a selected urban catchment in the city of Osijek, Croatia. Model simulations were performed to evaluate differences in peak discharge, hydrograph shape and potential surcharge conditions within the sewer network. The results demonstrate that the choice of dimensionless hyetograph significantly affects predicted system response, particularly for short-duration, high-intensity storms. Hyetographs characterized by earlier precipitation concentration tend to generate higher and earlier peak flows, while those with delayed concentration can lead to sustained system loading and increased risk of surcharge in downstream sections. The findings emphasize that the method used to construct the design hyetograph is not a neutral modelling choice but a critical factor influencing hydraulic performance assessment and infrastructure design. A transparent and locally derived selection of the temporal precipitation pattern is therefore essential for reliable urban drainage analysis.

Key words

Design hyetograph, numerical model, Huff curves, Alternating Block Method, Urban floods.

1 Introduction

Urban drainage systems are commonly designed and evaluated using synthetic design storms derived from intensity–duration–frequency (IDF) relationships. Consequently, the selection of an appropriate design hyetograph represents one of the most important steps in hydraulic modelling, as the temporal distribution of rainfall directly affects runoff generation, peak discharge, surcharge occurrence and

flooding within the drainage network (Bonacci, 1994; Huff, 1967; Pilgrim and Cordery, 1975; Bezak et al., 2018; Krvavica and Rubinić, 2020). The use of high-resolution precipitation records is essential for the development of reliable IDF relationships and design storms. Detailed temporal rainfall information improves the representation of short-duration, high-intensity precipitation events, which are often responsible for surcharge conditions, flooding and rapid runoff generation in urban drainage systems (Dunkerley, 2008; Yin et al., 2016; Wartalska et al., 2020). Several approaches are available for constructing design storms. Among the most frequently applied methods are Huff hyetographs, which are derived from observed rainfall events and classified according to the temporal position of peak rainfall intensity (Huff, 1967; Nguyen and Chen, 2022), and the Alternating Block Method (ABM), which remains one of the most commonly used approaches in engineering design practice due to its simplicity and direct connection with IDF relationships (Bonacci, 1994; Bezak et al., 2018). Although both methods are widely used, they may produce substantially different hydraulic responses because of differences in rainfall temporal distribution.

The objective of this study is to evaluate the influence of different design storm approaches on the hydraulic performance of an urban drainage system. Two Huff hyetographs (Type 1 and Type 4) and two Alternating Block Method configurations (R-1 and R+1) were analysed for multiple return periods and storm durations using a SWMM model. Emphasis was placed on flooding indicators, outfall loadings and the identification of critical areas within the drainage network. Section 2 describes the study area, rainfall data, design storm construction and modelling methodology. Section 3 presents and discusses the simulation results, while the main findings and conclusions are summarized in Section 4.

2 Methods

2.1 Study area, catchment and drainage characteristics

The study was conducted in Donji Grad, an urban district of the City of Osijek located in eastern Croatia (Fig. 1a). The district has approximately 9,000 inhabitants and is characterized by predominantly residential land use combined with local roads, parking areas and public facilities. The terrain is generally flat, with an average elevation of approximately 94 m above sea level. According to the Köppen–Geiger climate classification, the area is characterized by a humid continental climate with warm summers and no pronounced dry season. The total catchment area of the study district is 171.97 ha, while 125.14 ha were included in the numerical model and considered hydraulically connected to the drainage system. The analysed stormwater drainage network consists of more than 400 manholes and conduits, with pipe diameters ranging from 300 to 1500 mm. The drainage system discharges through five outfalls (IDs 23, 154, 155, 464 and 479), which drain subcatchment areas of 5.36 ha, 3.7 ha, 2.5 ha, 93.4 ha and 20.1 ha, respectively. Outfall 464 represents the dominant drainage outlet and receives runoff from the largest portion of the study area. These outfalls do not represent the final receiving points of the drainage system but connect to larger trunk sewers conveying wastewater and stormwater from other parts of the city towards the municipal wastewater treatment plant. Consequently, the analysed network represents a hydraulically distinct subsystem within the broader urban drainage system of Osijek.

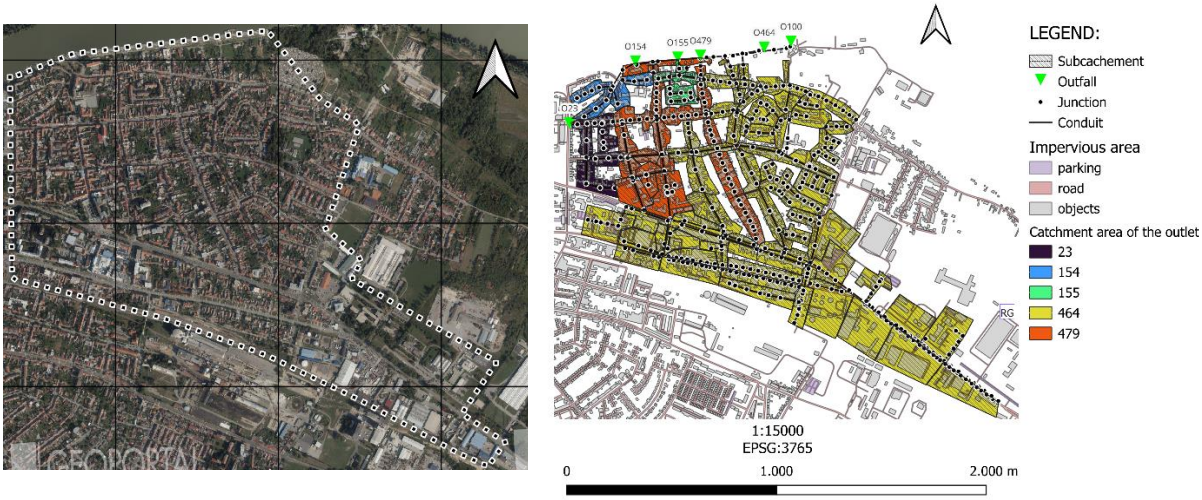


Figure 1. Study area: a) Satellite image, b) Numerical model

2.2 IDF curve and design hyetographs

Rainfall intensity–duration–frequency (IDF) relationships were derived from 5-min rainfall records collected during the period 2016–2025 from the meteorological station Osijek. Prior to the frequency analysis, individual precipitation events were identified and separated using the Kernel Density Estimation (KDE) approach proposed by Grubišić et al. (2026). The KDE method was selected because previous analyses demonstrated its ability to provide physically consistent event separation while reducing the subjectivity associated with fixed inter-event time criteria (Cao et al., 2023). The resulting IDF curves were used to construct design storms for three return periods (10, 20 and 50 years) and two storm durations (20 and 60 min). Two different design storm approaches were analysed: the Huff method and the Alternating Block Method (ABM). For the Huff method, Type 1 (T1) and Type 4 (T4) hyetographs were selected. These two storm patterns were identified as the most relevant for hydraulic analysis in previous studies conducted for the same climatic region (Grubišić et al., 2026). Type 1 represents storms with rainfall concentrated in the first quartile of the event, whereas Type 4 concentrates the dominant rainfall intensity in the final quartile. For the Alternating Block Method, design hyetographs were constructed directly from the derived IDF curves. Two rainfall distributions were considered: the R-1 configuration, where the maximum rainfall intensity occurs at the beginning of the event, and the R+1 configuration, where the maximum intensity occurs at the end of the event. These two variants were selected to investigate the influence of rainfall peak position on flooding generation and system response. Examples of the Huff curve and ABM hyetographs for the 50-year return period and t = 60 min are presented in Fig. 2.

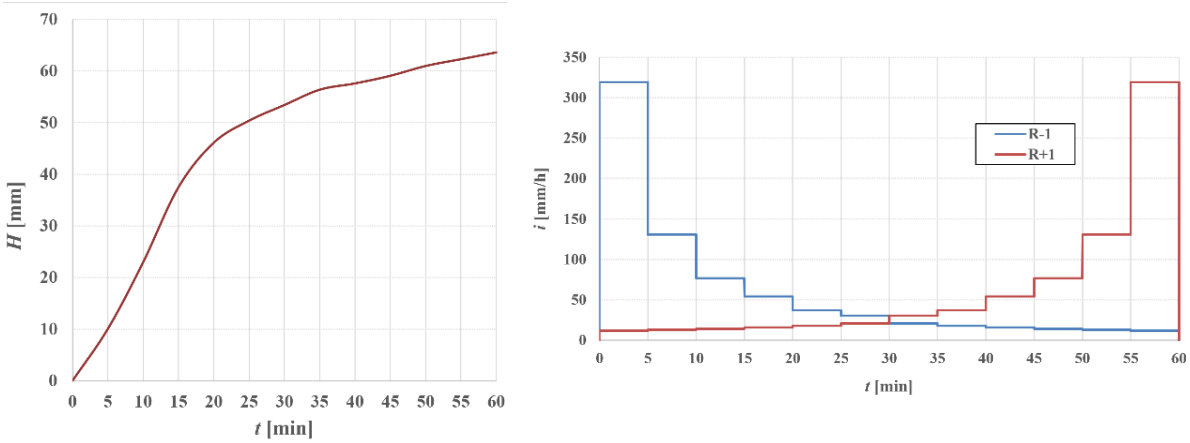


Figure 2. Representative design storms: a) Huff curve Type 1, b) ABM hyetographs

2.3 Numerical model setup

The numerical model was developed using the Storm Water Management Model (SWMM) and a GIS-based workflow. The drainage network geometry was derived from available geodetic documentation originally prepared in AutoCAD format. After georeferencing, the network layout was imported into the QGIS environment, where manholes and conduits were represented as point and line layers, respectively. A Digital Orthophoto Map (DOF, LiDAR 2025) was used as the background layer to support the delineation of subcatchment boundaries and the identification of local drainage directions. Subcatchment areas were obtained from GIS analysis, while conduit dimensions and elevations were imported directly from the geodetic database. Buildings, roads and parking areas were extracted from OpenStreetMap data and assigned to individual subcatchments. The resulting spatial layers were combined with the drainage network using the Generate SWMM INP plugin, which was subsequently used to create the SWMM model structure.

The final model consists of 90 subcatchments, 437 junctions, 442 conduits and 5 outfalls (Fig. 1b). The subcatchment width parameter was estimated according to recommendations provided in the SWMM Reference Manual, using the ratio between subcatchment area and the longest hydraulic flow path. To reduce the number of uncertain parameters, several model properties were assigned uniformly throughout the study area. Manning's roughness coefficient for conduits was set to 0.012, while the remaining hydraulic parameters were retained at their default SWMM values. Flow routing was performed using the Dynamic Wave approach.

2.4 Scenario analysis

The hydraulic performance of the drainage system was evaluated through a series of design storm simulations. Four design storm configurations were analysed: Huff Type 1 (T1), Huff Type 4 (T4), ABM (R-1), and ABM (R+1). Each storm configuration was analysed for three return periods (P = 10, 20 and 50 years) and two storm durations (t = 20 and 60 min). This resulted in a total of 24 simulation scenarios (4 storm configurations × 3 return periods × 2 durations). The analysed scenarios are summarized in Table 1.

Table 1. Analysed scenarios

Method	Variant	P [years]	t [min]
Huff	T1	10, 20, 50	20, 60
	T4	10, 20, 50	20, 60
ABM	R-1	10, 20, 50	20, 60
	R+1	10, 20, 50	20, 60

2.5 Evaluation Criteria

The simulated scenarios were evaluated using flooding, outfall loading and spatial performance indicators. Flooding performance was assessed through the number of flooded nodes, total flood volume, maximum flooding duration, maximum flooding rate and maximum flood volume recorded at an individual node. These indicators were selected to quantify both the extent and severity of flooding within the drainage system. The hydraulic response at the system outlets was evaluated using maximum discharge (Q_{max}) and average discharge (Q_{avg}). These parameters were used to assess the influence of rainfall distribution on peak loading and overall runoff generation. In addition, a spatial analysis of flooding patterns was performed. The analysis included identification of the most critical flooded nodes, assessment of the persistence of critical locations across different storm scenarios, and evaluation of the contribution of the most critical nodes to the total flood volume.

3 Results and Discussion

3.1 Huff design storm

The hydraulic response obtained using the Huff design storms was evaluated for Type 1 (T1) and Type 4 (T4) hyetographs. The results are discussed in terms of flooding characteristics and outfall loadings, followed by a direct comparison of the two Huff types.

3.1.1 Flooding

Flooding characteristics were first analysed separately for T1 and T4 considering the number of flooded nodes, flood volume, flooding duration and flooding rate. The persistence and spatial distribution of critical locations were also examined across the analysed return periods and storm durations.

3.1.1.1 Type 1

Results of the flooding analysis for the Huff Type 1 design storm are presented in Table 2. In all analysed scenarios, node 153 exhibited the longest flooding duration, indicating a persistent local hydraulic restriction independent of rainfall duration and return period. For return periods P10 and P20, rainfall duration had little influence on the total flood volume, although the spatial distribution of flooding differed. The 20-min storm produced a greater number of flooded nodes and higher flooding intensities, whereas the 60-min storm resulted in longer water retention at critical locations. For the extreme event (*P*50), the number of flooded nodes became nearly identical for both durations (122 and 119 nodes), while the 20-min storm generated approximately 49 % greater flood volume. These results indicate that the median Huff Type 1 storm is particularly sensitive to short-duration, high-intensity rainfall events. Critical flooding locations remained highly consistent across all scenarios, with nodes 850, 200, 72, 195, 396, 401, 135, 144 and 118 repeatedly appearing among the most affected areas.

Table 2. Flooding analysis for the Huff Type 1

P [year]	*t* [min]	Flooded Nodes	Total Flood Volume [10^6 l]	Max Hours Flooded [h] (Node ID)	Max Flooding Rate [l/s] (Node ID)	Max Node Flood Volume [10^6 l] (Node ID)
10	20	54	2.975	0.36 (153)	941 (275)	0.328 (850)
10	60	36	2.982	0.78 (153)	899 (144)	0.497 (850)
20	20	84	5.731	0.38 (153)	1520 (275)	0.428 (850)
20	60	53	5.721	0.97 (153)	754 (144)	0.753 (850)
50	20	122	10.958	0.46 (153)	2688 (356)	0.620 (850)
50	60	119	7.351	0.24 (153)	2326 (275)	0.473 (850)

3.1.1.2 Type 4

Results of the flooding analysis for the Huff Type 4 design storm are presented in Table 3. Similar to the Type 1, node 153 consistently exhibited the longest flooding duration in all analysed scenarios, confirming its role as one of the most critical locations within the system.

Increasing the return period resulted in higher flood volumes and a greater number of flooded nodes. For P10 and P20, the 20-min storm generally produced more flooded nodes, while total flood volumes remained similar for both durations. Unlike Type 1, however, the differences between the 20- and 60-min storms almost disappeared for the extreme event (*P*50), where both durations generated nearly identical flood volumes and numbers of flooded nodes. This behaviour indicates a lower sensitivity of Type 4 to rainfall duration. Critical flooding locations were largely identical to those identified for Type 1, with nodes 850, 200, 72, 195, 396, 401, 135, 144 and 118 repeatedly appearing among the most affected areas, confirming that the location of flooding is governed primarily by system hydraulics rather than by the selected design storm shape.

Table 3. Flooding analysis for the Huff Type 4

P [year]	*t* [min]	Flooded Nodes	Total Flood Volume [10^6 l]	Max Hours Flooded [h] (Node ID)	Max Flooding Rate [l/s] (Node ID)	Max Node Flood Volume [10^6 l] (Node ID)
10	20	52	2.898	0.26 (153)	743 (144)	0.288 (850)
10	60	30	2.586	0.42 (153)	776 (144)	0.584 (850)
20	20	64	5.398	0.37 (153)	913 (396)	0.356 (396)
20	60	37	5.114	0.49 (153)	648 (396)	0.753 (850)
50	20	92	10.035	0.40 (153)	1924 (356)	0.535 (396)
50	60	49	10.286	0.75 (153)	888 (396)	0.903 (850)

3.1.2 Outfall loadings

The hydraulic response at the system outlets was analysed for both Huff design storm types using maximum (Q_{max}) and average (Q_{avg}) discharge. The analysis focused on the effects of storm duration, return period and catchment size on outfall loading.

3.1.2.1 Type 1

Table 4 presents the results of the outfall loading analysis for the Huff Type 1 design storm. The analysis includes maximum (Q_{max}) flows for all analysed return periods and rainfall durations. The results indicate that the influence of rainfall duration on peak flows strongly depends on catchment size. The largest catchment (outfall 464) shows very low sensitivity to rainfall duration, whereas the smaller catchments (outfalls 154, 155 and 23) exhibit substantially higher peak flows for the 20-min storm. This behaviour confirms that short-duration, high-intensity rainfall events more efficiently activate small urban catchments with short concentration times. Increasing the return period results in higher peak flows at all outfalls, although the increase is considerably more pronounced for the smaller catchments than for the larger drainage areas.

Average flows Q_{avg} show a similar dependence on catchment size. Average flow increases with increasing return period for both rainfall durations, with the largest relative increases observed at outfall 23 and the smallest at outfall 464. These results indicate that average flows reflect the overall hydraulic loading of the system, while peak flows are more directly controlled by rainfall concentration and catchment response time. Overall, Huff Type 1 emphasises the influence of short-duration, high-intensity rainfall on the hydraulic response of smaller urban catchments.

Table 4. Maximum outfall discharge [l/s] for the Huff Type 1

Outfall	Area [ha]	Impervious [%]	*P*10 Q_{max} 60*	*P*10 Q_{max} 20*	Ratio	*P*20 Q_{max} 60	*P*20 Q_{max} 20	Ratio	*P*50 Q_{max} 60	*P*50 Q_{max} 20	Ratio
464	93.4	43	5267	5313	1.01	5326	5327	1.00	5339	5760	1.08
479	20.1	52	3172	3544	1.12	3631	3963	1.09	4157	4522	1.09
154	3.7	56	695	1220	1.76	835	1524	1.83	1113	1643	1.48
155	2.5	60	475	741	1.56	561	930	1.66	722	1338	1.85
23	5.36	54	543	878	1.62	831	990	1.19	1071	1284	1.20

Note: $Q_{max}60$ – maximum discharge for precipitation duration t = 60 min, $Q_{max}20$ – maximum discharge for t = 20 min

3.1.2.2 Type 4

Table 5 presents the results of the outfall loading analysis for the Huff Type 4 design storm. Similar to the Type 1, the influence of rainfall duration is strongly dependent on catchment size. The largest catchment (outfall 464) remains largely insensitive to rainfall duration, whereas the smaller catchments consistently produce higher peak flows for the 20-min storm. This effect is particularly evident for outfalls 154, 155 and 23, confirming the strong response of small urban catchments to short-duration rainfall events. Peak flows increase with return period at all outfalls, although the increase is substantially smaller for the largest drainage area.

Average flows increase progressively with return period for both rainfall durations. The largest relative increases are again observed at the smaller catchments, while outfall 464 shows only moderate changes. Compared with peak flows, average flows better represent the cumulative hydraulic loading of the system throughout the event. The results indicate that Huff Type 4 is also sensitive to rainfall duration, although the response is generally less pronounced than for Type 1, particularly for extreme events where differences between durations become smaller.

Table 5. Maximum outfall discharge [l/s] for the Huff Type 4

Outfall	Area [ha]	Impervious [%]	*P*10 Q_{max} 60	*P*10 Q_{max} 20	Ratio	*P*20 Q_{max} 60	*P*20 Q_{max} 20	Ratio	*P*50 Q_{max} 60	*P*50 Q_{max} 20	Ratio
464	93.4	43	5246	5328	1.02	5325	5339	1.00	5331	5352	1.00
479	20.1	52	2914	3472	1.19	3279	3862	1.18	3798	4536	1.19
154	3.7	56	536	824	1.54	658	1057	1.61	842	1392	1.65
155	2.5	60	370	556	1.50	448	667	1.49	556	970	1.74
23	5.36	54	174	817	4.70	546	928	1.70	876	1249	1.42

3.1.3 Comparison of Type 1 and Type 4

The comparison of results indicates that changing the Huff storm type does not alter the location of the critical areas within the drainage system. Regardless of return period and rainfall duration, the most affected locations are consistently associated with nodes 850, 200, 72, 195, 396, 401, 135, 144 and 118. Critical locations are marked in Fig. 3. Node 850 dominates most P10 and P20 scenarios, whereas node 200 becomes increasingly important during the most extreme events (P50). The persistence of these locations for both Huff types confirms that the identified critical areas represent actual hydraulic weaknesses of the system rather than artefacts of the selected design hyetograph.



Figure 3. Critical flooding locations

The main difference between Types 1 and 4 is reflected in the intensity and spatial distribution of flooding. Type 1 generally produces a larger number of flooded nodes, higher flood volumes and higher

flooding rates than Type 4, particularly for the extreme P50 event. In contrast, Type 4 tends to concentrate a larger proportion of the total flood volume within a smaller number of critical nodes, indicating a more localized flooding pattern. For both storm types, increasing the return period causes a transition from localized to distributed flooding, as the contribution of the ten most critical nodes gradually decreases and flooding spreads to a larger portion of the network.

The outfall analysis reveals that the sensitivity to storm shape strongly depends on catchment size. The largest catchment (outfall 464) shows almost identical peak flows for both storm types, whereas smaller catchments (154, 155 and 23) are considerably more sensitive. In these catchments, Type 1 consistently generates higher peak flows than Type 4, indicating that the influence of storm temporal distribution increases with decreasing catchment area and concentration time. A similar pattern is observed for average flows. At lower return periods, Type 1 generally produces higher average flows, while the differences gradually diminish as the return period increases. For the P50 event, average flows become nearly identical, suggesting that total rainfall depth becomes more important than rainfall distribution during extreme events.

Overall, Type 1 may be considered the more hydraulically critical of the two analysed Huff storm types because it generally results in larger flood volumes, more flooded nodes and higher peak flows in smaller catchments. However, the strong agreement in the location of critical areas significantly increases confidence in the identification of vulnerable parts of the system and confirms that these locations are governed primarily by the hydraulic structure of the network. The observed differences between Types 1 and 4 should also be interpreted in the context of the median Huff curves used in this study. Although both represent characteristic storm patterns within their respective quartiles, the median Type 1 curve exhibits a noticeably steeper rise within its dominant quartile than the median Type 4 curve. This results in a higher concentration of rainfall over a shorter period and consequently larger peak flows, greater flood volumes and more extensive flooding. Therefore, the differences between T1 and T4 cannot be attributed solely to the position of the storm peak, but also to the different rainfall concentration within the dominant quartile. Since median Huff curves were applied, the analysed scenarios do not represent the most critical storms possible within each quartile. The use of lower-percentile Huff curves (e.g., the 25th percentile) could potentially produce even higher peak flows and more severe flooding conditions.

3.2 Alternating block method

The hydraulic response obtained using the Alternating Block Method was evaluated for the R-1 and R+1 configurations. The analysis followed the same structure as for the Huff design storms, considering flooding characteristics and outfall loadings, followed by a direct comparison of the two variants.

3.2.1 Flooding

Flooding characteristics were analysed separately for R-1 and R+1 using the same evaluation criteria applied to the Huff design storms, enabling a consistent comparison of the effects of rainfall peak position on system response.

3.2.1.1 Variant R-1

Table 6 presents the flooding results obtained using the alternating block method with the peak rainfall intensity located at the beginning of the storm event (R-1). The number of flooded nodes increases with increasing return period, from 39 nodes for P10 to 101 nodes for P50, while rainfall duration has little influence on the number of affected locations within the same return period. In contrast, rainfall duration strongly affects both total flood volume and flooding duration. For all analysed return periods, the 60-min storm produces larger flood volumes and longer flooding durations than the 20-min storm, with the largest difference observed for the P50 event.

As observed for the Huff design storms, node 153 consistently exhibits the longest flooding duration, whereas node 850 dominates most scenarios in terms of flood volume. The critical flooding areas remain

highly consistent across all analysed scenarios and are mainly associated with nodes 850, 200, 72, 195, 396, 401, 135, 144 and 118. The proportion of flood volume concentrated within the ten most critical nodes decreases from approximately 76–78 % for P10 to 44–50 % for P50, indicating a gradual transition from localized to more distributed flooding. Overall, the R-1 variant primarily emphasizes prolonged system loading, with longer rainfall durations resulting in larger flood volumes and longer water retention at critical locations.

Table 6. Flooding analysis for the ABM R-1

P [year]	*t* [min]	Flooded Nodes	Total Flood Volume [10^6 l]	Max Hours Flooded [h] (Node ID)	Max Flooding Rate [l/s] (Node ID)	Max Node Flood Volume [10^6 l] (Node ID)
10	20	39	2.518	0.37 (153)	767 (144)	0.400 (850)
10	60	39	2.839	0.74 (153)	767 (144)	0.514 (850)
20	20	61	5.100	0.39 (153)	883 (200)	0.471 (850)
20	60	61	5.920	0.99 (153)	883 (200)	0.735 (850)
50	20	101	10.183	0.45 (153)	1649 (275)	0.644 (396)
50	60	101	12.272	1.10 (153)	1649 (275)	1.136 (850)

3.2.1.2 Variant R+1

Table 7 presents the flooding results obtained using the alternating block method with the peak rainfall intensity located at the end of the storm event (R+1). Compared with R-1, this configuration produces substantially greater hydraulic loading of the system. The number of flooded nodes increases from approximately 70 for P10 to about 120 for P50, while the total flood volume reaches 15.210 × 10^6 l for the P50, 60-min scenario, representing the highest value among all analysed design storm variants.

Table 7. Flooding analysis for the ABM R+1

P [year]	*t* [min]	Flooded Nodes	Total Flood Volume [10^6 l]	Max Hours Flooded [h] (Node ID)	Max Flooding Rate [l/s] (Node ID)	Max Node Flood Volume [10^6 l] (Node ID)
10	20	69	3.529	0.26 (153)	872 (144)	0.259 (200)
10	60	83	5.469	0.28 (153)	987 (144)	0.388 (850)
20	20	95	6.298	0.28 (153)	1087 (200)	0.373 (200)
20	60	105	8.990	0.32 (153)	1311 (275)	0.465 (850)
50	20	121	11.254	0.32 (153)	1513 (275)	0.555 (200)
50	60	120	15.210	0.38 (153)	1673 (830)	0.649 (200)

Although node 153 again exhibits the longest flooding duration in all scenarios, maximum flooding durations remain considerably shorter than those obtained for R-1. Unlike R-1, where flooding is concentrated within a limited number of dominant locations, R+1 produces a more spatially distributed flooding pattern. This is reflected by the lower contribution of the ten most critical nodes, which accounts for only 33–49 % of the total flood volume. Nevertheless, the core critical areas remain largely unchanged and are consistently associated with nodes 850, 200, 396, 401, 195, 135, 144 and 275. Overall, the R+1 variant promotes wider spatial spreading of flooding, as the delayed peak intensity allows the system to become partially filled before the most intense rainfall occurs.

3.2.2 Outfall loadings

Outfall loading for the Alternating Block Method was evaluated using maximum and average discharge at the five analysed outfalls. The influence of rainfall peak position, return period and storm duration is discussed below.

3.2.2.1 Variant R-1

Table 8 presents the maximum (Q_{max}) outfall flows obtained for the R-1 variant of the alternating block method. The results reveal a distinctive hydraulic response compared to the Huff design storms. Peak flows are identical for the 20- and 60-min storm durations at all analysed outfalls, indicating that the position of the maximum rainfall intensity at the beginning of the event effectively eliminates the influence of storm duration on Q_{max}. Under these conditions, peak flows are controlled primarily by return period and catchment size. While the largest catchment (outfall 464) exhibits only a minor increase in peak flow with increasing return period, smaller catchments show a substantially stronger response, reflecting their shorter concentration times and lower storage capacity.

Average flow increases progressively with increasing return period for all outfalls, with the largest relative increases observed at outfall 23 and the smallest at outfall 464. These results indicate that average flows better represent the cumulative hydraulic loading of the system, whereas peak flows are governed primarily by the initial rainfall pulse. Overall, the R-1 configuration highlights the influence of early rainfall concentration and demonstrates that smaller catchments are considerably more sensitive to increasing rainfall intensity than larger drainage areas.

Table 8. Maximum outfall discharge [l/s] for the ABM R-1

Outfall	Area [ha]	Impervious [%]	*P*10 Q_{max} 60	*P*10 Q_{max} 20	Ratio	*P*20 Q_{max} 60	*P*20 Q_{max} 20	Ratio	*P*50 Q_{max} 60	*P*50 Q_{max} 20	Ratio
464	93.4	43	5233	5233	1.00	5323	5323	1.00	5417	5417	1.00
479	20.1	52	3221	3221	1.00	3735	3735	1.00	4345	4345	1.00
154	3.7	56	1004	1004	1.00	1230	1230	1.00	1553	1553	1.00
155	2.5	60	596	596	1.00	747	747	1.00	1091	1091	1.00
23	5.36	54	630	630	1.00	890	890	1.00	1211	1211	1.00

3.2.2.2 Variant R+1

Unlike R-1, this configuration exhibits a moderate sensitivity to storm duration (Table 9). Although the largest catchment (outfall 464) shows nearly identical peak flows for both durations, smaller catchments generally produce slightly higher peak flows for the 60-min storm. This behaviour can be attributed to the delayed occurrence of the peak rainfall intensity, which allows the drainage network to become partially filled before the most intense rainfall occurs.

Peak flows increase with return period at all outfalls, although the increase is considerably more pronounced for smaller catchments than for the largest drainage area. Average flows follow a similar trend, showing a gradual increase with return period for both rainfall durations. However, compared with R-1, the relative increase in Q_{avg} is generally smaller, indicating a lower sensitivity of the system to changes in return period. Overall, the R+1 configuration demonstrates that delayed peak intensities can increase hydraulic loading by combining rainfall concentration with antecedent system filling, particularly within smaller urban catchments.

Table 9. Maximum outfall discharge [l/s] for the ABM R+1

Outfall	Area [ha]	Impervious [%]	*P*10 Q_{max} 60	*P*10 Q_{max} 20	Ratio	*P*20 Q_{max} 60	*P*20 Q_{max} 20	Ratio	*P*50 Q_{max} 60	*P*50 Q_{max} 20	Ratio
464	93.4	43	5350	5330	1.00	5360	5353	1.00	5359	5360	1.00
479	20.1	52	3962	3695	0.93	4549	4512	0.99	4550	4562	1.00
154	3.7	56	1233	1152	0.93	1524	1473	0.97	1666	1629	0.98
155	2.5	60	784	732	0.93	1095	1000	0.91	1439	1403	0.98
23	5.36	54	1013	898	0.89	1337	1213	0.91	1384	1384	1.00

3.2.3 Comparison of R-1 and R+1 variants

The comparison of results demonstrates that the position of the peak rainfall intensity has a significant influence on the hydraulic response of the drainage system. Although both variants are based on the same rainfall depth and return periods, they produce substantially different flooding and runoff patterns. The most pronounced differences are observed in flooding behaviour. In all analysed scenarios, the R+1 variant generates a greater number of flooded nodes and larger total flood volumes than R-1. The difference is particularly evident for longer storm durations. For example, for the P50, 60-min event, the total flood volume increases from 12.272×10^6 l for R-1 to 15.210×10^6 l for R+1. In contrast, R-1 produces considerably longer flooding durations at the most critical locations, with maximum flooding durations reaching 1.10 h compared with only 0.38 h for R+1. This indicates that R-1 creates more concentrated and persistent flooding, whereas R+1 results in a wider spatial distribution of flooding across the system. This interpretation is supported by the analysis of the ten most critical nodes. For R-1, the ten largest nodes account for approximately 44–78 % of the total flood volume, whereas their contribution decreases to 33–49 % for R+1. Despite these differences, the critical locations remain largely unchanged. Nodes 850, 200, 396, 401, 195, 135 and 144 repeatedly appear among the most vulnerable locations in both variants, confirming that the identified critical areas are controlled primarily by the hydraulic structure of the system rather than by the selected storm pattern.

The outfall analysis further highlights the influence of peak rainfall position. In the R-1 configuration, peak flows are independent of storm duration because the maximum rainfall intensity occurs immediately at the beginning of the event. In contrast, R+1 produces slightly higher peak flows for longer storm durations, particularly in smaller catchments, due to the gradual filling of the system before the peak intensity occurs. Both variants show increasing peak and average flows with increasing return period, although the sensitivity is generally higher for R-1 than for R+1. The largest differences are observed in the smaller catchments, whereas the largest catchment (outfall 464) exhibits nearly identical behaviour for both variants. Overall, R+1 can be considered the more hydraulically critical configuration. Although differences in outfall flows are relatively modest, R+1 consistently generates larger flood volumes and a greater number of flooded nodes. These results indicate that the most adverse hydraulic conditions occur when the peak rainfall intensity is delayed until the drainage network has already become partially filled, reducing the available storage and conveyance capacity of the system.

4 Conclusion

The results demonstrate that the selected design storm model significantly affects the intensity and spatial extent of flooding, while having a much smaller influence on the identification of critical areas within the drainage system. Regardless of the applied storm model, return period, or rainfall duration, the same locations repeatedly emerged as the most vulnerable parts of the network. This indicates that critical areas are governed primarily by the hydraulic structure and capacity limitations of the system rather than by the selected design hyetograph.

Type 1 generally produced larger flood volumes, a greater number of flooded nodes and higher outfall loadings than Type 4, although these differences became progressively smaller with increasing return period. This behaviour is associated with the steeper rise of the median Type 1 curve within its dominant quartile, resulting in a stronger concentration of rainfall over a shorter period. However, the differences between the two Huff types gradually decrease with increasing return period, suggesting that total rainfall depth becomes more influential than temporal rainfall distribution during extreme events. The Alternating Block Method exhibited greater sensitivity to the temporal position of peak rainfall intensity than the Huff method. While the R-1 variant produced more concentrated flooding and longer flooding durations at critical locations, the R+1 variant consistently generated larger flood volumes and a greater number of flooded nodes. These results indicate that the most severe flooding conditions occur when the rainfall peak is delayed until the drainage system has already become partially filled. The analysis of outfall flows further demonstrated that catchment size plays a key role in controlling system response. Large catchments showed limited sensitivity to storm shape and duration, whereas smaller catchments

exhibited substantially greater variations in both peak and average flows. This confirms that the influence of rainfall distribution decreases with increasing catchment area and concentration time.

Future urban development should also be considered when interpreting these results. An increase in built-up and impervious areas would reduce infiltration losses and increase both the volume and rate of surface runoff entering the drainage system. Consequently, higher discharges and more extensive flooding than those obtained under the present land-use conditions can be expected. The magnitude of this effect may also depend on rainfall temporal distribution. Storm patterns characterized by an early concentration of high rainfall intensities, such as T1 and R-1, may be particularly sensitive to increased imperviousness because reduced initial losses promote a more rapid runoff response. Overall, the results show that Huff design storms provide a relatively stable representation of system behaviour, whereas the alternating block method is considerably more sensitive to rainfall distribution within the event. Among the analysed design storms, the R+1 configuration represents the most conservative scenario for hydraulic assessment of existing urban drainage systems and may therefore be particularly suitable for evaluating future urban development and increasing catchment imperviousness.

Acknowledgements

Funded by the European Union – Next Generation EU. However, the views and opinions expressed are solely those of the author(s) and do not necessarily reflect those of the European Union or the European Commission. Neither the European Union nor the European Commission can be held responsible for them.

References

Bezak, N., Šraj, M., Rusjan, S. and Mikoš, M. 2018 Impact of the rainfall duration and temporal rainfall distribution defined using the Huff curves on the hydraulic flood modelling results. *Geosciences* 8 (2), 69.

Bonacci, O. 1994 *Oborine – analiza, obrada i primjena*. Građevinski institut Hrvatske, Zagreb, Croatia.

Cao, S., Diao, Y., Wang, J., Liu, Y., Raimondi, A. and Wang, J. 2023 KDE-based rainfall event separation and characterization. *Water* 15 (3), 580.

Dunkerley, D. 2008 Identifying individual rain events from pluviograph records: a review with analysis of data from an Australian dryland site. *Hydrological Processes* 22, 5024–5036.

Dunkerley, D. 2022 Regional rainfall regimes affect the sensitivity of the Huff quartile classification to the method of event delineation. *Water* 14 (7), 1047.

Grubišić, M., Šreng, Ž., Berbić, J. and Brleković, T. 2026 Systematic assessment of minimum inter-event time determination methods and precipitation thresholds for constructing design-critical Huff hyetographs. *Water* 18 (8), 976.

Huff, F.A. 1967 Time distribution of rainfall in heavy storms. *Water Resources Research* 3 (4), 1007–1019.

Krvavica, N. and Rubinić, J. 2020 Evaluation of design storms and critical rainfall durations for flood prediction in partially urbanized catchments. *Water* 12 (7), 2044.

Nguyen, D.T. and Chen, S.T. 2022 Generating continuous rainfall time series with high temporal resolution by using a stochastic rainfall generator with a copula and modified Huff rainfall curves. *Water* 14 (13), 2123.

Pilgrim, D.H. and Cordery, I. 1975 Rainfall temporal patterns for design floods. *Journal of the Hydraulics Division, ASCE* 101 (HY1), 81–85.

Wartalska, K., Kaźmierczak, B., Nowakowska, M. and Kotowski, A. 2020 Analysis of hyetographs for drainage system modeling. *Water* 12 (1), 149.

Yin, S., Xie, Y., Nearing, M.A., Guo, W. and Zhu, Z. 2016 Intra-storm temporal patterns of rainfall in China using Huff curves. *Transactions of the ASABE* 59 (6), 1619–1632.

CORRECT ADOPTION OF THE TWO-DIMENSIONAL DISPERSION TENSOR FOR POLLUTANT PROPAGATION IN WIDE RIVERS

Piotr ZIMA [1*]

[1] *Gdansk University of Technology, Faculty of Civil and Environmental Engineering, Poland*

E-mail: piotr.zima@pg.edu.pl

[*] *Corresponding author*

Abstract

This article addresses the issue of correctly determining two-dimensional dispersion tensor elements in real river flow conditions, with particular emphasis on wide channels with a pronounced velocity profile across the cross-section. This problem is of fundamental importance for modelling pollutant transport in surface waters, especially in situations involving accidental discharges of dissolved substances into rivers of large width, complex morphology, and the presence of terrain obstacles (e.g., islands, sandbars, spurs).

Key words

wide rivers, migration of pollutants in water, two-dimensional dispersion, mass dispersion, dispersion coefficients

1 Introduction

The process of transport and dispersion of pollutants in surface waters is one of the fundamental issues of contemporary environmental hydrodynamics and hydraulic engineering (Bear 1979,1988, Chapra 1997, Deng et al. 2001, Deng and Singh 2001). Modelling the migration of dissolved substances in large rivers is of particular importance, where, in the case of accidental pollutant discharges, it is necessary to quickly determine the direction of pollutant propagation, its transit time, and the potential impact on water intakes and the river ecosystem (Chapra 1997, Fischer et al. 1979, Rutherford 1994). In engineering practice, the advection-dispersion equation is commonly used to describe these processes, a key element of which is the correct determination of hydrodynamic dispersion coefficients (Bear 1988, Chapra 1997). The dispersion coefficient values assumed in pollutant transport models directly influence the results of numerical calculations. They determine the projected rate of plume spread, its shape, dilution rate, concentration field asymmetry, and the time it takes for pollutants to reach control cross-sections. In rivers and shallow coastal areas, these parameters should not be considered universal, as they depend on local hydraulic conditions, channel geometry, depth, turbulence structure, degree of mixing, and the scale of the process being analyzed.

The beginnings of research on hydrodynamic dispersion in open streams are associated with the classic works of Taylor (Taylor, 1953) and Elder (Elder, 1959), who demonstrated that a heterogeneous flow velocity distribution leads to an intensification of the longitudinal mixing process. Taylor demonstrated the fundamental role of turbulence and velocity gradients in the dispersion of solutes, while Elder proposed some of the first practical relationships enabling the estimation of longitudinal and transverse dispersion coefficients based on hydraulic flow parameters. In subsequent years, models were developed describing the dependence of dispersion coefficients on mean flow velocity, depth, hydraulic radius, and bed shear stress (Deng et al. 2001, Fischer 1968, 1973). A particularly significant contribution to the development of river dispersion theory was made by Fischer (1973), who demonstrated that the dispersion process in rivers is directly related to velocity gradients in the cross-section and to turbulent vertical and transverse mixing. Fischer also emphasized the importance of incomplete mixing of substances in the initial phase of plume propagation (Fischer 1968, 1979). Subsequent studies by

Rutherford (1994), Seo and Cheong (1998), Deng and Singh (2001), Kashefipour and Falconer (2002), and Valentine and Wood (1977) indicated that the use of constant dispersion coefficients can lead to significant errors in predicting pollutant transport, particularly in wide, multi-stream rivers with complex channel geometry. The authors noted that dispersion coefficient values depend not only on the hydraulic parameters of the flow but also on the local turbulence structure, channel geometry, and the presence of terrain obstacles.

In most modern pollutant transport models, however, the dispersion tensor is simplified to a diagonal form, which only considers longitudinal and transverse dispersion (Chapra 1997, Falconer and Lin 1997, Rodi 1993). This approach assumes no coupling between transport directions and ignores the influence of off-diagonal components of the dispersion tensor. In practice, this means disregarding the rotation of the principal axes of the pollutant plume and the asymmetric development of the concentration field (Sawicki and Zima 1997). Additionally, the values of the dispersion tensor coefficients are assumed incorrectly.

The assumption of a diagonal tensor shape may be sufficient for simple laboratory channels or narrow streams with uniform flow (Fischer, 1976). However, in real natural rivers, numerous factors disturb the flow structure, such as islands and sandbars, bends, local channel narrowing and widening, depth variations, reverse flows, wind effects, and stagnation zones near the banks.

These factors lead to the development of strong velocity gradients and local transport anisotropy (Nezu and Nakagawa 1993, Nikora and Roy 2012, Shen and Niu 2018). Particularly in wide rivers, a significant influence of the conjugate components of the dispersion tensor on the direction of plume migration and the rate of lateral mixing has been observed.

In recent years, interest in using the full dispersion tensor in environmental models has increased, particularly in analyses of pollutant transport in estuaries, coastal zones, and large lowland rivers (Shen and Niu 2018, Wang et al. 2015). However, field studies enabling the unambiguous determination of tensor coordinates based on actual measurement data are still lacking. Most available studies are based on laboratory analyses or adopt simplified assumptions regarding the velocity field and turbulence isotropy (Deng and Singh 2001, Rodi 1993).

A significant problem also remains distinguishing between true turbulent dispersion and the effect of incomplete mixing resulting from a non-uniform velocity distribution (Fischer, 1968, Rutherford 1994). In many cases, both phenomena are treated together, which complicates the physical interpretation of dispersion coefficients and limits their transferability across different hydraulic conditions.

The aim of this study is to analyze the significance of dispersion coefficient values adopted in modeling pollutant transport in rivers and shallow coastal areas. The study is not limited to the formal determination of dispersion coefficients, but focuses on assessing the modeling consequences resulting from the adoption of specific values for the horizontal dispersion tensor components. Particular attention is paid to how the values of longitudinal and transverse dispersion coefficients, as well as off-diagonal components, influence the shape, orientation, extent, and asymmetry of the pollutant plume. The study was conducted for a section of the Vistula River near Włocławek, using data from tracer measurements and numerical simulations based on the two-dimensional advection-dispersion equation. The analyzed case of a wide river channel with an island allows for the assessment of the impact of varying dispersion tensor values on pollutant propagation under conditions of a heterogeneous velocity field, local flow disturbances, and increased lateral transport. The hypothesis adopted in this study is that dispersion coefficient values used in models of rivers and shallow coastal areas should not be treated as universal parameters. Their selection directly impacts the reliability of concentration distribution forecasts, the assessment of coastal zone exposure, and the determination of environmental risk. Ignoring dispersion anisotropy or using typical values without reference to local hydraulic conditions can lead to an erroneous assessment of the extent of pollutant impact.

2 Methods

2.1 Mathematical model and solution area definition

2.1.1 Flow field characteristics

The analyzed section of the Vistula River near Włocławek is characterized by a significant channel width exceeding 200 [m] and the presence of an island that causes the main stream to split (Fig.1 and 2).



Figure 1. The analyzed section of the Vistula River near Włocławek.

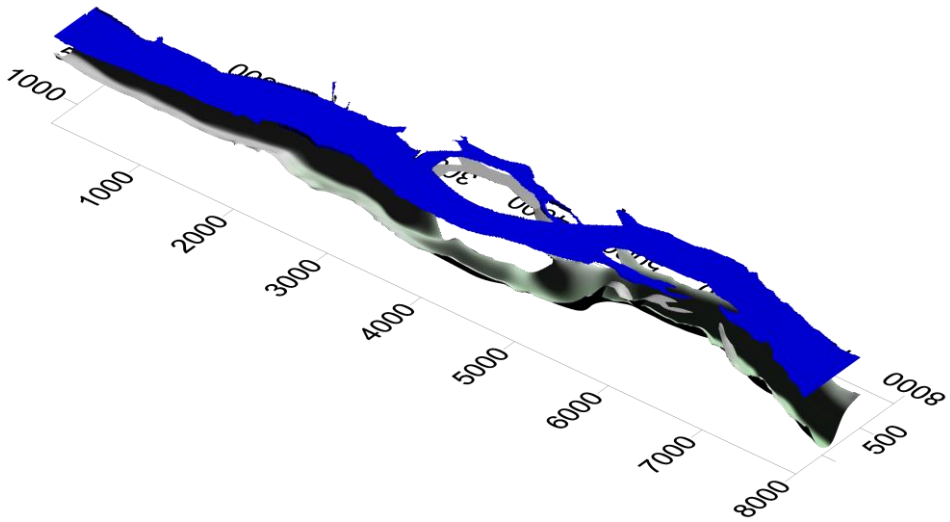


Figure 2. Generated numerical model of the bed and water table in the modeled section assuming a flow above the water table elevation for the mean low flow.

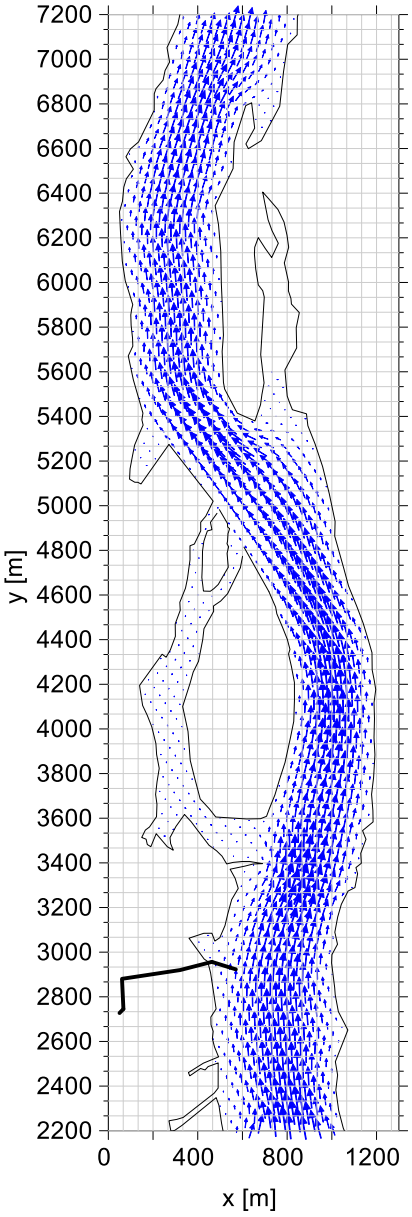


Figure 3. Calculated velocity distribution on the Vistula River section near Włocławek for the mean low flow.

As a result of variable flow geometry, a distinct differentiation of the velocity field was observed in both the longitudinal and transverse directions. This phenomenon is crucial for describing the transport of dissolved substances, as the heterogeneity of the velocity field leads to intensified hydrodynamic dispersion and an asymmetric concentration distribution (Fischer 1973, 1979, Rutherford 1994).

The velocity distribution on the Vistula River section in question was calculated using the Shallow Water Steady State Equations (Zima, 2018a, 2018b). The continuous solution region was divided into a discrete region using a square grid with sides $\Delta x = \Delta y = 5.0$ [m]. The calculated velocity distribution is shown in Fig.3.

The obtained velocity profiles indicate the occurrence of maximum velocity values (0.96 m/s) along the main stream axis, local zones of flow acceleration in narrowing areas, and areas of flow slowdown near the banks and behind the island. Local recirculation and stagnation zones could occur behind the river obstacle, which resulted in extended pollutant residence times in selected parts of the study area. Similar hydrodynamic effects are described in the literature as one of the significant mechanisms responsible for deviations from the classical, one-dimensional dispersion model (Nikora and Roy 2012, Valentine and Wood 1977).

The gradient nature of the velocity field resulted in a pronounced anisotropy of pollutant transport. Changes in the direction of velocity vectors in the area of the stream divide around the island proved particularly significant. These led to local rotation of the main axis of the plume propagation and to uneven development of the concentration field on both sides of the main stream. This means that the direction of maximum pollutant spread did not necessarily coincide with the geometric axis of the river or the direction of the main component of flow velocity (Shen and Niu 2018, Wang et al. 2015).

The results of the flow field analysis indicate that the assumption of a simplified, uniform velocity distribution would be insufficient in the analyzed case. In wide natural rivers, local hydraulic conditions, such as depth variations, the presence of islands, shoreline deformations, and the occurrence of free-flow zones, have a direct impact on the formation and movement of pollutant plumes (Nezu and Nakagawa 1993, Nikora and Roy 2012). The calculations were made for data near the planned sewage outlet ($Q = 0.7$ [m^3/s]), introduced through a pipe from the river bank (Fig. 2).

2.1.2 Assumptions for the pollutant transport model

The transport of dissolved substances in a river was described using a two-dimensional horizontal advection-dispersion equation (2DH) (Chapra 1997, Falconer and Lin 1997, Fischer 1979). It was assumed that the analyzed substance is passive and conservative, which means that chemical transformations, sedimentation, biodegradation, and thermal interactions are omitted (Bear 1988, Chapra 1997, Rutherford 1994). This assumption is commonly used in tracer analyses and in studies of hydrodynamic pollutant transport in rivers (Fischer 1979, Kilpatrick and Cobb 1985). In this study, it was assumed that: the flow is spatially unsteady but quasi-steady in time, the dominant transport mechanism is advection and turbulent dispersion, the vertical mixing process occurs faster than horizontal mixing, which allows for the use of a depth-averaged model (Falconer and Lin 1997, Nezu and Nakagawa 1993), the dispersion tensor is anisotropic. Then the transport equation was written in the form (Bear 1988, Shen and Niu 2018, Wang et al. 2015, Zima 2018, 2019, Zima and Sawicki 2024):

$$\frac{\partial(h\bar{c})}{\partial t}+\frac{\partial(h\overline{u_x}\bar{c})}{\partial x}+\frac{\partial(h\overline{u_y}\bar{c})}{\partial y}=\frac{1}{h}\frac{\partial}{\partial x}\left(hD_{xx}\frac{\partial\bar{c}}{\partial x}+hD_{xy}\frac{\partial\bar{c}}{\partial y}\right)+\frac{1}{h}\frac{\partial}{\partial y}\left(hD_{yx}\frac{\partial\bar{c}}{\partial x}+hD_{yy}\frac{\partial\bar{c}}{\partial y}\right) \quad (1)$$

where: x [m], y [m], t [s] - independent variables (spatial and time), h [m] – depth, $\bar{c}$ [kg/m^3]– depth-averaged concentration, $\overline{u_x}, \overline{u_y}$ [m/s] – depth-averaged components of the velocity vector, D_{xx}, D_{xy}, D_{yx}, D_{yy} [m^2/s] – coordinates of the dispersion tensor **D**:

$$[\mathbf{D}] = \begin{bmatrix} D_{xx} & D_{xy} \\ D_{yx} & D_{yy} \end{bmatrix} \tag{2}$$

Due to the transverse anisotropy of the dispersion process, the D_{ij} coefficients are expressed by local dispersion coefficients along the direction of velocity D_L [m^2/s] (longitudinal dispersion coefficient) and in the direction perpendicular to it D_T [m^2/s] (transverse dispersion coefficient):

$$\begin{aligned} D_{xx} &= D_L n_x^2 + D_T n_y^2 \\ D_{xy} &= D_{yx} = (D_L - D_T) n_x n_y \\ D_{yy} &= D_L n_y^2 + D_T n_x^2 \end{aligned} \tag{3}$$

where n_x [/] and n_y [/] are the coordinates of the **n** vector - cosines of the velocity vector **u**:

$$n_x = \frac{\overline{u_x}}{|\mathbf{u}|}, n_y = \frac{\overline{u_y}}{|\mathbf{u}|} \tag{4}$$

D_{xx} and D_{yy} denote the dispersion components in the principal directions of the coordinate system, respectively, while D_{xy} and D_{yx} are conjugate components describing the effect of the concentration gradient in one direction on the dispersion flux in the other direction.

The idea of solute mass dispersion is a compromise between the appropriateness of using average velocity distributions and the tendency to take consider the impact of the actual differentiation of these distributions. We owe a quantitative model of this process to Taylor (1953). In practice, for the free-surface flows in the coastal zone that interest us here, so the D_L and D_T coefficients are determined according to the classical proposal (Elder, 1959):

$$D_L = 5{,}93hu^*, \quad D_T = 0{,}23hu^* \tag{5}$$

where u^* [m/s] – shear velocity. This approach is correct mainly for straight channels with uniform flow (Fischer, 1976). In real natural rivers, however, the presence of islands, bends, stagnation zones and non-uniform velocity field causes transport anisotropy and rotation of the main dispersion axes (Nezu and Nakagawa 1993, Nikora and Roy2012, Shen and Niu 2018). In this work, the full dispersion tensor was adopted, enabling the description of the coupling between the longitudinal and transverse directions of plume propagation.

2.1.3 Numerical simulations of pollution plumes

Numerical simulations were performed for an actual river section using a computational mesh representing the geometry of the stream and the river island (Fig. 1 and 2). Boundary conditions included: a specified inflow in the upstream section (Q = 293 [m^3/s]), an open outflow condition in the downstream section, and impermeability conditions at the shorelines.

Two basic calculation variants were analyzed: dispersion coefficient coordinates selected for gravity flow, and a second variant with dispersion coefficients selected for drift flow (Zima 2024, Zima and Sawicki 2024). The comparative analysis assessed the impact of the assumed dispersion coefficient values on: plume shape, propagation rate, contamination zone width, bank exposure, concentration distribution asymmetry, location of the center of mass of the pollutant, time of arrival of the pollutant at the control cross-sections, and local concentration maxima in the riparian zones.

FEM and classical numerical procedures used in hydrodynamic models were used to solve the transport equation (Falconer and Lin 1997, Ferziger and Perić 2002, Zienkiewicz and Taylor 2000, LeVeque 2002), presented in previous papers (Zima 2018, 2019, 2014, Zima and Sawicki 2024). Comparison of calculation variants allowed for the assessment of the extent to which the adopted values of the dispersion tensor components influence the final result of pollutant transport modelling.

2.2 Traser measurements and analytical calculations

Field studies were conducted as part of previous work (Burdziakowski et al. 2021, Zima 2024). They covered the estuary section of the river and the coastal area. The analyzed section of the river is characterized by a width exceeding 200 m and the presence of an island dividing the stream. The study

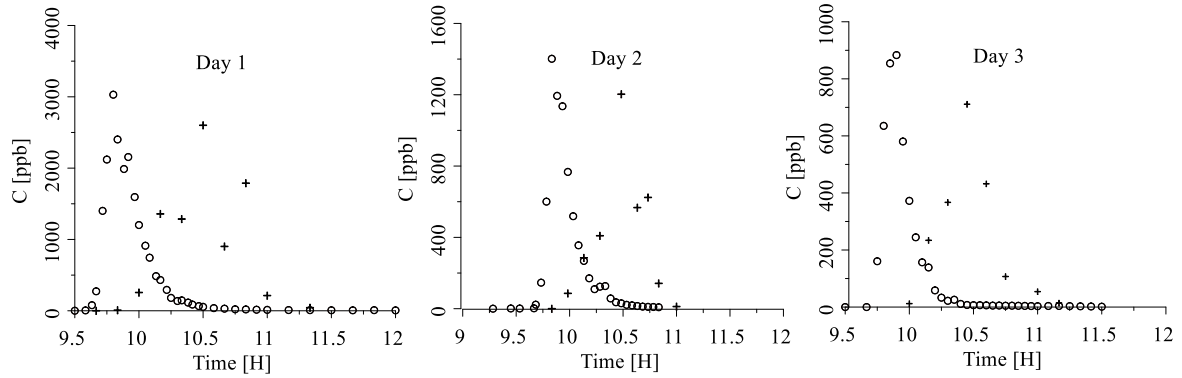


Figure 4. Results obtained from 2 points: at the river mouth into the sea (circles) and at a point 200 m away in the area of the coastal zone (crosses) (Burdziakowski et al. 2021).

employed the impulse tracer method, widely used in river mixing analyses (Kilpatrick and Cobb 1985, Rutherford 1994). Concentration changes were recorded in successive measurement cross-sections located downstream of the discharge point. Based on this, the longitudinal dispersion coefficient was determined. For the gradient velocity profile, the longitudinal dispersion coefficient D_L varied within the range of 0.35-0.56 [m^2/s], and for the drift velocity profile 1.33-2.57 [m^2/s] (Zima 2024). The analytically calculated longitudinal dispersion coefficients, presented in (Zima and Sawicki 2024), were respectively: for the gradient velocity profile $D_L = 0.17$ [m^2/s], for the drift profile $D_L = 89.94$ [m^2/s]. In this paper, the average values from tracing measurements were assumed, $D_L = 0.46$ [m^2/s] for the gradient profile and $D_L = 1.95$ [m^2/s] for the drift profile.

3 Results

3.1 Flow field characteristics

As a result of variable flow geometry, a distinct differentiation of the velocity field was observed in both the longitudinal and transverse directions. This phenomenon is crucial for describing the transport of dissolved substances, as the heterogeneity of the velocity field leads to intensified hydrodynamic dispersion and an asymmetric concentration distribution (Fischer 1973, 1979, Rutherford 1994).

The obtained velocity profiles for the mean low flow $Q = 293$ [m^3/s] indicate the occurrence of maximum velocity values in the main stream axis (0.96 m/s), local zones of flow acceleration in the narrowing areas, and areas of flow slowdown near the banks and behind the island. Local recirculation and stagnation zones could occur behind the river obstacle, which prolonged the pollutant residence time in selected parts of the study area. Similar hydrodynamic effects are described in the literature as one of the significant mechanisms responsible for deviations from the classical, one-dimensional dispersion model (Nikora and Roy 2012, Valentine and Wood 1977). The gradient nature of the velocity field resulted in a distinct anisotropy of pollutant transport. Changes in the direction of velocity vectors in the area of the stream divide around the island proved particularly significant. These led to local rotation of the main axis of the plume propagation and to uneven development of the concentration field on both sides of the main stream. This means that the direction of maximum pollutant spread did not necessarily coincide with the geometric axis of the river or the direction of the main component of flow velocity (Shen and Niu 2018, Wang et al. 2015).

The results of the flow field analysis indicate that the adoption of a simplified, uniform velocity

distribution would be insufficient in the analyzed case. In wide natural rivers, local hydraulic conditions, such as depth variability, the presence of islands, shoreline deformations and the presence of free flow zones, have a direct impact on the formation and movement of the pollution plume (Nezu and Nakagawa 1993, Nikora and Roy2012).

3.2 Propagation of pollution plume

Numerical simulations allowed us to analyze the temporal evolution of a pollutant plume following a pulsed discharge of a nonreactive substance into the river stream through an outlet located at some distance from the river bank towards its current. This is almost a steady state, after 5 hours of simulation. In the initial phase of propagation, advection was the dominant transport mechanism. The plume moved in the main flow direction, maintaining a relatively small lateral width. Maximum concentrations were maintained near the stream axis, where flow velocities were the highest.

With increasing distance from the discharge site, a turbulent dispersion process developed, leading to the plume's expansion and a decrease in maximum concentration values. However, this process was clearly asymmetric, resulting from the non-uniform velocity field and the presence of a river island. In the area of the island, the plume separated into two main streams, local deformations of the concentration field, and an increase in the pollutant retention time in zones of slower flow were observed.

The obtained results indicate that adopting incorrect dispersion coefficient values can lead to incorrect interpretations of plume development. In particular, it may result in overestimating the extent of pollution impact towards one of the banks and in an incorrect assessment of the time it takes for maximum concentrations to reach control cross-sections. This is particularly important in emergency analyses, where the precise determination of the time and location of the maximum threat has practical implications for the protection of water intakes and planning of interventions (Chapra 1997, Rutherford 1994).

In rivers, the tensor component values are strongly related to the velocity profile, the direction of the mainstream, and the channel geometry. Longitudinal dispersion usually remains dominant, but conjugate components can determine the plume's deflection and its contact with coastal zones. In shallow coastal areas, the tensor component values should reflect the more complex and multidirectional nature of transport, resulting from the effects of wind, waves, depth variations, and local currents.

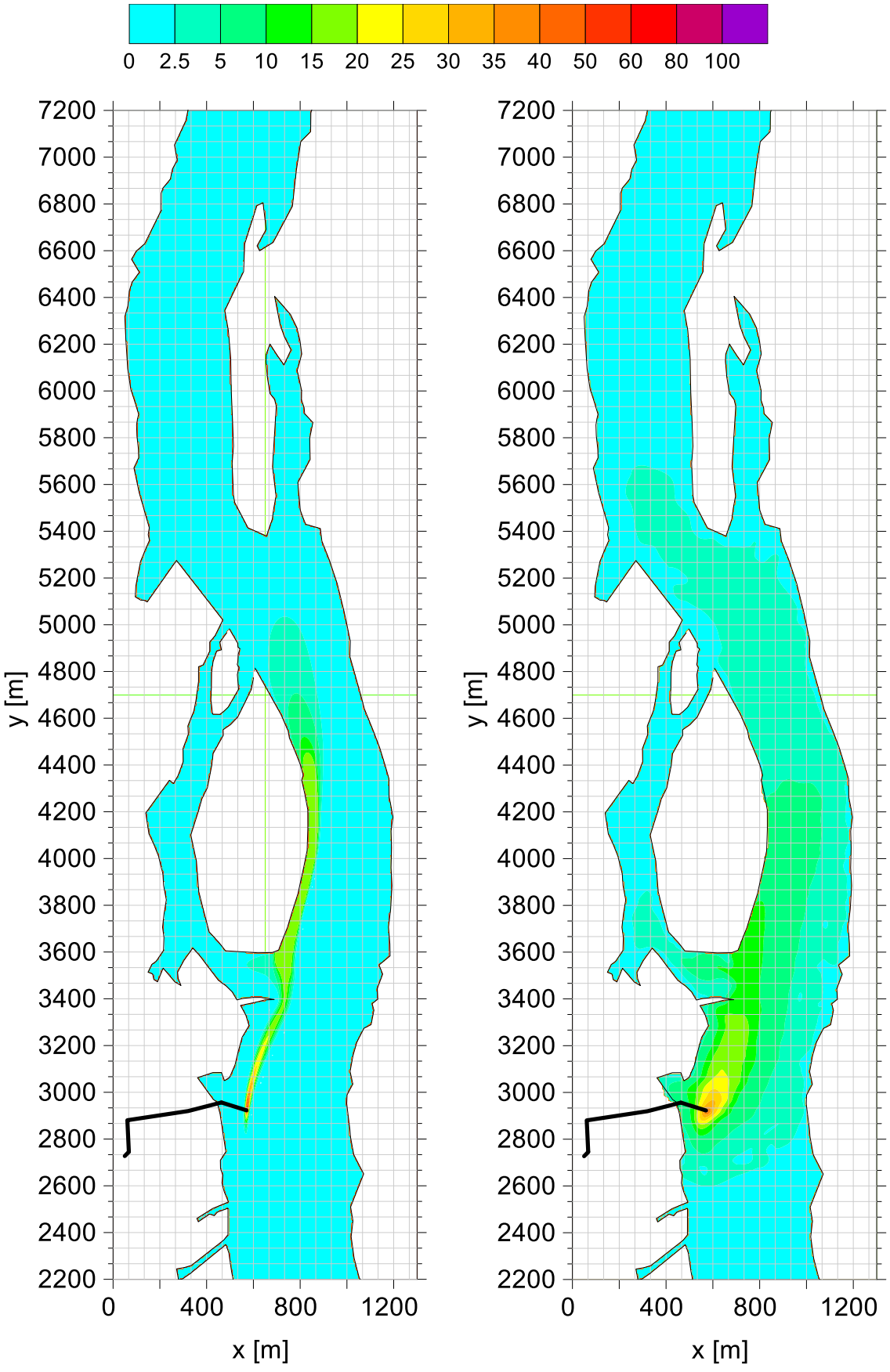


Figure 5. Results of numerical calculations of the propagation of the pollutant plume under the following conditions: a) dispersion coefficient values as for the gradient velocity profile - left, b) dispersion coefficient values as for the drift velocity profile - right.

3.3 Analysis of the development of coastal zones

A significant element of the study was the analysis of the impact of pollutant plumes on coastal zones. The results showed that depending on the dispersion coefficient values used, the exposure of the banks to pollutants varied.

The gradient model observed a more elongated distribution of pollutants (Fig.5a), with less exposure of the banks. The model with increased dispersion coefficient values (Fig.5b), characteristic of the velocity distribution in coastal areas, observed a more even concentration distribution, with greater exposure of the banks but lower concentrations. This approach can lead to underestimation of concentrations near the shore, particularly in areas with local slower flow or recirculation zones. In practice, this poses a risk of inaccurately assessing the impact of pollutants on coastal habitats, surface water intakes, and recreational areas.

The analysis of coastal zones also revealed that pollutants can persist longer in areas with low flow velocities. This leads to a locally prolonged exposure of the aquatic environment, even if the bulk of the pollutant has already been transported downstream. This phenomenon is consistent with the concept of dead zones and retention areas described in the literature on river dispersion (Valentine and Wood 1977). The obtained results confirm that accurate representation of dispersion coefficient values is crucial for environmental analyses related to the protection of water intakes, assessing the impacts of accidental discharges, planning water quality monitoring, and forecasting ecological risk. Particularly in wide rivers, it is not sufficient to assess only the longitudinal passage time of pluma. It is also necessary to determine its lateral migration and possible contact with costal zones.

3.4 Comparison of the obtained results

A comparison of both simulation results revealed that an inappropriate approach can lead to significant interpretation errors. The model with dispersion coefficients selected for gradient flow more realistically represented the pollutant migration process, indicating bank areas exposed to higher pollutant concentrations and providing a more realistic picture of the impact of pollutants on the aquatic environment (Shen and Niu 2018, Wang et al. 2015, Zima and Sawicki 2024). However, the model with dispersion coefficients selected for drift flow less accurately represented the pollutant propagation process, causing excessive "spreading" of the pollutant patch and a decrease in concentration at the banks.

The study results indicate that in wide natural rivers, using appropriate values for the dispersion tensor components is extremely important. This approach increases the reliability of predictive models used in water quality management systems and environmental risk analyses. This is particularly important for river sections containing islands, sandbars, meanders, stagnation zones, or other features that cause local flow field disturbances.

4 Discussion

The obtained results confirm that in wide natural rivers, the correct mapping of the dispersion tensor is crucial for realistic modeling of pollutant propagation. It turned out to be particularly important to take into account the off-diagonal components of the tensor, which influenced both the direction of plume development and the intensity of transverse mixing. These results are consistent with the observations reported by Fischer et al. (1979), who pointed out that the actual dispersion process in natural streams is strongly related to the heterogeneity of the velocity field and the occurrence of secondary flows.

In classical models of pollutant transport, the diagonal form of the dispersion tensor is usually assumed (Chapra 1997, Falconer and Lin 1997, Rodi 1993). This assumption is justified mainly for simple laboratory channels or homogeneous flows with low spatial variability. In the case of wide natural rivers,

however, this simplification may lead to significant interpretation errors. The presence of a terrain obstacle caused local flow acceleration, stream separation and the formation of recirculation zones. These effects led to strong transport anisotropy and an increase in the importance of the D_{xy} and D_{yx} conjugated components. Similar phenomena were described by Nikora and Roy (2012), pointing out the important role of secondary flows and local hydrodynamic disturbances in shaping river mixing processes.

The obtained results also indicate that the actual course of plume propagation is strongly dependent on the gradient velocity distribution in the cross-section. Maximum velocities occurring in the stream axis caused the plume to elongate in the longitudinal direction, while coastal areas with lower velocities favored local pollutant retention. This mechanism corresponds to the classical Taylor–Fischer dispersion theory (Fischer 1973, Taylor 1953), according to which the inhomogeneity of the velocity field generates an additional hydrodynamic mixing effect.

The physical interpretation of dispersion coefficients remains an important issue. Many studies emphasize that experimentally determined coefficients include both the actual turbulent dispersion and the effect of incomplete mixing (Deng and Singh 2001, Fischer 1968, Rutherford 1994). This issue is particularly significant in wide rivers, where the time of lateral mixing can be comparable to the time of advective plume transport. As a result, the observed values of dispersion coefficients may be strongly dependent on the spatial scale and time of observation. The conducted studies also point to the limitations of using classical empirical formulas, such as those of Elder (1959), Seo and Cheong (1998), and Kashefipour and Falconer (2002). These formulas were developed primarily for simple channels or rivers with relatively uniform flow and do not account for the effects of complex channel morphology and transport anisotropy. In the analyzed case, the presence of an island caused local changes in flow direction and the formation of stagnation zones, leading to significant deviations from classical dispersion models.

The results of the study are consistent with more recent studies on anisotropic dispersion in two-dimensional models (Shen and Niu 2018, Wang et al. 2015). These studies indicate the need to consider the full dispersion tensor in environmental analyses. The results obtained in this study confirm these observations for a real, wide, natural river. Additionally, the results are consistent with the assumption that when modeling the transport of pollutants in rivers with complex geometry, not only the values of longitudinal and transverse dispersion should be taken into account, but also the orientation of the main directions of the plume spread (Shen and Niu 2018, Wang et al. 2015, Zima and Sawicki 2024).

An important practical aspect is the influence of the dispersion tensor structure on environmental risk assessment. The drift model, typical of coastal areas, has been observed to underestimate the impact of pluma on coastal zones, which can lead to erroneous risk assessments for water intakes, protected areas, or recreational zones. In practice, this means that the use of simplified models can result in inappropriate planning of protective measures during industrial or transport emergencies.

However, it should be emphasized that the approach used also has certain limitations. A depth-averaged (2DH) model was adopted in this study, which ignores the vertical structure of flow and dispersion. In real river conditions, three-dimensional processes can play a significant role, particularly in flow zones around terrain obstacles and under thermal or density stratification conditions (Nezu and Nakagawa 1993). Furthermore, the analysis focused on the inert substance, without taking into account reaction processes, sedimentation, and biological interactions. Further research should include the development of three-dimensional models, analysis of the impact of variable unsteady flow, studies of the influence of secondary turbulence, determination of the dispersion tensor from ADCP data, and integration of hydrodynamic models with field monitoring. A particularly important research direction seems to be the development of methods enabling the dynamic determination of dispersion tensor coordinates directly from local flow parameters. Such an approach could significantly improve the accuracy of predictive models used in water quality management systems and environmental risk analyses.

5 Conclusion

Based on numerical simulations of pollutant propagation in a wide natural river for two sets of dispersion coefficient values (for the gradient and drift velocity profiles), the following conclusions were drawn:

1. In wide natural rivers with complex flow structures, the dispersion tensor is clearly anisotropic. The values of the tensor coordinates depend directly on the local velocity distribution, channel geometry, and the presence of terrain obstacles such as river islands or stagnation zones (Nikora and Roy 20212, Shen and Niu 2018, Wang et al.), as shown in the modeling results.
2. Taking into account the gradient dispersion tensor enables realistic representation of the concentration field asymmetry and the rotation of the principal axis of the plume propagation (Fig.5). In particular, the off-diagonal components D_{xy} and D_{yx} play an important role in disturbed and multidirectional flow conditions (Shen and Niu 2018, Wang et al. 2015, Sawicki and Zima 1997, Zima and Sawicki 2024).
3. The drifting distribution of flow velocity leads to significant deformations in the propagation of pollutant plumes in rivers as shown in Fig. 5. The pollutant plume is diffuse, while coastal areas with lower flow velocities favor local pollutant retention and increase the exposure time of the aquatic environment (Fischer 1973, 1979, Zima and Sawicki 2024). However, the concentrations of this pollutant are lower.
4. The largest differences between the gradient and drift models were observed in the river island region, where local flow accelerations, stream separation, secondary flows, and recirculation zones occurred. These conditions resulted in an increased importance of the tensor's conjugate components and intensified anisotropic mixing processes (Nikora and Roy 2012, Shen and Niu 2018, Wang et al. 2015, Zima and Sawicki 2024).
5. The research results indicate that incorrect assumption of the dispersion tensor components may lead to underestimation of the environmental risk, especially in relation to coastal zones, water intakes, protected areas and local concentration maxima.
6. Classical empirical relations used to determine dispersion coefficients may be insufficient for wide rivers with complex morphology. In such conditions, it is necessary to take into account the actual velocity field and local hydrodynamic effects (Elder 1959, Kashefipour and Falconer 2002, Seo and Cheong 1998).

The conducted research has shown that correctly assuming the dispersion tensor component values is essential for reliable modeling of pollutant propagation in wide natural rivers. These values should always be analyzed in the context of local hydraulic conditions, as their simplified selection can lead to significant errors in environmental risk assessment.

References

Bear J. 1988 *Dynamics of Fluids in Porous Media*. Dover Publications, New York.
Bear J. 1979 *Hydraulics of Groundwater*. McGraw-Hill, New York.
Burdziakowski P., Zima P., Wielgat P. & Kalinowska D. 2021 Tracking Fluorescent Dye Dispersion from an Unmanned Aerial Vehicle, *Sensors.* 21(11), 3905.
Chapra S.C. 1997 *Surface Water-Quality Modeling*. McGraw-Hill, New York.
Deng Z.Q., Bengtsson L. & Singh V.P. 2001 Longitudinal dispersion coefficient in straight rivers. *Journal of Hydraulic Engineering.* 127(11), 919–927.
Deng Z.Q. & Singh V.P. 2001 Mechanism of non-Fickian dispersion in rivers. *Journal of Hydraulic Engineering*. 127(2), 151–160.
Elder J.W. 1959 The dispersion of marked fluid in turbulent shear flow. *Journal of Fluid Mechanics.* 5, 544–560.
Falconer R.A. & Lin B. 1997 Modelling water quality processes using finite element methods. *Water Research*. 31(7), 1637–1646.
Ferziger J.H. & Perić M. 2002 *Computational Methods for Fluid Dynamics*. Springer, Berlin.
Fischer H.B. 1968 Discussion of simple method for predicting dispersion in streams. *Journal of*

Environmental Engineering Division. 94, 927–943.
Fischer H.B. 1973 Longitudinal dispersion and turbulent mixing in open-channel flow. *Annual Review of Fluid Mechanics.* 5, 59–78.
Fischer H.B. 1976 Mixing and dispersion in estuaries. *Annual Review of Fluid Mechanics*, 8, 107–133.
Fischer H.B., List E.J. & Koh R.C.Y., Imberger J., Brooks N.H. 1979 *Mixing in Inland and Coastal Waters*. Academic Press, New York.
Kashefipour S.M. & Falconer R.A. 2002 Longitudinal dispersion coefficients in natural channels. *Water Research*. 36, 1596–1608.
Kilpatrick F.A. & Cobb E.D. 1985 *Measurement of Discharge Using Tracers*. USGS Techniques of Water-Resources Investigations, Washington.
LeVeque, R.J. 2002 Finite Volume Method for Hyperbolic Problems. Cambridge University Press, New York.
Nezu I. & Nakagawa H. 1993 *Turbulence in Open-Channel Flows*. Balkema, Rotterdam.
Nikora V. & Roy A.G. 2012 Secondary flows in rivers: theoretical framework, recent advances and current challenges. *River Research and Applications*. 28, 1427–1438.
Rodi W. *Turbulence Models and Their Application in Hydraulics*. IAHR, Rotterdam, 1993.
Rutherford J.C. 1994 *River Mixing*. Wiley, Chichester.
Sawicki, J.M. & Zima, P. 1997 The Influence of Mixed Derivatives on The Mathematical Simulation of Pollutants Transfer, In: *Proc. of 4th International Conference on Water Pollution*, Bled, Slovenia, 18-20 June.
Seo I.W. & Cheong T.S.1998 Predicting longitudinal dispersion coefficient in natural streams. *Journal of Hydraulic Engineering.* 124(1), 25–32.
Shen C. & Niu J. 2018 Numerical simulation of anisotropic pollutant transport in wide rivers. *Journal of Hydrology.* 563, 927–941.
Taylor G.I. 1953 Dispersion of soluble matter in solvent flowing slowly through a tube. *Proceedings of the Royal Society A*. 219, 186–203.
Valentine E.M. & Wood I.R. 1977 Longitudinal dispersion with dead zones. *Journal of Hydraulic Engineering*. 103(9), 975–990.
Wang Y., Huai W. & Zeng Y. 2015 Two-dimensional anisotropic dispersion in natural rivers. *Environmental Fluid Mechanics*. 15, 907–926.
Zienkiewicz O.C. & Taylor R.L. 2000 *The Finite Element Method*. Butterworth-Heinemann, Oxford.
Zima, P. & Sawicki, J. 2024 Numerical Analysis of the Influence of 2D Dispersion Parameters on the Spread of Pollutants in the Coastal Zone. *Water*. 16(24), 3637.
Zima, P. 2018a Mathematical Modeling of the Impact Range of Sewage Discharge on the Vistula Water Quality in the Region of Włocławek. In: *Free Surface Flows and Transport Processes*. Kalinowska M, Mrokowska M, Rowiński P (eds), GeoPlanet: Earth and Planetary Sciences. Springer, Cham, 489-502.
Zima, P. 2018b Modeling of the Two-Dimensional Flow Caused by Sea Conditions and Wind Stresses on the Example of Dead Vistula. *Pol Marit Res.* 97, 166-171.
Zima, P. 2019 Simulation of the impact of pollution discharged by surface waters from agricultural areas on the water quality of Puck Bay, Baltic Sea. *Euro-Mediterr. J. Environ. Integr*. 4:16
Zima P. 2024 Testing The Parameters Of Two-Dimensional Horizontal Dispersion Phenomenon In The Coastal Zone. In: *Proc. of 18th International Symposium on Water Management and Hydraulic Engineering (WMHE 2024)*, Štrbské Pleso, Slovakia, 10-14 September.

URBAN AREAS AND GROUNDWATER FLOW ISSUESt

Jaromír ŘÍHA [1*], Tomáš JULÍNEK [2]

[1,2] *Brno University of Technology, Faculty of Civil Engineering, Dep. of Water structures, Czech Republic*

E-mail: Riha.j@vutbr.cz

E-mail: Tomas.Julinek@vut.cz

[*] *Corresponding author*

Abstract

In urban areas groundwater regime results both from natural conditions and by human interventions, namely by the construction of deep foundations of new buildings. Human activities are represented by a change of geological composition, leakage from water pipes, pumping from water wells, obstruction of the flow by deep foundations and construction of deep collectors. These factors influence the groundwater flow regime. Groundwater flow also affects a technical design of structures and foundation techniques. Special issue is the temporal change of the groundwater regime during floods when increased water stages in streams propagate to the floodplain and affect the groundwater regime in the areas along the streams. In river equipped by flood levees or floodwalls, the safety towards an internal erosion of the levee itself or of the subbase is crucial. Modelling groundwater flow enables both the evaluation of an impact of a structure on the groundwater regime and impact of groundwater on the subsurface structures. In the paper, the groundwater flow issues in urban areas are listed and demonstrated on practical examples. The use of models and the application of CAD and GIS tools for data pre- and post-processing is briefly described as well.

Key words groundwater flow, subsurface structures, urban areas, floods.

1 Introduction

In urban areas the groundwater regime results both from natural conditions and by human interventions, namely by the construction of deep foundations of new residential and other buildings. The natural conditions are related to aquifer morphology often containing the network of historical "subsurface" water courses partly draining the areas.

Human activities are represented by a change of geological composition (anthropogenic geological layers), leakage from water supply pipes, pumping from water wells, obstruction of the subsurface flow by deep foundations and construction of deep engineering network collectors. These factors influence the groundwater flow regime, on contrary, groundwater flow affects a technical design of aforementioned structures and foundation techniques at the site.

A special issue is the temporal change of the groundwater regime during floods when increased water stages in streams propagate to the floodplain and affect the groundwater regime in the areas along the streams (Fetter, 2001). In rivers equipped by flood levees or floodwalls, the safety towards an internal erosion of the levee itself or of the subbase is crucial. Increased water stages during floods can affect groundwater regime in the area adjacent to the river. The rise in the water level in a water course during a flood may result in temporary infiltration along the banks of the river and seepage propagation into the aquifer in the opposite direction to that of normal flow. High piezometric level may cause "groundwater flood" (Robins and Finch, 2012; CIRIA, 2013) which may endanger both flood protection elements and the structures in protected urbanized areas (MacDonald et al., 2012; Zhou and Li, 2011). This may result in waterlogging of the areas behind the flood barriers (Adams et al., 2010).

In summary, the issue has several aspects, out of which the most important ones are as follows:

- During the city development, new buildings are usually constructed with several subterranean floors with subsurface garages. Thus, subsurface parts of buildings frequently reach the groundwater level. Therefore it is necessary to take into account groundwater effects on the newly proposed structure and a reverse influence of the new structure on the groundwater flow regime and an impact on existing structures.
- In case of continuous line of flood protection, an “artificial” excess pressure occurs in the protected area as the increased flood level propagates into the aquifer and affects the structures in the protected area. In relation to permeability of the collector, the groundwater level advance can reach tens to hundreds of metres from the water course.

Groundwater flow modelling is used for the assessment of the states before and after the construction of subsurface parts of new buildings (Bear and Verruijt, 1992). This enables both the evaluation of an impact of a structure on the groundwater regime in the locality and impact of groundwater on the subsurface structures (water pressure on the foundation joints, uplift forces, etc.).

Experience shows that the aspects mentioned above cannot be overlooked during the preparation of extensive investment and that it is always worth checking local conditions in the framework of the project elaboration through geological and hydrogeological surveys and through the use of interrelated groundwater flow modelling to carry out relevant proposal for possible measures.

In the paper, the groundwater flow issues in urban areas are systematically listed and demonstrated on two practical examples located in the city of Brno, namely an impact of the Janacek Concert Hall on the groundwater regime in the locality and the impact of groundwater on flood protection and urbanisation along the Svitava river.

2 Methods

2.1 Basic considerations

The general method when solving groundwater flow issues in urban areas consists of the following steps:

- identification of hazards related to groundwater flow, defining hazard quantifiers,
- conceptual model containing methodology and necessary approximations,
- input data backup, verification and analysis,
- hydraulic modelling,
- quantification of hazards, outputs, recommendations.

2.2 Identification of hazards

Groundwater-induced hazards in urban areas can be divided into following categories:

- flood induced hazards due to an increase of piezometric level at areas adjacent to streams during flood events,
- hazards in areas protected by flood protection measures,
- hazards to the civil structures with deep foundations,
- change of groundwater regime due to anthropogenic activities,

The hazards can manifest themselves via (Fig. 1):

a) the rise of groundwater table represented by piezometric head $h(x, y, z, t)$; this may occur e. g. in the area protected against floods or "upstream" of the deep subterranean foundations of newly built structures, city collectors, subways, etc., the result can be:
   - increased pore water pressure $p(x, y, z, t)$ in a sub-base acting on subterranean parts of existing buildings,

- waterlogging of affected area,
- collapse of poorly permeable topsoil layers covering hydrogeological aquifer,

b) the seepage into flood protected areas during the floods which increases "inner water" amount,
c) increased hydraulic gradients **grad** $h(x, y, z, t)$ in sub-base, possibly under the civil or flood protection structures, represents a body load on soils susceptible to internal erosion.

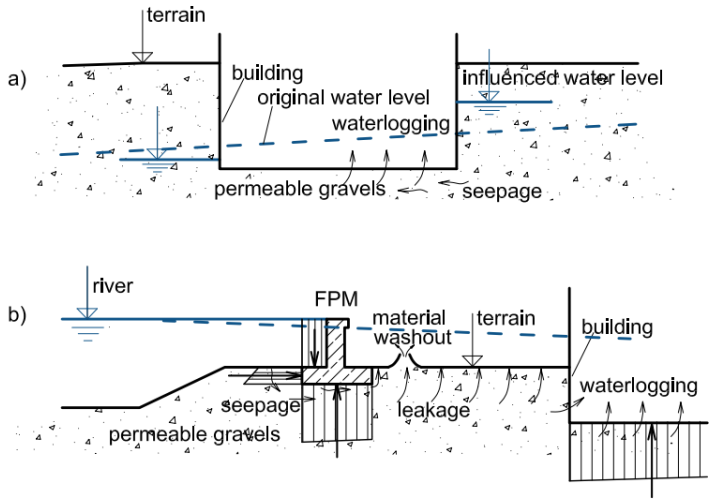


Figure 1. Types of hazard a) effect on buildings sub-base due to backwater, b) internal erosion and waterlogging

2.3 Conceptual model

As hydrogeological and hydrological conditions are usually highly complicated, simplifications of the reality are necessary. Their specification is a part of conceptual model which transforms reality into mathematical formulation of the problem. In specifying the simplifications and approximations the experience and knowledge about local conditions is employed, usually based on existing or on-purpose geological and hydrological survey including groundwater level monitoring.

The inhomogeneity is usually incorporated by applying different properties over specified sub-domains of entire flow domain.

Water levels in a stream usually represent the boundary condition for seepage along the river reach, the time course of the discharge and the water stage has to be determined. The theoretical "typical" flood hydrograph is used or the real flood wave is taken into account. As the shape of the hydrograph, namely flood duration is usually hardly predictable, in the design of flood protection structures the "infinite" steady state maximum flood is frequently taken into account to express the upper envelope of possible scenarios.

According to the prevailing direction of the seepage flow the dimensional simplifications may be applied. Thus generally three-dimensional (3D) seepage flow model may be approximated by two-dimensional (2D) in vertical or horizontal plane or even one-dimensional (1D) approximation may be adopted.

Existing topographical elements must be included into model. These can be local streams influencing ground water regime by certain leakage, impervious structural elements like slurry walls, concrete walls of cellars, etc. The drainage of groundwater may be caused by leaking sewer pipes which, conversely, may also obstruct groundwater flow in case of their large dimensions.

2.4 Input data analysis

As the first step in the evaluation of a potential groundwater threat, the available information must be

summarised:

- geographic and geodetic data on the studied area and related objects/structures or terrain (DMT),
- geological and hydrogeological data,
- hydrologic and hydraulic data,
- background information on the existing and proposed flood protection measures (FPM),
- data on building foundation, ground water uptake (wells).

Most of the background information is usually available through the contracting body and is often part of the urban plans, design plots of newly built structures, documentation of FPM in the evaluated area. Other providers are appropriate organizations such as the Czech Hydrometeorological Institute in case of hydrological data, river basin authorities for data on existing objects, government agency for surveying, mapping and cadastre or for geology survey.

The required data mostly have a spatial character and can be linked to spatial coordinates. For their analysis, preparation and representation, it is possible to successfully use CAD and/or geographic information systems (GIS), which can subsequently be applied also to the representation and analysis of solution results in the form of map outputs. It is always necessary to attach information to the provided data on the time of their acquisition, or validity (the time of investigation or surveying of the area, the validity of hydrological information, etc.).

2.5 Hydraulic modelling

The quantification of individual hazard characteristics is carried out using a hydraulic model. The type of the model is chosen based on the nature of the addressed problem defined by the spatial layout, morphology, geological and hydrogeological conditions of the site and also by the layout of structures in the area. The modelling typically consists of the following typical steps:

- Construction of the model
- Model calibration, resp. verification,
- Simulation of variants chosen.

The groundwater flow models, including a mathematical description and numerical methods, have been described in numerous monographs (Bear and Verruijt, 1992), the following text is limited only to general comments concerning the solution of problems relating to urban areas.

From the experience, most of the groundwater problems occur in municipalities where typically quaternary aquifers are covered by fluvial loams, which are in urban areas frequently substituted by heterogeneous anthropogenic layers. In these cases two-dimensional (2D) models of groundwater flow in a horizontal plane are a suitable tool for the solution. In complicated configuration, more complex (3D) models can be used.

The obtained numerical model should be subject to calibration and verification. For this purpose, sufficient data from groundwater level observation and corresponding pumped amounts has to be acquired. It is necessary to provide homogeneous sets in terms of time of observations and measurements. The accuracy of the monitoring data should be assessed in order to set down the convergence criteria for model calibration. As a rule, model verification is carried out using another data set than for calibration.

The calibrated model is finally used for the simulation of scenarios serving for answering the questions and achieving defined goals and objectives.

2.6 Processing and presentation of results

Very important point is an acquisition of the results, their processing, analysis and interpretation. For this, engineering approaches are combined with efficient methods of post-processing which enable

spatial and temporal data displaying using CAD systems and thematic maps within GIS tools. The GIS techniques also enable processing results of modelling and safety and reliability assessment of the urban areas behind the flood protection structures.

The results are usually presented as follows:

- The maps of piezometric head - piezometric contours.
- The maps of differences in water table, resp. piezometric head due to human intervention.
- The maps of pore pressures, pressure or hydraulic gradients.
- Vector maps of specific seepage, hydraulic gradients.
- The cross sections showing the water table, resp. piezometric head.
- The pore pressure diagrams.
- Hazard maps e.g. in terms of reliability maps, maps of overdimensioning or safety factor.
- The maps of water-logged areas, etc.

3 Practical examples

3.1 Janacek Concert Hall

The Janacek Concert Hall (JCH) is located in the centre of the city of Brno. This block originally housed a parking lot, currently it is a construction site where the underground buildings of the JCH, stage 1, are newly located. The actual construction has been divided into 2 stages (Fig. 2):

- Stage 1: underground parking house including connections and temporary pedestrian surface treatments.
- Stage 2: includes the extension of the lower structure towards the International Hotel and the upper structure - a multifunctional building with a multipurpose hall with administrative, commercial and operational areas.

In the locality the pre-Quaternary bedrock is represented by Neogene sediments composed mainly of calcareous relatively impermeable clays. These materials, identified at a depth of 6.5 to 13.4 m below the terrain (elevations 205.20 to 211.60 m above sea level) can be considered as basal insulator.
Quaternary deluvio-fluvial sediments, represented by relatively permeable sands and sandy gravels with a variable content of fine-grained admixtures, rest on the Neogene bedrock. The thickness of these layers forming the hydrogeological aquifer is 0.4 to 5.3 m. Pumping tests indicated transmissivity of these layers approximately $T = 2 \cdot 10^{-3}$ m^2/s with hydraulic conductivity value of $k \approx 2 \cdot 10^{-3}$ m/s. The subsurface layer consists of anthropogenic layers (fills) with the character of cohesive and non-cohesive soils, in places with remains of old building structures. These materials are quite heterogeneous with significantly different permeability. The groundwater flow comes approximately from the South/South-East and follows ancient "buried" stream coming along the Špilberk Castle.

Stage I of the JCH construction is represented by the foundation pit with dimensions of approximately 80 x 30 m with an extension on the northern side with dimensions of approximately 40 x 20 m. The construction pit in the IInd stage is an extension of the subsurface structures built in the Ist stage towards the south. This is an extension of approximately 50 x 10 m (western part) + 35 x 30 m (eastern part), see Fig. 3. The construction pit is about 7 m deep below the terrain, however peripheral sealing wall is rather deeper reaching relatively impermeable neogeneous bedrock. Thus, the foundation pit surrounded by the so-called "Milan diaphragm wall", which will remain after the construction is completed, obstructs the groundwater flow coming from the South-East. The "obstruction" across the groundwater flow direction is about 70 m wide and would dam the groundwater water table, resp. increase the piezometric head upstream of the pit.

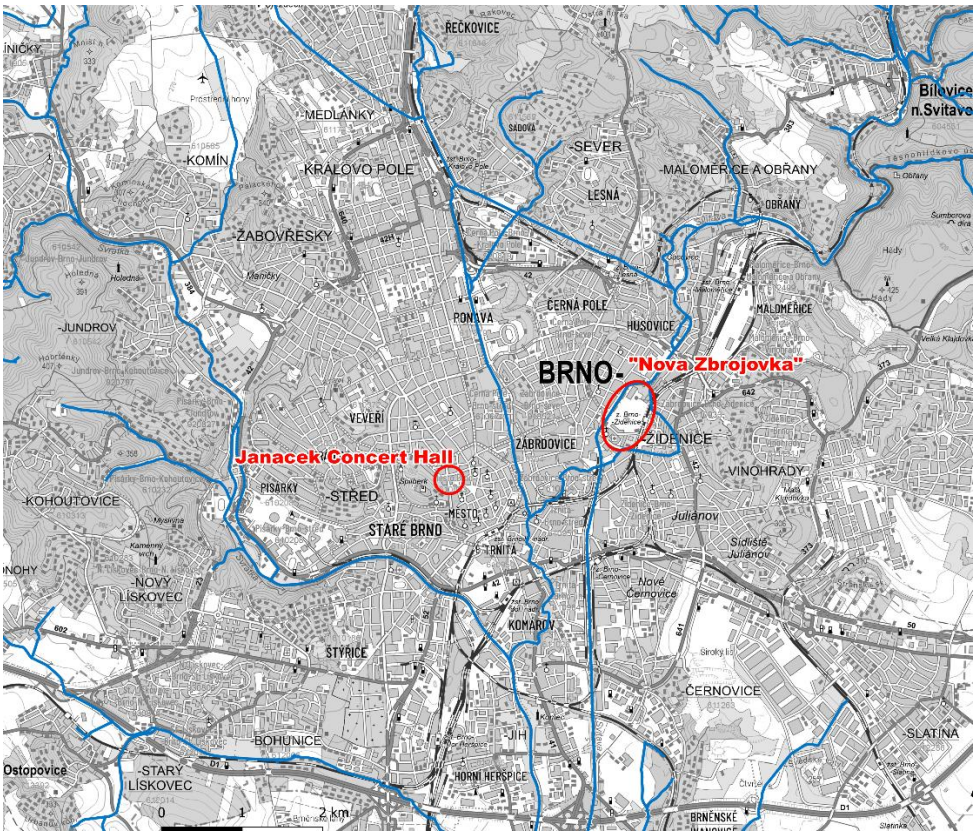


Figure 2. The location of described areas

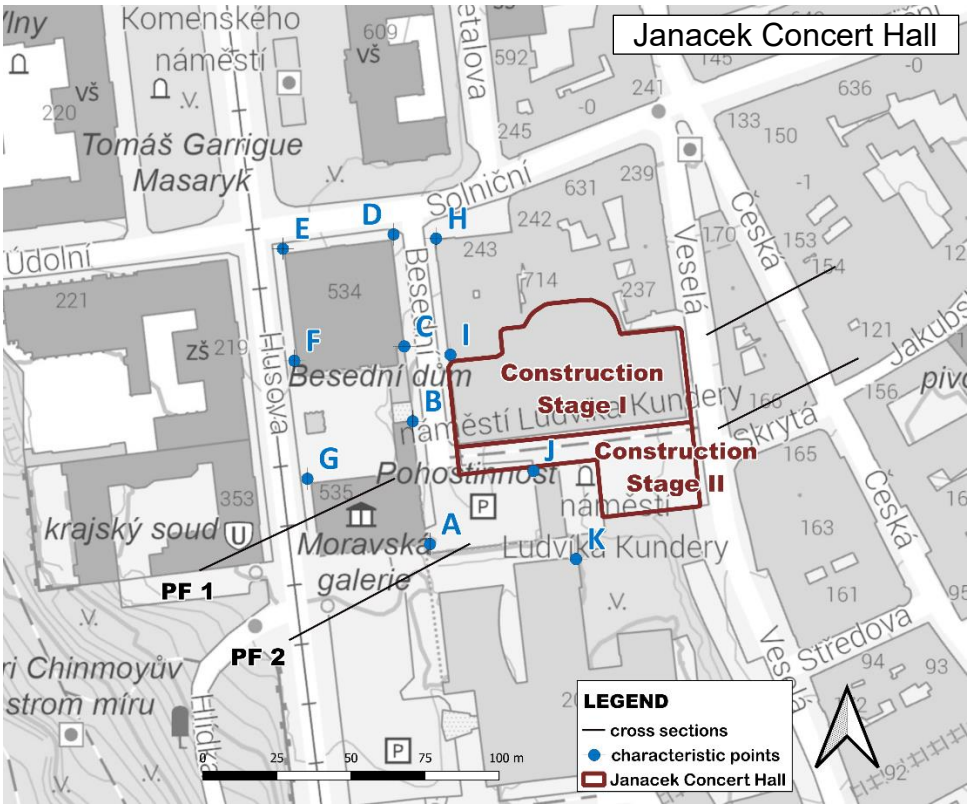


Figure 3. The layout of the Janacek Concert Hall

Hydraulic modelling was carried out using 2D horizontal model. The model calibration was performed based on measured water levels in boreholes obtained before the beginning of the construction. Hydraulic conductivity was determined from the results of the pumping test. In Fig. 4 one can see the

results of the model calibration in terms of piezometric level contours.

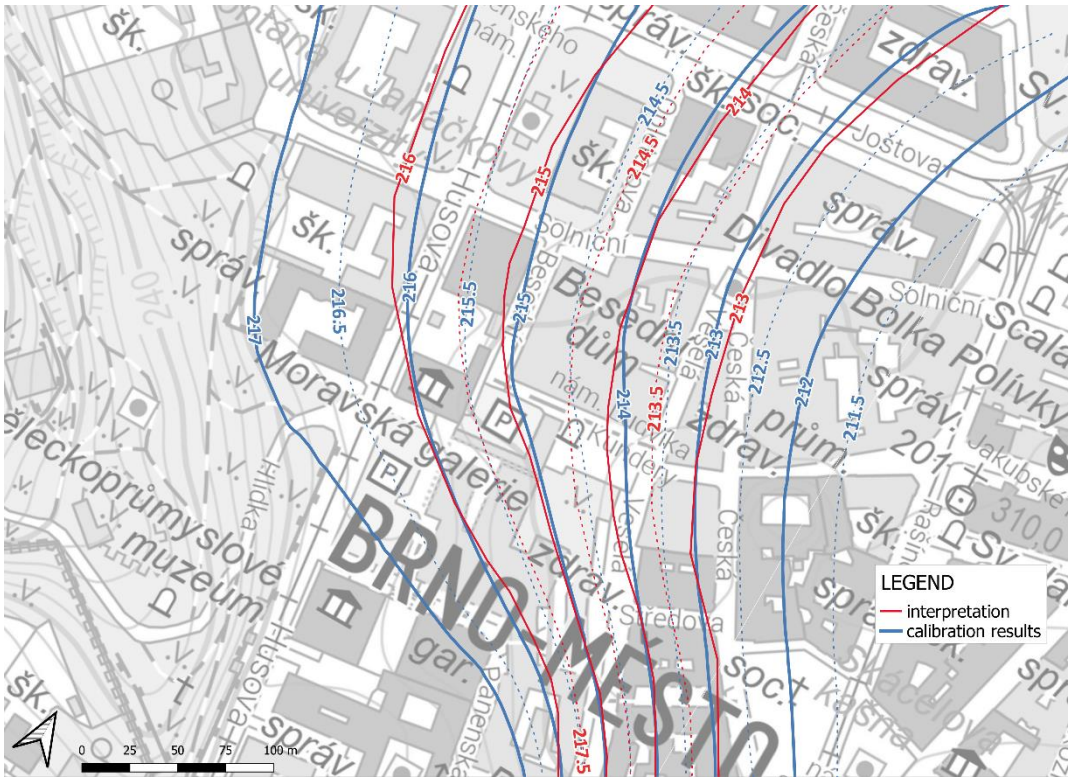


Figure 4. The calibration of the Janacek Concert Hall model

Into the calibrated model the foundation pit was implemented as "impermeable block". The results of the calculations were interpreted via the map and cross sections showing differences in water level due to the construction of the subsurface part of the hall (Figs. 5, 6).

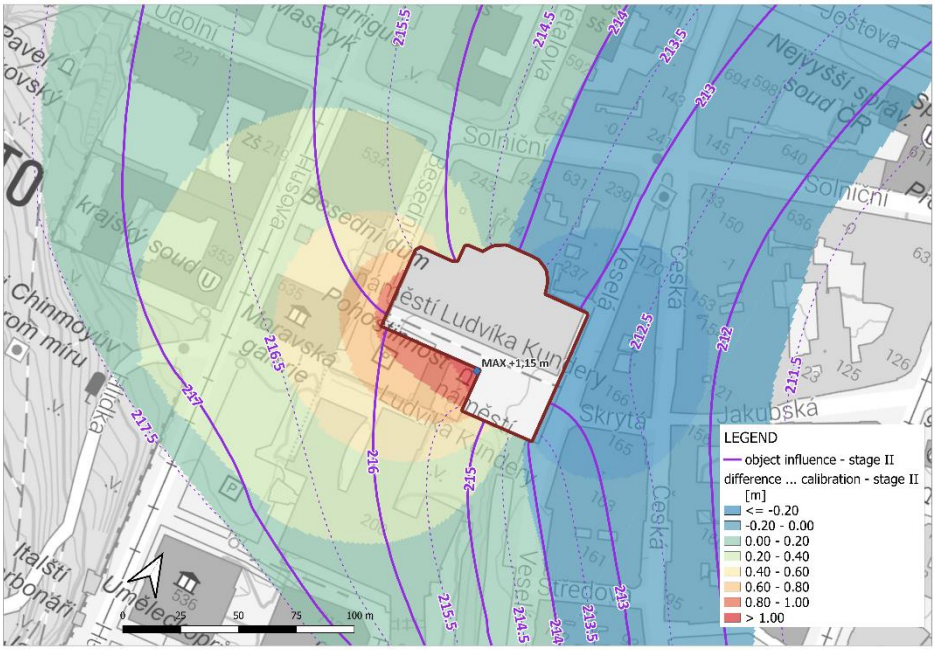


Figure 5. The map of differences in piezometric head due to JCH construction, construction stage II

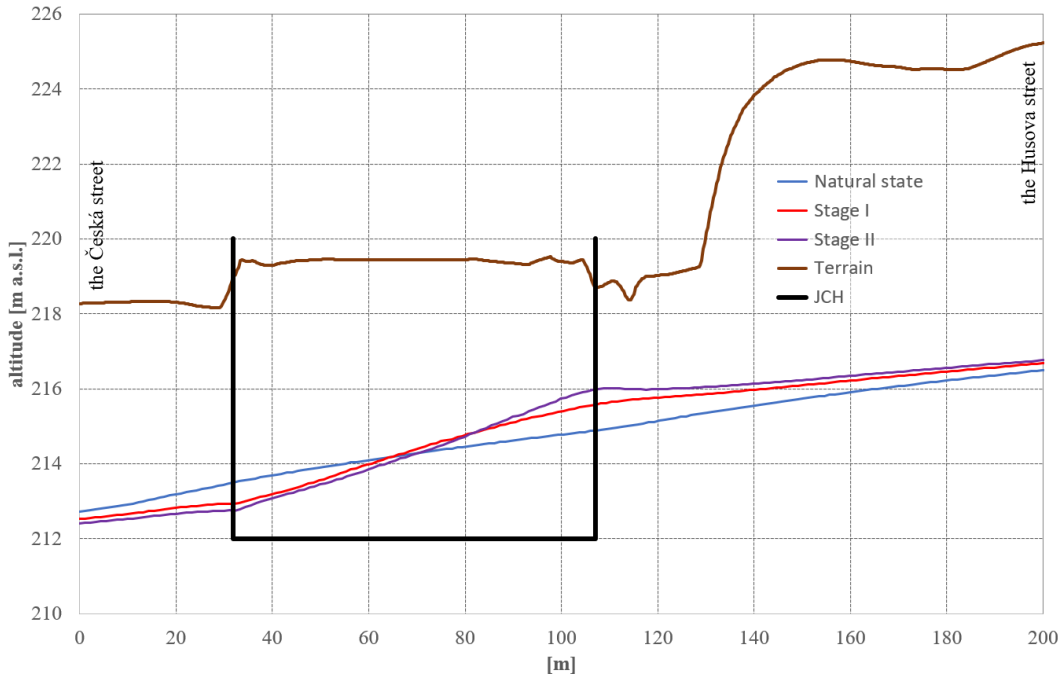


Figure 6. The section across the JCH with groundwater levels differences

The resulting water levels and their differences due to the construction of JCH were summarised for important locations (points) shown in Fig. 2. For both construction stages they are shown in Table 1.

Table 1. Resulting water stages and differences in groundwater levels in selected points in the locality

Point	State before JCH construction	1st stage of JCH construction		2nd stage of JCH construction	
	[m a. s. l.]	[m a. s. l.]	Difference [m]	[m a. s. l.]	Difference [m]
A	215.66	216.01	0.35	216.21	0.56
B	215.23	215.76	0.53	215.91	0.67
C	215.10	215.46	0.36	215.53	0.43
D	214.97	215.12	0.15	215.17	0.20
E	215.56	215.72	0.16	215.77	0.21
F	215.71	215.96	0.25	216.04	0.33
G	215.97	216.26	0.29	216.36	0.39
H	214.73	214.86	0.13	214.91	0.18
I	214.84	215.28	0.44	215.33	0.49
J	214.82	215.31	0.49	215.78	0.96
K	215.03	215.25	0.21	215.59	0.56

In summary, the highest rise of groundwater level due to construction is located in the edge of the pit on its southern part (Fig. 4) amounting to more than 1 m when compared with the pre-construction conditions. An expected increase at the western part at the place of present historical concert hall (points B, C in Fig. 2) is about 0.43 to 0.67 m. To assess potential negative effect of such increase (waterlogging, uneven vertical deformation), the site investigation and geodetic measurements in historical cellars are necessary.

3.2 Flood protection and new urbanisation along the Svitava river

The area of interest is located in Brno, in the city districts of Maloměřice, Husovice, Zábrdovice and Trnitá on both banks of the Svitava river (Fig. 7). The terrain in the area is flat, the existing development consists of both residential buildings and industrial buildings, especially production halls. In the areas with abandoned industrial facilities new construction is being considered, especially on the left bank of the Svitava river. Within the design of river revitalisation, the terrain level along the river is artificially decreased at many places. Moreover, the residential development is located just at the river bank at the

removed soil along the river bank.

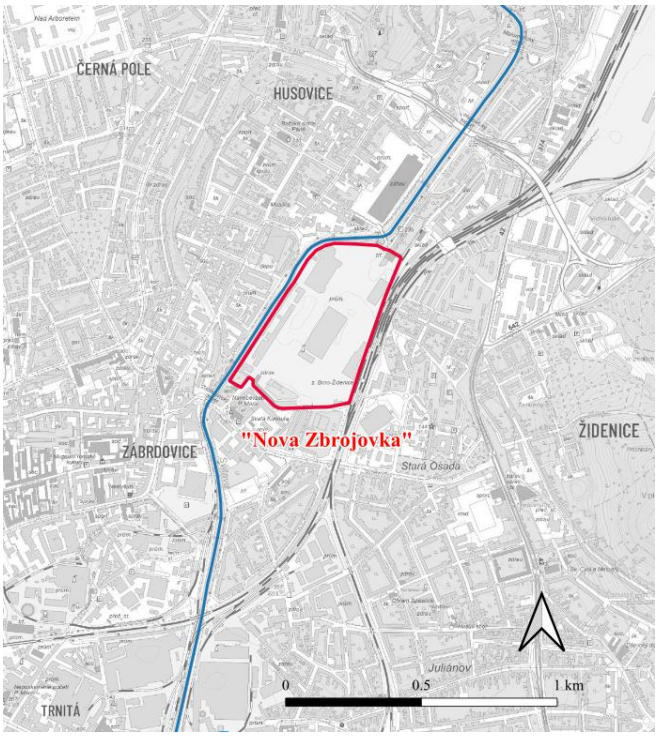


Figure 7. The Svitava river reach with flood protection and intended new urbanisation

In the area the pre-Quaternary are mainly represented by relatively impermeable diorites and granodiorites. The Quaternary cover is primarily formed by fluvial deposits of the Svitava River. In the lower part there are mainly coarse gravels and gravel-sands with a thickness of about 4 to 8 m, which are covered by 1 to 4 m thick layer of relatively impermeable clayey soils. The clays are absent in many places where they are substituted by approximately 3 m thick highly heterogeneous deposits. The groundwater flow is in close hydraulic connection with the Svitava river. A detailed survey indicated the hydraulic conductivity in the range of $1.87 \cdot 10^{-4}$ to $6.01 \cdot 10^{-3}$ m/s, the exception being the relatively high value of $k = 1.95 \cdot 10^{-3}$ m/s obtained in the area of newly proposed residential block of flats Nová Zbrojovka on the left bank of the river (Fig. 8). The following analysis is focused on this locality.

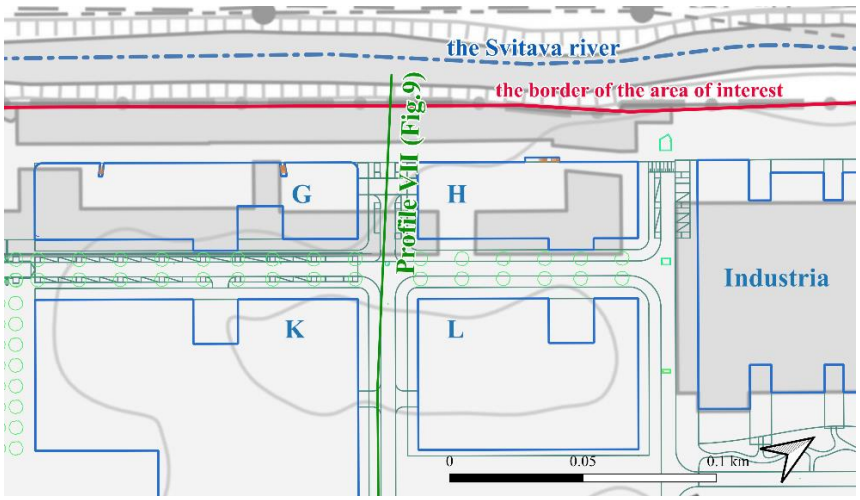


Figure 8. The residential area "Nova Zbrojovka"

The present study focuses on the residential buildings A, B, G, and H located just along the right bank of the Svitava River (Fig. 8). The buildings are designed as a watertight concrete structure, so-called

"white tank". Special attention is paid to the profile along the vacant lot between houses (blocks G and H) where the terrain is excavated in the slope to the Svitava river. The flood water level at the entrance to the vacant lot is 1.9 m above the terrain behind the mobile floodwall (Fig. 9).

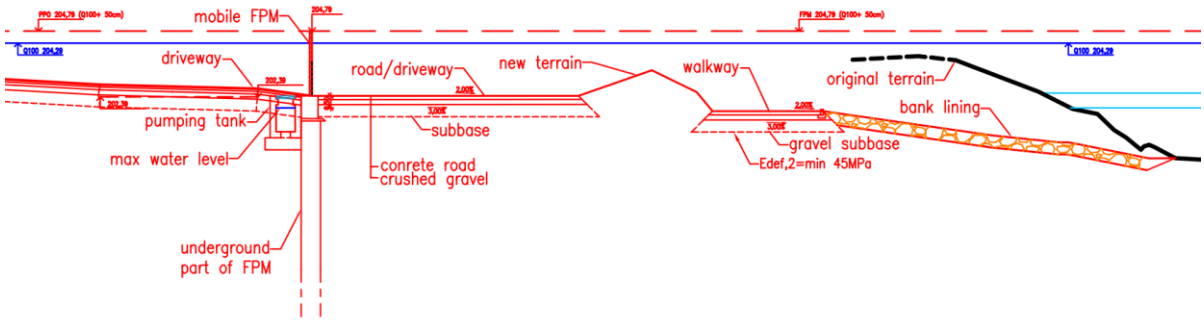


Figure 9. The cross section along the vacant lot between blocks G and H

To avoid high hydraulic gradients below the mobile floodwall the completely penetrating slurry wall was designed extended 18 m below the residential blocks (Fig. 10). The seepage during the flood peak amounting to about 30 l/s will be trapped by 7 drainage wells connected with collecting tank from which seepage will be pumped during the flood situation. The arrangement is shown in Fig. 10.

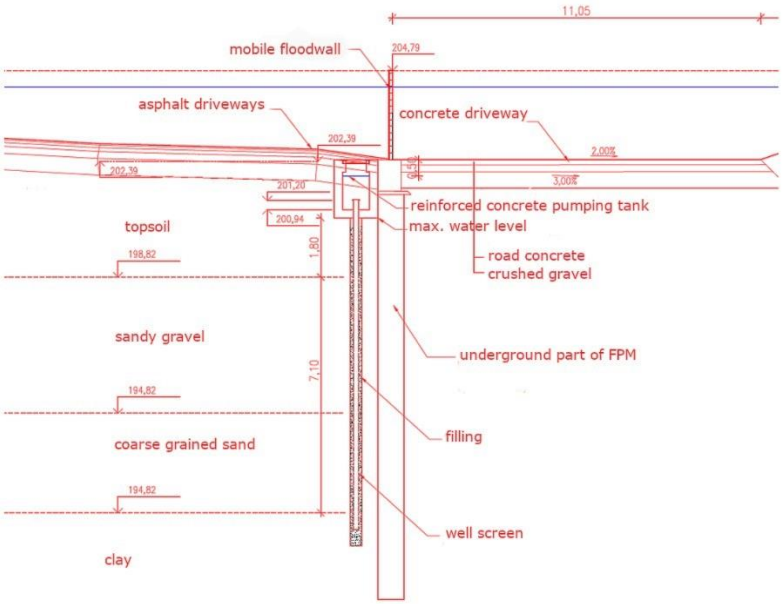


Figure 10. Vertical section along the vacant lot

From the arrangement it is clear that during the floods special attention should be paid to this singularity, at which fire brigade providing the rescue and flood management services during floods has to install sufficiently powerful pumps and after installation the mobile wall has to pump seepage water back to the river. Moreover, such arrangements call for extra investment cost for the slurry wall, drillholes, collecting tank and other corresponding structures. Conversely, if the terrain remained on the original (present) level, floodwall height will reduce to few decimetres with no need of deep slurry wall.

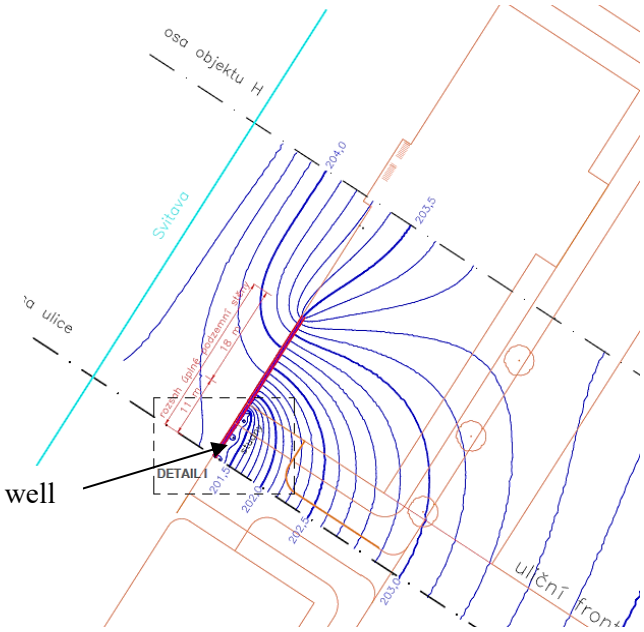


Figure 11. Ground plan of the vacant lot, mobile floodwall, extended slurry wall and piezometric contours

4 Conclusions

In the paper, several problems are mentioned which are connected with the groundwater flow in the urbanised area. The issue has several aspects, out of which the most important ones are chosen:

- In the framework of the city development, these days buildings are constructed with several subterranean floors. The purpose is to use relatively expensive plots as efficiently as possible by placing e.g. subsurface garages in building basements. Thus, subsurface parts of buildings frequently reach the groundwater level. When proposing structures arranged in this way, it is necessary to take into account groundwater effects (uplift pressures on the foundation base, aggressive impact) on the newly proposed structure and a reverse influence of new structure on the groundwater flow regime and an following impact on existing structures. This usually manifests itself as an increase in the groundwater level "upstream" of the obstruction.
- In case of constructing a continuous line of flood protection, an “artificial” excess pressure occurs in the hydrogeological collector from the river side and the flood level gets propagated into the aquifer. Though the flood water does not overflow the protected area, it propagates into permeable alluvial gravels towards the protected area by terms of groundwater flow. Then structures are strained by water pressures invoked by the groundwater advance in the offshore zone. In relation to permeability of alluvial fluvial loose sediments, the groundwater level advance can reach the tens to hundreds of metres wide strip along the water course.
- The revitalisation and renaturation of the streams in urban areas needs special care. The less sensitive excavation works can significantly worsen the local groundwater flow conditions and increase impact of the structures. This usually evokes additional cost for the management of changed groundwater regime and extra remedial measures.

Experience shows that these aspects cannot be overlooked during the preparation of extensive investment and that it is always worth checking local conditions in the framework of the project elaboration through geological and hydrogeological surveys and through the use of interrelated model hydraulic calculations to carry out conceptual proposal for possible measures. They have to guarantee a sufficient protection of structures themselves against unfavourable groundwater effects and to eliminate, in a suitable way, groundwater flow regime changes and a possible impact on the adjacent civil structures and environment.

Acknowledgements

This study is part of the project TACR SS07010401, "Water Management Analysis of Restoring Natural Floodplains and Increasing the Transformation Effect of Floodplains", which includes administrative and technical support.

References

Adams B., Bloomfield J.P., Gallagher A.J., Jackson C.R., Rutter H.K. and Williams A.T. 2010 An early warning system for groundwater flooding in the Chalk. *Quarterly Journal of Engineering Geology and Hydrogeology* 43(2), 185–193.

Bear J. and Verruijt A. 1992 *Modeling Groundwater Flow and Pollution*. D. Reidel Publishing Company, Dordrecht, The Netherlands.

CIRIA 2013 The International Levee Handbook. CIRIA, London (in collaboration with the U.S. Army Corps of Engineers).

Fetter C.W. 2001 *Applied Hydrogeology*, 4th edn. Prentice Hall, Upper Saddle River, NJ.

MacDonald D., Dixon A., Newell A. and Hallaways A. 2012 Groundwater flooding within an urbanised flood plain. *Journal of Flood Risk Management* 5, 68–80.

Robins N.S. and Finch J.W. 2012 Groundwater flood or groundwater-induced flood? *Quarterly Journal of Engineering Geology and Hydrogeology* 45(1), 119–121. https://doi.org/10.1144/1470-9236/10-040

Zhou Y. and Li W. 2011 A review of regional groundwater flow modeling. *Geoscience Frontiers* 2(2), 205–214.

APPLICATION OF THE ENTROPY THEORY IN A CASE OF THE MEANDER IN A COMPLEX MORPHODYNAMICS MEDIA

Bojan ĐURIN [1*], Marko ŠRAJBEK [1], Tanja TRABE BARANAŠIĆ [2], Farhad BAHMANPOURI [3]

[1] *University North, Department of Civil Engineering, Varaždin, Croatia*

E-mail: bojan.durin@unin.hr

E-mail: msrajbek@unin.hr

[2] *University North, Department of Geodesy and Geomatics, Varaždin, Croatia*

E-mail: ttrabebaranasic@unin.hr

[3] *Research Institute for Geo-Hydrological Protection, National Research Council (CNR-IRPI), 06128 Perugia, Italy*

E-mail: farhad.bahmanpouri@irpi.cnr.it

[*] *Corresponding author*

Abstract

Entropy theory, based on the principle of maximum entropy, is used to determine the velocity distribution across the cross-profile section relative to the maximum surface velocity. This method reliably determines the final result: the average flow value for the analyzed watercourse profile. This research will analyze velocity distributions in the meander of the Bednja River in Croatia at the analyzed location, Lovrentovec. The results are expected to differ from those for rectilinear flow, that is, in the direction of the water flow. We will determine maximum velocity using a propeller-based current meter and compare its results with those of the Acoustic Doppler Velocity device. We will reconstruct velocities across the cross-profile section using the Heat mapping procedure, supported by Python. Another challenge is the changing geological structure of the meander relative to the existing sedimentary rocks that form the bottom and sides of the trough, running lengthwise along the watercourse at the analyzed location. This research is important for understanding flow and velocity distributions, which affect the hydraulic and hydrological attributes of watercourses in general. This is particularly important for sizing and constructing embankment regulation facilities, flood protection, and other hydrotechnical facilities (hydropower plants, dams, etc.).

Keywords

meander, flow, velocity, entropy, hydrometry

1 Introduction

Modern hydrometry aims to use inexpensive, uncomplicated measurement devices and procedures to obtain velocity distributions and flow values. However, many models and calculation procedures are available to solve these tasks. Reliable results require reliable input data, but because of the complexity of watercourse behavior and limited equipment, it is often not possible to obtain accurate results for the sizing and construction of many hydrotechnical facilities.

The presented research will show an adequate procedure usable for solving many engineering tasks in watercourses, along with a scientific contribution. The complex situation of meanders in watercourse analysis will be investigated through a real case study on the Bednja River in Croatia, focusing on a meander curve. Another impediment is complex watercourse geometry, with changes in the riverbed and longitudinal and transversal profiles, as well as changes in water velocity and direction.

Determining the velocity distribution in river meanders is a well-known research topic (Hooke, 2023),

especially when water flows through alluvium or karst media. In general, research on meanders is divided into hydrology and morphology (Zamyshlyaev, 2025). Research by Bradley and Smith (1984) shows that changes in flow affect meander changes, i.e., river geometry. With increasing flow, the watercourse width at the meander starts to extend due to the impact of the velocity and water stroke. Laboratory models were also used to determine functional dependencies between hydrological and morphological parameters (Yılmazer and Arı Güner, 2024), but they cannot replace field conditions or the irregular profiles of watercourses (Jamaludin et al., 2025).

To simplify this complex task, researchers have developed many methods, procedures, and models to gain insight into the quality and quantity of information on velocity, river geometry, and flow values. Camera-based methods such as large-scale particle image velocimetry (LSPIV) have also been used to estimate river surface velocities and discharge (Fujita et al., 1998; Le Boursicaud et al., 2016), but they were not applied in the present study. The research presented by Biggs et al. (2023) and Despax et al. (2016) provides wide application and insight into the actual state-of-the-art of river hydrometry. This research is based on entropy theory and compares measured maximum surface velocity values from a propeller-based current meter with results from the Acoustic Doppler Velocity (ADV) device. We selected and measured four profiles on the river meander at the analyzed location, Lovrentovec.

2 Methods

At each cross section, velocities were measured at verticals spaced 0.5 m apart, following a professional rule of thumb of 1/20 of the total width of the cross profile. At each vertical, we measured at a fraction of the depth: 0.6 of the depth below 0.5 m, and for depths greater than 0.5 m, at 0.2 and 0.8 of the depth at each vertical. The measurement duration at each point, depth, and vertical was 40 s.

The velocity distribution based on the entropy method along the defined verticals is presented in Bahmanpouri et al. (2022a) and Bahmanpouri et al. (2022b):

$$U(x_i, y) = \frac{U_{\max v}(x_i)}{M} \ln\left[1 + (e^M - 1)\frac{y}{D(x_i) - h(x_i)} \exp\left(1 - \frac{y}{D(x_i) - h(x_i)}\right)\right] \quad i = 1...N_v \tag{1}$$

Where U is the time-averaged velocity, $U_{maxv}(x_i)$ is the maximum value of U along the ith vertical, x_i is the distance of the ith sampled vertically from the left bank, $h(x_i)$ is the dip, i.e., the depth of $U_{maxv}(x_i)$ below the water surface, $D(x_i)$ the flow depth, y is the distance of the velocity point from the bed, and N_v is the number of verticals sampled across the river section.

M is the entropic parameter and can be calculated using the linear entropic relation (Bahmanpouri et al., 2024):

$$U_m = \left(\frac{e^M}{e^M - 1} - \frac{1}{M}\right) U_{max} = \phi(M) U_{max} \tag{2}$$

U_{max} surmises the maximum value of $U_{maxv}(x_i)$ sampled in the cross-sectional flow area. The maximum value of the velocity refers to the position of the maximal depth-wise velocity magnitude, i.e., the velocity dip phenomenon.

3 Results and Discussion

Figure 1 shows the analyzed site and the locations of four cross profiles through the meander. Water flows from P1 to P4. In the wide analyzed area, River Bednja flows through sand and gravel media, but in the analyzed section it flows through an interlayer of carbonate limestone.

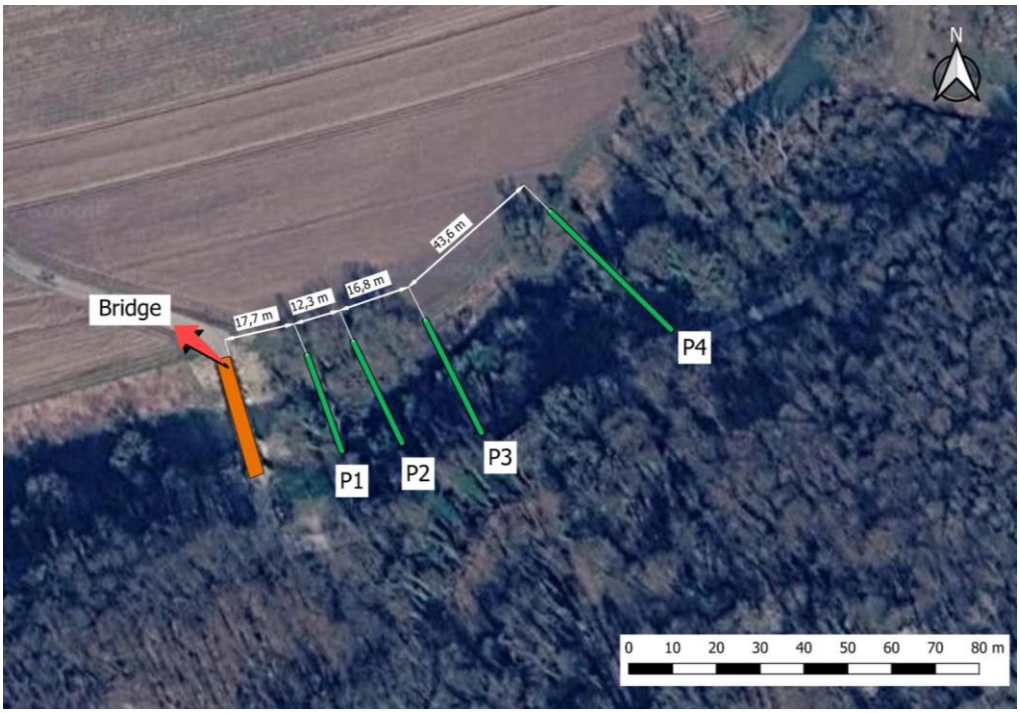


Figure 1. Analyzed site and location of four analyzed profiles (Google Maps, 2026)

Profiles 1 and 4 are the beginning and, respectively, the ending of the analyzed meander. Figures 2-5 show the perspective of each profile, together with an example of the measurement procedures. Application of the ADV is shown in Figures 2 and 5. Figures 3 and 4 show measurements for a propeller-based current meter. The distance between vertical transverse stations was 0.5 m, in accordance with professional rules (ISO standard) and for uniformity of measurement.



Figure 2. Cross profile P1

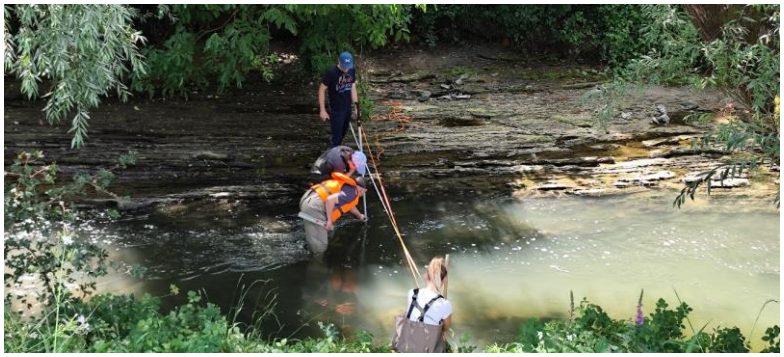


Figure 3. Cross profile P2

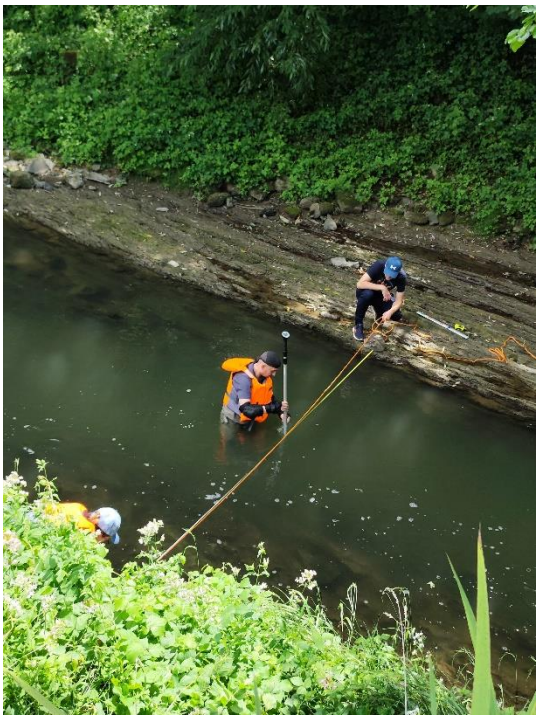


Figure 4. Cross profile P3



Figure 5. Cross profile P4

Cross profile P4 is the only one in the alluvium surroundings, while the other three profiles are in the carbonate limestone media. This combination implies flow dynamics different from those expected with a single soil type.

Figures 6 to 9 show depth and maximum surface velocity distributions for each profile.

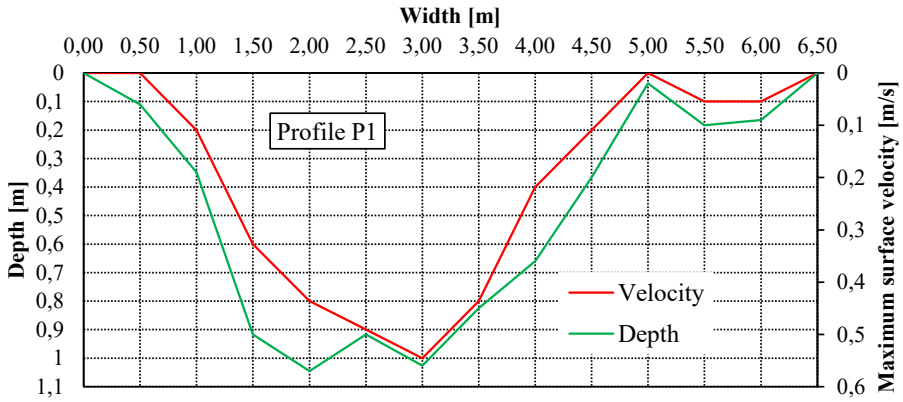


Figure 6. Depth and maximum surface velocity distributions for profile P1

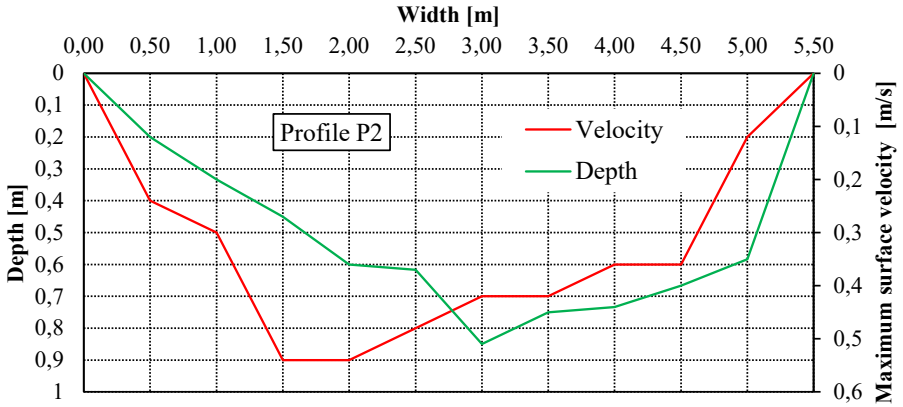


Figure 7. Depth and maximum surface velocity distributions for profile P2

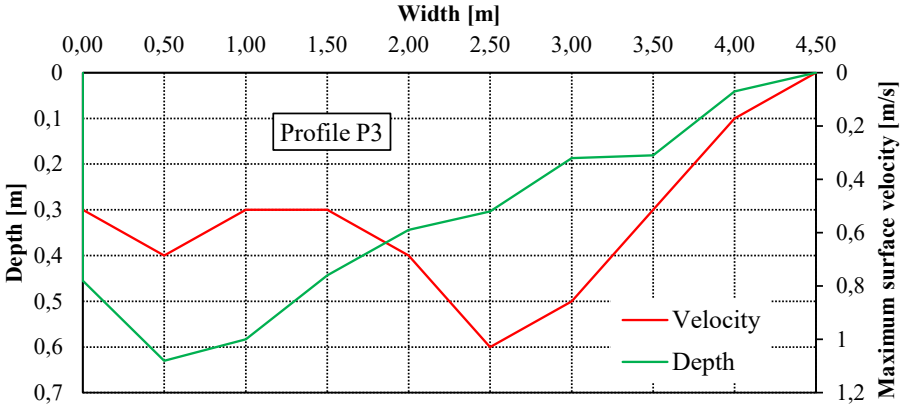


Figure 8. Depth and maximum surface velocity distributions for profile P3

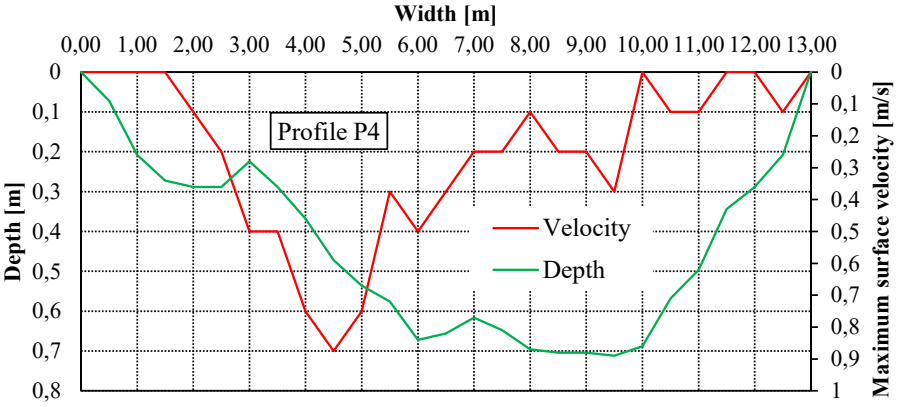


Figure 9. Depth and maximum surface velocity distributions for profile P4

Profiles P2 and P3 show rock erosion due to a change in the rectilinear movement of water due to the curvature of the meander. Also, the velocity profiles on the mentioned profiles do not overlap with the depth profiles. Differences in channel geometry and bed roughness may contribute to these velocity patterns, but the present measurements cannot determine their individual effects. Normally, depth increases with velocity. Profile P1 is of a regular shape, due to a straight, long inlet of a river with constant and unchanged layers. Profile P4 is on the outlet part of the river, and after 20 meters there is another meander, so this is an explanation for the irregular shape of the cross profile P4, as well as the uneven distribution of the velocity.

Figure 10 shows Pseudo-code for the heat-mapping procedure for velocity-field reconstruction, based on maximum surface velocity.

```
procedure ANALYZE(measured data)
    Read measured coordinates x, depths d, and velocities v
    Remove invalid or missing measurements
    Determine characteristic values:
        x_max  ← x at maximum(v)
        U_max  ← maximum(v)
        x_last ← maximum(x)
    Construct computational domains:
        x_left  □ [0, x_max]
        x_right □ [x_max, x_last]
    Compute analytical velocity distributions:
        v_e(x) ← elliptic velocity model
        v_p(x) ← parabolic velocity model
    Interpolate measured velocity:
        v_m(x) ← interp(x, v)
    Compute integrated velocities:
        A_m ← ∫ v_m(x) dx
        A_e ← ∫ v_e(x) dx
        A_p ← ∫ v_p(x) dx
    Compute mean velocities:
        v¯_m ← A_m / L
        v¯_e ← A_e / L
        v¯_p ← A_p / L
    Compute cross-sectional area:
        A_cs ← ∫ d(x) dx
    Estimate discharge:
        Q_e ← v¯_e · A_cs
        Q_p ← v¯_p · A_cs
    Generate two-dimensional computational mesh (x, y)
    Evaluate velocity fields:
        V_e(x, y)
        V_p(x, y)
    Apply bathymetry mask:
        Remove points where y > d(x)
    Interpolate bathymetry:
        d_bath(x) ← interp(x, d)
    Visualize velocity fields and bathymetry
    Export bathymetry data
    return Q_e, Q_p, d_bath
end procedure
```

Figure 10. Pseudo-code for the heat-mapping procedure

Figures 11 to 14 show the distribution of average velocities through cross profiles P1-P4 using entropy theory (equations 1 and 2). We used parabolic and elliptic distributions for each calculation. Tables 1 to 4 show the summary of the results obtained by ADV measurement and entropy theory.

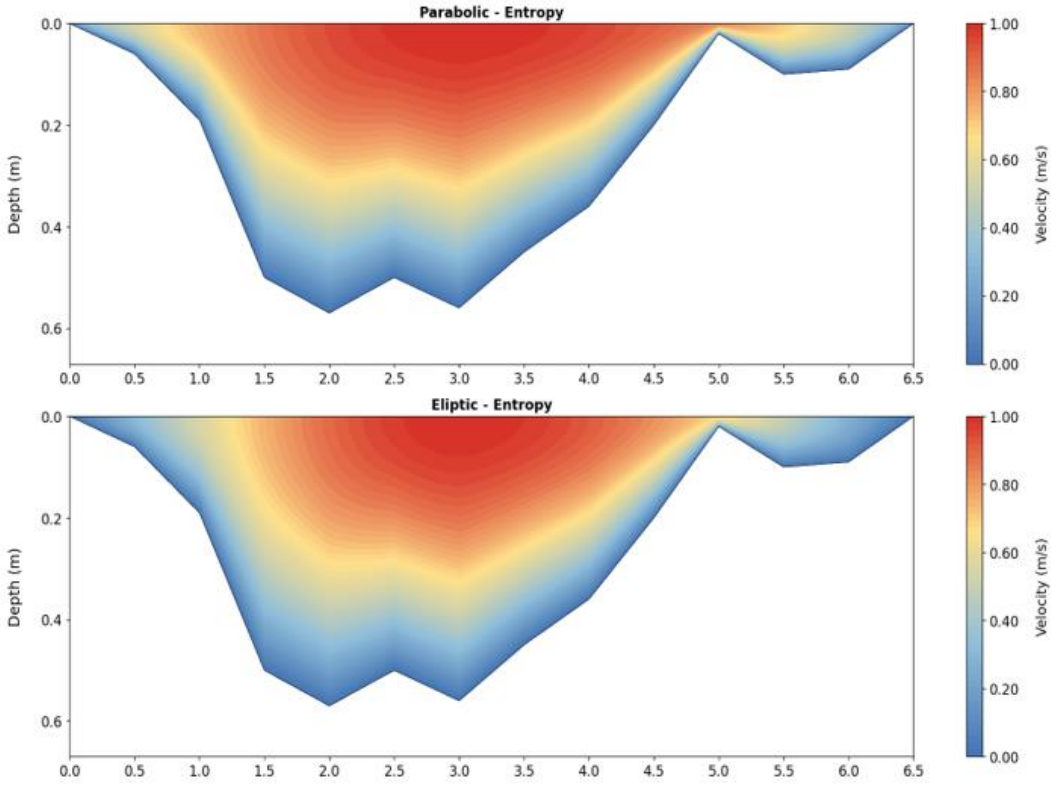


Figure 11. Obtained distribution of the average velocities by Entropy theory through cross profile P1

Table 1. Obtained results by measurements and Entropy theory for the cross profile P1

Area under measured curve:	2.550 m²
Area under elliptic curve:	5.100 m²
Area under parabolic curve:	4.333 m²
Percentage of measured area vs elliptic:	99.98%
Percentage of measured area vs parabolic:	69.92%
Mean velocity (measured by ADV):	0.39 m/s
Mean velocity (elliptic):	0.78 m/s
Mean velocity (parabolic):	0.67 m/s
Cross-sectional area *A*:	1.800 m²
Discharge *Q* (elliptic, v_mean*A):	1412 l/s
Discharge *Q* (parabolic, v_mean*A):	1200 l/s
Discharge *Q* (measured by ADV):	756 l/s

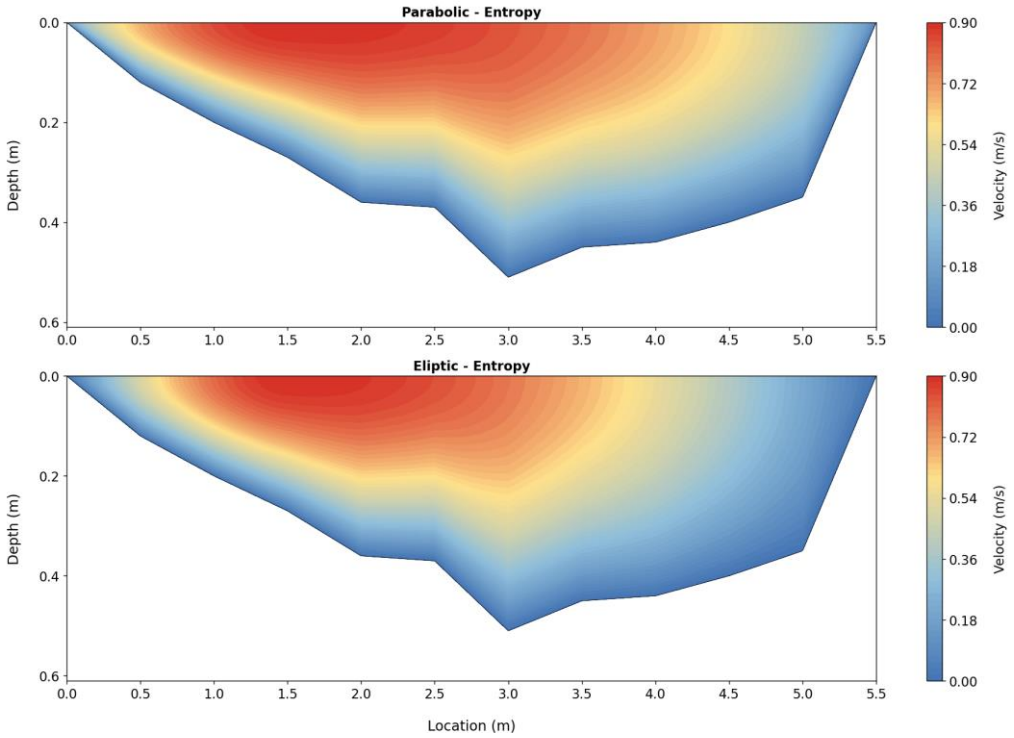


Figure 12. Obtained distribution of the average velocities by Entropy theory through cross profile P2

Table 2. Obtained results by measurements and Entropy theory for the cross profile P2

Area under measured curve:	3.150 m²
Area under elliptic curve:	3.883 m²
Area under parabolic curve:	3.300 m²
Percentage of measured area vs elliptic:	23.30%
Percentage of measured area vs parabolic:	4.76%
Mean velocity (measured by ADV):	0.57 m/s
Mean velocity (elliptic):	0.71 m/s
Mean velocity (parabolic):	0.60 m/s
Cross-sectional area *A*:	1.735 m²
Discharge *Q* (elliptic, v_mean*A):	1225 l/s
Discharge *Q* (parabolic, v_mean*A):	1041 l/s
Discharge *Q* (measured by ADV):	745 l/s

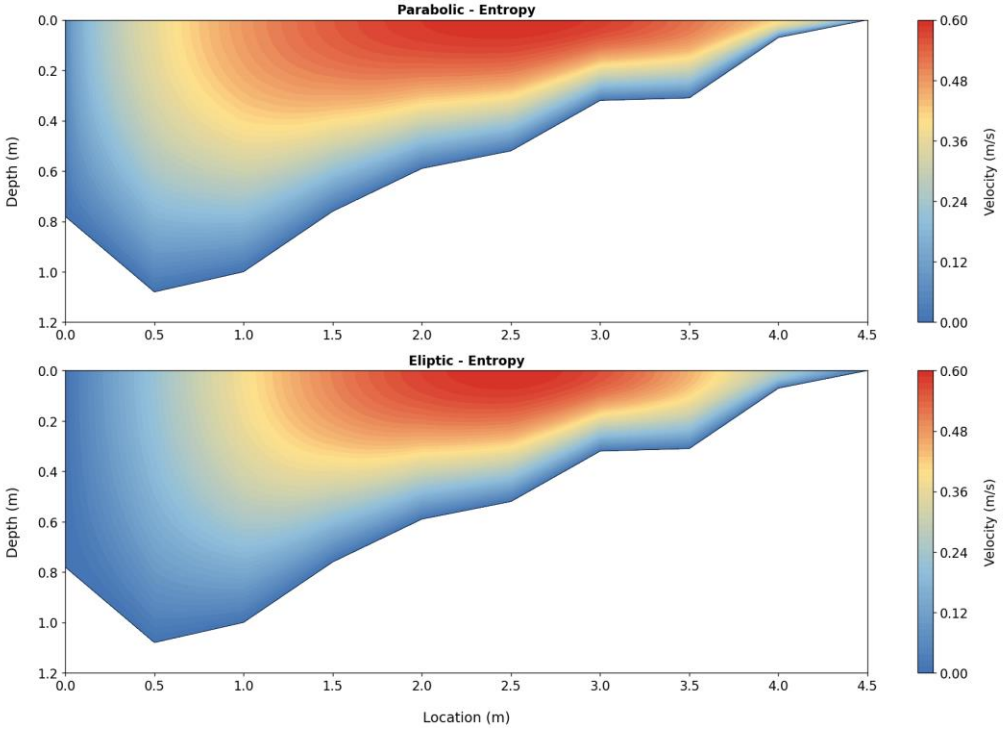


Figure 13. Obtained distribution of the average velocities by Entropy theory through cross profile P3

Table 3. Obtained results by measurements and Entropy theory for the cross profile P3

Area under measured curve:	1.525 m²
Area under elliptic curve:	2.118 m²
Area under parabolic curve:	1.800 m²
Percentage of measured area vs elliptic:	38.89%
Percentage of measured area vs parabolic:	18.01%
Mean velocity (measured by ADV):	0.34 m/s
Mean velocity (elliptic):	0.47 m/s
Mean velocity (parabolic):	0.40 m/s
Cross-sectional area *A*:	2.520 m²
Discharge *Q* (elliptic, v_mean*A):	1186 l/s
Discharge *Q* (parabolic, v_mean*A):	1008 l/s
Discharge *Q* (measured by ADV):	707 l/s

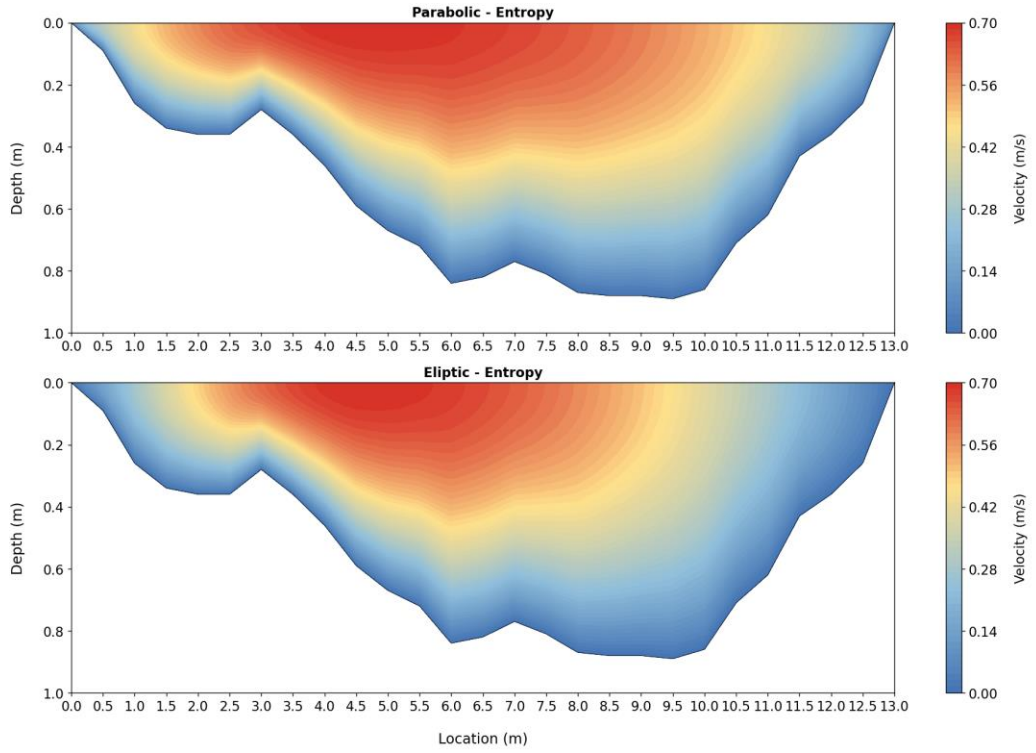


Figure 14. Obtained distribution of the average velocities by Entropy theory through cross profile P4

Table 4. Obtained results by measurements and Entropy theory for the cross profile P4

Area under measured curve:	2.751 m²
Area under elliptic curve:	7.139 m²
Area under parabolic curve:	6.066 m²
Percentage of measured area vs elliptic:	159.52%
Percentage of measured area vs parabolic:	120.51%
Mean velocity (measured by ADV):	0.10 m/s
Mean velocity (elliptic):	0.55 m/s
Mean velocity (parabolic):	0.47 m/s
Cross-sectional area *A*:	7.320 m²
Discharge *Q* (elliptic, v_mean*A):	3978 l/s
Discharge *Q* (parabolic, v_mean*A):	3380 l/s
Discharge *Q* (measured by ADV):	739 l/s

The largest difference between measured and calculated flow occurred at profile P4, at 3239 l/s. Applying the elliptic distribution leads to a larger deviation than the parabolic distribution, and these results should be taken with caution. Nevertheless, even parabolic distribution gives the largest deviations for all profiles. This may be explained by drastic changes in the depth values of all cross profiles, which affect the actual velocity distribution and, later, the flow values. The impact of the meander is also significant, because at the same location and on upstream profiles without meanders (Šamanović et al., 2026), such analysis shows smaller differences between measured and calculated values. Also, water flow through sand or gravel produces a more regular cross-profile section than in rock media, such as carbonate limestone. In general, low-depth water courses with such small flow values and drastic velocity changes should be treated with caution, because applying entropy theory may lead to large discrepancies in the measured values.

4 Conclusion

The presented research has shown that meandering flow properties are very complex compared with flow on the straight part of the watercourse. Channel geometry and bed roughness may affect the measured velocity distributions and the resulting discharge estimates. For future measurements, use a smaller width (i.e., the distance between verticals on the cross-profile stationing) to get more precise insight into the velocity distribution. At least more measurements, as many as possible, should be done at the same locations. Future work will assess whether camera-based surface image velocimetry using an unmanned aerial vehicle or smartphone can provide suitable input velocities for the entropy model.

Acknowledgements

This research was supported by the scientific project 'Advanced Numerical and Statistical Methods in the Analysis of Surface and Groundwater Resource Use and Protection Scenarios', Project No. UNIN-TEH-26-1-2, University North, Varaždin, Croatia, 2026.

References

Bahmanpouri, F., Barbetta, S., Gualtieri, C., Ianniruberto, M., Filizola, N., Termini, D., & Moramarco, T. 2022a Prediction of river discharges at confluences based on Entropy theory and surface-velocity measurements. *Journal of Hydrology*, 606, 127404. https://doi.org/10.1016/j.jhydrol.2021.127404

Bahmanpouri, F., Eltner, A., Barbetta, S., Bertalan, L., & Moramarco, T. 2022b Estimating the Average River Cross-Section Velocity by Observing Only One Surface Velocity Value and Calibrating the Entropic Parameter. *Water Resources Research*, 58(10), e2021WR031821

Bahmanpouri, F., Lazzarin, T., Barbetta, S., Moramarco, T., & Viero, D. P. 2024 Estimating velocity distribution and flood discharge at river bridges using entropy theory – insights from computational fluid dynamics flow fields. *Hydrology and Earth System Sciences Discussions*, 28(16), 1-29. https://doi.org/10.5194/hess-28-3717-2024

Biggs, H., Smart, G., Doyle, M., Eickelberg, N., Aberle, J., Randall, M., & Detert, M. 2023 Surface Velocity to Depth-Averaged Velocity—A Review of Methods to Estimate Alpha and Remaining Challenges. *Water*, 15(21), 3711. https://doi.org/10.3390/w15213711

Bradley, C., & Smith, D. G. 1984, Meandering channel response to altered flow regime: Milk River, Alberta and Montana. *Water Resour. Res.*, 20(12), 1913–1920, doi:10.1029/WR020i012p01913

Despax, A., Perret, C., Garçon, R., Hauet, A., Belleville, A., Le Coz, J., & Favre, A.-C. 2016 Considering sampling strategy and cross-section complexity for estimating the uncertainty of discharge measurements using the velocity-area method. *Journal of Hydrology*, 533, 128–140. https://doi.org/10.1016/j.jhydrol.2015.11.048

Fujita, I., Muste, M., & Kruger, A. 1998 Large-scale particle image velocimetry for flow analysis in hydraulic engineering applications. *Journal of Hydraulic Research*, 36(3), 397–414. https://doi.org/10.1080/00221689809498626

Google Maps 2026. https://www.google.com/maps Access date 15.06.2026.

Hooke, J. 2023 Morphodynamics of active meandering rivers reviewed in a hierarchy of spatial and temporal scales. *Geomorphology* 493 (108825), doi: 10.1016/j.geomorph.2023.108825

Jamaludin, A. N. I., Jumain, M., Ibrahim, Z., Wan Mustafah Kamal, W.N.A., Ismail, F. N. A., Abdul Karim, M.U.H., & Makhtar, M.R. 2025 Hydraulics and morphodynamics of a meandering channel with angled baffles. *IOP Conf. Ser.: Earth Environ. Sci.* 1453 012060 doi: 10.1088/1755-1315/1453/1/012060

Le Boursicaud, R., Pénard, L., Hauet, A., Thollet, F., & Le Coz, J. 2016 Gauging extreme floods on YouTube: application of LSPIV to home movies for the post-event determination of stream discharges. *Hydrol. Process.*, 30: 90–105. doi: 10.1002/hyp.10532

Šamanović, S., Đurin, B., Cetl, V., & Bahmanpouri, F. 2026 Determination of the Surface Watercourse Velocities by Using the Propeller Current Meter, Unmanned Aerial Vehicle, and Mobile Phone. *Water* 18, 273. https://doi.org/10.3390/w18020273

Yılmazer, C., & Arı Güner, H.A. 2024 Physical and Numerical Modeling of Flow in a Meandering Channel. *Water*, 16, 1547. https://doi.org/10.3390/w16111547
Zamyshlyaev, V. I. 2025 "Meandr" and "Izluchina" as morphological units of planimetry of a meandering channel: analysis of existing concepts. *Soil erosion and channel processes* 3(1-9).

INNOVATIVE TREND ANALYSIS (ITA) OF GROUNDWATER QUALITY PARAMETERS AT THE BARTOLOVEC WELLFIELD (CROATIA)

Marko ŠRAJBEK [1*], Bojan ĐURIN [1], Mihael MIKIĆ [1], Nikolina NOVOTNI-HORČIČKA [2]

[1] *University North, Department of Civil Engineering, Varaždin, Croatia*

E-mail: msrajbek@unin.hr

E-mail: bojan.durin@unin.hr

E-mail: mimikic@unin.hr

[2] *Varkom d.d., Trg bana Josipa Jelačića 15, 42000, Varaždin, Croatia*

E-mail: nnovotni@varkom.com

[*] *Corresponding author*

Abstract

Groundwater is one of the most important sources of drinking water, especially in regions exposed to intensive agricultural and urban pressures, where long-term changes in water quality are increasingly evident. Continuous monitoring and analysis of groundwater quality are therefore essential for sustainable water resource management and the timely identification of potential contamination processes. In this study, long-term trends in groundwater-quality parameters at the Bartolovec wellfield in northern Croatia are analysed using the Innovative Trend Analysis (ITA) method. The analysis is based on a 30-year time series (1994–2023), which provides a robust basis for detecting temporal variations in groundwater quality. The selected parameters include nitrate and chloride concentrations, pH, electrical conductivity and oxidizability. The ITA method is used as an advanced and highly sensitive approach to trend detection. Unlike conventional statistical approaches, such as linear regression analysis, the ITA method does not require strict assumptions regarding data distribution, serial correlation or sample size and enables a more detailed and visually interpretable assessment of trends. The analysis is performed using annual average values, providing insight into long-term changes in groundwater quality. The results indicate statistically significant increases in electrical conductivity and nitrate concentration in the upper aquifer, whereas both parameters decreased in the lower aquifer. Oxidizability showed statistically significant decreasing trends in both aquifer layers, while chloride concentration decreased significantly only in the lower aquifer. The results contribute to an improved understanding of the temporal development of groundwater quality and support the development of effective groundwater-protection and management strategies. The study further highlights the importance of applying innovative analytical methods to long-term environmental datasets, particularly amid increasing anthropogenic pressures and the need for sustainable groundwater-resource management.

Key words

groundwater quality, innovative trend analysis (ITA), long-term monitoring, wellfield, nitrates

1 Introduction

Groundwater is a strategic natural resource for public water supply, agriculture, industry and ecosystem preservation. Although generally less exposed to rapid quality changes than surface water, contaminants reaching an aquifer may persist for long periods because of slow groundwater movement and limited

natural renewal (Juntakut et al., 2019; Kyte et al., 2023). Groundwater-quality changes are therefore often gradual and may remain undetected without long-term systematic monitoring. Urbanisation, industrial development, transport infrastructure, municipal wastewater and intensive agriculture can exert considerable pressure on groundwater resources, particularly in highly permeable alluvial aquifers (Dyvak et al., 2021; Zhao et al., 2022; Craswell, 2021). Continuous monitoring of physicochemical groundwater-quality parameters is therefore essential for detecting deterioration and supporting timely protection measures (Li et al., 2020; Mester et al., 2024). Parameters such as pH, electrical conductivity, oxidizability, chloride and nitrate concentrations are commonly monitored because they provide complementary information on groundwater quality and its temporal variation (Kurwadkar et al., 2020; Barbieri et al., 2023; Chowdhury et al., 2025). This issue is particularly relevant in the Varaždin region of northern Croatia, characterised by dense settlement, intensive agriculture and considerable economic activity. Previous studies have shown pronounced spatial and temporal changes in groundwater quality caused by both diffuse and point pollution sources, with nitrate contamination representing the most important long-term problem (Nemčić-Jurec et al., 2007; Šrajbek et al., 2020; Šrajbek et al., 2022; Kovač et al., 2025). Earlier investigations associated elevated nitrate concentrations with changes in the groundwater-flow regime following construction and operation of hydropower facilities on the Drava River (Grđan, 1989), whereas more recent studies indicate that present contamination is primarily related to point and diffuse sources within or near wellfield recharge areas (Šrajbek et al., 2022). Until the mid-1990s, the Varaždin wellfield was the principal source of drinking water for the regional water-supply system, but persistently elevated nitrate concentrations caused a gradual reduction in groundwater abstraction and its withdrawal from regular operation in 2004. This increased the importance and abstraction capacity of the Bartolovec wellfield. Groundwater at Bartolovec is abstracted from upper and lower aquifer layers, largely separated by a semi-permeable silty and clayey aquitard. The upper aquifer is more directly exposed to surface influences, whereas the intervening fine-grained deposits provide partial protection to the lower aquifer. Previous investigations consequently showed generally better groundwater quality in the lower aquifer (Kovač et al., 2017). Nevertheless, the entire system remains highly vulnerable to anthropogenic contamination, emphasising the need for continuous monitoring and effective protection of the recharge area (Larva et al., 2023; Umar et al., 2022).

Previous monitoring results also indicate differences in groundwater quality among regional wellfields and between the two aquifer layers (Šrajbek et al., 2024). The arithmetic mean values presented in Table 1 show substantially higher nitrate concentrations at the Varaždin wellfield than at Bartolovec and Vinokovščak. At Bartolovec, nitrate and chloride concentrations were lower in the lower aquifer, whereas pH, oxidizability and ammonia concentrations were relatively similar between analysed locations. These findings confirm the importance of analysing groundwater-quality parameters separately for the upper and lower aquifer layers. The values in Table 1 provide an overview of groundwater-quality conditions during the earlier monitoring period and highlight the need to assess their temporal development. Previous research at the Bartolovec wellfield using conventional statistical procedures identified significant differences between aquifer layers and parameter-specific temporal changes, particularly for nitrate and chloride concentrations (Šrajbek et al., 2024). However, groundwater-quality time series may exhibit behaviour that cannot be adequately represented by a single linear or monotonic trend. Low, medium and high values of the same parameter may develop differently over time because of changes in pollution sources, land use, groundwater abstraction, precipitation and aquifer recharge. Innovative Trend Analysis (ITA) provides a graphical and quantitative approach for identifying such changes. The method divides a time series into two equal subseries, sorts their values in ascending order and compares them in a Cartesian coordinate system. Values near the 1:1 line indicate no trend, whereas deviations above or below the line indicate increasing or decreasing trends. ITA also enables separate assessment of low, medium and high value ranges and can therefore identify non-monotonic patterns that may remain undetected by conventional methods. Furthermore, it does not require strict assumptions regarding data distribution, serial correlation or sample size (Şen, 2012; Kişi and Ay, 2014).

Table 1. Arithmetic means of certain groundwater quality parameters in the period 1993–2017 (Šrajbek et al., 2024)

Parameter	Varaždin 1*	Varaždin 2**	Bartolovec 1*	Bartolovec 2**	Vinokovščak
pH	7.40	7.43	7.40	7.48	7.36
$KMnO_4$ (mg/L O_2)	0.75	0.62	0.61	0.61	0.60
Ammonia (NH_4^+ mg/L)	0.008	0.000	0.007	0.007	0.011
Nitrates (NO_3 mg/L)	79.74	54.68	20.55	11.04	24.45
Chlorides (Cl mg/L)	19.21	13.96	22.94	8.56	13.83

* upper aquifer layer
** lower aquifer layer

Accordingly, the objective of this study is to apply ITA to annual average groundwater-quality data from the Bartolovec wellfield for the 30-year period 1994–2023. Five physicochemical parameters are analysed: pH, electrical conductivity, oxidizability, chloride concentration and nitrate concentration. The analysis is performed separately for the upper and lower aquifer layers to determine the direction, magnitude and statistical significance of long-term trends and to identify possible differences among low, medium and high values. The results are intended to provide a more detailed understanding of temporal groundwater-quality changes and support effective monitoring, protection and sustainable management of the Bartolovec aquifer system.

2 Materials and Methods

2.1 The Study Area

The study area is located in Varaždin County in northern Croatia and includes the Bartolovec wellfield, situated approximately 8.5 km east of the city of Varaždin (Fig. 1). In a broader geographical context, the area lies along the western margin of the Pannonian Plain and in the immediate vicinity of the Drava River. The terrain is predominantly flat to gently undulating and is characterised by a temperate continental climate, with warm summers and cold winters. Varaždin County is one of the most densely populated and economically developed regions in Croatia, with intensive agricultural production, urban areas, industrial activities and major transport infrastructure. These characteristics result in considerable demand for drinking water and simultaneously create potential pressures on groundwater quality. Organised public water supply in the Varaždin region began during the 1960s with the establishment of the Varaždin Regional Water Supply System. The system is supplied primarily from the Bartolovec, Varaždin and Vinokovščak wellfields and provides drinking water to approximately 150,000 inhabitants in 216 settlements through about 46,000 service connections. The Bartolovec wellfield was commissioned in 1972 and has gradually become the principal source of drinking water for the regional water-supply system. Its importance increased considerably after elevated nitrate concentrations caused a reduction in pumping from the Varaždin wellfield, which was withdrawn from regular operation in 2004. The abstraction capacity of Bartolovec was consequently expanded over several decades through the construction of additional wells. The wellfield currently consists of nine wells abstracting groundwater from the upper and lower aquifer layers, with a total capacity exceeding 500 l/s. The location of the Bartolovec wellfield and the spatial distribution of the production wells are shown in Fig. 1.

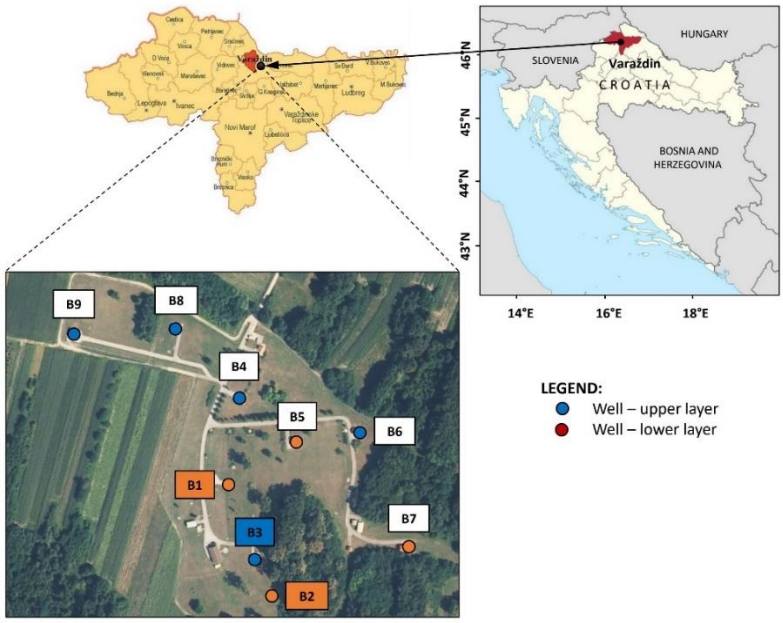


Figure 1. Location of the Bartolovec wellfield and spatial distribution of wells

2.2 Geological and Hydrogeological Conditions

The Bartolovec wellfield is located within the Quaternary alluvial deposits of the Drava River valley. The aquifer is predominantly composed of highly permeable gravel and sand, with locally occurring finer-grained deposits of silt and clay (Šimunić et al., 1982; Urumović et al., 1990). In the Bartolovec area, the aquifer is approximately 100 m thick and consists of upper and lower permeable layers that are largely separated by a semi-permeable aquitard, as shown in Fig. 2. This intermediate layer provides partial protection to the lower aquifer, whereas the upper layer is more directly exposed to surface influences. Nevertheless, the high permeability of the alluvial sediments and intensive land use within the recharge area make the aquifer system vulnerable to anthropogenic contamination (Larva et al., 2023).

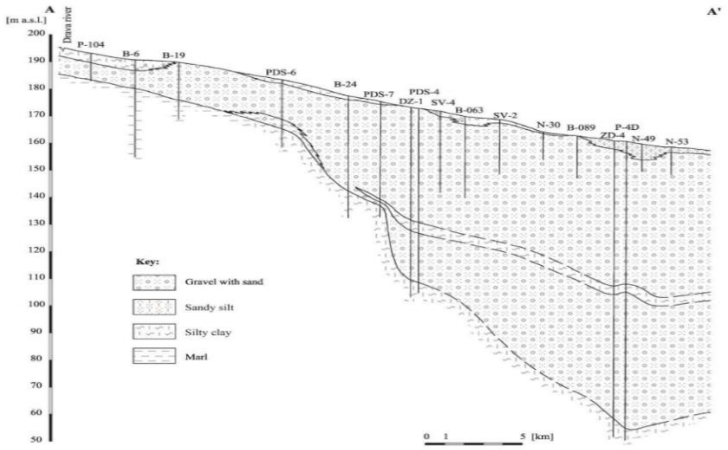


Figure 2. Longitudinal lithological profile of the Varaždin aquifer (Larva et al., 2023)

2.3 Experimental Data

Groundwater quality at the Bartolovec wellfield is systematically monitored at nine production wells, four of which abstract water from the upper aquifer layer and five from the lower aquifer layer. Chemical analyses are performed by the authorised laboratory of the Varkom d.d. utility company. Since only wells B1 and B2 in the upper aquifer and well B3 in the lower aquifer were continuously active throughout the entire observation period, the databases used in this study were formed using

measurements from these three wells. Groundwater samples were collected at least once a week whenever the respective wells were in operation, resulting in more than 1,000 individual measurements for each analysed parameter at each well. The analysis covers the 30-year period from 1994 to 2023 and includes five physicochemical groundwater-quality parameters: pH, electrical conductivity, oxidizability, chloride concentration and nitrate concentration. Annual arithmetic mean values were calculated from the available measurements for each parameter. The values obtained for wells B1 and B2 were combined to represent the upper aquifer layer, whereas the values measured at well B3 represented the lower aquifer layer. The resulting annual time series were used as input data for the Innovative Trend Analysis.

2.4 Methodology

Long-term trends in the selected groundwater-quality parameters were analysed using the Innovative Trend Analysis (ITA) method. The original annual time series was first divided into two equal subseries. Since the analysed period comprised 30 years, the first subseries represented 1994–2008, while the second represented 2009–2023. The values within both subseries were independently arranged in ascending order. The sorted values from the first half were plotted on the horizontal axis, whereas the corresponding values from the second half were plotted on the vertical axis of a Cartesian coordinate system. The 1:1 line, inclined at 45°, represents the no-trend condition. Data points located above this line indicate an increasing trend, while points below it indicate a decreasing trend. The distance of the points from the 1:1 line reflects the magnitude of the observed change. In addition to the general trend, the data range was divided into low, medium and high-value groups to identify possible non-monotonic behaviour within different parts of the time series (Şen, 2012; Šrajbek et al., 2025). The ITA trend slope was calculated as:

$$s = \frac{2(\overline{y_2} - \overline{y_1})}{n} \tag{1}$$

where *s* is the straight-line slope of the trend line represented by the ITA method; $\overline{y_2}$ and $\overline{y_1}$ are the arithmetic means of the first and second halves of the dependent variable; and *n* is the number of years of data. A positive value of s indicates an increasing trend, whereas a negative value indicates a decreasing trend. The standard deviation of the sampling slope was calculated as:

$$\sigma_s = \frac{2\sqrt{2}}{n\sqrt{n}}\sigma\sqrt{1-r} \tag{2}$$

where σ_s is the standard deviation of the sampling slope; σ is the standard deviation of the entire time series; and *r* is the correlation coefficient between the ascending sorted arithmetic means of the two halves. The lower and upper confidence limits were then determined as:

$$CL_{1-\alpha} = 0 \pm s_{cri} \cdot \sigma_s \tag{3}$$

where $CL_{1-\alpha}$ is the upper and lower confidence limits at α level of significance; σ_s is the standard deviation of sampling slope; and s is the slope value. In view of the methodology presented, the null hypothesis H0 is established, which means that there is no significant trend in the observed time series at the significance level α:

$$H0: |s| < \left|CL_{1-\alpha(95\%)}\right| \tag{4}$$

$$H0: |s| < \left|CL_{1-\alpha(99\%)}\right| \tag{5}$$

Conversely, an alternative hypothesis H1 is also set up, which confirms the existence of a trend in the observed time series at the significance level α:

$$H1: |s| > \left|CL_{1-\alpha(95\%)}\right| \tag{6}$$

$$H1: |s| > \left|CL_{1-\alpha(99\%)}\right| \tag{7}$$

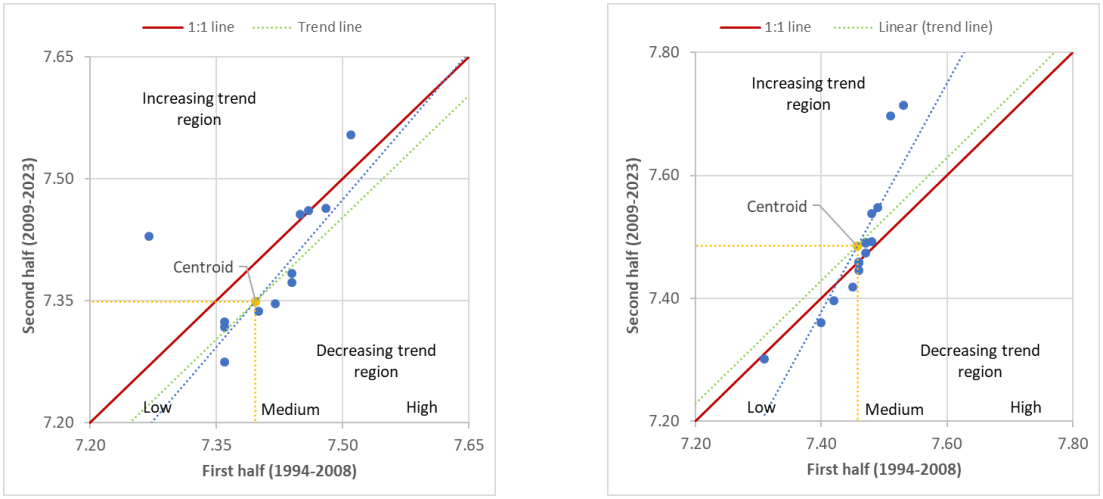
A positive (negative) value of s indicates an increasing/decreasing trend in the time series.

3 Results

3.1 pH

The ITA results for pH indicate opposite long-term trends in the two aquifer layers (Fig. 3). In the upper aquifer, most of the sorted values from the second subperiod are positioned below the 1:1 line, resulting in a negative trend slope of s=−0.00317. In the lower aquifer, the data are generally positioned above the 1:1 line and the calculated slope is positive (s=0.00187). As shown in Table 2, both slope values exceed the corresponding confidence limits at the 99% significance level, indicating a statistically significant decreasing trend in the upper aquifer and a statistically significant increasing trend in the lower aquifer. Nevertheless, the absolute slope values are small in both layers, showing that the long-term changes in pH were relatively limited.

The statistical indicators presented in Table 2 further show that the standard deviation was slightly higher in the upper aquifer (σ=0.09681) than in the lower aquifer (σ=0.08549), while the correlation between the sorted subseries was stronger in the lower layer (r=0.87166) than in the upper layer (r=0.69917). The ITA diagrams in Fig. 3 also show that the low, medium and high pH values remain relatively close to the no-trend line, confirming the generally stable behaviour of this parameter despite the statistically significant trends. Accordingly, the null hypothesis H0 is rejected for both aquifer layers, while the alternative hypothesis H1 is accepted, confirming a statistically significant decreasing pH trend in the upper aquifer and a statistically significant increasing trend in the lower aquifer at the 99% significance level.



(a) (b)

Figure 3. ITA diagrams of pH values in the (a) upper and (b) lower aquifer layers

3.2 Electrical conductivity

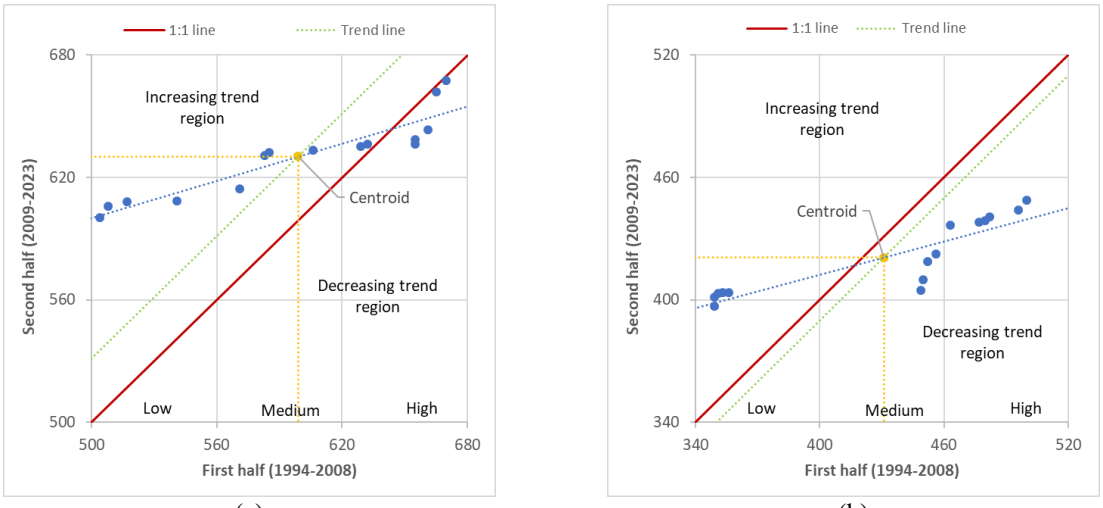
The ITA results for electrical conductivity indicate different long-term trends in the two aquifer layers (Fig. 4). In the upper aquifer, most of the sorted values from the second subperiod are positioned above the 1:1 line, indicating an increasing trend. The calculated slope is positive (s=2.09161) and exceeds the upper confidence limits at both significance levels. As shown in Table 2, the increasing trend is therefore statistically significant at the 99% level. A more detailed inspection of Fig. 4a shows that the low and medium electrical-conductivity values were generally higher in the second subperiod, whereas the highest values were greater in the first subperiod. This indicates that the overall increase was mainly associated with changes in the lower and central parts of the data range rather than with an increase in the highest recorded values.

In the lower aquifer, the points are generally distributed slightly below the 1:1 line, resulting in a negative slope of s=−0.67356. The slope exceeds the lower confidence limit at the 95% level but remains within the confidence limits at the 99% level. Consequently, Table 2 indicates a statistically significant

decreasing trend at the 95% level. The absolute slope is considerably smaller than that observed in the upper aquifer, indicating a less pronounced temporal change. Figure 4b shows a similar distribution pattern, with low and medium values generally higher in the second subperiod and the highest values greater in the first subperiod. The correlation between the sorted subseries is high in both layers, with values of r=0.92361 for the upper aquifer and r=0.87918 for the lower aquifer. Overall, electrical conductivity increased significantly in the upper aquifer, whereas a weaker decreasing trend was identified in the lower aquifer during the period 1994–2023. Accordingly, the null hypothesis H0 is rejected for both aquifer layers, while the alternative hypothesis H1 is accepted, confirming a statistically significant increasing trend in the upper aquifer at the 99% significance level and a statistically significant decreasing trend in the lower aquifer at the 95% significance level.

Table 2. ITA results for the analysed groundwater-quality parameters in the upper and lower aquifer layers (CL – confidence limits at the 1% and 5% significance levels)

Parameter	Layer	s	σ	r	σs	±CL (1%)	±CL (5%)	Significance level	Trend
pH	Upper	−0.00317	0.09681	0.69917	0.00091	0.00236	0.00179	99%	−
	Lower	0.00187	0.08549	0.87166	0.00053	0.00136	0.00103	99%	+
Electrical conductivity	Upper	2.09161	46.61294	0.92361	0.22176	0.57214	0.43465	99%	+
	Lower	−0.67356	43.94342	0.87918	0.26292	0.67833	0.51532	95%	−
Oxidizability	Upper	−0.01779	0.24700	0.98190	0.00057	0.00148	0.00112	99%	−
	Lower	−0.01063	0.24966	0.91728	0.00124	0.00319	0.00242	99%	−
Chlorides	Upper	−0.02804	3.48522	0.93853	0.01487	0.03837	0.02915	–	no trend
	Lower	−0.06467	1.76926	0.98049	0.00425	0.01097	0.00834	99%	−
Nitrates	Upper	0.15467	6.85680	0.95678	0.02454	0.06331	0.04809	99%	+
	Lower	−0.32951	3.88456	0.94518	0.01566	0.04039	0.03068	99%	−



(a) (b)

Figure 4. ITA diagrams of electrical conductivity in the (a) upper and (b) lower aquifer layers

3.3 Oxidizability

The ITA results for oxidizability indicate statistically significant decreasing trends in both aquifer layers (Fig. 5). In the upper aquifer, most of the sorted values from the second subperiod are positioned below the 1:1 line, resulting in a negative trend slope of s=−0.01779. As shown in Table 2, the absolute slope value exceeds the corresponding confidence limits at the 99% significance level, confirming a highly significant decreasing trend. A similar pattern is observed in the lower aquifer, where the calculated slope is also negative (s=−0.01063) and statistically significant at the 99% level. The decrease is therefore evident in both aquifer layers, although it is somewhat more pronounced in the upper aquifer. The statistical parameters presented in Table 4 show very similar standard deviation values in the upper and lower aquifers, amounting to σ=0.24700 and σ=0.24966, respectively. The correlation between the sorted subseries is high in both layers, particularly in the upper aquifer, where r=0.98190, compared with r=0.91728 in the lower aquifer. The ITA diagrams in Fig. 5 show that the decreasing pattern is present across the low, medium and high-value groups. Overall, oxidizability values, expressed in mg O_2/L, were lower in the second half of the analysed period in both aquifer layers, representing one of the most pronounced and consistent decreasing trends among the analysed groundwater-quality parameters. Accordingly, the null hypothesis H0 is rejected for both aquifer layers, while the alternative hypothesis H1 is accepted, confirming statistically significant decreasing trends in oxidizability in both the upper and lower aquifers at the 99% significance level.

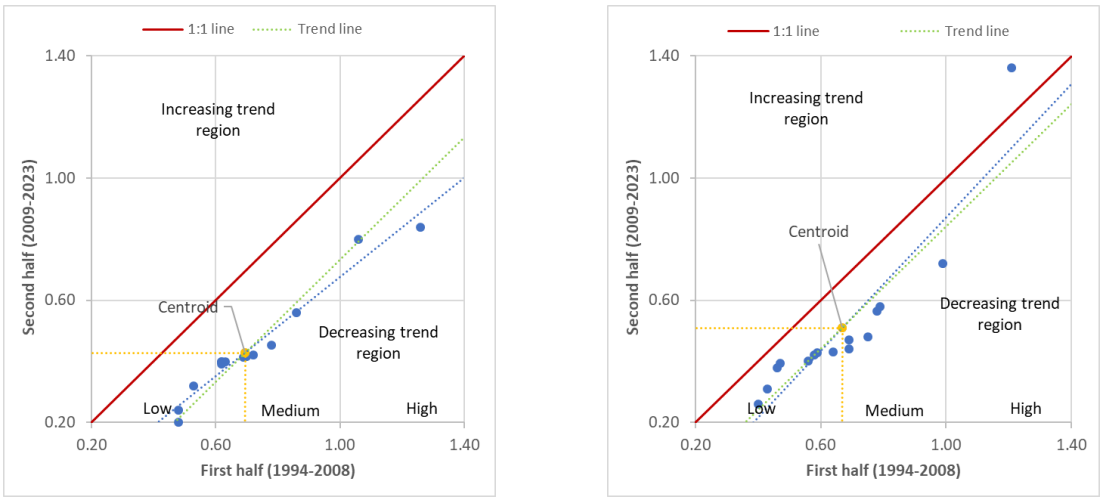


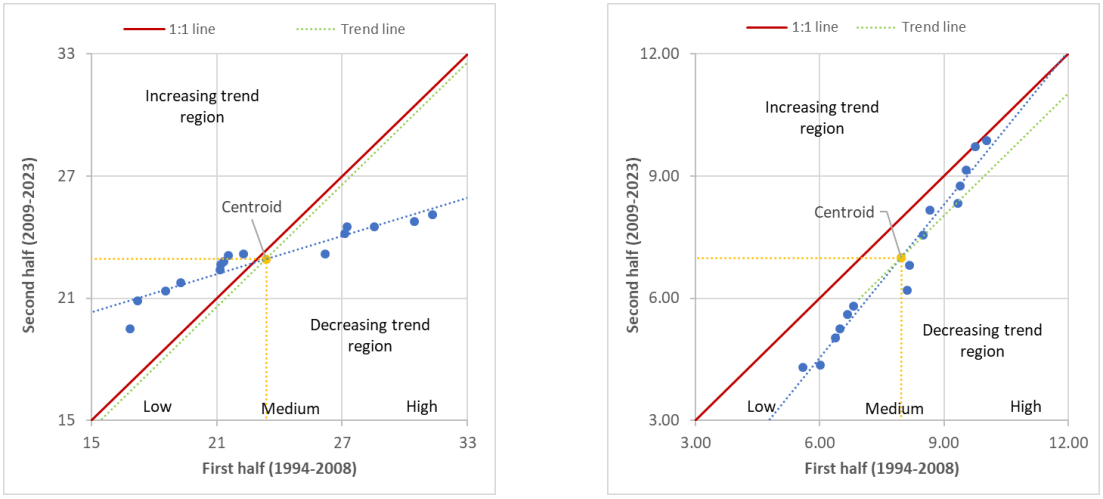
Figure 5. ITA diagrams of oxidizability in the (a) upper and (b) lower aquifer layers

3.4 Chlorides

The ITA results for chloride concentration indicate decreasing tendencies in both aquifer layers, although their statistical significance differs (Fig. 6). In the upper aquifer, the calculated slope is slightly negative (s=−0.02804), and the data points are generally distributed close to the 1:1 line. As shown in Table 2, the slope remains within both the 95% and 99% confidence limits, indicating that the observed decrease is not statistically significant. A more detailed inspection of Fig. 6a shows that the low chloride-concentration values were generally higher in the second subperiod, whereas the high values were lower than in the first subperiod. These opposite changes across the value range offset each other, which explains why no statistically significant overall trend was detected in the upper aquifer. Therefore, further analysis should divide the time series into additional subperiods to examine these temporal variations in greater detail.

A more pronounced decrease is observed in the lower aquifer, where most of the sorted values from the second subperiod are positioned below the 1:1 line. The calculated slope of s=−0.06467 is lower than the corresponding lower confidence limits at both the 95% and 99% significance levels. Consequently, Table 2 confirms a statistically significant decreasing trend at the 99% level. The correlation between the sorted subseries is high in both aquifer layers, amounting to r=0.93853 in the upper aquifer and

r=0.98049 in the lower aquifer. Overall, the results indicate no statistically significant long-term change in chloride concentration in the upper aquifer, while a clear and highly significant decrease was detected in the lower aquifer during the period 1994–2023.



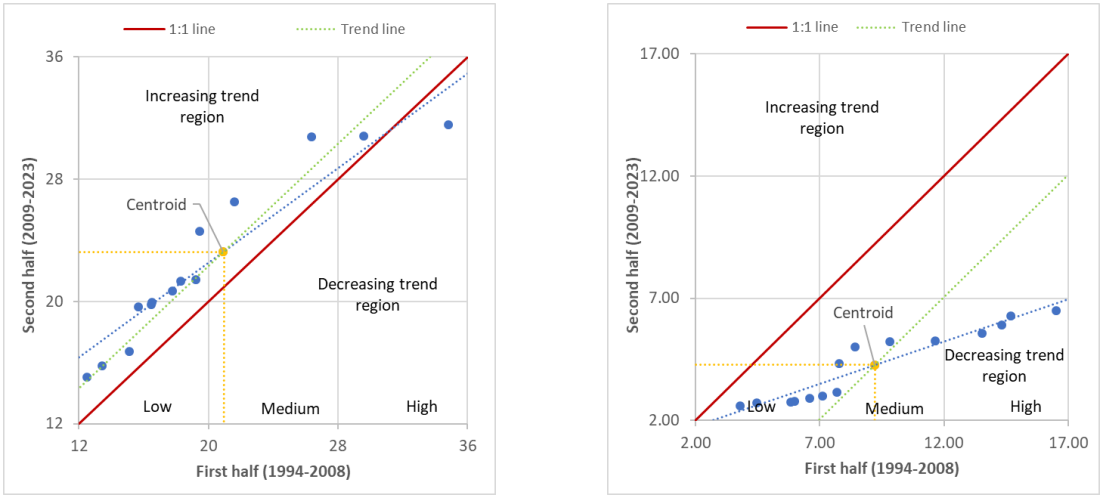
(a) (b)

Figure 6. ITA diagrams of chloride concentration in the (a) upper and (b) lower aquifer layers

3.5 Nitrates

The ITA results for nitrate concentration indicate statistically significant but opposite long-term trends in the two aquifer layers (Fig. 7). In the upper aquifer, most of the sorted values from the second subperiod are positioned above the 1:1 line, resulting in a positive trend slope of s=0.15467. As shown in Table 2, this value exceeds the upper confidence limits at both the 95% and 99% significance levels, confirming a statistically significant increasing trend. In contrast, the lower aquifer shows a pronounced negative slope of s=−0.32951, with most data points positioned below the 1:1 line. The absolute slope value exceeds the lower confidence limits at the 99% significance level, indicating a highly significant decreasing trend.

The statistical parameters presented in Table 6 show greater variability in the upper aquifer, where the standard deviation is σ=6.85680, compared with σ=3.88456 in the lower aquifer. The correlation between the sorted subseries is high in both layers, amounting to r=0.95678 in the upper aquifer and r=0.94518 in the lower aquifer. The ITA diagrams in Fig. 7 indicate that the increasing tendency in the upper aquifer is generally present across the analysed value range, while the lower aquifer shows a consistent decrease. Overall, nitrate concentrations increased significantly in the upper aquifer but decreased markedly in the lower aquifer during the period 1994–2023. These opposite trends further indicate different long-term behaviour of the two aquifer layers. Accordingly, the null hypothesis H0 is rejected for both aquifer layers, while the alternative hypothesis H1 is accepted, confirming a statistically significant increasing trend in nitrate concentration in the upper aquifer and a statistically significant decreasing trend in the lower aquifer, both at the 99% significance level.



(a) (b)

Figure 7. ITA diagrams of nitrate concentration in the (a) upper and (b) lower aquifer layers

4 Discussion

The results summarised in Table 3 demonstrate that long-term groundwater-quality changes at the Bartolovec wellfield are both parameter-specific and dependent on aquifer depth. Although statistically significant trends were identified for most parameters, their directions differed considerably between the upper and lower aquifer layers. The upper aquifer is more directly exposed to surface-derived influences, whereas the semi-permeable aquitard provides partial protection to the lower layer (Dragon, 2013). This interpretation is consistent with previous investigations of the Varaždin aquifer, which identified its high vulnerability to anthropogenic contamination and generally better groundwater quality in the deeper aquifer layer (Larva et al., 2023; Šrajbek et al., 2024).

Although statistically significant but opposite pH trends were detected in the two layers, the corresponding slope values were very small. The decreasing trend in the upper aquifer and increasing trend in the lower aquifer therefore represent only minor long-term changes, and pH can generally be considered stable over the analysed period. The limited variation may be associated with the natural buffering capacity of the alluvial aquifer sediments.

As shown in Table 3, electrical conductivity exhibited a statistically significant increasing trend in the upper aquifer at the 99% significance level, whereas a decreasing trend was detected in the lower aquifer at the 95% significance level. The increase in the upper layer indicates a gradual rise in the overall concentration of dissolved ionic substances. However, the ITA diagrams showed that the behaviour was not uniform across the entire value range, because low and medium values were generally higher in the second subperiod, while the highest values were greater in the first subperiod. This confirms the usefulness of ITA in identifying changes that cannot be fully described by a single overall trend.

Table 3. Summary of ITA trend directions and statistical significance for the analysed groundwater-quality parameters

Parameter	Upper layer	Lower layer
pH	↓	↑
Electrical conductivity	↑	↘
Oxidizability	↓	↓
Chlorides	→	↓
Nitrates	↑	↓

→ No significant trend
↘ Negative trend at the 95% significance level
↓ Negative trend at the 99% significance level
↑ Positive trend at the 99% significance level

The nitrate results require particular attention. A statistically significant increasing trend at the 99% significance level was identified in the upper aquifer, while a statistically significant decreasing trend at the same significance level was found in the lower aquifer. The increase in the upper layer is particularly important because elevated nitrate concentrations have already represented a serious groundwater-quality problem in the Varaždin region. Persistently high nitrate concentrations previously caused a reduction in groundwater abstraction and ultimately the withdrawal of the Varaždin wellfield from regular operation. Earlier studies identified both diffuse and point pollution sources, particularly agricultural activities and other surface-derived pressures, as important contributors to nitrate contamination in the Varaždin aquifer (Nemčić-Jurec et al., 2007; Šrajbek et al., 2020; Šrajbek et al., 2022; Wendland et al., 2020). Consequently, the significant positive nitrate trend in the upper aquifer should be treated as an important warning signal, even if the measured concentrations remain within the currently permitted limits. Particular attention should therefore be given to nitrate concentrations in the forthcoming monitoring period, together with a more detailed assessment of agricultural activities, fertiliser application, wastewater impacts, precipitation, aquifer recharge and groundwater abstraction within the wellfield recharge area.

In contrast, the decreasing nitrate trend in the lower aquifer indicates more favourable long-term behaviour and supports the protective role of the intermediate fine-grained deposits. Nevertheless, the lower layer should not be considered completely isolated from surface influences because the aquitard is semi-permeable and hydraulic connections between the two aquifer layers may occur. The opposite nitrate trends therefore indicate that contaminant transport and groundwater-quality development differ considerably with depth.

Oxidizability showed statistically significant decreasing trends at the 99% significance level in both aquifer layers. This was the most consistent result among the analysed parameters, with decreasing behaviour observed across the low, medium and high-value groups. Lower oxidizability values during the second subperiod may indicate a reduction in oxidisable substances in groundwater and therefore represent a favourable development in both layers.

Chloride concentration also showed different behaviour between the aquifer layers. A statistically significant decreasing trend at the 99% level was identified in the lower aquifer, whereas no significant overall trend was detected in the upper aquifer. However, the absence of a general trend in the upper layer does not mean that chloride concentrations remained unchanged across the entire data range. Low chloride values were generally higher in the second subperiod, whereas high values were lower than in the first subperiod. These opposite changes offset one another and resulted in the absence of a statistically significant overall trend. This non-uniform behaviour suggests that future chloride analysis should divide the time series into additional subperiods to identify possible changes in the dominant temporal pattern.

Overall, Table 3 shows that the lower aquifer generally exhibited more favourable long-term behaviour, with decreasing trends in electrical conductivity, oxidizability, chloride and nitrate concentrations. In contrast, the upper aquifer showed statistically significant increases in electrical conductivity and nitrate concentration, indicating continued sensitivity to anthropogenic surface pressures. Among all analysed results, the positive nitrate trend in the upper aquifer is the most important from the perspective of groundwater protection and public water supply. Continued monitoring should therefore be accompanied by more detailed seasonal and subperiod analyses and by the inclusion of groundwater levels, pumping rates, meteorological conditions, land use and agricultural practices to determine the causes of the observed trends more reliably.

5 Conclusion

This study applied Innovative Trend Analysis to a 30-year series of groundwater-quality data from the Bartolovec wellfield for the period 1994–2023. Five physicochemical parameters were analysed separately for the upper and lower aquifer layers: pH, electrical conductivity, oxidizability, chloride

concentration and nitrate concentration. The results confirmed that long-term groundwater-quality changes are both parameter-specific and dependent on aquifer depth. The upper aquifer showed statistically significant increasing trends in electrical conductivity and nitrate concentration at the 99% significance level, indicating continued sensitivity to surface-derived anthropogenic pressures. The increasing nitrate trend is particularly important because elevated nitrate concentrations have already caused serious groundwater-quality problems in the Varaždin aquifer system and contributed to the withdrawal of the Varaždin wellfield from regular operation. In contrast, electrical conductivity and nitrate concentration decreased in the lower aquifer, while oxidizability decreased significantly in both aquifer layers. Chloride concentration decreased significantly in the lower aquifer but showed no significant overall trend in the upper layer, where low values generally increased and high values decreased between the two subperiods. Statistically significant but weak and opposite pH trends were also identified, although the small slope values indicate generally stable pH conditions.

Overall, the lower aquifer exhibited more favourable long-term trends, supporting the protective role of the semi-permeable aquitard separating the two groundwater-bearing layers. Nevertheless, the increasing nitrate concentration and electrical conductivity in the upper aquifer emphasise the need for continued monitoring and effective protection of the Bartolovec wellfield recharge area. The results also demonstrate the usefulness of ITA for identifying the direction, magnitude and statistical significance of changes across low, medium and high-value groups. Further research should include more detailed seasonal analyses and subdivision of the available time series into additional subperiods, particularly for parameters showing non-uniform behaviour. Future studies should also integrate groundwater-quality data with groundwater levels, pumping rates, land use, agricultural practices and meteorological records to better determine the causes of the observed trends and support effective groundwater-management and protection measures.

References

Barbieri M., Barberio M.D., Banzato F., Billi A., Boschetti T., Franchini S., Gori F. and Petitta M. 2023 Climate change and its effect on groundwater quality. *Environmental Geochemistry and Health* 45, 1133–1144. https://doi.org/10.1007/s10653-021-01140-5

Chowdhury T.N., Battamo A., Nag R., Zekker I. and Salauddin M. 2025 Impacts of climate change on groundwater quality: a systematic literature review of analytical models and machine learning techniques. *Environmental Research Letters* 20. https://doi.org/10.1088/1748-9326/adb8ff

Craswell E. 2021 Fertilizers and nitrate pollution of surface and ground water: an increasingly pervasive global problem. *SN Applied Sciences* 3, 518. https://doi.org/10.1007/s42452-021-04521-8

Dragon K. 2013 Groundwater nitrate pollution in the recharge zone of a regional Quaternary flow system: Wielkopolska region, Poland. *Environmental Earth Sciences* 68, 2099–2109. https://doi.org/10.1007/s12665-012-1895-5

Dyvak M., Rot A., Pasichnyk R., Tymchyshyn V., Huliiev N. and Maslyiak Y. 2021 Monitoring and mathematical modeling of soil and groundwater contamination by harmful emissions of nitrogen dioxide from motor vehicles. *Sustainability* 13, 2768.

Grđan D. 1989 Utjecaj površinskih akumulacija na režim podzemnih voda (na primjeru akumulacija na rijeci Dravi) [in Croatian]. PhD thesis, Faculty of Mining, Geology and Petroleum Engineering, University of Zagreb, Zagreb, Croatia.

Juntakut P., Snow D.D., Haacker E.M.K. and Ray C. 2019 The long-term effect of agricultural, vadose zone and climatic factors on nitrate contamination in Nebraska's groundwater system. *Journal of Contaminant Hydrology* 220, 33–48. https://doi.org/10.1016/j.jconhyd.2018.11.007

Kişi O. and Ay M. 2014 Comparison of Mann–Kendall and innovative trend method for water quality parameters of the Kızılırmak River, Turkey. *Journal of Hydrology* 513, 362–375. https://doi.org/10.1016/j.jhydrol.2014.03.005

Kovač I., Kovačev-Marinčić B., Novotni-Horčička N., Mesec J. and Vugrinec J. 2017 Komparativna analiza koncentracije nitrata u gornjem i donjem sloju Varaždinskog vodonosnika [in Croatian]. Radovi Zavoda za znanstveni rad Varaždin 28, 41–57. https://doi.org/10.21857/9e31lh4zem

Kovač I., Šrajbek M., Sakač N. and Nemčić-Jurec J. 2025 Comparative analysis of nonlinear models

from different domains: a case study on the quality of groundwater in an alluvial aquifer in Northwestern Croatia. *Water* 17, 1378. https://doi.org/10.3390/w17091378
Kurwadkar S., Kanel S.R. and Nakarmi A. 2020 Groundwater pollution: occurrence, detection, and remediation of organic and inorganic pollutants. *Water Environment Research* 92, 1659–1668.
Kyte E., Cey E., Hrapovic L. and Hao X. 2023 Nitrate in shallow groundwater after more than four decades of manure application. *Journal of Contaminant Hydrology* 256, 104200. https://doi.org/10.1016/j.jconhyd.2023.104200
Larva O., Brkić Ž. and Marković T. 2023 Vulnerability and risk of contamination of the Varaždin aquifer system, NW Croatia. *Sustainability* 15, 16502. https://doi.org/10.3390/su152316502
Li J., Shi Z., Wang G. and Liu F. 2020 Evaluating spatiotemporal variations of groundwater quality in Northeast Beijing by self-organizing map. *Water* 12, 1382. https://doi.org/10.3390/w12051382
Mester T., Szabó G., Kiss E. and Balla D. 2024 Long-term spatiotemporal changes in nitrate contamination of municipal groundwater resources after sewerage network construction in the Hungarian Great Plain. *Environmental Science and Pollution Research* 31, 61114–61137. https://doi.org/10.1007/s11356-024-35280-9
Nemčić-Jurec J., Mesić M., Bašić F., Kisić I. and Zgorelec Ž. 2007 Nitrate concentration in drinking water from wells at three different locations in northwest Croatia. *Cereal Research Communications* 35, 845–848.
Şen Z. 2012 Innovative trend analysis methodology. *Journal of Hydrologic Engineering* 17(9), 1042–1046. https://doi.org/10.1061/(ASCE)HE.1943-5584.0000556
Šimunić A., Pikija M. and Hećimović I. 1982 Osnovna geološka karta SFRJ 1:100 000, Tumač za list Varaždin L 33–69 [in Croatian]. Institut za geološka istraživanja, Zagreb; Savezni geološki zavod, Belgrade.
Šrajbek M., Kovač I., Novotni-Horčička N. and Kranjčević L. 2020 Assessment of average contributions of point and diffuse pollution sources to nitrate concentration in groundwater by nonlinear regression. *Environmental Engineering and Management Journal* 19(1), 95–104.
Šrajbek M., Kranjčević L., Kovač I. and Biondić R. 2022 Groundwater nitrate pollution sources assessment for contaminated wellfield. *Water* 14, 255. https://doi.org/10.3390/w14020255
Šrajbek M., Kovač I., Đurin B. and Gilja G. 2024 *Trend and correlation analysis of groundwater quality at the Bartolovec wellfield in Croatia*. In: Proc. of the 18th International Symposium Water Management and Hydraulic Engineering (WMHE 2024), M. Červeňanská, A. Šoltész, D. Baroková et al. (eds), Slovak University of Technology in Bratislava, Bratislava, Slovakia, pp. 232–244.
Šrajbek M., Đurin B., Gnjato S. and Popov T. 2025 Regional innovative trend analysis of annual and seasonal discharges of rivers in Bosnia and Herzegovina. *Earth* 6, 30. https://doi.org/10.3390/earth6020030
Umar M., Khan S.N., Arshad A., Aslam R.A., Khan H.M.S., Rashid H., Pham Q.B., Nasir A., Noor R., Khedher K.M. and Anh D.T. 2022 A modified approach to quantify aquifer vulnerability to pollution towards sustainable groundwater management in Irrigated Indus Basin. *Environmental Science and Pollution Research* 29, 27257–27278. https://doi.org/10.1007/s11356-021-17882-9
Urumović K., Prelogović E., Hlevnjak B. and Mayer D. 1990 Hidrogeološki odnosi varaždinskog vodonosnika [in Croatian]. *Geološki vjesnik* 43, 149–158.
Wendland F., Bergmann S., Eisele M., Gömann H., Herrmann F., Kreins P. and Kunkel R. 2020 Model-based analysis of nitrate concentration in the leachate—the North Rhine-Westfalia case study, Germany. *Water* 12, 550. https://doi.org/10.3390/w12020550
Zhao X., Wang D., Xu H., Ding Z., Shi Y., Lu Z. and Cheng Z. 2022 Groundwater pollution risk assessment based on groundwater vulnerability and pollution load on an isolated island. *Chemosphere* 289, 133134.

TRANSBOUNDARY WATER COOPERATION BETWEEN EU MEMBER STATES AND THE THIRD COUNTRIES

Luka JURETIĆ [1], Lidija TADIĆ[1*], Tamara BRLEKOVIĆ[1], Eniko Anna TÁMAS[2], Dániel KOCH[2]

[1] *Faculty of Civil Engineering and Architecture University of Osijek, Croatia*

E-mail: ljuretic@gfos.hr

E-mail: ltadic@gfos.hr

E-mail: tamaradadic@gfos.hr

[2] *Ludovica University of Public Services, Hungary*

E-mail: Tamas.Eniko.Anna@uni-nke.hu

E-mail: Koch.Daniel@uni-nke.hu

[*] *Corresponding author*

Abstract

Transboundary water cooperation within the EU is subject to a highly harmonised legal regime dominated by the EU's Water Framework Directive (WFD). EU member states are also under a "best-effort" obligation to implement the objectives of the WFD vis-à-vis third countries in shared river basins. Project titled “Transboundary water cooperation between EU member States and third countries: governance resilience analysis and hydropolitical model-building” (TWCEU) will try to fill the gap by comparative analysis of the legal and institutional framework of cooperation in the relevant sub-basins, including the effectiveness of existing water management. Project aims to map out the interactions between EU, national and international water policy and law in four river basins shared by EU and non-EU countries (the Rhône, the Rhine, the Po and the Danube). In the first stage of project implementation, the focus is on the analysis of hydrological water management problems in the basins, specifically in sub-basins shared by EU and non-EU countries alike. Their geographical, hydrological and environmental characteristics and water management practices will be the starting point for the understanding of conflict and cooperation over shared rivers from an international relations, international law, and political science perspective.

Key words

transboundary cooperation, third countries, water management

1 Introduction

The European Union is perceived to have one of the most robust transboundary water governance regimes in the world (Moss et al., 2020). It has been originated on the long history of European water management, upgraded by the EU Water Framework Directive (WFD, 2000) and supplemented by a range of additional secondary EU legislation with significant or ancillary transboundary relevance. For example, the Floods Directive, the Groundwater Directive, the Priority Substances Directive or the Urban WasteWater Treatment Directive, etc.

The evolution and main features of EU transboundary water governance within the European Union have been analysed from theoretical, economic or hydropolitical point of view (Reichert, 2016; Jager, 2016; Baranyai, 2020).

However, less straight-forward cooperation is over basins shared by EU and non-EU countries. Although the WFD puts member states under a “best-efforts” type of obligation to implement its

objectives vis-à-vis third countries, the relevant basins vary grossly in terms of political and hydrological complexity. There are many excellent examples of individual basins in which EU and non-EU countries have long and efficient cooperation, such as the Sava basin (Komatina and Grošelj, 2015), or the Tisza sub-basin (Dumitrache et al, 2018).

The most important thing is that there is no systematic research of these relations on an empirical basis, especially from a multidisciplinary perspective (including water sciences, policy and law). Consequently, there is no database of quantity and quality management regarding EU/non-EU transboundary relations.

In order to explore this problem, four large transnational river basins have been selected - the Rhône, Rhine, Po and Danube basins. From the water management point of view, they have certain similarities, especially in this age of climate change. Snow and ice melting from the European Alps intensifies and extreme rainfall events result in more frequent flooding across the Europe. Population density across these basins is growing, pollution from agricultural runoff is increasing together with warming air and water temperatures.

This study represents the first stage of the project "Transboundary Water Cooperation between EU Member States and Third Countries: Governance Resilience Analysis and Hydropolitical Model-Building" (TWCEU) and focuses on the development of a common spatial database for the four selected river basins. The database includes information on transboundary catchments, land use, population, monitoring networks and water management infrastructure. These data will be combined with institutional and governance information in the next stages of the project to analyse transboundary water cooperation and governance resilience. The hydropolitical analysis itself is therefore outside the scope of the present paper.

The findings of the TWCEU project could complement existing knowledge of EU/non-EU cooperation in the four relevant sub-basins and contribute to the understanding of the effectiveness of EU and international legal instruments as well as customary international water law. They could also help refine existing models of hydropolitics by incorporating hydrological information from water sciences.

2 Methods

2.1 Data sources

Data were compiled for the Rhône, Rhine, Po and Danube basins, from a range of international, national and European spatial datasets. The primary sources used in the study, together with a description of the data provided and their application within the analytical framework, are listed in Table 1. Collected data can be divided into several groups: basic spatial data including land cover data, hydrological data, monitoring and infrastructure. They are described in more details in Table 1.

Table 1. Spatial datasets used in the analysis of transboundary catchments

Source / Dataset	Basin(s)	Category	Used in this study
HydroBASINS (Lehner and Grill, 2013) and HydroLAKES (Messager et al., 2016)	All four basins	Base spatial data	Primary delineation of study basins and all transboundary sub-basins (threshold: area greater than 1,000 km²); lake polygons for all major lakes within the four study basins.
GADM (GADM, 2022)	All four basins	Base spatial data	Identification of EU and non-EU territory per sub-basin; spatial overlay for country-share calculation.
CORINE Land Cover 2018 (European Environment Agency, 2019) / ENI CLC 2024 (European Environment Agency, 2025)	All four basins	Base spatial data	Dominant land cover class per basin and sub-basin.
GHS-POP R2023A (Schiavina et al., 2023).	All four basins	Base spatial data	Population total and density per sub-basin.
ICPDR (DanubeHIS, TNMN, DanubeGIS)	Danube	Monitoring and infrastructure	River discharge, water level and water temperature monitoring network; chemical and ecological water quality monitoring network; dams and weirs; morphological alterations; impoundments; urban wastewater treatment plants, etc.
DanubeSediment (DanubeSediment Interreg Project, 2019)	Danube	Monitoring and infrastructure	Sediment pressure points (infrastructure); suspended sediment transport monitoring network.
FOEN / BAFU	Rhine, Rhône, Po	Monitoring and infrastructure	River discharge, water level and water temperature monitoring; chemical water quality monitoring of surface waters; dams under federal supervision; urban wastewater treatment plants; groundwater bodies. Applied as the key non-EU comparator across three basins.
OFB	Rhine, Rhône	Monitoring and infrastructure	Surface and groundwater abstraction points; all in-stream barriers (dams, weirs, culverts, fords); urban wastewater treatment plants.
BfG	Rhine	Monitoring and infrastructure	Dams and weirs; navigation locks; chemical status monitoring of groundwater bodies; quantitative status monitoring of groundwater bodies; ecological and chemical status monitoring of surface waters.
EEA WISE WFD (European Environment Agency, 2016)	Rhine and Rhône	Monitoring	Surface water and groundwater monitoring station network; groundwater body polygons.
ADBPO	Po	Monitoring and infrastructure	Surface water monitoring network; groundwater monitoring network; groundwater bodies; drinking water abstraction points; urban wastewater treatment plants.
EEA UWWTD (European Environment Agency, 2025)	All four basins	Infrastructure	Urban wastewater treatment plants with treatment level attribute; applicable across all four basins.
GDW — Global Dam Watch (Lehner et al., 2024)	Rhine, Rhône, Po	Infrastructure	Large dam points where national open-access GIS registries are unavailable.
GRDC (BfG, Koblenz)	All four basins	Monitoring	River discharge monitoring stations.

2.2 Identification and delineation of transboundary catchments

The spatial units of analysis were delineated using the HydroBASINS dataset, which provides a hierarchical subdivision of the global land surface into nested river basins based on a hydrologically conditioned digital elevation model derived from SRTM data at approximately 90 m resolution. For each of the four study basins (Danube, Rhine, Rhône and Po) the appropriate Pfafstetter level was selected such that the resulting basin polygon matched the officially reported total catchment area as closely as possible. Official basin areas reported by river basin authorities and international commissions were used as reference values. Where necessary, multiple HydroBASINS polygons were merged to obtain the best match with the reported basin extent. Within each main basin, all sub-basins exceeding 1,000 km² were identified as the primary spatial units for the analysis. This threshold was selected to exclude very small catchments while retaining sufficient spatial detail for comparative analysis.

Besides, there are many direct sub-catchments shared by two countries on the rivers that are borders between them. These units were delineated by subtracting all attributed tributary catchments from the total basin polygon and then intersecting the remainder with national administrative boundaries derived from GADM (version 4.1). Each direct drainage unit was assigned to the corresponding transboundary country combination.

To ensure meaningful comparisons among national portions of transboundary catchments, only countries representing at least 3% of the total catchment area were retained for further analysis.

All spatial operations were performed in QGIS 3.40.15 (QGIS Development Team, 2024). There are also several transboundary lakes. They were delineated using the HydroLAKES database and treated as separate spatial units in subsequent analyses.

2.3 Spatial land cover and population data

Each transboundary catchment and direct drainage unit was characterised using land cover and population indicators. All calculations were performed separately for the EU and non-EU portions of each catchment, as defined in Section 2.2.

Land cover characteristics were derived from the CORINE Land Cover 2018 dataset (CLC2018). For Ukraine and the Republic of Moldova, which are not covered by the standard CLC dataset, the ENI CLC dataset was used. Individual land cover classes were aggregated into five major categories: artificial surfaces, agricultural areas, forests and semi-natural areas, wetlands, and water bodies. For each national catchment portion, the area and relative share of each category were calculated.

Population characteristics were derived from the GHS-POP R2023A dataset representing projected population distribution for 2030. Population totals were extracted for each national catchment portion using zonal statistics. Based on these results, total population, population density and the share of national population located within each catchment were calculated.

2.4 Monitoring network and hydrological assessment

Monitoring station datasets listed in Table 1 were assigned to individual catchments and direct drainage units using point-in-polygon analysis. The stations were then classified as belonging to the EU or non-EU part of each catchment using GADM national boundaries.

For the Danube River Basin, monitoring information was obtained from the TNMN, DanubeHIS and DanubeSediment datasets. For the Rhine, Rhône and Po basins, monitoring information was compiled from national monitoring systems and European reporting platforms, including FOEN/BAFU, BfG, AdbPo and WISE-WFD. GRDC discharge stations were used for all four basins to provide a common dataset for comparing hydrological monitoring coverage.

The number and distribution of monitoring stations were evaluated for each catchment and compared between EU and non-EU territories. Where available, information on monitored parameters and measurement frequency was obtained from official documentation accompanying the respective monitoring networks.

Not all monitoring datasets provided complete metadata in GIS format. Information on monitoring network characteristics was therefore supplemented using official documentation where available.

2.5 Water infrastructure assessment

Infrastructure objects were assigned to individual catchments and direct drainage units following the same spatial procedure described for monitoring stations in Section 2.4. Infrastructure datasets were linked to the corresponding catchments using point-in-polygon analysis and subsequently attributed to either the EU or non-EU portion of each catchment.

The available infrastructure categories differed among river basins and data sources. Depending on data availability, the analysis included continuity interruptions, dams and weirs, morphological alterations, navigation structures, urban wastewater treatment plants (UWWTPs), water abstraction points and sediment pressure points. The datasets listed in Table 1 were combined into a geospatial database and analysed at the catchment level.

The amount of information available for individual infrastructure objects also differed between datasets. Some included attributes such as dam height, reservoir storage capacity, operational status and infrastructure type, while others provided only basic information. For this reason, a common threshold based on infrastructure size or capacity could not be applied at this stage of the project.

3 Results and Discussion

3.1 Characteristics of identified transboundary catchments

Application of the methodology described in Section 2 resulted in the identification of transboundary catchments, direct drainage units and major transboundary lakes within all four study basins. The type and number of analysed units are summarised in Table 2.

Table 2. Number of transboundary catchments, direct transboundary catchments and major lakes identified within each study basin.

Basin	Tributary catchments	Direct transboundary catchments	Lakes	Total analysed units
Danube	21	7	0	28
Rhine	1	2	1	4
Rhône	3	2	1	6
Po	2	0	2	4

The spatial distribution of all identified transboundary catchments, direct drainage units and major transboundary lakes across the four study basins is illustrated in Fig. 1.

The number of identified transboundary catchments varied considerably among the four basins. The Danube Basin contained the largest number of analysed units, comprising 21 major tributary catchments and seven direct transboundary drainage units. This is related to the size of the basin and the number of countries it covers. In contrast, the Rhine Basin included the Aare catchment, two direct transboundary catchments and Lake Constance, while the Rhône Basin comprised the Saône, Ain and Arve catchments, two direct transboundary catchments and Lake Geneva. The Po Basin contained the Adda and Ticino catchments together with the transboundary lakes Lago Maggiore and Lago di Lugano.

The Danube accounted for most of the transboundary units identified in this study. The other three basins contained considerably fewer units and included several transboundary lakes. This difference in the number and type of spatial units needs to be taken into account when comparing monitoring and infrastructure data between the four basins.

Following the delineation of transboundary catchments and direct drainage units, the proportion of EU and non-EU territory was calculated for each basin using GADM national boundaries. The results are summarised in Table 3.

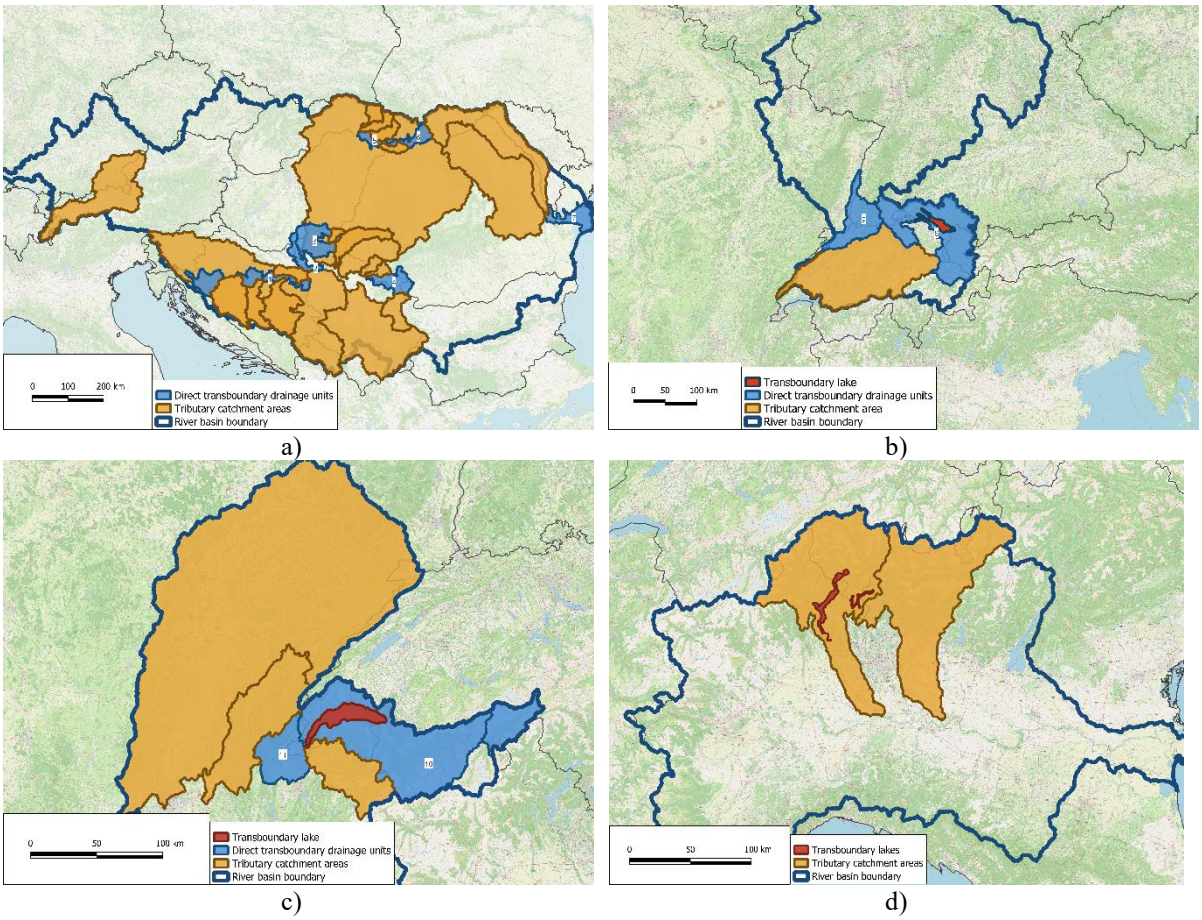


Figure 1. Transboundary catchments, direct drainage units and major transboundary lakes identified within the four study basins: a) Danube Basin; b) Rhine Basin; c) Rhône Basin and d) Po Basin

The number of identified transboundary catchments varied considerably among the four basins. The Danube Basin contained the largest number of analysed units, comprising 21 major tributary catchments and seven direct transboundary drainage units. This is related to the size of the basin and the number of countries it covers. In contrast, the Rhine Basin included the Aare catchment, two direct transboundary catchments and Lake Constance, while the Rhône Basin comprised the Saône, Ain and Arve catchments, two direct transboundary catchments and Lake Geneva. The Po Basin contained the Adda and Ticino catchments together with the transboundary lakes Lago Maggiore and Lago di Lugano.

The Danube accounted for most of the transboundary units identified in this study. The other three basins contained considerably fewer units and included several transboundary lakes. This difference in the number and type of spatial units needs to be taken into account when comparing monitoring and infrastructure data between the four basins.

Following the delineation of transboundary catchments and direct drainage units, the proportion of EU and non-EU territory was calculated for each basin using GADM national boundaries. The results are summarised in Table 3.

Table 3. EU and non-EU area shares of the analysed transboundary catchments and direct drainage units by river basin.

Basin	EU share (%)	Non-EU share (%)
Danube	61.7	38.3
Rhine	29.4	70.6
Rhône	85.9	14.1
Po	75.6	24.4

The Danube Basin contained the largest number of transboundary units and had the most balanced distribution between EU and non-EU territory among the four basins. The Rhine Basin had the largest share of non-EU territory, mainly due to the large Swiss contribution. In contrast, the analysed transboundary areas of the Rhône and Po basins were predominantly located within the EU.

3.2 Land use and population characteristics

The land cover composition and population density of EU and non-EU portions of the analysed transboundary catchments and direct drainage units are summarised in Table 4.

Table 4. Land cover composition and population density in EU and non-EU portions of the analysed transboundary catchments and direct drainage units by river basin.

	EU					Non-EU				
Basin	Artif. (%)	Agric. (%)	Forest & semi-nat. (%)	Wetl. + Water (%)	Pop. density (inh/km²)	Artif. (%)	Agric. (%)	Forest & semi-nat. (%)	Wetl. + Water (%)	Pop. density (inh/km²)
Danube	5.5	52.5	40	2	78	3.3	47.6	48	1.1	83
Rhine	7.8	40.4	46.7	5.1	201	8.5	36.3	50.8	4.4	281
Rhône	5.7	51.2	40.8	2.3	102	4	16.5	70.6	8.9	246
Po	9.2	25.3	61.7	3.8	288	4.5	4	89.3	2.2	103

Land cover differs both among the four basins and between their EU and non-EU portions. Within the Danube Basin, agricultural land represented the dominant land cover category in most EU portions, whereas forests and semi-natural areas accounted for a larger proportion of non-EU territories. The strongest contrasts were observed between intensively cultivated lowland catchments and forest-dominated Carpathian catchments.

In the Rhine Basin, forests and semi-natural areas represented the dominant land cover category in both EU and non-EU portions. Agricultural land remained an important component throughout the basin, while artificial surfaces occupied a relatively larger share than in most Danube catchments.

The Rhône Basin exhibited a clear contrast between the French and Swiss portions. Agricultural land dominated the French territory, whereas forest and semi-natural areas prevailed in the Swiss Alpine catchments. Population was concentrated in a limited number of urban areas, particularly around Geneva.

The Po Basin was characterised by predominantly Alpine landscapes within the analysed transboundary catchments. Forest and semi-natural areas dominated both Italian and Swiss portions, while agricultural land and urban areas were concentrated in the lower parts of the basin.

Across the four basins, non-EU portions generally contain a larger share of forest and semi-natural areas, while agricultural land is more prominent in the EU portions. However, population density does not follow the same pattern. It is higher in the non-EU portions of the Danube, Rhine and Rhône, but substantially lower in the non-EU portion of the Po. The results therefore do not support a simple interpretation in which EU territories are consistently more urbanised or densely populated than non-

EU territories. Geographic setting and the location of major urban areas appear to be important alongside EU membership when interpreting these spatial differences.

3.3 Monitoring data availability

Monitoring data were identified for all four river basins, but their organisation and accessibility differed considerably. The Danube Basin is covered by several basin-wide datasets, including TNMN and DanubeHIS, which provide hydrological, meteorological and water-quality information across both EU and non-EU countries.

Additional sediment monitoring information was obtained from the DanubeSediment project. However, these datasets were only available for countries participating in the project, resulting in less complete spatial coverage than that provided by TNMN or DanubeHIS.

For the Rhine, Rhône and Po basins, monitoring information had to be collected from several national and European sources, including FOEN/BAFU, BfG, AdbPo and WISE-WFD. As a result, data collection required the integration of multiple datasets originating from different institutions and reporting systems.

The main difference observed among the basins is therefore not simply whether monitoring data exist, but how those data are organised and made available. In the Danube Basin, common databases facilitate the identification and comparison of monitoring information across national borders. In the other three basins, relevant data are available, but their distribution among several institutions makes compilation and harmonisation more complex. This difference also limits direct comparison of monitoring coverage. A larger number of stations identified in one basin does not necessarily indicate a denser or more developed monitoring network, because the number of stations captured by the analysis also depends on the coverage and reporting criteria of the source datasets. Station counts should therefore be interpreted together with the characteristics of the databases from which they were obtained.

The Global Runoff Data Centre (GRDC), hosted by BfG in Koblenz under a WMO mandate, was additionally used as a harmonised reference dataset for hydrological discharge monitoring across all four basins. GRDC provides a common source for inter-basin comparison of discharge monitoring coverage. However, it complements rather than replaces the basin-specific and national monitoring datasets, which contain additional information and differ in their spatial and temporal coverage.

3.4 Water management infrastructure data availability

Infrastructure data were available for all four analysed river basins, although their availability and organisation differed considerably between basins and countries. The Danube Basin provided the most comprehensive source of infrastructure information through the DanubeGIS platform, which includes datasets on continuity interruptions, impoundments, morphological alterations and urban wastewater treatment plants.

For the Rhine, Rhône and Po basins, infrastructure information had to be collected from several national and international sources, including FOEN/BAFU, OFB, BfG, AdbPo, the European Environment Agency (EEA) and the Global Dam Watch database. As a result, the data collection process was more fragmented and required the integration of multiple datasets.

Data accessibility also differed among countries and datasets. Most datasets were available for direct download, while some infrastructure data had to be requested from the responsible institutions. For example, several DanubeGIS infrastructure layers were obtained through formal data requests.

These differences in data availability limited direct comparison between the basins. The available infrastructure data therefore reflect both the information provided by individual databases and differences in data access between countries.

3.5 Discussion and limitations

Several limitations need to be taken into account when comparing the four river basins. They are mainly related to differences in spatial datasets and to the availability and completeness of monitoring and infrastructure data.

Catchment boundaries were delineated using HydroBASINS and major lakes using HydroLAKES. For most catchments, the calculated areas were close to the official values reported by river basin authorities and international commissions. However, differences were found for some catchments and lakes. Since the same datasets and delineation procedure were used for all four basins, the spatial units remain comparable, but they do not always fully correspond to official boundaries. This can also affect the calculated area shares and other spatial indicators.

Land cover data were not equally complete for all countries. CORINE Land Cover 2018 does not fully cover Ukraine and Moldova, so ENI CLC was used for these areas. Some gaps still remained. No ENI CLC data were available for the Ukrainian parts of the Siret and Prut catchments, and coverage was only partial for some non-EU parts of the Direct Danube drainage unit. Land cover results for these areas are therefore less complete and should be interpreted accordingly.

3.5.1 Availability and organisation of monitoring data

Monitoring data for the Danube Basin were available through several basin-wide systems, including TNMN, DanubeHIS and DanubeSediment. For the Rhine, Rhône and Po basins, data had to be collected from several national and international sources. This made the collection and comparison of monitoring data more complex in these three basins.

There were also differences in the coverage of individual datasets. DanubeSediment includes only countries participating in the project and therefore does not cover the entire Danube Basin. In the Rhône Basin, no single open monitoring database for French territory comparable to FOEN/BAFU or DanubeHIS was identified, so French monitoring data were mainly obtained from WISE-WFD.

These differences limit direct comparison of monitoring networks between the four basins. The number of stations identified in the analysis depends partly on the coverage and availability of the datasets used and does not necessarily represent differences in actual monitoring intensity.

3.5.2 Infrastructure data consistency

A common threshold for water infrastructure could not be used because the available datasets differed in content and level of detail. Some datasets include information on dam height, reservoir storage capacity or treatment level, while others provide only the location and basic type of infrastructure. Therefore, all infrastructure objects available in the selected datasets were included.

This limits direct comparison between the basins because the reported numbers depend partly on the information available in each dataset. A higher number of identified objects does not necessarily mean that a basin has more infrastructure.

3.5.3 Differences in data accessibility

Data accessibility also varied between countries and datasets. Several infrastructure layers for the Danube Basin were not available for direct download and had to be obtained through formal data requests. Data availability therefore depends partly on how individual countries and institutions provide access to their data. This can influence the amount of information available for comparison between basins.

Despite these differences, the collected data were sufficient to create a common spatial database for the

four basins. However, the database is not equally complete for all countries and data categories. These gaps need to be taken into account in the next stages of the TWCEU project, particularly when the database is used for governance and hydropolitical analyses.

4 Conclusion

This study developed a GIS-based database for the comparative assessment of transboundary river basins shared by EU Member States and non-EU countries across the Danube, Rhine, Rhône and Po river basins. Using a common spatial framework, catchments, direct transboundary drainage units and major transboundary lakes were identified and characterised with respect to land use, population distribution, monitoring networks and water management infrastructure.

Differences were found in the availability and organisation of data between the four basins. The Danube has several basin-wide data sources coordinated through ICPDR, while data for the Rhine, Rhône and Po had to be collected from several national and international sources. This made data collection and harmonisation less straightforward in these three basins.

The comparison of EU and non-EU territories showed that non-EU areas tend to have larger proportions of forest and semi-natural land, while EU territories more often feature intensive agricultural land use and urbanisation. This pattern was not uniform across all basins. Switzerland, for example, combines high population density with extensive forest cover. The results also showed that differences in data availability and monitoring organisation are not determined by EU membership alone. Institutional arrangements, reporting practices and national data-sharing policies play an equally important role.

The main purpose of this first stage of the TWCEU project was to collect and harmonise the spatial data needed for further research. Therefore, the present paper focuses on the development of the database and the main differences and limitations identified during this process, rather than on analytical assessment of transboundary water governance and cooperation. These analyses will be carried out in the next stages of the project using the database developed in this study.

Acknowledgements

This research is carried out and financed within the framework of the second Swiss Contribution MAPS-2024-7047.

References

Baranyai, G. 2020 *European Water Law and Hydropolitics: An Inquiry into the Resilience of Transboundary Water Governance in the European Union.* Springer International Publishing.

Bundesanstalt für Gewässerkunde (BfG) BfG Geoportal - Federal Waterways and Monitoring Datasets. Bundesanstalt für Gewässerkunde, Koblenz, Germany. https://geoportal.bafg.de/(accessed April 17th 2026)

DanubeSediment Project 2019 DanubeSediment Interactive Maps. Interreg Danube Transnational Programme. https://dtp.interreg-danube.eu/approved-projects/danubesediment/section/interactive-maps (accessed June 1st 2026)

Dumitrache, R., Ion, B., & Godeanu, E. 2018 *Strengthening Cooperation Between River Basin Management Planning and Flood Risk Prevention to Enhance the Stats of Waters of the Tisza River Basin*. International Multidisciplinary Scientific GeoConference: SGEM, 18(3.1), 655-661

European Environment Agency 2016 WISE WFD Reference Spatial Datasets reported under Water Framework Directive 2016 - Public version. European Environment Agency, Copenhagen, Denmark. https://www.eea.europa.eu/en/datahub/datahubitem-view/a50d10f6-e0f6-496b-a6e2-27eb5ad204e8 (accessed May 21st 2026)

European Environment Agency 2019 CORINE Land Cover 2018 (raster 100 m), Europe, 6-yearly - version 2020_20u1. European Environment Agency, Copenhagen, Denmark. https://doi.org/10.2909/960998c1-1870-4e82-8051-6485205ebbac (accessed May 5th 2026)
European Environment Agency 2025a Corine Land Cover 2024 in Eastern Partnership Countries (ENI CLC), version 01.00. European Environment Agency, Copenhagen, Denmark. https://sdi.eea.europa.eu/catalogue/srv/api/records/96de1349-108a-417e-a7fe-d0ca8ce946f7
European Environment Agency 2025b Urban Waste Water Treatment Directive, Treatment Plants Reported under UWWTD Data Call 2023 - Public Final Version. European Environment Agency, Copenhagen, Denmark. https://www.eea.europa.eu/en/datahub/datahubitem-view/6244937d-1c2c-47f5-bdf1-33ca01ff1715 (accessed April 23rd 2026)
GADM 2022 Database of Global Administrative Areas, version 4.1. https://gadm.org
Global Runoff Data Centre (GRDC) GRDC Data Portal. Global Runoff Data Centre of WMO, Federal Institute of Hydrology (BfG), 56068 Koblenz, Germany. https://grdc.bafg.de (accessed June 1st 2026)
International Commission for the Protection of the Danube River (ICPDR) Danube Geographic Information System (DanubeGIS). ICPDR, Vienna, Austria. https://www.danubegis.org (accessed May 31st 2026)
International Commission for the Protection of the Danube River (ICPDR) Danube Hydrological Information System (DanubeHIS). ICPDR, Vienna, Austria. https://www.danubehis.org (accessed June 3rd 2026)
International Commission for the Protection of the Danube River (ICPDR) TransNational Monitoring Network (TNMN) - Water Quality Database. ICPDR, Vienna, Austria. https://wq-db.icpdr.org (accessed April 14th 2026)
Jager, N. W. 2016 Transboundary Cooperation in European Water Governance–A set-theoretic analysis of International River Basins. Environmental policy and governance, 26(4), 278-291
Komatina, D. and Grošelj, S. 2015 T*ransboundary water cooperation for sustainable development of the Sava River Basin. In: The Sava Rive*r, R. Milačič, J. Ščančar and M. Paunović (eds), The Handbook of Environmental Chemistry 31, Springer, Berlin, Heidelberg, pp. 1–25.
Lehner, B. and Grill, G. 2013 Global river hydrography and network routing: baseline data and new approaches to study the world's large river systems. *Hydrol. Process*. 27 (15), 2171–2186.
Lehner, B., Beames, P., Mulligan, M., Zarfl, C., De Felice, L., van Soesbergen, A., Thieme, M., Garcia de Leaniz, C., Anand, M., Belletti, B., Brauman, K.A., Januchowski-Hartley, S.R., Lyon, K., Mandle, L., Mazany-Wright, N., Messager, M.L., Pavelsky, T., Pekel, J.-F., Wang, J., Wen, Q., Wishart, M., Xing, T., Yang, X. and Higgins, J. 2024 The Global Dam Watch database of river barrier and reservoir information for large-scale applications. *Sci. Data* 11, 1069. https://doi.org/10.1038/s41597-024-03752-9
Messager, M.L., Lehner, B., Grill, G., Nedeva, I. and Schmitt, O. 2016 Estimating the volume and age of water stored in global lakes using a geo-statistical approach. *Nat. Commun*. 7, 13603.
Moss, T., Bouleau, G., Albiac Murillo, J., and Slavíkova, L. 2020 The EU water framework directive twenty years on: Introducing the special issue. *Water Alternatives* 13(3): 446-457
Office Français de la Biodiversité (OFB) French National Water Information Systems — BNPE, ROE, STEU. Office Français de la Biodiversité, Vincennes, France. https://www.ofb.gouv.fr/
Po River Basin District Authority (ADBPO) 2021 Piano di Gestione del Distretto Idrografico del Fiume Po 2021 (PdGPo 2021) - Spatial Data Portal. Autorità di Bacino Distrettuale del Fiume Po, Parma, Italy. https://www.adbpo.it/
Reichert, G. 2016 Transboundary water cooperation in Europe: a successful multidimensional regime? *Brill Research Perspectives in International Water Law*, 1(1), 1-111.
Schiavina, M., Freire, S. and MacManus, K. 2023 GHS-POP R2023A — GHS population grid multitemporal (1975-2030). European Commission, Joint Research Centre (JRC). https://doi.org/10.2905/2FF68A52-5B5B-4A22-8F40-C41DA8332CFE
Swiss Federal Office for the Environment (FOEN/BAFU) Swiss Water Geodata Portal. Federal Office for the Environment, Bern, Switzerland. https://www.bafu.admin.ch/en/water-geodata

STRATEGIC RECONNECTION OF FLOODPLAINS FOR IMPLEMENTING THE EU 2030 BIODIVERSITY STRATEGY IN LEVEE MANAGEMENT

Tomáš JULÍNEK [1*], Jaromír ŘÍHA [1], Jiří SKOKAN [1], Stanislav KOTAŠKA [1]

[1]*Brno University of Technology, Faculty of Civil Engineering, Dep. of Water structures, Czech Republic*

E-mail: Tomas.Julinek@vut.cz

E-mail: Jaromir.Riha@vut.cz

E-mail: Jiri.Skokan@vut.cz

E-mail: Stanislav.Kotaska@vut.cz

[*] *Corresponding author*

Abstract

Flood levees have historically played a vital role in flood risk management, with more than half a million kilometres of such structures built worldwide. However, by disconnecting rivers from their natural floodplains, levees influenced natural water retention capacity and riverine ecosystems processes. The EU 2030 Biodiversity Strategy and the Nature Restoration Regulation call for the restoration of freshwater ecosystems, specifically aiming to revitalize at least 25,000 km of rivers by removing obsolete and redundant barriers, including non-functional sections of flood levees. This study proposes a comprehensive three-step methodology to identify and evaluate opportunities for reconnecting floodplains with rivers. The first step involves a preliminary classification of the levee system to identify sections suitable for further analysis. This classification is based on four key criteria, such as flood protection effectiveness, financial implications of reconstructing or decommissioning, the technical condition of the structure, and any secondary functions the levee might serve, such as transportation or recreation. Each criterion is assigned a score and a weight, with flood protection and financial issues being the most significant factors in the decision-making process. Following the identification of suitable sections, the second step involves the specification of realistic management variants. These range from maintaining the current state to complete levee removal, partial removal, or decommissioning the levee from official records to allow for spontaneous ecological succession. The final step employs multicriterial optimization (MCDA) to select the optimal variant, integrating hydraulic modelling, cost-benefit analysis, and socio-economic, technical, and environmental considerations. The methodology was demonstrated on a pilot localities along the Morava River in the Czech Republic representing typical landuse characteristics and river morphology. The analysis identified specific levee reaches where the primary function was merely the protection of agricultural land, making them candidates for reconnection. The multicriterial evaluation indicated that in certain cases, the most effective approach is to leave the levee without maintenance and remove it from official water structure registries, thereby facilitating a gradual return to natural floodplain dynamics. This integrated approach provides a robust decision-support tool for water managers, authorities and stakeholders to balance public safety with the urgent need for ecological restoration as mandated by the Biodiversity 2030 requirements.

Key words

Flood levee, floodplain reconnection, EU 2030 Biodiversity Strategy.

1 Introduction

In Europe, flood protection levees have been designed and constructed systematically since the beginning of the 19th century, although the history of flood protection (FP) dates back to the Middle Ages (EUCOLD 2018). While riverbank levees safeguard human populations and socio-economic assets from the destructive impacts of flooding, the confinement of extensive floodplains can, conversely, exacerbate downstream peak flood discharges. This phenomenon occurs because these linear structures severely restrict the landscape's natural capacity to attenuate and retain water during high-flow events.

Concurrently, river floodplains represent dynamic systems that play a critical role in the hydro-ecological functioning of watercourses. Where a floodplain remains laterally connected to the river channel and undergoes regular inundation, the interactions among various environmental components sustain natural processes that benefit both fluvial ecosystems and, ultimately, human society. Evidently, linear flood protection levees disrupt these vital lateral interactions. This socio-ecological trade-off underscores an urgent need for a comprehensive reassessment of levee management strategies at the catchment scale.

To ensure the effective design and management of levee systems, the application of optimization frameworks is highly appropriate (Hui 2014). Within levee engineering, optimization can address the macro-level spatial layout (van Vuren et al. 2016), technical specifications, such as crest height (freeboard), bank revetment (Pilarczyk 1998), and seepage control—as well as broader economic and environmental variables. Various methodological approaches can be employed to achieve this, including game theory and risk-based decision analysis (Hui et al. 2015). Notably, research emphasizes that what frequently appears to be a fragmented collection of individual structures is, from a functional perspective, a deeply interconnected system, even though each levee segment has traditionally been designed, managed, and maintained in isolation.

In many instances, aging levees have lost their original protective function, prompting discussions regarding their decommissioning or complete removal (van Vuren et al., 2016). Conversely, in other contexts, these structures can serve multi-purpose functions, such as transportation corridors, or provide additional ecosystem services alongside flood mitigation (Hue et al. 2019). While conventional levee optimization primarily relies on economic metrics—such as relative and absolute cost-effectiveness or payback periods the governance of complex levee networks necessitates a more comprehensive multi-criteria decision analysis (MCDA) (Shafiei and Bozorg-Haddad 2005). This approach requires balancing flood risks to human life and property, structural integrity, environmental impacts, and socio-economic consequences, while simultaneously exploring opportunities to enhance the hydro-ecological potential of the river corridor and its floodplain in compliance with regulatory frameworks, water management directives, and overarching water policies (Directive 2000). Previous studies (Serra-Llobet et al. 2022) have documented selected projects focusing on the rehabilitation, setback (alignment relocation), or removal of flood protection levees, while a synthesis of the regulatory and procedural requirements for evaluating these systems can be found in (FEMA 2020, USACE 2024).

Optimizing the configuration of levee systems requires the evaluation of numerous indicators, which in turn demands the acquisition of extensive and heterogeneous baseline datasets. Given the high complexity, spatial context, varying spectral and spatial resolutions, and temporal dynamics of these indicators, the integration of Remote Sensing (RS) data and products represents an ideal solution. Remote sensing serves as an indispensable source of information across virtually all disciplines monitoring the state and processes of the Earth’s surface and atmosphere; a comprehensive review of RS applications across various environmental matrices is provided in (Dahl et al. 2017).

Primarily due to the long-term, systematic satellite missions of the National Aeronautics and Space Administration (NASA 2026) and the complementary programs of the European Space Agency (ESA 2026), it is now possible to conduct retrospective analyses of landscapes and their characteristics. Utilizing data from the reflective and thermal spectral regions at various spatial scales (ranging from kilometres to meters), researchers can leverage established products to analysed land cover and land use

change (LCLUC) as well as thermal regimes dating back to approximately 1975. Furthermore, RS datasets frequently serve as vital inputs for predictive models simulating spatial phenomena and hazard behaviours (Senay et al., 2023). To achieve the ultra-high spatial resolution necessary for localized or site-specific assessments, data from airborne sensors and Unmanned Aerial Vehicles (UAVs) (Sharma et al. 2021) are increasingly deployed. Furthermore, topographic, vegetation, and built-environment elevation characteristics can be precisely captured via Light Detection and Ranging (LiDAR) / airborne laser scanning. Several of these techniques are already implemented within national mapping programs at regular intervals, allowing validated methodologies to be adopted without incurring additional data acquisition costs.

2 Methods

2.1 Basic considerations

Within this context, the EU Biodiversity Strategy 2030 (2021) places a significant emphasis on the ecological restoration of floodplains, specifically aiming to reinstate lateral connectivity between river channels and adjacent alluvial areas. In practice, operationalizing this strategy requires the strategic removal or modification of anthropogenic structures that restrict natural flood inundation, disrupt the continuous flux of sediments and nutrients, and fragment aquatic and riparian ecosystems.

Crucially, the Strategy targets "obsolete barriers"—structures that no longer fulfill their original technical or socio-economic purpose. Consequently, a systematic classification of the function, current condition, and structural necessity of individual linear features (such as levees) is required to establish their degree of obsolescence. Given the competing socio-ecological and safety priorities involved, any decision-making process regarding the reconfiguration of a levee system must be underpinned by a robust multi-criteria decision analysis (MCDA).

To address this challenge, a comprehensive three-step analytical framework is proposed:

- Preliminary System Classification: Identifying and screening specific river reaches and levee segments to determine their suitability for further socio-ecological and technical analysis.
- Scenario Definition: Developing realistic design variants and alternative spatial arrangements of the levee system, focusing primarily on restoring lateral connectivity.
- Multi-Criteria Optimization: Utilizing MCDA frameworks to evaluate the trade-offs between the proposed variants and identify the optimal management strategy.

As a foundational step toward the implementation of this broader framework, the scope of the present study is dedicated exclusively to the development, description, and validation of the preliminary classification of the system.

2.2 Preliminary Classification of Dike System Reaches

2.2.1 Segmentation of Levee Systems into Reaches

The initial step of the methodology involves segmenting the river dike network into distinct spatial reaches (segments) to facilitate the subsequent preliminary classification. The spatial boundaries of each reach are defined based on the homogeneity of the following characteristics:

- **Flood Protection Level:** The dike reach constitutes a continuous, integrated flood defence element protecting a specific spatial asset, delineated by clear upstream and downstream boundaries.
- **Technical Condition:** The technical state, structural integrity, and engineering properties are uniform throughout the entire length of the reach.
- **Functional Uniformity:** The dike serves identical primary and secondary purposes along the whole segment.
- **Ancillary Hydraulic Infrastructure:** The reach may encompass co-dependent structures, such

as water intake works, weirs, or other ancillary facilities essential for its operation.

2.2.2 Methodology for the Preliminary Classification of Dike Reaches

The preliminary classification serves as a screening tool, providing an initial assessment of the suitability of individual dike reaches for decommissioning or modification to reconnect the wider floodplain. This assessment is systematically applied to each predefined reach (Section 2.2.1). Based on their suitability for floodplain reconnection, the reaches are categorized into four distinct classes (see also Table 1).

The final classification is subsequently visualized cartographically using a standardized color-coded scale (see Fig. 1). The evaluation relies on four core classification criteria (i), each assigned a scoring value P_i within the closed interval <-1, 1>:

1. **Flood Protection** (P_1)
2. **Financial/Economic Aspect** (P_2)
3. **Technical/Structural Condition** (P_3)
4. **Ancillary Functions** (P_4)

Positive scores (P_i) indicate that the dike reach is recommended for further detailed, site-specific evaluation regarding floodplain opening. Conversely, negative scores denote critical sections where removal or alteration is highly undesirable due to safety or technical constraints.

Table 1. Classification of the levee section

Category	Total score P	Colour
Unsuitable for floodplain opening	$\langle -1.0; -0.5 \rangle$	Blue
Inadvisable for floodplain opening	$(-0.5; 0\rangle$	Green
Conditionally suitable for floodplain opening	$(0;\ 0.5\rangle$	Yellow
Suitable for floodplain opening	$(0.5;\ 1.0\rangle$	Red

The total performance score P for each dike reach is calculated as a weighted average, summing the products of the individual criteria scores (P_i) and their respective weights (w_i), expressed as follows:

$$P = \sum_{i=1}^{4} (P_i \cdot w_i) \tag{1}$$

where n = 4 represents the total number of evaluation criteria. The resulting composite score P determines the definitive suitability of the given dike reach for floodplain reconnection.

2.2.3 Evaluation Criteria and Scoring Parameters

The preliminary assessment relies on four fundamental criteria (P_1 to P_4). Each criterion is evaluated within a closed normalized interval of <-1, 1>, where negative scores indicate a critical need to retain the structure and positive scores denote suitability for floodplain reconnection.

Flood Protection (P_1)
This parameter evaluates the discrepancy between the actual flood protection provided by the dike and the required protection level determined via GIS and land-use datasets (e.g., INSPIRE). In the Czech Republic, standard evaluations leverage existing flood hazard maps for Q_5, Q_{20}, Q_{100}, and Q_{500} scenarios. Scoring is defined as follows:

- **Extreme Risk <-1; -0.5):** Reconnection causes critical socio-economic and environmental losses, threatening public health and human life.
- **High Risk <-0.5; 0):** Significant economic and environmental damage; potential risks to human life.
- **Medium Risk <0; 0.5):** Moderate losses with localized social impacts or temporary health risks.

- **Low Risk <0.5; 1>:** Minimal social disruption; low economic or environmental exposure with zero risk to human life.

Financial and Economic Aspect (P_2)
This criterion accounts for all induced expenditures associated with dike modification, including decommissioning, structural removal, and the potential construction of set-back levees.

- **Extremely High Costs <-1; -0.5):** Extensive civil engineering works required in the newly opened floodplain, making the project financially unfeasible.
- **High Costs <-0.5; 0):** Substantial financial demands; investment is only conditionally feasible.
- **Medium Costs <0; 0.5):** Moderate capital expenses; optimization or removal is financially viable.
- **Low Costs <0.5; 1>:** Only minor ancillary expenditures required; the intervention is highly cost-effective.

Technical and Structural Condition (P_3)
The structural integrity and asset safety are verified through field investigations, adhering to standardized engineering frameworks (e.g., USACE methodologies) (USACE 2024).

- **Very Good <-1; -0.5):** Structure is in excellent condition with low maintenance demands; removal is strongly discouraged.
- **Acceptable <-0.5; 0):** Sound structural condition requiring only routine annual maintenance and minor repairs.
- **Conditionally Acceptable <0; 0.5):** Identifiable structural deficiencies require partial rehabilitation. Reliability is compromised, though primary flood defense is temporarily maintained.
- **Unacceptable <0.5; 1>:** Unsatisfactory structural safety during high-flow events; highly favorable for decommissioning.

Ancillary Functions (P_4)
This metric evaluates non-safety services provided by the dike, such as maintaining navigation depths, supporting water sports, facilitating water abstraction (drinking water, irrigation, hydropower), reinforcing weir backwaters, or serving as socio-communal infrastructure (e.g., cycle paths).

- **Strong Influence <-1; -0.5):** Multiple critical functions that are technically or financially difficult to compensate.
- **Moderate Influence <-0.5; 0):** Existing secondary functions that require formal compensation or relocation prior to floodplain opening.
- **Minor Influence <0; 0.5):** Negligible ancillary functions requiring little to no remedial action.
- **Absent <0.5; 1>:** The structure serves no secondary purpose.

2.2.4 Criteria Weighting

To establish the relative importance of each aspect, criteria weights were derived using a multi-step approach combining pairwise comparison matrices (Ramík 2020) and preferential ranking methods (Ramík 2020, Saaty, 1977). Initial broader preferences were sequentially refined to capture the distinct trade-offs between flood safety, financial investment, structural condition, and ancillary uses.

While the exhaustive mathematical derivation of these weights lies beyond the scope of this paper, the definitive weighting coefficients obtained via Saaty's Analytic Hierarchy Process (AHP) are consolidated and presented in Table 2.

Table 2. Weights assigned to the evaluated aspects.

Aspect	Weight w_i
Flood protection (P_1)	0.32
Financial issue (P_2)	0.36
Technical condition (P_3)	0.22
Other functions (P_4)	0.10

2.2.5 Final evaluation

The scores for the aspects discussed above have to be assigned to every single levee section and incorporate in the "Levee card" (see Table 2) elaborated for each levee section. In the card descriptive data are mentioned together with the scoring, weights and final score P (see Eq. 1) related to the levee section.

Based on the final score P the levee section is classified into one of the four categories according to Table 3. The categories reflect the suitability of the levee section for opening and reconnecting the floodplain. For further visualisation in the maps, the classes of levee sections are assigned by the colour (see Table 3, Fig. 1).

3 Practical examples

3.1 Levee sections classification

The proposed methodology described in Chapter 2 was applied at the four different levee systems along the Morava River basin. Each system has between 20 and 35 levee sections identified. The resulting classification of the levee sections is displayed in Fig. 1, where the sections of levees are coloured according to the proposed classification (see Table 1).

First picture (number 1 in Fig. 1) represents foothill regions. Levee reconstruction or removal typically interacts with steep catchment hydrology and rapid runoff response. These areas often exhibit narrow floodplains, coarse sediment transport, and higher stream power. Proximity of settlements and transport corridors in foothill valleys requires careful evaluation of residual flood risk. In such settings, levee removal is often combined with set-back levees or controlled inundation zones to maintain acceptable protection levels while restoring ecological processes. The sections classified as suitable for floodplain opening (green colour) are related to location with secondary levees constructed around settlements.

At confluences of major rivers, the Morava River and the Bečva River (picture number 2), where surrounding urban development is common, levee removal presents a different set of challenges. These areas are characterized by complex hydraulic interactions, backwater effects, and high exposure of built-up zones. Here, levee removal can partially improve flood conveyance, but only if accompanied by detailed hydraulic modelling and strategic land-use planning. The presence of critical infrastructure, such as bridges and transport networks (road, railways, etc.), often limits the spatial extent of restoration. The picture shows sections of levees along the Morava can modified in order to enhance the flood resilience of the broader river inundation corridor.

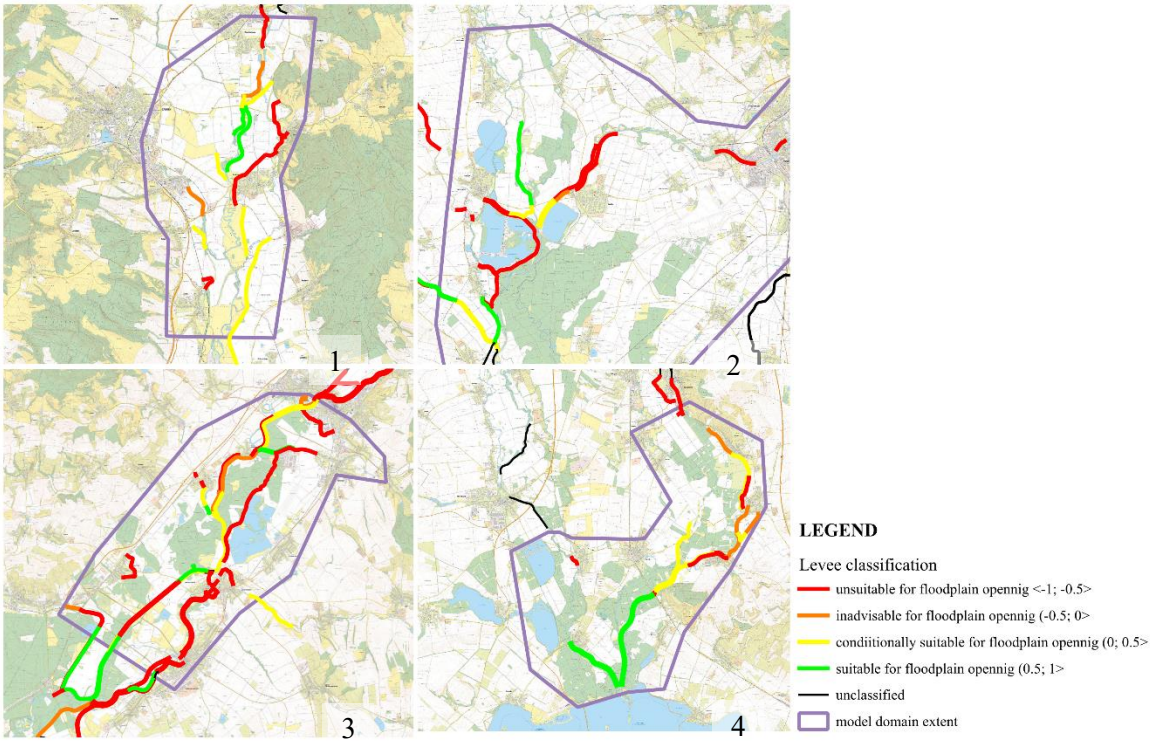


Fig. 1 Evaluated levee sections at considered localities

In lower floodplains, where the landscape is typically wide, and intensively used for agriculture, levee adaptation or even removal offers potential for restoring natural inundation regimes. Reconnecting the river with its floodplain can improve groundwater recharge, support nutrient retention, and enhance biodiversity. However, in the considered area of Uherský Ostroh (number 3 in Fig. 1) the Morava River floodplain is influenced by number of small streams and trenches conveying water. The area also include water-abstraction structures, irrigation systems, navigation channel (The Bata canal) and also settlements. These structures complicate hydrological management. Agricultural stakeholders are concerned about prolonged soil saturation and reduced land availability. An adaptive management strategy including structures to regulate inundation, definition of seasonal flooding zones, compensation schemes or change in land use are to be proposed.

Finally, confluence zone of the Svratka River and the Jihlava River upstream to Nove Mlyny Dam (number 4 in Fig. 1) has due to abandoned meanders and riparian forests represent locality with high potential for floodplain reopening. These areas often retain natural hydromorphology, including oxbow lakes, side channels, and wetlands. The locality is less urbanized, so the socio-economic constraints are lower. The design of restoration scenarios in this locality is currently under development.

Across all landscape types, floodplain reopening including potential levee removal must be supported by robust hydraulic modelling, stakeholder engagement, and long-term monitoring. The hydraulic modelling is part of evaluation of proposed variant for floodplain reconnection.

3.2 Scenario Generation and Variant Development

For levee reaches identified in the preliminary assessment as suitable or conditionally suitable for management interventions, a series of alternative scenarios (variants) must be developed. These variants are subsequently subjected to a rigorous multi-criteria optimization framework that incorporates detailed risk analysis.

The proposed variants must strictly reflect local socio-ecological constraints and the existing configuration of the flood protection system. Representative management scenarios typically include:

- **Status Quo (No-Action Alternative):** Maintenance of the current state, serving as the

benchmark/baseline scenario against which all other alternatives are evaluated.

- **Complete Dike Removal:** Total structural deconstruction of the levee segment. While often presenting the highest initial capital costs, this variant ensures maximum lateral connectivity and functional restoration between the river channel and its floodplain.
- **Partial Dike Removal (Breaching/Lowering):** Strategic removal or lowering of specific levee sections to facilitate managed or controlled inundation of the adjacent floodplain.
- **Administrative Decommissioning:** Reclassifying the levee to legally revoke its status as critical water infrastructure. This involves removing the assets from material registries and converting the structure into an unmaintained earthen embankment, thereby allowing spontaneous ecological succession.
- **Structural Rehabilitation or Modification:** Engineering interventions aimed at upgrading structural safety, altering freeboard allowances, or strategically increasing/decreasing the local level of flood protection.
- **Hybrid Scenarios:** Integrated combinations of the aforementioned variants tailored to unique site-specific conditions and reach dynamics.

The performance and trade-offs of these developed variants are subsequently quantified using multi-criteria decision analysis (MCDA).

3.3 Multi-Criteria Optimization and Selection of the Optimal Variant

The optimization procedure begins with the consolidation and analysis of a comprehensive spatial database. This database integrates heterogeneous baseline datasets that vary in spatial resolution, accuracy, and epistemic reliability.

The optimization framework is operationalized through the selection of relevant evaluation criteria, the mathematical derivation of their respective weights, and the objective scoring of each criterion across the proposed scenarios. The final evaluation is executed by computing a multi-attribute objective function subject to predefined technical, environmental, and financial boundary conditions.
The optimization protocol directly builds upon an established, certified methodology.

4 Conclusion

This study presents a streamlined methodology for the preliminary classification of levee segments, aimed at facilitating floodplain reconnection via structural removal or spatial optimization. Representing the first phase of a comprehensive three-step framework for floodplain restoration, this screening approach aligns directly with the strategic mandates of the EU 2030 Biodiversity Strategy (2021).

As a primary output, representative levee reaches within the study area were systematically identified, categorized, and visualized using a standardized, color-coded cartographic layout. This preliminary classification functions as a decision-support tool, enabling the prioritization of specific levee sections for subsequent, high-resolution evaluations of alternative management scenarios. Future research will encompass the formal design of these restoration variants and their comprehensive evaluation through robust multi-criteria optimization procedures.

Acknowledgements

This study is part of the project TACR SS07010401, "Water Management Analysis of Restoring Natural Floodplains and Increasing the Transformation Effect of Floodplains", which includes administrative and technical support.

References

Dahl T.A., Theiling C.H. & Echevarria W. 2017 Overview of levee setback projects and benefits. ERDC/CHL CHETN-VII-17, U.S. Army Engineer Research and Development Center, Vicksburg, MS. https://doi.org/10.21079/11681/22767

Directive 2000/60/EC 2000 Directive of the European Parliament and of the Council establishing a framework for Community action in the field of water policy. Official Journal of the European Communities L 327.

ESA 2026 The European Space Agency. https://www.esa.int

EU Biodiversity Strategy for 2030 2021 Barrier Removal for River Restoration. European Commission, Luxembourg.

EUCOLD Working Group on Levees and Flood Defences 2018 European and US Levees and Flood Defences: Characteristics, Risks and Governance.

FEMA 2020 Guidance for Flood Risk Analysis and Mapping: Levees. Guidance Document 95, Federal Emergency Management Agency, Washington, DC.

Hue N.H., Huong D.C. & Thanh N.H. 2019 A technical solution to improve the existing river dikes for both flood prevention and transportation purposes. IOP Conference Series: Materials Science and Engineering 507, 012012. https://doi.org/10.1088/1757-899X/507/1/012012

Hui R. 2014 Optimal Design of Levee and Flood Control Systems. PhD thesis, University of California, Davis.

Hui R., Lund J.R. & Madani K. 2015 Game theory and risk-based leveed river system planning with noncooperation. *Water Resources Research* 52. https://doi.org/10.1002/2015WR017707

NASA 2026 Earthdata. National Aeronautics and Space Administration. https://www.earthdata.nasa.gov

Pilarczyk K.W. 1998 Dikes and Revetments: Design, Maintenance and Safety Assessment. A.A. Balkema, Rotterdam.

Ramík, J.: Pairwise Comparisons Method: Theory and Applications in Decision Making. Lecture Notes in Economics and Mathematical Systems, Springer Nature (2020). https://doi.org/10.1007/978-3-030-39891-0.

Saaty, T.: A scaling method for priorities in hierarchical structures. J. Math. Psychol. 15, 234–281 (1977).

Senay G., Parrish G., Schauer M., MacKenzie F., Khand K., Boiko O., Kagone S., Dittmeier R., Arab S. & Ji L. 2023 Improving the operational simplified surface energy balance evapotranspiration model using the forcing and normalizing operation. *Remote Sensing* 15(1), 260. https://doi.org/10.3390/rs15010260

Serra-Llobet A., Tourment R., Montané A. & Buffin-Bélanger T. 2022 Managing residual flood risk behind levees: comparing USA, France, and Quebec (Canada). *Journal of Flood Risk Management* 15(2), e12785. https://doi.org/10.1111/jfr3.12785

Shafiei M.S. & Bozorg-Haddad O. 2005 Optimization of levee's setback: a new GA approach. In: Proc. of the 6th WSEAS International Conference on Evolutionary Computing, Portugal, pp. 400–406.

Sharma A.B., Bhandari M., Bandini F., Pizarro A., Perks M., Joshi D.J., Wang S., Dogwiler T., Ray R.L., Kharel G. & Sharma S. 2021 Unmanned aerial vehicles in hydrology and water management: applications, challenges, and perspectives. *Water Resources Research* 57(11), e2021WR029925. https://doi.org/10.1029/2021WR029925

USACE (U.S. Army Corps of Engineers) 2024 Engineer Circular 1165-2-218: Levee Safety Program. Washington, DC.

van Vuren S., de Vriend H. & Barneveld H. 2016 A stochastic model approach for optimisation of lowland river restoration works. *Journal of Earth Science* 27, 55–67. https://doi.org/10.1007/s12583-016-0629-0

CARTOGRAPHIC MICROZONATION OF NITRATE VULNERABILITY IN THE VARAŽDIN AQUIFER THROUGH INTEGRATION OF FIELD MEASUREMENTS, HISTORICAL TIME SERIES AND LAND COVER DATA

Jelena LOBOREC [1], Lucija PLANTAK [1*], Karlo LESKOVAR [1], Ranko BIONDIĆ [1]

[1] *University of Zagreb Faculty of Geotechnical Engineering, Croatia*

E-mail: jelena.loborec@gfv.unizg.hr

E-mail: lucija.plantak@gfv.unizg.hr

E-mail: karlo.leskovar@gfv.unizg.hr

E-mail: ranko.biondic@gfv.unizg.hr

[*] *Corresponding author*

Abstract

The Varaždin aquifer is one of the most important drinking water resources in northwestern Croatia and has been affected by elevated nitrate concentrations for several decades. Long-term contamination has already resulted in the closure of one of the three major wellfields, highlighting the need for a more precise assessment of nitrate vulnerability. This study proposes a methodology for nitrate vulnerability microzonation based on advanced GIS cartographic modelling and spatial data integration. Current nitrate vulnerable zone delineations are intended for regional-scale management and regulatory purposes and do not fully capture the local hydrogeological heterogeneity that controls nitrate transport within the aquifer. The proposed microzonation provides a higher-resolution assessment of spatial variability in groundwater vulnerability. The approach combines long-term nitrate concentration records from groundwater abstraction wells with recent field measurements in groundwater and surface water. Georeferenced nitrate data are mapped and spatially interpolated to generate continuous concentration surfaces, which are compared with historical monitoring data to identify persistent hotspots, emerging risk areas, and temporal trends. Nitrate concentration maps are integrated with CORINE Land Cover information and maps of cover deposits describing lithology and protective layer thickness above the aquifer. Multi-criteria spatial analysis evaluates relationships between nitrate occurrence, land-use intensity, and hydrogeological conditions, supporting groundwater protection planning and long-term protection of drinking water resources.

Key words

Varaždin aquifer, Nitrate vulnerability microzonation, GIS, CORINE Land Cover

1 Introduction

Groundwater represents one of the most important sources of drinking water worldwide and plays a crucial role in ensuring water security, ecosystem stability, and socio – economic development (Freeze and Cherry, 1979; Fetter and Kreamer, 2018; WHO, 2022). However, increasing anthropogenic pressures, particularly intensive agricultural practices, have significantly affected groundwater quality in many European aquifers (European Environment Agency, 2018). Among the various contaminants, nitrates are considered one of the most widespread pollutants due to their high mobility in the subsurface environment and their strong association with agricultural fertilization and livestock production. The Varaždin aquifer, located in northwestern Croatia, is one of the most important groundwater resources in the country and serves as a primary source of drinking water for the surrounding population. Previous

studies have documented elevated nitrate concentrations within the aquifer over several decades, primarily as a consequence of intensive agricultural activities and the extensive use of nitrogen – based fertilizers (Karlović, 2022). The severity of the problem is reflected in the closure of one of the three major groundwater abstraction sites in the Varaždin area due to nitrate concentrations exceeding regulatory thresholds. In addition to environmental concerns, elevated nitrate concentrations pose significant public health risks. After ingestion, nitrates may be converted into nitrites, which can cause methemoglobinemia in infants, commonly known as "blue baby syndrome" (Park and Rhee, 2025). Long – term exposure has also been associated with adverse reproductive and developmental outcomes, including spontaneous abortions, premature births, low birth weight, congenital malformations, and increased neonatal mortality. Although extensive groundwater monitoring datasets exist for the Varaždin aquifer, current assessments are primarily based on monitoring data from abstraction wells and do not fully integrate information from surface waters, spring waters, geological characteristics, or land – use patterns. Consequently, important spatial relationships controlling nitrate occurrence and transport remain insufficiently understood. Furthermore, existing nitrate vulnerable zone classifications often fail to capture local – scale heterogeneity in hydrogeological conditions and contamination pathways. To address these limitations, this study proposes a methodology for nitrate vulnerability microzonation based on advanced cartographic modelling and spatial data integration within a Geographic Information System (GIS) environment. Nitrate vulnerability microzonation is defined as the process of subdividing the study area into relatively homogeneous microzones according to their susceptibility to nitrate contamination, based on detailed local-scale investigations and the integration of multiple environmental datasets. Unlike conventional regional nitrate vulnerable zone delineations, which are necessarily generalized, microzonation incorporates site-specific hydrogeological, geological, land-use, hydrological and groundwater quality data to achieve substantially higher spatial resolution. The methodology presented in this paper represents the initial phase of the proposed microzonation framework. At this stage, historical monitoring data, recent field measurements and preliminary GIS analyses are used to establish the methodological basis for the subsequent delineation of nitrate vulnerability microzones. The final outcome of the research will be a GIS-based nitrate vulnerability microzonation map, classifying the aquifer into microzones with different levels of vulnerability to nitrate contamination. The approach combines long – term nitrate monitoring data from groundwater abstraction wells with recent field measurements in groundwater and surface waters. These datasets will be integrated with land-use information, geological and hydrogeological characteristics, and environmental parameters to identify spatial patterns of nitrate occurrence and delineate areas of increased vulnerability. The primary objective of the study is to develop a scientifically robust and reproducible framework for nitrate vulnerability microzonation that can support groundwater protection planning, optimization of monitoring networks, implementation of good agricultural practices, and sustainable management of drinking water resources. The proposed microzonation should therefore not be interpreted as a replacement of the officially designated Nitrate Vulnerable Zones, but rather as a complementary, local-scale decision-support tool that identifies spatial differences in vulnerability within those zones. Additionally, the methodology is designed to be transferable to other alluvial aquifers with similar hydrogeological characteristics.

2 Methodology

The study focuses on the Varaždin aquifer, located within the Drava River alluvial plain in northwestern Croatia. The aquifer represents one of the most productive groundwater systems in the country and constitutes a strategically important source of drinking water for the regional population. Geologically, the aquifer is composed predominantly of Quaternary alluvial deposits consisting of gravel and sand layers characterized by high permeability and hydraulic conductivity (Urumović et al., 1990). These hydrogeological conditions enable significant groundwater recharge but simultaneously increase vulnerability to contamination originating from surface activities. Land use within the study area is dominated by intensive agricultural production, including arable farming and livestock breeding (Larva et al., 2023). The widespread application of nitrogen fertilizers and manure has been identified as the primary source of nitrate contamination. In addition to agricultural land, the area includes urban settlements, transportation infrastructure, and smaller industrial zones, all of which may contribute to

groundwater quality pressures. Hydrologically, the Varaždin aquifer is closely connected to the Drava River and associated surface water bodies (Urumović et al, 1990). Variations in precipitation patterns and river discharge significantly influence groundwater recharge processes and nitrate transport dynamics. The combination of highly permeable deposits, shallow groundwater levels, and intensive agricultural activities creates conditions that favour the infiltration and migration of nitrate contaminants into the saturated zone. The proposed methodology relies on the integration of multiple spatial and temporal datasets describing groundwater quality, environmental conditions, and hydrogeological characteristics.

2.1 Groundwater Nitrate Monitoring Data

Organic nitrogen includes all the nitrogen that is part of living animals, animal wastes and the remains of living things. Organic forms of nitrogen must be broken down into inorganic forms to be used by plants. Nitrate (NO_3) is the most common form of inorganic nitrogen found in waterways (Camargo and Alonso, 2006). Nitrates are odorless, colorless, and tasteless so it is important to test feed and drinking water to determine levels of nitrate. Long – term nitrate concentration records obtained from groundwater abstraction wells constitute the primary dataset used in this study. These monitoring records provide valuable information on temporal trends, seasonal variability, and long-term changes in groundwater quality. Historical monitoring data are supplemented by measurements from observation wells and piezometers where available. The Varaždin aquifer is subject to continuous monitoring of nitrate concentrations due to its importance as a major drinking water resource and the long – standing pressures from agricultural activities. Several regulatory frameworks have been established to protect groundwater quality and support sustainable water management. The study area is designated as a Nitrate Vulnerable Zone (Official Gazette No. 130/2012) under Croatian legislation (Figure 1), requiring the implementation of measures aimed at reducing nitrate inputs from agricultural sources.

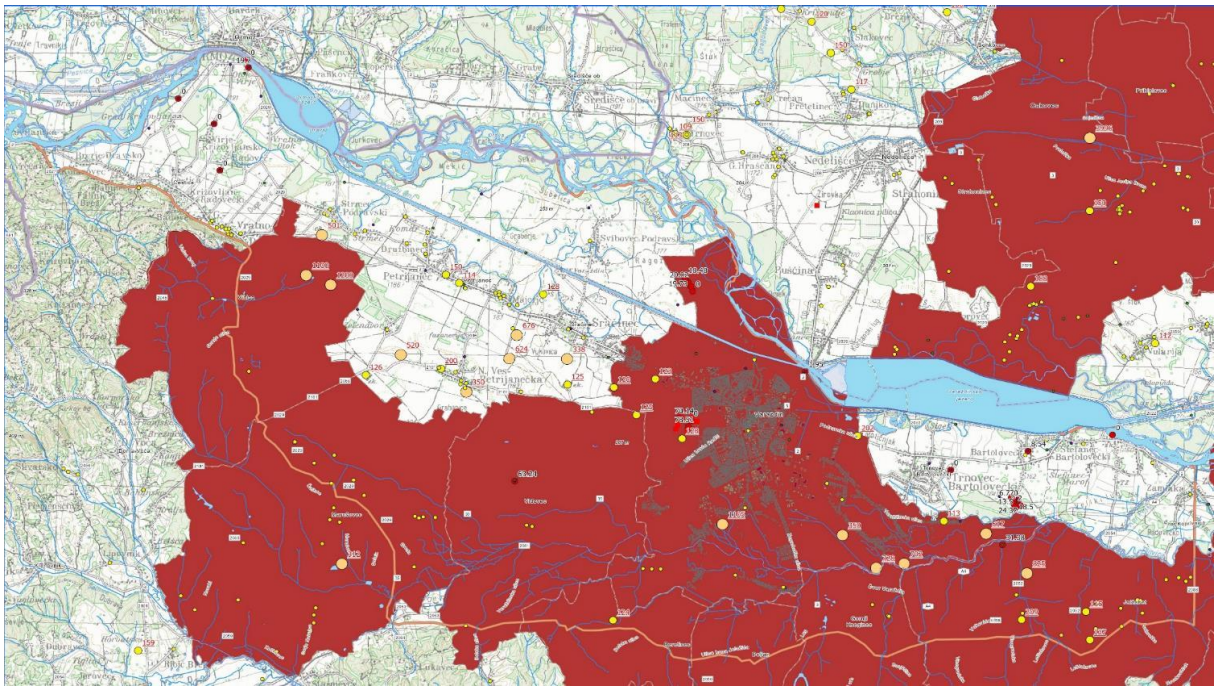


Figure 1. Nitrate Vulnerable Zone in Varaždin area (marked red)

In addition, almost the entire aquifer area is encompassed by sanitary protection zones of public water supply sources, providing an additional level of protection against groundwater contamination. According to the River Basin Management Plan (RBMP) for the period up to 2027 (Official Gazette No. 84/2023), the Varaždin section of the Drava River Basin is classified as having a good quantitative status, indicating sufficient groundwater availability, while its chemical status remains poor due to

elevated nitrate concentrations. From a climate change adaptation perspective, these regulatory measures play an important role in enhancing the resilience of the water resource system. Measures aimed at reducing hydraulic loads on drainage infrastructure during extreme precipitation events can help mitigate the rapid transport of contaminants, while maintaining adequate groundwater recharge may contribute to the dilution of nitrate concentrations within the aquifer. Together, these approaches support both groundwater protection and long-term adaptation to increasing climatic variability.

Nitrates concentrations were collected from water pumping extraction sites Varaždin (Figure 2), Vinokovščak (Figure 3) and Bartolovec (Figure 4) from water distributor Varkom d.o.o. It should be noted that the monitoring dataset contains discrete sampling measurements collected during regular monitoring campaigns. Consequently, short-term concentration peaks should be interpreted as snapshots of groundwater quality at the time of sampling rather than as continuous annual trends.

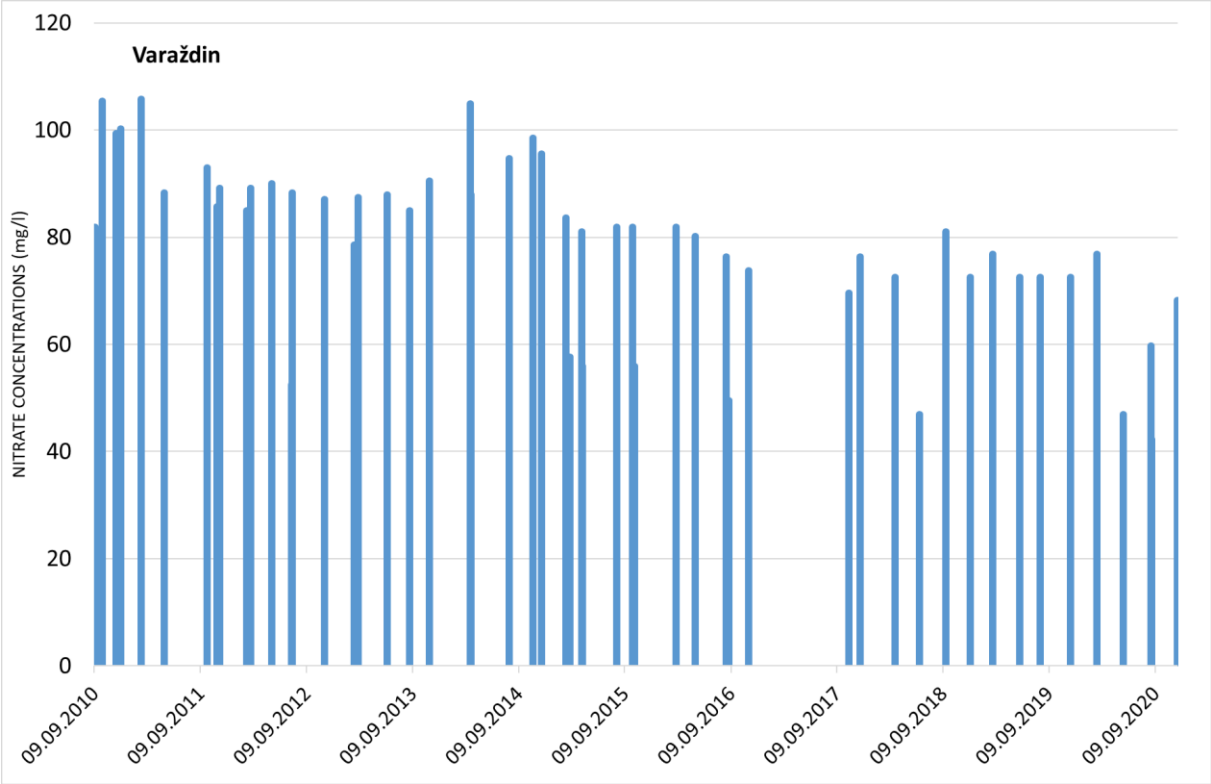


Figure 2. Nitrates concentration in mg/l in Varaždin water extraction site from 2010 till 2020

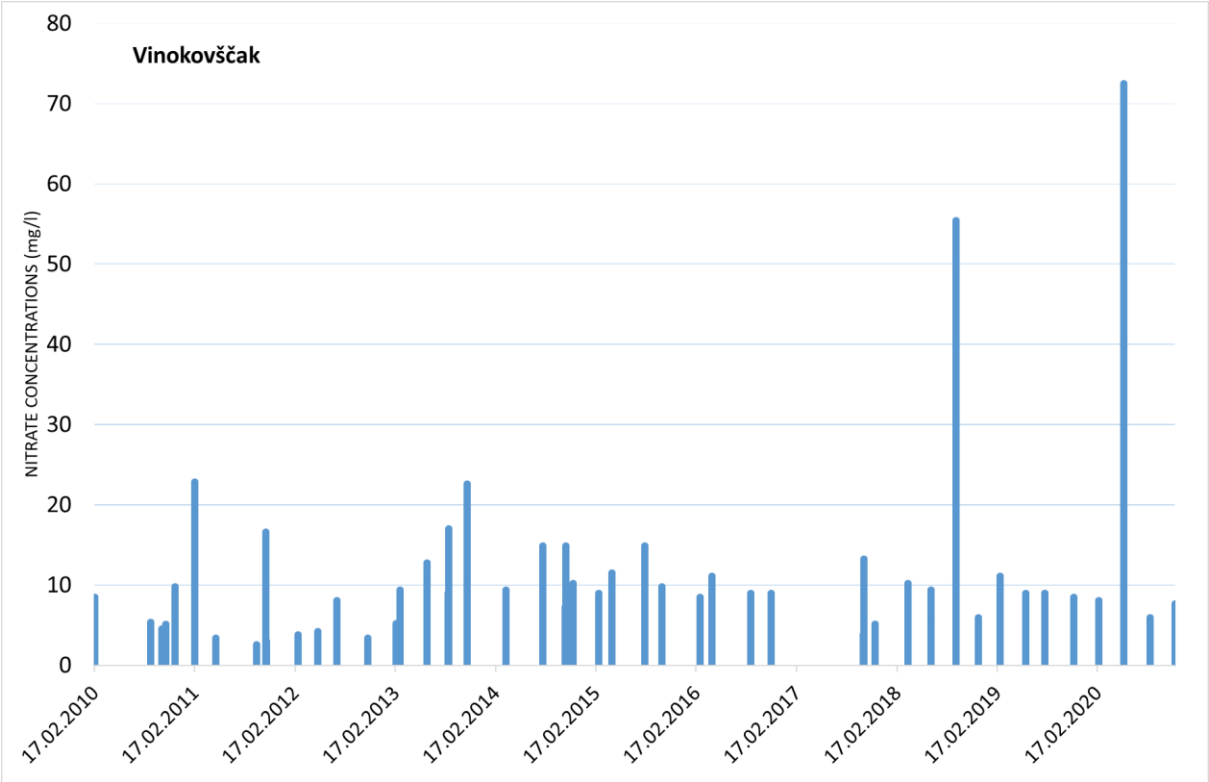


Figure 3. Nitrates concentration in mg/l in Vinokovščak water extraction site from 2010 till 2020

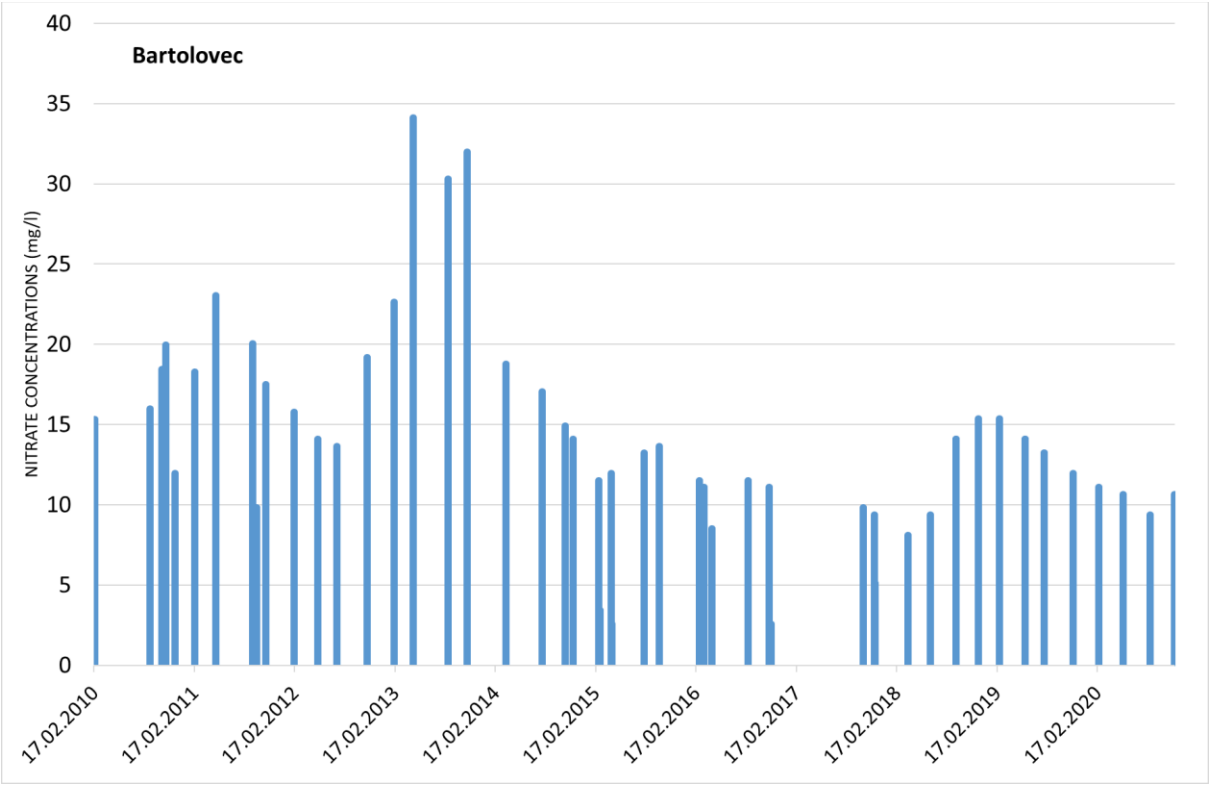


Figure 4. Nitrates concentration in mg/l in Bartolovec water extraction site from 2010 till 2020

Long-term groundwater quality monitoring has revealed elevated nitrate concentrations throughout the aquifer, particularly in areas influenced by intensive agricultural activities. Among the three wellfields, the Varaždin wellfield experienced the most severe deterioration in groundwater quality, with nitrate concentrations repeatedly exceeding the maximum allowable concentration (MAC) of 50 mg/l NO_3^-

which is also prescribed by Croatian legislation, namely the Regulation on Compliance Parameters, Analytical Methods and Monitoring of Water Intended for Human Consumption (Official Gazette No. 64/2023). As a consequence of persistent exceedances of this threshold, the Varaždin wellfield was permanently taken out of operation. In contrast, the Bartolovec and Vinokovščak wellfields remain active and continue to be regularly monitored, although elevated nitrate concentrations have also been recorded at certain locations within their capture zones. This especially applies to particularly pronounced nitrate peaks observed at the Vinokovščak wellfield during 2019 and 2020. Although the present study does not specifically investigate the causes of these short-term fluctuations, previous studies indicate that nitrate concentrations in the Varaždin aquifer are controlled by a combination of agricultural nitrogen inputs, groundwater recharge conditions, hydrogeological characteristics, and groundwater abstraction regimes. In particular, changes in pumping patterns following the closure of the Varaždin wellfield may have influenced groundwater flow paths and consequently affected nitrate concentrations at the remaining active wellfields. These observations further support the need for an integrated assessment combining long-term monitoring data with hydrogeological, climatic and land-use information, which is one of the main objectives of the proposed nitrate vulnerability.

2.2 Field Measurements

To improve spatial coverage and better understand nitrate distribution within the hydrological system, additional field investigations are conducted. Water samples are collected from groundwater monitoring locations, surface water bodies, and selected springs within the study area. Measured nitrate concentrations are georeferenced and incorporated into a GIS database for further spatial analysis. Nitrates analysis in groundwater is carried out periodically from September 2024 till end of the April 2026. During the period from September 2024 till May 2025, three sampling was conducted in different hydrological conditions.

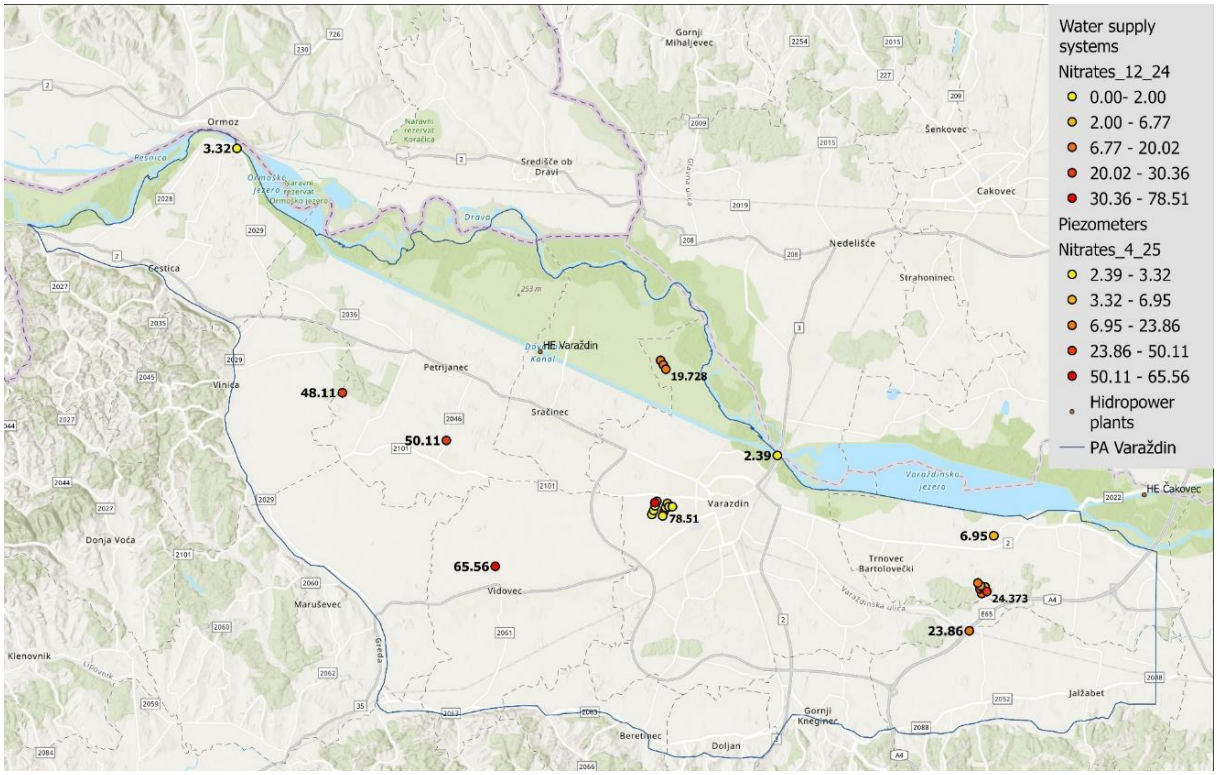


Figure 5. Measured nitrate concentration in study area

Figure 5 presents the spatial distribution of nitrate concentrations measured at water supply wells and monitoring piezometers within the Varaždin aquifer during 2024. The results reveal considerable spatial

variability, with the highest nitrate concentrations recorded in the central and southwestern parts of the study area, where several monitoring locations exceed the drinking water limit of 50 mg/l NO_3^-. In contrast, lower nitrate concentrations are generally observed in the northern part of the aquifer and in areas adjacent to the Drava River. The observed distribution pattern suggests a strong influence of local hydrogeological conditions and agricultural land use on nitrate occurrence and transport. These preliminary findings provide an important basis for subsequent GIS – based vulnerability assessment and the delineation of nitrate vulnerability microzones within the aquifer.

3 Preliminary Results and Discussion

The proposed methodology is based on GIS – supported cartographic modelling and multi-criteria spatial analysis aimed at developing a robust framework for nitrate vulnerability microzonation within the Varaždin aquifer. In the initial phase of the research, available datasets were standardized, georeferenced, and integrated into a unified GIS database. Historical nitrate concentration records from groundwater abstraction wells were combined with recent field measurements collected within the study area to establish a comprehensive spatial dataset.

As a first step, nitrate concentration measurements were processed to generate preliminary spatial distribution maps using interpolation techniques such as Inverse Distance Weighting (IDW) and Ordinary Kriging (Figure 6). The resulting concentration surfaces reveal considerable spatial variability across the aquifer, with several localized zones exhibiting elevated nitrate concentrations. In particular, concentrations exceeding the drinking water threshold of 50 mg/l were identified in the central and southwestern sectors of the study area, indicating potential contamination hotspots. These preliminary results demonstrate the capability of GIS – based spatial analysis to identify areas requiring further investigation and enhanced monitoring.

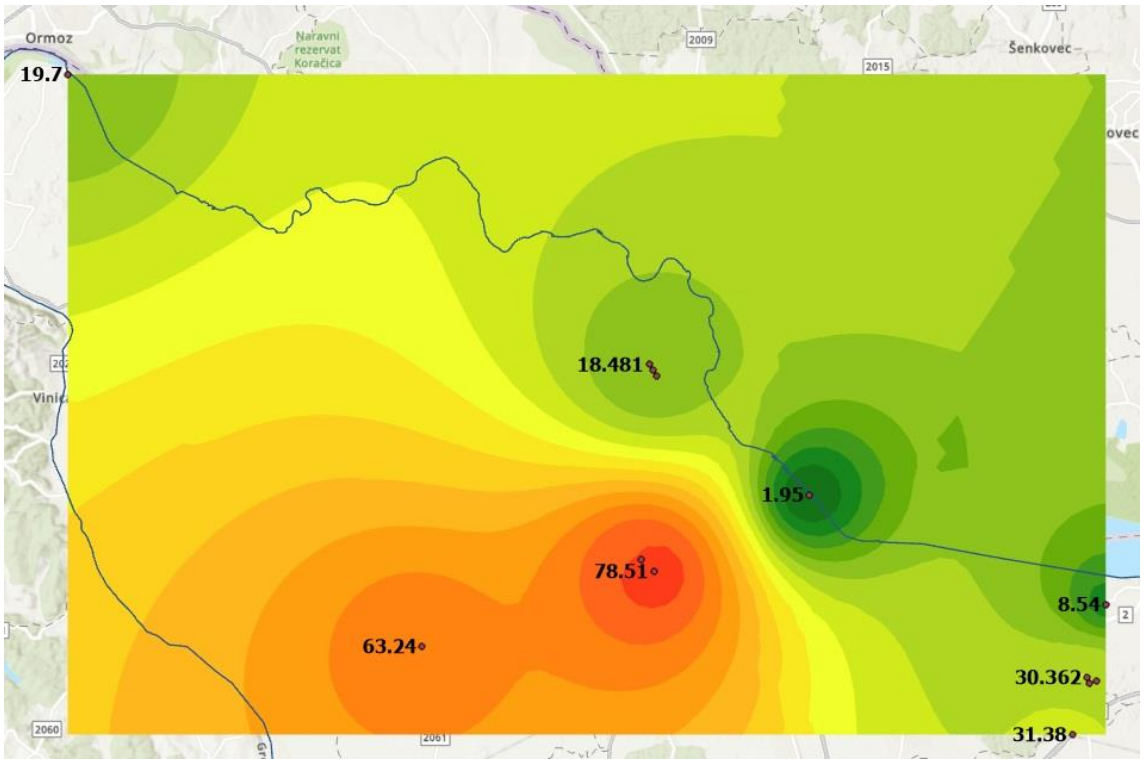


Figure 6. GIS generated nitrate concentration map

The generated nitrate concentration map, such as primarily results shown on Figure 6, represent the first stage of the proposed microzonation methodology. In subsequent phases, these spatial datasets will be quantitatively compared with long – term nitrate time series from groundwater abstraction sites to identify persistent contamination hotspots, emerging risk areas, and temporal variability patterns

associated with hydrological conditions and recharge dynamics.

A key component of the methodology involves the spatial overlay and cross – analysis of nitrate concentration maps with thematic environmental datasets. These include land – use information derived from the CORINE Land Cover database, geological maps describing lithological composition, and maps of cover deposits indicating the thickness and protective capacity of superficial sediments above the aquifer. Such datasets provide essential information for understanding the environmental controls governing nitrate transport and accumulation.

Particular attention is given to areas characterized by highly permeable gravel and sand deposits combined with reduced thickness of low – permeability cover layers. These hydrogeological conditions facilitate rapid infiltration and vertical transport of nitrates from agricultural land toward the groundwater table, thereby increasing vulnerability to contamination. The preliminary concentration patterns observed in the study area suggest that geological and hydrogeological characteristics play a significant role in controlling nitrate distribution and should therefore be incorporated into vulnerability assessments.

The next stage of the research will apply multi – criteria spatial analysis to evaluate relationships between nitrate occurrence, agricultural land-use intensity, hydrogeological conditions, and the protective function of cover deposits. Through the integration of these parameters, preliminary nitrate vulnerability microzones will be delineated and classified according to their relative contamination risk. The resulting maps are expected to provide substantially greater spatial detail than currently available nitrate vulnerable zone classifications.

To ensure the reliability and practical applicability of the methodology, future model outputs will be verified through targeted field investigations and comparison with independent monitoring data. This validation process will support the development of a scientifically robust and transferable framework for nitrate vulnerability microzonation, providing a basis for groundwater protection planning, optimization of monitoring networks, implementation of good agricultural practices, and long – term preservation of drinking water resources in the Varaždin aquifer and similar hydrogeological environments.

4 Conclusion

This study presents a methodology for nitrate vulnerability microzonation in the Varaždin aquifer based on GIS – supported cartographic modelling, spatial data integration, and multi-criteria environmental analysis. The proposed framework combines long-term groundwater quality monitoring data with recent field measurements and environmental datasets describing land use, geological characteristics, hydrogeological conditions, and protective cover deposits. Preliminary spatial analyses demonstrate significant spatial variability in nitrate concentrations and indicate the presence of localized contamination hotspots that require further investigation.

The integration of nitrate concentration maps with thematic environmental layers provides a scientifically sound basis for identifying areas with increased intrinsic and specific vulnerability to nitrate contamination. Particular importance is attributed to the combined influence of intensive agricultural land use, highly permeable gravel and sand deposits, and reduced thickness of low-permeability protective layers, which collectively facilitate the transport of nitrates toward the groundwater table. The resulting microzonation approach offers substantially greater spatial resolution than existing nitrate vulnerable zone classifications and can support more targeted groundwater protection measures.

Beyond the GIS – based vulnerability assessment, the presented methodology establishes the foundation for the development of advanced artificial intelligence (AI) models capable of analysing complex spatial and temporal relationships within the aquifer system. Future research will incorporate machine learning

(ML) and deep learning (DL) techniques to process long – term monitoring datasets from groundwater, surface water, spring water, and meteorological observations. Particular emphasis will be placed on evaluating the predictive capabilities of algorithms for forecasting nitrate concentration dynamics under variable hydrological and climatic conditions.

The integration of AI – based predictive modelling with GIS – derived vulnerability maps will enable the development of a hybrid decision – support framework that combines environmental monitoring, spatial analysis, and data – driven forecasting. Such an approach has the potential to function as an early warning system for nitrate contamination, allowing water utilities and environmental authorities to anticipate periods of elevated nitrate concentrations and implement preventive management measures in a timely manner.

The proposed methodology contributes to the digital transformation of groundwater management by integrating environmental data science, geospatial technologies, and artificial intelligence into a unified analytical framework. In addition to its application within the Varaždin aquifer, the methodology is designed to be transferable to other alluvial aquifers with similar hydrogeological characteristics, thereby supporting broader implementation of innovative approaches for groundwater protection, climate change adaptation, and sustainable management of drinking water resources.

Acknowledgements

Part of this research was carried out within the Interreg Central Europe project CE0100184 „Management of urban water resources in Central Europe facing climate change MAURICE" and is additionally funded by the European Union – Next Generation EU through the project Development of a Methodology for Microzonation of Nitrate Vulnerability Using Artificial Intelligence and Multiple Data Sources (DIMRAN), project code: NPOO GFV-IP-006/2025.

References

Camargo, J. A. and Alonso, Á. 2006 Ecological and toxicological effects of inorganic nitrogen pollution in aquatic ecosystems: A global assessment, *Environment International*, 32(6), pp. 831–849.
European Environment Agency 2018 *European Waters: Assessment of Status and Pressures 2018*. EEA Report No. 7/2018. Copenhagen: European Environment Agency.
Fetter, C. W. and Kreamer, D. 2018. *Applied Hydrogeology*. 5th edn. Long Grove, IL: Waveland Press.
Freeze, R. A. and Cherry, J. A. 1979 Groundwater. Englewood Cliffs, NJ: Prentice Hall.
Karlović, I. 2022 Origin, fate and transport modelling of nitrate in the Varaždin aquifer. Zagreb. Faculty of Mining, Geology and Petroleum Engineering.
Larva, O., Brkić, Ž. and Marković T. 2023 Vulnerability and Risk of Contamination of the Varaždin Aquifer System, NW Croatia, *Sustainability*. 15(23), 16502, DOI:10.3390/su152316502.
Official Gazette 2012 Decision on Determining Vulnerable Areas in the Republic of Croatia (Official Gazette No. 130/2012).
Official Gezette 2023 Regulation on Compliance Parameters, Analytical Methods and Monitoring of Water Intended for Human Consumption (Official Gazette No. 64/2023)
Official Gezette 2023 River Basin Management Plan up to 2027, Croatia (Official Gazette No. 84/2023).
Park, S. M. and Rhee, M. S. 2025 Investigating the possible role of foodborne nitrite-producing bacteria during digestion in infant methemoglobinemia, *Trends in Food Science & Technology*. 159.
Urumović, K., Hlevnjak, B., Prelogović, E. and Mayer, D. 1990 Hydrogeological Conditions Of The Varaždin Aquifer. *Geološki Vjesnik*, 43, 149–158.
World Health Organization. 2022 *Guidelines for Drinking-water Quality*. 4th edn., incorporating the 1st and 2nd addenda. Geneva: World Health Organization

A FRAMEWORK FOR URBAN CLIMATE RESILIENCE: REGULATION ELEMENTS FOR GROUNDWATER PROTECTION IN THE VARAŽDIN AQUIFER

Lucija PLANTAK [1*], Karlo LESKOVAR [1], Hrvoje MEAŠKI [1], Ranko BIONDIĆ [1]

[1] *University of Zagreb Faculty of Geotechnical Engineering, Croatia*

E-mail: lucija.plantak@gfv.unizg.hr

E-mail: karlo.leskovar@gfv.unizg.hr

E-mail: hrvoje.measki@gfv.unizg.hr

E-mail: ranko.biondic@gfv.unizg.hr

** Corresponding author*

Abstract

Urban aquifer management in highly permeable alluvial environments requires an integrated approach due to increasing pressures from anthropogenic activities and climate change. Applying Integrated Water Resources Management (IWRM) principles can enhance the climate resilience of the Varaždin aquifer, a strategically important drinking water resource in northwestern Croatia. The Varaždin aquifer is characterized by high hydraulic conductivity, strong surface water-groundwater interactions, and documented nitrate contamination originating from agricultural and urban activities. Climate change, particularly more frequent extreme precipitation events and prolonged droughts, intensifies pollutant leaching, alters nitrate dynamics, and increases hydraulic stress on urban drainage systems. This study evaluates spatial planning regulation elements (REs) as IWRM instruments using a multi-criteria assessment framework that considers contaminant reduction potential, climate resilience benefits, implementation feasibility, and synergy with natural attenuation processes. Hydrogeological indicators are integrated with regulatory and infrastructural parameters to link planning measures with expected groundwater performance. The analysis shows that sanitary protection zones around abstraction sites provide the most effective regulatory protection. Wastewater network expansion, water-supply infrastructure upgrades, and decentralized infiltration systems reduce pollution pressures while enhancing flood mitigation. By combining hydraulic buffering, pollutant retention, and urban heat mitigation, these measures strengthen adaptive capacity. The qualitative assessment indicates that effective urban IWRM requires coordinated spatial planning, technical infrastructure, and nature-based solutions to improve groundwater resilience under climate change.

Key words

IWRM, Regulation Elements, Climate Change Adaptation, Groundwater Protection.

1 Introduction

Groundwater resources in highly permeable alluvial aquifers are increasingly exposed to multiple pressures arising from urbanization, intensive agriculture, and climate change (La Vigna, 2022). The Varaždin aquifer in northwestern Croatia represents a strategically important drinking water resource supplying the City of Varaždin and surrounding municipalities. Characterized by high hydraulic conductivity and strong surface water-groundwater interactions, the aquifer is highly productive but also highly vulnerable to contamination.

Local hydrogeological studies have documented the presence of nitrates, nitrites, and microbial

indicators in parts of the Varaždin aquifer, originating mainly from agricultural practices, the food industry, and improper disposal of poultry waste (Ožanić, 2016). The vulnerability of the aquifer is further amplified by its permeable gravel-sand deposits, which facilitate rapid transport of contaminants from the surface to groundwater (Rawat et al. 2022). Climate change introduces additional challenges through increasing frequencies of extreme precipitation events, prolonged drought periods, and altered recharge patterns (Mas-Pla and Menció, 2019). These processes may accelerate pollutant leaching, increase hydraulic stress on urban drainage systems, and modify groundwater quality dynamics (Dao et al., 2024). The spatial planning framework of Varaždin provides instruments to regulate land-use and mitigate these risks. The General Spatial Plan of City of Varaždin (Official Gazette of the City of Varaždin, 2022) and the Spatial Plan of Varaždin County, 2024 define zones of special protection, water management infrastructure, and land-use restrictions in sensitive areas. In addition, the study Protection of Wellfields in the Regional Water Supply System of Varaždin (Bačani et al., 2010) delineated sanitary protection zones for pumping stations such as Bartolovec and Vinokovščak, using 3D numerical groundwater flow models, in line with the Regulation on Sanitary Protection Zones of Water Sources (OG 55/02, 66/11, 47/13).

Recent infrastructure projects, notably the EU-funded "Aglomeracija Varaždin" (Varkom d.d., 2022), have also targeted groundwater quality protection through the expansion of the wastewater collection system and construction of new treatment facilities. This reduces direct pollutant pressures from urban and peri-urban areas, complementing regulatory land-use measures.

Integrated Water Resources Management (IWRM) provides a framework for addressing these challenges by combining regulatory, technical, and ecosystem-based measures (La Vigna, 2022). The objective of this study is to evaluate spatial planning regulation elements (REs) as instruments for enhancing groundwater quality resilience in the Varaždin aquifer and to assess their contribution to climate adaptation and sustainable groundwater management.

2 Methodology

The evaluation of spatial planning REs for the Varaždin area builds on the framework set by national legislation, such as the Regulation on Sanitary Protection Zones of Water Sources (OG 55/02, 66/11, 47/13), and is implemented through local planning instruments, primarily the Spatial Plan of Varaždin County, 2024 and the General Spatial Plan of City of Varaždin (Official Gazette of the City of Varaždin, amendments up to 2022). These plans define zones of special protection, land-use conditions, and infrastructure development requirements, all of which are crucial for safeguarding groundwater resources. In evaluating REs, particular attention is given to the specific hydrogeological setting of the Varaždin aquifer, characterized by high infiltration capacity and strong interaction between surface water and groundwater. This makes the aquifer highly productive but also vulnerable to contamination from both urban and agricultural activities, as well as from potential impacts of hydropower accumulation dynamics along the Drava River.

The evaluated measures included sanitary protection zones, agricultural land-use controls, wastewater infrastructure upgrades, stormwater management systems, green infrastructure, riparian buffer restoration, and hydropower operation management. A qualitative ranking approach was used to determine the relative priority and effectiveness of each measure.

The evaluation matrix of spatial planning REs was developed using a multi-criteria assessment (MCA) approach. The methodology is designed to systematically compare heterogeneous REs that differ in scale, implementation level, and functional mechanisms, while ensuring relevance to climate-resilient groundwater quality restoration in areas with a heavily modified water regime.

The MCA approach combines qualitative expert judgment with evidence-based assessment derived from local and regional spatial planning documents (City of Varaždin and Varaždin County), national regulatory frameworks, hydrogeological studies and monitoring results for the Varaždin aquifer, and

project objectives related to climate change (CC) resilience and groundwater quality restoration. The methodology follows four sequential steps shown in Figure 1.

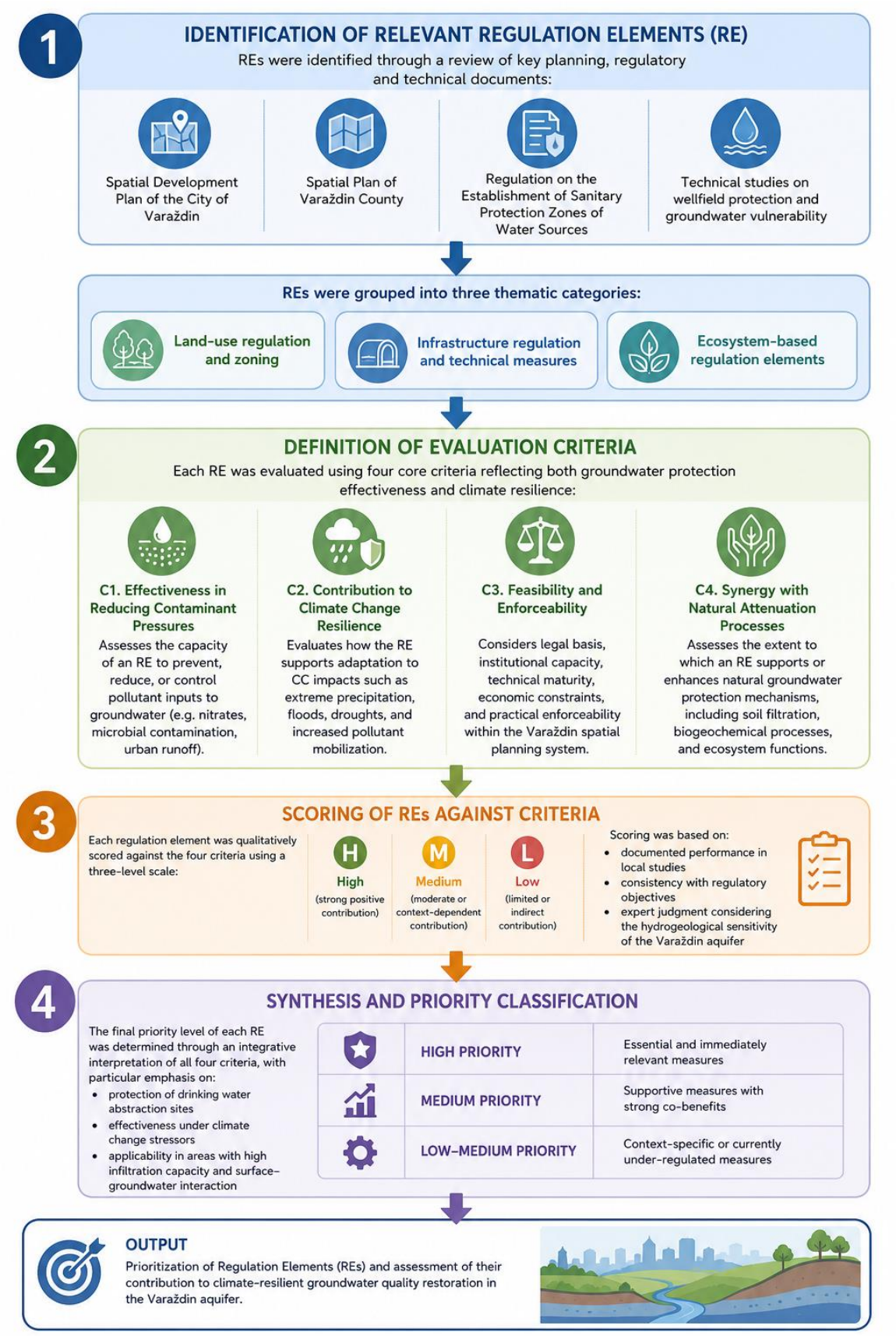


Figure 1. Methodology of the RE's evaluation (AI generated)

The assessment was based on existing planning documents, hydrogeological studies, groundwater protection regulations, and infrastructure development programs. REs were grouped into three categories:

1. Land-use regulation and zoning measures
   Sanitary protection zones: Defined for all major water abstraction sites, are the cornerstone of groundwater protection. Restrictions include bans on hazardous industry, controlled agricultural use, and limits on construction. Their legal basis is the Regulation on Sanitary Protection Zones of Water Sources (OG 55/02, 66/11, 47/13), and their spatial delineation is included in county and city plans.

   Agricultural land regulation: The Varaždin spatial plan highlights agriculture as a key land use. However, documented nitrate contamination indicates a need for stricter zoning controls in SPZs and recharge areas. Reduced fertilizer and pesticide use, alongside incentives for organic farming, would directly benefit groundwater quality.

   Urban development control: The General Spatial Plan of City of Varaždin integrates conditions for infrastructure, including requirements for wastewater connection and surface permeability, but further emphasis on green infrastructure (e.g. permeable pavements, green roofs) would increase resilience.

2. Infrastructure regulation and technical measures
   Wastewater management (Aglomeracija Varaždin): The project expands the sewerage system and constructs new wastewater treatment plants, addressing one of the main sources of groundwater contamination.

   Stormwater regulation: Local plans require regulated discharge, but opportunities exist for more widespread use of infiltration systems and retention basins to filter pollutants before recharge.

   Hydropower accumulation regulation: While not yet explicitly addressed in city or county spatial plans, the interaction between hydropower reservoirs and the aquifer suggests the need for operational rules that minimize rapid water-level fluctuations, which can accelerate contaminant transport.

3. Ecosystem-based and nature-based solutions
   Wetlands and riparian zones: While limited in the immediate urban area, county-level plans emphasize ecological corridors and river protection. Strengthening riparian buffers along the Drava and Plitvica Rivers could enhance pollutant retention before infiltration.

   Afforestation and soil conservation: Increasing forested cover in recharge areas would provide long-term protection against erosion and leaching.

   Green infrastructure in urban areas: Introducing green belts could reduce the pollutant burden from urban runoff.

All evaluation criteria were considered equally important for groundwater quality resilience and therefore no numerical weighting was assigned. This was motivated by the research nature of the framework and the absence of empirical evidence supporting differential criterion importance within the Varaždin aquifer context. Based on expert interpretation of the combined criteria, the scoring process combined evidence from planning documents, groundwater protection regulations, hydrogeological studies, and published scientific literature. For each regulation element, the available evidence was evaluated against each criterion using the definitions provided in Table 1. Where evidence indicated a direct and well-established contribution to groundwater protection, a High score was assigned. Where performance depended on implementation conditions or local context, a Medium–High or Medium score was assigned. Low scores were assigned where the contribution was indirect or limited.

Table 1. Scoring of the REs

Score	Definition
High (H)	Strong and direct contribution to the criterion, supported by regulatory requirements, documented effectiveness, or well-established scientific evidence of strong influence on groundwater protection
Medium–High (MH)	Strong contribution but dependent on implementation conditions or spatial context
Medium (M)	Moderate contribution with indirect or site-specific effects
Low (L)	Limited contribution or weak direct influence on groundwater protection

This study does not attempt to quantify pollutant reduction, recharge enhancement, or flood mitigation effects. Instead, it applies a qualitative MCA based on document review and expert judgment to identify and prioritize REs that are expected, according to existing scientific and regulatory knowledge, to contribute to groundwater resilience.

3 Results and Discussion

Of the identified REs, four were selected for the comparative MCA based on their direct relevance to the Varaždin urban area and the availability of sufficient evidence for assessment, while the remaining measures are discussed qualitatively as complementary measures. The resulting evaluation matrix is presented in Table 2.

Table 2. Evaluation Matrix of REs in Varaždin area

Regulation Element (REs)	Effectiveness in Reducing Contaminants	Contribution to CC Resilience	Feasibility & Enforcement	Synergy with Natural Attenuation
Sanitary protection zones for water supply wells (Bartolovec, Vinokovščak)	High – Proven through modelling and monitoring studies (Bačani et al., 2010)	High – Provides buffer against extreme pollutant inputs	Medium-High – Already established, but enforcement remains a challenge	High – Reduces pollutant loads, allowing soil and aquifer processes to function
Land-use regulation in high infiltration areas (agriculture restrictions, organic incentives)	Medium-High – Addresses nitrate and pesticide pressures (Ožanić, 2016)	High – Reduces risk under heavy rainfall and drought	Medium – Requires cooperation with farmers and policy incentives	Medium-High
Wastewater and sewerage system expansion (Aglomeracija Varaždin)	High – Key urban pollutant reduction (Varkom, 2022)	Medium-High – Prevents overflows and leakage under CC extremes	High – EU project funded and implemented	Medium
Permeable surfaces / green infrastructure in urban planning	Medium	High – Enhances infiltration, reduces floods	Medium – Requires new planning standards	Medium

The assessment identified sanitary protection zones as the most effective regulatory instrument for groundwater protection (Foster et al, 2002; Zektser and Everett, 2004). Existing ones surrounding the Bartolovec, and Vinokovščak abstraction sites provide a legally enforceable framework for restricting potentially hazardous activities and controlling agricultural and urban development. Their effectiveness is enhanced by their direct influence on recharge areas and pollutant source control.

Agricultural land-use regulation also demonstrated high effectiveness due to its capacity to reduce nitrate and pesticide loading (Follett and Hatfield, 2001; Sebilo et al., 2013; Mas-Pla and Menció, 2019). The implementation of fertilizer restrictions, controlled pesticide application, and incentives for organic farming would significantly decrease diffuse contamination pressures. Such measures are particularly important given the documented nitrate contamination within the aquifer system. The results indicate that stricter controls in high-infiltration recharge zones could substantially reduce future groundwater quality deterioration while increasing resilience to climate-induced changes in recharge and contaminant transport.

The evaluation demonstrated that wastewater infrastructure improvements and sustainable urban drainage systems are among the most effective measures for simultaneously improving groundwater quality and climate resilience (Daigger, 2009; UNESCO, 2022). The ongoing Aglomeracija Varaždin project significantly reduces pollutant inputs from urban and peri-urban areas through the expansion of sewerage networks and modernization of wastewater treatment facilities.

In addition to conventional infrastructure upgrades, the assessment identified a comprehensive set of sustainable urban drainage and green infrastructure measures that integrate natural hydrological processes into urban planning. These measures are tailored to different urban land-use categories and transport infrastructure types.

For densely built-up roads with limited available space, the most suitable interventions include permeable edge strips, rain gardens, permeable parking surfaces, green barriers, and curb openings that direct runoff toward vegetated infiltration areas. These measures reduce stormwater runoff volumes, lower flood risk, and increase green space within highly urbanized environments.

Roads undergoing reconstruction present opportunities for the installation of underground infiltration systems, bioswales, green filtration belts, and rain gardens. Such interventions modernize drainage systems by replacing conventional conveyance approaches with natural retention and filtration processes that reduce pollutant transport and hydraulic stress on sewer networks.

Where sufficient space is available for expansion, the incorporation of double rows of trees, large bioswales, retention depressions, and vegetated infiltration corridors can contribute to increasing infiltration capacity while enhancing biodiversity and improving urban environmental quality. Similar benefits were identified for newly planned transport corridors, where sustainable drainage systems can be integrated from the design stage through permeable pavements, retention basins, infiltration channels, green roofs, and vegetated drainage networks. These measures maximize the use of natural processes and improve the long-term resilience of transport infrastructure to climate extremes.

The analysis further highlighted the importance of green infrastructure within public squares, parks, parking facilities, industrial zones, and residential developments. Permeable paving, rain gardens, retention areas, infiltration lawns, wetland zones, green roofs, and stormwater harvesting systems contribute to runoff reduction, pollutant filtration, groundwater recharge, and urban cooling. In industrial and commercial areas, large retention facilities and rainwater reuse systems can substantially reduce environmental impacts while improving water-use efficiency. Residential areas benefit from decentralized retention and infiltration measures that strengthen local resilience to extreme rainfall events and improve overall quality of life. Nature-based solutions were identified as critical components of groundwater quality protection and climate adaptation (City of Zagreb, 2022). Riparian buffer restoration along the Drava and Plitvica Rivers, wetland rehabilitation, afforestation of recharge areas, and urban greening measures contribute directly to natural attenuation processes by enhancing filtration, nutrient uptake, and pollutant retention.

The assessment indicates that green infrastructure measures provide multiple ecosystem services beyond groundwater protection. Urban parks incorporating retention ponds, wetland zones, rain gardens, and infiltration trenches increase water retention capacity while supporting biodiversity, recreational functions, and environmental education. Green roofs and green walls were found to be particularly

effective in densely urbanized areas, where they reduce stormwater runoff, mitigate urban heat island effects, and compensate for the loss of permeable surfaces. These ecosystem-based measures also enhance resilience to climate change by reducing flood peaks during extreme rainfall events and improving water availability during drought periods. Their contribution is particularly significant in highly permeable alluvial aquifers, where surface processes rapidly influence groundwater conditions.

The results demonstrate that the effectiveness of REs depends not only on their technical performance but also on the existence of an appropriate implementation framework. Successful application of sustainable urban drainage and groundwater protection measures requires interdisciplinary cooperation among urban planners, hydrogeologists, water managers, engineers, and environmental specialists. Several enabling conditions were identified as essential for long-term implementation: development of technical design standards, establishment of regular maintenance programs, provision of financial incentives and EU funding mechanisms, systematic monitoring and performance evaluation, integration of measures into statutory planning documents, and public education initiatives. These components collectively support the operationalization of IWRM principles at the local scale (Nydrioti et al., 2024).

Overall, the results indicate that groundwater resilience in the Varaždin aquifer cannot be achieved through isolated measures. Instead, resilience emerges from the interaction between land-use regulation, wastewater infrastructure, sustainable drainage systems, and nature-based solutions. Sanitary protection zones provide the regulatory backbone of groundwater protection, while green infrastructure and sustainable urban drainage systems create additional hydraulic buffering capacity, pollutant retention, and climate adaptation benefits. The integration of these measures within a coherent governance framework represents a practical pathway for strengthening groundwater quality resilience under future climate and land-use pressures.

The proposed methodology provides a qualitative prioritization rather than quantitative estimates of environmental performance. No hydrological modelling, economic assessment, or scenario analysis was undertaken. Consequently, the results should be interpreted as a strategic decision-support tool rather than a prediction of measurable groundwater quality improvements.

4 Conclusion

The Varaždin aquifer represents a highly vulnerable but strategically important groundwater resource whose protection requires integrated management under increasing climate and land-use pressures. The evaluation of spatial planning REs indicates that sanitary protection zones remain the most effective groundwater protection measure, forming the regulatory backbone of the system. Agricultural land-use controls and wastewater infrastructure improvements provide additional high-priority interventions capable of significantly reducing contamination risks.

Nature-based solutions, including riparian buffers, wetlands, afforestation, and urban green infrastructure, complement regulatory and technical measures by enhancing natural attenuation processes and increasing climate resilience. The combined implementation of these measures supports groundwater quality protection, flood mitigation, hydraulic buffering, and urban climate adaptation.

The qualitative assessment indicates that effective urban groundwater management requires the integration of spatial planning, infrastructure development, and ecosystem-based solutions within a coherent IWRM framework. The methodology identifies REs that are expected to contribute to groundwater quality resilience based on expert assessment and existing evidence, providing a transferable model for groundwater resilience in medium-sized European cities facing similar environmental challenges. The evaluation of REs for the Varaždin aquifer highlights that sanitary protection zones remain the most effective and established measure for safeguarding groundwater quality, particularly at critical abstraction sites. Their delineation and enforcement, as defined in the Spatial Plan of Varaždin County, the General Spatial Plan of City of Varaždin, and the Regulation on Sanitary Protection Zones of Water Sources (OG 55/02, 66/11, 47/13), form the regulatory backbone of

groundwater protection. Additionally, land-use regulation in high infiltration zones is of high importance, especially restrictions and incentives related to agricultural practices. Given the documented nitrate and microbial pressures on the aquifer, stricter control of fertilizer and pesticide use, combined with promotion of organic and nature-based practices, should be considered a priority.

On the infrastructure side, the EU project "Aglomeracija Varaždin" is a key intervention, ensuring improved wastewater collection and treatment. This significantly reduces pollutant inputs from urban and peri-urban sources, enhancing both water quality and system resilience to climate change.

Ecosystem-based measures, such as riparian buffer zones, wetland restoration, and afforestation in recharge areas, provide multiple co-benefits for flood regulation, pollutant retention, and biodiversity. While not yet fully integrated into local spatial planning, their role in supporting natural attenuation and increasing resilience under extreme events is recognized.

In conclusion, the evaluation shows that the highest-priority REs for Varaždin are:

1. Strict enforcement and periodic revision of SPZs for water supply wells.
2. Strengthening land-use controls in recharge areas, particularly for agriculture.
3. Full implementation of wastewater and stormwater infrastructure projects.

Through the integration of green infrastructure, modern drainage solutions, and systematic planning, the city of Varaždin can enhance resilience to climate change, reduce environmental risks, and improve the quality of urban life. Consistent implementation, supported by clear standards, financing mechanisms, and public engagement, will ensure long-term effectiveness and contribute to a healthier and more sustainable urban environment.

Acknowledgements

This research was carried out within the Interreg Central Europe project CE0100184 „Management of urban water resources in Central Europe facing climate change MAURICE" and is additionally funded by the European Union – Next Generation EU through the project Development of a Methodology for Microzonation of Nitrate Vulnerability Using Artificial Intelligence and Multiple Data Sources (DIMRAN), project code: NPOO GFV-IP-006/2025.

References

Bačani A., Posavec K. and Vlahović T. 2010 *Protection of wellfields in the regional water supply system of Varaždin*. In: Proc. of the 4th Croatian Geological Congress with International Participation, Zagreb, Croatia, pp. 182–183.

City of Zagreb 2022 Manual of Nature-Based Solutions. City Office for Economy, Ecological Sustainability and Strategic Planning, Zagreb, Croatia.

Daigger G.T. 2009 Evolving urban water and residuals management paradigms. *Water Environment Research* 81, 809–823.

Follett R.F. and Hatfield J.L. 2001 Nitrogen in the environment: sources, problems, and management. *The Scientific World Journal* 1 (Suppl. 2), 920–926.

Foster S., Hirata R., Gomes D., D'Elia M. and Paris M. 2002 *Groundwater Quality Protection: A Guide for Water Utilities, Municipal Authorities and Environment Agencies*. World Bank and World Health Organization, Washington DC, USA.

La Vigna F. 2022 Review: Urban groundwater issues and resource management, and their roles in the resilience of cities. *Hydrogeology Journal* 30, 1657–1683.

Mas-Pla J. and Menció A. 2019 Groundwater nitrate pollution and climate change: learnings from a water balance-based analysis of several aquifers in a western Mediterranean region (Catalonia). *Environmental Science and Pollution Research* 26, 2184–2202.

Nydrioti I., Sebos I., Kitsara G., et al. 2024 Effective management of urban water resources under

various climate scenarios in semiarid Mediterranean areas. *Scientific Reports* 14, 28666.
Ožanić T. 2016 *Kakvoća podzemne vode varaždinskog vodonosnog sustava*. MSc thesis, Rudarsko-geološko-naftni fakultet, Sveučilište u Zagrebu, Zagreb, Croatia.
Phuong Uyen Dao, Heuzard A.G., Thi Xuan Hoa Le, Zhao J., Yin R., Shang C. and Fan C. 2024 The impacts of climate change on groundwater quality: A review. *Science of the Total Environment* 912, 169241.
Rawat M., Sen R., Onyekwelu I., Wiederstein T. and Sharda V. 2022 Modeling of groundwater nitrate contamination due to agricultural activities—A systematic review. *Water* 14 (24), 4008.
Regulation on Sanitary Protection Zones of Water Sources. Official Gazette 55/02, 66/11, 47/13, Republic of Croatia.
Sebilo M., Mayer B., Nicolardot B., Pinay G. and Mariotti A. *2013 Long-term fate of nitrate fertilizer in agricultural soils*. Proceedings of the National Academy of Sciences of the United States of America 110, 18185–18189.
Spatial Plan of Varaždin County 2024 Official Gazette of Varaždin County, Varaždin, Croatia.
The General Spatial Plan of the City of Varaždin 2022 Official Gazette of the City of Varaždin, Varaždin, Croatia.
UNESCO 2022 The United Nations World Water Development Report 2022: *Groundwater – Making the Invisible Visible*. UNESCO, Paris, France.
Varkom d.d. 2022 EU Project Aglomeracija Varaždin. Varkom d.d., Varaždin, Croatia. Available from: https://www.voda.hr/hr/eu/projekti/varazdin (accessed 11 September 2025).
Zektser I.S. and Everett L.G. 2004 *Groundwater Resources of the World and Their Use*. UNESCO, Paris, France.

PROPOSAL OF FISHPASSES BASED ON MONITORING

Marian DOBRANSKÝ [1], Martina ZELENAKOVA [2]

[1] *Institute of Technology, Economics and Management in Construction, Technical University of Košice, 040 00 Košice, Slovak Republic*

E-mail: marian.dobransky.2@tuke.sk

[2] *Department of Environmental Engineering, Faculty of Civil Engineering, Technical University of Košice, Slovak Republic*

E-mail: martina.zelenakova@tuke.sk

[*] *Corresponding author*

Abstract

River fragmentation caused by hydraulic structures significantly affects ecological connectivity and fish migration. Fishpass effectiveness depends not only on hydraulic parameters within the structure, but also on the ability of fish to locate the entrance under real field conditions. This paper presents a monitoring-based approach for supporting fishpass proposal and entrance positioning using underwater video monitoring. The study is based on practical experience from two reference fishpasses in Slovakia where underwater camera systems were implemented for post-construction monitoring. These examples are used to identify the type of behavioural information obtainable from video records and to transfer selected monitoring principles to the pre-design phase. Particular attention is given to fish aggregation zones, preferred movement corridors, repeated passage attempts, and locations where fish abandon upstream migration. A camera placement strategy is proposed for two representative barrier types: a larger weir structure with a developed stilling basin and a smaller concrete drop structure. The proposed approach does not replace ichthyological surveys, telemetry, or hydraulic and habitat modelling, but complements them by providing direct behavioural observations. Future automated image analysis may further improve the processing of long-term video records.

Key words

fish migration, ecological connectivity, underwater camera monitoring, fish behaviour, migration barriers, fishpass entrance positioning.

1 Introduction

River systems have been extensively modified by dams, weirs, hydropower facilities, and flood-control structures, resulting in significant fragmentation of river networks and disruption of longitudinal connectivity. Such barriers alter natural migration routes and limit access to spawning, feeding, and refuge habitats required by many fish species during various stages of their life cycle. Recent assessments indicate that river fragmentation remains one of the most important pressures affecting freshwater biodiversity worldwide. Although fishpasses are widely implemented to mitigate these impacts, their effectiveness varies depending on local hydraulic conditions, barrier characteristics, and fish behaviour (Branco et al., 2023; Belletti et al., 2020). Fishpasses are therefore considered an essential component of modern river restoration and connectivity management. However, successful fish migration depends not only on the hydraulic capacity of the fishpass itself but also on the ability of fish to locate and enter the structure under real field conditions (Calles et al., 2021).

Therefore, the design of fishpasses is traditionally based on hydraulic criteria including flow velocity, water depth, turbulence characteristics, and energy dissipation. These parameters remain fundamental for ensuring fish passage; however, information regarding fish behaviour at migration barriers is often

unavailable during the design phase. As a result, fishpass entrances are frequently positioned using hydraulic assumptions rather than direct observations of fish movement and aggregation patterns.

Several studies have identified fishpass entrance location as one of the critical factors influencing overall passage efficiency. Even well-designed fishpasses may exhibit reduced performance when attraction flow conditions do not correspond with the natural behavioural responses of target fish species. Consequently, fish may accumulate below barriers, experience migration delays, or fail to locate the fishpass entrance despite favourable hydraulic conditions within the structure itself (Romão et al., 2021; Tan et al., 2021). These limitations highlight the need for complementary approaches capable of providing site-specific information on fish behaviour prior to fishpass construction.

Recent advances in monitoring technologies have created new opportunities for collecting behavioural data directly at migration barriers. Underwater camera systems, image-processing techniques, and artificial intelligence tools increasingly enable continuous observation of fish movement under field conditions. Compared to conventional sampling methods, video-based monitoring can provide long-term, non-invasive observations while minimizing disturbance to aquatic organisms. Monitoring of fish migration is commonly applied after fishpass construction to evaluate passage efficiency and fulfil environmental assessment requirements. While standardized post-construction monitoring methodologies are increasingly available, the application of comparable monitoring approaches during the fishpass design phase remains limited (Decree No. 383/2018 Coll.). However, the same technologies may also support the design process by identifying locations where fish naturally aggregate, concentrate, or repeatedly attempt to overcome migration barriers. Such information may contribute to improved fishpass entrance positioning and more effective attraction flow design. In addition, recent developments in automated image analysis and modelling of fish movement have improved the capacity to process behavioural data and support interpretation of fish activity near migration barriers (Mawer et al., 2023).

This paper presents a monitoring-based approach for supporting fishpass proposal at migration barriers. The study focuses on the application of underwater camera systems for identifying fish aggregation zones below barriers and evaluating their potential use during the fishpass design process. Two reference fishpasses with implemented underwater camera monitoring were used to derive practical experience, and the resulting approach was applied conceptually to selected migration barriers. Particular attention is given to camera placement strategies, behavioural observations, and the potential contribution of monitoring data to fishpass entrance positioning and overall fishpass design.

2 Methods

The methodology focuses on evaluating how monitoring techniques commonly used for post-construction fishpass assessment can be adapted to support fishpass proposal. Existing monitoring approaches, operational camera systems, and behavioural observations of fish are used to develop a conceptual framework for camera deployment below migration barriers prior to fishpass construction.

2.1 Existing methodology for post-construction fishpass monitoring

The effectiveness of newly constructed fishpasses is commonly verified through post-construction ichthyological monitoring. The monitoring process focuses on fish occurrence, species composition, migration activity, and the ability of target species to successfully pass through the structure.

Among the available monitoring techniques, underwater camera systems represent one of the officially recognized methods for evaluating fishpass functionality. According to current monitoring guidelines, camera systems can be used for both qualitative and quantitative assessment of fish migration (Decree No. 383/2018 Coll.). Their advantages include non-invasive operation, continuous data collection, and the possibility of repeated evaluation of recorded observations. However, the applicability of camera systems is influenced by water transparency, species detectability, and regular maintenance requirements associated with long-term operation.

The primary objective of post-construction monitoring is to verify the migration success of target fish species and assess the effectiveness of implemented fishpass structures. Existing monitoring methodologies do not focus exclusively on fishpass performance. Telemetry-based approaches are also used to identify migration routes and locations where fish accumulate below barriers, providing information relevant for the positioning of fishpass entrances and attraction flows. Such information may contribute to the optimization of fishpass entrance placement and attraction conditions.

Although these methodologies were developed for evaluating completed fishpasses, many of the monitored parameters remain equally relevant during the planning stage. Information regarding fish occurrence, aggregation zones, preferred migration routes, and temporal migration activity may provide valuable support for fishpass proposal before construction begins. Consequently, selected monitoring principles currently applied during post-construction assessment may also be transferred to the pre-design phase to improve understanding of fish behaviour in the vicinity of migration barriers.

2.2 Reference fishpasses with existing camera monitoring

To evaluate the applicability of video monitoring during the fishpass planning phase, experience obtained from existing fishpasses equipped with operational underwater camera systems was considered. The author participated in the design process of multiple fishpasses where camera-based monitoring was subsequently implemented for post-construction assessment. Two representative case studies were selected to demonstrate practical monitoring conditions and information obtainable from underwater video records.

2.2.1 The fishpass in the Veľké Kozmálovce dam

The fishpass located at the *Veľké Kozmálovce* dam on the *Hron* River, *Slovakia* was selected as one of the reference sites used in this study. The structure was designed to restore longitudinal river connectivity at an existing migration barrier and to provide suitable conditions for upstream fish migration. The fishpass consists of a nature-like bypass channel designed to mimic natural hydraulic and habitat conditions occurring within the *Hron* River basin. The total length of the fishpass is approximately 485 m with a design discharge ranging between 1.0 and 1.5 $m^3 \cdot s^{-1}$.



Figure 1. Location of the Veľké Kozmálovce fishpass and its position relative to the migration barrier (*source: ortho-photo map from GKÚ Bratislava, NLC*).

Following construction, the fishpass was equipped with an underwater video monitoring system intended for post-construction assessment of fish migration and fishpass functionality. The monitoring system was installed within the fishpass infrastructure and enabled continuous observation of fish movement under real operating conditions. Compared to conventional field observations, the camera system provided long-term records of fish occurrence and migration activity while minimizing disturbance to aquatic organisms. The site represents a practical example of long-term application of underwater video monitoring within a functioning fishpass (Dobranský et al., 2023).

A partial monitoring report from the 2020 migration season provides quantitative evidence of the scale of video-based post-construction monitoring at this site. During the monitoring period, video records from camera No. 1, installed behind the operating inlet opening, and camera No. 6, installed in the outlet structure, were evaluated. The records were analysed manually using the VS Player HikVision software, and fish occurrence was recorded by date, time, and species identification when image quality allowed reliable determination (Andreji, 2020).



Figure 2. Underwater camera installation used for post-construction fishpass monitoring.

2.2.2 The fishpass in the Turiec weir (in RS 7.530)

The second reference site considered in this study is the fishpass located at the weir on the *Turiec* River in the city of *Martin*, *Slovakia*. The structure was designed as part of a project focused on restoring longitudinal river connectivity at a migration barrier situated at river station 7.530. The original fishpass incorporated within the weir structure was identified as unsuitable for the target fish species and did not comply with the requirements for the designated fish zone. Consequently, a new nature-like fishpass was proposed to replace the existing structure.

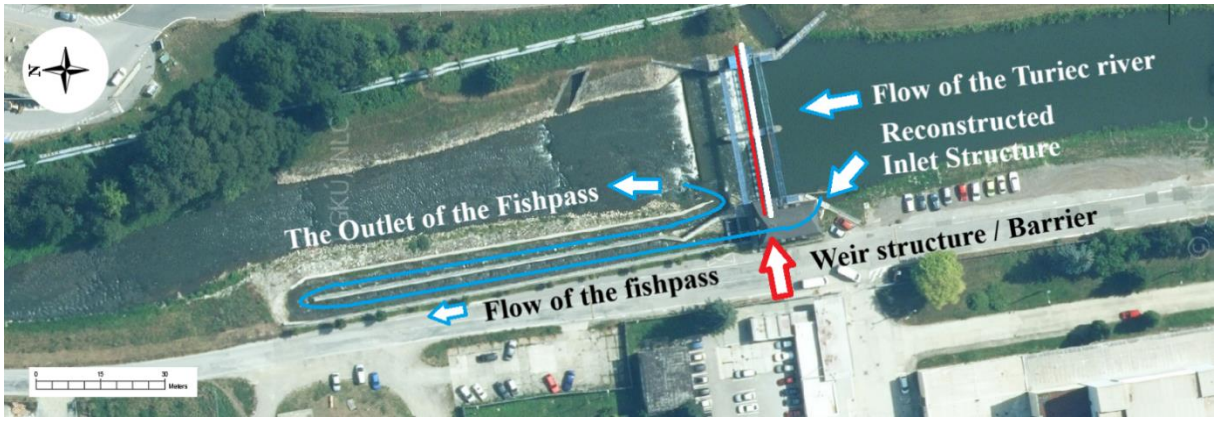


Figure 3. Location of the *Turiec* fishpass and its position relative to the migration barrier (*source: ortho-photo map from GKÚ Bratislava, NLC*).

The proposed fishpass was designed as a barrier-free bypass corridor with rapid-like elements intended to imitate natural habitat conditions occurring within the *Turiec* River. The structure was developed for characteristic fish species of the grayling zone and incorporated natural substrate, boulders, resting areas and flow heterogeneity to support upstream fish migration. The total length of the fishpass is approximately 235 m, with a design discharge of 1.0 $m^3 \cdot s^{-1}$ and an average longitudinal slope ranging from 1.25 to 1.35%.

As part of the project, an underwater monitoring system was incorporated into the fishpass design. Monitoring cameras were proposed at both the inlet and outlet sections of the fishpass to enable continuous observation of fish movement and migration activity. The monitoring system was intended to provide video records for evaluating fishpass functionality and to support long-term assessment of fish migration through the structure.



Figure 4. Underwater camera installation and its protection for post-construction fishpass monitoring.

The *Turiec* fishpass represents a complementary reference site to the *Veľké Kozmálovce* installation, demonstrating the application of underwater video monitoring within a different hydraulic and structural configuration. Together, both case studies provide practical examples of camera-based fish monitoring implemented under real operating conditions.

2.3 Information obtainable from underwater video monitoring

Underwater video monitoring provides several categories of information that may support fishpass planning and barrier assessment. The most basic information includes the presence of fish species, species composition, and observations of migration activity within the monitored area. Continuous monitoring allows repeated observations over extended periods and can therefore reveal behavioural patterns that may not be detectable during short-term field surveys. One of the most valuable outputs of video monitoring is the identification of fish aggregation zones below migration barriers. Repeated occurrence of fish within specific locations may indicate areas where migrating individuals naturally concentrate while searching for upstream passage routes. Such locations can provide valuable information regarding fish attraction and may contribute to more effective positioning of fishpass entrances.

Video records may also reveal preferred migration routes and behavioural responses to local hydraulic conditions. Fish often exhibit repeated movement patterns when approaching barriers, including concentration within specific flow corridors, avoidance of highly turbulent zones, or repeated attempts to overcome obstacles at particular locations. These observations may improve understanding of site-specific migration behaviour and provide complementary information to hydraulic analyses. In addition, long-term monitoring enables evaluation of temporal migration activity. Seasonal migration periods, daily activity patterns, and responses to changing hydrological conditions can be identified from continuous observations. Such information may help determine periods of highest migration intensity and improve understanding of target species behaviour within the vicinity of migration barriers.

Despite these advantages, the applicability of underwater video monitoring remains influenced by several limitations, including water transparency, lighting conditions, biofouling of camera lenses, and species detectability. Nevertheless, when suitable monitoring conditions are achieved, underwater camera systems can provide valuable behavioural information that is difficult to obtain using conventional survey methods alone. The information obtained from underwater monitoring may therefore extend beyond post-construction evaluation and can potentially support decision-making during the fishpass planning process.

2.4 Transfer of monitoring principles from post-construction evaluation to the pre-design phase

Fishpass proposal is commonly supported by ichthyological surveys, telemetry studies, topographic surveys, and hydraulic modelling. Each method provides specific information regarding fish occurrence, migration, or hydraulic conditions. However, direct observations of fish behaviour in the vicinity of migration barriers are often limited. Underwater video monitoring may therefore serve as a complementary tool capable of providing continuous behavioural observations prior to fishpass construction.

Table 1. Comparison of selected methods supporting current fishpass proposals.

Method	Primary purpose	Information provided	Temporal coverage	Main limitations
Ichthyological survey	Fish community assessment	Species composition, abundance, target species	Short-term campaigns	Limited behavioural information
Telemetry	Fish movement tracking	Migration routes, residence time, barrier passage success	Long-term	Limited number of tagged individuals, higher costs
Hydraulic modelling	Hydraulic assessment	Flow velocity and patterns, depth, potential attraction flow	Simulation-based	Predictive only; no direct observation of fish behaviour
Underwater video monitoring	Behavioural observation	Fish occurrence, aggregation zones, migration behaviour, preferred routes	Continuous	Visibility, lighting, maintenance requirements

The proposed approach does not aim to replace conventional monitoring techniques. Instead, underwater camera systems are considered an additional source of information that may support the identification of fish aggregation zones, preferred migration routes, and behavioural responses to local hydraulic conditions. These observations may subsequently contribute to more informed decisions regarding fishpass entrance positioning and attraction flow design.

2.5 Proposed camera placement strategy

The proposed monitoring approach was developed for a selected migration barrier located on the *Hornád* River in the City of *Košice*, *Slovakia*. The site represents a typical example of a regulated river reach where several sources of information are already available, including topographic surveys, hydrological data followed by hydrodynamic modelling results, and ichthyological data obtained from previous monitoring activities. These datasets provide valuable information regarding hydraulic conditions and fish species occurrence; however, direct observations of fish behaviour in the immediate vicinity of the migration barrier remain unavailable.

Although existing methodologies such as ichthyological surveys, telemetry, habitat modelling, and hydraulic simulations provide essential information for fishpass design, they do not continuously document how fish interact with the barrier itself. In particular, information regarding fish aggregation zones, preferred migration routes, repeated passage attempts, and locations where fish abandon migration efforts are often missing. Understanding these behavioural patterns may significantly contribute to the positioning of future fishpass entrances and improve attraction efficiency.

The objective of the monitoring is not to determine the presence of fish species alone, but to investigate fish behaviour immediately downstream of migration barriers. Particular attention is focused on identifying locations where fish repeatedly concentrate, routes most frequently used during upstream movement attempts, and zones where migration attempts terminate. Two representative barrier types were identified within the study area: a large weir structure on the *Hornád* River, the *Vyšné Opátske* weir, and a smaller concrete drop structure located on the *Myslavský* Stream. Due to differences in hydraulic conditions and spatial extent of the affected area, different monitoring strategies are proposed

for each barrier type.



Figure 5. Photos of the *Vyšné Opátske* weir on the *Hornád* River (left) and small concrete drop structure on the *Myslavský* stream (right).

For the larger structure, represented by the *Vyšné Opátske* weir, a multi-camera arrangement is proposed within the stilling basin downstream of the barrier. Cameras should be positioned to monitor the main flow concentration zones, areas adjacent to structural elements such as piers and wing walls, and the downstream counter-threshold of the stilling basin. Such an arrangement enables observation of fish aggregation behaviour, repeated passage attempts, movement between hydraulic zones, and downstream departure following unsuccessful migration attempts.

For the smaller concrete drop structure on the *Myslavský* Stream, a simplified monitoring configuration is proposed. Due to the limited spatial extent of the hydraulic influence zone, camera placement is focused directly on the stilling basin and counter-threshold area where fish are expected to accumulate prior to attempting barrier passage. Monitoring of this zone may provide information regarding the frequency of migration attempts, fish residence time below the obstacle, and preferred movement paths within the affected reach. The proposed camera locations are shown in Fig. 6 and marked by purple-white circles.

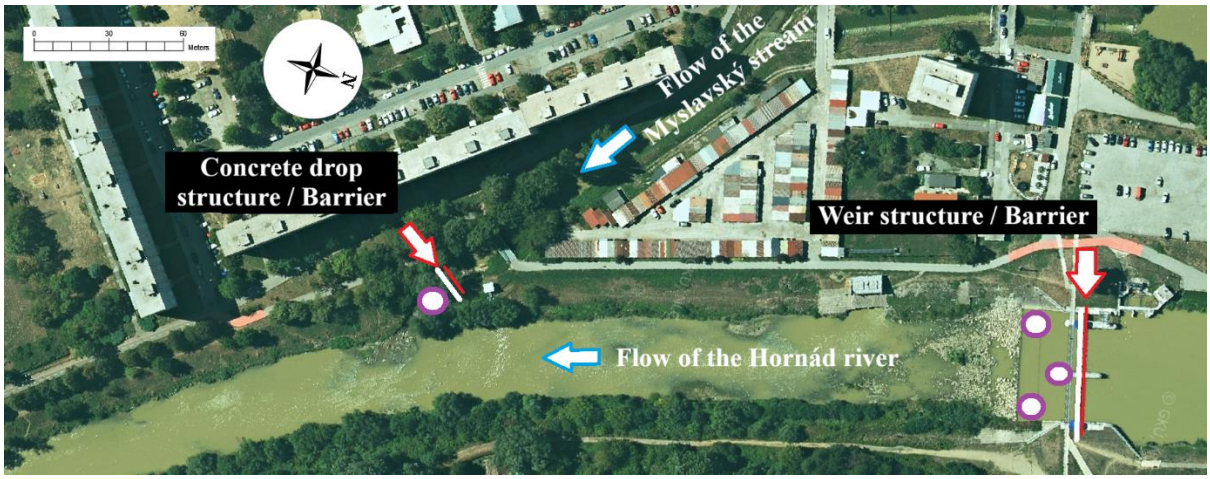


Figure 6. Location of the *Vyšné Opátske* Weir on the *Hornád* River and small concrete drop structure with marked proposed placement of underwater camera monitoring system

The proposed monitoring concept aims to complement existing hydraulic and biological datasets by providing direct observations of fish behaviour under real field conditions. The information obtained from such monitoring may subsequently support fishpass proposal, entrance positioning, and future verification of fish migration restoration measures.

3 Results and Discussion

The results of this study are primarily methodological and demonstrate how underwater video monitoring can complement conventional approaches used in fishpass proposal and assessment. The method is **not intended to replace** ichthyological surveys, telemetry, hydrodynamic modelling, or habitat modelling, but rather to provide direct observations of fish behaviour in the vicinity of migration barriers.

The methodological concept is supported by quantitative information from the 2020 post-construction monitoring of the Veľké Kozmálovce fishpass. In this monitoring, more than 2,050 hours of video records were analysed from camera No. 1 and more than 1,476 hours from camera No. 6. In total, 3,526 hours of underwater video were evaluated, resulting in more than 5,800 records confirming fish presence. More than 4,500 fish-positive records were obtained from camera No. 1 and almost 1,300 records from camera No. 6. The difference between cameras was partly caused by the later installation of camera No. 6 and by the absence of records from this camera between 13 May and 27 May 2020 (Andreji, 2020).

Table 2. Quantitative indicators from the 2020 underwater video monitoring of the Veľké Kozmálovce fishpass.

Indicator	Camera No. 1	Camera No. 6	Total / Comment
Analysed monitoring period	12 Apr.–6 Jul. 2020	20 Apr.–6 Jul. 2020	Camera No. 6 had missing records from 13–27 May 2020
Analysed video duration	>2,050 h	>1,476 h	3,526 h
Fish-positive records	>4,500	~1,300	>5,800
Fish species recorded	13 species	11 species	Based on identifiable video records
Non-identifiable fish records	~30%	~50%	~40% overall
Main uncertainty sources	reflection, camera angle, bubbles, turbidity, poor lighting, dirty camera glass	reflection, camera angle, bubbles, turbidity, poor lighting, dirty camera glass	Practical limitations of underwater video monitoring

The reference fishpasses at Veľké Kozmálovce and Turiec confirm that underwater camera systems can be successfully integrated into fishpass infrastructure and operated under real conditions. The Veľké Kozmálovce monitoring also demonstrates that such systems can generate large datasets over a single migration season. However, the results show that the value of the recorded data depends strongly on camera placement and site-specific hydraulic and optical conditions. Poor positioning, unfavourable light conditions, turbulence, air bubbles, turbidity, floating material, dirty camera glass and camera movement may significantly reduce the reliability of species identification and behavioural interpretation.

Compared with other monitoring and modelling approaches, underwater cameras provide a unique source of information. Ichthyological surveys describe species composition and abundance, telemetry tracks the movement of tagged individuals, and hydraulic or habitat models identify areas with suitable physical conditions. However, these methods do not directly document how fish respond to a barrier. Video monitoring therefore serves as a link between hydraulic conditions and actual fish behaviour. This role is especially relevant during the pre-design phase. Hydrodynamic and habitat models can predict locations with suitable attraction flows or migration conditions, but these predictions require field verification. Camera monitoring can confirm whether fish actually use these areas, avoid them, or concentrate elsewhere. Consequently, video monitoring should be viewed as a tool that supports and refines model-based assumptions rather than replacing them.



Figure 7. Example frames from underwater video monitoring in the *Veľké Kozmálovce* fishpass.

Based on the reference monitoring experience, future pre-design camera campaigns should include basic quality-control and behavioural indicators. These should include total video duration, number of fish-positive records, proportion of non-identifiable records, visibility conditions, dominant obstruction sources, species identification confidence, movement direction, residence time within the monitored zone, repeated passage attempts and downstream departure after unsuccessful migration attempts. Such indicators would allow the monitoring output to be interpreted not only qualitatively, but also as a structured dataset supporting fishpass entrance positioning.

The proposed camera placement strategy reflects the scale of the monitored structure. For larger weirs with developed stilling basins, multiple cameras are recommended to capture fish movement across different hydraulic zones. Monitoring near structural elements, flow concentration areas, and the downstream counter-threshold can help identify locations where fish naturally aggregate and repeatedly attempt upstream passage. For smaller concrete drop structures, monitoring can be focused on the stilling basin and counter-threshold area, where fish activity is expected to be concentrated.

The method also has limitations. Monitoring quality may be affected by turbidity, air bubbles, suspended material, poor lighting, or biofouling of camera lenses. In addition, camera systems alone cannot reliably quantify migration efficiency and are most effective when combined with complementary methods such as telemetry or trapping. Therefore, underwater video monitoring should primarily be considered a behavioural and qualitative assessment tool. Despite these constraints, underwater cameras offer an important advantage: continuous long-term observation. They can record fish activity during different flow conditions, times of day, and migration periods, providing information that may be missed during short-term field surveys. Future developments in automated image analysis and deep-learning-based fish detection could further improve data processing and enable efficient identification of fish occurrence, movement patterns, and aggregation hotspots.

Overall, underwater video monitoring provides behavioural information that is not directly available from conventional survey and modelling methods. By documenting fish responses to migration barriers, it can support the identification of suitable fishpass entrance locations and contribute to more informed fishpass proposals.

4 Conclusion

This paper presents a monitoring-based approach for supporting fishpass proposal at migration barriers. The study demonstrates that principles commonly applied during post-construction fishpass monitoring can also provide useful information during the pre-design phase. Underwater video monitoring should not be considered a replacement for ichthyological surveys, telemetry, hydrodynamic modelling, or habitat modelling. Its main contribution lies in providing direct behavioural observations of fish in the vicinity of migration barriers. Such observations can help identify aggregation zones, preferred movement corridors, repeated passage attempts, and areas where fish abandon upstream migration.

The proposed camera placement strategy shows that monitoring design should reflect the type and scale of the barrier. For larger weir structures with developed stilling basins, a multi-camera arrangement is recommended to capture fish movement across different hydraulic zones. For smaller concrete drop structures, monitoring can be focused on the stilling basin and counter-threshold area, where fish activity is expected to concentrate.

The results indicate that underwater video monitoring can serve as a complementary pre-design tool linking hydraulic conditions with observed fish behaviour. This information may support more informed positioning of fishpass entrances and improve the overall basis for fishpass proposal. The method remains limited by water transparency, lighting conditions, turbulence, biofouling, and maintenance requirements. Future integration of automated image analysis and deep-learning-based fish detection may further improve the processing of long-term video records and support the interpretation of fish behaviour below migration barriers.

Acknowledgements

This work was supported by the VEGA Grant Agency under Contract No. 1/0588/24 “Research of extreme hydroclimatic phenomena in watersheds and mitigation proposals in the context of natural based solutions” and SWIM2025 “Sustainable Water and Integrated Management of Fish Migration and their Habitats in the Danube River Basin and NW Black Sea”.

References

Andreji, J. 2020. Monitoring of fishpass permeability at the Veľké Kozmálovce Water Structure. *Partial report for 2020* [in Slovak]. Slovak University of Agriculture in Nitra, Nitra, Slovakia.

Belletti, B., Garcia de Leaniz, C., Jones, J., Bizzi, S., Börger, L., Segura, G., Castelletti, A., van de Bund, W., Aarestrup, K., Barry, J., Belka, K., Berkhuysen, A., Birnie-Gauvin, K., Bussettini, M., Carolli, M., Consuegra, S., Dopico, E., Feierfeil, T., Fernández, S., Fernandez Garrido, P., Garcia-Vazquez, E., Garrido, S., Giannico, G., Gough, P., Jepsen, N., Jones, P.E., Kemp, P., Kerr, J., King, J., Łapińska, M., Lázaro, G., Lucas, M.C., Marcello, L., Martin, P., McGinnity, P., O’Hanley, J., Olivo del Amo, R., Parasiewicz, P., Pusch, M., Rincon, G., Rodriguez, C., Royte, J., Schneider, C.T., Tummers, J.S., Vallesi, S., Vowles, A., Verspoor, E., Wanningen, H., Wantzen, K.M., Wildman, L. and Zalewski, M. 2020 More than one million barriers fragment Europe’s rivers. *Nature* 588, 436–441 DOI: 10.1038/s41586-020-3005-2

Branco P., Mascarenhas A.M., Duarte G., Romão F., Quaresma A., Amaral S.D., Ferreira M.T., N.Pinheiro A. and Santos J.M. 2023 Vertical Slot Fishways: Incremental Knowledge to Define the Best Solution. *Biology* 12(11), 1431 DOI: 10.3390/biology12111431

Calles, O., Elghagen, J., Nyqvist, D., Harbicht, A. and Nilsson, P. A. 2021 Efficient and timely downstream passage solutions for European silver eels at hydropower dams. *Ecological Engineering*, 170, Article 106350 DOI: 10.1016/j.ecoleng.2021.106350

Dobranský M., Škrinár A., and Zeleňáková M. 2023 The inlet structure of the fishway in the Veľké Kozmálovce Dam. *Structural and Physical Aspects of Construction Engineering 2022 (SPACE 2022)*

5th International Scientific Conference, High Tatras, Slovakia, 14-16 October 2022 DOI:10.1063/5.0181243

Mawer R., Pauwels I., Bruneel S., Goethals P., Kopecki I., Elings J., Coeck J. and Schneider M. 2023 Individual based models for the simulation of fish movement near barriers: Current work and future directions. *Journal of environmental management* 335, 117538 DOI:10.1016/j.jenvman.2023.117538

Ministry of the Environment of the Slovak Republic. 2018. Decree No. 383/2018 Coll. of the Ministry of the Environment of the Slovak Republic of 10 December 2018 on the technical conditions for the design of fishways and monitoring of the migration permeability of fishways. *Collection of Laws of the Slovak Republic*. [in Slovak]

Romão, F., Quaresma, A.L., Santos, J.M., Amaral, S.D., Branco, P. and Pinheiro, A.N. 2021 Multislot Fishway Improves Entrance Performance and Fish Transit Time over Vertical Slots. *Water*, 13, 275 DOI: 10.3390/w13030275

Tan J., Tan H., Goerig E., Ke S., Huang H., Liu Z. and Shi X. 2021 Optimization of fishway attraction flow based on endemic fish swimming performance and hydraulics. *Ecological Engineering*, 170, 106332 DOI: 10.1016/j.ecoleng.2021.106332

OPTIMIZATION OF THE MANNING´S ROUGHNESS COEFFICIENT VALUE FOR 1-D FISH PASS NUMERICAL MODELLING

Adela RUTZKÁ [1*], Alexandra VIDOVÁ [1], Lea ČUBANOVÁ [1]

[1] *Department of Hydraulic Engineering, Faculty of Civil Engineering, Slovak University of Technology in Bratislava, Radlinského 2766/11, 810 05 Bratislava, Slovak Republic*

E-mail: adela.rutzka@stuba.sk

E-mail: alexandra.vidova@stuba.sk

E-mail: lea.cubanova@stuba.sk

[*] *Corresponding author*

Abstract

Nature-like fish passes require precise hydraulic modeling, which relies on detailed geometric input data. Advances in photogrammetric surveying allow for efficient acquisition of high-resolution spatial data, but the effect of terrain detail and channel geometry on model calibration is still underexplored. This study surveyed a fish pass using photogrammetric scanning to create a dense point cloud of its morphology, generating terrain models with raster resolutions of 1, 5, 10, and 25 cm. Field measurements of water levels and discharge provided reference data for model calibration and validation. Hydraulic simulations utilizing HEC-RAS software employed a one-dimensional steady non-uniform flow model with varying terrain details. The models were calibrated by adjusting Manning's roughness coefficient, resulting in optimized n values between 0.026 and 0.035. Statistical comparisons between simulated and observed water levels yielded MAE values of 14.8 – 27.2 mm, RMSE values of 19.7 – 34.4 mm, and high coefficients of determination (R^2 = 0.976 – 0.986). The findings indicate that higher-resolution terrain models enhance the representation of local hydraulic conditions and confirm the reliability of photogrammetric surveying for hydraulic modeling of nature-like fish passes.

Key words

Roughness coefficient, topography, fish pass, numerical modeling.

1 Introduction

Manning's roughness coefficient (n) is one of the key parameters in hydraulic calculations and numerical modelling of open channel flow, as it represents the resistance exerted by channel boundaries on the flowing water. Its value depends on a wide range of factors, including bed material, channel irregularities, vegetation, and flow conditions, and is typically determined empirically (Chow, 1959; Henderson, 1966; French, 1986). Due to the variability of natural and engineered channels, the estimation of n remains inherently uncertain and often subjective, which directly affects the accuracy of hydraulic simulations (Vidová, 2023; Schügerl, 2023). This issue becomes particularly significant in the design and modelling of close-to-nature fish passes. These structures intentionally incorporate various roughness elements such as boulders, stones, and sills to mimic natural river conditions and to create hydraulically diverse environments suitable for fish migration (Jaworowski, 2022; Magaju, 2020; Baek, 2022; Dumitran, 2020). The presence of such elements introduces complex flow patterns, including turbulence, secondary currents, and spatial variability of velocity fields, making the determination of an appropriate Manning's coefficient even more challenging (Schügerl, 2020; Máčka, 2009; Gualtieri, 2011). Moreover, the effective roughness may vary with discharge, submergence of structural elements, and seasonal changes in vegetation (French, 1986; Schügerl, 2023). Traditional approaches for estimating Manning's coefficient rely on empirical relationships or tabulated values derived from grain

size characteristics (Haan, 1994; Chanson, 2004). However, these methods are often insufficient for fish passes, where the internal environment is highly heterogeneous and not fully represented by standard assumptions. A promising alternative is the calibration of roughness coefficients based on measurements from existing structures, which allows for a more realistic representation of hydraulic conditions (Velísková, 2017; Liu, 2023). Recent advances in drone-based photogrammetry enable detailed and high-resolution mapping of fish pass geometry and surface characteristics. This technique provides accurate digital elevation models and allows for the analysis of bed morphology and roughness elements at a level of detail not achievable with conventional surveying methods (Liu, 2023; Purinton, 2019; Bunte, 2001; Marcus, 2008; Dietrich, 2017). Such data can be effectively used in numerical models, such as HEC-RAS, to improve the calibration of Manning's roughness coefficient (Fošumpaur, 2010; U.S. Army Corps of Engineers, 2021). The aim of this study is to optimize Manning's roughness coefficient for 1D numerical modelling of a fish pass using HEC-RAS, based on field measurements and varying levels of terrain detail obtained from drone surveys. By comparing calibrated roughness values for different geometric representations, the study seeks to improve the reliability of hydraulic simulations and provide recommendations for more accurate modelling of fish pass hydraulics.

2 Materials and methods

2.1 Photogrammetry-Based Survey and Terrain Data Preparation

Recent developments in Unmanned Aerial Vehicle (UAV) technology, high-precision Global Navigation Satellite System (GNSS), and Structure-from-Motion (SfM) photogrammetry have significantly expanded the possibilities of detailed topographic mapping and terrain reconstruction (Kulikovska, 2026; Tuan, 2026; Dlamini, 2025). UAV-based photogrammetry enables the generation of dense point clouds and high-resolution Digital Elevation Models (DEMs) suitable for hydraulic applications, particularly in complex fluvial environments (Villanueva, 2025; Tuyet, 2025). Compared to conventional surveying methods, low-altitude UAV acquisition enables the accurate capture of small-scale morphological features (Chen, 2025), including riverbed roughness, boulders, and channel irregularities, which significantly influence flow conditions, provided that the channel is dry or nearly dry, since water cover can obscure these microtopographic features, although limited bathymetric information may still be obtained in shallow and optically clear water. The quality of the reconstructed terrain depends on image overlap (Fudala, 2025), flight altitude, and resulting Ground Sampling Distance (GSD), with sub-centimeter resolutions (Liu, 2026) achievable under optimized acquisition conditions. The accuracy of the reconstructed surface is also strongly influenced by site characteristics, as dense vegetation, water surfaces, and steep or vertical banks may obscure the terrain and reduce the reliability of the photogrammetric reconstruction. High-resolution rasterized DEMs derived from photogrammetry can subsequently serve as terrain inputs for hydraulic modelling software like HEC-RAS, where they are used to define channel geometry, cross-sections, and hydraulic characteristics. This approach enhances the representation of channel morphology and improves the reliability of simulated water levels and flow velocities in engineered channels, for example, fish passes (Keshk, 2026).

The survey was carried out over the Veľké Kozmálovce fish pass, with the primary objective of capturing the microtopography of the channel bed. The survey was performed using a DJI Mavic 3 Enterprise UAV equipped with a high-resolution camera, flying at a low altitude of approximately 6 m above the channel surface. This configuration resulted in an effective GSD of approximately 1.6 mm. To ensure full visibility of the channel bed, the fish pass was drained before data acquisition.

The acquired imagery was processed in Agisoft Metashape Professional (Agisoft, 2019) using high-accuracy image alignment and dense point cloud generation. The resulting point cloud was subsequently filtered and optimized in CloudCompare (Girardeau-Montaut, 2016) to remove noise and improve data consistency while preserving fine-scale morphological features. A representative 100 m-long segment of the fish pass was selected for further analysis to reduce computational demands while maintaining hydraulic and morphological representativeness. The selected reach was characterized by a constant longitudinal slope and a nearly uniform cross-sectional geometry, with no significant influence from the

inlet structure or other hydraulic controls such as bridge crossings. These conditions provided an appropriate domain for the development of steady, gradually varied flow. The processed point cloud was used to generate a continuous surface model, which was subsequently rasterized into a high-resolution DEM. The selected grid cell size defined the spatial resolution of the DEM and controlled the level of geometric detail available for subsequent hydraulic modelling. The resulting terrain model accurately captured small-scale roughness elements, individual boulders, and channel irregularities, providing a reliable geometric basis for numerical flow simulations.

2.2 Roughness Analysis

The analysis of Manning's roughness coefficient can be performed using various approaches, such as empirical equations applicable to specific boundary conditions (primarily based on the Strickler formula and grain size analysis of the bed material), tabulated values, visual assessment and stream classification (Cowan's method), or measurements of basic hydraulic parameters within a stream reach. In the latter case, methods such as the step-by-step method or numerical modelling can be applied, where the roughness coefficient is obtained through model calibration.

2.2.1 Empirical Equations

Empirical equations based on the Strickler formula (Equation (1)) (Mäsiar, 2001) depend on characteristic grain diameters of the riverbed material. These parameters can be derived from the grain size distribution curve. The sieve method is most commonly used to determine granulometry; however, it is often not applicable in the environment of fish passes. Therefore, more suitable approaches for determining grain size distribution include photographic methods, such as optical granulometry (Raplík, 1983), or, more recently, the use of drone-based photogrammetry combined with automated grain size analysis (Figure 1) (Diepenbroek, 1992; Diepenbroek, 2007).

$$n = \frac{1}{a} \cdot d^{x} \tag{1}$$

Where: a – constant (-);
d – characteristic grain diameter (m);
x – exponent (-).

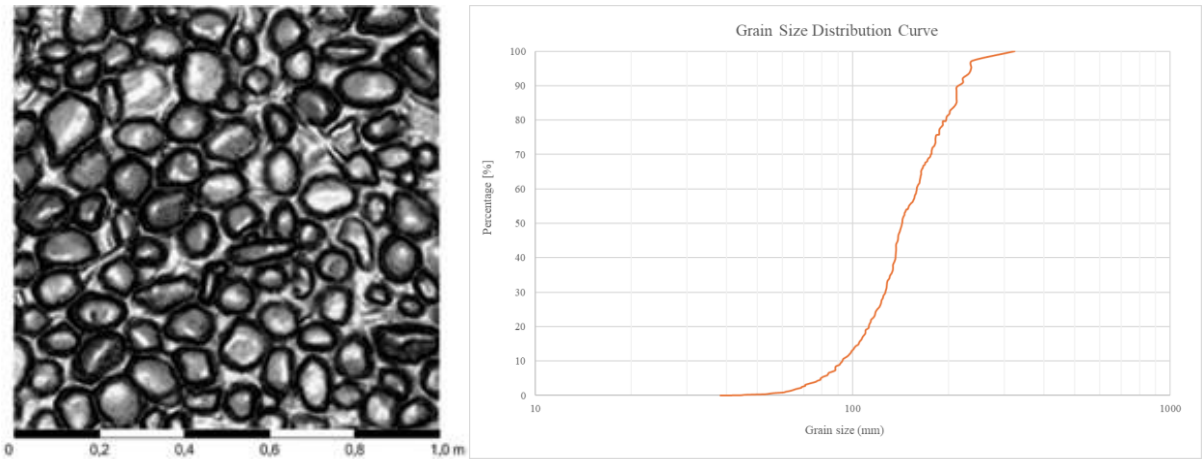


Figure 1. Sample processing from drone-based photogrammetry: identification of individual grains and the resulting grain size distribution curve of the fish pass

2.2.2 Standard Open-Channel Equation

This approach requires measured field data, including the geometric characteristics of the channel cross-sections (cross-sectional area, wetted perimeter, hydraulic radius, water level at individual cross-sections, and the distance between cross-sections for slope determination), as well as hydraulic

parameters (discharge and mean cross-sectional velocity). For steady non-uniform flow, which is expected in a fish pass channel, the following equation for the Manning's roughness coefficient can be derived (Equation (2)) (Dušička, 2015; Schügerl, 2023):

$$n = \sqrt{\frac{\Delta y - Q^2 \frac{\alpha}{2g}\left(\frac{1}{A_1^2} - \frac{1}{A_2^2}\right)}{l}} \frac{A_{average}}{Q} R_{average}^{2/3} \quad (2)$$

Where Δy – change of water level position between downstream and upstream profile (m);
Q – value of the steady discharge ($m^3 \cdot s^{-1}$);
α – coefficient expressing the uneven distribution of velocity in the profile (–);
g – gravity acceleration ($m \cdot s^{-2}$);
A_1, A_2 – flow area of the downstream and upstream profile (m^2);
L – the length of the section between the downstream and upstream profile (m);
$A_{average}$ – mean value of the flow area (m^2);
$R_{average}$ – mean value of the hydraulic radius (m).

2.2.3 Numerical Model and High-Resolution Survey Data Utilization

Fish pass roughness can be estimated by combining a one-dimensional numerical hydraulic model (e.g., HEC-RAS (U.S. Army Corps of Engineers Hydrologic Engineering Center, 2021) with highly accurate geometric data obtained from drone-based surveying. A dense point cloud generated through UAV photogrammetry provides detailed information about the fish pass geometry, including bed irregularities, slopes, boulder placement, and structural elements. The point cloud is processed into a digital terrain model and imported into the hydraulic model to define cross-sections and channel characteristics. Roughness coefficients in the form of Manning's n are then calibrated by comparing simulated hydraulic parameters—such as water depth, velocity, and energy slope - with measured field conditions. Through iterative adjustment of the roughness parameter, the model can reproduce observed flow behavior, resulting in a realistic estimate of hydraulic roughness along the fish pass. This approach improves model reliability and enables a more accurate assessment of flow conditions relevant to fish pass hydraulic behavior.

2.3 One-Dimensional Hydraulic Model in HEC-RAS

The processed digital elevation model derived from the photogrammetric survey served as the primary terrain input for the development of the one-dimensional (1D) hydraulic model in HEC-RAS 6.4 (U.S. Army Corps of Engineers Hydrologic Engineering Center, 2021). Although the photogrammetric survey provided terrain data suitable for 2D or 3D hydraulic modelling, a 1D HEC-RAS approach was intentionally selected because such models remain widely used in engineering practice due to their simplicity, computational efficiency, and straightforward parameterization. Moreover, Manning's roughness coefficients commonly used in hydraulic modelling were historically derived and calibrated primarily within the framework of 1D open-channel flow calculations based on relationships between discharge, hydraulic radius, slope, and flow resistance. Therefore, the use of a 1D model also ensures consistency with the traditional interpretation and application of Manning-based roughness characterization in hydraulic engineering practice.

To evaluate the influence of geometric detail on hydraulic model performance, several terrains represented by raster files with different cell resolutions (Table 1) were generated from the photogrammetric point cloud. These raster variants represented different levels of topographic detail and were subsequently used as terrain inputs for individual HEC-RAS model configurations.

The DEMs were imported into RAS Mapper, where they formed the basis for defining the geometric framework of the model. The channel centerline, bank lines, and cross-sections were delineated directly from the terrain data. Elevation profiles of the cross-sections were extracted from the DEMs, ensuring

that the channel geometry was based on measured terrain data obtained from the photogrammetric survey. In addition to varying raster resolutions, multiple geometric configurations with different numbers and spacing of cross-sections were prepared to assess the influence of channel representation on hydraulic simulation results (Table 2). Cross-sections were initially generated at regular intervals and subsequently adjusted manually to better reflect local channel morphology and hydraulic controls (Figure 2). Attention was paid to sections located near structural elements, including large boulders and abrupt changes in channel geometry, where significant variations in flow conditions occur.

Table 1. Raster file size comparison

Raster Cell (cm)	Raster Size width x height (px)	Size of File (MB)
1.0	4,261 x 9,405	269.00
5.0	853 x 1,882	13.00
10.0	427 x 941	3.26
25.0	171 x 377	0.54

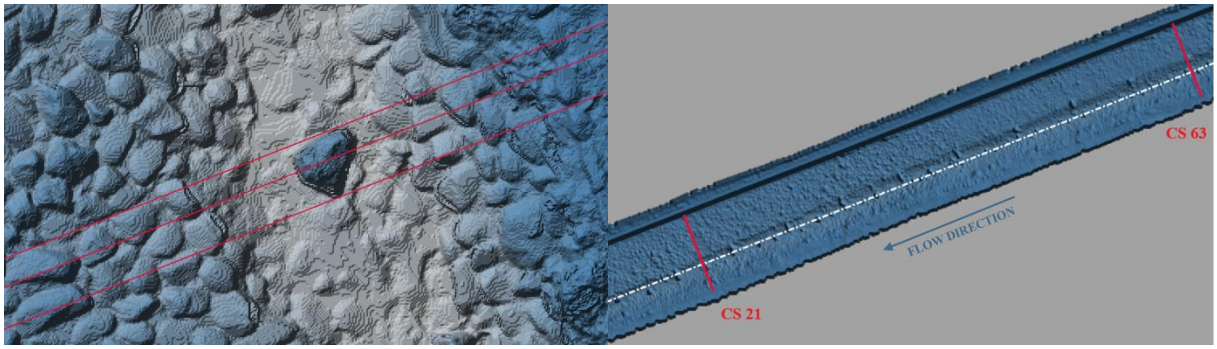


Figure 2. Cross-section placement around a solitary boulder

The minimum cross-section spacing remained constant for all geometric configurations, as profiles were systematically positioned immediately upstream, directly across, and immediately downstream of perturbation boulders to capture their influence on local hydraulic conditions. This approach ensured that important hydraulic features influencing water surface profiles were adequately represented within the model geometry.

Table 2. Individual geometries

Geometry	Cross-sections	The spacing of cross-sections (m)		
		Minimal	Maximal	Average
G1	234	0.1	1.1	0.41
G2	133	0.1	2.6	0.74
G3	118	0.1	4.7	0.77
G4	79	0.1	4.9	1.30

Hydraulic simulations were performed in HEC-RAS using a one-dimensional steady non-uniform flow model, which is appropriate for the analyzed fish pass conditions. The simulations assumed subcritical flow throughout the modelled reach, corresponding to Froude number values lower than 1 ($Fr < 1$). Boundary conditions were defined using measured discharge values and downstream water surface elevations obtained during field measurements. For the analyzed fish pass section, the discharge was 0.904 m^3/s, while the measured downstream water level of 172.48 m a. s. l. was applied as the boundary condition.

3 Results

Manning's roughness coefficient was used as the primary calibration parameter representing hydraulic resistance caused by bed material, channel irregularities, and flow obstructions. Initial roughness values were estimated based on empirical tables published by Ven Te Chow (Chow, 1959) and subsequently refined through iterative calibration to achieve the best agreement between simulated and measured water surface elevations. The calibrated results obtained for different terrain and geometric configurations were then compared with field observations to evaluate the influence of geometric detail on hydraulic model performance.

3.1 Empirical Estimation of Manning's Roughness Coefficient

The first step of the analysis consisted of estimating the Manning roughness coefficient using empirical equations (Equation (1) based on characteristic grain diameters derived from the photogrammetric survey and grain-size analysis. The calculated values are summarized in Table 3. The resulting roughness coefficients ranged from 0.0285 to 0.0662, depending on the applied empirical relationship and representative grain diameter.

Table 3. Manning roughness coefficients calculated using empirical equations

Autor	a	x	Based on diameter	unit	n
Strickler	24.4	0.167	d_{50}	m	0.0296
Garde, Raju	21.3	0.167	d_{50}	m	0.0339
Henderson	29.4	0.167	d_{50}	ft	0.0299
Keulegan	25.3	0.167	d_{50}	m	0.0285
Bray	16.86	0.179	d_{50}	m	0.0418
Mattas	10.31	0.196	d_{50}	m	0.0662
Raudkivi	76.9	0.167	d_{65}	mm	0.0305
Irmay	24	0.167	d_{65}	m	0.0308
Bray*	17.83	0.179	d_{65}	m	0.0406
Henderson*	26.31	0.167	d_{75}	m	0.0286
Lane, Carlson	21.14	0.167	d_{75}	m	0.0356
Mattas*	8.7	0.376	d_{84}	m	0.0638
Mayer-Peter, Müller	26	0.167	d_{90}	m	0.0297
Bray**	20.2	0.160	d_{90}	m	0.0386
Pirkovský	19.4	0.167	d_e	m	0.0346
					Average value = 0.0375

Note: */** denote cases where a single author developed several roughness equations differing in the empirical coefficient a, exponent x and/or the characteristic particle diameter d.

The observed variability between empirical equations confirms the uncertainty associated with roughness estimation in highly heterogeneous fish pass environments. The differences are primarily related to the sensitivity of individual equations to characteristic grain size and to the assumptions under which the equations were originally derived. Since nature-like fish passes contain large boulders, irregular bed forms, and localized flow contractions, empirical equations alone cannot fully represent the effective hydraulic resistance of the structure. Consequently, the empirically derived values were not directly used as final model inputs but instead served as a physically based reference range for the

subsequent calibration of Manning's coefficient.

3.2 Manning's Roughness Coefficient Derived Using the Standard Open Channel Equation

Manning's roughness coefficient was also calculated using the standard open-channel equation based on measured hydraulic characteristics between two surveyed cross-sections (Equation (2)). The calculation used in situ field measurements provided by the Water Research Institute (WRI), including surveyed channel bed geometry and measured water levels at cross-sections 63 and 21 (Fig. 2). Hydraulic parameters such as cross-sectional area, wetted perimeter, hydraulic radius, and energy slope were subsequently derived from the surveyed geometry and measured water surface elevations together with the measured discharge. Unlike the photogrammetry-based hydraulic modelling approach, this calculation was performed only once using the measured field data. The resulting Manning's roughness coefficient of 0.0275 (Table 4) represented the hydraulic resistance of the investigated fish pass under the measured flow conditions.

Table 4. Manning's roughness coefficients calculated using the standard open-channel equation

Parameters		Terrain	
		CS 63	CS 21
Q	($m^3 \cdot s^{-1}$)	0.904	
Water Level	(m a. s. l.)	172.71	172.56
A	(m^2)	0.95	1.54
Wetted Perimeter	(m)	4.83	5.95
R	(m)	0.197	0.259
l	(m)	42	
Δy	(m)	0.15	
n	(-)	0.0275	

3.3 Calibration of the HEC-RAS Hydraulic Model

Calibration was performed in a structured workflow combining initial physically based parameter estimation and subsequent numerical optimization. The hydraulic model was calibrated independently for each combination of terrain resolution and geometry. Calibration was performed by iteratively adjusting the Manning roughness coefficient until the simulated water surface profile matched the measured water levels along the analyzed fish pass reach. Each geometric configuration was combined with four terrain raster resolutions (1 cm, 5 cm, 10 cm, and 25 cm), resulting in a total of 16 individual HEC-RAS simulation scenarios.

The calibration process demonstrated that the required Manning coefficient depended on both the raster resolution and the density of cross-sections used to represent the channel geometry. Models based on finer terrain resolutions generally required slightly lower Manning coefficients compared to coarser raster representations (Table 5, Figure 3). This behavior indicates that detailed terrain models explicitly incorporate a larger proportion of flow resistance through the geometric definition of the channel morphology itself. To support the comparison of model performance, the standard deviation of water levels expressed in percentage was used, providing a dimensionless measure of variability that enables consistent evaluation across different stations and flow magnitudes.

Similarly, geometric configurations with denser cross-section spacing provided a more detailed representation of local channel irregularities and hydraulic controls. As a result, these configurations reproduced measured water surface elevations with lower calibration error and more stable roughness values. Configurations with simplified geometric representation produced smoother hydraulic profiles

and larger local deviations from measured water levels, particularly near sections containing boulders.

Table 5. Optimized Manning's n values across all configurations

Geometry	Terrain 1 cm		Terrain 5 cm		Terrain 10 cm		Terrain 25 cm	
	n (-)	σ (%)	n (-)	σ (%)	n (-)	σ (%)	n (-)	σ (%)
G1	0.0260	1.439	0.0260	1.634	0.0260	1.658	0.0260	1.853
	0.0261	1.390	0.0261	1.658	0.0261	1.658	0.0261	1.877
	0.0263	1.439	0.0263	1.634	0.0263	1.634	0.0263	1.853
	0.0265	1.463	0.0265	1.585	0.0265	1.634	0.0265	1.853
	0.0270	1.439	0.0270	1.561	0.0270	1.658	0.0270	1.853
	0.0300	1.536	0.0300	1.414	0.0300	1.463	0.0300	1.682
	0.0330	1.707	0.0330	1.707	0.0330	1.682	0.0330	1.658
G2	0.0260	1.341	0.0260	1.439	0.0260	1.463	0.0260	1.853
	0.0261	1.365	0.0261	1.414	0.0261	1.463	0.0261	1.853
	0.0263	1.317	0.0263	1.414	0.0263	1.487	0.0263	1.853
	0.0265	1.317	0.0265	1.439	0.0265	1.536	0.0265	1.853
	0.0270	1.292	0.0270	1.317	0.0270	1.463	0.0270	1.780
	0.0300	1.463	0.0300	1.414	0.0300	1.390	0.0300	1.609
G3	0.0260	1.126	0.0260	2.174	0.0260	2.174	0.0260	2.567
	0.0261	1.152	0.0261	2.174	0.0261	2.174	0.0261	2.567
	0.0263	1.127	0.0263	2.174	0.0263	2.200	0.0263	2.567
	0.0265	1.152	0.0265	2.095	0.0265	2.200	0.0265	2.514
	0.0270	1.126	0.0270	2.017	0.0270	2.226	0.0270	2.448
	0.0300	1.493	0.0300	1.886	0.0300	1.964	0.0300	2.252
	0.0330	1.676	0.0330	1.833	0.0330	1.859	0.0330	2.095
	0.0350	1.781	0.0350	2.069	0.0350	2.148	0.0350	2.069
G4	0.0260	2.149	0.0260	2.475	0.0260	2.502	0.0260	2.502
	0.0265	2.094	0.0265	2.420	0.0265	2.420	0.0265	2.556
	0.0270	2.121	0.0270	2.257	0.0270	2.339	0.0270	2.420
	0.0300	1.713	0.0300	1.958	0.0300	1.985	0.0300	2.013
	0.0310	1.605	0.0310	1.849	0.0310	1.931	0.0310	2.067
	0.0320	1.632	0.0320	1.686	0.0320	1.822	0.0320	1.877
	0.0330	1.686	0.0330	1.768	0.0330	1.741	0.0330	1.822
	0.0350	1.795	0.0350	1.741	0.0350	1.768	0.0350	1.819

Note: Highlighted yellow values indicate the optimized Manning's roughness coefficients with the lowest standard deviation for each simulation scenario. Green and red colors represent lower and higher tested roughness values, respectively

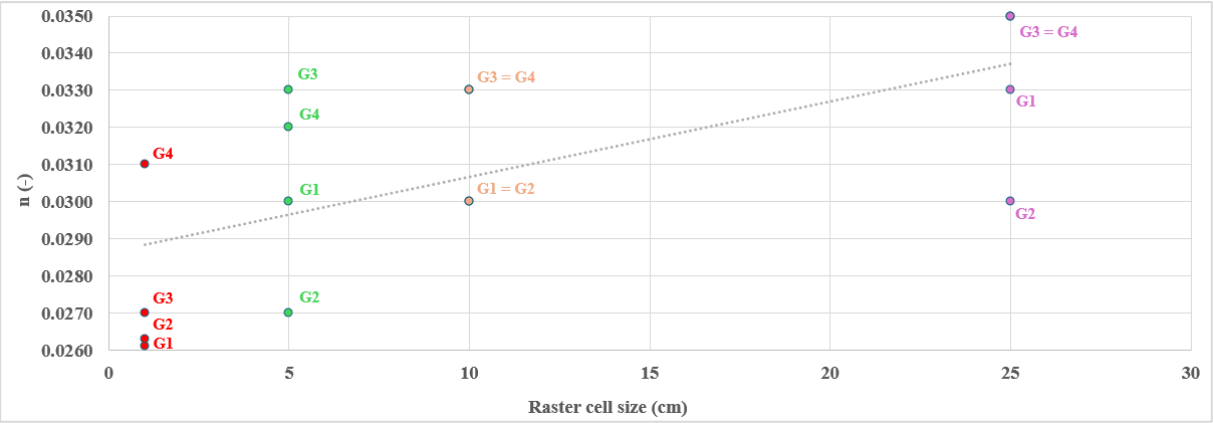


Figure 3. Effect of Raster Resolution on Calibrated Manning's Roughness Coefficient

Model performance of the geometrical configurations combined with the optimized Manning roughness values (identified in Table 5 based on the standard deviation criterion) was subsequently evaluated using the root mean square error (RMSE), mean absolute error (MAE), and coefficient of determination (R^2) between measured and simulated water surface elevations (Table 6). RMSE (Equation (3)) and MAE (Equation (4)) were used to quantify the magnitude of residual errors, while R^2 (Equation (5)) was used to assess the agreement between measured and simulated longitudinal water surface profiles.

$$\mathrm{RMSE} = \sqrt{\frac{1}{n}\sum_{i=1}^{n}(y_i - \hat{y}_i)^2} \tag{3}$$

$$\mathrm{MAE} = \frac{1}{n}\sum_{i=1}^{n}|y_i - \hat{y}_i| \tag{4}$$

$$R^2 = \frac{\sum_{i=1}^{n}(y_i - \hat{y}_i)^2}{\sum_{i=1}^{n}(y_i - \bar{y})^2} \tag{5}$$

Where: y_i – measured value (m);
$\hat{y}_i$ – simulated value (m);
$\bar{y}$ – mean of measured values (m);
n – number of observations (-) (n = 29).

Table 6. Model performance statistics (RMSE, MAE, R^2)

Geometry	Terrain (cm)	n (-)	MAE (mm)	RMSE (mm)	R^2 (-)
G1	1	0.0261	19.7	24.3	0.986
	5	0.0300	20.0	24.1	0.985
	10	0.0300	20.7	25.5	0.984
	25	0.0330	23.4	27.0	0.985
G2	1	0.0263	18.6	24.4	0.983
	5	0.0270	18.6	24.8	0.985
	10	0.0300	19.7	25.5	0.983
	25	0.0300	22.8	27.8	0.983
G3	1	0.0270	14.8	19.7	0.986
	5	0.0330	24.1	31.5	0.976
	10	0.0330	24.5	32.4	0.977
	25	0.0350	27.2	34.4	0.976
G4	1	0.0310	20.7	26.3	0.984
	5	0.0320	21.0	27.9	0.980
	10	0.0330	22.1	28.2	0.983
	25	0.0350	23.4	30.3	0.981

4 Discussion

The statistical comparison between measured and simulated water surface elevations revealed a clear dependency between hydraulic model performance and the level of geometric detail incorporated into the terrain and cross-section representation. Configurations based on higher-resolution terrain models and denser cross-section spacing consistently achieved lower residual errors, whereas simplified configurations showed reduced accuracy in reproducing local hydraulic conditions.

Although RMSE and MAE increased with decreasing terrain resolution and geometric simplification, the coefficient of determination (R^2) remained consistently high across all configurations. This indicates that even simplified models can reproduce the overall longitudinal trend of the water surface profile, while the main loss of accuracy is associated with local hydraulic variability rather than general flow behavior.

The influence of terrain resolution was particularly evident in sections containing large boulders and abrupt local slope variations. High-resolution DEMs preserved small-scale morphological features that were progressively smoothed in coarser terrain variants, affecting the extracted hydraulic geometry and resulting water surface profiles. Consequently, coarser DEMs produced smoother hydraulic gradients and larger local deviations from measured water levels.

This behavior highlights the trade-off between explicit geometric roughness represented by detailed terrain morphology and implicit hydraulic resistance represented by Manning's roughness coefficient. When geometric detail is reduced, the hydraulic model compensates by increasing Manning's n to maintain agreement with observed water levels.

The Manning's roughness coefficients obtained using different estimation approaches showed relatively consistent ranges. Empirical equations based on bed material characteristics produced values of n = 0.0285–0.0662, while standard open-channel equations yielded values of n = 0.0275. Calibration of the one-dimensional hydraulic model using the standard deviation criterion resulted in optimized Manning's coefficients ranging from n = 0.026 – 0.035, depending on the simulation scenario. The calibrated values, therefore remained within the lower to middle portion of the empirically derived intervals,

suggesting that part of the hydraulic resistance was already explicitly represented by the detailed channel geometry captured in the high-resolution terrain models.

The obtained roughness coefficients are consistent with values commonly reported for coarse-bed natural channels and nature-like fish passes. Previous studies on gravel- and cobble-bed streams and coarse alluvial channels report Manning's n values typically in the range of approximately 0.030–0.050 for similar bed materials (Chow, 1959). Studies on nature-like fish passes with comparable coarse-bed and boulder-dominated substrates report values in the range of approximately 0.023–0.040 depending on hydraulic conditions and estimation methods (Čubanová, 2023; Čubanová, 2025).

From a modelling perspective, the results demonstrate that geometric discretization directly affects both calibration accuracy and the spatial distribution of residuals along the channel. Simplified terrain and cross-section configurations tend to smooth hydraulic gradients, leading to increased deviations in areas influenced by local hydraulic controls such as boulder clusters and abrupt bed variations.

From an engineering standpoint, simplified terrain models may still be acceptable for preliminary design or feasibility studies where only general water level trends are required. However, for detailed hydraulic analysis, calibration studies, or ecological assessments of fish migration conditions, high-resolution photogrammetric terrain data combined with dense geometric discretization is strongly recommended.

Overall, the study demonstrates that hydraulic resistance in numerical models shifts between explicitly represented channel morphology and the empirically calibrated roughness parameter depending on the level of geometric detail included in the model. This finding has important implications for interpreting calibrated Manning's coefficients in complex nature-like hydraulic structures where geometry and roughness effects are strongly coupled.

5 Conclusion

The study demonstrates a strong coupling between geometric representation and the calibrated Manning's roughness coefficient in modelling nature-like fish passes. Manning's n behaves as an effective parameter that compensates for unresolved geometric complexity rather than representing a purely material property, with lower terrain resolution leading to higher calibrated roughness and high-resolution DEMs shifting part of the resistance into explicitly resolved morphology. UAV-based photogrammetry provides an efficient means of generating high-resolution terrain data that improves physical realism in one-dimensional hydraulic models and reduces calibration dependence. From an engineering perspective, all model configurations remained stable and reproduced the general water surface profile, indicating that simplified terrain may be suitable for preliminary assessments. However, accurate calibration and prediction of local hydraulic conditions require high-resolution terrain representation. Overall, the results emphasize that Manning's n must be interpreted in relation to geometric resolution, as it directly affects its calibrated value and transferability in complex natural channels.

Acknowledgements

This contribution was developed within the framework and based on the financial support of the APVV-23-0447, APVV-20-0023 projects, and Vega projects No.1/0699/25 and No. 1/0161/24. Acknowledgement is also given to the Program for Supporting Young Researchers for supporting the project entitled Flow Dynamics in Fish Passes: Hybrid Modeling for the Optimization of Migratory Connectivity.

References

Agisoft Metashape User Manual: Professional Edition, Version 1.5. 2019, Agisoft LLC.

Baek, K.-O., Lee, J.-M., Han, E.-J., Kim, Y.-D. 2022 Evaluating Attraction and Passage Efficiencies of Pool-Weir Type Fishways Based on Hydraulic Analysis. *Applied Sciences.* 12 (4), 1880.

Bunte, K.; Abt, S.R. 2001 *Sampling Surface and Subsurface Particle-Size Distributions in Wadable Gravel-and Cobble-Bed Streams for Analyses in Sediment Transport, Hydraulics, and Streambed Monitoring*; U.S. Department of Agriculture: Fort Collins, CO, USA, 2001.

Chanson, H. 2004 *Hydraulics of Open Channel Flow: An Introduction.* Elsevier Butterworth-Heinemann, 634 p.

Chow, V.T. 1959 *Open-Channel Hydraulics*, 1st ed.; McGraw-Hill: New York, NY, USA.

Čubanová, L., Rumann, J., Vidová, A., Almikaeel, W., Rebenda, F. 2023 Verification of Hydraulic Parameters of Nature-like Fish Pass. *Water.* 15 (13), 2478.

Čubanová, L., Rumann, J., Rutzká, A., Vidová, A., Dušička, P. 2025 Verification of the Manning's Roughness Coefficient of Fish Pass Riverbeds Using Drone-Based Photogrammetry. *Water.* 17 (10), 1409.

Diepenbroek, M., Bartholoma, A., Ibbeken, H. 1992 How round is round? A new approach to the topic 'roundness' by Fourier grain shape analysis. *Sedimentology*, 39 (3), 411–422.

Diepenbroek, M., De Jong, C. 2007 Quantification of textural particle characteristics by image analysis of sediment surfaces - examples from active and paleo-surfaces in steep, coarse-grained mountain environments. In *Ergenzinger P., Schmidt K. H. (Eds) Dynamics and Geomorphology of Mountain Rivers, Lecture Notes in Earth Sciences, Springer*, 52, 301–314.

Dietrich, J. T. 2017 Bathymetric Structure from Motion: Extracting shallow stream bathymetry from multi-view stereo photogrammetry. *Earth Surface Processes and Landforms*. 42, 355–364.

Dumitran, G. E., Vuță, L. I. 2020 Design of Rock Ramps for Ensuring Fish Migration. *Scientific Bulletin of the University Politehnica of Bucharest*, 82 (3), 240–243.

Dušička, P., Květon, R. 2015 *Canal Water Power Plants – Hydraulic Research of the Operation of Derivation Canals, Basic Hydraulic Research (in Slovak: Kanálové vodné elektrárne – hydraulický výskum prevádzky derivačných kanálov, Základný hydraulický výskum).* Bratislava: STU in Bratislava, STU Publishing House, 92 p.

Fošumpaur, P.; Králík, M.; Zukal, M. 2020 Physical and Numerical Modelling in the Research of Hydraulic Structures. In *Proceedings of the International Conference on Modelling and Simulation*, Prague, Czech Republic, 22–25 June 2010.

French, R. H. 1986 *Open-Channel Hydraulics*. McGraw-Hill, 705 p.

Girardeau-Montaut, D. 2016 *CloudCompare*; 5th ed.; EDF R&D Telecom ParisTech: France.

Gualtieri, C, Chanson, H. 2011 Hydrodynamics and turbulence in a positive surge. A comparative study. In *Proceedings 34th IAHR World Congress*, *Engineers Australia Publication*, Brisbane, Australia, 26 June – 1 July, 2452–2459.

Haan, C. T., Barfield, B. J., Hayes, J. C. 1994 *Design Hydrology and Sedimentology for Small Catchments*. Academic Press, 588 p.

Henderson, F.M. 1967 Open Channel Flow. *J. Fluid Mech*. 29, 414–415.

Jaworowski, A. 2022 *Manning's roughness coefficient in small scale nature-like fish passages. Field study and evaluation.* Master's thesis. Division of Water Resources Engineering, Department of Building & Environmental Technology, Lund University, Lund, Sweden.

Liu, L. 2023 Drone-Based Photogrammetry for Riverbed Characteristics Extraction and Flood Discharge Modeling in Taiwan's Mountainous Rivers. *Measuremen*t. 220, 113386.

Magaju, D., Montgomery, J., Franklin, P., Baker, C., Friedrich, H. 2020 A New Framework for Assessing Roughness Elements in Promoting Fish Passage at Low-Head Instream Structures. *Journal of Ecohydraulics.* 5 (2), 152–164.

Marcus, W.A.; Fonstad, M.A. 2008 Optical Remote Mapping of Rivers at Sub-meter Resolutions and Watershed Extents. *Earth Surf. Process. Landf*. 33, 4–24.

Máčka, Z. 2009 Determination of Flow Velocity and Discharge in a Small Stream (in Czech: Stanovení rychlosti proudění a průtoku na malém vodním toku). Study Materials for the Course PřF: Z7051 Environmental Geography Practice, Project 4, 6 p. Online (02.04.2024), https://is.muni.cz/el/1431/jaro2010/Z7051/um/10137516/Projekt_4_-_odhad_prutoku.pdf

Mäsiar, E.; Kamenský, J. 2001 *Hydraulics (In Slovak: Hydraulika)*, 3rd ed., Slovak University of Technology: Bratislava, Slovakia.

Purinton, B.; Bookhagen, B. 2019 Introducing PebbleCounts: A Grain-Sizing Tool for Photo Surveys of Dynamic Gravel-Bed Rivers. *Earth Surf. Dyn*., 7, 859–877.

Raplík, M.; Macura, V. 1983 Analysis of the Granulometry of Gravel-Sand Riverbeds Using Photographic Methods (In Slovak: Analýza granulometrie štrkopieskových korýt fotografickou metódou). In *Proceedings of the Specialist Seminar: Surface Water Flow and Its Effects on the Environment*, Proceedings of Papers; Tatranská Štrba, Slovakia, pp. 31–38.

Schügerl, R., Velísková, Y. 2023 Change of the Manning´s coefficient in small stream influenced by vegetation. *Acta Hydrologica Slovaca*. 24 (1), 134-140.

Schügerl, R., Velísková, Y., Sočuvka, V., Dulovičová, R. 2020 Effect of aquatic vegetation on Manning´s roughness coefficient value – case study at the Šúrsky channel. *Acta Hydrologica Slovaca*. 21 (1), 123-129.

U.S. Army Corps of Engineers 2021 *HEC-RAS Hydraulic Reference Manual*, Version 6.0. Hydrologic Engineering Center, Davis, CA.

Velísková, Y., Dulovičová, R., Schügerl, R. 2017 Impact of Vegetation on Flow in a Lowland Stream During the Growing Season. *Biologia* 72, 840-846.

Vidová, A. 2023 *Verification of the functionality of the nature-like fish pass (in Slovak: Overenie funkčnosti prírode blízkeho typu rybovodu)*. Diploma thesis. Department of Hydraulic Engineering, Faculty of Civil Engineering, Slovak University of Technology, Bratislava, 81 p.

SOFTWARE TOOL FOR OPERATIONAL CONTROL OF THE GABČÍKOVO HYDROPOWER PLANT ON THE DANUBE: LINKING WATER FLOW SIMULATIONS AND ENERGY MANAGEMENT

Peter ŠULEK [1], Martin ORFÁNUS [1], Michaela ČERVEŇANSKÁ [1*]

[1] *Department of Hydraulic Engineering, Faculty of Civil Engineering,*

Slovak University of Technology in Bratislava, Radlinského 11, 810 05 Bratislava, Slovakia

peter.sulek@stuba.sk

martin.orfanus@stuba.sk

michaela.cervenanska@stuba.sk

[*] *Corresponding author*

Abstract

The Gabčíkovo Hydropower Plant (GHP) is the largest power plant in Slovakia in terms of generated electricity. The primary objective of its operational management is to optimise the utilisation of the hydroelectric potential of the Danube River to meet the required power output schedule (load-following). At the same time, all other functions of the Gabčíkovo Project must be ensured, and the constraints resulting from its multipurpose character and the hierarchy of priorities for fulfilling its individual functions, as defined by the operating rules, must be respected. These functions include, for example, the flood protection, ensuring water withdrawals, and maintaining navigation conditions in accordance with international regulations governing navigation on the Danube River. This paper aims to describe a software tool developed at the Department of Hydraulic Engineering of the Faculty of Civil Engineering, Slovak University of Technology in Bratislava, designed for planning and operational management of the GHP in the environment of a liberalised electricity market. The tool ensures that all functions of the hydraulic structure are fulfilled while preventing any threat to navigation safety, particularly the deterioration of navigation channel parameters caused by the GHP's hydropeaking.

Key words

Gabčíkovo Hydropower Plant, hydropeaking, HEC-RAS water flow simulation, navigation demands

1 Introduction

The primary objective in managing the Gabčíkovo hydropower plant (GHP) is the optimal utilization of the hydroelectric potential of the Danube River to meet the requirements of the hourly power dispatch schedule. At the same time, all other functions of the Gabčíkovo Project must be ensured, and the constraints arising from its multipurpose nature and the hierarchy of importance of fulfilling individual functions must be respected, as established by the operating rules. These functions include, for example, the flood protection, ensuring water withdrawals, guaranteeing international navigation, and others. The GHP's load-following (i.e., reducing and increasing the power output of the GHP based on the demands of the energy system – the so-called "load-following") can only be applied to a limited extent, because the equalizing reservoir of the Nagymaros Project has not been constructed. The Nagymaros Project was intended, in addition to equalizing the peak outflow from the GHP, to ensure the parameters of the navigation channel in the reach of the Danube downstream of the GHP by raising the water level even during low flow conditions. The non-completion of the Gabčíkovo–Nagymaros system therefore results in the navigation conditions being directly affected by flow management at the GHP. A sudden drop in

flow through the GHP can reduce the navigable depth below the safe threshold, leading to the risk of a vessel running aground. Such a navigational accident may have dangerous consequences for crews, passengers, cargo, and the vessels themselves, and poses a serious threat to navigation safety. Flow management at the GHP must therefore not cause a reduction in navigable depths below the limit values prescribed by regulations (27 dm); during periods of low flows on the Danube, the GHP must not, through flow management, reduce the currently reported navigable depth values. From the perspective of the risk of water level drop in the navigation channel, the critical sections are the shoals, i.e., sections where the minimum navigable depths occur. For the safety of navigation operations, it is therefore essential to understand the influence of flow management at the GHP turbines on the flow regime and on the water level regime in this river section.

The planning of hydroelectric power plant operations regarding maintaining navigation conditions in rivers is an active area of research. This has been confirmed by numerous scientific publications in recent years (Hatamkhani et al., 2023a; Hatamkhani et al., 2021; Hatamkhani et al., 2023b; Jia et al., 2019; Moura De Figueiredo et al., 2023; Tianlong & Jianzhong, 2018; Xiangyu, 2023; Yizi, 2017).

With the aim of optimizing the load-following of the GHP, a software tool for the optimal operational management of the GHP was developed at the Department of Hydraulic Engineering of the Faculty of Civil Engineering at the Slovak University of Technology in Bratislava. This tool links water flow simulations with energy management. Compared to tools used in the past, it enables more comprehensive and efficient planning and utilization of the GHP, also because it optimizes the operation of the GHP regarding ensuring adequate navigation parameters of the international Danube waterway. The aim of this paper is to describe the functions and principles of the implemented software.

2 Materials and Methods

2.1 Water Flow Simulation

The software uses HEC-RAS (Hydrologic Engineering Center River Analysis System) for water flow simulation in open channels. For unsteady flow simulation, HEC-RAS implements a numerical solution to the Saint-Venant equations for 1D flow. The system consists of two partial differential equations.

$$\frac{\partial A}{\partial t} + \frac{\partial(\phi Q)}{\partial x_c} + \frac{\partial[(1-\phi)Q]}{\partial x_f} = 0 \tag{1}$$

$$\frac{\partial Q}{\partial t} + \frac{\partial}{\partial x_c}\left(\phi^2 \frac{Q^2}{A_c}\right) + \frac{\partial}{\partial x_f}\left[(1-\phi)^2 \frac{Q^2}{A_f}\right] + gA_c\left(\frac{\partial H}{\partial x_c} + S_{fc}\right) + gA_f\left(\frac{\partial H}{\partial x_f} + S_{ff}\right) = 0 \tag{2}$$

where t is the time, x is the distance between two independent variables, x_c is the distance along the channel, and x_f is the distance along the floodplain. Q is the total discharge in the cross-section, g is the gravitational acceleration, H is the water surface elevation, A is the total cross-sectional area, A_c is the cross-sectional area of the channel, A_f is the cross-sectional area of the floodplain parts, S_{fc} and S_{ff} are the hydraulic slopes describing the friction losses along the channel and floodplain, respectively. The coefficient ϕ describes the discharge distribution between the channel and the floodplain. Equation (1) describes the mass balance in an open channel, and equation (2) represents the momentum balance. A more detailed description of the equations is given in (Brunner, 2016).

2.2 HEC-RAS Controller

The key technical element is the use of the Application Programming Interface (API), known as the *HEC-RAS Controller*. This tool enables:

- controlling simulations using external scripts, e.g. in Visual Basic or Visual Basic for Applications,
- automating the opening of projects, setting boundary conditions, and extracting data without

manual user intervention,

- manipulation of HEC-RAS ASCII files of the **.uXX* type (Unsteady Flow Files), thereby replacing work in the graphical user interface.

Figure 1 shows an example of a Visual Basic script used to open and run a HEC-RAS project without the need to launch the HEC-RAS application itself.

```
'Initiate the HEC-RAS Controller class
Dim HRC As New HECRASController

'The path and filename of the desired HEC-RAS Project
Dim strProjectFilename As String
strProjectFilename = App.Path & "\Project.prj"

'Hide HEC-RAS computation window
HRC.Compute HideComputationWindow

'Open HEC-RAS project
RC.Project Open (strProjectFilename)

'Set HEC-RAS plan as current
Dim strCurrentPlanName As String
strCurrentPlanName = "Plan"
Dim blnDidIt SetCurrentPlan As Boolean
blnDidIt SetCurrentPlan = RC.Plan SetCurrent(strCurrentPlanName)

'Compute the current plan
Dim lngMessages As Long 'number of messages returned by the HEC-RAS Controller (returned)
Dim strMessages() As String 'array of messages returned by the HEC-RAS Controller (returned)
Dim blnDidIt ComputeCurrentPlan As Boolean
blnDidIt ComputeCurrentPlan = RC.Compute CurrentPlan(lngMessages, strMessages(), True)
'computes the current plan (returns TRUE, if the computation worked properly, FALSE if not)

'Close HEC-RAS project
RC.QuitRas
```

Figure 1. Visual Basic script for opening and running the HEC-RAS project.

Figure 2 shows an example of a script used to edit a HEC-RAS text file **.uXX*, which contains the parameters of the boundary and initial conditions of unsteady flow.

```
'Set the restart file in Usteady flow file *.uXX to use for next time simulation
Dim strFlowFile As String
strFlowFile = App.Path & "\RAS Model\Project.uXX" 'the path and filename of the Unsteady flow file
Dim strNewFlowFile As String
strNewFlowFile = App.Path & "\RAS_Model\Project.tempuXX" 'the path and filename of the
temporary Unsteady flow file
  Open strFlowFile For Input As #1 'open the Unsteady flow file
  Open strNewFlowFile For Power output As #2 'open the temporary Unsteady flow file
     Do While Not EOF(1)
     Line Input #1, strLine
       If InStr(strLine, "Restart Filename=") Then 'search string "Restart Filename="
         Print #2, "Restart Filename=Project.pXX.DDMONTHYYYY hhmm.rst" 'change the
         restart file to use
       Else
         Print #2, strLine
       End If
     Loop
  Close #1 'close the Unsteady flow files
  Close #2 'close the temporary Unsteady flow files
```

Figure 2. Visual Basic script for editing text file **.uXX*.

2.3 GHP's Management Model: Energy and Economic Optimization

While HEC-RAS handles the water flow simulation, the GHP's Management Model focuses on production planning.

2.3.1 Main Inputs and Outputs

The main inputs of the management model are (see Figure 3):
1. hydrological forecast,
2. electricity price maps in the trading schedule,
3. design parameters and limits of the Gabčíkovo Project,
4. required operations at the Gabčíkovo Project,
5. outages and restrictions of technological equipment,
6. navigation demands.

The main output of the model is the electricity generation plan for the GHP on an hourly basis.

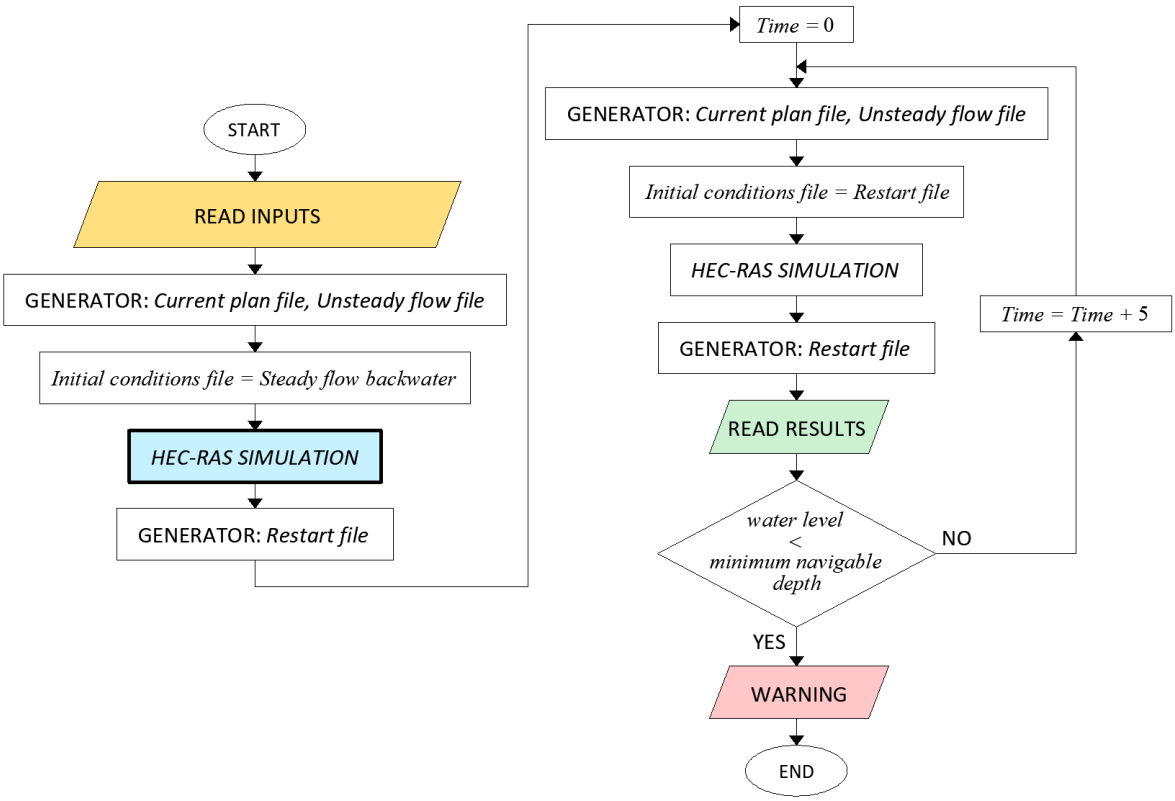


Figure 3. Flowchart of the work process.

The described procedure allows the user to intuitively modify the discharge through the GHP for individual hours of the planning period using a trial-and-error approach until a solution is obtained in which the water depth in the navigation channel along the entire Danube reach affected by GHP operation is greater than or equal to the required minimum navigable depth. Within the software tool, this approach is referred to as the *simulation mode*. However, this procedure is relatively labor-intensive and time-consuming. Therefore, an *optimization mode* was developed within the software tool, as described in Section 2.3.2.

2.3.2 Optimization Criterion

For an arbitrary length of the planning period and considering time step i, the optimization objective can be described by the objective function (3). The goal of the optimization is to maximize the profit from energy production, while satisfying all design and operational constraints.

$$F = \sum_{i=1}^{T} c_i . ST_i . P_i = \sum_{i=1}^{T} c_i . (ST_i . 9{,}81 . Q_i . H_i . \eta_i . 10^{-3}) \rightarrow max \quad (3)$$

where T is the number of time intervals (planning period), i is the index of the time interval of the

solution, c_i is a weighting factor (the so-called electricity price), ST_i is a bivalent variable describing the operational state of the GHP (1 – hydropower plant in operation, 0 – hydropower plant out of operation), P_i is the dispatched power output of the GHP in [MW] and Q_i is the flow through the GHP in [$m^3 \cdot s^{-1}$]. H_i is the average head at the GHP in [m] (where $H_{k,i} = f(Q_i, V_{in})$), where V_{in} is the initial volume of water in the Hrušov reservoir [m^3], η_i is the energy conversion efficiency at the GHP [-] (where $\eta_i = f(Q_i, H_i)$). The variables Q_i (i.e., the GHP operation plan) are then the result of maximizing the objective function (3), which must be supplemented during the solution with constraining conditions derived from the restrictions, or from constraints and navigation demands.

Subject to hydro plant operation limits:

$$ST_i \, Q_{min} <= Qi <= ST_i \, Q_{max} \tag{4}$$

Subject to Hrušov reservoir storage capacity limits:

$$V_{min} <= V_i <= V_{max} \tag{5}$$
$$V_0 = V_{in} \quad \text{and} \quad V_T = V_{fin} \tag{6}$$

where Q_{min} is minimum discharge of hydro plant [m^3/s], Q_{max} is maximum discharge of hydro plant [m^3/s], V_{min} is Hrušov reservoir's minimum storage volume [m^3], V_{max} is Hrušov reservoir's maximum storage volume [m^3], V_{in} is Hrušov reservoir's initial storage volume [m^3] and V_{fin} is Hrušov reservoir's final (target) storage volume [m^3].

The water balance for reservoir during hour i is given by:

$$V_i = V_{i-1} - 3600 Q_i + I_i \tag{7}$$

where V_i is Hrušov reservoir storage volume at the end of an hour i [m^3], I_i is inflow including the evaporation losses, leakage and other non-energy withdrawals [m^3].

Subject to navigation limits:

$$WL_i >= WL_{min}$$

where WL_i is water level in the fairway and WL_{min} is minimum navigable water level (see Section 2.5).

Due to the complexity of the mathematical formulation of unsteady open-channel flow using the Saint-Venant equations, the objective function (3) cannot be solved using conventional numerical optimization methods. Therefore, the software tool employs a heuristic approach based on genetic algorithms (GA) to maximize the objective function. Since GA are optimization algorithms designed to solve unconstrained optimization problems, the constraints defined by Equations (4)–(7) must be transformed into penalty functions.

2.4 Visual Basic-HECRAS Interface Design: The "Power – Flow" Link

In the real-world electricity trading environment, trading is not conducted in terms of flow, but in power blocks. Standard HEC-RAS, however, does not allow power to be entered as a boundary condition. The relationship between power and flow is non-linear and depends on the current head (the difference in water level upstream and downstream of the hydropower plant). The *Visual Basic-HECRAS interface* resolves this problem by dividing the simulation into 5-minute steps. The flowchart of the work process is shown in Figure 3. At each step, the system:

1. calculates the turbine flow according to the current head from the previous simulation step,
2. Visual Basic scripts automatically overwrite the HEC-RAS text files *.*uXX*, thereby replacing manual operator inputs,
3. to ensure simulation continuity, after each step the system generates a so-called *Restart File*

(*.*rst*), which serves as the initial condition for the next simulation step,

4. data extraction: the results of the water flow simulation are retrieved from binary *DSS files* and interpreted in the user interface of the GHP management model (see Figure 7).

2.5 Navigation Conditions

A critical aspect of operations is compliance with the threshold depth, which is set at 25 dm (plus a safety margin of 2 dm) for international navigation on the Danube River.

2.5.1 Limiting River's Reaches and Shoals (Fords)

According to the Gabčíkovo Operating Rules, the key monitoring point on the Danube River is the ford at river km 1796 (Čičov), but the system enables monitoring of the entire section as far as Komárno. Older management methods based on static tables with permitted durations of negative flow manipulation were difficult to apply in practice and imprecise. It is precisely the combination of economic optimization and accurate hydraulic simulation (using the Visual Basic-HECRAS interface) that enables maximum utilization of the Danube's energy potential without negative impacts on international transport. The unsteady flow simulation enables continuous evaluation of:

- Depth reduction: It alerts the operator if the proposed production plan risks a drop in water level below the limit value at the fords,
- Translatory waves: It simulates positive and negative waves arising from sudden changes in power output, which may compromise the manoeuvrability of vessels.

Model calibration and verification was carried out using real operational data from 2020 to 2023 at 17 gauging stations and demonstrated an accuracy of ± 10 cm, which is essential for safe navigation in reaches with intensive sediment transport.

The required simulation accuracy in the negative direction (i.e., −10 cm) is particularly important because the safety margin added to the minimum navigable water depth is only 0.2 m. Consequently, even if the simulation error reaches the allowable limit, a residual safety margin of 0.1 m remains in the fairway. The required simulation accuracy in the positive direction (i.e., +10 cm) is related to the accuracy of the power-to-flow conversion, since a simulation error exceeding 10 cm would lead to the accumulation of errors in the power-to-flow transformation at each computational time step.

3 Implementation and Results (Case Study – the Gabčíkovo hydropower plant)

The above-mentioned approach was implemented in the real-world planning and management environment of the Gabčíkovo Hydropower Plant on the Danube River in Slovakia (Figure 4). This hydropower plant, with a capacity of 720 MW and a maximum turbine flow of 5,000 $m^3 \cdot s^{-1}$, is an integral part of the extensive Gabčíkovo Project on the Danube River (Figure 5). Its basic parameters are listed in Table 1. The total length of the modelled sections is 149.2 km with 762 cross-sectional profiles. The average annual flow in the given section of the Danube reaches approximately 2,000 $m^3 \cdot s^{-1}$, while during flood situations it can rise to as much as 10,000 $m^3 \cdot s^{-1}$. Maximum flows occur primarily in spring and early summer. Conversely, periods of low water levels are typical of the autumn and winter months. It is precisely during this period that vessel contact with the bed of the navigation channel may occur, which can lead to damage to towing lines and loss of vessel manoeuvrability.

An example of the proposed operation of the GHP management model in its own user interface, with the basic inputs and outputs indicated, is shown in Figure 6. An example of the water level simulation in the intake channel of the GHP and in the section of the Danube downstream of the GHP for the proposed operation of the hydropower plant is shown in Figure 7.



Figure 4. The Gabčíkovo Hydropower Plant (Source: TASR/Martina Baumann).

Table 1. The parameters of the Gabčíkovo hydropower plant

Parameter	Value
Location	Gabčíkovo, Slovakia
River	Danube River
Type of Dam	Concrete gravity dam
Installed Capacity	720 MW
Number of Turbines	8 Kaplan turbines
Turbine Power Output	90 MW each
Runner – diameter – number of blades	∅9300 mm – 4
Turbine Capacity	636 $m^3 \cdot s^{-1}$ each
Average Annual Production	Approximately 2,200 GWh
Head	16 ~ 23.6 meters
Reservoir Capacity	38.9 million m^3
Reservoir Area	~ 40 km^2
Dam Height	25 meters
Length of Dam	500 meters
Commissioning Year	1992
Primary Purpose	Hydropower generation, flood control, navigation improvements
Operator	Vodohospodárska výstavba

Key findings from the implementation:

- Dispatch efficiency: The operator receives real-time alerts if the planned production schedule poses a risk to navigation safety in the following 24 hours (see Figure 6).
- Visual monitoring: The interface provides graphical outputs of the water level regime in both the headrace canal and the tailrace canal (see Figure 7), facilitating rapid decision-making.
- It was confirmed that a 5-minute time step is optimal for maintaining accuracy of ± 10 cm during sharp changes in power output. Shorter steps increase computation time without a significant gain in accuracy.

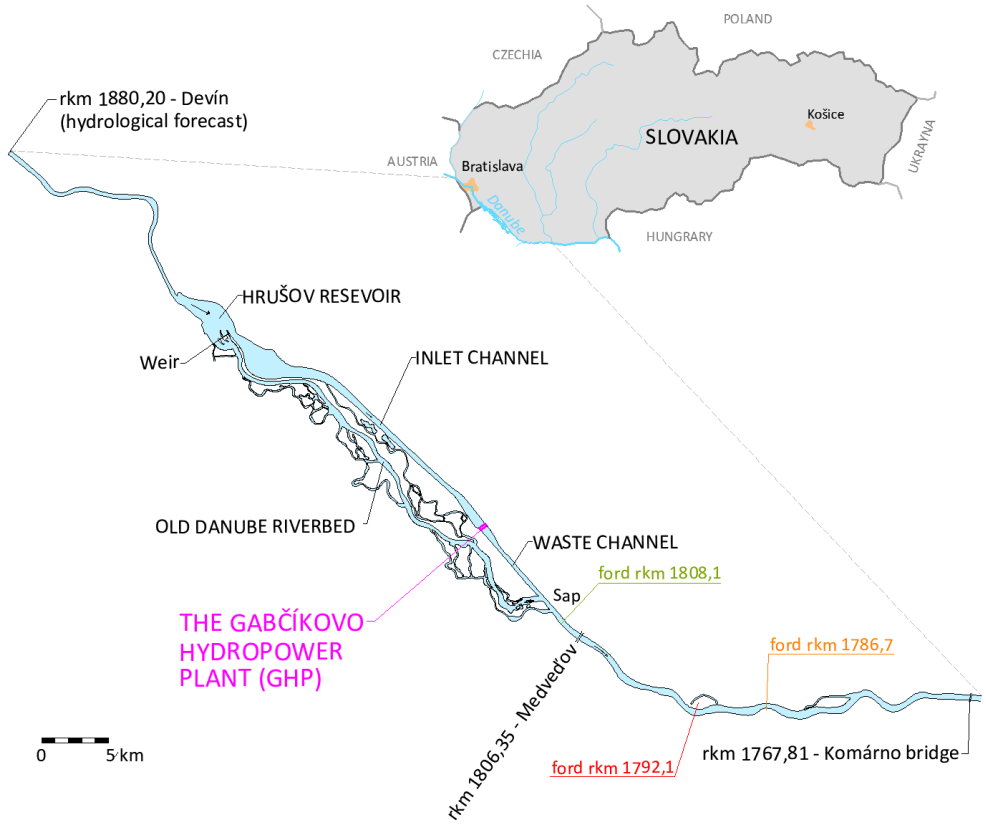


Figure 5. Location of The Gabčíkovo Project in Slovakia.

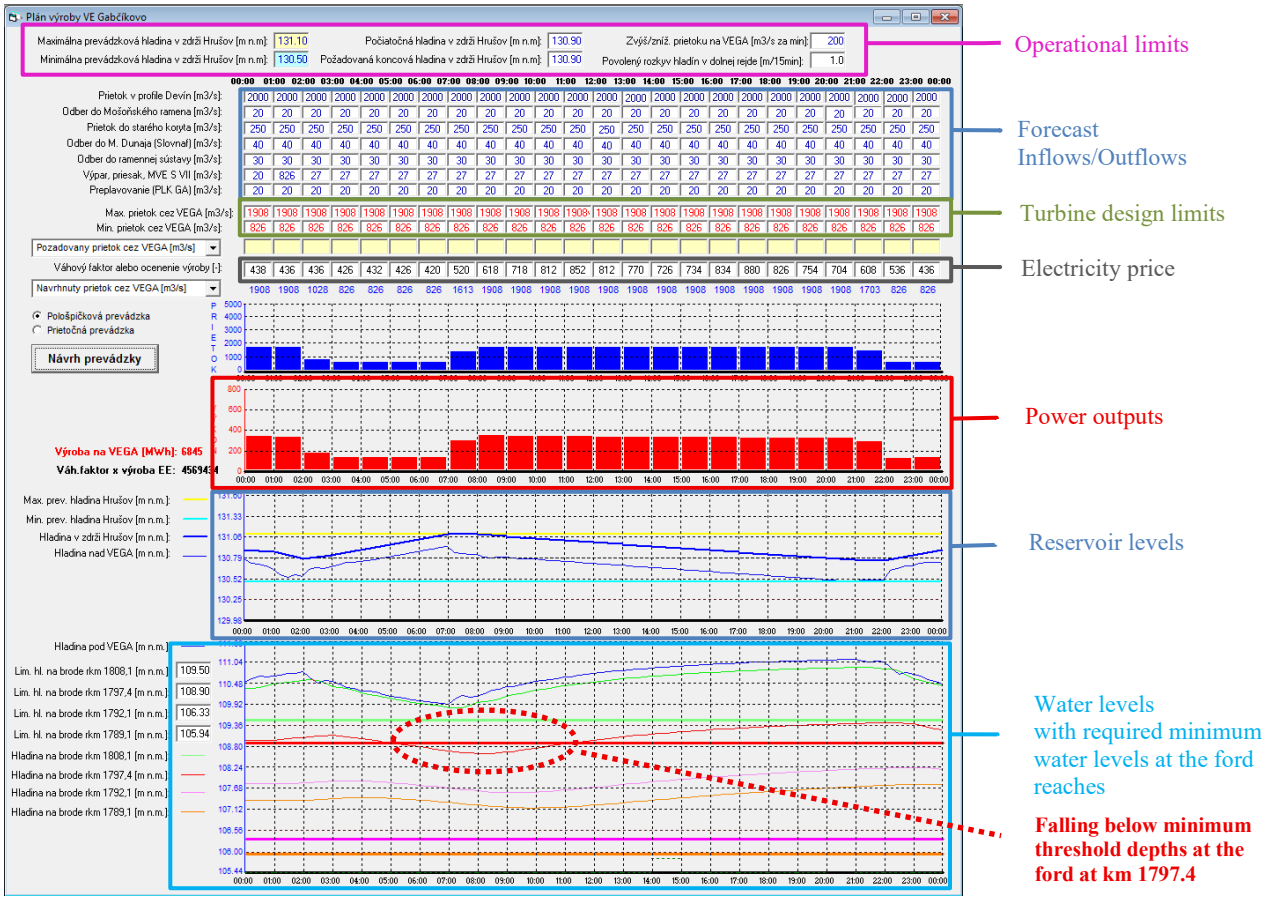


Figure 6. Example of a proposed daily operation plan for the GHP by management model in its own user interface, with the basic inputs and outputs indicated.

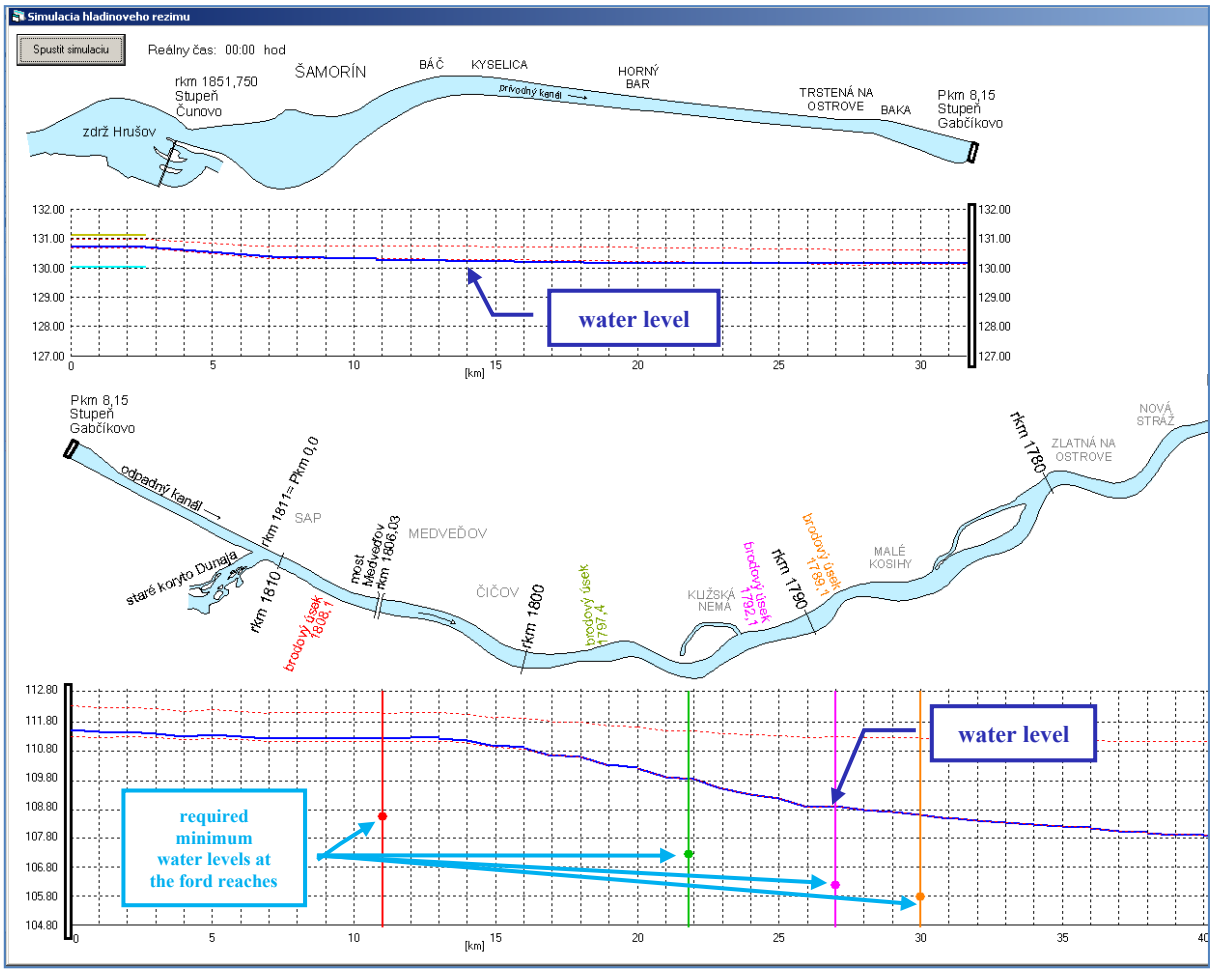


Figure 7. Example of water level simulation in the intake channel of the GHP and in the downstream of the GHP for the proposed operation of the GHP – state at 24:00.

4 Conclusions and Discussion

The newly developed software tool (GHP Management Model) represents a comprehensive solution that integrates hydrological forecasts, energy requirements, and navigation constraints. The optimization objective is described by an objective function that takes into account the energy pricing in individual hours of the trading schedule. The combination of energy management and accurate water flow simulation enables maximum utilization of the Danube's energy potential without negative impacts on international navigation.

The main advantages of automating simulations through the integration of HEC-RAS and Visual Basic tools include, above all, increased operational efficiency, computational accuracy, and navigation safety.

The key contributions are:

- Direct input of energy requirements: Automation allows the power plant output to be entered directly as a boundary condition of the water flow simulation. Standard hydraulic models require manual approximation of power output via turbine flow, which is impractical in real electricity market conditions where trading is conducted in power blocks.
- Increased efficiency and elimination of human errors: The automated process removes the need for manual adjustment of input files and restarting the simulation after each time step. This saves time and significantly reduces the risk of errors in hydroelectric power plant management planning.
- Accurate modelling of non-linear relationships: The relationship between plant power output

and flow is non-linear and depends on the current head. The automated interface can recalculate the required flow at each step based on current water levels, thereby achieving high simulation accuracy of up to ± 10 cm.

- Enhanced navigation safety: The system can evaluate whether the planned plant operation will cause the water level to drop below the threshold depth or result in the formation of dangerous translatory waves. In the event of a risk, the operator can adjust the production plan in a timely manner.
- Customised graphical user interface: Thanks to automation, the complex HEC-RAS hydraulic environment can be concealed behind a simplified graphical interface tailored directly to the needs of energy dispatchers.
- Interdisciplinary collaboration: This integration enables experts in the field of energy to utilise advanced hydraulic analyses, thereby optimising the operation of hydraulic structure regarding both energy and environmental requirements.
- Versatility: The proposed software architecture is applicable to any river system with one or more hydropower plants, provided that high-quality input data are available.

Future development of the system focuses on integration with HEC-RAS 2D, which could bring the following advantages and challenges:

- Assessment of transverse flow components: While the current model uses 1D simulation based on the Saint-Venant equations, a 2D model would enable assessment of the influence of transverse velocity components on the safety of vessel movement.
- Enhanced safety at the ship locks: This extension is particularly important in the vicinity of ship locks and their approaches, where vessel manoeuvres are most demanding and where transverse currents can divert a vessel from its ideal course.
- More accurate modelling in open water: The 2D approach would provide a more detailed view of flow dynamics, which is important for assessing the stability of a vessel's trajectory.
- Computational demand: The authors also note that as model complexity increases (such as the transition to 2D) and the volume of data grows, computation time slows significantly. This would require further performance optimisation to keep the system viable for real-time operational management.

Acknowledgments

This work was carried out within the project “Strategic partnership for green and sustainable energy research using AI for major waterworks” – AIHydroHUB, which is co-funded by the European Union under the Programme Slovakia.

This contribution was developed within the framework and based on the financial support of the Slovak grant scheme VEGA No. 1/0161/24.

References

Brunner G.W. 2016 *HEC-RAS River Analysis System Hydraulic Reference Manual; US Army Corps of Engineers*; Report No. CPD-69; Hydrologic Engineering Center (HEC): Davis, CA, USA.

Hatamkhani A., Moridi A., Haghighi A. T. 2023a *Incorporating ecosystem services value into the optimal development of hydropower projects.* Renewable Energy, Volume 203, 495-505. https://doi.org/10.1016/j.renene.2022.12.078

Hatamkhani A., Shourian M., Moridi A. 2021 *Optimal Design and Operation of a Hydropower Reservoir Plant Using a WEAP-Based Simulation–Optimization Approach*. Water Resources Management, Volume 35, 1637–1652. https://doi.org/10.1007/s11269-021-02821-7

Hatamkhani A., Moridi A., Randhir T. O. 2023b *Sustainable planning of multipurpose hydropower reservoirs with environmental impacts in a simulation–optimization framework*. Hydrology Research, Volume 54 (1). 31–48. https://doi.org/10.2166/nh.2022.084
Jia T., Qin H., Yan D., Zhang Z., Liu B., Li C., Wang J., Zhou J. 2019 *Short-term multi-objective optimal operation of reservoirs to maximize the benefits of hydropower and navigation*. Water, Volume 11(6), 1272. https://doi.org/10.3390/w11061272
Moura De Figueiredo N., Cavalcante Blanco C.J., Pinheiro Campos Filho L.C., Amarante Mesquita A.L. 2023 *Muwos - multiple use water optimization system for the power generation and navigation trade-offs analysis.* Renew. Energy 203, 205–218. https://doi.org/10.1016/j.renene.2022.12.004
Tianlong J., Jianzhong Z. 2018 *A daily power generation optimized operation method of hydropower stations with the navigation demands considered.* MATEC Web of Conferences International Symposium on Water System Operations (ISWSO 2018), Volume 246. https://doi.org/10.1051/matecconf/201824601065
Xiangyu M., Shengli L., Benxi L., Hongye Z., Chuntian C., Huaying S. 2023 *Multi-objective solution and decision-making framework for coordinating the short-term hydropeaking-navigation-production conflict of cascade hydropower reservoirs*. *Journal of Cleaner Production,* Volume 422. https://doi.org/10.1016/j.jclepro.2023.138602
Yizi S., Xiaofei L., Xuerui G., Yanxiang G., Yuntao Y., Ling, S. 2017 *Influence of Daily Regulation of a Reservoir on Downstream Navigation.* Journal of Hydrologic Engineering, Volume 22, Issue 8. https://doi.org/10.1061/(ASCE)HE.1943-5584.0001522

SAFETY ASSESSMENT OF HYDRAULIC STRUCTURES USING RISK ANALYSIS

Jaromír ŘÍHA [1*]

[1] *Brno University of Technology, Faculty of Civil Engineering, Dept. of Water structures, Czech Republic*

E-mail: Jaromir.Riha@vut.cz

[*] *Corresponding author*

Abstract

The paper gives a comprehensive summary of the research carried out in the field of safety and risk analysis of natural and dam-break floods in the Department of Hydraulic Structures, at the Brno University of Technology. In the period until 2010 the prerequisites were created for the compilation of guidelines for the implementation of risk analysis in the field of protection against natural floods. In parallel, risk analysis of hydraulic structures, especially dams, was studied. In the period from 2008 to 2024, a number of tasks related to the implementation of risk analysis at water retaining structures was elaborated. These include: (1) modelling dam failure due to overtopping and piping, study of the resistance of earth materials subject to flow, derivation of the dam break hydrograph; (2) internal erosion in soils, the study of the erodibility of sands and the process of backward erosion piping in embankments and their foundations; (3) assessment of impacts in the area of loss of human life during floods; (4) spatial analysis of hazard due to flooding and seepage using GIS; and (5) developing methodology for combining risk in the material sphere, loss of human life and operational impacts. From the list of particular problems, two examples of risk based approach at the safety of hydraulic structures in the Czech Republic are shown and discussed, namely the assessment of the financial efficiency of emergency spillway rehabilitation at the dam Šance and the tolerability of losses of human lives when assessing flood protection in the city of Krnov.

Key words

hydraulic structures, dam safety, flood protection, risk analysis, flood losses.

1 Introduction

Risks in hydraulic engineering are primarily perceived in connection with potential flooding of areas, both due to natural floods and as a result of the failure of water-retaining structures such as dams, protective levees, and flood walls (man-made floods). Although flooding caused by natural and extraordinary floods has its own specific characteristics, the two phenomena often occur in combination, with flooding resulting from the failure of a water control structure during an extreme hydrological event. The methods of risk analysis (RA) are similar in both cases and risk management procedures are also based on similar principles and approaches.

In recent decades, significant progress has been made in European countries regarding natural floods, particularly in connection with the implementation of Directive 2007/60/EC of the European Parliament and of the Council on the assessment and management of flood risks. The concept of assessing protection against natural floods and the associated risks is thus well-defined and has been implemented for more than 20 years (Říha et al., 2005; Dráb & Říha, 2010; Drbal et al., 2019). Less developed are the tasks related to the application of risk analysis in the safety assessment of hydraulic structures, the failure of which could lead to the occurrence of a dam-break flood.

Hydraulic structures damming water belong among the most significant engineering works. The function of these structures, which is primarily to retain a significant amount of water (or other material),

imposes high demands on their safety and reliability. These demands stem from the far-reaching impacts and potentially catastrophic damage in the event of a critical failure of the damming structure.

The risk of failure stems from a number of factors, including in particular:

- deficiencies in the water structure itself resulting from:
  - the complexity and limited predictability of the natural conditions,
  - defects and errors in the design of the structure,
  - deficiencies in construction,
  - deficiencies in the operation and maintenance of the structures,
- negative human factors, e.g., operational failures, improper handling, intentional damage, and others,
- negative environmental impacts, e.g., erosion and abrasion, natural floods, landslides, etc.,
- aging of the materials and technological components used.

The types of failures in hydraulic structures and the circumstances leading to them have been examined in a number of studies on the design, construction, and operation of hydraulic structures, drawing on historical records and experience (DSO, 1992; Singh, 1996; Bulletin 99, 1995; Bulletin 111, 1998; Bulletin 130, 2005; Wahl, 1998; Jandora & Říha, 2008; Bernard-Garcia & Mahdi, 2020). The assessment of failures, safety, and risks of hydraulic structures remains a crucial issue worldwide. In many countries, the safety assessment of hydraulic structures using risk analysis is incorporated into national regulations (e.g. CFBR, 2015).

In the assessment of the safety and reliability of hydraulic structures, traditional methods based on the safety factor or the partial factor method (Frank et al., 2004; Bond et al., 2013) still predominate. Formalized procedures for risk analysis and risk management are used only sporadically and rather exceptionally in our context. The wider use of contemporary reliability analysis methods in the field of hydraulic engineering continues to face challenges related to securing and providing accessible data; it is often difficult to find the financial resources to carry out time-consuming analyses.

In this study, two practical examples of risk based approach at the safety of hydraulic structures in the Czech Republic are shown and discussed, namely the assessment of the financial efficiency of emergency spillway rehabilitation at the dam Šance and the tolerability of losses of human lives when assessing flood protection in the city of Krnov.

2 Methods

2.1 Definition of Risk

Most often, the risk is expressed as the "probability of an undesirable event" which results in adverse effects on life, health, property, or the environment. Risk is then the combination of hazard, vulnerability, and exposure.

If the continuous distribution of the consequences of an adverse event (structural failure, flood event, etc.) and its probability distribution can be expressed, the risk can be defined as follows:

$$RI(\mathbf{D}) = \int_0^\infty C(u|\mathbf{D}) \cdot g(u) \cdot du \tag{1}$$

where $RI(\mathbf{D})$ is the risk, $C(\mathrm{u}\,|\,\mathbf{D})$ is the "continuous" function of consequences, u is an event quantifier dependent on the vector of measures and decisions **D** (structural modifications, operations on the water structure, timely evacuation, etc.), which influences the consequences of an extreme event. $g(u)$ is the probability density of the occurrence of an event (hazard scenario) with consequences $C(\mathrm{u}\,|\,\mathbf{D})$.

Equation (1) expresses the so-called mean (expected) value of risk in the form of average annual damage.

2.2 Risk in material sphere, effectiveness

Risk analysis often includes an assessment of the effectiveness of safety measures using a cost-benefit analysis. This approach is primarily used to assess the "cost-effectiveness" of proposed risk-reduction measures. Applying this approach typically requires the spatial distribution of damages in an area affected by a natural or man-made flood resulting from the failure of a hydraulic structure, as well as the estimation of their magnitude. The necessary tools for these analyses are GIS tools with supporting databases (registers of census districts and economic entities, etc.) and software for evaluating efficiency indicators. Risk analysis is then supplemented by the following steps within the framework of risk management:

- Identifying scenarios involving remedial measures. These involve constructing new flood protection measures, modifying existing spillway, etc. Preliminary design of modifications is required.
- Investment cost estimates for individual risk reduction measures.
- Cost estimates corresponding to flood-related damages for individual hazard scenarios.
- A multi-criteria evaluation of the options and scenarios through a cost-benefit analysis.

The annual expected damage RIR can be determined either by modifying Eq. (1):

$$RI_R = \int_{Q_A}^{Q_B} C(Q) \cdot u(Q) \cdot dQ \tag{2}$$

where RI_R is the average annual economic flood risk, $C(Q)$ is the loss corresponding to the discharge Q, $u(Q)$ is the probability density of annual peak discharges, Q_A is the discharge with a return period A at which losses begin (harmless discharge given, for example, by the channel or spillway capacity), Q_B is the extreme discharge with a return period B, at which the probability of the loss es is already close to zero (e.g., a discharge corresponding to return period $N >> 10{,}000$ years).

Here, the damage $C(Q)$ represents the sum of damages across all categories of objects affected by the flood:

$$C(Q) = \sum_{j=1}^{PK} C_j(Q) \tag{3}$$

where PK is the number of categories or types of structures or areas affected by the flood.

Using a hydraulic model, flood characteristics in the affected area are determined for individual hazard scenarios. These characteristics include local water depth and velocity. The direct loss in a given area is derived from these characteristics using so-called damage curves. Flow-related loss $C(Q)$ can be related to its return period N, i.e. $C(N)$. Equation (3) then takes the form:

$$RI_R = \int_{A}^{B} C(N) \cdot \mathrm{d}N \tag{4}$$

The integral in equation (4) is calculated numerically based on the assumption, derived from the shape of the N-year flow curve, that the damage $C(N)$ is linearly dependent on the logarithm of the return period in intervals corresponding to individual values of N_i (Fig. 1), for which the damage $C_i(Ni)$ is determined. In natural flood protection, the standard return periods are $N = 5$, 20, 100, and 500 years; for hydraulic structures, the return periods are selected individually up to $N = 10{,}000$ years.

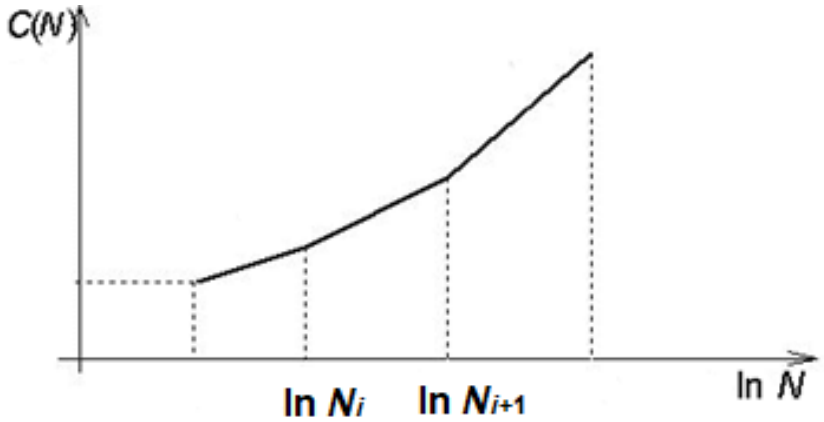


Figure 1. Diagram illustrating the derivation of the average annual risk

For further evaluation, the present value of risk RI_S (total loss, capitalized risk) is determined:

$$RI_S = RI_R \cdot \frac{1-(1+DS)^{-T_0}}{DS} \tag{5}$$

where DS is the discount rate, and T_0 is the length of the evaluation period in years. For water related projects, the USACE recommended a discount rate of 7% in 2016; the Czech National Bank reports a discount rate ranging from 3.5% to 5.25% for 2024 (CNB, 2024).

In studies conducted between 2002 and 2008, a discount rate of 3% was used. The length of the evaluation period T_0 depends on the technical lifespan of the structure. In preliminary evaluations of hydraulic structures with a long lifespan of more than 100 to 500 years (e.g., the Jordán Pond and other historical structures), the length of the evaluation period is often not taken into account for simplicity:

$$RI_S = \frac{RI_R}{DS} \tag{6}$$

As part of the cost-benefit analysis, indicators are used to compare the loss with the costs of measures. Suitable indicators include:

The ratio EF_P expresses the relative economic efficiency of an investment. It represents a ratio of the reduction in the present loss to the total investment cost of the measure:

$$EF_P = \frac{RI_{s_PRED} - RI_{s_PO}}{I} \tag{7}$$

where RI_{S_RED} an RI_{S_PO} are the present value of risk before and after the measure is implemented. I represents the total investment costs of implementing the measure (If the indicator is greater than 1, the investment is profitable in the long term).

The absolute efficiency EF_A expresses the efficiency of the investment in absolute monetary units:

$$EF_A = \left(RI_{s_PRED} - RI_{s_PO}\right) - I \tag{8}$$

The indicator expresses the total long-term financial effect of the proposed measure in monetary units. Positive values of the indicator indicate the economic profitability, while negative values indicate the economic disadvantage of implementing a measure. The indicator is used to compare the effect of measures with the same EF_P. It is particularly relevant for large investments.

The period T_n is used to compare the payback of individual measures with values based on experience:

$$T_n = \frac{I}{RI_{R_PRED} - RI_{R_PO}} \tag{9}$$

where RI_{R_PRED} and RI_{R_PO} denote the average annual risk before and after the implementation of the measure.

2.3 Risk of loss of life

In addition to considerations of the economic effectiveness of measures reducing the risk, it is important to assess the risk of loss of life. Risk analysis in this area includes the following steps:

- estimation of the number of people at risk (*PAR* - Population At Risk),
- estimation of the number of fatalities (*LOL* - Loss Of Life),
- estimation of the number of fatalities (*LOL* - Loss Of Life),
- assessment of the acceptability of loss of life using F-N diagrams,
- analysis ALARP (As Low As Reasonably Practicable).

The population at risk *PAR* is derived from the distribution of residential and industrial buildings in the affected (flooded) area. Similarly to the assessment of material damage, for each hazard scenario it is necessary to analyse the parameters of the flood wave (Říha & Kotaška, 2019) and to determine total number of inhabitants in the affected area.

When estimating the number of human lives lost *LOL*, or the annual expected number of fatalities E(*LOL*), factors reducing *PAR* are used. They express the main factors that can influence the number of fatalities, namely the hazard, posed by the flood characteristics (water depth and velocity, etc.), warning and preparedness of inhabitants, including conditions for evacuation, etc. The number of fatalities can be estimated using techniques mentioned in the available literature [Brown, Gosden 2002], [Brázdová, Říha, 2014].

The societal risk RI_{OR} is expressed by annual expected number of fatalities E(I):

$$RI_{OR} = \mathrm{E}(LOL) = \int_0^\infty LOL \cdot \mathrm{d}F(LOL) \tag{10}$$

where $F(LOL)$ is distribution function of the loss *LOL*. The integral in equation (10) is calculated numerically.

the acceptability of risk of loss of life is assessed via so-called *F-N* curves, which graphically illustrate the relationship between the annual probability of exceeding $p = G(LOL) = 1 - F(LOL)$ and the number of losses of life *LOL*.
The exceedance probability $p = G(LOL)$can be evaluated using the formula:

$$p = 1 - e^{-\frac{1}{N}} \tag{11}$$

where *N* is the return period.

In the following text the notation *F* and *N* used in the literature for the frequency and number of victims has the meaning *G* (probability) and *LOL* (loss of life), see Fig. 2.

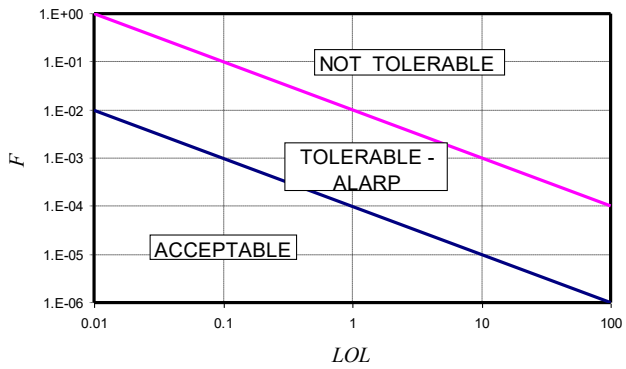


Figure 2. The concept of *F-N* curves

F-N diagrams are typically divided into three zones (Fig. 2):

- Acceptable risk represents the level that the society is prepared to accept. No additional measures are required.
- Tolerable risk is an agreed level of risk determined in order to ensure certain profits. It expresses the belief that the risk is adequately managed, is under control and is possibly reduced. If further risk reduction is difficult or financially demanding, the ALARP (As Low As Reasonably Practicable) analysis must be performed. The description of the analysis is beyond the scope of this study.
- Intolerable risk - risk-reduction measures must be adopted.

The margins between zones were developed for the Czech Republic within past research (Drbal et al., 2011). The relations for the acceptable risk RI_P and tolerable risk RI_T are expressed via the corresponding constants C_P and C_T using so-called "aversion factors", k_P and k_T:

$$RI_P = G_P(LOL) \cdot LOL^{k_P} = C_P; \qquad RI_T = G_T(LOL) \cdot LOL^{k_T} = C_T \tag{12}$$

where $G_P(LOL)$ and $G_T(LOL)$ are the exceedance probabilities for acceptable and tolerable risk, respectively.

Based on experience from other fields and countries the constants proposed for the Czech Republic are as follows:

$C_P = 10^{-3}$, for $LOL = 1$, $C_P = 10^{-5}$, for $LOL = 10$, $k_P = 2$,
$C_T = 10^{-1}$, for $LOL = 1$, $C_T = 10^{-4}$, for $LOL = 100$, $k_T = 1.5$.

3 Case studies

3.1 Quantitative risk and cost effective analysis for the dam Šance

The floods in 1997 showed insufficient capacity of the emergency spillway at the dam Šance (Fig. 3). To justify the designed arrangement, quantitative risk analysis with subsequent cost benefit analysis was carried out. The dam break analysis and the modelling of the dam break propagation indicated the area 126.6 km^2 endangered by flooding due to the Šance dam collapse, the area of the affected buildings is 42.0 km^2, approximately 86,000 inhabitants are at risk. The flood wave would propagate to lower-lying Poland only to a limited extent, the impacts on the territory of Poland are not taken into account in the analysis. The estimated investment costs for the reconstruction of the Šance dam were 420 mill. CZK. An extent of the affected area is shown in Fig. 4. The losses caused by the dam-break flood wave were determined using damage curves derived for the assessment of hydrological floods. These were modified for the assessment of the effects of the dam-break flood so that in cases where the water depth exceeded 3 m or the flow velocity was greater than 5 m/s, the complete destruction of the affected structures was considered. The total material loss was determined to be approximately CZK 99.288 billion. It can be assumed that the actual damage would be somewhat higher due to the propagation of the extraordinary flood in Poland and also to the unaccounted indirect damage. The cost-benefit analysis was based on the above-mentioned analysis of impacts and derived damage.



Figure 3. Insufficient capacity of the spillway at the dam Šance

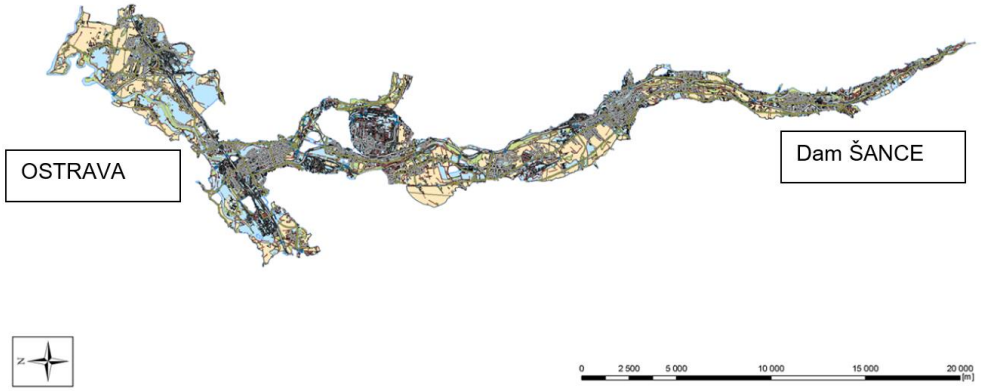


Figure 4. Affected area by the collapse of the Šance dam

The probability of losses was determined using the following input assumptions:

- currently, a dam breach corresponds to a return period of $N = 2000$ years, which corresponds to the current capacity of the spillway,
- the analysis considered a single hazard scenario, which is a dam break due to overtopping, technical and safety supervision did not indicate a risk of another type of failure (internal erosion, loss of stability),
- losses start at the hydrological discharge corresponding to a return period of $N = 1000$ years, the losses increase linearly from zero at $N = 1000$ years to a total loss (CZK 99 billion) during the inflow into the reservoir with a probability corresponding to $N = 2000$ years. The dependence of flood damage on the return period N is shown in Fig. 5.

The values of individual economic indicators were determined using the procedure described in Chapter 2.2, Eq. (7), (8), (9). The summary of the results including economic indicators is in Tab. 1. It can be seen that the cost-benefit analysis has demonstrated a high profitability of the reconstruction of the spillway, with the return on investment corresponding to approximately 6 years and the absolute efficiency approaching CZK 2 billion.

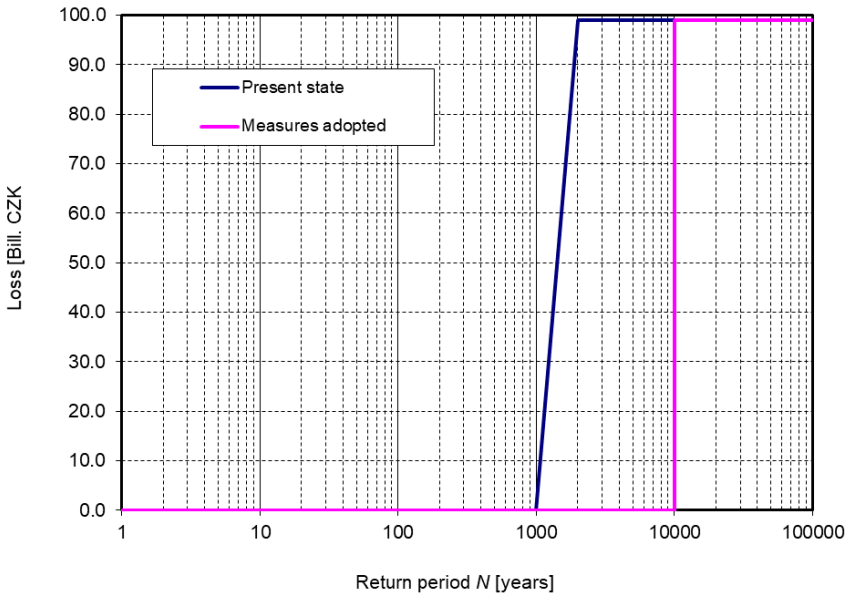


Figure 5. The dependence of flood damage on the return period N

Table 1. Results of cost benefit analysis for the Šance dam reconstruction

	Before improvement	After reconstruction	Units
Average annual risk (RI_R)	80,632	8,887	[mill. CZK/year]
Discount rate (DS)	3%	3%	
Capitalised risk (RI_S)	2687,722	296,222	[mill. CZK]
Investment cost (I)	0	420,000	[mill. CZK]
Relative effectiveness (EF_P)	5,694		[-]
Absolute effectiveness (EF_A)	1971,500		[mill.CZK]
Repayment period (T_n)	6		[years]

3.2 Loss of life assessment for the town of Krnov

For the demonstration of the loss of life assessment, the town of Krnov, which lies on the Opava River in the north of the Czech Republic was chosen. The analysis was carried out for floods corresponding to the return periods $N = 2, 5, 10, 20, 50, 100$ and 500 years. The exceedance probability was evaluated using Eq. (11). For the assessment, for individual flood scenarios flooded area, LOL and $p = G(LOL)$ were determined according to [Brázdová, Říha, 2014]. The dependence $p = G(LOL)$ was plotted on a logarithmic scale in a so-called F -N ($G(LOL)$ - LOL) diagram and compared with acceptable and tolerable risk margins (Fig. 6).

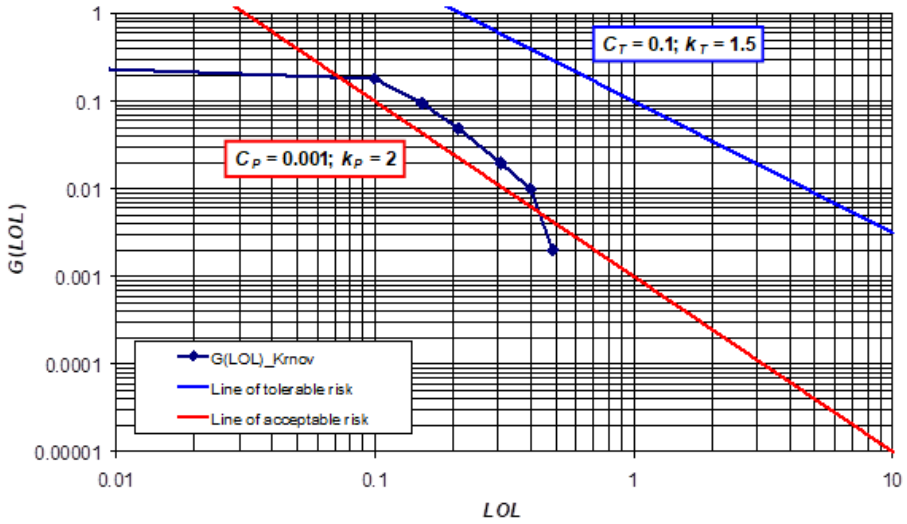


Figure 6. F-N curve for the Krnov locality

Figure 6 shows that floods with return periods of 5 to 100 years do not agree with the acceptable risk requirements. Based on the analysis, in this case the acceptable risk for the locality will be guaranteed by the newly prepared flood-protection scheme including the dam Nové Heřminovy at the Upper Opava river.

4 Conclusions

In the paper, theoretical background for the quantitative risk analysis both in material and societal sphere are described. The risk based approaches are demonstrated on two examples in the Czech Republic, particularly at the safety improvement of the dam Šance and at the assessment of the flood protection in the city of Krnov.

The analysis shows the necessity of risk reduction in both cases. The reconstruction of the spillway at the Šance dam shows high rentability and small repayment period of the investment. The loss of life analysis in the Krnov municipality indicates the need of risk reduction which is currently in progress when preparing the Nové Heřminovy scheme which should provide 100-years flood protection of the Krnov town.

Acknowledgements

This study is the part of the project TACR SS07010401 *Water management analysis of restoring natural floodplains and increasing the transformation effect of floodplains*.

References

Bernard-Garcia, M. & Mahdi, T.-F. 2020 A Worldwide Historical Dam Failure's Database. Https.//DOI.ORG/10.5683/SP2/E7Z09B, Scholars portal dataverse, V1.
Bond, A., Schuppener, B., Scarpelli, G. & Orr, T. 2013 Eurocode 7: Geotechnical Design Worked examples. JRC, Luxembourg, 2013, 172 s.
Brázdová, M. & Říha, J. 2014 A Simple Model for the Estimation of the Number of Fatalities Due to Floods in Central Europe. *Natural Hazards And Earth System Sciences*, 14, 1663–1676.
Brown, A. J. & Gosden, J. D. 2015 Interim guide to quantitative risk assessment for UK reservoirs. Thomas Telford, London.
Bulletin 99. 1995. Dam Failures Statistical Analysis. ICOLD Bulletin No. 99, Paris, France.

Bulletin 111. 1998. Dam Break Flood Analysis. ICOLD Bulletin No. 111, Paris, France.
Bulletin 130. 2005. Risk Assessment in Dam Safety Management, a Reconnaisance of Benefits, Methods and Current Applications, ICOLD Bulletin No. 130, Paris, France
CFBR, 2015. *Recommandations pour la justification de la stabilité des barrages et des digues en remblai*, Octobre 2015, 132 s.
CNB. 2024. *Discount rate development.* https://www.cnb.cz/cs/casto-kladene-dotazy/Jak-se-vyvijela-diskontni-sazba-CNB/.
Directive. 2007. Directive 2007/60/EC of the European Parliament and of the Council of 23 October 2007 on the assessment and management of flood risks.
DNRM 2002 *Queensland Dam Safety Management Guidelines.* Department of Natural Resources and Mines. 2/2002.
Dráb, A. & Říha, J. 2010. The implementation of flood risk directive in the CR. *Nat. Hazards Earth Syst. Sci.*, 10, 1977–1987
Drbal, K. et al. 2011 *Risk maps resulting from flood danger in the Czech Republic*. Final report. Brno (In Czech)
Drbal, K. ed. 2019 *Guidelines for the development of flood hazard and risk maps*. VÚV T.G.M. Brno. (In Czech).
DSO. 1992 *Technical note 1 – Dam break inundation analysis and downstream hazard classification.* Dam Safety Office. Olympia, Washington, USA. 34 p.
Frank, R., Bauduin, C., Driscoll, R., Kavvadas, M., Ovesen, N. K., Orr, T. & Schuppener, B. 2004 *Designers' Guide to EN 1997-1 Euro-code 7: Geotechnical Design - General Rules*, Thomas Telford, 2004, 232 s.
Jandora, J. & Říha, J. 2008 *The Failure of Embankment Dams due to Overtopping*, VUTIUM.
Říha, J. ed. 2005 *Flood risk analysis,* Monographs of the Department of Hydraulic Structures, FCE, BUT Brno. Vol. 7
Singh, V. P. 1996 *Dam Breach Modeling Technology.* Louisiana State University, Kluwer Academic Publishers, Baton Rouge, USA, Dodrecht
USACE. 2016 *Discount Rates in the Economic Evaluation of U.S. Army Corps of Engineers*, CRS Report R44594, 41 p. https://crsreports.congress.gov.
Wahl, T., L. 1998 *Prediction of Embankment Dam Breach Parameters.* Dam Safety Research Report, DSP-98-004, Water Resources Research Laboratory

ADAPTIVE DISCRETIZATION FOR 3D BRIDGE FLOW WITH SCALE-RESOLVING AIR-WATER MULTIPHASE SIMULATION

Jiří SKOKAN [1*], David DUCHAN [1], Aleš DRÁB [1]

[1] *Brno University of Technology, Czech Republic*

E-mail: Jiri.Skokan@vut.cz

E-mail: David.Duchan@vut.cz

E-mail: Ales.Drab@vut.cz

[*] *Corresponding author*

Abstract

This study presents a computationally optimized approach for simulating 3D air-water flow around a haunched slab bridge deck under three hydraulic regimes: fully overtopped, marginally overtopped, and pressurized. Methodology leverages adaptive mesh refinement and the Scale-Resolving simulation turbulence model to dynamically refine mesh based on free-surface gradients, strain-rate fields, and wall boundary conditions. Experimental validation using Particle Image Velocimetry confirms model's ability to reliably capture flow separation, wake dynamics, and intake vortex formation while achieving approximately 87% fewer cells and 75% less computational time compared to uniform meshing. A custom Python-based post-processing tool ensures consistent time-averaged evaluations on spatially varying meshes. This approach is easily implementable in Ansys Fluent and demonstrates significant efficiency gains for flood-induced bridge hydraulics simulations.

Key words

CFD, adaptive mesh refinement, scale-resolving simulation, bridge flow, computational efficiency, PIV.

1 Introduction

Bridges and other transport infrastructure can significantly alter natural river flow, particularly during flood events, where assessing hydraulic characteristics such as flow capacity, velocity distributions, and pressure fields is critical for ensuring structural safety (Ahmari et al., 2021; Ahmadi and Ahmadi, 2023). Computational Fluid Dynamics (CFD) is an essential tool for resolving the complex multiphase (air-water) flows around bridge decks, where free-surface tracking, velocity gradients, and boundary layer resolution are paramount. However, high-fidelity 3D simulations often require excessively fine meshes, leading to prohibitive computational costs (Menter, 2015).

Traditional approaches rely on global or local mesh refinement, which uniformly increases cell counts without considering local flow features (Roache, 1994). Adaptive Mesh Refinement (AMR) offers a more efficient alternative by dynamically refining regions of interest, such as free surfaces, high strain rates, or near-wall zones, while coarsening less critical areas (Berger and Colella, 1989). This study applies AMR with the Scale-Resolving simulation (SRS) turbulence model (Menter and Egorov, 2010; Menter and Matyushenko, 2025) to simulate three distinct hydraulic regimes around a haunched slab bridge deck: fully overtopped, marginally overtopped, and pressurized flow without overtopping. Results are validated against Particle Image Velocimetry (PIV) measurements and demonstrate substantial improvements in computational efficiency with reasonable accuracy.

2 Methods

This study combines physical modelling and CFD to investigate the flow field around a haunched slab bridge deck under three hydraulic conditions. A laboratory-scale physical model was used to experimentally measure velocity fields using PIV, providing high-resolution reference data. In parallel, a three-dimensional numerical model was developed to simulate corresponding flow conditions using SRS turbulence approaches (Menter and Egorov, 2010). CFD results were compared with experimental measurements to assess the ability of CFD model to reproduce mean flow characteristics, flow separation, and wake development beneath and downstream of bridge deck.

2.1 Physical model

Experiments were conducted in the Laboratory of Water Management Research (LVV) at Brno University of Technology (BUT). A plexiglass flume, 5 meters long and 0.2 meters wide with haunched slab bridge deck. Three hydraulic regimes were investigated, defined by discharge Q and downstream water levels h_d relative to bridge soffit, as summarized in Table 1. PIV measurements used a double-pulse laser (532 nm, 120 mJ) and a 1600 × 1200 pixel camera to capture 2D velocity fields in vertical plane of symmetry (Dantec Dynamics, 2006). Polyamide seeding particles (100 μm, 1050 kg/m³) ensured accurate flow tracing.

Table 1. Hydraulic conditions for the physical model experiments during overtopping regime

Regime	Q (l/s)	h_b[1)] (mm)	h_d[2)] (mm)	Re[3)] (-)
A – fully overtopped	12.4	120	156	~ 24 000
B – Marginally overtopped	8.7	120	139	~ 18 000
C - Pressurized	6.4	120	130	~ 14 000

[1)] distance between bridge deck and bottom
[2)] tailwater depth relative to bottom
[3)] Reynolds number (Batchelor, 2000)

In Regime A, fully overtopped condition, upstream water level significantly exceeded deck elevation, resulting in strong flow separation beneath deck and a highly turbulent wake downstream. Regime B, marginally overtopped condition, exhibited reduced separation and a shorter wake, representing transitional behavior between free-surface overflow and pressurized flow. In Regime C, pressurized condition, water level remained below top of bridge deck, and flow passed entirely beneath deck, dominated by confined acceleration and pressure-driven effects with minor separation.

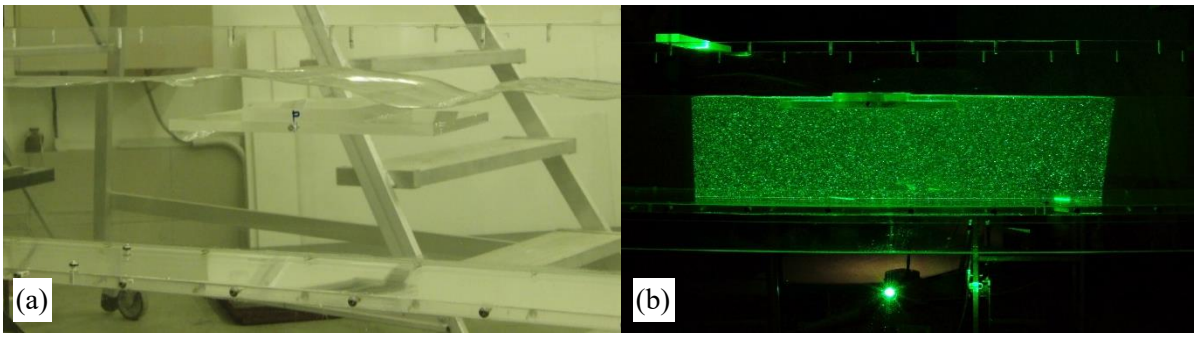


Figure 1 (a) Experimental setup with submerged bridge deck. (b) Flow visualization using PIV: laser sheet illumination of seeding particles around bridge deck cross-section.

2.2 CFD model

Flow was modeled as a 3D, incompressible, turbulent flow of a Newtonian fluid under influence of gravitational forces (Batchelor, 2000). Multiphase flow was captured using explicit Volume of Fluid

(VOF) method (Youngs, 1982), while turbulence was modeled using the Scale-Adaptive Simulation (SAS) model coupled with Generalized *k-ω* (GEKO) model. Surface tension and wall adhesion were modeled according to Brackbill et al. (1992). System of equations was solved using a pressure-based finite volume method (FVM) with a pressure-velocity coupled solver (Darwish and Moukalled, 2008). Computational domain Ω (Fig. 2) was designed to minimize influence of artificial boundary conditions on flow field around bridge deck. At inlet boundary Γ_I, a velocity profile based on the logarithmic law of the wall (Schlichting and Gersten, 2000) was prescribed along with water volume fraction. Outlet boundary Γ_O was defined by a hydrostatic pressure distribution corresponding to downstream water level, including specification of water volume fraction in regions of possible backflow. The open boundary Γ_A was set to atmospheric pressure, while all solid boundaries, including channel walls Γ_W and bridge deck Γ_B, were modeled using a no-slip condition and assumed to be hydraulically smooth. Turbulent quantities (such as turbulent kinetic energy k and specific dissipation rate ω) for all non-wall boundary conditions were extrapolated from within domain, using nearest cells.

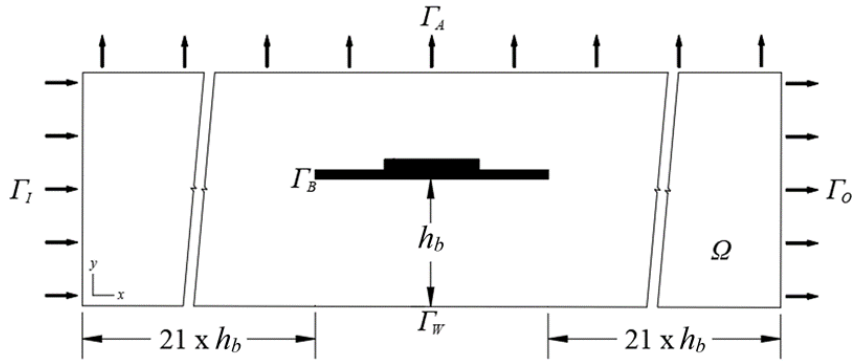


Figure 2. Conceptual model of 3D domain (comparison with PIV experiment).

Computational domain was discretized using orthogonally structured hexahedral elements with local refinement applied in regions of strong velocity gradients, flow separation, and free-surface deformation. Rather than uniform refinement, mesh was dynamically adapted based on local flow characteristics using criteria originally proposed by Berger and Colella (1989) and previously applied to multiphase flows by Zeng et al. (2022).

AMR criteria included free-surface tracking based on gradients of water volume fraction, strain-rate adaptation for separation zones, and wall resolution control based on the dimensionless wall distance y^+ (Wilcox, 2006). Mesh refinement was performed symmetrically by splitting orthogonal cells (ANSYS, 2026) into four sub-cells (Fig. 3). Base mesh spacing was 0.01 m, with a minimum resolution of 6.25×10-4 m at refinement level 4.

- For free-surface tracing:

Refine if:
$$\frac{\partial \alpha}{\partial x_{ij}} > 0.06 \tag{1}$$

Coarsen if:
$$\frac{\partial \alpha}{\partial x_{ij}} < 0.05 \tag{2}$$

- For strain rate (scaled by maximum), thus separation tracing:

Refine if:
$$\alpha \geq 0.5 \text{ and } \frac{\partial \left(S_{ij}/S_{max}\right)}{\partial x_{ij}} > 0.06 \tag{3}$$

Coarsen if:
$$\frac{\partial \left(S_{ij}/S_{max}\right)}{\partial x_{ij}} < 0.05 \tag{4}$$

where α is water volume fraction.

- And adjusting y^+ values as (except for separation zone, strain rate tracing has priority):

Refine if: $\alpha \geq 0.5$ and $y^+ > 100$ (5)

Coarsen if: $y^+ < 30$ (6)

These conditions were integrated into software using user-defined expressions. Strain rate and y^+ tracing works by definition in water phase only.

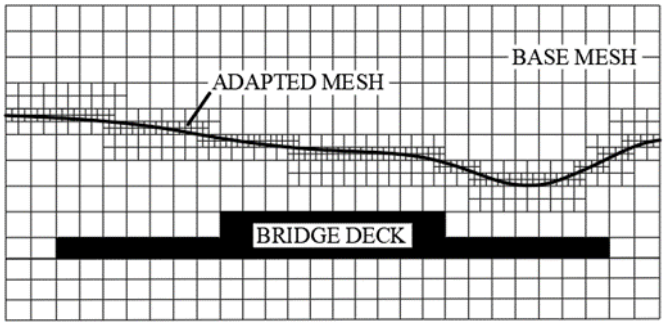


Figure 3. Example of adaptive mesh for free surface tracking.

To handle time-varying AMR meshes, a Python-based multi-layer averaging grid method was developed. Reference domain was discretized using 2500 points in longitudinal direction and 500 points in vertical direction. Instantaneous velocity components were interpolated from the unstructured AMR mesh onto this structured grid using Inverse Distance Weighted (IDW) interpolation of scattered data (with power parameter $P = 1$) (Shepard, 1968). Reconstructed fields were used to compute spatial-temporal statistics, including time-averaged velocities. This procedure enabled consistent evaluation of time-averaged flow features independently of evolving AMR mesh.

3 Results and Discussion

SAS model with AMR acceptably reproduced key flow features across all three regimes. In Regime A, fully overtopped condition, model captured strong flow separation reasonably well beneath deck (Fig. 4). Model is somewhat inaccurate in wake region at lower end of bridge deck, where it poorly predicts velocity recovery.

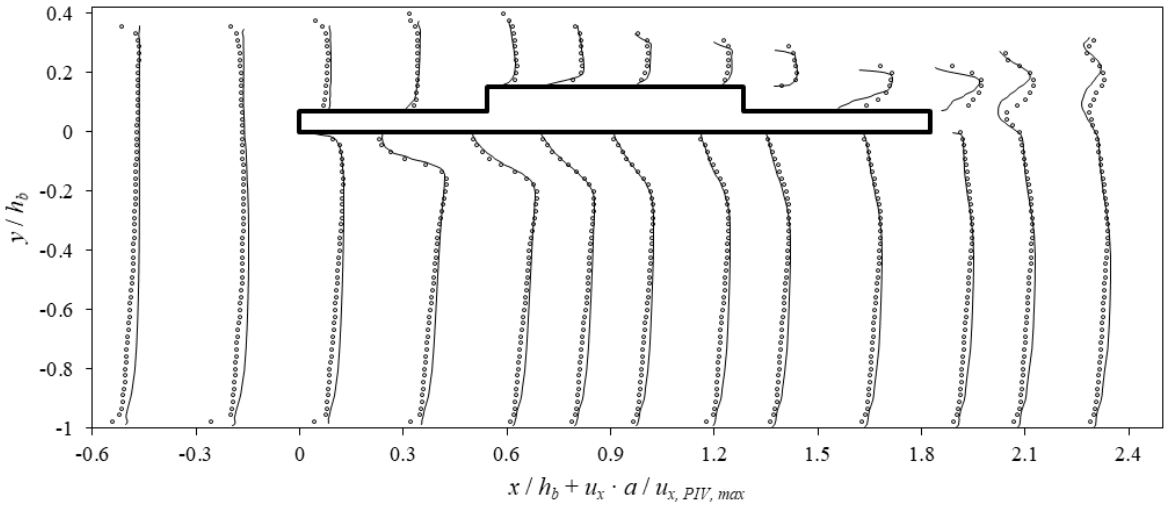


Figure 4. Regime A: Time-averaged x-velocity u_x (— CFD, ○ PIV, $a = 6$).

For Regime B, marginally overtopped condition, model closely reproduced reduced separation beneath deck and shorter wake compared to Regime A and additionally captured vortex formation at inlet (Fig.

5), but did not capture reattached air under bridge deck (Fig. 6).

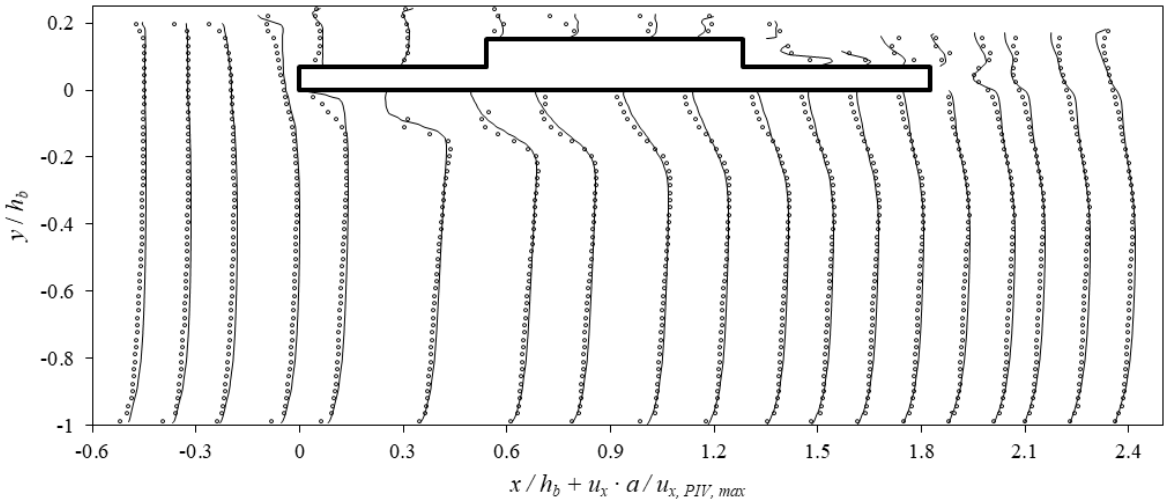


Figure 5. Regime B: Time-averaged x-velocity u_x (— CFD, ○ PIV, a = 6)).

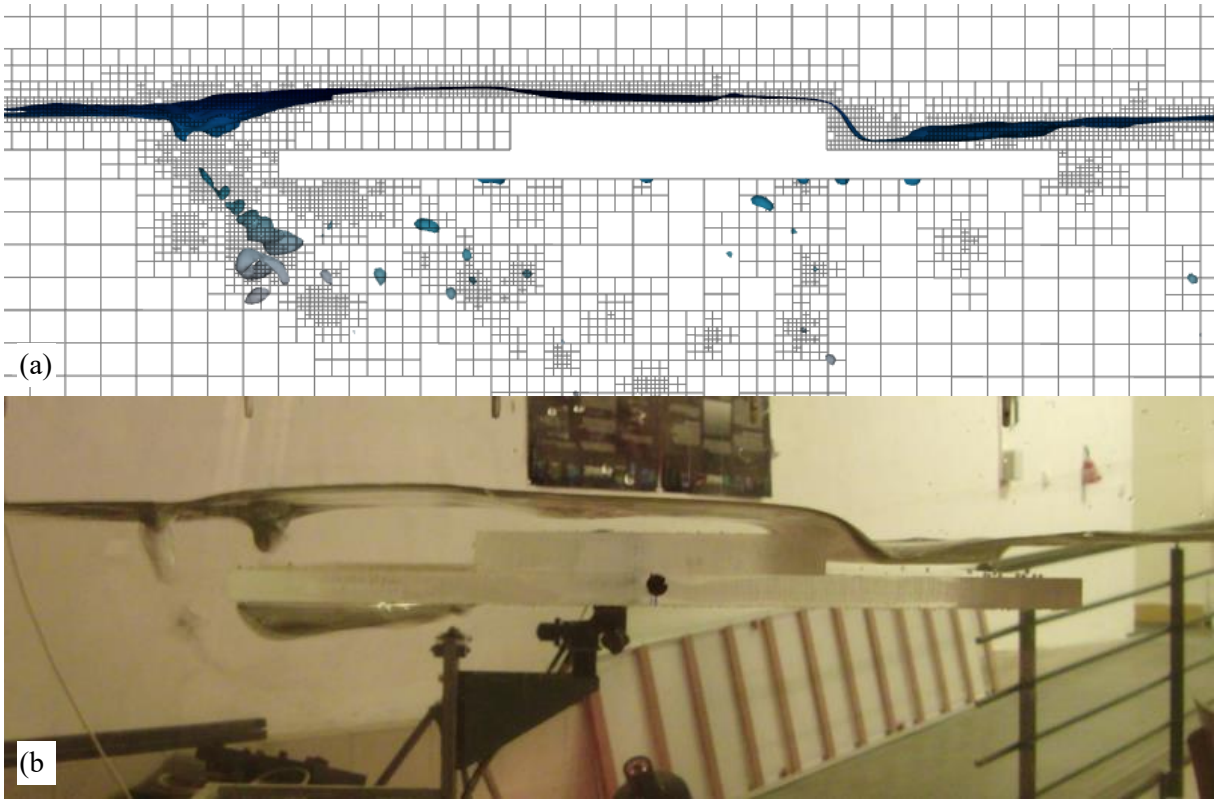


Figure 6. (a) Tracing the free surface with AMR, resolved intake vortex in CFD, but unresolved reattached air under bridge deck. (b) Intake vortex and reattached air under bridge deck in physical experiment.

In Regime C with pressurized flow condition, model captured flow entirely beneath the deck, dominated by confined acceleration and pressure-driven effects, as well as small localized separation beneath deck soffit (Fig. 7).

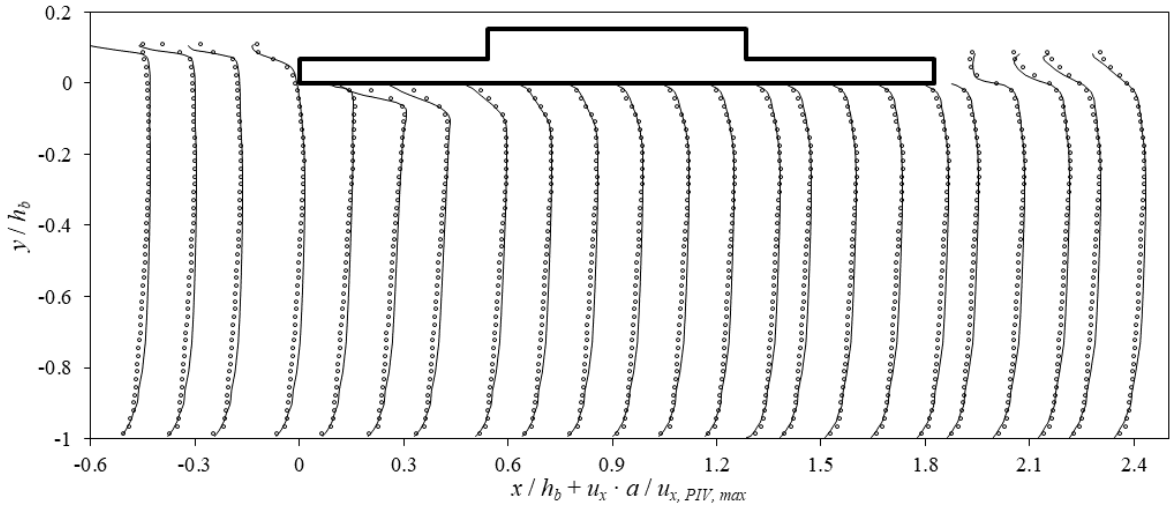


Figure 7. Regime C: Time-averaged x-velocity u_x (— CFD, ○ PIV), a = 6).

Fig. 8 illustrates ability of adaptive mesh to trace free surface, separation beneath deck and in negative step of the upper deck, and the downstream wake.

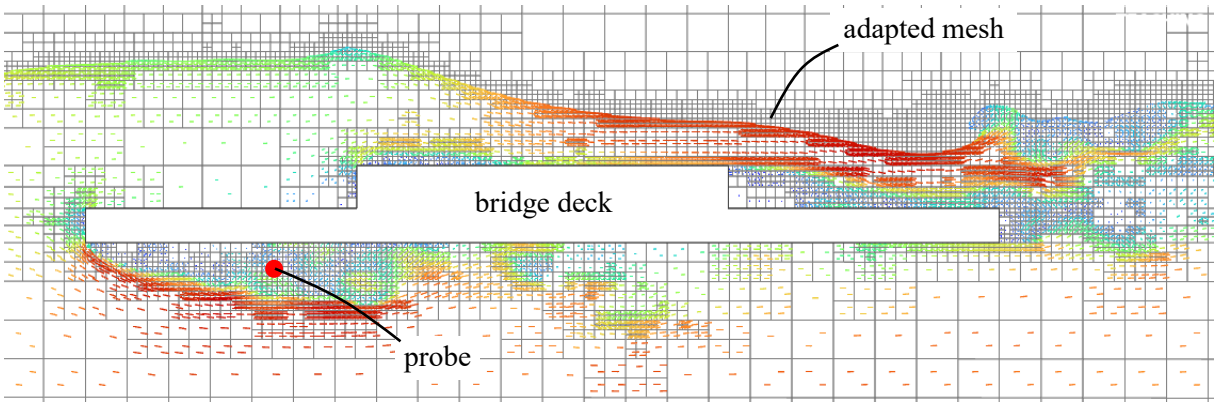


Figure 8. Resolved free surface separation and wake dynamics as colored velocity vectors.

Velocity fluctuations were assessed based on distribution of local deviations. Histograms of velocity deviations at selected probe locations (for example in Fig. 8) exhibit a symmetric profile centered around zero, indicating an unbiased statistical sample with no or minimum net mean offset (Fig. 9).

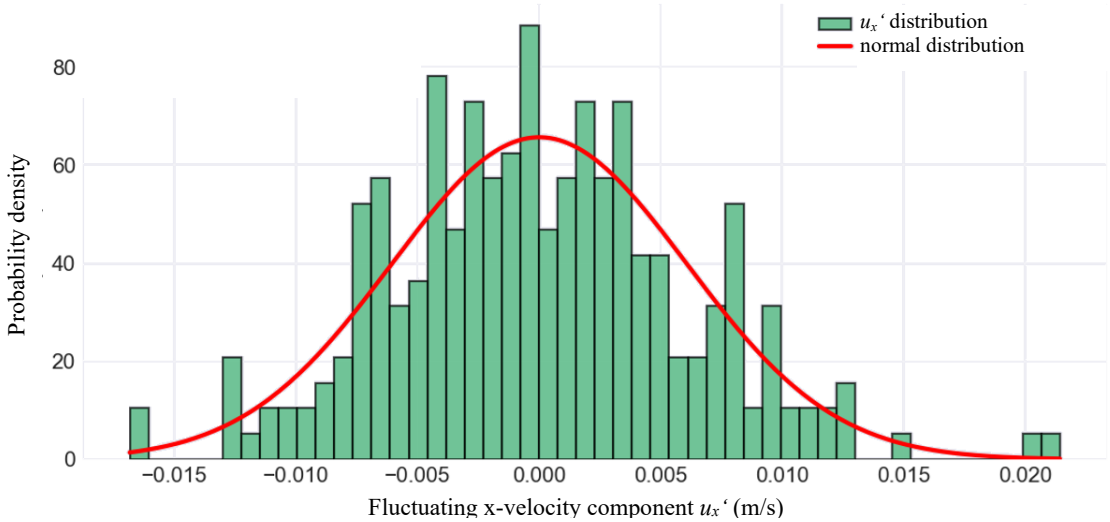


Figure 9. Resolved fluctuating x-velocity u_x' component in studied fully developed turbulent flow

Furthermore, temporal convergence was evaluated by computing progressive cumulative averages (Fig. 10). Cumulative mean rapidly asymptotes to a steady value and exhibits negligible subsequent variations, demonstrating that transient simulation is sufficiently resolved in time for robust statistical evaluation.

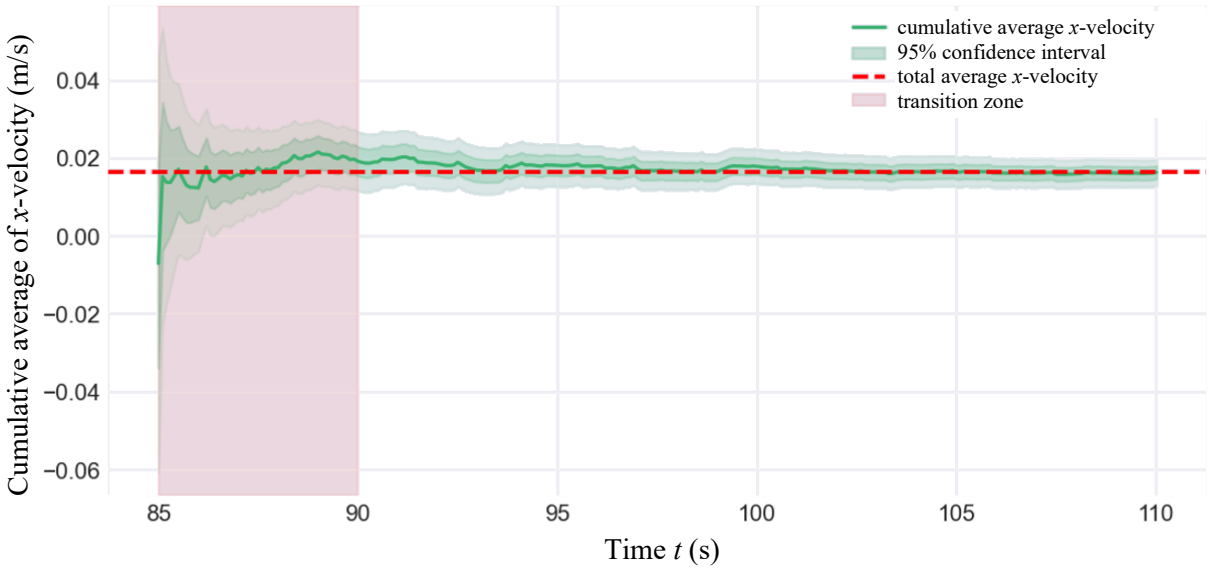


Figure 10. Analysis of time-averaged statistics for *x*-velocity component

Adaptive meshing approach significantly improved computational efficiency across all regimes. Total number of cells was reduced by 87%, computational time by 75%, and memory usage by 60% compared to a uniform mesh (Tab. 2). Calculations on uniform mesh were not completed due to low efficiency, and "computational time" parameter in Tab. 2 was extrapolated from results attained.

The adaptive mesh effectively captured the water-air interface across all regimes. It quite well resolved separation and reattachment zones. Wall resolution was maintained with y^+ values between 30 and 100 near walls and $y^+ \leq 5$ in high-strain regions, ensuring accurate representation of boundary layers and flow separation.

Table 2. Efficiency metrics

Metric	Uniform mesh	AMR	Improvement
Total cells	~ 35 mil.	2 ~ 4.5 mil.	87 ~ 94 % ↓
Computational time (30 s simulation for time-averaged statistics)	288 CPU hours (estimated)	72 CPU hours	75 % ↓
Memory usage (RAM only, without scratch memory)	75 GB RAM	30 GB RAM	60 % ↓

AMR methodology was implemented using User-Defined Expressions (UDEs) in Ansys Fluent. Dynamic mesh adaptation was achieved through UDEs hooks for gradient-based and maximum/minimum value refinement. The GEKO-SAS model was activated with default coefficients, and post-processing was automated via Python scripts for interpolation and averaging.

Steps for replication include defining a base mesh with a spacing of 0.01 m, setting AMR criteria for free surface, strain rate, and y^+, running a transient simulation with adaptive time-stepping (CFL < 1), and applying Python post-processing for time-averaged fields using uniform grid.

4 Conclusion

This study presented a computationally efficient CFD framework for simulating 3D air-water flows around bridge decks under various hydraulic regimes, integrating Scale-Adaptive Simulation (SAS) with dynamic Adaptive Mesh Refinement (AMR). High-fidelity validation against PIV measurements confirmed that the developed AMR criteria successfully captured key flow features - such as free-surface deformation, flow separation, and wake dynamics - while achieving an approximately 87% reduction in cell count and a 75% speedup compared to uniform meshing.

Proposed workflow is straightforward to implement in Ansys Fluent using described UDE configurations and automated Python post-processing. Consequently, it represents a practical tool for large-scale engineering applications in flood-induced bridge hydraulics. Future research will extend this methodology to alternative bridge deck configurations and broader hydraulic structures, with a specific focus on evaluating time-averaged pressure fields and transient dynamic loads, which are subject of research at LVV.

Acknowledgements

This article was elaborated with the support of the project: FAST-S-26-9009 Analysis of flow past hydraulic structures during flood flows.

Computational resources were provided by the e-INFRA CZ project (ID:90254), supported by the Ministry of Education, Youth and Sports of the Czech Republic.

References

Ahmadi, S.M. and Ahmadi, M.T. 2023 Hydrodynamic considerations for improving the design/evaluation of over-topped bridge decks during extreme floods. *Structure and Infrastructure Engineering.* 20(11), 1819-1833.

Ahmari, H., Hummel, M., Chao, S., Imran, S.M., Pervaiz, K.F., Acharya, B.R., Dean, M. and Mowla, Q.A. 2021 *Identify and analyze inundated bridge superstructures in high velocity flood events.* Technical report FHWA/TX-21/0-7068-1, The University of Texas at Arlington, Arlington, USA

ANSYS. 2026 Ansys Fluent [software]. https://www.ansys.com/products/fluids/ansys-fluent

Batchelor, G.K. 2000 *An introduction to fluid dynamics.* Cambridge University Press, Cambridge.

Berger, M.J. and Colella, P. 1989 *Local adaptive mesh refinement for shock hydrodynamics*. Journal of Computational Physics, 53(3), 64-84.

Brackbill, J.U., Kothe, D.B. and Zemach, C. 1992 *A continuum method for modeling surface tension*. Journal of Computational Physics. 100, 335-354.

Dantec Dynamics. 2006 3D stereoscopic PIV Reference manual. Dantec Dynamic A/S, Denmark.

Darwish, M. and Moukalled, I.S.F. 2008 *A coupled finite volume solver for the solution of incompressible flows on unstructured grids*. Journal of Computational Physics. 228(2009), 180-201.

Menter, F.R. 2015 Best Practice: Scale-Resolving Simulations in Ansys CFD. Version 2.00

Menter, F.R. and Egorov, Y. 2010 *The scale-adaptive simulation method for unsteady turbulent flow predictions. Part 1: Theory and model description*. Flow Turbulence Combust. 85, 113-138.

Menter, F.R. and Matyushenko, A. 2025 *Generalized k−ω (GEKO) Two-Equation Turbulence Model.* AIAA Journal, 63(11), 4590-4606.

Roache, P.J. 1994 *Perspective: A method for uniform reporting of grid refinement studies*. Journal of Fluids Engineering. 116, 405-413.

Schlichting, H. and Gersten, K. 2000 *Boundary-Layer Theory*. 8th edn, Springer-Verlag, Berlin.

Shepard, D. 1968 A two-dimensional interpolation function for irregularly-spaced data. In *Proceedings of the 1968 ACM National Conference,* Rosenberg 27–29 August, 517–524.

Wilcox, D.C. 2006 *Turbulence modeling for CFD.* 3rd ed. Birmingham Press, La Cañada
Youngs, D.L. 1982 Time-dependent multi-material flow with large fluid distortion. In: *Numerical Methods in Fluid Dynamics*, K.W. Morton & M.J. Baines (eds.), Academic Press, Aldermarston, pp. 273-285.

UNCERTAINTY QUANTIFICATION OF WAVE TRANSMISSION OF PI-TYPE FLOATING BREAKWATERS

Damjan BUJAK [1*], Veronika MENDEŠ [1], Lovro ŠTEFAN [1], Dalibor CAREVIĆ [1]

[1] *Faculty of Civil Engineering, University of Zagreb, Croatia*

E-mail: damjan.bujak@grad.unizg.hr

E-mail: veronika.mendes@student.grad.hr

E-mail: lovro.stefan@grad.unizg.hr

E-mail: dalibor.carevic@grad.unizg.hr

[*] *Corresponding author*

Abstract

This paper deals with the quantification of uncertainties in wave transmission for π-type floating breakwaters, increasingly applied in the protection of small harbors and marinas. The introduction explains the fundamental concepts of wave climate and the role of the transmission coefficient in assessing structural efficiency. The methodology is based on the application of existing calculation equations and numerical data processing using Sandia Dakota and Python. A total of 24 uncertainty quantification tests were carried out on models 4320BRK and 5320BRK, analyzing different wave, tidal, and geometric conditions. The results show that safety factors SF_{80} and SF_{95} increase in a nonlinear manner, with variations being more pronounced for higher quantiles. It was found that the relative depth parameter (d/L) has a weaker influence on safety factors compared to the width-to-wavelength ratio (w/L), while the transmission coefficient Kt exhibits increased sensitivity in certain regions, while small sensitivity in others. It is concluded that the design of π-type breakwaters requires the application of higher safety factors to ensure functional reliability under conditions of pronounced nonlinearity.

Key words

wave climate, floating breakwater, pontoon, transmission coefficient, safety factor, probabilistic analysis, uncertainty

1 Introduction

Floating breakwaters are increasingly used as an alternative to conventional coastal protection structures, particularly in small harbors, marinas, and recreational waterfront areas. Compared with traditional rubble-mound or vertical-wall breakwaters, floating systems offer several advantages, including lower construction costs, simplified installation, adaptability to varying water depths, and reduced environmental impacts. However, their hydraulic performance is generally more sensitive to changing wave conditions, making reliable prediction of wave attenuation an important aspect of engineering design (Oliver et al., 1994; Hales, 1981).

Incident wave energy interacting with a floating structure may be partially reflected, dissipated through turbulence and friction, or transmitted to the sheltered area behind the breakwater. The proportion of transmitted wave energy is commonly quantified using the wave transmission coefficient, Kt, defined as the ratio between transmitted and incident wave heights. As one of the primary indicators of floating breakwater effectiveness, the transmission coefficient directly reflects the ability of the structure to reduce wave action in protected areas (Ruol et al., 2013; Wiegel, 1960). Previous studies have shown that wave transmission depends on both environmental conditions and structural characteristics,

including wave height, wave period, water depth, breakwater width, and draft depth (Wiegel, 1960; Goda, 2010). Consequently, a proper characterization of wave climate is essential for the design and assessment of floating breakwaters, as it directly affects their protective capacity, durability, and reliability under varying marine conditions (Oliver et al., 1994; Suh et al., 2012). Wave climate therefore provides the link between theoretical predictions, experimental investigations, and real sea conditions, making it a fundamental aspect of coastal structure design and analysis.

Among the various floating breakwater configurations, π-type floating breakwaters have attracted considerable attention due to their improved wave attenuation characteristics. The characteristic geometry consists of a floating pontoon equipped with two submerged vertical plates, which enhance wave energy dissipation and modify wave-structure interactions. As a result, π-type breakwaters generally achieve lower transmission coefficients than conventional pontoon systems (Ruol et al., 2013; Martinelli et al., 2008). Several empirical formulations have therefore been proposed to estimate wave transmission for π-type floating breakwaters and to support preliminary engineering design (Ruol et al., 2013). Experimental investigations have additionally demonstrated the influence of geometric configuration on transmission efficiency and overall hydraulic performance (Martinelli et al., 2008).

Despite the availability of empirical prediction models, uncertainties associated with environmental loading conditions remain an important challenge. Variability in wave heights, wave periods, tides, storm surges, and geometric parameters may significantly influence predicted transmission coefficients and consequently affect the reliability of engineering designs. Traditional deterministic approaches provide a single prediction value and therefore do not adequately represent the variability that exists in real operating conditions (Burcharth, 1992; Schüttrumpf et al., 2007).

Probabilistic methods have increasingly been applied in coastal engineering to quantify uncertainty and assess the reliability of hydraulic structures. Such approaches allow uncertainties associated with input parameters to be propagated through numerical or empirical models, resulting in statistical distributions of predicted responses rather than a single deterministic estimate. Among the available sampling techniques, *Latin Hypercube Sampling* (*LHS*) has proven particularly efficient for uncertainty propagation because it provides good statistical coverage of the input space while requiring fewer simulations than conventional Monte Carlo approaches (Karatzetzou, 2024; Hajihassanpour et al., 2023).
Therefore, the objective of this study is to quantify uncertainties associated with wave transmission predictions for π-type floating breakwaters. A probabilistic framework based on Latin Hypercube Sampling and the Dakota software package is applied to propagate uncertainties in environmental and geometric parameters through an empirical wave transmission model. The resulting probability distributions are used to evaluate safety factors and identify the parameters that most strongly influence transmission behaviour and design reliability.

2 Methods

2.1 Wave transmission model

The hydraulic performance of floating breakwaters is commonly described using the wave transmission coefficient, *Kt*, defined as the ratio between transmitted and incident wave heights:

$$K_t = \frac{H_t}{H_i} \tag{1}$$

where H_t denotes the transmitted wave height behind the structure and H_i represents the incident wave height.

One of the earliest and most widely adopted formulations involving this coefficient was proposed by Macagno (1954) for rectangular breakwaters. The model relates wave transmission to the geometric

characteristics of the structure and the incident wave conditions through the following expression:

$$k_{tM} = \frac{1}{\sqrt{1 + \left[kw \frac{\sinh k\,h}{2\cosh(kh - kd)}\right]^2}} \tag{2}$$

where (k) is the wave number, (w) is the breakwater width, (h) is the water depth, and (d) is the draft of the structure.

The present study focuses on π-type floating breakwaters consisting of a rectangular pontoon equipped with two submerged vertical plates attached to the side walls. These additional plates increase the effective draft of the structure and enhance wave energy dissipation, resulting in improved attenuation performance compared with conventional pontoon-type breakwaters. The geometry of the investigated breakwater configuration is shown in Figure 1.

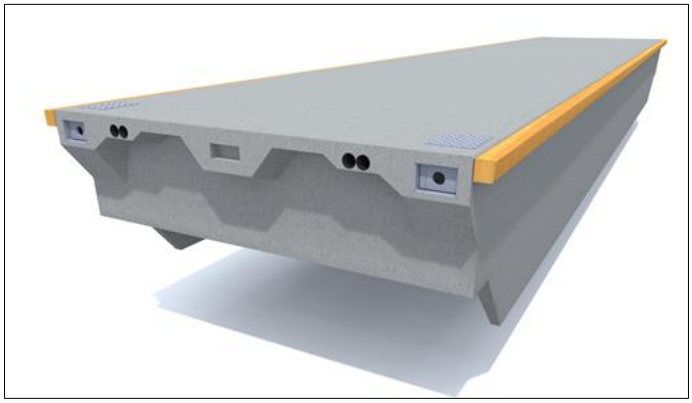


Figure 1. Geometry of the π-type floating breakwater (PIANC, 2003)

Although widely used, the original Macagno formulation does not account for the dynamic response of floating structures and wave radiation effects. Consequently, significant discrepancies may occur when estimating wave transmission through π-type floating breakwaters. To overcome these limitations, Oliver et al. (1994) proposed a modified empirical approach in which the interaction between wave characteristics and structural dynamics is represented through a dimensionless parameter based on the ratio between the peak wave period, T_p, and the natural heave period of the structure, T_n, which corresponds to the natural period of vertical oscillation of the floating breakwater. Since T_n cannot be determined directly due to the complex geometry of π-type floating breakwaters, a simplified approximation based on the dynamic characteristics of the system was adopted. The natural circular frequency of vertical oscillation is given by:

$$\omega_h = \sqrt{\frac{K}{M}} \tag{3}$$

where K denotes the hydrostatic restoring coefficient and M represents the total oscillating mass of the system. The total mass consists of the structural mass of the floating breakwater and the hydrodynamic added mass generated by the surrounding water. Since the added mass depends on the geometry of the structure and the flow conditions, a direct determination of the natural heave period is not straightforward. For a simplified rectangular floating body, the hydrostatic restoring coefficient can be expressed as:

$$K = \rho g A_w \tag{4}$$

where ρ is the water density, g is the gravitational acceleration, and A_w is the waterplane area.
The corresponding natural period of vertical oscillation is given by:

$$T_n = \frac{2\pi}{\omega_h} \tag{5}$$

Based on dimensional analysis and experimental observations, Oliver et al. (1994) proposed a simplified approximation of the parameter $\frac{T_p}{T_n}$ that avoids the direct calculation of the natural period while preserving the dominant geometric and hydrodynamic effects governing wave transmission. The resulting dimensionless parameter is expressed as:

$$\chi = \frac{T_p}{2\pi}\sqrt{\frac{g}{d + 0.35w}} \tag{6}$$

where T_p is the peak wave period, d is the draft of the breakwater, w is the breakwater width, and g is the gravitational acceleration.

The proposed parameter was found to provide a more consistent description of wave transmission behaviour than the traditionally used width-to-wavelength ratio (w/L), particularly for π-type floating breakwaters.

Based on regression analysis of experimental results, Oliver et al. (1994) derived an empirical correction function that relates the measured transmission coefficients to those predicted by the original Macagno formulation. The correction factor can be expressed as:

$$\beta = \frac{1}{1 + \left(\frac{\chi - \chi_o}{\sigma}\right) e^{-\left(\frac{\chi-\chi_o}{\sigma}\right)^2}} \tag{7}$$

where $\beta(\chi)$ is an empirical correction factor dependent on the introduced dimensionless parameter χ, $\chi_0 \approx 0.79$ and $\sigma \approx 0.19$ are empirical parameters obtained from experimental measurements. This modified formulation was adopted in the present study as the deterministic model for evaluating wave transmission through π-type floating breakwaters and subsequently served as the basis for the uncertainty quantification analysis.

2.2 Uncertainty characterization

The transmission model described in the previous section was used for forward uncertainty propagation. Four environmental parameters were treated as uncertain: significant wave height (H_{m0}), peak wave period (T_p), astronomical tide (η), and storm surge (ss). Water depth, breakwater draft and width, and the empirical model parameters were held fixed within each test case at the values reported in Table 4. Each uncertain input was represented by a normal distribution centred on its case-specific mean. The inputs were sampled independently, and no correlation model between waves, tide, and storm surge was introduced. This assumption isolates the effect of the marginal variability assigned to each input, but it does not represent the joint dependence that may occur during individual storm events.

Table 1 summarizes literature-based CoV values reported for key hydrodynamic parameters, including significant wave height (H_{m0}), peak wave period (T_p), mean wave period (T_m), storm surge, and tidal level. These uncertainty estimates are typically derived from direct measurements, numerical modelling, empirical prediction methods, and observational datasets reported in previous studies (Suh et al., 2012; PIANC, 2003; Burcharth et al., 1992; Schüttrumpf et al., 2007; EurOtop II., 2018; Kortenhaus, 2003; Katalinić et al., 2020; Kim et al., 2013; Suh et al., 2010). The reviewed values served as the basis for selecting the uncertainty levels adopted in the present study.

Table 1. Literature-based coefficients of variation (*CoV*) reported for hydrodynamic parameters used in uncertainty analyses

Parameter	Symbol	Estimation method	CoV (σ′)
Significant wave height	H_{m0}	Measurements	0.05–0.10 0.022–0.036
		Hindcast (SMB method)	0.10–0.20 0.040–0.049
		Numerical model	0.10–0.20 0.040–0.044
		Manual calculation	0.15–0.35
		Visual observations	0.2 0.044–0.052 0.05 0.09–0.125 0.05 0.1 0.1–0.2
Peak wave period	T_p	Measurements	0.028–0.029
		Hindcast	0.048–0.055
		Numerical model	0.043
		Visual observations	0.036–0.047 0.05 0.2 0.12
Mean wave period	T_m	Measurements	0.02
		Visual observations	0.15 0.05 0.1–0.2
Sea level (astronomical tide and storm surge)	$\eta + ss$	–	0.15–0.30 0.03
Astronomical tide	η	Sinusoidal approximation	0.707A
		Measurements	Calculated from measurements
Storm surge	ss	Numerical model	0.1–0.25

Based on the reviewed literature and engineering judgement, the coefficients of variation adopted in the present study are presented in Table 2.

Table 2. Coefficients of variation adopted for uncertainty propagation in the present study

Parameter	Symbol	CoV (σ′)	STD (σ)
Significant wave height	H_{m0}	0.10	–
Peak wave period	T_p	0.08	–
Astronomical tide	η	–	0.707A
Storm surge	ss	0.15	–

A = tidal amplitude

The adopted uncertainty levels were subsequently used to define the probability distributions of the input parameters. These distributions served as the basis for uncertainty propagation using the Latin Hypercube Sampling (*LHS*) method. *LHS* was selected because it provides efficient coverage of the input parameter space while requiring fewer simulations than conventional Monte Carlo sampling techniques (Karatzetzou, 2024; Hajihassanpour et al., 2023).

The uncertainty analysis was implemented using the Dakota software package coupled with Python routines developed for automated evaluation of the transmission model. For each investigated case, 1000 realizations of the input parameters were generated and propagated through the deterministic transmission model described in Section 2.1. The resulting distributions of transmission coefficients and transmitted wave heights were subsequently used to derive the safety factors presented in the following sections.

2.3 Investigated breakwater configuration

The uncertainty analysis was performed for two commercially available π-type floating breakwater models manufactured by Marinetek, designated 4320BRK and 5320BRK. Both configurations are based on the π-type geometry illustrated in Figure 1 and differ primarily in their geometric characteristics, including width, draft, freeboard, and structural mass. These properties directly influence wave transmission behaviour and the dynamic response of the structure.

The principal characteristics of the investigated breakwater models are summarized in Table 3. To evaluate the influence of uncertainty under different hydraulic conditions, a total of 24 uncertainty quantification tests were performed using various combinations of wave parameters, water levels, and geometric configurations.

Table 3. Geometric and structural characteristics of the investigated π-type floating breakwater models

Characteristic	4320BRK	5320BRK
Length (m)	19.90	19.90
Overall width including fenders (m)	4.3	5.3
Concrete width (m)	4.0	5.0
Height (m)	1.8	1.8
Weight (t)	41.1	52.4
Net load capacity (kN/m^2)	6.0	6.0
Freeboard (m)	0.60	0.60
Joint strength (kN)	2 × 812	2 × 812
Joint spacing (mm)	90	90

3 Results and Discussion

A total of 24 uncertainty quantification tests were performed to investigate the influence of environmental and geometric variability on wave transmission through π-type floating breakwaters. The test matrix was divided into two groups according to the incident significant wave height: the first group

(Tests 1–12) considered H_{m0} = 0.7 m, while the second group (Tests 13–24) was based on H_{m0} = 0.5 m. This approach enabled the evaluation of uncertainty propagation under different wave conditions.

The scenarios investigated included uncertainty in wave height, wave period, tidal level, and storm surge, together with different values of water depth and breakwater geometry. Three installation depths (3 m, 5 m, and 7 m) were analyzed for both investigated breakwater configurations (4320BRK and 5320BRK), while uncertainty associated with the transmission model itself was kept constant throughout the analysis. In addition, two representative Adriatic locations, Rovinj and Dubrovnik, were considered in order to account for differences in local tidal conditions and their associated uncertainties. The input parameters used in the uncertainty analysis are summarized in Table 4. The uncertainty associated with significant wave height was assumed to be 10% of its mean value, while the uncertainty of the peak wave period was taken as 8% of the corresponding mean value. Tidal oscillations and storm surge effects were introduced through their respective mean values and standard deviations, providing a realistic representation of environmental variability encountered under operational conditions. Tidal uncertainty is specified directly for Rovinj (0.35 m) and Dubrovnik (0.16 m).

The uncertainty propagation analysis generated probability distributions of transmitted wave heights and transmission coefficients for each investigated case. In addition to the deterministic transmission coefficient *Kt*, the median value and the 80% and 95% quantiles of transmitted wave height distributions were determined. The corresponding safety factors were obtained by comparing the quantile-based transmission coefficients with the deterministic solution, providing a more comprehensive assessment of structural performance than a conventional deterministic approach.

Figure 2 presents the variation of the safety factors SF_{80} and SF_{95} as a function of the relative depth parameter (d/L) for the Rovinj and Dubrovnik locations. In both cases, the safety factors remain within a relatively narrow range. However, SF_{95} exhibits larger variations than SF_{80}, reflecting the stronger influence of uncertainty at higher non-exceedance probabilities. An overall increase in safety factors with increasing relative depth can be observed, although slight deviations from this trend occur for intermediate values of (d/L). These results indicate that the installation depth of the floating breakwater plays an important role in the uncertainty associated with wave transmission predictions.

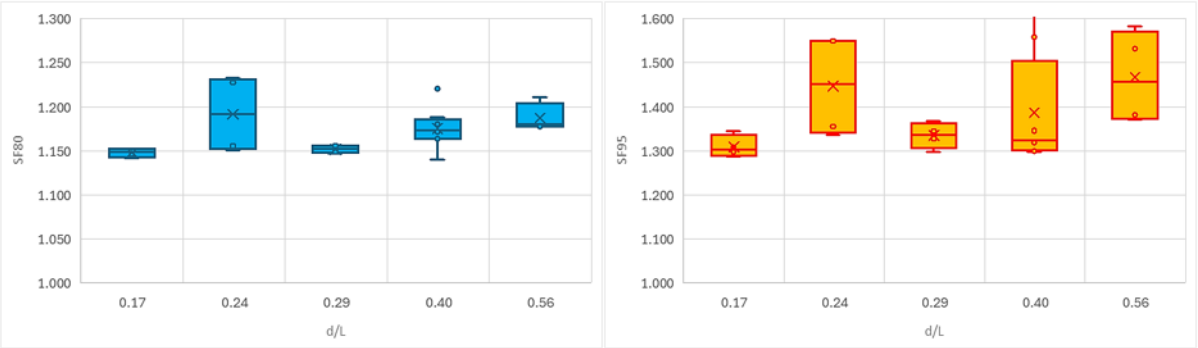


Figure 2. Dependence of the safety factors SF_{80} (left) and SF_{95} (right) on the relative depth parameter (d/L) for Rovinj and Dubrovnik

The influence of the width-to-wavelength ratio (w/L) on the safety factors is illustrated in Figure 3. Similar to the previous analysis, the values of SF_{80} remain relatively stable, whereas SF_{95} exhibits a more pronounced response to changes in geometry. Compared with the relative depth parameter, the width-to-wavelength ratio has an even stronger influence on the resulting safety factors, with larger values of w/L generally corresponding to increased design uncertainty and higher safety factors.

Table 4. Input parameters used for the uncertainty quantification analysis

N	$H_{m0,i,mean}$ (m)	$H_{m0,i,st.dev}$ (m)	H_{m0}/L_0 (–)	L_0 (m)	$T_{p,mean}$ (s)	$T_{p,st.dev}$ (s)	$Tide_{mean}$ (m)	$Tide_{st.dev}$ (m)
1	0.7	0.07	0.04	17.50	3.35	0.268	0.000	0.350
2	0.7	0.07	0.04	17.50	3.35	0.268	0.000	0.350
3	0.7	0.07	0.04	17.50	3.35	0.268	0.000	0.350
4	0.7	0.07	0.04	17.50	3.35	0.268	0.000	0.160
5	0.7	0.07	0.04	17.50	3.35	0.268	0.000	0.160
6	0.7	0.07	0.04	17.50	3.35	0.268	0.000	0.160
7	0.7	0.07	0.04	17.50	3.35	0.268	0.000	0.350
8	0.7	0.07	0.04	17.50	3.35	0.268	0.000	0.350
9	0.7	0.07	0.04	17.50	3.35	0.268	0.000	0.350
10	0.7	0.07	0.04	17.50	3.35	0.268	0.000	0.160
11	0.7	0.07	0.04	17.50	3.35	0.268	0.000	0.160
12	0.7	0.07	0.04	17.50	3.35	0.268	0.000	0.160
13	0.5	0.05	0.04	12.50	2.83	0.226	0.000	0.350
14	0.5	0.05	0.04	12.50	2.83	0.226	0.000	0.350
15	0.5	0.05	0.04	12.50	2.83	0.226	0.000	0.350
16	0.5	0.05	0.04	12.50	2.83	0.226	0.000	0.160
17	0.5	0.05	0.04	12.50	2.83	0.226	0.000	0.160
18	0.5	0.05	0.04	12.50	2.83	0.226	0.000	0.160
19	0.5	0.05	0.04	12.50	2.83	0.226	0.000	0.350
20	0.5	0.05	0.04	12.50	2.83	0.226	0.000	0.350
21	0.5	0.05	0.04	12.50	2.83	0.226	0.000	0.350
22	0.5	0.05	0.04	12.50	2.83	0.226	0.000	0.160
23	0.5	0.05	0.04	12.50	2.83	0.226	0.000	0.160
24	0.5	0.05	0.04	12.50	2.83	0.226	0.000	0.160

N	Storm $surge_{mean}$ (m)	Storm $surge_{st.dev}$ (m)	Water depth, d (m)	Draft (m)	Width, w (m)	d/L (–)	w/L (–)	Location
1	0.07	0.0105	3	1.2	5	0.17	0.29	Rovinj
2	0.07	0.0105	5	1.2	5	0.29	0.29	Rovinj
3	0.07	0.0105	7	1.2	5	0.40	0.29	Rovinj
4	0.07	0.0105	3	1.2	5	0.17	0.29	Dubrovnik
5	0.07	0.0105	5	1.2	5	0.29	0.29	Dubrovnik
6	0.07	0.0105	7	1.2	5	0.40	0.29	Dubrovnik
7	0.07	0.0105	3	1.2	4	0.17	0.23	Rovinj
8	0.07	0.0105	5	1.2	4	0.29	0.23	Rovinj
9	0.07	0.0105	7	1.2	4	0.40	0.23	Rovinj
10	0.07	0.0105	3	1.2	4	0.17	0.23	Dubrovnik
11	0.07	0.0105	5	1.2	4	0.29	0.23	Dubrovnik
12	0.07	0.0105	7	1.2	4	0.40	0.23	Dubrovnik
13	0.05	0.0075	3	1.2	5	0.24	0.40	Rovinj
14	0.05	0.0075	5	1.2	5	0.40	0.40	Rovinj
15	0.05	0.0075	7	1.2	5	0.56	0.40	Rovinj
16	0.05	0.0075	3	1.2	5	0.24	0.40	Dubrovnik
17	0.05	0.0075	5	1.2	5	0.40	0.40	Dubrovnik
18	0.05	0.0075	7	1.2	5	0.56	0.40	Dubrovnik
19	0.05	0.0075	3	1.2	4	0.24	0.32	Rovinj
20	0.05	0.0075	5	1.2	4	0.40	0.32	Rovinj
21	0.05	0.0075	7	1.2	4	0.56	0.32	Rovinj
22	0.05	0.0075	3	1.2	4	0.24	0.32	Dubrovnik
23	0.05	0.0075	5	1.2	4	0.40	0.32	Dubrovnik
24	0.05	0.0075	7	1.2	4	0.56	0.32	Dubrovnik

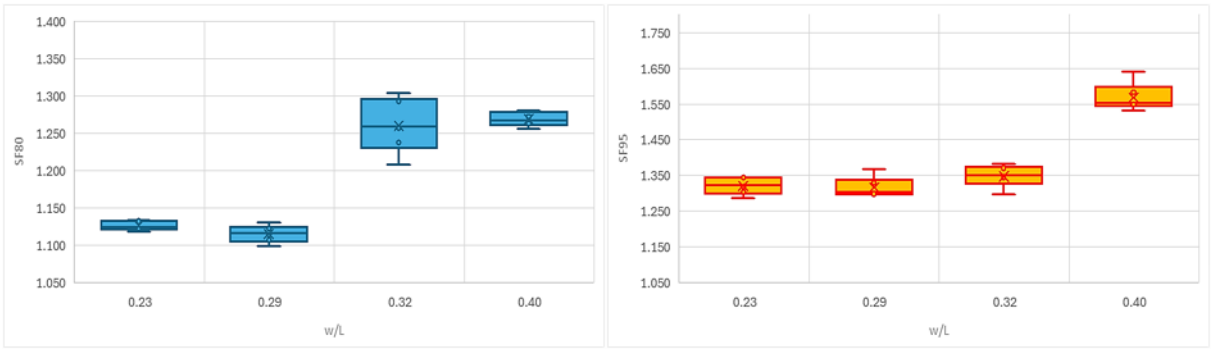


Figure 3. Dependence of the safety factors SF_{80} (left) and SF_{95} (right) on the width-to-wavelength ratio (w/L) for Rovinj and Dubrovnik

Finally, Figure 4 shows the relationship between the transmission coefficient and the corresponding safety factors. The results demonstrate that the increase in safety factors is highly nonlinear, particularly for SF_{95}. In certain regions, relatively small variations in the transmission coefficient produce a significant increase in the required safety factor, indicating increased sensitivity of the transmission model to uncertainty. This behaviour is a consequence of the nonlinear nature of the empirical transmission equations and highlights the importance of adopting a probabilistic design approach when evaluating the hydraulic performance of π-type floating breakwaters.

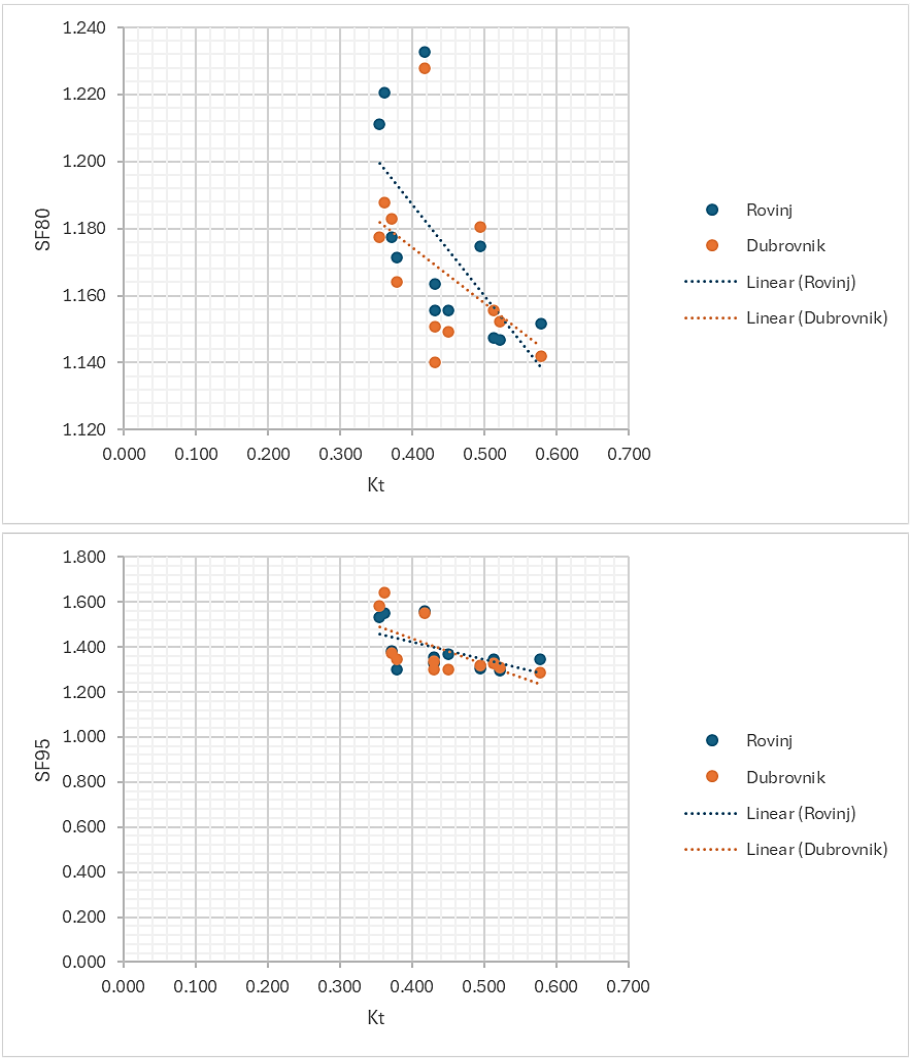


Figure 4. Relationship between the transmission coefficient (Kt) and the safety factors SF_{80} (above) and SF_{95} (below) for Rovinj and Dubrovnik.

4 Conclusion

The results demonstrated that the wave transmission coefficient (K_t) is the primary parameter governing the hydraulic performance of π-type floating breakwaters, as it directly controls the reduction of wave energy transmitted behind the structure. The uncertainty analysis showed that, within nonlinear regions of the transmission relationship, relatively small variations in input parameters such as wave height, wave period, tidal level, and storm surge can produce significant changes in predicted transmission coefficients K_t. Consequently, uncertainties associated with the input parameters are amplified through the transmission model, resulting in increased safety factors.

The results further indicate that the safety factor (SF_{95}) provides a more conservative assessment of structural performance, as it accounts for more extreme scenarios and ensures a larger margin of safety in engineering design. Compared with (SF_{80}), greater variability was observed for (SF_{95}), reflecting the increased influence of uncertainty at higher non-exceedance probabilities. Nevertheless, this characteristic makes (SF_{95}) a more reliable basis for design applications and engineering decision-making.

Furthermore, the analysis revealed that the relative depth parameter (d/L) has a significant influence on safety factor values, while the width-to-wavelength ratio (w/L) plays an even more pronounced role in determining transmission behaviour. These findings highlight the importance of accurately representing both geometric and hydraulic parameters when assessing the performance of floating breakwaters.

Overall, the uncertainty quantification framework successfully identified the parameters and operating conditions that most strongly influence wave transmission predictions. The results indicate that the design of π-type floating breakwaters should be based on a careful evaluation of transmission uncertainty and the application of appropriate safety factors, particularly (SF_{95}). Such an approach contributes to more reliable design, reduces the risk of underestimating transmitted wave energy, and improves the long-term functionality and resilience of floating breakwaters operating under variable marine conditions.

Acknowledgements

This work was supported by the Croatian Science Foundation under the project number (HRZZ-DOK-2025-02-3371).

This study was conducted within the framework of the institutional project of the University of Zagreb Faculty of Civil Engineering – [HOPIK – Enhancement of hydrological and oceanographic data for assessing the exposure of transport infrastructure to climate change], under the programme line for enhancing scientific excellence, financed through the National Recovery and Resilience Plan 2021–2026. The project is funded by the European Union – NextGenerationEU. The views and opinions expressed are solely those of the authors and do not necessarily reflect those of the European Union or the European Commission. Neither the European Union nor the European Commission can be held responsible for them.

References

Burcharth, H.F. 1992 *Uncertainty Related to Environmental Data and Estimated Extreme Events*. Report of Subgroup B, PIANC PTC II Working Group 12, Aalborg Universitetsforlag, Aalborg, Denmark.

EurOtop 2018 *Manual on Wave Overtopping of Sea Defences and Related Structures. An Overtopping Manual Largely Based on European Research, but for Worldwide Application*, 2nd edn. Van der Meer, J.W., Allsop, N.W.H., Bruce, T., De Rouck, J., Kortenhaus, A., Pullen, T., Schüttrumpf, H., Troch, P. and Zanuttigh, B. (eds). www.overtopping-manual.com

Goda, Y. 2010 *Random Seas and Design of Maritime Structures*, 3rd edn. Advanced Series on Ocean Engineering, Vol. 33, World Scientific, Singapore.
Hajihassanpour, M., Kesserwani, G., Pettersson, P. and Bellos, V. 2023 Sampling-based methods for uncertainty propagation in flood modeling under multiple uncertain inputs: finding out the most efficient choice. *Water Resources Research* 59, e2022WR034011.
Hales, L.Z. 1981 *Floating Breakwaters: State-of-the-Art Literature Review*. Technical Report No. 81-1, U.S. Army Corps of Engineers, Coastal Engineering Research Center, Fort Belvoir, VA, USA.
Karatzetzou, A. 2024 Uncertainty and Latin hypercube sampling in geotechnical earthquake engineering. *Geotechnics* 4 (4), 1007–1025.
Katalinić, M. and Parunov, J. 2020 Uncertainties of estimating extreme significant wave height for engineering applications depending on the approach and fitting technique—Adriatic Sea case study. *Journal of Marine Science and Engineering* 8 (4), 259.
Kim, S.-W. and Suh, K.-D. 2013 Performance analysis of vertical breakwaters designed by partial safety factor method. *Journal of Coastal Research* SI 65, 296–301.
Kortenhaus, A. 2003 *Probabilistische Methoden für Nordseedeiche*. PhD thesis, Leichtweiß-Institut für Wasserbau, Technische Universität Braunschweig, Braunschweig, Germany.
Martinelli, L., Ruol, P. and Zanuttigh, B. 2008 Wave basin experiments on floating breakwaters with different layouts. *Applied Ocean Research* 30 (3), 199–207.
Oliver, D.L., McDougal, W.G. and Hall, K.R. 1994 Dynamics of floating breakwaters. *Coastal Engineering*, 22 (3-4), 221-238.
PIANC 2003 *Breakwaters with Vertical and Inclined Concrete Walls*. Report of Working Group 28 of the Maritime Navigation Commission, PIANC General Secretariat, Brussels, Belgium.
Ruol, P., Martinelli, L. and Pezzutto, P. 2013 Formula to predict transmission for π-type floating breakwaters. *Journal of Waterway, Port, Coastal, and Ocean Engineering* 139 (1), 1–8.
Schüttrumpf, H., Kortenhaus, A., Peters, K. and Fröhle, P. 2007 Expert judgement of uncertainties in coastal structure design. In: *Proc. of the 30th International Conference on Coastal Engineering*, San Diego, CA, USA, 3–8 September 2006, World Scientific, Singapore, pp. 5267–5278.
Suh, K.-D., Kim, S.-W., Mori, N. and Mase, H. 2012 Effect of climate change on performance-based design of caisson breakwaters. *Journal of Waterway, Port, Coastal, and Ocean Engineering* 138 (3), 215–225.
Suh, K.-D., Kwon, H.-D. and Lee, D.-Y. 2010 Some statistical characteristics of large deepwater waves around the Korean Peninsula. *Coastal Engineering* 57 (4), 375–384.
Wiegel, R.L. 1960 Transmission of waves past a rigid vertical thin barrier. *Journal of the Waterways and Harbors Division, ASCE* 86 (WW1), 1–12.

HIGH-RESOLUTION UAV LASER SCANNING OF THE CHANNEL MORPHOLOGY – COMPARISON WITH TRADITIONAL SURVEYING TECHNIQUES

Michaela ČERVEŇANSKÁ [1*], Pavol PECHO [2], Jakub CHROMČÁK [3], Juraj PAPČO [4], Roman TÓTH [1], Adela RUTZKÁ [1], Dmitrii PAVLOV [1], Natália BILČÍKOVÁ [1]

[1] *Department of Hydraulic Engineering, Faculty of Civil Engineering, Slovak University of Technology in Bratislava, Slovakia*

E-mail: michaela.cervenanska@stuba.sk

E-mail: roman.toth@stuba.sk

E-mail: adela.rutzka@stuba.sk

E-mail: dmitrii.pavlov@stuba.sk

E-mail: natalia.bilcikova@stuba.sk

[2] *Department of Air Transport, Faculty of Operation and Economics of Transport and Communications, University of Žilina, Slovakia*

E-mail: pavol.pecho@fpedas.uniza.sk

[3] *Department of Geodesy, Faculty of Civil Engineering, University of Žilina, Slovakia*

E-mail: jakub.chromcak@uniza.sk

[4] *Department of Theoretical Geodesy and Geoinformatics, Faculty of Civil Engineering, Slovak University of Technology in Bratislava, Slovakia*

E-mail: juraj.papco@stuba.sk

[*] *Corresponding author*

Abstract

Traditionally, data describing riverbed morphology are collected through topographic surveys using total stations or Real-Time Kinematic (RTK) Global Navigation Satellite System (GNSS) receivers. However, these methods have limitations, including coarse sampling densities and time-intensive field efforts. To overcome the limitations, remote sensing technologies such as aerial laser scanning (ALS) or drone laser scanning (DLS) have been utilised to survey riverbed morphology. The aim of the research on the Rye Island drainage channel system in Slovakia was to combine and compare traditional surveying with DLS to obtain the channel bed morphology. An Unmanned Aerial Vehicle (UAV) DJI Matrice 300 RTK carrying an ultra-light Light Detection and Ranging (LiDAR) system of Slovak origin, Lidaretto, was used to obtain data describing the morphology of two channels which are artificially fed with water of groundwater quality (originating as a seepage through the dykes of the Gabčíkovo supply channel). The processed LiDAR data covering the entire channel area were then compared with point data measured at several cross-sections using RTK GNSS. The results show that in clear, shallow water, DLS achieved performance comparable to that of RTK GNSS. The mean elevation bias calculated for cross-sections varied from 0.01–0.50 meters. The differences in results were mainly in profiles with a thick layer of bottom fine sediments or vegetation.

Key words

drainage channels, riverbed morphology, UAV, LiDAR, DLS

1 Introduction

Channel morphology or channel metrics (e.g., cross-sectional area, width, depth, and slope) has been traditionally characterised through topographic surveys using total stations and Real-Time Kinematic (RTK) Global Navigation Satellite System (GNSS) receivers (Backes et al., 2020; Resop et al., 2024). However, the use of such equipment is restricted to easily accessible sites, and in relatively shallow waters with a slow flow (Backes et al., 2020). Moreover, these methods are limited by time-intensive field surveys, coarse sampling densities, and difficulties in surveying complex morphology (Resop et al., 2010; Resop et al., 2024).

Remote sensing technologies, such as imagery and LiDAR, have revolutionised the way topographic data are collected (Backes et al., 2020). These technologies rely on a range of platforms including satellite, aerial, terrestrial, mobile, and, more recently, drone systems for measuring physical riverscape properties (Resop et al., 2021). The availability of terrestrial (TLS) and aerial laser scanning (ALS), the use of unmanned aerial vehicles (UAVs; i.e., drones) and recent advances in photogrammetric techniques such as drone-based imagery, also known as Structure-from-Motion (SfM), has led to heightened interest in applying these technologies to hydrological and biological studies. More recently, ultra-light Light Detection and Ranging (LiDAR) systems have become integrated with UAV systems (Resop et al., 2019).

Airborne LiDAR allows rapid and accurate measurements of topography over large areas; however, their main disadvantage lies in their price. An efficient alternative to labour-intensive terrestrial and costly airborne surveys is the use of small, inexpensive UAVs, commonly known as drones (Backes et al., 2020). While drones are more limited than ALS surveys in terms of total area of extent, they provide the ability to scan the environment closer to the earth's surface. Lower altitude scans can produce much higher density point clouds than ALS and improved detail of hard-to-scan features, making drone-based lidar or drone laser scanning (DLS) well suited for surveying the topography of complex riverscapes (Resop et al., 2019). These low-altitude remote sensing platforms can carry a passive lightweight optical sensor and LiDAR sensors (active remote sensing equipment) (Backes et al., 2020). Both remote sensing technologies have advantages and disadvantages (Resop et al., 2021).

UAVs with passive optical sensors have become popular for reconstructing topography using SfM photogrammetry (MacDonell et al., 2023). In recent years, technological progress and miniaturisation of sensors, such as the appearance of high-performance, miniature inertial measurement units (IMU), enabled the development of UAV-borne LiDAR systems (Backes et al., 2020). Vegetation penetration and shadowing, challenges associated with SfM photogrammetry, can be overcome by UAV-borne LiDAR systems since LiDAR is better suited for producing 3D point clouds and penetrating vegetation canopy, thus providing much higher resolution point clouds in comparison with traditional methods (MacDonell et al., 2023; Resop et al., 2021; Resop et al., 2024). Even though UAV systems still have limited endurance, they can provide a flexible and relatively inexpensive monitoring solution for a limited area of interest (Backes et al., 2020).

Drone laser scanning has only recently been applied to measure channel morphology. However, little research has been carried out to directly compare cross sections measured using traditional surveying methods to those extracted using DLS (Resop et al., 2024).

Resop et al. (2024) studied a 1.3-km reach of Stroubles Creek (Blacksburg, VA, USA), which underwent a restoration in 2010, and was surveyed twice with a total station (2010 and 2021) and twice with DLS (2017 and 2021). A direct comparison between the total station and DLS data in 19 cross sections was performed for 2021 since it was the only time both methods were utilized with the mean elevation bias between the drone LiDAR digital terrain model (DTM) and the total station points of 0.093 m.

As already illustrated, only a little research has been carried out to directly compare cross sections measured using traditional surveying methods to those extracted using DLS. Therefore, the main objective of this paper is to present the results of research on the Rye Island drainage channel system,

Slovakia, combining a traditional surveying method (RTK GNSS) and the use of DLS for obtaining the channel bed morphology.

2 Methods

2.1 The area of interest

Rye Island, the area between the Danube River and the rivers Little Danube and Váh, is part of the Podunajska lowland located in the southwest of Slovakia. It is the largest river island in Europe and the warmest region of Slovakia with the longest growing season and the richest water resources, both surface and underground. Because of the very low slope of the inland island, a network of irrigation and drainage channels was built to manage drainage and irrigation in the area.

The Rye Island channel system, with its damming and dividing structures and pumping stations, can now be considered multi-purpose. While in the past it was built for draining waterlogged soils, especially in the wet spring season and during floods, nowadays an equally important purpose is related to irrigation and to regulating the water level regime. The Rye Island channel system, with its capacity, thus represents an important source of irrigation water, which can be regulated in time and space on the entire territory of the island. The channel network consists of ten systems (in the past referred to as systems I – X) and is geographically divided into two parts – the upper and lower Rye Island, with the Chotárny channel (S VI) creating a natural boundary between the two parts.

There are three main water sources for the lower part of the Rye Island channel system (Fig. 1):

- inflow from the supply canal of the Gabčíkovo hydraulic structure to the Gabčíkovo-Topoľníky channel (S VII) through a small hydropower plant with a capacity of 8.0 m^3/s;
- inflow from the left-side seepage channel of the Gabčíkovo hydraulic structure to the channels Vojka-Kračany (A VII), Šuľany-Jurová (B VII) and Baka-Gabčíkovo (C VII), and subsequently to the Gabčíkovo-Topoľníky channel (S VII);
- by draining the groundwater.

It is evident that system VII plays a crucial role in supplying water to the lower part of the channel system and is one of the reasons for choosing this part of the island as the area of interest. The channels A VII and B VII were chosen because of the quality of the water artificially fed into them – it is a seepage through the dykes of the Gabčíkovo supply canal, with clear water of groundwater quality. Additionally, in some parts, the depth of the water is only in tens of centimetres, making it a suitable area for research on the potential use of DLS for obtaining data about channel morphology.

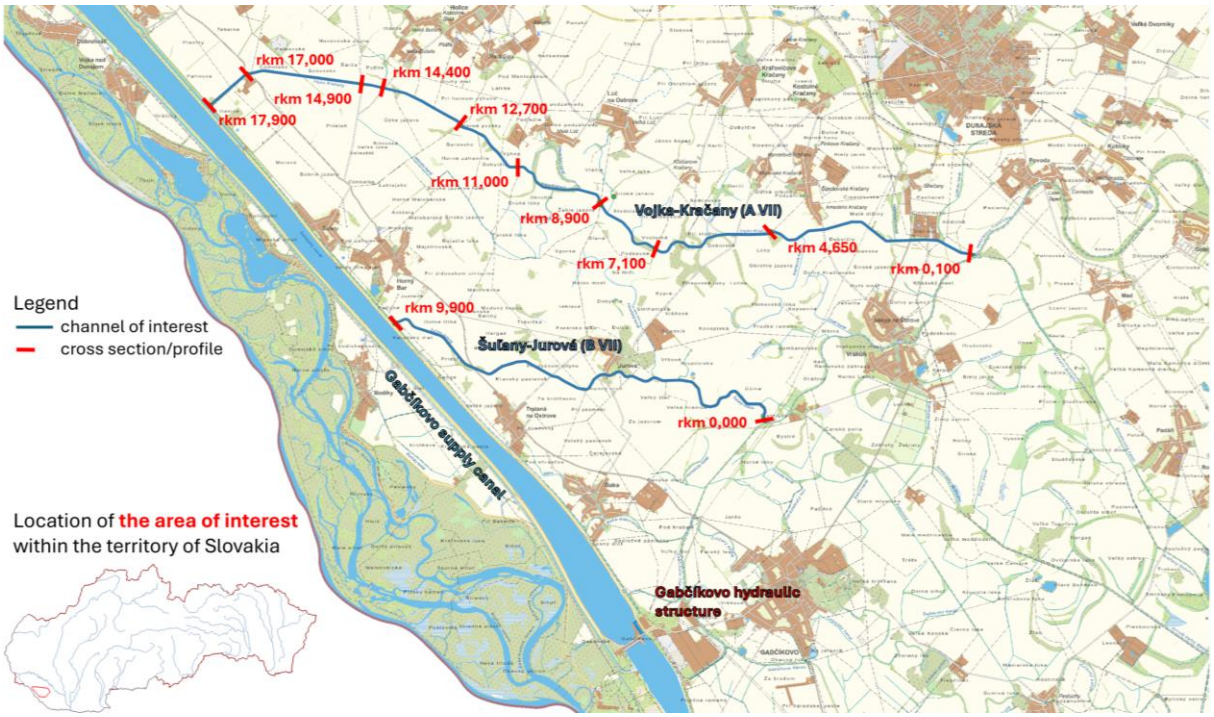


Figure 1. The area of interest

2.2 LiDAR and GNSS Data Collection

The DLS system used (Fig. 2) consisted of a carrier DJI Matrice 300 RTK (DJI, USA) with an ultra-light LiDAR system of Slovak origin, Lidaretto (GEOTECH, Slovakia).

The DJI Matrice 300 RTK uses DJI's own flight control system with integrated GPS, GLONASS, BeiDou, and Galileo satellite positioning, along with an RTK module for centimetre-level positioning accuracy (horizontal 1 cm, vertical 1.5 cm), and pairs with the DJI Pilot app for mission planning, execution, and live telemetry. The drone has a maximum payload capacity of 2.7 kg (sensors, cameras) and uses dual redundant intelligent flight batteries (TB60, 6.3 kg) that together enable a maximum flight time of up to 55 minutes (unloaded). It features a six-directional sensing and positioning system for omnidirectional obstacle avoidance, an IP45 ingress protection rating for operation in light rain and dust, an operating temperature range of -20 °C to 50 °C, and a maximum transmission range of up to 15 km under interference-free conditions. It supports up to three payload sensors simultaneously and offers a maximum take-off weight of approximately 9 kg.

The Lidaretto, a classical topographic scanner, is a lightweight, multiplatform system that makes it a versatile payload well-suited for a wide range of UAV-, vehicle-, and backpack-mounted survey applications. The system uses a Novatel OEM7 GNSS/IMU unit with 555 channels and dual-GNSS capability, supporting GPS, GLONASS, Galileo, and BeiDou signals on L1/L2, paired with a Hesai XT32 LiDAR puck and onboard computer for self-contained, autonomous data acquisition. The LiDAR system is capable of recording up to two returns per pulse, with a maximum range of 120 m and a typical range accuracy of ±1 cm and uses a NIR wavelength of 905 nm.

According to Resop et al. (2021), NIR LiDAR pulses are almost completely absorbed or scattered at the water surface, leaving data gaps within the wetted channel. Thus, another objective of the study was either to confirm or deny this statement in specific conditions – shallow, clear water.

DLS surveys were flown on March 23 and 24, 2026. The flight was carried out at a time when the area was within the Aerodrome Traffic Zone (ATZ) and in accordance with the applicable rules and safety

procedures for the UAV under Decision no. 2/2019 of 14 November 2019. For the elimination of shadows from buildings and vegetation, during the flight, the sun was as high as possible above the horizon and with light meteorological conditions. The 19-km-long channel A VII was divided into 8 sections for short drone flights, and each section was scanned separately over two days. The approx. 10-km-long channel B VII was scanned over 6 short drone flights during the first day.



Figure 2. Unmanned Aerial System (UAS) – DJI Matrice 300 RTK carrying Lidaretto (photo: authors).



Figure 3. Channel bed measurements using Leica Viva GS15 GNSS RTK receiver and Leica CS15 controller (photo: authors).

Along with the DLS, on March 24 and 25, 2026, a survey (Fig. 3) for measuring the channel bed was carried out using a Leica Viva GS15 GNSS RTK receiver (RTK accuracy: horizontal 8 mm, vertical 15 mm), with a Leica CS15 controller (Leica Geosystems, Switzerland) in the Slovak reference coordinate and height system S-JTSK and BvDAA. Ten cross sections of the A VII channel and 2 cross sections of the B VII channel were irregularly measured (Fig. 1).

2.3 LiDAR Data Processing

LiDAR data were processed using Lidaretto Creator (GEOTECH, Slovakia), generating georeferenced point clouds by combining the raw scan data with the post-processed GNSS/IMU trajectory. QGIS (QGIS.org/Open Source Geospatial Foundation, OSGeo) was used to clip the georeferenced point clouds so that only the channel (from the left-side channel bank to the right-side) was left and later processed in comparison of two methods used for data collection. Along the A VII channel with the channel (clipped) area (from one bank line to the other) of 270,860 m^2, DLS collected a little more than 739,500,000 points, which corresponds to an overall density of 2,730 points/m^2. Along the B VII channel with the channel area of 151,775 m^2, almost 228,000,000 points were obtained with the density of 1,500 points/m^2. In comparison, 150 points (approx. one point for every 0.5 meter in each cross section) were measured in both channels using GNSS RTK.

The generated point clouds were imported into a third-party software for further processing – classification and digital terrain model (DTM) generation.

3 Results and Discussion

Profile tool (Terrain profile) in QGIS was used for the extraction of cross sections from the DTM. The extracted cross sections were then compared with the GNSS RTK point data measurements (Fig. 4, 6). For better understanding of each cross section as well as for better perspective, the actual state of the representative cross sections can be seen in Fig. 5 and 7. Representative cross sections were selected to include all channel bottom types in the study area (gravel/fine-grained material), different flow conditions (flow with/without turbidity) and different tracing (in a straight section or arc).

For the comparison of absolute values of the differences between the two methods used for the data collection, Tab. 1 and 2 were created.

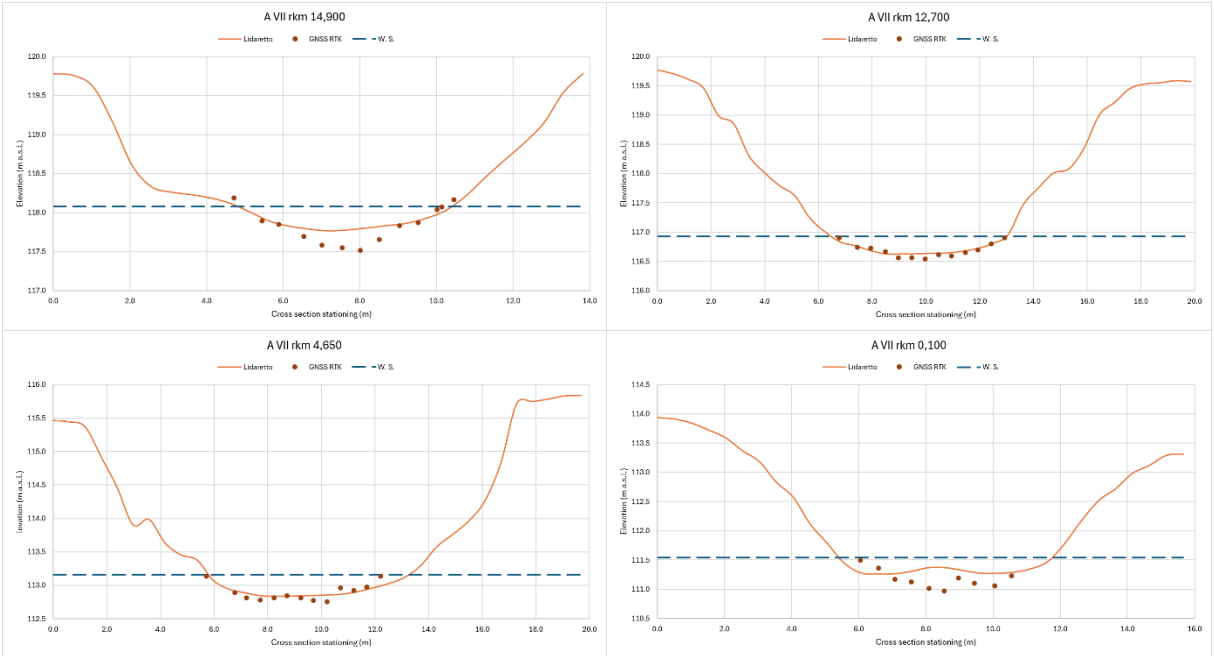


Figure 4. Representative cross sections of the A VII channel – comparison of DTM (obtained using LiDAR) data and GNSS RTK point data (*rkm* – river kilometre, *W. S.* – water surface).



Figure 5. The actual state of the representative cross sections of the A VII channel. The photos' order follows Fig. 4 – top left rkm 14,900; top right rkm 12,700; bottom left rkm 4,650 and bottom right rkm 0,100 (photos: authors).

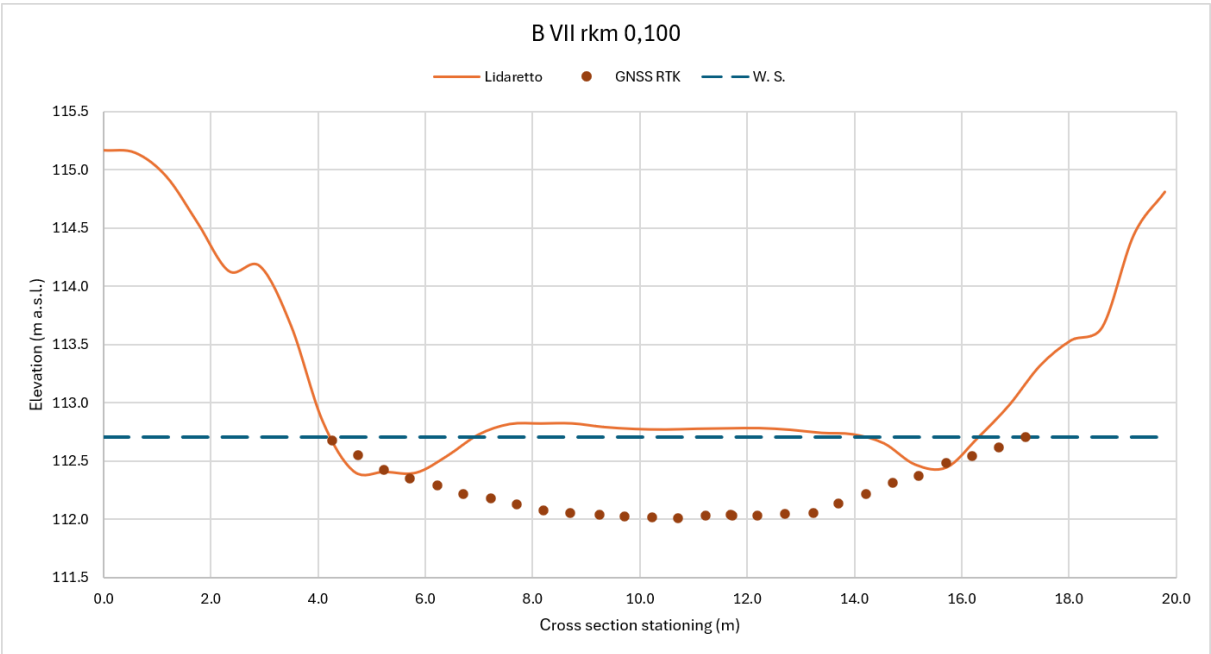


Figure 6. Representative cross sections of the B VII channel – comparison of DTM (obtained using LiDAR) data and GNSS RTK point data (*rkm* – river kilometre, *W. S.* – water surface).



Figure 7. The actual state of the representative cross sections of the B VII channel (photo: authors).

As can be seen from Fig. 4, LiDAR pulses were able to penetrate the water surface in all representative cross sections of the A VII channel. The generated DTM aligns perfectly with the data measured using GNSS RTK in cross sections at rkm 12,700 and 4,650, with the mean elevation bias being 2 cm and 1 cm respectively. The absolute differences in these two cross sections vary from 1 cm up to 14 cm (Tab. 1). The reason is the material at the bottom of the channel – mainly gravel without vegetation (Fig. 5). Moreover, the water is clear in every representative cross section of the A VII channel, which enables good penetration of the pulses. Cross sections at rkm 14,900 and 0,100 show higher differences (varying from 1 cm up to 28 cm and 6 cm up to 40 cm respectively with the mean elevation bias of 6 cm and 13 cm, Tab. 1). At rkm 14,900, the water flow is influenced by the temporary damming structure built one day prior to the measurements (compensating for the sluice gate currently in renovation, Fig. 5), creating scours in the channel bed. The bottom material (sediments) was being transported, polluting the previously clear water, causing the refraction of the LiDAR pulses. At rkm 0,100, there is fine-grained material at the bottom of the channel along with vegetation at the bottom and the channel banks. The pulses were most likely refracted due to the vegetation. Moreover, the fine sediments caused the GNSS RTK to sink into them, making it hard to measure the exact top of the sediment layer.

Table 1. Comparison of the collected data for each representative cross section of the A VII channel

Profile in rkm; water depth *h* (mean elevation bias between Lidaretto and GNSS RTK)	GNSS RTK (m a.s.l.)	Lidaretto (m a.s.l.)	Absolute difference (m)
rkm 14,900; h = 0.56 m (mean elevation bias 0.06 m)	118.07	118.00	-0.07
	118.17	118.10	-0.07
	118.04	117.98	-0.06
	117.87	117.90	0.03
	117.83	117.85	0.02
	117.65	117.82	0.16
	117.51	117.79	0.28
	117.55	117.77	0.22
	117.58	117.77	0.19
	117.69	117.79	0.10
	117.85	117.86	0.01
	117.89	117.93	0.04
	118.19	118.09	-0.09
rkm 12,700; h = 0.39 m (mean elevation bias 0.02 m)	116.91	116.84	-0.06
	116.74	116.76	0.01
	116.72	116.68	-0.04
	116.67	116.63	-0.04
	116.56	116.63	0.07
	116.56	116.63	0.06
	116.54	116.63	0.09
	116.61	116.64	0.03
	116.59	116.65	0.06
	116.66	116.68	0.03
	116.70	116.72	0.02
	116.80	116.80	-0.01
	116.90	116.92	0.02
rkm 4,650; h = 0.41 m (mean elevation bias 0.01 m)	113.13	112.99	-0.14
	112.98	112.94	-0.04
	112.92	112.89	-0.03
	112.96	112.86	-0.09
	112.75	112.85	0.10
	112.77	112.85	0.07
	112.81	112.84	0.03
	112.85	112.84	-0.01
	112.81	112.84	0.02
	112.78	112.84	0.07
	112.81	112.88	0.07
	112.89	112.92	0.03
	113.14	113.20	0.07
rkm 0,100; h = 0.58 m (mean elevation bias 0.13 m)	111.23	111.29	0.06
	111.06	111.27	0.21
	111.10	111.29	0.18
	111.19	111.33	0.14
	110.97	111.36	0.40
	111.02	111.37	0.35
	111.13	111.30	0.18
	111.17	111.26	0.09
	111.36	111.26	-0.10
	111.49	111.28	-0.21

Table 2. Comparison of the data collected for each representative cross section of the B VII channel

Profile in rkm (mean elevation bias between Lidaretto and GNSS RTK)	GNSS RTK (m a.s.l.)	Lidaretto (m a.s.l.)	Absolute difference (m)
rkm 0,100; h = 0.69 m (mean elevation bias 0.46 m)	112.68	112.71	0.03
	112.55	112.41	-0.14
	112.42	112.41	-0.02
	112.35	112.40	0.05
	112.29	112.50	0.21
	112.22	112.64	0.42
	112.18	112.76	0.58
	112.13	112.82	0.69
	112.08	112.82	0.74
	112.05	112.82	0.77
	112.04	112.80	0.75
	112.02	112.78	0.76
	112.02	112.77	0.75
	112.01	112.77	0.76
	112.03	112.78	0.75
	112.04	112.78	0.74
	112.03	112.78	0.75
	112.04	112.78	0.75
	112.05	112.77	0.72
	112.05	112.75	0.69
	112.14	112.73	0.60
	112.22	112.70	0.48
	112.32	112.60	0.29
	112.37	112.47	0.10
	112.48	112.44	-0.04
	112.55	112.65	0.10
	112.62	112.88	0.26
	112.71	113.16	0.45

Figure 6 shows the reflection of the pulses off almost across the whole cross section (maximum absolute difference 77 cm, mean elevation bias 46 cm, Tab. 2). The main reason may be the water containing fine-grained material from the bottom of the channel (Fig. 7), causing the LiDAR pulses to reflect off the water surface. Due to the lack of vegetation on the left channel bank, approx. 1 m of the cross section shows the alignment of the LiDAR data (from the DTM) and the GNSS RTK point data (the absolute difference from 2 cm up to 21 cm, Tab. 2, corresponding to the absolute differences measured in A VII channel, Tab. 2). That is, however, not the case on the right channel bank with the vegetation (Fig. 7) since LiDAR pulses cannot perfectly penetrate riparian vegetation to measure ground. The absolute differences thus vary up to 45 cm (Tab. 2).

Resop et al. (2024) observed the mean elevation bias between the drone LiDAR DTM and the total station points of 9.3 cm indicating DLS over-estimated ground elevation compared to the total station. Our research reached the same conclusion (Tab. 1 and 2). A slight over-estimation of elevation by the DLS was expected, since LiDAR pulses cannot perfectly penetrate riparian vegetation to measure ground. The mean bias of the bank points (9.5 cm) in the study by Resop et al. (2024) was slightly larger than the bed points (8.2 cm), which met the expectation – the LiDAR bias would be greater under the water surface due to NIR absorption. However, the bias was not as significant as anticipated, most likely due to conducting the DLS surveys during baseflow with the observed depth between 0.13 and 0.34 m (conditions a little different than in our study with the water depths around 40–70 cm). For most cross sections, the bias under the water surface was within the overall bias observed between the total station and DLS measurements.

4 Conclusion

This study compared drone laser scanning (DLS) using a UAV-mounted Lidaretto system with traditional RTK GNSS surveying for characterising channel bed morphology in two drainage channels (A VII and B VII) of the Rye Island system, Slovakia. Under the clear, shallow-water conditions surveyed, DLS produced results broadly comparable to those obtained with RTK GNSS, with a mean elevation bias between the two methods ranging from 0.01 to 0.50 m across the representative cross sections. The closest agreement (mean bias of 1–2 cm) was found in cross sections with unvegetated, gravel-dominated beds and undisturbed, clear water.

The largest discrepancies occurred where the bed and banks were affected by fine sediments, disturbed or turbid water, or riparian vegetation. Fine sediment layers on the channel bed caused refraction and scattering of the LiDAR pulses and made it difficult to locate the true bed surface with the GNSS RTK rod, while bank vegetation prevented LiDAR pulses from reaching the ground, leading to a consistent overestimation of elevation by DLS – a pattern consistent with the findings of Resop et al. (2024). Contrary to Resop et al. (2021), who reported that near-infrared LiDAR pulses are almost completely absorbed or scattered at the water surface, the results show that in clear, shallow water, DLS pulses can penetrate the water column and reach the channel bed with an accuracy approaching that of RTK GNSS, at least at the water depths of 40–70 cm observed in this study.

Beyond accuracy, DLS provided a substantially denser representation of channel morphology – between 1,500 and 2,730 points/m² – compared with the roughly one point every 0.5 m obtained along the traditionally surveyed cross sections, enabling a continuous characterisation of the channel bed and banks rather than sparse point sampling. These findings indicate that DLS is a viable and considerably more efficient alternative to traditional cross-sectional surveying for mapping the morphology of small drainage channels with clear, shallow water, although caution is warranted where fine sediments, turbidity, or dense riparian vegetation are present.

From a practical standpoint, these results carry direct benefits for the management of drainage and irrigation networks such as the Rye Island system. A single UAV-mounted DLS flight can capture a continuous, high-density record of an entire channel reach in a fraction of the time needed for point-by-point RTK GNSS surveying, and without requiring surveyors to wade into the channel or access steep or overgrown banks. This makes DLS particularly well suited to the routine monitoring by water management authorities. The resulting dense morphological data can support more informed decisions on maintenance prioritisation (e.g., where to schedule dredging or vegetation clearance), on assessing changes in channel capacity that affect flood conveyance, and on tracking long-term sedimentation and erosion trends, provided that surveys are scheduled during periods of clear, shallow water. DLS therefore offers water managers and hydraulic engineers a scalable, faster, and more cost-effective complement to traditional surveying for keeping small drainage channels in good operating condition. Furthermore, since DLS captures a continuous bed surface rather than interpolated cross sections, it also provides hydraulic modellers with the detailed bathymetric input needed for reliable flow and sediment-transport simulations.

Future work should extend this comparison across a wider range of water depths, turbidity levels, and vegetation covers, and examine the influence of flow conditions and seasonal change on DLS performance, in order to better define the operational limits of drone laser scanning for monitoring riverine and drainage channel morphology.

Acknowledgements

Funded by the EU NextGenerationEU through the Recovery and Resilience Plan for Slovakia under the project No. 09I03-03-V04-00274.
This contribution was developed within the framework and based on the financial support of the Slovak grant scheme VEGA No. 1/0699/25 Optimization of water resources exploitation for sustainable

development of agriculture on the Rye Island.

References

Backes, D., Smigaj, M., Schimka, M., Zahs, V., Grznárová, A. and Scaioni, M. 2020 River morphology monitoring of a small-scale alpine riverbed using drone photogrammetry and LiDAR. In *The International Archives of the Photogrammetry, Remote Sensing and Spatial Information Sciences*, Volume XLIII-B2-2020, 2020 XXIV ISPRS Congress (2020 edition), 1017–1024. https://doi.org/10.5194/isprs-archives-XLIII-B2-2020-1017-2020

MacDonell, C.J., Williams, R.D, Maniatis, G., Roberts, K. and Naylor, M. 2023 Consumer-grade UAV solid-state LiDAR accurately quantifies topography in a vegetated fluvial environment. *Earth Surface Processes and Landforms*, 48, 11, 2211–2229. https://doi.org/10.1002/esp.5608

Resop, J.P. and Hession, W.C. 2010 Terrestrial Laser Scanning for Monitoring Streambank Retreat: Comparison with Traditional Surveying Techniques. *Journal of Hydraulic Engineering*, 136, 10, 794–798. https://doi.org/10.1061/(ASCE)HY.1943-7900.0000233

Resop, J.P., Lehmann, L. and Hession W.C. 2019 Drone Laser Scanning for Modeling Riverscape Topography and Vegetation: Comparison with Traditional Aerial Lidar. *Drones*. 3 (2), 35. https://doi.org/10.3390/drones3020035

Resop, J.P., Lehmann, L. and Hession, W.C. 2021 Quantifying the Spatial Variability of Annual and Seasonal Changes in Riverscape Vegetation Using Drone Laser Scanning. *Drones*, 5, 91. https://doi.org/10.3390/drones5030091

Resop, J.P., Hendrix, C., Wynn-Thompson, T. and Hession, W.C. 2024 Channel Morphology Change after Restoration: Drone Laser Scanning versus Traditional Surveying Techniques. *Hydrology*, 11, 54. https://doi.org/10.3390/hydrology11040054

ADVANCING THE TEMPORAL DYNAMICS ANALYSIS OF THE BULAŽ SPRING CATCHMENT WATER BALANCE WITH GLOBAL MODERATE RESOLUTION SOIL MOISTURE DATASETS

Bojana HORVAT [1*], Maja OŠTRIĆ [2], Maja RADIŠIĆ [3], Josip RUBINIĆ [4]

[1] *University of Rijeka, Faculty of Civil Engineering, Radmile Matejčić 3, 51000 Rijeka, Croatia*

E-mail: bojana.horvat@uniri.hr

[2] *Hrvatske vode, VGO Rijeka, Đure Šporera 3, 51000 Rijeka, Croatia*

E-mail: maja.ostric@voda.hr

[3] *MaLu, Pomerio 11, 51000 Rijeka, Croatia*

E-mail: maja8radisic@gmail.com

[4] *GEO-5, d.o.o., Carera 59, 52210 Rovinj, Croatia*

E-mail: rubinic.josip@gmail.com

[*] *Corresponding author*

Abstract

Highly heterogeneous and vulnerable, karst springs with the underlying karst aquifers are critical to water supply in the Adriatic Sea coastal region. Estimating the availability of water that can meet the increasing demand for potable water is essential but complex and often difficult task. Researchers are frequently confronted with the lack of data hence preliminary water budget investigations were usually conducted using the various empirical methods e.g., Turc (1954) and Langbein (1949) methods that require minimum input data, such as precipitation and air temperature. Over the past decades, advances in remote sensing technology enabled data collection using Earth observation satellites and overcoming the data availability gap, including in water budget estimation. Copernicus Land Monitoring Service (CLMS) and ERA5 Land derived from the ERA5 ECMWF (European Centre for Medium-Range Weather Forecasts) reanalysis offer long time series (CLMS for period 2021-today, ERA5 Land for period 1950-today) of spatial distribution of soil moisture data at various temporal and spatial resolutions. Bulaž Spring, located in the northern Istria with catchment area spanning over 105 km2 serves as the secondary water source in the water supply system. The paper describes the approach to analysing monthly dynamics of water balance in the soil-atmosphere system based on the modified Palmer's two-layer soil moisture model and using the monthly meteorological ground observations and satellite-derived soil water observations. Strong correlation between satellite-derived mean monthly soil water and observed total discharges indicates strong hydrological connection between the parameters. Comparison of estimated (Palmer's) and measured runoff coefficients also indicate strong correlation although estimations are overestimated, depending on a month of the year. Interrelationship between estimated groundwater recharge and the observed spring discharges is used to demonstrate monthly storage/release dynamics of the underlying aquifer: water is usually stored during winter months and released during spring and summer. These preliminary results are in accordance with the existing knowledge of the catchment dynamics, and validate the existing hypothesis. However, further development of the research that focuses on further leveraging the connection between the ground measurements and remotely sensed data is needed to improve our understanding of quantitative relationship between the water balance components in the catchment.

Key words

Copernicus Land Monitoring Service (CLMS), ERA5 Land, soil-atmosphere water

balance, Palmer's two-layer soil moisture model, Bulaž Spring.

1 Introduction

Constantly increasing water supply demands is critical for long-term water supply planning, especially in regions with increased migrations on seasonal level, such as Adriatic coast. As the only accessible water resource in coastal region, the underlying karst aquifer directly influences regional development and climate-change resilience. Karst aquifers are highly sensitive – high permeability and rapid flows are making them highly vulnerable to contamination, and over-abstraction may easily affect the groundwater dynamics and induce seawater intrusion. Management of such water resources relies on detailed characterisation of karst aquifers however it requires knowledge of the spatial and temporal characteristics of its storage potential i.e., detailed insight into the spatio-temporal variability of the inflows and outflows. The basis for all hydrological calculations in that respect is determination of the catchment area size and extent (Bonacci et al., 2006). Delineation of catchment boundaries in karst aquifers is specifically complex task as the hydrological boundary rarely matches the topographical boundary and is temporally variable, depending on the groundwater dynamics. Hence it requires extensive geological, hydrological and hydrogeological investigations that are not often feasible. Commonly used approach to determine the catchment area is applying hydrological methods of estimating the water budget, i.e., effective rainfall. Selection of the appropriate method mostly depend on the data availability. Karst springs are usually not adequately monitored hence lack the discharge data, with gaps during the most critical periods such as droughts and floods. If the spring is used for the local water supply system, the pumping records are often incomplete. In general, the data available is usually scarce, often only precipitation and air temperatures.

Preliminary annual water budget investigations in Dinaric karst were usually conducted using the various empirical methods e.g., Turc (1954) and Langbein (1949) methods that require minimum input data, such as precipitation and air temperature, assuming the negligible changes in soil water storage. Detailed temporal analysis, e.g., seasonal or monthly water budgets were usually estimated using the Palmer's approach but that required more detailed data on soil moisture dynamics, which was rarely available.

Over the past decade, lots of effort was to put to produce global soil moisture products that can facilitate in estimating the soil water dynamics. One such product is ERA5 Land soil water data. It is, in general, a high temporal resolution global dataset derived from the ERA5 reanalysis, produced by replying the land component of the ECMWF ERA5 climate reanalysis (Muñoz-Sabater et al., 2021). It is not directly derived from the satellite remote sensing data however the satellite products are often used to evaluate ERA5 datasets. ERA5 Land provides detailed data (about 50 variables) for the land surface component of the ERA5 reanalysis but with higher spatial detail at resolution of 0.1° (app. 9 km). Temporal resolution is hourly to monthly and the available datasets span from 1950 till present (Okal et al., 2023). One of the key variables is soil water at various depths: 0-7 cm, 7-28 cm, 28-100 cm, 100-289 cm. It has been used extensively to improve modelling rainfall-runoff processes, hazard prediction etc.

This paper develops a monthly water budget of the Bulaž Spring catchment using the modified Palmer's approach, and supported by the spatially and temporally variable ERA5 Land soil water dataset along with the meteorological and the hydrological observations.

2 Methods

2.1 Study area

Bulaž Spring is an ascending karst spring in Mirna River watershed (Fig. 1), forming a lake approximately 50 m in diameter and 21 m deep. The total catchment area is estimated at 105 km^2 (Bonacci & Magdalenić, 1984; Magdalenić, 1988), mostly located in Croatia while only 16 % of the

catchment stretches into Slovenian territory. It is predominantly hilly flysch region with a well-developed torrential drainage network terminating in several ponors (Bazuje, Pašudija, Šterna, Malinska, ponors in Oprtaljska draga valley and Zrenjska vala creek) at the contact of limestone plateau and the alluvial Mirna River valley. Ponors enable focused discharge from the flysch terrain towards the spring and directly influence the abundance of the spring and its water quality.

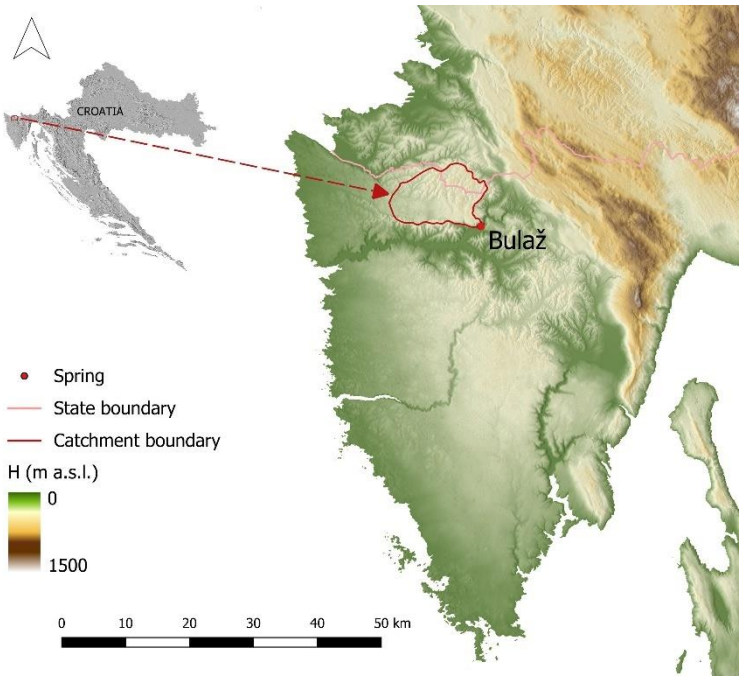


Figure 1. Location of the Bulaž Spring

The spring is part of the regional water supply system Istarski vodovod, d.o.o. but mostly as the reserve source, with infrastructure connecting Bulaž to other springs and the Butoniga reservoir.

2.2 Methodological framework

The approach often used in estimating the catchment water balance in Dinaric karst is the Palmer's two-layer soil model e.g., (Bonacci et al., 2006; Pandžić et al., 2009). It divides the soil into the two layers of various depth (Palmer, 1965), in which the loss of water from the lower (subsurface) layer depends on the initial water content, evapotranspiration rate and the water retention capacity. Evapotranspiration removes the water from the upper (surface) layer and when it reaches the potential rate, the lower layer starts losing the moisture. The root zone in the lower layer is not recharged as long as the upper layer does not reach maximum water retention capacity. Input data consists of precipitation, air temperatures and soil water content mean monthly values.

Monthly potential evapotranspiration, *PET* (mm) is calculated using the Eagleman's equation (Bonacci et al., 2006; Eagleman, 1967; Pandžić et al., 2009):

$$PET = C_t \cdot e_{max} \cdot (100 - RH)^{\frac{1}{2}};\ e_{max} = 6{,}1 \cdot e^{17{,}1 \cdot T/(234{,}2+T)} \tag{1}$$

where RH is the relative humidity (%), e_{max} mean monthly maximum water vapor pressure and Ct stand for the coefficient depending on temperature, T (°C):

$$C_t = \begin{cases} 0{,}6 & for\ \ T < 0\ °C \\ 0{,}63 + 0{,}024 \cdot T & for\ \ 0\ °C \leq T \leq 21\ °C \\ 1{,}13 & for\ \ T > 21\ °C \end{cases} \tag{2}$$

Palmer's water balance divides the soil profile into two layers, hence available soil water consists of two components: the soil moisture content of the upper layer, S_1 and the soil moisture content of the lower layer, S_2. Because of the rockiness of the soil and the various soil depth, soil moisture capacity in karst aquifers is significantly decreased. Maximum soil water holding capacities of the upper and lower layer are adopted from previous research (Andrić, 2014; Pandžić, 1985; Pandžić et al., 2009): for the upper soil layer S_{MAX1} = 0-2 mm and for the lower soil layer S_{MAX2} = 100-200 mm. The maximum (potential) amount of water in the soil (potential recharge) is computed as the difference between the maximum soil moisture holding capacity and the soil moisture stored in both soil layers (Eq. 3):

$$PR = S_{MAX} - (S_1 + S_2) \tag{3}$$

while potential runoff, PRO is the total soil moisture (Eq. 4):

$$PRO = S_{MAX} - PR \tag{4}$$

When evapotranspiration rate exceeds available precipitation, the water deficit is complemented with the soil moisture from the upper and partially from the lower soil layer (Yu et al., 2019). Potential loss, PL is the amount of moisture that would be lost if there were no precipitation in the observed month. PL in the upper layer equals PET if it does not exceed soil moisture in that layer. Lower layer contributes to PL depending on the relative soil moisture content of the lower layer in comparison with the maximum water holding capacity (Eq. 5):

$$\begin{gathered} PL = PL_1 + PL_2 \\ PL_1 = \min(PET, S_1)\,;\; PL_2 = (PET - P) \cdot \frac{S_2}{S_{MAX}} \end{gathered} \tag{5}$$

The actual soil moisture loss from both layers ($L = L_1 + L_2$) in Palmer's approach is the function of the water deficit (PET-P) and the soil moisture content in the observed layer (Eq. 6):

$$L_1 = \begin{cases} PET - P & for \quad PET - P > 0 \; i \; PET - P < S_1 \\ S_1 & for \quad PET - P > 0 \; i \; PET - P \geq S_1 \\ 0 & for \quad S_1 = 0 \end{cases}$$

$$L_2 = \begin{cases} 0, & for \quad L_2 \leq 0 \\ (PET - P - L_1) \cdot \dfrac{S_2}{S_{max}} & for \quad 0 < L_2 < S_2 \\ S_2, & for \quad L_2 \geq S_2 \end{cases} \tag{6}$$

Infiltration starts with the excess precipitation (P-PET). Recharging starts at the upper layer until it reaches its maximum capacity, then continues to infiltrate the lower layer. Surface runoff is generated when both layers reach their maximum water holding capacity, i.e. (Eq. 7):

$$\begin{cases} R = 0 & RO = 0 & for & P - PET \leq 0 \\ R = P - PET & RO = 0 & for & 0 < P - PET \leq S_{max} - S \\ R = S_{max} - S & RO = P - PET - R & for & P - PET > S_{max} - S \end{cases} \tag{7}$$

Actual evapotranspiration in Palmer's approach depends on the excess precipitation and the soil moisture loss (Eq. 8):

$$ET = \begin{cases} PET, & for \; P - PET \geq 0 \\ P + L, & for \; P - PET < 0 \end{cases} \tag{8}$$

The described equations ensure that losses cannot exceed the available water content and distributes the deficit proportionally between the layers, preserving the mass balance.

Finally, monthly runoff coefficients are calculated for the "normal" conditions using the CAFEC

precipitation (Climatologically Appropriate For Existing Conditions) i.e., precipitation needed to maintain a normal soil moisture level (Antofie et al., 2015; Yu et al., 2019) (Eq. 9):

$$P'_i = \alpha \cdot ET_i + \beta \cdot R_i + \gamma \cdot RO_i - \delta \cdot L_i = ET'_i + R'_i + RO'_i - L'_i \quad (9)$$

where α, β, γ, δ are correction coefficients calculated as the ratio between mean actual and mean potential monthly value of water balance components. Monthly runoff coefficient, C_{0i} is then calculated as the ratio between the corrected surface runoff and CAFEC precipitation (Eq. 10):

$$C_{0i} = {RO'_i}/{P'_i} \quad (10)$$

Methodological framework is illustrated in the Fig. 2.

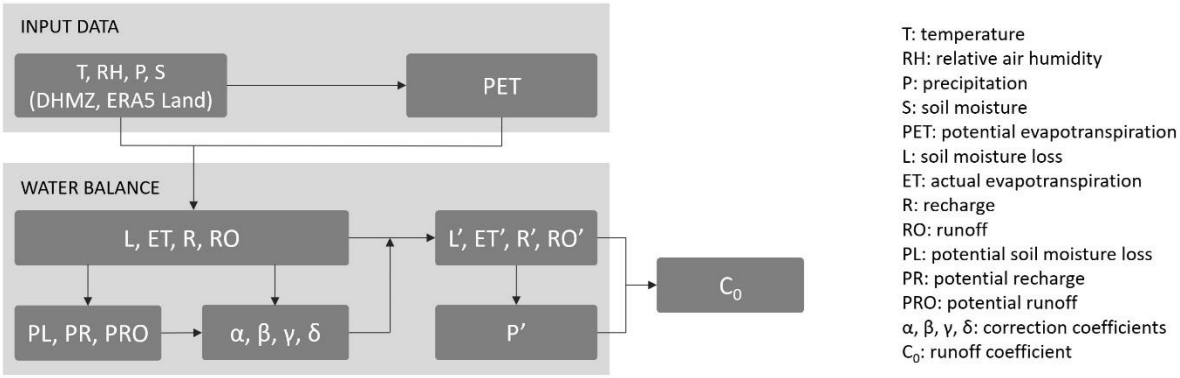


Figure 2. Methodological framework (C_0: runoff coefficient)

2.3 Data

2.3.1 Climate and hydrological data

Long term precipitation and air temperature data (1995-2023) are available from main meteorological, climate and rain gauge stations on the Istrian peninsula. Precipitation regime is strongly influenced by the relief: it shows a decrease towards the west coast and significant increase in central Istria and towards the Učka and Ćićarija. Precipitation in Istria is a mixture of maritime and continental type, with annual totals ranging from 700 mm on the western coast to more than 2500 mm at the Učka mountain (1961-1990) (Gajić-Čapka & Zaninović, 2008). Maximum precipitation occurs during autumn and winter while minimum precipitation occurs in summer (Fig. 3a). Mean annual air temperatures range from 8°C in higher elevation to 13 °C at the coast. The lowest temperatures are specific for the winter and the highest temperatures occur in summer (July) (Fig. 3b).

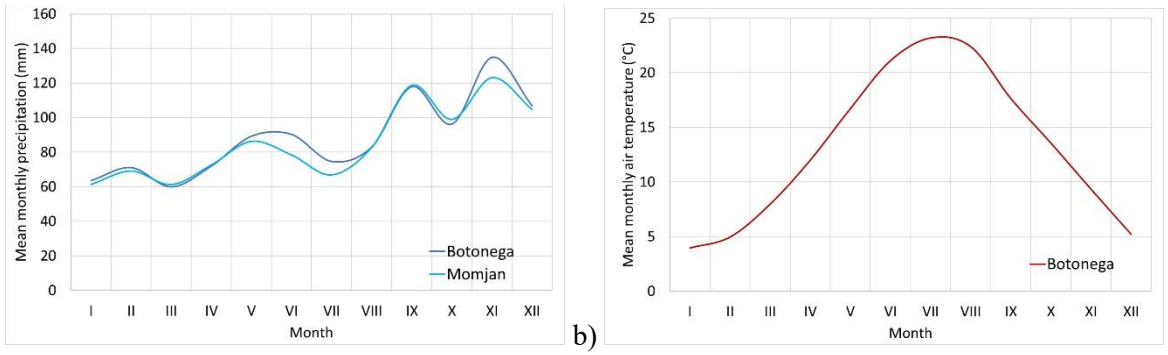


Figure 3. a) Mean monthly precipitation at the gauging stations Botonega and Momjan (1995-2023); b) Mean monthly air temperatures at the gauging station Botonega (1995-2023)

Hydrological monitoring at the spring began in 1988 when it became an alternative water source for the regional water supply system, covering only the peak water needs during the summer when water supply from St. Ivan and Gradole springs cannot meet the water demand. Minimum discharges occur at the end of summer while maximum occurs in late autumn and winter (Fig. 4a) but it should be taken into consideration that temporal interannual distribution of the discharges is partially influenced by the water extraction that reaches its maximum in August and minimum in April and November (Fig. 4b).

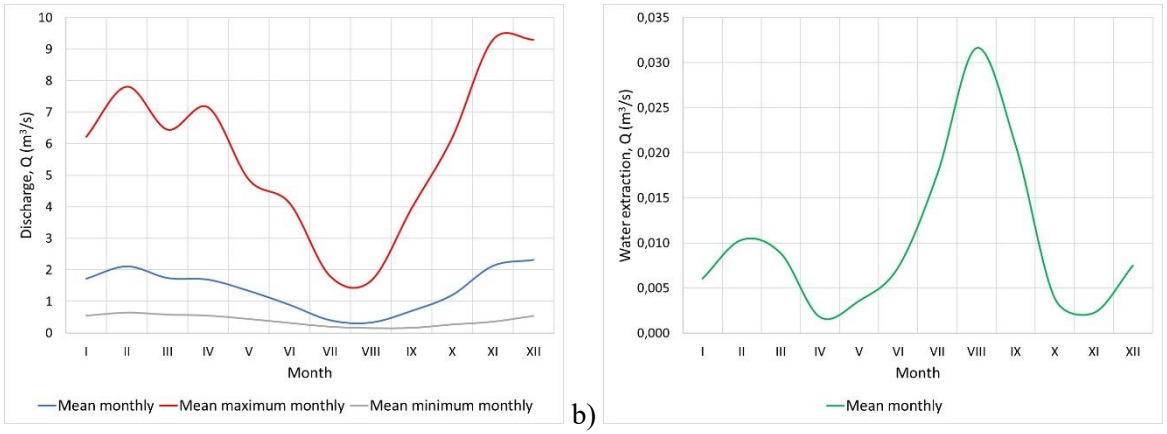


Figure 4. Mean monthly discharges at the Bulaž Spring (1988-2023): a) measured discharge; b) water extraction

2.3.2 ERA5 Land soil water and linkage to discharge

Multi year monthly mean soil water content in the two layers was extracted from the previously described ERA5 Land dataset (resampled to 0-2 mm depth of the upper layer and 100-200 mm depth of the lower layer) and resampled for the time period 1995-2023. Soil water content in ERA5 Land dataset is model-derived, not directly measured. The soil column is discretised into four layers at the depths 0-7 cm, 7-28 cm, 28-100 cm and 100-289 cm. Each layer contains the volumetric water content ($m^3\ m^{-3}$), representing a single bulk-average value for the entire depth of the layer. To calculate soil water content, the ERA5 Land volumetric water content is multiplied with the maximum soil water holding capacities of two soil layers (upper, S_{1MAX} and lower, S_{2MAX}). Soil water content of the upper layer (S_1) is calculated using the volumetric water content data of the top ERA5 Land layer (0-7 cm), while the soil water content of the lower layer (S_2) is calculated using the volumetric water content data of the bottom ERA5 Land layer (7-289 cm).

With the resolution of 9 km, spatial distribution in both layers describes general soil moisture conditions within the catchment area: higher soil moisture values in the eastern parts of the peninsula (higher altitudes) are gradually decreasing towards the coast in the west and north west (Fig. 5).

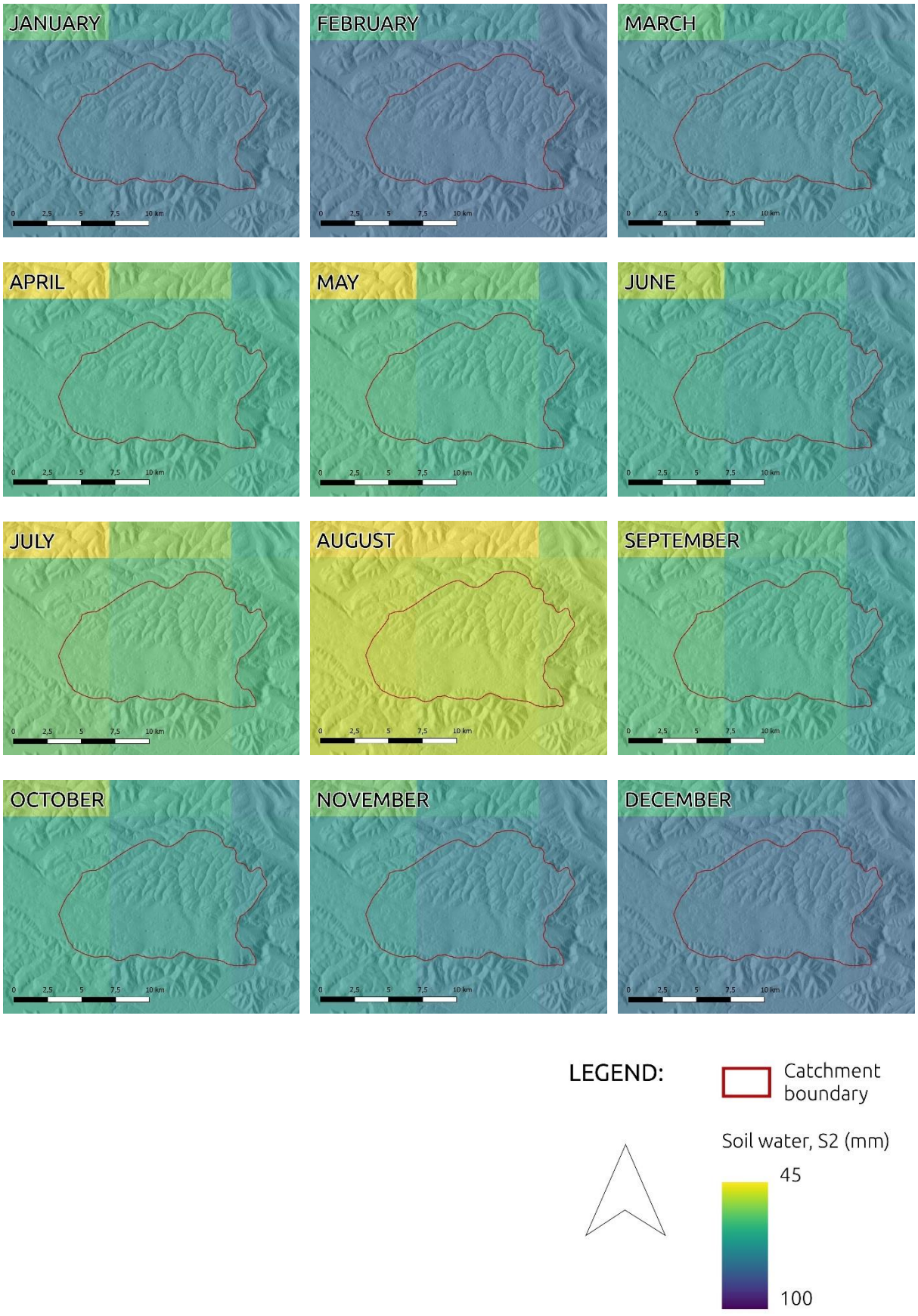


Figure 5. Monthly spatial distribution of the ERA5 Land soil water in the lower soil layer, S_2 = 100-200 mm (1995-2023)

Interannual distribution shows the lowest soil moisture in both layers during summer, with minimum in August in both layers and maximum in late autumn and winter (November for the upper layer and January for the lower layer) (Table 1, Fig. 6).

Table 1. Mean monthly total soil water (1995-2023)

	I	II	III	IV	V	VI	VII	VIII	IX	X	XI	XII	Year
TOTAL SOIL WATER, S (mm)													
MEAN	78.7	78.4	77.2	75.5	73.2	69.3	63.8	60.5	61.9	68.2	74.9	78.4	860.1
σ	2.9	3.3	3.6	3.8	3.8	4.1	3.3	4.4	6.0	7.0	5.7	4.0	33.3
MAX	82.9	84.3	83.4	82.8	79.5	76.2	69.1	72.9	79.7	79.9	83.8	83.2	925.3
MIN	71.1	71.0	70.8	69.6	65.3	59.0	54.7	51.5	50.2	56.3	61.9	65.4	778.6
SOIL WATER IN UPPER LAYER. S1 (mm)													
MEAN	0.76	0.75	0.73	0.71	0.69	0.61	0.53	0.53	0.64	0.72	0.77	0.76	8.20
σ	0.03	0.04	0.05	0.06	0.07	0.08	0.09	0.11	0.09	0.05	0.03	0.03	0.35
MAX	0.80	0.82	0.81	0.78	0.79	0.75	0.73	0.75	0.77	0.79	0.82	0.80	8.96
MIN	0.68	0.66	0.62	0.52	0.47	0.37	0.37	0.35	0.49	0.61	0.65	0.69	7.13
SOIL WATER IN LOWER LAYER. S2 (mm)													
MEAN	77.9	77.7	76.5	74.8	72.5	68.7	63.2	59.9	61.3	67.5	74.2	77.7	851.9
σ	2.9	3.3	3.6	3.7	3.7	4.0	3.3	4.3	6.0	7.0	5.6	4.0	33.0
MAX	82.1	83.5	82.6	82.0	78.7	75.5	68.6	72.1	78.9	79.1	83.0	82.4	916.5
MIN	70.3	70.3	70.2	69.0	64.8	58.6	54.3	51.1	49.7	55.6	61.2	64.7	771.5

MEAN: mean monthly soil water; σ: standard deviation of the mean monthly soil water; MIN: minimum mean monthly soil water; MAX: maximum mean monthly soil water

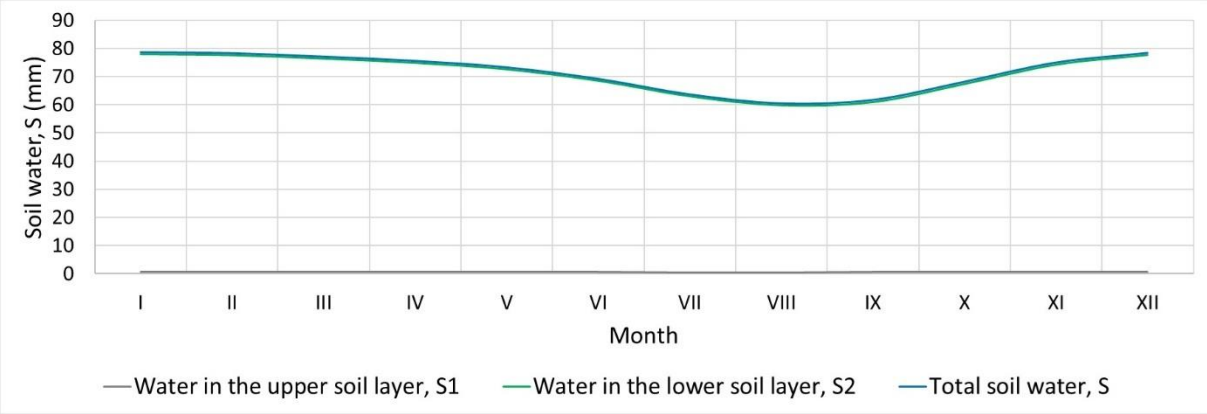


Figure 6. Interannual distribution of the ERA5 Land soil water (1995-2023)

3 Results and Discussion

Comparison of the monthly precipitation and discharges (Fig. 7a) for the selected time period (hydrological years 1995/1996-2022/2023) shows seasonality in parameters variation: the precipitation is highest in November, followed by the peak discharges in December, suggesting accumulation of the precipitation in the aquifer during winter and delayed groundwater response. Minimum discharges in summer, especially in July, reflect dry period and slow infiltration.

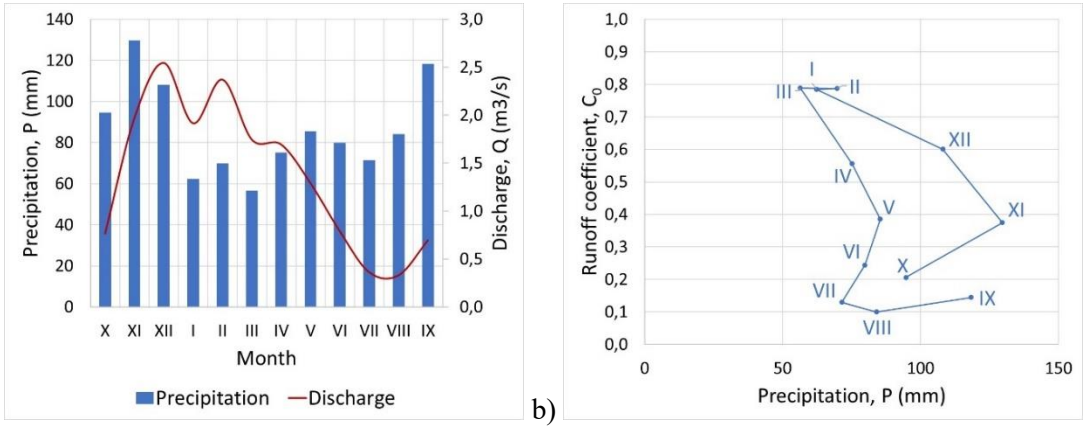


Figure 7. Mean monthly rainfall and runoff characteristics (1995/1996-2022/2023): a) interannual distribution of the mean monthly precipitation and the spring discharges; b) relationship between the mean monthly runoff coefficients and rainfall

Runoff coefficients are therefore the highest during January-March and the lowest in August (Table 2, Fig. 7b).

Table 2. Mean monthly runoff coefficients (1995/1996-2022/2023)

	X	XI	XII	I	II	III	IV	V	VI	VII	VIII	IX	Year
Q (mm)	19.5	48.6	64.9	48.9	54.9	44.5	41.8	32.9	19.5	9.3	8.4	17.1	410.4
P (mm)	94.7	129.6	108.0	62.3	69.7	56.4	75.1	85.4	79.8	71.4	84.1	118.3	1,034.9
$C_{0\text{-}M}$	0.206	0.375	0.601	0.784	0.788	0.789	0.556	0.386	0.244	0.130	0.100	0.145	0.425

Q: discharge measured at the Bulaž Spring; P: precipitation; $C_{0\text{-}M}$: measured runoff coefficient

The relationship between precipitation and runoff coefficients suggests prolonged groundwater discharge from the aquifer from January to August. During that time maximum runoff coefficients observed between January and March continuously decrease until reaching minimum values in August. Maximum precipitation is observed from September to December however, runoff response, observed in January to March, is delayed indicating prolonged water retention within the aquifer at the end of the year. Water retention is initially more pronounced at the beginning when the groundwater level is lowest since it was preceded by a prolonged period of aquifer discharge.

A strong correlation between integrated soil water content derived from ERA5 Land and Bulaž Spring discharge (r=0.9384) indicates a strong functional relationship between the catchment scale soil moisture storage and the spring discharge (Fig. 8). This initially supports the use of ERA5 Land soil water dataset as the substitute for the unavailable soil moisture measurements.

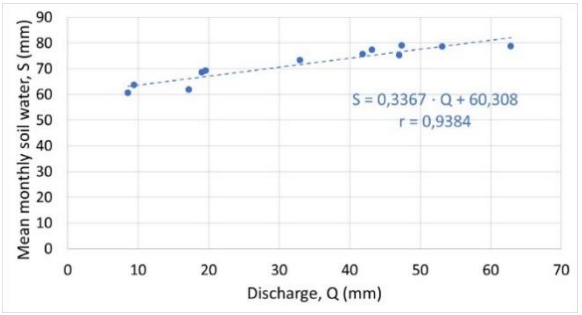


Figure 8. Correlation between the ERA5 Land soil water content and the spring discharge (1995-2023)

The maximum soil moisture capacities are set to 2 mm and 200 mm, reflecting local soil conditions (Bonacci et al., 2006; Bonacci & Andrić, 2015; Pandžić, 1985; Pandžić et al., 2009).

Water balance components were computed using previously described modified Palmer's approach adjusted to CAFEC precipitation, with spatially variable soil moisture dataset (Table 3).

Table 3. Summary of water balance components for the CAFEC precipitation (1995/1996-2022/2023)

	X	XI	XII	I	II	III	IV	V	VI	VII	VIII	IX	Year
ET' (mm)	39.4	26.0	16.7	15.9	19.8	29.0	41.8	65.3	98.4	121.3	109.1	64.5	647.3
R' (mm)	23.8	22.7	21.5	20.9	20.9	21.0	21.2	21.5	21.9	22.6	23.5	24.0	265.4
RO' (mm)	34.7	38.4	42.1	44.1	44.2	44.0	43.3	42.4	41.1	38.8	35.7	34.0	482.9
L' (mm)	5.2	3.9	2.7	2.8	3.4	4.9	6.9	10.4	15.1	17.5	14.4	8.2	95.2
P' (mm)	92.8	83.2	77.6	78.2	81.5	89.1	99.4	118.8	146.3	165.2	153.8	114.3	1,300.3

ET': corrected actual evapotranspiration; R': corrected recharge; RO': corrected runoff; L': corrected soil moisture loss; P': corrected (CAFEC) precipitation

Runoff coefficients are then calculated as the ratio between surface runoff and CAFEC precipitation and compared to the measured values (Table 4).

Table 4. Runoff coefficients (1995/1996-2022/2023)

	X	XI	XII	I	II	III	IV	V	VI	VII	VIII	IX	Year
$C_{0\text{-}P}$	0.374	0.462	0.543	0.564	0.542	0.494	0.436	0.357	0.281	0.235	0.232	0.297	0.401
$C_{0\text{-}M}$	0.206	0.375	0.601	0.784	0.788	0.789	0.556	0.386	0.244	0.130	0.100	0.145	0.425

$C_{0\text{-}P}$: calculated runoff coefficient; $C_{0\text{-}M}$: measured runoff coefficient

The described approach results in overestimation of the runoff coefficients during the months with maximum precipitation (October-November) as well as the minimum discharges (June-September). At the annual level, the difference between measured and estimated runoff coefficients is rather small. The mean annual discharge, based on the measured discharges at the Bulaž Spring, is Q_M = 1.37 m^3/s. Accordingly, the mean annual discharge based on the calculated runoff coefficient is Q_P = 1.46 m^3/s, overestimating the measured discharge by 6.4 %. Comparison between mean monthly runoff coefficients shows a strong correlation (r=0.9187) between the measured and the estimated values (Fig. 9).

The discharge overestimation during the months with maximum precipitation and underestimation during the rest of the year may be explained by the conceptual definition of the runoff component in the Palmer's method. Runoff is defined as a residual (eq. 7) and does not take into consideration physical factors that influence runoff. After meeting ET demand, precipitation that is left refills first the surface and then the underlying soil layer water deficit. Runoff is generated when both layers reach their full water holding capacity. Furthermore, it is often the case that the available water capacities are underestimated. The soil layer in karst is thin and the set maximum soil water holding capacity (S_{1MAX}, S_{2MAX}) captures only the capacity of the shallow soil mantle that cannot be fully representative of the much larger karst reservoir beneath. That leads to filling the soil layer at rate much smaller than underlying karst aquifer can absorb. The excess water is then recognized by the model as the residual i.e., runoff, leading to overestimation of the runoff. Similarly, when precipitation is small, there is no residual after meeting the ET demand and the soil layers water deficit resulting in runoff underestimation.

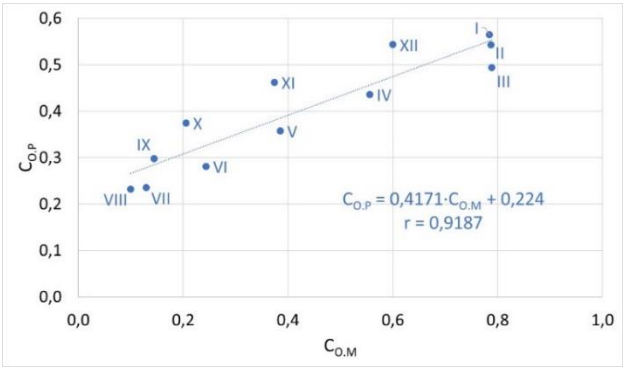


Figure 9. Correlation between the calculated, $C_{0.P}$ and the measured runoff coefficient, $C_{0.M}$ (1995/1996-2022/2023)

Soil moisture data used as the input data for the described model is derived from the ERA5 Land soil water data, with spatial resolution of app. 9 km. Such a coarse resolution is more appropriate for the global analysis. Catchment level of the analysis requires higher level of spatial detail, especially in karst regions, to enable capturing the heterogeneity of the karst systems. Bulaž Spring catchment is located at the contact of the hilly flysch area with the limestone plateau and the alluvial valley of the Mirna River, with hydrologically heterogeneous characteristics at the scale of few to tens of meters. With 9 km of spatial resolution, ERA5 Land data averages the soil moisture conditions and smooths out the extremes. Vertical resolution is another issue: ERA5 Land soil water dataset divides the soil column into four vertical layers at the depths of 0-7 cm, 7-28 cm, 28-100 cm and 100-289 cm, neglecting the vertical downward movement of water below the lowest layer. However, epikarst extends beyond that level and water that would normally be retained and recharge the deeper epikarst becomes the excess runoff by the model.

4 Conclusion

Soil moisture is an important component governing the water budget dynamics but its estimation is rather difficult due to lack of the necessary data, which is often the case in karst aquifers. The integration of the ERA5 Land derived spatial distribution of the soil moisture into the described modified two-layer Palmer methodological approach provides a practical way to approximate monthly soil moisture where in situ measurements are not available. Although the spatial distribution of the dataset is still quite coarse (~9 km) for the catchment scale analysis, temporal resolution is very high (hourly to monthly), providing valuable information on soil water dynamics. Demonstrated hydrological relevance of this dataset for the Bulaž Spring catchment water balance (strong correlation between soil moisture and the measured discharge) significantly improved the analysis of the seasonal and monthly water budget of the complex karst environment, such as Bulaž Spring catchment.

The described modified Palmer's approach is designed as the full water balance model, using minimum input data (precipitation, air temperature and soil moisture) and rather simple equations in describing the main processes in the soil-atmosphere system. Although the representation of the components is very simplified description of the real interactions within the system, especially in highly heterogeneous and complex terrain such as Bulaž Spring catchment, the approach proved to be very useful in regions with limited data and provides reasonable estimates for the long-term, monthly assessment of the water balance components.

Resolving the monthly water balance components as described in the paper, with spatially distributed soil moisture data derived from ERA5 Land, enables better understanding and interpretation of the water storage dynamics in the karst aquifers and hence provides relevant information for better water supply planning, drought assessment and protection of the karst water resources. Given its moderate data requirements and compatibility with moderate resolution ERA5 Land products, the proposed

methodology can easily be transferred to other karst systems with similar data constraints.

Acknowledgements

This research is the result of work carried out within the UNIRI Institutional Research Project "*Droughts Analysis with Application of the Space-born Earth Observation Technologies (ASOZ-s)*" (uniri-iz-25-40), approved by the Ministry of Science, Education and Youth (funded by the European Union - NextGenerationEU).

References

Andrić, I. 2014 *Primjena tehnologija temeljenih na hidroakustici, radaru i tlačnim senzorima kod praćenja i analize kretanja vode u kršu (Application of technologies based on hydroacoustics, radar and pressure sensors in monitoring and analysis of water movement in karst)* [Disertacija]. Sveučilište u Splitu.

Antofie, T., Naumann, G., Spinoni, J., and Vogt, J. 2015 Estimating the water needed to end the drought or reduce the drought severity in the Carpathian region. *Hydrology and Earth System Sciences*, *19*(1), 177–193. https://doi.org/10.5194/hess-19-177-2015

Bonacci, O., and Andrić, I. 2015 Karst spring catchment: an example from Dinaric karst. *Environmental Earth Sciences*, *74*(7), 6211–6223. https://doi.org/10.1007/s12665-015-4644-8

Bonacci, O., Jukić, D., and Ljubenkov, I. 2006 Definition of catchment area in karst: case of the rivers Krčić and Krka, Croatia. *Hydrological Sciences Journal*, *51*(4), 682–699. https://doi.org/10.1623/hysj.51.4.682

Bonacci, O., and Magdalenić, A. 1984 *Studija sliva izvora Bulaž u Istri*.

Eagleman, J. R. 1967 Pan Evaporation, Potential and Actual Evapotranspiration. *Journal of Applied Meteorology*, *6*(3), 482–488. https://doi.org/10.1175/1520-0450(1967)006<0482:PEPAAE>2.0.CO;2

Gajić-Čapka, M., and Zaninović, K. 2008 Klima Hrvatske / Climate of Croatia. In K. Zaninović (Ed.), *Klimatski atlas Hrvatske / Climate atlas of Croatia 1961-1990, 1971-2000* (pp. 13–17). Državni hidrometeorološki zavod / Meteorological and Hydrological Service of Croatia.

Magdalenić, A. 1988 *Zone sanitarne zaštite izvora Bulaž u Istri*.

Muñoz-Sabater, J., Dutra, E., Agustí-Panareda, A., Albergel, C., Arduini, G., Balsamo, G., Boussetta, S., Choulga, M., Harrigan, S., Hersbach, H., Martens, B., Miralles, D. G., Piles, M., Rodríguez-Fernández, N. J., Zsoter, E., Buontempo, C., and Thépaut, J.-N. 2021 ERA5-Land: a state-of-the-art global reanalysis dataset for land applications. *Earth System Science Data*, *13*(9), 4349–4383. https://doi.org/10.5194/essd-13-4349-2021

Okal, H. A., Molnar, P., Molnar, D., Mantel, S., Hughes, D., and Tanner, J. 2023 *ERA5-Land Data: New Possibilities in Hydrological Modelling and Water Resources Assessment in the Data-Scarce Regions of Sub-Saharan Africa*. https://doi.org/10.5194/egusphere-egu23-12695

Palmer, W. C. 1965 Meteorological Drought. In *Research paper No. 45*. U.S. Department of Commerce.

Pandžić, K. 1985 Bilanca voda na istočnom primorju Jadrana (Water balance on the eastern Adiatic coastal region). *Hrvatski Meteorološki Časopis*, *20*(20), 21–29.

Pandžić, K., Trninić, D., Likso, T., and Bošnjak, T. 2009 Long-term variations in water balance components for Croatia. *Theoretical and Applied Climatology*, *95*(1–2), 39–51. https://doi.org/10.1007/s00704-007-0366-5

Yu, H., Zhang, Q., Xu, C.-Y., Du, J., Sun, P., and Hu, P. 2019 Modified Palmer Drought Severity Index: Model improvement and application. *Environment International*, *130*, 104951. https://doi.org/10.1016/j.envint.2019.104951

FLOOD RISK ASSESSMENT AND HYDRAULIC CAPACITY ANALYSIS OF THE UNGAUGED ROKALOVO KARST CATCHMENT

Danko HOLJEVIĆ [1], Toni HOLJEVIĆ [2*]

[1] *Hrvatske vode, Croatia*

E-mail: Danko.Holjevic@voda.hr

[2] *Hidroprojekt-ing, Draškovićeva 35/1, 10000 Zagreb, Croatia Croatia*

E-mail: tholjevic@hp-ing.hr

[*] *Corresponding author*

Abstract

Hydrological analysis of ungauged karst catchments represents a significant challenge for urban planning and infrastructure safety, particularly in Mediterranean regions characterized by rapid responses to intense precipitation. This paper examines the Rokalovo stream catchment, for which historical measurements are unavailable, with the aim of defining flood risks for existing and future critical utility infrastructure. The focus of the work is on providing pragmatic engineering solutions by integrating the SCS (NRCS) method and Manning's equation. The results indicate that local, partial interventions are insufficient. Instead, it is necessary to adopt a holistic catchment management approach, emphasizing the importance of integrated regulation and the strategic use of retention areas to ensure the long-term resilience of the urban environment and vital infrastructure systems.

Key words

ungauged karst catchments, Rokalovo stream, infrastructure protection, parametric sensitivity, holistic management

1 Introduction

Hydrological analysis of ungauged karst catchments represents a significant challenge for urban planning and infrastructure safety, especially in Mediterranean regions characterized by the rapid response of torrential catchments to intense precipitation. Determining the relevant flows for such torrential watercourses requires a careful approach because quick and rough estimates of peak flows using simpler methods (such as the rational method) do not provide information on the shape and duration of the flood wave. For adequate flooding analysis and reliable dimensioning of protective structures in ungauged catchments, it is extremely important to define complete runoff hydrographs, which necessitates the use of finer and more detailed methods.

The need for such a detailed analysis of the Rokalovo stream catchment arose from the fact that the existing facility and the planned expansion project of the Stupe Wastewater Treatment Plant (WWTP) in the city of Split are located in a potentially flood-prone area. The Rokalovo torrent is a typical Mediterranean torrential watercourse, characterized by steep terrain slopes and an extremely short time of concentration in the event of intense precipitation, representing a high flood risk. The catchment forms on the southern slopes of Mount Mosor (Fig. 1), extends through the administrative areas of the City of Split (Cadastral Municipalities of Kučine, Kamen, and Žrnovnica), and flows into the Vrbovnik stream, which is the main recipient, in the industrial-commercial zone (TTTS).



Figure 1. The Rokalovo torrent catchment at the foot of Mount Mosor

The total catchment area is 1.92 km². The topography is characterized by significant elevation differences in a small area, with a maximum altitude of H_{max} = 358 m a.s.l. in the source area and a minimum altitude of H_{min} = 9 m a.s.l. at the confluence with the Vrbovnik stream. The average slope of the entire catchment system is 5.3%.

The risk of flooding, apart from natural predispositions, is today drastically exacerbated by general catchment urbanization and significant anthropogenic interventions within the catchment area. The trend of converting natural green and agricultural areas into construction land (such as residential and commercial zones in the settlements of Kamen and Korešnica) directly reduces the possibility of water infiltration into the soil and significantly increases the runoff coefficient. Due to this urbanization and land use change, historically relevant flows lose their reliability, and the threat of overflow and flooding grows uncontrollably. This imposes the necessity of finding a new torrential channel regulation solution based on updated high water flows.

The threat of overflow is further increased by specific infrastructure projects in the catchment:

- Karepovac landfill remediation: Large impermeable cover surfaces have been formed, from which stormwater is directly discharged into Rokalovo via a newly designed drainage channel, generating a rapid peak inflow (Institut IGH, 2015; Fig. 2).
- Construction of the Trogir – Omiš expressway: The project envisages additional discharge of stormwater drainage from the new Karepovac interchange directly into the torrent (Geoprojekt, 2024).
- Expansion of the Stupe WWTP itself: The newly formed plant plateau is planned to be expanded to the north, with the plateau elevation situated about 7.0 meters lower than the natural bottom of the Rokalovo stream channel, on the very edge of the active torrent (Hidroprojekt-consult, 2016).
- Any overflow from the channel would result in a flood wave falling directly onto the sensitive plant equipment (Fig. 3).



Figure 2. Regulated stormwater flow of the Karepovac landfill



Figure 3. Stupe plant set at a lower elevation relative to the Rokalovo torrent

The aim of this paper is to define the relevant high water values for return periods of 50 and 100 years, conduct a hydraulic analysis of the existing channel capacity, and propose an optimal engineering regulation solution that will ensure long-term stability and protection of critical infrastructure, integrating the needs of flood protection and stormwater drainage of the urbanized area.

2 Methods

Given that this is a hydrologically ungauged catchment without historical flow measurements, the SCS (NRCS - Natural Resources Conservation Service) unit hydrograph method was selected for the transformation of precipitation into runoff. This method is widely accepted in Croatian engineering practice, particularly in the coastal and island Mediterranean karst areas.

Based on the conducted GIS analysis, and to achieve greater calculation accuracy, the entire Rokalovo stream catchment was divided into five characteristic sub-catchments (Fig. 4).

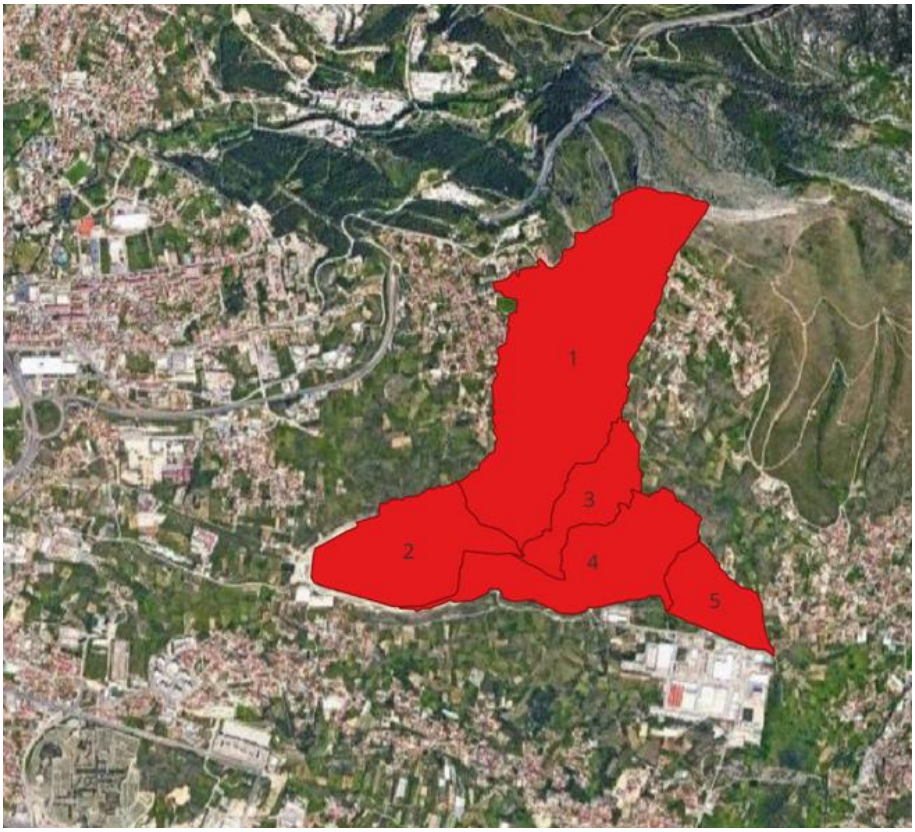


Figure 4. Schematic representation of the division of the Rokalovo torrent catchment into 5 sub-catchments

Figure 5 shows the analyzed 1.4 km long section of the Rokalovo torrent.



Figure 5. Analyzed section of the Rokalovo torrent

To estimate the time of concentration (t_c), the SCS Lag method (TR-55) was applied. The time of concentration is derived from the lag time (t_{lag}), which represents the shift between the center of mass of effective precipitation and the hydrograph peak, according to the expression:

$$t_c = t_{lag} / 0.6 \approx 1.67 \cdot t_{lag} \quad (1)$$

The lag time (t_{lag}) itself in hours is calculated based on three physical catchment parameters according to the formula:

$$t_{lag} = (L^{0.8} \cdot (S_p + 1)^{0.7}) / (1900 \cdot Y^{0.5}) \quad (2)$$

Where:

- t_{lag} = Lag time (hours)
- L = Hydraulic flow length (in feet, ft)
- Y = Average catchment slope (in percent, %)
- S_p = Maximum potential catchment retention (in inches, in)

The retention parameter (S_p) directly depends on the adopted runoff curve number (CN):

$$S_p = (1000 / CN) - 10 \quad (3)$$

Although Mediterranean karst catchments exhibit complex infiltration mechanisms, the SCS-CN unit hydrograph and TR-55 lag method (USDA-SCS, 1986) represent standard and reliable engineering tools in regional practice (Hrvatske vode, 2023). To account for the inherent uncertainties of karst hydrogeology and soil classification, conservative hydrological soil group parameters were adopted, ensuring an adequate safety margin for the design of protection structures.

Based on a detailed land cover analysis (Urban Atlas) and the hydrological soil group, a weighted CN value was calculated for the entire catchment according to the corresponding sub-catchments (Table 1).

Table 1. Results of weighted CN value calculations

Land Cover Class	Area km² (1+2+3)	Area km² (4)	% (1+2+3+4)	CN Class (B)	CN Class (C)	CN Class (D)	1+2+3 (B)	1+2+3 (C)	1+2+3 (D)	4 (C)
Continuous urban fabric (S.L. > 80%)	0.00		0%	92	94	95	0.00	0.00	0.00	0.2
Discontinuous dense urban fabric (S.L.: 50% - 80%)	0.18	0.24	12%	85	90	92	10.61	11.23	11.48	10.7
Discontinuous medium density urban fabric (S.L.: 30% - 50%)	0.01		0%	75	83	87	0.00	0.00	0.00	0.2
Industrial, commercial, public, military and private units	0.00	0.01	1%	90	93	94	0.18	0.18	0.19	0.5
Other roads and associated land	0.02	0.03	2%	98	98	98	1.48	1.48	1.48	1.6
Mineral extraction sites and dump sites	0.23	0.27	14%	98	98	98	16.24	16.24	16.24	13.7
Land without current use	0.01	0.01	0%	86	91	94	0.42	0.44	0.46	0.3
Sports and leisure facilities	0.01	0.01	0%	79	86	89	0.37	0.40	0.41	0.3
Arable land (annual crops)	0.08	0.25	13%	85	90	93	4.56	4.83	4.99	11.0
Pastures	0.37	0.53	26%	69	79	84	17.81	20.39	21.68	19.1
Forests	0.08	0.08	4%	60	73	79	3.29	4.00	4.33	2.4
Herbaceous vegetation associations (natural grassland, etc.)	0.45	0.48	25%	71	81	89	22.46	25.63	28.16	18.0
TOTAL	**1.42**	**1.92**	**100%**				**77**	**85**	**89**	**78**

Statistical processing of precipitation data was carried out according to the guidelines from the "Adriatic Hydrological Study - Book 3" (VEPAR project). The design return periods of 50 and 100 years (Pr = 50 and Pr = 100 years) were selected in accordance with long-standing Croatian engineering practice and national regulatory criteria for the flood protection of critical municipal utility infrastructure (such as the Stupe WWTP) and adjacent dense industrial-commercial zones. The analytical IDF (Intensity-Duration-Frequency) curves derived for the Split Marjan rain gauge station (code 070) in power-law form were used as relevant data:

- For Pr = 50 years (Annual Exceedance Probability 2%): $I = 12.875 \cdot t^{-0.653}$
- For Pr = 100 years (Annual Exceedance Probability 1%): $I = 14.176 \cdot t^{-0.652}$

The calculation of flow and capacity in the open sections of the channel (both existing and newly

designed state) was performed using Manning's equation for steady and uniform flow:

$$Q = A \cdot v = A \cdot (1/n) \cdot R_h^{2/3} \cdot S_0^{1/2} \quad (4)$$

Where:

- Q = Calculated flow (profile capacity) [m³/s]
- A = Flow area [m²]
- R_h = Hydraulic radius [m]
- S_0 = Channel bottom slope [m/m]
- n = Manning's roughness coefficient.

For calculation purposes, the following values were adopted:

- n = 0.035 (for natural channel - profiles P1-P10, P12-P27)
- n = 0.013 (for concrete culvert P11, analyzed separately)

3 Results and Discussion

Iterative hydrological calculations for different rainfall durations determined the relevant peak flows at key profiles (Hidroprojekt-ing, 2025). The final relevant flow at the discharge profile towards the Vrbovnik stream (point J4) is 18.06 m³/s for a 50-year return period and 20.76 m³/s for a 100-year return period. Hydraulic verification of the existing state undoubtedly points to a critical channel capacity deficit along the entire section, but particularly at three locations:

- Profile P11 (Pipe culvert)
- Section P1 - P5 (Existing concrete channel)
- Section P20 - P5 (Rip-rap channel)

In the current state of the Rokalovo torrent channel, the occurrence of extreme precipitation and consequent runoff leads to flooding and overflow north of the WWTP location. This, combined with the fact that the WWTP plateau is expected to expand and further lower relative to the natural channel, would certainly cause significant damage to the newly built Stupe wastewater treatment plant. Considering the aforementioned, the dimensioning of a new regulation for the Rokalovo torrent was undertaken. Two options were analyzed: a rectangular reinforced concrete invert lined with rough stone, and a trapezoidal channel lined with stone.

The optimal engineering solution selected is a single, hydraulically continuous open rectangular reinforced concrete (RC) invert with a lining of rough crushed stone embedded in concrete. The stone lining increases the roughness coefficient, which purposefully slows the flow and encourages kinetic energy dissipation. The hydraulic parameters of the newly designed rectangular RC invert are: dimensions 3.0 × 2.2 m, longitudinal slope of 1%, design average velocity of 3.57 m/s, wall safety freeboard of 0.27 m, Froude number of 0.82, and a total profile capacity of 20.67 m³/s.

Due to the uncertainty in defining exact hydrological soil groups across the ungauged Rokalovo karst catchment, conservative (unfavorable) Curve Number (CN) values were intentionally selected. A sensitivity analysis showed that a variation of the weighted CN by ± 5% results in a peak discharge variation of approximately ± 9% for the 100-year event, confirming the stability and predictability of the hydrological model under extreme rainfall events. Furthermore, evaluating the hydraulic robustness across different rainfall durations demonstrated that the proposed rectangular RC channel, with its designed safety freeboard, possesses sufficient reserve capacity. It can safely convey extreme flow rates exceeding the calculated 100-year peak flow without overtopping or endangering the adjacent WWTP plateau.

Regarding ecological and morphodynamic aspects, nature-based or unlined bioengineered channel

solutions were considered but deemed unfeasible. Given the steep longitudinal catchment slope and high design flow velocities, an unlined or vegetated channel would suffer catastrophic bed erosion and bank scouring during flash floods. Therefore, a rigid reinforced concrete profile lined with rough crushed stone embedded in concrete was adopted as the optimal technical compromise, ensuring absolute structural stability and roughness-induced kinetic energy dissipation within a minimal spatial footprint. The analyzed alternative solution with an open trapezoidal channel, although meeting the required capacity, was rejected for two key reasons:

- Excessive footprint: The crest width of the trapezoidal channel would be as much as 6.40 m. Such a wide corridor would directly encroach upon the roadway of Mosorska Street and private parcels, causing long-term property and legal disputes.
- Unfavorable flow regime: The trapezoidal profile would result in supercritical/rapid flow. To achieve the design longitudinal regulation slope, the construction of a series of water steps is planned in accordance with the existing terrain configuration.

4 Conclusion

The presented example of analyzing floodwaters in the ungauged Rokalovo torrential catchment confirms the specificities and engineering challenges in the process of finding optimal solutions aimed at ensuring the long-term resilience of the urban environment and vital infrastructure systems. The conducted hydrological-hydraulic analysis confirms that existing local and partial interventions on the Rokalovo torrential stream cannot meet the flood safety criteria for the existing and future urban infrastructure. The existing state of the channel, and particularly the critical pipe culvert P11, represents a direct threat to the functioning of the Stupe WWTP and surrounding commercial facilities in the TTTS zone. The implementation of comprehensive regulation in the form of a 3.00 m wide rectangular RC channel with stone lining and water steps successfully transitions the flow into a controlled subcritical regime, ensuring the safe accommodation of relevant 100-year flood waves, but also raises the question of future regulation works in the wider catchment area of this part of Split.

References

Geoprojekt d.d. 2024 Trogir – Omiš expressway, section: from Mravince interchange to TTTS interchange. Folder 04: Stormwater drainage and water protection, Split.
Hidroprojekt-consult d.o.o. 2016 Expansion of the Stupe wastewater treatment plant – Preliminary design, proj. no. S/701 - 1/3 GR, Zagreb.
Hidroprojekt-ing d.o.o. 2025 Hydrotechnical analysis of the Rokalovo stream catchment: Hydrological-hydraulic calculation for defining relevant high waters of 50 and 100 year return periods, Zagreb.
Hrvatske vode 2023 *Adriatic Hydrological Study - Book 3: Improvement of hydrological bases. Project for the improvement of non-structural flood risk management measures in the Republic of Croatia* (VEPAR), Zagreb.
Institut IGH d.d. 2015 *Karepovac landfill waste disposal site in Split – Book 5: Amendment to the main design of the road and drainage channel with stormwater drainage to the "Rokalovo" stream, proj. no. 3400-0259/2015*, Split.
USDA-SCS 1986 *Urban Hydrology for Small Watersheds*. Technical Release 55 (TR-55), United States Department of Agriculture, Soil Conservation Service, Engineering Division, Washington D.C. management

EVALUATION OF REANALYSIS AND CLIMATE PRODUCTS FOR WIND FORCING OF A MID-ADRIATIC NUMERICAL WAVE MODEL

Lovro ŠTEFAN [1*], Damjan BUJAK [1], Hanna MILIČEVIĆ [1], Dalibor CAREVIĆ [1]

[1] *University of Zagreb Faculty of Civil Engineering, Croatia*

E-mail: lovro.stefan@grad.unizg.hr

E-mail: damjan.bujak@grad.unizg.hr

E-mail: hanna.milicevic@grad.unizg.hr

E-mail: dalibor.carevic@grad.unizg.hr

[*] *Corresponding author*

Abstract

Accurate atmospheric forcing is essential for reliable numerical wave modelling in semi-enclosed basins with complex island-mainland geometry such as the mid-Adriatic area of coastal Croatia. Multiple reanalysis and climate products provide wind fields of varying spatial and temporal resolution, yet their performance as forcing for regional wave simulations requires systematic evaluation. This study assesses selected products (ERA5, CERRA, ICON-DREAM, MERIDA) as wind forcing for a high-resolution numerical wave model of the Croatian mid-Adriatic area. Wave simulations were performed using SWAN, implemented on an unstructured computational grid covering the coastal-island system and validated against buoy wave measurements. Solution verification was conducted by simulating the most severe recorded storm event using ERA5 forcing. Three mesh configurations of varying cell sizes and three directional resolutions were tested to quantify numerical sensitivity to spatial and spectral discretization. Preliminary results indicate that mesh refinement and directional resolution have little influence on model results for the tested storm event below a cell area of 100 000 m^2. Model calibration was subsequently carried out by adjusting the Janssen whitecapping coefficient for each wind product. The findings underline the importance of careful model development when applying reanalysis and climate products as wind forcing for regional SWAN-based modelling.

Key words

numerical wave model, SWAN, wind forcing, atmospheric reanalysis products, Adriatic Sea

1 Introduction

The Adriatic Sea is a semi-enclosed basin of the Mediterranean, extending approximately 800 km from the Gulf of Trieste in the northwest to the Strait of Otranto in the southeast, with a mean width of around 170 km. Its eastern coastline is among the most complex in the Mediterranean, characterized by a large number of islands, channels, and bays that create highly variable wave conditions across short distances. The wave climate of the Adriatic is dominated by two regional wind systems: the bora, a strong northeast orographic wind with limited fetch, and the sirocco, a southeast wind with considerably longer fetch extending along the entire basin (Katalinić and Parunov, 2018; Bonaldo et al., 2017). These wind regimes, combined with complex coastal geometry, produce wave fields that are strongly spatially heterogeneous and difficult to characterize from sparse point measurements alone.

Reliable wave data are essential for the design of coastal and offshore structures, assessment of extreme sea states, coastal zone management, analysis of coastal processes, and flood risk assessment (Dutour

Sikirić et al., 2018; Ruol et al., 2022; Cavaleri et al., 2018). Wave parameters can be obtained through in situ measurements, satellite altimetry, and numerical modelling. While wave buoys and platforms provide high-quality local time series, their spatial coverage is inherently limited. Satellite altimetry allows for wider spatial coverage and can be used for validation of hindcast datasets, but its applicability is restricted in narrow basins and within approximately 20 km of the coastline (Katalinić and Parunov, 2018; Barbariol et al., 2021).

Numerical spectral wave models of the third generation, which solve the wave action balance equation, have become the primary tool for wave climate analysis and forecasting in coastal and semi-enclosed seas (WMO, 2018). In such environments, model accuracy depends critically on the quality of the bathymetric description and, above all, on the quality of the wind forcing (Cavaleri et al., 2018; Cavaleri et al., 2020). In the Adriatic, wind forcing is of particular importance due to the complex orography and strong spatial gradients in wind fields. Several studies have demonstrated that errors in wind input lead to systematic underestimation of significant wave height, particularly during extreme events and under bora and sirocco conditions (Dutour Sikirić et al., 2018; Lončar et al., 2010; Barbariol et al., 2022). Lončar et al. (2010) showed that model agreement with buoy measurements was strongly conditioned by the quality of ALADIN wind fields, while Dutour Sikirić et al. (2018) demonstrated that an operationally applied unstructured-grid model reproduced the general wave climate well but consistently underestimated peak wave heights, a deficiency also attributed to insufficient wind forcing. Barbariol et al. (2022) further showed that a portion of this error can be reduced through statistical downscaling of the input wind field. The parameterization of whitecapping dissipation serves as the primary calibration mechanism in most spectral wave models and is commonly used to compensate for deficiencies in wind forcing (Cavaleri et al., 2018). This approach was systematically applied by Bujak et al. (2023), who calibrated the Janssen whitecapping coefficient separately for ERA5 and ALADIN forced SWAN models in the fetch-limited mid-Adriatic region near Split, demonstrating that careful whitecapping calibration can bring ERA5-forced model performance to a level comparable with a finer-resolution regional wind product, despite the considerably coarser spatial resolution of ERA5.

Wave climate projections for the Adriatic under climate change scenarios consistently indicate a general reduction in mean wave energy, though with pronounced spatial variability (Benetazzo et al., 2012; Bonaldo et al., 2020; Moulin et al., 2024). Studies based on high-resolution SWAN implementations further highlight the importance of fine spatial resolution for capturing wave extremes in complex coastal geometries (Denamiel et al., 2020).

The mid-Adriatic coastal area of Croatia presents modelling challenges due to its dense island archipelago, restricted fetch conditions, strong island sheltering effects, and rapid spatial variations in wind direction. This study focuses on this region and assesses the performance of four wind forcing datasets, ERA5, CERRA, ICON-DREAM-EU, and MERIDA, as input to a high-resolution SWAN wave model implemented on an unstructured computational grid. The sensitivity of model results to spatial and spectral discretization is examined through solution verification, and the Janssen whitecapping coefficient is calibrated independently for each forcing dataset against buoy wave measurements from an October 2018 storm event.

2 Methods

2.1 Study area

The model domain covers part of the central Adriatic Sea along the Croatian coast. It extends from Drvenik Mali Island in the northwest and the island of Vis in the southwest to the Mali Ston Bay in the southeast. Korčula Island and Pelješac Peninsula form the southern border of the research area, while in the north it extends to Kaštela bay. The area has a complex topography and bathymetry, as shown in Figure 1. Three large islands (Hvar, Brač and Šolta) are located within the domain, as well as several smaller islands and numerous islets. The deepest point of the domain is roughly on the western boundary, at a depth of approximately 120 m. The area is characterized by a number of narrow channels between

the islands and the coast. Many beaches and marinas in the region make it highly attractive, especially for nautical tourism.

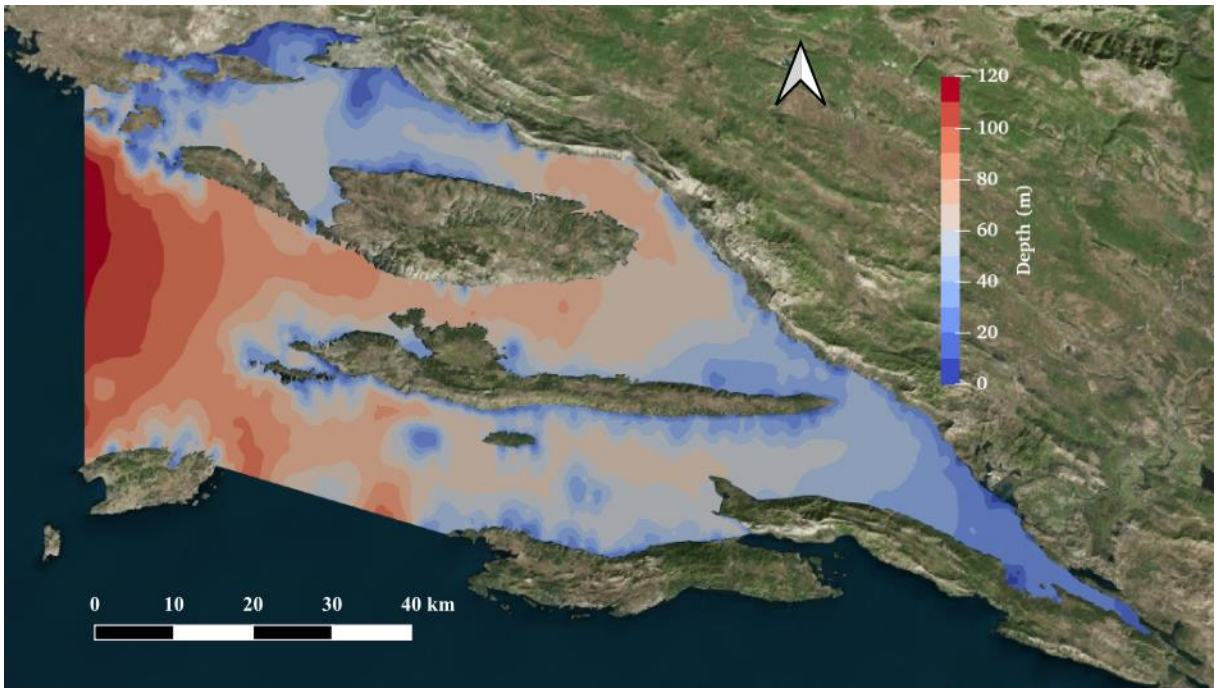


Figure 1. Bathymetry of the study area

2.2 Wind forcing data

Wind forcing for the numerical wave simulations was obtained from four atmospheric reanalysis and regional climate datasets, which differ in spatial resolution, temporal coverage, and geographic extent. The key characteristics of each product are summarized in Table 1.

ERA5, produced by the European Centre for Medium-Range Weather Forecasts (ECMWF) as part of the Copernicus Climate Change Service, is a global atmospheric reanalysis providing hourly wind fields at a horizontal resolution of approximately 31 km, or 0.25° (Copernicus Climate Change Service, 2023; Hersbach et al., 2020). Its long temporal coverage, from 1940 to the present, and global availability make it a widely used atmospheric forcing dataset in wave modelling studies. In this study, ERA5 is used as the baseline dataset for model verification.

CERRA, the Copernicus European Regional ReAnalysis, is a regional reanalysis produced using the HARMONIE-ALADIN limited-area numerical weather prediction system. It provides atmospheric fields over Europe at a horizontal resolution of 5.5 km. Analysis fields are available at 3-hourly intervals, while forecast fields are available at hourly resolution (Schimanke et al., 2021). Compared with ERA5, the finer spatial resolution of CERRA may provide a better representation of mesoscale wind features relevant to the complex coastal topography of the study area.

ICON-DREAM-EU, the European-domain component of ICON-DREAM, is a regional reanalysis developed by the German Meteorological Service, DWD. It is based on the ICOsahedral Nonhydrostatic, or ICON, modelling framework. The dataset provides hourly wind fields over Europe at a horizontal resolution of 6.5 km and is available from 2010 onwards (Valmassoi et al., 2025).

MERIDA, the MEteorological Reanalysis Italian DAtaset, is a dynamical downscaling of ERA5 over Italy and the surrounding region. The standard MERIDA product has a horizontal resolution of 7 km, while the high-resolution version, MERIDA HRES, provides fields at 4 km resolution from 1986 onwards (Bonanno et al., 2019; Viterbo et al., 2024). Given that the MERIDA domain encompasses the Adriatic Sea and the surrounding region, it may provide an improved representation of local wind

patterns within the complex island–mainland geometry of the Croatian mid-Adriatic compared with coarser global products.

Table 1. Wind data source comparison

Wind data	Spatial resolution	Temporal resolution	Spatial availability	Temporal availability
ERA5	0.25° (~31 km)	1h	global	1940 – present
CERRA	5.5 km	3h (analysis), 1h (forecast)	Europe	1984 – present
ICON-DREAM-EU	6.5 km	1h	Europe	2010 – present
MERIDA	7 km 4 km (HRES)	1h	Italy and surrounding region	1990 – 2024 1986 – 2024 (HRES)

ERA5, ICON-DREAM-EU and MERIDA wind data are provided as two separate component datasets, u10 m and v10 m wind speed components (zonal and meridional 10 m wind speeds). CERRA data, on the other hand, is provided as 10 m wind direction and 10 m wind speed variables. Prior to running the simulations, wind fields were modified if needed, from curvilinear to rectangular, i.e. to match the Croatian HTRS96 reference coordinate system in which the computational mesh was produced.

2.3 Numerical wave model

Third generation numerical wave model SWAN was used for wave modelling. It is a wind wave model based on the dynamic spectral balance equation with sinks and sources (1).

$$\frac{\partial N}{\partial t} + \frac{\partial C_x N}{\partial x} + \frac{\partial C_y N}{\partial y} + \frac{\partial C_\sigma N}{\partial \sigma} + \frac{\partial \theta N}{\partial \theta} = \frac{S}{\sigma} \tag{1}$$

Left side in the equation (1) represents kinematic component, i.e. action (energy) density change in space, time, frequency and direction, whereas the right-hand side of the equation shows the total source of wave energy. The total source term includes wind-related energy input, white-capping dissipation, nonlinear quadruplets wave energy transfer, triad nonlinear interaction, and dissipation caused by depth-related wave breaking (The SWAN team, 2024a,b).

The computational domain is discretized using an unstructured triangular mesh, as shown in Figure 2. The mesh covers the Croatian mid-Adriatic coastal-island system, conforming to the complex shoreline geometry of the mainland coast and the surrounding islands. Two open boundaries are defined along the western (Drvenik Mali to Vis) and southern (Vis to Korčula) edge of the domain, through which wave energy can propagate into the domain. Also shown in Figure 2 is the location of the wave measurement buoy, indicated by the yellow marker. Buoy records were used to identify a severe storm event in October 2018, which serves as the basis for all simulations conducted in this study. This event was selected for model verification, calibration of the whitecapping coefficient, and the subsequent comparison of wave model results obtained using the four wind forcing datasets.

Boundary conditions were prescribed using wave spectra obtained from the Copernicus Marine Environment Monitoring Service (CMEMS, 2024). Wave parameter time series were extracted at two points, each corresponding to one of the open boundaries, and the extracted series were applied uniformly along the full length of the respective boundaries, assuming spatial homogeneity of the incoming wave field along each boundary line.

The wave model was run in non-stationary, two-dimensional mode on the unstructured triangular mesh described above. The spectral space was defined using a full 360° directional circle and a frequency range from 0.05 to 2.00 Hz.

Wave generation and dissipation physics were configured using the third-generation formulation (GEN3) with the Janssen wind input and whitecapping scheme. The Janssen scheme describes exponential wave growth driven by atmospheric forcing and dissipation through whitecapping, with the whitecapping rate controlled by the coefficient *Cds*, which was adjusted during model calibration as described in Section 2.3.2. Default SWAN formulations were adopted for the remaining source terms. Depth-induced wave breaking was activated using the constant breaker index formulation of Battjes and Janssen, with a proportionality coefficient $\alpha = 1.0$ and a breaker index $\gamma = 0.73$. Bottom friction dissipation was modelled using the JONSWAP formulation.

The convergence criterion for the iterative solver was defined using the STOPC option, requiring that the absolute change in significant wave height between iterations be less than 0.005 m, the relative change less than 0.01, and the curvature of the iteration curve less than 0.005, with all conditions satisfied in more than 95% of wet grid points. The model was run with a time step of 10 minutes over the simulation period, with output recorded at hourly intervals.

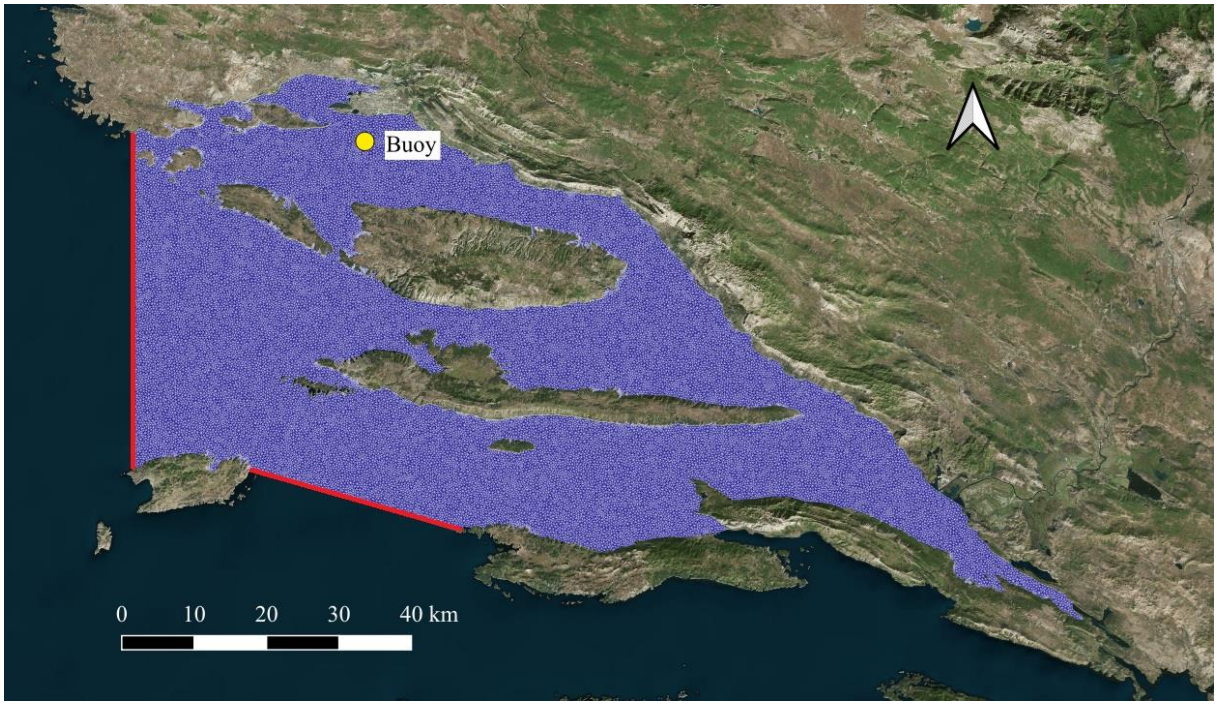


Figure 2. Computational grid with open boundaries highlighted in red and the wave measurement buoy location shown in yellow.

2.3.1 Verification

Solution verification was performed to assess the sensitivity of model results to spatial discretization and directional resolution. Seven simulations of the October 2018 storm event were conducted using ERA5 wind forcing, with varying mesh configurations and numbers of directional bins. Three mesh configurations were tested: coarse, medium, and fine, with maximum cell areas of 100 000 m², 50 000 m², and 25 000 m² (Figure 3), in combination with directional discretization into 18, 24, and 36 bins. The results are summarized in Table 2 and illustrated in Figure 4.



Figure 3. Mesh detail south of Split showing coarse, medium, and fine mesh resolutions from left to right.

Table 2. Solution Verification

N	Start	End	Wind data	Mesh size	Dir. res.	Janssen - *Cds*	RMSE	R	NBIAS	Comp. time (s)
1	26.10.2018. 18:00	30.10.2018. 18:00	ERA5	coarse	36	2.76	0.249	0.799	0.04	9874
2	26.10.2018. 18:00	30.10.2018. 18:00	ERA5	medium	36	2.68	0.247	0.803	0.05	17743
3	26.10.2018. 18:00	30.10.2018. 18:00	ERA5	fine	36	2.61	0.249	0.800	0.06	37956
4	26.10.2018. 18:00	30.10.2018. 18:00	ERA5	coarse	18	2.74	0.255	0.786	0.05	5947
5	26.10.2018. 18:00	30.10.2018. 18:00	ERA5	medium	18	2.67	0.252	0.793	0.04	11559
6	26.10.2018. 18:00	30.10.2018. 18:00	ERA5	fine	18	2.66	0.253	0.793	0.04	21159
7	26.10.2018. 18:00	30.10.2018. 18:00	ERA5	coarse	24	2.58	0.244	0.808	0.05	7241

Maximum cell size per mesh: coarse – 100 000 m^2, medium – 50 000 m^2, fine – 25 000 m^2

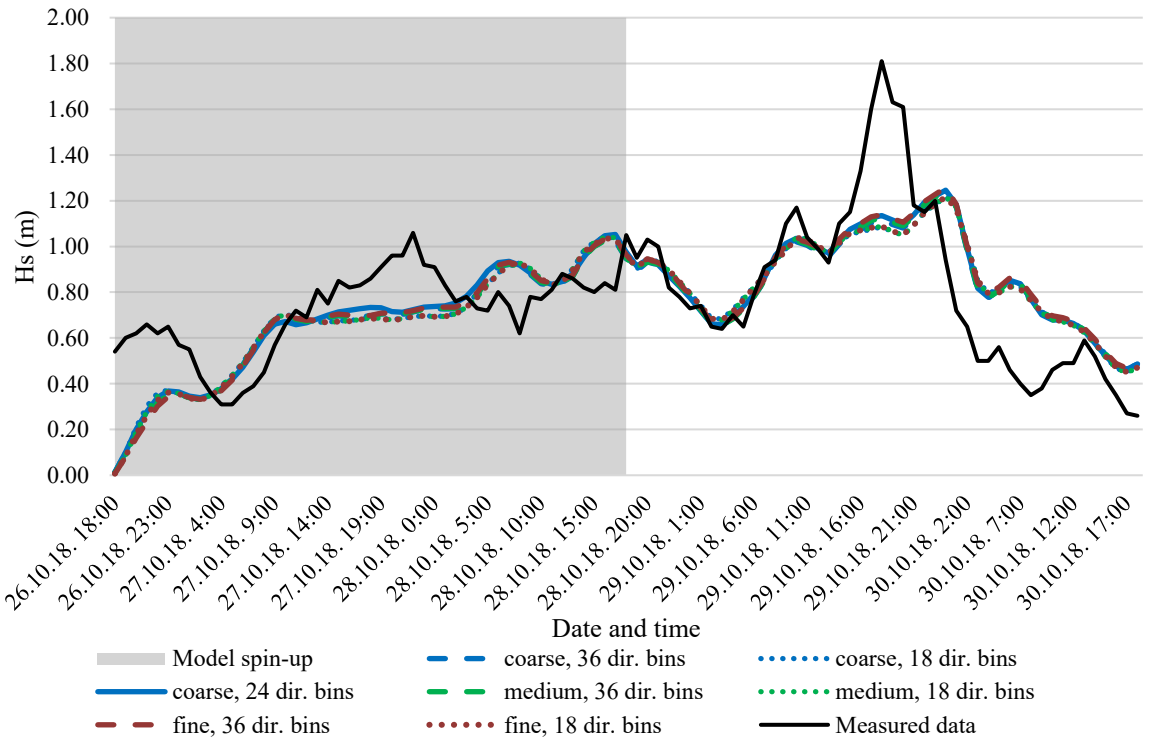


Figure 4. Time series of modelled significant wave height at the buoy location for varying mesh size and directional discretization

The simulated significant wave height time series at the buoy location show very little sensitivity to either mesh refinement or directional resolution, as evident from Figure 4. The RMSE values across all seven simulations range narrowly from 0.244 to 0.255 m, indicating that model performance is largely insensitive to the tested discretization parameters. Computational time, however, varies considerably. Refining the mesh from coarse to fine increases computation time approximately fourfold for a given directional resolution, while doubling the number of directional bins from 18 to 36 roughly doubles the computational cost, with no meaningful gain in accuracy.

Based on these results, the coarse mesh configuration with 24 directional bins is adopted for all subsequent simulations, as it provides accurate results at a fraction of the computational cost of finer configurations.

2.3.2 Calibration of the Janssen whitecapping coefficient

Model calibration was performed by adjusting the Janssen whitecapping dissipation coefficient *Cds* for each of the four wind forcing datasets, using the coarse mesh configuration with 24 directional bins as determined in the previous section. The whitecapping dissipation coefficient is commonly used as a tuning parameter in spectral wave models to compensate for deficiencies in wind forcing (Cavaleri et al., 2018). Calibration was carried out using the Dakota toolkit (Sandia National Laboratories), an open-source software package for optimization and model calibration (Adams et al., 2026). The Efficient Global Optimization method was employed, with the *Cds* coefficient constrained to the range [0, 4] and RMSE of simulated significant wave height against buoy observations as the objective function.

The calibrated *Cds* values are summarized in Table 3. Considerable variation is observed across the four forcing datasets, with values ranging from 1.18 for ICON-DREAM EU to 3.36 for MERIDA, indicating substantial differences in wind energy input between the datasets. The ERA5 and CERRA datasets yield intermediate values of 2.58 and 2.67, respectively. The spread in calibrated Cds values across the four products reflects differences in the effective wind energy input delivered by each dataset to the wave model.

Table 3. Calibration

N	Start	End	Wind data	Janssen - *Cds*	Mesh refinement	Dir. res.	RMSE	R	NBIAS
1	26.10.2018. 18:00	30.10.2018. 18:00	ERA5	2.58	coarse	24	0.244	0.808	0.05
2	26.10.2018. 18:00	30.10.2018. 18:00	CERRA	2.67	coarse	24	0.167	0.909	0.08
3	26.10.2018. 18:00	30.10.2018. 18:00	ICON-DREAM -EU	1.18	coarse	24	0.183	0.897	-0.03
4	26.10.2018. 18:00	30.10.2018. 18:00	MERIDA	3.36	coarse	24	0.172	0.886	0.03

3 Results and Discussion

Figure 5 shows the spatial distribution of significant wave height and wave direction across the model domain at 18:00 on 29 October 2018, corresponding to the period of measured peak wave activity during the observed storm event, as simulated using each of the four wind forcing datasets. The overall spatial patterns are broadly consistent across the four simulations, with the highest wave heights occurring in the open western part of the domain where the fetch is largest, and progressively lower wave heights in the sheltered channels between the islands. However, notable differences between the forcing datasets are visible, particularly in the area east of Brač island, marked with a blue circle in Figure 5. At this location, simulated significant wave heights differ substantially across the four products: ERA5 yields the lowest value at approximately 0.85 m, followed by MERIDA at 1.34 m and CERRA at 1.81 m, while

ICON-DREAM-EU produces the highest estimate at 2.28 m, nearly three times the ERA5 value. These spatial differences are an expected consequence of the single-point calibration approach adopted in this study, where the Janssen *Cds* coefficient was tuned to match observations at one buoy location only. It is therefore likely that the calibrated model performs differently across the domain, and that additional measurement points would be needed to better constrain the spatial variability of model performance.

Figure 6 presents a comparison of the simulated and measured significant wave height time series at the buoy location over the full duration of the storm event. At the beginning of the simulation, all four models underestimate the observed wave heights, which is attributable to model spin-up, as the wave field requires some time to develop from the initial conditions. It is also notable that the first local peak of approximately 1.1 m, observed at around 22:00 on 27 October 2018, is not reproduced by any of the four simulations, suggesting that the wind forcing datasets may not adequately capture the meteorological conditions responsible for this event.

During the main storm peak, occurring around 18:00 on 29 October 2018, the measured significant wave height reaches approximately 1.81 m. ICON-DREAM reproduces this peak most closely at 1.76 m, followed by CERRA at 1.69 m, while MERIDA underestimates the peak slightly at 1.57 m. ERA5 significantly underestimates the storm peak, reaching only approximately 1.09 m. The relatively poor performance of ERA5 at the storm peak is consistent with the known tendency of coarser global reanalysis products to smooth out wind extremes and may also reflect its lower spatial resolution compared to the regional datasets (Barbariol et al., 2021; Dutour Sikirić et al., 2018).

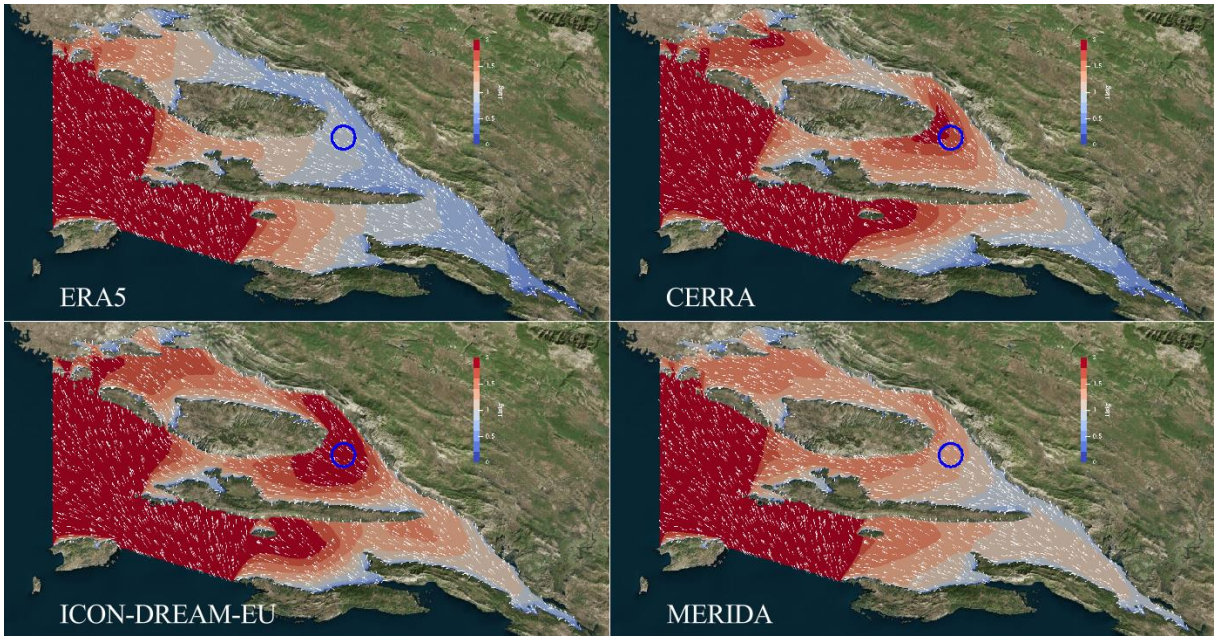


Figure 5. Numerical model results obtained using different wind input datasets. Significant wave height and wave direction on 29 October 2018 at 18:00. The blue circle marks an area east of Brač island where notable differences in simulated significant wave heights were obtained between the forcing datasets.

The degree of ERA5 underestimation observed in this study contrasts with the findings of Bujak et al. (2023), who reported that a calibrated ERA5-forced SWAN model in the same general area achieved performance comparable to a higher resolution ALADIN-forced model. Several factors may explain this discrepancy. First, the October 2018 event was a particularly severe sirocco storm, with measured significant wave heights reaching 1.81 m, well above typical wave conditions encountered in the Bujak et al. (2023) study, where the maximum recorded daily significant height was 1.29 m. At such extreme conditions, the spatial smoothing inherent to ERA5 is more likely to result in significant underestimation of peak wind speeds and consequently wave height. Second, the calibration differs: Bujak et al. (2023) calibrated over a period of approximately six weeks covering multiple storm events, while the present study calibrates against a single storm event. Single-event calibration may not adequately constrain

model behaviour beyond the conditions of that specific event. The calibrated *Cds* values are considerably different between the two studies, suggesting that the optimal whitecapping coefficient is sensitive to both the choice of wind forcing and calibration conditions.

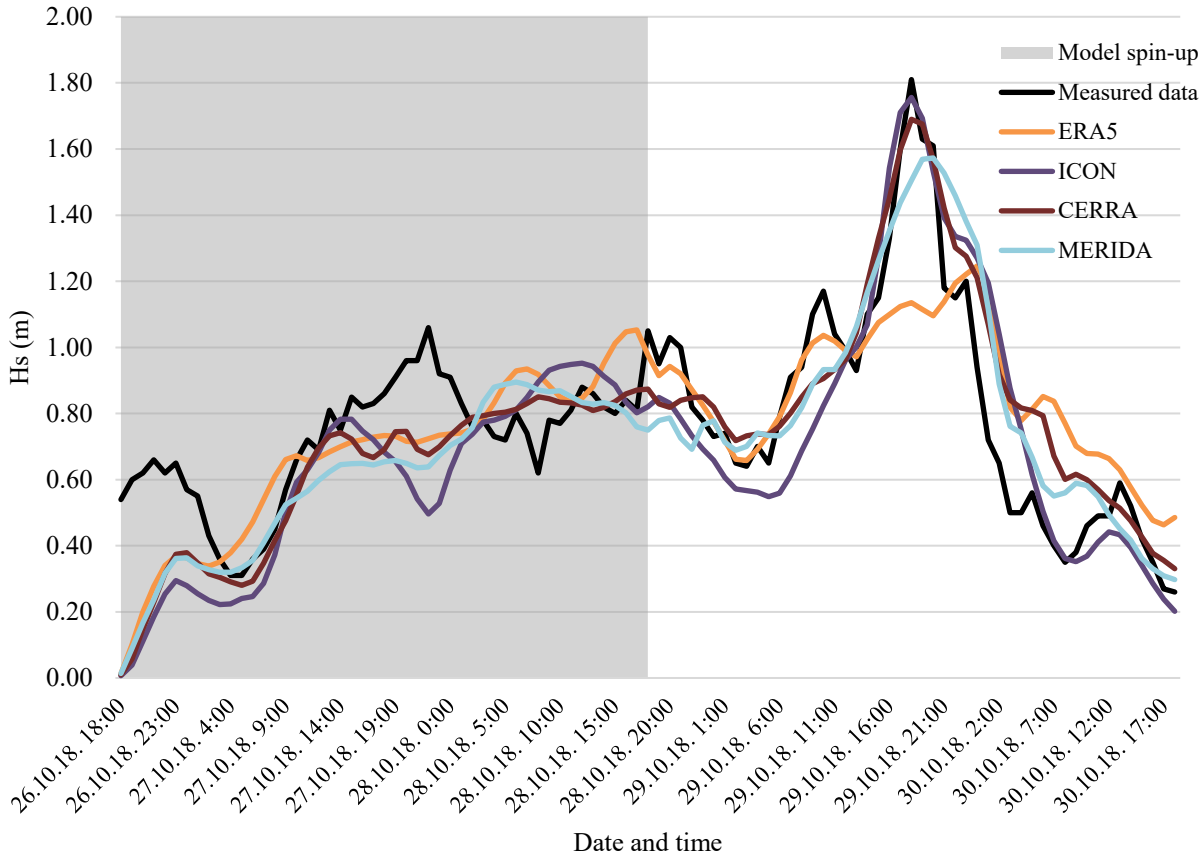


Figure 6. Comparison of measured and modelled significant wave height using different wind input datasets

4 Conclusion

This study assessed four atmospheric reanalysis and regional climate datasets: ERA5, CERRA, ICON-DREAM-EU, and MERIDA as wind forcing for a high-resolution SWAN wave model of the Croatian mid-Adriatic, a region characterized by complex island-mainland geometry, restricted fetch conditions, and strong spatial gradients in wind fields. Model simulations were performed on an unstructured computational grid and evaluated against buoy wave measurements from a severe storm event in October 2018.

Solution verification demonstrated that model results are largely insensitive to spatial and directional discretization below a maximum cell area of 100 000 m², with RMSE values varying only between 0.244 and 0.255 m across all tested configurations. Computational cost, however, increased four times with mesh refinement and roughly doubled with directional resolution, justifying the adoption of the coarse mesh with 24 directional bins for all subsequent simulations. Model calibration via the Janssen whitecapping coefficient yielded considerably different *Cds* values across the four datasets, reflecting substantial differences in the effective wind energy input between products.

The comparison of simulated and measured significant wave height during the storm event shows that ICON-DREAM-EU and CERRA best reproduce the storm peak significant wave height, while ERA5 significantly underestimates, consistent with the known limitations of coarse global reanalysis products in fetch-limited regions with complex topography. Spatial wave field comparisons reveal notable differences between datasets, particularly east of Brač island, highlighting that single-point calibration

is insufficient to constrain model performance across the full domain.

Several limitations of this study should be acknowledged. The analysis is based on a single storm event, which limits the statistical robustness of the conclusions. The October 2018 event was sirocco-driven, and the relative performance of the tested wind products may differ for bora-dominated events, which are characterized by shorter fetch and stronger spatial gradients in wind speed. Calibration against a single buoy introduces spatial uncertainty in model performance, as demonstrated by the notable differences in simulated wave heights observed across the domain, particularly east of Brač island. These spatial differences suggest that buoy-calibrated model performance may be locally representative but not spatially transferable across a geometrically complex domain. The assumption of uniform boundary conditions along each open boundary is a further simplification that may affect results in the southern part of the domain.

The findings presented here are intended as a foundation for a broader study covering the full Adriatic Sea, which will include multiple storm events spanning both bora and sirocco conditions, a denser network of validation points, and an extended temporal coverage enabling seasonal analysis. That study will allow more statistically robust conclusions regarding the relative performance of ERA5, CERRA, ICON-DREAM-EU, and MERIDA as wind forcing for regional wave modelling in the Adriatic.

Acknowledgements

This work was supported by the Croatian Science Foundation under the project number (HRZZ-DOK-2025-02-3371). This study was conducted within the framework of the institutional project of the University of Zagreb Faculty of Civil Engineering – [HOPIK – Enhancement of hydrological and oceanographic data for assessing the exposure of transport infrastructure to climate change], under the programme line for enhancing scientific excellence, financed through the National Recovery and Resilience Plan 2021–2026. The project is funded by the European Union – NextGenerationEU. The views and opinions expressed are solely those of the authors and do not necessarily reflect those of the European Union or the European Commission. Neither the European Union nor the European Commission can be held responsible for them.

References

Adams, B.M., Bohnhoff, W.J., Bolstad, M.B., Dalbey, K.R., Ebeida, M.S., Eddy, J.P., Eldred, M.S., Geraci, G., Hooper, R.W., Hough, P.D., Hu, K.T., Jakeman, J.D., Khalil, M., Maupin, K.A., Monschke, J.A., Portone, T., Prudencio, E.E., Ridgway, E.M., Rizzi, F., Robbe, P., Rushdi, A.A., Seidl, D.T., Stephens, J.A., Swiler, L.P., Tran, A., Winokur, J.G., Menhorn, F. and Zeng, X. 2026 Dakota 6.24.0 documentation. Technical Report SAND2026-20988O, Sandia National Laboratories, Albuquerque, NM. http://snl-dakota.github.io (Accessed on 10 June 2026)

Barbariol, F., Davison, S., Falcieri, F.M., Ferretti, R., Ricchi, A., Sclavo, M. and Benetazzo, A. 2021 Wind waves in the Mediterranean Sea: an ERA5 reanalysis wind-based climatology. *Frontiers in Marine Science* 8, 760614.

Barbariol, F., Pezzutto, P., Davison, S., Benetazzo, A., Bertotti, L., Carniel, S. and Sclavo, M. 2022 Wind-wave forecasting in enclosed basins using statistically downscaled global wind forcing. *Frontiers in Marine Science* 9, 1002786.

Benetazzo, A., Fedele, F., Carniel, S., Ricchi, A., Bucchignani, E. and Sclavo, M. 2012 Wave climate of the Adriatic Sea: a future scenario simulation. *Natural Hazards and Earth System Sciences* 12 (6), 2065–2076.

Bonaldo, D., Bucchignani, E., Ricchi, A. and Carniel, S. 2017 Wind storminess in the Adriatic Sea in a climate change scenario. *Acta Adriatica* 58 (2), 195–208.

Bonaldo, D., Bucchignani, E., Pomaro, A., Ricchi, A., Sclavo, M. and Carniel, S. 2020 Wind waves in the Adriatic Sea under a severe climate change scenario and implications for the coasts. *International Journal of Climatology* 40 (12), 5389–5406.

Bonanno, R., Lacavalla, M. and Sperati, S. 2019 A new high-resolution Meteorological Reanalysis Italian Dataset: MERIDA. *Quarterly Journal of the Royal Meteorological Society* 145 (723), 2537–2554.
Bujak, D., Lončar, G., Carević, D. and Kulić, T. 2023 The feasibility of the ERA5 forced numerical wave model in fetch-limited basins. *Journal of Marine Science and Engineering* 11 (1), 59.
Cavaleri, L., Abdalla, S., Benetazzo, A., Bertotti, L., Bidlot, J.R., Breivik, Ø., Carniel, S., Jensen, R.E., Portilla-Yandun, J., Rogers, W.E. et al. 2018 Wave modelling in coastal and inner seas. *Progress in Oceanography* 167, 164–233.
Cavaleri, L., Barbariol, F. and Benetazzo, A. 2020 Wind–wave modeling: where we are, where to go. *Journal of Marine Science and Engineering* 8 (4), 260.
Copernicus Climate Change Service, Climate Data Store 2023 ERA5 hourly data on single levels from 1940 to present. *Copernicus Climate Change Service (C3S) Climate Data Store (CDS)*. DOI: 10.24381/cds.adbb2d47 (Accessed on 10 June 2026).
Denamiel, C., Pranić, P., Quentin, F., Mihanović, H. and Vilibić, I. 2020 Pseudo-global warming projections of extreme wave storms in complex coastal regions: the case of the Adriatic Sea. *Climate Dynamics* 55 (9–10), 2483–2509.
Dutour Sikirić, M., Ivanković, D., Roland, A., Ivatek-Šahdan, S. and Tudor, M. 2018 Operational wave modelling in the Adriatic Sea with the Wind Wave Model. *Pure and Applied Geophysics* 175 (11), 3801–3815.
Hersbach, H., Bell, B., Berrisford, P., Hirahara, S., Horanyi, A., Munoz-Sabater, J., Nicolas, J., Peubey, C., Radu, R., Schepers, D. et al. 2020 The ERA5 global reanalysis. *Quarterly Journal of the Royal Meteorological Society* 146, 1999–2049.
Katalinić, M. and Parunov, J. 2018 Wave statistics in the Adriatic Sea based on 24 years of satellite measurements. *Ocean Engineering* 158, 378–388.
Lončar, G., Ocvirk, E. and Andročec, V. 2010 Usporedba modeliranih i mjerenih površinskih vjetrenih valova. *Građevinar* 62 (3), 197–206.
Mediterranean Sea Waves Reanalysis (CMEMS Med-Waves, MedWAM3 system). 2024 E.U. Copernicus Marine Service Information (CMEMS). Marine Data Store (MDS). DOI: 10.25423/CMCC/MEDSEA_MULTIYEAR_WAV_006_012 (Accessed on 10 June 2026).
Moulin, A., Mentaschi, L., Clementi, E., Verri, G. and Mercogliano, P. 2024 Projections of the Adriatic wave conditions under climate changes. *Frontiers in Climate* 6, 1409237.
Ruol, P., Martinelli, L., Favaretto, C., Barbariol, F. and Benetazzo, A. 2022 Representative and morphological waves along the Adriatic Italian coast in a changing climate. *Water* 14 (17), 2678.
Schimanke, S., Ridal, M., Le Moigne, P., Berggren, L., Undén, P., Randriamampianina, R., Andrea, U., Bazile, E., Bertelsen, A., Brousseau, P., Dahlgren, P., Edvinsson, L., El Said, A., Glinton, M., Hopsch, S., Isaksson, L., Mladek, R., Olsson, E., Verrelle, A. and Wang, Z.Q. 2021 CERRA sub-daily regional reanalysis data for Europe on single levels from 1984 to present. *Copernicus Climate Change Service (C3S) Climate Data Store (CDS)*. DOI: 10.24381/cds.622a565a (Accessed on 10 June 2026).
The SWAN team 2024a SWAN Scientific and Technical Documentation: Cycle III, Version 41.51. Delft University of Technology, Faculty of Civil Engineering and Geosciences, Delft, The Netherlands. http://www.swan.tudelft.nl (Accessed on 10 June 2026).
The SWAN team 2024b SWAN User Manual: Cycle III, Version 41.51. Delft University of Technology, Faculty of Civil Engineering and Geosciences, Delft, The Netherlands. http://www.swan.tudelft.nl (Accessed on 10 June 2026)
Valmassoi, A., Keller, J.D., Anlauf, H., Cress, A., Becker, A., Fundel, F., Hanisch, T., Kaspar, F., Krebber, S., Lange, M., Steinert, T., Wahl, S., Zängl, G. and Potthast, R. 2025 ICON-DREAM – ICON Dual resolution Reanalysis for Emulators, Applications and Monitoring. *Deutscher Wetterdienst (DWD), Climate Data Center (CDC)*. DOI: 10.5676/dwd/icon-dream_v1 (Accessed on 10 June 2026).
Viterbo, F., Sperati, S., Vitali, B., D'Amico, F., Cavalleri, F., Bonanno, R. and Lacavalla, M. 2024 MERIDA HRES: a new high-resolution reanalysis dataset for Italy. *Meteorological Applications* 31 (6), e70011.
World Meteorological Organization 2018 *Guide to Wave Analysis and Forecasting*. WMO-No. 702. Geneva: WMO.

WATER RETENTION MEASURES IN THE CENTER OF TURANY NAD ONDAVOU VILLAGE

Rastislav FIJKO [1*], Anatolii KUHAL [1], Martina ZELENAKOVA [1]

[1] *Department of Environmental Engineering, Faculty of Civil Engineering, Technical University of Kosice, Slovakia*

E-mail: rastislav.fijko@tuke.sk

E-mail: anatolii.kuhal@tuke.sk

E-mail: martina.zelenakova@tuke.sk

[*] *Corresponding author*

Abstract
The paper presents the project that captures and controls rainwater from the Turany nad Ondavou municipal office roof and surrounding areas. Rainwater is directed via gravity-fed pipes to rain gardens and impermeable foil-lined retention areas, maximizing subsoil absorption. The design integrates vegetation, permeable paving, and recycled materials, enhancing sustainability, microclimate, and urban aesthetics. This approach supports effective on-site water management, ecological balance, and architectural harmony.

Key words
rainwater measures, rainwater drainage, rain gardens, retention capacity

1 Introduction

Natural water retention measures encompass a range of strategies adopted by many industries or considered in various planning procedures pertaining to water, food safety, biodiversity preservation, climate change adaptation, or urban development. While some of these actions are intended to directly alter the ecosystem, others are meant to alter how economic actors operate (Zelenakova et al., 2017).

One multipurpose type of green infrastructure that can be very helpful in managing the risk of flooding in a catchment is water retention measures. An increasing number of people recognize that traditional grey infrastructure-based flood prevention measures in metropolitan areas can be supplemented with green infrastructure based on natural processes. By improving or restoring natural hydrologic processes including interception, evapotranspiration, infiltration, and ponding, upstream detention techniques based on the idea of "stormwater detention where it falls" can help lower the risk of flooding downstream. A better understanding of the likely reduction in flood risk in downstream cities, the institutional structures required to manage risk. Mutually agreeable compensation schemes for farms are necessary to identify situations where the introduction of water retention measures may be warranted (Collentine and Futter, 2018).

The need to handle urban stormwater concerns is growing due to climate change and ongoing population increase. Using nature-based solutions, especially sustainable technology for managing urban stormwater, is a viable approach for mitigating climate change. These technologies are essential components of nature-based measures (Koiv-Vainik, et al. 2022).

Significant changes to current stormwater management techniques are required to reduce infrastructure damage from stormwater-related hazards, save natural ecosystems, and regulate flooding in metropolitan areas. The greatest way to reduce the risk of urban flooding and encourage a healthy natural environment may be to integrate stormwater management with urban planning. An environmentally friendly substitute for conventional stormwater control techniques is green infrastructure. Rain gardens

are crucial for lowering stormwater levels and flows, shielding property from damage, filtering pollutants from urban runoff, and replenishing groundwater. Through several methods, rain gardens can filter pollutants, pathogens, heavy metals, nutrients, and hydrocarbons out of runoff (Sharma and Malaviya, 2021).

The project provides for the capture and controlled drainage of rainwater from the roof of the Turany nad Ondavou municipal office building and its surroundings so that it is diverted in a controlled manner over the site and at the same time to be retained in its subsoil to the maximum extent possible.

The project is designed so that rainwater is controlled by gravity pipes to rain gardens with reserve retention capacity, or spatial depressions (two retention areas with an impermeable foil). In this case, three field depressions are designed on the site, which are technically connected and supplemented by objects for local water retention in the technical element. The project also foresees the planting of vegetation.

The aim of the paper is to present design of green solution for water retention in the municipality. The aim of the design is to complement the environment as appropriately as possible in terms of architectural function and in terms of functional design, offering the possibility to manage rainwater on the user's land.

2 Methods

2.1 Study area

The area in consideration is in the cadastral territory of the municipality of Turany nad Ondavou (Figure 1). Turany nad Ondavou lies in the eastern part of the valley of the middle Ondava River, at an altitude of about 172 m. The slightly undulating deforested surface of the area is formed by the Tertiary flysch. The size of the cadastre is 959 ha. A sulphurous spring springs up in the wooded part of the village. There is also a rain gauge station in the village. The surroundings of the village are suitable for hiking and agrotourism.



Figure 1. Location of the Study Area.

The area where the landscaping and water retention measure is implemented is currently used as an asphalt-concrete parking area, which occupies a relatively large part of the courtyard area. The area of asphalt on the area in question is 554 m^2 per courtyard and 119,7 m^2 is the area of impermeable pavements around the building. The building is situated between two streets which are connected by the pavements on both sides of the building. The walkway on the north side is used by the inhabitants of the village and the footpath on the south side of the building is in the courtyard of the kindergarten and is closed on both sides.

2.2 Project Description

From the urban planning point of view, the project is designed to create conditions for controlled retention of precipitation water from the reconstructed area of the parking lot and pedestrian road or rest area, the influence of which will be returned to the water cycle back to nature. A green permeable to semi-permeable paved area will be created in the central part of the village, which provides a new dimension to the area and replaces the asphalted area, with a green 'island' in the central part of the village in front of the main building entrance and the transition between the streets, where it will functionally connect them. It will also demonstrate the appropriate use of mats of recycled materials for the needs of parking lot renovation and the use of rainwater and its retention on site impact.

The scope of the project will make the overall area of the village in front of the cultural and administrative building more pleasant and cultural. The whole created area is visually divided into three parts: on the left from the entrance there is a green infrastructure, the central is the landscaped entrance and paved bituminous area, and to the right are arranged parking spaces (Figure 2).



Figure 2. Revitalization of the village center (before and proposal).

The project envisages the renovation of existing 8+1 parking spaces for the disabled. The number remains unchanged and does not increase the original number of parking spaces. The parking stalls are designed as permeable with permeable base. Long-term parking is not anticipated. A short-term parking is expected. While this will create a parking area, it is emphasised that an area such as a car park does not just act as an impermeable asphalt surface, but as an area that can provide, in the warm summer months, pleasant cooling of the surroundings. In total, 554 m^2 of asphalt will be removed and partly replaced with a permeable surface. The remaining area required for vehicle access will be restored as bituminous, but to a lesser extent than present one.

From an urban planning point of view, the building is designed to create conditions for controlled retention of precipitation and surface water from the site. The project considers the composition of the vegetation cover, which is in harmony with its infiltration capacity, operational needs, durability in relation to grade changes saturation of the filtration environment and their suitability to the relevant geomorphological and climatic characteristics of the area of the site.

3 Construction part of Water Retention objects

The construction part focuses mainly on the modification of paved areas (permeable, semi-permeable and the restoration of the access road), construction of the storm sewerage system and construction of water retention measures to which the storm sewerage system is connected to (Figure 3). A system of rain gardens, spatial depressions and retention areas provided with impermeable PVC sheets that are interconnected.

3.1 Water Retention Lines

The A and C lines (Figure 4) is designed as a gravity drainage from the roof of the adjacent building through a set of two underground tanks and through control shafts. The line is designed as a gravity drainage from the roof of the adjacent building through a set of two underground tanks and through control shafts. The total length of the line is 75,36 m. Two underground tanks with a capacity of 6,0 m^3 are proposed along the route as a new and an existing one with a capacity of approximately 50 m^3 as a reconstructed disused cesspit. The surroundings of the route are in a natural gradient. If the tank is full, it will be drained, and water will be used for watering green areas of vegetation.

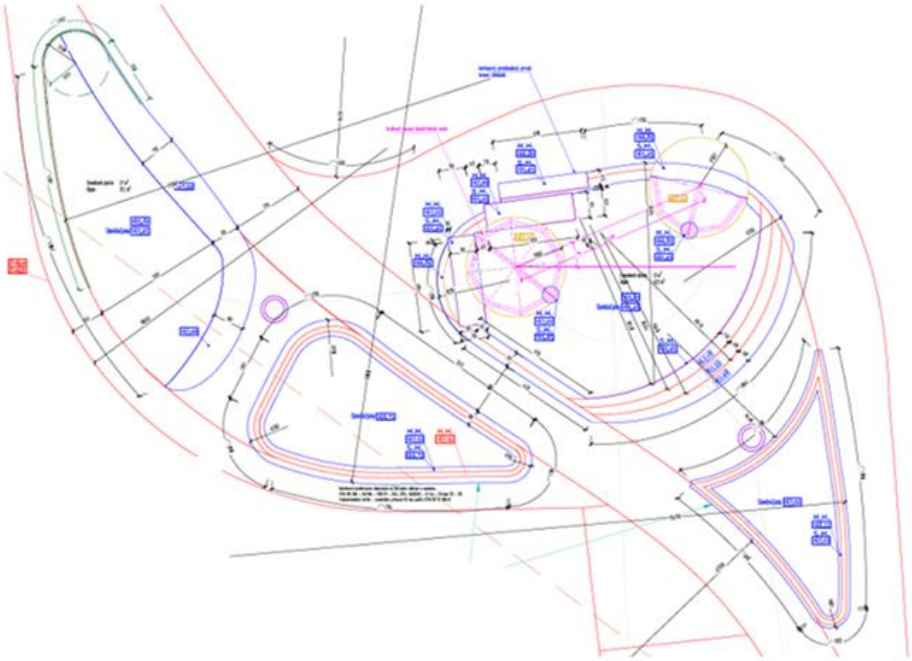


Figure 3. Schematic description of the water retention constructions.

The line begins with a connection from the storm drain through the roof silt trap. It connects at the inspection shaft where the pipe breaks and continues for a length of 18,3 m. A connection pipe from the rainwater outfall is connected to the manhole. The line is connected to an underground retention tank with a proposed volume of 6,0 m^3 from where it continues. At the manhole the pipe breaks and continues. After its connection, the pipe breaks again, and the route continues along the fence. There is a short connection line with a total length of 16,99 m, which runs from the north and is connected to the shaft by two downpipes. After this shaft, the line changes dimension and continues through the inspection shaft to the existing underground structure (old cesspit). This is an existing non-functional building with a volume of approximately 50 m^3.

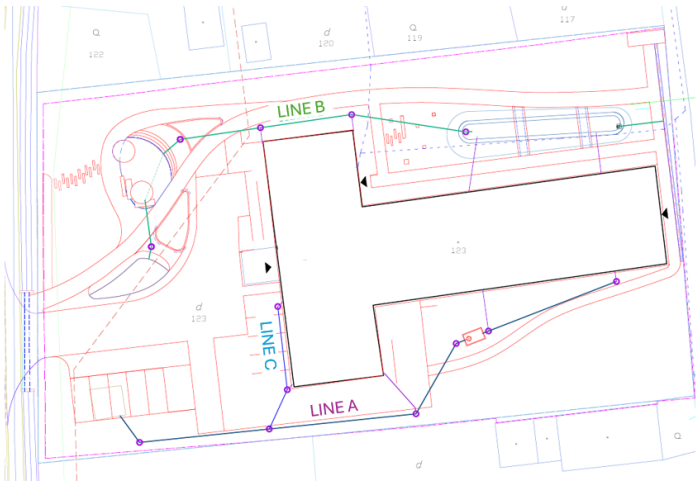


Figure 4. Schematic description of the water retention constructions – line A and line C.

Line B is formed by two water retention areas which are functionally connected by gravity storm sewers. The route starts on the eastern side of the building with an inflow into the gutter, which ensures water retention from the road body and prevents the accumulation of water to the entrance of the kindergarten. The gutter is designed with a width of 300 mm, sloping down towards the inlet and is secured along its entire length by a grating. The gutter is installed in place of the original fence wall, which is being removed. The gutter is dropped to the centre of the rigoll, from where it is diverted via a system inlet to the retention area. An end check valve is fitted in the concrete face of the riprap to prevent the water level from rising, protected against floating objects by the side walls of the riprap. Line B is divided into two restraint spaces which are functionally connected.

3.2 Landscaping

The vegetation arrangements are designed to reflect the character of the surrounding urban environment, the proposed use of the area and to respect the protection zones of utility networks. The species composition of the proposed trees is adapted to the conditions of the area under consideration and consider adaptation to climate change. The aim of the modifications is to increase the prospective, microclimatic, hygienic, ecological and aesthetic value of the vegetation.

It is a semi-closed transition area between the municipal office building and the surrounding buildings, supplemented by rest areas for meeting of citizens with suitable furnishings. The central part of the courtyard has the character of a terraced group of trees, with undergrowth lawn and solitary shrubs. Ornamental tree species with flowers or autumn colouring are added to seasonally enliven the space. The significant proportion of trees proposed creates a pleasant living space in the shade under the tree canopy. In the peripheral parts, or outside the main residence areas, lawns will be replaced with an understorey of grassland community or meadow lawns.

Two dry polders (depressions) for rainwater are proposed in the area - "rain gardens", which are formed by a slight reduction of terrain. The bottom and slopes will be planted with plants suitable for the given habitat - ornamental grasses will predominate, supplemented by spot woody plants.

In front of the entrances to the apartment buildings between the pavement and the road there are existing front gardens with benches. As part of the revitalisation of the area, the benches will be unified in terms of material, and the cycle racks to encourage cycling. Within the front gardens, planting measures will be carried out - inappropriate or collision trees are proposed for removal. Front gardens will be planted with solitary shrubs, lower shrubs, shrubs, undercover plants, perennials to unify the aesthetic appearance of the entrance areas.

3.3 Construction Impact to the Environment

It is necessary to prevent mud and debris from polluting the roads construction material, to prevent air pollution by exhaust gases, excess idling of engines and to prevent damage to original buildings and vegetation unaffected by construction. From the point of view of nature protection during construction, care must be taken to prevent the release of oil from machinery into streams and the surrounding countryside. When carrying out construction work, ensure compliance with the principles of general nature and landscape protection. During demolition works, the different types of waste will be sorted and temporarily stored on the site to ensure protection of the environment. Plastic or jute sacks for sorted commodities are used for separate collection (paper, glass and plastics). The recoverable waste is taken to a collection point or waste recovery facility. Other to a non-hazardous waste landfill.

4 Conclusion

The project aims to enhance the environmental sustainability of the Turany nad Ondavou municipal office building by implementing an advanced rainwater management system. The primary contributions of the project include:

- controlled rainwater capture and drainage: the project ensures the systematic capture of rainwater from the building's roof and surrounding areas. By using gravity pipes, rainwater is directed to specific rain gardens and spatial depressions, where it is managed and retained effectively,
- maximized groundwater recharge: the design emphasizes maximizing the retention of rainwater in the subsoil, which helps replenish local groundwater levels and reduces surface runoff, thereby minimizing erosion and potential flooding,
- creation of rain gardens and retention areas: the installation of three interconnected field depressions, supplemented with impermeable foil-lined retention areas, enhances the site's capacity to manage and retain rainwater. These features serve as reservoirs that temporarily store excess rainwater and facilitate its gradual infiltration into the ground,
- vegetation and landscaping integration: the project includes the planting of vegetation, which not only contributes to the aesthetic enhancement of the site but also supports the rainwater management system by improving soil absorption and providing additional water retention capacity through root systems,
- architectural and functional harmony: the project is designed to blend seamlessly with the existing environment, both architecturally and functionally. This ensures that the rainwater management system does not disrupt the site's appearance or usability but rather complements and enhances its ecological function,
- sustainable land use: by offering a practical solution for on-site rainwater management, the project promotes sustainable land use practices. This approach reduces reliance on external drainage systems and minimizes the impact of urban development on the natural water cycle.

The project contributes to the environmental resilience of the Turany nad Ondavou area by implementing a comprehensive rainwater management system that harmonizes with the local landscape and supports sustainable water practices. The paper should as an example for other similar projects for increasing the climate resilient municipality.

Acknowledgements

This work was supported by project VEGA 1/0588/24 and by project HUSK/2302/1.2/060.

References

Collentine, D., Futter, M.N. 2018 Realising the potential of natural water retention measures in

catchment flood management: Trade-offs and matching interests, *Journal of Flood Risk Management*, 11(1), pp. 76-84.
Kõiv-Vainik, M., Kill, K., Espenberg, M., Uuemaaa, E., Teemusk, A., Maddison, M., Palta, M. M., Törökc, L., Mander, Ü., Scholz, M., & Kasak, K. 2022 Urban stormwater retention capacity of nature-based solutions at different climatic conditions. *Nature-Based Solutions*, 2, 100038. https://doi.org/10.1016/j.nbsj.2022.100038
Sharma, R., Malaviya, P. 2021 Management of stormwater pollution using green infrastructure: The role of rain gardens, *Wiley Interdisciplinary Reviews: Water*, 8.2, 1507.
Zelenakova, M., Diaconu, D.C., Haarstad, K. 2017 Urban water retention measures, *Procedia engineering*, 190, pp. 419-426.

REVITALIZATION OF A DRAVA RIVER SIDE BRANCH USING 2D NUMERICAL MODELLING

Antonija HARASTI [1*], Gordon GILJA [1], Dorian TATARIN [2], Igor TOŠIĆ [3]

[1] *University of Zagreb Faculty of Civil Engineering, Laboratory for river and sediment dynamics, Croatia*

E-mail: antonija.harasti@grad.unizg.hr

E-mail: gordon.gilja@grad.unizg.hr

[2] *Hidroing d.o.o. Osijek, Croatia*

E-mail: dorian.tatarin@hidroing-os.hr

[3] *Croatian Waters, Varaždin, Croatia*

E-mail: igor.tosic@voda.hr

[*] *Corresponding author*

Abstract

Floodplain side channels provide important hydraulic and ecological functions, but their connectivity is frequently reduced by river regulation and sediment accumulation. This study evaluates the extent to which localized inlet modifications can improve hydraulic connectivity and identifies the limitations of such measures in the Podravska Moslavina side channel of the Drava River, Croatia. A two-dimensional HEC-RAS model was applied under low- and higher-flow conditions. The existing inlet sill was compared with two variants involving different degrees of sill lowering. Under low-flow conditions, the existing sill restricted inflow to two narrow openings, producing a concentrated high-velocity jet followed by extensive low-velocity zones. Lowering the sill widened the inflow section, reduced velocity gradients and produced a more uniform velocity distribution within the upstream reach. However, improvements diminished downstream, where sediment deposits, scour holes, residual transverse structures and channel geometry continued to control flow patterns. Additional sill lowering produced only marginal benefits and did not establish continuous conveyance throughout the side channel. Under higher-flow conditions, differences among the scenarios were minor because the original sill was submerged. The results demonstrate that localized inlet modification can improve low-flow connectivity but cannot independently restore the hydraulic functionality of a morphologically degraded side channel.

Key words

river restoration, river side branch, numerical 2D model, sill, hydraulic connectivity

1 Introduction

Floodplain side channels are integral components of alluvial river systems, supporting hydraulic connectivity, sediment transport, nutrient exchange and habitat diversity across river corridors (Ward et al., 2002). Their periodic connection with the main channel sustains a wide range of geomorphological and ecological processes, including sediment redistribution, fish migration, spawning, and the maintenance of heterogeneous aquatic habitats (Tockner & Stanford, 2002). Consequently, preserving or restoring hydrological connectivity between the main channel and floodplain water bodies has become a central objective of river restoration worldwide and is strongly promoted through the European Water Framework Directive and the EU Biodiversity Strategy.

Over the past century, extensive river regulation has substantially altered the natural hydromorphological functioning of many large alluvial rivers. Channelization, bank stabilization, construction of groynes and revetments, flood protection levees, and navigation improvements have

simplified channel morphology and reduced lateral connectivity between rivers and their floodplains (Nilsson et al., 2005). As a consequence, many formerly active side channels have become partially or completely disconnected from the main channel, resulting in reduced flow exchange, and increased sediment deposition. These processes diminish habitat diversity, restrict fish migration, and reduce the ecological integrity of floodplain ecosystems. Restoring hydrological connectivity has therefore become one of the principal objectives of river restoration projects worldwide and is strongly supported by the European Water Framework Directive and the EU Biodiversity Strategy.

A common approach to restoring disconnected side channels is excavation of the channel bed and removal of accumulated sediments to re-establish flow connectivity. While excavation can effectively restore hydraulic exchange, it is often associated with considerable environmental and economic costs (Kondolf, 1997). Extensive dredging disturbs established riparian and aquatic habitats, removes stored sediments mixed with nutrients, and may require repeated maintenance where sediment deposition continues. Although restoration measures frequently focus on reconnecting side channels through excavation, inlet widening or removal of artificial barriers, can offer permanent solution. Relatively small modifications of inlet geometry may substantially alter the distribution of discharge between the main channel and the side branch, thereby influencing velocity patterns, sediment transport capacity and habitat conditions, while minimizing engineering interventions. Consequently, understanding the hydraulic mechanisms governing flow distribution is essential for designing effective restoration measures (Palmer et al., 2005). Advances in two-dimensional hydraulic modelling have provided powerful tools for evaluating such restoration scenarios, allowing spatially distributed analyses of water depth, velocity and flow conveyance under different hydrological conditions before implementation.

Previous restoration projects have predominantly focused on changes in water levels, whereas relatively few studies have characterized spatial flow-velocity fields (Roni et al., 2008). Spatial velocity distributions determine zones of erosion and deposition, control hydraulic habitat diversity and strongly influence the persistence of low-flow connectivity within restored channels. Quantifying these hydraulic responses therefore provides an important basis for assessing restoration effectiveness and optimizing engineering design.

The present study investigates the hydraulic restoration of the Podravska Moslavina side channel along the Drava River in Croatia using two-dimensional hydraulic modelling in HEC-RAS. The objective of this study is to evaluate the extent to which localized modifications of an inlet sill can improve hydraulic connectivity in a regulated floodplain side channel and to identify the hydraulic limitations of such interventions under contrasting hydrological conditions. The central hypothesis is that modest morphological modifications at the channel entrance can substantially improve flow conveyance and restore a more natural longitudinal velocity distribution without requiring extensive excavation works.

2 Methods

2.1 Study area

The study was conducted on Drava River side branch located near the village of Podravska Moslavina, Croatia (river kilometre 98; Fig. 1). The approximately 1.8 km long side channel is situated within the active floodplain of the Drava River, one of the last semi-natural large alluvial rivers in Central Europe. The study area forms part of the Natura 2000 ecological network and is characterized by floodplain forests, gravel bars and diverse aquatic habitats of high ecological value.

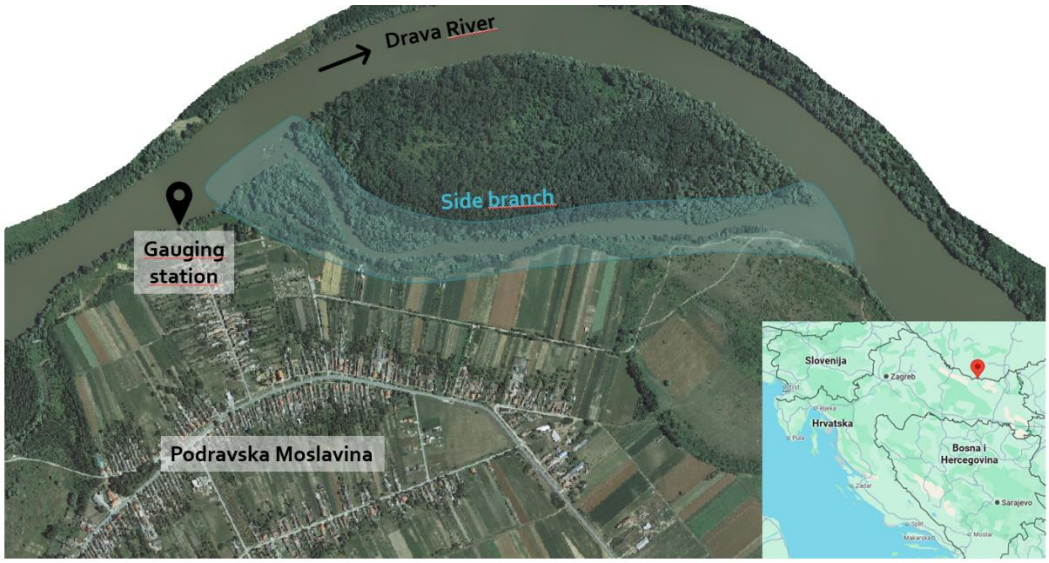


Figure 1. Location of Podravska Moslavina side branch

Despite the side channel is still hydraulically connected to the main channel at both the upstream and downstream ends, currently it experiences severely reduced flow conveyance during low-flow conditions. The main reason is an artificial rock sill at the channel entrance. Its crest elevation is 91.60 m a.s.l., so water enters the side channel only when the water level exceeds approximately the 35% exceedance stage (Ekonerg, 2020). Consequently, the side channel remains poorly connected to the main channel during approximately two-thirds of the year, promoting sediment deposition, stagnant water conditions and progressive ecological degradation. Additional hydraulic disturbances are caused by remnants of an older downstream sill and by extensive sediment accumulation within the channel, resulting in highly non-uniform flow conditions.

The restoration objective considered in this study was to improve hydraulic connectivity during ecologically critical low-flow periods through localized modification of the inlet sill while preserving the overall morphology of the side channel and minimizing physical disturbance within the protected floodplain.

2.2 Model setup and calibration

Hydraulic conditions within the study reach were simulated using the two-dimensional (2D) module of HEC-RAS. The HEC-RAS 2D solver simulates depth-averaged unsteady flow by solving the vertically integrated shallow-water (Saint-Venant) equations of continuity and momentum over a two-dimensional computational domain. The governing equations are derived from the Reynolds-averaged Navier–Stokes equations under the assumption of hydrostatic pressure and negligible vertical accelerations, resulting in a depth-averaged representation of the flow field. Unsteady flow simulations were performed using the Diffusion Wave solver. Although simplified compared with the full shallow-water equations, the Diffusion Wave formulation is appropriate for gradually varied flow conditions typical of lowland floodplain channels and provides robust numerical performance for restoration scenario analysis.

The model was employed to evaluate the effects of alternative restoration scenarios on the hydraulic behaviour of the side channel by comparing the existing channel configuration with proposed modifications of the inlet sill. A uniform computational mesh with a cell size of 1×1 m was adopted to adequately resolve the complex channel geometry while maintaining numerical stability.

Boundary conditions were established using long-term hydrological observations (01.01.1995. - 31.12.2024.) from the Podravska Moslavina gauging station that is located just upstream of the side branch inlet. During the analysed period, the minimum recorded discharge was 175.4 m³/s, the mean discharge was 514.9 m³/s, and the maximum recorded discharge was 2,166 m³/s.

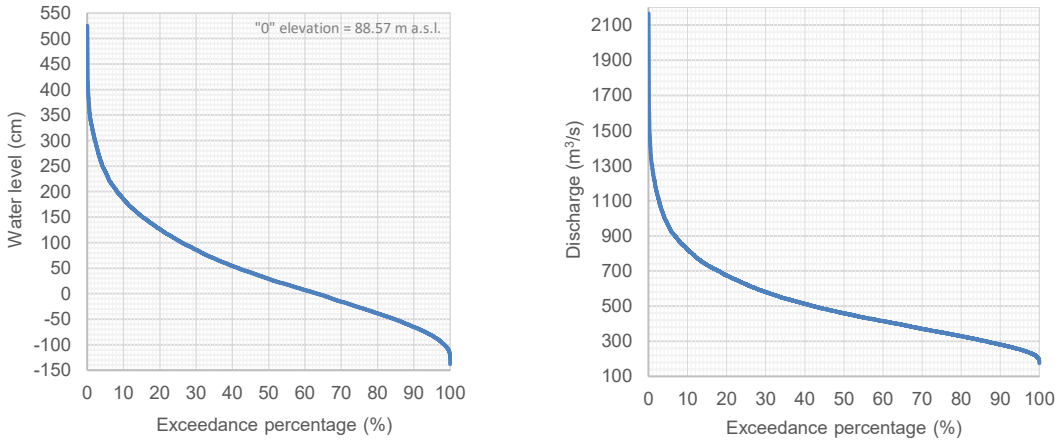


Figure 2. Flow duration curve for water levels (left) and discharges (right) for gauging station "Donji Miholjac C.S." 50 m upstream of the side branch.

Two representative hydrological conditions were selected to evaluate restoration performance under contrasting hydraulic regimes: a low-flow event corresponding to the 80% exceedance water level and a higher-flow event corresponding to the 25% exceedance water level. These conditions represent periods when hydraulic connectivity is respectively most restricted and fully established.

Water levels at the side-channel outlet were estimated based on the known distance from, and the recorded measurements at, the downstream gauging station. For the low-flow simulation, an upstream water level of 90.68 m a.s.l. and a downstream water level of 90.44 m a.s.l. were prescribed, corresponding to a characteristic discharge of 329 m³/s in the main river. For the higher-flow simulation, upstream and downstream water levels of 91.96 m a.s.l. and 91.72 m a.s.l., respectively, were applied, representing a main-channel discharge of 624 m³/s.

Model calibration was performed by iteratively adjusting the inflow entering the side channel and Manning's roughness coefficient until the simulated upstream water level matched the observed stage under each hydrological condition. The calibrated inflow amounted to 3.5 m³/s for the low-flow simulation and 39 m³/s for the higher-flow simulation. The corresponding Manning's roughness coefficients were 0.038 and 0.037, respectively.

Table 1. Calibrated model parameters and reference water levels

Hydrological event	Side channel discharge inflow [m^3/s]	Manning's roughness coefficient	Upstream water level [m a.s.l.]	Downstream water level [m a.s.l.]
High-flow	48.0	0.037	92.05	91.72
	40.0	0.037	91.97	91.72
	38.0	0.037	91.95	91.72
	39.0	0.037	91.96	91.72
Low-flow	3.0	0.030	90.60	90.44
	3.0	0.035	90.63	90.44
	3.0	0.040	90.66	90.44
	3.5	0.035	90.66	90.44
	3.5	0.037	90.67	90.44
	3.5	0.038	90.68	90.44

2.3 Restoration scenarios

The reference scenario retained the existing sill crest at 91.60 m a.s.l. In Variant A, the crest was lowered to 89.25 m a.s.l., approximately 1 m below the 95% exceedance stage, to maintain an open inflow section during low flows. Variant B lowered the crest further to 88.77 m a.s.l. to test whether additional excavation would provide a measurable hydraulic benefit. The two proposed cross-sections are shown in Fig. 3.

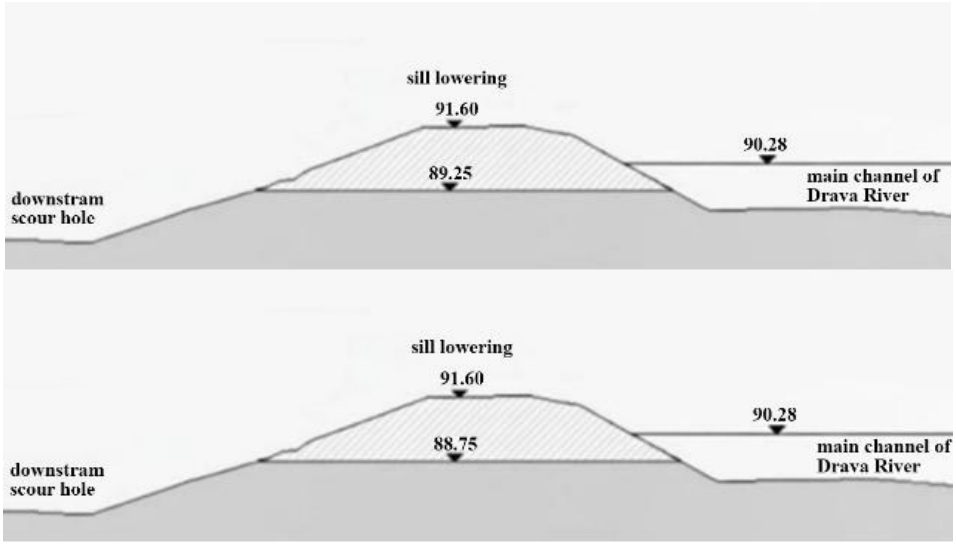


Figure 3. Cross section of inlet sill for lowering crest to 89.25 m a.s.l. - variant A (top) and 88.77 m a.s.l. – variant B (bottom)

2.4 Hydraulic assessment

Performance was evaluated from the spatial distribution of depth-averaged velocity under both hydrological conditions. The assessment focused on the active inlet width, continuity of the principal flow path, activation of the secondary branch, and the extent of low-velocity zones associated with weak conveyance.

Velocity was treated as an integrated hydraulic indicator rather than a direct measure of sediment transport or habitat quality. Improvements were defined as a less abrupt entrance transition and a more continuous longitudinal velocity field without creating new areas of excessive local acceleration.

3 Results and Discussion

3.1 Hydraulic conditions under the existing configuration

The hydraulic simulations of the existing side branch geometry indicate that the inlet sill exerts a dominant control on flow exchange between the main channel and the side branch during low-flow conditions. Under the representative low-flow scenario (80% exceedance water level), inflow into the side channel is restricted to two narrow openings within the inlet sill, with a width of approximately 12 m. This pronounced flow contraction generates locally high flow velocities reaching approximately 0.7 m/s immediately downstream of the sill.

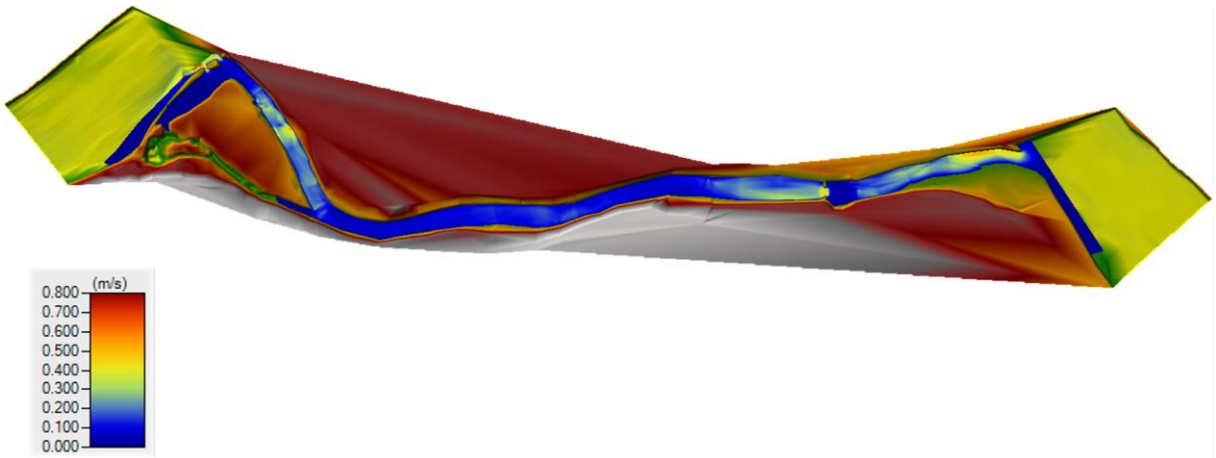


Figure 4. Flow velocities distribution of low-flow scenario under existing side branch configuration

The accelerated inflow entered a wider scour pool more than 4.5 m deep, where simulated velocities declined sharply and extensive low-velocity areas developed. This transition indicates that the inlet geometry controls not only the active inflow width but also the hydraulic organisation of the entrance reach.

Farther downstream, the channel divides into a principal and a secondary branch. The secondary branch was largely inactive at low flow, while the principal branch conveyed the discharge through locally shallow, sediment-affected reaches where velocities increased to approximately 0.3 m/s.

A second hydraulic discontinuity occurred near the remnants of a former transverse structure about 1.35 km downstream. Local velocity increased to approximately 0.5 m/s and then fell below 0.03 m/s in the adjoining scour pool. Near the outlet, flow was again concentrated along the concave bank beside the gravel bar, with velocities approaching 0.5 m/s. Overall, the existing low-flow condition was characterised by short zones of acceleration separated by broad areas of weak conveyance.

At the 25% exceedance stage, partial submergence of the inlet sill activated both channel branches and improved longitudinal continuity (Fig. 5). However, the velocity field remained strongly controlled by channel morphology. Velocities of approximately 0.5–1.0 m/s occurred at contractions, concave banks, and the residual downstream structure, whereas broader and deeper sections generally remained at 0.1–0.2 m/s.

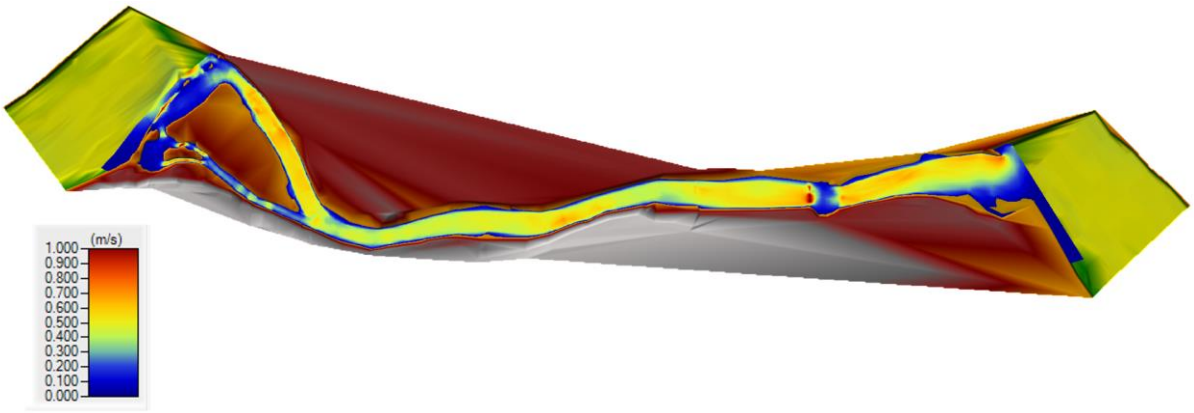


Figure 5. Flow velocities distribution of high-flow scenario under existing side branch configuration

3.2 Response of the velocity field to inlet sill lowering

Lowering the sill substantially changed the entrance hydraulics under low-flow conditions. In both variants, the active inlet widened and the concentrated high-velocity zone associated with the two existing openings disappeared. The resulting velocity field was more evenly distributed across the entrance.

Variant A produced a smoother transition from the main channel into the side channel and reduced the abrupt velocity gradients in the upstream reach (Fig. 6). The effect diminished downstream, where sediment deposits, bed-level variations, scour pools, and the residual transverse structure continued to determine the principal flow path and the location of low-velocity zones.

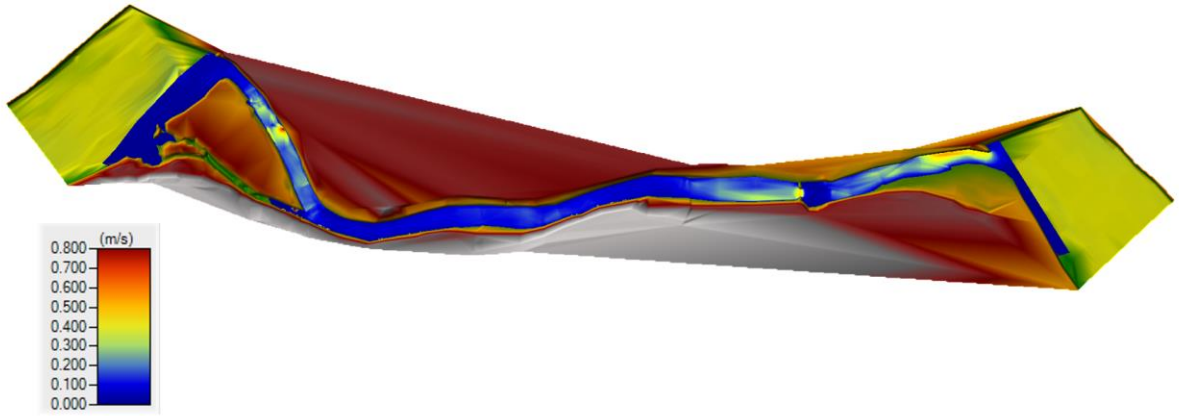


Figure 6. Flow velocities distribution under low-flow conditions for Variant A

Variant B produced only minor additional changes relative to Variant A (Fig. 7). Although the inlet was more deeply lowered, the central and downstream velocity patterns remained similar. The secondary branch was only partly activated, and a continuous channel-wide flow path was not established.

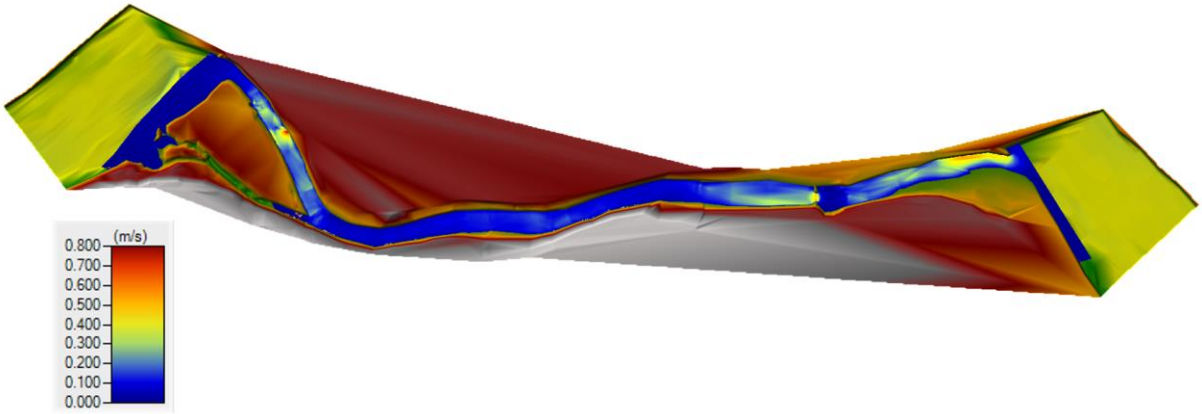


Figure 7. Flow velocities distribution under low-flow conditions for Variant B

These results indicate that lowering the inlet sill primarily affects the hydraulic boundary condition at the channel entrance rather than the overall hydraulic behaviour of the side channel. Once water enters the channel, flow patterns remain strongly controlled by the inherited morphology, including local bed depressions, residual transverse structures and sediment deposits that developed during decades of reduced connectivity. Consequently, localized modification of the inlet geometry alone is insufficient to restore the longitudinal continuity of the velocity field.

3.3 Effects under contrasting hydrological conditions

The effectiveness of the proposed restoration measures depended strongly on the prevailing hydrological conditions. During low-flow conditions, when the inlet sill represented the dominant hydraulic control, lowering the sill noticeably increased hydraulic exchange between the main channel and the side branch. The most pronounced changes occurred within the entrance reach, where flow became less concentrated and velocity gradients were reduced. Nevertheless, hydraulic improvements gradually diminished downstream as channel morphology increasingly controlled flow distribution.

Under higher-flow conditions, differences between the existing configuration and the two restoration variants became considerably smaller. As water levels exceeded the crest elevation of the original inlet sill, the hydraulic control imposed by the structure was substantially reduced even under existing conditions. Consequently, both restoration variants produced velocity distributions that closely resembled those of the reference scenario, with the principal flow paths controlled by natural channel curvature, local constrictions and residual bed morphology rather than by the inlet geometry. Similar patterns of accelerated flow were observed near concave banks and the remnants of the downstream sill, while deeper channel sections maintained relatively low and spatially uniform velocities.

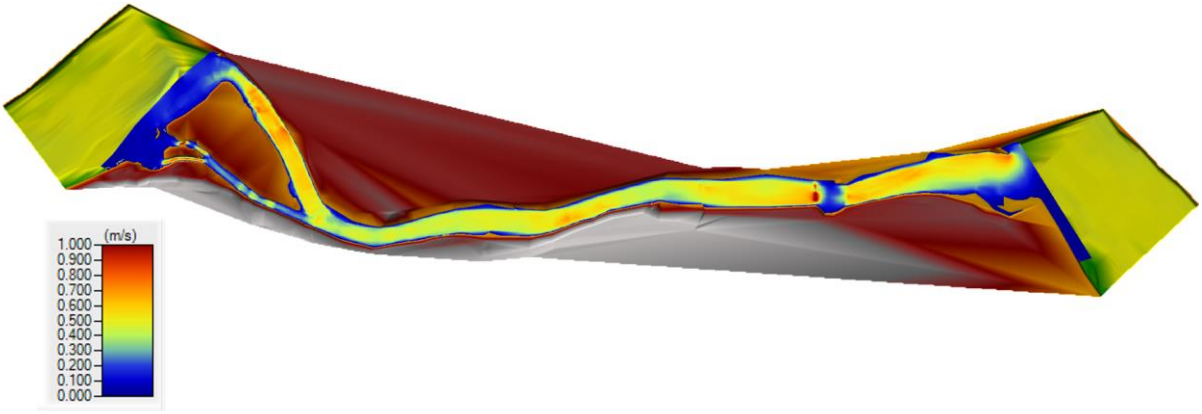


Figure 8. Flow velocities distribution of under higher-flow conditions for Variant A.

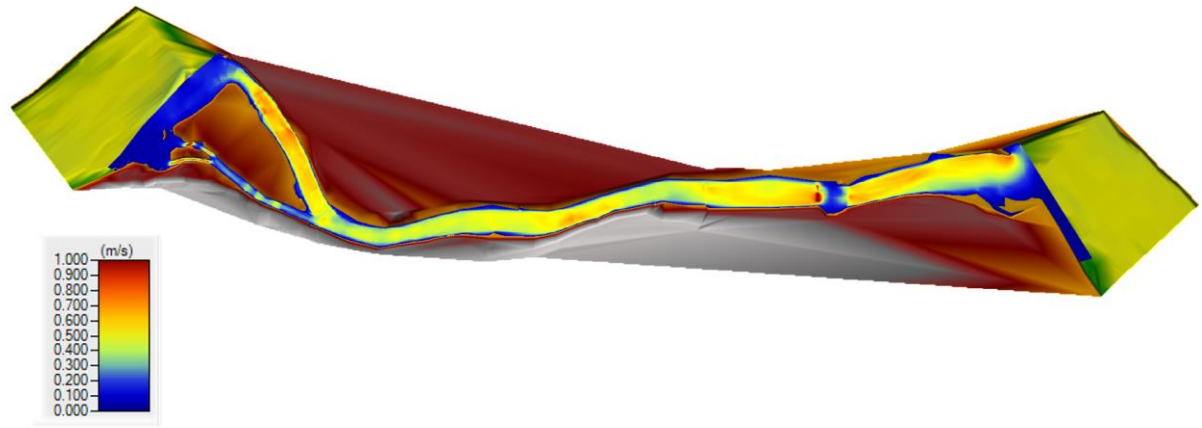


Figure 9. Flow velocities distribution of under higher-flow conditions for Variant B.

These findings demonstrate that the influence of localized restoration measures is highly dependent on hydrological regime. Modifying the inlet sill has the greatest hydraulic significance during ecologically critical low-flow periods, whereas its influence progressively decreases as river stage increases and the hydraulic control exerted by the sill becomes submerged.

4 Conclusion

This study evaluated the hydraulic response of the Podravska Moslavina side channel to localized inlet restoration measures using a two-dimensional hydraulic model developed in HEC-RAS. The objective was to assess the extent to which lowering the inlet sill could improve hydraulic connectivity under contrasting hydrological conditions and to identify the hydraulic limitations of such interventions.

The two-dimensional simulations show that the existing inlet sill is the dominant hydraulic control during low-flow conditions. It concentrates inflow through narrow openings and creates an abrupt entrance transition, while downstream sediment deposits, scour pools, and residual structures fragment the longitudinal velocity field.

Localized sill modification is therefore a useful low-disturbance measure for improving entrance conditions, but it is insufficient for channel-wide revitalization. Effective restoration should consider the inlet together with sediment accumulation and residual transverse structures. Spatial velocity patterns provide a practical screening metric, provided that their interpretation is supported by appropriate validation and, for detailed design, sediment and full-momentum analyses.

The findings highlight that the effectiveness of localized restoration measures depends strongly on hydrological conditions. Their influence is greatest during ecologically critical low-flow periods, whereas under higher discharges the hydraulic behaviour of the side channel is controlled primarily by channel morphology rather than inlet geometry. This demonstrates that successful restoration requires consideration of the entire hydraulic system instead of focusing exclusively on reconnecting the channel entrance.

Finally, this study demonstrates that the spatial organization of the velocity field provides a valuable process-based indicator for evaluating restoration effectiveness. Beyond describing hydraulic conditions, velocity distributions reveal the governing mechanisms controlling flow continuity, sediment redistribution and hydraulic connectivity. The proposed approach therefore offers a practical framework for assessing restoration alternatives and identifying the hydraulic limitations of localized interventions before implementation. Such process-based evaluation can support the design of more effective and less intrusive restoration strategies in regulated floodplain rivers, particularly in ecologically sensitive areas where minimizing physical disturbance is a primary management objective. Future research should combine field validation with sediment-transport modelling and should test combined inlet and downstream interventions across a broader range of hydrological conditions.

Acknowledgements

This work was supported by the RIVET project through the National Recovery and Resilience Plan 2021–2026; funded by the European Union – NextGenerationEU.

References

EKONERG d.o.o. 2020. Technical report: Hrvatske vode Glavna ocjena prihvatljivosti zahvata za ekološku mrežu: Zahvat – Obnova rukavca i proširenje korita na rijeci Dravi na lokacijama: Miholjački Martinci (C.6) i Podravska Moslavina (C.7).

Kondolf, G. M. 1997 PROFILE: Hungry Water: Effects of Dams and Gravel Mining on River Channels. *Environmental management*, 21(4), 533-551. https://doi.org/10.1007/s002679900048

Nilsson, C., Reidy, C. A., Dynesius, M., & Revenga, C. 2005 Fragmentation and flow regulation of the world's large river systems. *Science*, 308(5720). https://doi.org/10.1126/science.1107887

Palmer, M. A., Bernhardt, E. S., Allan, J. D., et al. 2005. Standards for ecologically successful river restoration. *Journal of Applied Ecology*, 42(2), 208-217. https://doi.org/https://doi.org/10.1111/j.1365-2664.2005.01004.x

Roni, P., Hanson, K., & Beechie, T. 2008 Global Review of the Physical and Biological Effectiveness of Stream Habitat Rehabilitation Techniques. *North American Journal of Fisheries Management*, 28(3), 856-890. https://doi.org/10.1577/M06-169.1
Tockner, K., & Stanford, J. A. 2002 Riverine flood plains: present state and future trends. *Environmental Conservation*, 29(3), 308-330. https://doi.org/10.1017/S037689290200022X
Ward, J. V., Tockner, K., Arscott, D. B., & Claret, C. 2002 Riverine landscape diversity. *Freshwater Biology*, 47(4), 517-539. https://doi.org/10.1046/j.1365-2427.2002.00893.x

INTEGRATING HYDRODYNAMIC HABITAT MODELLING AND NATURE-BASED SOLUTIONS FOR THE RESTORATION OF THE NOSKOVAČKA BARA SIDE-ARM

Antonija BARIŠIĆ LASOVIĆ [1*], Igor TADIĆ [1], Gabrijela SABO [1], Nikola BATAKOVIĆ [2]

[1] *Hidroing d.o.o. Osijek, Croatia*

E-mail: antonija.barisic-lasovic@hidroing-os.hr

E-mail: igor.tadic@hidroing-os.hr

E-mail: gabrijela.sabo@hidroing-os.hr

[2] *Hrvatske vode, Croatia*

E-mail: nikola.batakovic@voda.hr

[*] *Corresponding author*

Abstract

Noskovačka Bara is a former side arm of the Drava River in Croatia, located within the UNESCO Transboundary Biosphere Reserve Mura–Drava–Danube and the Natura 2000 network. Due to long-term hydrological disconnection, sedimentation, and altered groundwater dynamics, the site has experienced significant degradation of ecological status and habitat functionality. Within the SWIMM (Sustainable Water and Integrated Management of Fish Migration and Their Habitats in the Danube River Basin and NW Black Sea) project, this study evaluates nature-based solutions for restoring hydrological connectivity and improving habitat conditions for asp (*Aspius aspius*), a representative rheophilic fish species. The research combines ecohydrological assessment, field surveys, and hydrodynamic habitat modelling to support restoration planning. Baseline data included bathymetric surveys, water-level monitoring, and fish assemblage analyses. Proposed restoration scenarios involve selective sediment removal, channel reshaping, and restoration of surface-water and groundwater connectivity with the Drava River. Modelling results indicate that the proposed measures enhance inundation frequency and duration, improve hydraulic conditions, and maintain suitable water depths during low-flow periods. Habitat suitability analysis suggests improved spawning and refuge opportunities for asp. The study demonstrates a transferable framework for restoring degraded floodplain side arms and integrating ecohydrological approaches into river restoration planning within the Danube River Basin.

Key words

Noskovačka Bara, oxbow restoration, ecohydrology, fish habitat modelling, nature-based solutions, Drava River, floodplain management

1 Introduction

Floodplain ecosystems represent highly dynamic and ecologically valuable components of large river systems, providing essential habitats for aquatic biodiversity and supporting key ecological processes. However, extensive river regulation, channelisation, and hydrological disconnection have substantially altered natural river–floodplain interactions across Europe, leading to habitat simplification, reduced lateral connectivity, and degradation of ecological status, particularly in large lowland rivers such as those of the Danube River Basin (Habersack et al., 2016; Poff et al., 1997; Schmutz and Sendzimir, 2018). These pressures are closely linked to the disruption of the natural flow regime, which is a

fundamental driver of habitat variability and ecosystem functioning (Acreman et al., 2014; Poff et al., 1997).

From an ecohydrological perspective, effective restoration must address the coupled relationships between hydrological dynamics, hydraulic conditions, and habitat structure. Environmental flow approaches emphasise that flow quantity, timing, and variability are all relevant for sustaining ecological integrity in both natural and altered river systems (Acreman et al., 2014). In this context, hydrodynamic habitat modelling offers a mechanistic framework for translating physical river conditions into biologically meaningful habitat metrics and for comparing alternative restoration measures before implementation (Maddock et al., 2013; Park et al., 2024; Tomsic et al., 2007).

In recent years, nature-based solutions (NbS) have become increasingly important in river restoration because they seek to restore natural processes while simultaneously enhancing biodiversity, ecosystem services, and climate resilience (European Commission, 2020). In large river floodplains, NbS typically include side arm reconnection, sediment management, restoration of variable bathymetry, preservation of riparian vegetation, and reduction of purely structural engineering interventions. Such approaches are strongly aligned with the objectives of the EU Water Framework Directive, the EU Biodiversity Strategy, and contemporary Danube basin restoration policy (European Commission, 2020; Habersack et al., 2016; Schmutz and Sendzimir, 2018).

The Drava River floodplain, which forms part of the UNESCO Transboundary Biosphere Reserve Mura–Drava–Danube, contains numerous former side arms that are today partially or fully disconnected from the main channel. A representative example is Noskovačka Bara, located near Noskovačka Dubrava in Virovitica-Podravina County, Croatia. The site lies within protected floodplain landscape units and the Natura 2000 network and has undergone progressive degradation due to sedimentation, reduced floodplain exchange, and altered groundwater–surface water interactions (DHMZ, 2023; HIDROING d.o.o., 2024). Historically, the side arm functioned as a dynamic floodplain water body, but in its present condition it receives insufficient freshwater exchange under ordinary hydrological conditions, which has reduced habitat quality and accelerated terrestrial succession (Fig. 1).

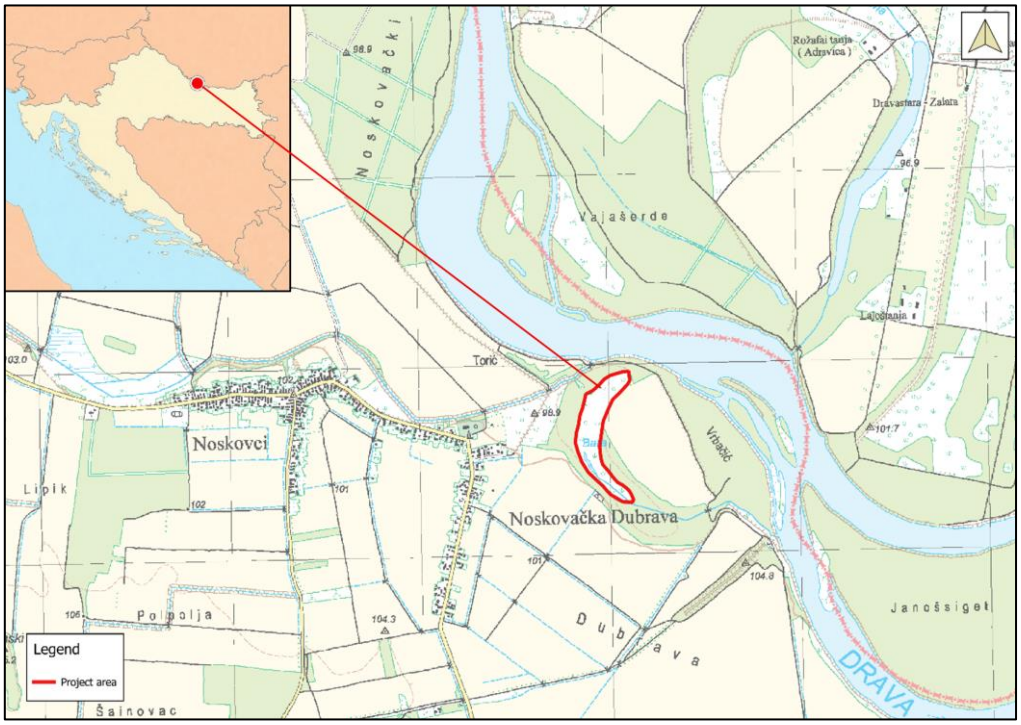


Figure 1. Study area and proposed restoration layout of Noskovačka Bara, showing the side arm system and phased intervention zones.

Despite the increasing use of NbS in river restoration projects, there remains a practical need for

integrated assessment frameworks that explicitly couple restoration design with hydrodynamic habitat evaluation. This is especially important in side arm restoration, where the ecological outcome depends not only on reconnection itself, but also on the resulting spatial pattern of depths, velocities, inundation persistence, and habitat diversity across fish life stages (Maddock et al., 2013; Park et al., 2024; Tomsic et al., 2007; Waddle, 2001).

The restoration of Noskovačka Bara is being developed within the SWIMM project. The aim of this study is to assess the potential effectiveness of alternative NbS restoration measures in improving hydrological connectivity and habitat suitability for fish species of conservation interest. Particular emphasis is placed on the use of hydrodynamic habitat modelling as a decision-support tool for identifying the most ecologically favourable restoration variant under variable flow conditions.

2 Methods

The methodology implemented in this study integrates baseline ecohydrological assessment, restoration scenario development, hydrodynamic evaluation, and habitat suitability analysis. The workflow was designed to support restoration planning in a data-limited but ecologically sensitive floodplain environment, while remaining consistent with nature-based restoration principles (Acreman et al., 2014; European Commission, 2020; Maddock et al., 2013).

2.1 Study area and baseline data collection

Noskovačka Bara is a former Drava side arm with a total area of approximately 18.7 ha, located in the inundation zone near the settlement of Noskovci. In its present condition, the water body is only periodically connected to the Drava River, while large parts of the former aquatic area are affected by sediment infilling, vegetation overgrowth, and hydrological stagnation (HIDROING d.o.o., 2024). According to project documentation, present-day floodplain water surfaces vary approximately between 10 and 15 ha depending on river stage, while the remaining area is occupied by marsh vegetation, shrubs, and willow stands (HIDROING d.o.o., 2024).

Baseline assessment was based on geodetic and hydrographic survey data, orthophotos, bathymetric information, historical interpretation of former channel morphology, and review of hydrological records from the wider Drava sector (DHMZ, 2023; HIDROING d.o.o., 2024). These datasets were used to define the present geometry of the side arm, identify critical disconnection points, and characterise the physical constraints controlling water exchange with the main river. Particular attention was given to inlet and outlet conditions, bed elevations, sediment accumulation, and the persistence of shallow isolated zones, as these factors directly influence habitat suitability for fish spawning, juvenile refuge, and seasonal survival.

2.2 Development of restoration scenarios

A total of six restoration variants were developed during the conceptual design phase, ranging from simple regulated channel configurations to more naturalistic meandering layouts incorporating internal islands and variable bed elevations (HIDROING d.o.o., 2024). All scenarios aimed to improve lateral connectivity between the Drava River and the side arm while maintaining compatibility with the ecological sensitivity of the floodplain and minimizing unnecessary engineering intervention.

The proposed measures included:
- reopening or reshaping of the upstream connection,
- improvement of downstream drainage and controlled outflow,
- selective excavation of accumulated sediment,
- formation of variable-depth aquatic zones,
- creation of shallow littoral areas and deeper refuge habitats,
- preservation of a natural meandering planform where feasible.

A qualitative comparison of the six restoration variants was undertaken considering their morphological configuration, environmental integration, hydrological performance, habitat potential, and implementation complexity (Table). The assessment was based on the conceptual design analysis and was used to identify the alternative that best balances long-term water retention, morphological diversity, habitat functionality, and environmental integration.

Table 1. Qualitative comparison of the six restoration variants for Noskovačka Bara.

Variant	Configuration	Main advantages	Main limitations
1-A	Straight, uniformly shaped channel with a bed elevation of 92.5 m a.s.l.	Simple and visually unobtrusive solution; basic reconnection during higher Drava water levels.	Artificial, uniform morphology with limited habitat diversity; water retention is low during low-flow periods.
1-B	Wider straight channel (approximately 35 m), with a uniform bed elevation of 92.5 m a.s.l.	Larger water surface and storage volume than Variant 1-A; improved visual integration into the surrounding landscape.	Regular channel form and uniform bed level limit hydraulic and habitat diversity; substantial water loss may occur during dry periods.
2-A	Meandering channel with two islands and a uniform bed elevation of 92.5 m a.s.l.	More natural appearance, improved landscape integration, and greater hydraulic and habitat variability than Variants 1-A and 1-B.	Water retention remains limited because the bed elevation is uniform; lower resilience during prolonged low-flow conditions.
2-B	Broad meandering channel with two islands and extensive open-water areas; uniform bed elevation of 92.5 m a.s.l.	High visual and morphological diversity; large open-water area and a diverse range of fish habitats.	Uniform bed elevation limits water retention during low flows; more technically complex to implement than simpler variants.
2-C	Meandering channel with one island, variable channel widths, and a uniform bed elevation of 92.5 m a.s.l.	Natural channel appearance, large open-water area, and relatively high water-storage capacity; favourable habitat diversity.	Hydrological resilience remains constrained by the uniform bed elevation; lower retention capacity than Variant 3 during drought conditions.
3	Meandering channel with two islands and differentiated bed elevations of 92.0 and 92.2 m a.s.l.	Highest hydraulic, morphological, and habitat diversity; increased effective storage volume; longest water retention and lowest drying risk.	Most technically complex alternative to implement.

Although Variant 3 is technically more complex than the simpler channel configurations, its differentiated bed elevations and greater effective storage volume provide a clear hydrological advantage. In particular, the lower bed elevations enable inflow at lower Drava River stages and reduce the risk of drying in the deeper northern part of the side arm. Together with the meandering planform and internal islands, these characteristics create the most diverse hydraulic conditions and the most favourable habitat mosaic for different fish life stages. Variant 3 was therefore selected for detailed hydrodynamic and habitat suitability assessment.

The existing state and the hydrodynamic effects of the proposed interventions are illustrated in Figure 2, which compares the currently disconnected conditions (Fig. 2a) with the hydraulic response of the restored system under Variant 3 (Fig. 2b). The layout of the selected restoration scenario is shown in Fig. 2c (HIDROING d.o.o., 2024).

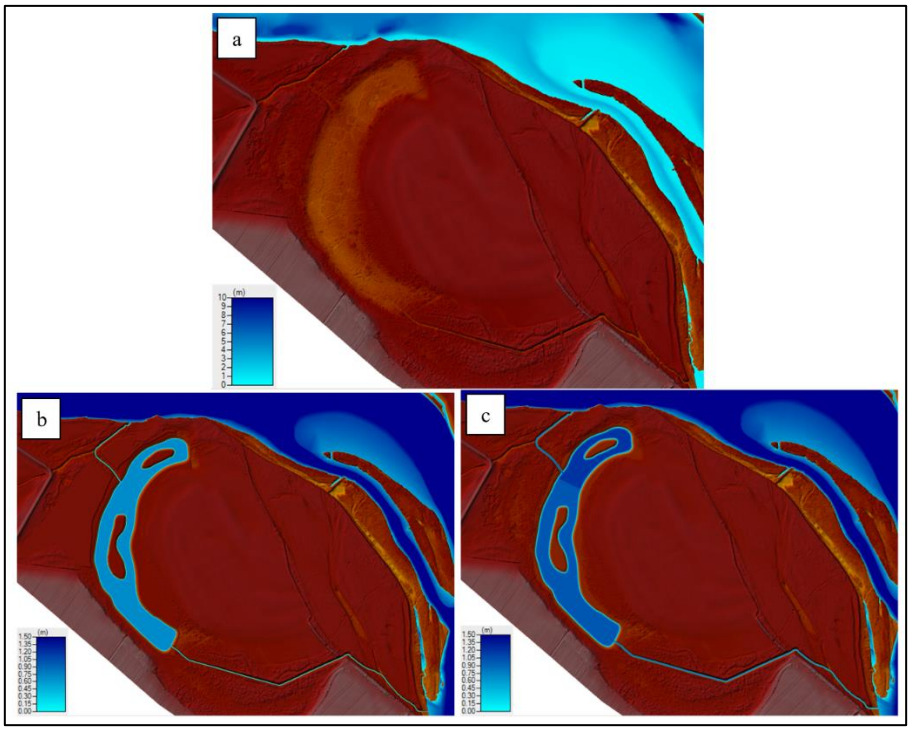


Figure 2. Hydrodynamic modelling results and selected restoration scenario: (a) simulated water depth under existing conditions; (b) simulated water depth for Variant 3 under identical boundary conditions; (c) layout of the selected restoration scenario (Variant 3) used for subsequent ecohydraulic assessment.

2.3 Hydrodynamic modelling concept

The study area was modelled using a two-dimensional (2D) hydrodynamic model in HEC-RAS v6.5. Model geometry was derived from a digital terrain model created from surveyed XYZ points and processed into a 1 m × 1 m raster. The computational domain covered Noskovačka Bara and the adjacent Drava River reach approximately 1.5 km upstream and downstream of the inlet/outlet channels. A 2 m × 2 m 2D mesh was generated in HEC-RAS v6.5, and hydraulic roughness was parameterized using Manning's coefficient.

The selected mesh resolution represented a balance between computational efficiency and adequate representation of terrain variability. Simulations were performed under unsteady-flow conditions using discharge at the upstream boundary and stage at the downstream boundary as model forcing.

The modelled discharge range of 0.10–1.80 m³/s represents local flows through the restored side-arm system and should not be interpreted as the total discharge of the Drava River. Hydrological data from the nearby Terezino Polje and Donji Miholjac gauging stations, analysed for the 1995–2024 period, indicate substantially larger main-channel flows. The long-term mean annual discharges were 499.8 m³/s at Terezino Polje and 514.9 m³/s at Donji Miholjac, while the recorded annual minimum discharges were 121 m³/s and 175 m³/s, respectively. Therefore, the analysed scenarios represent low local exchange flows entering and circulating through Noskovačka Bara under low- to medium-stage conditions in the Drava River, when the persistence of aquatic habitats in the side arm is most critical. The corresponding river water levels were derived from the characteristic water levels at both gauging stations and interpolated along the 75.3 km river reach, using calculated water-surface slopes of approximately 12.7–13.0 cm/km (Hidoring d.o.o., 2024).

Model outputs (water depth and velocity fields) were used as inputs for subsequent habitat suitability and WUA analyses. Due to the conceptual design stage of the project, model calibration and validation were not performed; instead, the model was applied as a comparative tool for evaluating restoration

scenarios. Therefore, model outputs were interpreted comparatively among restoration scenarios rather than as absolute predictions of hydraulic conditions.

The assessment focused on the hydraulic consequences of alternative restoration geometries and on the resulting suitability of the restored side arm for fish habitat functions. The conceptual modelling approach linked surveyed topography and bathymetry with restoration geometry scenarios in order to evaluate the expected changes in water retention, depth distribution, and flow pattern under representative hydrological conditions.

Because the restoration is currently in the planning and design phase, the modelling was used primarily as a comparative decision-support tool rather than as post-project validation. The objective was to determine which restoration layout is most likely to maintain ecologically favourable hydraulic conditions during periods of hydrological stress, particularly under low and medium flow conditions when side arm habitats are often most vulnerable to fragmentation and drying (Maddock et al., 2013; Park et al., 2024; Tomsic et al., 2007). In this context, morphological complexity was treated as a key design variable because heterogeneous channel forms generally improve the diversity of local hydraulic environments and therefore support broader ecological functionality (Schmutz and Sendzimir, 2018; Tomsic et al., 2007).

2.4 Habitat suitability assessment

Habitat suitability assessment was performed using a Habitat Suitability Index (HSI) approach focused on *Aspius aspius* as a representative rheophilic target species. This species is ecologically relevant for the Drava floodplain and is particularly suitable for evaluating the restoration potential of side arm habitats because different life stages respond differently to depth and flow conditions. The analysis considered two habitat functions:

- juvenile habitat, which generally favours shallow and lower-velocity marginal areas,
- spawning habitat, which requires somewhat deeper and hydraulically stable conditions.

The habitat suitability curves for water depth and flow velocity were developed from literature-derived habitat preference ranges and expert-based interpretation of the ecological requirements of *Aspius aspius*. These curves were used to derive composite HSI values ranging from 0 to 1, where higher values indicate more suitable habitat (Maddock et al., 2013; Park et al., 2024; Waddle, 2001). Composite HSI values were calculated by multiplying depth and velocity suitability indices, resulting in a final suitability score ranging from 0 to 1. For juveniles, optimum suitability (HSI = 1.0) was assigned at a depth of 0.6 m and a flow velocity of 0.25 m/s, while for spawning habitat optimum suitability occurred at a depth of 1.2 m and a flow velocity of 0.5 m/s (Fig. 3).

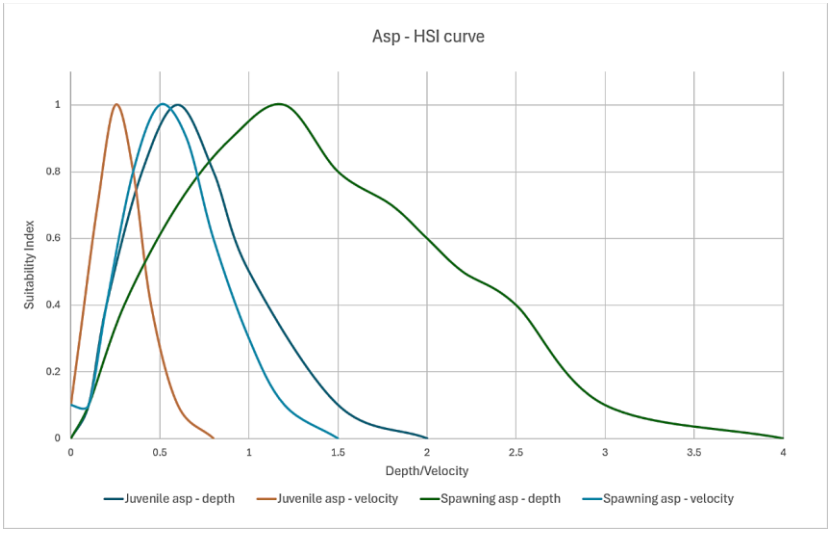


Figure 3. Habitat suitability curves (HSI) for juvenile and spawning stages of *Aspius aspius* based on water depth and flow velocity.

To complement spatial HSI interpretation, habitat response to discharge was quantified using PHABSIM (Physical Habitat Simulation System) to calculate the Weighted Usable Area (WUA) as a key indicator of habitat availability (Waddle, 2001). WUA was computed as the sum of habitat-weighted cell areas:

$$WUA = \sum_{i=1}^{n} A_i * HSI_i \quad (1)$$

where A_i is the area of cell i and HSI_i is the composite suitability value (0–1). For comparability across reaches, WUA values are reported as m² per 1,000 m of reach (m²/1,000 m). WUA was normalized per 1,000 m reach length to enable comparison between habitat patches of different spatial extents. Throughout this paper, discharge values are expressed in m³/s.

In addition to reach-integrated WUA values, longitudinal WUA outputs were used to visualize the spatial distribution of habitat availability along the side arm at selected discharges. In these plots, the reach is subdivided into longitudinal–lateral segments, and each coloured rectangle represents a range of local WUA values (m²/1,000 m) for the corresponding segment.

3 Results and Discussion

The analysis revealed a clear contrast between the current degraded condition of Noskovačka Bara and the hydraulic and ecological potential of the proposed restoration variants. Under representative boundary conditions, the existing configuration does not provide sufficient inflow to maintain wet conditions within the side arm; model results indicate that the oxbow remains largely dry (Fig. 2a). This confirms that sedimentation, inlet degradation, and simplified internal morphology currently limit floodplain exchange and habitat functionality (HIDROING d.o.o., 2024). Such degradation patterns are typical of regulated lowland rivers, where channelization and reduced lateral connectivity simplify habitat structure and diminish ecological resilience (Habersack et al., 2016; Poff et al., 1997; Schmutz and Sendzimir, 2018).

All six conceptually assessed restoration options are expected to improve hydraulic connectivity to some extent; however, their anticipated ecological value differs markedly. Simpler geometries with relatively regular channel sections restore water exchange but still produce fairly uniform hydraulic conditions. In contrast, the more naturalistic Variant 3, with its meandering planform, internal islands, and differentiated bed elevations, generates continuous inundation along the full side-arm length and a wider range of depths and retention zones (Fig. 2b), thereby increasing hydraulic heterogeneity and reducing the probability of complete habitat homogenisation during lower flows (HIDROING d.o.o., 2024). This result is consistent with previous ecohydraulic restoration studies showing that physically complex restoration layouts generally provide more functionally diverse habitats than simplified engineered channels (Maddock et al., 2013; Tomsic et al., 2007).

For the juvenile stage of *Aspius aspius*, high HSI values are concentrated along shallow channel margins and around the internal islands, where relatively low velocities and moderate depths create favourable nursery conditions. Suitability is highest in sheltered marginal zones and decreases toward deeper or hydraulically more uniform parts of the restored side arm. This pattern agrees with the ecological expectation that early life stages depend strongly on shallow, low-energy microhabitats that reduce energetic stress and provide refuge (Maddock et al., 2013; Park et al., 2024), as shown in Fig. 4.



Figure 4. Spatial distribution of Habitat Suitability Index (HSI) for juvenile *Aspius aspius* in the restored side arm, based on combined depth and velocity criteria.

For the spawning stage, habitat suitability shifts toward somewhat deeper and more hydraulically stable sections of the side arm. In the analysed scenario, the highest suitability occurs in the central and northern portions of the restored channel, where water depth and velocity better correspond to spawning requirements. Compared with juvenile habitat, spawning habitat is less spatially extensive but more continuous, indicating that the same restored morphology can support different ecological functions in different subzones of the side arm. This contrast between juvenile and spawning outputs confirms the importance of designing a heterogeneous habitat mosaic rather than a single uniform excavated channel (Maddock et al., 2013; Park et al., 2024; Tomsic et al., 2007), as shown in Fig. 5.



Figure 5. Spatial distribution of Habitat Suitability Index (HSI) for spawning *Aspius aspius* in the restored side arm, based on combined depth and velocity criteria.

The PHABSIM-based WUA analysis provides a quantitative interpretation of habitat response to discharge (Fig. 6). Juvenile habitat availability increased from approximately 6,110 m²/1,000 m at Q = 0.10 m³/s to a maximum of 7,818 m²/1,000 m at Q = 0.20 m³/s, and then decreased progressively with increasing discharge to 3,072 m²/1,000 m at Q = 1.00 m³/s and 1,588 m²/1,000 m at Q = 1.80 m³/s. Spawning habitat showed the opposite pattern: WUA increased from 3,366 m²/1,000 m at Q = 0.10 m³/s to a maximum of 7,342 m²/1,000 m at Q = 0.65 m³/s, remaining relatively high at Q = 1.00 m³/s (6,880 m²/1,000 m) before gradually declining toward 6,194 m²/1,000 m at Q = 1.80 m³/s. Selected WUA values are summarized in Table 2.

This divergence indicates that no single hydraulic condition maximizes habitat suitability for both life stages simultaneously, underlining the need for morphologically diverse restoration layouts that maintain a mosaic of low-velocity shallow margins and deeper hydraulically stable zones (Fig. 6). The contrasting discharge optima indicate that maintaining ecological functionality for different life stages requires a range of hydraulic conditions rather than a single target flow value. Such trade-offs between life stages are commonly observed in floodplain ecosystems and highlight the importance of maintaining habitat diversity across a range of flow conditions. These findings strongly support restoration strategies aimed at increasing morphological complexity and hydraulic diversity within floodplain side arms.

Although WUA provides a useful quantitative indicator of habitat availability, restoration performance should also be interpreted in relation to habitat connectivity, refuge availability, and the long-term persistence of aquatic habitats during low-flow periods. Therefore, WUA results were considered together with the spatial distribution and continuity of suitable habitat patches, as well as the overall hydraulic functioning of the side arm. In particular, the capacity of the proposed design to retain water in deeper sections while maintaining shallow, low-velocity marginal habitats was considered essential for supporting different life stages of *Aspius aspius* under variable flow conditions.

Table 2. Weighted Usable Area (WUA) for juvenile and spawning *Aspius aspius* at selected discharges (from Fig. 6)

Discharge, Q (m³/s)	WUA Juvenile (m²/1,000 m)	WUA Spawning (m²/1,000 m)
0.10	6,110	3,366
0.20	7,818	4,822
0.35	6,684	6,152
0.50	5,452	6,964
0.65	4,696	7,342
1.00	3,072	6,880
1.80	1,588	6,194

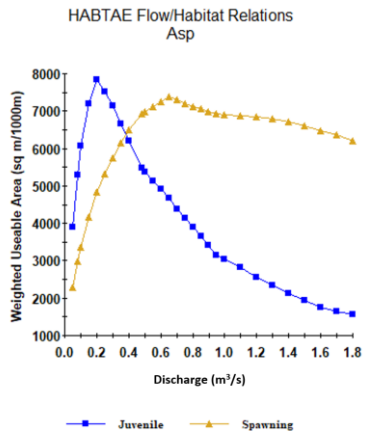


Figure 6. Relationship between discharge and weighted usable area (WUA) for juvenile and spawning stages of *Aspius aspius,* obtained using PHABSIM-based habitat evaluation.

Longitudinal WUA outputs further support the "habitat mosaic" interpretation by showing where along the reach WUA is concentrated at selected discharges (Fig. 7). For juveniles, the discharge close to the peak WUA (Q = 0.2 m³/s) corresponds to patchy but extensive distributions of usable habitat, whereas

at Q = 0.3 m³/s the spatial pattern changes in both extent and continuity (Fig. 7a–b). Spawning-stage longitudinal WUA at Q = 0.2–0.3 m³/s similarly demonstrates spatially heterogeneous patterns across the side arm (Fig. 7c–d), indicating that hydraulically diverse restoration layouts support multiple life-stage functions through spatial differentiation rather than uniform conditions.

The preferred restoration concept is consistent with Nature-Based Solution principles because it restores natural hydrological and geomorphological processes rather than relying primarily on structural engineering interventions. The creation of variable-depth habitats, low-velocity refuge zones, and a meandering channel planform is expected to enhance ecological resilience while simultaneously improving hydrological connectivity.

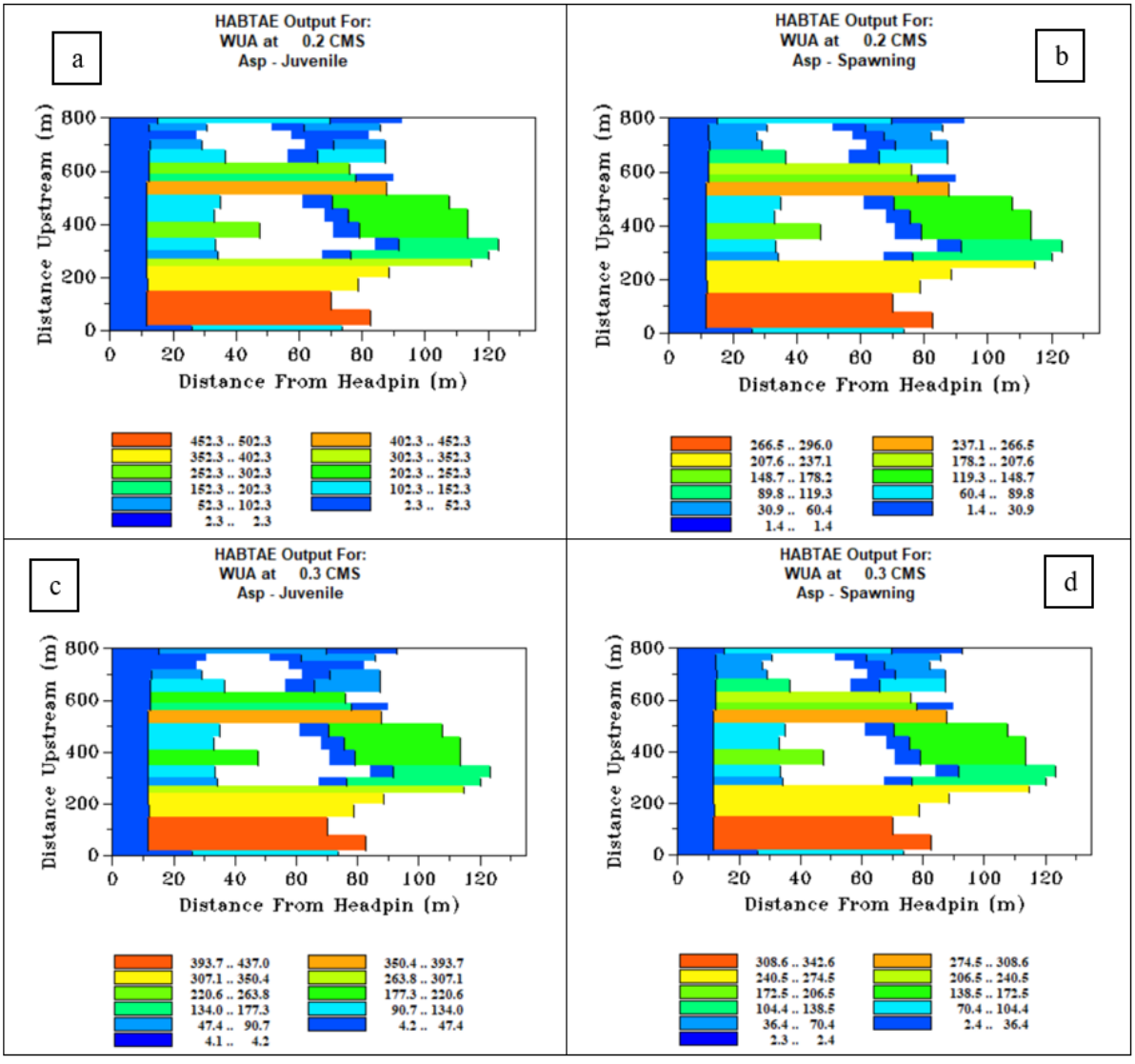


Figure 7. Longitudinal distribution of local WUA (m²/1,000 m) for *Aspius aspius* along Noskovačka Bara at selected discharges: (a) juvenile, Q = 0.2 m³/s; (b) juvenile, Q = 0.3 m³/s; (c) spawning, Q = 0.2 m³/s; (d) spawning, Q = 0.3 m³/s.

Overall, the results indicate that increasing morphological complexity leads directly to improved habitat functionality. From a conservation perspective, the restoration of such habitat diversity is essential for maintaining the favourable status of the Natura 2000 network, as it supports the specialized life-cycle requirements of protected rheophilic fish species within the Drava River floodplain. While all reconnection scenarios have some hydraulic benefit, the ecologically strongest response is associated with the scenario that best reproduces floodplain channel diversity through variable depths, low-velocity refuge zones, increased shoreline length, and retention of water in deeper compartments (HIDROING

d.o.o., 2024; Schmutz and Sendzimir, 2018; Tomsic et al., 2007). In this sense, the restoration design does not merely reconnect the side arm to the Drava River but creates a more functional hydraulic template for multiple fish life stages.

Taken together, the results show that hydrodynamic habitat modelling is a useful planning instrument for side arm restoration because it allows alternative NbS scenarios to be compared on ecological grounds before implementation. In the case of Noskovačka Bara, the most morphologically diverse restoration option also provides the most favourable combination of hydraulic connectivity, habitat diversity, and flow-stage resilience, which supports its selection as the preferred restoration concept.

4 Conclusion

Noskovačka Bara represents a characteristic example of a degraded floodplain side arm in a large regulated lowland river system, where long-term hydrological disconnection and sedimentation have reduced ecological functionality. The present study shows that integrated ecohydrological assessment and hydrodynamic habitat modelling can provide a robust basis for selecting restoration measures in such environments.

The analysis demonstrates that hydrological reconnection, while necessary, is insufficient on its own; ecological success relies on morphological complexity. The most promising outcomes are associated with restoration layouts that create morphological and hydraulic diversity within the side arm. In the Noskovačka Bara case, the preferred Variant 3 provides the best balance of water retention, heterogeneous depth structure, and habitat suitability for different life stages of *Aspius aspius*. As the project is currently in the planning and design phase, the presented findings should be interpreted as scenario-based evidence of restoration potential rather than proof of achieved ecological recovery. Nevertheless, the applied methodology offers a strong decision-support framework for restoration planning and may serve as a transferable model for similar side arm systems in the Drava and wider Danube River Basin.

The results of this study provide practical decision support for water management authorities, nature conservation practitioners, project designers, and river restoration practitioners when selecting restoration measures among multiple technical alternatives. They may also support policy-makers and other stakeholders in planning and prioritising ecohydrological restoration measures in the Drava River floodplain and in comparable side-arm systems across the Danube River Basin.

The presented assessment is based on hydrodynamic and habitat modelling supported by currently available ecological data. Future post-restoration monitoring will be required to verify habitat responses under real hydrological conditions and to further refine habitat suitability relationships for target species. Such monitoring will provide an important basis for adaptive management and long-term evaluation of restoration effectiveness.

Acknowledgements

This work was supported by the SWIMM project (Sustainable Water and Integrated Management of Fish Migration and Their Habitats in the Danube River Basin and NW Black Sea), co-funded by the European Union under the Danube Region Programme. The authors would like to thank the project partners and stakeholders for their cooperation and support during the field investigations, conceptual design development, and ecological assessment process.

References

Acreman, M., Arthington, A.H., Colloff, M.J., Couch, C., Crossman, N.D., Dyer, F., Overton, I., Pollino, C.A., Stewardson, M.J. and Young, W. 2014 Environmental flows for natural, hybrid, and novel riverine ecosystems in a changing world. F*rontiers in Ecology and the Environment* 12(8), 466–473.

DHMZ 2023 Hydrological Yearbook of the Republic of Croatia. Meteorological and Hydrological Service, Zagreb.

European Commission, 2020 Nature-Based Solutions: State of the Art in EU-Funded Projects. Publications Office of the European Union, Luxembourg.

Habersack, H., Hein, T., Stanica, A., Liska, I., Mair, R., Jäger, E., Hauer, C. and Bradley, C. 2016 Challenges of river basin management: Current status of, and prospects for, the River Danube from a river engineering perspective. *Science of the Total Environment* 543, 828–845.

HIDROING d.o.o., 2024, Technical Report Conceptual Design of the Noskovačka Bara Restoration. Internal technical reports prepared for the SWIMM project, Osijek, Croatia.

Maddock, I., Harby, A., Kemp, P. and Wood, P. 2013 *Ecohydraulics: An Integrated Approach*. John Wiley & Sons, Chichester.

Park, J., Jang, S., Lee, H., Gou, J. and Song, I. 2024 Evaluation of fish habitat suitability based on stream hydrodynamics and water quality using SWAT and HEC-RAS linked simulation. *Scientific Reports* 14, 19236.

Poff, N.L., Allan, J.D., Bain, M.B., Karr, J.R., Prestegaard, K.L., Richter, B.D., Sparks, R.E. and Stromberg, J.C. 1997 The natural flow regime. *BioScience* 47(11), 769–784.

Schmutz, S. and Sendzimir, J. (eds.) 2018 *Riverine Ecosystem Management: Science for Governing Towards a Sustainable Future*. Springer, Cham.

Tomsic, C.A., Granata, T.C., Murphy, R.P. and Livchak, C.J. 2007 Using a coupled eco-hydrodynamic model to predict habitat for target species following dam removal. *Ecological Engineering* 30(3), 215–230.

USACE Hydrologic Engineering Center, 2024 HEC-RAS River Analysis System: User's Manual, Version 6.5. Davis, CA, USA.

Waddle, T.J. 2001 PHABSIM for Windows: User's Manual and Exercises. U.S. Geological Survey, Fort Collins.

NATURE-BASED SOLUTIONS IN THE WATER SECTOR IN SERBIA AND THE EU: FROM REGULATORY ALIGNMENT TO IMPLEMENTATION CHALLENGES

Jelena BATICA [1*], Žarko SRETENOVIĆ [1], Nikola RAKONJAC[1,2]

[1] *Jaroslav Cerni Water Institute LLC Belgrade, Serbia*

E-mail: jelena.batica@jcerni.rs

E-mail: zarko.sretenovic@jcerni.rs

[2] *Wageningen University, The Netherlands*

E-mail: nikola.rakonjac@jcerni.rs

** Corresponding author*

Abstract

Nature-based solutions (NbS) have become a central concept in European water and climate policy, particularly through their integration into the Water Framework Directive, the Floods Directive, and the EU adaptation agenda. In parallel, Serbia is aligning its water and environmental acquis under Chapter 27 (Environment and climate change), which is part of Cluster 4 - Green Agenda and Sustainable Connectivity in the revised EU enlargement methodology, supported by substantial EU technical and financial assistance in the water sector. This study examines the extent to which this regulatory convergence has translated into the systematic use of NbS in Serbian water and flood risk management. The analysis follows a three-pillar framework. First, key EU water, flood risk and climate documents are compared with Serbian laws, strategies and plans to assess the explicit and implicit integration of NbS or functionally equivalent concepts. Second, quantitative and qualitative indicators characterise the structural context for implementation, including wastewater service coverage, treatment levels, water body status and the presence of NbS or natural water retention measures in flood risk management plans. Third, institutional and implementation aspects are assessed through national NbS and climate adaptation reports, project documentation and pilot initiatives. Preliminary results indicate substantial policy alignment but a pronounced implementation gap, with Serbian investments still dominated by grey infrastructure. The study identifies institutional fragmentation, lack of technical standards and project-level risk aversion as key barriers and outlines actionable measures to embed NbS in planning and investment.

Key words

Nature-based solutions, water sector, flood risk management, European Union, Serbia, environmental policy, implementation gap.

1 Introduction

Nature-based solutions (NbS) have become an increasingly important component of European environmental and climate policy because they address water-related risks while also providing broader ecological and societal co-benefits. The European Environment Agency (2021), in its report Nature-based solutions in Europe: Policy, knowledge and practice for climate change adaptation and disaster risk reduction, emphasized that NbS are gaining strategic importance across climate adaptation, disaster risk reduction and ecosystem-based management.

In the water sector, this shift is closely associated with the European Union's core regulatory framework. Directive 2000/60/EC of the European Parliament and of the Council, commonly referred to as the Water

Framework Directive, established an integrated river basin management approach aimed at preventing the deterioration of aquatic ecosystems and achieving good status of surface and groundwater bodies (European Commission, 2000; European Commission, 2026). Directive 2007/60/EC on the assessment and management of flood risks, known as the Floods Directive, complemented this framework by introducing requirements for preliminary flood risk assessment, flood hazard and risk mapping, and the preparation of flood risk management plans (European Parliament and Council, 2007). Within this broader policy context, the European Commission has increasingly promoted green infrastructure, natural water retention measures, and other NbS-related approaches as instruments that can support both water management and flood risk reduction objectives (European Commission, 2014; Wild et al., 2023). Serbia is advancing the alignment of its environmental legislation with the EU acquis under Chapter 27, which forms part of Cluster 4 - Green Agenda and Sustainable Connectivity in the revised EU enlargement methodology. According to the Swedish Environmental Protection Agency (2024), this approximation process includes substantial institutional reform, directive-specific alignment and major infrastructure investment needs in the water sector.

However, policy alignment does not automatically lead to implementation. The European Environment Agency (2021) noted that, despite clear progress in policy recognition, the practical uptake of NbS remains constrained by governance, planning, and implementation barriers across Europe. In Serbia, the United Nations Development Programme (2021) and subsequent scoping work on NbS in Serbia have shown that, although the concept is increasingly recognized in climate and disaster risk reduction discussions, it is still only weakly embedded in mainstream water management and flood risk management practice. Against this background, this study examines the extent to which EU-oriented regulatory alignment has translated into the systematic uptake of NbS in the Serbian water sector, with particular attention to water management and flood risk management

2 Methods

2.1 Analytical framework

The study applies a comparative analytical framework designed to examine the relationship between regulatory alignment and the practical implementation of NbS in the Serbian water sector. The framework is based on the assumption, widely recognized in recent NbS literature, that the formal inclusion of NbS in strategic and policy documents does not automatically lead to their operational uptake in planning, investment, and implementation practice. Martin et al. (2025) describe this as an "implementation gap", highlighting the role of institutional, legal, regulatory, and financial barriers in constraining the wider mainstreaming of NbS. Similar conclusions were drawn by Morita and Matsumoto (2021), who emphasized that effective NbS implementation depends on the alignment of policies, institutions, and actors across sectors and governance levels.

To capture this gap, the analysis is structured around three interconnected dimensions. The first dimension addresses policy and regulatory alignment, focusing on how NbS and related concepts are reflected in EU and Serbian water, flood, and climate-related documents. The second dimension addresses the structural implementation context, using selected indicators to assess whether existing service deficits and sectoral priorities create conditions that facilitate or constrain the uptake of NbS. The third dimension addresses institutional and governance conditions, examining whether the existing allocation of responsibilities, planning routines, and implementation instruments support or hinder the practical integration of NbS.

This three-part framework is consistent with broader NbS policy literature, which identifies policy integration, institutional coordination, and enabling governance arrangements as critical conditions for successful implementation and scaling-up (European Environment Agency, 2021; Morita and Matsumoto, 2021; Martin et al., 2025). In the present study, the framework is used to compare the EU policy orientation with the Serbian implementation context in relation to water management and flood risk management.

The analytical framework is summarised in Figure 1, distinguishing between policy and regulatory alignment, structural implementation context, and institutional and governance conditions, all of which influence the uptake and mainstreaming of NbS in Serbian water and flood risk management.

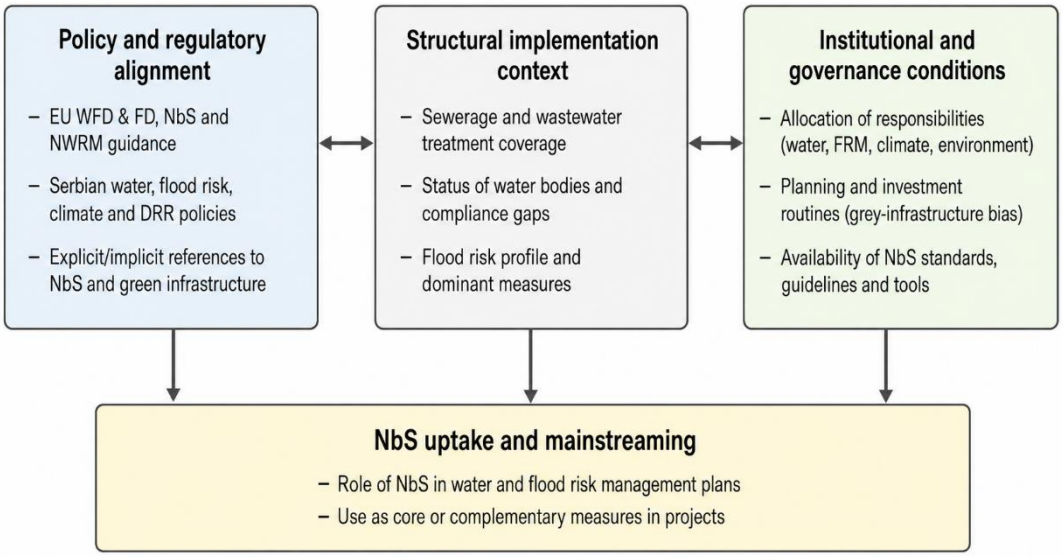


Figure 1: Analytical framework for assessing policy alignment, structural conditions, and governance factors influencing the uptake of nature-based solutions in the Serbian water and flood risk management sectors

2.2 Data sources

The analysis draws on three main groups of data sources: (i) European Union policy and guidance documents, (ii) Serbian legal and strategic documents, and (iii) secondary statistical and analytical sources related to the Serbian water sector and flood risk management.

The first group comprises core EU directives and policy documents relevant to water management, flood risk management and NbS. These include the Water Framework Directive (Directive 2000/60/EC), which establishes the overall framework for integrated river basin management in the EU, and the Floods Directive (Directive 2007/60/EC), which sets requirements for the assessment and management of flood risks (European Commission, 2000; European Parliament and Council, 2007). In addition, the analysis uses Commission guidance on natural water retention measures and recent EU assessments of NbS for water policy implementation, including the EU policy document on natural water retention measures, the Joint Research Centre report Nature-based Solutions for Water Management: From Pilot to Standard and the European Environment Agency report Nature-based Solutions in Europe: Policy, Knowledge and Practice for Climate Change Adaptation and Disaster Risk Reduction (European Commission, 2014; European Commission, 2022; European Environment Agency, 2021; Wild et al., 2023).

The second group comprises Serbian framework legislation, national strategies, and sectoral plans in water management, the environment, climate change, and disaster risk reduction. This includes the primary water and flood risk management planning documents, climate and adaptation strategies, and EU approximation support materials related to Chapter 27 and Cluster 4 (Swedish Environmental Protection Agency, 2024; GFDRR and Government of Serbia, 2021; Delegation of the European Union to Serbia, 2021; Nikolić Popadić, 2023). Particular attention is given to national studies that explicitly address NbS or nature-based climate solutions in Serbia, which provide a systematized overview of the institutional, policy, and legal framework and identify key challenges and entry points for NbS mainstreaming (United Nations Development Programme, 2021; Ministry of Environmental Protection, 2021; European Environment Agency, 2025).

The third group includes secondary data and analytical reports that characterise the structural

performance of the Serbian water sector. These sources provide information on sewerage coverage, wastewater treatment levels, investment needs, and current compliance gaps, as well as contextual information on flood hazard and risk (Klima 101, 2025; NALED, 2023; GFDRR and Government of Serbia, 2021; Swedish Environmental Protection Agency, 2024). Where possible, these data are compared with EU averages and benchmarks reported in European assessments to situate Serbia's implementation context relative to that of EU Member States (European Environment Agency, 2021; European Commission, 2022; Revised Urban Waste Water Treatment Directive 2024/3019; Sustainable Development Goal 6 Progress Report).

These three groups of sources correspond to the analytical dimensions shown in Figure 1. EU and Serbian water, flood and climate documents provide the basis for assessing policy and regulatory alignment, structural performance indicators are used to characterise the implementation context, while national NbS and climate adaptation studies, project documentation and pilot initiatives provide evidence on institutional and governance conditions and practical implementation experience.

2.3 Indicators and comparative approach

To assess the implementation context for nature-based solutions in the Serbian water sector, the study applies a small set of structural and policy-related indicators. The purpose of these indicators is not to provide a full performance evaluation of the sector, but to identify whether existing infrastructure deficits, service gaps, and planning practices create favourable or constraining conditions for the uptake of NbS.

The first group of indicators relates to wastewater and basic water service performance. These include the share of population connected to sewerage systems, the proportion of generated wastewater collected, and the share of wastewater undergoing treatment, particularly at the secondary level or above. These indicators were selected because they reflect the overall maturity of water service infrastructure and the extent to which sectoral investments are still dominated by basic compliance needs. Available evidence shows that only about 14.7% of wastewater in Serbia undergoes at least secondary treatment, compared with an EU average of approximately 80%, while sewerage services are available to only around half of the population. Similarly, just 15% of Serbia's population is connected to at least secondary wastewater treatment, far below the EU average of 81%, highlighting significant structural deficiencies in the country's wastewater infrastructure (NALED, 2023; Serbia Water Security Diagnostics, 2022; ICPDR, 2020; EUROSTAT, 2022).

The second group of indicators relates to water status and environmental compliance, including available information on the condition of water bodies and broader compliance gaps in relation to EU water requirements. These indicators are used as contextual variables rather than as direct measures of NbS uptake, since poor environmental performance often reinforces policy preference for conventional grey infrastructure and end-of-pipe solutions (European Commission, 2022; European Environment Agency, 2021).

The third group of indicators relates to flood risk management planning and NbS relevance. Here, the analysis considers whether flood risk management plans and related strategic documents explicitly refer to natural water retention measures, floodplain restoration, green infrastructure, or comparable nature-based approaches. In line with the EU policy document on natural water retention measures, such references are treated as a proxy for the degree to which flood risk planning moves beyond structural defence and opens space for more integrated catchment-based solutions (European Commission, 2014). Additional attention is given to the presence of pilot projects or programme documents that connect flood risk reduction with retention, restoration, or hybrid green-grey approaches (GFDRR and Government of Serbia, 2021; Delegation of the European Union to Serbia, 2021).

The comparative approach is therefore qualitative-quantitative and benchmark-oriented. Serbia is not compared to a single EU Member State, but to the general policy direction, benchmarks, and implementation logic emerging from EU legislation, guidance, and assessment reports. This makes it

possible to distinguish between formal policy convergence and the more limited operational uptake of NbS in the Serbian context.

2.4 Qualitative rating scheme

To provide a more transparent link between the analytical framework and the results, each of the three dimensions is assigned a qualitative rating (low, medium, high) for Serbia, based on the combination of indicators and documentary evidence described above. A 'high' rating indicates that conditions are largely favourable for systematic NbS uptake in that dimension; a 'medium' rating indicates mixed but partially enabling conditions; and a 'low' rating indicates that prevailing conditions strongly constrain NbS implementation. The ratings are not intended as a formal index, but as a transparent summary of the comparative assessment underpinning the discussion in Section 3. For clarity, the main elements assessed under each dimension are:

- Focusing on **policy alignment**, we qualitatively assessed river basin planning structures, explicit references to NbS/NWRM, and availability of technical guidance and design standards.
- For the **structural context**, we used indicators on sewerage and wastewater treatment coverage, share of wastewater receiving ≥ secondary treatment, and share of water bodies in good status.
- For **institutional and governance** conditions, we examined the allocation of responsibilities across sectors, planning and investment routines, and the presence of NbS standards, guidelines and tools.

3 Results and Discussion

3.1 NbS in the EU water policy framework

Within the European Union, nature-based solutions have emerged as an important complement to conventional grey infrastructure in achieving water policy objectives. The Water Framework Directive (Directive 2000/60/EC) introduced an integrated river basin management approach with the overarching goal of preventing deterioration and achieving good ecological and chemical status of surface waters and good quantitative and chemical status of groundwater (European Commission, 2000). The Floods Directive (Directive 2007/60/EC) subsequently established a common framework for the assessment and management of flood risks, requiring Member States to prepare flood hazard and risk maps and flood risk management plans for river basins and coastal areas at significant risk (European Parliament and Council, 2007).Building on these two core directives, subsequent policy developments and technical guidance have increasingly promoted NbS-related concepts as means to support both water quality and flood risk objectives. The EU Policy Document on Natural Water Retention Measures explicitly presents measures such as floodplain restoration, wetland creation, retention ponds, buffer strips, and green roofs as tools that can reduce flood peaks, improve water quality, and contribute to the achievement of Water Framework Directive objectives, while also delivering climate adaptation and biodiversity benefits (European Commission, 2014). The document emphasises that such measures should be considered in both river basin management plans and flood risk management plans, in order to strengthen synergies between the two directives.

Recent EU assessments further consolidate the position of NbS in the water policy domain. The European Environment Agency (2021) report on nature-based solutions in Europe highlights an expanding body of experience with NbS for climate adaptation and disaster risk reduction, including numerous water-related applications such as river and floodplain restoration, urban green-blue infrastructure, and natural water retention at the catchment scale. The Joint Research Centre's report Nature-based Solutions for Water Management: From Pilot to Standard documents how NbS are being tested and evaluated in urban and agricultural contexts, providing evidence on their effectiveness, costs, and co-benefits and arguing for their progressive integration into mainstream water management and planning (European Commission, 2022). In parallel, more targeted analyses of NbS impacts on water quality and waterbody conditions demonstrate that NbS can support the implementation of the Water Framework Directive by addressing diffuse pollution, runoff, and hydromorphological pressures, while also contributing to wider environmental policy goals (Wild et al., 2023).Despite this increasingly

favourable policy and knowledge environment, European-level reviews also underline that the uptake of NbS remains uneven and that governance, institutional, and financial barriers continue to limit its wider deployment (European Environment Agency, 2021; Martin et al., 2025). This broader EU experience provides the reference against which Serbia's regulatory alignment and implementation context are examined in the subsequent sections.

3.2 Regulatory alignment in Serbia

Serbia's alignment with the European Union water and environmental acquis takes place within Chapter 27, which forms part of Cluster 4 - Green Agenda and Sustainable Connectivity in the revised enlargement methodology. As noted by the Swedish Environmental Protection Agency (2024), this approximation process requires not only legal harmonisation with EU directives but also substantial institutional strengthening and large-scale infrastructure investment, particularly in the water sector. In that sense, Serbia's policy trajectory is formally oriented toward the same objectives that underpin the Water Framework Directive and the Floods Directive.

In the field of water management, Serbia has already adopted planning instruments that mirror the logic of the EU Water Framework Directive. The River Basin Management Plan for the territory of the Republic of Serbia for the period 2021-2027 adopts the river basin as the main planning unit and defines good status of water bodies as a central long-term objective, consistent with the WFD approach. This indicates a significant degree of formal convergence at the level of strategic planning. However, the extent to which this convergence translates into operational measures that favour nature-based approaches remains less clear.

A similar pattern is visible in flood risk management. Following the 2014 floods, Serbia intensified the development of flood hazard maps, flood risk maps, and flood risk management planning in line with the Floods Directive, supported by extensive EU technical and financial assistance. According to the Delegation of the European Union to Serbia (2021), this support has been directed toward the preparation of flood risk management plans for the main Serbian river basins and toward strengthening the institutional capacities of the national water authorities. EU support documents also explicitly indicate that future planning should promote multipurpose and nature-based solutions for climate adaptation. Nevertheless, the dominant framing of flood policy in Serbia still appears to be centred on structural protection, preparedness, and conventional defence measures.

The position of NbS becomes more visible in the climate adaptation domain than in core water sector planning. The Study on Nature-based Climate Solutions in Serbia, prepared by the United Nations Development Programme (2021), represented one of the first systematised efforts to assess the applicability of NbS in the Serbian context and to identify links between NbS, climate resilience, and sectoral policy needs. More recently, Serbia adopted the Programme for Adaptation to Changed Climate Conditions for the period 2023–2030 with an accompanying action plan, thereby strengthening the institutional basis for adaptation planning at the national level. According to available summaries and tracking assessments, this programme provides an important entry point for the integration of NbS into adaptation policy and acknowledges the need to improve resilience of natural resources and critical infrastructure.

At the same time, recent scoping work on NbS in Serbia suggests that the concept remains unevenly embedded across policy domains. The 2025 study Enhancing Nature-Based Solutions in Serbia: The Role of Ecosystems in Climate Change and Disaster Risk Reduction concludes that Serbia has relevant policy entry points for NbS, especially in climate change adaptation and disaster risk reduction, but still faces important legal, institutional, and governance barriers to mainstreaming. This implies that Serbia's regulatory alignment is real, but partial in functional terms: EU-compatible planning structures and adaptation instruments are increasingly in place, while the systematic translation of NbS into mainstream water management and flood risk management practice remains limited.

Taken together, these elements justify a high rating for policy and regulatory alignment, even if the

functional integration of NbS into planning instruments remains partial.

To operationalise the policy and regulatory alignment dimension, a simple qualitative alignment matrix is used to compare selected NbS-relevant criteria between the EU framework and the Serbian context. The criteria and ratings are indicative, but they make the underlying assessment more transparent.

Table 1: Alignment matrix for NbS-relevant policy criteria

Criterion	EU	Serbia	Alignment level
River basin planning	Yes (WFD fully in force)	Yes (RBMP 2021-2027 adopted)	High
NWRM integration	Strong in guidance and plans	Limited and project-specific	Medium
NbS terminology	Explicit and consolidated	Partial and uneven	Medium
Technical guidance	Extensive EU guidance suites	Limited national documents	Low

The matrix confirms that Serbia is strongly aligned with the EU in terms of river basin planning structures, while the integration of NWRM and NbS terminology, and especially the availability of national technical guidance, still lag. This justifies a high rating for overall policy alignment, but only medium to low alignment for the more operational aspects of NbS implementation.

3.3 Structural context of implementation

The structural performance of the Serbian water sector is characterised by significant infrastructure and service gaps, particularly in the area of wastewater collection and treatment. Available national and international assessments show that a substantial share of the population is not connected to sewerage systems, and that only a relatively small fraction of collected wastewater undergoes at least secondary treatment, placing Serbia among the weakest performers in Europe in this domain. This indicates that a large part of current and planned investments is still directed towards basic service provision and compliance with conventional environmental requirements, rather than toward more innovative or multifunctional approaches.

In parallel, assessments of water status and environmental compliance suggest that a considerable proportion of water bodies in Serbia fail to achieve good status, due to a combination of organic pollution, nutrient loads, hydromorphological alterations, and legacy pressures. These pressures further reinforce a prevailing policy and investment preference for end-of-pipe and structural measures, which are perceived as necessary to address the most pressing compliance gaps. In such a context, nature-based solutions and hybrid measures may be recognised at the level of discourse but struggle to compete with conventional infrastructure in budget allocation and project prioritisation.

A similar picture emerges in flood risk management. While flood hazard and risk mapping and flood risk management plans have been developed in line with EU requirements, the dominant risk reduction measures remain structural flood defences, channel regulation, and emergency protection. References to natural water retention measures, floodplain restoration, or other NbS-related options are generally limited or appear as complementary rather than central components of the measure portfolios. This reflects both the historical path-dependency of flood defence practice and the perception that large-scale NbS require additional space, time, and coordination efforts that may not align with short-term risk reduction imperatives.

Table 2 provides a schematic overview of selected structural indicators for the Serbian water sector and illustrates the extent to which basic service deficits and compliance gaps shape the conditions for NbS implementation. The values in Table 2 confirm that Serbia is still in a phase of catching up with basic water service and compliance requirements, which structurally constrain the extent to which nature-based solutions can be mainstreamed as a central element of water and flood risk management.

Table 2: Selected structural indicators relevant for NbS implementation in the Serbian water sector

Indicator	Unit	Latest value (Serbia)	Reference/source
Population connected to public sewerage	% of total population	Around 50% of the population is connected to sewerage	World Bank, 2022; ICPDR, 2020; Statistical Office of the Republic of Serbia, 2024.
Population served by wastewater treatment	% of total population	Around 15% of the population is served by wastewater treatment	World Bank, 2022; ICPDR, 2020
Population connected to at least secondary wastewater treatment	% of total population	Around 15% of the population is connected to secondary or higher treatment	EUROSTAT, 2022.
Share of wastewater receiving ≥ secondary treatment	% of generated wastewater	14.7% of wastewater receives at least secondary treatment	World Bank, 2022; Statistical Office of the Republic of Serbia, 2024; SDG6 progress report (indicator 6.3.1).
Share of water bodies with good ecological status	% of classified water bodies	Around 40% of surface water bodies are in at least good status	Government of the Republic of Serbia, 2023 (RBMP); BIOEAST, 2022.
Presence of NWRM/NbS in FRM plans	Qualitative	Limited; mostly referenced as complementary measures	GFDRR & Government of Serbia, 2021; Delegation of the EU to Serbia, 2021.

3.4 Key implementation challenges

Despite formal convergence with the EU water and climate acquis and the existence of clear policy entry points, several structural and governance-related factors constrain the practical uptake of nature-based solutions in Serbia.

A first challenge is **institutional fragmentation and path dependency in the water and flood risk sectors**. Responsibilities for water management, flood protection, spatial planning, environmental protection, and climate adaptation are distributed across several ministries, agencies, and public enterprises, with a limited tradition of integrated, cross-sectoral planning. Existing planning and implementation routines in both water services and flood defence are strongly shaped by historical reliance on grey infrastructure, such as sewer networks, treatment plants, dykes, and channel regulation. This path dependency makes it difficult for NbS to be considered as a primary option, particularly when administrative procedures, design standards, and cost-benefit assessments are tailored to conventional solutions.

A second challenge is the **absence of detailed technical standards, design guidelines, and mainstreamed methodologies for NbS** in the Serbian water sector. While EU guidance on natural water retention measures and international experience provide a growing body of technical knowledge, there are still few nationally adopted documents that translate these concepts into operational design criteria, sizing rules, performance indicators, and monitoring requirements suitable for Serbian regulatory and hydrological conditions. In such a situation, project developers and engineers face additional uncertainty when proposing NbS or hybrid solutions, which in turn reinforces risk-averse preferences for established grey designs.

A third challenge relates to **financing frameworks and project selection practices**. Given the magnitude of investment needs for basic water infrastructure, particularly in sewerage and wastewater treatment, national and donor funding is largely directed toward projects that close the most critical service and compliance gaps. Under these conditions, NbS are often perceived as optional or complementary measures rather than as core elements of investment projects. Limited experience with the economic valuation of NbS co-benefits, combined with conventional cost-benefit methodologies that focus on single-sector outcomes, further reduces the visibility of NbS in project pipelines. Together, these factors contribute to an implementation environment in which nature-based solutions are

recognised at the level of policy discourse but face significant obstacles in becoming a routine component of water and flood risk management practice in Serbia.

To make this assessment more transparent, Table 3 summarises the main institutional and governance indicators used in this study and the corresponding qualitative ratings for Serbia.

Table 3: Institutional and governance indicators relevant for NbS implementation in Serbia

Indicator	Main finding for Serbia	Rating
Allocation of responsibilities across sectors	Responsibilities for water management, flood protection, spatial planning, environmental protection and climate adaptation are fragmented across several institutions, with limited cross-sectoral coordination.	Low
Planning and investment routines	Planning and implementation remain strongly oriented toward grey infrastructure and conventional sectoral solutions.	Low
Availability of NbS standards, guidelines and tools	Nationally adopted technical standards, design guidance, and operational methodologies for NbS remain limited.	Low
Position of NbS in project pipelines	NbS are generally treated as complementary or pilot measures rather than as core investment options.	Low
Overall institutional and governance conditions	Existing governance arrangements offer some policy entry points, but prevailing institutional and implementation conditions still constrain the systematic uptake of NbS.	Low

4 Discussion

The results show that Serbia has achieved a relatively high degree of formal alignment with the EU water, flood risk, and climate policy framework, but that this alignment has not yet translated into the systematic uptake of nature-based solutions in practice. This finding is consistent with broader European experience, in which regulatory recognition of NbS has often remained ahead of implementation.

At the same time, the Serbian case points to a more specific implementation constraint. While many EU Member States face governance barriers such as fragmented responsibilities, limited cross-sectoral coordination and insufficient technical standards for NbS, Serbia also faces pronounced structural deficits in basic water services and environmental compliance. Low wastewater treatment coverage, persistent water quality pressures and high investment needs continue to direct policy attention and financial resources toward conventional grey infrastructure.

This means that Serbia faces a double implementation challenge. On the one hand, it shares the same institutional and governance barriers that have slowed NbS mainstreaming elsewhere in Europe. On the other hand, these barriers are reinforced by a sectoral context in which basic compliance and service delivery gaps remain unresolved, reducing the political, financial and administrative space for the wider use of NbS and hybrid solutions.

Taken together, the analysis suggests that Serbia should not be viewed as an exception, but rather as a case in which the broader European implementation gap is intensified by a substantial infrastructure backlog. This helps explain why NbS are increasingly visible in policy discourse, yet still appear only marginally in mainstream water and flood risk management practice.

5 Conclusion

This study explored how far Serbia's formal alignment with the EU water, flood risk and climate acquis has translated into the practical use of nature-based solutions (NbS) in the water sector. The analysis shows that Serbia has adopted many of the key planning instruments and strategic frameworks linked to the Water Framework Directive and the Floods Directive and has strengthened its climate adaptation framework, including a national adaptation programme and dedicated NbS studies (Swedish

Environmental Protection Agency, 2024; United Nations Development Programme, 2021; European Environment Agency, 2025). However, this regulatory and strategic convergence has so far led only to limited and uneven integration of NbS into day-to-day water management and flood risk management practice (Swedish Environmental Protection Agency, 2024; United Nations Development Programme, 2021; European Environment Agency, 2025).

The structural context helps explain why. Serbia still faces large gaps in sewerage coverage and wastewater treatment, with only about 14-15% of wastewater receiving at least secondary treatment and substantial investment needs identified for basic water infrastructure (NALED, 2023; World Bank, 2022). Many water bodies remain under pressure from pollution and hydromorphological changes, and flood risk management continues to rely predominantly on conventional structural measures and emergency protection, even though hazard and risk maps and flood risk management plans have been developed with EU support (GFDRR and Government of Serbia, 2021; Delegation of the European Union to Serbia, 2021). In this environment, it is natural that projects which close the most urgent service and compliance gaps with familiar grey infrastructure are prioritised, while NbS tend to appear as complementary or pilot measures rather than as central elements of investment portfolios (NALED, 2023; World Bank, 2022; GFDRR and Government of Serbia, 2021; Delegation of the European Union to Serbia, 2021).

The institutional and governance dimension further reinforces this pattern. Responsibilities for water, flood management, environment, climate and spatial planning are distributed across several institutions, and nationally adopted technical standards and design guidelines specifically for NbS are still missing. EU guidance and international experience provide an expanding knowledge base, but their translation into Serbian regulatory practice and everyday planning tools remains limited (European Commission, 2014; European Commission, 2022). In line with wider European findings on the NbS "implementation gap", the Serbian case illustrates that policy alignment and high-level recognition, although necessary, are not sufficient to ensure systematic NbS uptake in the absence of enabling structural conditions, clear technical frameworks and supportive financing and project selection practices (European Environment Agency, 2021; European Commission, 2014; European Commission, 2022; Martin et al., 2025).

From a policy perspective, the results point to several practical entry points for strengthening the role of NbS in Serbia's water and flood risk management. These include targeted use of NbS in priority river basins where flood risk, water quality problems and land-use pressures intersect; systematic integration of NbS into upcoming cycles of river basin management plans, flood risk management plans and climate adaptation measures; and the development of national technical guidance that adapts existing EU and international NbS standards to Serbian hydrological, institutional and legal conditions (European Commission, 2014; European Commission, 2022; United Nations Development Programme, 2021). In parallel, project appraisal and financing frameworks could be adjusted to better account for the multiple co-benefits of NbS and hybrid solutions, thereby increasing their visibility and competitiveness in investment pipelines (European Environment Agency, 2021; Martin et al., 2025). Taken together, such steps could help move Serbia from predominantly formal alignment towards more substantive, implementation-oriented convergence with EU practice in the use of NbS in the water sector (European Commission, 2022; European Environment Agency, 2025).

Acknowledgements

The authors would like to thank the Jaroslav Černi Water Institute for the institutional support provided during the preparation of this paper.

References

Delegation of the European Union to Serbia. 2021 *Urgent Action against Flood Risks – EU Support to Flood Risk Management in Serbia*. Delegation of the European Union to Serbia, Belgrade, Serbia.

European Commission. 2000 *Directive 2000/60/EC of the European Parliament and of the Council Establishing a Framework for Community Action in the Field of Water Policy (Water Framework Directive)*. Official Journal of the European Communities L 327/1.
European Commission. 2007 *Directive 2007/60/EC on the Assessment and Management of Flood Risks (Floods Directive).* Official Journal of the European Union L 288/27.
European Commission. 2014. *EU Policy Document on Natural Water Retention Measures.* European Commission, Brussels, Belgium.
European Commission. 2023 *Nature-based Solutions – Research and Innovation Policy.* Directorate-General for Research and Innovation, Brussels, Belgium.
European Commission. 2022 *Nature-based Solutions for Water Management: From Pilot to Standard.* Publications Office of the European Union, Luxembourg.
European Environment Agency. 2021 *Nature-based Solutions in Europe: Policy, Knowledge and Practice for Climate Change Adaptation and Disaster Risk Reduction*. EEA Report No. 01/2021, European Environment Agency, Copenhagen, Denmark.
European Environment Agency. 2025 *Water Management - Adaptation in EU Policy Sectors. Climate-ADAPT,* European Environment Agency, Copenhagen, Denmark.
European Environment Agency. 2025 *Enhancing Nature-Based Solutions in Serbia: The Role of Ecosystems in Climate Change and Disaster Risk Reduction.* European Environment Agency, Copenhagen, Denmark.
EUROSTAT, Population connected to at least secondary wastewater treatment
GFDRR & Government of the Republic of Serbia. 2021 *Flood Hazard and Risk Mapping: Serbia - Component 2 of the National Disaster Risk Management Program.* Global Facility for Disaster Reduction and Recovery, Washington, DC.
Government of the Republic of Serbia. 2023a *River Basin Management Plan for the Territory of the Republic of Serbia for the Period until 2027.* Official Gazette of the Republic of Serbia No. 33/2023, Belgrade, Serbia. (in Serbian; English title used).
Government of the Republic of Serbia. 2023b. *Flood Prevention in the Republic of Serbia.* Presentation to the EUROSAI Working Group on the Audit of Funds Allocated to Disasters and Catastrophes, Kyiv, Ukraine
Institute for European Environmental Policy. 2025 *Bridging the Policy Gap: Bringing Nature-based Solutions to the Forefront of EU Strategies*. IEEP, Brussels, Belgium.
ICPDR 2020 *Serbia – Facts and Figures.* International Commission for the Protection of the Danube River, Vienna, Austria.
Klima 101 2025 *Serbia is at the Bottom of Europe When It Comes to Wastewater Treatment.* Klima 101, Belgrade, Serbia. (in Serbian).
Martin, J.G.C., Scolobig, A., Linnerooth-Bayer, J., Irshaid, J., Aguilera Rodriguez, J.J., Fresolone-Caparrós, A., & Oen, A. 2025 The nature-based solution implementation gap: A review of nature-based solution governance barriers and enablers. *Journal of Environmental Management.* 388, 126007.
Ministry of Environmental Protection Republic of Serbia 2021 *Nature-based Solutions for Climate Change Adaptation in Serbia.* Government of the Republic of Serbia, Belgrade, Serbia. (in Serbian; English title from official English version).
Ministry of Environmental Protection Republic of Serbia 2023 *Programme for Adaptation to Changed Climate Conditions for the Period 2023-2030 with Action Plan 2024-2026*. Government of the Republic of Serbia, Belgrade, Serbia. (in Serbian; English title used).
Ministry of European Integration Republic of Serbia 2020 *Negotiating Position of the Republic of Serbia for Chapter 27 - Environment and Climate Change.* Ministry of European Integration, Belgrade, Serbia. (in Serbian; English title used).
NALED 2023 *In Serbia, only 14.7% of Wastewater is Treated - In Europe Only Malta is Behind. National Alliance for Local Economic Development*, Belgrade, Serbia. (in Serbian).
Nikolić Popadić, S. 2023a Serbia on the Road to EU Accession: Securing Ambition for Chapter 27 – Environment and Climate Change. In: *Thematic Collection of Articles on EU Integration and the Environment*, Institute of Social Sciences, Belgrade, Serbia. (in Serbian; English title used).
Nikolić Popadić, S. 2023b. *Nature-based Solutions in Serbia: Policy Context and EU Approximation. In: Serbia on the Road to EU Accession: Securing Ambition for Chapter 27 – Environment and Climate*

Change, Institute of Social Sciences, Belgrade, Serbia. (in Serbian; English title used).
Stojković, S. & Zlatanović, N. 2017 Current State and Perspective of Water Management Policy in Terms of Climate Change – Case Study Republic of Serbia. *International Journal of Climate Change Strategies and Management.* 9(5), 626–645.
Swedish Environmental Protection Agency 2024 *Serbia – Supporting EU Approximation.* ENVAP Fact Sheet, Swedish Environmental Protection Agency, Stockholm, Sweden.
United Nations Development Programme 2021 *Study on Nature-based Climate Solutions in Serbia*. UNDP Serbia, Belgrade, Serbia.
Wild, T. et al. 2023 *Nature-Based Solutions Impacts on Water Quality & Waterbody Conditions.* European Commission, Valorisation of NBS Projects Initiative, Brussels, Belgium.
World Bank 2022 *Serbia Water Security Diagnostics.* International Bank for Reconstruction and Development / World Bank, Washington, DC.

COMPARATIVE HYDRAULIC ANALYSIS AND OPTIMISATION OF THE WATER SUPPLY SYSTEM IN A RESIDENTIAL AND TOURIST AREA

Elvis ŽIC [1*], Goran VOLF [1], Bojana HORVAT [1]

[1] *Faculty of Civil Engineering Rijeka, Croatia*

E-mail: elvis.zic@uniri.hr

E-mail: goran.volf@uniri.hr

E-mail: bojana.horvat@uniri.hr

[*] *Corresponding author*

Abstract

Seasonal variations in water demand are a major challenge for planning and managing water supply systems in tourist-intensive coastal areas. This paper presents a comparative hydraulic analysis and optimisation of the Novo Naselje water supply system (City of Poreč), focusing on water tower location, pumping station configuration and peak seasonal consumption. The analysis was based on demographic and tourist projections for a 30-year design period. Relevant water quantities were determined, including average daily, maximum daily and maximum hourly consumption, together with fire-fighting and safety reserves. Five system variants were analysed: three gravity-based variants with different water tower positions and elevations, and two variants with pumping inflow. Hydraulic simulations were performed primarily in WaterCAD V8i, while Urbano Hydra was used for a limited cross-model consistency check of selected governing outputs under identical input and boundary conditions. Pressures, velocities and flows were evaluated for different pipe materials and fire scenarios. The results show that water-tower position strongly affects pressure stability and network balance, while pumping-station configuration influences operational complexity and energy efficiency. Hydraulic modelling provided a structured decision-support basis for comparing the alternatives under seasonal and peak-load conditions.

Key words

hydraulic analysis, water supply system, numerical modelling, water tower, pumping station.

1 Introduction

Water supply systems in tourist-intensive areas are exposed to pronounced seasonal and daily demand fluctuations, especially during the summer period, when user numbers increase and the system must maintain reliable service, adequate pressures and fire-protection capacity. Under such conditions, hydraulic behaviour becomes sensitive to storage arrangement, pumping regimes and network configuration (Kara et al., 2016; Walski et al., 2003).

In coastal urban areas, where residential and tourist functions are spatially and operationally interrelated, water supply planning must consider not only average consumption conditions, but also peak demand and emergency scenarios. For this reason, comparative hydraulic analysis of alternative system layouts represents an important basis for technical and operational optimisation (Margeta, 2010; Mala-Jetmarova et al., 2018).

The case study is Novo Naselje, in the southern part of the City of Poreč, a residential and tourist zone combining permanent residents with seasonal hotel and private accommodation capacity. This makes it

suitable for examining the influence of seasonal variability on water consumption and hydraulic system performance (Kara et al., 2016).

The research is motivated by the need to identify the most favourable supply concept for an area with increased summer loads, variable operating conditions, service reliability requirements and fire protection needs.

The objective of this paper is to conduct a comparative hydraulic analysis and optimisation of the water supply system in Novo Naselje by assessing alternative arrangements of the water tower and pumping station. The analysis focuses on determining how different supply concepts affect operating pressures, flow velocities, discharge distribution, hydraulic stability and the operational reliability of the network (Muranho et al., 2014; Todini et al., 1988).

The study includes five system variants. Three variants are based on gravity inflow into the water tower, with different water-tower positions and elevations, while two variants are based on pumping inflow with different pumping-station arrangements. The hydraulic response of the system is additionally examined for different pipe materials and scenarios with different numbers of simultaneous fires.

2 Materials and methods

Novo Naselje is a mixed residential and tourist zone within the wider urban area of Poreč City. Its key planning characteristic is the coexistence of permanent residents and seasonal users. Hotels and private accommodation facilities significantly intensify summer water consumption and create peak-load conditions that must be included in the design procedure (Fig. 1). The system is therefore a representative coastal water supply zone for comparing alternative storage and pumping concepts under regular and peak operating conditions. Throughout the manuscript, the term water tower refers to the complete elevated storage structure, whereas water chamber refers specifically to the storage compartment within that structure.

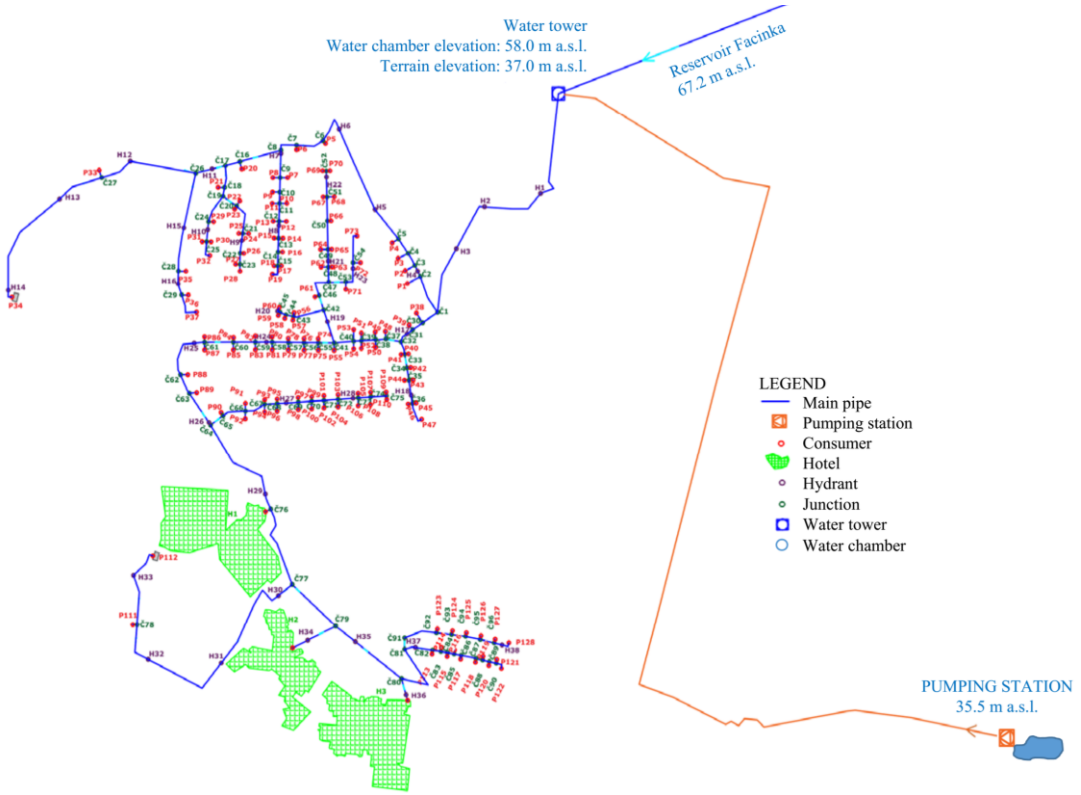


Figure 1. Location of the analysed area and schematic layout of the water supply network.

The planning assumption was that the system must be sized for average demand and pronounced summer peak loads caused by tourism. The methodology therefore focused on maximum daily and hourly demand and on reliable operation under fire scenarios. The first analytical step determined the water quantities required for hydraulic modelling and sizing: average daily, maximum daily and maximum hourly consumption, together with fire-fighting demand, operating reserve and safety reserve.

Table 1. General design assumptions and hydraulic criteria.

Parameter	Unit	Value	Note
Design period	years	30	project horizon
Daily non-uniformity coefficient	–	1.7 / 1.6 / 1.4 / 1.8	permanent residents / hotel*** / hotel**** / private accommodation
Hourly non-uniformity coefficient	–	2.4 / 2.2 / 2.5 / 2.2	same category order as above
Basic fire-fighting flow	L/s	10	one simultaneous fire in the governing design scenario
Fire duration	h	2	governing fire scenario
Pump operating period	h/day	10	pumping variants
Operating-pressure acceptance range	bar	2.5–6.0	hydraulic criterion
Maximum velocity in main pipelines	m/s	2.0	hydraulic criterion

Five alternative system variants were developed and analysed. The first three variants, denoted as WT1, WT2 and WT3, are based on gravity inflow into the water tower (Table 2). These variants differ in the spatial position and elevation of the water tower, and were introduced to assess the influence of storage arrangement on pressure distribution, flow conditions and overall hydraulic stability within the network (Chang et al., 2018; Mala-Jetmarova et al., 2018).

Table 2. Overview of the analysed variants.

Variant	Supply concept	Main characteristic	Expected hydraulic implication
WT1	Gravity inflow	Water-tower position 1	Pressures and velocities satisfy the requirements, although the minimum pressures are closest to the lower limit of 2.5 bar. In the case of one fire, the flow increases by 10 L/s and the pressure decreases by approximately 0.13 bar, but remains acceptable.
WT2	Gravity inflow	Water-tower position 2	The water-tower position provides stable pressures within the allowable range, with small differences depending on pipe material. During two simultaneous fires, the flow increases by 20 L/s, pressures remain above 2.5 bar, and the water chamber empties rapidly during the fire.
WT3	Gravity inflow	Water-tower position 3	The higher elevation of the water tower provides higher operating pressures and a better pressure reserve in the network. Even with three simultaneous fires, hydrant pressures remain above the permissible lower limit, with increased flows and velocities.
PS1	Pumping inflow	Pumping-station position /configuration 1	The pumping station conveys water to the water tower through a pressure pipeline, so the highest flows and velocities occur on the sections leading to the water chamber. Ten-hour pump operation causes cyclic filling and emptying of the water tower during the day.
PS2	Pumping inflow	Pumping-station posit. /configuration 2	Series operation of two pumps increases the available head and enables inflow through a longer pressure pipeline. The hydraulic response is stable, but the system is more dependent on the proper pump operating regime and standby pumps.

The remaining two variants, denoted as PS1 and PS2, are based on pumping inflow into the water tower (Table 2). These variants differ in the position and configuration of the pumping station, and were developed to assess the influence of the pumping concept on storage operation, continuity of supply and hydraulic response under peak water-demand conditions.

All variants were also analysed for different pipe materials and simultaneous-fire scenarios to assess hydraulic robustness and operational reliability.

WaterCAD V8i served as the primary modelling environment. The model represented network geometry, nodal demands, the water tower, pumps and operating scenarios, and provided pressures, velocities and discharges for each variant (Bentley Systems, 2026; Walski et al., 2003).

Selected governing simulations were additionally reproduced in Urbano Hydra to cross-check whether the same input data and boundary conditions produced consistent flows and velocities in a second modelling environment. This exercise was not intended as model validation, because no field measurements were available. Its purpose was to identify possible implementation or data-transfer inconsistencies and to support an internal consistency check of the primary WaterCAD V8i model. The overall modelling strategy was designed to size individual system elements, compare alternative supply concepts under realistic operating conditions and identify the most favourable solution in terms of hydraulic adequacy, reliability and practical operation (Muranho et al., 2014; Arjun et al., 2015; Junaid et al., 2022; StudioARS, 2023).

A simplified conceptual representation of the five variants is provided in Figure 2 to make the differences in water-tower location, elevation, pressure-pipeline length and pump arrangement easier to compare.

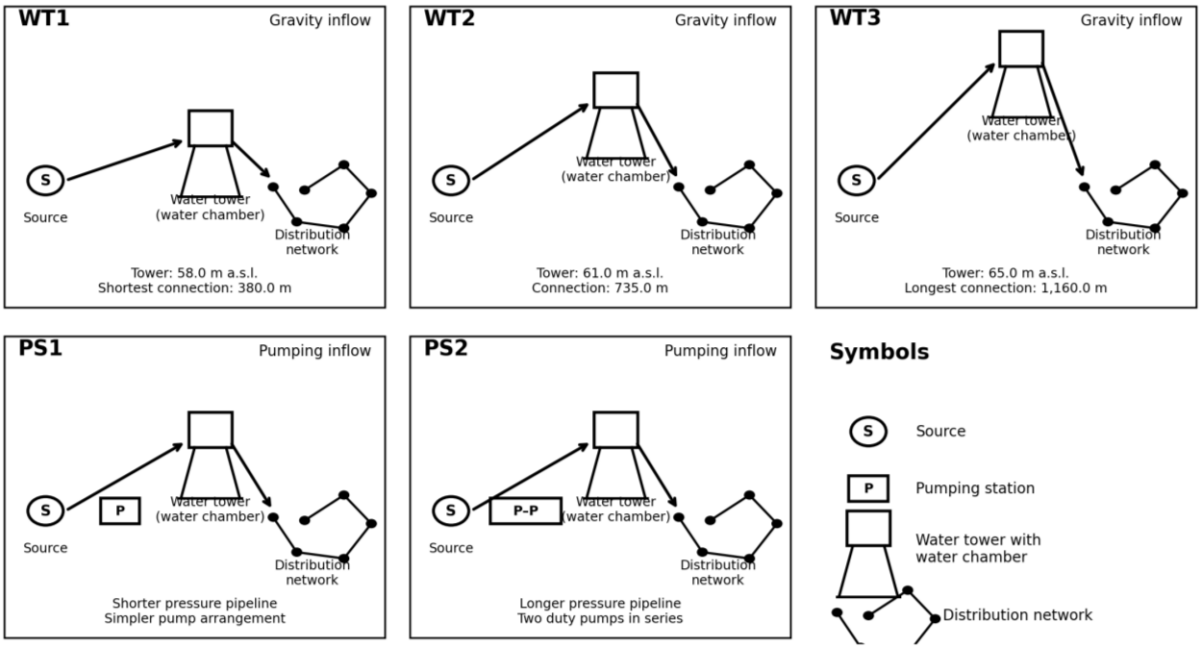


Figure 2. Conceptual representation of the analysed gravity and pumping-station variants (not to scale).

3 Calculation of design quantities and system definition

The calculation of design quantities provides the basis for defining the system and comparing the analysed variants. This section presents water demand, water-chamber volume, pumping-station requirements and the scenarios used in the hydraulic analysis.

The observed system is located in the southern part of the City of Poreč. Because of its tourist function, the governing loads are determined not only by the permanent population, but also by hotel and private accommodation demand during the summer period.

Water demand was calculated by user categories: permanent population, hotel***, hotel**** and private

accommodation. For each category, the specific water consumption, average daily consumption, maximum daily consumption and maximum hourly consumption were determined. This approach enables a clear separation of the basic water demand of the population from seasonally induced tourist water demand (Margeta, 2010).

The relatively high specific consumption values, including 300 L/person/day for permanent residents, were retained from the original project design requirements. They represent gross peak-season design allowances for a mixed residential and tourist area, including elevated summer use and associated service demand, rather than typical domestic consumption alone.

The total number of users at the end of the design period was calculated as 3,835, of which 538 are permanent residents and 3,297 are tourists. The largest share of the tourist load is represented by hotels****, with a total of 1,630 users, followed by hotel*** with 875 users and private accommodation with 792 users (Table 3).

Table 3. Calculated water demands for individual user categories.

User category	Number of users [persons]	Specific consumption [L/person/day]	Average daily consumption [m^3/day]	Maximum daily consumption [m^3/day]	Maximum hourly consumption [L/s]
Permanent population	538	300	161.40	274.38	7.62
Hotel ***	875	400	350.00	560.00	14.26
Hotels ****	1,630	500	815.00	1,141.00	33.02
Private accommodation	792	300	237.60	427.68	10.89
Total	3,835	-	1,564.00	2,403.10	65.79

The calculation follows conventional water-supply planning methodology: demand is derived from user structure and specific consumption and is then adjusted using non-uniformity coefficients. The resulting aggregate design flows define the storage and pumping requirements and the hydraulic loading conditions (Swamee and Sharma, 2008) (Table 4).

Table 4. Relevant aggregate water quantities for the analysed system.

Parameter	Symbol	Quantity	Unit
Average daily water consumption	$\bar{Q}_{avg,d}$	1,564.00	m^3/day
		18.10	L/s
Maximum daily water consumption	$Q_{max,d}$	2,403.10	m^3/day
		27.82	L/s
Maximum hourly water consumption	$Q_{max,h}$	236,829.17	L/h
		65.79	L/s

Total average daily consumption is 1,564.00 m^3/day, maximum daily consumption is 2,403.10 m^3/day (27.82 L/s) and maximum hourly consumption is 65.79 L/s, the governing hydraulic load.

Tourists account for approximately 86% of peak-period users. Hotels**** contribute 33.02 L/s, about half of the maximum hourly demand.

For the purpose of comprehensive system sizing, additional water quantities were determined for fire-fighting, the water supply system's own operational needs and losses (Republic of Croatia, 2006). For a

settlement of up to 5,000 users, the governing scenario is one simultaneous fire lasting 2 h, with a flow of 10 L/s, which gives a fire-fighting volume of 72.00 m^3. The water supply system's own operational needs are adopted as 156.40 m^3/day, while losses in the system are estimated at 480.62 m^3/day.

The water chamber is sized to equalise demand, provide fire-fighting water and ensure a safety reserve. Its total volume is the sum of operating, fire-fighting and safety reserves. Gravity conveyance assumes continuous 24 h inflow, while pumping inflow occurs during the selected 10 h/day pump operating period (Table 5).

The operating reserve is 567.13 m^3 for gravity inflow and 456.59 m^3 for pumping inflow. Although the pumping value is smaller, this regime requires additional checks of pump reliability and operational safety. The total calculated water-chamber volume is 798.91 m^3 for gravity inflow and 660.74 m^3 for pumping inflow. The larger gravity value is governing, while a standard 1,000 m^3 water chamber is adopted for operational safety and reserve capacity.

Table 5. Comparison of water-chamber volumes for gravity and pumping inflow.

Volume component	Gravity inflow	Pumping inflow
Operating reserve, V_{OR} [m^3]	567.13	456.59
Fire-fighting reserve, V_{FR} [m^3]	72.00	72.00
Safety reserve, V_{SR} [m^3]	159.78	132.15
Total calculated volume, V_{TOT} [m^3]	798.91	660.74
Adopted water-chamber volume [m^3]	1,000.00	1,000.00

Pumping was considered as an alternative means of conveying water from the source to the water tower. Variants PS1 and PS2 were sized from maximum daily consumption assuming 10 h/day pump operation. The design pumping flow is approximately 67 L/s, with a DN 250 mm pressure pipeline in both variants. Their main differences are pumping-station position, pipeline length and required manometric head (Table 6).

The same centrifugal pump type, 200-CVE-400-30/1, was selected for both variants. At 67 L/s, one pump provides a head of approximately 21 m, so two pumps in series are required, with standby pumps provided for operational reliability. The difference between PS1 and PS2 results from pressure-pipeline length and total head. PS1 has a shorter pipeline (1,842 m) and lower required head (~ 40 m), whereas PS2 has a longer pipeline (2,108 m) and slightly higher head (~ 42 m), causing higher energy losses.

Pumping-station configuration affects energy use and operation. A shorter pipeline and lower head reduce pumping energy, while pumps in series overcome the required manometric head. Standby pumps improve reliability but increase investment and maintenance requirements (Sârbu, 2016).

Table 6. Basic indicators for pumping stations PS1 and PS2.

Indicator	PS1	PS2
Pumping-station elevation [m a.s.l.]	35.5	36.0
Source elevation [m a.s.l.]	31.5	31.5
Water-tower elevation [m a.s.l.]	58.0	58.0
Pressure-pipeline length [m]	1,842	2,108
Pressure-pipeline diameter [mm]	250	250
Design pumping flow [L/s]	67	67
Required head [m]	~ 40	~ 42
Selected pump type	200-CVE-400-30/1	200-CVE-400-30/1
Pump efficiency, η [-]	0.75	0.75
Number of duty pumps in series	2	2
Total number of pumps including standby units	4	4

Several scenarios covered peak and reduced demand, fire-fighting loads, pipe materials, and gravity or pumping conveyance to assess system behaviour under relevant operating and boundary conditions (Table 7).

Table 7. Scenario analysis of the water supply system.

Scenario group	Scenario description	Purpose of analysis
Pipe material	cast-iron, PVC and steel pipes	comparison of hydraulic losses and material suitability
Water consumption	minimum hourly, average daily, maximum daily and maximum hourly water consumption	checking system operation under different loads
Fire-fighting load	basic scenario with one simultaneous fire; possibility of checking additional fire loads	checking available flow and pressures under critical conditions
System supply mode	gravity water inflow and pumping inflow	comparison of operating regimes and water-chamber volume
Layout of facilities	different positions of the water tower and pumping station	assessment of the influence of elevation relationships and pipeline length
Peak tourist regime	demand including hotel and private accommodation	determination of the governing seasonal load

The fire-fighting scenario is based on 10 L/s over 2 h, or 72 m^3. The basic calculation considers one simultaneous fire, while additional scenarios test system sensitivity to larger fire loads. Pipe-material scenarios compare the effect of roughness on hydraulic losses and operating pressures. Water-demand scenarios check network behaviour under minimum and maximum loads, including possible excessive pressures and the adequacy of flows at the most unfavourable operating moment.

The comparison of gravity and pumping supply modes is important because it affects water-chamber volume, operating costs and reliability. Gravity inflow gives a governing volume of 798.91 m^3, while

pumping inflow gives 660.74 m^3, but requires operational control, energy availability and standby equipment. These scenarios therefore support assessment of technical compliance, operational safety and energy efficiency.

4 Results of the hydraulic analysis

The hydraulic analysis checked operating pressures, flow velocities, water-chamber level behaviour and fire-fighting loads for several variants. Extended 24 h simulations focused on maximum hourly demand from 07:00 to 09:00, when residential, tourist and fire-fighting demands may occur simultaneously.

Operating pressures of 2.5–6.0 bar and main-pipeline velocities below 2.0 m/s were adopted as acceptance criteria. All variants satisfy these requirements, but differ in water-tower position, pipeline length, pressure level, velocity and operational efficiency.

The gravity variants WT1, WT2 and WT3 differ by water-level elevation, position relative to consumers and connecting-pipeline length. In all cases, the water-chamber volume is approximately 1,017.9 m^3, corresponding to the adopted 1,000 m^3 volume.

In variant WT1, the water level in the water tower is at an elevation of 58 m a.s.l., while the bottom of the water chamber is at 53 m a.s.l. In the maximum hourly water-demand scenario, the highest flow velocity is 1.24 m/s, occurring on the section from the source to the water chamber of the water tower. Operating pressures for cast-iron pipes range from 2.62 to 4.79 bar, while for PVC pipes they range from 2.69 to 4.74 bar. Minimum pressures are close to the lower permissible limit, but do not fall below 2.5 bar, so the variant satisfies the hydraulic requirements.

In variant WT2, the water level in the water tower is at an elevation of 61 m a.s.l., while the bottom of the water chamber is at 56 m a.s.l. The maximum flow during the period of maximum hourly water demand is 59.22 L/s, while the maximum velocity is 1.23 m/s. Pressures for cast-iron pipes range from 2.66 to 4.82 bar, and for steel pipes from 2.71 to 4.85 bar. Compared with WT1, the WT2 position provides a slightly more favourable distribution of minimum pressures, but with a longer connecting pipeline.

In variant WT3, the water level in the water tower is at an elevation of 65 m a.s.l., while the bottom of the water chamber is at 60 m a.s.l. The maximum system flow is 74.69 L/s, while the maximum flow velocity is 1.52 m/s. Pressures range from 3.10 to 5.22 bar for PVC pipes and from 3.04 to 5.19 bar for steel pipes (Table 8). This variant provides the highest minimum operating pressures, but due to the higher water-tower elevation and longer connecting pipeline, it has less favourable constructional and economic characteristics.

Table 8. Comparison of results for gravity variants.

Variant	Water level in the water tower [m a.s.l.]	Pipeline length to the first node [m]	Pressure range [bar]	Maximum velocity [m/s]	Fire scenario	Assessment
WT1	58.0	380.0	2.62-4.79 / 2.69-4.74	1.24	1 fire, 10 L/s	Hydraulically satisfactory; shortest connecting pipeline
WT2	61.0	735.0	2.66-4.82 / 2.71-4.85	1.23	2 fires, 20 L/s	Stable pressures; greater pipeline length
WT3	65.0	1,160.0	3.10-5.22 / 3.04-5.19	1.52	3 fires, 30 L/s	Highest pressures; longest connecting pipeline

Water-tower position mainly affects operating pressures and connecting-pipeline length. A higher elevation increases network pressures, as in WT3, but also increases pipeline length, investment cost and potential linear losses.

All three gravity scenarios satisfy the condition that pressure does not fall below 2.5 bar. The most favourable relationship between hydraulic functionality and pipeline length is achieved by variant WT1, because it has the shortest connecting pipeline of 380.0 m, satisfactory pressures and flow velocities, and acceptable behaviour of the water chamber during peak load (Fig. 3).

Water-level oscillations are most pronounced during maximum demand and fire-fighting loads. The water-level drop is approximately 0.10 m in WT1, 0.11 m in WT2 and 0.20 m in WT3. These changes do not endanger operation, but show the chamber's sensitivity to fire-fighting demand.

The pumping variants were analysed for two pumping-station layouts, denoted as PS1 and PS2. In both variants, water is pumped from the source to the water chamber of the water tower, with the design pumping flow determined as 67 L/s. Pump operation is organised over 10 h/day, in the periods 05:00-10:00, 13:00-16:00 and 19:00-21:00 (Table 9).

Table 9. Comparison of pumping station variants PS1 and PS2.

Indicator	PS1	PS2
Pumping-station elevation [m a.s.l.]	36.5	36.0
Source elevation [m a.s.l.]	31.5	31.5
Pressure-pipeline length [m]	1,794.7	2,116.35
Pressure-pipeline diameter [mm]	250	250
Design pumping flow [L/s]	67.0	67.0
Pump configuration	1 duty + 1 standby	2 duty pumps in series + 2 standby
Head [m]	42.00	48.58
Maximum velocity [m/s]	2.23	1.48
Operating regime	10 h/day	10 h/day
Assessment	Shorter pipeline and simpler operation	Lower velocities, but longer pipeline and more complex operation

In variant PS1, the pumping station is located at an elevation of 36.5 m a.s.l., while the source is at 31.5 m a.s.l. Water is conveyed through a pressure pipeline 1,794.7 m long and 250 mm in diameter. The model uses one duty pump and one standby pump, where the duty pump lifts a flow of 67 L/s to a head of 42 m. The highest velocities and flows occur on the sections leading to the water chamber of the water tower. The maximum velocity in the pressure pipeline is approximately 2.23 m/s.

In variant PS2, the pumping station is located at an elevation of 36.0 m a.s.l. and is 8 m from the source. Water is conveyed through a pressure pipeline 2,116.35 m long and 250 mm in diameter. The model includes two duty pumps connected in series and two standby pumps. Each duty pump lifts a flow of 23.48 L/s to a head of 24.29 m, giving a total head of approximately 48.58 m. The maximum velocity in the system is 1.48 m/s, on the section leading to the water chamber of the water tower.

Both variants that include a pumping station ensure stable operation and required inflow to the water chamber. Water-level oscillations follow pump operation, decreasing during off-periods and increasing

after the pumps are switched on at 05:00, 13:00 and 19:00.

PS1 is operationally advantageous because of its shorter pressure pipeline and simpler pump arrangement, despite a higher maximum velocity of 2.23 m/s. PS2 limits velocity to 1.48 m/s but requires a longer pipeline and two series pumps. PS1 uses one duty pump, whereas PS2 requires coordinated operation of two series pumps. The choice is therefore between simpler construction and operation in PS1 and lower velocities in PS2.

Cast-iron (CI), PVC and steel pipes were considered (Table 10). Pipe material affects roughness, linear losses and pressure distribution, but the pressure differences between materials are relatively small, averaging about 0.05 bar. Therefore, material selection should not be based solely on hydraulic indicators.

In WT1, PVC pipes provide slightly higher minimum pressures than cast-iron pipes (2.69 bar compared with 2.62 bar), indicating the minor hydraulic benefit of lower roughness. In WT2 and WT3, pressure differences between materials are also small and do not change the acceptability of the variants. WT3 maintains pressures well above the minimum permissible value, and velocities remain below the allowable limit (Table 10).

The influence of fire scenarios was analysed for one, two and three simultaneous fires. Each fire increases demand by 10 L/s for a duration of 2 h during the maximum hourly demand period. One fire was analysed in WT1, two simultaneous fires in WT2 and three simultaneous fires in WT3.

In all fire scenarios, operating pressures remain above 2.5 bar, confirming that the system satisfies fire-fighting supply requirements. In WT1, the pressure decreases by approximately 0.13 bar during one fire, but remains above the permissible limit. In WT3, under the scenario with three fires, the minimum pressures at hydrants are 3.53 bar, 3.41 bar and 4.58 bar, indicating a considerable safety reserve.

Pipe material mainly affects small changes in pressure and energy losses, while simultaneous fires directly increase flow, reduce pressure and accelerate water-chamber emptying. All combinations remain within permissible hydraulic limits.

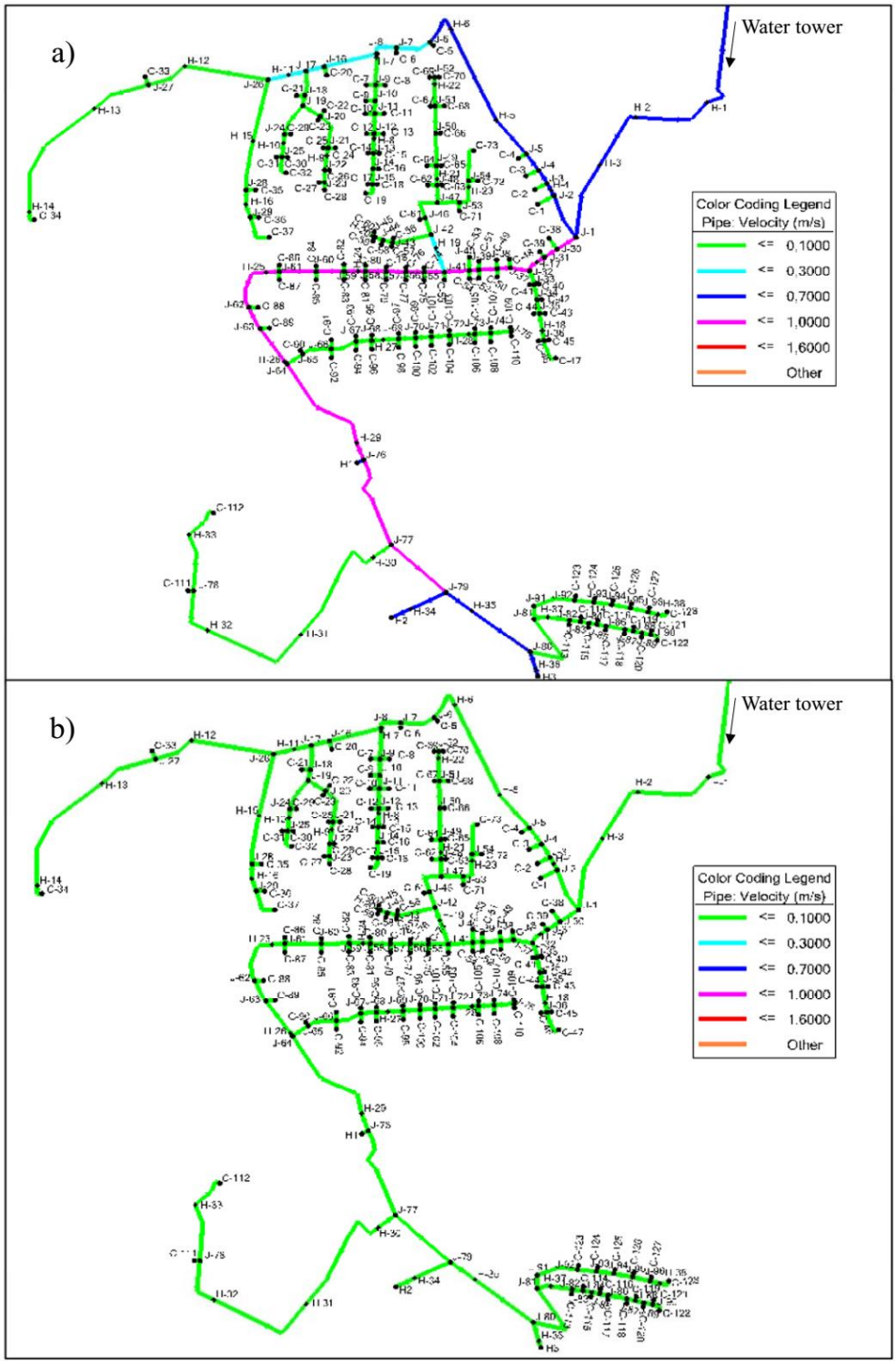


Figure 3. Water velocities in the water supply network for variant WT1
a) during maximum hourly demand, b) during minimum hourly demand.

Table 10. Comparative overview of scenarios according to operating pressures, velocities and assessment.

Scenario	Pipe material	Fire load	Minimum pressure [bar]	Maximum pressure [bar]	Maximum velocity [m/s]	Assessment
WT1	cast iron (CI)	1 × 10 L/s	2.62	4.79	1.24	Satisfactory, but minimum pressure close to the limit
WT1	PVC	1 × 10 L/s	2.69	4.74	1.24	Hydraulically more favourable than CI pipes
WT2	cast iron (CI)	2 × 10 L/s	2.66	4.82	1.23	Stable, satisfies the fire scenario
WT2	steel	2 × 10 L/s	2.71	4.85	1.23	Very similar results, slightly higher pressures
WT3	PVC	3 × 10 L/s	3.10	5.22	1.52	Highest pressure reserve
WT3	steel	3 × 10 L/s	3.04	5.19	1.52	Stable, but with a longer connecting pipeline

WaterCAD V8i was used as the primary environment for the extended 24 h hydraulic simulations, while Urbano Hydra was used for a limited cross-model consistency check. The comparison covered the maximum hourly demand period from 08:00 to 09:00 and the governing main section from the water tower to the first downstream node. As shown in Table 11, both programs produced a flow of 65.81 L/s and a velocity of 0.68 m/s for this section. This agreement indicates consistency for the selected outputs under identical inputs and it should not be interpreted as validation against field measurements.

Table 11. Cross-model consistency check for the governing main section during maximum hourly demand.

Indicator	WaterCAD V8i	Urbano Hydra	Relative difference
Flow [L/s]	65.81	65.81	0.00%
Velocity [m/s]	0.68	0.68	0.00%

The optimal variant was determined using five criteria: supply reliability, hydraulic stability, fire safety, operational flexibility and energy/constructional acceptability. Because all variants satisfy the basic hydraulic requirements, pipeline length, operational simplicity, water-chamber operating behaviour and additional equipment were also considered (Table 12).

A detailed bill-of-quantities cost estimate was not available for this study. Therefore, the economic comparison is qualitative. WT1 is expected to have the lowest capital cost among the gravity variants because its connecting pipeline is only 380.0 m long, whereas WT3 is expected to be the most expensive gravity option because of its 1,160.0 m pipeline and higher-elevation construction. Among the pumping alternatives, PS1 is expected to be less expensive than PS2 owing to its shorter pressure pipeline and simpler pump arrangement. Both pumping alternatives would also incur energy, maintenance and standby-equipment costs that are not associated with the selected gravity solution.

Table 12. Assessment of variants according to selection criteria.

Variant	Reliability of supply	Hydraulic stability	Fire safety	Operational flexibility	Energy / construct. acceptability	Overall assessment
WT1	good	good	satisfactory	good	most favourable due to the shortest pipeline	most favourable gravity variant
WT2	good	good	satisfactory for 2 fires	good	moderately favourable	acceptable
WT3	very good	very good	satisfactory for 3 fires	good	less favourable due to the longest pipeline	Hydraul. safe, less favourable in terms of construction
PS1	good	good	depends on pump operation	good	favourable due to the shorter pipeline and simple pump arrangement	more favourable pumping variant
PS2	good	good	depends on pump operation	medium	less favourable due to the longer pipeline and two pumps connected in series	acceptable, but more complex

WT1 is the most favourable gravity variant, with the water level at 58 m a.s.l., pressures of 2.62–4.79 bar for cast iron and 2.69–4.74 bar for PVC, a maximum velocity of 1.24 m/s and adequate supply for one 10 L/s fire. WT1 also has the shortest connecting pipeline: 380.0 m, compared with 735.0 m in WT2 and 1,160.0 m in WT3, reducing construction scope, cost and linear losses. Although WT3 provides the greatest pressure reserve, WT1 meets all hydraulic criteria. PS1 and PS2 are stable but depend on energy supply, pump operation and standby equipment. WT1 is therefore optimal because it combines acceptable pressures and velocities, fire safety, the shortest connecting pipeline and gravity operation.

5 Discussion

Hydraulic efficiency in a tourist-loaded system cannot be judged only by minimum pressure and permissible velocity. Variant selection must also consider pressure distribution, water-tower position, pipeline length, operational complexity and stability under seasonal and fire loads.

Differences between gravity variants primarily result from water-tower position and elevation, which determine the available piezometric head and affect operating pressures and hydraulic balance in the network. WT1 offers the most favourable relationship between hydraulic functionality and constructional simplicity. Although it does not provide the largest pressure reserve, it achieves permissible pressures with the shortest connecting pipeline and the smallest spatial intervention. WT2 and WT3 confirm that higher water-tower elevation can improve pressures and fire-fighting robustness, but also increases pipeline length. A hydraulically stronger solution is therefore not automatically optimal when feasibility and long-term maintenance are considered.

For pumping variants, operational arrangement is as important as hydraulic capacity. PS1 has a shorter pipeline and simpler configuration, whereas PS2 achieves the required head with series pumps and depends more strongly on equipment and standby reliability. Pumping-station configuration directly affects energy use. Greater head, a longer pressure pipeline and more complex operation increase system sensitivity and potential life-cycle costs, requiring careful management, maintenance and standby-operation planning.

Seasonal variability is decisive because Novo Naselje experiences several-fold demand increases during the tourist season. The selected solution must withstand peak hours, maximum summer days and fire scenarios without unnecessary oversizing.

The professional contribution is the comparative evaluation of water supply variants according to reliability, pressure stability, velocities, fire safety, pipeline length and operational complexity, enabling a more realistic selection of the optimal solution in tourist areas.

Water-tower position and elevation govern pressure distribution, while pumping configuration affects energy use, safety and management complexity. The preferred solution balances hydraulic reliability, constructional simplicity and rational operation.

Additional value arises from the limited cross-model consistency check between WaterCAD V8i and Urbano Hydra. The agreement of the selected flow and velocity outputs supports internal verification of the model implementation and data transfer, but it cannot replace validation against field measurements.

6 Conclusion

This paper presented a comparative hydraulic analysis of the Novo Naselje water supply system in Poreč, a residential and tourist area with pronounced seasonal demand. Based on a 30-year user projection, governing water quantities were determined for average, peak and fire-fighting conditions. Five conceptual variants were compared: three gravity variants with different water-tower positions (WT1-WT3) and two pumping-inflow variants with different pumping-station configurations (PS1 and PS2). This enabled assessment of the influence of storage position, connecting-pipeline length and conveyance method on network stability.

Operating pressures, velocities, flows, water-level oscillations, water reserves and fire-scenario behaviour were used as key indicators. Pipe material influenced pressures only slightly and did not change the acceptability of the variants. The limited comparison of selected results obtained in WaterCAD V8i and Urbano Hydra showed agreement for the governing flow and velocity values. This finding indicates computational consistency under identical input conditions, but does not constitute model validation in the absence of field measurements.

Variant WT1 was identified as the optimal variant, namely the gravity solution with the water level in the water tower at 58 m a.s.l. This variant achieves acceptable pressures and velocities, satisfies fire-fighting requirements, has the shortest connecting pipeline to the network and does not require continuous pump operation, thereby providing the most favourable relationship between hydraulic reliability, constructional simplicity and operational safety.

The results are applicable to coastal and tourist-loaded water supply systems where seasonal demand is the decisive design condition. Further research should include detailed energy and economic analysis, measured consumption time series, drought resilience and water-quality verification.

Acknowledgements

This research is the result of work carried out within the UNIRI Institutional Research Project "*Challenges of water resource management in times of climate change with regard to drinking-water production*" (uniri-iz-25-18), approved by the Ministry of Science, Education and Youth (funded by the European Union - NextGenerationEU).

References

Arjun, K., Kankesh, K., Bharanidharan, B., Neha, M., Eshita, D., Mahan, S. and Neeraj, M. 2015. Design of Water Distribution System using EPANET. *International Journal of Advanced Research*, 3(9).
Bentley Systems. 2026. *WaterCAD V8i / OpenFlows WaterCAD User Documentation*. Bentley Systems
Chang, Y., Choi, G., and Kim, J. 2018. Energy cost optimization for water distribution networks using demand pattern and storage facilities. *Sustainability*, 10(4), 1118.
Junaid, C. T. and Izinyon, O. C. 2022. Hydraulic and water quality modelling of water distribution networks using EPANET software. *Niger. J. of Environ. Sci. Technol.*, 6(1), 172-179.
Kara, S., Karadirek, I. E., Muhammetoglu, A. and Muhammetoglu, H. 2016. Hydraulic modeling of a water distribution network in a tourism area with highly varying characteristics. *Procedia Engineering*, 162, 521-529.
Mala-Jetmarova, H., Sultanova, N. and Savic, D. 2018. Lost in optimisation of water distribution systems? A literature review of system design. *Water*, 10(3), 307.
Margeta, J. 2010. *Water Supply of Settlements: Planning, Design, Management*, *Water Treatment*. University of Split, Faculty of Civil Engineering and Architecture, Split.
Muranho, J., Ferreira, A., Sousa, J., Gomes, A. and Sá Marques, A. 2014. Technical performance evaluation of water distribution networks based on EPANET. *Procedia Engineering*, 70, 1201-1210.
Republic of Croatia. 2006. *Pravilnik o hidrantskoj mreži za gašenje požara*. Narodne novine, br. 8/2006.
Republic of Croatia. 2023. *Zakon o vodama*. Narodne novine, No. 66/2019, 84/2021, 47/2023.
Sârbu, I. 2016. A study of energy optimisation of urban water distribution systems using potential elements. *Water*, 8(12), 593.
Swamee, P.K. and Sharma, A.K. 2008. *Design of Water Supply Pipe Networks*. New Jersey: John Wiley and Sons.
StudioARS. 2023. *Urbano Hydra – Water Distribution and Hydraulic Calculation Documentation*. StudioARS Ltd.
Todini, E. and Pilati, S. 1988. A gradient algorithm for the analysis of pipe networks. In B. Coulbeck and C. H. Orr (Eds.), *Computer Applications in Water Supply, Vol. 1: Systems Analysis and Simulation*, Research Studies Press, Letchworth, Hertfordshire, England, pp. 1-20.
Walski, T., D.V, C., Savic, D., Grayman, W., Beckwith, S. and Koelle, E. 2003. *Advanced Water Distribution Modelling and Management*. Waterbury, CT, USA: Haestad Press.

HYDRAULIC ANALYSIS AND OPTIMISATION OF AN ANNULAR WATER SUPPLY SYSTEM IN AN URBAN AREA

Elvis ŽIC [1*], Goran VOLF [1], Bojana HORVAT [1]

[1] *Faculty of Civil Engineering Rijeka, Croatia*

E-mail: elvis.zic@uniri.hr

E-mail: goran.volf@uniri.hr

E-mail: bojana.horvat@uniri.hr

[*] *Corresponding author*

Abstract

The planning and optimisation of urban water supply systems require reliable hydraulic performance, energy-efficient operation and adequate safety under peak and emergency conditions. This paper presents a variant hydraulic analysis of a section of the looped water supply system in the City of Vinkovci, aimed at evaluating the arrangement of a water tower, low-level reservoir and pumping stations within the regional water supply system of Eastern Slavonia. The analysis included residential, tourist and industrial water demands, average daily, maximum daily and maximum hourly consumption, fire-fighting requirements, system needs and water losses. Three variants were analysed: two with pumping to a 30 m high water tower followed by gravity distribution, and one with gravity inflow to a low-level reservoir followed by pumping into the network. Hydraulic simulations were performed in WaterCAD V8i. Selected corresponding pipes and nodes were additionally checked in Urbano Hydra as a limited cross-software consistency check rather than as independent validation. Pressures, velocities and flows were evaluated for different pipe materials and emergency fire scenarios. The results show that all variants are hydraulically acceptable, while the third variant provides the highest operational flexibility and pressure control.

Key words

hydraulic modelling, looped water supply system, reservoir layout, pumping station, water resources management.

1 Introduction

Urban water supply systems must provide reliable service, acceptable pressures and velocities, and sufficient quantities under regular and emergency conditions, including fire-load scenarios (Safitri et al., 2023). Reservoir layout, pumping regime and pressure regulation strongly affect energy efficiency and operational stability (Serafeim et al., 2023; Kim and Jang, 2024; Elhay et al., 2025).

Looped water supply systems are important in urban areas because they enable distribution from several directions and increase resilience during peak demand, fire events or temporary pipe failures (Orime et al., 2024; Ismail et al., 2025). Therefore, alternative conceptual solutions should be compared before selecting the final system layout (Gomes Jr. et al., 2024; Sidiropoulos et al., 2025).

The subject of this paper is the hydraulic analysis and optimisation of a section of the looped water supply system of the City of Vinkovci, Figure 1. The analysis focuses on assessing the functionality of the system in terms of pressure distribution, velocities and flows, as well as the ability of the system to meet consumer demand under regular and fire-flow conditions.

Three development concepts were analysed within the regional water supply system of Eastern Slavonia: two involving pumping to a water tower followed by gravity distribution, and one using a low-level reservoir and pumping station for pressure regulation.

The study aims to identify the most favourable arrangement of the water tower, low-level reservoir and pumping stations by balancing hydraulic reliability, energy efficiency and controllability. Optimisation considered operating pressures, velocities and flows, particularly under fire loads and different operating regimes (Tian et al., 2023; Alsaydalani, 2024; Elhay et al., 2025).

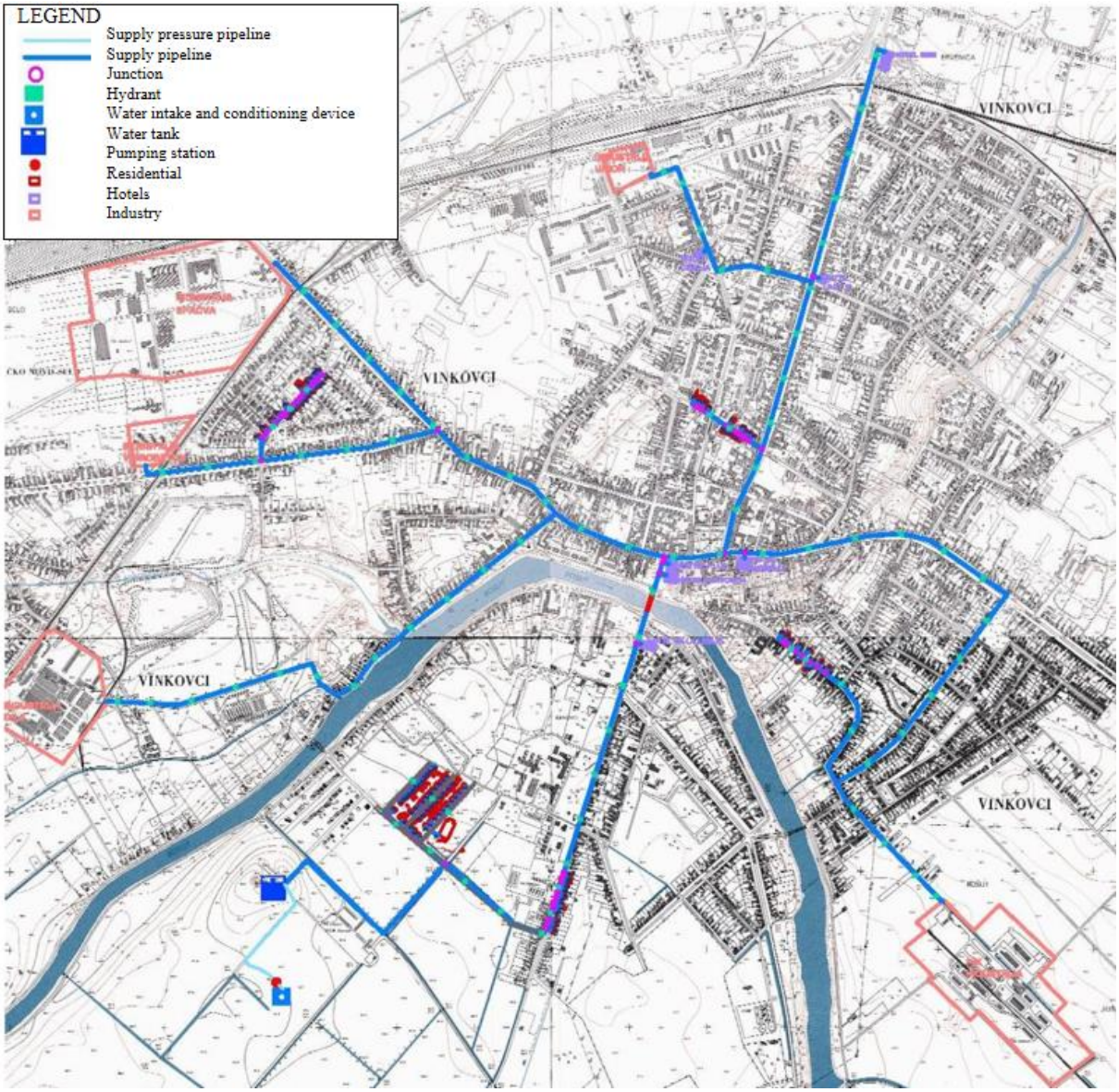


Figure 1. Layout of the analysed water supply network.

2 Materials and methods

The analysed area covers part of the urban water supply system of the City of Vinkovci, developed as a looped network that must ensure reliable supply, adequate pressures and fire-safety conditions for different consumer groups.

The Kanovci water intake and planned water-conditioning facility are the common source in all variants, connecting the local network to the regional system. Consumers were classified as residents, tourists and industrial users for demand calculation and hydraulic modelling.

The analysis included user numbers, specific consumption, daily and hourly non-uniformity coefficients, industrial and fire-fighting demand, internal needs and estimated losses.

The calculation included 6,740 inhabitants, tourist capacities and five industrial consumers: PIK, Spacva, Dilj, Unior and Vibrobeton.

Relevant water quantities were determined from consumer categories, specific consumptions and non-uniformity coefficients ($k_{max,d}$, $k_{max,h}$). Industrial demand, fire-fighting quantities, internal needs and estimated losses were then added (Table 1).

The relatively high specific consumption values were taken from the underlying project design documentation and retained as governing inputs for the 30-year planning horizon. They represent a conservative design criterion that includes peak seasonal, commercial and service-related demand rather than current household-only metered consumption.

Table 1. Characteristic water demands in the analysed system.

Calculation step	Input data / method	Value	Unit
Number of inhabitants	Projected number of users	6,740	users
Tourist users	Hotels and private accommodation	1,526	users
Total number of users for the fire-flow calculation	Population + tourists	8,266	users
Specific consumption of residents	Adopted value	300	L/(user·day)
Specific hotel water consumption	Depending on facility category	300-400	L/(user·day)
Non-uniformity coefficient for residents	$k_{max,d}$; $k_{max,h}$	1.50; 1.80	–
Non-uniformity coefficient for hotels	$k_{max,d}$; $k_{max,h}$	1.60; 2.20	–
Non-uniformity coefficient for private accommodation	$k_{max,d}$; $k_{max,h}$	1.80; 2.20	–
Average daily demand	Sum of all user categories	2,512.45	m^3/day
Maximum daily demand	$Q_{max,d}$	3,865.72	m^3/day
Maximum hourly demand	$Q_{max,h}$, sum of consumer categories	approximately 84.4	L/s
Industrial demand	PIK, Spacva, Dilj, Unior, Vibrobeton	1,558.8	m^3/day
Settlement fire load	1 fire, 2 h, 15 L/s	108.0	m^3/day
Industrial fire load	1 fire, 2 h, 20 L/s	144.0	m^3/day
Total fire load	Settlement + industry	252.0	m^3/day
Internal needs of the water supply system	Adopted higher calculated value	251.2	m^3/day
Water losses	20% of $Q_{max,d}$ + Q_{ind}	1,084.9	m^3/day

Three development variants were analysed. All use the Kanovci water intake, but differ in the layout of the main facilities, the method of conveying water and the possibilities for managing hydraulic conditions. Variant 1 is based on pumping water from the intake to a 30 m high water tower, with a water level elevation of 131 m a.s.l. After filling the water chamber, water is distributed by gravity through the looped network (Figure 1). Variant 2 applies the same principle as Variant 1, but with a different layout of the water tower and pumping station. This allows assessment of the influence of facility position and pressure-pipeline length on pressures, flows and operating conditions. Variant 3 uses gravity inflow from the intake to a low-level reservoir, followed by a pumping station that provides the required network pressures and flows. This concept was analysed to examine more active pressure management under variable demand and night-time operation. In this paper, water tower denotes the

complete elevated facility, whereas water chamber denotes only its storage compartment. A comparative schematic of the three concepts is provided in Figure 2.

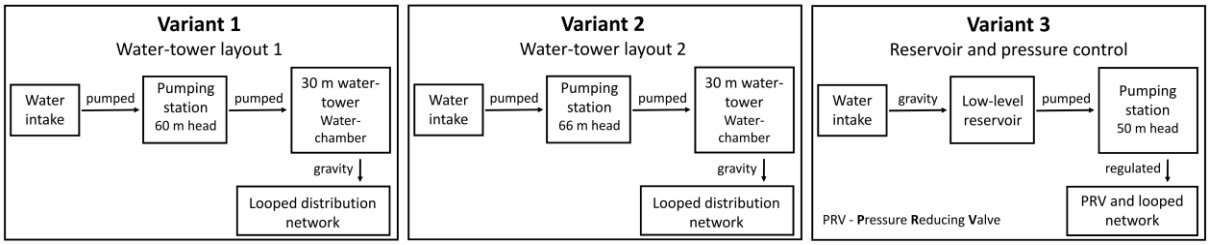


Figure 2. Schematic comparison of the three analysed system variants.

The comparison therefore covers two conventional water tower solutions and one reservoir-pumping solution with greater potential for operational adaptability and pressure regulation. The hydraulic analysis was performed in WaterCAD V8i (Safitri et al., 2023). The model included the looped network, demand nodes, pipelines, water tower or low-level reservoir, pumping stations and fire-load scenarios. For each variant, flows, pipe velocities and nodal pressures were calculated under regular and fire-load conditions. Selected corresponding network elements were subsequently exported in EPANET format and checked in Urbano Hydra (StudioARS, 2023) solely as a cross-software consistency check. This secondary calculation was not treated as field validation or as an independent basis for variant selection.

3 Calculation and system definition

This section defines the main facilities and numerical basis for variant comparison.

3.1 Calculation of relevant water demand

Water demand was calculated from user numbers, specific consumption and non-uniformity coefficients (Table 2), including residential, tourist and industrial demand, fire-fighting requirements, internal needs and losses.

Table 2. Input data for the water demand calculation.

Consumer group	Number of users / unit	Adopted specific consumption	Unit
Population	6,740 users	300	L/(user·day)
Hotel Admiral	150 users	350	L/(user·day)
Hotel Slavonija	210 users	350	L/(user·day)
Villa Lenije	50 users	400	L/(user·day)
Hotel Cibalia	48 users	350	L/(user·day)
Hotel Gem	145 users	350	L/(user·day)
Hostel Plus	67 users	300	L/(user·day)
Hotel Lady M	56 users	300	L/(user·day)
Private accommodation	800 users	300	L/(user·day)
PIK industry	11 h of operation	9	L/s
Spacva industry	10 h of operation	10	L/s
Dilj industry	9 h of operation	9	L/s
Unior industry	9 h of operation	9	L/s
Vibrobeton industry	9 h of operation	8	L/s

The adopted coefficients were $k_{max,d}$ = 1.50 and $k_{max,h}$ = 1.80 for residents, 1.60 and 2.20 for hotels, and 1.80 and 2.20 for private accommodation. Table 3 summarises the resulting quantities used to size the reservoir and water tower.

Table 3. Summary of relevant calculated water quantities.

Calculated quantity	Symbol	Value	Unit
Average daily demand of residents and tourist users	$Q_{avg,d}$	2,512.45	m^3/day
Maximum daily demand of residents and tourist users	$Q_{max,d}$	3,865.72	m^3/day
Maximum hourly demand of residents and tourist users	$Q_{max,h}$	84.39	L/s
Total industrial demand	Q_{ind}	1,558.80	m^3/day
Settlement fire load	$Q_{fire,settl.}$	108.00	m^3/day
Industrial fire load	$Q_{fire,ind.}$	144.00	m^3/day
Total fire load	$Q_{fire,tot.}$	252.00	m^3/day
System internal needs	$Q_{inter.}$	251.20	m^3/day
Water losses in the system	Q_{losses}	1,084.90	m^3/day
Total daily load relevant for main facilities	$Q_{tot,d}$	5,424.52	m^3/day

3.2 Calculation of the water tower and reservoir

The required storage volume was calculated as the sum of operational, fire-fighting and safety reserves. In Variants 1 and 2, this is the volume of the water chamber within the water tower. In Variant 3, it is the storage volume of the low-level reservoir. Two inflow regimes were considered: pumped inflow into a water tower and gravity inflow into a low-level reservoir (Table 4).

Table 4. Comparative calculation of storage volume by variant.

Variant	Facility	Inflow regime	Operational reserve, V_{OR} (m^3)	Fire-fighting reserve without neutralisation, V_{FR} (m^3)	Safety reserve, V_{SR} (m^3)	Calculated volume, V_{TOT} (m^3)	Adopted volume (m^3)
Variant 1	Water tower	Pumped inflow	1,191.2	252.0	360.8	1,804.0	2,000.0
Variant 2	Water tower	Pumped inflow	1,191.2	252.0	360.8	1,804.0	2,000.0
Variant 3	Low-level reservoir	Gravity inflow	1,068.6	252.0	330.2	1,650.8	2,000.0

In the water tower variants, the operational reserve in the water chamber is higher due to scheduled pumping, whereas gravity inflow to the low-level reservoir is more continuous. In all variants, an adopted storage volume of 2,000.0 m^3 ensures the required operational, fire-fighting and safety functions.

3.3 Pumping station calculation

In Variants 1 and 2, pumping stations fill the water tower before gravity distribution. In Variant 3, the downstream station pressurises the distribution network (Table 5).

Table 5. Pumping station calculation by variants.

Variant	Function of pumping station	Required flow (L/s)	Required manometric head (m)	Selected pump type	Operating configuration	Standby configuration
Variant 1	Pumping water to the water tower	107.63	60	150-CVE-350-23	Two parallel branches, each with two pumps connected in series	Standby branch with the same characteristics
Variant 2	Pumping water to the water tower in a different layout	107.63	66	250-CVE-460-38	Three pumps connected in series in the main branch	Standby branch with the same characteristics
Variant 3	Pressurising water from the low-level reservoir to the network	129.39	50	250-CVE-460-32	One operating pump	One standby pump with the same characteristics

Variants 1 and 2 pump from the source to the water tower, with Variant 2 requiring greater head because of its layout and longer pressure pipeline. In Variant 3, the station directly regulates network pressures under variable demand.

3.4 Definition of analysis scenarios

Regular and emergency scenarios were defined to verify hydraulic reliability, with fire loads governing pressure, flow and velocity checks (Table 6).
Variant 1 included one remote hydrant fire of 15 L/s, Variant 2 two simultaneous fires, and Variant 3 two fire loads plus industrial demand.
Pipe-material effects were also examined. Ductile iron, PVC and steel were compared in Variants 1 and 2, while Variant 3 used PVC. The scenarios supported comparison of roughness, losses, pressures, velocities, technical acceptability and operational flexibility.

Table 6. Hydraulic analysis scenarios.

Variant	Regular regime	Emergency scenario	Purpose of verification
Variant 1	Regular demand and gravity distribution from the water tower	One fire at a hydrant	Verification of fire impact on pressures, flows and velocities in a remote part of the network
Variant 2	Regular demand and gravity distribut. from the water tower	Two simultaneous fires	Verification of network resilience to a higher fire-fighting load
Variant 3	Pressure distribution from the low-level reservoir via the pumping station	Two fires and additional industrial loading	Verification of pressure-management capability and system stability under unfavourable conditions

4 Results of the hydraulic analysis

The hydraulic analysis covered the three conceptual variants of the Vinkovci looped water supply system. Results are presented for relevant operating conditions, with emphasis on maximum hourly demand, fire loads, pressure distribution, pipe velocities and operation of the main facilities.

4.1 Results for Variant 1

Variant 1 pumps water from the intake to a 30 m high water tower and then distributes it by gravity through the looped network. The water tower stabilises network pressures, while the pumping station primarily fills the water chamber (Figure 3).

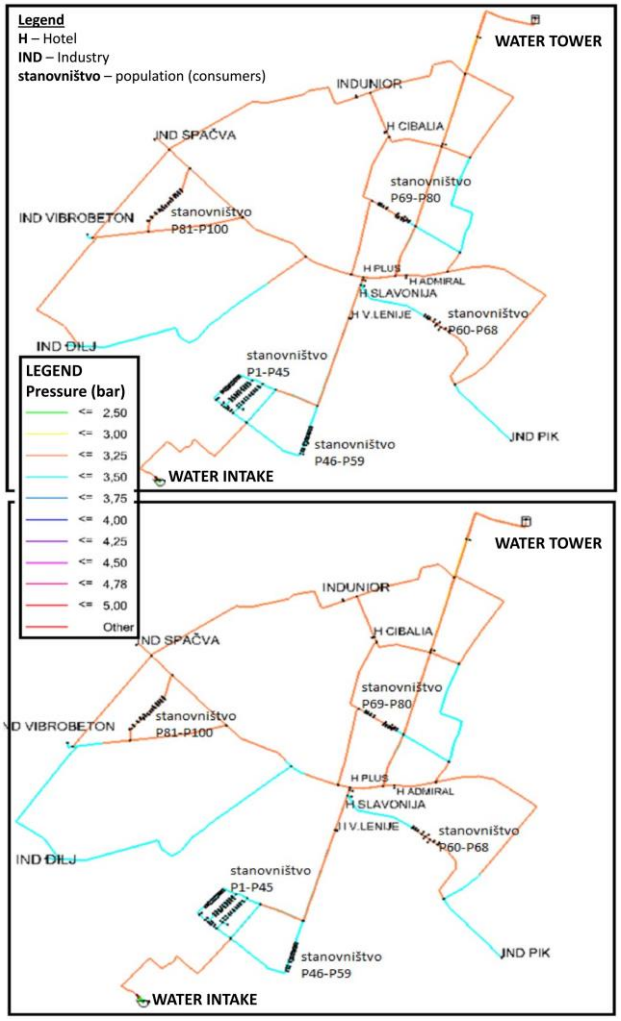


Figure 3. Change in operating pressures at 11:00, Variant 1; top - maximum water level, bottom - minimum water level in the water chamber of the water tower.

All section velocities are below 2.0 m/s. The highest values occur between the pumping station and water tower because of concentrated chamber inflow, whereas short peripheral sections have very low velocities (Figure 4). For ductile iron and PVC pipes (Figure 5), pressures mostly remain within 2.5-6.0 bar.

A local pressure of about 6.10 bar occurs at node J-240, immediately downstream of the pumping station. Both materials are technically acceptable, while PVC gives slightly lower losses and more favourable hydraulic behaviour.

During maximum hourly demand, a 15 L/s fire flow was applied at hydrant H-70. Flow in section P-92 rises from about 9 to 24 L/s, while pressure at H-70 falls by only about 0.18 bar and remains safe.
Pump operation depends on the initial water level in the water chamber. Depending on whether the initial level is maximum or minimum, the total daily pump operating time ranges from approximately 12 to 16 h, confirming that the selected configuration can cover variable demand.

Label	Start Node	Stop Node	Diameter (mm)	Material	Hazen-Williams C	Flow (L/s)	Velocity (m/s)
P-300	J-240	VODOTORANJ	350,0	Ductile Iron	130,0	132,05	1,3725
P-301	J-97	VODOTORANJ	450,0	Ductile Iron	130,0	- 129,39	0,8136
P-89(2)(2)(2)...	H-51	J-79b	200,0	Ductile Iron	130,0	25,35	0,8069
P-89(2)(2)(1)...	J-79a	H-51	200,0	Ductile Iron	130,0	25,35	0,8069
P-86(2)(2)(2)...	H-55	H-56	450,0	Ductile Iron	130,0	- 126,89	0,7978
P-275	J-78a	H-55	450,0	Ductile Iron	130,0	- 126,89	0,7978
P-274(1)	H-56	J-97	450,0	Ductile Iron	130,0	- 126,89	0,7978
P-248	VODOZAHVAT	PMP-1	350,0	Ductile Iron	130,0	66,03	0,6863
P-249(1)	PMP-1	PMP-2	350,0	Ductile Iron	130,0	66,03	0,6863
P-249(2)	PMP-2	J-240	350,0	Ductile Iron	130,0	66,03	0,6863

Figure 4. Ten sections with the maximum water-flow velocities - Variant 1.

Label	Elevation (m)	Demand (L/s)	Hydraulic Grade (m)	Pressure (bars)
HOTEL GEM	93,60	1,90	121,23	2,70
J-97	93,50	0,40	121,23	2,71
J-77	89,80	1,71	120,55	3,01
HOTEL LADY M	89,80	0,63	120,56	3,01
J-78	89,80	0,78	120,56	3,01
J-77a	89,62	1,36	120,42	3,01
HOTEL CIBALIA	89,60	0,63	120,42	3,02
J-79	89,60	0,49	120,42	3,02
J-79b	89,31	2,18	120,15	3,02
INDUSTRIJA UNIOR	89,30	9,00	120,14	3,02

Label	Elevation (m)	Demand (L/s)	Hydraulic Grade (m)	Pressure (bars)
HOTEL GEM	93,60	1,90	121,51	2,73
J-97	93,50	0,40	121,51	2,74
J-77	89,80	1,71	120,99	3,05
HOTEL LADY M	89,80	0,63	120,99	3,05
J-78	89,80	0,78	120,99	3,05
J-77a	89,62	1,36	120,89	3,06
HOTEL CIBALIA	89,60	0,63	120,89	3,06
J-79	89,60	0,49	120,89	3,06
J-79b	89,31	2,18	120,68	3,07
INDUSTRIJA UNIOR	89,30	9,00	120,67	3,07

Label	Elevation (m)	Demand (L/s)	Hydraulic Grade (m)	Pressure (bars)
J-240	84,80	0,00	147,09	6,10
J-51	83,50	1,32	119,67	3,54
HOTEL VILLA LENIJE	83,50	0,75	119,67	3,54
P23	84,00	0,03	119,09	3,43
J-1	84,20	1,24	119,09	3,42
J-11	84,50	0,09	119,09	3,39
P11	84,50	0,02	119,09	3,39
J-2	84,50	0,28	119,09	3,39
J-12	84,50	0,08	119,09	3,39
P2	84,50	0,02	119,09	3,39

Label	Elevation (m)	Demand (L/s)	Hydraulic Grade (m)	Pressure (bars)
J-240	84,80	0,00	143,97	5,79
J-51	83,50	1,43	120,30	3,60
HOTEL VILLA LENIJE	83,50	0,81	120,30	3,60
P23	84,00	0,03	119,77	3,50
J-1	84,20	1,35	119,78	3,48
J-11	84,50	0,09	119,78	3,45
P11	84,50	0,02	119,78	3,45
J-2	84,50	0,30	119,77	3,45
J-12	84,50	0,09	119,77	3,45
P2	84,50	0,02	119,77	3,45

a) b)

Figure 5. a) Ten minimum and maximum operating pressures for ductile iron pipes - Variant 1, b) ten minimum and maximum operating pressures for PVC pipes - Variant 1.

4.2 Results for Variant 2

Variant 2 also pumps water to the water tower followed by gravity distribution, but with a changed layout of the main facilities and pressure pipeline. This affects the pressurized part of the water supply system and network pressure distribution.

Velocities remain below 2.0 m/s, with the highest values between the intake, pumps and water tower and the lowest in short terminal sections.

With ductile iron and steel pipes, pressures are generally within 2.5-6.0 bar, although about 6.87 bar occurs at J-240. The revised layout requires greater pumping head and less favourable station operation than Variant 1.

Two simultaneous fires were imposed at H-33 and H-34. Flow in P-60 rises from about 9 to 39 L/s, while hydrant pressures fall to about 2.6 bar, remaining just above the lower limit. Variant 2 is therefore acceptable but offers no clear pressure advantage and requires a more demanding pumping system.

4.3 Results for Variant 3

Variant 3 receives gravity inflow to a low-level reservoir and pumps into the network, enabling pressure control. With PVC pipes, velocities remain below 2.0 m/s (Figure 6), peaking between the intake and reservoir. Pressures range from 2.5 to 6.0 bar, with the maximum at J-263 downstream of the station.

Start Node	Stop Node	Diameter (mm)	Material	Hazen-Williams C	Flow (L/s)	Velocity (m/s)	Headloss Gradient (m/m)
VODOZAHVAT	VODOSPREMA	300,0	PVC	150,0	122,51	1,7331	0,007
VODOSPREMA	PMP-1	350,0	PVC	150,0	129,39	1,3449	0,004
PMP-1	J-263	350,0	PVC	150,0	129,39	1,3449	0,004
J-263	PRV-1	350,0	PVC	150,0	129,39	1,3449	0,004
PRV-1	J-1	350,0	PVC	150,0	129,39	1,3449	0,004
J-54a	H-57	200,0	PVC	150,0	40,44	1,2874	0,007
J-54	J-54a	250,0	PVC	150,0	52,49	1,0693	0,004
H-6	H-7	350,0	PVC	150,0	96,34	1,0014	0,002
J-52	J-53	350,0	PVC	150,0	94,24	0,9795	0,002
J-53	J-54	350,0	PVC	150,0	93,33	0,9701	0,002

Figure 6. Ten sections with maximum flow velocities, PVC pipes - Variant 3. (Vodozahvat = Water intake, Vodoosprema = Reservoir, PMP-1 = Pump station, J = Junction, H = Hotel, PRV = pressure reducing valve)

A key advantage of Variant 3 is active pressure management. The longitudinal profile towards Hotel Gem shows an increase in the piezometric line at the pumping station and subsequent reduction by the pressure-reducing valve. During night-time hours, this valve lowers pressures above 6 bar to about 5 bar, improving operational safety (Figure 7).

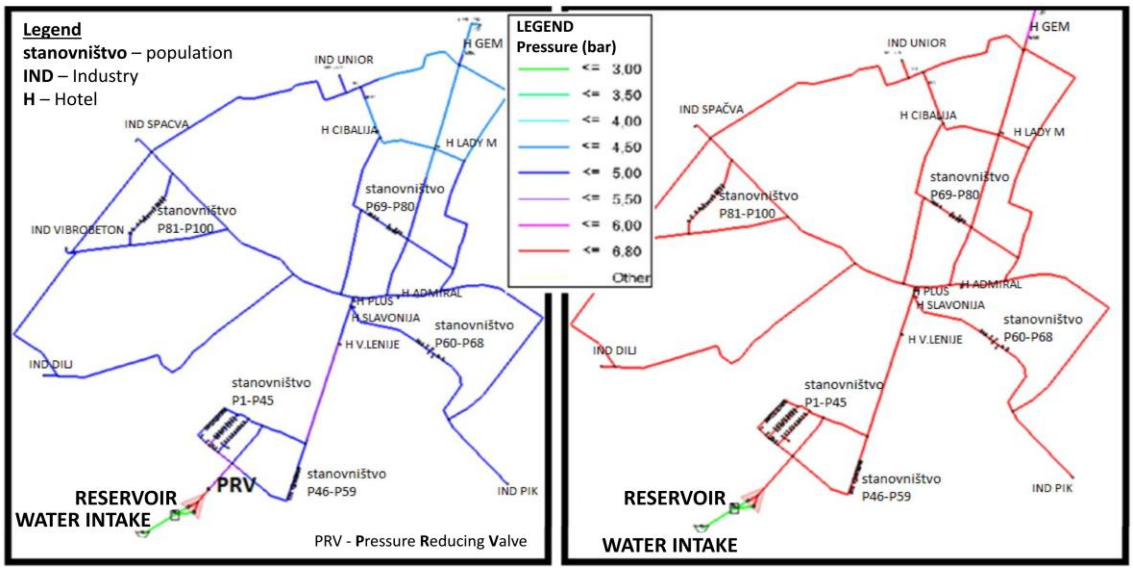


Figure 7. Influence of the pressure-reducing valve on operating pressures in the water supply system during night-time hours; left - system with a pressure reducing valve, right - system without a pressure reducing valve.

The 5 bar outlet setpoint was selected primarily to preserve the required pressure reserve at hydraulically critical and elevated nodes during peak and fire-flow conditions. It was not imposed by high-rise building requirements. A dynamically controlled pressure-reducing valve with a higher setpoint activated during fire events could provide additional flexibility, but this control strategy was outside the scope of the present analysis.

Variant 3 was tested with two simultaneous fires near the Unior industry plus industrial fire demand, and with fires near Hotel Gem and Unior during maximum hourly demand.

Critical pressures remain above the limit: about 2.62 bar at H-57, 3.17 bar at H-56, 2.56 bar at Hotel Gem and 3.0 bar near Unior. Variant 3 therefore remains safe under combined fire and industrial loading. Variant 3 offers greater flexibility through direct pressure control, reducing excessive night-time pressures, losses and adverse operating conditions.

4.4 Comparison of Variants

All variants are hydraulically acceptable; their main differences concern pressure distribution, pumping demand, regulation and resilience (Table 7).

Table 7. Comparison of hydraulic characteristics of the analysed system variants.

Comparison criterion	Variant 1 - water tower and pumping	Variant 2 - water tower and pumping, different layout	Variant 3 - low-level reservoir and pumping station
Basic concept	Pumping to the water tower, followed by gravity distribution	Pumping to the water tower, followed by gravity distribution, with changed position of main facilities	Gravity inflow to a low-level reservoir, followed by pressurisation towards the network
Velocities in pipelines	Within allowable limits, below 2.0 m/s	Within allowable limits, below 2.0 m/s	Within allowable limits, below 2.0 m/s
Critical sections	Pressure pipeline between the pumping station and water tower	Sections between the water intake, pumping station and water tower	Section between the water intake and reservoir, and sections downstream of the pumping station
Pressure distribution	Stable in most of the network; local pressure increase downstream of the pumping station	Stable in the network, but with a more pronounced local pressure downstream of the pumping station	Stable, with the possibility of pressure regulation by a pressure-reducing valve
Hydraulic stability	Good, especially due to gravity distribution from the water tower	Good, but with higher requirements in the pressurized part of the water supply system	Very good, with active pressure management
Energy requirements	Moderate to higher due to pumping towards the water tower	Higher than in Variant 1 due to the less favourable layout and greater head	More favourable in terms of a shorter pressure system and pump-operation regulation
Management flexibility	Limited, dependent on the water level in the water chamber	Limited, similar to Variant 1	Highest, due to the pumping station downstream of the reservoir and the pressure-reducing valve
Fire safety	Satisfied for one fire	Satisfied for two simultaneous fires, with pressures close to the lower limit	Satisfied for more complex scenarios: two fires and industrial loading
Overall assessment	Technically acceptable and hydraulically stable	Technically acceptable, but operationally more demanding	Most favourable in terms of controllability, flexibility and pressure adjustment
Relative cost implications (qualitative)	Moderate: water tower and pumping equipment; lower required head than Variant 2	Higher: greater required head and a more demanding pumping arrangement	Moderate to higher capital cost for reservoir, pumps, PRV and controls; potentially lower operating losses through active pressure management

Only a qualitative cost comparison was possible because detailed bills of quantities, energy tariffs and maintenance costs were not available. Variant 2 is expected to be the most expensive of the two water-tower solutions because of its higher required head and more demanding pumping configuration, whereas Variant 1 is comparatively less costly. Variant 3 avoids construction of a 30 m water tower but requires a low-level reservoir, pumping station, pressure-reducing valve and control equipment. Its initial cost may therefore be comparable, while active pressure management may reduce leakage-related and energy-related life-cycle costs.

The water tower variants provide stable gravity distribution but limited active pressure regulation. Variant 2 does not significantly improve hydraulic conditions compared with Variant 1 and requires less favourable pumping operation. Variant 3 provides the best pressure-management capability and remains safe under more complex fire scenarios.

4.5 Cross-software consistency check: WaterCAD V8i and Urbano Hydra

A limited cross-software consistency check was performed for selected representative conditions in one water-tower variant and one low-level-reservoir variant (Figure 8), rather than as validation of either

model. The WaterCAD V8i model was exported in EPANET format and imported into Urbano Hydra while preserving the network topology, pipe properties, nodal demands, boundary conditions and operating settings.

Figure 8 compares the same physical pipe sections and associated nodes in Variant 1 under maximum hourly demand. The element labels differ because the EPANET transfer applies software-specific naming conventions (correspondence was established from pipe endpoints, diameters and network connectivity). The displayed values therefore represent the same hydraulic locations rather than different network sections. Minor differences arise from the treatment of intermediate geometry points and numerical precision.

a)

Label	Start Node	Stop Node	Diameter (mm)	Material	Hazen-Williams C	Flow (L/s)	Velocity (m/s)
P-300	J-240	VODOTORANJ	350,0	Ductile Iron	130,0	132,05	1,3725
P-301	J-97	VODOTORANJ	450,0	Ductile Iron	130,0	- 129,39	0,8136
P-89(2)(2)(2)...	H-51	J-79b	200,0	Ductile Iron	130,0	25,35	0,8069
P-89(2)(2)(1)...	J-79a	H-51	200,0	Ductile Iron	130,0	25,35	0,8069
P-86(2)(2)(2)...	H-55	H-56	450,0	Ductile Iron	130,0	- 126,89	0,7978
P-275	J-78a	H-55	450,0	Ductile Iron	130,0	- 126,89	0,7978
P-274(1)	H-56	J-97	450,0	Ductile Iron	130,0	- 126,89	0,7978

b)

Naziv	N1	N2	L [m]	Din [m...	Q [l/s]	▼v [m/s]	hL [m]	hL [...
p-1_1	J-240	p-1_1	7,43	350,00	126,64	1,32	0,03	4,70
p-2_4	p-2_3	VODOTORANJ	39,02	450,00	129,39	0,81	0,06	1,44
p-2_3	p-2_2	p-2_3	196,47	450,00	129,39	0,81	0,28	1,44
p-2_2	p-2_1	p-2_2	113,78	450,00	129,39	0,81	0,16	1,44
p-2_1	J-97	p-2_1	182,55	450,00	129,39	0,81	0,26	1,44
p-3_2	p-3_1	J-79b	0,18	200,00	25,35	0,81	0,00	3,63
p-4_1	J-79a	H-51	45,78	200,00	25,35	0,81	0,17	3,65
p-3_1	H-51	p-3_1	42,08	200,00	25,35	0,81	0,15	3,65
p-6_1	J-78a	H-55	64,92	450,00	126,89	0,80	0,09	1,39
p-7_1	H-56	J-97	15,16	450,00	126,89	0,80	0,02	1,39
p-5_1	H-55	H-56	180,13	450,00	126,89	0,80	0,25	1,39

Figure 8. Cross-software consistency check for the same physical pipe sections and associated nodes in Variant 1: a) WaterCAD V8i and b) Urbano Hydra. Element labels differ after EPANET transfer, but the rows correspond by pipe endpoints, diameter and network connectivity. Note: VODOTORANJ = Water tower

For Variant 3, selected pressure and flow indicators were also checked under representative operating conditions. Urbano Hydra was used only to examine the consistency of the principal trends and to support preparation of longitudinal profiles (it was not treated as field validation). The design conclusions remain based on the WaterCAD V8i analysis, and calibration against measured field data was outside the scope of the available study.

5 Discussion

All variants are hydraulically acceptable, but differ in pressure distribution, pumping requirements, regulation and resilience to complex loads.

Variant 1 provides satisfactory hydraulic stability through pumping to a water tower and gravity distribution. Velocities and pressures are generally acceptable, and the fire scenario at H-70 causes only a small pressure decrease of about 0.18 bar. Its main limitation is the required pump operation of approximately 12 to 16 h/day, depending on the initial water level in the water chamber.

Variant 2 is technically acceptable but offers no clear advantage over Variant 1. Its layout requires greater head and less favourable pumping, while two fires reduce pressures at H-33 and H-34 to about 2.6 bar, near the lower limit.

Variant 3 has the most favourable management characteristics. Its low-level reservoir, downstream pumping station and pressure-reducing valve enable active control and reduce excessive night-time pressures and losses.

Under two simultaneous fires and additional industrial demand, Variant 3 maintains pressures above the lower limit at H-57, H-56, Hotel Gem and the Unior industrial area.

Water-tower variants provide passive stability, whereas Variant 3 better accommodates daily demand fluctuations, night-time operation and industrial loads, making it preferable where pressure control is important.

The results emphasise appropriate placement of pumps and control elements. In Variant 3, the downstream pumping station actively shapes network pressures and enables further optimisation of pump operation.

The analysis was focused on hydraulic behaviour, including pressures, flows, velocities and fire scenarios. Future work should include a detailed quantitative economic and energy comparison based on bills of quantities, energy tariffs and life-cycle maintenance, together with variable pump-operation regimes, possible pump or pipe failures and additional resilience scenarios.

Overall, the best solution is not simply the one that satisfies limit values, but the one that combines technical safety with adaptability, rational operation and emergency resilience. In this respect, Variant 3 is the most favourable hydraulic and operational concept. The limited cross-software check supports the consistency of selected results but does not constitute independent or field-based validation.

6 Conclusion

This paper presented a variant hydraulic analysis of a section of the Vinkovci looped water supply system, with the aim of assessing technical acceptability, operational efficiency and management possibilities. Three concepts were analysed: two water-tower variants with gravity distribution and one low-level reservoir variant with pumping into the network.

All variants are hydraulically acceptable under regular and fire-flow conditions. The water-tower concepts provide stable gravity distribution but limited active control, and Variant 2 requires a less favourable pumping regime without materially improving Variant 1.

Variant 3 is the most favourable because its low-level reservoir and pumping station allow better pressure regulation under variable conditions. The pressure-reducing valve limits night-time pressures, while the system remains stable under combined fire and industrial loads.

Pipe-material differences affect losses and pressure distribution, but do not change the basic acceptability of the variants. A limited consistency check in Urbano Hydra showed close agreement for selected corresponding pipes and nodes; however, the design conclusions are based on the WaterCAD V8i analysis, and field validation remains outside the scope of this study. The most favourable concept for the observed system is therefore the low-level reservoir with pumping station and pressure regulation, as it maintains hydraulic safety while providing greater controllability, operational flexibility and adaptation to actual urban water supply conditions.

Acknowledgements

This research is the result of work carried out within the UNIRI Institutional Research Project "*Challenges of Water Resources Management in Times of Climate Change with Respect to Drinking Water Production*" (uniri-iz-25-18), approved by the Ministry of Science, Education and Youth (financed by the European Union - NextGenerationEU).

References

Alsaydalani, M. O. 2024. Hydraulic Modelling for Leakage Reduction in Water Distribution Systems Through Pressure Control. *The Open Civil Engineering Journal*, 18.

Elhay, S., Fischer, M., Piller, O., Deuerlein, J., Simpson, A. R. 2025. Modelling Flow and Pressure Controlled Pump Stations with Application to Optimal Pump Scheduling. *Cambridge Prisms: Water*, 3. DOI: 10.1017/wat.2025.10005.

Gomes Jr., M. N., Benites, I. M., Elsherif, S. M., Taha, A. F., Giacomoni, M. H. 2024. Modeling and Design Optimization of Looped Water Distribution Networks Using MS Excel: Developing the Open-Source X-WHAT Model. *arXiv preprint*, arXiv:2405.09044.

Ismail, A., Rahman, M. H., Mortula, M., Atabay, S., Ali, T. 2025. Water Distribution Network Resilience Management Using Global Resilience Analysis-Based Index. *Sustainability*, 17(6), 2353, DOI: 10.3390/su17062353.

Kim, D.H. and Jang, D.W. 2024. Optimization of Water Distribution Network Demand Patterns Using Real-Coded Genetic Algorithms. *Water*, 16(20), 2971, DOI: 10.3390/w16202971.

Orime, H., Tait, S., Boxall, J., Shepherd, W., Schellart, A. 2024. Evaluating the Performance of Water Distribution Network Deterioration Using Customer-Oriented Performance Indices. *Water Supply*, 24(11), 3759-3775, IWA Publishing.

Safitri, A., Wahyudi, S. I., Soedarsono. 2023. Simulation of Pipe Networks Using EPANET to Optimize Water Supply: A Case Study for Arjawinangun Area, Indonesia. *Archives of Hydro-Engineering and Environmental Mechanics*, 70(1), 17-28, DOI: 10.2478/heem-2023-0002.

Serafeim, A. V., Perdios, A., Fourniotis, N. T., Langousis, A. 2023. Towards More Efficient Hydraulic Modeling of Water Distribution Networks Using the EPANET Software Engine. *Environmental Sciences Proceedings*, 25, 46, DOI: 10.3390/ECWS-7-14166.

Sidiropoulos, P., Papadomanolakis, A., Lyra, A., Mylopoulos, N., Vasiliades, L. 2025. A Modelling Framework for the Hydraulic Simulation of a Water Distribution System Under Data Scarcity: Application in the City of Farsala, Greece. *Applied Sciences*, 15(11), 6124, DOI: 10.3390/app15116124.

StudioARS. 2023. *Urbano Hydra – Water Distribution and Hydraulic Calculation Documentation*. StudioARS Ltd.

Tian, Y., Gao, J., Chen, J., Xie, J., Que, Q., Munthali, R. M., Zhang, T. 2023. Optimization of Pressure Management in Water Distribution Systems Based on Pressure-Reducing Valve Control: Evaluation and Case Study. *Sustainability*, 15(14), 11086, DOI: 10.3390/su151411086.

HYDROLOGICAL MODEL CALIBRATION USING SWAT-CUP

Karlo LESKOVAR [1*], Damir BEKIĆ [2], Lucija PLANTAK[1], Hrvoje MEAŠKI[1]

[1] *University of Zagreb Faculty of Geotechnical Engineering, Croatia*

E-mail: karlo.leskovar@gfv.unizg.hr

E-mail: lucija.plantak@gfv.unizg.hr

E-mail: hrvoje.measki@gfv.unizg.hr

[2] *University of Zagreb Faculty of Civil Engineering, Croatia*

E-mail: damir.bekic@grad.unizg.hr

[*] *Corresponding author*

Abstract

Model calibration can be done manually, when user alters calibration parameters, or by using specific calibration software. This paper presents results of SWAT model calibration and validation in the case of the Sill River catchment in Austria. Model calibration was performed using the sequential uncertainty fitting 2 (SUFI-2) algorithms of the SWAT Calibration Uncertainty Programs (SWAT-CUP). The algorithm in SWAT-CUP uses a Latin hypercube sampling method to calculate the 2.5% and 97.5% levels of a given parameter's cumulative distribution to get the 95% of the data (95PPU). Two factors describing the quality of the fit between the calculated and observed data (in this example, streamflow) are mandatory: the P-factor and R-factor. Several investigations tackled the problem of SWAT-CUP calibration in snowmelt-influenced mountainous basins, where particularly the Nash-Sutcliffe Efficiency (NSE) and Pearson's coefficient of determination (R^2) were found as effective indicators of goodness of fit. According to prior investigations in similar regions, a specific set of calibration parameters important for model performance was identified. A total of three stages of calibration were performed where the selected model statistics, namely, R^2 and NSE, were increased from 0.51 and 0.17 to 0.93 and 0.90, respectively, for the calibration period, and 0.91 and 0.84 for the validation period. It was effectively shown that a thought-out selection of calibration parameters and the respective physically valid ranges can increase model performance in complex snowmelt-influenced mountainous basins.

Key words

hydrological modelling, SWAT, snowmelt, mountainous catchment, model calibration, Sill River

1 Introduction

Hydrological models have become indispensable tools for investigating watershed processes, supporting water resources management, flood forecasting, climate change impact assessment, and hydropower planning. However, the predictive capabilities of any hydrological model strongly depend on the quality of the calibration. This challenge is particularly pronounced in alpine catchments, where runoff generation is influenced by complex terrain, pronounced precipitation gradients, snow accumulation and snowmelt and groundwater dynamics.

The Soil and Water Assessment Tool (SWAT) is one of the most widely accepted watershed-scale hydrological models. Although SWAT has demonstrated good performance in snow-dominated environments, its successful application requires careful calibration of climate, snowmelt, surface

runoff, and groundwater-related parameters. Manual calibration can be time-consuming and subjective, particularly in large watersheds characterized by substantial parameter uncertainty.

To address this challenge, the SWAT Calibration and Uncertainty Programs (SWAT-CUP) provide several automatic calibration algorithms, among which the Sequential Uncertainty Fitting Version 2 (SUFI-2) approach is one of the most widely applied. Besides parameter optimization, SUFI-2 enables uncertainty analysis through the estimation of prediction uncertainty bands and the evaluation of model performance using indicators such as the p-factor and r-factor.

The objective of this study is to demonstrate the calibration and validation of a SWAT model for the snowmelt-dominated Sill River catchment in the Austrian Alps using the SUFI-2 algorithm. Particular emphasis is placed on the selection of calibration parameters, the calibration strategy for alpine catchments, and the evaluation of model performance using both conventional hydrological goodness-of-fit method and statistical metrics, i.e. the widely accepted Pearson's coefficient of determination and the Nash-Sutcliffe efficiency. Furthermore, the model skill is evaluated using two different precipitation inputs: measured station observations and the remotely sensed gridded CHIRPS precipitation product. To our knowledge this is the first study evaluating different precipitation products over Austrian Alps as inputs to the SWAT hydrological model. The research further demonstrated the applicability of SWAT model in high mountainous catchments, as already successfully presented in the Italian Alps (Tuo et al. 2016, 2018).

2 Methods

The Soil Water Assessment Tool (SWAT) is a physically-based, semi-distributed watershed simulation model initially developed by (Arnold et al. 1998; Neitsch et al. 2011) for comprehensive modelling of the impacts of management practices on water yield, sediment yield, crop growth and agricultural chemical yields in large ungagged basins (Arnold et al. 1998). It can also be used for snowmelt modelling, as proven by several investigations, i.e. Fontaine *et al.* (Fontaine et al. 2002), Grusson *et al.* (Grusson et al. 2015) and Tuo *et al.* (Tuo et al. 2018). As a result of intensive data collection and data file creation efforts involved with large-scale modelling, SWAT is designed to use GIS (Geographic information system) to extract parameter values and input data from map layers and databases (Fontaine et al. 2002). Hydrologic processes calculated in the model are precipitation, interception, surface runoff, soil and root zone infiltration, evapotranspiration and soil and snow evaporation and groundwater flow, described in eq. (1) (Arnold et al. 1998; Fontaine et al. 2002; Neitsch et al. 2011):

$$\Delta SW = (P - Q - ET - DP - QR) \quad (1)$$

Where ΔSW is the soil water content, P is precipitation, Q is the runoff, ET evapotranspiration, DP deep percolation, and QR is the return flow, all units in mm.

2.1 Study area

The Sill River catchment, with an area of 854.8 km^2, is located in North Tyrol, Austria (Figure 1.), north of Innsbruck and south of the Brenner Pass. The basin's south-west and west border are made by Stubaier Alps with the highest peak Zuckerhütl (3507 m a.s.l.), while the Brenner Pass forms the southern border. The Zillertaller (Hochfeiler – 3510 m a.s.l.) and Tuxer Alps (Lizumer Reckner – 2886 m a.s.l.) form the east border, and the city of Innsbruck with the Inn River form the north border od the basin.

The snow and glacier-melt dominated river has its source at an elevation of 2342 m a.s.l. in the municipality Gries am Brenner, just below the Wildseespitze (2733 m) mountain peak in the Zillertaller Alps. From its source until the mouth in the Inn River near Innsbruck, the flow length is 42.2 km and flow direction mainly north. The most significant tributary of the Sill River is the Ruetz river, which conferences with the Sill approx. 8 km north of Innsbruck, other memorable left tributaries are the

Gschnitzbach stream and Obernberger Seebach. The right tributaries are much smaller, streams, i.e., Valser Bach, Navisbach and Mühlbach.

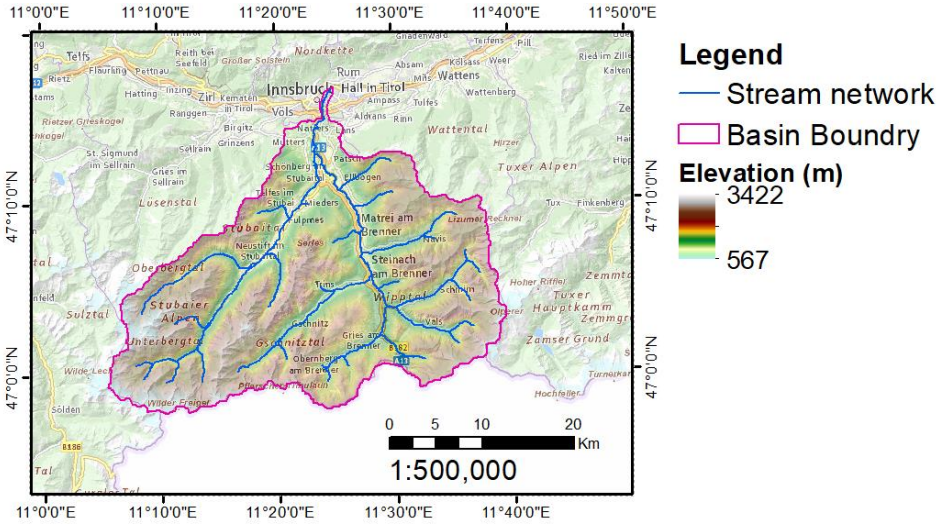


Figure 1. Sill River catchment

2.2 Input data

Meteorologically measured precipitation data and runoff data received from the GIS portal eHYD (https://ehyd.gv.at/) of the Austrian Bundesministerium für Nachhaltigkeit und Tourismus and sites of the Autonomous Province of Bozen/Bolzano – South Tyrol meteorological service (https://weather.provinz.bz.it/download-data.asp). The eHYD portal provides meteorological data on precipitation – (P) [mm], snow depth – (SD) [cm] and fresh snow [cm] and hydrological related data like runoff - (Q) [m3/s], water level [m], water temperature [°C], suspended sediment (load) [t], hydrogeological data related to groundwater, i.e., groundwater level [m a.s.l.] and groundwater temperature [°C] and water source data, i.e., water conductivity [µS/cm], spring discharge [l/s] and water temperature [°C]. The portal of the Province Bolzano provides daily timestep data on precipitation (P) [mm] and minimum (Tmin) and maximum (Tmax) air temperature [°C]. The used precipitation data from both portals and runoff data from eHYD are all available at daily timestep, while some groundwater-related data from eHYD is only available in weekly or monthly timescales.

All 14 precipitation gauges used as inputs for the model calibration and validation are presented in Figure 2 (a). The meteorological stations Pflersch and Ridnaun are located in Italy and are part of the Meteorological Service of the Province of Bolzano. The remaining 12 stations, namely: Gries im Sellrain, Obernberg am Brenner, Trins, Matrei am Brenner, Schönberg im Stubaital, Telfes im Stubai, Innerschmirn-Obern, Dresdner Hütte, Neustift i. St.-Volderau, Axams, Navis and Gschnitz-Obertal are under the jurisdiction of the Austrian Bundesministerium für Nachhaltigkeit und Tourismus.

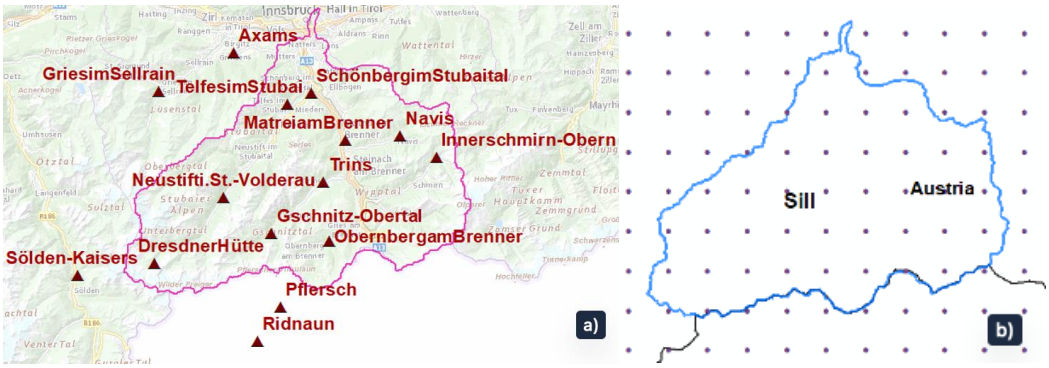


Figure 2. Precipitation gauges in and around the Sill River catchment (a); CHIRPS product data points (b)

Climate Hazards Group InfraRed Precipitation with Station (CHIRPS-V2.0) (Funk et al. 2015) dataset provides quasi-global (50S-50N) high resolution 0.05° (Figure 2 - b) precipitation gridded dataset. The product is based on the monthly precipitation climatology CHPclim (Climate Hazards Center's Precipitation Climatology version 1) that is created using rain gauge stations collected from FAO (Food and Agriculture Organization) and GHCN (Peterson and Vose 1997) (Global Historical Climatology Network), which are combined with 5 satellite products (Tropical rainfall Measuring Mission 2B31 microwave precipitation estimates (Huffman et al. 2007), CMORPH microwave plus-infrared based precipitation estimates (Joyce et al. 2004), monthly mean geostationary infrared brightness temperatures (Janowiak et al. 2001) and land surface temperature estimates (Wan 2014), all resampled to 0.05 degrees (Funk et al. 2015). The dataset is available from 1981 to near-real-time from the Climate Hazard Center server (ftp://ftp.chg.ucsb.edu/pub/org/chg/products/CHIRPS-2.0/).

2.3 SWAT-CUP calibration software and model evaluation

The calibration and validation of the model was done using the sequential uncertainty fitting 2 (Abbaspour et al. 2004) (SUFI-2) algorithm of the SWAT Calibration Uncertainty Programs (Abbaspour 2011) (SWAT-CUP). Several investigators have successfully used the SUFI-2 algorithm (Abbaspour et al. 2004, 2015; Tuo et al. 2018). In the SUFI-2 algorithm the modelling uncertainty is expressed as ranges of model parameters an account for all uncertainties, i.e. input data like precipitation or air temperature, the conceptualisation f the model or observed data (Abbaspour et al. 2007). The algorithm uses Latin Hypercube Sampling to generate parameter sets and derives the 95% Prediction Uncertainty (95PPU) from the 2.5th and 97.5th percentiles of the resulting model simulations (Abbaspour et al. 2015). Basically, there isn't a single true model output, but rather an envelope of solutions defined by the 95PPU within the model parameter ranges. In order to quantify the fit between the modelled solutions and the observation, two factors describing the quality of the fit between the calculated and observed data (in this example, streamflow) are mandatory, the P-factor and R-factor (Abbaspour et al. 2004, 2007).

The uncertainty analysis of the SUFI-2 algorithm is illustrated in Figure 3. It is shown that a single value of a parameter would result in a single model output, a line. If the parameter is considered a range (example b), the model result can be considered as the 95PPU illustrated as a shaded are, furthermore, with an increase in parameter uncertainty, the 95PPU band, also widens (example c). Therefore, in SUFI-2 a large parameter uncertainty within a physically meaningful range is assumed, which later gets decreased during calibration steps. In each step, previous parameter ranges are updated by calculating the sensitivity matrix (or Jacobian) and a equivalent Hessian matrix, covariance matrix, 95% confidence intervals of the parameters, and correlation matrix. Parameters are then adjusted so that the new ranges are always smaller than the previous ones and centred around the best simulation (Abbaspour 2011).

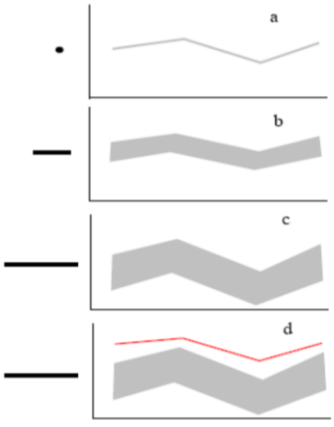


Figure 3. Conceptual illustration of the parameter uncertainty (taken from: **(**Abbaspour 2011**)**)

P-factor varies from 0 to 1 and inherits the data contained within the 95PPU band, as for streamflow calibration, values > 0.7 or 0.75 are adequate (Abbaspour et al. 2015). The R-factor refers to the

wideness of the 95PPU band, and the standard deviation of the measured parameter, values < 1.5, is considered adequate (Abbaspour et al. 2015). A successful calibration goal is to find the right balance between these two parameters. If the initially set parameter ranges equal to the maximum physically meaningful ranges cannot find a 95PPU that brackets any or most of the data (example d), then the problem is not parameter calibration or range, but the conceptual model must be re-examined.

SUFI-2 offers up to 10 objective functions statistical parameters, which describe the goodness of the fit between calibrated streamflow and observed values. According to prior investigations of snowmelt driven basins, i.e. (Grusson et al. 2015; Koycegiz and Buyukyildiz 2019; Tuo et al. 2018), NSE and R^2 are often chosen as indicators of the goodness of the calibration. As described by (D. N. Moriasi et al. 2007), the coefficient of determination R^2 (Eq. (2)(2)) is considered very sensitive to extreme values, such as peak flow therefore, R^2 is a good indicator of goodness of fit when modelling snowmelt driven basins to get as good as possible volume and magnitude of spring peak flow.

$$R^2 = \left[\frac{\sum_{i=1}^{n}(Q_i - \bar{Q})\left(Q'_i - \bar{Q}'\right)}{\sqrt{\sum_{i=1}^{n}(Q_i - \bar{Q})^2 \sum_{i=1}^{n}\left(Q'_i - \bar{Q}'\right)^2}} \right]^2 \tag{2}$$

where: Q_i is the observed runoff, $\bar{Q}$ the mean observed runoff, Q'_i is the predicted runoff and $\bar{Q}'$ the mean predicted runoff.

Typically, values greater than 0.5 mean a good fit of calculated and observed values (D. N. Moriasi et al. 2007). Therefore, the second statistical parameter we choose is the Nash-Sutcliffe efficiency (NSE) (3).

$$NSE = 1 - \frac{\sum_i (Q_i - Q'_i)^2}{\sum_i (Q_i - \bar{Q})^2} \tag{3}$$

NSE determines the relative magnitude of the residual variance, compared to the observed data (D. N. Moriasi et al. 2007; Nash and Sutcliffe 1970), where ranges from 0.75 – 1.0 indicate good model performance (D. N. Moriasi et al. 2007; Rahman et al. 2013).

Percent Bias (PBIAS) measures the average tendency of simulated discharge to be larger or smaller than the corresponding observed values, with values close to zero indicating minimal overall bias and therefore better model skill. According to Moriasi et al. (2007), for streamflow simulations, |PBIAS| < 10% indicates very good, 10–15% good, 15–25% satisfactory, and >25% unsatisfactory model performance; in the formulation used in this study, negative values indicate underestimation, whereas positive values indicate overestimation.

$$PBIAS = \frac{\sum_{i=1}^{n}(Q'_i - Q_i) \times 100}{\sum_{i=1}^{n} Q_i} \tag{4}$$

The Root Mean Square Error (RMSE) quantifies the average magnitude of prediction errors by measuring the square root of the mean squared differences between simulated and observed discharge values, with lower values indicating better model performance.

$$RMSE = \sqrt{\frac{\sum_{i=1}^{n}(Q_i - Q'_i)^2}{n}} \tag{5}$$

where: Q_i is the observed runoff and Q'_i is the predicted runoff.

2.4 SWAT model – calibration

The calibration was performed using the SUFI-2 algorithm implemented in SWAT-CUP. Initial parameter ranges were selected through expert judgement and literature review, while parameter optimization and uncertainty analysis were performed automatically by SUFI-2. Starting values for parameters have been checked in similar investigations in the European Alps region, i.e. (Tuo et al. 2018), where alpine basins in Italy have been examined, around 100 km southwest of our area of the investigation. Also, similar publications investigating SWAT snowmelt modelling around the globe have been consulted for mountainous regions similar to the European Alps (Abbaspour et al. 2015; Rahman et al. 2013; Tuo et al. 2018).

SWAT-CUP offers three types of parameter changes, a relative change, an absolute change and replacing the parameter value. When absolute change "A_" is chosen, the values from the selected range are added or subtracted from the parameter's default value. Setting the relative change, "R_" means relative change, where the default value gets multiplied by 1 + a value from the selected range, or in other words, the default value gets changed by the percentage value from the selected range. This type of change is used when calibrating spatially dependent parameters like CN2. The third type of change is referred to as replacing "V_", where the parameter's default value gets changed with the best fitting value from the selected range. This change is used when a parameter is constant over a basin or subbasin area, i.e., PLAPS or TLAPS.

The calibration process in SWAT-CUP consisted of a total of 4 iterations. First, an initial uncalibrated simulation, where the goal is to assess if the initially set parameter ranges result in a 95PPU that overlaps with most of the observed data, the run can be assumed successful. Then we proceed with the calibration of weather parameters (Table.), namely, temperature and precipitation lapse rates, therefore a total of 100 simulations are run. After a valid range of precipitation and temperature lapse rates is found, they are set to a fixed range, and as next step, the five snow-related parameters (Table 1.) are calibrated. Calibrating snowmelt related parameters, i.e. SFTMP, SMTMP, SMFMX, SMFMN, TIMP, is essential in snowmelt dominated watersheds, as shown by Ahl *et al.* (Ahl et al. 2008), who proved that the default SWAT snowmelt parameters caused to early peaks in streamflow, a 75-80 days earlier peak in streamflow. A total of 300 simulations of snow-melt related parameter calibration parameters are run. Although the suggested ranges for calibrating the melt factors SMFMX and SMFMN are 0 – 10, which led to errors, the automatic calibrating procedure calculated the values of SMFMN higher than the values of SMFMX, which is not correct for the northern hemisphere, where the investigated basins are located. Therefore, we adjusted the calibration ranges of the parameters, as shown in Table. Similar problems were observed by others (Tuo et al. 2018). Furthermore, calibrating snowmelt parameters extends the recession limb of the hydrograph. The most significant impact on model performance had TIMP and SMTMP (Ahl et al. 2008). Again, when satisfied with the results, the parameters were fixed, following the same procedure as in the second iteration.

Table 1. Calibration ranges of climate, snowfall and snowmelt related parameters

Parameter	Description	Calibration Range
V_TLAPS.sub	Temperature lapse rate (°C/km)	-8 – -2
V_PLAPS.sub	Precipitation lapse rate (mm/1000 m)	0 – 100
V_SFTMP.bsn	Snowfall temperature (°C)	-5 – 5
V_SMTMP.bsn	Snowmelt temperature (°C)	-5 – 5
V_SMFMX.bsn	Maximal snowmelt factor – 21st of June (mm/day)	5 – 10
V_SMFMN.bsn	Minimal snowmelt factor – 21st of December (mm/day)	0 – 5
V_TIMP.bsn	Snow temperature lag factor (-)	0 – 1

Note: the "V_" term means the existing parameter value is to be replaced by a given value, and "R_" means a relative change to the parameter, where a current parameter value is multiplied by (1+ a given value).

As the last step, surface runoff and groundwater-related parameters are calibrated (Table 2.). Again, all three possible parameter change types were used, absolute change "A_" and replace "V_" for spatially not sensitive parameters, i.e., GWQMN or GW_DELAY, which are considered constant over the entire watershed, and "R_" relative change for spatially sensitive parameters like the CN curve number which highly depends on the landcover type and changes over the range of the watershed. To calibrate the surface runoff and groundwater-related parameters 500 model simulations are run.

Table 2. Final calibration and validation ranges for the Sill basin

		Sill basin	
Parameter	**Description**	**Calibration range**	**Fitted value**
R_CN2.mgt	Soil conservation services (SCS) runoff curve number	-0.2 – 0.2	0.081
A_GWQMN.gw	Threshold depth of water in shallow aquifer for return flow (mm)	0 – 300	250.50
R_ESCO.hru	Soil evaporation compensation coefficient	-0.25 – 0.25	0.103
V_GW_DELAY.gw	Delay time for aquifer recharge (days)	0 – 300	33.90
A_SLSUBBSN.hru	Average slope length (m)	-9 – 115	13.44
R_GW_REVAP.gw	Groundwater "revap" coefficient	0 – 0.2	0.028
R_REVAPMN.gw	Threshold depth of water in the shallow aquifer for "revap" or percolation to occur (mm H_20)	-0.2 – 0	-0.109
V_ALPHA_BF.gw	Baseflow alpha factor (1/days)	0 – 1	0.427
R_SOL_AWC().sol	Available water capacity of the soil layer (mm H_20/mm soil)	-0.05 – 0.05	0.034
V_RCHRG_DP.gw	Deep aquifer percolation fraction	0 – 1	0.251

Note: the "V_" term means replacing the value of the parameter, "R_" means a relative change to the parameter, where the parameter gets changed by percentage (value given in the calibration range), while "A_" means absolute change, where the provided calibration range values get added or subtracted from the default parameter value

3 Results and Discussion

The modelling results with the emphasis on calibration and validation of the model with SWAT-CUP are presented on the example of the upper Sill River catchment in the Austrian Alps. In order to further prove the effectiveness of SWAT and calibration capabilities of SWAT-CUP, the procedure has been repeated for two different precipitation inputs to the hydrological model. First, the model was built and calibrated with precipitation data measured at precipitation gauges from the Austrian and Italian meteorological services. Upon successful calibration and validation, the model was rebuilt with exactly the same input data, except for the precipitation input, which in this case was a remotely sensed gridded precipitation dataset, namely the CHIRPS V2.0 dataset. The data used in the models included the period from 01.01.1991 to 31.12.2013. In addition, model calibration was performed in the SWAT-CUP

software on the period from 01.01.1996. to 31.12.2005. The model was validated on the period of 01.01.2009. to 31.12.2013. During model calibration and validation, 4 evaluation metrics were selected and monitored: SWAT-CUP related p-factor and r-factor, and the often-used metrics in hydrological forecasting, coefficient of determination R^2 and Nash-Sutcliffe Efficiency NSE. Additionally, to measure the model error in regards of under or overestimation and peak-flow and baseflow simulation, quantitative bias measures have been included, namely PBIAS and RMSE. The results presented in each table are divided into three sections, initial model, basic model with default parameter values set up in ArcSWAT, and final calibration, representing the calibrated model, period 01.01.1996. to 31.12.2005. and validation representing the model validation on period 01.01.2009. to 31.12.2013.

A global uncertainty analysis was considered when identifying parameters that influence the modelling result. Therefore, the t-Stat and P-Value are evaluated, where parameters with larger absolute t-Stat are considered more sensitive, while the P-Value determines the significance of the parameter (Abbaspour 2011). In the case of the upper Sill catchment the most sensitive paraments are the Snow temperature lag factor TIMP, Baseflow alpha factor ALPHA-BF, precipitation lapse rate PLAPS, snowmelt temperature SMTMP and Groundwater "revap" coefficient GW-REVAP, all resulting in a P-Value lower than 0.05, meaning they all can be considered statistically significant for the model outcome.

Table 3. Initial model and calibration results for the Sill River catchment with measured precipitation input

Subbasin	b1_KRO_m	b1_PUI_m	b1_INN_m
Initial model setup			
p-factor	0.02	0.09	**0.13**
r-factor	0.00	0.00	**0.00**
R^2	0.23	0.56	**0.51**
NSE	-0.02	0.19	**0.17**
PBIAS	-20.41	-12.72	**-12.28**
RMSE	5.06	6.83	**15.03**
Final Calibration			
p-factor	0.73	0.73	**0.76**
r-factor	0.70	1.02	**1.00**
R^2	0.81	0.89	**0.93**
NSE	0.76	0.87	**0.90**
PBIAS	-13.82	-7.65	**-8.52**
RMSE	2.20	2.21	**4.37**
Validation			
p-factor	0.63	0.80	**0.77**
r-factor	0.61	0.91	**0.84**
R^2	0.88	0.88	**0.91**
NSE	0.78	0.85	**0.84**
PBIAS	-16.69	-11.21	**-15.22**
RMSE	2.37	2.67	**6.42**

The modelling with measured precipitation resulted not very satisfactory initial result, with R^2 value of 0.51 and NSE value of 0.17 at the catchment outlet gauge in city of Innsbruck. For the upstream gauges the results very similar or worse. The model achieved very good statistical performance according to NSE and R^2, while PBIAS values indicate good to satisfactory agreement in terms of simulated water balance (D. N. Moriasi et al. 2007). We can note an increase in both R^2 values across all three gauging points (0.81, 0.89 and 0.93), and NSE values (0.76, 0.87 and 0.9), respectively. In order to validate the model run on unseen data, a validation run has been performed, which showed also very satisfactory

result with R^2 values between 0.88 and 0.91, and NSE values between 0.78 and 0.84. Calibration substantially reduced the magnitude of discharge errors, decreasing RMSE at the catchment outlet from 15.03 m³/s in the initial simulation to 4.37 m³/s after calibration. The validation period maintained relatively low errors (RMSE = 6.42 m³/s), indicating satisfactory transferability of the calibrated parameter set. The negative value of the PBIAS across model results indicate underestimation of the modelled discharge, especially during validation we observe an increase in the PBIAS value for the basin outlet, while both subbasins show a successful model calibration in terms of PBIAS.

In many mountainous catchments, often, a lack of gauging station network is present; therefore, gridded remotely sensed precipitation products are considered valid inputs to hydrological models. These products are often obtained by combining satellite-based remote sensing imagery with ground measurements from nearby gauging stations. The initial, uncalibrated model for the Sill catchment, fed with gridded CHIRPS precipitation data, produced similar results to the uncalibrated model based on traditionally measured precipitation. Upon a successful calibration, again a significant increase in model skill was achieved, where values of R^2 rose to 0.89 and NSE to 0.87 for the model outlet station in Innsbruck. Again, a validation run on unseen data has been performed, where the highly satisfactory results could be validated, with values of R^2 ranging from 0.83 to 0.93 across the catchment gauges, and NSE values ranging from 0.69 to 0.87. The overall underestimation of the discharge observed during modelling with measured precipitation input, is also noticeable while modelling with the CHIRPS gridded product, with negative PBIAS values across initial, calibrated and validated model. As before, an increase in model performance can be observed, supported by a decrease in RMSE values across both upstream subbasins and the model outlet gauge (from 15.13 m³/s to 5.99 m³/s during calibration and to 5.69 m³/s during validation at the catchment outlet).

Table 4. Initial model and calibration results for the Sill River catchment with CHIRPS gridded precipitation input

Subbasin	b1_KRO_c	b1_PUI_c	b1_INN_c
Initial model setup			
p-factor	0.04	0.12	**0.10**
r-factor	0.00	0.00	**0.00**
R^2	0.29	0.48	**0.49**
NSE	0.15	0.13	**0.16**
PBIAS	-27.19	-15.02	**-8.87**
RMSE	4.62	7.09	**15.13**
Final Calibration			
p-factor	0.63	0.73	**0.77**
r-factor	0.53	0.78	**0.79**
R^2	0.80	0.85	**0.89**
NSE	0.68	0.81	**0.87**
PBIAS	-24.34	-13.19	**-9.68**
RMSE	2.82	3.35	**5.99**
Validation			
p-factor	0.62	0.68	**0.70**
r-factor	0.52	0.84	**0.80**
R^2	0.83	0.89	**0.93**
NSE	0.69	0.84	**0.87**
PBIAS	-13.40	-13.40	**-13.66**
RMSE	2.72	2.72	**5.69**

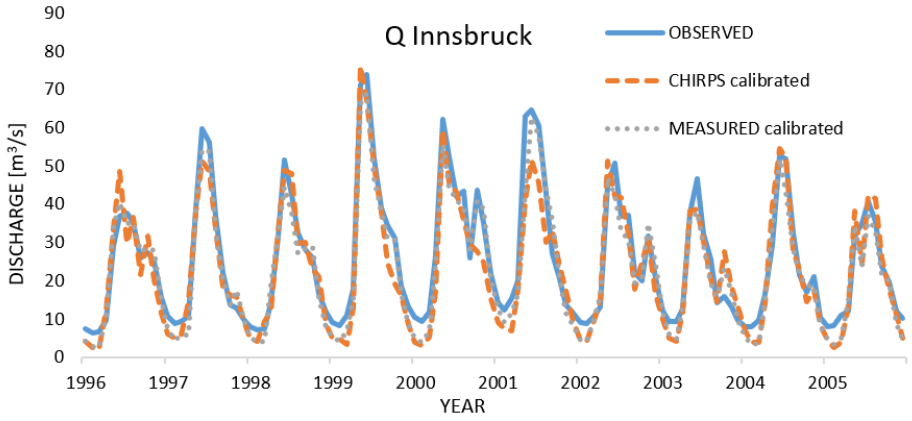


Figure 4. Resulting model hydrograph compared with observed discharge – calibration period

The gridded precipitation model of the Sill catchment slightly overestimates the maximum observed discharge and underestimate the minimum runoff. The measured precipitation model slightly underestimates the maximum runoff. However, it significantly underestimates minimum runoff as the gridded precipitation product model (Figure 4), where the underestimation of the baseflow is evident for both precipitation inputs. As for the mean runoff, the measured and CHIRPS models underestimate the mean runoff slightly. Both precipitation inputs capture most of the peak flows well, with slight advantage for the measured precipitation input.

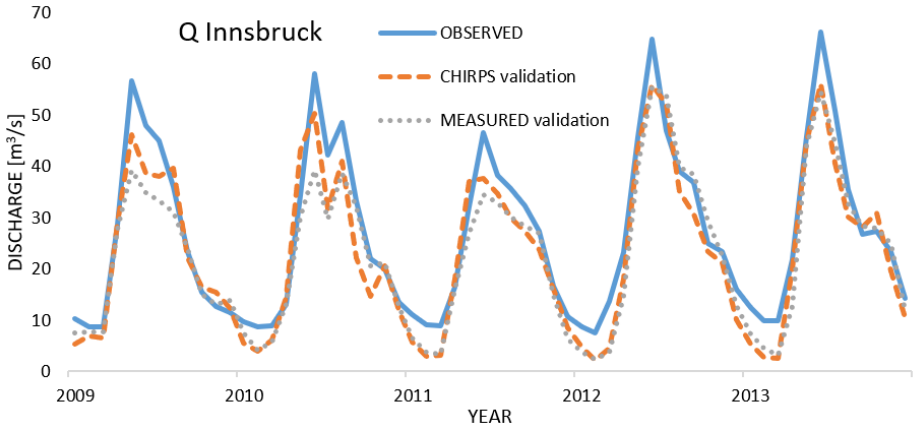


Figure 5. Resulting model hydrograph compared with observed discharge – validation period

In terms of the base flow and the mean discharge values, similar results are present for the validation period (Figure 5) where both precipitation inputs underestimate the base flow by a larger margin. In the case of the validation period, slight edge can be given to the CHIRPS product in terms of the peak flows, especially in 2009. and 2010 where it outperforms the measured precipitation as model input. The flow dynamics (timing) are well captured by both products.

4 Conclusion

The presented study demonstrates the successful application of the SWAT-CUP software and the SUFI-2 calibration algorithm for improving hydrological simulations in a snowmelt-dominated alpine watershed. The initial SWAT model showed limited predictive capability, whereas the calibrated model achieved substantial improvements in all evaluation metrics. For the catchment outlet, calibration increased R^2 from 0.51 to 0.93 and NSE from 0.17 to 0.90 when measured precipitation data were used, while similarly high performance was achieved using the CHIRPS gridded precipitation product. The calibration process also reduced the RMSE from 15.03 m³/s in the initial simulation to 4.37 m³/s after calibration and 6.42 m³/s during the validation period. Similar results were observed with the CHIRPS gridded product as precipitation input, where a decrease in RMSE from 15.13 m³/s to 5.99 m³/s for the

catchment outlet during calibration, and 5.69 m³/s during validation can be reported. Both measured and gridded precipitation products as precipitation inputs to the SWAT model resulted in a negative PBIAS, meaning both types of precipitation yielded slightly less discharge than was observed during the modelled period.

The results confirm that careful calibration of climate, snowmelt, surface runoff, and groundwater-related parameters is essential for accurately reproducing streamflow dynamics in mountainous catchments. In particular, calibration of snow-related parameters and lapse rates proved critical for representing the timing and magnitude of snowmelt-driven runoff.

The comparison between measured and gridded precipitation inputs demonstrated that remotely sensed precipitation products can provide a viable alternative in regions with sparse meteorological monitoring networks. Although measured precipitation data generally produced slightly better results, the calibrated CHIRPS-based model achieved comparable performance and successfully reproduced the observed flow dynamics.

Overall, the study highlights the effectiveness of the SUFI-2 algorithm for reducing model uncertainty and improving predictive performance in complex alpine environments. The presented calibration framework can serve as a practical guideline for future SWAT applications in snowmelt-influenced mountainous watersheds.

References

K.C. Abbaspour 2011 *SWAT-CUP: SWAT calibration and uncertainty programs–a user manual*. Swiss Federal Institute of Aquatic Science and Technology, Dübendorf.

Abbaspour, K.C., Johnson, C.A. and van Genuchten, M.Th. 2004 Estimating Uncertain Flow and Transport Parameters Using a Sequential Uncertainty Fitting Procedure. *Vadose Zone J.* 3 (4), 1340–1352.

Abbaspour, K.C., Rouholahnejad, E., Vaghefi, S., Srinivasan, R., Yang, H. and Kløve, B. 2015 A continental-scale hydrology and water quality model for Europe: Calibration and uncertainty of a high-resolution large-scale SWAT model. *J. Hydrol.* 524, 733–752.

Abbaspour, K.C., Vejdani, M. and Haghighat, S. 2007 SWAT-CUP calibration and uncertainty programs for SWAT. *MODSIM07 - Land, Water and Environmental Management: Integrated Systems for Sustainability, Proceedings*, 1596–1602.

Ahl, R.S., Woods, S.W. and Zuuring, H.R. 2008 Hydrologic calibration and validation of SWAT in a snow-dominated Rocky Mountain watershed, Montana, U.S.A. *J. Am. Water Resour. As.* 44 (6), 1411–1430.

Arnold, J.G., Srinivasan, R., Muttiah, R.S. and Williams, J.R. 1998 Large Area Hydrologic Modeling and Assessment Part I: Model Development. *J. Am. Water Resour. Assoc.* 34 (1), 73–89.

D. N. Moriasi, J. G. Arnold, M. W. Van Liew, R. L. Bingner, R. D. Harmel, and T. L. Veith 2007 Model Evaluation Guidelines for Systematic Quantification of Accuracy in Watershed Simulations. *Transactions of the ASABE* 50 (3), 885–900.

Fontaine, T.A., Cruickshank, T.S., Arnold, J.G. and Hotchkiss, R.H. 2002 Development of a snowfall-snowmelt routine for mountainous terrain for the soil water assessment tool (SWAT). *J. Hydrol.* 262 (1–4), 209–223.

Funk, C., Peterson, P., Landsfeld, M., Pedreros, D., Verdin, J., Shukla, S., Husak, G., Rowland, J., Harrison, L., Hoell, A. and Michaelsen, J. 2015 The climate hazards infrared precipitation with stations - A new environmental record for monitoring extremes. *Sci. Data.* 2 (1), 1–21.

Grusson, Y., Sun, X., Gascoin, S., Sauvage, S., Raghavan, S., Anctil, F. and Sáchez-Pérez, J.M. 2015 Assessing the capability of the SWAT model to simulate snow, snow melt and streamflow dynamics over an alpine watershed. *J. Hydrol.* 531, 574–588.

Huffman, G.J., Adler, R.F., Bolvin, D.T., Gu, G., Nelkin, E.J., Bowman, K.P., Hong, Y., Stocker, E.F. and Wolff, D.B. 2007 The TRMM Multisatellite Precipitation Analysis (TMPA): Quasi-global, multiyear, combined-sensor precipitation estimates at fine scales. *J. Hydrometeorol.* 8 (1), 38–55.

Janowiak, J.E., Joyce, R.J. and Yarosh, Y. 2001 A real-time global half-hourly pixel-resolution infrared dataset and its applications. *Bull. Am. Meteorol. Soc.* 82 (2), 205–217.
Joyce, R.J., Janowiak, J.E., Arkin, P.A. and Xie, P. 2004 CMORPH: A method that produces global precipitation estimates from passive microwave and infrared data at high spatial and temporal resolution. *J. Hydrometeorol.* 5 (3), 487–503.
Koycegiz, C. and Buyukyildiz, M. 2019 Calibration of SWAT and two data-driven models for a data-scarce mountainous headwater in Semi-Arid Konya Closed Basin. *Water* 11 (1).
Nash, J.E. and Sutcliffe, J.V. 1970 River flow forecasting through conceptual models part I - A discussion of principles. *J. Hydrol.* 10 (3), 282–290.
S.L. Neitsch, J.G. Arnold, J.R. Kiniry & J.R. Williams 2011 *Soil and Water Assessment Tool User's Manual Version 2005.* Texas Water Resources Institute, TEMPLE, TEXAS.
Peterson, T.C. and Vose, R.S. 1997 An Overview of the Global Historical Climatology Network Temperature Database. *Bull. Am. Meteorol. Soc.* 78 (12), 2837–2849.
Rahman, K., Maringanti, C., Beniston, M., Widmer, F., Abbaspour, K. and Lehmann, A. 2013 Streamflow Modeling in a Highly Managed Mountainous Glacier Watershed Using SWAT: The Upper Rhone River Watershed Case in Switzerland. *Water Resour. Manag.* 27 (2), 323–339.
Tuo, Y., Duan, Z., Disse, M. and Chiogna, G. 2016 Evaluation of precipitation input for SWAT modeling in Alpine catchment: A case study in the Adige river basin (Italy). *Science of the Total Environment* 573, 66–82.
Tuo, Y., Marcolini, G., Disse, M. and Chiogna, G. 2018 Calibration of snow parameters in SWAT: comparison of three approaches in the Upper Adige River basin (Italy). *Hydrol. Sci. J.* 63 (4), 657–678.
Wan, Z. 2014 New refinements and validation of the collection-6 MODIS land-surface temperature/emissivity product. *Remote Sens. Environ.* 140, 36–45.

NUMERICAL ASSESSMENT OF AN IMPROVED HYDRODYNAMIC VORTEX SEPARATOR FOR STORMWATER TREATMENT

MAHAVEER [1*], Piotr ZIMA [1]

[1] *Faculty of Civil and Environmental Engineering, Gdańsk University of Technology, Narutowicza street 11/12, 80-233 Gdańsk, Poland*

E-mail: mahaveer.mahaveer@pg.edu.pl

E-mail: piotr.zima@pg.edu.pl

[*] *Corresponding author*

Abstract

Urbanization and climate change have significantly increased the volume and degraded the quality of stormwater entering receiving water bodies. Hydrodynamic vortex separators (HDVS) are effective devices for removing suspended solids from urban runoff, but their performance depends heavily on internal geometric configuration. This paper presents a numerical assessment of an HDVS design to evaluate its hydrodynamic characteristics and particle capture efficiency. Three-dimensional CFD simulations were performed using the Reynolds Stress Model (RSM) for turbulence closure and a Eulerian-Eulerian approach for multiphase flow. The proposed geometry was evaluated based on velocity distribution, tangential flow profile, and dispersed phase volume fraction. Quantitative analysis indicates a theoretical hydraulic residence time of 6.6 s and a calculated separation efficiency of 87.4% for 100 μm particles, with a mass balance closure error below 0.5%. The design achieves effective flow stabilization in the settling zone and high phase separation, providing a numerical basis for designing compact HDVS units for sustainable urban water management.

Key words

computational fluid dynamics, Reynolds Stress Model, multiphase flow, stormwater treatment, separation efficiency.

1 Introduction

Hydrodynamic vortex separators (HDVS) have become indispensable unit operations in urban stormwater management and municipal wastewater treatment to reduce the discharge of solids and pollutants into receiving water bodies (He et al., 2022). Inspired by natural rotational phenomena (i.e., hurricanes, and whirlpools), the HDVS is effective in separating particulate matter, suspended solids, and emerging pollutants from liquid streams (Kwon et al. 2012; Meroney et al., 2016; Lekuona-Orkaizagirre et al., 2025; Mahaveer et al., 2025). In addition to providing contaminant separation, the HDVS generates sufficient centrifugal force to move particulates or suspended solids toward the walls for removal. While HDVS have been implemented extensively throughout the world for many years, the overall performance of the HDVS tends to decrease as the inflow rate increases. Increased inflow rates cause reduced residence time and increased decay of the swirl generated within the HDVS. Thus, increasing the efficiency of pollutant removal from stormwater at higher inflow rates presents a formidable challenge (He et al., 2022; He et al., 2024). Although many HDVS prototype designs have been evaluated via laboratory studies and full-scale demonstrations over the past few decades, the current commercial HDVS designs continue to rely upon empirical relationships derived from the specific geometry of individual manufacturers. Therefore, a need exists for generalizable design equations that can predict removal efficiency based on design inflow rates, fluid and particle characteristics, and key geometric features of the unit (Mahaveer and You, 2021). Recent reviews have identified the key factors governing vortex separator performance, including inlet-outlet configurations,

internal baffling, vortex-forming elements, and dimensional similarity principles (Mahaveer and Zima, 2026). The HDVS is used to remove suspended solids, particulate matter, and emerging pollutants such as microplastics from stormwater and industrial wastewater. As compact, high-efficiency treatment systems become increasingly necessary in urban drainge systems, there is a need for improved HDVS designs assessment supported by numerical models. the aim of this study are : (i) to analyze the internal flow field and disphered phase behavior of an HDVS using an Eulerian-Eulerian multi-phase flow model, and (ii) to quantify the hydrodynamic indicators governing particle capture, including tangential velocity decay, axial flow reversal, hydraulic residence time, short-circuiting fraction, and dispersed phase mass balance, for an HDVS geometry configured using literature-recommended dimensional ratios (Mahaveer and Zima, 2026). The results establish a numerical basis for HDVS design evaluation applicable to municipal and industrial pretreatment systems.

2 Methods

The approach combines a three-dimensional geometric model of the HDVS with the use of advanced turbulence and multiphase modelling approaches. In particular, fluid turbulence is simulated with the Reynolds Stress Model (RSM) to enable the correct prediction of the anisotropic turbulence and strong rotational flow fields typical of vortex separators. The Eulerian-Eulerian approach is used to simulate the flow in the HDVS as a turbulent, incompressible two-phase flow. In this model, the continuous (water) and dispersed (sediment) phases are considered as interpenetrating continua, each with its own set of momentum and continuity equations with a common pressure field. The dispersed phase was assigned a granular viscosity of 0.1 Pa·s. Sensitivity analyses indicated that values in the range 0.01-1.0 Pa·s had negligible effect (< 2%) on predicted separation efficiency, while values below 0.01 Pa·s introduced numerical instability due to excessive phase segregation. The value of 0.1 Pa·s was selected as it provided the best balance between numerical stability and computational efficiency. In this way, the distribution of the phases, the exchange of momentum between the phases, and the collection efficiency of the particles can be predicted as a function of the geometric and operational parameters of the HDVS.

2.1 Geometric model

Literature-recommended dimensional ratios were used for the geometric configuration of the HDVS in order to improve the centrifugal separation effect and minimize short-circuiting. The primary separation chamber is a cylindrical separation tank with a diameter of 500 mm and a total height of 810 mm, resulting in an aspect ratio (H/D) of 1.62, a value reported in the literature as favourable for the formation of a stable vortex in the separation tank. The tangential inlet pipe is 160 mm in diameter to provide a strong initial swirl. A central vortex finder (overflow pipe) of the same diameter is located at the top to remove the clarified fluid. The underflow section includes a baffle plate to facilitate the collection and removal of coarse particles that settle. The full geometric configuration can be seen in (Figure. 1), and key geometric parameters are summarized in Table 1.

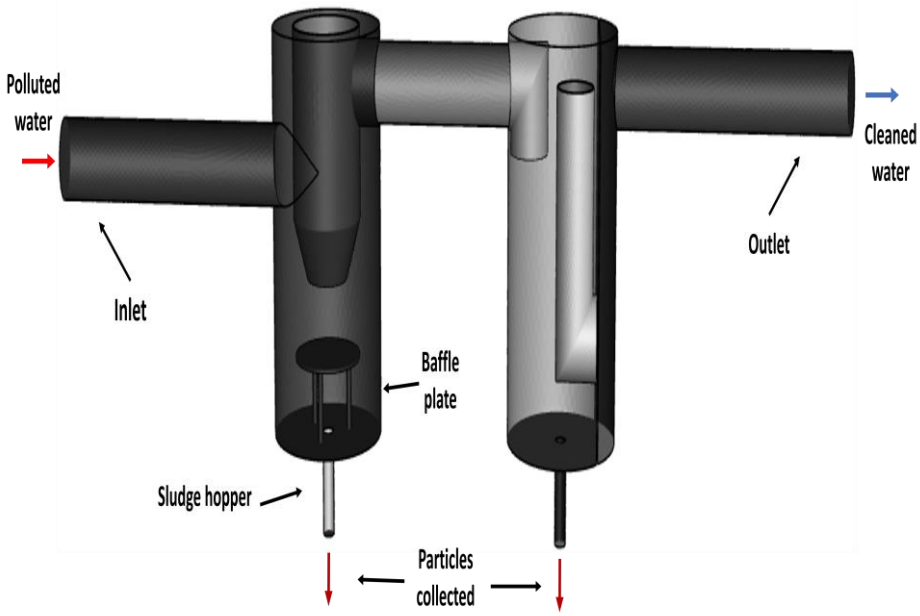


Figure 1. Geometric design of the HDVS.

Table 1. Geometric parameters.

Parameter	Value
Tank diameter (D)	500 mm
Total height (H)	810 mm
Inlet pipe diameter (D_{in})	160 mm
Overflow pipe diameter (D_o)	160 mm
Aspect ratio (H/D)	1.62

2.2 Model discretization

To capture the complex, highly rotational flow within the separator, a high-quality three-dimensional mesh was created using ANSYS Meshing software, which included inflation layers of tetrahedral elements. The mesh density was increased in regions of high velocity gradients, specifically around the tangential inlet, inner cylinder wall, and overflow outlet zone. The final computational mesh, shown in (Figure 2), contained approximately 1.0×10^6 elements, chosen to achieve a good compromise between the resolution of the flow field and computational cost.



Figure 2. Computational mesh of the HDVS.

2.3 Model verification and validation

2.3.1 Mesh independence

Three mesh densities (0.6×10^6, 1.0×10^6, and 2×10^6 elements) were tested. The peak tangential velocity on the mid-height plane and the underflow phase-2 mass flux varied by less than 3% between the medium (adopted) and fine mesh, confirming mesh independence. Grid Convergence Index (GCI) values for tangential velocity and separation efficiency are below 4%.

2.3.2 Turbulence closure justification

The Reynolds Stress Model (RSM) was selected over the k-ε and k-ω models because it resolves the anisotropic Reynolds stresses of the Rankine-type combined vortex that governs the flow inside the HDVS. Previous validation against Laser Doppler Anemometry measurements in hydrocyclones has shown that RSM provides superior prediction of tangential and axial velocity profiles compared to isotropic closures (Delgadillo and Rajamani, 2005). RSM has also been identified as the required closure for capturing swirl-induced anisotropy in CFD simulations of hydrocyclone-type separators (Narasimha et al. 2007), and a recent review of HDVS modelling confirmed it as the most reliable RANS-based closure for strongly swirling separator flows when combined with Eulerian-Eulerian multiphase formulations (Mahaveer et al., 2025). On this basis, RSM combined with the Eulerian-Eulerian multiphase formulation is applied in the present work.

2.3.3 Qualitative validation against literature

The predicted flow field reproduces the expected features of swirl separator flows: a two-region Rankine vortex composed of an inner forced-vortex core and an outer free-vortex annulus, reverse axial flow with a downward outer annulus and an upward inner core, and tangential velocity decay along the chamber height. These features are consistent with classical descriptions of swirl-based separators reported in the literature (Hsieh and Rajamani, 1988; Chine and Concha, 2000), supporting the physical validity of the simulated flow structure. Direct quantitative comparison with experimental measurements is reserved for future work pending prototype testing.

2.4 Governing equations

2.4.1 Eulerian-Eulerian multiphase model

In the Eulerian-Eulerian approach, the continuous water phase and the dispersed sediment phase are treated as interpenetrating continua. This approach solves separate continuity and momentum equations for each phase while assuming a single shared pressure field. The continuity equation for phase q is expressed as:

$$\frac{\partial}{\partial_t}\left(\alpha_q \rho_q\right) + \nabla \cdot \left(\alpha_q \rho_q \overrightarrow{v_q}\right) = 0 \tag{1}$$

where α_q, ρ_q and $\overrightarrow{v_q}$ are the volume fraction, density, and velocity vector of q phase respectively. The volume fractions of all phases are constrained by: $\sum_q \alpha_q = 1$

The momentum conservation equation for phase q is:

$$\frac{\partial}{\partial_t}\left(\alpha_q \rho_q \overrightarrow{v_q}\right) + \nabla \cdot \left(\alpha_q \rho_q \overrightarrow{v_q}\,\overrightarrow{v_q}\right) = -\alpha_q \nabla_p + \nabla \cdot \overline{\overline{\tau_q}} + \alpha_q \rho_q \vec{g} + \vec{F}drag, q + \vec{F}lift, q + \vec{F}vm, q \tag{2}$$

where p is the pressure shared by all the phases, $\overline{\overline{\tau_q}}$ is the phase stress-strain tensor, and $\vec{g}$ is the gravitational acceleration vector. The terms $\vec{F}_{drag,\ q}$, $\vec{F}_{lift,\ q}$, and $\vec{F}_{vm,\ q}$, represent the interphase drag, lift and virtual mass forces respectively. The interphase momentum exchange is dominated by the drag force, which is calculated as:

$$\vec{F}drag, q = K_{pq}\left(\overrightarrow{v_p} - \overrightarrow{v_q}\right) \tag{3}$$

where K_{pq} is the interphase momentum exchange coefficient, computed using the Schiller-Naumann drag model:

$$K_{pq} = \frac{\left(\alpha_p \alpha_q \rho_q f\right)}{\tau_p} \tag{4}$$

where $\tau_p = \frac{\rho_p d_p^2}{18\,\mu_q}$, is the particle relaxation time, and f is the drag function defined as:

$$f = \frac{C_D Re_p}{24} \tag{5}$$

The drag coefficient C_D, and particle Reynolds number Re_p are given by:

$$C_D = \begin{cases} \frac{24}{Re_p}\left(1 + 0.15\, Re_p^{0.687}\right) & Re_p < 1000 \\ 0.44 & Re_p \geq 1000 \end{cases} \tag{6}$$

$$Re_p = \frac{\rho_q \left|\overrightarrow{v_q} - \overrightarrow{v_p}\right| d_p}{\mu_q} \tag{7}$$

2.4.2 Reynolds stress model (RSM)

The RSM is applied to the continuous phase (water) to resolve the highly anisotropic turbulence generated by strong swirl and secondary flows inside the HDVS. Unlike isotropic eddy-viscosity models, RSM solves individual transport equations for each Reynolds stress component, accurately capturing streamline curvature and rotational effects. The steady-state transport equation for the Reynolds stress tensor $\overline{u_i}\overline{u_j}$ is written as:

$$\frac{\partial}{\partial x_k}\left(\rho \overline{u_k}\,\overline{u_i}\overline{u_j}\right) = P_{ij} + \phi_{ij} + D_{ij} - \varepsilon_{ij} + F_{ij} \tag{8}$$

where P_{ij}, ϕ_{ij}, D_{ij}, ε_{ij} and F_{ij} represent the production, pressure-strain, diffusion, dissipation terms, and rotation term respectively. The $\frac{\partial}{\partial x_k}\left(\rho\overline{u_k}\ \overline{u_i'u_j'}\right)$ is the mean convection (or transport by mean flow). This approach provides high accuracy in resolving tangential and axial velocity profiles and recirculation zones within the HDVS.

2.5 Boundary conditions

A uniform velocity inlet was used at the tangential inlet with a given initial volume fraction of the dispersed (particulate) phase. All solid walls were modeled as a no-slip condition, and the central overflow and bottom underflow were modeled as pressure outlets with gauge pressure set to zero. The simulation parameters are summarized in Table 2. The SIMPLE algorithm with second-order upwind discretization of the momentum, turbulence, and volume fraction transport equations was used to obtain steady-state solutions for pressure-velocity coupling. Convergence was declared when normalized residuals fell below 10^{-4} for all equations.

Table 2. Operating conditions and physical properties.

Properties	Value
Inlet velocity	1.2 m/s
Operating pressure	101,325 Pa
Gravitational acceleration	9.8 m/s^2
Water density	1000 kg/m^3
Water viscosity	0.001kg m^{-1} s^{-1}
Sand density	2650 kg/m^3
Sand viscosity	1.7894×10^{-5} kg^{-1} s^{-1}
Sand particle diameter	100 µm
Inlet volume fraction (Sand)	5%

2.6 Flow regime characterization

The flow regime within the HDVS is characterized by the inlet Reynolds number ($R_e = \frac{\rho V_{in}\, D_{in}}{\mu} \approx 1.92 \times 10^5$), Froude number ($Fr = \frac{V_{in}}{\sqrt{gD_{tank}}} \approx 0.54$), and Stokes number ($Stk = \frac{\tau_p V_{in}}{D_{tank}} \approx 3.5 \times 10^{-3}$), which quantify the relative importance of inertial, gravitational, and particle response effects, respectively. The high Reynolds number ($Re > 4000$), confirms fully turbulent flow. The Froude number ($Fr < 1$), indicates that gravitational forces remain significant relative to the inlet inertia. The low Stokes number ($Stk < 1$), suggests strong fluid-particle coupling, meaning particles closely follow the fluid streamlines; consequently, separation is achieved primarily through cumulative centrifugal drift within the vortex rather than high-inertia impaction.

2.6.1 Velocity distribution

The velocity field in three-dimensional swirling flow consists of tangential, axial, and radial components. The resultant velocity magnitude contours are shown in (Figure. 3). The tangential inlet maintains a maximum velocity of 1.20 m/s, corresponding to a volumetric flow rate of 0.0241 m³/s. The velocity drops significantly upon entering the main chamber, creating a low-velocity bulk zone favourable for particle settling. Using the active separation volume of 0.159 m³ and the inlet flow rate, the theoretical hydraulic residence time is ($\tau = V/Q = 0.159/0.0241 = 6.6$ s). High-velocity regions near the underflow sump and overflow pipe indicate flow acceleration and potential short-circuiting paths. Integration of axial velocity profiles reveals that short-circuiting flow accounts for the total inlet flow. Mass balance verification shows the inlet dispersed phase mass flow rate (3.196 kg/s) matches the combined underflow (2.793 kg/s) and overflow (0.403 kg/s) rates, with a closure error below 0.5%, confirming numerical accuracy.

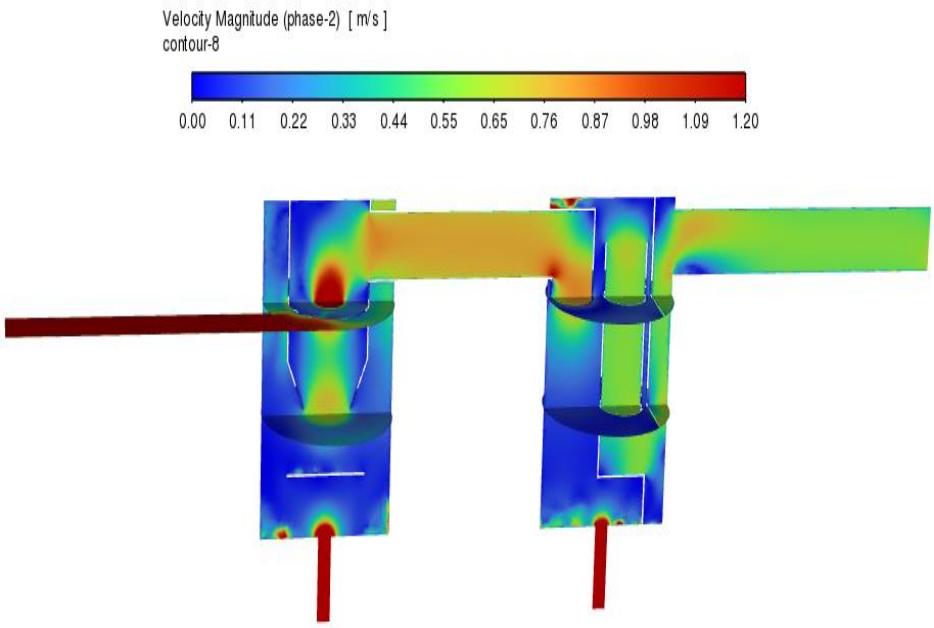


Figure 3. Velocity magnitude contour of the vortex separator.

2.6.2 Tangential velocity analysis

The tangential velocity distribution in the longitudinal plane is shown in (Figure. 4). Maximum tangential velocities occur at the inlet (1.20 m/s) with a decay to 0.36-0.64 m/s at mid-height and a further reduction to below 0.18 m/s in the lower sump zone. Minimal tangential motion in the lower sump (v_θ < 0.18 m/s) indicates effective swirl dissipation. This distribution ensures particle separation through strong centrifugal forces in the upper chamber (v_θ = 0.64-1.20 m/s), promoting radial migration of particles toward the walls, while the low-tangential-velocity underflow region enables deposited particles to settle without re-entrainment

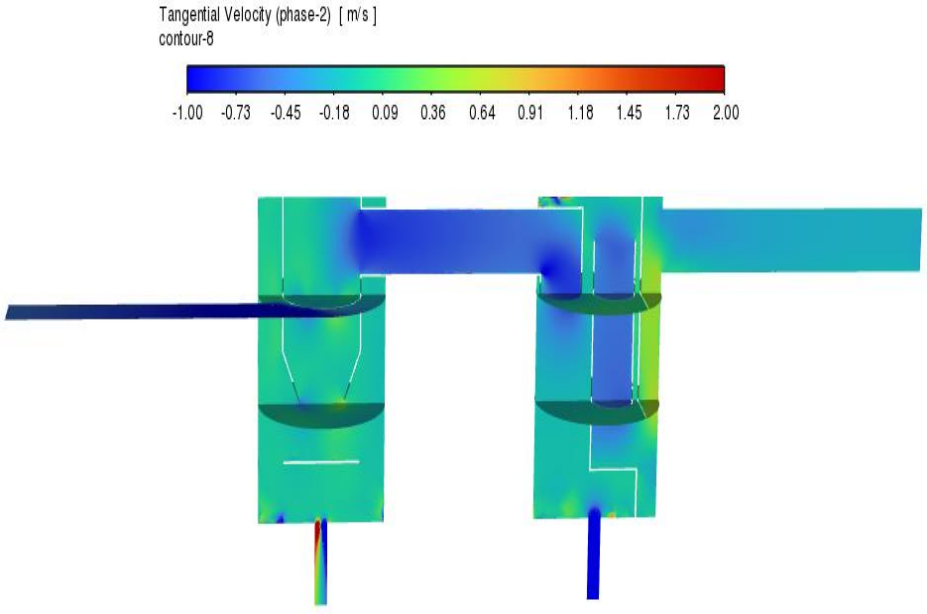


Figure 4. Tangential velocity contour on the longitudinal plane of the vortex separator.

2.6.3 Axial velocity analysis

Figure. 5 shows the axial velocity distribution in horizontal cross-sectional planes of the dispersed phase. The outer annular region exhibits net negative axial velocities (-0.46 to -1.0 m/s), indicating downward flow that transports captured particles toward the underflow sump. The inner core displays net positive

axial velocities (0.35 to 0.89 m/s), driving clarified fluid upward to the central overflow pipe. The axial velocity reversal boundary, where Vz = 0, is located at r/R ≈ 0.4, demarcating the capture zone from the short-circuiting core.

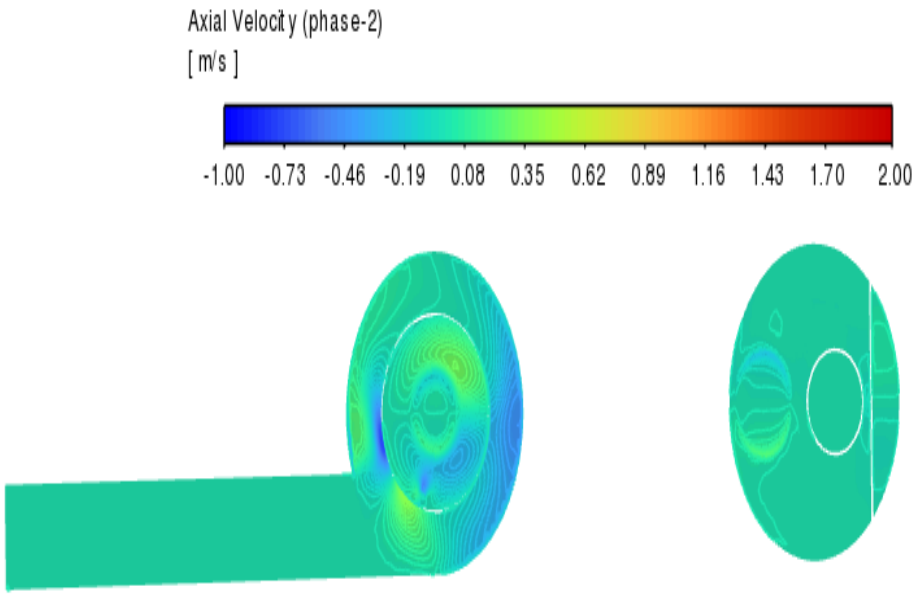


Figure 5. Axial velocity contour on a horizontal cross-section of the vortex separator.

2.6.4 Radial velocity analysis

Figure. 6 displays the radial velocity distribution of the dispersed phase in cross-sectional planes. The outer annular zone exhibits low radial velocities below 0.36 m/s, confirming that centrifugal forces dominate particle migration toward the walls. The inner core shows distinct radial gradients with peak values of 1.27-2.00 m/s near the inlet, decaying to below 0.55 m/s at mid-height. The radial velocity at the vortex core (r/R < 0.2) is suppressed below 0.18 m/s, reducing central turbulence and stabilizing the up-flow.

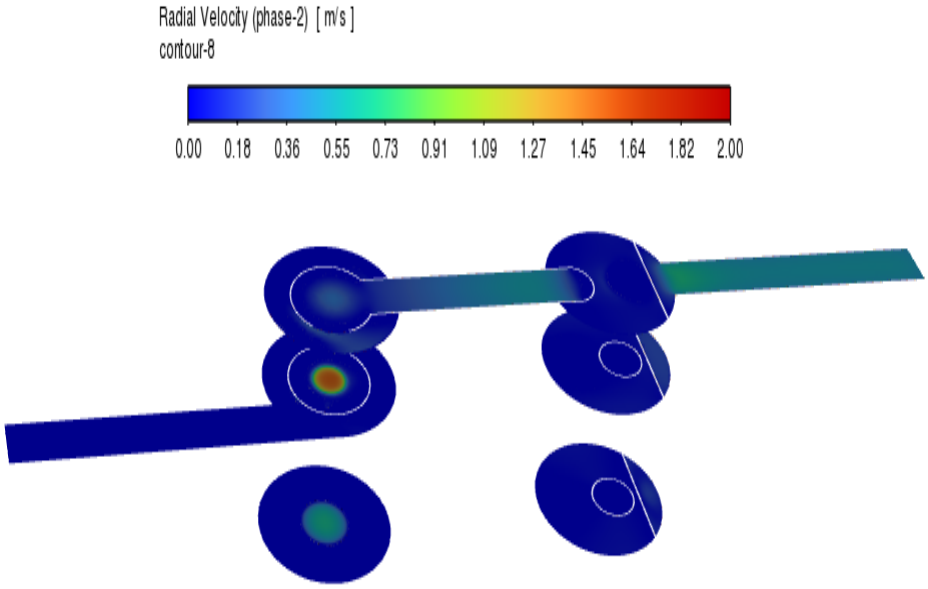


Figure 6. Radial velocity contours across the horizontal planes of the vortex separator.

2.7 Volume fraction profile

Figure. 7 illustrates the dispersed phase volume fraction distribution. The vertical profile (Figure 7a) demonstrates effective phase separation, characterized by a dilute concentration in the main chamber and a dense sediment layer in the bottom sump, reaching a maximum volume fraction of 0.20. The horizontal cross-sections (Figure 7b) confirm low particle dispersion in the upper zones and high concentration in the lower collection areas. This distinct stratification indicates that centrifugal and gravitational forces are efficient in routing solid particles into the collection space.

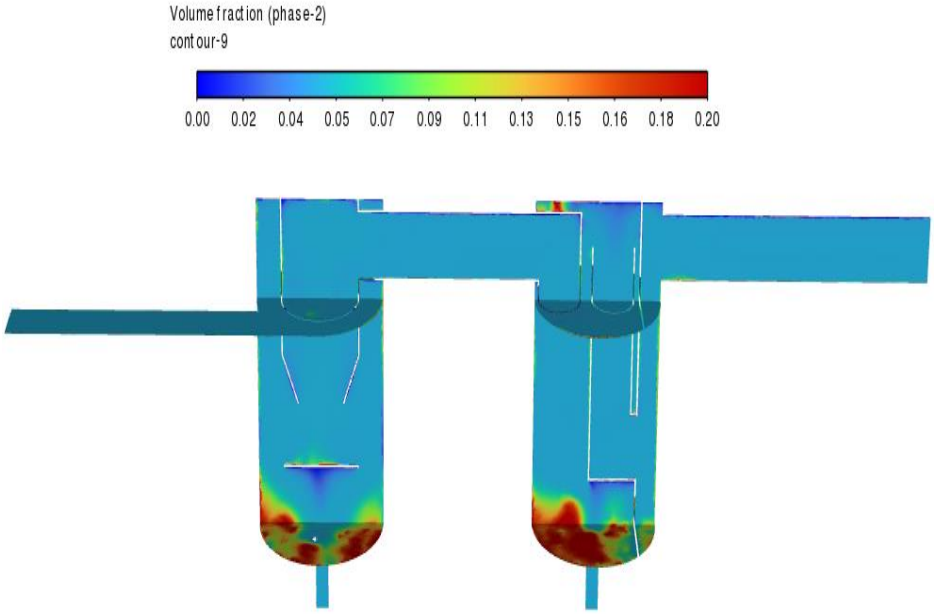


Figure 7a. Volume fraction contours of the dispersed phase across the vertical profile.

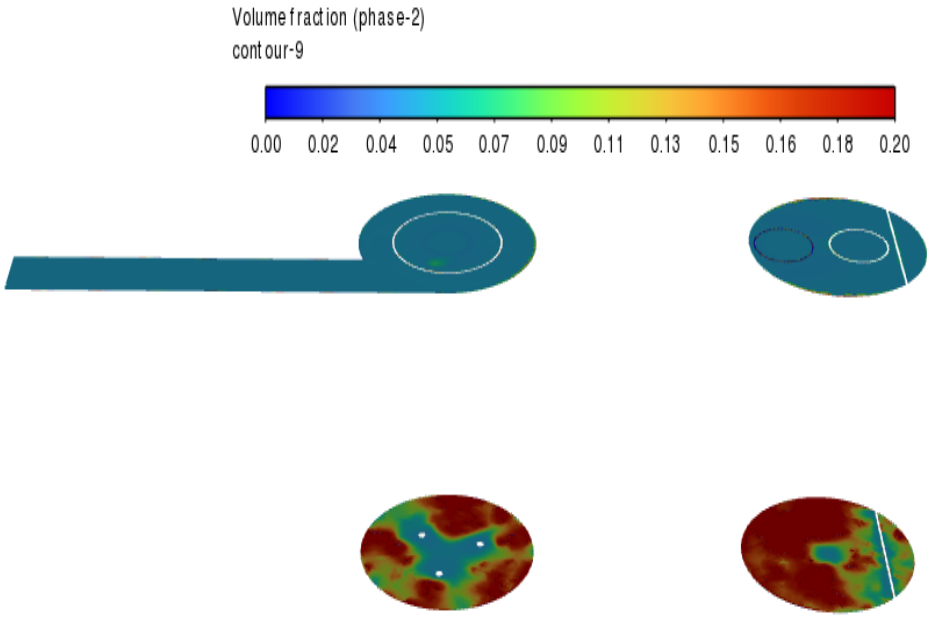


Figure 7b. Volume fraction contours of the dispersed phase across the horizontal cross-section.

2.7.1 Separation efficiency

The overall separation efficiency η is defined as the ratio of the mass flow rate of particles captured in the underflow sump to the total mass flow rate of particles entering through the inlet:

$$\eta = \frac{\int A_{underflow} \alpha_p \rho_p (\vec{v} . \vec{n})\, dA}{\int A_{inlet} \alpha_p \rho_p (\vec{v} . \vec{n})\, dA} \times 100\ \% \quad (9)$$

where α_p is the local volume fraction of the dispersed phase, ρ_p is the particle density, and $\vec{n}$ is the outward-facing normal vector at each boundary surface. The separation efficiency for (100 μm) particles, calculated using the (Equation 9), is 87.4%. This value was obtained from the ratio of the underflow dispersed phase mass flow rate (2.793 kg/s) to the inlet mass flow rate (3.196 kg/s), with 0.403 kg/s exiting through the overflow. The mass balance closure error is below 0.5%, confirming numerical conservation.

3 Discussion

The numerical analysis demonstrates effective phase separation through a stable low-velocity bulk zone and well-defined flow reversal patterns. The calculated separation efficiency represents a theoretical prediction based on the simulated mass fluxes at the underflow and inlet boundaries. Direct comparison with alternative geometries was not performed within this study, as the focus was on characterizing the flow field and separation performance of the specific HDVS configuration evaluated. The results provide a validated numerical framework for understanding the hydrodynamics of vortex separation, though experimental validation is required to confirm absolute performance metrics. Future work should include physical testing against the Ecol-Unicon Gdańsk prototype to establish empirical validation of the numerical predictions.

4 Conclusion

This study demonstrates that effective phase separation and internal flow stability are achieved through the numerical assessment of the proposed HDVS geometry. The combination of the Eulerian-Eulerian model and the RSM accurately resolves the Rankine vortex and anisotropic turbulence required for particle separation. Quantitative analysis confirms a separation efficiency of 87.4% for 100 μm particles, driven by a stable low-velocity bulk zone (residence time of 6.6 s). The primary significance of this research is establishing a clear relationship between the geometric configuration and dispersed phase accumulation at the underflow. These results provide a robust numerical basis for predicting HDVS performance, reducing reliance on physical prototyping and supporting the development of scalable, high-efficiency stormwater treatment systems.

Acknowledgements

The authors gratefully acknowledge the support, resources, and encouragement provided by the Gdańsk University of Technology, Poland. The design dimensions and prototype of the vortex separator were provided by Ecol-Unicon Gdańsk, for which we are also grateful.

References

Chiné B. and Concha, F. 2000 Flow patterns in conical and cylindrical hydrocyclones, *Chemical engineering journal*, 80, pp. 267–273, doi: 10.1016/S1383-5866(00)00101-5.
Delgadillo J. A. and Rajamani, R. K. 2005 A comparative study of three turbulence-closure models for the hydrocyclone problem, *Int. J. Miner. Process*. 77, pp. 217–230, doi: 10.1016/j.minpro.2005.06.007.
He, C., Chittibabu, P., Nguyen, D. and Rochfort, Q. 2022 Investigating the Effectiveness of Vortex-Enhanced Particle Settling in a Hydraulic Separator Using Physical Modelling, *Journal of Environmental Engineering*, 148, doi: 10.1061/(asce)ee.1943-7870.0002004.
He, C., Chittibabu, P., Nguyen, D. and Rochfort, Q. 2024 Particle separator with vortex claw: an efficient and new technology, *Water Science and Technology*, 89, pp. 1441–1453, doi: 10.2166/wst.2024.072.

Hsieh K. T. and Rajamani, K. 1988 Phenomenological model of the hydrocyclone: Model development and verification for single-phase flow, *Int. J. Miner. Process*., 22, pp. 223–237, doi: 10.1016/0301-7516(88)90065-8.
Kwon, K. H., Kim, S. W., Kim, L. H., Kim, J. H., Lee, S. and Min, K. S. 2012 Particle removal properties of stormwater runoff with a lab-scale vortex separator, *Desalination Water Treat*. 38, pp. 349–353, doi: 10.5004/dwt.2012.3589.
Lekuona-Orkaizagirre, A., Meaurio, M., Madrazo-Uribeetxebarria, E., Garmendia Antín, M. and Gredilla, A. 2025 Assessment of the influence of hydrodynamic vortex separators (HDVS) on runoff water quality in a real urban environment, *Journal of Water Process Engineering*, 79, doi: 10.1016/j.jwpe.2025.109057.
Mahaveer and You, X. Y. 2021 Optimization of hydrodynamic vortex separator for removal of sand particles from storm water by computational fluid dynamics, *Desalination Water Treat*., 223, pp. 54–70, doi: 10.5004/dwt.2021.27099.
Mahaveer, Zima, P., Qaisrani, M. A. and Kalwar, M. A. 2025 *Review of current approaches and gaps in modeling hydrodynamic vortex separator for enhanced separation efficiency*, Elsevier B.V. doi: 10.1016/j.dwt.2025.101426.
Mahaveer and Zima, P. 2026 Progress and key influencing factors in vortex separator technologies: A comprehensive review on optimization and similarity principles, *Water Res*., 305, p. 126531, doi: 10.1016/j.watres.2026.126531.
Meroney, R. N. and Sheker, R. E. 2016 Removing Grit During Wastewater Treatment:CFD Analysis of HDVS Performance, *Water Environment Research*. 88, pp. 438–448, doi: 10.2175/106143015x14212658614478.
Narasimha, M., Brennan, M. and Holtham, P. N. 2007 A Review of CFD Modelling for Performance Predictions of Hydrocyclone, *Engineering Applications of Computational Fluid Mechanics*, 1, pp. 109–125, doi: 10.1080/19942060.2007.11015186.

MODELLING OF SNOWMELT USING SWAT IN THE CASE OF THE UPPER DRAVA CATCHMENTS

Karlo LESKOVAR[1*], Damir BEKIĆ [2], Hrvoje MEAŠKI[1], Ranko BIONDIĆ[1]

[1] *University of Zagreb Faculty of Geotechnical Engineering, Croatia*

E-mail: *karlo.leskovar@gfv.unizg.hr*

E-mail: hrvoje.measki@gfv.unizg.hr

E-mail: ranko.biondic@gfv.unizg.hr

[2] *University of Zagreb Faculty of Civil Engineering, Croatia*

E-mail: damir.bekic@grad.unizg.hr

[*] *Corresponding author*

Abstract

The SWAT (Soil Water Assessment Tool) is a physically based, semi-distributed, watershed simulation model initially developed for comprehensive modelling of the impacts of management practices on water yield, sediment yield, crop growth, and agricultural chemical yields in large, ungagged basins. SWAT has also been shown to be an effective tool for snowmelt modelling; however, intensive data collection and data file creation efforts are mandatory. ArcSWAT was developed as a GIS (Geographic Information System) add-on to simplify the user interface for SWAT model development and the process of extracting parameter values and necessary input data from map layers and databases. The hydrologic processes calculated in the model are precipitation, interception, surface runoff, soil and root zone infiltration, evapotranspiration, soil and snow evaporation and groundwater flow. In SWAT, the modelling domain is delineated into subbasins, and later, based on unique Land Use/Land Cover (LULC), soil characteristics and digital elevation model (DEM) into Hydrologic Response Units (HRU). The water content of any HRU is represented as soil water content ΔSW which is calculated based on the precipitation P, runoff Q, evapotranspiration ET, deep percolation DP, return flow QR, with all units being represented as height of water in mm. Snowpack accumulation and snow in general, in SWAT, are considered as Snow Water Equivalent (SWE) of the snowpack, which denotes the amount of melted water in mm from a given amount of snow. SWE gets increased with snowfall (precipitation treated as snow), while being reduced via snowmelt and snow evaporation. Snow accumulation and the precipitation type depend on the average air temperature and catchment characteristics. Since in mountainous basins the network of meteorological gauging stations is often scarce, SWAT uses a lapse rate method in order to account for precipitation amount and air temperature changes with elevation change. Snowmelt is calculated by the degree-day method, where the melting coefficient of snow is calculated based on time (day of the year) and maximum and minimum melting factors. This paper provides detailed insights into the snow melting and accumulation processes within SWAT while emphasising potential drawbacks of the method. The pilot area are the headwaters of the Drava River basin in the Italian and Austrian Alps.

Key words

hydrological model; SWAT; snowmelt; snow water equivalent; mountainous catchments; Drava River

1 Introduction

Snow accumulation and snowmelt are among the dominant hydrological processes governing runoff generation in mountainous catchments. In alpine environments, seasonal snow storage acts as a natural reservoir that controls the timing and magnitude of river discharge, making reliable simulation of snow processes essential for water resources management, hydropower production, flood forecasting, and climate change impact assessments. However, accurate modelling of snow dynamics is often challenged by complex topography, strong elevation gradients, and limited availability of meteorological observations.

Physically-based hydrological models have become important tools for investigating runoff formation in such environments. Among them, the Soil and Water Assessment Tool (SWAT) has been widely applied for watershed-scale hydrological simulations and has demonstrated satisfactory performance in snow-dominated basins. The model incorporates snow accumulation and melt routines based on temperature-index methods and allows the representation of elevation-dependent variations in precipitation and air temperature through lapse-rate corrections.

The objective of this study is to present the implementation of the SWAT model for simulating snowmelt processes in the upper catchments of the Drava River located in the Austrian and Italian Alps. Particular emphasis is placed on the representation of snow accumulation and melt processes within SWAT, the preparation of input data required for mountainous catchments, and the evaluation of model performance.

2 Methods

The Soil Water Assessment Tool (SWAT) is a physically-based, semi-distributed watershed simulation model initially developed by (Arnold et al. 1998; Neitsch et al. 2011) for comprehensive modelling of the impacts of management practices on water yield, sediment yield, crop growth and agricultural chemical yields in large ungagged basins (Arnold et al. 1998). It can also be used for snowmelt modelling, as proven by several investigations, i.e. Fontaine *et al.* (Fontaine et al. 2002), Grusson *et al.* (Grusson et al. 2015) and Tuo *et al.* (Tuo et al. 2018). As a result of intensive data collection and data file creation efforts involved with large-scale modelling, SWAT is designed to use GIS (Geographic information system) to extract parameter values and input data from map layers and databases (Fontaine et al. 2002). Hydrologic processes calculated in the model are precipitation, interception, surface runoff, soil and root zone infiltration, evapotranspiration and soil and snow evaporation and groundwater flow, described in eq. (1) (Arnold et al. 1998; Fontaine et al. 2002; Neitsch et al. 2011):

$$\Delta SW = (P - Q - ET - DP - QR) \tag{1}$$

Where *ΔSW* is the soil water content, *P* is precipitation, *Q* is the runoff, *ET* evapotranspiration, *DP* deep percolation, and *QR* is the return flow, all units in mm.

As snowmelt mainly depends on air temperature, Fontaine *et al.* (Fontaine et al. 2002) suggested creating a local temperature lapse rate following the experiences from other investigations involving snowmelt runoff modelling. The local basin mean lapse rate (dT/dZ) [°C/1000 m] is calculated as a regression from mean annual temperatures measured on weather stations over the basin for several years. The calculated temperature lapse rate is then multiplied by the difference in band midpoint elevation (Z_B) and station elevation (Z). The updated elevation band temperature (T_a) is then calculated following eq. (2) (Fontaine et al. 2002):

$$T_a = T + (Z_B - Z)\frac{dT}{dZ} \tag{2}$$

A similar approach is suggested for calculating the precipitation lapse rate since the model selects only one meteorological station for each subbasin. Precipitation lapse rate (dP/dZ) [mm/1000 m] is calculated as a regression when plotting precipitation data vs station elevation (Fontaine et al. 2002).

The adjusted precipitation value for each elevation band is then calculated following the eq. (3) (Fontaine et al. 2002):

$$P_B = P + (Z_B - Z)\frac{dP}{dZ} \tag{3}$$

The corrected elevation band temperature (eq. (1)) is then used to determine the precipitation type for each subbasin, when this temperature is below a critical temperature (SFTMP), all precipitation is considered as snow, a similar method is successfully applied in other investigations, i.e. (Martinec and Rango 1986).

Snowpack accumulation in SWAT is treated as snow water equivalent (SWE). For each timestep, SWE is calculated following eq. (4):

$$SWE_t = SWE_{t-1} + P_{SB} - M - E_s \tag{4}$$

where P_{SB} is snowfall, M is snowmelt and E_s is the snow sublimation (Fontaine et al. 2002). Rain is not considered in eq. (4), following the above statement that all precipitation during events with air temperature T_a bellow SFTMP is considered as snow. When T_a is higher than SFTMP, P_{SB} equals zero, and rain is not added to the SWE_t, rather it is considered as rain on bare ground. Meltwater M (or SNO_{mlt_t}) is only released when the snowpack exceeds a threshold temperature, commonly set as 0 °C. However, the temperature for the entire snowpack isn't the same, it's affected by multiple factors, such as air temperature, snowpack depth, exposure and snowpack density (Fontaine et al. 2002), and can be calculated following the eq. (5):

$$T_{snow_t} = T_{snow_{t-1}}(1.0 - TIMP) + T_a \times TIMP \tag{5}$$

Where T_{snow_t} is the updated snowpack temperature, TIMP is the coefficient that relates to the daily mean temperature T_a to snowpack temperature $T_{snow_{t-1}}$. Snowpack lag factor TIMP ranges from 0 (low dependency on air temperature, areas with deeper snowpack) to 1 (highly dependent on air temperature, sites with shallow snowpack). For shallow snowpacks, TIMP is usually chosen to be between 0.5 and 1 (Fontaine et al. 2002).

A strong correlation was found between maximum SWE and the point when air temperature reached 0 °C, therefore, Fontaine *et al.* (Fontaine et al. 2002) suggest using a melt coefficient (b_{mlt_t}) which defines the amount of meltwater (SNO_{mlt_t}) released, eq. (6):

$$SNO_{mlt_t} = b_{mlt_t} \times sno_{cov_t} \times \left(\left(\frac{T_{snow_t} + T_a}{2}\right) - SMTMP\right) \tag{6}$$

where sno_{cov_t} is the basin area fraction covered by snow on given day.

In mid-latitudes areas, like the Alps in Austria, solar radiation affects the snowmelt rate (Fontaine et al. 2002). Neitsch *et al.* (Neitsch et al. 2011) describe the melting coefficient b_{mlt_t} as a sine wave with its minimum occurring on 21st of December and its maximum occurring on 21st of June, Eq. (7):

$$b_{mlt_t} = \frac{SMFMX + SMFMN}{2} + \frac{SMFMX - SMFMN}{2} \cdot \sin\left[\frac{2\pi}{365}(t - 81)\right] \quad (7)$$

where the melt coefficient ranges from 0.20 to 0.60 cm/°C (Fontaine et al. 2002; Neitsch et al. 2011; Rango and Martinec 1995; Tuo et al. 2018).

2.1 Study area

The upper catchments of the Drava River consist of the actual Drava River source catchment with a size of 669 km^2, and the Isel River catchment with a catchment area of 1200.86 km^2 (Figure 1.), located in East Tyrol, located in East Tyrol, westwards and north-western of the city of Lienz, and eastwards of the Italian town of Dobiacco. The fluvio-glacial Drava River originates from the Sexten Dolomites between Dobbiaco and San Candido, at an elevation of 1450 m a.s.l. Before the city of Lienz, the Drava River has only three right tributaries, namely Sägerbach, Gailbach and Galitzenbach streams. The left tributaries are of a larger scale, i.e., the Villgratenbach stream and Kristeinbach stream. The length of the Isel River is 57.3 km, and is a glacier-fed river that originates from the Umbalkees glacier in the Hohe Tauern National Park near the summit of Rötspitze mountain at an elevation of approximately 2400 m a.s.l. Important left tributaries of the Isel are the Juaernbach stream and the Kaiser Bach stream, which feeds the river with water from the Großglockner peak area. The most significant right tributary is the Schwarzach stream from the Defereggental valley. Even though the Isel River is more prominent, with higher discharge, the river takes the name Drava after the confluence in the city of Lienz.

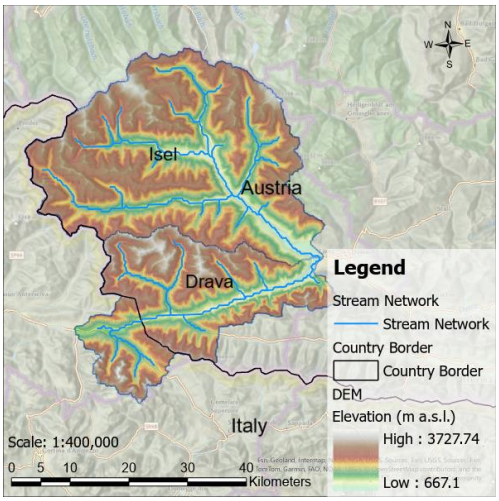


Figure 1. Upper Drava River catchments

2.2 Input data

The EU-DEM v1.1 (EU-DEM — Copernicus Land Monitoring Service 2009) digital elevation model (DEM) is a hybrid product based on Shuttle Radar Topography Mission (SRTM) and Advanced Spaceborne Thermal Emission and Reflection Radiometer (ASTER) Global Digital Elevation Model GDEM data fused by a weighted averaging approach. The ESDB v2 soil data 1 km x 1km raster files were acquired from the European Soil Data Centre (ESDAC). The dominant STU raster data was used according to FAO85 (Panagos et al. 2012) classification. CORINE (Coordination of information on the environment) Land Cover (CLC) (CORINE Land Cover — Copernicus Land Monitoring Service 2018) inventory was initiated in 1985 to standardize data collection on land use in Europe and to support environmental policy development. For this study, the CLC2006 version was used. CLC2006 is one of the Corine Land Cover (CLC) datasets produced within the Copernicus Land Monitoring Service frame, referring to land cover/land use status of the year 2006 +/- 1 year with a satellite accuracy of ≤ 25 m.
Meteorologically measured precipitation data and runoff data received from the GIS portal eHYD (https://ehyd.gv.at/) of the Austrian Bundesministerium für Nachhaltigkeit und Tourismus and sites of the Autonomous Province of Bozen/Bolzano – South Tyrol meteorological service

(https://weather.provinz.bz.it/download-data.asp). The eHYD portal provides meteorological data on precipitation – (P) [mm], snow depth – (SD) [cm] and fresh snow [cm] and hydrological related data like runoff - (Q) [m^3/s], water level [m], water temperature [°C] etc. The portal of the Province Bolzano provides daily timestep data on precipitation (P) [mm] and minimum (T_{min}) and maximum (T_{max}) air temperature [°C]. The used precipitation data from both portals and runoff data from eHYD are all available at daily timestep. All 16 precipitation gauges used in modeling the upper Drava catchments are presented in Figure 2.



Figure 2. Available precipitation gauging stations in the upper Drava catchments

The meteorological stations Toblach, St. Magdalena in Gsies, Antholz–Obertal and Prettau are located in Italy and are part of the Meteorological Service of the Province of Bolzano. The remaining 12 stations, namely: Sillian, Hochberg, Innervillgraten, Anras, Obertilliach, Kartitsch, Prägraten, Matrei in Osttirol, St. Johann im Walde, Felbertauerntunnel-Süd, Zettersfeld and Hopfgarten i.Def. are under the jurisdiction of the Austrian Bundesministerium für Nachhaltigkeit und Tourismus.

2.3 ArcSWAT and model creation

ArcSWAT is an extension of ArcGIS-ArcView software, serving as a graphical interface for easier development of SWAT hydrological models and simplifying the loading process of required input data. For example, to create a SWAT model, several types of data are needed: a digital elevation model (DEM), soil data, land use and land cover data and the climate inputs, precipitation, min and max air temperature, air humidity, solar radiation, and wind speed.

First, the DEM of the basin is loaded into ArcMap (ArcSWAT), as presented in Figure 3. (an example for the Isel river basin), then, based on the DEM, the software calculates the stream network, if errors exist, a polyline shapefile of the main river can be used to burn-in the network. Next, the watershed is delineated, and the subbasins are defined with parameters calculated.

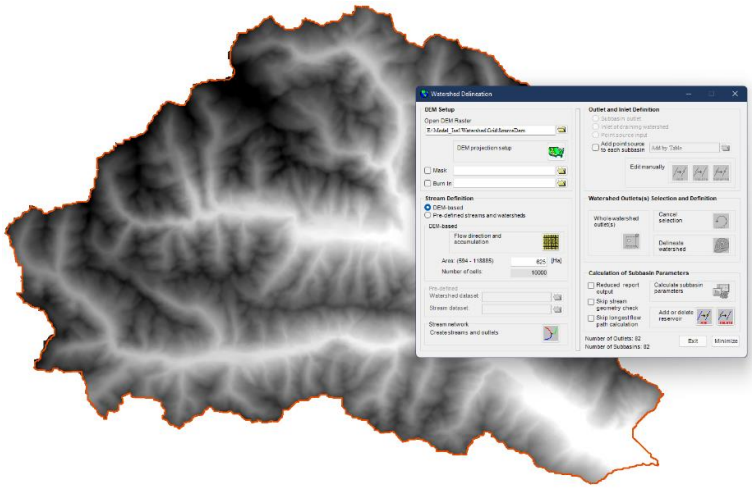


Figure 3. DEM loading and watershed delineation in ArcSWAT

Next, the Land Cover/Land Use data and soil type rasters are loaded, the loading and reclassification process for LULC data is shown in Figure 4. Since the Corine classification differs from the one used in the SWAT model, a user-defined lookup table is needed to reclassify the land use types correctly. Similarly, the process for loading FAO85 soil type data and reclassification is identical, with only the lookup table being prepared with different class pairs.

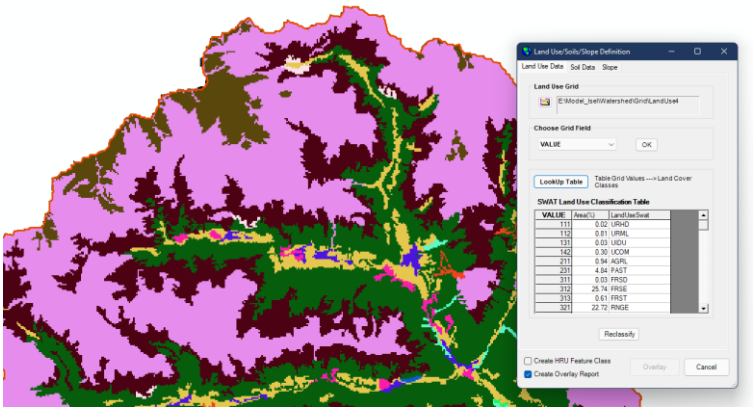


Figure 4. Example of LULC data loading and reclassification

Slope class definition is essential when creating a SWAT model in a mountainous basin. After researching several literature sources (Bieger et al. 2015; Yacoub and Foguet 2013), which investigated SWAT modelling in mountainous watersheds, 5 classes of slope provide a reasonable choice when creating the model. However, no clear pattern, or in other words, fixed values of slope ranges, can be found. Therefore, we decided to use the ranges presented in Table 1. The class ranges required by SWAT were determined using the Spatial analyst toolbox in ArcGIS. As SWAT divides slope in percentage, both percentage rise and degree slopes have been created for better understanding.

Table 1. Slope class ranges

Class	Slope (°)	Slope (% rise)
1	0 - 10	0 - 17
2	10 - 20	17 - 36
3	20 - 30	36 - 58
4	30 - 55	58 - 142
5	>55	>142



Figure 5. SWAT model setup

In the next step, the meteorological data is loaded through predefined and specially formatted .txt files. Next, the SWAT input tables are written with the weather data loaded, which are later used during the model run. Finally, the SWAT model setup is done Figure 5.), where the desired model properties are set. For this research, the model is run from 01.01.1991 to 31.12.2013, due to data availability, where the initial 3 years are selected as model warm-up period. The calculated discharge is formed as monthly averages. The 64-bit version of the SWAT.exe was used due to the operating system and the available CPU.

2.4 Model evaluation metrices

Two factors often associated with the quality of the fit between the calculated and observed data in SWAT are the P-factor and R-factor. P-factor varies from 0 to 1 and inherits the data contained in the 95PPU band, as for streamflow calibration, values > 0.7 or 0.75 are adequate (Abbaspour et al. 2015). The R-factor refers to the wideness of the 95PPU band, and the standard deviation of the measured parameter, values < 1.5, is considered adequate (Abbaspour et al. 2015). Additionally, (D. N. Moriasi et al. 2007) and other investigators suggest the coefficient of determination R^2 (Eq. (2)) and the Nash-Sutcliffe efficiency (NSE) as good model performance indicators when modelling with SWAT. R^2 is considered very sensitive to extreme values, such as peak flow therefore, it is a good indicator of goodness of fit when modelling snowmelt driven basins to get as good as possible volume and magnitude of spring peak flow.

$$R^2 = \left[\frac{\sum_{i=1}^{n} (Q_i - \bar{Q}) \left(Q'_i - \bar{Q}' \right)}{\sqrt{\sum_{i=1}^{n} (Q_i - \bar{Q})^2 \sum_{i=1}^{n} \left(Q'_i - \bar{Q}' \right)^2}} \right]^2 \tag{8}$$

where: Q_i is the observed runoff, $\bar{Q}$ the mean observed runoff, Q'_i is the predicted runoff and $\bar{Q}'$ the mean predicted runoff.

Typically, values greater than 0.5 mean a good fit of calculated and observed values (D. N. Moriasi et al. 2007). Therefore, the second statistical parameter we choose is the Nash-Sutcliffe efficiency (NSE) (3).

$$NSE = 1 - \frac{\sum_i (Q_i - Q'_i)^2}{\sum_i (Q_i - \bar{Q})^2} \tag{9}$$

NSE determines the relative magnitude of the residual variance, compared to the observed data (D. N. Moriasi et al. 2007; Nash and Sutcliffe 1970), where ranges from 0.75 – 1.0 indicate good model performance (D. N. Moriasi et al. 2007; Rahman et al. 2013).

Percent Bias (PBIAS) measures the average tendency of simulated discharge to be larger or smaller than the corresponding observed values, with values close to zero indicating minimal overall bias and

therefore better model skill. According to Moriasi et al. (2007), for streamflow simulations, |PBIAS| < 10% indicates very good, 10–15% good, 15–25% satisfactory, and >25% unsatisfactory model performance; in the formulation used in this study, negative values indicate underestimation, whereas positive values indicate overestimation.

$$PBIAS = \frac{\sum_{i=1}^{n}(Q'_i - Q_i) \times 100}{\sum_{i=1}^{n} Q_i} \tag{10}$$

The Root Mean Square Error (RMSE) quantifies the average magnitude of prediction errors by measuring the square root of the mean squared differences between simulated and observed discharge values, with lower values indicating better model performance.

$$RMSE = \sqrt{\frac{\sum_{i=1}^{n}(Q_i - Q'_i)^2}{n}} \tag{11}$$

where: Q_i is the observed runoff and Q'_i is the predicted runoff.

2.5 Model calibration

The calibration was performed using the SUFI-2 algorithm implemented in SWAT-CUP. Initial parameter ranges were selected through expert judgement and literature review, while parameter optimization and uncertainty analysis were performed automatically by SUFI-2. The algorithm uses Latin Hypercube Sampling to generate parameter sets and derives the 95% Prediction Uncertainty (95PPU) from the 2.5th and 97.5th percentiles of the resulting model simulations (Abbaspour et al. 2015) meaning, there isn't a single true model output, but rather an envelope of solutions defined by the 95PPU within the model parameter ranges. Starting values for parameters have been checked in similar investigations in the European Alps region, i.e. (Tuo et al. 2018), where alpine basins in Italy have been examined, around 100 km southwest of our area of the investigation. Also, similar publications investigating SWAT snowmelt modelling around the globe have been consulted for mountainous regions similar to the European Alps (Abbaspour et al. 2015; Rahman et al. 2013; Tuo et al. 2018).

The calibration process in SWAT-CUP consisted of a total of 4 iterations. First, an initial uncalibrated simulation, where the goal is to assess if the initially set parameter ranges result in a 95PPU that overlaps with most of the observed data, the run can be assumed successful. Then we proceed with the calibration of weather parameters (Table 2.), namely, temperature and precipitation lapse rates, therefore a total of 100 simulations are run. After a valid range of precipitation and temperature lapse rates is found, they are set to a fixed range, and as next step, the five snow-related parameters (Table 2.) are calibrated. Calibrating snowmelt related parameters, i.e. SFTMP, SMTMP, SMFMX, SMFMN, TIMP, is essential in snowmelt dominated watersheds, as shown by Ahl *et al.* (Ahl et al. 2008), who proved that the default SWAT snowmelt parameters caused to early peaks in streamflow, a 75-80 days earlier peak in streamflow. A total of 300 simulations of snow-melt related parameter calibration parameters are run. Although the suggested ranges for calibrating the melt factors SMFMX and SMFMN are 0 – 10, which led to errors, the automatic calibrating procedure calculated the values of SMFMN higher than the values of SMFMX, which is not correct for the northern hemisphere, where the investigated basins are located. Therefore, we adjusted the calibration ranges of the parameters, as shown in Table. Similar problems were observed by others (Tuo et al. 2018). Furthermore, calibrating snowmelt parameters extends the recession limb of the hydrograph. The most significant impact on model performance had TIMP and SMTMP (Ahl et al. 2008). Again, when satisfied with the results, the parameters were fixed, following the same procedure as in the second iteration.

Table 2. Calibration ranges of climate, snowfall and snowmelt related parameters

Parameter	Description	Calibration Range
V_TLAPS.sub	Temperature lapse rate (°C/km)	-8 – -2
V_PLAPS.sub	Precipitation lapse rate (mm/1000 m)	0 – 100
V_SFTMP.bsn	Snowfall temperature (°C)	-5 – 5
V_SMTMP.bsn	Snowmelt temperature (°C)	-5 – 5
V_SMFMX.bsn	Maximal snowmelt factor – 21st of June (mm/day)	5 – 10
V_SMFMN.bsn	Minimal snowmelt factor – 21st of December (mm/day)	0 – 5
V_TIMP.bsn	Snow temperature lag factor (-)	0 – 1

Note: the "V_" term means the existing parameter value is to be replaced by a given value, and "R_" means a relative change to the parameter, where a current parameter value is multiplied by (1+ a given value).

As the final step, surface runoff and groundwater-related parameters are calibrated (Table 3). Again, all three possible parameter change types were used, absolute change "A_" and replace "V_" for spatially not sensitive parameters, i.e., GWQMN or GW_DELAY, which are considered constant over the entire watershed, and "R_" relative change for spatially sensitive parameters like the CN curve number which highly depends on the landcover type and changes over the range of the watershed. To calibrate the surface runoff and groundwater-related parameters 500 model simulations are run.

Table 3. Final calibration and validation ranges for the Drava and Isel catchments

		Isel catchment		Drava catchment	
Parameter	**Description**	**Calibration range**	**Fitted value**	**Calibration range**	**Fitted value**
R_CN2.mgt	Soil conservation services (SCS) runoff curve number	-0.2 – 0.2	-0.066	-0.2 – 0.2	-0.143
A_GWQMN.gw	Threshold depth of water in shallow aquifer for return flow (mm)	-300 – 0	-90.30	-300 – 300	145.80
R_ESCO.hru	Soil evaporation compensation coefficient	-0.25 – 0.25	0.019	-0.25 – 0.25	0.151
V_GW_DELAY.gw	Delay time for aquifer recharge (days)	0 – 300	23.10	0 – 300	24.90
A_SLSUBBSN.hru	Average slope length (m)	-9 – 115	2.53	-9 – 115	90.324
R_GW_REVAP.gw	Groundwater "revap" coefficient	-0.2 – 0	-0.183	-0.2 – 0.2	0.199
R_REVAPMN.gw	Threshold depth of water in the shallow aquifer for "revap" or percolation to occur (mm H_20)	0 – 0.2	0.067	-0.2 – 0.2	-0.058
V_ALPHA_BF.gw	Baseflow alpha factor (1/days)	0 – 1	0.177	0 – 1	0.147
R_SOL_AWC().sol	Available water capacity of the soil layer (mm H_20/mm soil)	-0.05 – 0.05	-0.047	-0.05 – 0.05	0.04
V_RCHRG_DP.gw	Deep aquifer percolation fraction	0 – 1	0.155	0 – 1	0.543

Note: the "V_" term means replacing the value of the parameter, "R_" means a relative change to the parameter, where the parameter gets changed by percentage (value given in the calibration range), while "A_" means absolute change, where the provided calibration range values get added or subtracted from the default parameter value

3 Results and Discussion

In this investigation only the initial modelling results and the calibrated model will be presented for both upper Drava River catchments. Since in the initial run SWAT only uses the default model parameters,

without any calibration, often, the initial run presents a not very well functioning model. The case is especially true, for cases of complex catchments, in advanced terrain with pronounced slopes and high amounts of precipitation. Often such conditions are present in mountainous basins, like the source area of the Drava River, valid for both the upper Isel and Drava catchment, modelled in this article. When properly calibrated, the SWAT model performance is noticeably better. The previously described evaluation metrices for the initial run and final calibrated SWAT model are presented in Table . The results are presented across the two selected catchments and their respective sub catchments, selected according to available gauging stations for evaluation reasons. As for the upper Drava catchment, the selected gauges are Ausservillgraten (b2_AUS), Rabland (b2_RAB) and Lienz-Falkensteinsteg (b2_LIE) and in the Isel catchments, the selected gauges are Hopfgarten (b3_HOP), Brühl (b3_BRU) and Lienz (b3_LIE). The model skill is evaluated according to the p-factor, r-factor, Pearsons coefficient of determination (R^2) and the Nash-Sutcliffe efficiency (NSE). Those factors are often considered in similar research where complex catchments are modelled with the SWAT model (Abbaspour et al. 2007; D. N. Moriasi et al. 2007; Tuo et al. 2018).

Table 4. Initial model results for the upper Drava and Isel River catchments

	Drava catchment			Isel catchment		
Initial model setup	b2_AUS_m	b2_RAB_m	**b2_LIE_m**	b3_HOP_m	b3_BRU_m	**b3_LIE_m**
p-factor	0.05	0.11	**0.08**	0.09	0.05	**0.06**
r-factor	0.00	0.00	**0.00**	0.00	0.00	**0.00**
R^2	0.28	0.62	**0.64**	0.48	0.31	**0.39**
NSE	-0.71	-0.96	**-1.08**	0.33	0.10	**0.17**
PBIAS	1.53	12.29	**22.99**	-25.63	-24.88	**-20.53**
RMSE	1.42	6.68	**11.32**	5.82	17.16	**28.76**
Final Calibration						
p-factor	0.58	0.76	**0.77**	0.77	0.69	**0.79**
r-factor	1.05	0.99	**1.03**	0.58	0.43	**0.54**
R^2	0.27	0.73	**0.78**	0.91	0.96	**0.95**
NSE	0.21	0.71	**0.67**	0.87	0.91	**0.93**
PBIAS	1.03	7.00	**17.54**	-12.55	-19.36	**-10.84**
RMSE	0.96	2.58	**4.48**	2.58	5.52	**8.38**

The following hydrographs plots (Figure 6 and Figure 7) compare the observed and simulated discharges for the calibration period at the outlet gauges of the upper Drava (station Lienz-Falkensteinsteg) and Isel (station Lienz) catchments. In both catchments, calibration substantially improves the agreement between simulated and observed discharge compared to the initial model setup. The calibrated models reproduce the seasonal snowmelt-driven discharge regime well, with the timing of the spring runoff peaks generally captured sufficiently well. The initial simulations considerably overestimated several peak flows and exhibited larger deviations throughout the recession periods, whereas calibration significantly reduced these discrepancies.

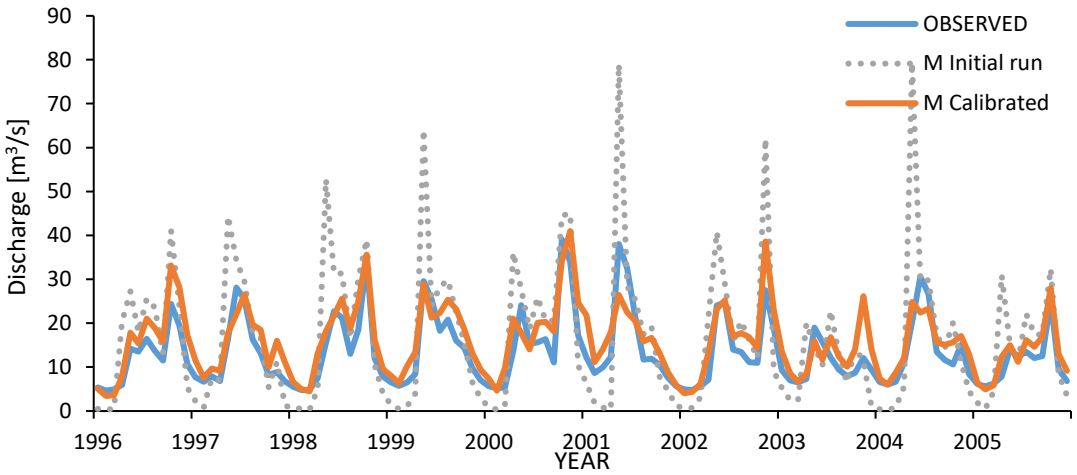


Figure 6. Resulting model hydrograph – Drava catchment – observed, initial model and calibrated discharge

For the Drava catchment (Figure 6), the calibrated model captures the overall annual flow pattern but still shows noticeable differences in the magnitude of several flood peaks and multiple recession limbs. These remaining discrepancies are reflected in the lower NSE (0.21–0.71) and R^2 (0.27–0.78) values obtained after calibration. In contrast, the Isel catchment (Figure 7) exhibits an excellent agreement between observed and simulated hydrographs, with both the timing and magnitude of the dominant snowmelt peaks reproduced consistently throughout the calibration period. This is consistent with the higher model performance (NSE = 0.87–0.93 and R^2 = 0.91–0.96, respectively).

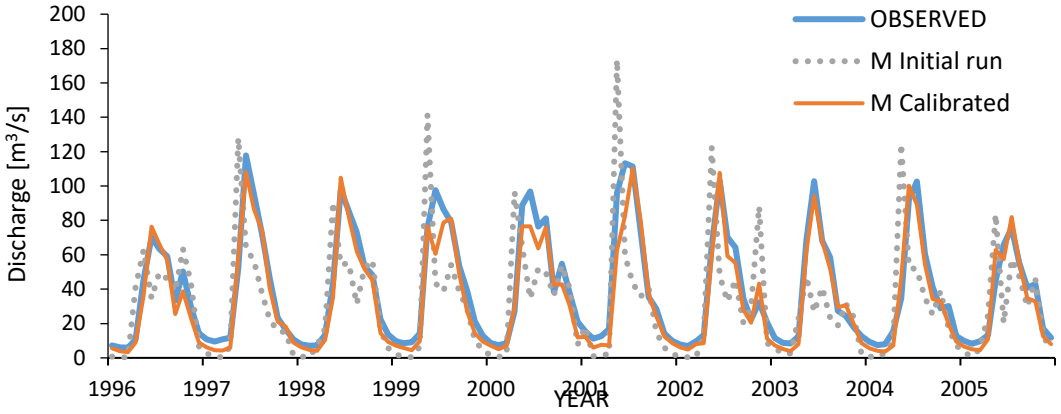


Figure 7. Resulting model hydrograph – Isel catchment – observed, initial model and calibrated discharge

In Figure the evaluation according to R^2 and NSE metrices is presented. The most notable difference can be observed between the evaluation metrices values across the two upper catchments, where the model performance over the Isel catchment is significantly better. Averaged over the three gauging station the Isel catchment model exhibited higher R^2 and NSE values when compared with the Drava catchment.

The reasons for worse physical model performance can only be speculated since both catchments are located at similar high altitudes, and also, the climate conditions are very similar due to close location, especially between Drava and Isel basins. The density and number of precipitation gauging stations can be considered satisfactory (Figure .), considering the smaller catchment area of the upper Drava catchment.

Although the calibrated Drava model exhibits relatively small discharge bias (PBIAS between 1.0 and 17.5%), NSE remains considerably lower (0.21–0.71) than in the Isel catchment (0.87–0.93). This indicates that the lower performance cannot primarily be attributed to systematic over- or underestimation of discharge volume, but rather to an inadequate representation of the temporal

variability and flow dynamics. A likely explanation is the regulation of the Drava River by the Tassenbach reservoir and diversion tunnel towards the Amlach hydropower plant (Netzwerk Wasser Osttirol - Niedergang eines Flusses 2006), which alters the natural discharge regime and is not represented in the current SWAT model configuration. After the plant in Amlach, just before Lienz, the water is rerouted to the Drava River.

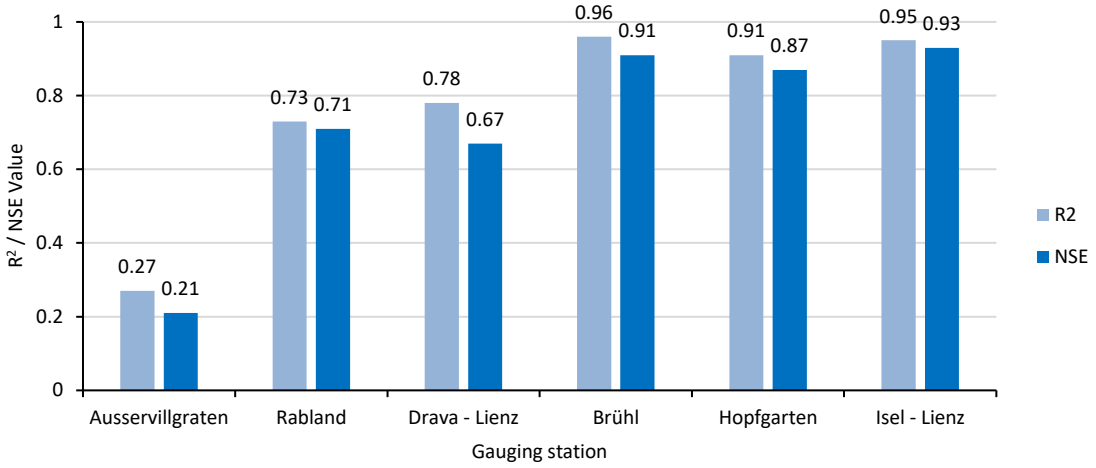


Figure 8. Final modelling metrics for the upper Drava catchments

4 Conclusion

This study demonstrated the applicability of the SWAT hydrological model for simulating snowmelt-driven runoff in the upper Drava River catchments in the Austrian Alps. The results showed that the initial model was unable to adequately reproduce the observed discharge dynamics, highlighting the importance of calibration when modelling complex mountainous basins. Following calibration, model performance improved substantially across all evaluation metrics. In the Isel catchment, the calibrated model achieved R^2 values between 0.91 and 0.96 and NSE values between 0.87 and 0.93, indicating very good agreement between simulated and observed streamflow. The upper Drava catchment also showed considerable improvement after calibration, although the achieved performance (R^2 = 0.27–0.78; NSE = 0.21–0.71) remained noticeably lower than in the Isel catchment.

The investigation confirmed that SWAT's temperature-index snow routine, combined with elevation-dependent corrections of precipitation and air temperature, can successfully represent the dominant hydrological processes governing runoff generation in alpine catchments. The additional evaluation metrics further showed that the calibrated models reduced discharge bias and prediction errors, while the hydrograph analysis demonstrated a substantial improvement in reproducing the seasonal snowmelt runoff regime and the timing of peak flows.

Despite these improvements, the analysis also revealed limitations associated with anthropogenic alterations of the natural flow regime. Although the calibrated Drava model exhibited relatively small discharge bias, its lower NSE and R^2 values indicate difficulties in reproducing the temporal variability of streamflow rather than the overall water balance. This is likely a consequence of hydropower infrastructure and water diversions in the upper Drava catchment, which are not explicitly represented within the current SWAT model setup.

Overall, the presented methodology provides a practical framework for snowmelt modelling in data-scarce mountainous regions and confirms the suitability of SWAT for investigating hydrological processes in snow-dominated alpine catchments. Future research should focus on incorporating water management infrastructure into the model and evaluating model performance under changing climatic conditions to improve simulations in regulated mountain river systems.

References

Abbaspour, K.C., Rouholahnejad, E., Vaghefi, S., Srinivasan, R., Yang, H. and Kløve, B. 2015 A continental-scale hydrology and water quality model for Europe: Calibration and uncertainty of a high-resolution large-scale SWAT model. *J. Hydrol.* 524, 733–752.

Abbaspour, K.C., Yang, J., Maximov, I., Siber, R., Bogner, K., Mieleitner, J., Zobrist, J. and Srinivasan, R. 2007 Modelling hydrology and water quality in the pre-alpine/alpine Thur watershed using SWAT. *J. Hydrol.* 333 (2–4), 413–430.

Ahl, R.S., Woods, S.W. and Zuuring, H.R. 2008 Hydrologic calibration and validation of SWAT in a snow-dominated Rocky Mountain watershed, Montana, U.S.A. *J. Am. Water Resour. As.* 44 (6), 1411–1430.

Arnold, J.G., Srinivasan, R., Muttiah, R.S. and Williams, J.R. 1998 Large Area Hydrologic Modeling and Assessment Part I: Model Development. *J. Am. Water Resour. Assoc.* 34 (1), 73–89.

Bieger, K., Hörmann, G. and Fohrer, N. 2015 Analyse spatiale détaillée du ruissellement et de l'apport de sédiments simulés par SWAT dans un bassin versant montagneux en Chine. *Hydrol Sci J* 60 (5), 784–800.

CORINE Land Cover — Copernicus Land Monitoring Service 2018 https://land.copernicus.eu/pan-european/corine-land-cover (accessed 11 September 2018).

D. N. Moriasi, J. G. Arnold, M. W. Van Liew, R. L. Bingner, R. D. Harmel, and T. L. Veith 2007 Model Evaluation Guidelines for Systematic Quantification of Accuracy in Watershed Simulations. *Transactions of the ASABE* 50 (3), 885–900.

EU-DEM — Copernicus Land Monitoring Service 2009 https://land.copernicus.eu/imagery-in-situ/eu-dem (accessed 22 April 2021).

Fontaine, T.A., Cruickshank, T.S., Arnold, J.G. and Hotchkiss, R.H. 2002 Development of a snowfall-snowmelt routine for mountainous terrain for the soil water assessment tool (SWAT). *J. Hydrol.* 262 (1–4), 209–223.

Grusson, Y., Sun, X., Gascoin, S., Sauvage, S., Raghavan, S., Anctil, F. and Sáchez-Pérez, J.M. 2015 Assessing the capability of the SWAT model to simulate snow, snow melt and streamflow dynamics over an alpine watershed. *J. Hydrol.* 531, 574–588.

Martinec, J. and Rango, A. 1986 Parameter values for snowmelt runoff modelling. *J. Hydrol.* 84 (3–4), 197–219.

Nash, J.E. and Sutcliffe, J.V. 1970 River flow forecasting through conceptual models part I - A discussion of principles. *J. Hydrol.* 10 (3), 282–290.

S.L. Neitsch, J.G. Arnold, J.R. Kiniry & J.R. Williams 2011 *Soil and Water Assessment Tool User's Manual Version 2005.* Texas Water Resources Institute, TEMPLE, TEXAS.

Netzwerk Wasser Osttirol - Niedergang eines Flusses 2006 http://www.wasser-osttirol.at/netzwerk.php?Sel=597 (accessed 14 March 2022).

Panagos, P., Van Liedekerke, M., Jones, A. and Montanarella, L. 2012 European Soil Data Centre: Response to European policy support and public data requirements. *Land Use Policy* 29 (2), 329–338.

Rahman, K., Maringanti, C., Beniston, M., Widmer, F., Abbaspour, K. and Lehmann, A. 2013 Streamflow Modeling in a Highly Managed Mountainous Glacier Watershed Using SWAT: The Upper Rhone River Watershed Case in Switzerland. *Water Resour. Manag.* 27 (2), 323–339.

Rango, A. and Martinec, J. 1995 Revisiting the Degree-Day Method for Snowmelt Computations. *J. Am. Water Resour. As.* 31 (4), 657–669.

Tuo, Y., Marcolini, G., Disse, M. and Chiogna, G. 2018 Calibration of snow parameters in SWAT: comparison of three approaches in the Upper Adige River basin (Italy). *Hydrol. Sci. J.* 63 (4), 657–678.

Yacoub, C. and Foguet, A.P. 2013 Slope effects on SWAT modeling in a mountainous basin. *J. Hydrol. Eng.* 18 (12), 1663–1673.

DISCREPANCIES BETWEEN AN UPDATED 1000-YEAR DESIGN HYDROGRAPH AND RECONSTRUCTED HISTORICAL FLOOD EVENTS

Juraj ŠKVARKA [1*]

[1] *Faculty of Civil Engineering STU in Bratislava, Slovakia*

E-mail: juraj.skvarka@stuba.sk

Abstract

Design flood hydrographs are a fundamental input for the design and assessment of the flood safety of hydraulic structures; however, in small catchments, their estimation may be subject to substantial uncertainty. This study compares the 2024 SHMI Q_{1000} design hydrograph, prescribed for the reservoir's flood-safety assessment, with the documented 1999 and 2024 flood events. The reconstruction of the inflow hydrographs was based on a reverse volumetric balance of the reservoir, using measured reservoir water levels, an updated reservoir storage curve, and the rating curves of the outlet structures, namely the safety spillway and bottom outlets. The updated Q_{1000} design hydrograph reaches a peak discharge of 17.2 $m^3 s^{-1}$. The reverse-balance reconstructed hydrograph of the 1999 flood reached a peak discharge of approximately 110 $m^3 s^{-1}$, while the reverse-balance reconstructed 2024 hydrograph had a maximum calculated inflow of 35.33 $m^3 s^{-1}$. However, the peak segment of the latter event is affected by uncertainty due to a failure of measurements. The estimated parameters of both documented events exceed those of the updated SHMI Q_{1000} design hydrograph. These findings confirm the need to verify design hydrological data against real extreme hydrological events.

Key words

flood hydrograph, reverse inflow calculation, reservoir volumetric balance, flood wave routing, dam safety

1 Introduction

The assessment of the flood safety of hydraulic structures requires reliable determination of design and verification flood hydrographs. For many older hydraulic structures, the design flood parameters of these hydrographs were derived from hydrological records, methodological procedures, and design assumptions available at the time of their preparation. At present, however, longer series of operational, hydrological, and meteorological observations are available, allowing the adequacy of the original design inputs to be verified against actually recorded extreme hydrological events. At the same time, the importance of uncertainty associated with the potential non-stationarity of hydrological processes is increasing, particularly due to changes in short-duration rainfall characteristics and the broader manifestations of climate change (Milly et al., 2008; Fluixá-Sanmartín et al., 2018; Földes et al., 2022). In engineering practice, design hydrological loading is often expressed primarily by a peak discharge with a specified return period. However, this approach may not sufficiently represent the actual effect of a flood on a reservoir, since the maximum water level reached during flood routing depends mainly on the shape of the hydrograph, i.e., the flood volume and duration, the initial reservoir water level, the available flood storage, and the capacity of the outlet works. For this reason, design floods should be evaluated as a multidimensional problem in which the joint characteristics of peak discharge, volume, and hydrograph duration are of decisive importance (Mediero et al., 2010; Requena et al., 2013; Gräler et al., 2013; Papaioannou et al., 2016). In reservoirs, the influence of hydrograph shape and initial water level is particularly important, because these factors directly affect the flood attenuation capacity of the reservoir and the resulting maximum water level during a flood (Gioia, 2016; Gabriel-Martin et al., 2019).

The need for regular reassessment of hydrological inputs is particularly important for small catchments and older reservoirs. In such cases, the available observation records may be short, the original design assumptions simplified, and the catchment response to extreme rainfall rapid. Under Slovak conditions, the effect of changes in short-duration rainfall on design floods was examined by Földes et al. (2022). Procedures for deriving check flood hydrographs and assessing flood risk for reservoirs have also been addressed in other Slovak case studies (Liová et al., 2022; Výleta et al., 2023). In this study, climate change is therefore considered as a broader context supporting the need to update safety assessments, but not as a directly demonstrated cause of any specific historical flood event in the absence of an independent trend analysis.

The aim of this paper is to compare the updated design hydrograph of the Slovak Hydrometeorological Institute (SHMI) for Q_{1000} with the documented flood events of 1999 and 2024 at the Lozorno II reservoir. The comparison focuses on peak discharge, flood volume, duration, time to peak, recession time, and the overall hydrograph shape. In addition to the values reported in older technical documentation for the 1999 flood event (Slaninka et al., 2000), the inflow hydrographs are also reconstructed from the observed reservoir water-level record using a reverse volumetric balance. This comparison makes it possible to assess the adequacy of the current design hydrological loading and to discuss the implications of real extreme events for the evaluation of flood safety at small reservoirs.

2 Data and Methods

2.1 Case study reservoir

The reservoir under study is located on the Suchý Stream in the western part of Slovakia, within the Morava River basin (Fig. 1). It was constructed as a multipurpose reservoir providing flood-retention, storage, and water-management functions. From the perspective of this study, the key aspects are the technical and hydrological characteristics that influence flood wave routing and enable the reverse reconstruction of the inflow hydrograph from the observed development of the reservoir water level.



Figure 1. Location of the reservoir under study

The catchment area at the dam profile is 19.10 km², and the long-term mean discharge of the Suchý Stream is 0.100 m³ s⁻¹. It is therefore a small catchment with a potentially rapid hydrological response to intense rainfall episodes. For the reconstruction of the hydrograph, knowledge of the basic reservoir characteristics, i.e., the elevation–storage curve, is essential. For illustration, the principal water levels

and storage zones of the reservoir are presented in Table 1.

Table 1. Principal water levels and storage zones of the reservoir

Reservoir storage zone	Water-level range [m a.s.l.]	Storage volume [m³]	Flooded area [ha]
Permanent storage	208.00–211.00	240,629	9.4
Active storage	211.00–218.60	1,669,871	33.2
Flood storage	218.60–219.00	140,446	34.7
Total reservoir storage	208.00–219.00	2,050,946	34.7

Outflow from the reservoir is controlled by a combined outlet structure and an ungated safety spillway. The crest of the safety spillway is located at an elevation of 218.60 m a.s.l., corresponding to the maximum operating water level. The spillway is ungated and double-sided, with a total crest length of 14 m (2 × 7 m). In addition to the safety spillway, the outlet structure includes two bottom outlets, with their axes located at elevations of 208.80 and 210.00 m a.s.l. Their effect during an extreme flood event depends on the current operational regime and on the operational decisions made during the flood (Slovenský vodohospodársky podnik, 2025).

For the purposes of the hydrological analysis, the reservoir was schematized using two basic functional relationships: the reservoir elevation–storage curve, and the rating curves of the outlet structures. The elevation–storage curve was used to convert the measured reservoir water level into the volume of stored water. The rating curves of the safety spillway and bottom outlets were then used to determine the reservoir outflow at individual reservoir water levels. These relationships represent the input boundary conditions for the reverse volumetric balance, on the basis of which the inflow hydrographs of the 1999 and 2024 flood events were reconstructed.

2.2 The 1999 flood event

The flood event of July 1999 was used in this study as a historical reference event for comparison with the Q_{1000} design flood hydrograph. Its selection is justified by the fact that it produced the highest reservoir water level recorded during the operation of the hydraulic structure. On 11 July 1999, the reservoir water level reached 219.66 m a.s.l., exceeding the maximum operating water level by 1.06 m and the maximum flood-retention water level by 0.66 m (Slaninka et al., 2000). During the event, the third degree of flood activity was declared. The measured reservoir water-level hydrograph at hourly intervals is shown in Fig. 2.

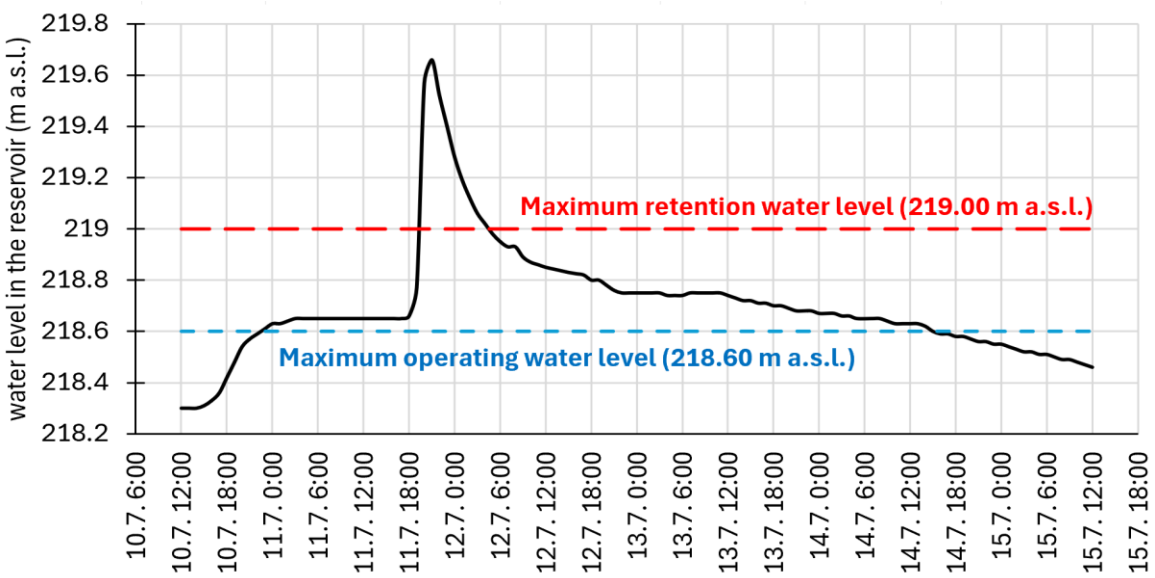


Figure 2. Reservoir water-level development during the 1999 flood event

According to the available documentation, part of the event was associated with an intense rainfall episode on 10 July, with a maximum hourly rainfall total of 22.9 mm. A second rainfall wave affected the catchment on 11 July 1999, when a maximum hourly total of 55 mm was recorded between 18:00 and 19:00. The reservoir water level peaked at 20:30. The passage of the flood wave was associated with damage to the stilling basin and outlet channel, slope failures, and the flooding of several structures along the stream course (Fig. 3).



Figure 3. View of the damaged outlet channel after the passage of the 1999 flood wave (adapted from Sviteková, 2024, contrast enhanced for readability)

2.3 Archival reconstruction of the 1999 inflow hydrograph

Slaninka et al. (2000) reconstructed the 1999 inflow hydrograph using the Klemeš reverse-transformation method. The method derives the inflow hydrograph by reversing the reservoir-routing calculation using the recorded reservoir water-level development and the estimated reservoir outflow. In the available documentation, the flood-wave volume associated with the Slaninka et al. (2000) hydrograph is reported as 1,927,000 m³, which substantially exceeded the design assumption used at that time. In the present study, the reported hydrograph was adopted without modification and used as the inflow boundary condition for forward reservoir routing in scenarios S2 and S3.

2.4 Inflow hydrograph reconstruction based on a reverse reservoir water balance

The new reverse reconstruction of the inflow hydrographs for the 1999 and 2024 flood events was based on the inverse solution of the reservoir water balance. In contrast to conventional flood wave routing, where the inflow hydrograph is known and the time development of the reservoir water level is calculated, the measured time series of the reservoir water level was used as the input in this case. The objective of the calculation was to retrospectively derive an inflow hydrograph that is hydrologically consistent with the recorded change in water level, i.e. the corresponding change in reservoir storage, and with the calculated outflow through the outlet structures. The calculation is based on the conservation equation for the volume of water stored in the reservoir:

$$\frac{dS}{dt} = I - O \tag{1}$$

where S is the volume of water stored in the reservoir$[m^3]$,
I is the inflow into the reservoir$[m^3\ s^{-1}]$,
O is the total outflow from the reservoir$[m^3\ s^{-1}]$,
t is time $[s]$.

At each time step, the volume of stored water in the reservoir was determined from the measured water level using the elevation–storage curve. An updated elevation–storage curve was used for the calculation. In the source documentation, this curve was refined on the basis of the DMR 5.0 digital terrain model. The differences from the original curve given in the operating regulations within the flood-control storage zone of the reservoir were assessed as minor to negligible.

The outflow over the safety spillway was determined from the spillway rating curve. According to the operating regulations of the hydraulic structure, discharge through the bottom outlets is restricted from the water level of 218.70 m a.s.l. until they are fully closed. Subsequently, the entire flood discharge is conveyed only through the safety spillway. If the water level reaches 219.00 m a.s.l. and continues to rise, the bottom outlets may be reactivated, even at the cost of exceeding the non-damaging discharge downstream of the dam. The capacity of the regulated channel downstream of the dam was considered in the available documentation to be approximately 8 $m^3\ s^{-1}$.

Based on all available information, the computational procedure was as follows. For each water level H_i, the corresponding reservoir storage S_i was calculated using the updated elevation–storage curve. Subsequently, the change in storage between two consecutive time steps was calculated:

$$\Delta S_i = S_i - S_{i-1} \tag{2}$$

and the corresponding storage-change discharge:

$$\Delta Q_{S,i} = \frac{\Delta S_i}{\Delta t} \tag{3}$$

The reconstructed inflow was then calculated as the sum of the discharge required to account for the change in reservoir storage ($\Delta Q_{S,i}$) and the total reservoir outflow, expressed as the sum of the outflow over the safety spillway ($O_{BP,i}$) and the outflow through the bottom outlets ($O_{DV,i}$):

$$I_i = \Delta Q_{S,i} + O_{BP,i} + O_{DV,i} \tag{4}$$

The hydrograph obtained in this way represents a reverse estimate of the inflow into the reservoir derived from the observed water-level development. For the purpose of comparing the design hydrograph with the historical flood events, not only the maximum peak discharge but also the hydrograph volume was evaluated. A reference discharge of Q_{ref} = 4.4 $m^3s^{-1}$was selected (threshold value), corresponding to the discharge through both fully open bottom outlets at the maximum operating water level of 218.60 m a.s.l. The beginning and end of the analysed flood wave were defined as the times at which the inflow hydrograph exceeded and subsequently fell below this value. The flood wave volume was then calculated by numerical integration of the part of the hydrograph exceeding the reference discharge:

$$W_{>Q_{ref}} = \int_{t_1}^{t_2} \left[Q_{in}(t) - Q_{ref} \right] dt \tag{5}$$

where $W_{>Q_{ref}}$ is the above-threshold flood wave volume [m^3],
$Q_{in}(t)$ is the inflow into the reservoir [$m^3\ s^{-1}$],
Q_{ref} is the reference discharge of 4.4 $m^3\ s^{-1}$,
t_1 is the time of the first exceedance of Q_{ref},
t_2 is the time of the subsequent decrease below Q_{ref}.

The volume defined in this way does not represent the total hydrograph volume, but only the part of the hydrograph above the selected threshold value. It was subsequently compared among the SHMI Q_{1000} design hydrograph, the Slaninka et al. (2000) reconstructed 1999 inflow hydrograph, and the reverse-balance reconstructed inflow hydrographs for the 1999 and 2024 flood events.

3 Results and Discussion

3.1 Reservoir water-level computations for flood safety assessment

To obtain the time development of the reservoir water level, calculations were performed for three basic scenarios. In all scenarios, the initial water level was set to 218.60 m a.s.l., corresponding to the crest elevation of the safety spillway and, at the same time, to the maximum operating water level of the reservoir. This initial condition represents an unfavourable state in which the available storage is already fully used before the arrival of the flood wave, and any further rise in the water level is governed mainly by the inflow into the reservoir and the capacity of the safety spillway.

Table 2. Overview of the individual scenarios used for flood wave routing

Scenario	Initial water level [m a.s.l.]	Flood wave	Safety spillway	Bottom outlet No. 1	Bottom outlet No. 2
S1	218.60	SHMI Q_{1000}	yes	no	no
S2	218.60	1999 - Slaninka et al. (2000)	yes	no	no
S3	218.60	1999 - Slaninka et al. (2000)	yes	yes	yes

Scenario S1 represents the reference design condition, in which the reservoir is loaded by the SHMI Q_{1000} design flood wave and the reservoir outflow is conveyed exclusively through the ungated safety spillway. The results obtained for this scenario also confirmed that the assumed mode of flood wave release is consistent with the rules specified in the operating regulations of the hydraulic structure.

Scenario S2 represents an analogous unfavourable condition for the historical 1999 flood reported by Slaninka et al. (2000), without considering outflow through the bottom outlets. This scenario enables assessment of the water level that would be reached during the passage of the historical flood if the safety spillway were the only effective outlet structure. Scenario S3 uses the same reconstructed 1999 inflow hydrograph reported by Slaninka et al. (2000) but assumes that both bottom outlets are open in addition to the safety spillway. The calculated and measured reservoir water-level developments are shown in Fig. 4.

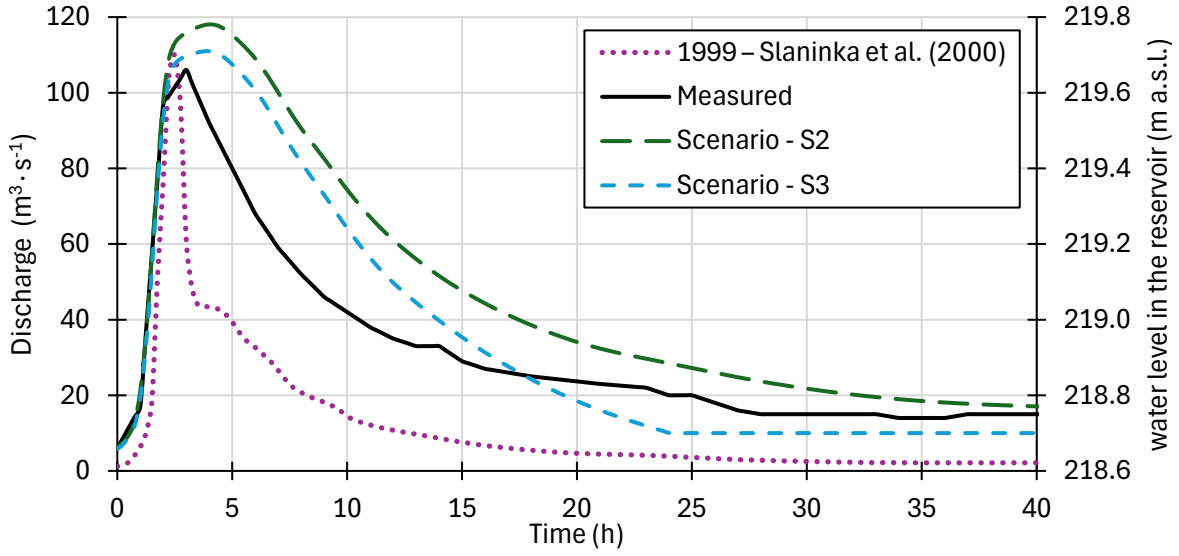


Figure 4. Comparison of the measured and calculated reservoir water-level development for scenarios S2 and S3

The comparison of the calculated and measured reservoir water levels shows that the reconstructed 1999 inflow hydrograph reported by Slaninka et al. (2000) does not reproduce the observed water-level development during the flood. In scenario S2, in which the reservoir outflow was considered only through the safety spillway, the calculated water level substantially exceeded the measured values.

Including both bottom outlets in scenario S3 reduced the calculated water level; however, sufficient agreement with the observed course was still not achieved. The calculated water level remained higher than the measured water level. This discrepancy indicates that the Slaninka et al. (2000) hydrograph probably overestimates the flood-wave volume or does not adequately represent the temporal distribution of inflow during the event. Therefore, a new inflow hydrograph was derived using a reverse reservoir water balance.

3.2 Reverse-balance reconstruction of the 1999 inflow hydrograph

Following the methodology described in Section 2.4, a new 1999 inflow hydrograph was derived using a reverse reservoir water balance. The reconstructed hydrograph was subsequently used in a forward flood-wave routing calculation considering the probable operational regime of the outlet structures. The hydrograph derived in this way was subsequently used in a forward flood wave routing calculation, in which the probable operational regime of the outlet structures during the event was considered. A comparison between the calculated and measured reservoir water-level development is shown in Fig. 5.

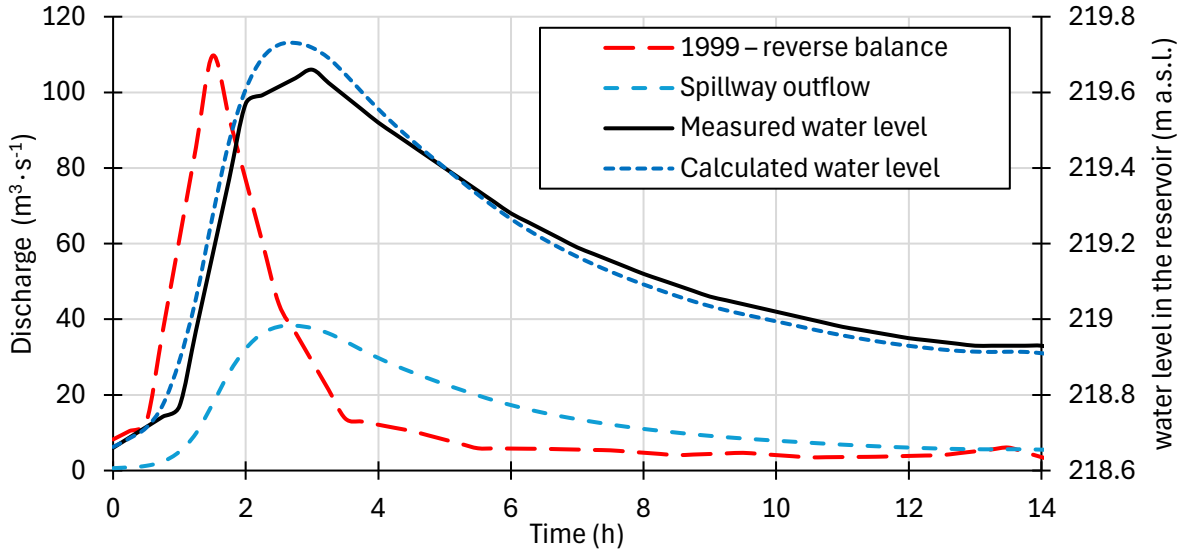


Figure 5. Reverse-balance reconstructed inflow, spillway outflow, and comparison of the calculated and measured reservoir water levels in 1999

The results of the subsequent verification calculation showed very good agreement between the calculated and measured reservoir water-level development. A minor difference was observed only in the region of the peak. The maximum measured water level reached 219.66 m a.s.l. at 3.0 h, whereas the calculated maximum water level reached 219.731 m a.s.l. at 2.5 h. This difference should be interpreted with regard to the fact that the measured water levels were recorded at hourly time intervals; therefore, the exact time and value of the peak may not have been captured precisely in the record.

3.3 Reverse-balance reconstruction of the 2024 inflow hydrograph

The flood event of September 2024 occurred after a period of heavy rainfall, which led to a rapid increase in inflow into the reservoir. At the beginning of the analysed period, on 14 September 2024 at 10:00, the reservoir water level was 215.85 m a.s.l., i.e., substantially below the maximum operating water level, and the reservoir therefore had a considerably larger available storage volume than during the 1999 event. According to the elevation–storage curve used, the corresponding volume of water stored in the reservoir was approximately 1.10 million m³. The reconstruction of the inflow hydrograph was performed using a reverse volumetric balance, analogously to the reconstruction of the 1999 flood event. At each time step, the inflow was derived from the change in reservoir storage and the outflow from the reservoir.



Figure 6. View of the safety spillway during the 2024 flood situation (Vodohospodárska výstavba, 2024)

The most significant limitation of the reconstruction is the failure of automatic measurement, or data transmission, on 15 September 2024, approximately between 06:00 and 14:00. This outage occurred precisely during the critical part of the flood event, when the reservoir water level rose from 217.33 m a.s.l. to 218.94 m a.s.l. In terms of storage volume, this represents an increase of approximately 0.522 million m³ over 8 h. The calculated inflow value for this interval therefore does not represent the instantaneous peak discharge, but only the average balance value over the entire period of the data outage.

The highest calculated hourly inflow value in the available time series was 35.33 $m^3 s^{-1}$ at 06:00. During the subsequent eight-hour data outage, the average balance inflow was 24.42 $m^3 s^{-1}$. However, the exact shape of the peak segment of the hydrograph cannot be determined unambiguously from the available data.

The water-level record indicates that water began to pass over the safety spillway during the measurement outage. The first available value after the record was restored, at 14:00, already documents a water level of 218.94 m a.s.l., i.e., 0.34 m above the spillway crest. The maximum reservoir water level was reached at 16:00 at an elevation of 219.00 m a.s.l., corresponding to the maximum flood-retention water level. The complete course of this flood event is shown in Fig. 7. The results of the analysis indicate that this was a bimodal flood, i.e., it had two peaks: the first, smaller peak with an inflow of 12.8 $m^3 s^{-1}$, and the second, larger peak, whose value cannot be determined unambiguously (35.33 $m^3 s^{-1}$) because of the aforementioned measurement outage.

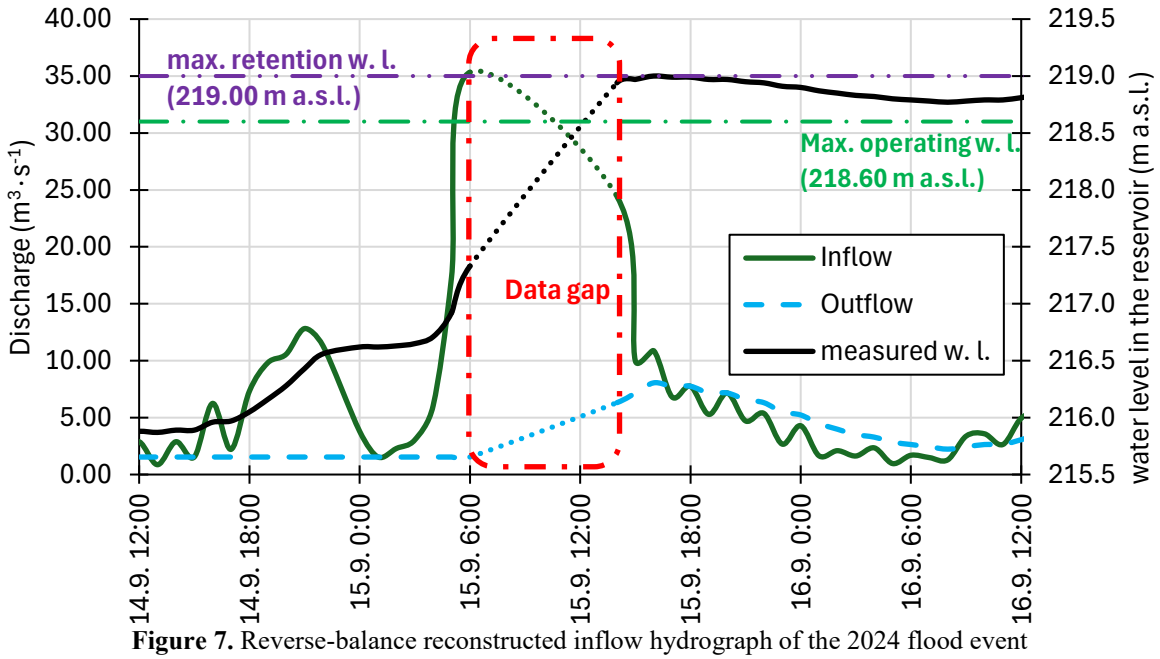


Figure 7. Reverse-balance reconstructed inflow hydrograph of the 2024 flood event

For the above reasons, the reconstructed hydrograph of the 2024 flood event should be interpreted as a balance-based estimate of the inflow into the reservoir. The result provides a basis for assessing the course of the flood event; however, it does not allow the exact shape of the peak segment of the hydrograph to be determined reliably.

3.4 Comparison of parameters of considered flood waves

To compare the design and historical flood events, four hydrographs were analysed: the updated SHMI Q_{1000} design hydrograph, the reconstructed 1999 inflow hydrograph reported by Slaninka et al. (2000), and the reverse-balance reconstructed inflow hydrographs for the 1999 and 2024 flood events derived from the measured reservoir water-level records (Fig. 8). All hydrographs were resampled to a common 15-min computational grid for numerical integration and comparison. This resampling did not increase the temporal resolution of the original observations.

The SHMI Q_{1000} hydrograph was selected because it represents the required flood-safety loading for the assessed hydraulic structure and was officially updated by SHMI in 2024. However, the hydrological data provided by SHMI are classified as reliability class III according to STN 75 1400, which indicates a lower level of reliability and introduces additional uncertainty into the interpretation of the Q_{1000} design hydrograph provided by SHMI. The pronounced discrepancy between the Q_{1000} hydrograph and both reconstructed 1999 hydrographs may result from uncertainty in extrapolating extreme floods for a small ungauged catchment. Although both 1999 reconstructions yielded similar peak discharges, their different flood volumes indicate uncertainty in the hydrograph shape.

The reconstructed peak discharge of approximately 110 $m^3 s^{-1}$ is exceptionally high for a catchment area of 19.10 km^2. Its magnitude may reflect the very intense short-duration rainfall recorded during the event, including an hourly rainfall total of 55 mm, and the rapid hydrological response of the small catchment. However, because the inflow was not measured directly, the peak should be interpreted as a balance-based estimate whose plausibility cannot be independently confirmed without rainfall–runoff modelling.

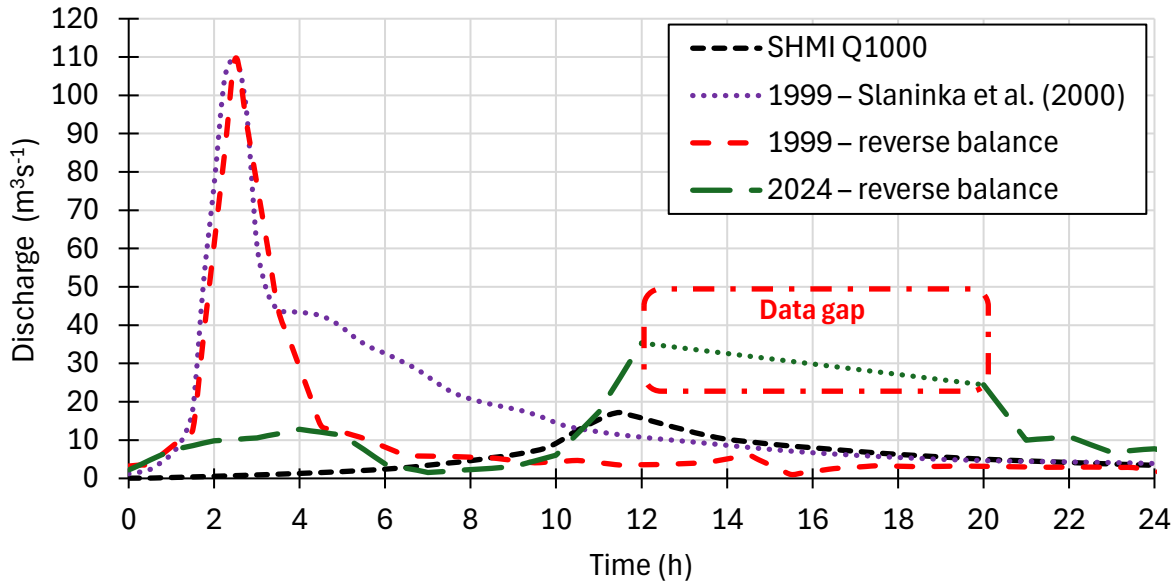


Figure 8. Comparison of the SHMI design hydrograph with the reconstructed hydrographs (1999 and 2024)

For each hydrograph, the basic flood wave characteristics were determined: peak discharge, flood wave volume, total wave duration, time to peak, and recession time. To enable an objective comparison of the individual flood waves in terms of hydraulic-structure safety, the beginning and end of each flood wave were defined using a uniform rule for all analysed hydrographs. The beginning of the wave was defined as the time when the inflow exceeded the reference discharge Q_{ref} = 4.4 $m^3 s^{-1}$, i.e., the capacity of the

bottom outlets, meaning that water must also pass over the safety spillway. Similarly, the flood wave volume was calculated only above this threshold. The comparison results are presented in Table 3.

Table 3. Comparison of flood wave parameters above reference flow (Q_{ref} = 4.4 m^3s^{-1})

Parameter	SHMI Q_{1000}	1999-Slaninka	1999-reverse balance	2024-reverse balance
peak discharge (m^3s^{-1})	17.2	110.01	109.69	35.33*
flood wave volume (m^3)	424,726	1,538,123	842,152	1,379,184*
flood wave duration (h)	13.57	20.55	14.26	30.75
time to peak (h)	3.67	1.72	1.93	14.39
recession time (h)	9.90	18.83	12.33	16.36

*In the interval from 06:00 to 14:00 on 15 September 2024, a measurement outage occurred; therefore, the actual shape of the peak segment of the hydrograph cannot be determined unambiguously.

3.5 Uncertainties of the reconstructed inflow hydrograph

The applied procedure for reverse reconstruction of the inflow hydrograph is based on the reservoir water balance. The accuracy of the resulting hydrograph therefore depends on the quality of the input water-level data, the reliability of the reservoir elevation–storage curve, the accuracy of the rating curves of the outlet structures, and knowledge of the actual operational regime during the flood event.

The first source of uncertainty is the measured development of the reservoir water level. In the reverse balance calculation, the difference in storage between two consecutive time steps enters the computation, while the measurement time step was one hour. Even a small deviation in water level may therefore result in a significant error in the calculated storage change, particularly during the phase of rapid water-level rise.

The second source of uncertainty is the relationship between reservoir water level and storage volume. In this study, an updated elevation–storage curve derived from the digital terrain model DMR 5.0 was used. It should be noted, however, that only very small to negligible differences exist between the updated storage curve and the storage curves included in the older operating regulations from 1997 and 2003.

The third limitation is the determination of reservoir outflow. The outflow over the safety spillway was determined from its rating curve, whereas the outflow through the bottom outlets depended on the selected operational scenario. For the historical 1999 flood event, the exact timing of the operation of the bottom outlets cannot be retrospectively verified with complete certainty. For this reason, the reconstructed hydrograph should be interpreted as a balance-consistent estimate rather than as a directly measured inflow record.

The fourth source of uncertainty is the temporal resolution of the input data. In rapid flash-flood events, the length of the time step may affect primarily the estimated peak discharge.

Another source of uncertainty is the definition of the beginning and end of the flood wave. This choice has a smaller effect on the peak discharge, but it may affect the calculated flood wave volume. Therefore, a uniform rule was applied to all analysed hydrographs. Nevertheless, the volume comparison should be interpreted with the awareness that a long recession limb of the hydrograph may increase the total calculated volume.

These limitations do not prevent the use of the reverse reservoir water balance for comparing the reconstructed flood events of 1999 and 2024 with the SHMI Q_{1000} design hydrograph. However, they require cautious interpretation of the absolute peak-discharge values, particularly for the 2024 event, where the measurement outage affected the decisive part of the peak. The key finding is that the estimated parameters of both historical events exceeded those of the design flood in terms of peak

discharge and flood-wave volume.

4 Conclusion

Two representations of the 1999 inflow hydrograph were considered. The first was the reconstructed 1999 inflow hydrograph reported by Slaninka et al. (2000). The second was newly reconstructed in this study from the observed reservoir water-level record using a reverse reservoir water balance, as described in Section 2.4. The aim of this paper was to compare the updated SHMI Q1000 design hydrograph, representing the prescribed flood-safety loading for the structure, with the documented flood events of 1999 and 2024. For this purpose, a reverse reservoir water balance was applied, based on the measured reservoir water-level development, the updated elevation–storage curve, and the rating curves of the outlet structures.

The results showed that flood assessment based solely on peak discharge is not sufficient. When peak discharge, duration, and the above-threshold volume of the inflow hydrograph above the reference value $Q_{ref} = 4.4$ m^{3}s^{-1} were compared, both analysed historical events represented a loading that exceeded the updated Q_{1000} design hydrograph. The 1999 flood had a substantially higher peak discharge, whereas the 2024 event was significant mainly in terms of volume and duration.

The reverse reservoir water balance proved to be a useful tool for reconstructing historical inflow hydrographs in cases where direct inflow measurements are not available. However, the results should be interpreted as balance-consistent estimates, the accuracy of which depends on the quality of the water-level record, the elevation–storage curve, the rating curves, and knowledge of the operational regime during the flood. The findings support the need for regular verification of design hydrological data against documented real extreme events, particularly in small catchments with a rapid hydrological response. Further research will focus on refining the assessment of the reservoir's flood safety. The planned work includes the development of a physical model of the safety spillway, the derivation of verification flood hydrographs using rainfall–runoff models, and the subsequent assessment of the hydraulic structure under extreme hydrodynamic loading.

Acknowledgements

This article was created with the support of the Ministry of Education, Science, Research and Sport of the Slovak Republic within KEGA grant No. 015STU-4/2026. The author also acknowledges the Slovak Water Management Enterprise, state enterprise, for providing data used in this study.

References

Fluixá-Sanmartín, J., Altarejos-García, L., Morales-Torres, A. & Escuder-Bueno, I. 2018 Review article: Climate change impacts on dam safety. *Natural Hazards and Earth System Sciences.* 18, 2471–2488.

Földes, G., Labat, M.M., Kohnová, S. & Hlavčová, K. 2022 Impact of changes in short-term rainfall on design floods: Case study of the Hnilec River basin, Slovakia. *Slovak Journal of Civil Engineering.* 30(1), 68–74.

Gabriel-Martin, I., Sordo-Ward, A., Garrote, L. & Granados, I. 2019 Hydrological risk analysis of dams: The influence of initial reservoir level conditions. *Water.* 11(3), 461.

Gioia, A. 2016 Reservoir routing on double-peak design flood. *Water* 8(12), 553.

Gräler, B., van den Berg, M.J., Vandenberghe, S., Petroselli, A., Grimaldi, S., De Baets, B. & Verhoest, N.E.C. 2013 Multivariate return periods in hydrology: A critical and practical review focusing on synthetic design hydrograph estimation. *Hydrology and Earth System Sciences.* 17, 1281–1296.

Liová, A., Valent, P., Hlavčová, K., Kohnová, S., Bacigál, T. & Szolgay, J. 2022 A methodology for

the estimation of control flood wave hydrographs for the Horné Orešany reservoir. *Acta Hydrologica Slovaca.* 23(1), 52–61.
Mediero, L., Jiménez-Álvarez, A. & Garrote, L. 2010 Design flood hydrographs from the relationship between flood peak and volume. *Hydrology and Earth System Sciences.* 14, 2495–2505.
Milly, P.C.D., Betancourt, J., Falkenmark, M., Hirsch, R.M., Kundzewicz, Z.W., Lettenmaier, D.P. & Stouffer, R.J. 2008 Stationarity is dead: Whither water management? *Science.* 319(5863), 573–574.
Papaioannou, G., Kohnová, S., Bacigál, T., Szolgay, J., Hlavčová, K. & Loukas, A. 2016 Joint modelling of flood peaks and volumes: A copula application for the Danube River. *Journal of Hydrology and Hydromechanics* 64(4), 382–392.
Requena, A.I., Mediero, L. & Garrote, L. 2013 A bivariate return period based on copulas for hydrologic dam design: Accounting for reservoir routing in risk estimation. *Hydrology and Earth System Sciences.* 17, 3023–3038.
Slaninka, V., Virág, P. & Uríča, J. 2000 *Flood on the Lozorno Hydraulic Structure in 1999*, Slovak Water Management Enterprise, Bratislava/Malacky, Slovak Republic (in Slovak).
Slovak Water Management Enterprise 2025 *Manipulation Rules for the Lozorno II Reservoir on the Suchý Stream at river km 8.5,* Slovak Water Management Enterprise, Danube River Basin Branch, Bratislava, Slovak Republic (in Slovak).
Sviteková, J. 2024 *Lozorno II: Summary Periodic Surveillance Report for the Entire Operation Period up to 2023,* Vodohospodárska výstavba, Bratislava, Slovak Republic (in Slovak).
Vodohospodárska výstavba, state enterprise. 2024 Lozorno II: Assessment of Dam Safety under Flood Loading within Technical Safety Supervision. Vodohospodárska výstavba, state enterprise, Bratislava, Slovak Republic, 67 pp. (in Slovak).
Výleta, R., Rončák, P., Liová, A., Valent, P., Bacigál, T., Gribovszki, Z., Danáčová, Z., Šurda, P., Vitková, J. & Hlavčová, K. 2023 The testing of a multivariate probabilistic framework for reservoir safety evaluation and flood risks assessment in Slovakia: A study on the Parná and Belá Rivers. *Journal of Hydrology and Hydromechanics.* 71(4), 449–463.

IMPACT OF PRIMARY PRECIPITATION DATA PROCESSING ON DIMENSIONLESS HYETOGRAPHS

Željko ŠRENG [1*], Marin GRUBIŠIĆ [1], Jadran BERBIĆ [2], Tamara BRKLEKOVIĆ [1]

[1] *Josip Juraj Strossmayer University of Osijek, Faculty of Civil Engineering and Architecture Osijek, Vladimira Preloga 3, 31000 Osijek, Croatia*

E-mail: zsreng@gfos.hr

E-mail: marin.grubisic@gfos.

E-mail: tamaradadic@gfos.hr

[2] *University of Zagreb, Faculty of Civil Engineering, Fra Andrije Kačića-Miošića 26, 10000 Zagreb, Croatia*

E-mail: jadran.berbic@grad.unizg.hr

[*] *Corresponding author*

Abstract

Primary precipitation data processing plays a crucial role in the construction of dimensionless design hyetographs used in urban drainage analysis. The definition of independent precipitation events and the application of precipitation depth thresholds directly influence statistics and the temporal distribution of precipitation within events. This study investigates the impact of precipitation event separation and threshold selection on dimensionless hyetographs derived using both the Huff curves and the Method of Average Variability (hereinafter MAV). High-resolution (5-minute) precipitation data from Čepin/Osijek meteorological station in Croatia, covering a 10-year period, were analysed, and precipitation events were separated using two approaches: an autocorrelation-based method (hereinafter AC) and a statistical method based on the Kolmogorov–Smirnov and Poisson tests with the Kernel Density Estimation method of function smoothing (hereinafter the KDE method). A minimum precipitation threshold of $P \geq 1$ mm was applied, and precipitation events with durations not exceeding 120 min were considered. For each processing variant, dimensionless hyetographs were constructed using both the Huff and MAV methods. Results indicate that the choice of event separation method significantly affects the duration and total depth of precipitation events, which consequently alters the shape of derived dimensionless hyetographs. The AC method generally produces fewer events, consistent with its tendency to merge neighbouring precipitation bursts, while the KDE method preserves a larger number of short and concentrated precipitation patterns. Although both Huff and MAV approaches capture dominant precipitation patterns, their sensitivity to primary processing differs, emphasising the need for transparent and methodologically consistent event definition in design applications. The findings highlight that primary precipitation data processing is not merely a technical preprocessing step but a decisive factor in defining design storm structure for urban drainage systems.

Key words

Precipitation data processing, Huff curves, Method of Average Variability, Urban drainage

1 Introduction

The analysis of precipitation data and the construction of dimensionless hyetographs are important components of hydrological and hydraulic studies, particularly in the planning and design of urban drainage systems. Dimensionless hyetographs describe the temporal distribution of precipitation within a storm event and are commonly combined with intensity–duration–frequency (IDF) relationships to derive design storms for engineering applications (Bonacci, 1994; Bezak et al., 2018). Their shape influences runoff generation, peak discharge and the hydraulic response of urban catchments, making an appropriate representation of precipitation temporal patterns essential for reliable urban drainage analyses.

Several methods have been developed for constructing design hyetographs, including the Huff method, the Method of Average Variability (MAV), the Chicago method and the triangular method (Bonacci, 1994; Ellouze et al., 2009). Among them, Huff curves and MAV hyetographs are frequently used because they are derived directly from observed precipitation records and preserve the temporal characteristics of real precipitation events. The Huff method, originally proposed by Huff (1967), classifies precipitation events according to the position of maximum precipitation intensity within the storm duration and represents precipitation variability through dimensionless cumulative precipitation curves. Its applicability has been demonstrated in numerous studies conducted under different climatic conditions (Bonta, 2004; Yin et al., 2016; Wartalska et al., 2020; Nguyen and Chen, 2022). More recently, Nguyen and Chen (2022) introduced an additional fifth Huff type to represent approximately uniform precipitation distributions over time. In contrast, the MAV approach, originally developed by Pilgrim and Cordery (1975), is based on the ranking of precipitation intensities within storms of similar duration and the averaging of their temporal variability. Several studies have shown that MAV-based hyetographs provide a useful representation of design precipitation and can serve as an alternative to more traditional design storm approaches (Krvavica et al., 2018; Krvavica and Rubinić, 2020).

Regardless of the selected method, the construction of dimensionless hyetographs begins with the primary processing of precipitation records. This process includes the identification of independent precipitation events and the application of precipitation thresholds, both of which directly influence the number of selected events, their duration, total precipitation depth and temporal structure. The importance of appropriate event delineation has been highlighted by numerous authors (Bonacci, 1994; Dunkerley, 2008; Dunkerley, 2010; Medina-Cobo et al., 2016; Dunkerley, 2022; Tu et al., 2023). In particular, the definition of the minimum inter-event time (MIT) represents one of the key methodological decisions because different separation criteria can produce substantially different samples of precipitation events and consequently different design storm characteristics.

The sensitivity of dimensionless hyetographs to event delineation procedures has received increasing attention in recent years. Dunkerley (2022) showed that Huff quartile classifications can be significantly influenced by the selected event separation method and by regional precipitation characteristics. Similarly, Cao et al. (2023) emphasized the importance of statistically based approaches for determining event separation criteria, while Bonacci (1994) stressed the need to distinguish between convective and cyclonic precipitation because of their fundamentally different temporal structures. Short-duration convective storms are particularly relevant for urban drainage applications since they are commonly associated with high precipitation intensities, rapid runoff generation and surcharge conditions in stormwater systems (Bonacci, 1994; Yin et al., 2016). Recent research conducted using high-resolution precipitation data from eastern Croatia further demonstrated that different MIT determination approaches, including autocorrelation-based (AC) and kernel density estimation (KDE) methods, may lead to noticeable differences in precipitation event characteristics and in the resulting Huff hyetographs (Grubišić et al., 2026). These findings suggest that the effects of primary precipitation data processing may extend beyond Huff analysis and potentially influence other types of dimensionless hyetographs as well.

Therefore, the objective of this study is to examine how two commonly used precipitation event separation approaches, namely the AC and KDE methods, influence the construction of dimensionless

Huff and MAV hyetographs. The analysis is based on a 10-year series of 5-minute precipitation data recorded at the Čepin meteorological station in eastern Croatia. Particular attention is given to precipitation events with durations not exceeding 2 h, which are commonly associated with convective precipitation and are of particular interest in urban drainage design. A minimum precipitation threshold of $P \geq 1$ mm is applied, while the temporal discretization within MAV duration classes is defined to ensure block durations not exceeding 15 min. Section 2 presents the study area and methodology, Section 3 presents and discusses the obtained results, and Section 4 summarises the main conclusions of the study.

2 Methods

2.1 Study Area and Precipitation Data

The analysis was conducted using precipitation data from the automatic meteorological station Čepin, located in the vicinity of the city of Osijek in eastern Croatia. According to the Köppen–Geiger climate classification, the area is characterised by a humid continental climate with warm summers and no pronounced dry season.

A continuous series of 5-minute precipitation data covering the period 2016–2025 was used. The high temporal resolution enables reliable identification of short-duration precipitation events and detailed analysis of their temporal structure. Additional information regarding the study area and data set can be found in Grubišić et al. (2026).

2.2 Methodology

The methodology applied in this study follows the framework presented by Grubišić et al. (2026) and consists of five main steps:

(i) preparation and quality control of the input precipitation data,
(ii) separation of independent precipitation events (AC and KDE methods),
(iii) construction of dimensionless Huff and MAV hyetographs,
(iv) analysis of precipitation event characteristics, and
(v) comparison of the resulting hyetographs.

The analysis was performed using two precipitation event separation approaches: the autocorrelation-based method (AC) and the kernel density estimation method (KDE). Following event separation, a minimum precipitation threshold of $P \geq 1$ mm was applied. Only precipitation events with durations not exceeding 120 min were considered, as such events are commonly associated with convective precipitation and are of particular interest for urban drainage applications.

2.3 Precipitation Event Separation Methods

Independent precipitation events were identified using two methods previously evaluated by Grubišić et al. (2026). The first approach is based on the autocorrelation structure of the precipitation time series (AC method), where the minimum inter-event time is determined from the lag at which the autocorrelation becomes statistically insignificant (Bonacci, 1994; Pohle et al., 2018; Cao et al., 2023). The second approach combines Kolmogorov–Smirnov and Poisson statistical tests with Kernel Density Estimation (KDE) and determines the minimum inter-event time from the relationship between theoretical and empirical distributions of dry periods (Restrepo-Posada and Eagleson, 1982; Vantas and Sidiropoulos, 2021; Cao et al., 2023).

Both methods were applied to the same 5-minute precipitation record. The resulting precipitation events formed the basis for the subsequent construction of dimensionless hyetographs.

2.4 Construction of Huff and MAV Hyetographs

Dimensionless Huff hyetographs were constructed following the methodology originally proposed by Huff (1967). Each precipitation event was normalised with respect to duration and cumulative precipitation depth and classified according to the position of the maximum precipitation intensity within the event duration. Five precipitation types (T1–T5) were considered, including the additional type representing approximately uniform precipitation distributions (Nguyen and Chen, 2022). Median Huff curves were used as representative dimensionless hyetographs.

MAV hyetographs were constructed according to the Method of Average Variability originally proposed by Pilgrim and Cordery (1975). Precipitation events were first grouped into duration classes: C1 (10–20 min), C2 (20–40 min), C3 (40–60 min), C4 (60–90 min) and C5 (90–120 min). Within each class, a fixed number of temporal blocks was selected so that the block duration did not exceed 15 min for the longest precipitation event in the class. For each event, precipitation depths were aggregated within the defined blocks and converted into relative contributions to the total precipitation depth. The blocks were subsequently ranked according to their precipitation contribution, and average rank characteristics were determined for all events within a class. The resulting average temporal distribution was then used to construct the representative MAV hyetograph for each duration class.

2.5 Comparison of Hyetograph Variants

The influence of precipitation event separation methods on the resulting hyetographs was evaluated through a comparison of the basic physical characteristics of the identified precipitation events and the shapes of the corresponding dimensionless hyetographs. For each Huff type and MAV duration class, the number of precipitation events, average and maximum precipitation depth, average and maximum duration, and maximum 10-, 15- and 20-minute precipitation intensities were determined.

In addition, the median and mean dimensionless hyetographs were analysed together with the 5–95 % variability range to assess the sensitivity of the resulting precipitation patterns to the selected event separation method. The comparison was performed separately for Huff and MAV hyetographs in order to evaluate whether the influence of primary precipitation data processing is consistent across both approaches.

3 Results and Discussion

3.1 Huff Hyetographs

The results of the Huff classification show that the selected precipitation event separation method has a clear influence on the number of identified precipitation events, while the relative distribution among Huff types remains broadly similar. The results are presented in Table 1 and Fig. 1. The KDE method identified 259 precipitation events, whereas the AC method identified 123 events. In both cases, Type 1 and Type 5 events were the most frequent, while Type 2 events were the least represented. This indicates that the KDE method mainly increases the total number of detected short-duration events but does not substantially change the general distribution of events among Huff types.

The average precipitation depths were relatively similar for most Huff types obtained by the two methods. The largest differences were observed for Type 5, where the average precipitation depth was lower for KDE, and for Type 3, where KDE produced slightly higher average values. The maximum precipitation depth was generally comparable between the two methods, except for Type 1, where KDE identified a substantially larger maximum value. This suggests that the KDE-based separation preserves some short but intense early-peak precipitation events that are merged into longer events when the AC method is applied.

The average event durations also show only moderate differences between the two methods. For most

Huff types, the average durations obtained by AC and KDE are close, with Type 4 events having the longest average duration and Type 5 events the shortest.

Table 1. Statistics of Huff precipitation events identified using AC and KDE event separation methods

	AC					KDE				
Type	T1	T2	T3	T4	T5	T1	T2	T3	T4	T5
Type criteria	>=0 to <=25%	>25 to <=50%	>50 to <=75%	>75 to <=100%	uniform	>=0 to <=25%	>25 to <=50%	>50 to <=75%	>75 to <=100%	uniform
Number of precipitation events, *n* [-]	37	13	17	21	35	79	36	33	42	69
Precipitation depth, P [mm]										
P_{avg}	5.44	4.31	5.19	3.96	4.95	5.75	4.47	5.71	3.77	3.99
P_{std}	6.96	6.72	5.2	5.5	7.23	8.49	5.23	5.23	5.18	6.34
P_{cv} [%]	127.8	156.1	100.2	138.8	145.9	147.6	117	91.6	137.4	158.8
P_{iqr}	5.15	1.73	6.73	1.83	2.55	4.5	2.65	6.33	2.1	1.53
$\boldsymbol{P_{max}}$	28.5	26.5	20.5	23.3	38.5	54.7	26.5	20.5	23.3	38.5
Precipitation duration, t [min]										
t_{avg}	72.4	63.5	70	80.5	54.6	71.9	58.1	70.8	80	51.9
t_{std}	31.3	34.3	40.3	27.4	34	28.9	32.1	39.6	26.1	32.2
t_{cv} [%]	43.3	54.1	57.5	34.1	62.3	40.2	55.4	56	32.6	62.1
t_{iqr}	47.5	56.3	85	50	48.8	48.8	57.5	81.3	50	47.5
Maximum intensities, i [mm/min]										
i (10 min)	1.22	0.99	2.04	1.09	2.44	3.28	0.99	2.04	1.15	3.17
i (15 min)	1.073	0.96	1.367	0.833	1.207	2.533	0.96	1.367	0.9	1.207
i (20 min)	0.935	0.935	0.56	0.635	1.185	1.975	0.935	0.92	0.72	1.185
Total No. of precipitation events, *n* [-]			**123**					**259**		

Abbreviations: avg – average, std – standard deviation, cv – coefficient of variation, iqr – interquartile range, *i* (10 min) maximum 10 min intensity, max - maximum

The comparison of maximum short-duration intensities further supports the observed differences between the two event separation methods. The most pronounced differences occur for Type 1, where KDE produces considerably higher maximum 10-, 15- and 20-minute intensities than AC. Higher values are also observed for Type 5. For Types 2 and 3, the differences are smaller, while Type 4 shows only minor differences between the two methods. These results indicate that KDE is more sensitive to short, intense precipitation bursts, particularly when the maximum precipitation occurs near the beginning of the event.

The shapes of the median Huff curves confirm the statistical results. For Type 1, both methods produce steep early-rising curves, indicating strong precipitation concentration in the first part of the event. The KDE curve is slightly steeper in the early part, which is consistent with the higher short-duration intensities obtained for this type. Type 2 and Type 3 curves show a more gradual accumulation pattern, with relatively small differences between AC and KDE. Type 4 curves clearly reflect late-peak precipitation events, where most of the cumulative precipitation occurs in the final part of the event. Type 5 curves are located close to the diagonal line, confirming their approximately uniform temporal distribution. The variability range of event durations is wider for KDE, particularly for Type 1 and Type

5, reflecting the greater heterogeneity of the identified event sample.

Overall, the Huff results indicate that the AC and KDE methods produce broadly similar median curve shapes for most Huff types but differ in the number of identified precipitation events and in the representation of short, intense events. The AC method produces fewer events, which is consistent with the longer minimum inter-event time applied by this method and its tendency to merge neighbouring precipitation bursts into longer events.

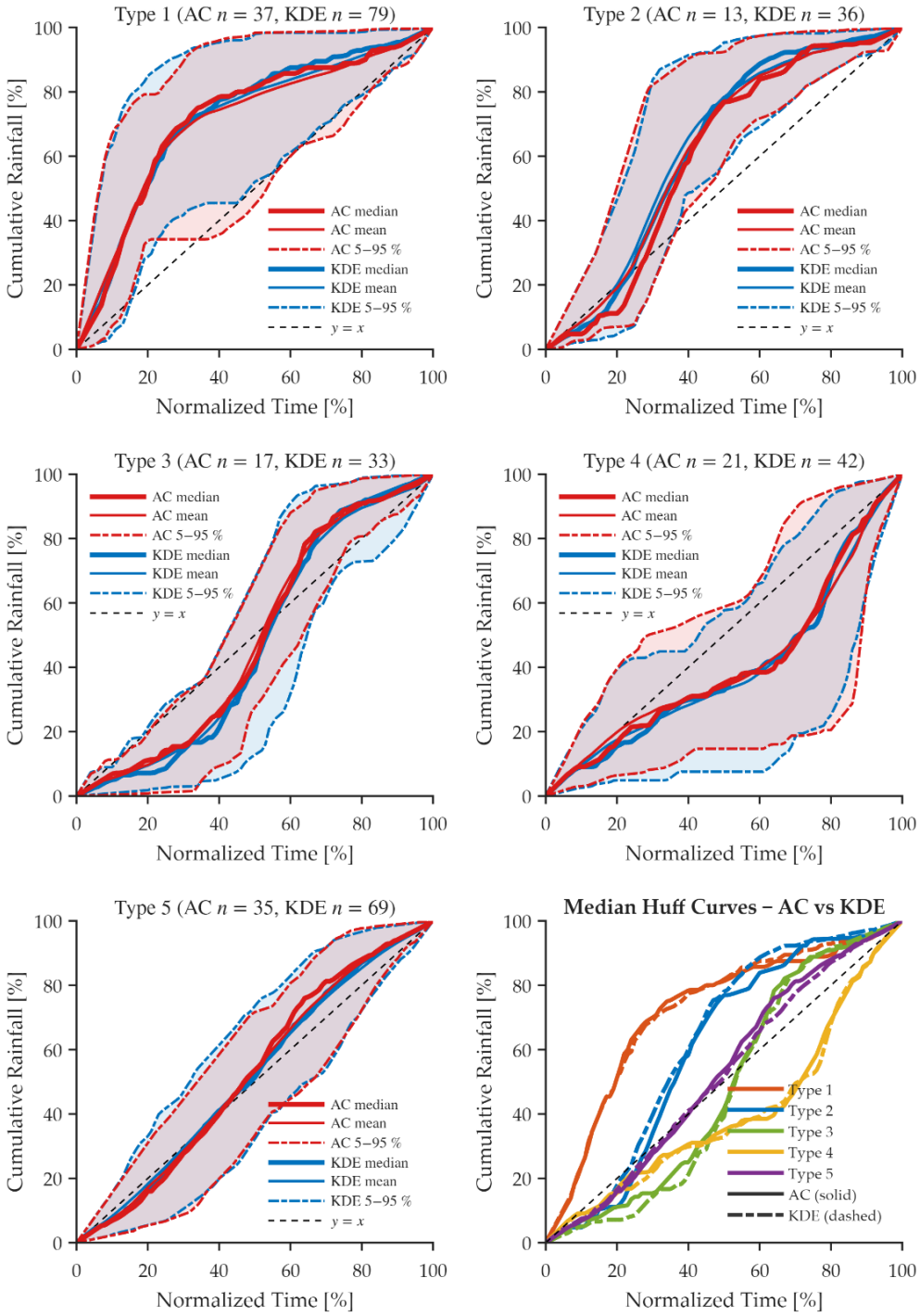


Figure 1. Huff hyetographs obtained using AC and KDE event separation methods

3.2 MAV Hyetographs

The MAV classification provides a different perspective on the temporal structure of precipitation events because the events are grouped according to duration classes rather than according to the position of the maximum intensity. The results are presented in Table 2 and Fig. 2. The same total number of events was used as in the Huff analysis, with 123 events identified using the AC method and 259 events using the KDE method. For both separation methods, the number of events generally increases with duration class, with the largest samples observed in C4 and C5, while C1 contains the smallest number of events. This reflects the fact that very short precipitation events between 10 and 20 min are less frequent than events with durations between 60 and 120 min.

Table 2. Statistics of MAV duration classes identified using AC and KDE event separation methods

	AC					KDE				
Classes	C1	C2	C3	C4	C5	C1	C2	C3	C4	C5
Duration interval	>=10 to <=20 min	>20 to <=40 min	>40 to <=60 min	>60 to <=90 min	>90 to <=120 min	>=10 to <=20 min	>20 to <=40 min	>40 to <=60 min	>60 to <=90 min	>90 to <=120 min
Number of blocks, *m* [-]	4	4	6	8	10	4	4	6	8	10
Number of precipitation events, *n* [-]	15	21	18	32	37	32	45	41	75	66
Precipitation depth, P [mm]										
P_{avg}	7.34	4.07	6.66	3.28	4.91	5.56	3.63	6.93	3.29	5.54
P_{std}	7.21	3.33	9.77	4.48	6.87	7.28	3.54	10.78	3.80	6.90
P_{cv} [%]	98.24	81.70	146.63	136.48	139.83	130.99	97.72	155.63	115.29	124.56
P_{iqr}	9.15	2.63	4.10	1.55	2.43	4.45	2.78	4.95	1.85	5.40
$\boldsymbol{P_{max}}$	24.40	13.00	38.50	23.80	28.50	31.70	19.50	54.70	23.80	33.80
Precipitation duration, t [min]										
t_{avg}	15.00	32.38	53.61	76.09	107.84	15.78	32.00	53.54	77.33	107.65
t_{std}	3.78	5.84	5.64	8.96	9.39	3.62	5.68	5.27	9.17	9.08
t_{cv} [%]	25.20	18.02	10.52	11.77	8.71	22.92	17.75	9.85	11.85	8.44
t_{iqr}	7.50	11.25	10.00	15.00	16.25	5.00	11.25	10.00	15.00	15.00
Maximum intensities, i [mm/min]										
i (10 min)	2.44	1.01	1.34	1.22	1.11	3.17	1.34	3.28	1.22	1.11
i (15 min)	1.37	0.73	1.21	0.94	1.07	1.37	1.12	2.53	0.95	1.07
i (20 min)	0.54	0.56	1.19	0.80	0.94	0.54	0.92	1.98	0.80	0.94
Block with the highest intensity	2	2	1	2	1	2	2	1	2	1
Total No. of precipitation events, *n* [-]			**123**					**259**		

Abbreviations: avg – average, std – standard deviation, cv – coefficient of variation, iqr – interquartile range, *i* (10 min) maximum 10 min intensity, max - maximum

Within the AC method, the highest average precipitation depth occurs in C1, followed by C3 and C5,

while the lowest average precipitation depth is observed in C4. This indicates that the shortest events can still contain relatively high precipitation amounts, which is particularly relevant for urban drainage applications. The maximum precipitation depth is highest in C3, suggesting that events with durations between 40 and 60 min include some of the most intense precipitation episodes in the analysed data set. A similar pattern is visible in the maximum short-duration intensities: C1 has the highest 10-minute intensity, while C3 has the highest 20-minute intensity. The block with the maximum intensity occurs in the second block for C1, C2 and C4, and in the first block for C3 and C5, indicating that the dominant precipitation concentration often appears in the early part of the event.

An additional insight is provided by the position of the block with the highest average precipitation contribution. For both event separation methods, the same dominant pattern was obtained. The maximum precipitation contribution occurs in the second block for classes C1, C2 and C4, whereas classes C3 and C5 exhibit the highest contribution in the first block. This indicates that the temporal position of the dominant precipitation burst is remarkably stable and largely independent of the selected event separation method. Although the AC and KDE methods produce different numbers of precipitation events and different intensity characteristics, both approaches identify the same characteristic location of the most intense part of the event within each duration class.

For the KDE method, the general differences between duration classes are even more pronounced. The largest number of events is again observed in C4 and C5, while C1 contains the smallest number of events. The highest average precipitation depth occurs in C3, followed by C1 and C5, whereas C4 has the lowest average precipitation depth. The maximum precipitation depth is also highest in C3, reaching a value considerably larger than in the corresponding AC class. This confirms that the KDE method preserves short and medium-duration precipitation events with high precipitation amounts that may be partly merged into longer events when the AC method is used. The highest maximum 10-, 15- and 20-minute intensities are also observed in C3, which indicates that precipitation events lasting between 40 and 60 min are particularly important for the analysed data set from the perspective of short-duration intensity.

The MAV hyetographs show that the temporal distribution of precipitation differs among duration classes. In both AC and KDE results, C1 and C2 show a more gradual increase of cumulative precipitation, while C3, C4 and C5 exhibit more pronounced temporal concentration. This is especially visible in the MAV hyetographs, which represent the reconstructed average variability pattern and therefore provide the most relevant curve for interpretation. For longer classes, particularly C4 and C5, a substantial part of precipitation is concentrated in the first half of the event, indicating that longer short-duration events are not necessarily temporally uniform but may contain a dominant early precipitation segment.

The comparison between AC and KDE shows that the two methods produce similar general MAV patterns, but with noticeable differences in the degree of temporal concentration. The KDE method generally identifies a larger number of events in every duration class, approximately doubling the sample size compared with AC. Despite this difference, the average durations within each class are almost identical for the two methods, which confirms that the class-based grouping is consistent and that the main effect of the separation method is not on the duration class itself, but on the number and internal structure of the events assigned to each class.

The clearest differences between AC and KDE are observed in C3. In this class, KDE produces a higher maximum precipitation depth and substantially higher maximum short-duration intensities than AC. This indicates that the KDE method is more sensitive to intense precipitation events of intermediate duration. In C1 and C2, the differences between the two methods are smaller in terms of hyetograph shape, although KDE still identifies more events and slightly different intensity characteristics. In C4 and C5, the MAV hyetographs obtained by the two methods are relatively similar, suggesting that the influence of the event separation method decreases for longer duration classes.

Overall, the MAV results confirm that primary precipitation data processing influences not only the

number of identified precipitation events but also the derived temporal structure of dimensionless hyetographs. The influence is most evident in the intermediate duration class C3, where the KDE method captures stronger precipitation concentration and higher short-duration intensities. At the same time, the similarity of the AC and KDE MAV curves in several classes suggests that the MAV approach may be somewhat less sensitive to event separation than the Huff classification, because events are grouped by duration rather than by the position of the maximum intensity.

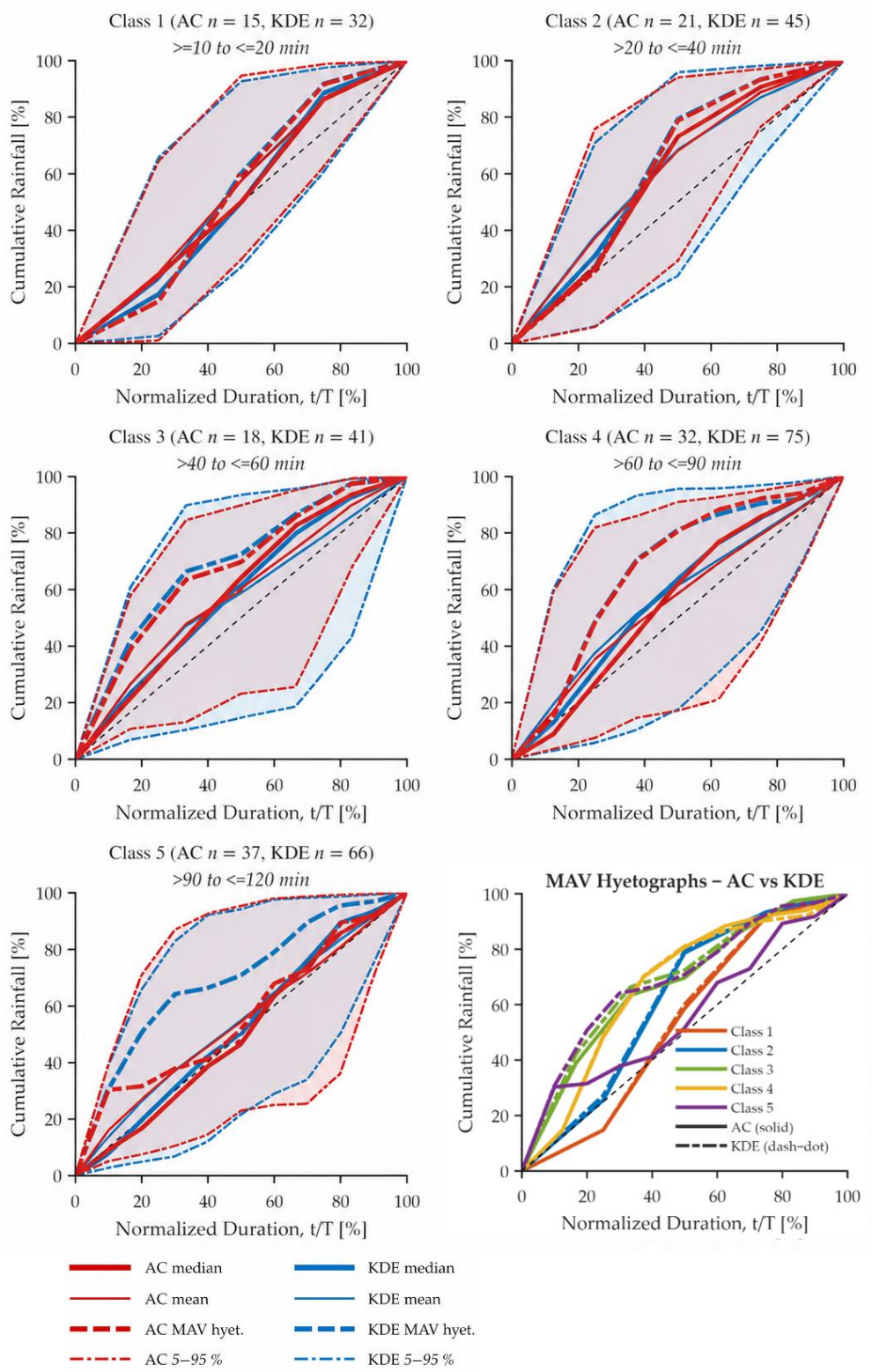


Figure 2. MAV hyetographs obtained using AC and KDE event separation methods

4 Conclusion

This study investigated the influence of primary precipitation data processing on the construction of dimensionless hyetographs using two precipitation event separation approaches (AC and KDE) and two hyetograph development methods (Huff and MAV). The analysis was performed using 5-minute precipitation data from the Čepin meteorological station and focused on short-duration precipitation events (≤ 120 min), which are particularly relevant for urban drainage applications.

The results showed that the selected precipitation event separation method significantly affects the number and characteristics of identified precipitation events. The KDE method identified more than twice as many precipitation events as the AC method, indicating a greater ability to preserve short and temporally concentrated precipitation bursts. These differences were reflected in both Huff and MAV hyetographs, confirming that primary precipitation data processing represents an important step in the development of design precipitation patterns.

The Huff analysis revealed that the largest differences between the AC and KDE methods occur for Type 1 events, where KDE produced substantially higher maximum 10-, 15- and 20-minute intensities. Although the general shapes of the median Huff curves remained relatively similar, the KDE method consistently preserved more intense early-peaked precipitation events.

The MAV analysis showed that the event separation method influences the number of precipitation events and intensity statistics within individual duration classes. However, the position of the dominant precipitation block remained identical for both AC and KDE methods, indicating that the characteristic temporal location of the most intense part of the event is relatively stable regardless of the selected event separation procedure. The greatest differences between the two methods were observed for Class C3 (40–60 min), where KDE produced considerably higher precipitation depths and short-duration intensities than AC.

A comparison of the Huff and MAV approaches provides additional insight into the temporal structure of intense precipitation events. While the Huff classification describes the position of the maximum precipitation intensity within an event, the MAV method characterises its duration-dependent temporal distribution. The highest 10-minute precipitation intensity identified using the KDE method in the Huff analysis occurred for Type 1 events. Similarly, within the MAV framework, the highest short-duration intensities were observed in Class C3. This suggests that the most critical precipitation events for urban drainage systems are characterised not only by high short-duration intensities, but also by a pronounced concentration of precipitation at the beginning of events lasting approximately 40–60 min.

Overall, the results indicate that Huff and MAV hyetographs provide complementary rather than competing descriptions of precipitation temporal structure. Huff curves appear more sensitive to changes in precipitation event delineation because they are directly linked to the timing of the maximum intensity, whereas MAV hyetographs preserve the dominant temporal concentration patterns more consistently across different event separation methods. The methodological framework applied in this study can also be transferred to regions with different precipitation regimes, including karst areas of Croatia, without fundamental changes to the event separation or hyetograph construction procedures. However, the derived MIT values and the resulting Huff and MAV hyetographs should be determined from local high-resolution precipitation records, particularly because differences in precipitation regime and orographic effects may influence event duration, intensity and temporal distribution. The adopted precipitation threshold, maximum event duration and MAV duration classes should also be evaluated with respect to local precipitation characteristics and the intended application. Therefore, the methodology can be considered transferable, whereas the resulting parameters and dimensionless hyetographs remain site-specific. The findings highlight the importance of transparent and methodologically consistent precipitation event definition when developing design hyetographs for urban drainage applications.

Acknowledgements

Funded by the European Union – Next Generation EU. However, the views and opinions expressed are solely those of the author(s) and do not necessarily reflect those of the European Union or the European Commission. Neither the European Union nor the European Commission can be held responsible for them.

References

Bezak, N., Šraj, M., Rusjan, S. and Mikoš, M. 2018 Impact of the rainfall duration and temporal rainfall distribution defined using the Huff curves on the hydraulic flood modelling results. *Geosciences* 8 (2), 69.

Bonacci, O. 1994 *Oborine – analiza, obrada i primjena*. Građevinski institut Hrvatske, Zagreb, Croatia.

Bonta, J.V. 2004 Development and utility of Huff curves for disaggregating precipitation amounts. *Applied Engineering in Agriculture* 20 (5), 641–653.

Cao, S., Diao, Y., Wang, J., Liu, Y., Raimondi, A. and Wang, J. 2023 KDE-based rainfall event separation and characterization. *Water* 15 (3), 580.

Dunkerley, D. 2008 Identifying individual rain events from pluviograph records: a review with analysis of data from an Australian dryland site. *Hydrological Processes* 22, 5024–5036.

Dunkerley, D. 2010 How do the rain rates of sub-event intervals such as the maximum 5- and 15-min rates (I5 or I30) relate to the properties of the enclosing rainfall event? *Hydrological Processes* 24, 2425–2439.

Dunkerley, D. 2022 Regional rainfall regimes affect the sensitivity of the Huff quartile classification to the method of event delineation. *Water* 14 (7), 1047.

Ellouze, M., Abida, H. and Safi, R. 2009 A triangular model for the generation of synthetic hyetographs. *Hydrological Sciences Journal* 54 (2), 287–299.

Grubišić, M., Šreng, Ž., Berbić, J. and Brleković, T. 2026 Systematic assessment of minimum inter-event time determination methods and precipitation thresholds for constructing design-critical Huff hyetographs. *Water* 18 (8), 976.

Huff, F.A. 1967 Time distribution of rainfall in heavy storms. *Water Resources Research* 3 (4), 1007–1019.

Krvavica, N., Jaredić, K. and Rubinić, J. 2018 Methodology for defining the design storm for sizing the infiltration system. *Građevinar* 70 (8), 657–669.

Krvavica, N. and Rubinić, J. 2020 Evaluation of design storms and critical rainfall durations for flood prediction in partially urbanized catchments. *Water* 12 (7), 2044.

Medina-Cobo, M.T., García-Marín, A.P., Estévez, J. and Ayuso-Muñoz, J.L. 2016 The identification of an appropriate minimum inter-event time (MIT) based on multifractal characterization of rainfall data series. *Hydrological Processes* 30, 3507–3517.

Nguyen, D.T. and Chen, S.T. 2022 Generating continuous rainfall time series with high temporal resolution by using a stochastic rainfall generator with a copula and modified Huff rainfall curves. *Water* 14 (13), 2123.

Pilgrim, D.H. and Cordery, I. 1975 Rainfall temporal patterns for design floods. *Journal of the Hydraulics Division*, ASCE 101 (HY1), 81–85.

Pohle, I., Niebisch, M., Müller, H., Schümberg, S., Zha, T., Maurer, T. and Hinz, C. 2018 Coupling Poisson rectangular pulse and multiplicative microcanonical random cascade models to generate sub-daily precipitation time series. *Journal of Hydrology* 562, 50–70.

Restrepo-Posada, P.J. and Eagleson, P.S. 1982 Identification of independent rainstorms. *Journal of Hydrology* 55, 303–319.

Tu, A., Zeng, J., Liu, Z., Zheng, H. and Xie, S. 2023 Effect of minimum inter-event time for rainfall event separation on rainfall properties and rainfall erosivity in a humid area of southern China. *Geoderma* 431, 116332.

Vantas, K. and Sidiropoulos, E. 2021 Intra-storm pattern recognition through fuzzy clustering. *Hydrology* 8 (2), 57.
Wartalska, K., Kaźmierczak, B., Nowakowska, M. and Kotowski, A. 2020 Analysis of hyetographs for drainage system modeling. *Water* 12 (1), 149.
Yin, S., Xie, Y., Nearing, M.A., Guo, W. and Zhu, Z. 2016 Intra-storm temporal patterns of rainfall in China using Huff curves. Transactions of the ASABE 59 (6), 1619–1632.

POSSIBILITIES OF WATER RESOURCES USE FROM DRAINAGE CANALS ALONG RESERVOIRS ON THE DRAVA RIVER, CROATIA

Oriol ROCA TORRES[1], Dijana OSKORUŠ[2*], Hrvoje MEAŠKI[2], Saša ZAVRTNIK[2]

[1] *Polytechnic University of Catalonia, Faculty of Civil Engineering*

E-mail: oriolrocatorres@gmail.com

[2] *University of Zagreb, Faculty of Geotechnical Engineering*

E-mail: doskorus@gfv.hr

E-mail: hmeaski@gfv.hr

E-mail: zavrtnik@gfv.hr

[*] *Corresponding author*

Abstract

Drainage canals constructed along hydropower reservoirs of the Drava River play a fundamental role in controlling seepage, maintaining embankment stability and regulating interactions between groundwater and surface water. Despite their operational importance, their hydrological behavior, water quality and potential for secondary water use have received limited scientific attention. This paper summarizes the main findings of a master thesis focused on the drainage canal system associated with the Varaždin, Čakovec and Dubrava hydropower reservoirs in northern Croatia, with detailed field and laboratory analyses in the Dubrava area. Field measurements, laboratory analyses and historical operational data were used to characterize flow regime, groundwater-reservoir connectivity, physicochemical parameters, nutrients, trace metals, microbiological indicators and sediment composition. Results show that drainage canal water is predominantly groundwater-derived and strongly influenced by reservoir operation. Although hydraulic conditions are relatively stable, microbiological contamination and some trace-metal results, particularly chromium in pumped groundwater restrict direct human use, irrigation and aquaculture. In contrast, stable flows and existing infrastructure indicate limited potential for hydropower production and environmental enhancement.

Key words

Drainage canals, hydropower reservoirs, water quality, groundwater-surface water interaction, Drava River, water reuse, trace metals.

1 Introduction

The Drava River hydropower system in northern Croatia is an example of a regulated river corridor where energy production, groundwater dynamics and water-management objectives are closely connected. Along the reservoirs and derivation canals, drainage channels were constructed to collect seepage water, protect embankments and maintain hydraulic stability. These channels form part of the broader groundwater-reservoir system, yet their water quality, hydrological role and possible secondary uses have received limited scientific attention.

The relevance of this topic has increased under climate change, which is expected to intensify hydrological variability, modify groundwater recharge and increase pressure on water resources. Within the Interreg Central Europe MAURICE project, the Faculty of Geotechnical Engineering, University of Zagreb, carried out research on urban water resources and groundwater dynamics in the Varaždin region.

This study contributes to that framework by evaluating whether drainage canal water can be considered an additional resource or whether it should be understood as redistributed water within the same integrated hydrological system.

The main objectives were: (i) to analyse the hydrological functioning and water quality of the drainage canals, including groundwater interactions and hydro chemical characteristics; (ii) to evaluate the suitability of different secondary water uses in relation to measured water quality and existing infrastructure; and (iii) to provide technical insight to support future water-management strategies in regulated river systems.

2 Study area and drainage canal system

The Drava River is approximately 710 km long and flows from the Italian Alps through Austria, Slovenia and Croatia before joining the Danube (Fig. 1). In the Croatian section, which extends for approximately 166 km, three main hydropower plants form the downstream part of the Drava hydropower cascade: HPP Varaždin, HPP Čakovec and HPP Dubrava (Fig. 2). These are low-head, run-of-river and diversion-type hydropower plants designed for coordinated operation, energy production, flow regulation and water management.

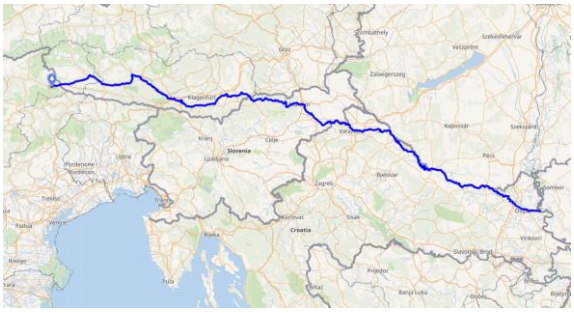


Figure 1. Map of the Drava River (Source: OpenStreetMap).

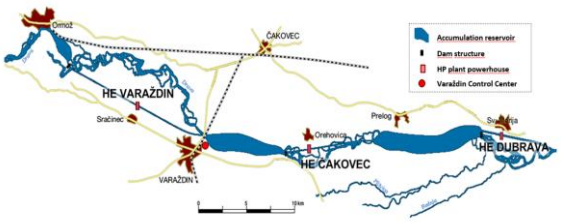


Figure 2. Croatian Drava hydropower cascade (Source: HEP, PP Sjever).

The three Croatian plants were commissioned in 1975, 1982 and 1989, respectively. Together, they have an installed capacity of about 246 MW and an expected annual production of roughly 1150 GWh. The operation is coordinated from the Control and Dispatch Centre in Varaždin, while each facility includes a gated dam, a headrace canal, a powerhouse equipped with Kaplan turbines and a tailrace canal. A mandatory ecological flow of 8 m3/s is continuously released into the old Drava riverbed.

Drainage canals run parallel to the reservoirs, headrace canals and embankments. They are excavated mainly in gravel and sand and act as controlled outlets that intercept seepage water and shallow groundwater. Their geometry and discharge capacity vary between hydropower plants because each section of the system was adapted to local hydrological and geomorphological conditions. These technical parameters are summarised in Table 1.

Table 1. Technical parameters of the drainage channels.

Hydropower plant	Drainage-channel width (m)	Flow range (m^3/s)
HPP Varaždin	1-2	0.04-0.3
HPP Čakovec	2-5	0.5-4
HPP Dubrava	3-7	2.5-8

The Dubrava reservoir is the most downstream and largest reservoir in the Croatian system. It is bordered by lateral embankments and located within a permeable alluvial environment, where groundwater is shallow and hydraulic gradients are strongly influenced by reservoir water levels. For

this reason, the Dubrava area was selected for detailed field measurements, water sampling and sediment analysis.

3 Materials and methods

The research combined field measurements, laboratory analyses, historical operational information and a qualitative multi-criteria assessment. Fieldwork focused on the drainage-channel system around Donja Dubrava and Veliki Bukovec. Sampling points included the left drainage canal, right drainage canal, fishpond outlet and pumped groundwater from 9 m depth (Fig. 3). Hydraulic measurements were carried out in selected cross-sections to characterise flow velocity and channel geometry.

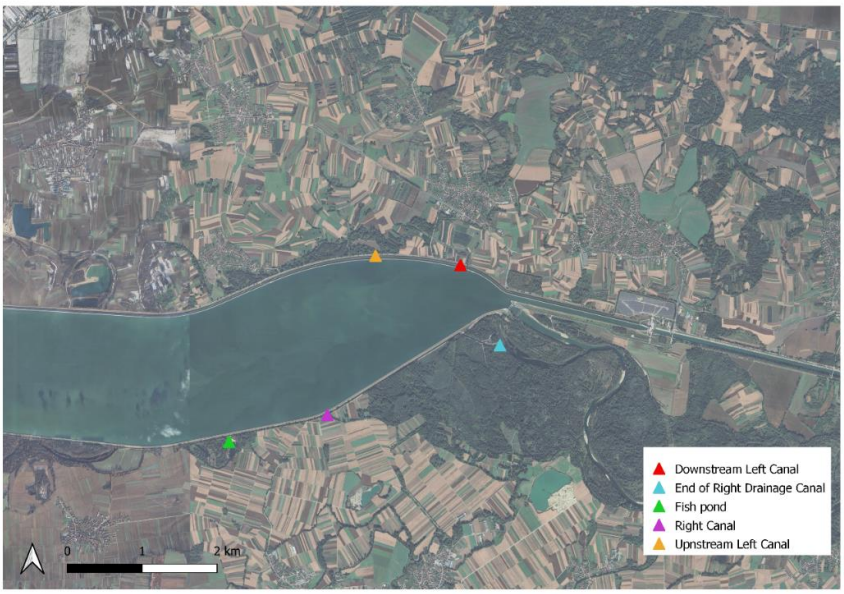


Figure 3. Donja Dubrava drainage-channel sampling and hydraulic measurement locations (Source: author's QGIS elaboration).

Water quality was assessed through measurements of pH, electrical conductivity, total dissolved solids, major ions, nutrients, total organic carbon, trace metals and microbiological indicators. Trace metals included Cu, Cr, Zn, Cd, Pb, As, Ni, Hg, Fe and Mn. Cr, Cu, Zn, Fe and Mn were analysed by FAAS technique and are reported in mg/L, while As, Cd, Ni and Pb were analysed by GFAAS technique, and Hg by CVAAS technique on Atomic Absortion Spectrometaer AAnalyst PerkinElmer; these latter results are reported in µg/L. Microbiological analyses included total coliform bacteria, Escherichia coli, intestinal enterococci, heterotrophic plate counts at 22 °C and 36 °C, and Clostridium perfringens.

Sediment collected from the end of the right drainage canal was analysed through granulometry and chemical characterisation. Grain-size results were used to calculate effective particle diameters, while geochemical analyses supported interpretation of metal retention and sediment-water interactions. Finally, potential uses of drainage canal water were evaluated for human use, hydropower, irrigation, aquaculture, environmental value and recreation. The assessment considered chemical suitability, microbiological quality, hydro morphology, operational compatibility and safety.

4 Results and Discussion

4.1 Groundwater-reservoir connectivity and hydraulic behaviour

The results support the interpretation that drainage canal water is not an independent resource, but a redistributed component of the reservoir-aquifer system. The drainage canals therefore function

primarily as engineered groundwater drains designed to maintain acceptable groundwater levels behind the embankments and reduce flood risk in adjacent agricultural and residential areas. The Varaždin alluvial aquifer consists mainly of permeable Quaternary gravels and sands with local silt and clay interbeds. Groundwater flow generally follows a north-west to south-east orientation, approximately parallel to the Drava River and the hydropower reservoirs. Because fine-grained cover is thin or discontinuous in several areas, the aquifer is vulnerable to rapid infiltration and hydraulic responses (Bačani & Posavec, 2008; Karlović, 2022).

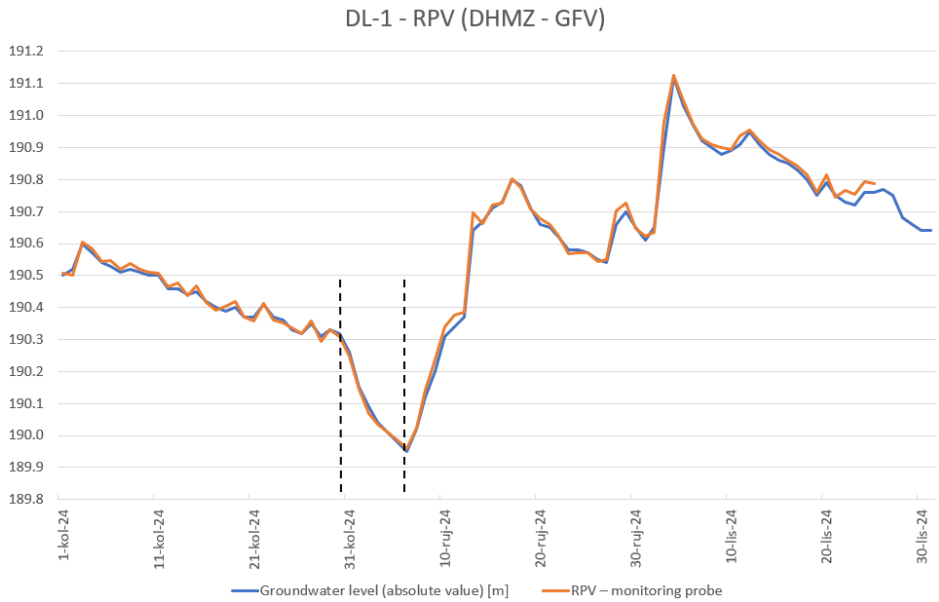


Figure 4. Groundwater level in piezometer DL-1 situated on the right bank of the Ormož reservoir and water level in the Ormož reservoir illustrating hydraulic connectivity between the reservoir and the alluvial aquifer (Source: MAURICE project unpublished data).

Monitoring data of the groundwater level in piezometer DL-1 situated on the right bank of the Ormož reservoir, and water level in the Ormož reservoir (Fig. 2) show that groundwater levels follow reservoir-level fluctuations with reduced amplitude and a slight temporal delay (Fig. 4). This confirms strong hydraulic coupling between reservoirs and the adjacent aquifer. Drainage canals connected to the shallow aquifer are therefore expected to reflect the same reservoir-controlled boundary conditions. In practical terms, this means that using drainage canal water may indirectly affect the broader groundwater-reservoir balance and should not be treated separately from the hydropower system.

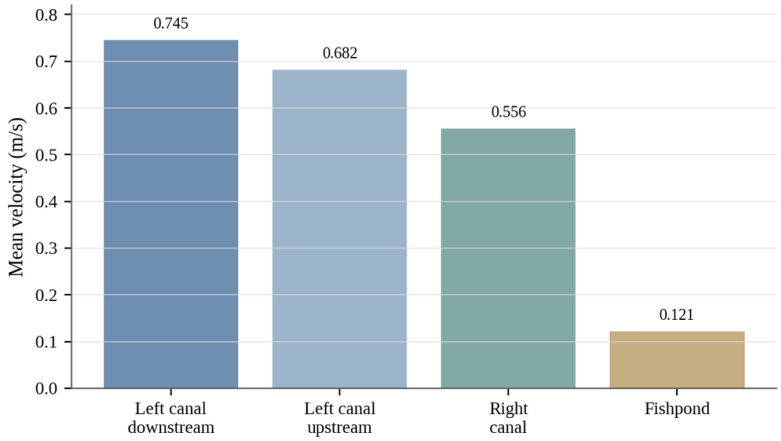


Figure 5. Mean velocities measured in selected hydraulic sections (Source: Author's own elaboration).

Measured flow velocities (Fig. 5) indicate clear differences between sections. The highest mean velocity was recorded in the left canal downstream section (0.745 m/s), followed by the left canal upstream

section (0.682 m/s) and the right canal (0.556 m/s). The fishpond section showed much lower velocity (0.121 m/s), reflecting different hydraulic conditions and reduced conveyance. These results are consistent with the role of the main drainage canals as active seepage collectors and with the more stagnant character of the fishpond system.

4.2 Water quality and trace metals

Physicochemical parameters were relatively stable among sampling locations (Table 4). pH ranged from 7.76 in pumped groundwater to 8.03 in the right canal, conductivity ranged from 336 to 355 µS/cm and total dissolved solids ranged from 168.7 to 176.9 mg/L. These values indicate broadly similar hydro chemical conditions and support the interpretation of common groundwater-reservoir influence across the sampling points. Nitrate and ammonia concentrations were low, with nitrates between 0.1 and 0.5 mg/L and ammonia between 0.02 and 0.07 mg/L.

Trace-metal interpretation (Fig. 6; Table 5) depends on the analytical method and reporting unit. Cr, Cu, Zn, Fe and Mn are reported in mg/L, whereas As, Cd, Ni, Pb and Hg are reported in µg/L. The highest As and Cd values were measured in the right canal, with As = 1.779 µg/L and Cd = 0.497 µg/L; these values are not mg/L. Left canal water contained As = 0.502 µg/L and Cd = 0.035 µg/L, while pumped groundwater showed Cr = 0.095 mg/L and Cd = 0.126 µg/L. In this dataset, the main chemical exceedance relevant to direct human use is Cr in pumped groundwater, while untreated use is also restricted by microbiological indicators.

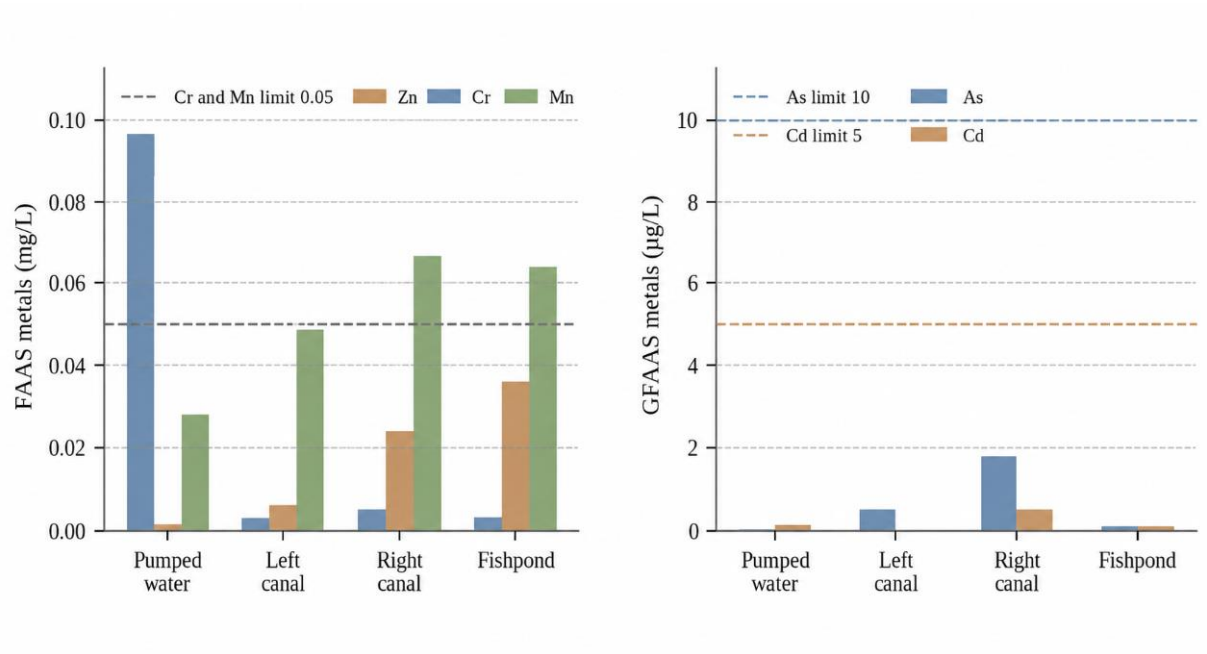


Figure 6. Selected dissolved metals in water samples. FAAS elements are reported in mg/L, while GFAAS elements are reported in µg/L; dashed lines indicate drinking-water reference limits (Source: Author's own elaboration).

The spatial pattern suggests that metal concentrations are not controlled only by one point source, but by a combination of groundwater composition, sediment interaction and local hydraulic conditions. The downstream accumulation of fine sediments in slower sections can favor adsorption and retention of trace elements, especially where fine particles and organic matter accumulate. Redox-sensitive Fe and Mn processes may also influence mobilization and retention of trace metals at the groundwater-surface water interface.

4.3 Water quality and trace metals

Microbiological analyses (Fig. 7; Table 6) indicate that canal water cannot be considered suitable for

human use or direct recreational contact. Total coliform bacteria were detected in all samples, with the highest value in pumped water (880 cfu/100 mL) and high values in both left and right canal samples. Escherichia coli was also detected in all samples analysed, ranging from 8 cfu/100 mL in the right canal on 16 November to 264 cfu/100 mL in the fishpond nearby right drainage canal at Veliki Bukovec. Intestinal enterococci ranged from 2 to 20 cfu/100 mL.

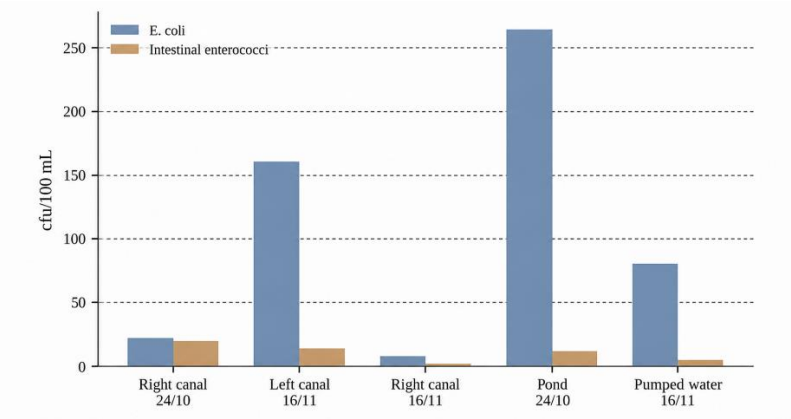


Figure 7. Microbiological indicators in sampled waters.

These results point to diffuse microbiological inputs, possibly associated with agricultural land use, wildlife, surface runoff or local groundwater vulnerability. Although contamination levels are not extreme compared with heavily polluted surface waters, they are incompatible with drinking-water requirements and impose restrictions on recreation, irrigation of edible crops and aquaculture. Seasonal variability may also be important, since storm events can mobilise sediments, organic matter and faecal indicators.

4.4 Sediment composition and geochemical implications

The right-canal sediment sample was coarse overall but included fine fractions that are important for metal retention (Fig. 8). Granulometric analysis yielded d10 = 0.13982 mm, d30 = 0.24267 mm and d60 = 5.23089 mm. The resulting hydraulic conductivity estimate was approximately 5.9×10^{-5} m/s, reflecting the hydraulic behaviour of the sampled sediment and not the regional alluvial aquifer. Chemical analysis showed alkaline conditions, high organic matter content and carbonate presence, with pH = 8.1, humus = 38.3%, organic carbon = 20.7% and carbonates = 3.93%.

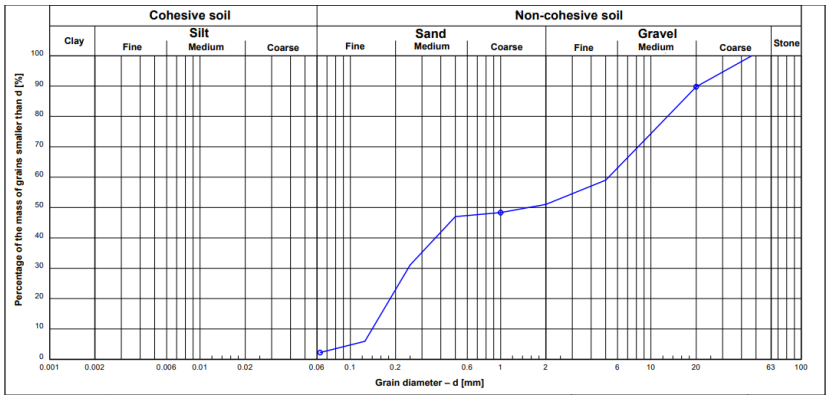


Figure 8. Grain-size distribution of the sediment sample.

Table 2. Trace metal concentrations in sediment.

Metal	Cu	Cr	Zn	Cd	Pb	As	Ni	Hg	Fe	Mn
Concentration (mg/kg)	6.33	15.11	145.06	0.28	43.46	3.21	10.83	0.00617	139.47	298.52

Sediment trace metals (Table 2) were generally below regulatory thresholds, but the sediment still plays an important role in the water-quality system. Measured concentrations included Zn = 145.06 mg/kg, Pb = 43.46 mg/kg, Cr = 15.11 mg/kg, Ni = 10.83 mg/kg, Cu = 6.33 mg/kg and As = 3.21 mg/kg. The combination of organic matter, carbonate content and fine sediment fractions provides surfaces for adsorption and may temporarily store metals that can later be remobilised under changing redox or hydraulic conditions.

4.5 Suitability of potential water uses

The suitability assessment (Table 3) shows strong contrasts between potential uses. Direct human use is not suitable without treatment because of microbiological contamination and the Cr exceedance observed in pumped groundwater. Irrigation and aquaculture should not be recommended without additional monitoring because suitability depends on trace-metal units, site-specific exposure criteria and microbiological quality. Recreational use is also restricted by water-quality concerns and unsafe embankment conditions.

Hydropower is the most feasible secondary use, because water quality does not limit energy production and the system already contains infrastructure designed to use drainage-channel flows. However, the potential is limited by available head, canal geometry and operational constraints. Environmental value is possible but limited; the channels provide habitat and landscape functions, but metal contamination and engineered morphology restrict biodiversity potential. Overall, drainage canal water should be managed as part of the integrated groundwater-reservoir system rather than as a freely available independent water source.

Table 3. Qualitative multi-criteria assessment of suitability for different potential uses of drainage canal water.

Use option	Chemical suitability	Microbiological suitability	Hydromorphology & habitat	Operational compatibility	Safety
Human use	Cr exceedance in pumped water; treatment required	Does not meet standards	Not relevant	Not practicable	Health risk
Hydropower	Not limiting	Not limiting	Limited head but stable flow	Operationally compatible	Safe
Irrigation	Requires trace-metal verification	Microbiological control required	Physically possible	Only after monitoring/treatment	Moderate
Aquaculture	Requires site-specific toxicity assessment	Low to moderate contamination	Poor habitat	Not practicable without control	Moderate
Environmental value	Trace-metal monitoring needed	Wildlife-typical levels	Limited but present	Occasional compatibility	Safe
Recreation	Water-quality concern	Not compliant	Unsafe embankments	Only indirectly compatible	High risk

4.6 Integrated system interpretation and hydraulic sections

The conceptual model and hydraulic cross-sections (Fig. 9; Fig. 10, Fig. 11, Fig. 12 and Fig. 13) provide the physical basis for interpreting the results. They show how seepage from the reservoir and local recharge are intercepted by the drainage canal, while site-specific channel geometry controls velocity, residence time and the potential accumulation of fine sediments.

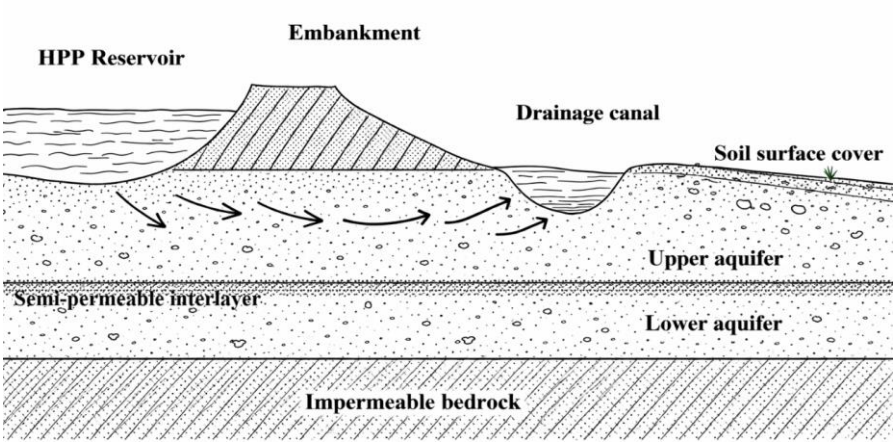


Figure 9. Conceptual model of the integrated groundwater-reservoir-drainage canal system.

The conceptual model shows the reservoir embankment, the drainage canal, the old Drava riverbed and the upper and lower aquifer. It illustrates why drainage canal water should be interpreted as part of a managed hydrogeological system rather than as a separate source. The reservoir and embankment generate hydraulic gradients, while the canal drains groundwater influenced by seepage and local recharge.

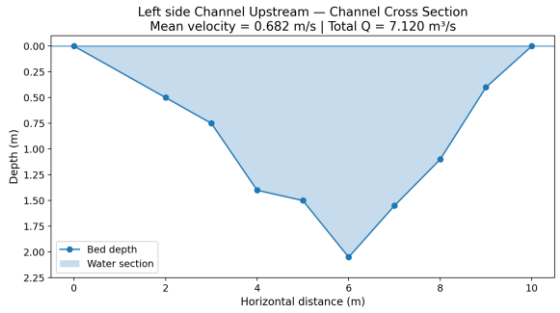


Figure 10. Left canal upstream cross-section.

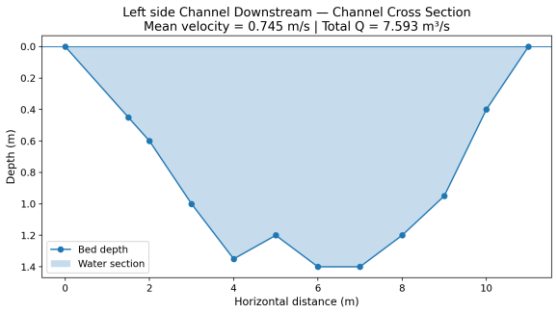


Figure 11. Left canal downstream cross-section.

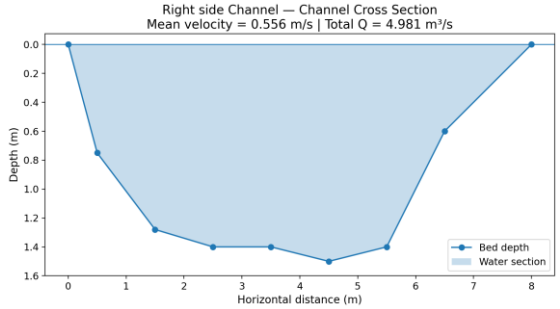


Figure 12. Right drainage canal cross-section.

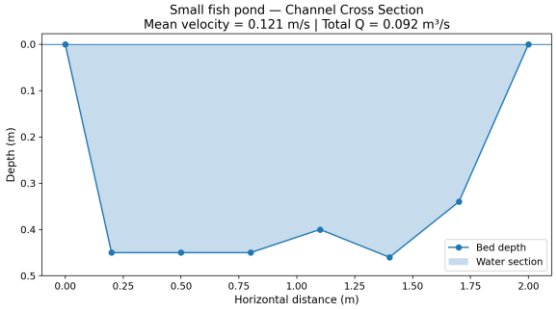


Figure 13. Fishpond cross-section.

The measured cross-sections (Fig. 10, Fig. 11, Fig. 12 and Fig. 13) show the contrasting hydraulic behaviour of the study sites. The left and right drainage canals present clearly defined flow sections and measurable velocities. By contrast, the fishpond, located along the right drainage channel near Veliki Bukovec was created by gravel excavation as part of the reservoir-drainage channel-groundwater system. When the reservoir water level is high, the pond is mainly filled by groundwater and excess water overflows into the right drainage channel; when the reservoir water level is low, the pond can be filled by water from the drainage channel. This explains why the fishpond section is wider and hydraulically slower than the main drainage canals, favouring longer residence time and the accumulation of fine sediments and aquatic vegetation.

Table 3. Qualitative multi-criteria assessment of suitability for different potential uses of drainage canal water.

Use option	Chemical suitability	Microbiological suitability	Hydromorphology & habitat	Operational compatibility	Safety
Human use	Cr exceedance in pumped water; treatment required	Does not meet standards	Not relevant	Not practicable	Health risk
Hydropower	Not limiting	Not limiting	Limited head but stable flow	Operationally compatible	Safe
Irrigation	Requires trace-metal verification	Microbiological control required	Physically possible	Only after monitoring/treatment	Moderate
Aquaculture	Requires site-specific toxicity assessment	Low to moderate contamination	Poor habitat	Not practicable without control	Moderate
Environmental value	Trace-metal monitoring needed	Wildlife-typical levels	Limited but present	Occasional compatibility	Safe
Recreation	Water-quality concern	Not compliant	Unsafe embankments	Only indirectly compatible	High risk

Table 4. Summary of physicochemical parameters, nutrients and TOC.

Location	pH	Conductivity (µS/cm)	TDS (mg/L)	NO3- (mg/L)	NH3 (mg/L)	TOC (mg/L)
Groundwater	7.76	339	169.4	0.4	0.02	0.76
Left canal	8.00	336	168.7	0.5	0.05	1.054
Right canal	8.03	346	173.7	0.4	0.05	2.700
Fishpond	7.90	355	176.9	0.1	0.07	2.754

Table 5. Selected dissolved metals controlling water-use suitability.
Source: Author's own elaboration. These elements have been analyzed below detection limits: Cr <0.003 mg/L; Zn <0.0015 mg/L; As <0.05 µg/L; Cd <0.002 µg/L; Ni <0.07 µg/L; Pb <0.05 µg/L; Hg <0.009 µg/L.

Sampling point	Cr (mg/L)	Zn (mg/L)	Cd (µg/L)	As (µg/L)	Mn (mg/L)	Main interpretation
Pumped water	0.095	<0.0015	0.126	<0.05	0.028	Cr exceeds 0.05 mg/L limit
Left canal	<0.003	0.006	0.035	0.502	0.049	Elements do not exceed limits
Right canal	0.005	0.024	0.497	1.779	0.067	Mn exceeds 0.05 mg/L limit
Fishpond	<0.003	0.036	0.109	0.115	0.064	Mn exceeds 0.05 mg/L limit

Table 6. Main microbiological indicators (cfu/100 mL).

Sampling location (date)	Total coliforms	E. coli	Intestinal enterococci	Interpretation
Right canal (24/10/2025)	142	22	20	Faecal indicators present
Left canal (16/11/2025)	688	160	14	High coliform and E. coli values
Right canal (16/11/2025)	520	8	2	Coliforms persist; lower E. coli
Fishpond - Veliki Bukovec (24/10/2025)	336	264	12	Highest E. coli value
Pumped water, 9 m (16/11/2025)	880	80	5	Groundwater sample also affected



Figure 14. HPP Dubrava hydropower structures. Source: HE Sjever.



Figure 15. HPP Dubrava reservoir and dam structures (Source: HE Sjever).

Together, the maps, cross-sections and photographs (Fig. 14 and Fig. 15) connect the study area, field design, hydraulic measurements and water-quality limitations. They show that drainage canal management depends on the combined effect of hydraulic connectivity, contamination risk and operational constraints.

4.7 Integrated system interpretation and hydraulic sections

The assessment identifies several practical implications for integrated water management. First, any reuse option must be evaluated together with groundwater and reservoir operation, because drainage canal flow is not an independent water supply. Second, water-quality limitations are more restrictive than water quantity in the studied canal sections, mainly because of microbiological indicators and certain trace-metal results. Third, the most promising use is energy-related, while uses involving human contact, food production or aquatic organisms require caution, regarding Cr and Mn content as well as microbiological activity, indicating the need for further monitoring.

For operational management, the most important recommendation is to establish longer-term monitoring that covers seasonal variability. The present dataset represents autumn conditions, when rainfall and reservoir operation were relatively stable. Summer low-water periods, storm events and maintenance drawdowns could modify flow velocity, sediment mobilisation, metal concentrations and microbiological contamination. Monitoring should therefore combine hydraulic, chemical, microbiological and sediment indicators, as summarised in Table 7.

Table 7. Recommended monitoring priorities for future management.

Monitoring priority	Reason	Suggested output
Seasonal discharge and velocity	To quantify variability under reservoir operation and rainfall events	Time series of canal flow and hydraulic response
Cr and Mn (mg/L)	Exceeding maximum allowable concentrations	Seasonal concentration ranges and detection-limit reporting
Microbiological indicators	E. coli, enterococci and coliforms restrict human contact and reuse	Identification of contamination peaks and possible sources
Sediment metals and grain size	Fine sediments and organic matter may retain or release metals	Spatial map of metal storage and mobilisation risk
Groundwater levels and reservoir stages	Needed to confirm hydraulic coupling and time lag	Coupled reservoir-aquifer-canal response model

These recommendations are directly aligned with the purpose of the MAURICE project, because they support adaptation to climate variability, improved groundwater protection and evidence-based water-management decisions. They also make the approach transferable to other regulated river systems where drainage canals are used primarily for infrastructure safety but may also appear attractive as secondary water resources.



Figure 16. Drainage canal landscape context and potential non-consumptive value.

A key final point is that reuse feasibility is not fixed, as illustrated by the drainage canal landscape context (Fig. 16). Hydropower potential depends mainly on stable flow, available head and infrastructure compatibility, whereas environmental enhancement depends on habitat quality, contamination control and maintenance practices. Therefore, future management should avoid treating the drainage canals as a single homogeneous resource and should instead evaluate each canal segment according to its hydraulic behaviour and water-quality profile.

5 Conclusion

Drainage canals along the Croatian Drava River hydropower cascade play an essential role in embankment stability, seepage control and groundwater regulation. The study confirms that they are hydraulically connected to the alluvial aquifer and strongly influenced by reservoir operation. Therefore, their water should not be considered an independent resource, but a redistributed component of the integrated groundwater-reservoir-drainage system.

Water quality is the main factor limiting potential use. Although physicochemical parameters and nutrients are relatively stable, microbiological contamination and certain trace-metal results, particularly Cr in pumped groundwater, restrict direct human use without treatment and require caution for irrigation, aquaculture and recreation. Sediment properties suggest that geochemical interactions and fine sediment accumulation may influence metal storage and mobilization, especially in slower canal sections.

Among the evaluated uses, limited hydropower production is the most compatible with existing conditions, because it is less affected by chemical and microbiological quality. Environmental enhancement may also be possible, but only if managed in a way that accounts for contamination risks and the engineered character of the channels. Future research should prioritise seasonal monitoring, expanded trace-metal speciation, sediment sampling along different canal segments and coupled groundwater-reservoir-canal modelling.

Acknowledgements

The author thanks Assistant Professor Dijana Oskoruš, Full Professor Hrvoje Meaški, Dr. Saša Zavrtnik, Assistant Professor Jelena Loborec, Professor Ana Jelčić, Assistant Professor Karlo Leskovar, the Faculty of Geotechnical Engineering, HEP staff and the Universitat Politècnica de Catalunya for their support during the development of the original master thesis.

References

Ayers, R.S. and Westcot, D.W. 1985 *Water Quality for Agriculture*. FAO Irrigation and Drainage Paper No. 29, Rev. 1, Food and Agriculture Organization of the United Nations, Rome.
Bačani, A. and Posavec, K. 2008 *Elaborat o zaštitnim zonama izvorišta Varaždin, Bartolovec i*

Vinokovščak. Rudarsko-geološko-naftni fakultet, Sveučilište u Zagrebu, Zagreb.
Council Directive 98/83/EC 1998 Council Directive 98/83/EC on the quality of water intended for human consumption. *Official Journal of the European Communities* L 330, 32–54.
Freeze, R.A. and Cherry, J.A. 1979 *Groundwater*. Prentice-Hall, Englewood Cliffs, New Jersey.
HE Sjever 2025 *Historical measurement records and original construction design documentation for the drainage canal system*. Unpublished operational data, HEP Proizvodnja PP HE Sjever, Varaždin.
Hrvatska Elektroprivreda and Elektroprojekt 2000 *Hydropower system documentation for the Drava River hydropower plants*. Internal technical documentation.
ICOLD 2015 *Internal Erosion of Existing Dams, Levees and Dikes, and Their Foundations*. Bulletin 164, International Commission on Large Dams, Paris.
Karlović, I. 2022 *Origin, Fate and Transport Modelling of Nitrate in the Varaždin Aquifer*. PhD thesis, University of Zagreb, Zagreb.
MAURICE 2023–2026 *Management of Urban Water Resources in Central Europe Facing Climate Change*. Interreg Central Europe project CE0100184, unpublished project data.

SONO-ELECTROCOAGULATION FOR SIMULTANEOUS SELENIUM AND STRONTIUM REMOVAL IN A MULTI-STAGE REACTOR

Katarina LICHT [1*], Ivan HALKIJEVIĆ [1], Domagoj NAKIĆ [1], Hana POSAVČIĆ [1]

[1] *Faculty of Civil Engineering, University of Zagreb, Croatia*

E-mail: katarina.licht@grad.unizg.hr

E-mail: ivan.halkijevic@grad.unizg.hr

E-mail: domagoj.nakic@grad.unizg.hr

E-mail: hana.posavcic@grad.unizg.hr

[*] *Corresponding author*

Abstract

This study investigated ultrasound-assisted electrocoagulation (sono-EC) for the simultaneous removal of selenium (Se) and strontium (Sr) in a multi-stage reactor. A D-optimal response surface design with 24 randomized runs was applied to assess the influence of current, treatment time, ultrasound power, electrode material, and pH regime. Se removal was generally high, exceeding 95% under most conditions, and was mainly governed by treatment time and pH value. In contrast, Sr removal was more dependent on operating conditions, with pH value identified as the dominant factor, followed by treatment time, current, and electrode material. Ultrasound had no consistently significant main effect on Sr removal but enhanced performance through interactions with pH value and time. Overall, sono-EC improved process robustness, although the adjustment of pH value remained essential for efficient Sr removal.

Key words

selenium, strontium, electrocoagulation, sonoelectrocoagulation, ultrasound

1 Introduction

Selenium (Se) and strontium (Sr) are two environmentally relevant trace elements that may occur in industrial, mining, and nuclear wastewaters. Although they differ considerably in their chemical behavior, their simultaneous presence can complicate water treatment and reduce the effectiveness of conventional methods. Se is an essential micronutrient, but the range between nutritional requirement and toxicity is narrow (Chapman et al., 2010; Okonji et al., 2021). Long-term exposure to elevated Se concentrations can cause serious health effects, including selenosis, while even low concentrations may affect aquatic ecosystems due to bioaccumulation in food webs (Chapman et al., 2010; He et al., 2018; Mehdi et al., 2013; Ruj et al., 2022). In aquatic environments, Se occurs predominantly in the inorganic forms selenate (SeO_4^{2-}, Se(VI)) under oxidizing conditions and selenite (SeO_3^{2-}/$HSeO_3^-$, Se(IV)) under moderately reducing conditions, whereas elemental selenium (Se^0) and selenide (Se(-II)) prevail under strongly reducing conditions; their distribution is governed primarily by pH and redox potential. Important anthropogenic sources include mining, industrial production, petroleum refining, and agriculture (Aliaskari et al., 2023; Okonji et al., 2021; Santos et al., 2015; Ullah et al., 2023).

Sr is an alkaline earth metal with chemical properties similar to calcium (Scott et al., 2020). Although generally not considered highly toxic at typical environmental concentrations, prolonged intake of elevated Sr levels may negatively affect bone tissue, particularly in children (Peng et al., 2021.; Scott et al., 2020; Watts and Howe, 2010). Natural Sr inputs into water are mainly associated with weathering of rocks and minerals, volcanic activity, and soil leaching, whereas anthropogenic sources include agriculture, metallurgy, oil and gas extraction, electronics production, ammunition production and

pyrotechnics (Frei et al., 2020; Musgrove, 2021; Scott et al., 2020). Additional concern is related to radioactive ^{90}Sr, which may originate from nuclear activities and improper radioactive waste disposal (Hwang et al., 2002).

Although chemically different, Se and Sr may co-occur in environments affected by sedimentary-carbonate geology, coal deposits, erosion, ammunition production and mining activities. Elevated concentrations of both elements have been reported in waters, sediments, and coals in several regions worldwide (Dai et al., 2012; Lin et al., 2018; Yudovich and Ketris, 2006). A notable example is the Raša coalfield in Istria, Croatia, where Paleogene coal and surrounding environmental compartments contain elevated Se and Sr concentrations, with contamination linked to mining, coal combustion, and inadequate waste management (Lieberman et al., 2020; Medunić et al., 2018, 2021).

Conventional methods for Se and Sr removal include adsorption, ion exchange, membrane processes, biological treatment, precipitation, and filtration (Ali and Shrivastava, 2021; Cai et al., 2020; Buecker et al., 2020; Hwang et al., 2002). However, these methods may be limited by secondary waste generation, high chemical consumption, reduced efficiency at low concentrations, and low selectivity in the presence of competing ions. Electrocoagulation (EC) offers a promising alternative, as pollutants are removed using coagulants generated in situ by the dissolution of sacrificial metal electrodes, most commonly Fe or Al (Lakshmi and Sivashanmugam, 2013; Sillanpää, 2020). The generated metal hydroxides destabilize colloidal and dissolved species, promoting their aggregation into flocs, while hydrogen bubbles formed at the cathode may enhance mixing and support pollutant removal by electroflotation (Al-Qodah et al., 2024; Garcia-Segura et al., 2017; Sillanpää, 2020). Compared with chemical coagulation, EC can reduce the addition of external reagents, secondary pollution, effluent salinity, and sludge production (Alattabi et al., 2017; Bazrafshan et al., 2015; Biswas and Goel, 2022; Dong et al., 2016).

Despite these advantages, EC performance can be limited by electrode passivation, mass-transfer constraints, and process sensitivity to operating conditions. Sono-electrocoagulation (sono-EC), or ultrasound-assisted EC, combines conventional EC with ultrasonic irradiation to intensify the process. Ultrasound cavitation and microjet formation can clean electrode surfaces, reduce passivation, improve mixing, and enhance mass transfer (Iloms et al., 2020; Moradi et al., 2021; Wood et al., 2017). Cavitation may also improve the distribution of metal hydroxide flocs and promote the formation of reactive radical species, contributing to pollutant degradation and removal (Moradi et al., 2021; Wood et al., 2017). Previous studies have shown that sono-EC can outperform EC or ultrasound alone in the treatment of various wastewaters, including dye-containing, distillery, brewery, landfill leachate, oily, and metal-complex wastewaters (Arka et al., 2022; Asaithambi et al., 2020; Chang et al., 2009; Dizge et al., 2018; Dubey et al., 2024). However, the use of ultrasound also increases energy demand, making process optimization essential (Mengistu et al., 2022).

This study investigates the application of sono-EC for the simultaneous removal of Se and Sr from synthetic wastewater in a multi-stage reactor. The work focuses on evaluating the influence of key operating parameters and improving process efficiency through optimized electrochemical and ultrasonic conditions.

2 Methods

2.1 Multi-stage reactor

The multi-stage reactor system was developed for the electrochemical removal of Se and Sr by combining electrochemical pH regulation with subsequent EC/sono-EC treatment. The system consisted of a three-compartment pH-control reactor, two rectangular EC/sono-EC reactors, two settling tanks, circulation pumps, and corresponding valves, enabling recirculating flow through all treatment stages (Fig. 1). In the pH-control reactor, the solution was divided into acidic and alkaline streams by ion-exchange membranes, while graphite electrodes were used to induce pH changes exclusively through

water electrolysis and selective ion transport. After pH adjustment, the solution was directed to the sono-EC reactors, where 4 Al or Fe electrodes generated metal hydroxide coagulants in situ. The immersed area of one electrode face was approximately 86.7 cm^2. Each sono-EC reactor had a working volume of 4 L and was equipped with mechanical stirring and ultrasonic transducers mounted on the bottom plate of the reactor. Four ultrasonic transducers were installed on each reactor, two with nominal power of 60 and two with 100 W, operating at a frequency of 45 kHz. An additional metal rod was mounted at the center of each transducer to enhance the direct transfer of ultrasonic energy into the solution volume, while the rods were electrically insulated to prevent any electrochemical contribution to the process. The transducers were connected to a separate ultrasonic generator, which enabled the application of ultrasound during electrocoagulation. This configuration enabled the investigation of the combined effects of pH regulation, electrode material, current intensity, treatment time, and ultrasound power on the simultaneous removal of Se and Sr. The inclusion of settling tanks allowed separation of the generated flocs after treatment, while the recirculation setup provided operational flexibility and more uniform treatment conditions throughout the system.

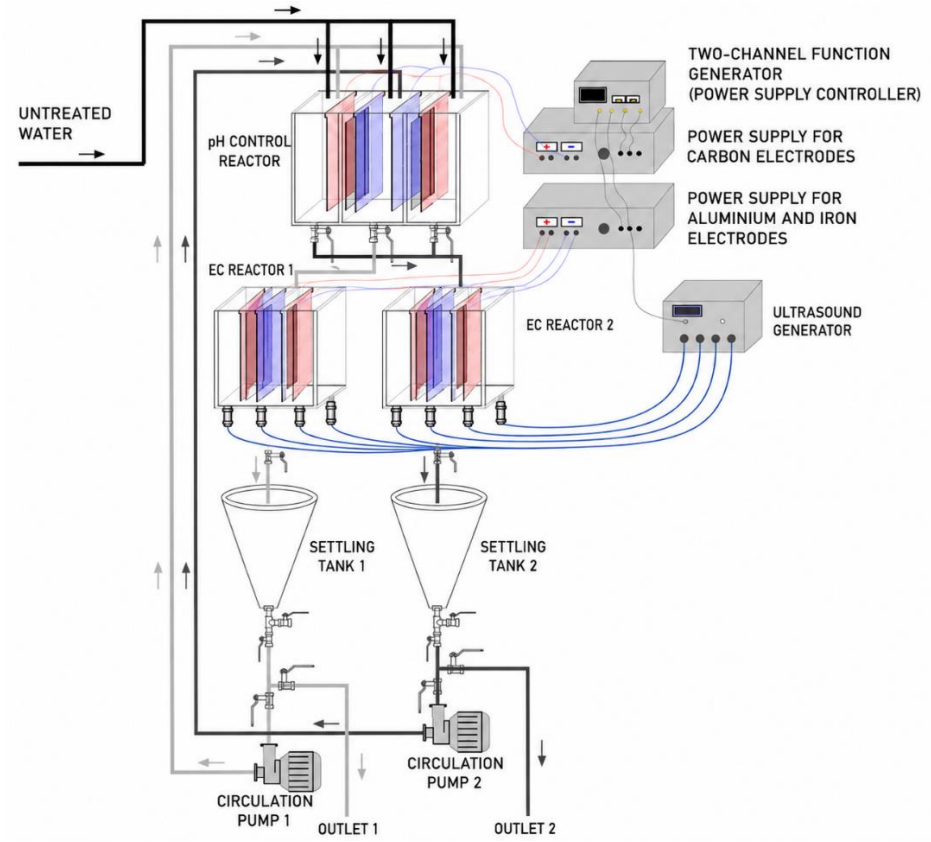


Figure 1. Schematic view of the multi-stage reactor

2.2 Statistical design of experiments

A D-optimal response surface design was applied to better understand the sono-EC process for the simultaneous removal of Se and Sr from synthetic wastewater. This approach enabled the evaluation of the individual effect of ultrasound, as well as its potential interactions with current intensity, treatment time, electrode material, and pH regime within the same experimental framework. Five parameters, presented in Table 1, were included in the experimental design. The pH regime and electrode material were defined as categorical process parameters, each tested at two levels. Al and Fe electrodes were used as the electrode materials. For the pH regime, the condition without pH adjustment refers to experiments in which the initial pH of the solution was not modified and the electrochemical pH-control stage was bypassed. In contrast, under the maximum pH range condition, the solution was first treated in the electrochemical pH-control reactor, where the pH was adjusted to 2.5–3.5 in the acidic compartment and 9.5–10.5 in the alkaline compartment. These values were achieved by applying 120

V to graphite electrodes for 15 min, during which a current of approximately 7–10 A was generated. Current intensity, treatment time, and ultrasound power were included as numerical factors and tested at three levels. The average cumulative removal efficiencies of Se (Y_1) and Sr (Y_2) at the end of treatment were used as the design responses. The removal efficiency of each element was calculated according to Eq. (1):

$$\eta = \frac{C_0 - C_{t,avg}}{C_0} * 100 \quad (1)$$

where η is the removal efficiency (%), C_0 is the initial concentration (mg/L), and $C_{t,avg}$ is the average concentration in both EC reactors at the end of the treatment (mg/L). Considering current, number of anodes and electrode surface, current intensity of 5 A corresponded to current density of 0.014 A/cm^2, 10 A to 0.029 A/cm^{2}and 15 A to 0.043 A/cm^2.

Table 1. Factors investigated and their characteristics

Factor	Unit	Type	Subtype	Minimum	Middle level	Maximum
A: current, I	A	Numeric	Continuous	5	15	25
B: treatment time,t	min	Numeric	Continuous	5	15	25
C: US power	W	Numeric	Continuous	150	300	450
D: electrode material		Categoric	Nominal	Al		Fe
E: pH regime		Categoric	Nominal	No pH adjustment		Maximum range

2.3 Experimental procedure

A mixed Se and Sr stock solution with a nominal concentration of 1000 mg/L for each element was prepared from strontium carbonate ($SrCO_3$) and selenous acid (H_2SeO_3) in distilled water. Accordingly, Se was introduced predominantly in the form of SeO_3^{2-}, whereas Sr was introduced as dissolved Sr^{2+}. The synthetic wastewater was prepared by diluting the stock solution with tap water to obtain initial concentrations of 10 mg/L Se and 10 mg/L Sr in a total volume of 7 L. The average physicochemical characteristics of the synthetic wastewater are presented in Table 2.

Table 2. Physiochemical characteristics of synthetic wastewater

Parameter	Average measured value
Electrical conductivity (μS/cm)	707 ± 14
pH value	6.73 ± 0.17
Total dissolved solids, TDS (mg/L)	354 ± 8
Dissolved oxygen (%)	80 ± 5
Temperature (ºC)	20.73 ± 0.25
Electric resistivity (MΩ*cm)	0.0014 ± 0.0001

Before each experimental run, all reactors were thoroughly rinsed with distilled water. The metal electrodes, Fe and Al, as well as the graphite electrodes, were mechanically cleaned with sandpaper, rinsed with distilled water, and dried. After cleaning, the graphite electrodes were placed in the pH-control reactor in an anode–cathode–cathode–anode (+--+) configuration, with both cathodes positioned in the larger central compartment and one anode placed in each of the two smaller side compartments. Depending on the experimental design, four of Fe or Al electrodes were installed in each EC reactor in an alternating anode–cathode configuration. Electrochemical pH adjustment was carried out by switching on the power supply connected to the graphite electrodes through a function generator set to the maximum output. Heat-exchange tubes were placed in each compartment to maintain a stable temperature. The electrochemical pH modulation was either skipped or performed for 15 min, with the possibility of extending the operation for several minutes if the target pH value was not achieved. After pH adjustment, the contents of the pH-control reactor were transferred to the EC reactors, ensuring

proper flow direction through the system. The acidic solution was directed into one EC reactor, while the alkaline solution was directed into the other. The function generator and the power supply for the metal electrodes were then switched on, and the current strength was adjusted according to the experimental design. The ultrasonic generator was also switched on, and the desired ultrasound frequency and power were set. The EC treatment was performed for the predefined time interval. After treatment, the power supply and stirrers were switched off, and the reaction mixture was discharged into the settling tanks. After settling, the valves of the settling tanks were opened toward the pump system, and the solution was returned to the pH-control reactor for the second treatment cycle, while the sludge was discharged. The water that had been in the acidic compartment during the first cycle was introduced into the alkaline compartment during the second cycle, and vice versa. The second cycle included the same sequence of procedures, measurements, and sampling as the first cycle. The concentrations of Se and Sr in the samples were determined by inductively coupled plasma optical emission spectrometry (ICP-OES; Agilent 5900 SVDV, Agilent Technologies).

3 Results and Discussion

The sono-electrocoagulation (sono-EC) process was evaluated for the simultaneous removal of Se and Sr by varying current intensity, treatment time, ultrasound power, electrode material, and pH regime. Overall, Se removal was highly efficient under most tested conditions, generally exceeding 95%, whereas Sr removal was more strongly dependent on the applied operating conditions. This indicates that the two elements respond differently to the sono-EC process, most likely due to differences in their aqueous speciation, precipitation behaviour, and affinity toward Fe/Al hydroxide flocs. The experimental matrix, achieved responses (Y_1 and Y_2), and predicted responses (Y_1' and Y_2') of the sono-EC process are presented in Table 3.

The obtained results were statistically evaluated using analysis of variance (ANOVA), and regression models were developed to describe and predict the removal efficiencies of Se and Sr. Separate regression models were developed for Se and Sr removal. The comparison of experimental Se and Sr removal efficiencies and those predicted by the obtained models show a relatively good fit, as can be seen in Fig. 2. For Se, a reduced quadratic model was selected after removing statistically insignificant terms. ANOVA results are listed in Table 4. The model was highly significant, with an F-value of approximately 47 and $p < 0.001$, and showed very good agreement with the experimental data, as indicated by $R^2 \approx 0.98$. The coded equation describes the obtained model in terms of coded factors and can be used to make predictions about the response for given levels of each factor (Eq.(2)). Treatment time was the dominant factor affecting Se removal, followed by pH regime. Current intensity, ultrasound power, and electrode material were also statistically significant, although their contribution was smaller. This indicates that Se removal was already highly efficient under the investigated conditions, while modulation of these parameters primarily supported further optimization of the process.

$$\eta(Se) = 97{,}53 + 1.96A + 7.57B + 1.41C - 1.70D + 4.28E - 1.68AB + 1.75AD - 1.54BC - 4.27BE - 1.78CE - 4.43B^2 - 3.31C^2 \quad (2)$$

Table 3. Experimental matrix, observed and predicted efficiencies

	A	B	C	D	E	Y_1	Y_1'	Y_2	Y_2'
Run	I (A)	t (min)	P_{US} (W)	material	pH	% Se	% Se	% Sr	% Sr
1	5	25	150	Fe	no pH adjustment	98.77	98.86	23.07	39.68
2	15	15	300	Fe	no pH adjustment	96.66	94.95	37.69	38.04
3	25	15	450	Fe	maximum pH range	100.00	100.00	88.31	89.23
4	15	5	300	Al	no pH adjustment	78.08	75.27	26.48	18.06
5	5	5	450	Fe	no pH adjustment	76.30	78.20	27.53	26.22
6	5	25	450	Fe	maximum pH range	99.34	98.62	85.73	85.27
7	5	25	150	Al	maximum pH range	95.29	95.53	72.29	77.08
8	15	5	450	Fe	maximum pH range	91.20	93.65	83.31	77.91
9	5	5	150	Al	no pH adjustment	60.36	61.84	8.00	7.97
10	5	5	150	Fe	maximum pH range	90.34	89.39	77.17	72.89
11	25	5	300	Fe	maximum pH range	98.05	97.67	79.29	83.04
12	25	25	150	Al	no pH adjustment	97.57	96.04	47.91	41.61
13	25	5	150	Fe	no pH adjustment	71.95	72.53	25.68	26.41
14	5	5	450	Al	maximum pH range	87.32	85.86	55.04	64.57
15	25	5	150	Al	maximum pH range	92.81	93.28	74.68	74.82
16	5	25	450	Al	no pH adjustment	96.01	95.28	45.79	41.42
17	25	25	150	Fe	maximum pH range	99.72	99.51	94.68	95.52
18	25	25	150	Fe	maximum pH range pH	99.13	99.51	93.97	95.52
19	5	25	450	Fe	maximum pH range pH	98.17	98.62	86.31	85.27
20	25	25	450	Fe	no pH adjustment pH	99.48	99.26	62.00	59.85
21	10	15	300	Al	maximum pH range pH	96.60	98.25	81.79	73.37
22	15	25	300	Al	no pH adjustment pH	95.72	98.96	35.48	41.51
23	25	5	450	Al	no pH adjustment pH	82.40	82.08	19.30	28.14
24	25	25	450	Al	maximum pH range pH	95.05	95.79	72.61	87.20

Several interaction terms were significant for Se removal, particularly the interaction between treatment time and pH regime. This indicates that increasing the treatment time was most beneficial under pH conditions favourable for the formation and stability of Fe/Al hydroxide flocs. Significant quadratic effects of treatment time and ultrasound power also suggested a saturation effect, meaning that further increases in these parameters resulted in a smaller additional improvement in Se removal.

For Sr removal, a reduced two-factor interaction (2FI) model was selected as the most appropriate. The model, described in Table 5, was also highly significant, with an F-value of approximately 70, $p < 0.001$, and $R^2 \approx 0.97$, confirming its good predictive ability. The obtained model in termes of coded factors is described by Eq. (3). In contrast to Se, Sr removal was dominated by the pH regime, which was by far the most important factor. Treatment time and current intensity also had significant positive effects, while electrode material was statistically significant, with Fe electrodes generally enabling higher peak Sr removal under favourable conditions.

$$\eta(Sr) = 56.98 + 5.09A + 8.97B + 2.48C - 4.13D + 23.06E - 2.75BE - 2.51CE \quad (2)$$

Table 4. Statistical model for Se removal

Source	Sum of Squares	df	Mean Square	F-value	p-value	
Model	2462.66	12	205.22	46.71	< 0.0001	significant
A-I	70.46	1	70.46	16.04	0.0021	
B-t	1176.56	1	1176.56	267.79	< 0.0001	
C-US	35.31	1	35.31	8.04	0.0162	
D-material	64.09	1	64.09	14.59	0.0028	
E-pH	405.54	1	405.54	92.30	< 0.0001	
AB	47.20	1	47.20	10.74	0.0074	
AD	53.04	1	53.04	12.07	0.0052	
BC	40.66	1	40.66	9.26	0.0112	
BE	374.85	1	374.85	85.32	< 0.0001	
CE	55.73	1	55.73	12.68	0.0045	
B^2	37.29	1	37.29	8.49	0.0141	
C^2	30.49	1	30.49	6.94	0.0232	
Residual	48.33	11	4.39			
Lack of Fit	48.33	9	5.37			
Pure Error	0.0000	2	0.0000			
Cor Total	2510.99	23				

The main effect of ultrasound power on Sr removal was not statistically significant at the 0.05 significance level, indicating that ultrasound alone did not consistently improve Sr removal across the entire experimental domain. However, the interaction between treatment time and pH regime was significant, while the interaction between ultrasound power and pH regime was close to significance. This suggests that ultrasound may contribute to Sr removal mainly through interactions with favourable pH conditions and sufficient treatment time, rather than acting as an independent controlling factor.

Table 5. Statistical model for Sr removal

Source	Sum of Squares	df	Mean Square	F-value	p-value	
Model	16789.31	7	2398.47	70.16	< 0.0001	significant
A-I	485.98	1	485.98	14.22	0.0017	
B-t	1679.50	1	1679.50	49.13	< 0.0001	
C-US	112.47	1	112.47	3.29	0.0885	
D-material	391.64	1	391.64	11.46	0.0038	
E-pH	12289.12	1	12289.12	359.50	< 0.0001	
BE	157.84	1	157.84	4.62	0.0473	
CE	115.67	1	115.67	3.38	0.0845	
Residual	546.94	16	34.18			
Lack of Fit	546.94	14	39.07			
Pure Error	0.0000	2	0.0000			
Cor Total	17336.25	23				

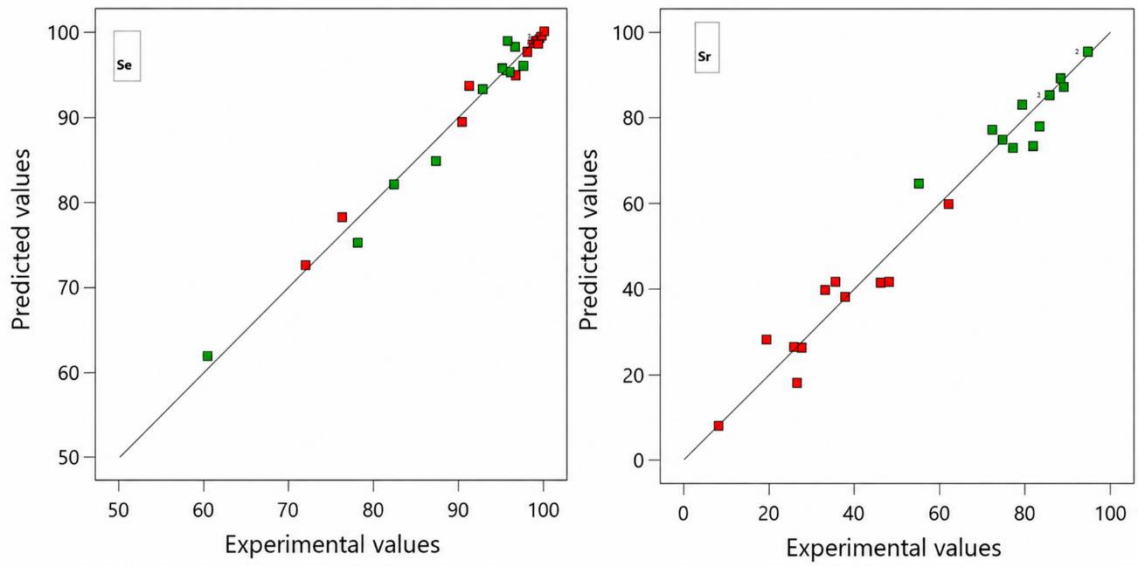


Figure 2. Comparison of experimental and predicted values for Se (left) and Sr (right) removal efficiencies

3.1 Contribution of ultrasound and cavitation intensity

The role of ultrasound in the sono-EC process was primarily associated with process intensification. Cavitation intensity was measured using Cav-meter-2 (MRC) in the filled EC reactor at three ultrasound power levels: 150, 300, and 450 W. The average measured cavitation intensities were approximately 750, 1230, and 1520 CAVIN, respectively, while the highest measured value was 2250 CAVIN, corresponding to approximately 114.3 W/L. These results confirmed that increasing ultrasound power increased cavitation intensity, although not linearly, which can be attributed to the nonlinear response of the liquid phase and the geometry of the reactor.

The spatial distribution of cavitation intensity showed that the highest values were measured in the lower zones of the reactor, particularly near the ultrasonic transducers and lower corners, while somewhat lower values were observed near the surface. Nevertheless, the measured values remained within the same order of magnitude, indicating a relatively uniform ultrasound field in the working volume. Therefore, the selected ultrasound power levels represented clearly distinguishable cavitation conditions and were suitable for evaluating the contribution of ultrasound to Se and Sr removal.

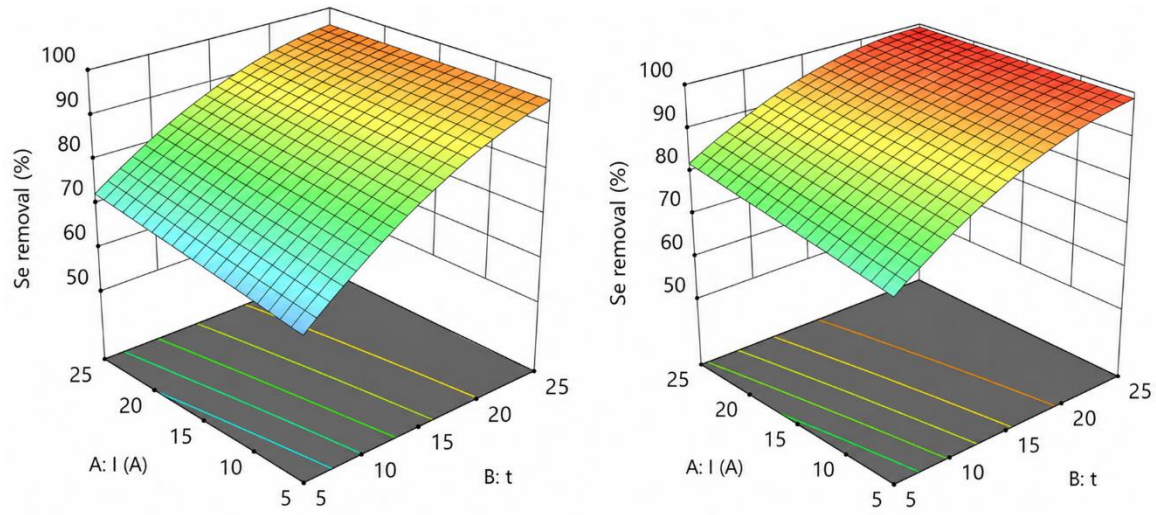


Figure 3. Removal efficiency of Se as a function of the interaction between treatment time and current intensity, without pH control, at ultrasound powers of 150 W (left) and 450 W (right)

For Se removal, increasing ultrasound power from 150 to 450 W improved process robustness. At low current intensity and short treatment time, Se removal was approximately 60–70%, while increasing current intensity and treatment time rapidly increased removal efficiency above 95%. At the highest current intensity and longest treatment time, almost complete Se removal was achieved. Higher ultrasound power increased the minimum removal efficiency to approximately 75–80% and expanded the operating region in which near-complete removal could be achieved, as shown in Fig. 3. Thus, ultrasound did not substantially increase the maximum attainable Se removal, but it enabled high removal efficiencies to be reached at lower current intensities and shorter treatment times.

Sr removal was more dependent on pH conditions. Without pH control, Sr removal remained relatively low, reaching approximately 40% at 150 W and increasing to about 50% at 450 W, as shown in Fig.4. This improvement indicates that stronger ultrasound can partially enhance Sr removal under non-optimized pH conditions, probably due to intensified cavitation, improved mixing, enhanced mass transfer, and partial cleaning of passivated electrode surfaces. However, the absolute removal efficiencies under these conditions remained insufficient.

When the maximum pH range was applied, Sr removal increased markedly, reaching approximately 85–90%, regardless of ultrasound power. Under these conditions, increasing ultrasound power from 150 to 450 W had little additional effect. This confirms that pH control was the key factor for efficient Sr removal and that ultrasound could not replace the need for a favourable pH range. Instead, ultrasound acted as an additional intensification factor that supported the effects of treatment time and pH, particularly when pH was not optimized.

Although pH values over 9.5 proved favourable for Sr removal, the cumulative Sr removal reported in this study cannot be attributed exclusively to a single acidic or alkaline compartment because the two water streams exchanged compartments between the first and second treatment cycles. Consequently, each stream was sequentially exposed to both acidic and alkaline conditions, and the reported response represents the average final removal from both treatment lines. The concentration profiles obtained during reactor development indicated that the pH-control stage contributed to Sr redistribution and removal through cation migration, whereas the alkaline conditions promoted precipitation of Sr-bearing carbonate/hydroxide phases. Subsequent electrocoagulation provided additional removal through adsorption and co-precipitation with Fe/Al hydroxide flocs. Thus, the improved Sr removal under the maximum-pH regime resulted from the sequential acidic–alkaline treatment rather than from one compartment acting independently.

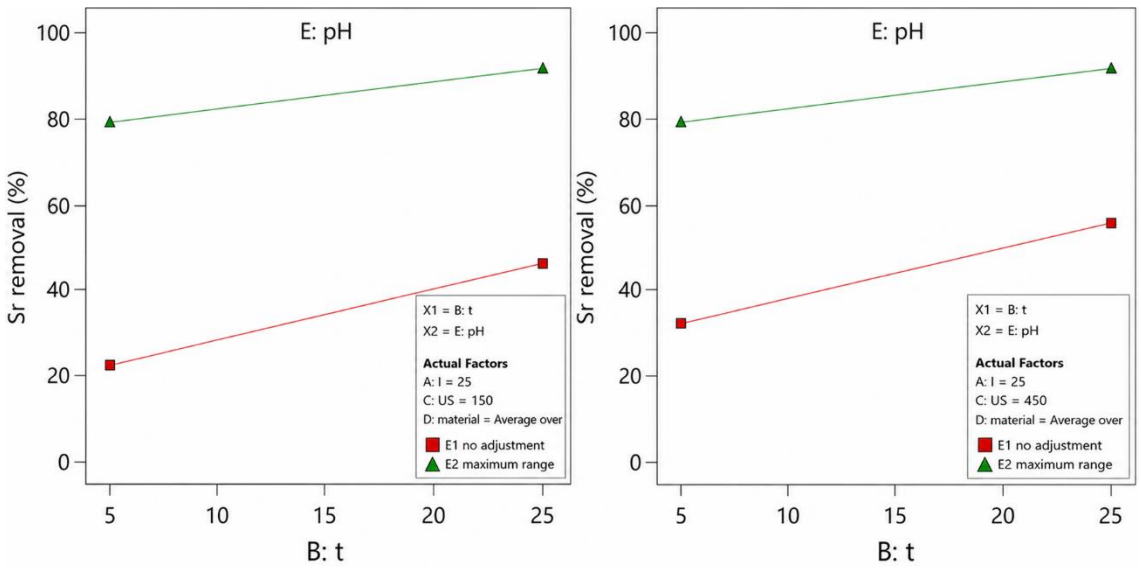


Figure 4. Effect of treatment time and pH value on Sr removal efficiency at ultrasound powers of 150 W (left) and 450 W (right), at a maximum current intensity of 25 A

Overall, the results show that ultrasound mainly intensified the sono-EC process rather than changing the fundamental removal mechanisms of Se and Sr. For Se, which was already removed very efficiently under favourable EC conditions, ultrasound allowed high removal efficiencies to be achieved faster and over a wider range of operating conditions. For Sr, pH remained the dominant controlling factor, while ultrasound provided only secondary improvement through enhanced hydrodynamic conditions and possible electrode surface cleaning.

Although cavitation measurements confirmed the presence of pronounced cavitation in the reactor, the effective local cavitation intensity near the electrode surfaces and within the floc zone may have been lower than the measured average. This may be explained by energy losses during ultrasound transmission from the transducers through the reactor wall into the liquid phase, as well as by reflection, absorption, and the formation of less active zones behind electrodes and structural elements. These limitations may partly explain why ultrasound did not produce more pronounced improvements, especially in Sr removal.

Residual dissolved Fe and Al concentrations in the treated water and the metal content of the generated sludge were not quantified in the present study. Consequently, although high Se and Sr removal efficiencies were achieved, the quality of the treated water with respect to residual electrode-derived metals could not be evaluated. This represents an important limitation because incomplete separation of Fe/Al hydroxide flocs may introduce secondary contamination and affect compliance with discharge or reuse requirements. Future work should therefore include dissolved and total Fe/Al measurements after settling and filtration, electrode mass-loss measurements, sludge characterization, and a complete metal mass balance.

4 Conclusion

This study demonstrated the applicability of ultrasound-assisted electrocoagulation (sono-EC) for the simultaneous removal of selenium (Se) and strontium (Sr) from synthetic wastewater in a multi-stage reactor system. Se was removed with high efficiency under most tested conditions, generally exceeding 95%. In contrast, Sr removal was more sensitive to operating conditions. Under the maximum pH range, Sr removal reached high efficiencies of approximately 85–90%, whereas without pH control the removal efficiency remained considerably lower. Ultrasound was expected to intensify the process through cavitation, microstreaming, improved mixing, enhanced mass transfer, and partial cleaning of the electrode surface, thereby reducing electrode passivation and improving contact between the generated Fe/Al hydroxide flocs and dissolved Se and Sr species. Overall, the results show that sono-EC can improve the efficiency and robustness of simultaneous Se and Sr removal, but the extent of improvement depended strongly on the target element and operating conditions. The multi-stage reactor configuration, combining electrochemical pH modulation, EC/sono-EC treatment, and settling, represents a promising approach for the treatment of wastewaters containing chemically different trace elements. Future work should focus on improving ultrasound energy transfer, reducing energy consumption, and testing the process on real wastewaters with more complex matrices and competing ions. Further investigations should also quantify residual dissolved Fe and Al, characterize the generated sludge, and establish complete Se, Sr, Fe, and Al mass balances.

Acknowledgements

This study was conducted within the framework of the institutional project of the University of Zagreb Faculty of Civil Engineering – [ARMOR – Advanced Treatment of Ammunition Production Wastewater Using Integrated Electrochemical and Adsorptive Technologies], under the programme line for enhancing scientific excellence, financed through the National Recovery and Resilience Plan 2021–2026. The project is funded by the European Union – NextGenerationEU. The views and opinions expressed are solely those of the author(s) and do not necessarily reflect those of the European Union

or the European Commission. Neither the European Union nor the European Commission can be held responsible for them.

References

Alattabi, A.W., Harris, C.B., Alkhaddar, R.M., Hashim, K.S., Ortoneda-Pedrola, M. & Phipps, D. 2017 Improving sludge settleability by introducing an innovative, two-stage settling sequencing batch reactor. *J. Water Process Eng.* 20, 207–216.

Ali, I. & Shrivastava, V. 2021 Recent advances in technologies for removal and recovery of selenium from (waste)water: A systematic review. *J. Environ. Manage.* 294, 112926.

Aliaskari, M., Ramos, R.L. & Schäfer, A.I. 2023 Removal of arsenic and selenium from brackish water using electrodialysis for drinking water production. *Desalination* 548, 116298.

Al-Qodah, Z., Al-Shannag, M., Hudaib, B. & Bani-Salameh, W. 2024 Enhancement of dairy wastewater treatment efficiency in batch chemical-assisted solar-powered electrocoagulation–adsorption system. *Case Stud. Chem. Environ. Eng.* 9, 100760.

Arka, A., Dawit, C., Befekadu, A., Debela, S.K. & Asaithambi, P. 2022 Wastewater treatment using sono-electrocoagulation process: Optimization through response surface methodology. *Sustain. Water Resour. Manag.* 8 (3), 61.

Asaithambi, P., Govindarajan, R., Busier Yesuf, M., Selvakumar, P. & Alemayehu, E. 2020 Enhanced treatment of landfill leachate wastewater using sono (US)–ozone (O_3)–electrocoagulation (EC) process: Role of process parameters on color, COD and electrical energy consumption. *Process Saf. Environ. Prot.* 142, 212–218.

Bazrafshan, E., Mohammadi, L., Ansari-Moghaddam, A. & Mahvi, A.H. 2015 Heavy metals removal from aqueous environments by electrocoagulation process—a systematic review. *J. Environ. Health Sci. Eng.* 13 (1), 74.

Biswas, B. & Goel, S. 2022 Electrocoagulation and electrooxidation technologies for pesticide removal from water or wastewater: A review. *Chemosphere* 302, 134709.

Buecker, B., Karlovich, D. & Djukanovic, V. 2020 Selenium removal from industrial wastewater. https://www.watertechonline.com/wastewater/article/14176337/selenium-removal-from-industrial-wastewater (accessed 27 July 2026).

Cai, Y.-H., Yang, X.J. & Schäfer, A.I. 2020 Removal of naturally occurring strontium by nanofiltration/reverse osmosis from groundwater. *Membranes* 10 (11), 321.

Chang, J.-H., Ellis, A.V., Yan, C.-T. & Tung, C.-H. 2009 The electrochemical phenomena and kinetics of EDTA–copper wastewater reclamation by electrodeposition and ultrasound. *Sep. Purif. Technol.* 68 (2), 216–221.

Chapman, P.M., Adams, W.J., Brooks, M.L., Delos, C.G., Luoma, S.N., Maher, W.A., Ohlendorf, H.M., Presser, T.S. & Shaw, D.P. (eds) 2010 *Ecological Assessment of Selenium in the Aquatic Environment*. CRC Press, Boca Raton, FL, USA.

Dai, S., Zou, J., Jiang, Y., Ward, C.R., Wang, X., Li, T., Xue, W., Liu, S., Tian, H., Sun, X. & Zhou, D. 2012 Mineralogical and geochemical compositions of the Pennsylvanian coal in the Adaohai Mine, Daqingshan Coalfield, Inner Mongolia, China: Modes of occurrence and origin of diaspore, gorceixite, and ammonian illite. *Int. J. Coal Geol.* 94, 250–270.

Dizge, N., Akarsu, C., Ozay, Y., Gulsen, H.E., Adiguzel, S.K. & Mazmanci, M.A. 2018 Sono-assisted electrocoagulation and cross-flow membrane processes for brewery wastewater treatment. *J. Water Process Eng.* 21, 52–60.

Dong, B., Fishgold, A., Lee, P., Runge, K., Deymier, P. & Keswani, M. 2016 Sono-electrochemical recovery of metal ions from their aqueous solutions. *J. Hazard. Mater.* 318, 379–387.

Dubey, S., Rekhate, C., Sharma, A., Joshi, A. & Kumar Prajapati, A. 2024 Optimizing distillery effluent treatment through sono-electrocoagulation: A response surface methodology approach. *Total Environ. Adv.* 9, 200093.

Frei, R., Frei, K.M., Kristiansen, S.M., Jessen, S., Schullehner, J. & Hansen, B. 2020 The link between surface water and groundwater-based drinking water—strontium isotope spatial distribution patterns and their relationships to Danish sediments. *Appl. Geochem.* 121, 104698.
Garcia-Segura, S., Eiband, M.M.S.G., de Melo, J.V. & Martínez-Huitle, C.A. 2017 Electrocoagulation and advanced electrocoagulation processes: A general review about the fundamentals, emerging applications and its association with other technologies. *J. Electroanal. Chem.* 801, 267–299.
He, Y., Xiang, Y., Zhou, Y., Yang, Y., Zhang, J., Huang, H., Shang, C., Luo, L., Gao, J. & Tang, L. 2018 Selenium contamination, consequences and remediation techniques in water and soils: A review. *Environ. Res.* 164, 288–301.
Hwang, E.D., Lee, K.W., Choo, K.H., Choi, S.J., Kim, S.H., Yoon, C.H. & Lee, C.H. 2002 Effect of precipitation and complexation on nanofiltration of strontium-containing nuclear wastewater. *Desalination* 147 (1–3), 289–294.
Iloms, E., Ololade, O.O., Ogola, H.J.O. & Selvarajan, R. 2020 Investigating industrial effluent impact on municipal wastewater treatment plant in Vaal, South Africa. *Int. J. Environ. Res. Public Health* 17 (3), 1096.
Lakshmi, P.M. & Sivashanmugam, P. 2013 Treatment of oil tanning effluent by electrocoagulation: Influence of ultrasound and hybrid electrode on COD removal. *Sep. Purif. Technol.* 116, 378–384.
Lieberman, N.R., Izquierdo, M., Muñoz-Quirós, C., Cohen, H. & Chenery, S.R. 2020 Geochemical signature of superhigh organic sulphur Raša coals and the mobility of toxic trace elements from combustion products and polluted soils near the Plomin coal-fired power station in Croatia. *Appl. Geochem.* 114, 104472.
Lin, R., Soong, Y. & Granite, E.J. 2018 Evaluation of trace elements in U.S. coals using the USGS COALQUAL database version 3.0. Part II: Non-REY critical elements. *Int. J. Coal Geol.* 192, 39–50.
Medunić, G., Kuharić, Ž., Krivohlavek, A., Đuroković, M., Dropučić, K., Rađenović, A., Lužar Oberiter, B., Krizmanić, A. & Bajramović, M. 2018 Selenium, sulphur, trace metal, and BTEX levels in soil, water, and lettuce from the Croatian Raša Bay contaminated by superhigh-organic-sulphur coal. *Geosciences* 8 (11), 408.
Medunić, G., Bilandžić, N., Sedak, M., Fiket, Ž., Crnić, A.P. & Geng, V. 2021 Elevated selenium levels in vegetables, fruits, and wild plants affected by the Raša coal mine water chemistry. *Rud.-Geol.-Naft. Zb.* 36 (1), 1–13.
Mehdi, Y., Hornick, J.L., Istasse, L. & Dufrasne, I. 2013 Selenium in the environment, metabolism and involvement in body functions. *Molecules* 18 (3), 3292–3311.
Mengistu, L.R., Samuel, Z.A., Kitila, C.D. & Bayu, A.B. 2022 Comparison study on sonodirect and sonoalternate current electrocoagulation process for domestic wastewater treatment. *Int. J. Anal. Chem.* 2022, 3477995.
Moradi, M., Vasseghian, Y., Arabzade, H. & Mousavi Khaneghah, A. 2021 Various wastewaters treatment by sono-electrocoagulation process: A comprehensive review of operational parameters and future outlook. *Chemosphere* 263, 128314.
Musgrove, M. 2021 The occurrence and distribution of strontium in U.S. groundwater. *Appl. Geochem.* 126, 104867.
Okonji, S.O., Achari, G. & Pernitsky, D. 2021 Environmental impacts of selenium contamination: A review on current issues and remediation strategies in an aqueous system. *Water* 13 (11), 1473.
Peng, H., Yao, F., Xiong, S., Wu, Z., Niu, G. & Lu, T. 2021 Strontium in public drinking water and associated public health risks in Chinese cities. *Environ. Sci. Pollut. Res.* 28 (18), 23048–23059.
Ruj, B., Bishayee, B., Chatterjee, R.P., Mukherjee, A., Saha, A., Nayak, J. & Chakrabortty, S. 2022 An economical strategy towards the managing of selenium pollution from contaminated water: A current state-of-the-art review. *J. Environ. Manage.* 304, 114143.
Santos, S., Ungureanu, G., Boaventura, R. & Botelho, C. 2015 Selenium contaminated waters: An overview of analytical methods, treatment options and recent advances in sorption methods. *Sci. Total Environ.* 521–522, 246–260.
Scott, V., Juran, L., Ling, E.J., Benham, B. & Spiller, A. 2020 Assessing strontium and vulnerability to

strontium in private drinking water systems in Virginia. *Water* 12 (4), 1053.
Sillanpää, M. 2020 *Advanced Water Treatment: Electrochemical Methods*. Elsevier, Cambridge, UK.
Ullah, H., Lun, L., Rashid, A., Zada, N., Chen, B., Shahab, A., Li, P., Ali, M.U., Lin, S. & Wong, M.H. 2023 A critical analysis of sources, pollution, and remediation of selenium, an emerging contaminant. *Environ. Geochem. Health* 45 (5), 1359–1389.
Watts, P. & Howe, P.D. 2010 *Strontium and Strontium Compounds*. Concise International Chemical Assessment Document 77, World Health Organization, Geneva, Switzerland.
Wood, R.J., Lee, J. & Bussemaker, M.J. 2017 A parametric review of sonochemistry: Control and augmentation of sonochemical activity in aqueous solutions. *Ultrason. Sonochem.* 38, 351–370.
Yudovich, Ya.E. & Ketris, M.P. 2006 Selenium in coal: A review. *Int. J. Coal Geol.* 67 (1–2), 112–126.

COMPARATIVE EVALUATION OF ELECTROOXIDATION, ULTRASOUND, AND OZONATION FOR THE INACTIVATION OF *ESCHERICHIA COLI* AND TOTAL COLIFORMS

Ivan HALKIJEVIĆ [1*], Katarina LICHT [1], Dora MILINOVIĆ [1], Dražen VOUK [1]

[1] *Faculty of Civil Engineering, University of Zagreb, Croatia*

E-mail: ivan.halkijevic@grad.unizg.hr

E-mail: katarina.licht@grad.unizg.hr

E-mail: dora2585@yahoo.com

E-mail: drazen.vouk@grad.unizg.hr

[*] *Corresponding author*

Abstract

The presence of faecal indicator bacteria in surface water is an important environmental and public health concern, emphasizing the need for effective disinfection technologies. This study evaluated electrooxidation (EO) with graphite electrodes, ultrasound (US), and ozonation (O_3) for the inactivation of *E. coli* and total coliforms in lake water spiked with environmentally isolated *E. coli*. Treatments were performed for 15 min at three intensity levels: EO at 1, 5, and 10 A; US at 20, 60, and 100% power; and ozonation at 1, 5, and 10 g/h O_3. Bacterial concentrations were determined using the automated TECTA B4 system, and treatment performance was assessed by log reduction and inactivation efficiency relative to untreated controls. Bacterial inactivation increased with treatment intensity and contact time. Ozonation showed the highest efficiency, achieving 99.00% inactivation of *E. coli* and 99.50% of total coliforms after 15 min, corresponding to 2.00 and 2.30 log reductions, respectively. EO was also effective, achieving 96.44% and 99.09% inactivation, while US showed limited standalone performance. Overall, ozonation was the most effective method, followed by EO.

Key words

disinfection, ultrasound, electrooxidation, ozone, *Escherichia coli*

1 Introduction

Water quality is determined by a complex interaction of physical, chemical, and microbiological parameters. Although chemical contaminants such as nutrients, metals, pesticides, pharmaceuticals, and disinfection by-products are important indicators of environmental pressure, microbiological contamination remains one of the most direct threats to public health. Surface water, groundwater, and treated wastewater may contain bacteria, viruses, protozoa, and other pathogenic microorganisms originating from municipal wastewater discharges, agricultural runoff, animal manure, leaking sewage systems, stormwater overflow, or resuspension of contaminated sediments (Buchanan, 2011; Rompré et al., 2002). Therefore, microbiological monitoring and efficient disinfection are essential components of water treatment, water reuse, and public-health protection (Rompré et al., 2002).

Among microbiological indicators, total coliforms and Escherichia coli (*E. coli*) are widely used for assessing faecal contamination and evaluating the efficiency of water disinfection processes (Solsona and Méndez, 2003). The coliform group includes Gram-negative, non-spore-forming, oxidase-negative rod-shaped bacteria that are defined mainly by shared biochemical characteristics rather than by strict taxonomic relationships (APHA, 1992). Total coliforms are useful as general indicators of sanitary quality and treatment performance, while *E. coli* is considered a more specific indicator of recent faecal

contamination because it is primarily associated with the intestinal tract of humans and warm-blooded animals (Rompré et al., 2002). *E. coli* is a Gram-negative bacterium with a complex cell envelope composed of an inner cytoplasmic membrane, a peptidoglycan layer, and an outer membrane containing phospholipids and lipopolysaccharides. This cellular structure influences bacterial resistance and the way in which different disinfectants damage the cell (Soares et al., 2024). Although many *E. coli* strains are harmless commensals, pathogenic strains transmitted through contaminated water or food can cause gastrointestinal infections and severe disease, which justifies its frequent use as an indicator organism in water disinfection studies (Rompré et al., 2002; Soares et al., 2024).

Disinfection is generally applied as the final step in water and wastewater treatment and represents the last barrier against pathogenic microorganisms before water is distributed, reused, or discharged into the environment. Its efficiency depends on disinfectant dose, contact time, pH, temperature, turbidity, organic matter content, mixing conditions, and the physiological properties of the target microorganisms. The basic disinfection concept is often expressed through the C × T relationship, where a defined disinfectant concentration must remain in contact with the water for a sufficient time to achieve the desired microbial inactivation (Solsona and Méndez, 2003).

Chlorination has historically been the most widely applied water disinfection method because of its relatively low cost, operational simplicity, high efficiency against many bacteria and viruses, and ability to maintain a residual disinfectant in distribution systems. Its main active form is hypochlorous acid, which is more effective than hypochlorite ion and is strongly influenced by pH (Collivignarelli et al., 2018). However, the use of chlorine is associated with several drawbacks, including unpleasant taste and odor, reduced effectiveness against chlorine-resistant protozoa such as Cryptosporidium and Giardia, chemical handling risks, and formation of disinfection by-products (DBPs) such as trihalomethanes and haloacetic acids (Solsona and Méndez, 2003; Vajnhandl et al., 2015). Because Cryptosporidium and Giardia are more resistant to conventional chlorination than many bacteria, advanced methods such as ozonation and UV irradiation have been investigated and implemented for improved pathogen control (Betancourt and Rose, 2004).

The limitations of conventional disinfection have stimulated interest in alternative and advanced treatment technologies that can inactivate microorganisms while reducing chemical consumption and DBP formation (Kraft, 2008; Martínez-Huitle and Brillas, 2008). Among these, ozonation, ultrasound, and electrooxidation are particularly relevant because they rely on different but partially overlapping mechanisms of microbial inactivation. Ozone acts mainly as a strong chemical oxidant; ultrasound produces physical and sonochemical effects through acoustic cavitation; and electrooxidation generates oxidizing species directly at electrode surfaces or indirectly in the bulk solution. Comparing these three technologies under the same experimental conditions is important because their efficiencies depend differently on water matrix composition, microbial group, contact time, energy input, oxidant formation, and operational parameters.

Ozone is a stronger oxidant than chlorine and reacts rapidly with microbial cell components, including membrane lipids, proteins, enzymes, and nucleic acids. The primary mechanism of bacterial inactivation involves oxidation of the cell envelope, modification of membrane permeability, leakage of intracellular material, and loss of cellular viability (Jyoti and Pandit, 2004). Ozone is effective against bacteria, viruses, and protozoan cysts, and it is often reported as particularly useful for microorganisms that are more resistant to chlorination, including Giardia and Cryptosporidium (Betancourt and Rose, 2004). Despite its high oxidation potential, ozonation also has important limitations. Ozone is unstable in water and decomposes relatively quickly, meaning that it must be generated on-site and does not provide a long-lasting residual disinfectant in the distribution system (Das et al., 2024). Its performance depends on ozone dose, gas–liquid transfer efficiency, water quality, pH, temperature, and the concentration of ozone-demanding substances such as natural organic matter (Barzegar et al., 2019). In waters containing bromide, ozonation can promote the formation of bromate and other brominated by-products, which must be controlled in practical applications (Solsona and Méndez, 2003). Nevertheless, ozonation remains attractive because it can achieve rapid microbial inactivation and can be combined with other treatment processes to improve overall disinfection efficiency.

Ultrasound is an alternative physical disinfection method based on the propagation of high-frequency sound waves through water (Naddeo et al., 2014). Its antimicrobial effect is mainly attributed to acoustic cavitation, which involves the formation, growth, and collapse of gas-filled microbubbles in the liquid (Gibson et al., 2008). During bubble collapse, localized extreme conditions are generated, including high pressures, high temperatures, shock waves, microjets, turbulence, and free radicals formed from water decomposition. These effects can mechanically damage bacterial cells and chemically oxidize cellular components (Blume and Neis, 2002; Vajnhandl et al., 2015). Cell disruption caused by ultrasound is often linked to shear forces and pressure gradients produced during cavitation collapse, while sonochemically generated radicals may additionally contribute to oxidative damage. The efficiency of ultrasound disinfection depends on frequency, acoustic power, treatment time, reactor geometry, microbial morphology, and water composition (Arrojo et al., 2008). Low-frequency ultrasound generally produces stronger physical cavitation effects, while higher frequencies may favor radical generation and sonochemical reactions (Song et al., 2024). However, ultrasound alone may require relatively high energy input for large-scale water treatment, and its practical implementation can be limited by energy efficiency, reactor design, and scale-up challenges (Vajnhandl et al., 2015). For this reason, ultrasound is often investigated not only as a standalone treatment but also as a process that can enhance ozonation, UV irradiation, or chemical disinfection.

Electrooxidation, also referred to as electrochemical oxidation or electrochemical disinfection, is based on the application of direct electric current between an anode and a cathode immersed in water (Biswas and Goel, 2022). At the electrode–water interface, electric current produces disinfecting species either from water itself or from ions dissolved in the water. Depending on the electrode material and water composition, microbial inactivation may occur through direct electron transfer at the anode, electroporation-like effects, local pH changes, and indirect oxidation by reactive species such as hydroxyl radicals, ozone, hydrogen peroxide, active chlorine, persulfate, percarbonate, or other oxidants (Ghernaout and Ghernaout, 2010; Kraft, 2008; Martínez-Huitle and Brillas, 2008). In chloride-containing waters, electrooxidation can generate free chlorine in situ through electrochemical oxidation of chloride to chlorine, followed by hydrolysis to hypochlorous acid and hypochlorite. In this way, the process can achieve disinfection without external dosing of chlorine-based chemicals (Kraft, 2008). A major advantage of electrooxidation is that disinfectants can be generated directly on site, reducing the need for chemical storage, transport, and manual dosing (Ghernaout, 2017). Moreover, the process can be adjusted according to treatment demand by controlling current, current density, electrode material, hydraulic retention time, and reactor configuration. However, electrochemical disinfection is strongly affected by the chloride concentration, conductivity, pH, temperature, organic matter content, and anode material. Stable and efficient electrodes, such as mixed metal oxide-coated titanium electrodes and boron-doped diamond (BDD) electrodes, have significantly improved the feasibility of electrochemical water disinfection (Ghernaout, 2019; Motta et al., 2018).

Given the different mechanisms and operational requirements of ozonation, ultrasound, and electrooxidation, a direct comparative evaluation is necessary to determine their relative effectiveness for the inactivation of *E. coli* and total coliforms. Ozonation is expected to provide rapid chemical oxidation but may be limited by ozone decay and oxidant demand. Ultrasound offers chemical-free physical treatment and cavitation-induced damage, but its efficiency may depend strongly on power input and exposure time. Electrooxidation can generate oxidants in situ and may combine direct and indirect microbial inactivation mechanisms, but its performance depends on electrode material and water chemistry. Therefore, the aim of this study is to comparatively evaluate electrooxidation, ultrasound, and ozonation for the inactivation of Escherichia coli and total coliforms in water. The comparison focuses on microbial reduction efficiency, treatment time, and the specific advantages and limitations of each technology.

2 Methods

2.1 General experimental setup

The study compared three water disinfection methods: electrochemical oxidation, ultrasound, and ozonation. Each method was tested at three different operating levels, while maintaining the same treatment volume of 5 L and total treatment time of 15 min. A control experiment was also conducted to evaluate the natural die-off of bacteria under the same hydraulic and mixing conditions but without application of any disinfection process. The water used in the experiments was collected from a nearby lake and subsequently mixed with tap water prior to experimental treatment. This step was performed to standardize the physicochemical properties of the water matrix and to provide sufficient electrical conductivity for the stable operation of the electrochemical oxidation process. At the same time, the use of lake water enabled the retention of naturally occurring organic matter, suspended particles, and other matrix components characteristic of surface water. To ensure comparable initial microbiological conditions in all experiments, the prepared water matrix was subjected to controlled inoculation with laboratory-grown cultures of *E.coli* and total coliforms. The purpose of inoculation was to obtain approximately similar initial bacterial concentrations in all experimental runs and to enable a reliable comparison of the disinfection efficiency of the tested methods. The average initial concentration of *E. coli* in the prepared samples corresponded to approximately 8.0×10^5 CFU/100 mL for *E. coli* and 1.34×10^7 CFU/100 mL for total coliforms.

The same reactor configuration was used for all treatments in order to ensure comparability between the tested methods. The reactor was a modified ultrasonic bath; however, ultrasound irradiation was activated only during the ultrasound experiments. During electrochemical oxidation, ozonation, and the control experiment, the ultrasonic bath served only as a reactor vessel and no ultrasound was applied. Throughout all experiments, the sample was continuously mixed using an overhead mechanical stirrer (IKA Werke RW27) to maintain homogeneous distribution of microorganisms, oxidants, and suspended particles in the reactor. Temperature control was ensured using heat-exchange coils placed in the reactor and connected to a cooling system consisting of an aluminum heat sink and a small fan powered by a McPower DF1730LCD power supply. The cooling system was used to remove excess heat generated during treatment and to prevent temperature increase from influencing bacterial inactivation. This was particularly important because both electrochemical oxidation and ultrasound can produce heat during operation.

2.2 Electrochemical oxidation

Electrochemical oxidation experiments were performed using four graphite electrodes, positioned parallel to each other and connected in an alternating anode-cathode configuration (Fig. 1). The electrodes were connected to a DC power supply Mean Well RST-5000-24 with a maximum power of 4800 W. The disinfection efficiency of electrochemical oxidation was tested at three current intensities: 1 A, 5 A, and 10 A. Each experiment lasted 15 min, and samples were collected at 0, 5, 10, and 15 min.

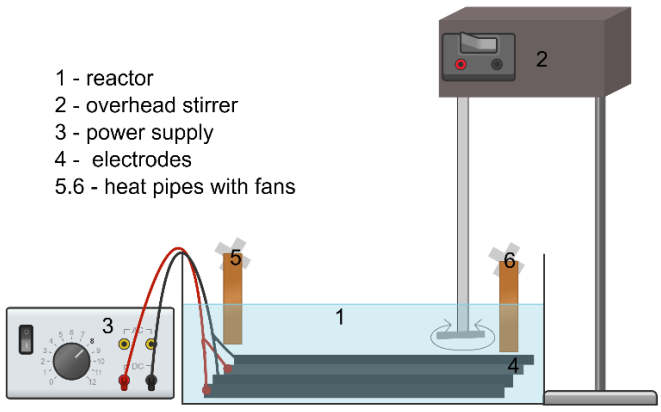


Figure 1. Experimental set-up for electrochemical disinfection

2.3 Ultrasound treatment

Ultrasound disinfection was performed using a combination of an ultrasonic bath and an immersed ultrasonic homogenizer, shown in Fig. 2. The ultrasonic bath was an Elma Ultrasonics TI-H10MF2 operating at a fixed frequency of 45 kHz. The ultrasonic homogenizer was a Bandelin Sonopuls HD2200.2 operating at a frequency of 25 kHz. The combined setup was used to enhance cavitation effects in the treated water. The ultrasound experiments were carried out at three different ultrasonic bath and homogenizer power settings: 20%, 60%, and 100%. Samples were collected at 0, 5, 10, and 15 min. Because two ultrasound sources were used, the cavitation intensity in the reactor was checked using a cavimeter (Cav-meter-2, MRC). Cavitation measurements were performed at three fixed points within the reactor, and the mean value was calculated as a relative physical indicator of cavitation intensity.

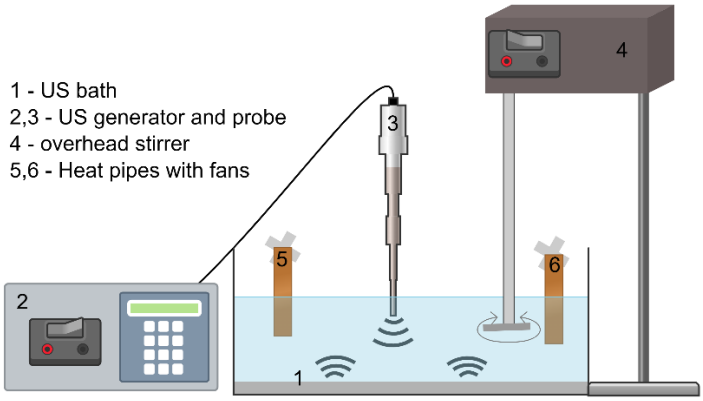


Figure 2. Ultrasonic treatment set-up

2.4 Ozonation

Ozonation experiments were conducted by introducing gaseous ozone directly into the water filled reactor, as shown in Fig.3. Ozone was generated from ambient air using a compact ozone generator Minus Longaeva PL-38869. The device draws air through a filter to reduce moisture before ozone generation. The generated ozone was introduced into the water through a flexible tube equipped with a diffuser placed in the reactor to improve gas distribution and contact with the water sample. The efficiency of ozonation was tested at three ozone production rates: 1 g/h, 5 g/h, and 10 g/h. Each ozonation experiment lasted 15 min, with samples collected at 0, 5, 10, and 15 min. The sample was continuously mixed using the overhead stirrer to improve ozone distribution in the reactor.

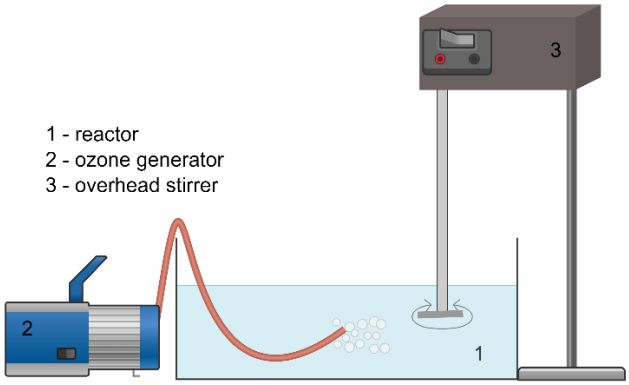


Figure 3. Ozonation set-up

2.5 Microbiological analysis

The microbiological analysis was focused on two indicator groups: *E. coli* and total coliforms. The bacterial concentration was expressed as colony-forming units per 100 mL of water sample (CFU/100 mL). For each sample, 100 mL of water was collected and analyzed using a fully automated TECTA™

B4 microbiological detection system.The TECTA™ B4 system is based on a directed enzyme-substrate method combined with optical fluorescence detection. The system detects target enzymatic activity associated with specific bacterial groups: β-D-glucuronidase activity for *E. coli* and β-D-galactosidase activity for total coliforms. The water sample was added to a dedicated test cartridge containing the appropriate nutrient substrate and then placed into the analyzer. During incubation at 35 °C, target bacteria metabolize the substrate and produce fluorescent metabolites. The instrument continuously monitors the fluorescence signal and automatically calculates the bacterial concentration in CFU/100 mL. The same analytical procedure was applied to all samples collected before and during the disinfection experiments.

3 Results and Discussion

The efficiency of each disinfection treatment was evaluated by comparing the bacterial concentration at each sampling time with the initial concentration measured before treatment. The results were expressed as remaining bacterial concentration in CFU/100 mL, percentage reduction, and log reduction. The logarithmic reduction (log kill) was calculated according to Eq. 1:

$$\log kill = log_{10}(N_0/N_t) \quad (1)$$

where (N_0) is the initial bacterial concentration before treatment, expressed as CFU/100 mL, and (N_t) is the concentration of surviving bacteria after a given treatment time. A 1-log reduction corresponds to a 90% reduction in the number of microorganisms, a 2-log reduction corresponds to 99% reduction, while a 3-log reduction corresponds to 99.9% reduction.

The control experiment confirmed that natural bacterial die-off during the 15 min experimental period was negligible. The calculated log reduction for both *E. coli* and total coliforms was approximately 0.00. This confirms that the observed bacterial removal in the treatment experiments was caused by the applied disinfection methods and not by spontaneous die-off under laboratory conditions. The disinfection efficiency of all tested treatments, expressed for each applied dose or intensity after 15 min, is presented in Table 1 for both *E. coli* and total coliform bacteria.

Table 1. The disinfection efficiency of all tested treatments

		Inactivation efficiency (%)		Log reduction log(No/Nt)	
Treatment	Dose	*E. coli*	Total coliforms	*E.coli*	Total coliforms
Electrochemical disinfection	10 A	96.44	99.09	1.45	2.04
	5 A	46.46	78.59	0.27	0.67
	1 A	36.30	79.18	0.20	0.68
Ultrasound	20 %	26.12	57.01	0.13	0.37
	60 %	43.38	82.74	0.25	0.76
	100 %	60.36	74.78	0.40	0.60
Ozone	10 g/h	99.00	99.50	2.00	2.30
	5 g/h	78.55	72.07	0.67	0.55
	1 g/h	46.57	76.76	0.27	0.63

Electrochemical oxidation showed a clear dependence on the applied current intensity. At the lowest current of 1 A, after 15 min of treatment, *E. coli* inactivation reached 36.30%, corresponding to a log reduction of 0.20. Total coliform removal was higher, reaching 79.18%, with a log reduction of 0.68. At 5 A, the efficiency of *E. coli* inactivation increased to 46.46%, corresponding to a log reduction of 0.27. Total coliform removal remained similar to that observed at 1 A, with a final inactivation of 78.59% and a log reduction of 0.67. This indicates that increasing the current from 1 A to 5 A did not substantially improve the removal of total coliforms, while only a moderate improvement was observed for *E. coli*. The highest efficiency of electrochemical oxidation was achieved at 10 A. Under these

conditions, the concentration *of E. coli* decreased 96.44% in 15 minutes, corresponding a 1.45-log reduction. The concentration of total coliforms showed a 2.04-log reduction. These results demonstrate that electrochemical oxidation can be highly effective, but only when a sufficiently high current intensity is applied. The inactivation trend also indicates that most of the bacterial reduction at 10 A occurred between 5 and 15 min of treatment. For *E. coli*, the log reduction increased from 0.11 after 5 min to 1.08 after 10 min and 1.45 after 15 min. For total coliforms, the increase was even more pronounced, from 0.78 after 5 min to 1.68 after 10 min and 2.04 after 15 min. This suggests that the formation of disinfecting species and the oxidative capacity of the system increased with treatment time.

Ultrasound was the least efficient disinfection method under the tested conditions. At 20% power, after 15 min of treatment, *E. coli* inactivation was 26.12%, corresponding to a log reduction of 0.13. Total coliform inactivation was higher, reaching 57.01%, with a log reduction of 0.37. At 60% power, *E. coli* inactivation increased to 43.38%, corresponding to a log reduction of 0.25. Total coliform removal reached 82.74%, with a log reduction of 0.76. This result indicates that increasing ultrasound power improved the inactivation of both microbial indicators, although the effect was more pronounced for total coliforms than for *E. coli.* At 100% power, ultrasound achieved its highest *E. coli* removal, 60.36% inactivation and a log reduction of 0.40. However, the inactivation efficiency of 74.78% and a 0.60-log reduction of total coliforms was less than at 60% power. Although ultrasound efficiency increased with power in the case of *E. coli*, the achieved log reductions remained low compared with ozonation and electrochemical oxidation. The results suggest that, within the applied treatment time of 15 min, ultrasound alone was not sufficient to achieve a high level of bacterial inactivation in the tested surface water matrix.

Ozonation showed the highest disinfection efficiency among the tested methods. At the lowest ozone dose of 1 g/h, after 15 min, *E. coli* inactivation reached 46.57%, with a log reduction of 0.27. Total coliform inactivation was higher, reaching 76.76%, corresponding to a log reduction of 0.63.At 5 g/h, *E. coli* inactivation increased to 78.55%, corresponding to a log reduction of 0.67. Total coliform inactivation was 72.07%, with a log reduction of 0.55. Although the increase in ozone dose improved *E. coli* removal, total coliform removal did not follow a strictly dose-dependent trend between 1 g/h and 5 g/h. The highest ozone dose of 10 g/h was the most effective treatment in the entire study. After 15 min, 99.50% inactivation and a 2.30-log reduction of total coliforms and 99% and 2-log reduction of *E.coli* was achieved. These results confirm the strong disinfection potential of ozone, especially at higher applied doses. The time-dependent results show that ozonation at 10 g/h produced rapid bacterial inactivation. For *E. coli*, log reduction increased from 0.49 after 5 min to 1.40 after 10 min and 2.00 after 15 min. For total coliforms, log reduction increased from 0.51 after 5 min to 1.70 after 10 min and 2.30 after 15 min. This indicates that ozone acted rapidly and continuously throughout the treatment period.

3.1 Comparison of tested disinfection treatments

A comparison of the three disinfection treatments after 15 min shows that ozonation at 10 g/h was the most efficient treatment for both microbial indicators. It achieved a 2.00-log reduction for *E. coli* and a 2.30-log reduction for total coliforms. Electrochemical oxidation at 10 A was the second most effective method, achieving a 1.45-log reduction for *E. coli* and a 2.04-log reduction for total coliforms. In contrast, ultrasound at 100% power showed the lowest disinfection performance, reaching only a 0.40-log reduction for *E. coli* and a 0.60-log reduction for total coliforms. Therefore, the overall efficiency of the tested methods can be ranked as follows: ozonation > electrochemical oxidation > ultrasound. This ranking was consistent for both microbial indicators, as can be seen in Figures 4 and 5. However, it is important to emphasize that none of the applied treatments resulted in complete bacterial elimination under the tested experimental conditions. Due to the very high initial bacterial concentrations, even high percentage removals left measurable numbers of surviving bacteria. Therefore, the results should be interpreted as a comparative evaluation of treatment efficiency rather than as evidence that the treated water met drinking-water microbiological standards.

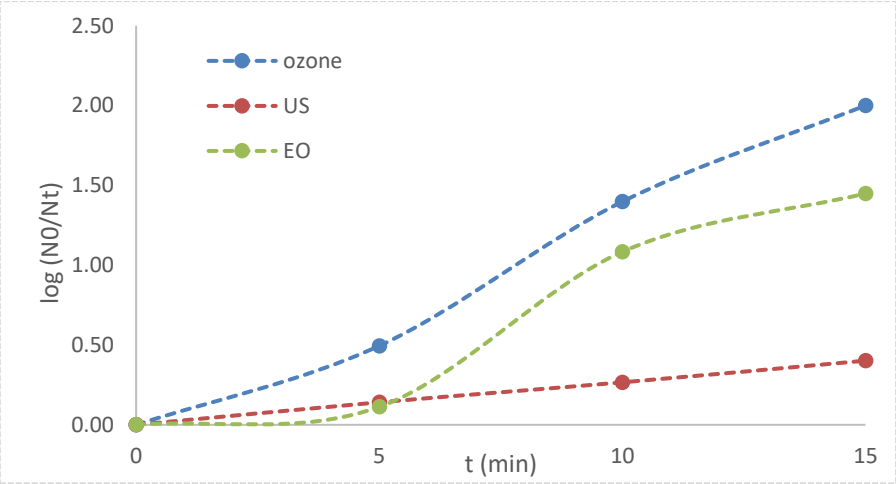


Figure 4. Comparison of *E. coli* inactivation efficiency achieved by ozone, ultrasound (US) and electrooxidation (EO) at the highest tested doses

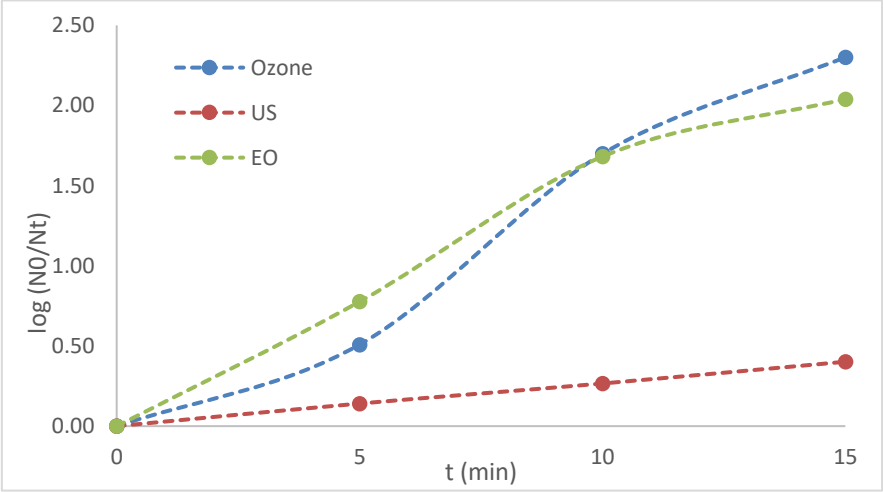


Figure 5. Comparison of total coliforms inactivation efficiency achieved by ozone, ultrasound (US) and electrooxidation (EO) at the highest tested doses

The obtained results show that the efficiency of bacterial inactivation strongly depended on the mechanism of action of each method. Ozonation and electrochemical oxidation were considerably more effective than ultrasound because both processes are based on the formation or application of strong oxidizing species. In contrast, ultrasound relies mainly on acoustic cavitation and mechanical effects, which were not sufficiently intense to achieve high bacterial removal within the tested treatment time.

Ozone acts as a strong chemical oxidant. It can damage bacterial cell walls and membranes, oxidize proteins and enzymes, alter membrane permeability, and cause leakage of intracellular material. These effects lead to rapid loss of cell viability. The high efficiency observed at 10 g/h is consistent with this mechanism, as a higher ozone dose increased the availability of oxidizing species in the water. The strong increase in log reduction between 5 and 15 min also suggests that sufficient ozone transfer and contact time are essential for effective microbial inactivation.

Electrochemical oxidation also relies on oxidative mechanisms, but the disinfecting species are generated within the water during the application of electric current. Depending on the water matrix and electrode material, electrochemical oxidation may produce hydroxyl radicals, hydrogen peroxide, ozone, active chlorine species, and other reactive oxidants. In addition, direct interaction between bacterial cells and the electrode surface or local electrical effects may contribute to inactivation. The strong improvement observed at 10 A indicates that a sufficiently high current intensity was required to generate enough disinfecting species for effective bacterial reduction.

Ultrasound treatment is based on acoustic cavitation, which involves the formation, growth, and collapse of microbubbles. The collapse of these bubbles can generate shear forces, microjets, pressure gradients, and localized high temperatures. These effects can damage bacterial cells, but in this study they were not strong enough to produce high log reductions. The results suggest that ultrasound alone, under the tested conditions, had limited disinfection capacity and would likely be more useful as a pretreatment or as part of a combined process.

Differences were also observed between the responses of *E. coli* and total coliforms. In most treatments, total coliforms showed higher apparent inactivation than *E. coli*. This was particularly evident during electrochemical oxidation at 1 A and 5 A, where total coliform removal was close to 79%, while *E. coli* inactivation remained below 50%. This difference may be related to the heterogeneous nature of the total coliform group, which includes bacteria with different physiological characteristics, resistance mechanisms, and tendencies to attach to particles or form aggregates. Therefore, the response of total coliforms does not necessarily follow the same pattern as that of *E. coli*. However, certain deviations from the expected dose-response trend were observed for total coliforms. For example, ozonation at 1 g/h resulted in slightly higher final total coliform inactivation than ozonation at 5 g/h, while ultrasound at 60% power showed higher total coliform inactivation than ultrasound at 100% power. These deviations should not be interpreted as a true reduction in the lethal effect of stronger treatments. A more likely explanation is the disruption of bacterial aggregates. If bacteria are present in clusters or attached to suspended particles, stronger physical or oxidative treatment can break these aggregates apart. This may increase the number of detectable colony-forming units, even when part of the bacterial population has already been damaged, leading to an apparent decrease in calculated inactivation efficiency.

The surface water matrix also played an important role in the observed treatment performance. The experiments were conducted using lake water, mixed with tap water and inoculated with laboratory-grown bacteria. Unlike synthetic laboratory solutions, this matrix contained natural organic matter, suspended particles, dissolved ions, and other constituents typical of surface water. These components can protect bacteria from disinfection, consume oxidants, interfere with ozone transfer, affect electrical conductivity, and influence cavitation distribution.

In ozonation, part of the applied ozone was probably consumed by organic matter and other ozone-demanding compounds instead of reacting directly with bacterial cells. This may explain why lower ozone doses showed only moderate efficiency, whereas 10 g/h produced strong inactivation. In electrochemical oxidation, the matrix affected both electrical conductivity and the generation of oxidizing species. Dissolved ions may support current flow and contribute to the formation of secondary oxidants, while organic matter can simultaneously consume reactive species. In ultrasound treatment, suspended particles and dissolved substances may influence cavitation intensity and the distribution of acoustic energy in the reactor, which could partly explain the relatively low efficiency of ultrasound as a stand-alone method.

3.2 Kinetic study

The time-dependent results indicate that bacterial inactivation increased with treatment time for all three treatments, although at different rates. The fastest inactivation was observed during ozonation at 10 g/h, followed by electrochemical oxidation at 10 A. The inactivation process can be approximately described using a first-order kinetic model (Eq. 2):

$$\ln(N_t/N_0) = -kt \tag{2}$$

where k is the inactivation rate constant and t is the treatment time. A higher k value indicates faster microbial inactivation. Kinetic interpretation is useful because it provides information not only on final treatment efficiency but also on the rate at which disinfection occurs. This is important for practical application, where shorter contact time can reduce reactor volume and operational costs.

For *E. coli*, the highest inactivation rate constant was obtained during ozonation at 10 g/h, with k value

of 0.3056 min^{-1} and R^2 of 0.9946. Electrochemical oxidation at 10 A also showed a relatively high inactivation rate, with a *k* value of 0.2180 min^{-1} and R^2 of 0.9543. In contrast, ultrasound at 100% power had a considerably lower rate constant of 0.0618 min^{-1}, regardless of very good model fit (R^2 = 0.9998). These results confirm that ozone caused the fastest *E. coli* inactivation, whereas ultrasound produced a slower but nearly linear decrease over the tested treatment period. A similar trend was observed for total coliform bacteria. Ozonation at 10 g/h again showed the highest inactivation rate, with *k* value of 0.3556 min^{-1} and R^2 0.9889. Electrochemical oxidation at 10 A achieved a comparable rate constant of 0.3375 min^{-1} with R^2 value of 0.9903, indicating that the process was also highly effective for total coliform inactivation. Ultrasound at 100% power showed a much lower rate constant of 0.0808 min^{-1}, confirming its weaker disinfection performance compared with the two oxidative treatments.

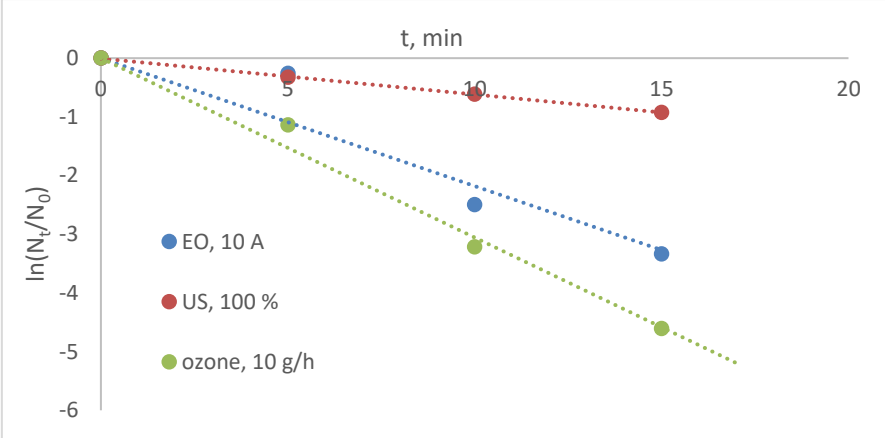


Figure 6. Kinetic models of *E. coli* inactivation by electrooxidation (EO), ultrasound (US) and ozone

As shown in Fig. 6, ozonation produced the steepest decline, indicating the fastest bacterial inactivation. Electrochemical oxidation also resulted in a pronounced decrease, especially for total coliforms, while ultrasound showed a slower and less intensive inactivation pattern. Therefore, the kinetic model provides additional evidence that ozonation and electrochemical oxidation were more suitable for rapid bacterial reduction under the tested conditions, whereas ultrasound alone had limited disinfection efficiency within the 15 min treatment time.

4 Conclusion

Overall, the results demonstrate that oxidative treatments were more effective than ultrasound for the inactivation of *E. coli* and total coliforms in the tested surface water. Ozonation showed the highest and fastest disinfection effect, while electrochemical oxidation also demonstrated strong potential at sufficiently high current intensity. Ultrasound alone was not sufficient to achieve high bacterial reduction within the applied treatment time, but its mechanical effects may still be useful in hybrid systems where cavitation could enhance mass transfer, disrupt bacterial aggregates, and improve the contact between microorganisms and oxidizing species.

Future research should focus on further optimization of operating conditions, including longer treatment times, lower initial bacterial loads, energy consumption per achieved log reduction, and monitoring of possible disinfection by-products. Special attention should be given to hybrid systems, such as ultrasound-assisted ozonation or ultrasound-assisted electrochemical oxidation, which could combine mechanical cavitation effects with strong oxidative inactivation and improve overall disinfection efficiency in complex surface water matrices.

Acknowledgements

The project „*A comprehensive AI-powered early warning system for digital management of water supply security, resilience, and sustainability (AquaGuardian)*" (DIGIT.2.1.02.001) is financed under the World Bank Loan No. 9558-HR for the project "Digital, Innovative and Green Technologies" (DIGIT Project).

References

American Public Health Association, American Water Works Association & Water Environment Federation 1992 *Standard Methods for the Examination of Water and Wastewater*, 18th edn, American Public Health Association, Washington, DC, USA.

Arrojo, S., Benito, Y. & Martínez Tarifa, A. 2008 A parametrical study of disinfection with hydrodynamic cavitation. *Ultrason. Sonochem.* 15 (5), 903–908.

Barzegar, G., Wu, J. & Ghanbari, F. 2019 Enhanced treatment of greywater using electrocoagulation/ozonation: Investigation of process parameters. *Process Saf. Environ. Prot.* 121, 125–132.

Betancourt, W.Q. & Rose, J.B. 2004 Drinking water treatment processes for removal of *Cryptosporidium* and *Giardia*. *Vet. Parasitol.* 126 (1–2), 219–234.

Biswas, B. & Goel, S. 2022 Electrocoagulation and electrooxidation technologies for pesticide removal from water or wastewater: A review. *Chemosphere* 302, 134709.

Blume, T. & Neis, U. 2002 Combined wastewater disinfection using ultrasound. In: *Proc. of the 3rd IWA World Water Congress*, Melbourne, Australia, 7–12 April.

Buchanan, K.M. (ed.) 2011 *Water Disinfection*. Nova Science Publishers, New York, USA.

Collivignarelli, M.C., Abbà, A., Benigna, I., Sorlini, S. & Torretta, V. 2018 Overview of the main disinfection processes for wastewater and drinking water treatment plants. *Sustainability* 10 (1), 86.

Das, P.P., Dhara, S., Samanta, N.S. & Purkait, M.K. 2024 Advancements on ozonation process for wastewater treatment: A comprehensive review. *Chem. Eng. Process. Process Intensif.* 202, 109852.

Ghernaout, D. 2017 Microorganisms' electrochemical disinfection phenomena. *EC Microbiol.* 9, 160–169.

Ghernaout, D. 2019 Greening electrocoagulation process for disinfecting water. *Appl. Eng.* 3 (1), 27–31.

Ghernaout, D. & Ghernaout, B. 2010 From chemical disinfection to electrodisinfection: The obligatory itinerary? *Desalin. Water Treat.* 16 (1–3), 156–175.

Gibson, J.H., Yong, D.H.N., Farnood, R.R. & Seto, P. 2008 A literature review of ultrasound technology and its application in wastewater disinfection. *Water Qual. Res. J. Can.* 43 (1), 23–35.

Jyoti, K.K. & Pandit, A.B. 2004 Ozone and cavitation for water disinfection. *Biochem. Eng. J.* 18 (1), 9–19.

Kraft, A. 2008 Electrochemical water disinfection: A short review. *Platin. Met. Rev.* 52 (3), 177–185.

Martínez-Huitle, C.A. & Brillas, E. 2008 Electrochemical alternatives for drinking water disinfection. *Angew. Chem. Int. Ed.* 47 (11), 1998–2005.

Motta, E.J.L., Rincón, G.J., Grau, L.E.D. & Jovanovich, K.D. 2018 Field testing of a small-scale continuous-flow wastewater electrodisinfection unit using direct current. *J. Environ. Eng.* 144 (1), 04017090.

Naddeo, V., Cesaro, A., Mantzavinos, D., Fatta-Kassinos, D. & Belgiorno, V. 2014 Water and wastewater disinfection by ultrasound irradiation—a critical review. *Glob. NEST J.* 16 (3), 561–577.

Rompré, A., Servais, P., Baudart, J., de-Roubin, M.R. & Laurent, P. 2002 Detection and enumeration of coliforms in drinking water: Current methods and emerging approaches. *J. Microbiol. Methods* 49 (1), 31–54.

Soares, B.S., Mello, R. & Motheo, A.J. 2024 Groundwater treatment and disinfection by electrochemical advanced oxidation process: Influence of the supporting electrolyte and the nature of the contaminant.

Appl. Res. 3 (2), e202300008.
Solsona, F. & Méndez, J.P. 2003 *Water Disinfection*. Report PAHO/CEPIS/PUB/03.89, Pan American Center for Sanitary Engineering and Environmental Sciences, Pan American Health Organization/World Health Organization, Lima, Peru.
Song, K., Liu, Y., Umar, A., Ma, H. & Wang, H. 2024 Ultrasonic cavitation: Tackling organic pollutants in wastewater. *Chemosphere* 350, 141024.
Vajnhandl, S., Željko, T., Majcen Le Marechal, A. & Volmajer Valh, J. 2015 Feasibility study of ultrasound as water disinfection technology. *Desalin. Water Treat.* 55 (5), 1393–1399.

WATER QUALITY ANALYSIS IN THE ORLJAVA RIVER BASIN AREA

Andreja MENĐEL [1*], Lidija TADIĆ [2]

[1] *Local development agency Požega, Industrijska 39, 34 000 Požega, Croatia*

E-mail: andreja.mendjel@pozega.hr

[2] *Faculty of Civil Engineering and Architecture Osijek, Vladimira Preloga 3, 31 000 Osijek, Croatia*

E-mail: ltadic@gfos.hr

[*] *Corresponding author*

Abstract

Water is a non-renewable resource that is the foundation of life, as well as the origin and development of all living beings, therefore, it can be described as the liquid of life. It is also an integral part of every segment of human activity, and is considered an irreplaceable resource in households, agriculture and the economy. Globalization and technological progress are becoming important for social development, but their progress leads to increased consumption of clean water and the generation of growing quantities of wastewater contaminated with various organic and inorganic substances. Ensuring an adequate supply of drinking water today represents one of the greatest global challenges. The availability of water in Croatia is considered highly sufficient, but its spatial and annual distribution can be assessed as unfavourable. Environmental changes caused by natural phenomena, as well as human activities, threaten water quality. The research area of this study is the Orljava river basin, from which four out of ten monitoring stations will be analysed, selected based on the availability of the longest data series (2001 to 2024). Based on the collected data for observed stations, water quality assessments are also carried out with a focus on nutrients – nitrates, total nitrogen and total phosphorus – in accordance with the Regulation on Water quality standards. The homogeneity of data series is examined using the RAPS method. Based on the obtained results, sub-periods and characteristics are analysed. At the same time, conclusions are drawn, along with plans for future that include measures for improving water quality.

Key words

The Orljava river basin, water quality, RAPS method

1 Introduction

Water is one of the most important natural resources and plays a crucial role in maintaining ecological balance, economic development and the quality of human life. The quality of surface waters is increasingly threatened by various forms of anthropogenic pollution, particularly through wastewater discharge and intensive agricultural production. Among the most significant indicators of watercourse pollution are nitrates, total nitrogen and total phosphorus, whose elevated concentrations may lead to eutrophication and deterioration of water quality.

Agricultural activities represent one of the main sources of nitrogen and phosphorus pollution, primarily due to the application of mineral and organic fertilizers. According to available public data from the Croatian Bureau of Statistics, the area of utilized agricultural land in Croatia did not significantly increase during the observed period, while a decrease in mineral fertilizer consumption was recorded after the last pronounced increase in 2021. At the same time, the quantity of treated wastewater showed a slight increase, while the total quantity of discharged wastewater decreased compared to the peak recorded in 2017. These indicators may suggest gradual changes in pressures on water resources and in

the efficiency of water protection measures.

The Orljava River basin is characterized by the combined influence of urban, industrial and agricultural activities, which makes monitoring changes in water quality particularly important for assessing the condition of water resources and identifying potential sources of nutrient pollution. Time series analysis enables the identification of changes in nutrient concentrations, possible trends and the occurrence of temporal inhomogeneities within the observed period.

The aim of this study is to analyse changes in nitrate, total nitrogen and total phosphorus concentrations at selected monitoring stations within the Orljava River basin during the period from 2000 to 2024. The RAPS method was applied to identify temporal inhomogeneities, characteristic subperiods and changes in nutrient concentrations, enabling the assessment of spatial and temporal variability in water quality. In addition, this study demonstrates the applicability of the RAPS method to long-term water quality monitoring and provides information that can support future river basin management and the evaluation of water protection measures.

2 Methods

This chapter presents the characteristics of the study area, water quality data and the RAPS method together with its application in the analysis of water quality time series.

2.1 Study area

The Orljava River basin covers an area of 1,616 km^2 and belongs to the Sava River basin. The Orljava River represents the main drainage recipient of the Požega Valley. For the purposes of this study, data collected by Hrvatske vode from 10 monitoring stations within the Orljava River basin were used, while 4 stations with the longest available data series were selected for detailed analysis: Orljava upstream from Požega, Orljava bridge Pleternica, Adžamovka lateral canal and Orljava under the highway. The spatial distribution of the monitoring stations and the course of the Orljava River are shown in Fig. 1. The study area is also influenced by municipal wastewater discharges and agricultural activities, which represent important potential sources of nutrient pollution (Hrvatske vode, 2014).

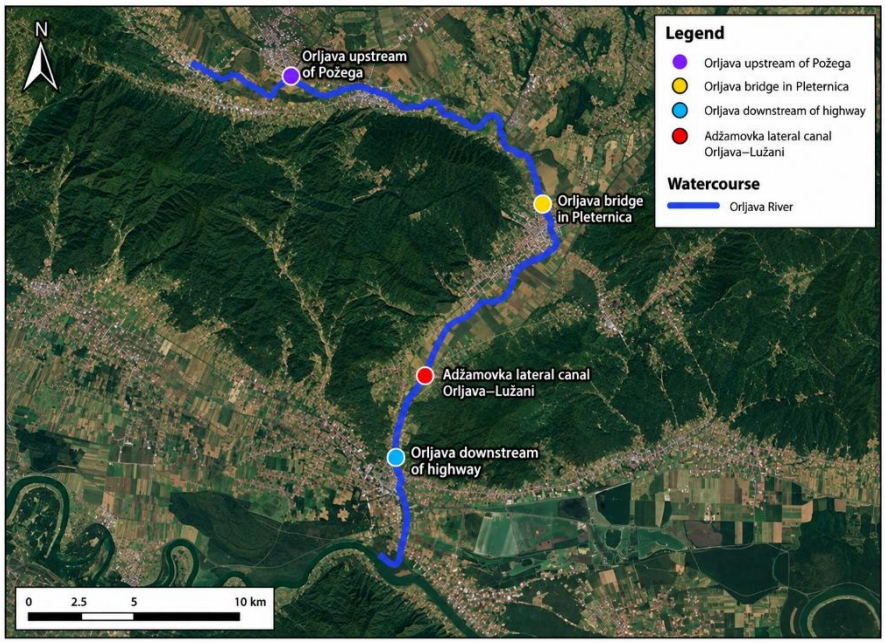


Figure 1. Spatial distribution of the analysed monitoring stations within the Orljava River basin (Source: authors, based on Google Maps and data from Hrvatske vode)

In the Požega area, the first phase of construction of the Central Wastewater Treatment Plant was completed in 2005, enabling mechanical wastewater treatment. At the end of 2024, an upgraded facility with tertiary treatment and nutrient removal was commissioned for trial operation, with a capacity of 33,500 population equivalents. The recipient of the treated wastewater discharged from the plant is the Orljava River water body (Hrvatske vode, 2014).

According to water body status data, the observed parameters characteristic of municipal wastewater indicate moderate to poor watercourse status, while total phosphorus was assessed as moderate, and total nitrogen concentrations were assessed as poor. Upstream water bodies, according to the conducted analysis, correspond to good ecological status (Riko, 2020).

2.2 Water quality data

Water quality is determined using physical, chemical, biological and microbiological indicators important for the management and monitoring of water as a natural resource. Chemical properties significantly affect the potential use of water, while nutrients are among the most important indicators. Nutrients are essential for primary organic matter production and the growth of algae and aquatic vegetation, and the most significant among them are nitrates, total nitrogen and total phosphorus (Vugrin, 2019), that are subject of this research.

Data for the selected monitoring stations were collected for the period from 2000 to 2024, represented a total period of 25 years, except for the station Adžamovka lateral canal, for which data were available for the period from 2015 to 2024. Despite the shorter observation period, this station was included in the study due to its location between two monitoring stations on the main course of the Orljava River, enabling a more detailed analysis of changes in the behaviour of the observed parameters.

A total of 842 input data were available for the station Orljava upstream from Požega (283 for nitrates and total nitrogen each and 270 for total phosphorus), 860 for the station Orljava bridge Pleternica (292 for nitrates and total nitrogen each and 276 for total phosphorus), 324 for the Adžamovka lateral canal station (111 for nitrates and total nitrogen each and 102 for total phosphorus) and 833 for the station Orljava under the highway (283 for nitrates and total nitrogen each and 267 for total phosphorus). The monitoring stations were analysed according to their position along the flow direction of the Orljava River.

Water quality assessment was carried out in accordance with the Regulation on Water Quality Standards (Narodne novine, 96/2019-1879), where the analysed indicators were classified into the categories very good, good and poor (unsatisfactory) status. The classification was performed according to the threshold values prescribed for the observed water body type.

2.3 RAPS method

The RAPS method (Rescaled Adjusted Partial Sums) is based on the analysis of cumulative deviations within a time series and enables the visualization and quantification of trend and fluctuations in the observed data series (Bonacci et al., 2008). RAPS values are calculated according to Eq. (1):

$$RAPS_k = \sum_{t=1}^{k} \frac{Yt - Ymean}{Sy} \quad (1)$$

where: Y_{mean} is the mean value of the observed series, Y_t is the value of the observed parameter at time (t) and S_y is the standard deviation of the series.

The graphical representation of RAPS values over time enables the identification of changes, fluctuations and possible inhomogeneities within the analysed time series (Bonacci, 2010). Due to its ability to detect regime shifts and temporal variability, the method is widely applied in hydrological, meteorological and environmental studies. Previous studies applied the RAPS method in analyses of air temperature, river discharge, precipitation trends and water quality parameters in Croatia and abroad

(Bonacci, 2010; Bonacci and Andrić, 2008; Shelton, 1998; Qijing et al, 2019).

In this study, the RAPS method was used to assess the homogeneity of selected water quality indicators. The identified break points were additionally evaluated using the F-test and t-test at a significance level of $p<0.01$. Based on the detected break points, characteristic subperiods were defined in order to analyse temporal changes and fluctuations in nitrate, total nitrogen and total phosphorus concentrations.

3 Results and Discussion

This chapter presents the results of the conducted analyses for nutrients, namely nitrates, total nitrogen and total phosphorus, at selected monitoring stations along the Orljava River basin during the period from 2000 to 2024.

3.1 Nitrates

The nitrate analysis included the assessment of nitrate concentration variations during the observed period, the application of the RAPS method for the identification of break points and characteristic subperiods, as well as the evaluation of nitrate water quality status.

3.1.1 General overview of nitrate concentrations

Nitrates are salts of nitric acid that enter the environment through agricultural activities, since they are a major component of mineral fertilizers. Nitrate concentrations in water largely depend on precipitation intensity, irrigation and cultivated crops (Jambrušić, 2016). Fig. 2 shows the variation in nitrate concentration at the monitoring stations included in this study. The lowest concentrations were recorded at the Orljava upstream station, while the highest concentrations were observed at the Orljava highway station, indicating an increase in nitrate concentrations downstream along the course of the Orljava river. Additional analysis of nitrate concentrations together with the corresponding flow and water level data at the Orljava Požega and Frkljevci-Orljava monitoring stations indicated a relationship between higher nitrate concentrations and increased flow and water level values. Linear trend analysis showed a decrease in nitrate concentrations at all observed stations, suggesting the implementation of certain water protection measures within the study area. However, since the observed decreases were not substantial, additional efforts and more intensive water protection measures are required in order to reduce nutrient inputs into watercourses.

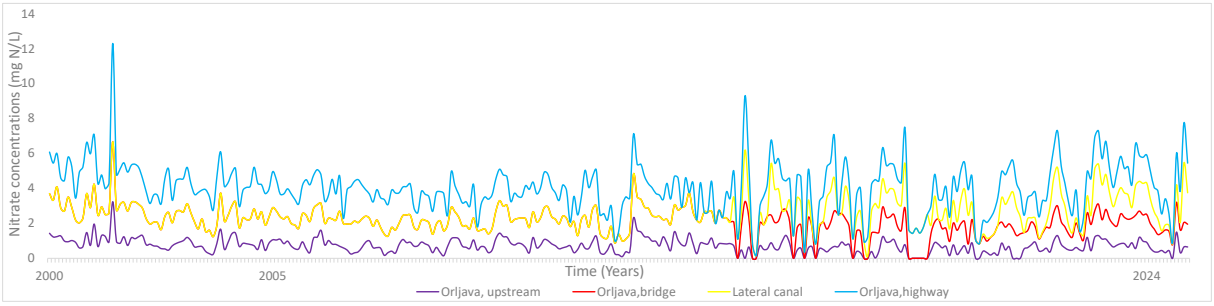


Figure 2. Nitrate concentrations at selected monitoring stations along the Orljava River

3.1.2 RAPS analysis of nitrate concentration by monitoring station

The RAPS analysis was applied to each nitrate concentration data set obtained on each monitoring station.

Orljava, upstream from Požega

The RAPS analysis identified 4 characteristic subperiods in the nitrate concentration series at the Orljava

upstream from Požega station (Fig. 3). The first subperiod was characterized by pronounced fluctuations and maximum concentrations, while later subperiods showed more stable values. A negative linear trend was observed in most subperiods, while the final subperiod showed a slight positive trend.

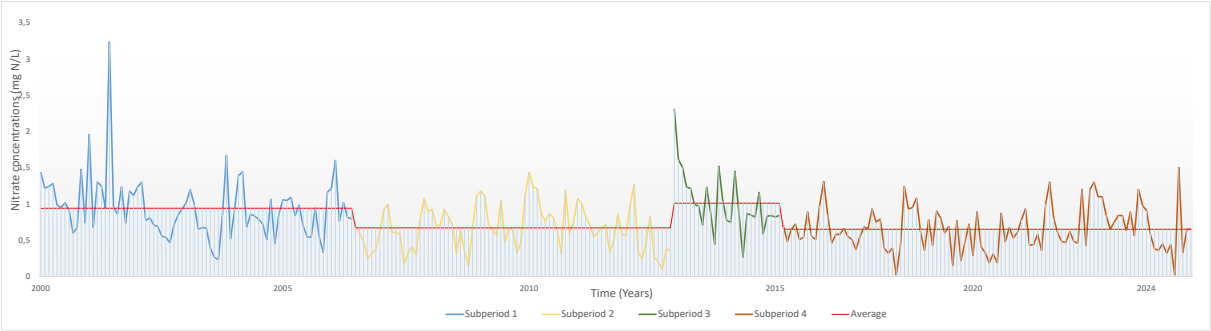


Figure 3. Subperiods of nitrate concentrations at the Orljava upstream from Požega monitoring station

Orljava bridge Pleternica

The RAPS analysis of nitrate concentrations at the Orljava bridge Pleternica station identified 6 characteristic subperiods (Fig. 4). The first subperiod was characterized by the highest nitrate concentrations and pronounced fluctuations, while later subperiods showed more stable concentrations, although occasional increases and stronger oscillations were observed in the middle part of the series. Negative linear trend prevailed in the later subperiods, while the final subperiod was characterized by relatively stable nitrate concentrations.

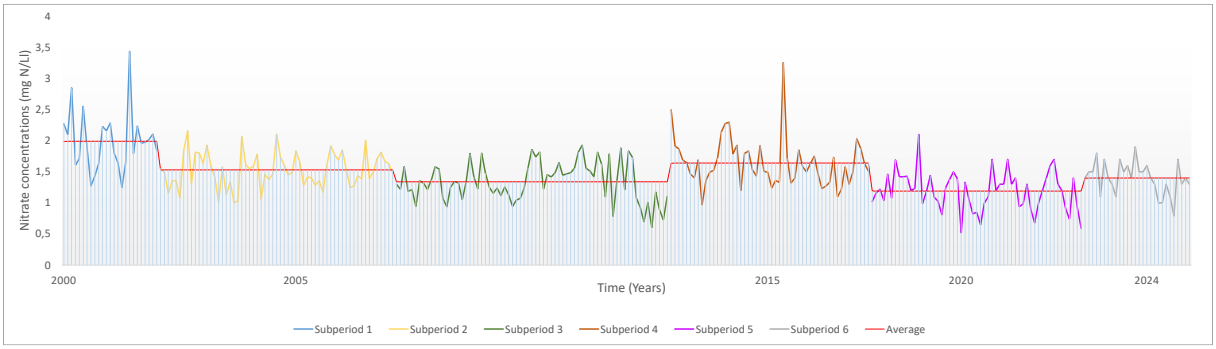


Figure 4. Subperiods of nitrate concentrations at the Orljava bridge Pleternica station

Adžamovka lateral canal, Orljava-Londža

The RAPS analysis of nitrate concentrations at the Adžamovka lateral canal station identified 4 characteristic subperiods (Fig. 5). The first subperiod was characterized by pronounced fluctuations and higher nitrate concentrations. During the second subperiod, concentrations became more stable with lower fluctuation intensity, while the third and fourth subperiods showed increased oscillations and occasional extreme values. Negative linear trends were observed in most subperiods, except for the second subperiod, where a slight positive trend was recorded.

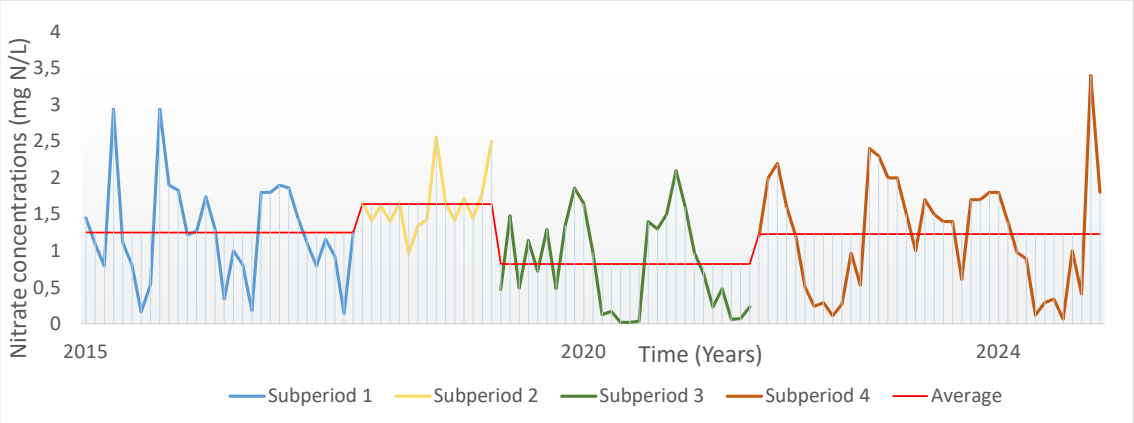


Figure 5. Subperiods of nitrate concentrations at the Adžamovka lateral canal, Orljava-Londža station

Orljava under the highway

The RAPS analysis of nitrate concentrations at the Orljava under the highway station identified 4 characteristic subperiods (Fig. 6). The first subperiod was characterized by the highest nitrate concentrations and pronounced fluctuations. In the second subperiod, concentrations became more stable with a negative linear trend, while the third subperiod showed increased oscillations and more pronounced decreased and increased values. The final subperiod was characterized by relatively stable concentrations with occasional fluctuations. Positive linear trend prevailed in most subperiods.

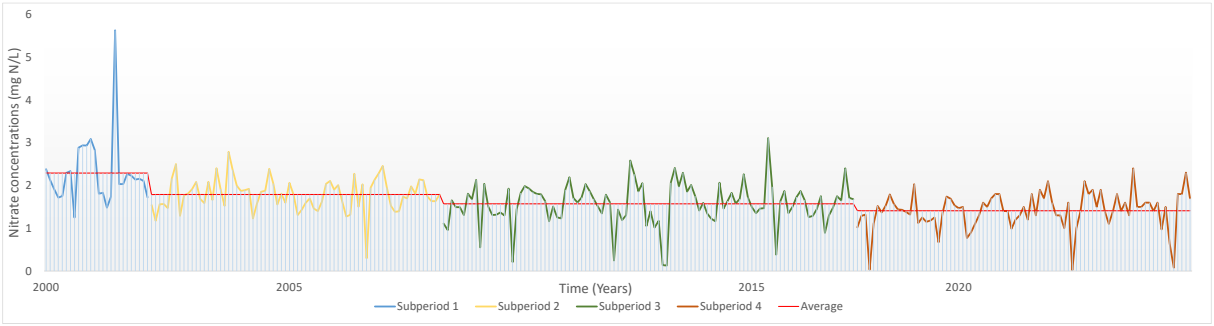


Figure 6. Subperiods of nitrate concentrations at the Orljava under the highway station

The results of the RAPS analysis of nitrate concentrations indicate the presence of temporal inhomogeneity at all observed monitoring stations. The identified break points differed among the stations, although certain years, particularly 2002, 2012 and 2017, appeared at multiple stations, which may indicate the influence of broader hydrological or anthropogenic changes within the observed area. The coefficient of variation showed the highest variability of nitrate concentrations at the Adžamovka lateral canal station (CV=60.97%) and the Orljava upstream station (CV=48.85%), while lower variability was observed at the Orljava under the highway (CV=33.15%) and the Orljava bridge Pleternica station (CV=27.03%).

3.1.3 Water quality classification

The classification of nitrate concentrations according to the Regulation revealed significant differences in water quality among the observed monitoring stations, as shown in Fig. 7. The highest share of "poor" category was recorded at the Orljava highway station, as well as at the Orljava bridge station. The most favourable results were observed at the Orljava upstream station, where the "good" and "very good" categories prevailed. The Lateral canal station showed greater variability in water quality, with all quality categories represented.

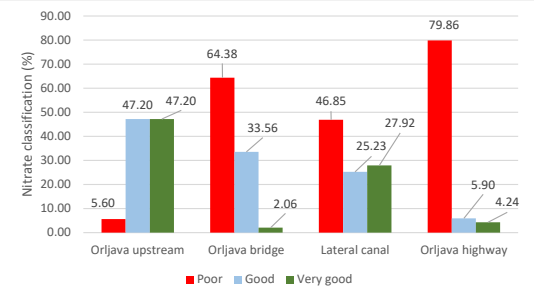


Figure 7. Water quality classification based on nitrate concentrations at selected monitoring stations

The analysis of water quality classification by subperiods indicates noticeable temporal changes in nitrate concentrations at the observed monitoring stations. At the station Orljava upstream from Požega, the share of "very good" water quality increased in later subperiods, while the proportion of "poor" quality decreased. In contrast, the stations Orljava bridge Pleternica and Orljava under the highway showed a dominant share of the "poor" category throughout most subperiods, indicating persistent nitrate pollution. The Adžamovka lateral canal exhibited alternating shares of "good" and "poor" categories between subperiods, suggesting increased temporal variability of nitrate concentrations.

The identified temporal inhomogeneities and characteristic subperiods are consistent with previous applications of the RAPS method in hydrological and environmental studies (Bonacci, 2010; Shelton, 1998), confirming its suitability for analysing long-term nutrient concentration series.

3.2 Total nitrogen

The analysis of total nitrogen included the evaluation of concentration changes during the observed period, the application of the RAPS method for identifying characteristic subperiods and break points within the time series, as well as the assessment of water quality status according to total nitrogen concentrations.

3.2.1 General overview of total nitrogen concentrations

Total nitrogen in water represents the sum of all nitrogen compounds present in water, while in wastewater commonly originates from nitrite, nitrate and ammonium ions, as well as from organic nitrogen compounds (Jambrušić, 2016). Figure 8 shows changes in total nitrogen concentrations at the observed monitoring stations during the analysed period. The highest total nitrogen concentrations were recorded at the Orljava bridge Pleternica station, while the lowest values were generally observed at the Orljava upstream from Požega station. At the Adžamovka lateral canal station, an extreme maximum total nitrogen concentration was recorded, significantly differing from the remaining measured values. Linear trend analysis indicated a more pronounced decrease in total nitrogen concentrations during the observed period compared to nitrates.

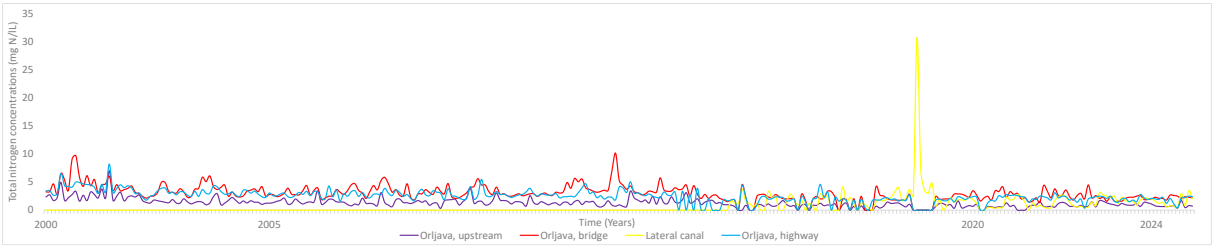


Figure 8. Total nitrogen concentrations at selected monitoring stations along the Orljava River

3.2.2 RAPS analysis of total nitrogen concentration by monitoring station

The RAPS analysis was applied to each total nitrogen concentration data set obtained on each monitoring station.

Orljava, upstream from Požega

The RAPS analysis of total nitrogen concentrations at the Orljava upstream from Požega station identifies 5 characteristic subperiods (Fig. 9). The first two subperiods were characterized by pronounced fluctuations and higher total nitrogen concentration, while the following subperiods showed more stable concentration values with occasional decreased and increased values. The final subperiod was characterized by relatively stable total nitrogen concentrations. Positive linear trends were observed in the first and last subperiods, while negative trends prevailed in the remaining periods.

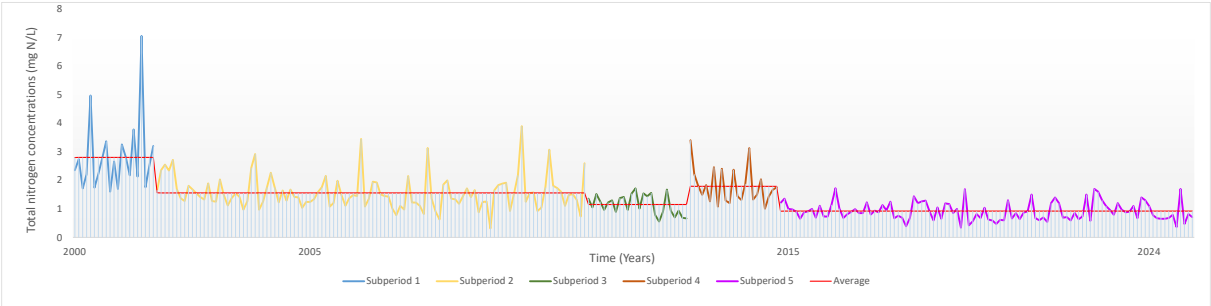


Figure 9. Subperiods of total nitrogen concentrations at the Orljava upstream from Požega monitoring station

Orljava bridge Pleternica

The RAPS analysis of total nitrogen concentrations at the Orljava bridge Pleternica station identified 4 characteristic subperiods (Fig. 10). The first two subperiods were characterized by pronounced fluctuations and elevated total nitrogen concentrations, including the maximum concentration, recorded during the observed period. In the following subperiod, concentrations gradually decreased and became more stable with lower oscillation intensity. A negative linear trend was observed in the first subperiod, while positive trends prevailed in the remaining periods.

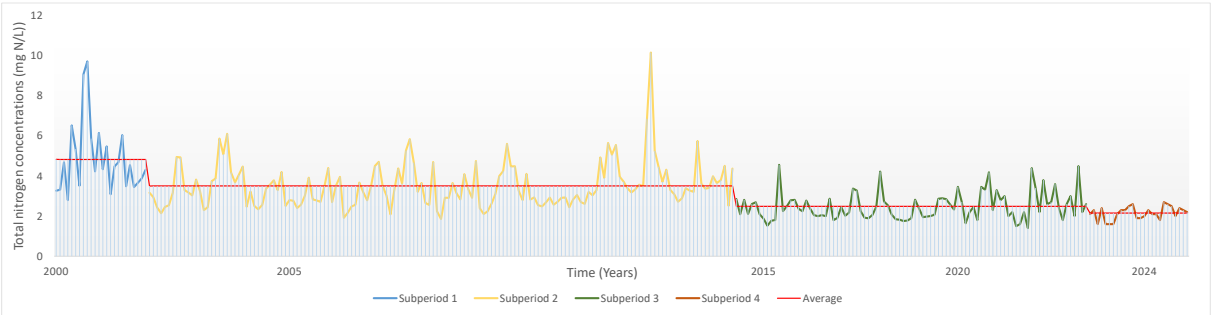


Figure 10. Subperiods of total nitrogen concentrations at the Orljava bridge Pleternica monitoring station

Adžamovka lateral canal, Orljava-Londža

The RAPS analysis of total nitrogen concentrations at the Adžamovka lateral canal station identified 3 characteristic subperiods (Fig. 11). The first subperiod was characterized by pronounced fluctuations and the occurrence of the maximum total nitrogen concentration recorded during the observed period. In the following subperiods, concentrations became more stable with lower oscillation intensity, although occasional fluctuations and slight increases in values were still observed. A positive linear trend was recorded in the first subperiod, while negative trend prevailed in the remaining periods.

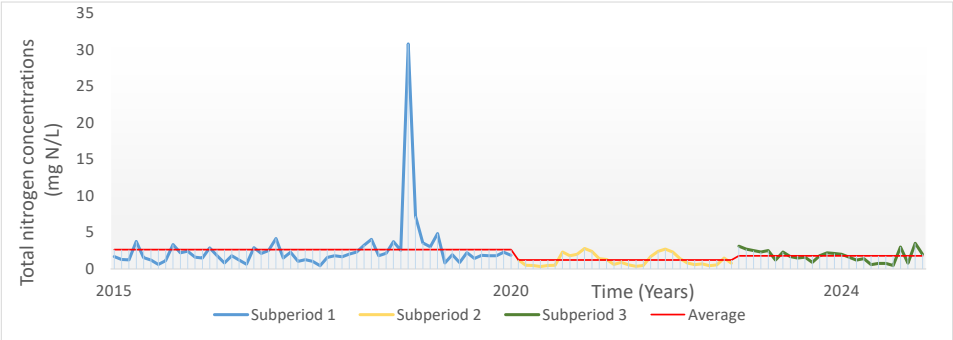


Figure 11. Subperiods of total nitrogen concentrations at the Adžamovka lateral canal, Orljava-Londža station

Orljava under the highway

The RAPS analysis of total nitrogen concentrations at the Orljava under the highway station identified 3 characteristic subperiods (Fig. 12). The first subperiod was characterized by the highest total nitrogen concentrations and pronounced fluctuations, including the maximum recorded concentration. In the following subperiods, concentrations became more stable and generally lower, although occasional fluctuations and minimum values were still observed. Negative linear trends prevailed throughout all identified subperiods.

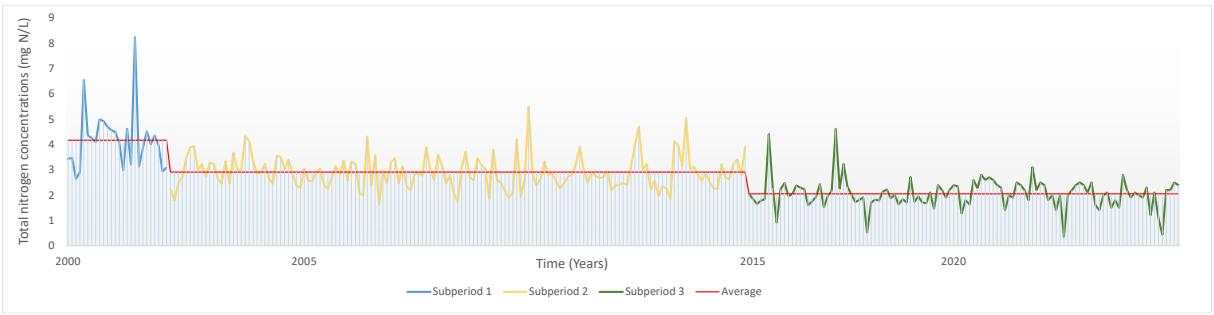


Figure 12. Subperiods of total nitrogen concentrations at the Orljava under the highway station

The results of the RAPS analyses of total nitrogen concentrations indicate the presence of temporal inhomogeneity at all observed stations. The identified break points differed among the stations, while the year 2014 appeared to be significant at multiple stations. At most stations, a gradual decrease in total nitrogen concentrations was observed during the analysed period, together with the stabilization of values in the later subperiods. The coefficient of variation showed the highest variability of total nitrogen concentration at the Adžamovka lateral canal station (CV=144.17%), indicating pronounced fluctuations and occasional extreme values. Higher variability was also observed at the Orljava upstream from Požega station (CV=54.45%), while lower variability was recorded at the Orljava bridge Pleternica station (CV=39.30%) and the Orljava under the highway station (CV=34.51%).

3.2.3 Water quality classification

The classification of total nitrogen concentrations, shown in Fig. 13, also revealed significant differences in water quality among the observed monitoring stations. The most favourable conditions were recorded at the Orljava upstream from Požega station, where the “good” and “very good” categories prevailed. In contrast, the Orljava bridge Pleternica and Orljava under the highway stations were characterized by a dominant share of the “poor” category. The Adžamovka lateral canal showed a more balanced distribution of all water categories.

The analysis of total nitrogen classification by identified subperiods indicates pronounced temporal changes in water quality at the observed monitoring stations. At the Orljava upstream from Požega station, an improving water quality trend was observed throughout the analysed subperiods, reflected in the increasing share of “good” and “very good” categories and the decreasing share of the “poor”

category in later subperiods. In contrast, the Orljava bridge Pleternica and Orljava under the highway stations were characterized by a dominant share of the "poor" category during most subperiods, indicating persistently elevated total nitrogen load. The Adžamovka lateral canal station showed greater variability in the distribution of water quality categories between subperiods, without a clearly expressed trend of improvement or deterioration.

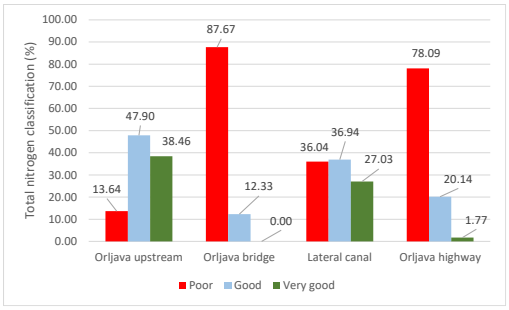


Figure 13. Water quality classification based on total nitrogen concentrations at selected monitoring stations

The obtained results further confirm that the RAPS method is an effective tool for detecting temporal changes in long-term water quality series, similarly to its successful application in previous hydrological and environmental studies.

3.3 Total phosphorus

The analysis of total phosphorus included the evaluation of concentration during the observed period, the application of the RAPS method for identifying characteristic subperiods and break points within the time series, as well as the assessment of water quality status according to total phosphorus concentration.

3.3.1 General overview of total phosphorus concentrations

Phosphorus represents one of the essential non-renewable elements whose presence is desirable within certain ranges, where it contributes to biological productivity in aquatic systems (Tutić et al., 2021). Fig. 14 shows changes in total phosphorus concentrations at the observed monitoring stations during the analysed period. Differences in fluctuation intensity and maximum values were observed among the stations, while some stations recorded more pronounced occasional increases in total phosphorus concentrations. Although linear trend analysis indicated a decrease in total phosphorus concentrations during the observed period, compared to nitrates and total nitrogen, total phosphorus showed the weakest decreasing trend.

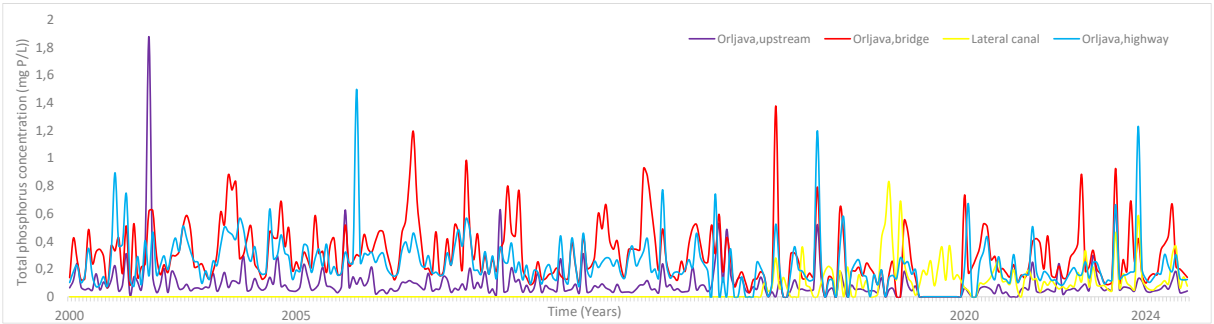


Figure 14. Total phosphorus concentrations at selected monitoring stations along the Orljava River

Orljava, upstream from Požega

The RAPS analysis of total phosphorus concentrations at the Orljava upstream from Požega station identified 2 characteristic subperiods (Fig. 15). The first subperiod was characterized by more pronounced fluctuations and higher maximum total phosphorus concentrations with a negative linear

trend. In the second subperiod, concentrations became more stable with occasional short-term increases in values and a positive linear trend.

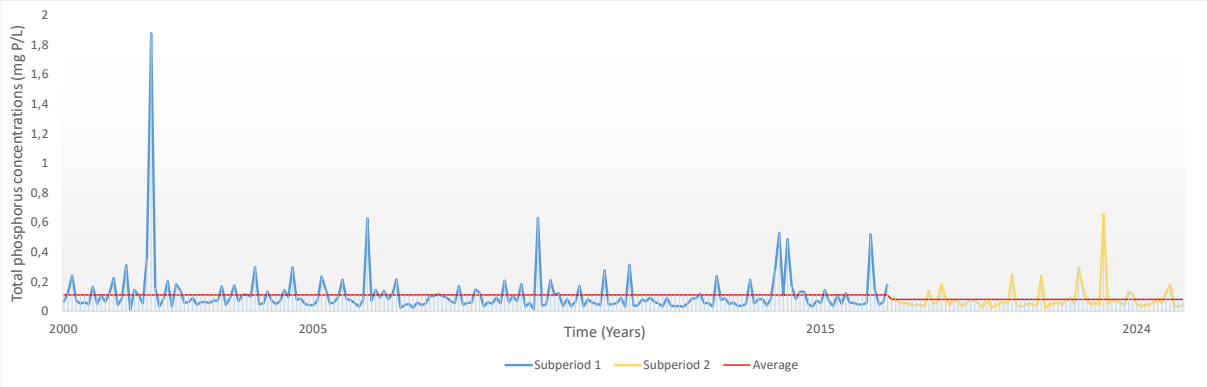


Figure 15. Subperiods of total phosphorus concentrations at the Orljava upstream from Požega monitoring station

Orljava bridge Pleternica

The RAPS analysis of total phosphorus concentrations at the Orljava bridge Pleternica station identified 5 characteristic subperiods (Fig. 16). The first two subperiods were characterized by pronounced fluctuations and occasional maximum concentration values, with positive linear trends. In the third subperiod, concentrations became lower and more stable, while the fourth and fifth subperiods showed increased variability and occasional higher concentration values. Negative linear trends were observed in the final two subperiods.

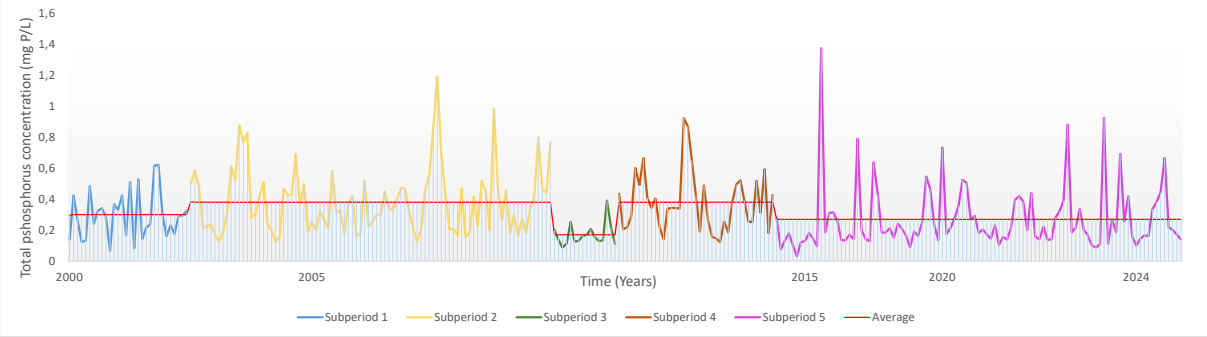


Figure 16. Subperiods of total phosphorus concentrations at the Orljava bridge Pleternica monitoring station

Adžamovka lateral canal, Orljava-Londža

The RAPS analysis of total phosphorus concentrations at the Adžamovka lateral canal station identified 3 characteristic subperiods (Fig. 17). The first subperiod was characterized by lower concentrations and moderate fluctuations with a negative linear trend. The second subperiod showed more pronounced oscillations and higher maximum concentration values, while the final subperiod was characterized by lower and more stable concentrations with occasional peak values towards the end of the observed period. A positive linear trend was observed in the final subperiod.

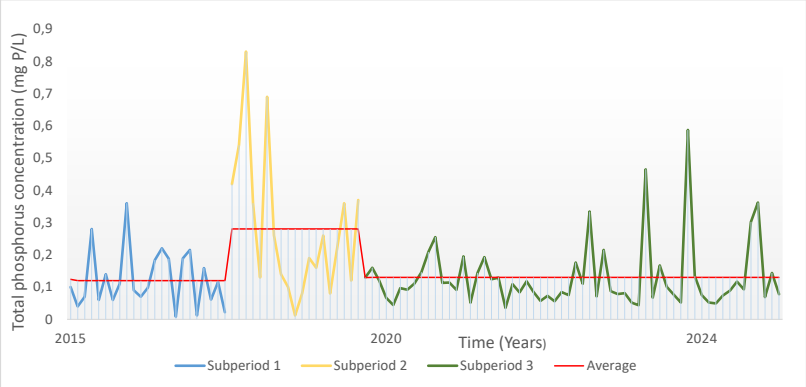


Figure 17. Subperiods of total phosphorus concentrations at the Lateral canal Adžamovka monitoring station

Orljava under the highway

The RAPS analysis of total phosphorus concentrations at the Orljava under the highway station identified 3 characteristic subperiods (Fig. 18). The first subperiod was characterized by lower concentrations and smaller oscillations with a negative linear trend. In the second and third subperiods, more pronounced fluctuations and higher maximum concentration values were observed, including the maximum concentration recorded during the analysed period. Negative linear trends prevailed throughout all identified subperiods.

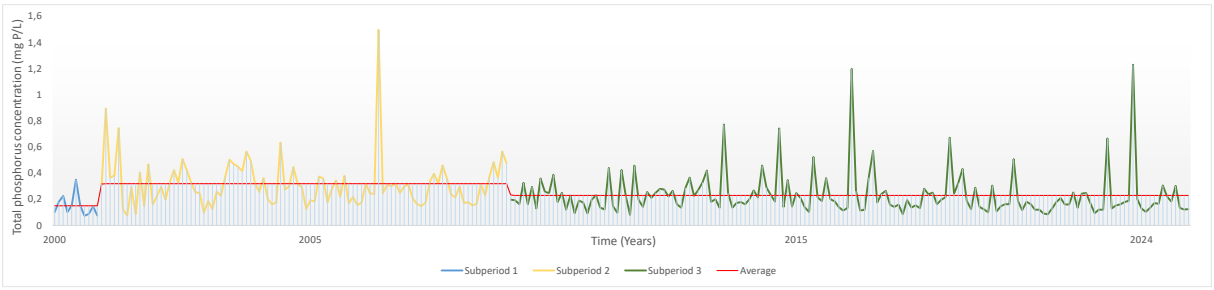


Figure 18. Subperiods of total phosphorus concentrations at the Orljava under the highway monitoring station

The results of the RAPS analysis of total phosphorus concentrations also indicate the presence of temporal inhomogeneity at all observed monitoring stations, with characteristic subperiods differing in concentration levels and fluctuation intensity. The identified break points varied among the stations, indicating spatial variability of total phosphorus concentrations within the basin. At most stations, pronounced fluctuations and occasional peak concentration values were observed, particularly in the later subperiods. Linear trend analysis indicated a decrease in total phosphorus concentrations during the observed period, however, compared to nitrates and total nitrogen, total phosphorus showed the weakest decreasing trend. The coefficient of variation showed the highest variability of total phosphorus concentrations at the Orljava upstream from Požega station (CV=139.68%), and the Adžamovka lateral canal station (CV=90.09%), while lower variability was observed at the Orljava under the highway station (CV=67.83%) and the Orljava bridge Pleternica station (CV=64.46%).

3.3.2 Water quality classification

The classification of total phosphorus concentrations, shown in Fig. 19, revealed significant differences in water quality among the observed monitoring stations. The most favourable conditions were recorded at the Orljava upstream from Požega station, where the “good” and “very good” categories prevailed, with the lowest share of the “poor” category. In contrast, the Orljava bridge Pleternica and Orljava under the highway station were characterized by a high share of the “poor” category, indicating increased total phosphorus load during the observed period. The Adžamovka lateral canal station showed a dominant share of the “good” category, with smaller shares of the “poor” and “very good” categories. Compared to nitrates and total nitrogen, total phosphorus showed the lowest share of the “very good” category,

indicating a less pronounced trend of water quality improvement during the observed period.

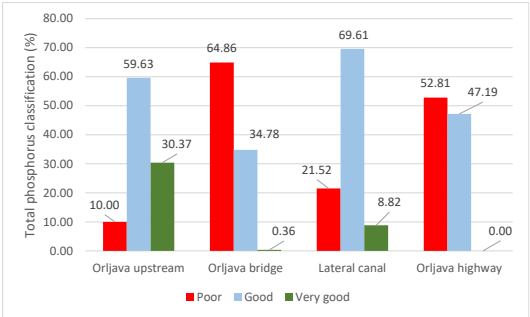


Figure 19. Water quality classification based on total phosphorus at selected monitoring stations

The analysis of total phosphorus classification by identified subperiods indicates an improving water quality trend at the Orljava upstream from Požega station. At the Orljava bridge Pleternica station, no clear improvement trend was observed. The Adžamovka lateral canal station was characterized by pronounced variability in water quality between subperiods, while the final subperiod showed a higher share of the "good" category. The Orljava under the highway station showed partial stabilization of water quality in the later subperiods, although the "poor" category remained significantly represented. The consistency of the identified temporal patterns across the analysed nutrient indicators supports the applicability of the RAPS method for assessing long-term changes in water quality and complements previous studies in which the method was primarily applied to hydrological and meteorological time series.

4 Conclusion

The conducted analysis of water quality within the Orljava River basin revealed significant spatial and temporal differences in nitrate, total nitrogen and total phosphorus concentrations at the observed monitoring stations. Data analysed indicated a gradual decrease in the concentrations of all analysed nutrients during the observed period, with the most pronounced decrease observed for total nitrogen, while total phosphorus showed the weakest decreasing trend.

The RAPS analysis confirmed the presence of temporal inhomogeneity at all observed monitoring stations, with characteristic subperiods differing in nutrient concentrations and fluctuation intensity. The identified break points varied among the stations, indicating spatial variability of water quality changes within the basin. However, certain break point years appeared at multiple stations, particularly 2002, 2012 and 2017 for nitrate concentrations, and 2014 for total nitrogen concentrations, which may indicate the influence of broader hydrological conditions, changes in watercourse load, or the implementation of specific water protection measures. The poorest water quality conditions were recorded at the Orljava bridge Pleternica and Orljava under the highway stations, while the Orljava upstream from Požega station showed the most favourable results. This indicates a lower influence of anthropogenic pollution sources in the upstream part of the basin.

The obtained results indicate the influence of agricultural activities, municipal wastewater and local anthropogenic pressures on changes in nutrient concentrations within the watercourses (Jambrušić, 2016; Hrvatske vode, 2014; Riko, 2020). The results also indicate that nutrient pollution remains significant in certain parts of the basin.

In order to reduce water pollution caused by nitrates, total nitrogen and total phosphorus, it is necessary to continue the modernization of wastewater drainage and treatment systems, increase the connection of the population to public sewerage systems and improve the efficiency of wastewater treatment plants. In addition, the implementation of sustainable agricultural practices, more rational use of mineral fertilizers and stricter control of agricultural pollution sources are of particular importance (Hrvatske vode, 2014; Riko, 2020). Continuous water quality monitoring and further time series analyses are

necessary for assessing the effectiveness of implemented measures and future changes in water resource conditions.

Considering the planned infrastructure projects and further improvements to wastewater treatment system within the Orljava River basin, similar analyses are recommended in the future in order to evaluate the effectiveness of implemented measures and long-term changes in water quality. By combining RAPS analysis with water quality classification according to the national regulation, the study provides a practical framework for interpreting long-term nutrient dynamics and supporting water management decisions.

References

Bonacci, O. 2010. Analysis of series of mean annual air temperatures in Croatia. *Građevinar, 62* (09.), 781-791

Bonacci, O. and Andrić, I. 2008 Sinking karst rivers hydrology – case of the Lika and Gacka (Croatia), Acta *Carsologica*, 37 (2-3), 185-196

Bonacci, O., Trninić, D. and Roje-Bonacci, T. 2008 Analysis of the relationship between air and water temperature on several major rivers in the continental part of Croatia [in Croatian]. *Hrvatske Vode*, 16 (2008), 62; 7-19-x

Croatian Bureau of Statistics, 2026 https://podaci.dzs.hr/?utm_source (accessed 30 May 2026)

Government of the Republic of Croatia (2019). Regulation on Water Quality Standards. Official Gazette of the Republic of Croatia (Narodne novine), No. 96/2019, 1879.

Hrvatske vode, 2014 Flood protection implementation plan for the protected area, sector D, middle and lower Sava, protected area 3: Orljava-Londža small basin area. https://www.voda.hr/sites/default/files/dokumenti/novosti/2022-07/bp_3_-_provedbeni_plan_obrane_od_poplava.pdf/, (accessed 15 April 2026)

Jambrušić, S. 2016 Determination of nitrogen compounds in wastewater treatment plants, final thesis, Međimurje Polytechnis in Čakovec. https://zir.nsk.hr/object/mev:500/ (accessed 30 April 2026)

Riko, 2020 Environmental protection study of the assessment procedure on need for an environmental impact assessment for project changes: upgrading the water supply, drainage and wastewater treatment system of the Požega agglomeration. https://mingo.gov.hr/UserDocsImages/UPRAVA-ZA-PROCJENU-UTJECAJA-NA-OKOLIS-ODRZIVO-GOSPODARENJE-OTPADOM/Opuo/OPUO_2024/13_03_2024_Elaborat_aglomeracija_Zagreb.pdf/ (accessed 15 May 2026)

Shelton, M.L. 1998 Seasonal hydroclimate change in the Sacramento river basin California, *Physical Geography*, 19:3, 239-255

Tutić, A., Zeko-Pivač, A, Landeka Dragičević, T. and Habuda-Stanić, M. 2021 Removal and recovery of phosphorus from wastewater, *Hrvatske vode*, 29 (2021), 115, 33-41

Vugrin, K. 2019 Water quality indicators and determination methods, final thesis, Varaždin, University of Zagreb, Faculty of Geotechnical Enginerring. https://repozitorij.gfv.unizg.hr/object/gfv:399/ (accessed 30 April 2026)

You, Q., Jiang, H., Liu, Y., Liu, Z. and Guan, Z. 2019 Probability analysis and control of river Runoff – sediment characteristics based on Pair-Copula functions: the case of the Weihe river and Jinge river, *Water 2019,* 11 (3), 510

METHODOLOGY FOR WHOLESALE WATER PRICING BETWEEN PUBLIC WATER UTILITIES IN CROATIA: LEGAL FRAMEWORK AND COST ALLOCATION

Hrvoje MOSTEČAK [1*], Dražen VOUK [2], Domagoj NAKIĆ [2], Dijana OSKORUŠ [3]

[1] *Building Technical School Zagreb, Croatia*

E-mail: hrvoje.mostecak@gmail.com

[2] *University of Zagreb Faculty of Civil Engineering, Croatia*

E-mail: drazen.vouk@grad.unizg.hr

E-mail: domagoj.nakic@grad.unizg.hr

[3] *University of Zagreb Faculty of Geotechnical Engineering, Croatia*

E-mail: doskorus@gfv.hr

[*] *Corresponding author*

Abstract

Wholesale water pricing between public water utilities remains insufficiently standardized despite the increasing interconnection of regional water supply systems. In Croatia, this regulatory ambiguity has resulted in long-lasting judicial disputes concerning the allocation of production, transmission, depreciation, labour and water loss costs. This paper analyses three court proceedings conducted between public water service providers during the period 2017–2026 and examines the evolution of different methodologies used to determine wholesale water prices. A comparative analysis of expert assessments, financial data, operational records and regulatory requirements was performed with the aim of developing a transparent and technically justified pricing framework. The results demonstrate that wholesale water prices are highly sensitive to methodological assumptions, particularly regarding cost allocation and the assessment of water losses. The progressive refinement of the methodology resulted in a reduction of the relative wholesale water price index from 1.00 to 0.16, demonstrating the significant influence of cost allocation assumptions on the final pricing outcome. Based on the findings, a delivery path methodology was developed, defining the physical and functional boundary of the system as the basis for cost allocation. Only costs directly attributable to water abstraction, treatment and transmission to the delivery point are included in the wholesale price, while losses occurring within downstream distribution networks are excluded. The proposed methodology improves transparency, consistency and legal certainty in wholesale water pricing and provides a transferable framework for interconnected water supply systems facing similar cost allocation challenges.

Key words

wholesale water pricing, water utilities, cost allocation, water losses, delivery path methodology

1 Introduction

Public water supply is one of the fundamental public utility services of particular social importance, whose primary objective is to ensure a continuous and safe supply of drinking water for human consumption (Hrvatski sabor, 2019a; European Union, 2020). Since water resources do not follow administrative boundaries, wholesale water supply between different public water service providers has become common practice in many countries, including the Republic of Croatia (Croatian Parliament, 2019b; Gereš, 2012; Margeta, 2010).

The construction of water abstraction, treatment and transmission systems requires substantial capital investment and a high level of technical and operational expertise (Margeta, 2010; Tušar, 2018). Consequently, regional water supply systems serving multiple service areas are often economically justified, as they enable economies of scale, more efficient utilisation of infrastructure and increased security of supply through system interconnections (Gereš, 2012; Henze et al., 1995; Tušar, 2018).

In the Republic of Croatia, wholesale water pricing is regulated by the Water Act (Croatian Parliament, 2019) and the Water Services Act (Croatian Parliament, 2019), which stipulate that the price charged between public water service providers must not exceed the cost of water production or procurement together with reasonable transmission costs (Government of the Republic of Croatia, 2023). However, despite the existence of a regulatory framework, there is no universally accepted methodology for determining which cost components should be included in wholesale water prices (Tušar, 2018). Similar engineering and economic challenges related to cost allocation in regional water supply systems and shared transmission infrastructure have been identified in several countries worldwide (Guerrini et al., 2011; March and Saurí, 2013; Renzetti and Kushner, 2004; Whittington et al., 2022).

Particular challenges arise in the allocation of labour costs, electricity consumption, maintenance expenses, infrastructure depreciation and water losses, especially in regional systems where the same infrastructure serves multiple service areas (Margeta, 2010; Tušar, 2018). The complexity of wholesale water pricing is further increased by differences in raw water quality and treatment requirements, which significantly affect production costs (Henze et al., 1995; Margeta, 2010; Tedeschi, 1997).

One of the most controversial issues concerns the treatment of water losses. In practice, different approaches are applied when incorporating water losses into wholesale water prices, although a significant portion of these losses may occur within distribution networks that are not directly related to the infrastructure used for wholesale water delivery. This raises the question of whether wholesale water pricing should be based on total system losses or only on losses attributable to the specific delivery path between two public water service providers.

This paper analyses the development of wholesale water pricing methodologies through three long-term court proceedings conducted between public water service providers in Croatia during the period 2017–2026. All three cases involved the same water abstraction, treatment and transmission system, allowing the comparison of different methodological approaches under identical technical conditions.

The objective of the study is to analyse existing approaches to wholesale water pricing and to develop a methodology based on the concept of a delivery path, defined as the infrastructure system used for water abstraction, treatment and transmission to the delivery point. Particular attention is given to cost allocation and the treatment of water losses, with the aim of distinguishing losses associated with the delivery path from those occurring within downstream distribution networks. The proposed methodology was evaluated through three long-term court proceedings and compared with alternative approaches used in regulatory and professional practice.

2 Methods

Due to the absence of a universally accepted methodology for determining wholesale water prices between public water service providers, this paper focuses on the analysis of approaches used in regulatory, professional and judicial practice, as well as on the development of a methodology that enables transparent and technically justified cost allocation.

The methodological approach applied in this study is based on the analysis of actual court proceedings in which issues related to water production costs, transmission costs, infrastructure depreciation, maintenance expenses, labour costs and water losses were examined over an extended period. Particular attention was given to identifying costs that can be directly associated with wholesale water supply and to developing the concept of the delivery path as the fundamental unit for cost allocation.

The following sections describe the subject of the research, data sources, analytical procedure and the main principles of the methodology developed on the basis of the study results.

2.1 Research Subject

The research presented in this paper is based on the analysis of three court proceedings conducted between public water service providers in Croatia during the period 2017–2026. The subject of all proceedings was the determination of wholesale water prices between public water service providers supplied from a common water production and transmission system.

To protect the confidentiality of data and business relationships between the parties involved, the analysed cases were anonymised and designated as Case A, Case B and Case C. Although the proceedings involved different water distributors, all of them relied on the same water abstraction, treatment and transmission system. This circumstance enabled the comparison of different methodological approaches without the influence of variations in production technology, raw water quality or transmission infrastructure characteristics.

A specific feature of the analysed cases is that all wholesale water customers were connected to the same production and transmission system and utilised the same infrastructure for water abstraction, treatment and transmission. Consequently, differences in the calculated wholesale water prices did not arise from different technical conditions but primarily from differences in cost allocation methodologies and the treatment of individual cost categories.

2.2 Data Sources

The analysed documentation included court expert assessments and their supplements, submissions of the parties, hearing records, financial and technical documentation of the water service providers, regulatory methodologies, legal regulations, and relevant professional and scientific literature.

2.3 Method of Analysis

The research was conducted using a comparative analysis of different approaches to wholesale water pricing. For each methodology, the scope of infrastructure included in the calculation, the cost allocation approach, the criteria for including individual cost categories, the assessment of water losses and the method of determining the unit water price were analysed.

The analysis was carried out to identify methodological differences affecting the final price and to determine the cost categories with the greatest impact on the calculation results. Particular attention was devoted to the consistency of the analysed approaches with the legal principle that wholesale water prices should reflect the cost of water production and the reasonable cost of its transmission.

The proposed methodology was not developed as a predefined model but was gradually shaped through a multi-year process involving the analysis of court cases, expert comments, regulatory opinions and supplementary expert assessments.

2.4 Delivery Path Concept

Based on the conducted analysis, a methodology founded on the delivery path concept was developed. The delivery path is defined as a functionally connected infrastructure unit comprising water abstraction, water treatment, transmission through trunk pipelines, associated facilities and equipment, and the delivery point to another public water service provider.

The fundamental principle of the methodology is that only costs directly associated with water production and transmission within the boundaries of the defined delivery path may be included in the wholesale water price. Costs related to the distribution of water to end users are excluded from the

wholesale water price calculation.

2.5 Cost Allocation

The analysis included labour costs, energy costs, water treatment costs, maintenance costs, depreciation, regulatory charges and water losses.

For each cost category, its relationship to the analysed delivery path was assessed. Where the same infrastructure or organisational unit served multiple functions within the system, appropriate allocation keys were applied to determine the portion of costs attributable to wholesale water supply.

2.6 Treatment of Water Losses

Different approaches to incorporating water losses into wholesale water pricing were analysed, including directly measured losses, empirically estimated unavoidable losses and total system losses.

The methodology assumes that only losses associated with the analysed delivery path may be included in the calculation. Priority is given to directly measured losses, while internationally accepted empirical methods may be used when measurements are unavailable. Total losses of the entire water supply system cannot be automatically attributed to the delivery path because they also include losses occurring within distribution networks and other parts of the system unrelated to wholesale water supply.

2.7 Presentation of Results

The analysed court proceedings covered the period during which Croatia transitioned from the Croatian kuna to the euro as its official currency and involved data originating from confidential contractual relationships between public water service providers.

To protect commercially sensitive information, actual unit water prices are not presented. Instead, a relative wholesale water price index was used, enabling comparison of different methodological approaches without disclosing actual contractual values. The reference value of the index was defined by assigning a value of **1.00** to the initial contractual wholesale water price, while all subsequent estimates are presented relative to that value.

3 Results and Discussion

3.1 Evolution of Wholesale Water Pricing Methodologies During the Study Period

The initial expert assessment was based primarily on publicly available financial and technical data. As the court proceedings progressed, additional financial, organisational and operational information became available, enabling a more detailed identification of water production and transmission costs.
The evolution of the applied methodologies is presented in Table 1.

In the Organizational-Cost Approach (2020), water losses were represented by total system losses without distinguishing between delivery path and distribution network losses.
The results demonstrate a gradual transition from general estimates based on publicly available information towards a methodology founded on detailed operational data and clearly defined infrastructure boundaries. The level of analytical detail increased throughout the proceedings, while the uncertainty associated with cost allocation gradually decreased.

Table 1. Development of the methodological approach for wholesale water pricing

Methodology Element	Initial Assessment (2017)	Financial-Analytical Approach (2018)	Organizational-Cost Approach (2020)	Delivery Path Methodology (2023)
Data Source	Submitted documentation	FINA* Data + technical documentation	Organizational and financial data	Complete technical and financial data
Labour Costs	Estimated	Estimated from reports	Organizational units	Actual employees
Electricity Costs	Estimated	Actual data	Actual data	Actual data
Water Treatment Costs	Estimated	Actual data	Actual data	Actual data
Depreciation	Entire infrastructure	Entire infrastructure	Entire infrastructure	Delivery-path analysis
Water Losses	Not analysed	Not recognised without evidence	System losses	Unavoidable annual real losses (UARL)
Delivery Path Defined	No	Partially	Partially	Yes

* Financial Agency (FINA), Croatia

To illustrate the impact of methodological development on the estimated wholesale water price, the results are presented using a relative index, where the initial contractual price is assigned a value of 1.00.

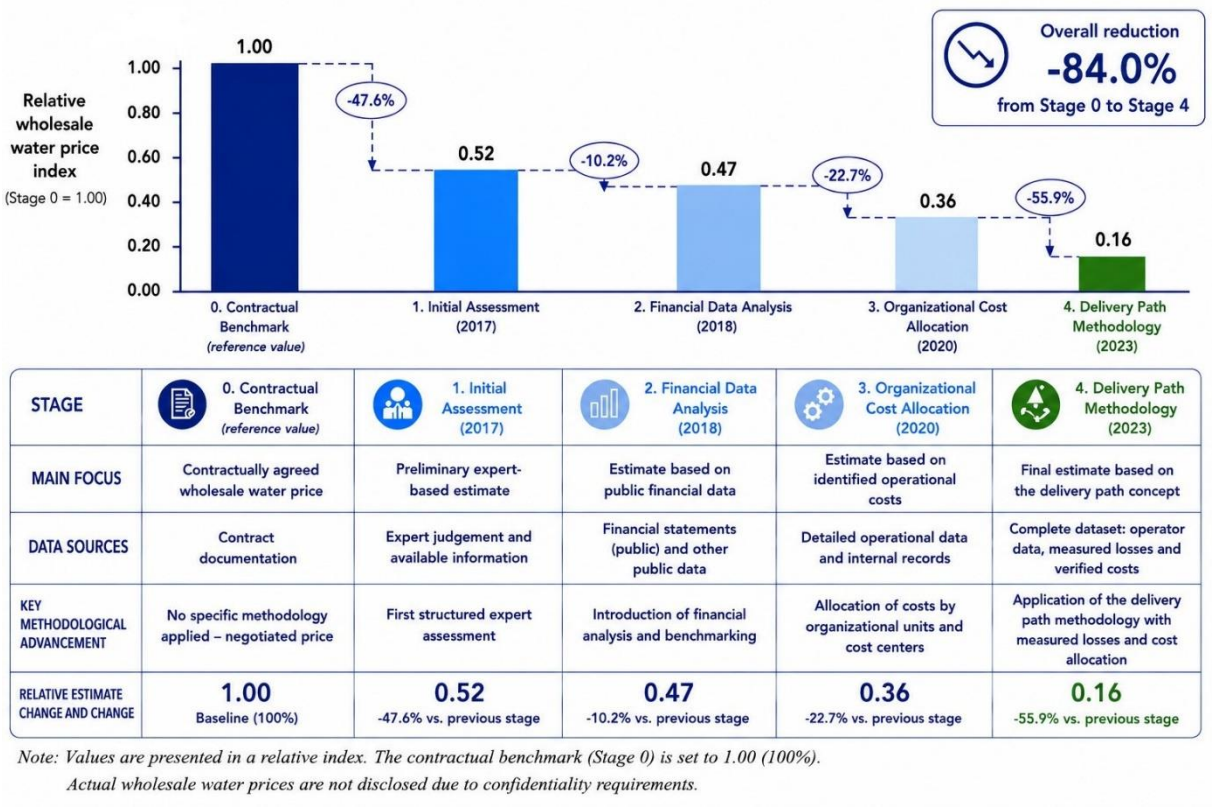


Figure 1. Evolution of wholesale water pricing methodologies during the study period

Figure 1 presents the evolution of wholesale water price estimates during the development of the delivery path methodology.

An important observation from Figure 1 is that each methodological refinement reduced the relative wholesale water price. This demonstrates that the largest source of uncertainty was not the production technology itself but the methodology used for allocating shared costs. The greatest improvements resulted from progressively defining infrastructure boundaries, identifying actual operational costs and introducing scientifically justified treatment of water losses.

The continuous decrease in the relative price index reflects progressively improved cost allocation resulting from more detailed operational and financial information.

The final delivery path methodology produced the lowest relative index value, indicating that part of the costs included in earlier assessments could not be directly attributed to the production and transmission of water supplied to another public water service provider.

Earlier methodological approaches remained in use primarily because detailed operational data, measured water losses and infrastructure-specific cost records were unavailable during the initial stages of the court proceedings. As additional technical and financial information became available, the methodology was progressively refined, resulting in more accurate cost allocation and a gradual reduction in the relative wholesale water price index.

3.2 Comparison of Analysed Methodological Approaches

The analysed methodologies differed primarily in terms of infrastructure boundaries, cost allocation principles and the assessment of water losses.

Early approaches generally considered the water supply system as a single operational entity and allocated costs using aggregated indicators. Later methodologies focused on identifying infrastructure elements and operational activities directly related to wholesale water supply.

The final methodology is based on the principle that only costs directly associated with water production and transmission within the defined delivery path may be included in the wholesale water price.
The general structure of wholesale water price determination is presented by Equation (1).

$$WWP = \frac{\Sigma_{i=1}^{n} D_{PC,i}}{Q} \tag{1}$$

where: WWP – wholesale water price [€/m^3], $D_{PC,i}$ – delivery path costs [€], Q – delivered water quantity [m^3].

The delivery path cost (D_{PC}) comprises the cost components specified in Equation (2):

$$D_{PC} = LC + EC + TC + OMC + ADC + RC + WLC + IC \tag{2}$$

where: LC – labour costs [€], EC – energy costs [€], TC – treatment costs [€], OMC – operation and maintenance costs [€], ADC – asset depreciation costs [€], RC – regulatory costs [€], WLC – water loss costs [€], IC – indirect costs [€].

The greatest methodological challenges were associated with labour costs, infrastructure depreciation and water losses, which required the largest number of supplementary analyses and expert opinions during the proceedings.

3.3 Influence of Individual Cost Categories on Wholesale Water Pricing

3.3.1 Labour Costs

Labour costs represented one of the most disputed cost categories in the analysed proceedings.

Initial calculations were based on financial statements and various allocation keys, making it impossible to determine precisely how many employees were directly involved in water production and transmission for wholesale supply.

Subsequently obtained information regarding employees assigned to the water abstraction and treatment facilities enabled a more accurate allocation of labour costs and significantly reduced uncertainty in the

calculation.

3.3.2 Infrastructure Depreciation

Infrastructure depreciation represented another major methodological issue.

The analysed transmission infrastructure was constructed several decades ago, primarily using public funding mechanisms available at the time. Consequently, a key question was whether wholesale water pricing should include depreciation of the entire infrastructure or only depreciation associated with more recent investments that had not yet been fully depreciated.

The results indicate that different approaches to depreciation accounting may substantially affect the final wholesale water price.

3.3.3 Maintenance Costs

Maintenance costs are essential for ensuring the safe and reliable operation of water supply systems. However, the proceedings demonstrated that not all maintenance activities can be directly associated with infrastructure used for wholesale water delivery.

For this reason, the proposed methodology includes only maintenance costs functionally related to the analysed delivery path.

3.4 Assessment of Water Losses

3.4.1 System Losses and Delivery Path Losses

The largest methodological differences among the analysed approaches were identified in the treatment of water losses. Total system losses can be expressed as following in Equation (3):

$$\mathrm{TSL} = \mathrm{DPL} + \mathrm{DNL} \tag{3}$$

where: TSL – Total System Losses, DPL – Delivery Path Losses, DNL – Distribution Network Losses.

In practice, it is often assumed that wholesale water customers should contribute to covering total system losses. However, such an approach neglects the fact that a significant proportion of losses occurs within secondary distribution networks, service connections, water meters and other system components that are not associated with wholesale water supply. The key question therefore arises: can wholesale water customers be charged for losses occurring on infrastructure they do not use? The results of the analysis indicate that such an approach is not fully consistent with the principle of cost causality.

3.4.2 The Challenge of Demonstrating Water Losses

During the court proceedings, it was repeatedly emphasised that actual losses along the analysed delivery path had not been directly measured. Since no appropriate measurement points existed on the relevant infrastructure, direct determination of actual losses was not possible. Under such circumstances, three possible approaches may be considered:

- use of total system losses;
- use of arbitrarily defined percentages;
- application of scientifically accepted empirical models.

Within this study, the position was adopted that water losses may be included in wholesale water pricing only if they are directly measured or estimated using scientifically accepted methods.

3.4.3 Unavoidable Water Losses

Where measured data on real losses were unavailable, the concept of Unavoidable Annual Real Losses (UARL), developed by the International Water Association (IWA), was applied (Alegre et al., 2016; Lambert et al., 1999).

$$UARL = \left(18L_m + 0{,}8N_c + 25L_p\right) \cdot P \tag{4}$$

where: L_m – length of transmission mains [km], N_c – number of service connections [-], L_p – length of service connection pipes [km], P – average system pressure [m].

The application of the UARL methodology enables the estimation of minimum physically unavoidable losses that may be expected even in well-maintained systems (Lambert et al., 1999). Compared with the use of total system losses or arbitrary percentages, this approach provides a more objective basis for water loss assessment (Frauendorfer and Liemberger, 2010; Marasović, 2020).

3.4.4 Impact of Water Losses on Wholesale Water Pricing

The analysis demonstrated that the assessment of water losses represents one of the most influential factors in determining the final wholesale water price.

The differences between methodologies based on total system losses and those recognising only losses attributable to the delivery path may be substantial. Consequently, water losses represent one of the key cost categories affecting the final pricing outcome.

The results further indicate that inappropriate allocation of water losses may lead to significant distortions in wholesale water pricing. This is particularly relevant in interconnected water supply systems, where a considerable proportion of losses may occur within downstream distribution networks that are not directly related to wholesale water delivery. Therefore, the accurate identification and allocation of water losses is essential for ensuring a technically justified and transparent pricing methodology.

Table 2. Comparison of water loss assessment approaches

Approach	Basis of Assessment	Advantages	Limitations
Losses Not Included	Losses not demonstrated	Conservative approach	Possible underestimation of costs
System Losses	Total system NRW	Simple application	Does not distinguish the location of losses
Fixed Percentage	Expert judgement	Simplicity	Lacks scientific justification
UARL Approach	IWA methodology	Technically justified	Requires input data
Measured Losses	Field measurements	Highest accuracy	High monitoring and measurement costs

3.5 Final Wholesale Water Pricing Methodology

The analysis of different methodological approaches applied during the court proceedings demonstrated that the greatest source of uncertainty in wholesale water pricing arises from the unclear definition of the infrastructure boundaries to which individual costs relate. In the early stages of the proceedings, costs were generally assessed at the level of the entire water supply system, making it impossible to determine which portion of individual cost categories resulted from the production and transmission of water quantities supplied to another public water service provider.

Based on the findings, a methodology founded on the delivery path concept was developed. The delivery path represents a functionally connected infrastructure unit comprising water abstraction, water treatment, transmission through trunk pipelines and the delivery point to another public water service provider.

The proposed methodology consists of five consecutive steps:

1. Identification of infrastructure elements forming the delivery path;
2. Identification of costs associated with water production and transmission;
3. Allocation of shared costs using appropriate allocation keys;
4. Determination of water losses attributable to the delivery path;
5. Calculation of the unit wholesale water price.

In the first step, all facilities, structures and equipment involved in water production and transmission to the delivery point are identified. This establishes the system boundary that serves as the basis for subsequent cost allocation. In the second step, all costs incurred within the boundaries of the defined delivery path are identified. These may include labour costs, electricity costs, water treatment costs, infrastructure maintenance, depreciation, regulatory charges and other costs directly attributable to the analysed infrastructure.

Due to confidentiality requirements arising from the analysed court proceedings, the relative contribution of individual cost categories cannot be disclosed. Nevertheless, the proposed methodology provides a transparent framework for identifying and allocating these costs within the defined delivery path.

The third step addresses the allocation of shared costs where facilities, equipment or organisational units perform multiple functions within the water supply system. Appropriate allocation keys are applied to determine the proportion of costs attributable to wholesale water supply.

The fourth step involves determining water losses associated with the analysed delivery path. Priority is given to directly measured losses, while internationally accepted empirical methods may be used where measurements are unavailable. Total system losses are not automatically included because a significant proportion of such losses occurs within distribution networks outside the analysed delivery path. In the final step, the unit wholesale water price is calculated by dividing the total delivery path costs by the volume of water supplied to another public water service provider.

The fundamental principle of the methodology is that only costs directly associated with water production and transmission to the delivery point are included in the wholesale water price. This ensures consistent application of the cost causality principle and reduces the likelihood of including costs arising from water distribution activities serving end users.

Figure 2 summarizes the proposed delivery path methodology. The methodology establishes a direct relationship between the physical infrastructure used for wholesale water delivery and the costs included in the wholesale water price calculation. By defining clear system boundaries, the approach enables consistent cost allocation and reduces the risk of including costs unrelated to wholesale water supply.

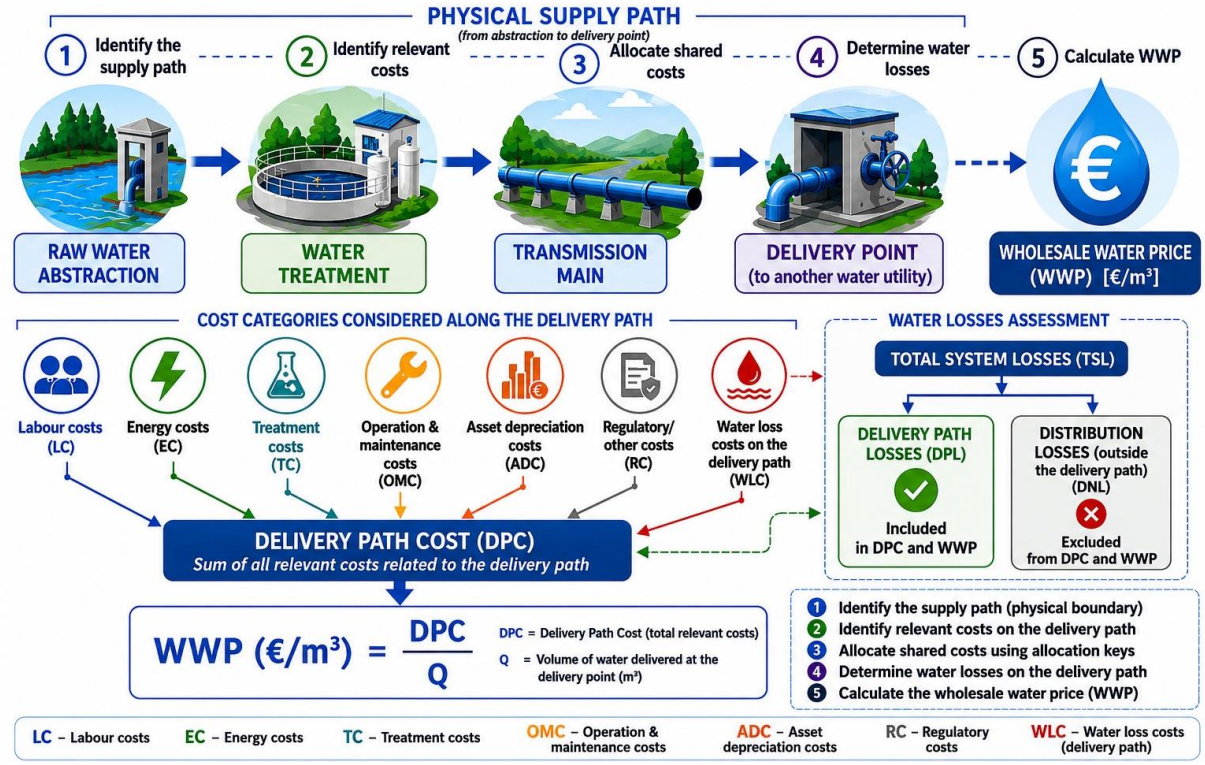


Figure 2. Conceptual framework of the delivery path methodology

3.6 Applicability of the Methodology

The originality of this research lies in developing a wholesale water pricing methodology derived from long-term judicial practice rather than from theoretical assumptions alone. Unlike previous studies, the proposed methodology evolved through successive expert assessments conducted under identical technical conditions, enabling the systematic identification of methodological shortcomings and the progressive refinement of cost allocation principles.

Although the methodology was developed within the Croatian regulatory framework and through specific court proceedings, its fundamental principles are not limited to the national context. The delivery path concept, the identification of infrastructure-related costs and the application of empirical methods for estimating unavoidable water losses can also be applied in countries where no detailed methodology for wholesale water pricing exists.

Similar engineering and economic challenges have also been reported in regional water supply systems in Europe and elsewhere (Guerrini et al., 2011; March and Saurí, 2013), as well as in cross-border and interregional systems worldwide (Renzetti and Kushner, 2004; Whittington et al., 2022).

A particular strength of the methodology lies in its applicability to regional water supply systems where multiple public water service providers share common infrastructure for water abstraction, treatment and transmission. The use of relative indices enables quantification of the influence of methodological assumptions on wholesale water pricing and demonstrates that the largest differences arise from the treatment of depreciation, shared costs and water losses. European studies similarly indicate that non-transparent treatment of capital costs and operational losses represents a major source of inefficiency and disputes within integrated water supply systems (Guerrini et al., 2011).

The results confirm that the delivery path methodology enables more transparent cost allocation, reduces the potential for disputes among system participants and supports a more consistent application of the cost causality principle (Renzetti and Kushner, 2004; Whittington et al., 2022).

Although the proposed methodology has not yet been incorporated into official Croatian regulations, it

could provide a practical framework for future national guidance on wholesale water pricing. Implementation could follow five consecutive stages: (i) definition of the delivery path, (ii) infrastructure inventory, (iii) cost allocation, (iv) assessment of delivery-path water losses, and (v) calculation and regulatory verification of the wholesale water price. Such an approach would improve transparency, reduce methodological inconsistencies and facilitate more consistent pricing practices among interconnected public water service providers.

Several limitations should be acknowledged. First, the methodology was developed on the basis of three long-term court proceedings related to a single production and transmission system. Second, the confidentiality of contractual data prevented the presentation of actual cost structures and unit prices. Third, direct measurements of delivery-path water losses were unavailable, requiring the application of internationally accepted empirical methods. Nevertheless, these limitations do not affect the conceptual validity of the proposed methodology, which is based on general engineering, economic and regulatory principles and can be adapted to other interconnected water supply systems.

4 Conclusion

This paper analysed the development of wholesale water pricing methodologies through three long-term court proceedings conducted between public water service providers in Croatia.

The results demonstrated that wholesale water prices are highly sensitive to cost allocation methodology. The largest differences between individual approaches were associated with labour costs, infrastructure depreciation and water losses. The analysis showed that the use of aggregated system-wide indicators may lead to the inclusion of costs that cannot be directly linked to the production and transmission of water supplied to another utility.

Based on the findings, a delivery path methodology was developed. The proposed approach defines the delivery path as a functional infrastructure unit consisting of water abstraction, treatment, transmission infrastructure and the delivery point to another utility. Only costs directly attributable to this infrastructure are included in the wholesale water price calculation.

Particular attention was given to water losses. The results indicate that system-wide losses should not automatically be allocated to wholesale water customers. Instead, losses should be determined through direct measurements or, where measurements are unavailable, through scientifically accepted empirical methods such as the IWA UARL approach.

The study also highlights the need for direct measurement of delivery-path water losses, as reliable separation of delivery-path and distribution network losses cannot be achieved using aggregated system data alone.

The progressive refinement of the methodology resulted in a substantial reduction of the relative wholesale water price index compared with the initial contractual benchmark, demonstrating the importance of transparent cost allocation and clearly defined infrastructural boundaries. The proposed methodology provides a technically justified and economically transparent basis for determining wholesale water prices and may also be applicable to other regional and interconnected water supply systems sharing common production and transmission infrastructure.

References

Alegre, H., Baptista, J.M., Cabrera Jr, E., Cubillo, F., Duarte, P., Hirner, W., Merkel, W. and Parena, R. 2016 *Performance Indicators for Water Supply Services*. IWA Publishing, London

Croatian Parliament: Water Services Act (Official Gazette of the Republic of Croatia, No. 66/19). https://narodne-novine.nn.hr/clanci/sluzbeni/2019_07_66_1327.html (accessed 11 June 2026)

European Union, Directive (EU) 2020/2184 of the European Parliament and of the Council of 16 December 2020 on the quality of water intended for human consumption. https://eur-lex.europa.eu/eli/dir/2020/2184 (accessed 11 June 2026)
Frauendorfer, R. and Liemberger, R. 2010 *The Issues and Challenges of Reducing Non-Revenue Water*. Asian Development Bank, Mandaluyong City, Philippines
Government of the Republic of Croatia: Methodology for Determining Water Services Charges (Official Gazette of the Republic of Croatia, No. 70/2023. https://narodne-novine.nn.hr/clanci/sluzbeni/2023_07_80_1268.html (accessed 21 June 2026)
Government of the Republic of Croatia: Water Management Strategy (Official Gazette of the Republic of Croatia, No. 91/08). https://narodne-novine.nn.hr/clanci/sluzbeni/2008_08_91_2825.html (accessed 11 June 2026)
Gereš, D. 2012 Razvoj regionalnih vodoopskrbnih sustava u Republici Hrvatskoj. *Hrvatska vodoprivreda*, XXI (201), 45–52.
Guerrini, A., Romano, G. and Campedelli, B. 2011 Factors affecting the operational efficiency of Italian water utility companies. *Water Resources Management*, 25 (10), 2483–2496.
Lambert, A., Brown, T.G., Takizawa, M. and Weimer, D. 1999 A review of performance indicators for real losses from water supply systems. *Water Science and Technology: Water Supply*, 49 (10), 227–237
Marasović, M. 2020 Primjena IWA metodologije za analizu vodnih gubitaka u vodoopskrbnim sustavima. In the Proceedings *Zbornik radova sa stručno-poslovnog skupa "Aktualna problematika u vodoopskrbi i odvodnji"*. Poreč, 21–25 listopada
March, H. and Saurí, D. 2013 The regionalization of water supply in the Metropolitan Area of Barcelona: Models, governance and conflicts. *Geoforum*, 47, 132–141.
Margeta, J. 2010 *Inženjerstvo vodoopskrbnih sustava*. Građevinsko-arhitektonski fakultet Sveučilišta u Splitu, Split.
Renzetti, S. and Kushner, J. 2004 Full cost accounting for water supply and sewage utilities: A case study. *Canadian Water Resources Journal*, 29 (1), 13–24.
Tedeschi, S. 1997 *Zaštita voda*. Građevinski fakultet Sveučilišta u Zagrebu, Zagreb
Tušar, B. 2018 *Ekonomika vodnih usluga i održivo upravljanje vodoopskrbnim sustavima*. Građevinski fakultet Sveučilišta u Zagrebu, Zagreb.
Whittington, D., Wu, X. and Shively, G. 2022 Wholesale water pricing and cost recovery in regional infrastructure systems. *Water Policy*, 24 (3), 415–432

CALIBRATION OF ANALYTICAL MODELS FOR WAVE PREDICTION

Damjan BUJAK [1*], Izabela JEDRIŠ [1], Lovro ŠTEFAN [1], Hanna MILIČEVIĆ [1],

[1] *Faculty of Civil Engineering, University of Zagreb, Croatia*

E-mail: damjan.bujak@grad.unizg.hr

E-mail: izabela.jedris@student.grad.hr

E-mail: lovro.stefan@grad.unizg.hr

E-mail: hanna.milicevic@grad.unizg.hr

[*] *Corresponding author*

Abstract

This paper analyzes the possibility of applying empirical formulas for wave estimation in the area of the Rijeka Bay, with a focus on verifying the reliability of using the revised SPM (1984) model, which provides significant wave heights and wave periods. The research was carried out on the basis of data obtained from measurements by the DATAWELL Waverider DWR MKIII wave buoy, located near the Port of Rijeka, and ERA5 reanalysis records for the period 2009-2011. After quality control and synchronization of the data, the input parameters were defined for use in the revised SPM (1984) model. Input variables comprise wind speed, storm duration, fetch lengths, and the values of the correction factors RL and RT. The obtained results showed that the basic model systematically underestimates the measured values, with the largest deviations observed in cases of higher waves and shorter fetch. The best agreement between the measured and calculated values was obtained by applying the factor RT = 1.1, while further improvement of the results can be achieved by a simple calibration correction. The conducted analysis showed that the revised SPM (1984) model, with certain corrections, provides satisfactory estimates of wave characteristics in the investigated area. However, due to its simplified approach and certain limitations, the application of such a model is recommended for basic analyses and simpler tasks.

Key words

wave prediction, significant wave height, calibration, SPM (1984), fetch

1 Introduction

Wave prediction represents an important component of coastal engineering applications and is widely used in the design of maritime structures, coastal management, navigation safety assessment, and sediment transport studies. Wave conditions strongly influence coastal processes and directly affect the stability and performance of coastal structures. In addition to generating loads on coastal infrastructure, waves play an important role in sediment transport and shoreline evolution (Kuspilić et al., 2017; WMO, 2018).

In Croatia, long-term and systematic wave measurements are relatively limited, while continuous monitoring networks have only recently begun to develop through projects such as METMONIC. Existing measurements are generally available only at limited locations and for relatively short observation periods, which often prevents reliable determination of long-term and extreme wave climate characteristics (Kuspilić et al., 2017). Consequently, indirect approaches based on wind observations are frequently applied in engineering practice for wave estimation.

The prediction of wave characteristics is a complex process because wave development and transformation depend on numerous factors. During propagation from deeper toward shallower water,

waves undergo several transformation processes including shoaling, refraction, diffraction, reflection, and wave seabed interactions (Dorrestein, 1960). Furthermore, in fetch limited environments wave development can be constrained by local basin geometry and available fetch length, resulting in wave characteristics that are controlled not only by wind forcing but also by local conditions.

Various methods are available for wave prediction, ranging from complex spectral numerical models to simplified empirical formulations. While numerical models can provide detailed results, empirical approaches remain attractive for preliminary engineering applications due to their simplicity and computational efficiency (Booij et al., 1999; Lefevre and Aouf, 2012). Among the available approaches, the revised Shore Protection Manual (SPM, 1984) model is one of the most commonly applied empirical methods for wave estimation under fetch limited conditions. The model estimates significant wave heights and wave periods based on wind speed, storm duration, and effective fetch length. Due to its relatively simple formulation and low computational requirements, the method is widely used for preliminary engineering analyses and practical applications. However, previous studies have shown that empirical approaches frequently require local calibration because model performance strongly depends on regional meteorological conditions and local basin characteristics (Hurdle and Stive, 1989; Bujak et al., 2025).

The primary objective of this study is to evaluate the applicability of the revised SPM (1984) method under fetch-limited conditions in Rijeka Bay. The secondary objective is to quantify the sensitivity of H_{m0} and T_p predictions to the R_t and R_l correction coefficients through three predefined configurations. Finally, an exploratory site-specific multiplicative correction is derived for the best-performing configuration. This final step is explicitly treated as an in-sample calibration rather than an independently validated predictive model.

2 Methods

2.1 Study area

The study was conducted in Rijeka Bay, located in the northern Adriatic Sea. Wave data were obtained from a measurement buoy deployed near the Port of Rijeka, while wind observations were collected from two nearby meteorological stations (Table 1). Geographically, Rijeka Bay forms part of Kvarner Bay, a semi-enclosed basin bounded by the Istrian coast to the west and the Vinodol–Velebit coast to the east. A series of islands (Cres–Lošinj, Krk–Rab–Pag) divide the basin into several smaller segments (Figure 1).

Due to the complex geographical configuration of the area, wave growth is strongly influenced by fetch-limited conditions. Therefore, the maximum wave height generated by a given wind event is limited by the distance over which the wind blows across the sea surface (fetch). However, this distance varies considerably depending on wind direction because of the surrounding topography. Measurements are performed in relatively deep-water conditions where the influence of depth-induced wave breaking is minimal (Lončar et al., 2019).

The study area is influenced by several dominant wind regimes. Bura (northeast wind) can reach considerable intensities, however, because it blows from land toward the open sea, it generates relatively short fetch conditions in the Rijeka area and consequently produces short, steep, and relatively small waves. In contrast, Jugo (southeast wind) and Lebić (southwest wind) propagate over significantly longer fetch distances and therefore generate larger wave conditions within Rijeka Bay. Changes in wind direction may significantly influence wave growth. For example, transitions from Jugo toward Lebić conditions may produce noticeable increases in wave heights near the Rijeka breakwater because southeast and southwest wind directions correspond to the longest available fetch lengths in the study area (Lončar et al., 2019). Therefore, wind direction and fetch characteristics represent important parameters for wave prediction analyses.

Table 1. Geographical location and main characteristics of the two land-based wind measurement stations used for retrospective estimation of significant wave heights at the wave buoy in Rijeka Bay

No.	Name	Symbol	Latitude	Longitude	Elevation (m)	Distance from buoy (km)
1	Rijeka	Ri	45.34° N	14.44° E	120	4
2	Malinska	Ma	45.12° N	14.52° E	10	25

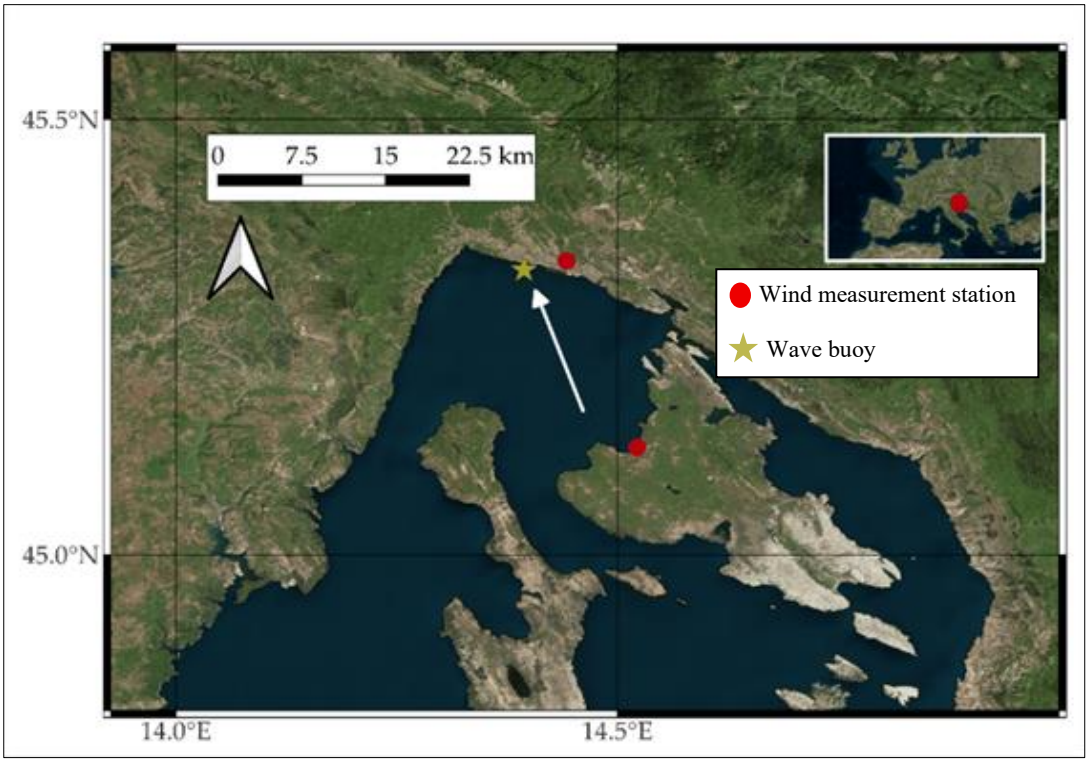


Figure 1. Study area in the northern Adriatic Sea; the yellow star indicates the wave buoy near Rijeka, the red circles indicate the two land-based wind measurement stations (Rijeka – northern station and Malinska – southern station), while the white arrow represents the main south-to-north fetch corridor controlling the development of local storm waves

2.2 Data acquisition and processing

Wave measurements used in this study were obtained from a DATAWELL Waverider DWR MKIII buoy deployed in cooperation with the Croatian Hydrographic Institute at coordinates 45.33° N and 14.39° E. The buoy continuously records significant wave height, wave direction, and peak wave period. The system also includes GPS tracking, allowing continuous monitoring of buoy position (Bujak et al., 2025). The 22 selected storm events were separated by at least a 12-hour below-threshold period.

The wave dataset used in this study covers a study period from June 2009 to June 2011. Wave measurements and wind observations were recorded at hourly intervals, although occasional interruptions in data availability occurred. During the quality control procedure, periods containing missing values or obvious measurement errors were removed, and only reliable simultaneous wind and wave observations were retained for further analyses (Bujak et al., 2025).

Additional wind data were obtained from the ERA5 reanalysis dataset, *ERA5 hourly data on single levels from 1940 to present*, developed by the European Centre for Medium-Range Weather Forecasts (ECMWF) (ERA5, 2018). The ERA5 dataset combines observations from multiple sources with numerical atmospheric models to provide spatially and temporally consistent estimates of

meteorological conditions. From the ERA5 data, the 10-m zonal and meridional wind components were extracted from the nearest atmospheric grid point to the buoy (45.25° N, 14.50° E), without spatial downscaling, and converted to wind speed and meteorological direction. Such data are particularly useful for areas such as Rijeka Bay, where they enable analysis of dominant wind directions, frequency of occurrence, and wind intensity.

The parameters used in the analysis are summarized in Table 2. Significant wave heights ($H_{m0,\ target}$), peak wave periods ($T_{p,target}$), wave directions, and sea temperatures were obtained from buoy measurements. Air temperature and storm duration were collected from the Rijeka and Malinska meteorological stations, while wind speed and wind direction used as model input parameters were extracted from ERA5 data. Effective fetch lengths were determined according to wind direction and surrounding coastal geometry. If air temperature data was missing, these cases were not considered in the analysis and were simply removed.

2.3 Empirical wave prediction methodology

As discussed previously, simplified wave prediction approaches are frequently used for estimating wave conditions, particularly in areas where direct wave measurements are unavailable. One such approach is presented in the *Shore Protection Manual (SPM, 1984)*, which describes wind-generated waves produced by a uniform wind acting over a known fetch length. The manual provides separate empirical formulations for wave prediction under different conditions, including developing waves in deep water, fully developed waves in deep water, and wave growth in shallow water.

However, difficulties arise at transition regions between different wave growth regimes, particularly during transitions from deep-water to shallow-water conditions. The objective is therefore to establish a unified set of equations applicable over all conditions in order to minimize inconsistencies that may lead to difficulties in engineering applications. Such an approach was proposed by Hurdle and Stive in Revision of SPM 1984 Wave Hindcast Model to Avoid Inconsistencies in Engineering Applications.

The primary limitations of the original SPM formulations arise from the use of separate equations for fetch-limited and fully developed sea states, as well as inconsistencies between shallow-water and deep-water formulations at large fetch lengths. In this paper, the fetch was calculated using the canonical effective fetch method established by the *Shore Protection Manual (SPM, 1984).*

The SPM (1984) methodology provides equations for fetch-limited wave growth under deep-water conditions:

$$\tilde{H}_s = 0.016\tilde{F}^{1/2} \tag{1}$$

$$\tilde{T}_m = 0.286\tilde{F}^{1/3} \tag{2}$$

$$\tilde{t}_{lim} = 68.8\tilde{F}^{2/3} \tag{3}$$

where H_s is the significant wave height, T_m represents the peak spectral energy period, F denotes fetch length (m) and t_{lim} is the limiting storm duration (s).

If storm duration is shorter than t_{lim}, the values of H_s and T_m are determined using a modified fetch length:

$$\tilde{F}' = \left(\frac{\tilde{t}}{68.8}\right)^{3/2} \tag{4}$$

When both t and t_{lim} exceed t_{full}, fully developed sea conditions are assumed. In this case, t_{full} = 71500 while significant wave height and wave period are obtained from:

$$\tilde{H}_s = 0.243 \tag{5}$$

$$\tilde{T}_m = 8.143 \tag{6}$$

For fetch-limited conditions in shallow water, the following equations apply:

$$\tilde{H}_s = 0.283 \tanh\left(0.53\tilde{d}^{3/4}\right) \tanh\left\{\frac{0.0056\tilde{F}^{1/2}}{\tanh\left(0.53\tilde{d}^{3/4}\right)}\right\} \tag{7}$$

$$\tilde{T}_m = 7.54 \tanh\left(0.833\tilde{d}^{3/8}\right) \tanh\left\{\frac{0.0379\tilde{F}^{1/3}}{\tanh\left(0.833\tilde{d}^{3/8}\right)}\right\} \tag{8}$$

where d denotes uniform water depth (m), while t_{lim} = (537*T_m)/3.

If storm duration is shorter than t_{lim}, values of H_s and T_m are determined according to Equations (7) and (8). The variation of significant wave height $H_s$with increasing fetch under shallow-water conditions was determined using Equation (7). The results indicate good agreement between the formulations for short fetch lengths. However, for intermediate fetch values, the equation produces approximately 20% lower values, while for large fetch lengths approximately 16% higher values are obtained. Similar deviations for T_m demonstrate abrupt transitions between shallow-water and deep-water formulations (Hurdle and Stive, 1989).

Following approximation and comparison between the revised and original equations for deep-water conditions under partially developed sea states, differences remained within approximately 5%, which was considered acceptable. On the other hand, larger deviations were observed under shallow-water conditions, indicating the need for revision of the original equations (Hurdle and Stive, 1989).

Consequently, revised equations were proposed:

$$\tilde{H}_{rev} = \tanh\left(0.6\tilde{d}^{0.75}\right) \tanh h^{0.5}\left[\frac{4.3 \times 10^{-5}\tilde{F}}{\tanh h^2\left(0.6\tilde{d}^{0.75}\right)}\right] \tag{9}$$

$$\tilde{T}_{rev} = \tanh\left(0.76\tilde{d}^{0.375}\right) \tanh h^{1/3}\left[\frac{4.1 \times 10^{-5}\tilde{F}}{\tanh h^3\left(0.76\tilde{d}^{0.375}\right)}\right] \tag{10}$$

For deep-water conditions with small fetch lengths:

$$\tilde{H}_{rev} \approx 0.0016\tilde{F}^{0.5} \tag{11}$$

$$\tilde{T}_{rev} \approx 0.286\tilde{F}^{1/3} \tag{12}$$

For deep-water conditions with large fetch lengths:

$$\tilde{H}_{rev} \approx 0.25 \;;\; \left(\tilde{d} \gg 1, \tilde{F} \gg 10{,}000\right) \tag{13}$$

$$\tilde{T}_{rev} \approx 8.3 \;;\; \left(\tilde{d} \gg 1, \tilde{F} \gg 10{,}000\right) \tag{14}$$

For shallow-water conditions with large fetch lengths:

$$\tilde{H}_{rev} \approx 0.25 \times 0.6d^{0.75} = 0.15d^{0.75} \tag{15}$$

$$\tilde{T}_{rev} \approx 8.3 \times 0.76d^{0.375} = 6.3d^{0.375} \tag{16}$$

All revised equations show close agreement or only minor deviations relative to the original SPM (1984) formulations.

Finally, for duration-limited conditions under all environmental states, the following expression is recommended:

$$t_{lim}(F) = \int_0^F \frac{1}{V_g(F^*)} dF^* \tag{17}$$

from which the modified fetch can be determined:

$$\widetilde{F}' = \left(\frac{\tilde{t}}{65.9}\right)^{3/2} \; ; \; \tilde{t} < \tilde{t}_{rev} \tag{18}$$

This unified set of equations enables smooth transitions between different wave growth regimes, including transitions from deep-water to shallow-water conditions and from short to long fetch lengths. Furthermore, the equations remain asymptotically consistent with the original *Shore Protection Manual (1984)* formulations within the regions where their performance is most reliable while simultaneously improving practical applicability and simplifying engineering implementation.

Wave conditions in the present study were analyzed using WaveLab 3.9 software based on the revised methodology proposed in *Revision of SPM 1984 Wave Hindcast Model to Avoid Inconsistencies in Engineering Applications*. As previously described, this represents an improved version of the original SPM (1984) methodology.

The software estimates wave characteristics, including wave height and wave period, based on wind data as input parameters.

The input parameters used in the software include:

- Elevation (z): height above mean sea level where wind speed is measured;
- Wind speed ($U_{(z)}$) : wind velocity at the specified elevation;
- Storm duration (t): storm duration in hours;
- Wind speed ratio over water and land (R_L);
- Air–sea temperature correction factor (R_T); in the absence of temperature information, R_T =1.1 is commonly used;
- Fetch length (F): distance over which the wind blows across the water surface;
- Water depth (h): water depth in meters.

Based on these parameters, the software first calculates the wind stress factor (U_A), accounting for the nonlinear relationship between wind stress and wind speed:

$$U_A = 0.71 \cdot U_{10}^{1.23} \tag{19}$$

where U_{10} is the wind speed measured at a height of 10 m above sea level.

The software then automatically determines whether wave growth is controlled by fetch length or storm duration. Under fetch-limited conditions, actual fetch values are applied, whereas under duration-limited conditions the software calculates a modified fetch according to Equation (18). In the analyzed cases, all events corresponded to fetch-limited conditions.

The final output parameters obtained from the model are significant wave height (H_{m0}) and peak wave period (T_p), calculated according to Equations (20) and (21).

Significant wave height (H_{m0}) is calculated as:

$$\frac{g \cdot H_{m0}}{U_A} = 0.25 \cdot tanh\left(0.6\left(\frac{g \cdot h}{U_A^2}\right)^{0.75}\right) \cdot tanh^{0.5}\left[\frac{4.3 \cdot 10^{-5} \cdot \frac{g \cdot F}{U_A^2}}{tanh^2\left(0.76\left(\frac{g \cdot h}{U_A^2}\right)^{0.375}\right)}\right] \quad (20)$$

Peak wave period (T_p) is calculated as:

$$\frac{g \cdot T_p}{U_A} = 8.3 \cdot tanh\left(0.76\left(\frac{g \cdot h}{U_A^2}\right)^{0.375}\right) \cdot tanh^{1/3}\left[\frac{4.1 \cdot 10^{-5} \cdot \frac{g \cdot F}{U_A^2}}{tanh^3\left(0.76\left(\frac{g \cdot h}{U_A^2}\right)^{0.375}\right)}\right] \quad (21)$$

3 Results and Discussion

The revised SPM methodology was calibrated using a dataset consisting of 22 selected storm events in Rijeka Bay, predominantly associated with Jugo wind conditions within the south-eastern sector (135°–175°), which represent the dominant wave-generating conditions in the investigated area. The analyzed events were characterized by effective fetch lengths ranging between 14 and 26 km and ERA5 wind speeds between approximately 7.7 and 16.6 m/s. These conditions are responsible for the generation of larger wave events in the study area and therefore provide a suitable basis for evaluating model performance. Figure 2 presents the measured significant wave heights together with wind speed observations obtained from the Rijeka and Malinska meteorological stations and ERA5 reanalysis data during the investigated period. Periods characterized by increased wind intensity generally correspond to higher significant wave heights, indicating the dominant role of wind forcing in wave development within Rijeka Bay. Compared with measurements from coastal meteorological stations, ERA5 data exhibit smoother temporal variations and generally higher peak values, providing a more representative description of offshore wind conditions. Based on these observations, 22 representative storm events were selected for further analysis and calibration of the revised SPM methodology. Table 2 summarizes the selected storm events together with the environmental input parameters and wave characteristics calculated using the three investigated methodological approaches:

- Methodology **M1**: correction coefficients R_T and R_L were determined according to the original procedure described in the methodology section.
- Methodology **M2**: the temperature correction coefficient was fixed at $R_T = 1.1$, while all remaining parameters followed the original procedure. Compared with methodology M1, this approach systematically increased predicted significant wave heights by approximately 16%, while peak wave periods increased by approximately 4.9%. In this method, we wanted to establish the accuracy of the method when no temperature data is available.
- Methodology **M3**: the temperature correction coefficient remained fixed at $R_T = 1.1$, while the wind speed ratio coefficient was additionally fixed at $R_L = 1$. In comparison with methodology M2, this approach produced a damping effect, reducing predicted significant wave heights such that values remained on average only approximately 3% higher than those obtained using methodology M1. Peak wave periods remained practically unchanged, with an average increase of approximately 0.7%.

The comparison between the investigated approaches enables assessment of the influence of correction coefficients on predicted significant wave heights and peak wave periods.

Table 2. Measured and calculated significant wave heights and corresponding input parameters used in the WaveLab software

Test No.	Date	Air temp. (°C)	Sea temp. (°C)	Effective fetch *F* (km)	Wind speed *U(z)* (m/s) - ERA5	Wind direction (°) - ERA5
1	6/6/2009 14:00			16.5	11.7	145
2	9/4/2009 12:00	29.8	21.7	24	7.7	160
3	10/22/2009 11:00	18.9	17.3	16.5	13.5	145
4	11/30/2009 18:00	17.6	14	20	14.8	150
5	12/8/2009 10:00	13.5	13.9	24	9.5	160
6	12/21/2009 18:00	7.4	12	23	11	165
7	12/22/2009 10:00	11.5	11.5	23	12.5	165
8	12/23/2009 5:00	14.4	11.8	23	13.5	165
9	12/25/2009 3:00			24	11.8	160
10	2/19/2010 14:00	13.8	10.1	14.5	16.6	140
11	3/30/2010 14:00	16.1	11.6	14.5	11.05	140
12	3/30/2010 22:00	14.4	11.3	16.5	10.5	145
13	5/3/2010 10:00	17.2	15.8	14.5	10.3	140
14	9/8/2010 14:00	21.6	19.2	14	11.2	135
15	10/5/2010 6:00	20	18.5	14	11.5	135
16	11/7/2010 22:00			21	10.2	155
17	11/21/2010 23:00			20	12.2	150
18	12/6/2010 18:00			23	11.5	165
19	12/7/2010 23:00			14.5	9.56	140
20	12/24/2010 4:00	14.8	12.2	20	11.5	150
21	12/24/2010 12:00	14.6	12.3	26	9.5	175
22	3/14/2011 4:00			14.5	11.58	140

Test No.	$H_{m0,calc}$ (m)	$T_{p,calc}$ (s)	Hm0,calc (RT = 1.1)	Tp,calc2 (RT = 1.1)	Hm0,calc (RL=1, RT=1.1)	Tp,calc (RL=1, RT=1.1)
1	1.24	4.2	1.24	4.2	1.1	4.04
2	0.739	3.75	1.05	4.22	0.794	3.84
3	1.15	4.1	1.4	4.37	1.32	4.28
4	1.26	4.36	1.66	4.78	1.62	4.74
5	1.13	4.32	1.22	4.44	1.03	4.19
6	1.17	4.35	1.18	4.37	0.917	4.01
7	1.3	4.51	1.5	4.73	1.41	4.63
8	1.24	4.44	1.63	4.86	1.55	4.78
9	1.48	4.73	1.48	4.73	1.34	4.59
10	1.38	4.26	1.49	4.37	1.59	4.47
11	0.984	3.8	1.05	3.89	0.965	3.78
12	0.823	3.66	1.1	4.03	0.967	3.86
13	0.779	3.55	1.05	3.89	0.885	3.67
14	0.832	3.67	1.09	4.03	0.921	3.8
15	0.879	3.64	1.09	3.92	0.996	3.8
16	1.25	4.38	1.25	4.38	1.05	4.13
17	1.31	4.41	1.31	4.41	1.28	4.38
18	1.36	4.57	1.36	4.57	1.21	4.39

Test No.	$H_{m0,calc}$ (m)	$T_{p,calc}$ (s)	Hm0,calc (RT = 1.1)	Tp,calc2 (RT = 1.1)	Hm0,calc (RL=1, RT=1.1)	Tp,calc (RL=1, RT=1.1)
19	0.959	3.77	0.959	3.77	0.808	3.56
20	1.01	4.04	1.31	4.41	1.19	4.27
21	0.861	4	1.13	4.39	0.934	4.11
22	1.24	4.11	1.24	4.11	1.02	3.85

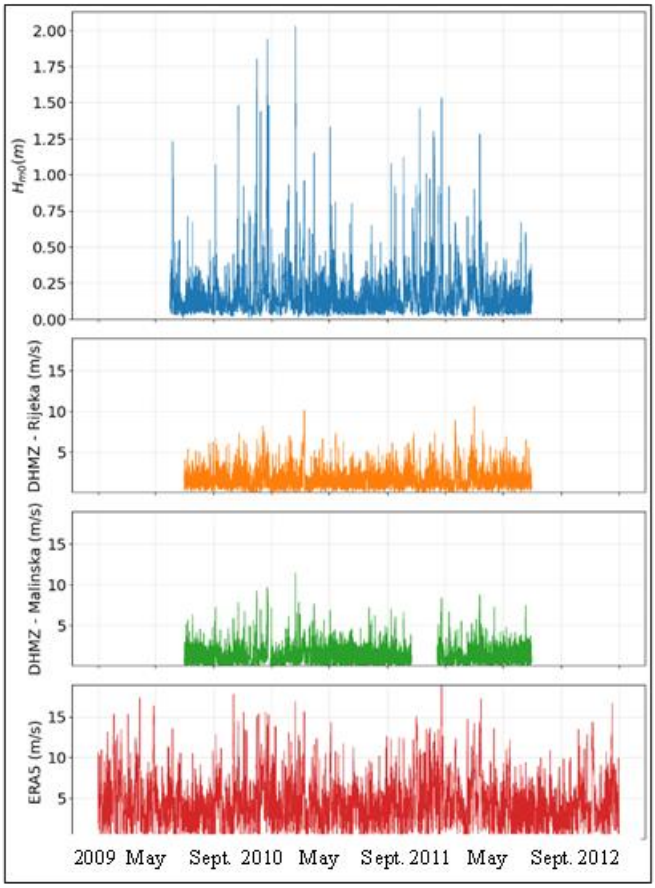


Figure 2. Time series of measured significant wave heights ($\boldsymbol{H_{m0}}$)and wind speed observations obtained from Rijeka and Malinska meteorological stations together with ERA5 reanalysis data during the investigated period.

The agreement between measured and predicted significant wave heights obtained using methodologies M1–M3 is presented in Figure 3. Results obtained using methodology M1 indicate systematic underestimation of measured wave heights, particularly for larger storm events. The largest deviations were observed for wave heights ranging approximately between 1.2 and 1.6 m. Statistical indicators confirmed this behaviour with RMSE = 0.348 m, MAE = 0.288 m, BIAS = -0.254 m and a moderate correlation coefficient of R = 0.554. The introduction of a fixed correction coefficient R_T = 1.1 methodology M2 considerably improved model performance. Predicted values moved closer to the ideal 1:1 relationship throughout the investigated range of wave conditions. Prediction errors were significantly reduced, with RMSE decreasing to 0.196 m and MAE to 0.138 m, while correlation increased to R = 0.792. Although slight underestimation remained for the largest wave events, the overall agreement with measurements improved substantially. Methodology M3, where R_T = 1.1 and R_L = 1 were simultaneously fixed, resulted in deterioration of the previously obtained agreement. Prediction errors increased again (RMSE = 0.289 m and MAE = 0.255 m), while stronger negative bias reappeared (BIAS = -0.231 m). Although correlation remained relatively high (R = 0.783), methodology M2 clearly provided the most reliable performance among the investigated approaches.

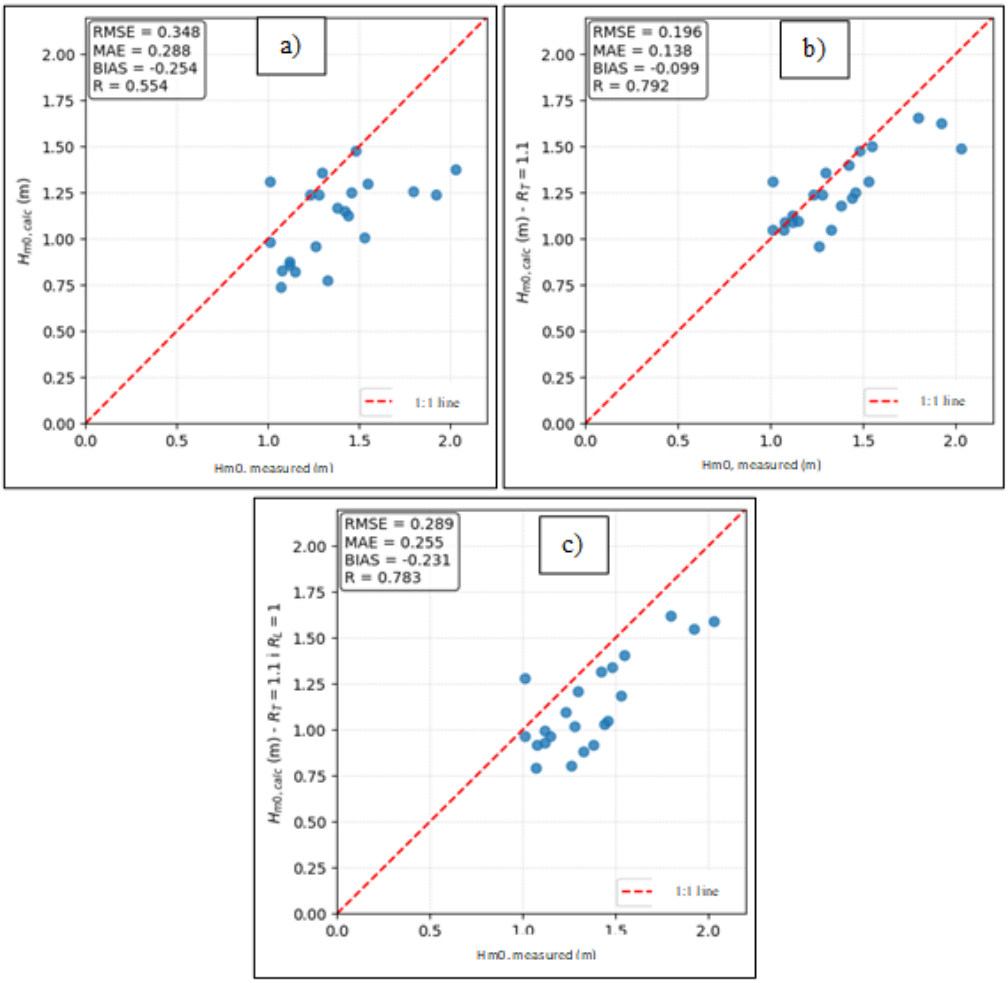


Figure 3. Comparison between measured and predicted significant wave heights using methodologies: (a) M1, (b) M2 and (c) M3

Similar comparisons were performed for peak wave periods, as presented in Figure 4. All investigated approaches systematically underestimated measured values. Methodology M1 produced the largest deviations, with RMSE = 0.652 s, MAE = 0.567 s, and BIAS = -0.510 s. Fixing the R_T coefficient to R_T = 1.1 in methodology M2 improved prediction accuracy and resulted in the most satisfactory agreement among the three investigated methods (RMSE = 0.486 s, MAE = 0.384 s, BIAS = -0.316 s and R = 0.50). Methodology M3 again reduced calculated wave periods and resulted in increased prediction errors (RMSE = 0.604 s, MAE = 0.523 s, BIAS = -0.485 s), despite a slight increase in correlation (R = 0.56).

Since methodology M2 showed the best overall agreement with measurements, an additional calibration procedure was performed to further improve prediction performance. Figure 5 presents the relationship between measured and predicted significant wave heights obtained using methodology M2. Regression analysis indicated a persistent proportional underestimation of wave heights, which became more pronounced for larger wave events. The obtained regression slope of 0.913 suggests that calculated values systematically underestimated measured wave heights across the investigated range of conditions. The statistical indicators for methodology M2 showed satisfactory performance (RMSE = 0.196 m, MAE = 0.138 m, and BIAS = -0.099 m), however, the remaining negative bias indicated that additional improvement could be achieved through a simple calibration procedure.

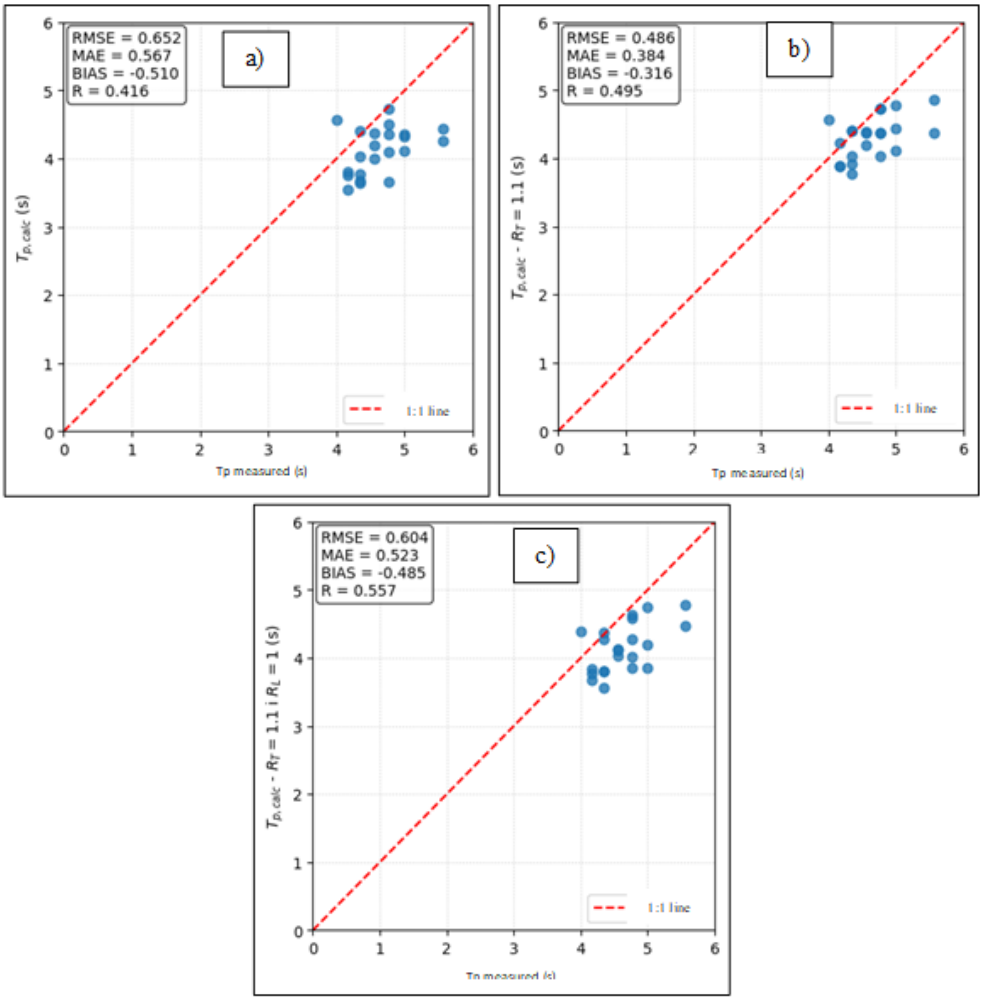


Figure 4. Comparison between measured and predicted peak wave periods using methodologies: (a) M1, (b) M2 and (c) M3

Based on the regression analysis, a multiplicative correction factor was introduced:

$$H_{m0,corr} = 1.095 \cdot H_{m0,calc} \tag{22}$$

Application of the proposed calibration factor further improved model performance and removed most of the systematic bias. The corrected results showed reduced prediction errors, with RMSE decreasing from 0.196 m to 0.169 m, while BIAS approached zero. In addition, the data distribution became more symmetrically concentrated around the ideal 1:1 relationship line, indicating improved agreement between predicted and measured wave heights.

The analysis contains only 22 storm-peak records from a narrow Jugo-sector range, and several records belong to the same synoptic storm sequence. The sample therefore provides limited information about sampling uncertainty and does not represent 22 independent storm realizations. In addition, M2 was selected and the factor 1.095 was derived and assessed using the same data. The calibrated improvement is consequently in-sample and may not transfer to other years, wind sectors, fetch ranges, or sites. ERA5's 0.25° grid also cannot resolve all local coastal-wind variability. Future work should test the coefficient configuration and correction on additional independent storms or by a temporally blocked cross-validation procedure.

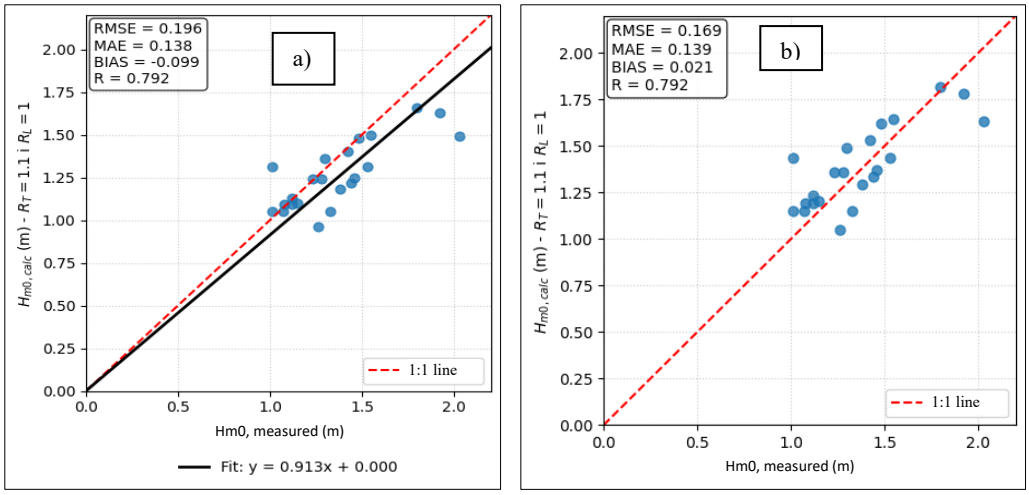


Figure 5. a) Linear regression between measured and predicted significant wave heights obtained using methodology M2 ($\boldsymbol{R_T = 1.1}$), b) Comparison between predicted significant wave heights before and after application of the calibration factor

4 Conclusion

The applicability of the revised SPM methodology for wave prediction under fetch-limited conditions in Rijeka Bay was evaluated using a dataset consisting of 22 storm events, predominantly associated with Jugo wind conditions (135°–175°), effective fetch lengths between 14 and 26 km, and ERA5-derived wind speeds ranging from approximately 7.7 to 16.6 m/s.

The results showed that adopting a fixed correction coefficient of R_T = 1.1 represents a suitable initial approach for estimating significant wave heights. This configuration provided the best agreement with measured values, resulting in a correlation coefficient of R = 0.792, together with relatively low prediction errors (RMSE = 0.196 m, MAE = 0.138 m, BIAS = -0.099 m). However, regression analysis indicated a systematic underestimation that increased with wave magnitude.

Application of a simple linear calibration factor $\left(H_{m0,corr} = 1.095\ H_{m0,calc}\right)$ significantly improved model performance by removing nearly all systematic bias and reducing prediction scatter ($RMSE$= 0.169 m, MAE = 0.139 m, $BIAS \approx 0$), while maintaining the same correlation level. The resulting distribution of predicted and measured values around the 1:1 relationship suggested that a single proportional correction factor is sufficient for significant wave height estimation under the investigated conditions.

For peak wave period $\left(T_p\right)$, all investigated methodological approaches (M1, M2, and M3) systematically underestimated measured values. The most accurate results were again obtained using R_T = 1.1, although only moderate agreement with measurements was achieved ($R \approx 0.50$).

The obtained results indicate that the revised SPM methodology, combined with a locally calibrated correction factor, can provide satisfactory wave predictions for preliminary engineering analyses and lower-sensitivity applications. However, for studies requiring a more accurate representation of wave fields and wave transformation processes in coastal environments, simplified empirical approaches remain insufficient. In such cases, the application of spectral wave models, such as SWAN or WW3, is recommended for obtaining more reliable long-term wave information and more accurate characterization of incident wave conditions.

Acknowledgements

This work was supported by the Croatian Science Foundation under the project number (HRZZ-DOK-2025-02-3371).

This study was conducted within the framework of the institutional project of the University of Zagreb Faculty of Civil Engineering – [HOPIK – Enhancement of hydrological and oceanographic data for assessing the exposure of transport infrastructure to climate change], under the programme line for enhancing scientific excellence, financed through the National Recovery and Resilience Plan 2021–2026. The project is funded by the European Union – NextGenerationEU. The views and opinions expressed are solely those of the authors and do not necessarily reflect those of the European Union or the European Commission. Neither the European Union nor the European Commission can be held responsible for them.

References

Aalborg University, Department of the Built Environment. WaveLab: Data Acquisition and Wave Analysis Software, version 3.9, SPM Hindcasting module.

Booij, N.; Ris, R.C.; Holthuijsen, L.H. 1999 A Third-Generation Wave Model for Coastal Regions: 1. Model Description and Validation. *Journal of Geophysical Research (Oceans)*. 104(C4), 7649–7666.

Bujak, D.; Miličević, H.; Lončar, G.; Carević, D. 2025 Hindcasting Extreme Significant Wave Heights Under Fetch-Limited Conditions with Tree-Based Models. *JMSE*. 13(7), 1355.

Coastal Engineering Research Center (CERC). 1977 *Shore Protection Manual*. Waterways Experiment Station, United States Army Corps of Engineers.

Dorrestein, R. 1960 Simplified Method of Determining Refraction Coefficients for Sea Waves. *Journal of Geophysical Research*. 65, 637–642.

Croatian Meteorological and Hydrological Service (DHMZ). 2022 METMONIC Project: First Meteorological-Oceanographic Buoy Deployed, 6 June 2022.

"ERA5 Hourly Data on Single Levels from 1940 to Present." 2018 *Climate Data Store*, Copernicus Climate Change Service.

Hurdle, D.P.; Stive, R.J.H. 1989 Revision of SPM 1984 Wave Hindcast Model to Avoid Inconsistencies in Engineering Applications. *Coastal Engineering*. 12, 339–345.

Kuspilić, N.; Ocvirk, E.; Beraković, B.; Carević, D.; Pršić, M. 2017 *Hidrotehničke građevine*. Građevinski fakultet Sveučilišta u Zagrebu, Zagreb, Croatia, pp. 177–195.

Lefevre, J.-M.; Aouf, L. 2012 Latest Developments in Wave Data Assimilation. *Proceedings of the European Centre for Medium-Range Weather Forecasts Workshop on Ocean Waves*. pp. 175–188.

Lončar, G.; Šreng, Ž.; Miličević, H.; Ostojić, S. 2019 Increase of Wave Height Due to Transition in Wind Direction—Example: Rijeka Bay. *Electronic Journal of the Faculty of Civil Engineering Osijek*. 10, 57–70.

World Meteorological Organization. 2018 *Guide to Wave Analysis and Forecasting*, 2nd ed.; WMO-No. 702; World Meteorological Organization: Geneva, Switzerland.

CROSS-SCALE ANALYSIS OF PRECIPITATION DATA FROM HIGH AND LOW TEMPORAL RESOLUTION DATASETS

Josip KAPUSTIĆ [1], Jadran BERBIĆ [2*], Željko ŠRENG [1], Marija ŠPERAC [1]

[1] *Josip Juraj Strossmayer University of Osijek, Faculty of Civil Engineering and Architecture Osijek, Vladimira Preloga 3, 31000 Osijek, Croatia*

E-mail: zsreng@gfos.hr

E-mail: msperac@gfos.hr

E-mail: jkapustic@gfos.hr

[2] *University of Zagreb, Faculty of Civil Engineering, Fra Andrije Kačića-Miošića 26, 10000 Zagreb, Croatia*

E-mail: jadran.berbic@grad.unizg.hr

[*] *Corresponding author*

Abstract

Precipitation extremes are commonly analysed using datasets that differ substantially in temporal and spatial resolution, ranging from high-frequency rain gauge observations to gridded reanalysis and climate models products. These differences can influence the characterization of precipitation events and consequently affect hydrological analyses and engineering applications. This study investigates cross-scale relationships between precipitation datasets for the Osijek area, Croatia, with a particular focus on precipitation extremes. Observed station data, ERA5 reanalysis, and CMIP6 climate model outputs were analysed using summary statistics, percentile-based indicators, correlation analysis, bias assessment, and extreme value metrics. The comparison addresses both temporal aggregation effects and spatial scaling effects between point observations and gridded datasets. Results indicate that precipitation characteristics are sensitive to both temporal and spatial resolution. ERA5 reproduces the temporal occurrence of precipitation events reasonably well but exhibits systematic differences in the representation of precipitation intensities and extremes. Similar effects are also observed in climate model outputs, where precipitation fields exhibit both temporal and spatial smoothing, resulting in a reduced representation of local precipitation intensities and extremes. Furthermore, climate projections suggest changes in the magnitude and frequency of extreme precipitation events. The findings highlight the importance of considering scale-related effects when interpreting precipitation extremes and comparing datasets with different temporal and spatial resolutions.

Key words

precipitation analysis, temporal resolution, temporal aggregation, climate projections, return period

1 Introduction

Hyetographs form the basis for runoff analysis, flood protection, and generally the design of infrastructure exposed to extreme precipitation. Traditionally, they are derived from historical meteorological data by applying statistical methods to maximum annual precipitation or peak-over-threshold precipitation for defined durations (e.g. 5, 10, 15, …, 60, 120, …, 1440 minutes). Primary analysis, extraction of intensities from rain gauge records, provides the foundation for secondary analysis and the construction of intensity-duration-frequency (IDF) curves, which are essential starting points for hyetograph creation and engineering design (Bonacci, 1994). This approach assumes that the statistical properties of precipitation remain stationary over time.

The assumption of stationarity is highly questionable (Milly et al., 2008), as the climate is defined as the 30-year average state of the atmosphere, and climate change can significantly affect hyetographs. Rising global air temperatures increase the atmosphere's capacity to retain water vapor, leading to more intense and frequent extreme precipitation events (Allen and Ingram, 2002, Yin et al., 2026). In addition, local climate characteristics and spatial variability influence the distribution and intensity of precipitation (Houze, 2012). Consequently, detailed analysis of historical, current, and future meteorological and climatological data is required to assess the influence of changing climate conditions on precipitation relevant for IDF curves and hyetograph construction.

In hydrological engineering, the estimation of design precipitation and rainfall intensities typically relies on long historical records with high temporal resolution. Longer observation periods provide a more reliable description of precipitation variability and improve the robustness of statistical analyses used for deriving design values. At the same time, temporal aggregation generally reduces peak rainfall intensities (Berne et al., 2004), although these peaks are often the most relevant parameter in runoff estimation, flood assessment, and hydraulic infrastructure design. In practice, however, long-term high-resolution precipitation records are rarely available (Kidd et al., 2017). Engineers and researchers therefore frequently rely on datasets with different temporal and spatial resolutions, including short-duration station measurements, reanalysis products, and climate model outputs. The increasing availability of reanalysis products and climate model simulations provides new opportunities for precipitation analysis but also raises questions regarding the consistency of precipitation characteristics across datasets with different temporal and spatial resolutions (Sunyer et al., 2016).

An additional complication arises from the inherently variable nature of precipitation. Rainfall is highly heterogeneous in both space and time, and extreme events often exhibit strong local characteristics (Berne et al., 2004). As a result, differences in temporal resolution, spatial resolution, and data origin may substantially influence the representation of precipitation extremes. Understanding these relationships is essential for the interpretation of precipitation extremes and their application in hydrological engineering. The challenge is to determine how these datasets relate to each other and to what extent information derived from one temporal or spatial scale can be transferred to another. To address these issues, this study investigates cross-scale relationships between observed precipitation data, ERA5 reanalysis, and CMIP6 climate model outputs for the Osijek area in eastern Croatia. The analysis focuses on the following research questions:

- How does temporal resolution influence the characterization of precipitation extremes?
- How well does ERA5 reanalysis reproduce observed precipitation characteristics and extremes at station scale?
- What is the impact of spatial aggregation on the representation of extreme precipitation events?
- To what extent are precipitation extremes consistent across datasets with different temporal and spatial resolutions?
- How might projected future changes in precipitation extremes affect the applicability of current IDF curves?

Although the statistical methods employed in this study are well established, the novelty lies in their integrated application across precipitation datasets with substantially different spatial and temporal resolutions. By simultaneously evaluating rain gauge observations, ERA5 reanalysis, and multiple CMIP6 climate models using a consistent statistical framework, this study provides a comprehensive assessment of scale-dependent precipitation characteristics relevant to hydrological engineering and climate impact studies.

2 Methods

2.1 Study Area and Datasets

Available data include daily precipitation (1970-2022) and 5-minute precipitation (2016-2024) from the main meteorological station Osijek-Čepin (Croatia), spatial ERA5 reanalyzed hourly data from

meteorological prognostic models (1940-2025), and daily spatial climate scenario data covering the area of interest (2015-2100) (DHMZ, 2025, C3S, 2025) from three different scenarios and three different models (Table 1). These datasets differ in both spatial resolution (local - station; global - reanalysis and climate models) and temporal resolution (from 5 minutes to 1 hour and 1 day).

Table 1. Overview of precipitation datasets used in the study

Dataset	Spatial Resolution	Grid Structure	Temporal Resolution	Period
MMS Osijek (Čepin)	Point	/	Daily	1970-2022
MMS Osijek (Čepin)	Point	/	5 min	2016-2024
ERA5	0.25 x 0,25°,~20 x 28 km	9 x 7	Hourly	1940-2025
CMIP6 HadGEM3-GC31-LL	1.875 x 1.25°, ~150 x 140 km	5 x 7	Daily	2015-2100
CMIP6 IPSLI-CM6A-LR	2.5 x 1.27°, ~200 x 140 km	4 x 7	Daily	2015-2100
CMIP6 MPI-ESM1-2-LR	1.87 x 1.865°, ~150 x 210 km	6 x 5	Daily	2015-2100

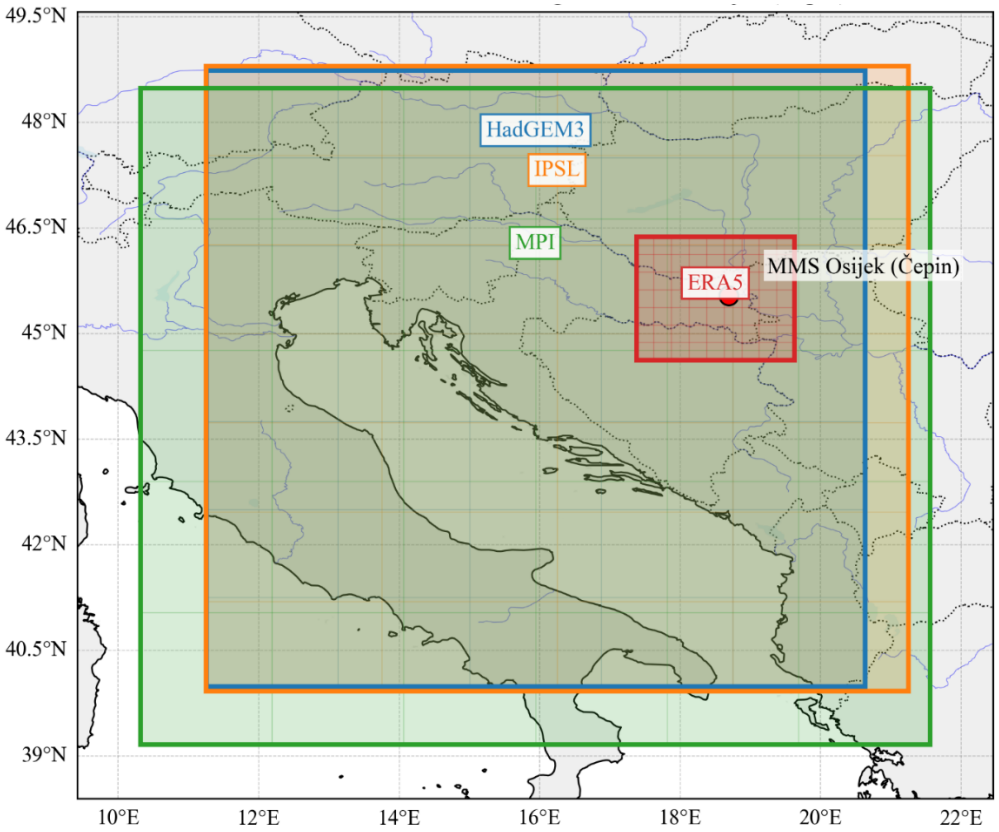


Figure 1. Study area and spatial coverage of the precipitation datasets: (a) location of the MMS Osijek (Čepin) station within Croatia and the ERA5 reanalysis grid; (b–d) spatial extent of the CMIP6 climate model grids used in the analysis: (b) HadGEM3, (c) MPI, (d) IPSL

2.2 Statistical Methods

Precipitation data were analysed using a combination of descriptive statistics, distribution fitting, and extreme value analysis. Seasonal variability was assessed through monthly percentile-based indicators (P2.5, P25, median, P75, P97.5) and interquartile ranges. Cross-dataset comparisons between station observations, ERA5 reanalysis, and CMIP6 model outputs were performed using Pearson and Spearman correlation coefficients, mean bias, and the two-sample Kolmogorov-Smirnov (KS) test to assess distributional differences.

For extreme value analysis, annual maximum series (AMS) were extracted from each dataset. Five theoretical distributions were fitted to the AMS: Gumbel, Generalized Extreme Value (GEV), Weibull, three-parameter Gamma, and Log-Pearson Type III (LP3). Distribution fitting was performed using maximum likelihood estimation (MLE), except for LP3 which was fitted using the method of moments in log space. Goodness-of-fit was evaluated using the root mean square error (RMSE) of the Q-Q plot. Return period quantiles were estimated for return periods of 2, 5, 10, 20, 50, and 100 years. All analyses were implemented in Python using the Anaconda distribution together with Pandas library for data handling and statistical processing (Van Rossum and Drake, 2009; Anaconda Inc., 2020; McKinney, 2010). Spatial maps and graphical outputs were produced using the Cartopy basemaps and Matplotlib library (Met Office, 2025, Hunter, 2007).

3 Results and Discussion

3.1 Temporal Variability and Precipitation Extremes

The seasonal precipitation pattern at MMS Osijek (based on the data from 1970 to 2022) is presented in Fig. 2. Monthly totals show a distinct seasonal cycle with the highest median values in June (76.3 mm) and July (57.4 mm), driven by convective activity during the warm season. Summer months also exhibit the greatest interquartile spread and extreme values, with recorded maxima reaching 239.5 mm in June and 273.5 mm in July, while winter months show lower and more consistent totals.

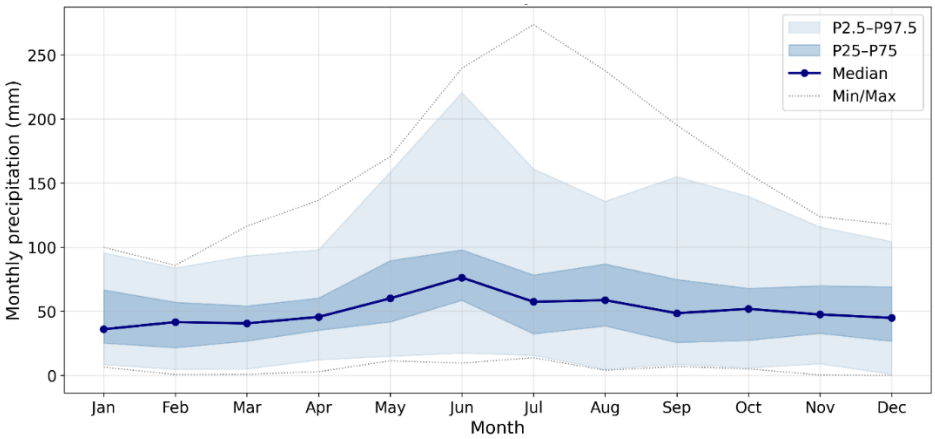


Figure 2. Seasonal precipitation pattern at MMS Osijek (Čepin)

Figure 3 compares annual maximum precipitation intensities obtained from different temporal resolutions over the common period 2016–2022. To enable direct comparison, all values were expressed as intensities (mm/h). Hourly station intensities were derived from aggregated 5-minute observations, whereas daily intensities were obtained by converting annual maximum daily precipitation totals into equivalent hourly intensities. An identical procedure was applied to ERA5 data. The results therefore isolate the influence of temporal aggregation and spatial averaging on the representation of precipitation extremes. When expressed as intensity (mm/h), finer temporal resolution consistently captures higher peak values. Annual maximum intensities from 5-minute data range from 80.4 to 225.6 mm/h, compared to 16.8-44.3 mm/h for hourly and 1.1–2.3 mm/h for daily station aggregates. ERA5 reanalysis shows considerably lower intensities across all resolutions, confirming that both temporal aggregation and spatial averaging systematically reduce the representation of peak precipitation.

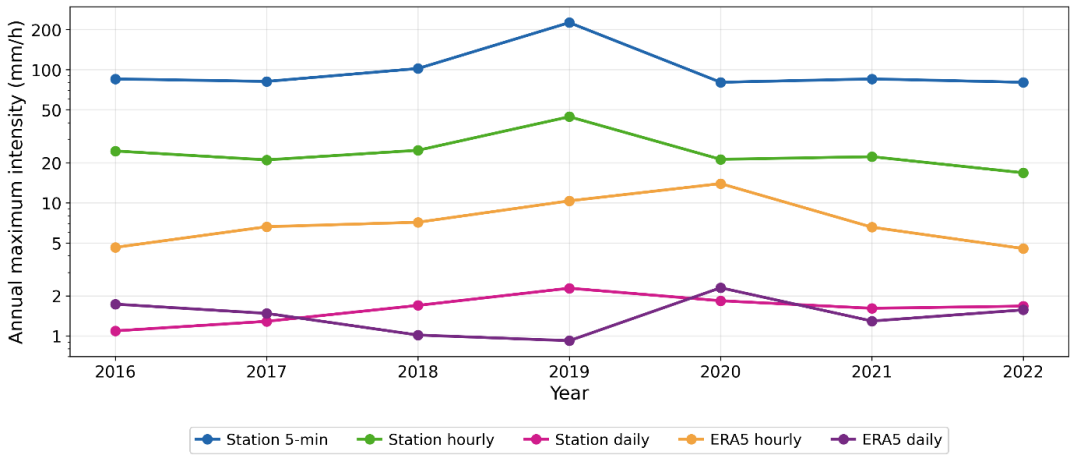


Figure 3. Effect of temporal aggregation on annual maximum precipitation intensity at MMS Osijek (Čepin), 2016–2022

3.2 Cross-scale comparison of station and ERA5 Data

Although ERA5 generally underestimates precipitation extremes, it exhibits substantial agreement with station observations and reproduces interannual variability reasonably well, as shown in Fig. 4. Notable peaks in station data, such as those recorded around 1971, 1981, and 2010, are partially reflected in ERA5, though with considerably lower magnitudes. Both datasets exhibit a weak positive trend over the study period. To identify the ERA5 grid cell most representative of the meteorological station, all 63 surrounding grid cells were evaluated using Spearman's rank correlation and bias against the observed precipitation series. Although several neighbouring cells exhibited very similar performance, the geographically closest grid cell consistently ranked among the best-performing cells, with differences in correlation coefficients below 0.01. Because these differences were negligible, the nearest grid cell was selected for all subsequent analyses. This approach minimizes spatial mismatch between point observations and gridded data while maintaining an objective and reproducible selection procedure.

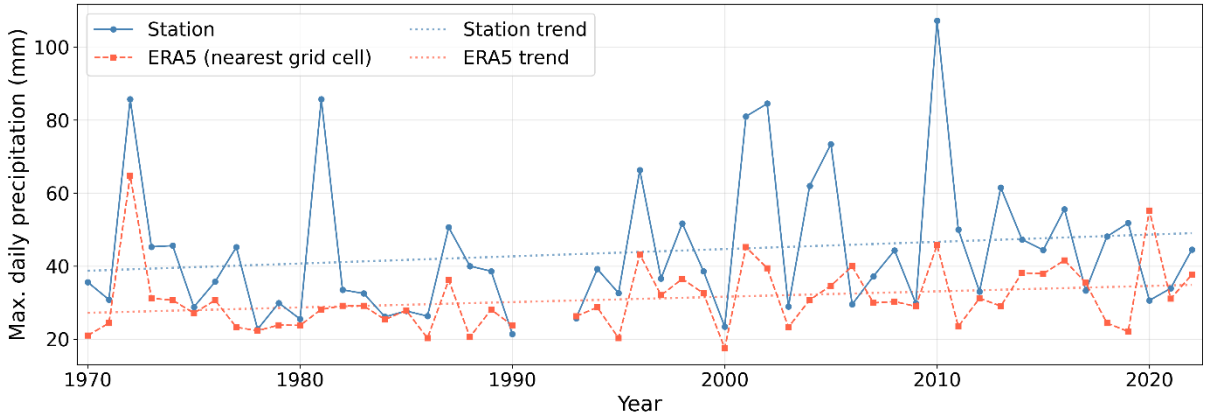


Figure 4. Annual maximum daily precipitation at MMS Osijek and the nearest ERA5 grid cell (1970–2022), with linear trends shown for both datasets

Table 2 presents KS statistics and precipitation percentiles for daily and hourly comparisons between MMS Osijek and ERA5 (Figs. 5 and 6). For daily data, the KS statistic is highest for all days ($D = 0.395$), largely due to differences in dry day frequency. When filtered to wet days ($P \geq 0.1$ mm/d), agreement improves substantially ($D = 0.084$). ERA5 systematically underestimates high percentiles, with P95 ratios of 0.80–0.91 and P99 ratios of 0.79 – 0.81, meaning ERA5 captures approximately 80 - 90% of observed extreme daily precipitation.

For hourly data, differences are considerably more pronounced, as visible in Fig. 6. The KS statistic reaches 0.649 for wet hours ($P \geq 1.0$ mm/h), with ERA5 capturing only 33% of station P95 and 27% of

P99. This strong underestimation of sub-daily intensities is consistent with the known limitation of ERA5 in representing convective precipitation events, which are responsible for the highest observed intensities.

Table 2. Comparison of P95 and P99 precipitation percentiles and Kolmogorov-Smirnov (KS) statistics between MMS Osijek station observations and ERA5 nearest grid cell

Resolution	Dataset	Scenario	KS	P95			P99		
				ST [mm]	ERA5 [mm]	Ratio	ST [mm]	ERA5 [mm]	Ratio
daily	MMS Osijek (d)	All days	0.395	10.80	9.85	0.91	23.80	18.97	0.80
	MMS Osijek (d)	P ≥ 0.1 mm/d	0.084	18.50	15.46	0.84	32.66	26.37	0.81
	MMS Osijek (d)	P ≥ 1.0 mm/d	0.130	22.20	17.82	0.80	36.47	28.77	0.79
hourly	MMS Osijek (h)	All hours	0.264	0.20	0.46	2.29	2.00	1.51	0.75
	MMS Osijek (h)	P ≥ 0.1 mm/h	0.309	4.00	1.92	0.48	10.07	3.34	0.33
	MMS Osijek (h)	P ≥ 1.0 mm/h	0.649	8.00	2.65	0.33	15.81	4.26	0.27

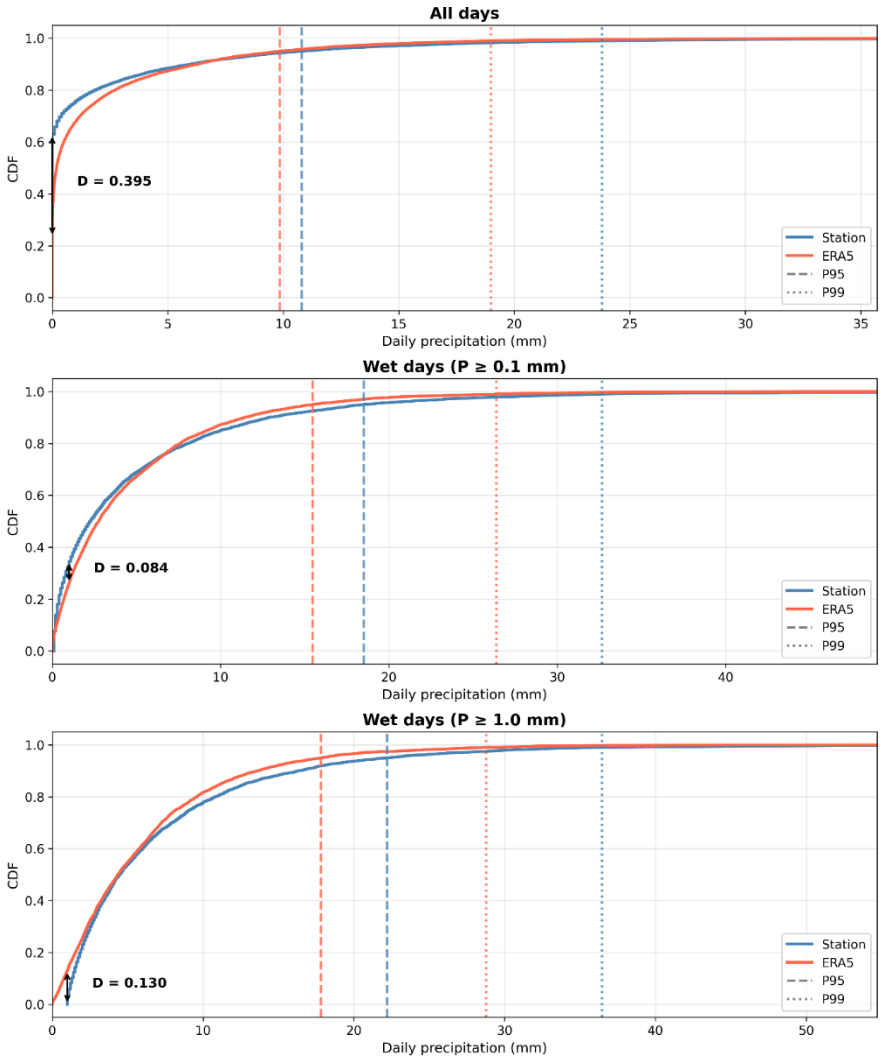


Figure 5. Empirical cumulative distribution functions (CDF) and KS statistics for daily precipitation at MMS Osijek and ERA5 (1970–2022)

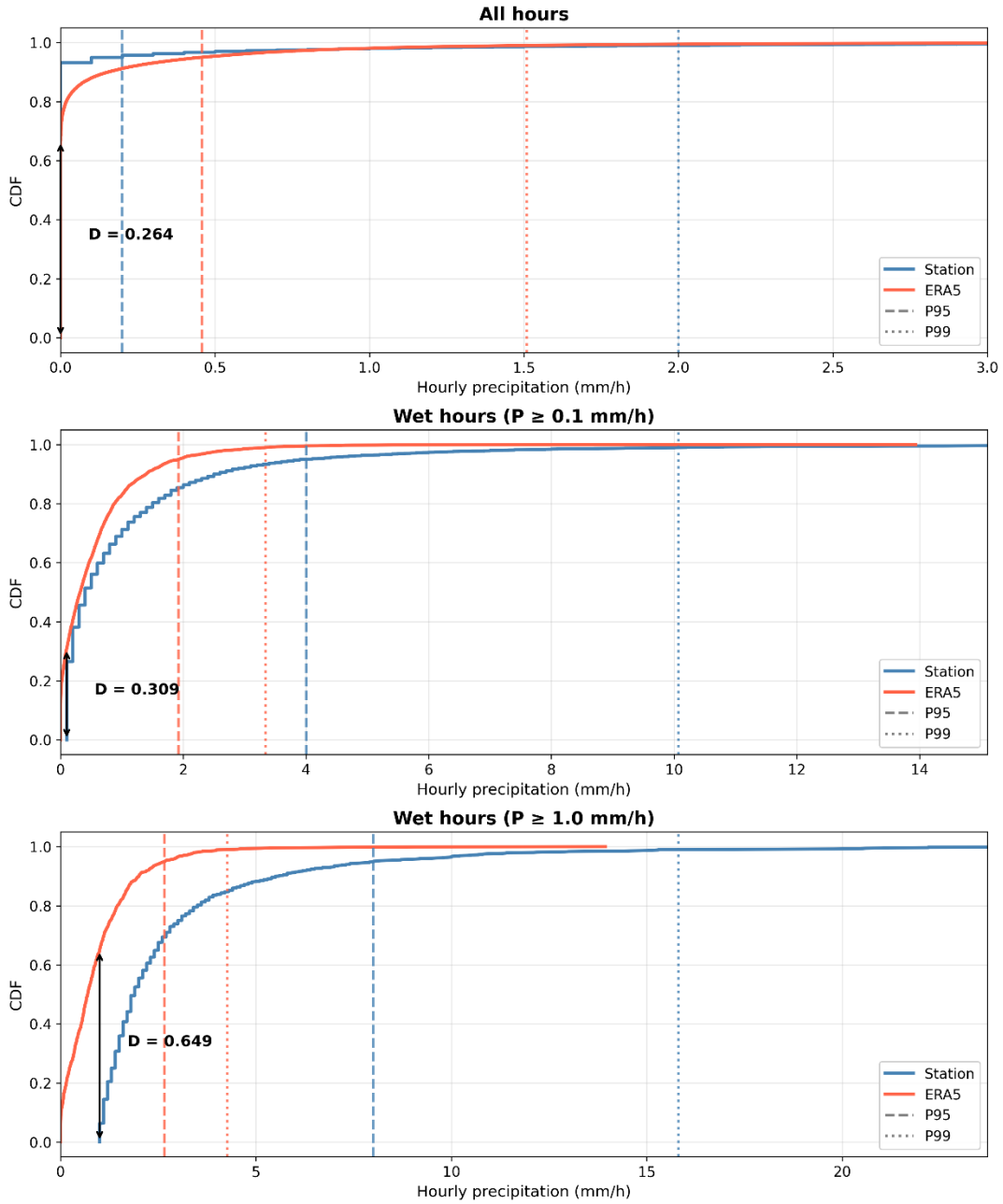


Figure 6. Empirical cumulative distribution functions (CDF) and KS statistics for hourly precipitation at MMS Osijek and ERA5 (2016–2024)

Figs. 7 and 8 show scatter plots of annual maximum precipitation between station observations and ERA5 for daily and hourly data, respectively. In both cases, ERA5 values consistently fall below the 1:1 line, confirming systematic underestimation of peak intensities. The underestimation is considerably more pronounced for hourly data, where ERA5 captures only a fraction of observed maximum intensities.

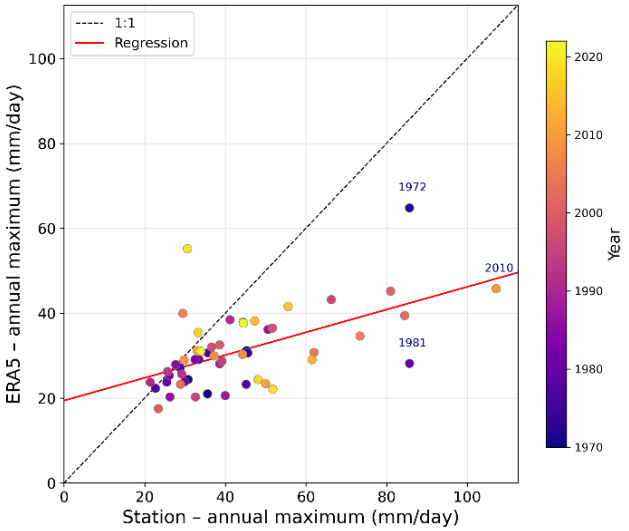


Figure 7. Relationship between observed and ERA5 daily precipitation totals

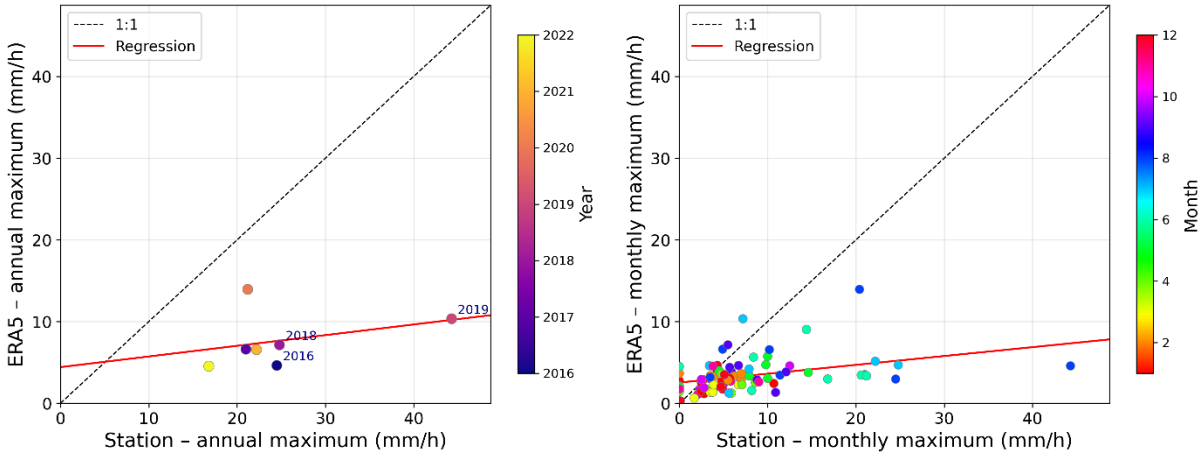


Figure 8. Relationship between observed and ERA5 hourly precipitation totals

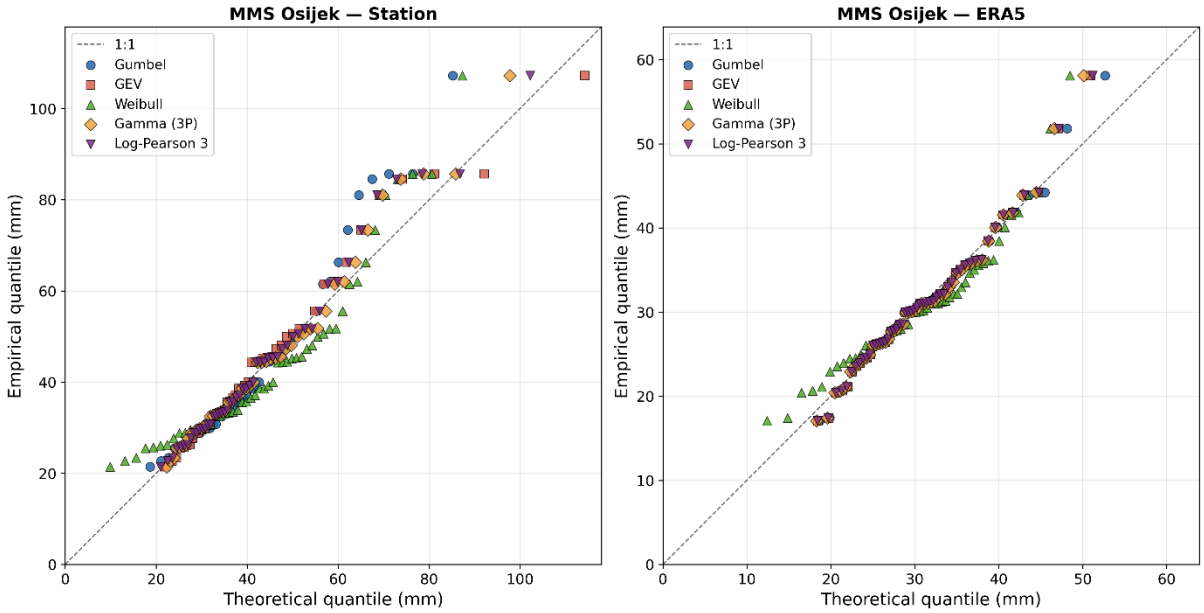


Figure 9. Comparison of maximum daily precipitation quantiles for selected return periods derived from station observations and ERA5 data

Fig. 9 presents Q-Q plots comparing empirical and theoretical quantiles for five fitted distributions, for both station data (left) and ERA5 (right). In addition to visual inspection of the Q-Q plots, the RMSE between empirical and theoretical quantiles was used as a quantitative goodness-of-fit measure, providing a practical measure of the predictive performance across the entire distribution of maxima. Based on RMSE evaluation, Gamma3 was selected as the best-fitting distribution for the station and Gumbel for ERA5, with the resulting return period quantiles presented in Table 3.

Table 3. Return period quantiles (mm/day) of annual maximum daily precipitation at MMS Osijek (Čepin) for selected probability distributions, where T denotes the return period in years.

Dataset	Distribution	T=2	T=5	T=10	T=20	T=50	T=100
MMS Osijek (Čepin)	Gamma3	38.9	56.5	69.1	81.3	97.1	108.9
ERA5 - MMS Osijek (Čepin)	Gumbel	29.8	37.0	41.8	46.4	52.4	56.9

The systematic underestimation of precipitation extremes by ERA5 reflects the inherent differences between point observations and gridded precipitation products. While temporal aggregation reduces peak rainfall intensities (Berne et al., 2004), gridded datasets further smooth the same precipitation event by averaging it over both space and time, reducing the representation of localized convective extremes (Sunyer et al., 2016). Consequently, ERA5 provides a reliable representation of regional precipitation patterns but should be used with caution when estimating local precipitation extremes.

3.3 Future climate projections and implications for IDF curve applicability

Spatial correlation and bias analysis between MMS Osijek (Čepin) and CMIP6 model grid cells revealed that correlation generally increases towards the northern part of the domain, while southern grid cells show negative or near-zero Spearman ρ values. Owing to the coarse spatial resolution of CMIP6 global climate models (approximately 150-200 km), statistical agreement between individual grid cells and station observations was considerably weaker than for ERA5. Since correlations between neighbouring grid cells and station observations were generally low, the geographically closest grid cell to the meteorological station was selected for each model, enabling a consistent comparison among different climate models.

A comparison of annual precipitation totals between station observations, ERA5, and CMIP6 model simulations for the overlapping period 2015–2022 is shown in Fig. 10. None of the analysed models reproduces observed annual precipitation totals satisfactorily. However, HadGEM3 generally exhibits the closest agreement with observations and may therefore be considered the most consistent among the analysed models for the overlapping period.

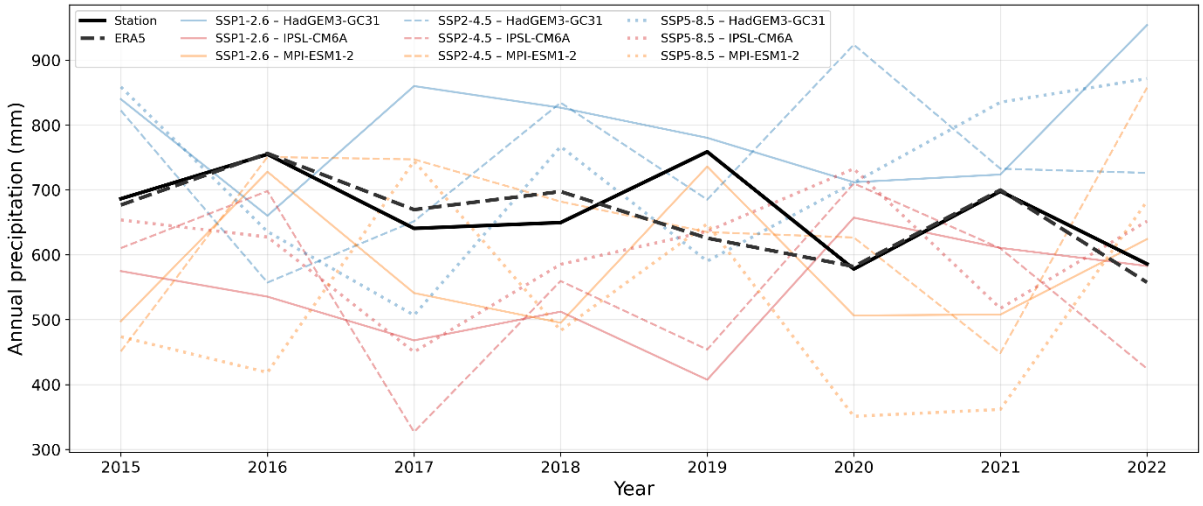


Figure 10. Comparison of annual precipitation totals between observations and CMIP6 simulations (2015–2022)

Return period quantiles derived from station observations, ERA5, and all three CMIP6 models under three emission scenarios are presented in Table 4, where for each dataset the best-fitting distribution based on Q-Q RMSE was applied. Results show considerable spread across models and scenarios, reflecting the uncertainty in climate projections. For HadGEM3-GC31-LL, SSP5-8.5 yields lower extremes than SSP1-2.6 at long return periods (91.7 vs. 121.9 mm for T=100), reflecting the variability of a single model realization rather than a physical signal.

Table 4. Return period quantiles (mm/day) of annual maximum daily precipitation for station observations, ERA5, and CMIP6 model simulations under selected emission scenarios

Dataset	Distribution	T=2	T=5	T=10	T=20	T=50	T=100
MMS Osijek (Čepin)	Gamma3	38.9	56.5	69.1	81.3	97.1	108.9
ERA5 - MMS Osijek (Čepin)	Gumbel	29.8	37.0	41.8	46.4	52.4	56.9
HadGEM3-GC31 (SSP1-2.6)	Log-Pearson 3	35.1	48.4	60.5	71.1	99.2	121.9
HadGEM3-GC31 (SSP2-4.5)	Log-Pearson 3	36.0	48.8	59.7	72.2	92.0	109.9
HadGEM3-GC31 (SSP5-8.5)	Log-Pearson 3	36.5	47.2	55.8	65.3	79.5	91.7
IPSL-CM6A (SSP1-2.6)	GEV	25.9	33.7	39.5	45.5	54.0	61.0
IPSL-CM6A (SSP2-4.5)	Log-Pearson 3	25.6	35.6	43.4	51.9	64.4	75.0
IPSL-CM6A (SSP5-8.5)	GEV	25.4	34.4	41.7	49.8	62.4	73.7
MPI-ESM1-2 (SSP1-2.6)	Gumbel	23.0	27.5	30.5	33.3	37.0	39.8
MPI-ESM1-2 (SSP2-4.5)	Log-Pearson 3	24.5	29.1	31.7	33.9	36.6	38.5
MPI-ESM1-2 (SSP5-8.5)	Gamma3	23.0	27.8	30.7	33.3	36.5	38.8

The spread among CMIP6 projections should also be interpreted in the context of the spatial representativeness of individual model grid cells. Owing to the coarse spatial resolution of global climate models, a single grid cell represents precipitation averaged over a large area rather than conditions at the station itself. Consequently, the selected grid cell may not fully capture the local precipitation regime, particularly for extreme events. A more rigorous comparison would involve an objective evaluation of neighboring grid cells, potentially combined with statistical bias adjustment or other calibration techniques, to ensure consistency between the overall statistical characteristics of climate model outputs and the observed precipitation regime during the common historical period.

4 Conclusion

The results demonstrate that both temporal and spatial scale have a strong influence on the characterization of precipitation extremes. Temporal aggregation substantially reduces peak precipitation intensities, while spatial aggregation smooths localized precipitation events and reduces the magnitude of extremes. ERA5 reanalysis reproduces the general precipitation variability reasonably well and represents an effective intermediate scale between point observations and climate model outputs. Despite differences in the representation of precipitation extremes, the observed relationships indicate potential for transferring information between datasets of different spatial and temporal resolutions. Future precipitation characteristics derived from CMIP6 simulations remain strongly model-dependent, highlighting the importance of considering scale effects and dataset-specific uncertainties when analysing precipitation extremes.

Acknowledgements

Funded by the European Union - Next Generation EU. However, the views and opinions expressed are solely those of the author(s) and do not necessarily reflect those of the European Union or the European

Commission. Neither the European Union nor the European Commission can be held responsible for them.

References

Allen M.R. and Ingram W.J. 2002 Constraints on future changes in climate and the hydrologic cycle. *Nature* 419, 224–232.

Anaconda Inc. 2020 Anaconda Distribution Documentation. Anaconda Inc., Austin, TX, USA.

Berne A., Delrieu G., Creutin J.D. and Obled C. 2004 Temporal and spatial resolution of rainfall measurements required for urban hydrology. *Journal of Hydrology* 299(3–4), 166–179.

Bonacci O. 1994 *Oborine: glavna ulazna veličina u hidrološki ciklus*. Geoing, Split, Croatia.

Copernicus Climate Change Service (C3S) 2025 ERA5 hourly data on single levels from 1940 to present. Copernicus Climate Data Store. DOI: 10.24381/cds.adbb2d47.

Copernicus Climate Change Service (C3S) 2025 Climate Data Store (CDS). CMIP6 Climate Projections. European Centre for Medium-Range Weather Forecasts (ECMWF), Reading, UK.

DHMZ (Croatian Meteorological and Hydrological Service) 2025 Relational meteorological database. Zagreb, Croatia.

Houze R.A. Jr. 2012 Orographic effects on precipitating clouds. *Reviews of Geophysics* 50(1), RG1001.

Hunter J.D. 2007 *Matplotlib: A 2D graphics environment*. Computing in Science & Engineering 9(3), 90–95.

Kidd C., Becker A., Huffman G.J., Muller C.L., Joe P., Skofronick-Jackson G. and Kirschbaum D.B. 2017 So, how much of the Earth's surface is covered by rain gauges? Bulletin of the American Meteorological Society 98(1), 69–78.

McKinney W. 2010 Data structures for statistical computing in Python. In Proceedings of the 9th Python in Science Conference, Pasadena, CA, USA, 28 June–3 July, pp. 51–56.

Milly P.C.D., Betancourt J., Falkenmark M., Hirsch R.M., Kundzewicz Z.W., Lettenmaier D.P. and Stouffer R.J. 2008 Stationarity is dead: Whither water management? *Science* 319(5863), 573–574.

Sunyer M.A., Madsen H., Rosbjerg D. and Arnbjerg-Nielsen K. 2016 Regional interdependency of precipitation extremes across scales: comparison of gridded data and rain gauge observations. *Hydrology and Earth System Sciences* 20, 759–772.

Van Rossum G. and Drake F.L. 2009 *Python 3 Reference Manual*. CreateSpace, Scotts Valley, CA, USA.

Yin J., Gao B. and Porporato A. 2026 Scaling of Rainfall Intensity and Frequency with Rising Temperatures.

QUANTIFYING WIND CONTRIBUTION TO WATER EXCHANGE IN MARINAS USING AN IMPROVED ANALYTICAL FORMULATION

Ivana LOVRIĆ [1*], Filip KALINIĆ [1], Goran LONČAR [2]

[1] *Zagreb University of Applied Sciences, Croatia*

E-mail: ilovric@tvz.hr

E-mail: fkalinic@tvz.hr

[2] *Faculty of Civil Engineering, Croatia*

E-mail: goran.loncar@grad.unizg.hr

[*] *Corresponding author*

Abstract

Water exchange is a key factor affecting environmental conditions in marina basins, particularly in microtidal environments where tidal forcing alone may not ensure adequate seawater renewal. This paper presents an improved analytical formulation that extends the classical tidal prism approach by incorporating the contribution of wind-induced circulation to water exchange. The formulation was developed using three-dimensional hydrodynamic simulations performed with MIKE 3 FM and tracer-based analyses of e-folding time. The investigation was carried out on hypothetical marina configurations with characteristic length-to-width ratios of L/B = 1 and L/B = 2, side-positioned entrances, and flushing culverts embedded in the breakwater structure. Numerical simulations showed that water exchange is significantly influenced by wind velocity, wind direction, tidal forcing, and exchange area. The characteristic wind directions E, SE, W, and NW produced the most efficient water exchange, while increasing wind velocity and effective exchange area generally resulted in shorter e-folding times. The proposed formulation was validated against numerical model results and also applied to Marina Opatija as a real-case study. The results showed good agreement between analytically calculated and numerically simulated e-folding times. The developed formulation provides a practical engineering tool for rapid assessment of short-term water exchange and comparison of marina design alternatives under microtidal conditions.

Key words

water exchange, marina, wind-forcing, tidal prism, e-folding time, MIKE 3 FM

1 Introduction

Marinas and small ports are semi-enclosed coastal basins where limited water exchange can result in the accumulation of pollutants and deterioration of water quality. Potential sources of pollution include vessel operation and maintenance, antifouling paints, hydrocarbons, sanitary wastewater, stormwater runoff, detergents, nutrients, and solid waste (US Environmental Protection Agency, 1993). Due to restricted circulation, these substances may remain within the basin for extended periods, affecting dissolved oxygen concentrations, nutrient levels, sediment quality, and biological communities. Efficient water renewal is therefore one of the key hydrodynamic conditions for maintaining acceptable environmental quality in marina basins (Schwartz and Imberger, 1988; Recreational Navigation Commission, 2008). The rate of water renewal in marinas depends on the hydrodynamic processes that drive seawater circulation, including tidal oscillations, wind, waves, freshwater inflows, and density-induced currents. Understanding the relationship between these circulation drivers and marina design is essential for achieving adequate seawater renewal and reducing pollutant concentrations within enclosed basins. Consequently, both natural forcing mechanisms and basin geometry play a crucial role in

determining the environmental performance of marina systems (Fischer, 1979).

Water exchange in marinas is commonly assessed using hydrodynamic time parameters such as flushing time, residence time, water renewal time, or e-folding time (Takeoka, 1984; Monsen, Cloern and Lucas, 2002). These parameters provide a simplified yet practical measure of the rate at which water within a semi-enclosed basin is replaced by surrounding seawater. Among the available approaches, the tidal prism method is one of the most widely applied analytical techniques for estimating water exchange in semi-enclosed coastal basins. It relates the exchange time to the basin volume, tidal prism, tidal period, and a return flow factor, which accounts for the fraction of exchanged water that re-enters the basin during subsequent tidal cycles (Sanford, Boicourt and Rives, 1992). Among the various exchange indicators, the e-folding time is frequently used in tracer-based analyses and is defined as the time required for the spatially averaged tracer concentration to decrease to 1/e, or approximately 37% of its initial value (Rodhe, 1992). Previous recommendations suggest that an e-folding time of approximately four days may be considered an indicator of adequate water exchange in marina basins (US Environmental Protection Agency, 1993; Recreational Navigation Commission, 2008).

Wind is considered one of the most important hydrodynamic drivers of water exchange in semi-enclosed coastal basins because it can generate surface currents, circulation cells, and shear-driven mixing processes (McKeehan, 1975). Wind-induced circulation may enhance mixing within the basin and accelerate exchange with the surrounding sea, particularly when wind direction aligns with marina entrances or additional openings in the breakwater. Previous studies have highlighted the importance of shear-driven circulation processes for water renewal in microtidal marinas, especially when tidal forcing is weak (Murphy, Deiber and Perrin, 2012). Similar conclusions were reported in studies investigating circulation in lagoons and marinas under wind forcing, where wind was shown to strongly influence flushing efficiency, residence times, and internal circulation patterns (Mestres, Sierra and Sánchez-Arcilla, 2007; Dumas *et al.*, 2012; Chen *et al.*, 2014; Safak *et al.*, 2015). Wind-driven circulation may also reduce the return flow factor and improve mixing efficiency within the basin (Cucco and Umgiesser, 2005).

Previous numerical and experimental studies have shown that incorporating additional openings or culverts embedded in breakwater structures can improve circulation and water renewal in microtidal marinas (Lončar *et al.*, 2016, 2017; Bartolić *et al.*, 2018; Carević *et al.*, 2019). Their effectiveness depends on the geometry, position, and alignment of the openings relative to dominant wind directions and circulation patterns. However, despite the recognized importance of wind-driven processes, their contribution to water exchange remains insufficiently represented in analytical formulations and is most often assessed using numerical modelling approaches.

This paper presents an improved analytical formulation for quantifying the contribution of wind to water exchange in marinas. The formulation extends the classical tidal prism approach by incorporating the effects of wind-induced circulation and is based on numerical investigations performed for hypothetical marina configurations. Its performance is evaluated against three-dimensional hydrodynamic simulations and its applicability is further assessed using a marina-domain model of Marina Opatija, whose computational domain is consistent with the assumptions adopted during the formulation development. Particular emphasis is placed on short-term water exchange processes in microtidal environments, where wind may become a dominant mechanism of water renewal. Accordingly, this study addresses the following research question: Can the classical tidal prism formulation be extended to incorporate the contribution of wind-induced circulation while providing a reliable and practical analytical tool for estimating short-term water exchange in microtidal marinas?

2 Methods

2.1 Model domain and investigated scenarios

The proposed analytical formulation is based on numerical investigations of hypothetical marina

configurations previously presented in Lovrić (2025). For completeness, the principal characteristics of these numerical investigations are briefly summarized below, as they provide the basis for the formulation evaluated in the present study. The results obtained from these simulations provided the basis for developing the proposed analytical formulation.

The investigated marina geometries were reduced to characteristic length-to-width ratios of L/B = 2 and L/B = 1 (Fig. 1). The numerical domain included only the marina basin, allowing detailed analysis of circulation and water exchange processes within the protected area. This domain configuration enabled the isolation of internal hydrodynamic processes while eliminating the influence of site-specific circulation patterns in the surrounding coastal area. However, the isolated domain does not account for the return flow of previously exported water from the surrounding aquatorium back into the marina basin. The hypothetical marina included submerged culverts (eight culvert pipes of 1 m diameter) integrated into the breakwater structure at position P2 (Fig. 1), following the configuration of Marina Opatija, where in-situ measurements were previously conducted (Bartolić *et al.*, 2018; Lovrić, 2025).

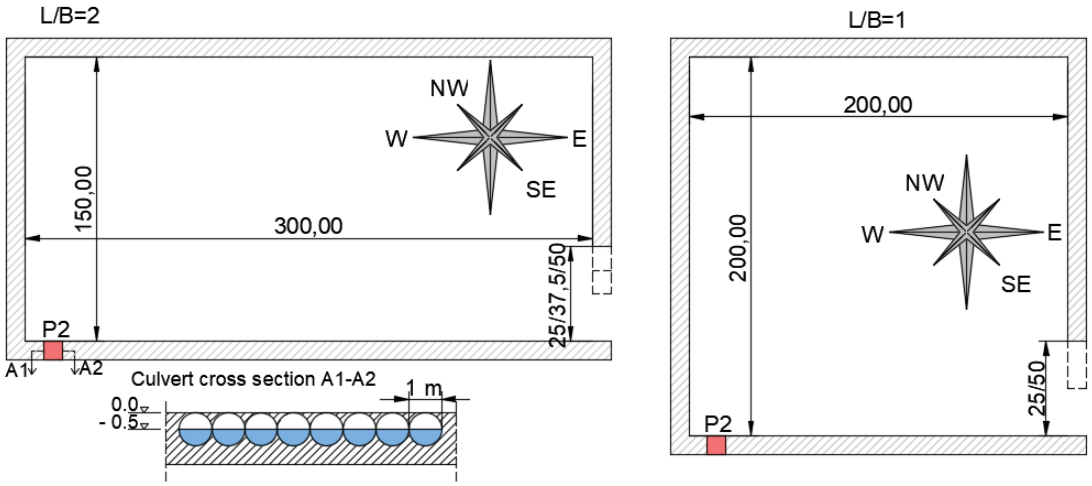


Figure 1. Schematic representation of the hypothetical marina configurations with L/B=2 and L/B=1 ratios, including the main geometric characteristics, culvert positioned at location P2, and characteristic wind directions

To ensure broader applicability of the results, simulations were performed for two representative Adriatic locations characterized by different tidal regimes: Rovinj in the northern Adriatic and Dubrovnik in the southern Adriatic. The analyses included variations in tidal forcing, wind speed and direction, entrance width, and marina geometry. For the analysis of wind contribution to e-folding exchange time (T_f), simulations were conducted for the following scenarios with culverts positioned at location P2 (Figure):

- Rovinj and Dubrovnik locations, marina geometry L/B=2:
  - wind intensities of 2, 3, 4, and 5 Beaufort,
  - four characteristic wind directions: E, SE, W, and NW,
  - three entrance widths: 25, 37.5, and 50 m,
  - homogeneous density conditions without spatial variations in temperature and salinity
- Dubrovnik location, marina geometry L/B=1:
  - wind intensities of 2, 3, 4, and 5 Beaufort,
  - four characteristic wind directions: E, SE, W, and NW,
  - two entrance widths: 25 and 50 m,
  - homogeneous density conditions without spatial variations in temperature and salinity.

The hypothetical marina model was used to analyse the influence of wind-induced circulation combined with tidal forcing on the e-folding exchange time (T_f) for different wind scenarios. The resulting numerical simulations form the basis of the analytical formulation described in Section 2.3.

2.2 Hydrodynamic and Tracer Transport Modelling

Three-dimensional hydrodynamic simulations were conducted using the MIKE 3 FM model (DHI, 2010). The numerical model solves the Reynolds-averaged Navier–Stokes equations with the finite-volume method on an unstructured mesh, while hydrodynamic circulation and tracer transport were simulated using the HD (Hydrodynamic) and AD (Advection–Dispersion) modules.

The computational domains of the hypothetical marinas (with L/B=2 and L/B=1) were discretized using an unstructured mesh composed of triangular finite-volume cells with an average horizontal cell area of approximately 25 m^2 (Fig. 2). In the vertical direction, the water column was discretized using seven sigma layers. The bottom geometry was defined with a constant slope ranging from 3 to 7 m water depth for both marina configurations. At culvert position, a group of eight circular culverts with a diameter of 1 m was incorporated into the breakwater structure. The invert elevation of the culverts was positioned at −0.5 m relative to the mean sea level (Fig. 2). Along solid vertical boundaries, the normal velocity component was prescribed as zero. Tidal forcing was introduced through time-varying sea-level boundary conditions derived from amplitudes and phases of the seven principal tidal constituents for the Rovinj and Dubrovnik locations (Janeković and Kuzmić, 2005). Water-level time series were imposed at the open boundaries located at the marina entrance and flushing culverts, enabling the simulation of tidal exchange between the marina basin and the surrounding sea. Simulations were performed under homogeneous density conditions. At the sea surface, the model was forced using spatially uniform and temporally constant wind fields (modelled scenarios in Section 2.1.).

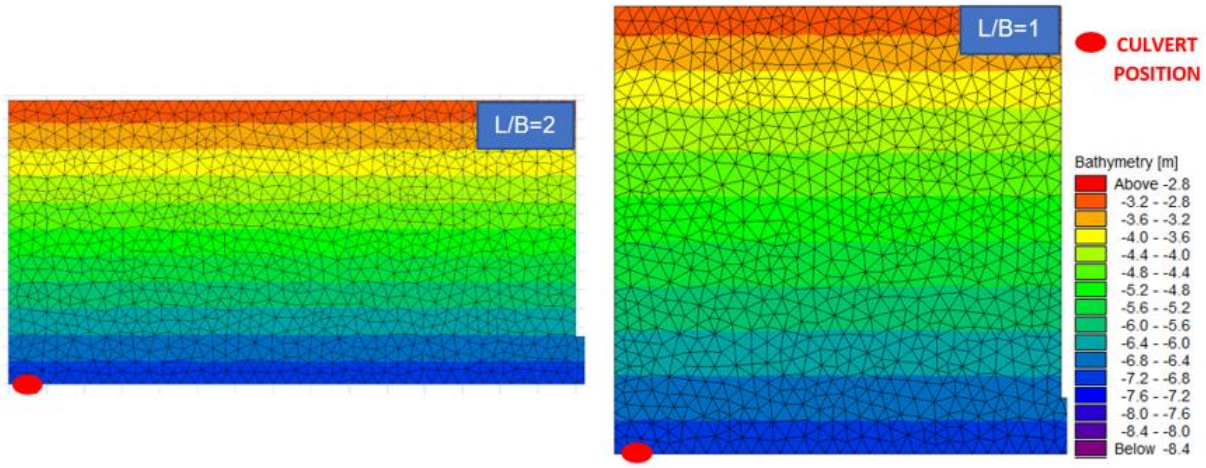


Figure 2. Spatial discretization of the model domains for marinas with L/B = 2 and L/B = 1 using triangular mesh elements, with a culvert located at position P2 and an entrance width of 25 m

The initial hydrodynamic condition corresponded to a stationary water body without any initial currents. Tracer transport simulations were conducted using a conservative tracer, uniformly distributed within the marina basin at the start of each simulation. The initial tracer concentration inside the marina was set as 100, while the concentration at the open boundaries was set to zero, assuming permanent removal of the tracer once exported from the marina basin. This assumption is consistent with a return flow factor equal to zero (b = 0), adopted in the development of the analytical formulation. Water exchange was quantified using the e-folding time (T_f), defined as the time required for the spatially averaged tracer concentration within the marina basin to decrease to 1/e (approximately 37%) of its initial value.

The Smagorinsky coefficient and bottom roughness were assumed to be spatially uniform with values of 0.2 and 0.01 m, respectively. The wind drag coefficient was set at 0.0024, according to Wu (1994).

2.3 Development of the Improved Analytical Formulation

Based on the numerical investigations summarized above, the classical tidal prism approach was extended in Lovrić (2025) to incorporate the contribution of wind-induced circulation to water exchange

in marina basins. The classical tidal prism formulation (Dyer and Taylor, 1973) expresses water exchange time as:

$$T_f = \frac{V_{AK} T_{po}}{(1-b) V_{po}} \ (h) \tag{1}$$

where V_{AK} (m^3) is the average basin volume, V_{PO} (m^3) is the tidal prism volume, T_{PO} (h) is the tidal period, and b (/) is the return flow factor.

The classical tidal prism formulation was first evaluated against numerical simulations performed under tidal forcing alone. Good agreement between analytical and numerical e-folding times confirmed its applicability under homogeneous density conditions. The numerical investigation then examined the influence of wind speed, wind direction, entrance width, and culvert configuration on water exchange. The results showed that winds aligned with the longitudinal axis of the marina and intersecting the entrance produced the most efficient exchange conditions. Consequently, winds from the E, SE, W, and NW directions (Fig. 1) were selected for the development of the analytical formulation.

Based on the numerical analyses, the following improved analytical formulation was proposed:

$$T_f = \frac{V_{AK}}{(1-b) \cdot \frac{V_{po}}{T_{po}} + k \cdot v \cdot p \cdot A} \ (h) \tag{2}$$

where k (/) is a calibration coefficient dependent on wind speed, wind direction, entrance cross-sectional area, and culvert geometry, v (m/s) is wind velocity, p (/) is a coefficient representing the influence of moored vessels as a function of the marina area occupied by berthed vessels, and A (m^2) is the marina water surface area. Although the proposed formulation includes parameter p to account for the influence of moored vessels, all analyses presented in this study assume an empty marina. Consequently, further research is needed to evaluate the formulation under different berth occupancy conditions and to validate the broader applicability of parameter p.

2.3.1 Assumptions and Limitations

Several assumptions were adopted during the development of the improved analytical formulation. The first relates to water density. Numerical investigations presented in Lovrić (2025) showed that non-homogeneous density conditions accelerated water exchange compared with homogeneous conditions. However, because density stratification depends strongly on local environmental conditions and seasonal variability, homogeneous density was adopted to obtain a simplified formulation with broader practical applicability.

The numerical simulations also revealed vertically separated circulation patterns under characteristic wind conditions. Depending on wind direction, surface inflow currents were accompanied by compensating bottom outflow currents, or vice versa. These circulation structures limited the recirculation of previously exported water into the marina basin, supporting the assumption of a zero return flow factor. Consequently, the proposed formulation is expressed as:

$$T_f = \frac{V_{AK}}{\frac{V_{po}}{T_{po}} + k \cdot v \cdot p \cdot A} \ (h) \tag{3}$$

The formulation was intentionally developed for marina-domain configurations. Extending the computational domain beyond the marina basin would introduce additional circulation and recirculation processes that are not represented by the simplified analytical formulation. Incorporating variable return-flow effects therefore remains a topic for future research.

Accordingly, the proposed formulation is applicable to homogeneous density conditions, wind velocities corresponding to 2–5 Beaufort, the characteristic wind directions E, SE, W, and NW, and marina configurations with length-to-width ratios of L/B = 1 and L/B = 2. The calibration covers combined entrance and culvert areas ranging from 171 to 324 m², corresponding to culvert-to-entrance area ratios between 0.02 and 0.04.

The adopted mesh resolution was selected to adequately represent the investigated marina configurations and hydrodynamic processes. Although a formal mesh sensitivity analysis was not performed, future research could include such an analysis to further assess the influence of mesh resolution on the numerical predictions and the proposed analytical formulation.

Finally, the applicability of the proposed formulation beyond the hypothetical marina configurations was evaluated using Marina Opatija (Bartolić *et al.*, 2017), a real marina located in the northern Adriatic Sea. Analytical e-folding times were compared with results obtained from a previously calibrated three-dimensional hydrodynamic model under selected wind conditions and characteristic wind directions.

3 Results and Discussion

3.1 Factors Influencing Water Exchange

The numerical simulations used in the formulation development demonstrated that water exchange within the investigated marina configurations is influenced by wind direction, wind velocity, tidal forcing, and the total exchange area formed by the marina entrance and culverts. As expected, e-folding times generally decreased with increasing wind velocity, reflecting the enhanced circulation and mixing generated by stronger winds within the marina basin (Fig. 3). In addition to wind velocity, wind direction was identified as a significant factor influencing water exchange. The characteristic wind directions E, SE, W, and NW consistently produced the shortest e-folding times and the most efficient water exchange. Their orientation relative to the marina geometry promotes circulation patterns that facilitate seawater renewal within the marina basin. Under wind-driven circulation, larger entrance widths further enhanced water exchange by increasing the effective exchange area between the marina basin and the surrounding sea. Nevertheless, wider entrances may also increase wave penetration into the marina basin, indicating the need to balance water renewal requirements with wave protection considerations during marina design. Larger tidal amplitudes also accelerated water renewal and resulted in shorter e-folding times, which is reflected in the consistently lower T_f values obtained for the Rovinj location compared to Dubrovnik.

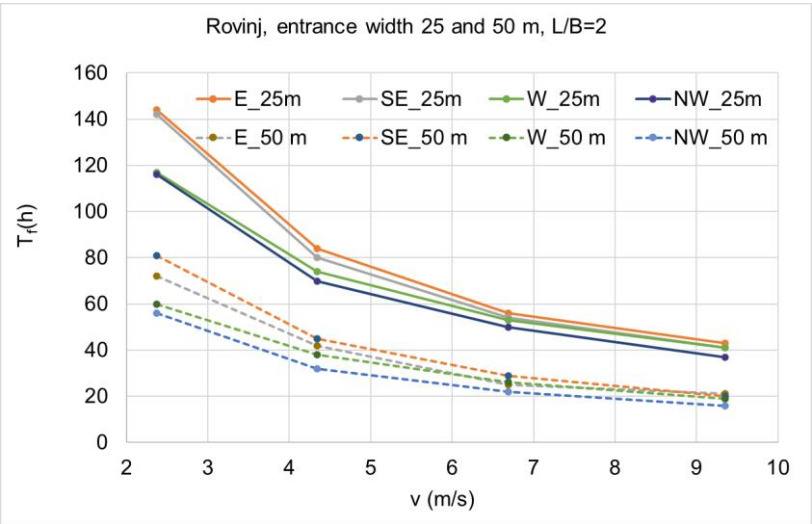


Figure 3. Numerically simulated e-folding time (T_f) for the marina with L/B = 2 under tidal forcing and characteristic wind directions (2–5 Beaufort), for the Rovinj, entrance widths of 25 and 50 m, and a culvert at position P2

Differences between characteristic wind directions became less pronounced with increasing wind velocity, suggesting that strong wind forcing dominates the influence of wind direction on exchange processes. The observed dependence of e-folding time on wind velocity, wind direction, and exchange area provided the basis for developing an improved analytical formulation capable of quantifying the contribution of wind to water exchange in marina basins.

3.2 Development and Validation of the Improved Analytical Formulation

Based on the numerical investigation described above, the proposed formulation extends the classical tidal prism approach by incorporating the contribution of wind-induced circulation to water exchange. Analysis of the numerical simulations enabled the derivation of empirical coefficients describing the influence of wind conditions and exchange area on water renewal. The empirical coefficients were determined through an iterative fitting procedure to achieve the best agreement between analytically calculated and numerically simulated e-folding times over the investigated range of scenarios. The calibration coefficient k, introduced in Eq. (3), consists of two empirical coefficients according to Eq. (4): k_1 which accounts for the effects of wind velocity and characteristic wind direction (E, SE, W, and NW), and k_2, which represents the influence of the effective exchange area, entrance and culvert area.

$$k = 10^{-6} \cdot k_1 \cdot k_2 \tag{4}$$

For elongated marinas with a side-positioned entrance, the values of coefficient k_1 can be determined directly from Fig. 4 as a function of wind velocity and characteristic wind direction. The coefficient k_2 can be calculated using Eq. (5) as a function of the effective exchange area A_{ent}(m^2) through which seawater is exchanged between the marina basin and the surrounding sea, defined as the combined area of the marina entrance and culverts.

$$k_2 = 0{,}0077 \cdot A_{ent} - 0{,}2192 \tag{5}$$

The resulting coefficient diagrams provide a practical framework for applying the proposed analytical formulation under the investigated conditions. The formulation was developed for wind velocities corresponding to 2–5 Beaufort, characteristic wind directions E, SE, W, and NW, and combined entrance and culvert areas ranging from 171 to 324 m².

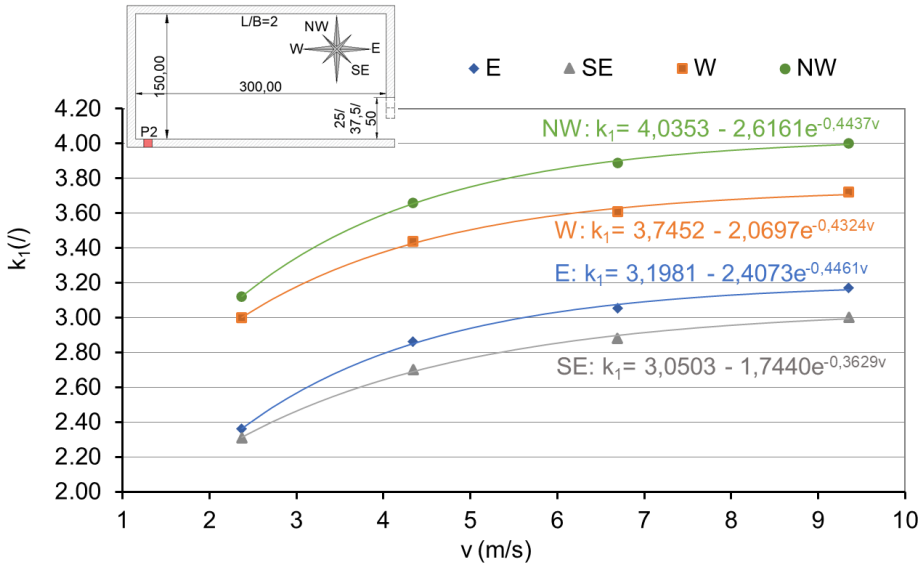


Figure 4. Coefficient k_1 as a function of wind velocity (2.37–9.35 m/s) and characteristic wind directions (E, SE, W, and NW), with a schematic representation of the marina geometry

The performance of the proposed formulation was evaluated by comparing analytically calculated e-folding times with the corresponding values obtained from the numerical model (Fig. 5). These

validation statistics also provide an estimate of the numerical uncertainty associated with the empirical calibration of the proposed formulation. The comparison demonstrated very good agreement across the investigated range of wind conditions and marina configurations. Coefficients of determination ranged from 0.93 to 0.97, while NSE values exceeded 0.90 for all characteristic wind directions. The highest agreement was obtained for the SE wind direction, whereas slightly larger deviations were observed for W and NW winds. These results confirm that the formulation reliably reproduces the effects of wind velocity, wind direction, and exchange area on short-term water exchange in marina basins.

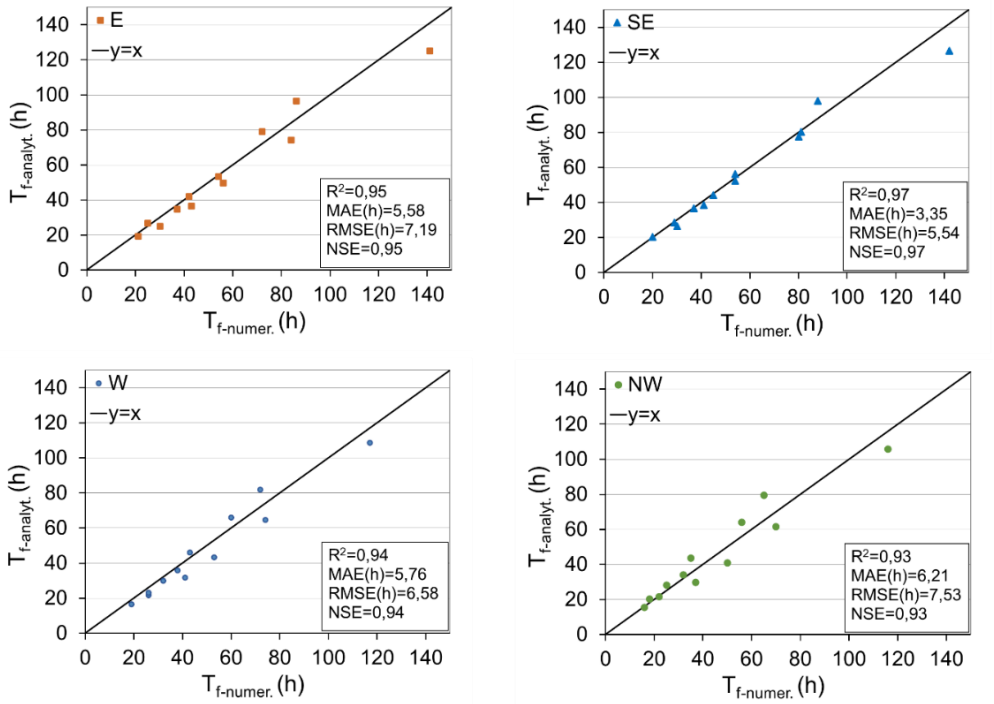


Figure 5. Comparison of analytically calculated and numerically simulated e-folding times (T_f) for the marina with L/B = 2 at the Rovinj location, considering entrance widths of 25, 37.5, and 50 m, characteristic wind directions (E, SE, W, and NW), wind intensities of 2–5 Beaufort, and a culvert at position P2

3.3 Application to Marina Opatija

To further evaluate the applicability of the proposed analytical formulation under conditions consistent with its assumptions, an additional comparison was performed using a marina-domain numerical model of Marina Opatija. This numerical model, previously developed by Bartolić et al. (2017), has a computational domain limited to the marina basin and is therefore consistent with the assumptions adopted in the development of the analytical formulation, particularly the assumption of a return flow factor equal to zero (b = 0). In contrast, the larger calibrated model (Bartolić et al., 2018; Lovrić, 2025), which includes the surrounding coastal area, captures additional site-specific circulation and possible recirculation of water between the marina and the adjacent aquatorium. Although such a model provides a more realistic representation of the complete hydrodynamic system, it includes processes that are not explicitly represented in the proposed analytical formulation. Therefore, the marina-domain model was selected as the reference for evaluating the applicability of the formulation.

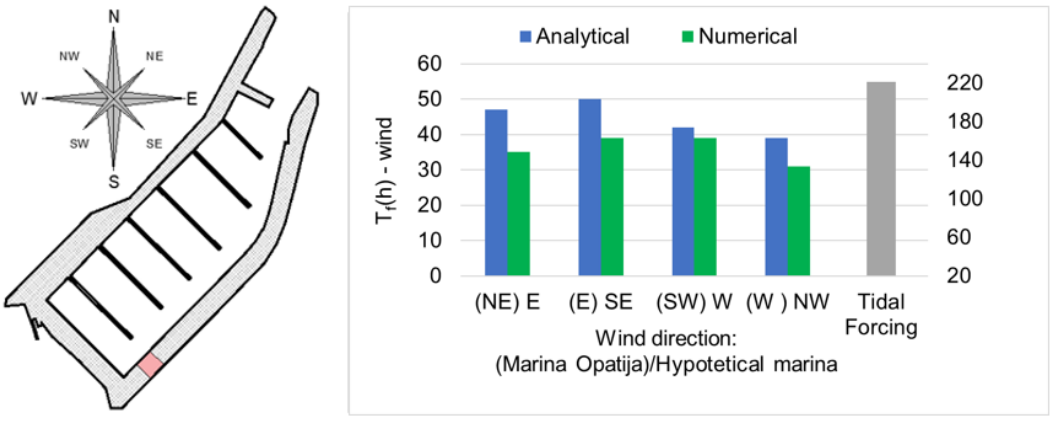
The comparison was performed for the characteristic wind directions E, SE, W, and NW under constant wind conditions corresponding to 4 Beaufort. To ensure consistency with the assumptions adopted during the development of the analytical formulation, freshwater inflows were excluded from the calibrated Marina Opatija model and the simulations were performed under barotropic conditions. Marina Opatija has a water surface area of 38,400 m² and a basin volume (V_{AK}) of 222,105 m³. The analytical calculations were performed using a tidal prism volume (V_{PO}) of 12,288 m³, a tidal period (T_{PO}) of 12.24 h, and an effective exchange area of 195 m², corresponding to the combined area of the marina entrance and flushing culverts. Analytically calculated e-folding times were subsequently

compared with the corresponding values obtained from the numerical model.

The wind directions used for Marina Opatija were selected according to the actual orientation of the marina entrance, breakwater, and flushing culverts (Fig. 6a). Therefore, the correspondence between wind directions in Marina Opatija and the hypothetical marina is not based on identical geographic directions, but on their relative orientation with respect to the marina geometry. For example, the W wind direction in Marina Opatija (Fig. 6a) corresponds approximately to the NW direction in the hypothetical marina configuration (Fig. 1).

Figure 6b presents a comparison between analytically calculated and numerically simulated e-folding times for Marina Opatija under characteristic wind directions and constant wind conditions corresponding to 4 Beaufort. For comparison, the figure also includes the e-folding time obtained using the classical tidal prism formulation under tidal forcing only. The substantially longer exchange time predicted by the classical formulation highlights the importance of wind-induced circulation and demonstrates the improvement achieved by incorporating wind effects into the proposed analytical formulation.

The comparison showed satisfactory agreement between the analytical formulation and the numerical model for all investigated wind directions. Relative deviations ranged from 7.7% to 34.3%, with an average deviation of approximately 24.3%. The smallest deviation was obtained for the (SW) W wind direction, while the largest deviation occurred for the (NE) E wind direction. In all investigated cases, the analytical formulation predicted slightly longer e-folding times than the numerical model. This difference can be attributed to the simplified representation of exchange processes in the analytical formulation, which describes water renewal through a limited number of parameters, while the numerical model additionally resolves local circulation structures, spatial variability of flow velocities, and three-dimensional hydrodynamic processes within the marina basin. Nevertheless, the formulation successfully reproduced the relative influence of different wind directions and provided e-folding times of the same order of magnitude as those obtained from the calibrated numerical model. These results demonstrate that the proposed formulation is capable of capturing the dominant mechanisms governing short-term water exchange under realistic conditions and may therefore be used as a practical tool for preliminary engineering assessments.



(a) **(b)**

Figure 6. (a) Schematic orientation of Marina Opatija and investigated wind directions; (b) comparison of analytically calculated and numerically simulated e-folding times for Marina Opatija under characteristic wind directions and constant wind conditions corresponding to 4 Beaufort, and under Tidal Forcing only

4 Conclusion

This study evaluated the applicability of an improved analytical formulation for estimating wind-

induced water exchange in marinas by comparing its predictions with numerical simulations for Marina Opatija. The results confirmed that water exchange is strongly influenced by wind velocity, wind direction, tidal forcing, and the effective exchange area formed by the marina entrance and culverts. Wind direction was identified as a particularly important factor, with the characteristic wind directions E, SE, W, and NW consistently producing the most efficient water renewal. Increasing wind velocity generally resulted in shorter e-folding times, indicating enhanced circulation and exchange processes within the marina basin. Additionally, larger exchange areas and greater tidal amplitudes contributed to faster water renewal and lower e-folding times.

The improved analytical formulation evaluated in this study extends the classical tidal prism approach by quantifying the contribution of wind-induced circulation to water exchange. The formulation incorporates the combined effects of wind velocity, wind direction, and exchange area through empirically derived coefficients. Validation against MIKE 3 FM simulations demonstrated a high level of agreement between analytical and numerical e-folding times, indicating that the formulation reliably reproduces the observed exchange behaviour and successfully captures the dominant mechanisms governing short-term water exchange in microtidal marinas. The comparison with the Marina Opatija marina-domain model further confirmed the applicability of the formulation under a realistic marina configuration consistent with the assumptions adopted during its development.

The proposed formulation may be applied for preliminary assessment of short-term water exchange in marinas with characteristic length-to-width ratios of $L/B = 1$ and $L/B = 2$ and a side-positioned entrance, operating under homogeneous density conditions in microtidal environments. Unlike the classical tidal prism approach, which considers only tidal forcing, the proposed formulation enables quantification of the contribution of wind-induced circulation to water renewal under specific wind conditions. Consequently, it can be used to evaluate the influence of wind velocity, wind direction, entrance width, and culvert configuration on marina flushing efficiency during short-term periods. Its applicability is limited to wind velocities corresponding to 2–5 Beaufort, characteristic wind directions E, SE, W, and NW, total exchange areas ranging from 171 to 324 m², and culvert-to-entrance area ratios between 0.02 and 0.04. Within these limitations, the formulation provides a practical engineering tool for rapid comparison of design alternatives and assessment of measures aimed at improving water exchange without the need for computationally demanding numerical simulations. Although the proposed formulation showed good agreement with numerical simulations, future research should include validation against field observations from different marina configurations and hydrodynamic conditions to further confirm its applicability under real environmental conditions.

References

Bartolić, I., Lončar, G., Bujak, D., Klapčić, S. and Mišura, I. 2017 Impact of wind, tidal variations, wave field and density gradient on the seawater exchange trough flushing culverts in marinas. Acta hydrologica Slovaca, 18 (2017), 2; 271-281

Bartolić, I., Lončar, G., Bujak, D. and Carević, D. 2018 The flow generator relations for water renewal through the flushing culverts in marinas, *Water (Switzerland)*, 10(7). Available at: https://doi.org/10.3390/w10070936.

Carević, D., Bujak, D., Lončar, G. and Bartolić, I. 2019 Use of culverts for improving exchange of seawater in ports, *Gradjevinar*, 71(3), pp. 197–207. Available at: https://doi.org/10.14256/JCE.2527.2018.

Chen, H., Malanotte-Rizzoli, P., Tieh-Yong, K., Guiting, Song. 2014 The relative importance of the wind-driven and tidal circulations in Malacca Strait, *Continental Shelf Research*, 88, pp. 92–102. Available at: https://doi.org/10.1016/j.csr.2014.07.012.

Cucco, A. and Umgiesser, G. 2005 Modeling the Venice Lagoon residence time, *Ecological modelling*, 194, pp. 34–51.

DHI 2010 "MIKE 21 & MIKE 3 FLOW MODEL FM Hydrodynamic Module Scientific Documentation." Available at: www.mikebydhi.com.

Dumas, F., Le Gendre, R., Thomas, Y. and Andréfouët, S. 2012 Tidal flushing and wind driven

circulation of Ahe atoll lagoon (Tuamotu Archipelago, French Polynesia) from in situ observations and numerical modelling, *Marine Pollution Bulletin*, 65(10–12), pp. 425–440. Available at: https://doi.org/10.1016/J.MARPOLBUL.2012.05.041.
Dyer, K.R. and Taylor, P.A. 1973 A simple, segmented prism model of tidal mixing in well-mixed estuaries, *Estuarine and Coastal Marine Science*, 1(4), pp. 411–418. Available at: https://doi.org/10.1016/0302-3524(73)90030-3.
Fischer, H.B. 1979 *Mixing in inland and coastal waters*. Academic Press.
Janeković, I. and Kuzmić, M. 2005 Numerical simulation of the Adriatic Sea principal tidal constituents, *Annales Geophysicae*, 23(10), pp. 3207–3218. Available at: https://doi.org/10.5194/angeo-23-3207-2005.
Lončar, G., Bekić, D., Carević, D., Bujak, D., Bartolić, I. and Beg Paklar, G. 2016 The impact of culverts on the seawater exchange and wave action in marina waters, *Hrvatske Vode*, 24(98).
Lončar, G., Carević, D., Bujak, D., Bartolić, I. and Beg Paklar, G. 2017 Analysis of the impact of winds, tide oscillations and density distribution on the sea exchange through culverts in the marinas as exemplified by the Ičići marina, *Hrvatske Vode*, 25(101).
Lovrić, I. 2025 *Contribution of wind to the seawater exchange in the marina through the culverts in the breakwater body*. University of Zagreb Faculty of Civil Engineering.
McKeehan, D.S. 1975 *Water Motion in Closed-end Canals*.
Mestres, M., Sierra, J.P.A.U. and Sánchez-Arcilla, A. 2007 Baroclinic and wind-induced circulation in Tarragona harbour (northeastern Spain), *Scientia Marina*, 71, pp. 223–238. Available at: https://doi.org/10.3989/scimar.2007.71n2223.
Monsen, N.E., Cloern, J.E. and Lucas, L.V. and Monismith, S.G. 2002 A comment on the use of flushing time, residence time, and age as transport time scales. *Limnology and Oceanography* 47(5), pp.1545–1553.
Murphy, E., Deiber, M. and Perrin, S. 2012 Shear-driven flushing of micro-tidal marinas, *Coastal Engineering Proceedings*, (33), p. 59. Available at: https://doi.org/10.9753/icce.v33.currents.59.
Recreational Navigation Commission 2008 *Protecting water quality in marinas*, pp. 26–26.
Rodhe, H. 1992 Modeling Biogeochemical Cycles, *International Geophysics*, 50, pp. 55–72. Available at: https://doi.org/10.1016/S0074-6142(08)62687-X.
Safak, I., Wiberg, P.L., Richardson, D.L. and Kurum, M. O. 2015 Controls on residence time and exchange in a system of shallow coastal bays, *Continental Shelf Research*, 97, pp. 7–20. Available at: https://doi.org/10.1016/j.csr.2015.01.009.
Sanford, L.P., Boicourt, W.C. and Rives, S.R. 1992 Model For Estimating Tidal Flushing of Small Embayment, *Journal of waterway, port, coastal, and ocean engineering*, 118, pp. 635–654.
Schwartz, R.A. and Imberger, J. 1988 Flushing behaviour of a coastal marina *Coastal Engineering Proceedings*, 1(21). Available at: https://doi.org/10.1061/9780872626874.196.
Takeoka, H. 1984 Fundamental concepts of exchange and transport time scales in a coastal sea, *Continental Shelf Research*, 3(3), pp. 311–326. Available at: https://doi.org/10.1016/0278-4343(84)90014-1.
US Environmental Protection Agency 1993 *Environmental Engineering for Small Boat Basins, Engineering Manual*, pp. 11–15.
Wu, J. 1994 The sea surface is aerodynamically rough even under light winds, *Boundary-Layer Meteorology*, 69(1–2), pp. 149–158. Available at: https://doi.org/10.1007/BF00713300.

We kindly thank those who have provided their support, including sponsorship, donation and material support, in organizing the 19th International Symposium “WATER MANAGEMENT & HYDRAULIC ENGINEERING”.

Silver sponsor

The company TEHNIX d.o.o. was founded in Donji Kraljevac in June 1991. This company has become one of the most successful in the field of design, production and servicing of machines and equipment for environmental protection and waste management under the name TEHNIX ECO INDUSTRY. The company is adapted to the ecological standards of the Republic of Croatia, has the necessary permits, attestations and certificates and keeps prescribed documentation and records. It also invests in education and equipment for environmental protection. Thanks to innovations and patents, the company is a leading manufacturer of machines, technologies and equipment for environmental protection and sustainable waste management in the Republic of Croatia and most of Europe and the world.

Company is a leader in the eco industry. TEHNIX is committed to the revolutionary design and application of technologies for environmental protection. Their mission is to create innovative solutions that promote sustainability, responsibility, and high standards in the environmental industry. Through expertise, transparency, and continuous research, TEHNIX stands for a positive impact on global ecology.

Bronze sponsors

Founded in 1990, Hidroing d.o.o. Osijek is a trusted Croatian engineering and consulting company based in Osijek, specialized in water supply, wastewater management, environmental protection and municipal infrastructure. Through high-quality design, expert technical supervision, feasibility studies and support in EU-funded projects, Hidroing Osijek delivers solutions that are technically sound, financially responsible and sustainable in the long term. With a strong focus on reliability, professional integrity and practical engineering, the company helps public utilities, municipalities and infrastructure investors turn complex infrastructure challenges into durable systems that serve communities and protect the environment.

Hidroprojekt-ing d.o.o. is one of the successor companies of Hidroprojekt, established in 1947, with a long-standing tradition and extensive experience in hydraulic engineering and water management. Operating throughout Croatia, the company provides professional services in planning, design, supervision, and project management. Its expertise covers water supply and drainage systems, drinking water and wastewater treatment, stormwater management, irrigation, and watercourse regulation. Today, Hidroprojekt-ing employs more than 40 professionals across three locations, bringing together highly qualified experts from various technical disciplines.

Donors



